JOINT EUROPEAN TORUS **JET**

JET
JOINT
UNDERTAKING

PROGRESS
REPORT 1989
Volume I

JET
JOINT
UNDERTAKING

PROGRESS
REPORT 1989

Volume I

March 1990

This document is intended for information only
and should not be used as a technical reference.

Printed in England

Contents

Volume I

Volume II

Reprints of JET Papers

Foreword

This is the seventh of the JET Progress Reports, which provides an overview summary and puts into context the scientific and technical advances made on JET during 1989. In addition, the Report is supplemented by appendices of contributions (in preprint form) of the more important JET articles published during the year, which set out the details of JET activities.

The Report provides a more detailed account of JET's scientific and technical progress than that contained in the JET Annual Reports. It is aimed not only at specialists and experts engaged in nuclear fusion and plasma physics, but also at a more general scientific community. To meet these general aims, the Report contains a brief summary of the background to the Project, describes the basic objectives of JET and the principal design aspects of the machine. In addition, the Project Team structure is included as it is within this structure that the activities and responsibilities for machine operation are carried out and the scientific programme is executed.

1989 proved to be an extremely successful year for JET, particularly for the impressive scientific results achieved. The Project entered the second half of its original programme by moving into its planned Phase III - Full Power Studies. The main aim of this phase is: to control the plasma density and improve the plasma purity, by use of beryllium; to consolidate the operation of the machine at full additional heating power; and to explore further the use of X-point operation as a means of improving confinement.

During the early part of 1989, the machine was in a scheduled shutdown period. The two main tasks during the shutdown were reinforcement of the vacuum vessel to withstand disruptive forces and inspection of a previously repaired ohmic heating coil. The experimental programme restarted in May following realignment of the carbon wall protective tiles. The programme was carried out in three steps:

- with Carbon as the first wall (May/June), to re-establish plasma in the modified vessel condition, and to obtain reference values against which new re sults with beryllium first wall could be compared;
- with a thin beryllium layer evaporated over the carbon first wall (June/July), to test beryllium as a first wall material and its gettering effects;

- with beryllium tiles on the limiters and RF antennae screens (and carbon tiles elsewhere).

This involved a further short shutdown in July and August to install the beryllium wall tiles. This operation was not difficult but for the first time, required personnel access to a beryllium contaminated vessel. All operations were carried out in safe conditions, beryllium contamination was well contained and considerable experience was gained. The smooth running of subsequent shutdowns demonstrated that beryllium operation and technical support for intervention in beryllium contaminated areas was well under control.

The number of pulses in 1989 was 2244, bringing the total number of cumulative JET pulses to 21030. A significant feature was the increasing number of discharges with plasma current exceeding 3 MA, which for 1989 brought the cumulative total to about 5800. A comparison between the current pulse distributions for 1988 and 1989 shows a continued movement to operation at higher current values in 1989 and a reduction in the number of low current (<1 MA) values. In spite of the limited time available for operation and hence the smaller number of pulses, 1989 was a year in which considerable technical advances were made and progress achieved in plasma performance was outstanding.

During the year, the successful operation of both the Octant No. 4 and Octant No. 8 neutral injection systems were further improved. No major difficulties or failures were encountered and a high degree of availability and reliability was maintained throughout all periods of tokamak operation. In addition, six of the sixteen beam sources and their associated power supplies were successfully converted from 80kV to 140kV operation enabling deeper penetration of the beams into the plasma. These improvements resulted in significant extensions to the plasma parameters achieved in JET, particularly the high ion temperature. In addition, the radio frequency (RF) heating system has been undergoing an upgrade of each of the eight generators from 3 MW to 4 MW each, which should permit 24MW power in the plasma for 20s duration. This upgrade is not complete (two generators were still being upgraded at the end of 1989) but a maximum power of about 18 MW for 2s has been coupled to the plasma.

The use of small pellets of solid deuterium is one of the possible methods of fuelling a fusion reactor. Experiments

have been carried out with a multi-pellet injector which JET and the US Department of Energy (USDoE) have jointly installed and are jointly operating under the umbrella of the Bilateral Agreement on Fusion Research. Using 2.7 and 4mm deuterium pellets at speeds up to 1.4 x 10^3 ms^{-1}, peaked density profiles with central densities up to 4×10^{20}m^{-3} have been achieved in material limiter and magnetic limiter configurations with decay times in the several seconds range. A further pellet launcher has been developed to provide pellet speeds up to 4×10^3 ms^{-1}, which should allow pellets to penetrate to the centre of plasmas at temperatures of a few keV. A prototype launcher is being installed ready for 1990 operation, in parallel with the existing pellet injector.

In late May 1989, an electrical fault was detected in the toroidal field system. Investigation showed that one coil exhibited low turn-to-turn insulation resistance between a number of turns. The fault did not prevent operation but was potentially a threat to the machine, since it was not possible to predict its evolution. It was decided to replace this faulty coil with one of the spare coils. The shutdown foreseen for November 1989 was brought forward to start in October 1989 and extended to allow for the coil replacement. The removal of a toroidal field coil is a major operation requiring a large effort in terms of organisation, preparation of work procedures and planning. By the end of December 1989, the in-vessel work required to separate one machine octant was complete and Octant No. 3 containing the faulty coil was ready to be lifted out of the machine.

During 1988, JET had operated with all-carbon walls, but production of impurities had increased with the input power to the plasma. At high power, the heat load on the carbon tiles was too high, and the plasma evolution presented a catastrphic behaviour, the so-called "carbon catastrophe" or "carbon bloom". Increased plasma dilution, increased power radiation, reduced neutral beam penetration and a threefold fall of the fusion yield resulted from the carbon influx. For lower input power with long duration, problems were also, encountered. Without fuelling, deuterium was pumped by the carbon and replaced by impurities, resulting in a large dilution of the plasma.

Consequently for 1989, to reduce the level of impurities generated and provide better density control and to further improve JET results, the carbon tiles and the inside of the vacuum vessel were first covered with evaporated beryllium, and then later, the belt limiter and RF antennae tiles were replaced by beryllium tiles. The effect of a beryllium first-wall on the impurity influxes was:

- Oxygen impurity was essentially eliminated from the plasma;
- the effective charge, Z_{eff}, was significantly reduced in ohmic plasmas (down to 1.2) and with strong additional heating (down to <2);
- a severe carbon influx ('carbon bloom') was still a problem for inner wall and X-point plasmas, and was a serious limitation in H-mode studies.

Even so, reduced impurity levels during 1989 allowed prolonged operation at higher densities and improved the general JET performance:

- the pumping of deuterium with Be was more effcient than with carbon walls. This permitted low density and high temperature (up to 30keV) operation for times >1s;
- the density limit increased to (nRq/B) ~ 30 (with a record peak density of 4×102^0m^{-3} with pellet fuelling). This limit is principally a fuelling limit and not a disruption limit as found with carbon limiters;
- H-modes were created with ICRH alone for periods >1s. Their confinement characteristics were similar to those with neutral beam (NB) heating alone;
- b values up to the Troyon limit were obtained in low field (B_T=1.4T) double-null X-point plasmas;
- the neutron yield doubled to 3.7×10^{16}ns^{-1} and the equivalent fusion factor Q_{DT} increased to ~0.8-0.9;
- the fusion product ($n_D \tau_E T_i$) increased to $8-9 \times 10^{20}$m^3 skeV for both high and medium temperatures, reaching near breakeven conditions and was within a factor 5-10 of that required in a reactor.

To date, the scientific results obtained in JET have been impressive. Plasma temperatures, plasma densities and confinement times have now reached individually those needed in a reactor, but not simultaneously. JET is the only machine in the world to have reached this stage. Both ion and electron temperatures over 10keV have been achieved at the same time, albeit at a lower density than required in a reactor. In some experiments, ion temperatures up to 30 keV were reached. Energy confinement times greater than 1.5s have been obtained in JET - the only machine to do so. Plasma densities have also reached values suitable for a reactor. Therefore, JET has successfully achieved and contained plasmas of thermonuclear grade.

Although JET is presently about a factor 5-10 below the simultaneous values of density, temperatures and confinement time required in a reactor, knowledge gained within the JET Programme enables us to define confidently the parameters of a fusion reactor. It is known that a reactor will be about two and a half times the linear dimensions of JET, have a plasma current capability of about 25-30 MA with a toroidal magnetic field of 3-5T and an output of several GW. In addition, the plasma must be maintained for very long times, such as 1 hour, rather than the 20-30s bursts in JET.

The impressive results obtained in JET were in a transient state and could not be sustained in a steady state. Ultimately, the influx of impurities caused a degradation in plasma parameters. However, by virtue of its size, its plasma performance and its long pulse capability, JET is in a good position to address the problem of impurity control in the basic geometry for the next step tokamak. Consequently, in the longer term, a new phase has been proposed for JET which aims to demonstrate effective methods of impurity control in operating conditions close to those of a next step tokamak in an axi-symmetric pumped divertor configuration. The objectives of the pumped divertor in

JET are to control impurities in the plasma, decrease the heat load on the target plates, control the plasma density, demonstrate exhaust capabilities.

A schedule for the JET programme in the new phase should allow for a pump divertor in JET in 1992. In the light of experimental results, further optimization would be likely ~ 18 months later. To provide time for the new phase, the use of tritium in JET would be postponed until end-1994. At this stage, all information on particle transport, exhaust and fuelling, first wall requirements and enhanced confinement regimes needed to construct the next step, should be available. Final tests with tritium, including α-particle heating studies could be performed in the two years following, leading to the completion of the JET programme by end 1996. The JET Council agreed to the proposed prolongations on JET and has invited the European Commission to make a proposal to the Council of the European Communities for amending the JET statutes to allow this prolongation.

Ultimately, JET will operate with deuterium-tritium plasmas, rather than pure deuterium ones, so that we can study the production of alpha-particles in a true thermonuclear plasma. This requires a tritium fuelling system and,

since JET will become active, remote handling equipment will be used. Preparations for D-T operations have continued. The Active Gas Handling Building is nearing completion and installation of the major subsystems has started. The planned commissioning programme in this area is consistent with a period of D-T operation during 1992.

The most impressive results obtained so far are a tribute to the dedication and skill of all those working on the Project. They also reflect the continuous co-operation and assistance received from the Associated Laboratories and from the Commission of the European Communities. I am confident that with such dedication of the staff and the support and guidance of the JET Council, JET Scientific Council and the JET Executive Committee, the Project will be able to meet these challenges to be encountered in future years and contribute substantially to crucial information for Next Step devices.

Dr. P.H. Rebut,
Director.
March 1990

Introduction, Background and Report Summary

Introduction

JET Progress Reports are aimed both at specialists in plasma physics and nuclear fusion research and at the more general scientific community. This contrasts with the JET Annual Reports, which provide overview descriptions of the scientific, technical and administrative status of the JET programme, and is directed to the average member of the public.

To meet these general aims, the Progress Report contains a brief summary of the background to the Project, describes the basic objectives of JET and sets out the principal design aspects of the machine. In addition, the Project Team structure is detailed, as it is within this framework that machine activities and responsibilities are organized and the scientific programme is carried out.

The main part of the 1989 Report provides overview summaries of scientific and technical advances made during the year, supplemented by appendices of detailed contributions (in preprint form) of the most important JET scientific and technical articles produced during the year. The final part of the Report briefly sets out developments underway to further improve JET's performance and plans for future experiments through to its foreseen completion.
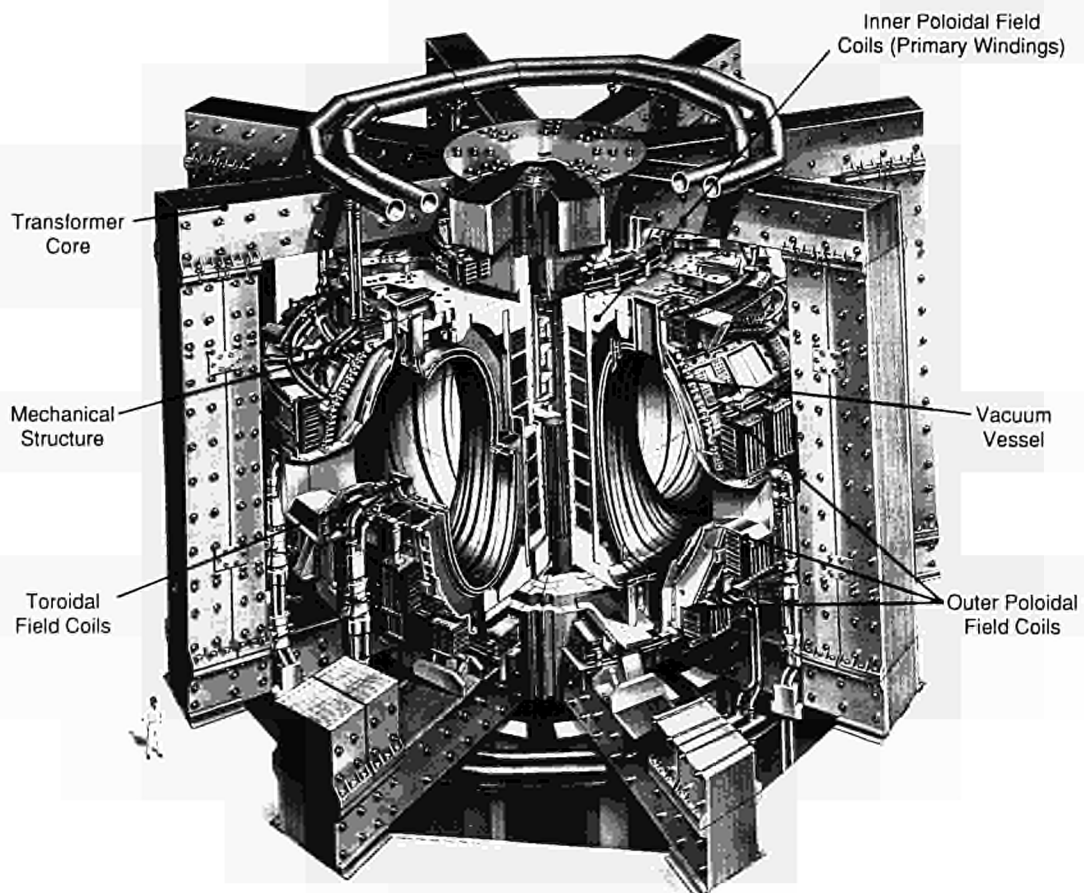

Fig.1: Diagram of the JET Tokamak.

Background

Objectives of JET

The Joint European Torus (JET) is the largest single project of the nuclear fusion research programme of the European Atomic Energy Community (EURATOM). The project was designed with the essential objectives of obtaining and studying plasma in conditions and with dimensions approaching those needed in a fusion reactor.

The studies are aimed at:

(a) investigating plasma processes and scaling laws, as plasma dimensions and parameters approach those necessary for a fusion reactor;

(b) examining and controlling plasma–wall interactions and impurity influxes in near–reactor conditions;

(c) demonstrating effective heating techniques (particularly, RF and Neutral Beam Heating), capable of approaching reactor temperatures in JET, in the presence of the prevailing loss processes;

(d) studying alpha–particle production, confinement and subsequent plasma interaction and heating produced as a result of fusion between deuterium and tritium.

Two of the key technological issues in the subsequent development of a fusion reactor are faced for the first time in JET. These are the use of tritium and the application of remote maintenance and repair techniques. The physics basis of the post–JET programme will be greatly strengthened if other fusion experiments currently in progress are successful. The way should then be clear to concentrate on the engineering and technical problems involved in progressing from an advanced experimental device like JET to a prototype power reactor.

Basic JET Design

To meet these overall aims, the basic JET apparatus was designed as a large tokamak device with overall dimensions of about 15m in diameter and 12m in height. A

Table I
Principal Parameters

Parameter	Value
Plasma minor radius (horizontally), a	1.25 m
Plasma minor radius (vertically), b	2.10 m
Plasma major radius, R_0	2.96 m
Plasma aspect ratio, R_0/a	2.37
Plasma elongation ratio, $e = b/a$	1.68
Flat top pulse length	25 s
Toroidal magnetic field (plasma centre)	3.45 T
Plasma current, D shaped plasma	7.0 MA
Volt-seconds available	42 Vs
Toroidal field peak power	380 MW
Poloidal field peak power	300 MW
Additional heating power (into torus)	~50 MW
Weight of vacuum vessel	108 t
Weight of toroidal field coils	364 t
Weight of iron core	2800 t

Table II
JET Departmental and Divisional Structure

Director
P.H. Rebut

Head of 'Staff' Office, Drawing Office and Quality Assurance
J.P. Poffé

Group   **Division**

Associate Director Administration
G.W. O'Hara

Associate Director HEAD of Machine and Development Department
M. Huguet

Deputy Head of Department
E. Bertolini

Deputy Director and HEAD of Experimental and Theory Department
M. Keilhacker

Associate Director HEAD of Heating and Operations Department
A. Gibson

Contracts — **L. Byrne**
Finance — **H. Spoor**
Personnel — **J-Y. Simon**

Machine Services
Fusion Technology — **R. Haange**
First Wall — **K.J. Dietz**
Magnet and Power Supplies — **E. Bertolini**

Theory — **D.F. Düchs**
Experimental II — **P.R. Thomas**
Experimental I — **P.E. Stott**
Diagnostics Engineering
Data Processing and Analysis

Machine Operations
CODAS — **H. Van der Beken**
Neutral Injection — **E. Thompson**
Radio Frequency — **J. Jacquinot**
Physics Operations

Fig.2: *Machine and Development Department, Group Structure (December 1989).*

diagram of the apparatus is shown in Fig.1 and its principal parameters are given in Table I. At the heart of the machine, there is a toroidal vacuum vessel of major radius 2.96m having a D-shaped cross-section 2.5m wide by 4.2m high. During operation of the machine, a small quantity of gas (hydrogen, deuterium or tritium) is introduced into the vacuum chamber and is heated by passing a large current through the gas. Originally, the machine was designed to carry 4.8MA, but has already been modified to achieve 7MA. This current is produced by transformer action using the massive eight-limbed magnetic circuit, which dominates the apparatus (see Fig.1). A set of coils around the centre limb of the magnetic circuit forms the primary winding of the transformer with the plasma acting as the single turn secondary. Additional heating of the plasma is provided by propagating and absorbing high power radio frequency waves in the plasma and by injection beams of energetic neutral atoms into the torus.

The plasma is confined away from the walls of the vacuum vessel by a complex system of magnetic fields, in which the main component, the toroidal field, is provided by 32 D-shaped coils surrounding the vacuum vessel. This field, coupled with that produced by the current flowing through the plasma, forms the basic magnetic field for the tokamak confinement system, which provides a full design field at the plasma centre of 3.45T. The poloidal coils, positioned around the outside of the vacuum vessel, shape and position the plasma in operation.

Initial experiments have been undertaken using hydrogen and deuterium plasmas, but in the later stages of the operation, it is planned to operate with deuterium-tritium plasmas, so that fusion reactions can occur to produce significant α-particle heating in the plasma.

In order to reach conditions close to those relevant to a fusion reactor, a plasma density of $\sim 10^{20} \mathrm{m}^{-3}$ at a temperature of 10-20keV would be needed. Even with a current of up to 7MA in JET, this would be inadequate to provide

MACHINE AND DEVELOPMENT DEPARTMENT

Head of Department: M. Huguet
Deputy Head of Department: E. Bertolini

D Carre	S McLaughlin
Mrs H Marriott	C Sborchia

MAGNET AND POWER SUPPLIES DIVISION
Head: E Bertolini

Mrs C Allen	D Halliwell	P Noll
P Bertoldi	M Huart	R Ostrom
T Bonicelli	F Jensen	P Presle
O Buc	J R Last	C Raymond
D Chiron	J McKeon	A Santaguistina
C Christadoulopoulos	J McKivett	S Shaw
R Claesen	V Marchese	M Tabellini
E Daly	G Marcon	S Turley
N Dolgetta	L Mears	J van Veen
P Doyle	P Mondino	C R Wilson
H T Fielding	G Murphy	G C Wilson
M Garriba	Mrs J Nolan	L Zanelli
J Goff		

FUSION TECHNOLOGY DIVISION
Head: R Haange

A C Bell	J Gowman	G Newbert
S J Booth	J L Hemmerich	A Nowak
P Brown	Mrs M E Jones	Miss S Perrissin-Fabert
T Businaro	L P D F Jones	T Raimondi
C Caldwell-Nichols	A Konstantellos	J Removille
P Chuilon	E Küssel	A Tesini
R Cusack	R Lässer	K D Walker
L Galbiati	J Mart	M Wykes
A Galetsas	P Milverton	

FIRST WALL DIVISION
Head: K J Dietz

W P Bailey	Mrs I Hyde	R Romain
H Buttgereit	G Israel	L Rossi
C Celentano	H Jensen	S Scott
Mrs D Cranmer	P Kupschus	K Sonnenberg
W Daser	E Martin	T Szabo
E Deksnis	P Macklin	R Thomas
D Flory	P McCarthy	E Usselmann
C Froger	J Orchard	M Watson
M Gadeberg	A Peacock	T Winkel
D Holland	M Pick	

Fig.3: Project Team Staff in Machine and Development Department (December 1989).

the temperature rquired using ohmic heating alone. Consequently, additional heating is required and two main systems are being used at JET, as follows:

- Injection into the plasma of highly energetic neutral atoms (Neutral Injection Heating);
- Coupling of high power electromagnetic radiation to the plasma (Radio Frequency (RF) Heating).

The total power into the torus will increase in discrete steps up to ~50MW.

Project Team Structure
The Project structure adopted, for management purposes, is divided into four Departments (see Table II):

- Machine and Development Department;
- Experimental and Theory Department;
- Heating and Operations Department;
- Administration Department.

In addition, some scientific and technical duties are carried out within the Directorate and in the Coordinating Staff Unit.

The main duties of the Administration Department have been described in previous JET Annual Reports. This Report concentrates on progress made in the scientific and technical areas during 1989. To aid this description, the functions of these Departments are described below.

Machine and Development Department
The Machine and Development Department is responsible for the performance capacity of the machine as well as equipment for the active phase, together with enhancements directly related to it (excluding heating) and the integration of any new elements on to the machine. In addition, the Department is responsible for machine services. The Department contains three Divisions:
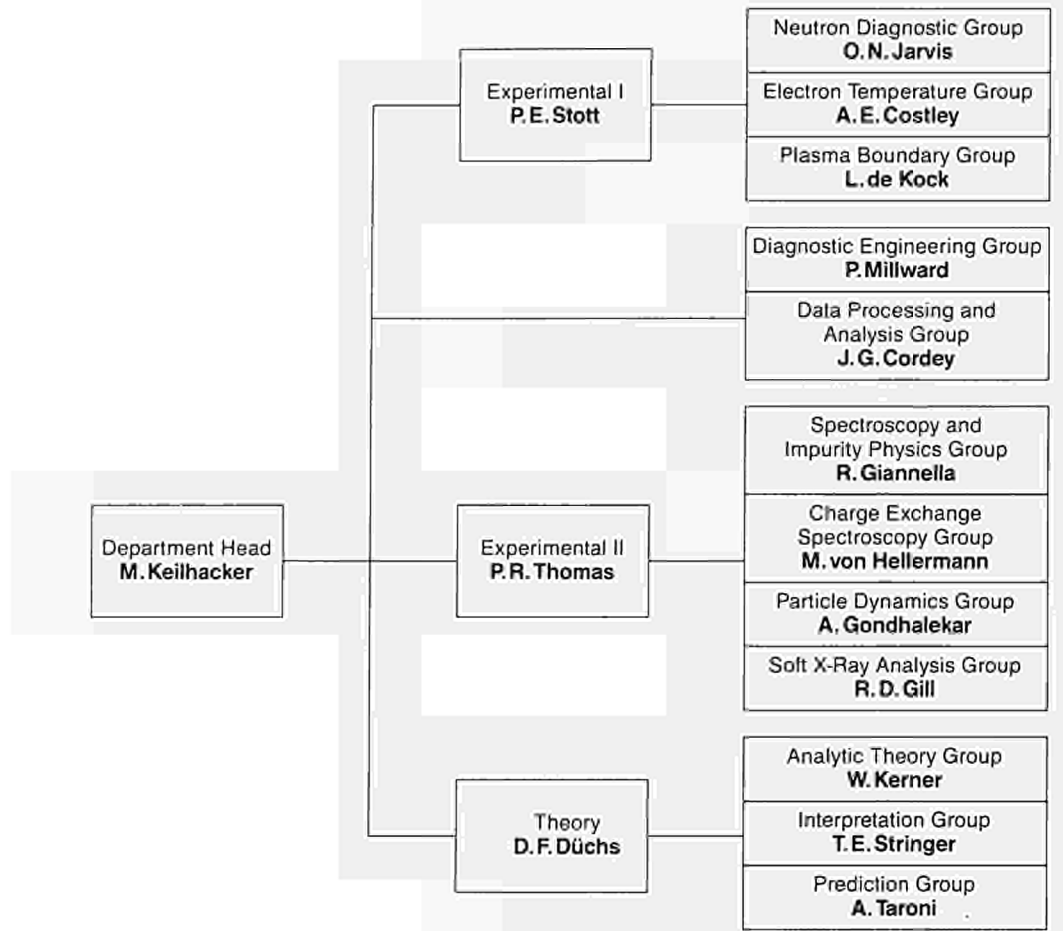
Fig.4: Experimental and Theory Department, Group Structure (December 1989).

(a) Magnet and Power Supplies Division, which is installation, operation, maintenance and modification of all power supply equipment needed by the Project. In addition, the Department is responsible for maintenance and operation of the coil systems, structural components and machine instrumentation;

(b) First Wall Division, which is responsible for the vital area of plasma wall interactions. Its main tasks include the provision and maintenance inside the vacuum vessel of conditions leading to high quality plasma discharges. The Division develops, designs, procures and installs first wall systems and components, such as limiters, wall protections and internal pumping devices. The area of responsibility encompasses the vacuum vessel as a whole, together with its associated systems, such as pumping, bakeout and gas introduction;

(c) Fusion Technology Division, which is responsible for the design and development of remote handling methods and tools to cope with the requirements of the JET device, and for maintenance, inspection and repairs. Tasks also include the design and construction of facilities for handling tritium.

The Structure of the Machine and Development Department to Group Leader level is shown in Fig.2 and the list of staff within the Department is shown in Fig.3.

Experimental and Theory Department

The main functions of the Department relate to the measurement and validation of plasma parameters and to the theory of tokamak physics. The main tasks are:

- to conceive and define a set of coherent measurements;
- to be responsible for the construction of necessary diagnostics;
- to be responsible for the operation of the diagnostics and the quality of measurements and the definition of the plasma parameters;
- to follow the theory of tokamak physics;
- to play a major role in interpretation of data.

The Department contains two Groups (Diagnostics Engineering Group and Data Processing and Analysis Group) and three Divisions:

(a) Experimental Division 1 (ED1), which is responsible for specification, procurement and operation of approximately half the JET diagnostic systems. ED1 undertakes electrical measurements, electron temperature measurements, surface and limiter physics and neutron diagnostics;

(b) Experimental Division 2 (ED2), which is responsible for specification, procurement and operation of the other half of the JET diagnostic systems. ED2 undertakes all

EXPERIMENTAL AND THEORY DEPARTMENT

Head of Department: M. Keilhacker

B Balet	M E Mynarends	Mrs R Thormaehlen
M Barnes	D O'Brien	A Tiscornia
K Blackler	R Oord	E van der Goot
J Christiansen	J Reid	G Vlases
J G Cordey	P J Roberts	M L Watkins
C J Hancock	Miss K Slavin	J Wesson
J Hoekzema	Mrs P Stubberfield	C H Wilson
J P Jéral	K Thomsen	D Wilson
P Millward		

EXPERIMENTAL DIVISION I

Head: P E Stott

Miss N Avery	C Gowers	C Nicholson
D Bartlett	Mrs M Harper	P Nielsen
B W Brown	P J Harbour	R Prentice
D Campbell	M Hone	P Roach
E Clipsham	I Hurdle	G Sadler
J Coad	O N Jarvis	A Stevens
A E Costley	B Laundy	D Summers
J Ehrenberg	M Loughlin	P van Belle
L de Kock	F Marcus	J Vince
J Fessey	G Neill	D J Ward

EXPERIMENTAL DIVISION II

Head: P R Thomas

G Braithwaite	A Gondhalekar	F Mompean
J L Bonnerue	N Gottardi	P Morgan
A D Cheetham	D Halton	H Morsi
S Corti	J Holm	J O'Rourke
Miss G B Denne	H Jaeckel	J Ryan
A Edwards	R Konig	D Pasini
Mrs A Flowers	L Lamb	M Stamp
R Giannella	G Magyar	M von Hellerman
R Gill	J L Martin	B Viaccoz

THEORY DIVISION

Head: D F Düchs

W Core	B Keegan	R Simonini
Mrs S Costar	W Kerner	E Springmann
L Eriksson	E Lazzaro	T E Stringer
A Galway	F Porcelli	A Taroni
Mrs S Hutchinson	H C Sack	F Tibone

Fig.5: Project Team Staff in the Experimental and Theory Department (December 1989).

spectroscopic diagnostics, bolometry, interferometry, the soft X–ray array and neutral particle analysis;

(c) Theory Division, which is responsible for prediction by computer simulation of JET performance, interpretation of JET data and the application of analytic plasma theory to gain an understanding of JET physics.

The structure of the Experimental and Theory Department to Group Leader level is shown in Fig.4 and the list of staff in the Department is shown in Fig.5.

Heating and Operations Department

Heating and Operations Department is responsible for heating the plasma, the organisation of experimental data, and the day–to–day operation of the machine. the main functions of the Department are:

- heating the plasma and analysis of its effects;
- centralising the interpretation of experimental results and investigating their coherence;

- organising data acquisition and computers;
- preparing and co–ordinating operation of the machine across the different Departments.

The Department is composed of three groups (Machine Operations Group, Physics Operation Group and Data Management Group) and three Divisions:

(a) Control and Data Acquisition System Division (CODAS), which is responsible for the implementation, upgrading and operation of computer–based control and data acquisition systems for JET;

(b) Neutral Beam Heating Division, which is responsible for the construction, installation, commissioning and operation of the neutral injection system, including development towards full power operation of the device. The Division also participates in studies of the physics of neutral beam heating;

(c) Radio Frequency Heating Division, which is responsible for the design, construction, commissioning and
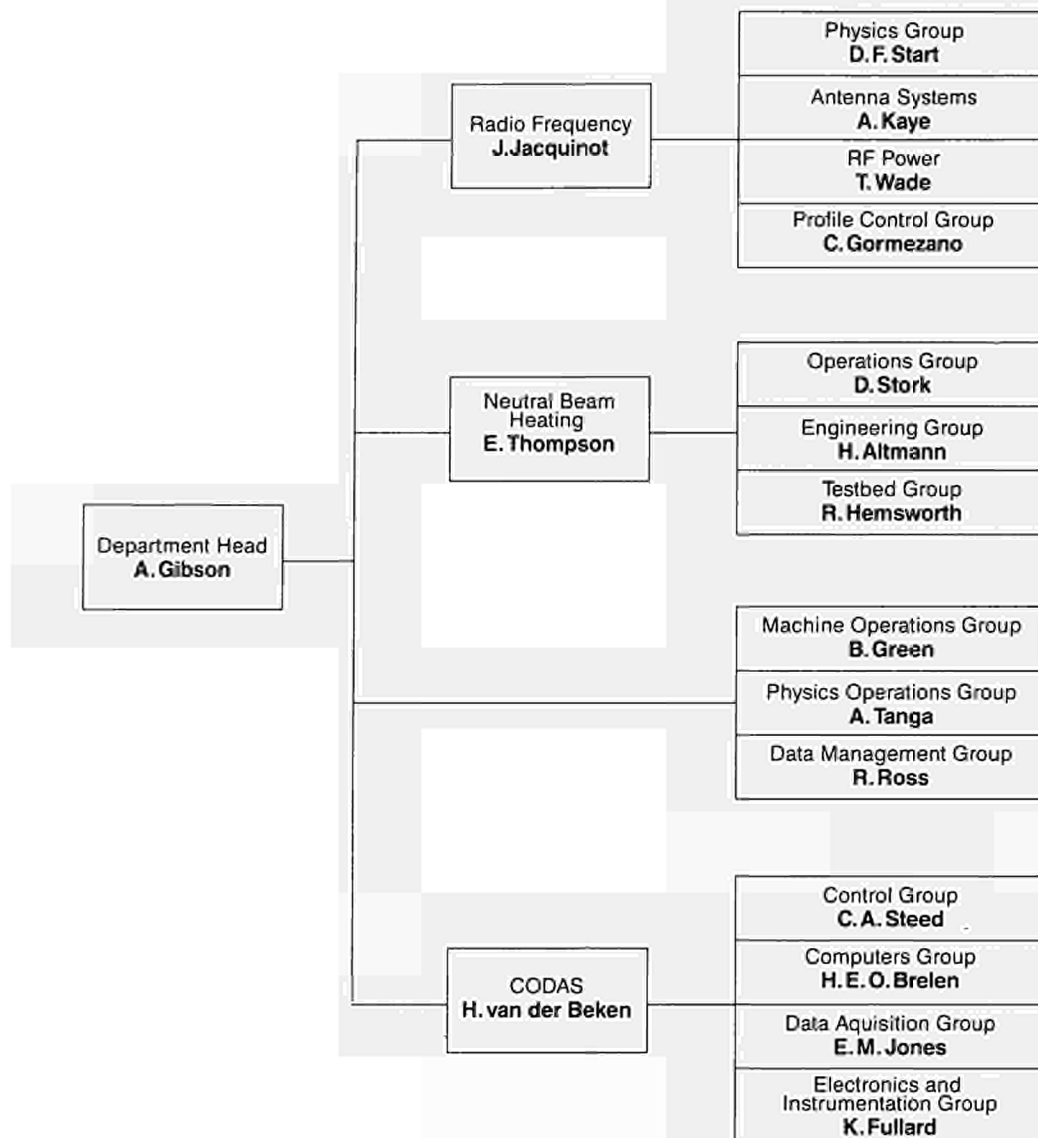
```
                                                  ┌──────────────────────────┐
                                                  │     Physics Group        │
                                                  │       D.F.Start          │
                                                  ├──────────────────────────┤
                          ┌─────────────────┐     │    Antenna Systems       │
                          │ Radio Frequency │     │       A.Kaye             │
                          │   J.Jacquinot   │─────┼──────────────────────────┤
                          └─────────────────┘     │       RF Power           │
                                                  │       T.Wade             │
                                                  ├──────────────────────────┤
                                                  │   Profile Control Group  │
                                                  │      C.Gormezano         │
                                                  └──────────────────────────┘

                                                  ┌──────────────────────────┐
                                                  │    Operations Group      │
                          ┌─────────────────┐     │       D.Stork            │
                          │  Neutral Beam   │     ├──────────────────────────┤
                          │    Heating      │─────│   Engineering Group      │
                          │  E.Thompson     │     │      H.Altmann           │
                          └─────────────────┘     ├──────────────────────────┤
                                                  │    Testbed Group         │
                                                  │    R.Hemsworth           │
                                                  └──────────────────────────┘

 ┌─────────────────┐                              ┌──────────────────────────┐
 │ Department Head │                              │ Machine Operations Group │
 │   A.Gibson      │                              │      B.Green             │
 └─────────────────┘                              ├──────────────────────────┤
                                                  │ Physics Operations Group │
                                                  │      A.Tanga             │
                                                  ├──────────────────────────┤
                                                  │  Data Management Group   │
                                                  │      R.Ross              │
                                                  └──────────────────────────┘

                                                  ┌──────────────────────────┐
                                                  │     Control Group        │
                                                  │      C.A.Steed           │
                          ┌─────────────────┐     ├──────────────────────────┤
                          │     CODAS       │     │    Computers Group       │
                          │  H.van der Beken│─────│    H.E.O.Brelen          │
                          └─────────────────┘     ├──────────────────────────┤
                                                  │  Data Aquisition Group   │
                                                  │      E.M.Jones           │
                                                  ├──────────────────────────┤
                                                  │    Electronics and       │
                                                  │  Instrumentation Group   │
                                                  │      K.Fullard           │
                                                  └──────────────────────────┘
```

Fig.6: Heating and Operations Department, Group Structure (December 1989).

operating the RF heating system during the different stages of its development to full power. The Division also participates in studies of the physics of RF heating.

The structure of the Heating and Theory Department to Group Leader level is shown in Fig.6, and the list of staff in the Department is shown in Fig.7.

In addition, all Divisions are involved in:
- execution of the experimental programme;
- interpretation of results in collaboration with other appropriate Divisions and Departments;
- making proposals for future experiments.

Directorate

Within the Directorate are one scientific and one technical group, (Scientific Assistants to the Director and Technical Assistant to the Director (including Publications Office)), whose main tasks are as follows:
- Scientific Assistants to the Director, who assist and

advise the Director on scientific aspects of JET operation and future development;
- Technical Assistant to the Director, who assists and advises the Director on organizational and technical matters related to JET operation and also acts as JET Publications Officer.

Coordinating Staff Unit

The Coordinating Staff Unit is responsible for the provision of engineering services to the Project and for the implementation of specific coordinating tasks at the Project level.

It comprises four Groups:
- Technical Services Group;
- Planning Group;
- Drawing Office;
- Quality Assurance Group.

The structure of the Directorate and Coordinating Staff

PLASMA HEATING AND OPERATION DEPARTMENT

Head of Department: A. Gibson

K Adams	J How	Mrs J Roberts
A Conway	M Hughes	R T Ross
D Cook	M Johnson	P Rutter
S Cooper	P Lomas	Ms D Samuel
T Dale	MrsP Longworth	P Smeulders
P Gaze	C Lowry	W Smith
B Green	M Macrae	A Tanga
N Green	Mrs M Pacco-Düchs	B Tubbing
Miss R Hausherr	D Pratt	M Walker
C Hookham	R Rigley	B Workman

NEUTRAL BEAM HEATING DIVISION
Head: E Thompson

H Altmann	H Falter	D Martin
A Bickley	R Hemsworth	P Massmann
A Browne	Mrs S Humphreys	C Mayaux
C D Challis	D Hurford	W Obert
D Cooper	J Z Jensen	S Papastergiou
J F Davies	A Jones	A J Parfitt
G Deschamps	T T C Jones	D Raisbeck
A Dines	D Kausch	Mrs M Sinclair
H P L de Esch	F Long	D Stork
D Ewers	J Lundqvist	

RADIO FREQUENCY HEATING DIVISION
Head: J Jacquinot

V Bhatnagar	A Franklin	M Pain
S C Booth	M Gammelin	J Plancoulaine
G Bosia	K Glasgow	F Riminini
M Brandon	B Glossop	M Schmid
H Brinkschulte	C Gormezano	Miss V Shaw
M Brusati	R Horn	A Sibley
M Bures	G Jessop	D Start
M Casson	A Kaye	T Wade
G Cottrell	M Lennholm	C Walker
T Dobbing	P Murray	M Zouhar
D T Edwards		

CONTROL AND DATA ACQUISITION SYSTEMS DIVISION
Head: H van der Beken

M Baronian	S Dmitrenko	J G Krom
Mrs A M Bellido	S E Dorling	D S Nassi
M J M Botman	K Fullard	C Perry
H E O Brelen	R F Herzog	C A Steed

Fig.7: Project Team Staff in the Heating and Operations Department (December 1989).

Unit to Group Leader level is shown in Fig.8 and the list of staff in these areas is shown in Fig.9.

Report Summary

The first section of this Report provides a brief introduction and background information relevant to the Report. The second and third sections set out an overview of progress on JET during 1989 and with a survey of scientific and technical achievements during 1989 sets these advances in their general context. This summary is specifically cross–referenced to reports and articles prepared and presented by JET staff during 1989. The more impor-

tant of these articles, which are of general interest, are reproduced as appendices to this Report.

The fourth section is devoted to future plans and certain developments which might enable enhancements of the machine to further improve its overall performance. Some attention has been devoted to methods of surmounting certain limitations and these are detailed in this section.

The Appendices contain a list of work topics carried out under Task Agreements with various Association Laboratories, and selected articles prepared by JET authors are reproduced in detail, providing some details of the activities and achievements made on JET during 1989. In addition, a full list is included of all Articles, Reports and Conference papers published by JET authors in 1989.
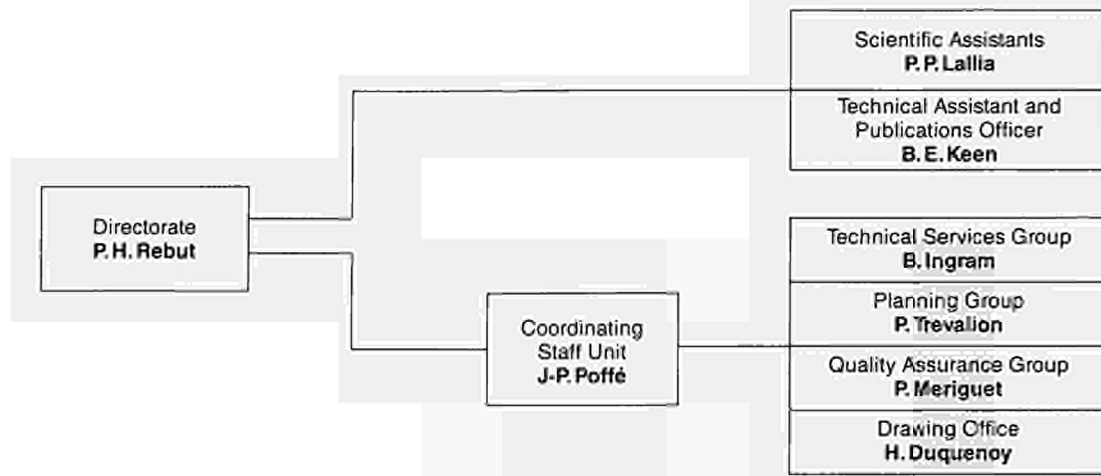
```
                                          ┌─────────────────────────┐
                                          │   Scientific Assistants │
                                          │      P. P. Lallia       │
                                          ├─────────────────────────┤
                                          │ Technical Assistant and │
                                          │  Publications Officer   │
                                          │       B. E. Keen        │
                                          └─────────────────────────┘

  ┌──────────────┐                        ┌─────────────────────────┐
  │  Directorate │                        │ Technical Services Group│
  │  P. H. Rebut │                        │       B. Ingram         │
  └──────────────┘                        ├─────────────────────────┤
                                          │     Planning Group      │
                  ┌────────────────┐      │      P. Trevalion       │
                  │  Coordinating  │      ├─────────────────────────┤
                  │   Staff Unit   │      │ Quality Assurance Group │
                  │   J.-P. Poffé  │      │       P. Meriguet       │
                  └────────────────┘      ├─────────────────────────┤
                                          │     Drawing Office      │
                                          │       H. Duquenoy       │
                                          └─────────────────────────┘
```

Fig. 8: Directorate and Coordinating Staff Unit, Group Structure (December 1989).

DIRECTORATE AND COORDINATING STAFF UNIT

Director: P-H Rebut

DIRECTORATE

Mrs S-J Ashwood	P P Lallia
D Boucher	J McMahon
M Drew	T O'Hanlon
Miss C Hampson	Mrs C Simmons
M Hugon	Ms M Straub
B E Keen	Mrs J Talbot

COORDINATING STAFF UNIT
Head: J-P Poffé

Ms L Ashby	Mrs E Harries
P Barker	F Hurd
G Dalle-Carbonare	B Ingram
Mrs D Dalziel	H Jones
N Davies	P Meriguet
H Duquenoy	H Panissie
L French	Ms A Reichenau
Ms D Field	R Smith
J A Green	P Trevalion
M Guillet	C Woodward

Fig. 9: Project Team Staff in the Directorate and Coordinate Staff Unit (December 1989)

Technical Achievements during 1989

Torus Systems

Following completion of the 1988/89 shutdown, operation resumed initially with graphite as the main first wall material. The new internal configuration of the vacuum vessel is shown in Fig 10, where the main change is that the vessel reinforcement rings are protected against the plasma by carbon fibre reinforced graphite.

Subsequently, beryllium was introduced into the JET vessel as a plasma facing material. Beryllium was first introduced in form of a thin evaporated layer at the inner surface of the vessel, and at a later stage the carbon tiles on the belt limiter and on the RF antennae were exchanged for beryllium tiles.

During 1989, the main effort on torus systems consisted of contributions towards the operation of JET (ie pellet injection, beryllium evaporation and gas introduction), the preparation and execution of in-vessel work for the introduction of the beryllium limiter and the coil exchange, and in the technical definition and in the preparation of the high speed prototype pellet launcher. These main contributions are described in the following sections, and in the conceptual design of the main in-vessel components for the Pumped Divertor.

In-vessel Components

One essential element in the exploration of beryllium as limiter and wall material [1] was the use of evaporators for covering the inside of the vacuum vessel with beryllium layers of up to a few micron thickness. Twenty six evaporations were made with four evaporators and about 260 grams of beryllium were deposited inside the vessel. Fig.11 shows one evaporator inside the vessel at the time of the installation of the beryllium limiter.
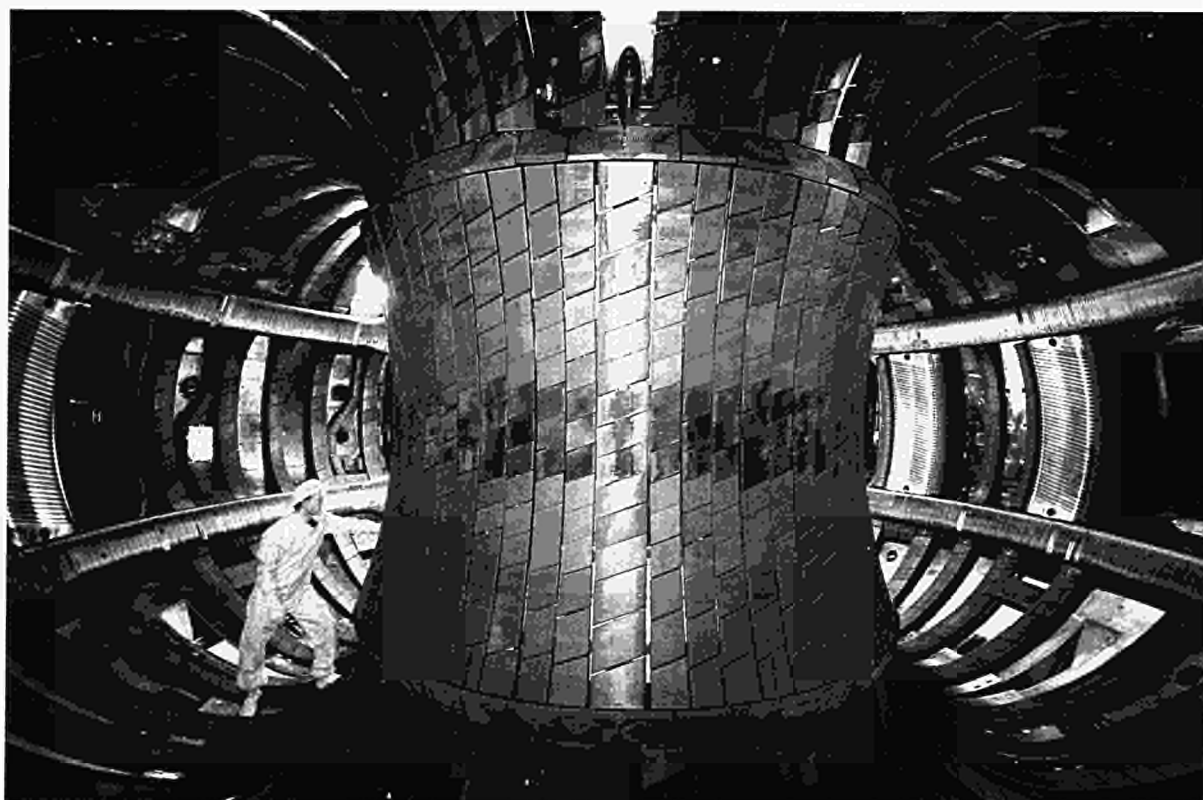
Fig 10: Internal View of JET Vacuum Vessel

Fig 11: A View of One Beryllium Evaporator inside the Vacuum Vessel

A beryllium laboratory was set up for the purpose of testing the evaporators before their use inside the vessel, to prepare samples (beryllium evaporated onto graphite) for test outside JET and to study basic material properties such as hydrogen diffusion, solubility and surface recombination rate. These were subsequently used to successfully explain the observed wall pumping inside JET.

During their use inside the JET vessel, the heads of the beryllium evaporators showed changes in the surface topology, and due to the related increase in emissivity the head temperature dropped and the evaporating rate decreased. This problem was reduced considerably by using cast heads instead of employing standard sintering techniques for their manufacture.

The second stage in the assessment of beryllium was the exchange of the limiter tiles, with the original graphite. The limiter design incorporated the facility of beryllium tiles on the belt limiter, this work had to be carried out with full protection, since the 'health physics' maximum permitted concentration of beryllium in air is 2 $\mu g \ m^{-3}$, and for higher values respiratory protection is required. Fig.12 shows installed beryllium tiles at the lower and upper belt and a suited worker during cleaning of the vacuum vessel before operation resumed.

During operation with the evaporated beryllium and the beryllium limiter, gas balance measurements [2,3] were carried out to assess the hydrogen retention on the vessel walls. This was undertaken to estimate tritium retention during the JET D-T phase and the inventory required to cope with this effect. It was found that the fraction of gas retained in the vessel with respect to the amount introduced was less for beryllium evaporation or beryllium limiters compared to that with a graphite machine. However, the stronger wall pumping observed with the introduction of beryllium required a larger input to achieve the same plasma density. Therefore, the number of particles retained was about the same for comparable discharges in a graphite or beryllium environment. More detailed analysis showed that this retention does not pose a problem for JET tritium operation.

Fig 12: Installed Beryllium Tiles on the Belt Limiter. A Suited Worker is Cleaning the Vessel Before Operation.

During 1989 operation, it became more apparent that one of the toroidal field coils had developed a fault which deteriorated during further operation. It became necessary to exchange this coil during the 1989/1990 shutdown. The reinforcement ring was installed just before this event and, in addition, respiratory protection was required to undertake work in the vacuum vessel. Octant removal prior to the coil exchange had to be planned and prepared in great detail. The effort and thoroughness which went into this preparation paid off and the Octant was removed for transfer into the Torus Hall, as planned. Fig.13 shows this Octant being removed from the Torus.

JET operated successfully during 1989 and achieved a plasma performance close to that required for the tritium phase, albeit only for a short time due to the influx of impurities into the plasma. Consequently the main problem which needs to be tackled now is impurity control. To that purpose, the Project has proposed a New Phase for JET involving a pumped divertor. The main components must be installed inside the vacuum vessel (coil, high heat flux components, cryo pumps). A conceptual design was carried out during the year and the preparation for Calls for Tender took place. At the end of the year, offers were being received so that first contracts could be placed in early-1990.
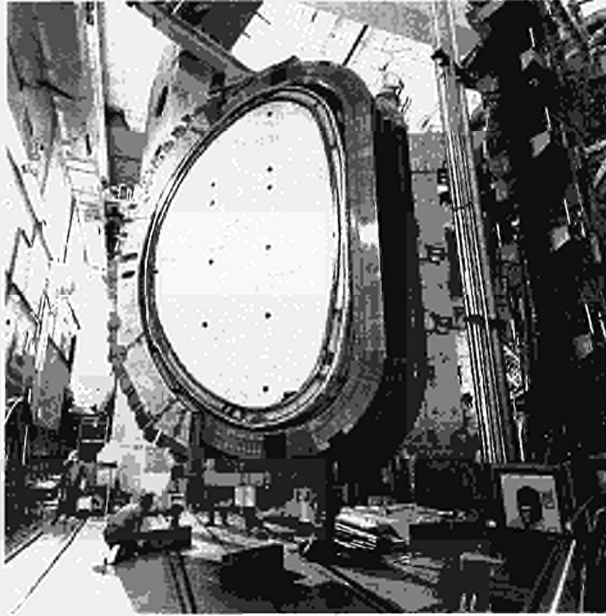
Fig 13: An Octant Being Removed from the Torus.

Vacuum System

The main issue was the assessment of the influence of beryllium on the vacuum system and its operation. The impact of interventions on vacuum components especially had to be studied and vessel openings for repairs required the application of techniques not used so far. To avoid the spread of beryllium dust from the vessel, modifications to hardware and in the operation of the pumping system were made. For example, the initial pump down of the vessel from atmospheric pressure is no longer carried out directly through a roughing line, but through fine filters at low initial pumping speed to avoid turbulence which can release and carry dust. Similarly, the venting of the torus is now undertaken slowly to avoid stirring up dust prior to vessel openings. For repairs and exchange of vacuum equipment, isolators are used which inhibit the spread of dust, but their use requires more detailed planning and this slows down the pace of work.

Generally, the vacuum system worked well, without any apparent problems. Improvements, incorporated during the 1988/89 shutdown (e.g. modification of the bellows for the gas introduction valves etc) made the operation more reliable, but still leak detection and leak repairs [4] were one of the main duties to be carried out.

The introduction of beryllium and the related higher wall pumping, together with the increased density limits, required the provision of more gas in shorter times. The gas introduction system was not designed to cope with these requirements simultaneously. It is not difficult to provide more gas, but the time response of the valves is now insufficient. Before the introduction of beryllium, typical pumping down times of the plasma density were tens of seconds, whereas with the beryllium limiter times of about one second are typical. At present, the gas introduction system cannot act fast enough and modifications will be required.

In preparation for the D-T phase, it will be necessary to develop radiation resistant vacuum instrumentation. Progress was made for the most difficult part, i.e. the residual gas analysers. The development of a radiation resistant instrument for the D-T phase requires to remove all sensitive electronics (preamplifiers, current sensor, RF - units) to locations about 100m apart. As currents in the 10^{-13}A range need to be measured, special techniques must be employed. The development was carried out with a small vacuum contractor and a prototype was built. Its operation had proven the feasibility of the schemes employed, but further work is required to improve sensitivity.

The vessel reinforcement ring which was installed during the 1988/89 shutdown was only one of the elements required to sustain radial disruptions at the 7MA plasma current level without undue stress in the vacuum vessel. The current decay time during disruption has increased with the introduction of beryllium limiters, and therefore the magnetic forces are reduced. However, it is still necessary, not only to limit the elongation of the vessel by the reinforcement ring, but also to dampen subsequent oscillations. For that purpose, dampers were designed, procured and installed during the 1989/90 shut-down. Tests on their effectiveness will not take place until the 1990 operating period.

Pellet Injection

This section summarises the contribution to the JET operation [5,6] the preparation for the advanced injector [7, 8] and the development of the prototype high-speed gun.

So far, the injection of solid hydrogen pellets is the only method of providing a particle source inside the recycling boundary layer of a future fusion reactor without simultaneously depositing excessive power. The ablation of the pellet by hot plasma electrons requires very high speeds for the pellet to penetrate beyond the q = 1 surface to the centre of the plasmas. The dependence of the penetration depth on the speed appears to be very weak ($\sim v^{\frac{1}{3}}$), but measurements have only been carried out in a limited velocity range, up to 1400 m s^{-1}. Therefore, JET plans to install a pellet launcher in 1990 capable of delivering pellets with 6mm diameter with speeds in excess of 4000 m s^{-1}. This will then enable an extension of the parameters of the ablation model to higher speeds and to study the velocity dependence of the pellet penetration in more detail. Should the weak dependence on speed be corroborated, speeds in excess of 10^4 m s^{-1} would be required and this has an important bearing on the fuelling problem in future reactors.

The 1989 operation was mainly devoted to the Beryllium first-wall assessment, and not much experimental time was left for particular pellet programmes. Nevertheless, some progress was made. It was possible to extend the pellet injection scenarios up to 5MA plasma current and to inject 6mm pellets successfully for the first time. The maximum central

peak density immediately after injection achieved so far was raised to 4 x 10^{20} m^{-3} for X-point and 2.8 x 10^{20} m^{-3} for limiter plasmas.

One essential milestone in developing a high speed injector was reached. Using a two-stage gun, it was possible to accelerate reliably and reproducibly 6mm diameter deuterium pellets to speeds of 4000 m s^{-1}. To acheive such velocities, the solid deuterium pellet had to be supported by sabots. It is now possible to separate them from the deuterium pellet in such a way that the holders and their fragments are not injected into the restraint tube situated between the launcher and the torus. This progress was achieved by establishing methods to produce deuterium ice pellets with good and reproducible mechanical properties, and by developing a sabot which acted as an efficient seal between the pellet and the hot (~5000°C) high pressure (~400 bars) driving gas. For separation from the pellet, the sabot splits into two halves and disintegrates at the middle due to the high pressure driving gas, as soon as it is no longer supported by the barrel. The reliability of the two stage gun and its driving piston has also been improved. The latter has so far survived 150 shots with no more than superficial scratch marks. This is remarkable since the metal (titanium) piston slides in a hardened stainless steel tube without requiring piston rings. The gun fired eight hundred pellets without failure. The cryostat forming an integral part of the prototype gun has been ordered and assembly will start at the beginning of 1990.

In parallel to tests of pellet acceleration and sabot separation, provisions were made for the installation, commissioning and operation of the prototype gun. The essential feature is that it will be assembled on the back of the existing pellet injector box.

The prototype launcher guns (one is optional to be installed perhaps at a later date) will use the two outer of the three gun lines existing below the torus midplane as a mirror image to the ORNL gun lines. Preparations for mounting the prototype are placed in order to minimise effort for later upgrades and for the advanced gun system which will be a multi-pellet gun. In particular, the necessary structural enhancements to provide mountings for the two-stage guns are already well established considering only one gun (assuming that simultaneous firing will not be needed or only performed by selected guns). A 8m long, 1.5m high carbon steel beam can support up to five two-stage guns of up to 5m in length on either side; the guns then can have barrel lengths in excess of 3m. The prototype will have initially a 3m pump tube and a 1.5m long barrel. Since the length of the beam will make use of the available space back to the corner of the Torus Hall, it was decided to take the weight of the beam (fully equipped up to 20 tonne) by the PIB platform and the wall but to anchor the force transferred to the beam under the momentum of the reversing piston (~80 tonnes for the prototype, up to 400 tonnes for upgraded

guns) fully in the concrete wall. Since the beam is blocking the peripheral haul passage for a number of larger components, it was conceived as a drawbridge allowing it to be lifted out of the way with a minimum of service interruptions. In particular, electrical cabling does not have to be disconnected.

The steelwork to the wall has already been erected, the support beam has been delivered and is being installed, and the required structural enhancements are being carried out. The prototype two-stage gun is delivered and is installed on the pellet Testbed. The related control electronics are being corrected. Progress for the implementation of the high-speed pellet launcher prototype is as planned and operation should be possible at the end of the 1989/90 shutdown.

The development of this JET prototype does not allow multiple injection (10-20 pellets) of high speed pellets in one discharge. The development aimed at multiple injection as well as at the related requirements of low maintenance, remote handling, and tritium compatibility is currently being undertaken by an Association and a design should emerge in the near future.

References

[1] K J Dietz et al., Beryllium in JET, A Report on the Experimental Experience, Proceedings of 13th Symposium on Fusion Engineering, Knoxville, USA, (1989).

[2] E Usselmann et al., Experimental Set-up for Gas Balance measurement at JET, Proceedings of 11th Int. Vac. Conf., Cologne, FRG, (1989).

[3] R Sartori et al., Gas Balance Measurements at JET, Proc. 16th Eur. Conf. Contr. Fusion and Plasma Physics. (Venice, Italy), Vol. 13 B, part III (1989), 963.

[4] T Winkel et al., Leak Evaluation in JET and its Consequences for Future Machines, Proceedings of 11th Int. Vacuum Congress, Cologne, FRG, (1989).

[5] G W Hammet et al., Transport Analysis of Pellet Enhanced ICRH Plasmas, Proc. 16th Europ. Conf. Contr. Fusion and Plasma Physics, (Venice, Italy) Vol. 13 B, part I (1989),131.

[6] S Milora et al., Summary of Energy and Particle Confinement in Pellet-Fuelled, Auxiliary Heated Discharges in JET, Proc. 16th Europ. Conf. Contr. Fusion and Plasma Physics, (Venice, Italy) Vol 13 B, part I (1989), 91.

[7] P Kupschus et al., Upgrading of the JET Pellet Injection by Employing a Two-Stage Light Gas Gun Prototype and Future Planning, Proceedings of 13th Symp. Fusion Engineering, Knoxville USA, (1989).

[8] P Kupschus, Fuelling of Magnetically Confined Fusion Reactor Plasmas, Course and Workshop on Tritium and Advanced Fuels in Fusion Reactors, Varenna, Italy, (1989), to be published in Il Nuovo Cimento.

Power Supplies and Magnet Systems

Introduction

The JET magnetic system is made up of the toroidal and poloidal coils with their mechanical structure, the purpose of which is to establish, maintain and control the tokamak magnetic configuration (see Fig.14). It includes the toroidal coils, the poloidal coil P1, acting as primary winding of the tokamak transformer and the coils P2, P3 and P4, to control plasma radial position, vertical position and shape, respectively. To perform these functions, the coils must be energised by suitable DC power supplies, whose voltages and currents are controlled in real-time by the plasma position and current control system (PPCC). Additional DC power supplies energize the neutral beam (NB) and radio frequency (RF) heating systems.
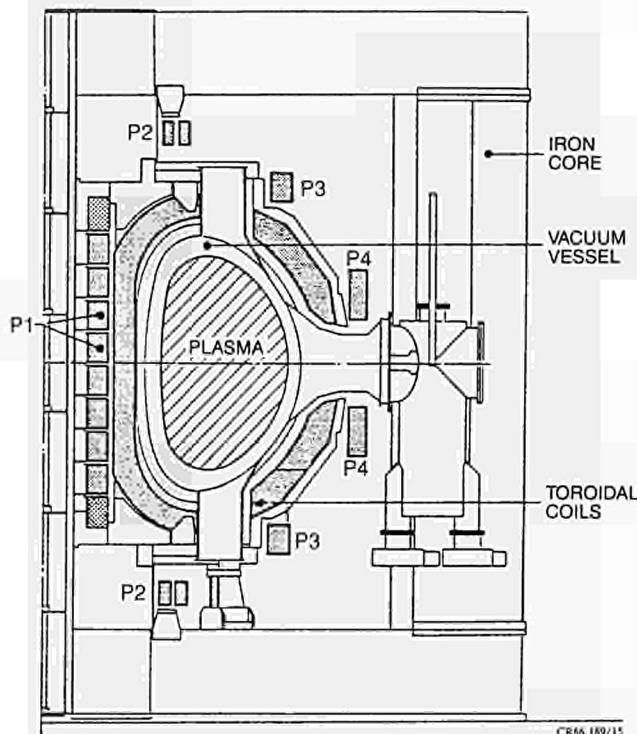
Fig.14: Cross-section of JET showing toroidal and poloidal coils.

The total installed DC power required by JET is well in excess of 1500MVA with a delivered power peak above 1000 MW and an energy content per pulse up to 10,000MJ. More than half of the power and of the energy is taken directly from the National Grid at 400kV and the rest is provided by two vertical shaft flywheel generators. Consequently, a major feature of the JET power supply scheme is the 400kV-33kV distribution system. Auxiliary power is supplied by the 20MVA, 11kV; 3.3kV; 415V distribution system.

The development programme to bring JET, first to its full design performance and subsequently well above, calls for continuous modification and upgrading of the electromagnetic system, of the plasma control and of the additional heating power supplies. The main objective of 1989 was to provide further tokamak and additional heating power supplies and upgrade the existing ones, including associated plasma control. Moreover, major new design work and new equipment procurement has been undertaken for the new project development phase.

The Electromagnetic System

The Magnet System

The Magnet System, following the major re-assessment and development for 7MA limiter operation and 5MA X-point operation during 1987-88, remained unchanged during 1989. However, improvements have been implemented to make Remote Handling Class 1 (routine) tasks possible. The following are being installed during the 1989-90 shutdown.

- *Modifications to link boards for poloidal field shaping coils:* These link boards allow the plasma shaping field configuration to be altered. The links have been made self-locating and equipped with handles to enable the Remote Handling manipulator to hold these;

- *New turn changing links on coils P3:* These turn changes also allow the field configuration to be changed. The links have been made self-locating and equipped with handles for the Remote Handling manipulators to hold and loose parts have been eliminated;

- *Jacks for supporting coil P2:* If the upper limbs of the magnetic circuit are removed, then coil P2 must be supported from the mechanical structure. These jacks allow the coil to be supported and positioned when the limbs are reassembled;

- *P1 single coil lifter:* This tool allows a single P1 coil to be lifted using remote handling equipment. It locates on the coil and has motor driven latches;

- *P1 whole stack lifter:* This existing tool will be modified to improve its guidance through the coil stack When it has engaged the coil lifting ring, it will be locked by a motor driven latch. The operation will be monitored by limit switches.

- *Central pillar lifter:* This existing tool will be modified to improve its guidance through the central pillar and will be driven by electric motors (instead of pneumatic cylinders) and monitored by limit switches.

The manufacture of the ohmic heating spare coil (P1) has taken place through the year. The steel support rings are completed, and four (out of six) coils have been wound and are awaiting resin impregnation. The first coil should be available by April 1990 and the set will be completed later in the year.

The poloidal busbars are being modified in the 1989-90 shutdown to allow:

- *Sweeping of the plasma X-point:* The X-point will be swept by modulating the current in the lower P3 coil. This will be undertaken by connecting the shaping circuit to the vertical field circuit and using the unbalance facility of the vertical field circuit;
- *Raising of P3 Coil upper for octant removal:* At present busbars passing over coil P3 have to be removed to allow the coil to be raised. The route will be slightly modified so that this is no longer necessary.

The coil system has been maintained and small improvements were implemented. The instrumentation system has also required maintenance and modifications, such as replacement of faulty transducers and electronic modules and relocation of transducers on modified equipment. The data acquisition will be rationalised in 1989/90 shutdown.

Toroidal Field Coil Fault

Detection of the Fault

A fault was first detected by the toroidal field (TF) coil fault detection system (DMSS). This system compares voltages across TF coils, which should all be the same, as the system is completely symmetrical. The indication was that Coil 3.1 (Octant No.3, 1st coil from left) had an out of balance voltage. At first, a fault in the detection system was suspected but, after thoroughly checking the detection system, measurements were made directly on the coils.

The measurements were;

(a) Voltage across each of the 32 coils while passing a small 50Hz current through the whole set: this showed a clear voltage reduction across coil 3.1 and adjacent coils. However this could have been due to another shorted loop coupling inductively within the coils;

(b) Resistance of each coil: this showed that all the coils had the same resistance, within the limits of measurement;

(c) Resistance of each turn of Coil 3.1 and of several other coils: this showed that Coil 3.1 deviated significantly from the normal pattern (see Fig.15).
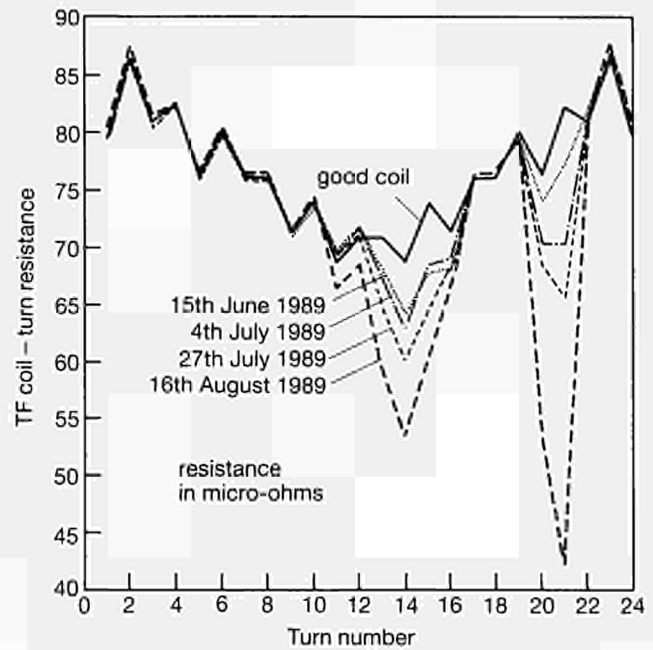
Fig.15: The TF Coil 3.1: Coil-turn resistance versus turn number as a function of time.

The resistance measurements (c) supported by the inductive measurements (a) could only be explained by the presence of interturn faults. In fact, four interturn faults were located as listed in Table III. It was probably coincidental, that problems were first noticed soon after the toroidal field had been reversed.

The existence of a coil fault explained some anomalies in the magnetic measurements (flux crossing the vacuum vessel) made on the machine. Re-examination of the magnetic data showed that the fault had been developing steadily since 1987, but more rapidly in 1989.

Characteristics of the fault were:

- multiple faults in adjacent regions
- linear resistance down to very low voltage (i.e. no threshold or breakdown voltage)
- moderate interturn resistance (ie only several times the single turn resistance)

These seemed to point to a water leak causing a conductive path between turns. Therefore, it was decided to attempt to detect and seal this leak and at the same time dry out the insulation and increase the fault

Table III

Date of measurement	Description of state	Fault resistances (between turns) (μΩ)			
		Nos. 11 &12	Nos. 13 &14	Nos. 15 &16	Nos. 17 &18
27th July	before heating	3200	240	410	200
16th August	after heating	510	100	220	22
12th September	after commissioning pulses	540	110	240	90

resistance using the following procedure;

- empty water out of coil
- dry out cooling hole by heating coil with electric current and passing dry gas through the cooling circuits
- evacuate each turn and make helium leak tests

When the coil was heated, the fault resistances reduced. This was expected due to reduced water resistivity at higher temperatures. However, when the heating was stopped, the fault resistances remained low, so some permanent damage had apparently occurred to the coil. The evolution of the fault resistances is shown in Table III.

No leaks to the outside of the coil were found but a trapped volume in turn No:15 was found. As no definite leak was found and as the fault resistance was not improved by drying (in fact the contrary), the planned leak sealing procedure was not carried out.

When the TF coils were next operated (during commissioning), the worst fault resistance (turns No:20 to No:21) suddenly increased during the pulse from 20μΩ. During subsequent operation similar (but smaller) sudden changes in fault resistance were also observed. This has not been explained but seems to indicate some moving part or particles inside the coil.

Nevertheless, it was decided to continue JET operations and this was considered safe because:

- the coils had operated in this condition with no detectable problems;
- analysis showed that the fault currents and associated fault forces were acceptable.

It was found that the coil protection system was sensitive to the rate of change of TF voltage. It was therefore possible to avoid trips by reducing the rate of rise of voltage. The voltage across the faulty coil was monitored to detect deterioration. Moreover, Rogowski coils were installed on the faulty coil and an adjacent one to monitor the turn difference.

Plans for replacing the coil and for improving diagnosis

The replacement of the faulty coil was planned as a major activity of the 1989-1990 shutdown. To change a TF coil, it was necessary to remove an Octant from the machine. However, replacement of an Octant had been foreseen and the machine was designed to facilitate this. Even so, it is still a major operation, but the design features (such as a modular torus and provision for moving the outer poloidal coils) have saved and will save a considerable amount of time and effort.

The procedure for removing an Octant is essentially a reversal of the original building procedure. The procedures have had to be somewhat revised to take account of the different state of some of the components and of beryllium and radiation precautions.

A spare octant including TF coils, structure and vacuum vessel is available but it was decided to change only a coil and not a complete octant. Therefore, the TF coil has to be changed when the Octant is in the

Assembly Hall. This operation has already been carried out on the spare octant to release the replacement TF coil. The preparatory work (ex-vessel) for removing the Octant was completed by the end of the year ready for moving it to the Assembly Hall at the beginning of 1990.

New instrumentation will provide more information about the coils so that the development of any future faults can be monitored. The modifications are:

- extend existing voltage measurement system, which compares the voltage across neighbouring coils;
- install Rogowski coils on all TF coils, so that signals can be integrated to give coil Ampere turns to compare with adjacent coils.

The different signals of TF coils Ampere-turns will be fed to trip modules to detect unequal values in adjacent coils. These will generate alarms and terminate the pulse.

A detailed analysis of the faulty coil will be undertaken, after replacement, since only limited measurements were possible with the coil in the machine. It is planned to proceed as follows:

Non destructive tests including

- visual inspection of exterior
- electrical test to determine location of fault
- leak detection cooling circuits

Other methods have been considered such as radiographic and ultrasonic testing may be tried but are probably unsuitable for this application.

Destructive tests, when maximum information has been obtained non-destructively, including some of the following:

- removal of ground insulation in selected areas
- cutting coil into sections
- separation of turns
- internal inspection of cooling channel

Due consideration is being given to the assessment of the status of the interturn insulation of the healthy coils, which have been tested electrically and they all exhibit expected behaviour. This is a difficult task since known non-destructive methods (applied to faulty coil) allow faults to be shown when the interturn resistance has degraded by a factor 10^3-10^4 from the design value, (which is in the kΩ range) due to the low copper turn resistance (80μΩ).

The Magnet Power Supplies

The Poloidal Vertical Field Boost Amplifier

This equipment is connected in series with the Vertical Field Amplifier (PVFA 3,4) and its purpose is to boost the amplifier's voltage to more accurately control the plasma radial position during the early phase of the

discharge. The commissioning of this equipment on inductive dummy load was successfully completed in January 1989. The tests included output current pulses up to the nominal value of 6kA DC, thermal capability test, measurement of the output characteristics, combined tests of the Boost Amplifier and PVFA 3-4 to check for correct operation and a terminal short circuit test.

The output characteristic was well in excess of specified value (indicated in brackets), namely: 10kV (9.2kV) at 900A, 8.9kV (5.5kV) at 3.6kA and 7.5kV (20kV) at 6kA. The peak current recorded during the short circuit test was 18.6kA, which the equipment withstood successfully.

The equipment was commissioned on the JET coils in March 1989 and subsequently with a plasma. It became quite noticeable that the plasma breakdown was greatly improved, in particular, at high premagnetization current.

Motor Operated Change-Over/Isolator for the Flywheel Generators

The braking of the flywheel-generators is achieved by stator phase reversal (AC plug braking) of the driving motor (Pony Motor). The existing AC plug braking system consists of an assembly of three motor operated three pole switches, mechanically and electrically interlocked. To overcome the mechanical problems experienced on these switches during operation, it has been proposed to replace them with a slow moving change-over/isolator, rated 11kV, 1250kA. The Technical Specifications have been defined and a Call for Tender issued and the manufacturer selected.

Upgrading of the Radial Field Amplifier

Sudden vertical plasma movement, such as experienced during a plasma disruption, can cause large induced current in the radial field circuit. Simulation of the behaviour of the thyristor crowbar of PRFA have been performed both for the existing 62mm thyristor and an alternative 75mm thyristor (used in the PVFA upgrade). The study showed that, in the latter case, the temperature excursion is well within the repetitive rating of the thyristor. All the crowbar thyristors will therefore be changed during the 1989-90 shutdown.

A computer program was set up to simulate two six-pulse rectifiers connected back-to-back, including the representation of the control loop circuits. The program was aimed at checking the transient behaviour of the equipment, in particular, the behaviour of the circulation current during rapid variation of the load current. The results of the analysis were applied to the existing equipment and a modification of the control loop system enabled the suppression of the large peak circulating current (~1000A) that had been observed during plasma disruption and which caused the PRFA equipment to trip.

Plasma Control

Plasma Position and Current Control

The plasma position and current control (PPCC) cubicle has been rebuilt to ease maintenance. The previous analogue control of radial position and shape has been replaced by a digital system (RPSC). Apart from vertical stabilisation, the PPCC is now a digital control system. In the course of operation, further tests of the vertical instability have been carried out to obtain a better estimate of forces expected in vertical disruptions of high current X-point plasmas and to revise the limits for safe operation.

The possible application of self tuning control (STC) in the vertical stabilisation system has been studied by the University of Manchester Institute of Technology (UMIST), UK, on the basis of a collaboration agreement between NET, UMIST and JET. The results are promising and indicate that the present stabilisation system could be improved by this technique. It has however been decided that STC should not be implemented for the present time to avoid compromising the development of a new fast stabilisation amplifier and JET operation, in general.

Disruption Feedback Amplifier

The purpose of this amplifier is to supply the eight saddle coils to be installed inside the vacuum vessel, to allow control of $m=1$, $m=2$ MHD instabilities. The contract was placed at end-1988.

The first Design Report was delivered in May 1989. The basic component is the Insulated Gate Bipolar Transistor (IGBT) of the family of fast power transistors. The building block is the module made up of an "H" bridge in which each arm consists of two IGBT's (200A, 1000V), in parallel. One unit consists of twelve parallel modules decoupled by the inductance of the coaxial cables foreseen between the local area and the junction cubicle. One Amplifier is made up of two units connected in series.

Each Amplifier has the following ratings:

Peak Voltage	: 1.5kV
Peak Current	
(variable with frequency)	: 3kA (in the range 0-1kHz)
	: 3kA/kHz (in the range 1-10kHz)
Peak Power	: 4.5MVA
Total Bandwidth	: 0-10kHz

The main elements of the Disruption Feedback Amplifier System are: a Rectifier Transformer with two secondaries reduces the voltage from 36kV to less than 1kV, to supply two Thyristor Converter Units; L-C filters in front of each Module, which is a DC/AC power converter, capable of four quadrant operation (inverter); Load Connecting Cables between the Amplifier and the Junction Cubicle that contains

Voltage and Current Transducers, Load Isolators and Load Earthing Switches.

Stage 2 involving manufacture of one amplifier made up of two units able to work independently, was released in late-May 1989, following the approval of the first Design Report. The approval of proposals for the various manufacturers followed soon afterwards, for all long delivery items. The tests on the bridge leg allowed a choice of parameters of the passive components (R,C) often called "spike killers", necessary for the correct operation of the bridge. After delivery of the IGBT's, the prototype modules were built and successfully tested in September, when the Final Design Report was also delivered.

Stage 3 of the Contract was placed at end-1989. The delivery schedule has been rearranged to suit plans that now foresee the installation of the saddle coils inside the vessel during the 1990-1991 shutdown. The first unit (Stage 2) should be delivered in October and the remaining three (Stage 3) in December 1990.

Additional Heating Power Supplies

There are three main systems of additional heating power supplies: for the ion cyclotron radio frequency (ICRF) and the neutral beam (NB) systems (already in operation) and for the lower hybrid current drive (LHCD) system. The latter system will become operational in mid-1990.

Radio Frequency Power Supplies

These power supplies were upgraded during 1988 to allow higher performance of the RF generators. They were operated without any significant problem during 1989 operation and only routine maintenance was required.

Lower Hybrid Power Supplies and Protections

Stage 1 of the Contract consists of three power supplies. Each has a design value of 100A at 65kV output voltage, and each is capable of supplying four klystrons. Stage 1 was completed during 1989, and all power supplies were tested on dummy load. One of these power supplies was also tested with the four klystrons as load up to the design value of 100A at 65kV. The second of the Stage 1 power supplies presently connected to the Lower Hybrid testbed equipped with two klystrons only. A conversion is being made to allow this power supply being switched between the testbed and the klystrons on the machine.

Stage 2 of the Contract also consists of three power supplies. Installation is completed and tests on dummy load are in progress. It is planned to complete these tests in early-1990.

The main protection of the klystrons relies on a crowbar made up of a string of ignitrons. This Contract

runs in parallel with the power supplies contract. Stage 1 comprises three crowbars and Stage 2 is for four crowbars. One of these seven crowbars is installed on the Lower Hybrid testbed while the six remaining are for the systems which will be connected to the machine. Three of the crowbars have been operated on the power supplies together with the klystrons. The remaining ones are being commissioned and will be tested once the klystrons are installed and ready.

Each crowbar consists of three ignitrons in series (Fig.16) and each ignitron has two trigger pins. The main triggering is achieved with a current loop to one of
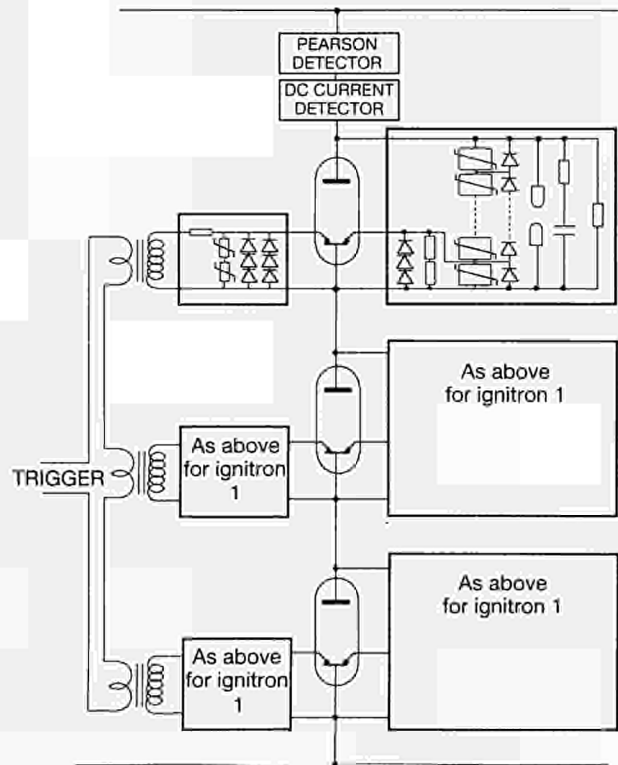
Fig.16: Schematic of a protection crowbar for the LHCD system.

the triggers of the three ignitrons connected in series. The second trigger is a back-up trigger and is supplied from a MOV circuit in parallel with the ignitron. In addition, there is a sparkgap, set at 30kV, in parallel with each ignitron. This is a final protection in case both the other trigger circuits fail. The current in the crowbar is sensed by a DC detector and a Pearson transformer, which will block the thyristors in the power supply if a current is detected.

Neutral Beam (NB) Power Supplies

During the year, several changes and improvements were undertaken to the NB power supplies. This resulted in a much higher reliability and allowed the NB system to inject on a regular basis into the plasma.

The Octant No.8 system was operational at 80kV, while on the Octant No.4 system the power supplies for six injectors were converted for 140kV operation.

Hardware modifications were carried out and some of the control circuits were altered. One of the hardware modifications was the addition of blocking diodes. These diodes decouple the two transmission lines for breakdowns in the injector. A high level of reliability was achieved by these power supplies both at 80kV and 140kV. Moreover, 140kV injection has allowed beam penetration to reach the plasma centre, thus further enhancing fusion reaction production. During the shutdown at the end-1989, the two remaining power supplies of the Octant No.4 system were being converted to 140kV operation.

The Power Distribution and the 400kV Grid

The 33kV Distribution System

A major extension of the 33kV switchgear compound has been completed to provide new feeders for the lower hybrid current drive (LHCD) power supplies, for the disruption feedback amplifier (DFAS), for the reactive power compensation (RPC) and for the 400kW gyrotron power supplies. To make the poloidal vertical field amplifier unit 2(PVFA 2) available for independent operation for the divertor coil, the PVFA 1,2,3,4 feeders were re-arranged. The distribution of loads on the 3 x 33kV busbar system were optimised to achieve a balanced effect in reducing voltage drops by the future use of the RPC system.

The design and modification work to use the spare 30MVA transformer in both 33kV-11kV and 11kV-33kV operating mode is well underway. This will allow a reduction in adverse effects on operation of JET and RF, LHCD, NB Testbeds during yearly maintenance of the 400kV and 132kV incoming lines and substations.

New Power Supplies: Layout and Installation

Work is underway and is due for completion during 1990, relating to: the DFAS (transformer - converter outdoor and indoor installation and coaxial cables run through the basement up to the Torus Hall for connections to the saddle coils); to the outdoor installation of the RPC; and the design of the outdoor/indoor layout for the new radial fast field amplifier (FPRFA) has been initiated.

Service Construction and Installation Work

A large number of activities were undertaken in this area to serve the needs of the Project. A considerable commitment has been required by the 415V supply, installation and modifications for the new tritium building (J25), for the beryllium handling facility, for the J25 chiller plant and for the 150 tonne crane. Cable termination for LHCD, NB and for the pellet injection (PI) system were implemented.

Further work is in progress for the extension of the radiological protection monitors throughout J1 building,

for the site water extension, for the RC snubber for PF amplifiers, for the cryogenic control panel and for the installation of the new neutral beam auxiliary power supplies G2 air cooled resistors. Design work for the electrical auxiliaries for the new divertor has been initiated.

Reactive Power Compensation

A contract has been placed for the supply of a reactive power compensation (RPC) system, to make up for the difference between the reactive power taken from the 400kV grid and the amount allowed in the supply contract with the Electricity Authority (475MVAR) and to control the voltage drop of 400kV with the contractual value (2.5%).

Following a full Call for Tender, the contract was placed for the supply of three x 50MVAR (Stage I) and of two x 50MVAR (Stage II). Therefore, two units (100MVAR in total) will be connected to two x 33kV busbars and one unit (50MVAR) to the third one. Provisions are made in the Contract to supply additional 50MVAR (Stage III) should it be required when the divertor with its power supplies comes into operation.

Each compensation unit (50MVAR) consists of three elements which are star connected. Its star-point is connected to the star-point of the secondary of the step-down transformer. Therefore, the voltage across each element of the star is well determined. Each element is made up of a large Capacitor Bank, two Vacuum Switches in series and the series of a Filter Reactor and a Damping Resistor connected in parallel.

Moreover, it was felt reasonable to add to the scope of the supply, three Snubber Circuits always connected to three busbars to damp high frequency oscillations (5-7kHz) noted on the busbars during pulses and probably caused by the stray capacitance of the load cables and the stray inductance of the 400/33kV transformers. Fig.17 shows a schematic of the Reactive Power Compensation Units and of the Snubber Circuit for Stage I.
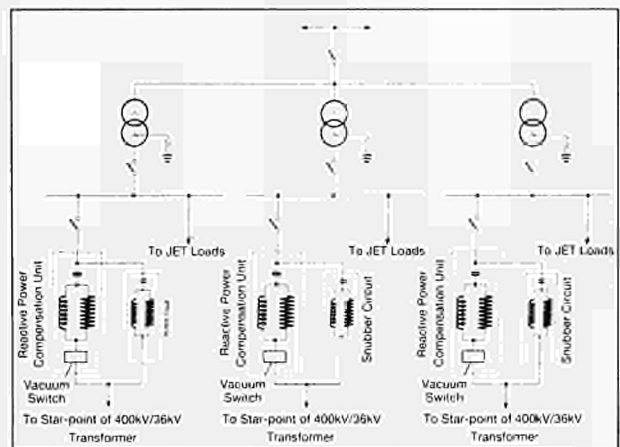
Fig.17: Schematic of the reactive power compensation system showing three 50MVAR units one per busbar (Stage I).

During the detailed design it was found that the amount of harmonics foreseen in the contract, due to both CEGB and the JET Loads, appeared too low: detailed calculations, confirmed that the harmonics to be expected during a JET pulse, at full performance, was higher than specified in the Contract. Upgrade of the Capacitor Banks, Filter Reactors and Damping Resistors was therefore necessary, and an amendment of the Contract was issued. Only Stage I has been released and the three units are due for delivery in July 1990. Stage II will be planned towards the end-1990, upon successful testing of Stage I. The layout has been fully defined: the indoor equipment (vacuum switches) will be installed in the J5 building, while the outdoor equipment (capacitor resistor and inductors) will be installed outdoor, east of J5 building.

Neutral Beam Heating System

Introduction

During the year, the successful operation of both the Octant No.4 and Octant No.8 injection systems has been further improved. No major difficulties or failures were encountered with either the mechanical or the power systems, and a high degree of availability and reliability was maintained throughout all periods of tokamak operation.

In addition, six of the sixteen beam sources and their associated power supplies have been successfully converted from 80kV to 140kV operation during planned shutdown periods. These improvements in conjunction with the use of beryllium as a first-wall material in the tokamak have resulted in significant extensions to the plasma parameters achieved in JET, both by NB heating alone and also in conjunction with RF heating. This has included:

- extension of the peak ion temperature to 26keV;
- extension of the peak D-D neutron rate to 3.7 $\times 10^{16}$ s^{-1};
- H-mode plasmas with a fusion product ($n_D T_i \tau_E$) = 8-9 x 10^{20}m^{-3} keV s.

Other activities have included assessments of the possibility of negative ion injection on JET (which will not be pursued) and also the technical feasibility of the use of the existing injectors for the injection of He^4 and He^3; preparation for handling neutral beam components in the event of contamination with beryllium and continuation of studies related to the ultimate conversion of one injector to 160kV tritium operation. In addition, a significant fraction of the engineering and cryogenic expertise is now allocated to tasks associated with the proposed New Phase of JET.

Neutral Beam Operations

The major new feature of this period was the commissioning and operation of 140kV deuterium beams on the beamline installed at Octant No.4. In the final period of operation in 1989, six of the eight sources had been converted to 140kV and had achieved injection into the tokamak at their full designated operating parameters of 30A extracted current at 140kV. The pulse length was restricted to less than two seconds for these first experiments. The electrical conditioning of the sources to full voltage and the commissioning of power systems and associated controls was remarkably quick and trouble-free. Major factors in this was the preconditioning of the sources in the neutral beam Testbed and the experience gained in the Testbed on modifications required to the power system for this type of operation (two ion beam accelerators were supplied in parallel from two x 80kV 60A power supplies connected in series).

Many JET discharges were obtained in which the injected beam power was in excess of 80% of the total 18.8MW available from the six x 140kV plus ten x 80kV sources. The calculated energy spectrum of the maximum power delivered to the plasma for the present configuration is shown in Table IV.

Table IV
Calculated Energy Spectrum for Maximum Injected-Power

Particle Energy (keV)	Power to Plasma (MW)
140	3.6
80	9.9
70	1.3
46.7	0.9
40	2.3
26.7	0.8

Even during the progressive upgrades of the 140kV sources, the availability and reliability of the total system remained high and comparable to the best levels obtained in 1988. The system availability (SA) is defined as:

$$SA = \left[\frac{TS - (TD + FD \times FS)}{TS} \right] \times 100\%$$

where TS = total time of operational shift

    TD = total down-time during shift (system 100% down)

    FD = total down-time in the shift with a fraction of the system down

    FS = fraction of system down (1 beam source = $^1/_{16}$)

For most of the operational periods, values of System Availability greater than 90% were obtained, which represents a considerable achievement for these complex systems and their associated services and, in

particular, their power systems. From rigorous fault logging procedures, it was found that the major limitation to availability was the power system. The following items were essentially fault free: CODAS and associated CAMAC electronics, the real-time control, interlock and data acquisition software, gas handling and gas introduction plus the cryopumps with their associated cryoplant and its control.

Reliability (defined as the ratio of total energy actually delivered to the plasma to that requested for a given pulse) was also high. Statistics were accumulated using the measured voltage and current waveforms from each beam source. The Neutral Beam data acquisition system logs faults responsible for premature termination of an injection pulse, enabling the causes to be identified. A graph of the reliability is shown in Fig.18. The injected energy exceeded 80% of that requested for 76% of the pulses. The major factors responsible for the shortfall in delivered power were equally divided between interruptions of the beam pulses due to electrical breakdowns in the (imperfectly conditioned) beam extraction and acceleration structures, and faults in the high voltage power supplies.

effect probes. Using a combination of the measured and computed magnetic field in the region of the duct, a full three-dimensional (3D) representation of the field was produced. This has been coupled to a 3D particle tracing code which follows the trajectories of ions borne throughout the duct to where they intercept the walls. By following many such trajectories, the spatial profile of the power density can be predicted. Good agreement between measured and predicted profiles is obtained for a wide variety of tokamak configurations. Furthermore, absolute values of the power density can be matched to within a factor x2 by using the measured value of the duct pressure to determine the gas target density responsible for the reionisation. Fig.19 shows injection into a 3MA double null X-point configuration. Although the main component of the measured stray magnetic field is due to the poloidal field equilibrium coils (P4) (the ampere-turns of which are directly related to the plasma current), the shaping coils have a significant effect in the double-null and the single-null configurations. Also, the stray radial magnetic field in the latter configuration which is generated by the unbalanced operation of the P4 coils, results in a strong vertical displacement of the reionised particles.

Fig.18 Reliability of total neutral beam system

Major progress has been made in the long standing problem of the power loading in the neutral beam duct (which connects the injectors to the torus) in terms of being able to both measure and predict the power densities in this region. The spatially extensive and diffuse source of energetic ions which are produced by ionisation of the neutral beams by collisions with the duct background gas is focussed by the stray poloidal field. In the past, this two dimensional focussing has resulted in catastrophic failure of the water-cooled duct liner due to burnout and subsequent melting of the liner. During this period, well instrumented copper protection plates were installed to extend the existing protection in the direction towards the torus. This allowed injection at lower values of plasma current (~2MA) and also enabled measurement of the magnitude and distribution of the deposited power. In addition, the various components of the magnetic field in the duct region were measured using an array of search coils and Hall-

Fig.19 Comparison of measured and predicted power densities of re-ionized particles in the neutral beam duct for a 3MA double-null plasma: (a) 3D plot of power density on duct protection plate as a function of vertical coordinate of duct; (b) power density on duct protection plate at z = 5cm, and z = -5cm as a function of distance along duct centre-line.

Studies of the vacuum behaviour of the beam duct (described in the 1988 Progress Report) have continued. The clean copper which now forms the surfaces of the duct, which are bombarded by the reionised fast atoms has proved to be very easily "conditioned". (Conditioning in this context describes the reduction in gas re-emission from the duct surfaces during beam operation.) Only a few "MW-seconds" of beam transmission are required to achieve duct pressures of <10^{-5}mbar during operation. This corresponds to an integrated reionisation probability of ~2%. An analytic model of the vacuum behaviour of the duct which uses the gas re-emission co-efficient Γ (molecules per incident atom) as a parameter shows that the duct pressure, and hence beam reionisation, will exponentiate during a beam pulse if $\Gamma > 32/N$, where $N \leq 8$ is the number of beams in the duct. The value of Γ has been determined experimentally during dedicated duct conditioning pulses. Values ~0.8 are obtained for a well conditioned duct, indicating a large margin of safety against exponentiation or beam blocking.

Neutral Beam Testbed

60kV PINI Operation

As detailed in the 1988 Progress Report, radio frequency interference (RFI) was a major factor responsible for the unreliability and difficulties encountered with previous operation of the Testbed high-voltage power supplies. The necessary additional screening and earthing of cables and chassis has been carried out. These (relatively minor) changes have resulted in quite remarkable improvements in reliability and availability of the power system. Correct operation was achieved even when using an open spark gap (at 160kV) in the absence of the snubber to simulate accelerator breakdown. This test is much more severe in terms of RFI than normal operation. Subsequently, successful operation of two beam sources operating in parallel from the common 160kV 60A supply was quickly achieved. Fig.20 shows the voltage and current waveforms obtained during the final stages of simultaneous conditioning of two beam sources and the ability of the improved power supply to handle repeated electrical breakdowns in the accelerator at full power. 160kV 40A operation of a single source corresponding to the parameters in excess of those to be expected for operation in tritium has also been demonstrated. Extensive measurements of the perveance of the JET beam sources have been carried out using H_2, D_2 and He^4 as working gas. The results based upon measurements of transmission and spatial profiles of both the neutral and the ion plus neutral beams are consistent to within +3%. The values obtained are ~15% higher than those obtained from the 80kV beam installed sources. The reason for this difference in perveance has not yet been identified.
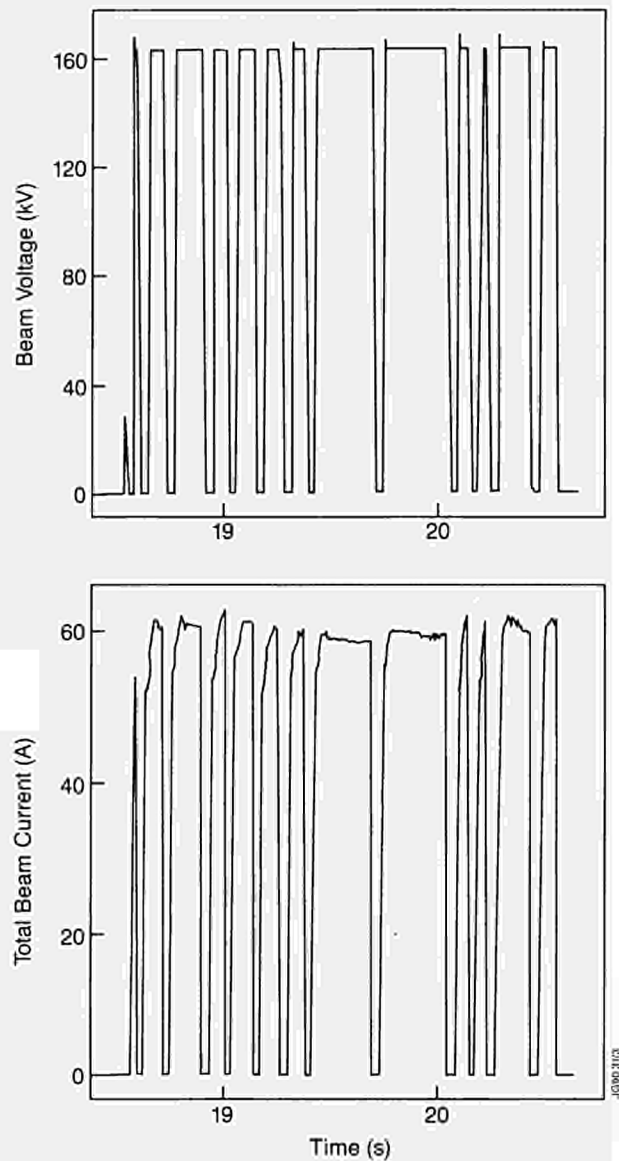
Fig.20 Voltage and current waveforms of Testbed power supply during simultaneous conditioning of two beam sources at full power.

Test of Simulated NET Divertor Element

The test programme for NET has been brought to completion using a configuration supplied by NET consisting of carbon tiles brazed to the surface of a hypervapotron element. The element was subject to pulses of 5s duration with a power density of 500Wcm^{-2}. The tests resulted in failure of many of the brazed joints.

Developments Related to the Tritium Injector

Ongoing work on development for the tritium injector has continued. Preliminary measurements on the performance of the deflection magnet and power profiles of the residual full energy ions in the ion dump have been obtained using 120kV He^4 neutrals to simulate 160kV T^+ beams. This indicates that satisfactory performance can be achieved, at least for the sources close to the mid-plane of the injector.

Measurements remain to be made using the other source which shares the same deflection magnet.

Considerable effort has been devoted to testing the feasibility of dispensing with the need to supply gas to the plasma sources at high potential during tritium operation. The present configuration utilises separate gas supplies for the plasma source (to replace the gas exhausted by the extracted ion beam) and the neutraliser (to provide the requisite gas target for neutralisation). Dispensing with the source gas would avoid tritium gas lines at high voltage. Apart from advantages with safety and inventory, it also avoids the possibility of tritium contamination with SF_6 and the resulting potential hazard for the gas separation plant. In addition, it offers the advantage of being able to exchange sources (if necessary) without disconnection of the gas feed. Tests have shown that it is feasible to supply all the gas at ground potential and only relatively minor modifications are necessary to minimise total usage of tritium. However, these measurements indicated that, although this type of operation is quite feasible, the accelerator which would operate at a factor ~x2 higher pressure, would be close to a limit due to long-path electrical breakdown. One JET source has been fitted with a transparent insulator to identify the regions responsible. Viewing the breakdown and glow discharges at high operating pressures has enabled critical regions to be identified and indications are that additional voltage stress shields will result in an improved operating margin at higher pressures.

Operation in the Testbed has revealed that a considerable fraction of the beam which is intercepted by various components, and, in particular, the calorimeter which collects the full beam, appears to be retained in the copper metal. This has been investigated using H_2, D_2 and He beams by observing the desorption of gas from the target following implantation by differing beams, e.g. desorption of He by H_2, etc. Qualitative results have also been obtained by studying the growth and decay of neutrons produced by the target when using deuterium beams or hydrogen beams
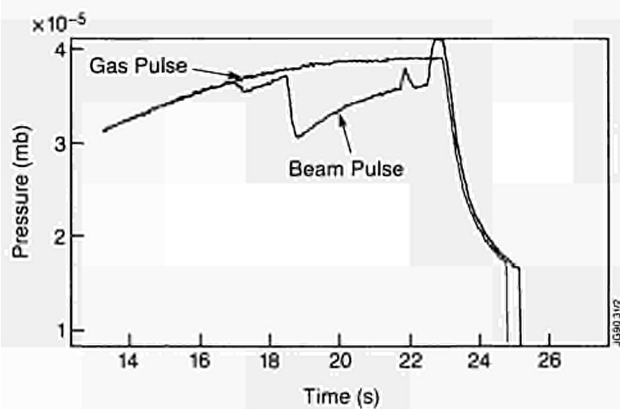
containing a trace of deuterium. This effective pumping is illustrated in Fig.21 which shows traces of the pressure in the Testbed during two pulses, one being gas only, the other being the same gas pulse with the beam operating. This clearly demonstrates "pumping" when the arc is struck within the plasma source followed by the stronger "pumping" of the beam particles. A first analysis indicates that the removal of beam particles is considerably greater than that to be expected by simple classical diffusion models for gas atoms in copper, but is in reasonable agreement with results obtained with "drive-in" targets for neutron generators. It is hypothesised that this high degree of retention may be due to radiation damage which results from high beam fluence. The implications on tritium retention for the tritium injector remains to be assessed.

Cryosorption Pumping of Helium

Studies are being carried out on pumping of gaseous helium using cryosorption on the liquid He cryocondensation pumps to determine the feasibility of using the injectors to inject beams of He^4 or He^3 into JET. It has been demonstrated that by first freezing a layer of argon onto the LHe pump surfaces, gaseous He is cryosorbed by the argon "frost". Pumping speed measurements have been made on both conventional chevron and open structure cryopumps. A value of the sticking coefficient of ~0.23 is obtained for helium on argon, which corresponds to a pumping speed of ~$2 \times 10^6 ls^{-1}$ for the JET injector. Fig.22 demonstrates the differing types of behaviour obtained by varying the ratio of pre-condensed argon to injected He gas.
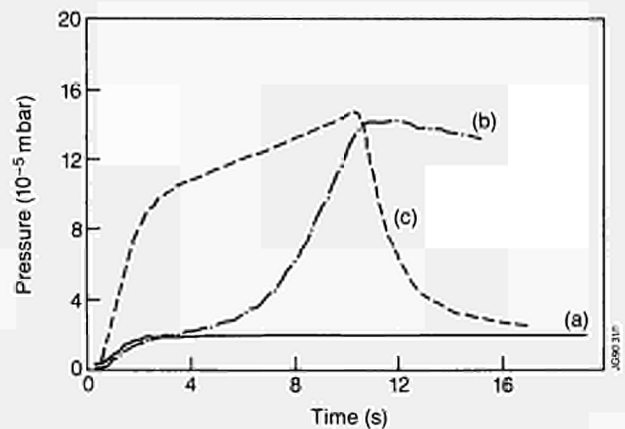
Fig.22 Pressure waveforms for various values of helium injection after condensing argon on the cryopump.

(a) He flow 5 mbar.ls⁻¹ ; Ar/He=160:1
(b) He flow 5 mbar.ls⁻¹ ; Ar/He=20:1
(c) He flow 5 mbar.ls⁻¹ ; Ar/He=20:1

Fig.21 Measured pressure in the Testbed demonstrating the 'pumping' of the plasma source and the beam.

Although cryosorption of He^4 has been demonstrated previously, the results of these measurements using He^3 show that cryosorption of this isotope is comparable to that of He^4 in spite of its higher vapour pressure at

4.2°K. As a result of these measurements, it is intended to carry out full scale tests on the JET injectors to determine the maximum number of beam sources which could be used for He^4 and He^3 injection experiments on JET.

Cryosystem and Cryopumps

The cryoplant has continued to operate with a very high degree of reliability and availability. All supplies of cryogens throughout the site, including various small users, e.g. diagnostics, are now supplied from the JET cryoplant. The plant has been upgraded to include enlarged high pressure storage of impure helium gas and a higher capacity helium recovery compressor. A major extension to the cryo-distribution system necessary to supply future large users (LHCD, tritium handling plant, and the pumped divertor) has been designed and is in manufacture.

The neutral injector and pellet injector cryopumps have continued their trouble-free operation throughout the year. A cryopump has been designed to pump the LHCD grill and a contract for manufacture by European industry is underway.

Engineering and Development Work

Maintenance and Upgrading of Beamlines

Prior to the start of operation, some of the single-ply Inconel bellows of the Full Energy Ion Dumps (FEIDs) on one injector suffered failures which appeared to be due to fatigue resulting from flow induced vibration. The failed bellows were replaced by double-ply stainless steel versions which have demonstrated fault-free operation. In addition, braid was fitted to all other single-ply bellows in order to damp out any destructive resonances and no further failures have been experienced.

The first set of improved FEIDs to ensure a satisfactory safety margin for long-pulse 140kV operation are scheduled for installation prior to operation in 1990. Delivery of improved neutralisers has been completed. One injector has been fully upgraded and the second will be completed during the 1989/90 shutdown.

In view of past failures of the duct liner assembly, a contract has been placed for the manufacture of two complete new assemblies. To maximise reliability, the new design utilises thick copper plates which are inertially cooled to collect the power and also avoids the use of thin walled bellows in the water circuit supplying the interpulse cooling. The designs for Octant No.8 and No.4 injectors are different in that Octant No.8 will only accept the beamline in its present orientation. However, Octant No.4 can accept the beamline in two configurations to allow for the option of using balanced injection. In this latter configuration, the direction of the beams oppose each other with one beam co- and one

counter to the plasma current. Delivery is planned prior to the 1990 shutdown.

Preparations are underway to upgrade the box scrapers which define the beam profile at the injector exit. This modification, to produce lower power densities on this element, will provide an enhanced safety margin with 160kV tritium beams to supply 12MW per injector compared with 10MW obtained with 80kV deuterium.

Beryllium Related Topics

The use of beryllium in the torus has introduced the possibility of beryllium contamination of components inside the neutral injectors. Consequently, a large Beryllium Controlled Area has been built in the Assembly Hall. This accommodates the complete cryopump assembly or the Central Support Column so that maintenance work can be carried out inside a controlled environment. The Area incorporates a recirculating water spraying system which is filtered to permit washing and decontamination of large neutral beam and other components. Following the first period of operation with beryllium, only low levels of contamination were measured on parts of the base of the injector and both the Central Support Column and cryopumps were uncontaminated.

Satisfactory procedures using isolators have been developed and used for changing the beam sources and the neutralisers. These ensure no release of beryllium in the event of significant contamination of these components.

Developments for the Tritium Injector

Work has continued on increasing system reliability and allowing elementary maintenance to be carried out by remote handling. A water drainage system is being fitted to allow rapid draining of the system in the event of a water leak. This will also minimise the potential production of tritiated water. Double walled components (bellows and ceramic insulated feedthroughs) are also in manufacture to progressively replace existing single-walled versions.

Components for the Pumped Divertor

Due to the similarity in technologies utilised in neutral injection and the pumped divertor - in particular high heat flux components and cryopumping - members of the Neutral Beam Engineering and Testbed Groups are participating in the proposed New Phase of JET.

Following the design and manufacture of a new test assembly, the testing of full size prototype elements for the high heat flux divertor plates is underway in the Testbed. These tests and the associated development/optimisation of the elements will form a major part of the 1990 Testbed programme. This work is being carried out in parallel with a strong participation in the detailed mechanical design and

preparations for the manufacture of the divertor plates and includes the finalization of the method of attaching the surface layer of beryllium.

Cryogenic and engineering expertise is also committed to the finalization of the design of the large cryopump and the preparations for its manufacture by European industry.

ICRF Heating and LH Current Drive Systems

The purpose of the powerful ion cyclotron resonance frequency (ICRF) heating and lower hybrid (LH) current drive systems are quite different:

- The ICRF heating system is used for highly localized heating of the JET plasma . The wide frequency band (23 to 57 MHz) allows variation in the position of heating as well as the ion species which is resonant with the wave (H or ^{3}He at present, D in the future D-T phase). The maximum design power is ~ 24 MW in the plasma. The system is not totally completed, but a maximum power of 18 MW has been coupled to the plasma.

- The LHCD (Lower Hybrid Current Drive) system (12 MW at 3.7 GHz) will be used to drive a significant fraction of the plasma current by direct acceleration of the plasma electrons, in order to stabilize sawtooth oscillations, thereby improving the overall JET performance. This will be the main tool for controlling the plasma current profile. This subject is discussed in a later section of this report ('Current Drive and Profile Control'). In this section, discussion is limited to technical achievements made during 1989.

Technical Achievements with the ICRF System

The original design power of the ICRF heating system was 15 MW for 20 s. However, the system has been undergoing an upgrade of each of the eight generators from 3 MW to 4 MW each. This upgrade is not yet complete (two generators were still being upgraded at the end of 1989) but a maximum power of about 18 MW for 2s has been coupled to the plasma. The maximum power was limited by arcs in the transmission and antennae components, while longer pulse lengths were not possible due to energy limitations on the vessel. Table V summarises the main characteristics of the RF system as used in 1989.

1989 proved to be a highly successful year for ICRH studies in JET. A number of enhancements to the power plant and antennae system were commissioned during the year. Most notable was the antenna-plasma matching system which is now used during the shot in a fully automated way acting both on the frequency and on the generator tuning stub length. These enhancements combined with the beneficial effects of a beryllium first-wall have increased the availability of high RF power and important contributions to various aspects of the JET experimental programme have been made.

Major achievements included:

- A record fusion yield [1] - 100 kW obtained from ^{3}He-D reactions with a ^{3}He minority accelerated by RF near the optimum of the fusion cross section (0.5 MeV);
- RF only H-mode [2] of a quality similar to NB H-modes;
- Simulation of α-particle heating [1] creating an energetic ^{3}He or H population similar in all respects, to the α-particle population in an ignited reactor (except for the anisotropy);
- Attainment of sawtooth-free periods of up to 5s (monsters) and, in combination with NB heating,

Table V
Nominal Characteristics of the ICRF plant in 1989

Frequency Range	23 to 57 MHz
6 Generators	4 MW output per module (20s)
2 Generators	3 MW output module (20s)
8 Antennae	• Nickel screen bars aligned with magnetic field
	• Two adjacent loops operated with either
	Monopole phasing (0,0) or Dipole phasing (0,π), or as a phased array
	• Getter pumps on vacuum transmission lines
16 transmission lines (Generator to antenna)	Each line 84m long rated at 50kW peak
	(ϕ ~ 230mm)
Feedback loops for control of:	• RF power level
	• Tetrode screen dissipation (acts on anode voltage)
	• Phase between the antennae
Feedback loops for impedance matching (plasma load)	• Frequency (Δv~ 1MHz)
	• Tuning stub (stepper motor)

a record D-D fusion yield in limiter plasmas;
- Suppression of specific ICRH impurity effects [3,4,5] on performance using both dipole phasing and evaporation of a beryllium film on the antennae screens. The density limit and the H-mode conditions are now independent of the heating method used, NB or ICRF heating. Fig. 23 shows the reduction to a negligible level of impurity ion sputtering from the screens;
- Demonstration of TTMP damping [6] of the fast wave in high ß plasmas.
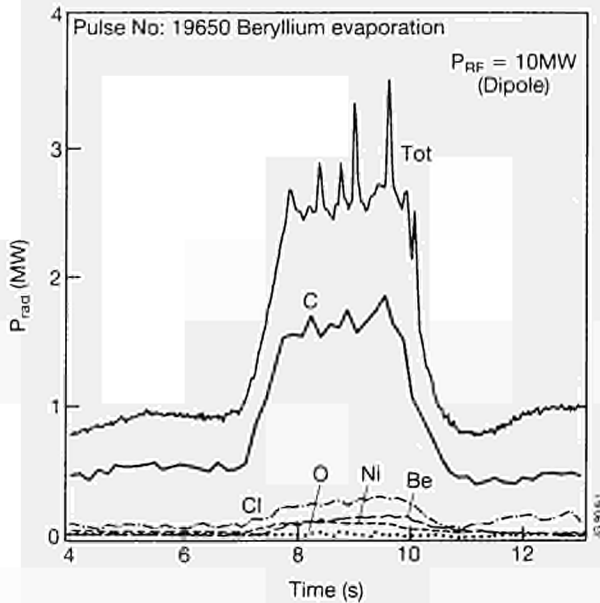
Fig 23: Total radiated power during an ICRH heated discharge (10 MW) after beryllium evaporation. Note the low level of radiation from oxygen, nickel and beryllium.

Fig.24 Reaction of the automatic matching system to a variation of the loading resistance during a long ICRF pulse. The figure represents the change of wave frequency and the error signal driving the stub length to perform proper impedance transformation of the coupling resistance. Generator power fed to one antenna and reflection coefficient during the long ICRF heating is also shown. The automatic matching system maintains a low reflection coefficient despite the variation of the coupling resistance.

Enhancement of the ICRH Plant Control Systems

A major difficulty for the ICRH plant is the rapid variation of the antenna load with plasma conditions. A good example of this is the change of the loading resistance (R_C) during a long monster sawtooth is shown in Fig. 24. The system was also used effectively to compensate partly for the change by a factor of x2 - 3 of R_C during L- to H-mode transitions. Considerable progress was made in adjusting rapidly the plant settings to varying plasma conditions. Two systems were developed and installed.

- Software calculates optimum plant settings corresponding to the plasma conditions of previous experiments. These settings can be downloaded and serve as an initial basis for an experimental campaign;
- During the discharge, a triple feedback loop adjusts the wave frequency, the length of tuning stubs and the electrical length of the antennae circuits to minimise the power reflected back to the generators. The frequency adjustment is fast (~50 ms) and of small amplitude (~50 kHz) due to the efficient

impedance transformation in the long coaxial line connecting the antenna to the tuning stub (~ 84 m). The adjustment of the tuning stub is relatively slow and can only compensate for about $0.5\Omega s^{-1}$. Nevertheless, high power coupling to the H-mode has been performed despite a large variation of the coupled resistance. Further progress is expected from an additional feedback loop, presently under construction, which will control the radial plasma position in order to maintain a requested value of the antenna loading resistance.

It has also been found necessary to modify a number of circuits to cope with the transient high voltages occurring during antennae arcs. A new control system has also been added. It protects the antennae and transmission equipment against certain arcs which appear to the generator as a tolerable load. This system is based on the measurement of the arc-induced asymmetry of the impedance of the two antenna sides powered by a generator. With this system, the damage observed previously on some antennae ceramics have been largely avoided.

Fig. 25 summarises the pattern of operation with the ICRH system in 1988 and 1989. It can be seen that the proportion of high power shots is larger in 1989 despite the short period of operation. This improvement is
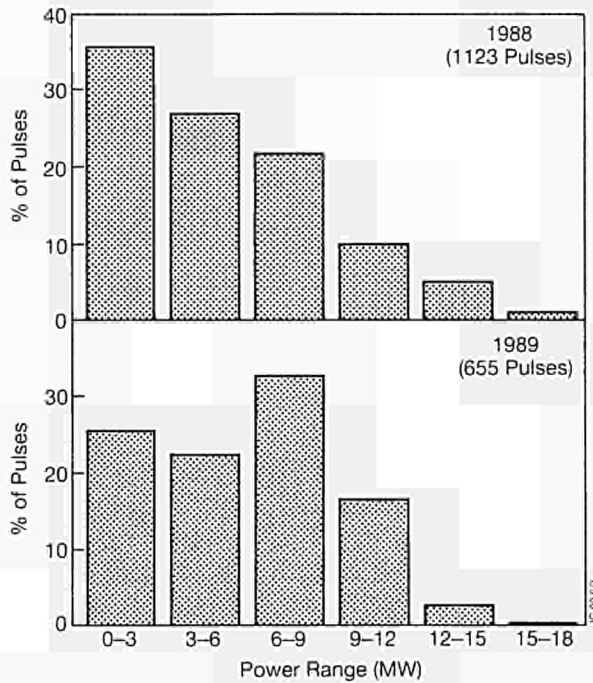
Fig 25: Histogram of the ICRF coupled power during 1988 and 1989. During 1989, the automatic system used was effective in reducing the percentage of low power coupling shots.

mainly due to the improved automation of the plant operation.

Beryllium Screens

JET undertook to replace the antenna screens made with nickel bars by a new screen assembly made of solid beryllium rods.

The change was motivated both by impurity physics aspects and by certain technical reliability considerations, as follows:

- Beryllium getters oxygen and has a very low self-sputtering coefficient which are dominant effects in impurity release due to RF sheath rectification on the screen [4]. Results obtained with beryllium evaporation have confirmed that impurity atoms released from the screens decreased by an order of magnitude [5] after the evaporation and that impurity effects specific to ICRF heating have been reduced to negligible levels [3].

- The good electrical conductivity of beryllium permits dispensing with circulating water inside the screen elements and eliminates the highly stressed weld between the elements and the water manifold. The heat can now be removed from the end of the elements by the water flowing in a manifold forming a "picture frame" which also supports the protecting tiles (beryllium or carbon), radiation cooled by nickel fins welded to the manifold as in the belt limiter structure.

By the end of the year, all the screen components had been delivered and high voltage tests had been

successfully performed. It is planned to resume plasma operation in 1990 with all eight antennae equipped with the new screens.

Fig. 26 shows a photograph of the new screen equipped, for safety reasons, with aluminium bars. The Nickel fins which are not equipped with the protecting tiles can be seen on each side. Contrary to the previous nickel version, there is optical shine-through between each bar.
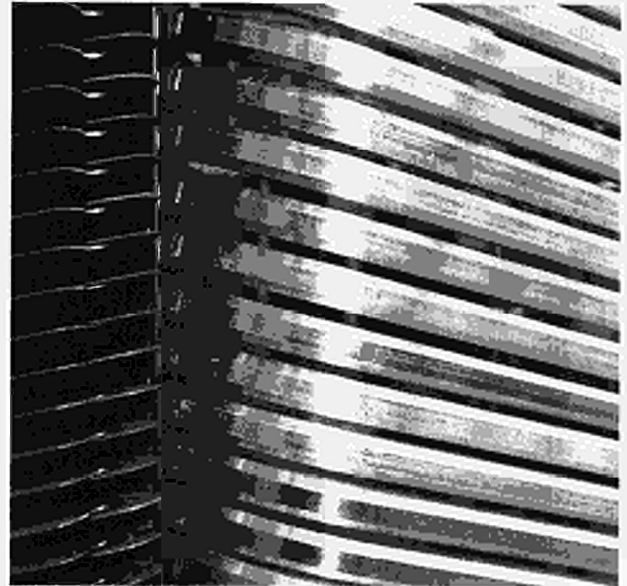
Fig 26: Detail of the construction of a beryllium screen (here equipped with aluminium bars for convenience) showing the open structure, the attachment of the bars and the cooling fins supporting the side protection tiles.

Technical Achievements with the Lower Hybrid Current Drive (LHCD) system

The JET LHCD system is powered by 24 klystrons operating at 3.7 GHz. The original power rating of 500 kW per klystron has been extended up to 650 kW by using newly developed high power circulators. The LHCD launcher will produce a narrow wave spectrum with a parallel wave index which can be varied from 1.4 to 2.4. The horizontal row producing this spectrum is composed of 32 waveguides: with 12 rows the total number of waveguides is 384. The system [6] is summarized in Table VI.

It will be installed in JET in two stages. The first stage, LO, will launch 4 MW and constitutes the prototype of the complete system, L1, intended to launch 12 MW power in the plasma. The first stage is composed of two prototypes, one built using the same technique as foreseen for the final system and one built by CEA Cadarache, France, using the technique used for Tore Supra design. They differ essentially in materials: carbonised copper-coated stainless steel is used for the JET design and zirconium copper for the Tore Supra design. The choice of stainless steel for JET has been based upon analysis of disruption forces and

Table VI
LHCD Systems

Generator	
Frequency	3.7GHz
No of klystrons	24
Power (generator) 10s pulse	25MW
20s pulse	12MW
Duty cycle	1/30
Efficiency	42%
Phase control	10 degrees
Maximum VSWR	1.8
Length of the transmission line	40m
Estimated insertion losses	1dB
Launcher	
Number of waveguides	384
(48 multijunctions)	
Waveguide material	stainless steel
Coating	copper+carbon
Maximum temperature	500˚C
Total weight	12 tons
Stroke	280mm
Response	15mm/15ms
Pumping	100 000 ℓ/s^{-1}

Fig 27: The prototype Klystron system.

on the mechanical properties of the launcher material at high temperature (~500C) which is necessary for HF conditioning.

The LO launcher will be powered by eight klystrons. The first row of four klystrons is shown in Fig 27. The module includes circulators, test loads, swiches and directional couplers. All four klystrons have been tested simultaneously at power level of 500 kW for 20 seconds. The necessary adjustments of the klystron parameters to reach the maximum HF rated power value of 650 kW are underway. The second module has been tested at his nominal power with electron beams only, the corresponding power control system are due for deliverying in early-1990.

The phase control system, which is needed to obtain a narrow wave spectrum and to control the current profile, cannot make use of phase measurement electronics close to the torus due to the high level of neutrons. To overcome this problem, it is proposed to make use of cross-talk between adjacent waveguides to assess the phase variation induced by thermal expansion during the HF pulse. The corresponding electronic system is complex and requires certain developments which are underway. It is anticipated that some of the main features of the phase control will be implemented during the prototype phase. The two klystrons in operation in the LH Testbed are routinely operated at power levels of 650 kW for 10 seconds, allowing acceptance tests and type tests of all the components of the LHCD system to be performed. All the critical components : HF windows, circulators, loads, etc are submitted to endurance testing.

The waveguides transmission lines linking the source generators to the Torus Hall are installed. Some of these have been tested at high power. In particular, the measured HF losses are within specifications. Parts of the transmission line in the Torus Hall, including hybrid junctions and loads, have been installed but were subsequently dismantled in order to allow Octant No. 3 to be removed from the Torus Hall.

The design of the prototype launcher has all the features of the complete LHCD system. In particular, all features related to the tritium phase of JET are taken into account, such as double containment and remote handling. Already tens of remote control flanges are installed in the waveguide transmission line. The main difference between the prototype and the complete launcher, (besides the number of waveguides), is a 10^5 ls^{-1} cryogenic pump which is under manufacture.

The LO launcher is ready for installation. The photograph of the grill mouth can be seen in Fig 28. The JET prototype is located at the bottom, and the Cadarache one at the top. The box shielding the launcher from disruption induced forces is also shown in the photograph together with the picture frame supporting the protecting carbon tiles. Langmuir probes and thermocouples are located in the carbon tiles. A honeycomb type structure is surrounding LOP and LOC in order to allow some pumping into the vacuum vessel to be obtained and to prevent HF power leakage in the back of the launcher. This structure will not be needed

Fig 28: The prototype launcher, with the JET launcher at the top and the Cadarache launcher at the bottom.

Fig 29: Photograph of complete prototype launcher (except picture frame protectives) leaving the Assembly Area.

for L1 since the shielding box will be fully occupied with multijunctions.

The carbonisation technique which is needed to avoid multipactoring has been shown to be effective in Testbed experiments, especially by retaining a negligible amount of gas when the Testbed chamber is filled to the same pressure as is used in the JET torus.

Testing of a multijunction under vacuum, at high temperature, with magnetic field and gas injection has allowed the following HF power to be reached:

- 200 kW for 20s on a short circuit
- 350 kW for 10s on a matched vacuum load,
  (e.g. 20% more than the required power rating)

The power handling capability of the short-circuit and of the vacuum load appear to be the limiting components of these tests. Nevertheless, these power levels are slightly above those foreseen during operation on JET.

An antimultipactoring technique allowing a thin layer of hydrocarbon to be deposited using Electron Cyclotron Resonance is being developed under an Article 14 Contract with IPP Garching, FRG. This technique may allow 'in situ' repair of the carbon coating, if needed.

A photograph of the complete LO launcher (with the exception of the picture frame) during its removal from the assembly area can be seen in Fig 29. The photograph of the LO launcher installed in its vacuum Testbed for hot leak testing, can be seen in Fig 30, showing the end plate which is equipped with eight vacuum windows. The vacuum windows have been installed using remote handling tools.

The two main areas related to the reactor aspects of JET which require special developments are the active position control of the launcher and the phase control of
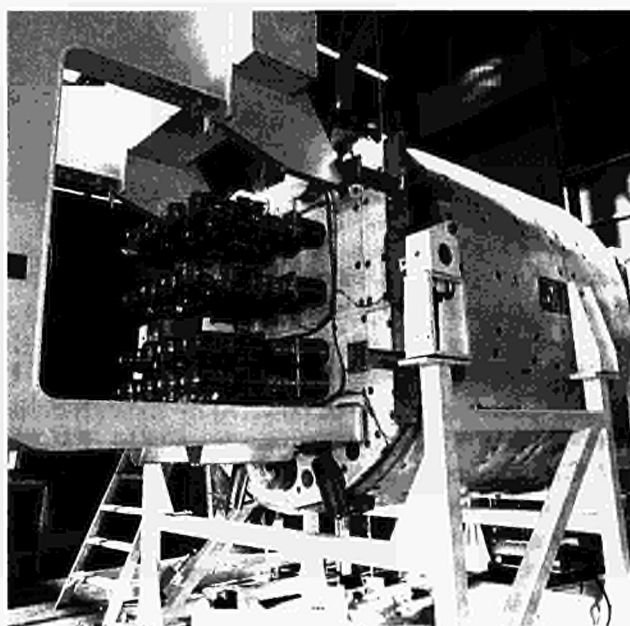
Fig 30: End plate equipped with eight HF vacuum windows.

the HF power at the grill mouth. The active position control system, which allows good matching during the pulse, is presently under test and will be implemented for the prototype launcher. The main components of the hydraulic system including the control cubicle have already been tested.

The algorithms required for the associated feedback control are under study. An infrared camera located on a top port and viewing the launcher mouth has been installed allowing hot spots at the grill mouth to be observed. High power tests on the LO launcher are being prepared, making use of the extended time duration of the shutdown. These tests will allow some

experience to be gained on conditioning and to start comissioning of the system before its implementation on JET.

References

[1] "Confinement of MeV Ions in JET created by Ion Cyclotron Resonance Heating", D.F.H. Start et al, IAEA Technical Committee Meeting on Alpha-Particles in Fusion Research, Kiev, USSR (1989), to be published.

[2] "H-mode in JET with Ion Cyclotron Resonance Heating alone", B.J.D. Tubbing, J. Jacquinot, D. Stork, A. Tanga, Nuclear Fusion, **29** p 1953 (1989)

[3] "Effect of Beryllium Evaporation on the performance of ICRH on JET", J. Jacquinot, V. Bhatnagar, M. Bures, D. Campbell, IAEA Technical Committee on ICRH Edge Physics (1989), to be published in a special issue of Fusion Engineering and Design.

[4] "Impurity Release by ICRF Antennae", D.A. D'Ippolito, J.R. Myra, M. Bures, M. Stamp, J. Jacquinot, IAEA Technical Committee on ICRH Edge Physics (1989), to be published in a special issue of Fusion Engineering and Design.

[5] "ICRH/Plasma Edge Interaction in JET with Beryllium Gettering", M. Bures, J. Jacquinot, M. Stamp, K. Lawson and P. Thomas, IAEA Technical Committee on ICRH Edge Physics (1989), to be published in a special issue of Fusion Engineering and Design.

[6] "The 15MW Microwave Generator and Launcher of the LHCD experiment on JET". M Pain et al, 13th Symposium on Fusion Engineering, (SOFE), Knoxville, USA (1989), to be published.

Remote Handling and Beryllium Handling

During the year, the Remote Handling Groups had a major commitment to preparation and implementation of shutdown activities involving a particularly large effort in preparing facilities and equipment for maintenance work on beryllium contaminated components. As a result, activities in the remote handling areas slowed down considerably. Main progress in these areas during 1989 is given below.

Remote Handling

Articulated Boom

In view of requirments to deal with heavy payloads, such as the Lower Hybrid antenna, the in-vessel articulated boom has been upgraded to a load capacity of 440 kg, from the previous value of 350 kg. This has involved redesign of the tilt actuator, using a cyclo-gearbox, and revision of several connections. A new structure was designed and ordered to accommodate the increased torque of the tilt actuator. Stiffer actuators for two horizontal joints have been installed and tested during operation. A larger unit for use in the experimental arm built for NET by KfK Jülich, FRG, has been directly derived from JET experience.

The control system has been improved with the use of feed forward networks, which give a tracking precision of 56 mm at 30% of full speed. The insertion into the vessel in "teach-repeat" mode takes place in approximately 7 minutes. The software for using the handbox has been improved to achieve a more friendly man-machine interface and it is now possible to create and edit "teach-repeat" files on a Silicon Graphics workstation and download them onto the boom local controller. These improvements have proved useful to reduce the time staff spend in the difficult working conditions of the enclosed Beryllium Controlled Area (BeCA) where the boom is being used during the present shutdown to replace antennae and limiters.

The boom has been installed on a stillage in the Assembly Hall at the level of the spare octant port, ready for mock-up tests. This has involved extensive rearrangement of cabling. Further studies on the dynamic response of the boom have been carried out using computer modelling. It seems possible to obtain some further improvements by using torque transducers. These would give a significant increase in the response speed and tracking precision, and provide more rapid perception of any forces applied accidentally to the vessel wall. This method will be applied on the articulated boom as second priority work as soon as time permits. It has been included in the "know-how" passed on to NET/KfK for use in the NET boom.

Telescopic Articulated Remote Mast (TARM)

The mechanical assembly of the TARM has been completed and preliminary load and functional tests have been carried out at the manufacturing site (see Fig.31). All rotary and telescopic movements proved satisfactory, with negligible backlash. The commissioning of the whole system, including high level and low level control of the 32° of freedom is planned in the early part of 1990. The cabling and 80% of the service cubicles have been installed. To ensure mechanical compatibility with the main crane, 3D photogrammetry was carried out on crane and TARM and checked using the CATIA facility.

Extensive cabling to link TARM to the control cubicles in the Assembly Hall and to the Remote Handling Control Room has been designed and partially installed.
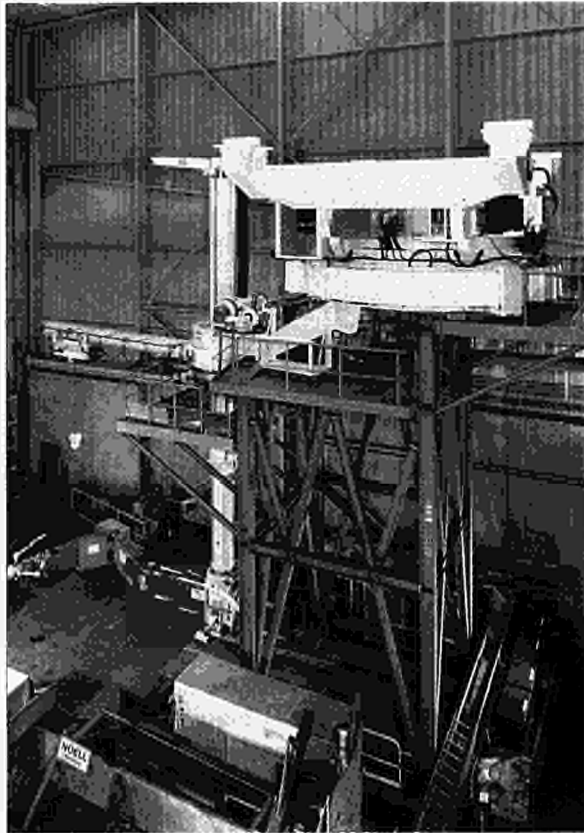
Fig.31 The Telescopic Articulated Remote Mast (TARM) in the final assembly phase.

Low Level Transporter

The drive controls and brakes have been improved to provide faster and easier manoeuvring. It was used to replace two turbo pumps in areas of difficult access and proved very satisfactory.

Servomanipulators

The first Mascot Master Unit has been installed in the Control Room with a faster and more user friendly man-machine interface. The following advanced functions have been commissioned and tested:
- teach and repeat
- tool-weight compensation
- preferential constraints
  (This requires further development).

Software has been prepared for automatic tracking of the "Cyclops" camera on the slave, and must now to be integrated into the system. Bench tests on unscrewing and tightening the bolts of a vacuum flange automatically using the teach-repeat function seemed most promising.

End Effectors

Considerable work has been carried out on the end effectors, to cope with new and diverse lifting requirements. After international tender the end effector for the LHCD has been procured and load tested, and

final commissioning is in progress. The beryllium screen shield, incorporating tilt motion, motorized latches and hooks, and improvments from previous experience, was designed and built. The "C-frame" to carry the LHCD hanger has been built.

In parallel with priority work for the shutdown, the conceptual designs of stillages for transferring tools and end effectors to and from the boom, and of the main remote connection of the boom were developed.

150 Tonne Crane

Additions and improvements of several crane sub-systems have taken place during 1989:
- The first version of the Crane Management System, which will be used to drive the crane remotely, has been completed as part of the TARM contract, to be installed in the second quarter of 1990;
- The cables in the reeling system have been replaced to include additional requirements of the TARM, including supply and fitting new termination and equipment cubicles on the crane itself;
- The method of clamping the cables, the drums and the reeler tower have been modified to improve reliability. At the same time, a fail-safe system has been installed which will flag mechanical faults in the reeling system before actual damage can occur;
- A prototype sealing box providing tritium containment of the cable was tested;
- The chain and sprocket assemblies for the position resolvers have been made and are ready for installation.

In-Vessel Inspection System (IVIS)

A new multimedia man-machine interface has been developed and used successfully in routine and emergency inspection campaigns (see Fig.32). The interface console contains four black and white monitors and a workstation. It is connected to the four

Fig.32 The man-machine interface console of the in-vessel inspection system (IVIS).

36

IVIS TV probes and provides manual and automatic tracking of areas of the vessel wall selected by the operator on a CAD graphical display. "Reference" photographs of the same areas shown on the monitors are also automatically displayed at the same time to facilitate interpretation of any possible defects. Fig.33 is a typical photograph taken with IVIS during an inspection campaign, showing melt marks on beryllium tiles of the belt limiter.
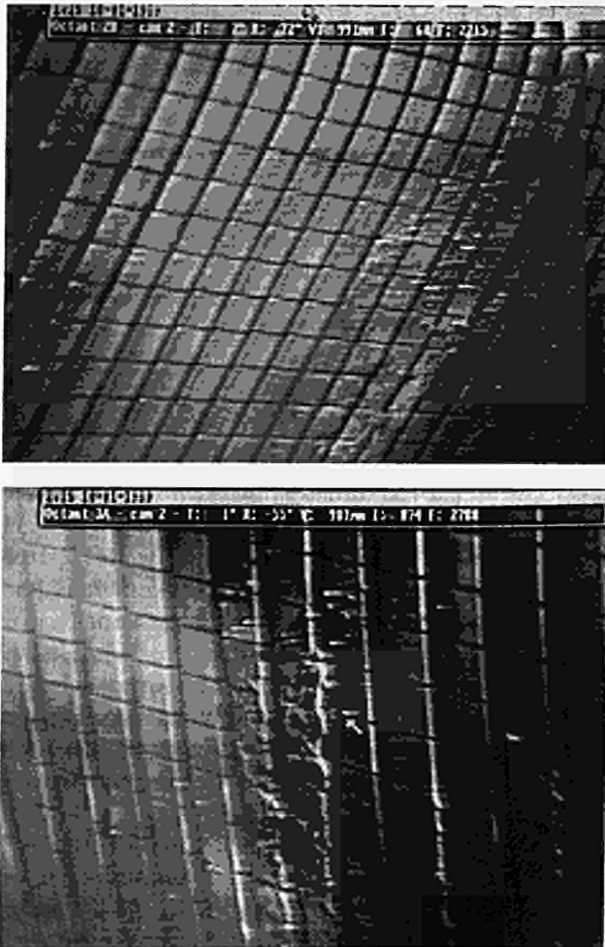
Fig.33 Photographs taken with IVIS showing melt marks on beryllium tiles of belt limiter.

The IVIS lighting system based on the light guides, has worked satisfactorily and is also normally used as in-vessel illumination during shutdowns. Loads imparted by IVIS during disruptions to the vessel ports have been evaluated by dynamic modelling of the system. This gave a better insight into the mode of oscillation of the vessel, which was checked experimentally. The need of a mechanical decoupling method has been identified and a design has been derived.

As a future IVIS improvement, a new TV probe, using flat sapphire window and prism suspended in the vacuum, allowing higher picture definition, is being developed in collaboration with ENEA, Italy.

Special Tools

The majority of the work on tools has involved development and use of existing designs for hands-on work in the JET shutdowns.

Two additional tool controllers have been built. Control software continues to be enhanced; dedication of controllers to individual tools has been eliminated and reliability improved. A tool simulator has been designed and built to aid commissioning of new software, and to allow comprehensive testing of new or repaired systems prior to actual use. The recent in-vessel cutting has highlighted the need for further equipment to diagnose faults quickly, particularly in wiring. These will be produced early in 1990. The controller has proved reliable during shutdown work.

Extensive use has been made of the new sleeve cutters and welders on the RF heating systems, and the LHCD assembly. It has been found necessary to incorporate weld pool viewing into the sleeve welder to reliably control the arc. This is required even during hands-on operation and so will be developed for use during remote operation.

A new set of cutting and welding trolleys for lip joints has been procured, commissioned and have been used on the Octant No.3 U-joint during the Octant replacement. The circular port welders used extensively in the past have been modified and requalified to produce an edge weld rather than a fillet to minimise the amount of port material wasted during the cutting process at each replacement.

The slitting saw for use primarily with the belt-limiter and RF antennae screen water pipe system has been modified to improve both its reliability and its maintainability. The drive train to the saw blade has been changed from a chain drive (which in the past proved to be rather unreliable) to a gear drive which has now been used successfully for cutting out the Octant No.3 pipework. The method of changing blades has been improved and the tool packaging for handling and decontamination has also been improved. Fig.34 shows the new cutting head design. The 50mm diameter orbital welder has undergone only small modifications to improve the reliability of service umbilical connections.

A review of the difficulties experienced in the installation and removal of RF antennae screens during previous shutdowns resulted in the design of new features and new handling tools for the beryllium screens to be installed in 1990. These tools facilitate the engagement and withdrawal onto its housing more reliably by allowing a greater compliance in alignment before final engagement and providing a foolproof visual indication of positive engagement/disengagement. The tools are designed for full remote handling.

The antennae screen and belt-limiter tile handling tools have been developed to a point now where they are both simple to use and highly reliable as
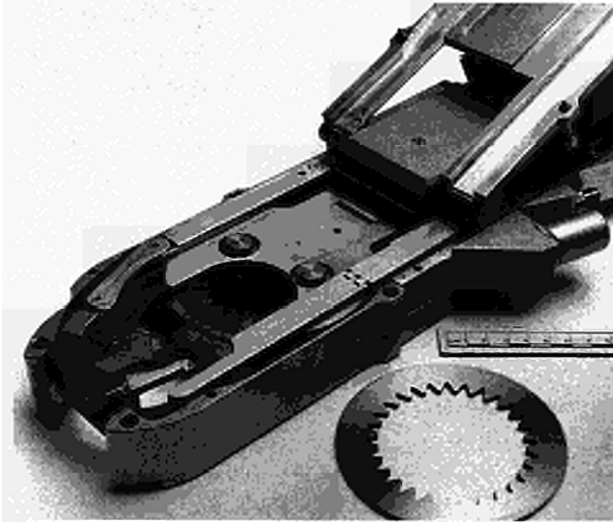
Fig.34 Remote handling pipe cutter.

demonstrated during the two major shutdowns of 1989 which involved the replacement of all belt-limiter tiles and one set of Be screen tiles. A few new handling tools for the Neutral Beam Neutralisers and the LHCD water pipe welding have been designed and manufactured during 1989.

Control Room

Work on the Remote Handling Control Room equipment has been primarily concerned with the provision of one complete SMMS for the Neutral Beam PINI mock-up work. This comprised a pair of Mascot master arms, one Remote Handling Workstation, one Common Panel and the associated video monitors and recorders. To achieve this the workstation hardware was completed by the addition of the two 9" colour video monitors, as shown in Fig.35.

The contract for supply of the 50 fixed cameras to be deployed on the Torus Hall walls during the D-T phase

Fig.35   Remote handling work station.

was completed and the cameras with their controller were delivered and commissioned in time for use with the PINI mock-up. These camera units comprise colour CCD camera with zoom lens all mounted on a pan/tilt head and with integral lighting and microphone. The camera controller has been interfaced to the RH control system on the Ethernet Local Area Network (LAN). This LAN is now being utilised for other tasks including the gathering of data for real-time graphical display of the Boom and TARM.

Collaboration with KfK Jülich, FRG, on real-time display of transporters has continued. The CATIA-RH Graphics Workstation link, which was developed at JET by KFK in 1988, has been extensively used to transfer 3-D models from CATIA for display in real-time of the TARM in its working environment within the Torus Hall. A hierarchy of models has been created and a simple method of creating displays of the requisite detail has started to be developed.

Mock-ups

There have been two major mock-up activities during 1989. The first and most complete is that of the PINI replacement and the second is for all In-Vessel remote handling tasks. Both activities were started in 1988 and continued in 1989 until major shutdown work required their dismantling to create space in the Assembly Hall.

The in-vessel mock-up rig underwent major modification due to the requirement to assemble the spare vacuum vessel with the other components to construct a full ninth Octant. A complete new support structure for the Octant on the bed-plate was designed and manufactured. The new ninth Octant mock-up was installed during May 1989.

Extensive work has been carried out on the PINI mock-up. During 1989 the fully remote phase of operations were carried out successfully and a number of reports and reviews are being produced. Fig.36 gives an overview of the mock-up facility. The task required over 25 separate operations and all these were ultimately performed under remote control from the Servo-Manipulator master station in the Remote Handling Control Room. The operations were performed with camera feedback from the Boom extension and Mascot B&W cameras supplemented by one colour facility camera. The tools required for the work were handled by the Mascot under remote control but the interconnection of tool services was not complete and the tools which could be were actuated under local control.

The main conclusions from the mock-up work have been the reinforcement of the importance of good viewing and the necessity to concentrate efforts in improving the man-machine interface for the viewing equipment. A wide range of other recommendations for improving the RH equipment are now being made.
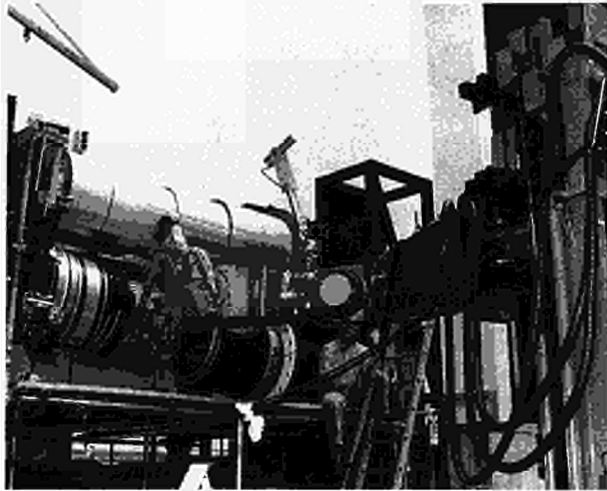
Fig.36   PINI Remote handling mock-up.

Beryllium Handling

The main effort in this area in 1989 has been the provision of equipment, services and expertise for the two shutdowns subsequent to the introduction of beryllium into JET in May 1989.

To coordinate the preparations for post-beryllium maintenance, a Beryllium Task Force was created. The preparatory work comprised major efforts for: the design, construction and commissioning of a new Beryllium Controlled Area Facility within the Assembly Hall; the setting up, resourcing and running of a PVC isolator and tent workshop/manufacturing facility; the design, construction and commissioning of a controlled area for access to Octant No.3 whilst it is being repaired in the Assembly Hall; and modifications to the Torus Access Cabin (TAC) ventilation and water systems. In addition a system was created for the handling, storage and disposal of both toxic and active waste and this is now in operation. Considerable time was invested in the definition of requirements for and the provision and recycling of protective clothing for work in controlled areas. This ranged from the fully pressurised suits used in the torus to simple disposable masks used in uncontaminated areas around the site.

Other beryllium related work consisted of preparing beryllium compatible remote handling equipment for the shutdown. Most notably, the Articulated Boom joints had to be fully gaitered, a tent to cover the boom when operating on the torus had to be installed and commissioned and a controlled transit storage cabin adjacent to the boom at Octant No.5 was designed and installed.

Torus Access Cabin (TAC)

With the use of beryllium in the torus, in-vessel intervention work supported from the TAC required for the first time, the use of all the service sub-systems. These include:

- HEPA filtered ventilation system

- Water wash system
- Breathing air system
- Intercom system
- Waste transfer system
- Controlled area barriers.

Since the TAC was designed, changes in the extent of in-vessel work and numbers of personnel required to carry out this work, have resulted in a number of modifications being required.

Ventilation Plant

Prior to the use of beryllium in the vessel, intervention work had been carried out from the TAC using a positive pressure ventilation system. Filtered air was pushed into the TAC Operations Box by two axial flow fans. The air exhaust was through openings in the vessel, normally at Octant No.5. The centrifugal fans of the TAC ventilation system maintained an airflow through the other areas of the TAC. Whilst this system protected the vessel from atmospheric dust, it was unacceptable for operations with beryllium.

During preparations for the July shutdown, the ventilation plant was reconfigured to the design mode for beryllium operations. The TAC fans draw air through two HEPA filtered circuits and discharge into the Torus Hall extract ductwork. The first circuit ventilates the change areas of the TAC. The second circuit provides an extract for the operations box and the vacuum vessel. Under normal conditions with no other openings in the vessel, a depression of ~200 Pa would be maintained in the second circuit with no air flow. This system was used for the ventilated suit operations.

For the October shutdown, the fan capacity was increased to provide an air flow through the torus of up to 10 airchanges per hour to facilitate in-vessel work for up to eight operatives wearing dust masks, assuming the levels of airborne beryllium dust could be reduced sufficiently. The modification involved the installation of two additional fans (one on stand-by) and a HEPA filter to form a separate circuit for the operations box and the torus to the remainder of the TAC, which is ventilated by the original fans. This system was used in the October shutdown, with rebalancing carried out for different operating regimes: i.e.

- full-suit operations with a single opening (Octant No.1)
- full-suit operations combined with boom operations at Octant No.5
- dust mask operations with Octant No.5 open.

Water Wash System

The pipework configuration to the holding tanks in the water wash system was modified to take account of the disposal method for beryllium contaminated water. A secondary factor was the increased volume of shower water resulting from the heavy work-load in the vessel. The TAC was designed to support 2-3 operatives wearing pressurised suits for normal in-vessel work. A

maximum of five suits can, however, be used for peak loads. During the July shutdown, it was demonstrated that with disciplined work procedures, four men could work safely in the vessel in pressurised suits. A fifth man could work in the operations box, at the same time. Consequently, during the October shutdown, the TAC supported five men in pressurised suits for three working sessions/day and six days/week.

The exit airlock from the operations box incorporates a suit shower. During these work periods, 15 exits/day produced about 1m³/day of contaminated wash water. Drainage from the shower and hand basin runs to a 2m³ collecting tank. Periodically, the water is transferred to the main site trades waste holding tanks in 1m³ containers, from which samples are taken for analysis. Typical beryllium concentrations of 10-15 µg/l were recorded.

A further modification to the system was the incorporation of an immersion heater into the shower supply tank. The decontamination of the PVC suits was improved by raising the water temperature from around 10°C to 30°C.

Fig.37 Beryllium handling facility.

Breathing Air System

Based on experience from other sites, the flow rates to the individual suits were estimated at about 200 l/min. This flow proved adequate for light work, but for strenuous work operatives were demanding up to 400l/min. Supplying five suits continuously at these flow rates - the maximum capacity of the compressor - resulted in an increase of the supply air temperature to 25°C. Early in the October shutdown, an in-line chiller was installed which reduced the supply temperature to 12°C.

Intercom System

The original conference intercom system had inputs for five suits plus an ex-vessel link plus the TAC controller. This was extended to form an 18 channel system. Direct communication is now possible between the TAC, in-vessel suit operators, waste transfer operations, boom operations at Octant No.5 and ex-vessel personnel. Overall control remains with the TAC controller who can connect the required channels.

Structural Modifications

To accommodate the increased flow of personnel through the TAC, an additional change cabin, incorporating a shoe barrier, was installed over the Alnor Access Cabin. A staircase access obviates the need to scale the original ladder carrying a pressurised suit.

Beryllium Handling Facility (J1A)

To carry out beryllium related work in the Assembly Hall, an enclosed facility was constructed and commissioned early in 1989 (see Fig.37). The facility
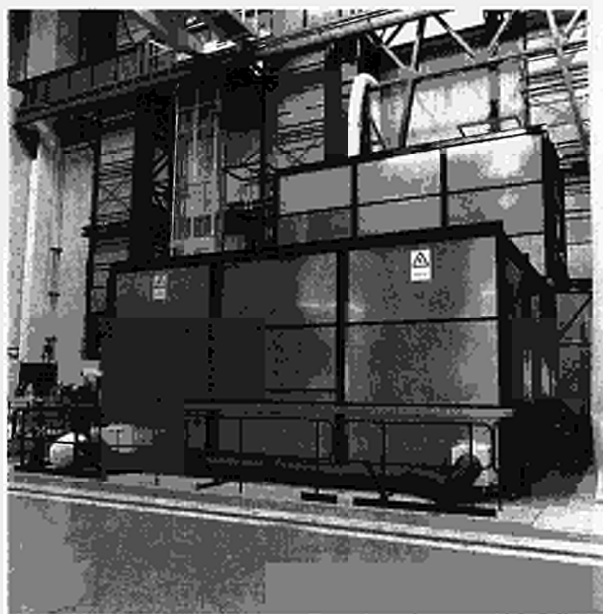
has a working area of 72 m² and includes an access and change area, a component transfer airlock, a HEPA filtered ventilation plant, electrical services and a water supply with filtered drainage system. Fume cabinets, ultrasonic cleaning baths and work benches have been installed. To meet necessary deadlines, the complete facility was designed, constructed and commissioned in-house in less than three months.

Tasks which have been performed in the facility include:

- Preparation of beryllium tiles for RF antennae and the belt limiters;
- Maintenance on potentially beryllium contaminated equipment;
- Decontamination of equipment from other beryllium controlled areas;
- Cleaning pressurised suits and other respiratory protection equipment.

The major activity during the in-vessel intervention period was cleaning of pressurised suits.

Isolator and Tent Workshop

A system was devised whereby any equipment detached from the outside of the torus during the beryllium phase which had potential for release of beryllium would be removed in a controlled way by use of 'isolators'. These are enclosed modules which are attached to both the equipment to be removed and the surrounding area of the machine to ensure a seal with respect to the Torus Hall environment whilst the equipment was being removed. Such an isolator is shown in Fig.38 and and is usually manufactured in clear PVC or polyurethane.

The workshop was been set up with one 3.5kW and two 1.5kW RF welding machines and has required a
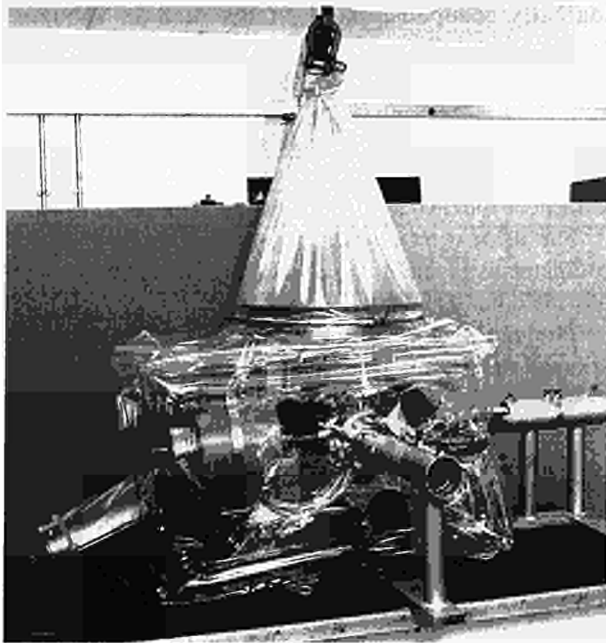
Fig.38 Isolator for maintenance of beryllium-contaminated components.

staff of 2-3 personnel. Over 50 different isolators have been manufactured in 1989 and a significant number of smaller tasks such as bags for tiles or protective gaiters for tools and control panels have been undertaken. The workshop also provides a repair and modification service and has undertaken extensive repairs of pressurised suits, tents and isolators.

Waste Management

Wastes generated by beryllium related operations and intervention work during 1989 can be separated into three major streams:

Beryllium Contaminated Solid Waste

The main items forming this waste stream include disposable clothing (coveralls, overshoes, gloves, dust masks etc), plastic sheeting, used isolators, cleaning materials and damaged equipment. All wastes leaving a beryllium controlled area are double bagged, labelled and packed into 200l steel drums. Disposal of waste is via an authorised waste disposal contractor and each batch must be authorised by the Local Authority. At peak periods during the shutdown, 25 drums/week were produced.

Beryllium Contaminated Water

Areas producing beryllium contaminated water include the TAC, Beryllium Handling Facility, Beryllium Evaporator Laboratory and the Beryllium Analytical Laboratory. Water from these areas is collected in 1 m^3 containers, which are individually sampled, before discharge into one of the main holding tanks of the site trades waste system. Following dilution, the tank contents are sampled and sentenced prior to off-site discharge.

Potentially Active Solid Waste (LLW)

Materials contacting the inside vessel wall are classified as potentially active for waste disposal purposes. These include overshoes, outer gloves and oversuits normally worn over pressurised suits. Damaged in-vessel components also fall into this category. These wastes are handled on-site in the same manner as beryllium wastes but a different colour coding is used for bags and drums. Following the results of a survey, it may be possible to recategorise some of this waste as beryllium contaminated waste. The disposal route for active wastes is through UKAEA Harwell Laboratory. Maximum arisings during shutdown operations have been around 5m per week.

Octant No.3 Beryllium Controlled Area in Assembly Hall

Due to the Beryllium contamination, it was necessary to provide a controlled man-access system to Octant No.3 after it had been removed to the Assembly Hall for replacement of the faulty toroidal field coil. This comprised a fully ventilated set of enclosures with shower and washing facilities, changing area and intercom equipment for communication between personnel in Octant No.3 and outside.

Suit Management

For beryllium work, a full one-piece pressurised suit is used. Air exhaust from the suit is via four cartridge filters. Entry to the suit is through a zippered opening in the rear with the assistance of a dresser who, together with the TAC controller, is in attendance throughout a working session. The suit is supplied with air via a 25m hose with an umbilical intercom connection. The airflow regulation is carried out on a rotameter at the main control console on request of the operator. The standard material for the suits is 0.012" laminated PVC, but nylon reinforced PVC and polyurethane have also been used. In an attempt to minimise the halogen impurity levels in the torus, a polyurethane oversuit is normally worn over the PVC suits.

During the October shutdown, 90 suits/week were used, from a complement of 300 suits. After each working session, the suits were double bagged and transferred to the suit cleaning facility. Suits were cleaned on the outside and the inside and then smeared for residual beryllium. Following an acceptably low analysis result, the suits were transferred out of the controlled area for inspection and repair.

A new facility for cleaning, repair, inspection and storage of the suits has been constructed and will be commissioned early in 1990. This will release the present facility for other beryllium related tasks.

Control and Data Acquisition (CODAS)

The Control and Data Acquisition System (CODAS) Division is responsible for the design, procurement, implementation, upgrade and operation of the computer based control and data acquisition system of JET. This system, based on a network of NORSK DATA minicomputers, allows centralised control and monitoring. The various components of JET have been logically grouped in subsystems such as Vacuum, Toroidal Field, Poloidal Field, etc. Each subsystem is controlled and monitored by one computer and the various computer actions are coordinated by supervisory software running on the machine console computer. This supervisory function includes the countdown sequences for each plasma discharge.

The allocation and configuration of all CODAS computers is given in Table VII, and Tables VIII and IX provide other quantitative data.

The main developments during 1989 and the orientation for 1990 are summarised below.

Table VII
CODAS Computer Configuration at the end of 1989

Subsystem	Usage	Model	Memory (MByte)	Disks (MByte)
AH*	NI Additional Heating (Oct 8)	ND110	3.5	1x70 1x450
AN*	Analysis and Storage	ND560	4.0	1x70 1x140 2x450
AS	Assembly Database	ND110	2.0	2x45
CB	Message Switcher B	ND110	2.0	1x70 2x140
CP	Cables Database	ND350	6.0	1x70 1x450
DA*	On-line Diagnostic	ND520	4.0	1x70 1x140
DB*	On-line Diagnostic	ND520	4.0	1x70 1x140
DC*	On-line Diagnostic	ND520	4.0	1x70 1x140
DD*	On-line Diagnostic	ND530	4.0	1x70 1x140
DE*	On-line Diagnostic	ND520	4.0	1x70 1x140
DF*	On-line Diagnostic	ND520	6.0	1x70 1x140
DG*	On-line Diagnostic	ND520	4.0	1x70 1x140
DH	Diagnostic Commissioning	ND550	6.0	1x70 1x450
EC*	Experimental Console	ND570	6.0	1x70 1x140
EL	Electronics	ND110	2.0	1x70 1x140
GS*	General Services	ND110	2.5	1x70 1x140
XC*	Pellet Testbed	ND110	4.0	2x70 1x140
LH	Lower Hybrid	ND110	3.0	1x70 1x140
MC*	Machine Console	ND110	2.5	1x70 1x140
PF*	Poloidal Field	ND110	3.0	1x70 1x140
PL*	Pellet Launcher	ND110	2.5	1x70 1x140
PM*	Pulse Management	ND550	6.0	1x70 1x140 1x450
RB*	Radio Frequency Testbed	ND110	2.25	1x70 1x450
RF*	Radio Frequency	ND100	3.0	1x70 1x140
RH	Remote Handling	ND110	2.5	1x70 1x140
SA*	Message Switching & JPF Collection	ND110	2.0	1x70 2x140
SB	Standby-system/Backup	ND110	4.0	2x70 1x450
SD	Built-in, Pool, Computer dB	ND110	2.25	2x45
SS*	Safety & Access	ND110	2.0	2x70 1x140
TB*	NI Testbed	ND110	2.5	1x70 1x450
TF*	Toroidal Field	ND110	2.5	1x70 1x140
TR	Tritium	ND110	2.5	1x70 1x140
TS	Test	ND520	4.0	1x70 2x450
VC*	Vacuum	ND110	3.5	1x70 2x140
YB	Integration	ND350	4.0	1x70 1x450
YC*	NI Additional Heating (Oct 4)	ND110	3.5	1x70 1x450
YD	Sc Dpt Development	ND570	6.0	1x70 1x450
YE	CODAS System Development	ND520	6.0	1x70 1x450

* Indicates on-line computers used for operation and testbed

Table VIII
Quantative Information on CODAS Installation

Item	End 1988	End 1989
CODAS interface cubicle	149	159
CAMAC Crates	232	247
CAMAC modules	3420	3382
Eurocard modules (signal conditioning and power supplies	7250	7346
CAMAC serial loop (fibre optic)	25	25
On-line computers	23	24
Off-line and commissioning computers	15	14
Size of JPF	17.6MB	21MB
Number of diagnostics on-line with CODAS	35	35
Number of diagnostics under commissioning with CODAS	4	4

Table IX
Review of CODAS Electronics Stock Holding
(Installed, pre-procurement and spares)

		End 1988	End 1989
1.	CAMAC systems modules	895	918
2.	CAMAC digital I/O modules	840	857
3.	Timing system CAMAC & Eurocard)	1273	1361
4.	CAMAC analogue I/O systems	1154	1224
5.	CAMAC dispaly modules	409	409
6.	CAMAC auxiliary controllers	152	152
7.	CAMAC powered crates	273	274
8.	U-port adaptor	200	200
9.	CISS modules	959	965
10.	CCTV	510	698
11.	Cubicle frames	345	345
12.	Console devices (not CAMAC)	518	524
13.	Power supply modules	1709	1848
14.	Intercom, Public address, Computer terminal network	617	635
15.	Pool instruments	964	1009
16.	Analogue I/O in Eurocard	2741	2853
17.	Digital I/O in Eurocard	4897	4909
18.	Eurocard sub-racks	970	997
		19426	20178
	Increase		3.9%

New Subsystems

No new subsystems were introduced this year, but significant extensions and modifications have been introduced. This is in line with the JET programme, where additional equipment is introduced in existing systems to expand JET capabilities.

Expansion, Enhancements and Modifications of Existing Systems

Extension and modification can be split into three main categories:

- Integration of new equipment into JET operation.
- Provision of new operational facilities.
- Improvement of existing facilities.

The main achievements of CODAS will be briefly reviewed under these headings.

Integration of New Equipment into JET Operation

The CODAS interface cubicles for the Lower Hybrid Current Drive (LHCD) System (8) have been manufactured, the software required for the first operation has been written and commissioning will be undertaken when operation resumes. The Central Interlock and Safety System (CISS) has been extended by an additional Programmable Logic Controller (PLC) devoted to the LHCD System protection. The hardware and software changes required by the operation of neutral beams at 140kV have been designed, implemented and commissioned.

Provision of New Operational Facilities

Software to facilitate the specification, execution and monitoring of all parameters required for a JET pulse has been made available to Session Leaders and Engineers-in-Charge. The current version will be used in the 1990 operation and reviewed in the light of experience. It allows Operation Staff to concentrate more on the physics issues and should make the routine part of operation more efficient.

The requirement to have long-pulse plasma discharges necessitated changes in many CODAS software products and modification of the logic of the Central Interlock and Safety System (CISS). These were successfully commissioned and a test pulse of 3 MA for 33s was achieved and a toroidal field of 1.7T for 66s. The ICRH antennae require conditioning from time to time. Based on the procedure devised and tested by RF Division a software procedure to automate this operation has been implemented.

To comply with HSE requirements new software for the JET Dosimetry Service was commissioned and accepted. It will be expanded later to include Tritium additions.

New hardware allowing the transmission of analog signals over long distances with a bandwidth compatible with that needed by the Disruption Feedback system has been successfully tested. The module design will be undertaken when all specifications have been agreed.

Software tools to record and process alarm occurrences have been implemented. The system includes real time software on the CODAS computers and usage of SAS on the JET IBM mainframe.

Some of the facilities available on CODAS consoles as part of the man-machine interface, have been made

available on computer terminals. This alleviates the requirements to provide additional consoles and console screens.

Improvements of Existing Facilities

For test purposes, a more powerful Central Processing Unit (CPU), has been installed in the communications computer. The JET Pulse File (JPF) collection speed was increased from 65 to 110kByte/s, showing that JPF collection time could benefit from more powerful CPU's. Some improvement of the software collecting the data and sending them to the IBM Mainframe have been introduced. This resulted in a significant decrease by ~ 220s of the time required to have data available on the IBM. The JPF growth and evolution of transfer time throughout the year is shown in Fig.39. Data compression is now in use on the mainframe reducing JPF storage requirements by about 70% and with no noticeable impact on data access times from application programmes.
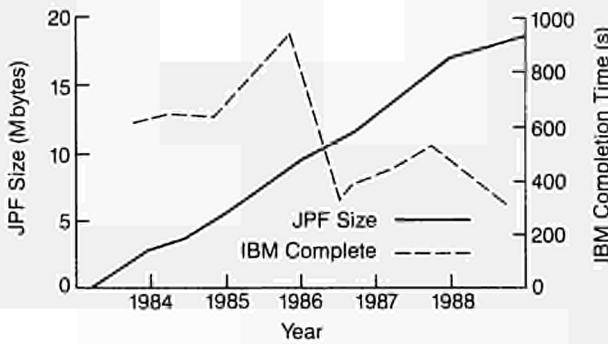
Fig 39: JPF Growth and Transfer Time over the Life of JET.

The modified computer configuration and the release of the operating system were successfully recommissioned when operation resumed. No major changes were introduced during operation. An active programme to bring all computers to their latest engineering level has been completed in order to improve the reliability and availability of CODAS.

ETHERNET controllers have been introduced on some machines in order to evaluate their suitability for the JET network. The tests were technically successful, but efficient usage of ETHERNET would require an upgrade of the operating system. This will be considered further in 1990.

The digital version of the feedback system for the plasma radial position and shape control has been fully commissioned and is routinely used in operation. This allowed the removal of the old system and the "clean-up" of related instrumentaton.

The introduction of beryllium into the machine significantly modified the gas pumping behaviour of the components. The behaviour of the plasma density feedback (PDF) system became unsatisfactory. A first set of measures was undertaken to remedy this. Further

analysis will lead to modification of the algorithm used. PDF, like other applications, uses the power of microprocessors to implement front-end processing with the flexibility of programmable devices. In this range of application the suitability of adaptative controls have been evaluated.

The development of the pellet launcher has continued together with the preparation for the new High-Speed Pellet Injector. Better operator facilities have been provided to take full advantage of the available and planned equipment.

At the present level of JET performance it is necessary to control discharge termination as smoothly as possible. The microprocessor based logic of the Pulse Termination Network has been upgraded to use pulse trains for fail safe operation. The termination of abnormal pulses also required a modification to the logic of CISS.

The overall management of all CISS information is being moved to a proper environment where control of the changes, programme development chain and logic verification will be integrated within the structure of a database system. Currently, all signal and cabling documentation has been computerised.

The site radio network has been improved to allow its use within shielded areas and to give better links with safety services. Continuous improvements have been made to the network facility for the IBM peripherals installed at JET. The constant effort required in this area, highlights the problems of using a remote mainframe.

The procedures to manage software distribution have been enhanced and most procedures are now fully automated. The efficiency of the JET backup strategy has been tested in a "Disaster Recovery" exercise. This exercise highlighted some weak points in the procedure documentation. These have been corrected and similar exercises will be carried out at regular intervals.

In addition to the nine LHCD system cubicles, expansions have been made to the Pellet Launcher (two cubicles), Remote Handling (two cubicles) and Diagnostics (one cubicle). There were also 385 fully documented design changes made to existing cubicles. Maintenance interventions were made on 420 occasions, in addition to routine preventive maintenance.

Main Orientation of Future Activities

During 1990, CODAS will continue to support and develop the facilities required for JET operation. As part of the development the final commissioning of the LHCD system and the High-speed Pellet Injector will continue. The design and organisation of the Pumped Divertor interface will begin. A significant effort will also be devoted to providing more convenient management tools for the large amount of information and for the documentation of all of the CODAS electronics modules, cables and cubicles.

In view of the proposed New Phase of JET, CODAS

has started a study on the best means to maintain services until the end of 1996. A comprehensive review of all electronic modules will be completed by September 1990 and a coherent plan of action should be ready by the end of 1990. For the control system, a feasibility study was made to evaluate the possible options and implementation measures are expected in 1990.

JET Data Management

The JET Data Management Group is responsible for the provision of a Mainframe Computing Service for scientific and engineering computing. This includes provision of appropriate software and hardware systems. The Group is also responsible for the management of JET data and for organisation and control of routine data processing.

The Computing Service is based on an IBM 3090/200E dual processor mainframe with a vector facility. There are 70GBytes of disc storage and a further 240GBytes of IBM mass storage. The JET Mainframe Data Processing Centre is housed in a specially designed building at UKAEA Harwell Laboratory and operated for JET under contract by a team from that Laboratory. The JET mainframe is also connected to the Harwell Laboratory CRAY2 computer.

The JET Computing Centre has been operating since June 1987 and the computing load has grown significantly since that date, such that at peak times the system is reaching its capacity. However, by careful tuning of the system, good response time is maintained for interactive users and for the CAD systems in the JET Drawing Office, although some deterioration is noted at peak times. Also the prompt execution of the intershot analysis is ensured. A background load of batch work is also serviced but the increasing long batch job work load, such as transport analysis and extensive structural analysis codes, now tends to be displaced outside daytime periods. Studies have indicated the need to upgrade the central processor in order to maintain the good service with the growing workload over the next few years. Plans are in place to upgrade the present IBM 3090/200E to the latest technology IBM 3090/300J early in 1990.

The Data Management Group provides the contact between the users, operators and system programmers, through the Help Desk Service, backed up by specialists in the Group. This ensures the smooth running of the system. The data communications between the JET site system and the Computer Centre are mainly the responsibility of CODAS Division and significant improvements in these areas are reported in that section.

The Group is also responsible for the storage of JET data and currently ~ 135GBytes of raw JET data (JPFs)

are stored on the cached Mass Store in a compressed form, and a further 35GBytes of analysed data are stored on the PPF online data base system. The Central Physics File (CPF), established during 1988 under the SAS environment, forms a complete higher level data selection and storage system. A subset of all data is extracted at time points of interest, determined by the Timeslice program and the interactive timeslice editor, TED, and stored in the SAS databases. These data are the basis for extended statistical analysis, and the source for other extracts such as the TRANSPORT bank. This complete system is a fully automated process, and is used by many physicists in the Project.

In addition to mainframe computing, the Group provides support for the increasing numbers of Personal Computers (PCs) on site which are used both as stand-alone workstations and terminals to the IBM and NORD computers, and for the AppleMac Systems introduced for word processing.

Diagnostic Systems

The status of JET's diagnostic systems at the end of 1989 is summarized in Table X and their general layout in the machine is shown in Fig.40. The staged introduction of the diagnostic systems onto JET has proceeded from the start of JET operation in June 1983 and is nearing completion. The present status is that, of 48 systems in total, 39 are in routine operation, 3 are being installed/commissioned, 4 have still to be constructed, one system is under development and one system is still under study. Operational experience has been good and most of the systems are now operating automatically with minimal manual supervision. The resulting measurements are of a high quality in terms of accuracy and reliability, and provide essential information on plasma behaviour in JET. Further details on specific diagnostics systems are given below.

Magnetics
The comprehensive system of magnetic flux-and field measurements has continued to work satisfactorily. The memory has been upgraded; slow signals recording information during the entire duration of the shot were extended from 1k to 4k word; the memory of many time windows used for detailed MHD fluctuation studies were also extended by a factor x4. Much time has been devoted to compensating for error fields picked-up by the diamagnetic loop. These appeared to be associated with the TF coil fault. The development of the TF coil fault could be traced back to late 1987 by using a set of saddle loops on the neighbouring Octant, in which the fault had a detectable effect. A subset of coils intended as sensors for the disruption feedback system were

45

Table X
Status of the JET Diagnostics Systems, December 1989

System	Diagnostic	Purpose	Association	Status	Compatibility with tritium	Level of automation
KB1	Bolometer array	Time and space resolved total radiated power	IPP Garching	Operational	Yes	Fully automatic
KC1	Magnetic diagnostics	Plasma current, loop volts, plasma position, shape of flux surfaces, diamagnetic loop, fast MHD	JET	Operational	Yes	Fully automatic
KE1	Single point Thomson scattering	T_e and n_e at one point several times	Risø	Operational	Yes	Fully automatic
KE3	Lidar Thomson scattering	T_e and n_e profiles	JET and Stuttgart University	Operational	Yes	Fully automatic
KE5	Fast ion and alpha-particle diagnostic	Space and time resolved velocity distributions	JET	Under Development	Yes	Not yet installed
KG1	Multichannel far infrared interferometer	$\int n_e ds$ on six vertical chords and two horizontal chords	CEA Fontenay-aux-Roses	Operational	Yes	Semi-automatic
KG2	Single channel microwave interferometer	$\int n_e ds$ on one vertical chord	JET and FOM Rijnhuizen	Operational	Yes	Fully automatic
KG3	Microwave reflectometer	n_e profiles and fluctuations	JET	Operational	Yes	Fully automatic
KG4	Polarimeter	$\int n_e B_p ds$ on six vertical chords	JET and CEA Fontenay-aux-Roses	Operational	Yes	Semi-automatic
KH1	Hard X-ray monitors	Runaway electrons and disruptions	JET	Operational	Yes	Fully automatic
KH2	X-ray pulse height spectrometer	Plasma purity monitor and T_e on axis	JET	Operational	Yes	Semi-automatic
KJ1	Soft X-ray diode arrays	MHD instabilities and location of rational surfaces	IPP Garching	Operational	No	Semi-automatic
KJ2	Toroidal soft X-ray arrays	Toroidal mode numbers	JET	Operational	Yes	Semi-automatic
KK1	Electron cyclotron emission spatial scan	$T_e(r,t)$ with scan time of a few milliseconds	NPL, UKAEA Culham and JET	Operational	Yes	Fully automatic
KK2	Electron cyclotron emission fast system	$T_e(r,t)$ on microsecond time scale	FOM Rijnhuizen	Operational	Yes	Fully automatic
KK3	Electron cyclotron emission heterodyne	$T_e(r,t)$ with high spatial resolution	JET	Operational	Yes	Semi-automatic
KL1	Limiter viewing	Monitor of hot spots on limiter, walls and RF antennae, divertor target tiles	JET	Operational	No	Fully automatic
KL3	Surface temperature	Surface temperature of limiter and target tiles	JET	Commissioning	No	Will be fully automatic
KM1	2.4 MeV neutron spectrometer	Neutron spectra in D-D discharges, ion temperatures and energy distributions	UKAEA Harwell	Operational	Not applicable	Semi-automatic
KM3	2.4 MeV time-of-flight neutron spectrometer		NEBESD Studsvik	Operational	Not applicable	Fully automatic
KM4	2.4 MeV spherical ionisation chamber		KFA Jülich	Commissioning	Yes	Semi-automatic
KM2	14 MeV neutron spectrometer	Neutron spectra in D-T discharges, ion temperatures and energy distributions	UKAEA Harwell	Under Construction	Yes	Not yet installed
KM5	14 MeV time-of-flight neutron spectrometer		SERC, Gothenberg	Under Construction	Yes	Not yet installed
KM7	Time-resolved neutron yield monitor	Triton burning studies	JET and UKAEA Harwell	Operational	Not applicable	Fully automatic
KN1	Time-resolved neutron yield monitor	Time resolved neutron flux	UKAEA Harwell	Operational	Yes	Fully automatic
KN2	Neutron activation	Absolute fluxes of neutrons	UKAEA Harwell	Operational	Yes	Semi-automatic
KN3	Neutron yield profile measuring system	Space and time resolved profile of neutron flux	UKAEA Harwell	Operational	Yes	Fully automatic
KN4	Delayed neutron activation	Absolute fluxes of neutrons	Mol	Operational	Yes	Fully automatic
KP3	Fusion product detectors	Alpha-particles produced by D-T fusion reactions	JET	Under study	Yes	Automatic
KR1	Neutral particle analyser array	Ion distribution function, $T_i(r)$	ENEA Frascati	Operational	No	Automatic
KR2	Active phase NPA	Ion distribution function, $T_i(r)$	ENEA Frascati	Under construction	Yes	Automatic
KS1	Active phase spectroscopy	Impurity behaviour in active conditions	IPP Garching	Operational	Yes	Semi-automatic
KS2	Spatial scan X-ray crystal spectroscopy	Space and time resolved impurity density profiles	IPP Garching	Operational	No	Not yet implemented
KS3	H-alpha and visible light monitors	Ionisation rate, Z_{eff}, impurity fluxes from wall and limiter	JET	Operational	Yes	Semi-automatic
KS4	Charge exchange recombination spectroscopy (using heating beam)	Fully ionized light impurity concentration, $T_i(r)$, rotation velocities	JET	Operational	Yes	Semi-automatic
KS5	Active Balmer α spectroscopy	T_D, n_D and Z_{eff} (r)	JET	Under Construction	Yes	Not yet implemented
KT1	VUV spectroscopy spatial scan	Time and space resolved impurity densities	CEA Fontenay-aux-Roses	Operational	No	Semi-automatic
KT2	VUV broadband spectroscopy	Impurity survey	UKAEA Culham	Operational	No	Fully automatic
KT3	Active phase CX spectroscopy	Fully ionized light impurity concentration, $T_i(r)$, rotation velocities	JET	Operational in '90	Yes	Not yet implemented
KT4	Grazing incidence + visible spectoscopy	Impurity survey	UKAEA Culham	Operational	No	Fully automatic
KX1	High resolution X-ray crystal spectroscopy	Central ion temperature, rotation and Ni concentration	ENEA Frascati	Operational	Yes	Fully automatic
KY1	Surface analysis station	Plasma wall and limiter interactions including release of hydrogen isotope recycling	IPP Garching	Operational	Yes	Automated, but not usually operated unattended
KY2	Surface probe fast transfer system		UKAEA Culham	Operational	Yes	
KY3	Plasma boundary probes	Vertical probe drives for reciprocating Langmuir and surface collecting probes	JET, UKAEA Culham and IPP Garching	Operational	Yes	
KY4	Fixed Langmuir probes (X-point and belt limiter)	Edge parameters	JET	Operational	Yes	Semi-automatic
KZ1	Pellet injector diagnostic	Particle transport, fuelling	JET and IPP Garching	Operational	No	Not automatic
KZ3	Laser injected trace elements	Particle transport, T_i, impurity behaviour	JET	Operational	Yes, after modification	Not automatic
Kγ1	Gamma-rays	Fast ion distributions	JET	Operational	Yes	Manual

P T7 (rev 17/1/90)

46
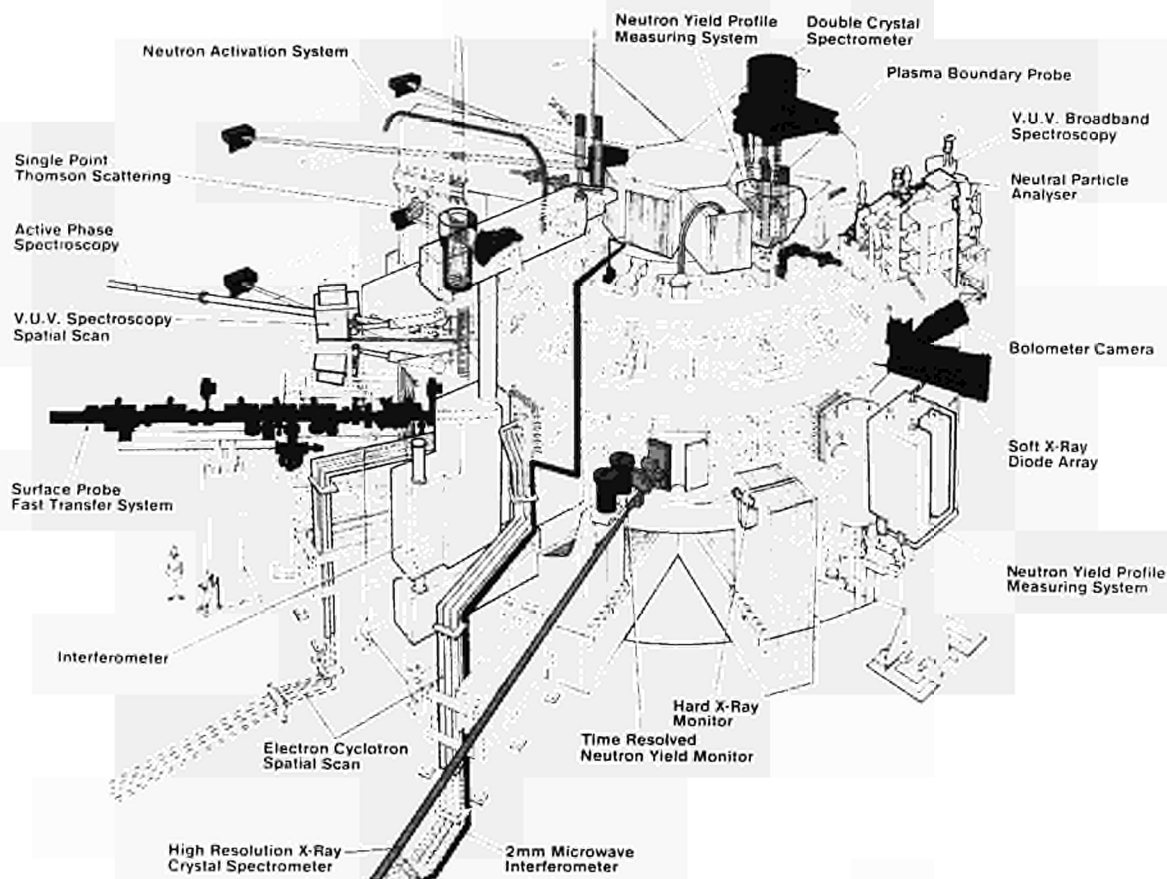
Fig.40: General layout of diagnostics in the machine.

installed in the vessel and found to operate according to expectation.

Plasma Boundary Probes

A large number of fixed probes were installed in target plates, limiters and RF antennae to provide routine measurements of the plasma parameters close to the plasma edge scrape-off layer (SOL). The fast moving reciprocating probe has been used regularly and with high reliability to provide extensive profile information, identification of the plasma boundary and of the carbon sputtering yield (deuterium on carbon plus self sputtering) measured on its tip as a function of surface temperature. The system for exposing time resolved collector probes at the top of the machine has been used for the first time in conjunction with its cassette under remote control.

Plasma Wall Interactions

The transition to Beryllium has made it difficult to examine wall materials exposed to discharges during this period and retrieved after an opening. However, surface analysis of complete tiles is still possible by ion beam techniques, especially Nuclear Reaction Analysis,

in air and in a beryllium isolator enclosure. This facility has been completed.

The integral exposure/analysis facility of Fast Transfer System (FTS) and Surface Analysis System (SAS) in which exposure, transfer and analysis are carried out under vacuum has been successfully operated throughout the campaign. It has provided direct measurements of the thickness of evaporated layers; a measurement of the evolution of an evaporated layer on a shot-by-shot basis (formation of beryllium oxide and carbide); and the time resolved deposition of carbon, beryllium, deuterium, etc, under various discharge conditions. Both Auger/XPS and ion beam techniques have been employed.

Limiter Observations

Up to eight different viewing ports have been available and five channels have routinely been recorded. Information from the CCD cameras has been used mainly to optimise plasma performance by avoiding arcing and hot spots, optimising the plasma contact with limiters, etc.

Cameras have been equipped with carousels containing filters for the observation of Hα, BeI, BeII

and Cl, II, III light and these have been used both for the beryllium limiters as well as for the divertor target plates to obtain spatially resolved influxes of the various elements.

Evaluation of video data has been greatly facilitated by the introduction of a PC based video analysis system. This has enabled more detailed analysis, particularly of temperature data, where problems due to the small dynamic range of the CCD cameras have been greatly reduced. Target temperatures at the X-point tiles of up to 2500°C have been measured using this facility. Viewing ports have been shared with other spectroscopic measurements to make correlations between the observations of impurity influxes.

A CCD camera has also been used successfully to observe the top of the reciprocating probe to give both the surface temperature as well as the carbon/beryllium influx. An increase in sputtering yield at elevated temperatures has been obtained up to 1500°C in reasonable agreement with other data from the literature on radiation enhanced sublimation.

Electron Cyclotron Emission (ECE) System

The ECE measurement system comprises four different types of spectrometer: rapid scan Michelson interferometers, Fabry-Perot interferometers, a twelve-channel grating polychromator and an eight channel heterodyne radiometer. The Michelson interferometers provide measurements of the whole ECE spectrum from which the spatial dependence of the electron temperature is derived. The Fabry-Perot interferometers and grating spectrometer provide the time dependence of the electron temperature at fixed points in the plasma, and the heterodyne radiometer provides temperature measurements in a limited region of the plasma with very high spatial resolution and sensitivity. One of the Michelson interferometers is linked to a real-time processing system which provides the electron temperature profile, or derivatives from it, for plasma monitoring or control of JET systems.

During 1989, the Michelson interferometer, Fabry-Perot interferometers and the grating spectrometer were not changed except the detector on the Michelson system, which was replaced due to failure of the detector cryostat. This meant that the continuity of ECE calibration, which had existed since 1984, was temporarily lost. Retrospective calibration at the end of the operation period restored the calibration to its normal accuracy (± 10% in absolute level).

Progress with the upgrade of the heterodyne radiometer from eight channels to 44 channels has continued. The detailed design was completed and all major system components ordered. Some key components not available commercially, for example non-polarizing beam-spitters which operate in oversized waveguide and a mulitplexing data acquisition system for calibration measurements, were developed in-house.

The existing eight channel radiometer was used in a wide range of studies: a new area of application was the study of high beta plasmas which are produced at toroidal fields ($B_T < 1.3$ T) below the operating range of the other ECE instruments (see Fig.41).
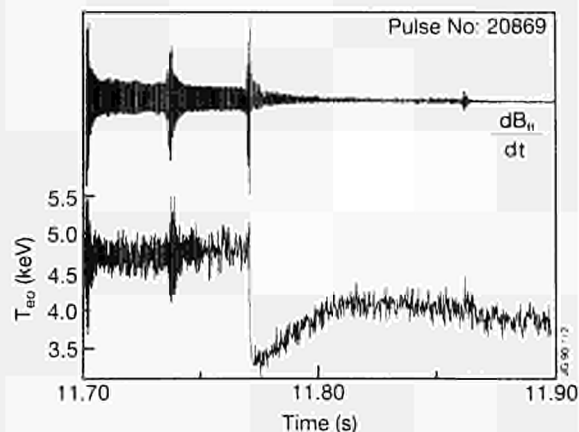
Fig.41: Heterodyne radiometer measurement of central electron temperature Teo in a high-β plasma ($B_T = 1.3T$) showing fishbones and β collapse.

The routine comparison of temperatures measured by ECE with those measured by LIDAR Thomson scattering continued and agreement on the level of the central plasma temperatures was generally obtained to within the measurement uncertainties (typically ± 10%). However, some discrepancies in the shape of the profile were observed and these are presently under investigation.

A novel technique for determining the total magnetic field in the plasma by combining data obtained with the ECE and LIDAR systems was developed. The technique exploits the facts that the ECE gives electron temperature as a function of cyclotron frequency, which is simply related to the magnetic field strength, while the LIDAR provides a spatial temperature profile directly. By identifying ECE frequencies with the spatial locations which the LIDAR shows to have the same temperature, the total magnetic field strength can be determined as a function of radial position. Subtraction of the vacuum toroidal field yields the magnitude and spatial dependence of the magnetic field due to the plasma (the internal field).

An error analysis has been performed by modelling the procedure numerically. It includes the effects of the principal uncertainties in the ECE measurements (relative calibration uncertainty and spectral resolution), in conjunction with the spatial resolution and statistical errors of the LIDAR measurements. The results show that the magnitude of the total magnetic field can be determined to an accuracy of > 3% depending on the shape of the temperature profile. This is sufficiently accurate to enable useful determinations of the internal field under some circumstances.

The internal field has been determined under a variety of JET plasma conditions: in particular, in

plasmas with monster sawteeth and strong additional heating. Comparisons with the JET magnetic equilibrium code (IDENTC) have been made and generally show good agreement (see Fig.42).

The planned experiments with lower hybrid current drive on JET will generate suprathermal electron populations and these will significantly affect the ECE. An investigation of the effects on the ECE and an assessment of the possible use of ECE measurements as a diagnostic tool for the suprathermal populations is in progress. The work is being carried out in collaboration with CNR Milan, Italy, where a code for numerical simulation of non-thermal spectra is being developed under an Article 14 contract.
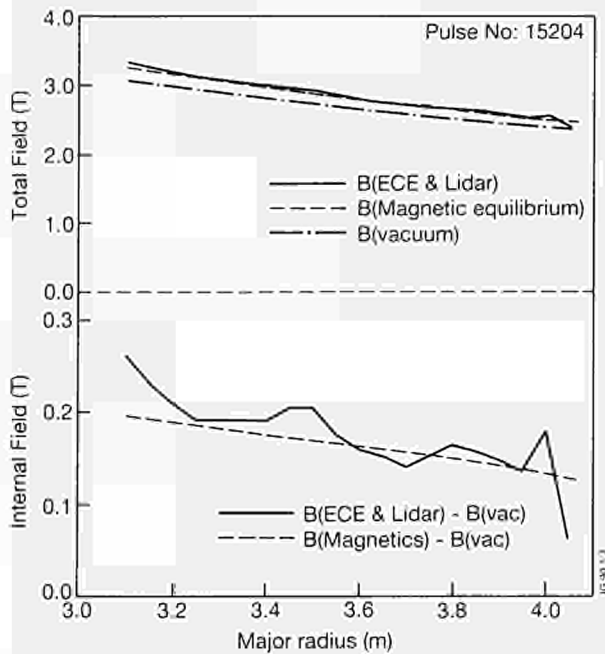
Fig.42: Magnetic fields deduced from ECE-LIDAR data compared with magnetic equilibrium calculations.

Microwave Transmission Interferometry and Reflectometry

The microwave transmission interferometer has continued routine use for measurements of the line-of-sight electron density and for plasma control purposes. It has operated with high reliability and essentially without modifications.

The multichannel reflectometer probes the plasma along a major radius with radiation propagating in the ordinary mode (E ∥ B) at 12 frequencies in the range 18 - 80 GHz and so probes electron densities in the range 0.4 - 8.0 x 10^{19} m^{-3}. It has been designed to have two modes of operation : narrow band swept, for measuring the electron density profile; and fixed frequency, for measuring movements of the different density layers on a relatively fast time-scale. During 1989, significant progress was made and, except for the two highest frequency channels, the system is now fully operational.

The principal system modification was the

installation in the vacuum vessel of a new antenna assembly. The new antennae have their apertures close to the plasma and so give a much improved coupling between launch and receive systems. Signals due to spurious reflections in the port are also significantly reduced. In addition, techniques were developed for reducing the effects of high frequency density fluctuations and it is now possible to measure the profile of the electron density with a spatial resolution ~ ± 5 cm and a time resolution ~ 5 ms under many conditions of interest.

The fixed frequency measurement capability has been exploited in several physics studies. It has been used to measure the movements of the different density layers following a sawtooth collapse. From the measurements the electron particle diffusion coefficient (D_p) is derived. This is compared with measurements of the thermal conductivity (χ_e) made on the same sawteeth by following the heat pulse propagation with ECE measurements. The ratio of χ_e/D_p is constantly found to be ~ 10. Measurements have also been made of the relative movements of the different density layers during times of rapid plasma change, for example during additional heating. This work is carried out in collaboration with the FOM Instituut voor Plasmafysica, Netherlands.

The swept frequency measurement capability was brought into successful operation towards the end of the tokamak operating campaign and measurements of the density profile in the edge region were made under a limited range of plasma conditions, mainly ohmic and H mode. The results have been compared with those obtained by transmission interferometry and in general good agreement has been obtained. The H-mode results are particularly interesting since they show that the density gradient can be very steep with gradient values >10^{21} m^{-4} (Fig.43).
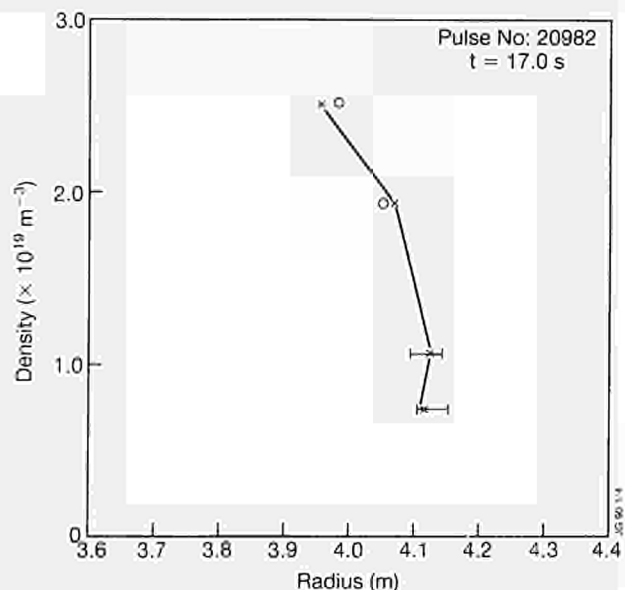
Fig.43: Electron density close to plasma edge from swept-frequency reflectometer diagnostic.

Measurements on density fluctuations have continued using correlation reflectometry. In this technique, two (or more) independent reflectometers operating at fixed, but slightly different, frequencies probe the plasma along the same line-of-sight. The cross power (coherence) and cross phase spectra are deduced from the data and, according to the theory of correlation reflectometry, the disperison curve and correlation length of the waves characterising the density fluctuations can be obtained.

Experiments were carried out with a correlation reflectometer operating with extraordinary mode radiation ($E\perp B$) at 76 and 77 GHz. The corresponding separation between the reflecting layers is ~1 cm. The results show a high level of coherence under conditions of additional heating but essentially no correlation for ohmically heated plasmas. This surprising result is possibly due to an effect not included in the original theory of correlation reflectometry, i.e. plasma rotation, and so the theory is presently being revised.

Thomson Scattering

During 1989, the work on Thomson scattering systems has concentrated on maintaining the operation of the LIDAR scattering system, whilst simultaneously proceeding with the phased installation of an upgrade to provide a 10 Hz repetition rate capability.

The first stage upgrade was successfully completed early in the year with the installation of high reflectivity (99%) broadband (400 - 750 nm) dielectric collection mirrors. These will allow reduced laser energy (1 - 2 J instead of 2 - 3 J) to be used for the future 10 Hz laser without a reduction in signal/noise for the measurement. In addition, a bandwidth enhancement of the digitizers (developed under contract by the Risø National Laboratory, Denmark) was commissioned to give a modest increase in the spatial resolution.

The system was operated routinely during the tokamak operating periods. Usually, it was operated with the 2-3 J ruby laser in 0.5 Hz/9 pulse mode but occasionally in ~ 1 Hz/6 pulse mode for improved time resolution, particularly for measurements with pellet fuelled discharges. The improved signal/noise afforded by the combination of the ruby laser and new mirror configuration revealed most notably the changes in the density profile when Be was introduced into JET as a wall material (see Fig.44). Use was also made of the simultaneity in space and time of LIDAR T_e and n_e profiles in discharges with unusually steep n_e gradients (see Fig.45). These profiles occurred in pellet fuelled RF heated discharges and persisted for much of the heating phase.

In the final 1989 operating period, the second phase of the 10 Hz upgrade was successfully implemented. This was the introduction of PC's as front ends to the digitizers interface to CODAS. The scheme was based on feasibility work carried under contract by the Risø
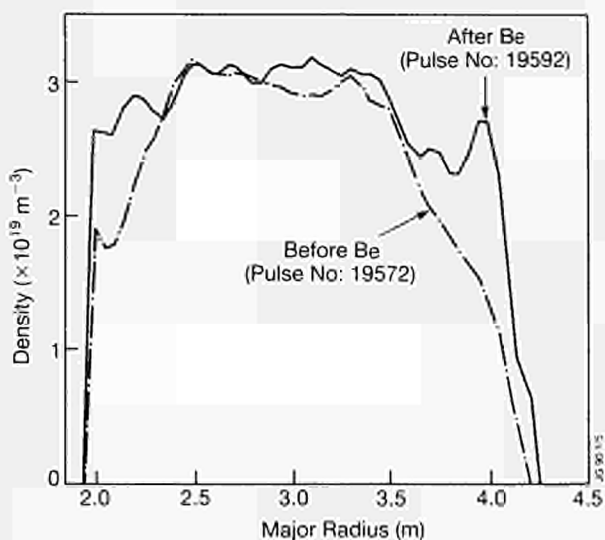
Fig.44: Density profiles using LIDAR, before and after Beryllium evaporation.
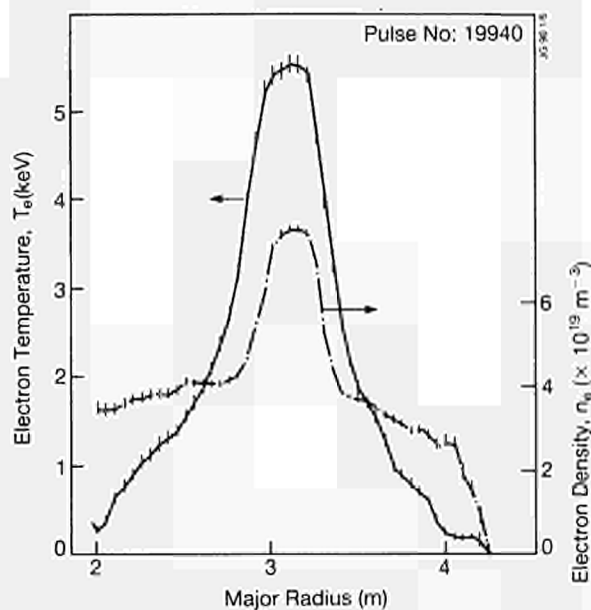
Fig.45: LIDAR electron temperature and density profiles with pellet injection and ICRF heating.

National Laboratory. The PC's facilitate fast data read-out and storage between laser pulses during a JET discharge. In addition, some data processing is possible in the 100 ms between laser pulses with this system, reducing the data transfer times throughout the computer network.

The Single Point Thomson scattering system has been operated mainly as a source for laser ablation measurements. During the year, the laser optics have been modified to produce a beam waist about 0.5 m above the JET equatorial plane. This is in preparation for its use as the light source for internal magnetic field measurements. By detecting the modulation of the scattered spectrum which occurs at angles orthogonal to the local magnetic field, the field strength and direction

can be determined [1]. The axicon based collection optics for the system have been designed and delivery is expected during the 1989/90 shutdown. The mechanical mounts are also being prepared also for installation during the shutdown. The detection system is being prepared by the UKAEA, Culham Laboratory, which is working in collaboration with JET on the magnetic field measurements.

Fast Ion and Alpha Particle Diagnostic

A diagnostic system to measure the velocity and spatial distributions of fast ions, including α-particles in the D-T phase, is in preparation. The system is based on collective scattering of radiation with a frequency ~140 GHz generated by a powerful gyrotron source. During 1989, substantial progress has been made with the scientific and technical design although the procurement of the major system components has not been initiated due to delays in gyrotron development. Nevertheless, the development of some key system components has been started.

The scientific design has concentrated on assessing the effects of the dielectric properties of the plasma. The principal effects are refraction of the launch and scattered beams, spreading of the beams due to density fluctuations, and modification of the scattering cross-section. Ray tracing codes have been used in conjunction with models of the plasma, including the presence of density fluctuations, to assess the magnitude of these effects. The scattering cross-section has been correctly evaluated taking into account the dielectric effect of the plasma. The results confirm the earlier predictions for scattering with radiation in the ordinary mode, but have also revealed that for scattering with radiation in the extraordinary mode, which is possible in the lower range of densities, the scattered signal can be enhanced by up to an order of magnitude [2]. The possibility of making detailed measurements of the bulk ion feature has also been examined.

The technical design has concentrated on the interfaces with the JET device and particularly on the in-vessel components, the high power transmission system and gyrotron installation. In addition, the detection system and control and data acquisition system have been designed. In each case, solutions to all the main technical problems have been obtained and potential suppliers identified. The in-vessel components are particularly important and so a mock-up of the proposed arrangement, including steerable mirrors, is under construction. This will be tested before the detailed design is completed. Development work is also in progress on a device (Vlasov convertor) which will convert the gyrotron output into a mode suitable for propagation in the oversized waveguide transmission system. An anode modulator unit which will allow modulation at high frequencies (up to 40 kHz) of the RF output of the gyrotron is also being developed.

It is interesting to predict the performance of the diagnostic with plasmas similar to the best obtained in JET in 1989 assuming D-T fuelling. The results show that it should be possible to measure the spatial and velocity distributions of the confined α-particles with energies in the range 0.5-3.5 MeV. For scattering with ordinary mode radiation, the signal/noise would be >10:1 assuming standard settings of the diagnostic.

The work on this system is supported by the Association Laboratories with contributions from the Riso National Laboratory, Denmark; ENEA Frascati, Italy; the FOM Instituut voor Plasmafysica, Netherlands; CRPP, Lausanne, Switzerland; and the UKAEA Culham Laboratory. The development of the Vlasov convertor is being carried out by the ECRH Group at the University of Stuttgart, FRG.

Neutron Yield Measurements

The instantaneous neutron yield from JET discharges is recorded with a set of fission chamber assemblies. During the year, a number of problems have come to light concerning both the absolute calibration of this diagnostic and the interpretation of measurements for additionally-heated discharges.

The calibration problem arose from the realization that there was now so much equipment attached to the main horizontal vessel ports that the use of a ^{252}Cf radioisotope neutron source to simulate 2.5MeV neutrons for in-vessel calibration studies was no longer acceptable. ^{252}Cf neutrons are emitted with a spread of neutron energies about a mean value of 2.12MeV; the lower energy neutrons are moderated and absorbed to a greater extent than are 2.5MeV neutrons. As a consequence, the calibration was now effected through activation techniques. For this purpose, a delayed-neutron counting system was used based on ^{232}Th and ^{238}U fission foils. This system was calibrated at a fission reactor against standard fission chambers and can determine neutron fluences to better than 3% accuracy. Neutron transport calculations were needed to relate the local fluence at the irradiation position to the total neutron yield. Employment of a new irradiation end positioned inside the vacuum vessel uncovered a modelling error in the neutron transport calculations. Despite these difficulties, the final calibration of the fission chambers was only 15% above the historical value which was traced back to January 1985.

The interpretation problem was related to the use of high power RF heating and was exacerbated by the recent introduction of beryllium belt limiters. Whenever ICRF heating is employed, a high energy tail of the minority ion species is formed (H or ^{3}He) and, in the case of H-minority, a high-energy tail of deuterons is also formed. These accelerated particles can attain energies of up to 10MeV and readily interact with thermal deuterons and also with beryllium impurity ions. Under certain conditions, giant sawteeth and low

electron densities, the neutron emission from RF-only heated discharges comes predominantly from fast ion-impurity reactions. However, with combined heating, the beam-plasma fusion reactions dominate, with less than 20% of the neutron emission being attributable to the RF-accelerated particles. Evidently, under these conditions, neutron and gamma spectroscopy have an important part to play in interpreting the nature of the neutron emission.

Positive evidence for fishbone instabilities adversely affecting the neutron emission was observed in high β discharges ($B_T = 1.2T$, $I_p = 2$ MA), (see section on MHD Topic Group). For these discharges, the neutron emission was too low for the fission chambers to give a noise-free signal. However, the NaI scintillators normally used to detect hard X-rays are also sensitive to neutron capture γ-rays and, hence, to the total neutron emission. The sudden drops in the neutron-induced signal was identified as being due to fishbones because of their coincidence with recognizable features in the ECE and magnetics signals. Through intercalibration with the fission chambers, the drops in intensity were found to be about 9%. Although small compared with the drops due to sawtooth oscillations, the associated losses of central energy content could be more significant due to their higher repetition frequency.

Neutron Emission Profiles

To explain the neutron emission from a JET discharge, it is necessary to supplement the data from the fission chambers with information on neutron emission profiles from the profile monitor and with neutron energy spectra derived from the most appropriate of the neutron spectrometers. For example, this combination permits the deuterium density in the plasma to be determined, independently from all other diagnostic information, for most normal discharges.

The neutron profile monitor has been operated routinely during all discharges run this year. It was mentioned in the 1988 JET Progress Report that the efficiency of the profile monitor apparently increased with neutron yield when D°-neutral beam heating was used; this effect is still not fully understood but is related to the strength of the background gamma-radiation and is worse when ICRF heating is additionally applied. It is only important for processed signal rates above the level that would normally be regarded as the upper limit for safe operation. Since JET neutron yields are continually rising, the profile monitor has to be fitted with inserts to reduce the collimated aperture and hence the count-rates and it has been difficult to keep the diagnostic in balance with the performance of the machine. A pragmatic correction for the efficiency problem is to scale the profile monitor rates with the instantaneous yields derived from the fission chambers.

Neutron Spectrometry

Several types of neutron spectrometers are operated

at JET so that a wide range of operating conditions can be covered. For normal well-behaved discharges, it is possible to unfold the neutron energy spectra to obtain good estimates of the plasma central ion temperature and the beam-plasma to thermal neutron emission strengths. In addition, by combining the analysis with data from the other neutron diagnostics, the beam-beam component can also be identified. However, for the interesting class of hot ion plasmas, this decomposition proves impossible because the neutron energy spectra from the three components become indistinguishable at high ion temperatures (>15keV). The reason is that the ion energy distributions of the reacting deuterons have also become indistinguishable; the separation of the reaction rates into the three components is computationally convenient, under these conditions, but is physically without meaning. These hot ion plasmas can be regarded as being in effect thermal and the neutron spectra can then be trivially interpreted in terms of the deuteron temperature. These temperatures tend to be rather lower than those provided by the active charge-exchange diagnostic.

With high power RF heating, the presence of fast (MeV) ion energy distributions means that the neutron spectra must always be inspected before activation measurements can be used for the absolute calibration of the fission chambers. As mentioned previously, with RF-only discharges the fast ions can interact with the beryllium impurity ions, producing very distorted neutron energy spectra. An example of this is shown in Fig.46, where a spectrum obtained before the introduction of beryllium is compared to one obtained under similar discharge conditions after the beryllium belt limiters had been installed. The difference is quite dramatic in this case, for which a detailed neutron analysis is clearly not possible.

Gamma-Radiation Spectrometry

The complex neutron energy spectra that are sometimes produced can be interpreted with the assistance of
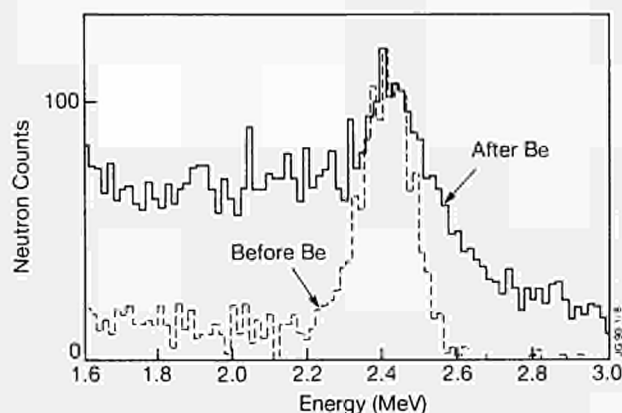
Fig.46: Neutron energy spectra recorded during RF-heated discharges, with hydrogen minority ion species. The presence of beryllium impurity ions gives rise to a very large contribution from neutrons produced by nuclear reactions with accelerated deuterons.

gamma-radiation energy spectra. These in turn, are quite complex and have to be understood by comparison with gamma spectra obtained, with the same detectors, from a particle accelerator under controlled conditions. Fig.47 shows a typical example of a gamma spectrum obtained during a discharge for which the neutron energy spectrum was highly distorted. In this instance, the RF minority ion species was hydrogen and a tail to the energy distribution was developed which extended to above 8MeV; the proton-beryllium reactions were the source of the extra neutron emission in this case.

Fig.48: Comparison of the 14MeV neutron time trace measured with the Si diode predictions derived from the 2.5MeV neutron emission. To obtain the good fit of prediction to measurement, it was necessary to include a loss term, operating from 6.5 to 8.5s into the discharge.

Fig.47: Gamma-radiation energy spectrum recorded during combined NB and RF heating (H-minority). The discharge is formed on the new beryllium belt limiters. The presence of strong lines due to $d(^9Be, {}^{10}B)n$ reactions explains the neutron spectrum in the previous figure.

Triton Burnup

The 1MeV tritons produced by the d(d,p)t reaction constitute nearly ideal test particles for simulating the single particle behaviour of the 3.5MeV α-particles to be generated in future D-T experiments. Triton burnup has been investigated extensively over the past few years and has been found to be classical, within the experimental errors. Most informative are the measurements of the time-dependence of the 14MeV triton burnup neutrons as derived from the pulse-height spectra recorded with a silicon diode. In general, both the absolute magnitude and the time-dependence of the count-rate in the diode can be predicted, within the expected errors, from the observed 2.5MeV neutron emission strength and the basic plasma parameters.

However, in a few recent (somewhat unusual) discharges, evidence has been obtained for very significant non-classical losses. The results of the burn-up measurement are shown in Fig.48. First, it should be noted that the extremely long slowing-down time, of more than 2s is a result of the low electron density ($<2\times10^{19}m^{-3}$) due to the strong pumping action of the beryllium limiters. However, the interpretation model

shows that about two-thirds of the tritons are missing at the time of the second peak in the emission of the 14MeV neutrons. This second peak is caused by a steady increase in electron density after beam switch-off. To simulate the apparent loss of confinement, it was necessary to apply a loss term, with a 0.9s decay time constant, from 6.5-8.5s into the discharge. Abrupt losses coincident with the sawtooth crashes do not reproduce the observed time dependence. The excellent agreement shown in Fig.48 demonstrates, simultaneously, record confinement times and significant non-classical losses.

Cold Fusion

A claim [4] that thermonuclear heating takes place in a heavy water electrolytic cell used to load deuterium into palladium metal received considerable publicity earlier this year. Whilst the original claim of measureable nuclear heating is simply unbelievable, the parallel observation [5] of a very weak emission of 2.5MeV neutrons appears more plausible, although surprising. De Ninno et al [6], in ENEA Frascati, Italy, carried out a simple variation on these experiments by subjecting titanium chips to deuterium gas at very high pressure; when cooled to 77K and allowed to warm up slowly, high (neutron) count-rates were recorded with simple, rather inefficient, Health Physics instrumentation. A possible explanation can be constructed for this observation in terms of crack propagation within the sample, with sudden development of local high voltages as the crystal planes separate, and consequent acceleration of deuterons to keV energies. The Frascati experiment was repeated at JET, in a collaboration with UKAEA Culham Laboratory staff [7].

Titanium samples were prepared, with up to 2.0 deuterons per titanium atom, in a pressure vessel suitable for insertion into one of the highly efficient neutron detector assemblies belonging to the delayed-neutron counting system. The pressure vessel was cooled in situ to 77K and was allowed to warm up

gradually. No neutron emission was observed. However, a tendency for proportional counters to generate extensive bursts of electrical noise which can be mistaken for neutron-induced signals was observed. The cause of this effect is thought to be related to the use of liquid nitrogen in the vicinity of the counters, allowing a microscopic quantity of moisture to penetrate through the electrical connector to the insulator at the HV end of the counter, from whence it cannot escape. This explanation is supported by the fact that no such spurious events were ever observed in the companion neutron detector assembly which was operated for control purposes, without liquid nitrogen in close proximity.

Survey of Light Impurity Behaviour

In 1989, JET operation offered a challenging variety of mixtures of light impurities in the hot plasma core, for analysis by spectroscopic means. Coverage of the vessel walls by a thin layer of evaporated beryllium and, in the second operation phase, the introduction of a beryllium tiled belt limiter, both caused a complete change in the visible spectrum. The gettered layer on the graphite tiled walls reduced the level of carbon emission and effectively eliminated oxygen. Beryllium became the dominant impurity.

Radial profiles of the effective ion charge, Z_{eff}, were determined from Abel inverted profiles of the multi-chord visible Bremsstrahlung signals and the simultaneous measurement of main light impurities by charge exchange spectroscopy. The dilution factor (n_d/n_c) was derived from the density of electrons and light impurities.

Four different cases are representative of campaigns in 1988 and 1989. These are denoted by

- the *Carbon* phase with carbon limiters and X-point target plates;
- the *Beryllium Gettering* phase with beryllium gettering on the graphite surfaces;
- the *Beryllium Limiter* phase where the graphite limiter tiles were replaced by beryllium components;
- *X-point with Beryllium* in the vacuum chamber.

A statistical summary of the impurity concentrations is given in Table XI. The number of samples used in each phase is also shown. The 1989 carbon phase data was not used because there was not enough time following the long shut-down to condition the machine and so bring oxygen down to 1988 levels. This is an important consideration because it appears that the reduction in the carbon levels during beryllium operation is associated with the elimination of the sputtering of carbon by oxygen.

Major progress has been achieved by the routine monitoring of the species mixture of the main light impurities. In a second order data processing chain, the neutral beam penetration code was corrected for the measured time dependent, impurity concentrations. Of particular interest is the observation that in high-power, high-fusion-yield plasmas the contributions of beryllium or carbon may change significantly over one JET pulse. The role of hollow impurity profiles and their implication for the prediction of neutron production was addressed.

A further point of interest was the establishment of a correlation between particle influx from the plasma boundary and changes in the bulk plasma. Typical delays of ~300 - 500ms were observed between the onset of particle influxes from limiter and wall surfaces and subsequent central increases of impurity concentrations. As a rule, the latter is much less dramatic than the events deduced from boundary emission suggest and sometimes even entirely suppressed, which indicates a screening effect between bulk plasma and edge phenomena. A comprehensive understanding and study of the link between impurity behaviour at the plasma boundary and in the plasma should play an important part in future experiments.

Spectroscopic Ion Temperatures

Spectroscopic ion temperature measurements at JET are based on the Doppler broadening of spectral lines emitted by either highly ionized impurity atoms (e.g. Ni^{26+}) in the case of high resolution X-ray spectroscopy, or by fully stripped light impurity ions (e.g. Be^{4+} or C^{6+}) in the case of Charge Exchange Recombination

Table XI
Statistical Summary of the Light Impurity and Deuterium Concentrations Obtained in each Operational Phase

Concentrations	Carbon Phase	Beryllium Gettering	Beryllium Limiter	X-Point with Beryllium
(Carbon) [%]	5.5(<7)	3.0(<5.0)	0.5(<1.5)	1.6(<3.0)
(Oxygen) [%]	0.9	0.05	0.05	0.05
(Beryllium) [%]	-	0.8(<1.0)	3.0(<4.0)	1.1(<2.0)
n_d (0)/n_e (0)	0.6(>0.45)	0.8(>0.65)	0.85(>0.8)	0.87(>0.6)
No. samples	2421	8524	1394	5979

(The figures in brackets correspond to the 66% level in each case)

Spectroscopy (CXRS). The passive emission of the resonance line of Ni^{26+} emanates from the hot plasma core, whereas the locations of the active charge exchange emission lines are defined by the intersection of neutral beam and a fan of viewing lines.

The sensitivity of the X-ray diagnostic and its analysis procedure have been significantly improved in 1989. These improvements have enabled the retrieval of central ion temperatures at nickel concentration levels as low as $n_{Ni}/n_e = 10^{-6}$. At high electron temperatures exceeding 10 keV, the inferred central ion temperatures must be corrected for profile effects resulting from the burn-out of helium-like nickel in the plasma centre. Modelling of the spectral emission by means of measured radial profiles of electron temperature, density and toroidal rotation, enables the deduction of consistent core ion temperatures.

CXRS is used routinely at JET to measure radial profiles of impurity ion temperatures using a fan of viewing lines intersecting the neutral heating beams at several radii in the torus mid plane. In 1989, radial ion temperature profiles were based on the spectral analysis of whichever was dominant of carbon or beryllium. Systematic errors due to energy dependent cross-sections for charge capture were analysed, but proved to be negligible even in hot-ion-mode plasmas with temperatures approaching 30keV.

For light impurity concentration levels exceeding 10^{-2}, and nickel concentrations greater than 10^{-6} three independent central ion temperatures could be compared in a wide range of different conditions. Generally the two main light impurity ion temperatures, and that of helium-like nickel, agreed within 20%. However, further attention is needed to investigate possible differences between temperatures measured perpendicular and parallel to the magnetic field.

In the periods prior to or after additional heating, the observed neutron production can be assumed to be entirely thermal, and central ion temperatures can be derived from a knowledge of deuteron density and measured neutron rates. Ion temperatures based on neutron yield agree during the ohmic heating phase within their estimated errors to spectroscopic measurements. Fig.49 illustrates the measure of agreement between the different ion temperature diagnostics for a pulse with a particularly high ion temperature.

Impurity Influx and Plasma Boundary
Visible Spectroscopy

Impurity influx measurements at JET are based on the visible spectroscopy of neutral atoms and low charge state ions at the plasma edge. The accuracy of the influxes depends mainly on the accuracy of the theoretical "photon efficiencies", which are dependent on suitable modelling using accurate atomic data.
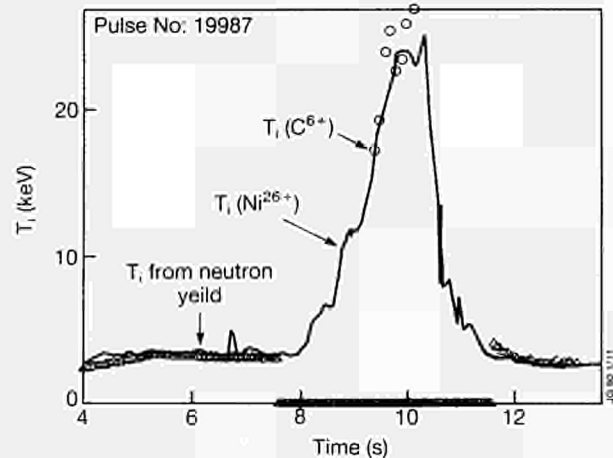
Fig.49: The comparison of the ion temperatures determined from the Doppler broadening of Ni^{26+}, the charge exchange recombination spectrum of C^{6+} and neutron emission.

Effective sputtering yields can be calculated from the influx measurements, and compared with the predictions of impurity production models. Such comparisons, over a range of plasma edge parameters, reveal:

● Large carbon sputtering yields in 1988 and early 1989 were attributable to large oxygen fluxes in the plasma edge;

● After the removal of oxygen by Be-gettering, carbon sputtering yields were still a factor of 1.5 higher than expected. This was probably because the sputtering models make no allowance for particles hitting the limiter surface at non-normal angles of incidence;

● Measured values of the effective sputtering yield of beryllium (<40%) were much higher than expected (<8%). This could be explained by increasing the self-sputtering yield in the sputtering model, in the same way as for carbon, but the enhancement factor required is ~3. Further investigations are needed to explain these data.

In preparation for beryllium operation in JET, a spectral survey (2000 to 8500 A) of beryllium emission in the UNITOR tokamak at the University of Düsseldorf, FRG, was carried out. The aim was to identify suitable visible spectral lines for monitoring beryllium in JET, and to assess the atomic modelling required for beryllium influx calculations. The need arose because many views are used to get a complete picture of the interior of the vacuum chamber for which visible spectroscopy is technically the most appropriate. Unfortunately, the visible lines tend to be weaker than the resonant UV lines and more sensitive to details of the atomic physics such as the excited state population densities. The expected spectral lines were identified, and their measured calibrated intensities were found to be in agreement with the emission modelling calculations, within the large shot-to-shot intensity variation that was observed.

Plasma Boundary Ion Temperatures

High resolution visible spectroscopy of neutrals and low charge state ions has been used to measure Doppler ion temperatures from ions near the plasma boundary. Fig.50 shows ion temperatures deduced from D_α (6561Å) and Be IV (4659Å). The Be IV temperature is higher than the D_α temperature. This was expected because Be IV radiates from further into the plasma than D_α. However both temperatures indicate that the boundary ion temperature is much larger than the electron temperature measured by Langmuir probes. The possibility that the ion temperature might be higher than the electron temperature had already been deduced by the inability of the Langmuir probe data to account for the power flow to the limiter.
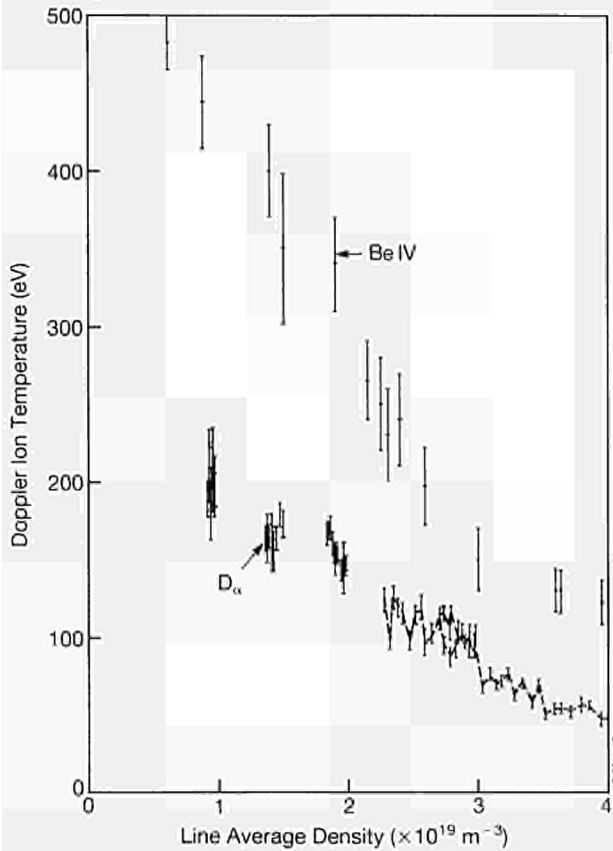
Fig.50: Ion temperatures measured near the boundary in an Ohmic heating density scan from the broadening of D_α spectrum emitted by the neutral beam as it crosses the plasma. The different Stark components are shown, which when folded with the instrumental resolution produce a curve which matches experiment well.

Z_{eff} Profile Measurement Using Active Balmer-Alpha Spectroscopy

Radial profiles of the effective ion charge, Z_{eff}, in a hot fusion plasma are usually derived by a multi-chord measurement of the Bremsstrahlung emission in the visible wavelength range and a subsequent Abel inversion. Active Charge Exchange Recombination Spectroscopy (CXRS) has given access to the measurement of local light impurity densities. Both the Abel inversion of visible Bremsstrahlung and the analysis of CXRS are sensitive to errors in absolute calibration and moreover require precise experimental data of electron density profiles.

The recent discovery at JET of motional Stark features in the excited Balmer-Alpha spectrum of injected fast neutrals has lead to a number of new tools for the diagnosis of local plasma parameters. The options encompass the measurement of fast neutral density, the density, temperature and velocity of deuterons, magnetic fields, and finally the effective ion charge.

Local values of Z_{eff} can be derived from the ratios of line intensities of the Doppler shifted Balmer-Alpha spectrum, which is associated with the ion impact excitation of the fast neutrals, and that of the thermal charge exchange D_α spectrum. The intensity of the first is a measure of the local ion density, that is fully stripped impurity ions plus bulk plasma ions. The intensity of the thermal CX feature is proportional to the local deuteron density. Fig.51 shows D_α charge exchange spectra for two discharges with different values of Z_{eff}. The increase in the proportion of Doppler shifted emission at the higher Z_{eff} can be seen clearly. It should be emphasized that the Active Balmer Alpha Spectroscopy technique does not depend on absolute calibration and is therefore not subject to coatings on observation windows which occur during plasma operation. Routine checks of absolute calibration are becoming increasingly cumbersome in the presence of beryllium and even more so in any future active phase device. Although it is clear from the spectra shown in Fig.51 that the method has great potential, some further work will be required on the charge exchange rate coefficients before it can be turned into a routine diagnostic.
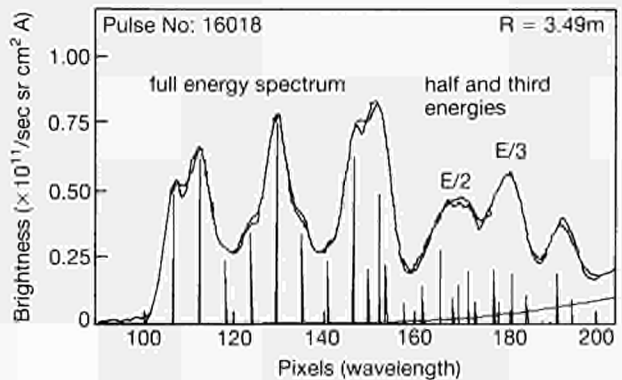
Fig.51: The full D_α spectrum showing the beam, charge exchange and edge emission for two discharges with different values of Z_{eff}. The ratio of beam to charge exchange components can be seen to respond to Z_{eff}.

Magnetic Field Measurements based on the Motional Stark Effect

The numerical procedure analyzing the observed Stark multiplet in the Doppler-shifted Balmer-alpha spectrum of fast neutrals has been further advanced. In the case

of known toroidal fields (from equilibrium calculations) and flux geometry, the measured wavelength splitting, $\Delta\lambda_{Stark} = const. \mathbf{v} \times \mathbf{B}$, leads to values of local poloidal fields which agree within 10% to predicted values as shown in Fig.52. However, the present state is rather a consistency check than an independent diagnostic. Detailed comparison has shown that total field values can be recovered by this technique with an error of <5%. Preliminary results obtained during a time resolved measurement (t = 50ms) indicate oscillations of the deduced field in phase with sawtooth activity. For future operation, a polarization sensitive detection facility will be implemented. This should enable measurement of both total magnetic field strength and its orientation. The advantage of this method is that it provides a local measurement of both poloidal and toroidal field which will be of considerable use in the study of MHD stability and Lower Hybrid Current Drive. A further aim is to investigate the options of higher resolutions in space and time.
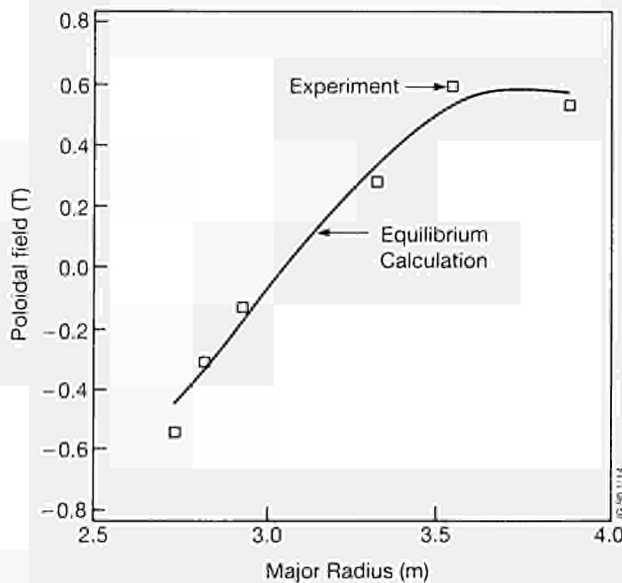
Fig.52: The poloidal magnetic field obtained from the Stark splitting of the beam D_α emission compared with that from the inversion of the magnetic diagnostics.

VUV/XUV Spectroscopy and Bolometry

In preparation for the JET Beryllium phase, several spectroscopic systems have been upgraded. A spatial scanning capability has been added to the XUV system. It has been mounted on a new frame which can be moved up and down by a hydraulic ram. The shortest scanning time is ~1s during which the line of sight is moved from ~10° below mid-plane to ~40° below mid-plane (to a point slightly above the X-point region).

Part of the direct view of this instrument is intercepted by a mirror at 45° for calibration purposes. Now an 8m long quartz fibre has been added to transfer visible light to a 0.6m Czerny-Turner instrument, equipped with a channel plate detector and an Optical Multichannel Analyser. The system has been calibrated

down to 2100Å and the 2270Å Carbon line has been observed. The system was mainly used to monitor the strongest Be lines at 3130.6, 3321, 3720 and 4573Å.

In anticipation of the installation of the LH system on Octant No.3, the VUV Broadband and the XUV Spectroscopy systems were transferred to Octant No.6, replacing the upper horizontal channel of the VUV Spatial Scan Spectroscopy System. Thus, all major spectroscopic systems are concentrated on Octant No.6 which will permit direct comparisons and cross calibrations.

The active-phase double Crystal X-ray Spectrometer has been brought to a state of reliability where it produces data routinely for the first time following commissioning in 1988. It was used to provide a monitor of the plasma oxygen content during the beryllium campaign. Fig.53 shows the development of the O concentration obtained from the 18.97Å line of O VIII at the time of the first beryllium gettering. As expected, the tight binding of oxygen to beryllium results in the virtual disappearance of oxygen from the plasma.
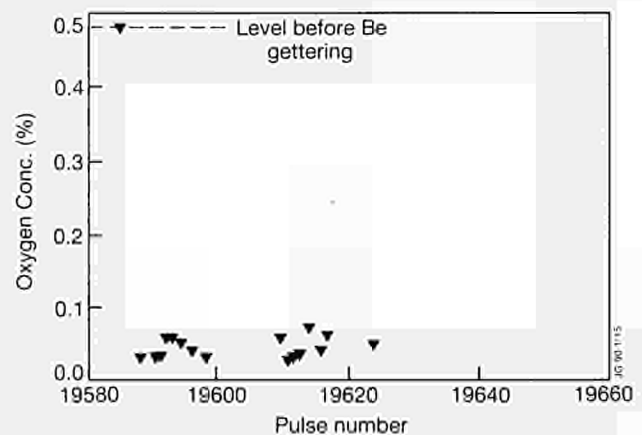
Fig.53: Oxygen concentration obtained with the active phase crystal spectrometer versus pulse number at the time of the first beryllium gettering.

Due to the relatively poor spatial resolution of the present bolometer system for the X-point region, a new, miniaturized X-point 12 channel bolometer camera has been limited with an expected resolution of ~70mm toroidally and with a much increased sensitivity. The camera and its associated electronics is being installed during the 1989-90 shutdown.

Soft X-Ray Diode Arrays

The 100 channels of the vertical and horizontal soft X-ray diode arrays continue to operate reliably and the toroidal arrays are also in full routine operation. An investigation has been made of the feasibility of using these arrays with the two filter technique to determine plasma temperature and density profiles on a rapid timescale (5µs) to study fast MHD phenomena. This method works reliably and a new set of filters will be fitted to the vertical camera with two thicknesses of Be

alternating between successive channels. This will be combined with the similar data already available from the horizontal camera to produce the temperature and density profiles.

A new trigger system has been introduced which allows any of the soft X-ray signals to be examined in real-time and particularly interesting events can be selected by suitable software. For example, an algorithmn for the detection of sawteeth is incorporated which permits data to be taken at high frequency in a short interval around the crash. Sophisticated programmable signal processing chips are employed in this system.

Development work has continued on the real-time tomography. The system is based on a PC with a serial link to a set of transputers which will carry out the tomographic inversions and also drive a real-time display. This system is now running on test data and inversion speeds considerably greater than required have been achieved. Typical data displayed on a high resolution graphics display is shown in Fig.54. The system will be in full operation in 1990.

Fig.54: High resolution graphical display of tomographically inverted soft X-ray data generated by the transputer system.

The signal processing techniques that are being developed will have wider applications in JET and NET. Intelligent data pre-processing is necessary for systems with a large number of signal channels in order to reduce the amount of data collected. Such considerations will become important for all data channels in NET since pulses will be 100-1000 seconds long. Data compression of this kind will be necessary for the high frequency imaging detectors which are being considered for installation in JET's spectroscopic systems. A transputer application is being considered which could invert the magnetic signals in real-time to provide control signals for amplifiers controlling the

shape and position of the JET plasma. Such a system could be supplied with additional information for the real-time X-ray tomography.

Pulse Height Analysis

This system provides X-ray spectra in the range 2 - 30 keV from which electron temperatures and medium to high-Z impurity concentrations can be obtained. For example it has been used to look at Nickel K lines following laser impurity blow-off (see Fig.55).
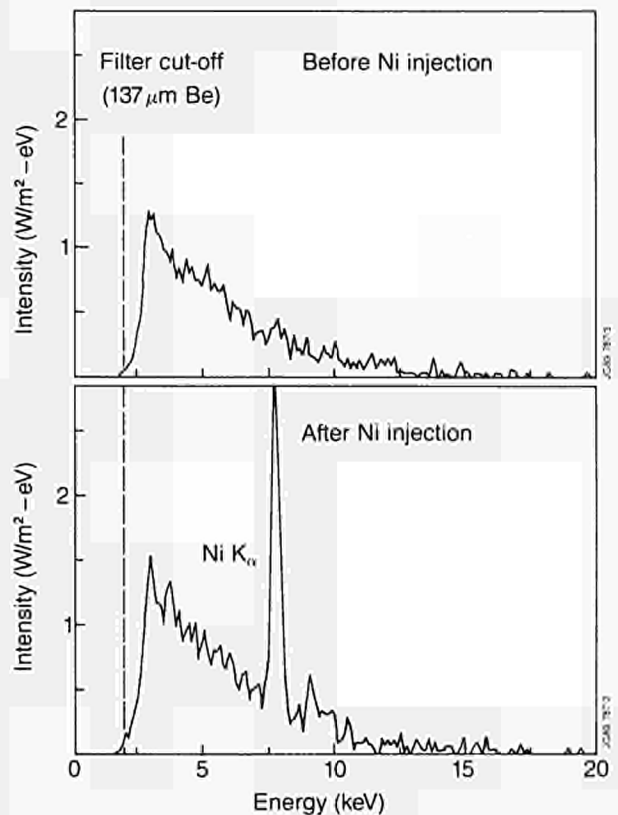
Fig.55: Soft X-ray spectrum from the pulse height spectrometer clearly showing the K-line of Ni produced by the injection.

The present three detector system can detect energies up to a maximum of 30keV. The Lower Hybrid Current Drive system will accelerate the current carrying electrons to energies of hundreds of keV. γ-rays with comparable energies will be produced by collisions between the electrons and the plasma ions. To diagnose the fast electron energy distribution a Ge detector has been procured which is sensitive up to hundreds of keV. This will be installed on the machine for the initial 2MW lower hybrid experiments.

Impurity Transport Following Laser Blow-Off

Small quantities of impurity ions have been injected into JET plasmas by a laser blow-off method. Since the impurities are all created at a well defined time, this is an excellent method for studying transport from the plasma edge to interior. The major part of this study has

used the soft X-ray diode arrays to measure the spatially resolved X-ray emission and then relies on modelling of the emission to determine transport coefficients. Typical signals are shown in Fig.56. The main results were obtained with Ni and Mo injection and tomographic inversion was used to obtain profiles of X-ray emission.
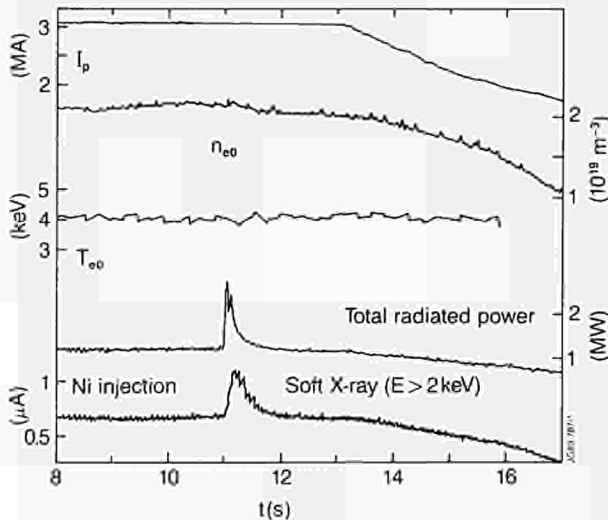
Fig.56: Overview showing the effects of laser induced injection of Ni into the plasma.

One of the most interesting results is the very important role of the q=1 surface in preventing inward diffusion of the impurities except during a sawtooth crash where partial but not complete in-filling of the core region occurs. Modelling of the observed signals have been made with a 1-D impurity transport (from CEA Cadarache, France). The data can be explained by a diffusion coefficient which is an order of magnitude larger at the edge compared with that at the centre. The central values of diffusivity are of the same order as given by neoclassical theory but are much higher than theory outside the q=1 surface. The convection velocity was also determined. During the sawtooth the diffusion coefficient must be substantially increased (by ~x10⁴) to reproduce the experimental measurements. It is possible that this technique can provide information on the sawtooth mechanism and investigations are under way. A change of transport within the q=1 surface of tokamaks has been long suspected and has been clearly demonstrated by these JET experiments.

Neutral Particle Analysis

A single Neutral Particle Analyzer (NPA) was installed at the bottom of Octant No.1, replacing the NPA array at Octant No.3, which was removed at the end of 1988 to make room for the Lower Hybrid System. 1989 operation reinforced the need to upgrade the NPA to allow measurement to higher energies, and to provide better immunity to neutron induced noise by discrimination and shielding. The new time-of-flight

analyzer under construction at ENEA-Frascati, Italy, will serve these needs, giving a reduction of ~10^3 in γ and neutron induced noise, and a further factor of ~10^2 will be gained by shielding. The new NPA will be usable in the presence of fluxes of ≈10^{20} neutrons/s, characteristic of the D-T phase. Calibration of the new analyzer has been performed in H, D, and He up to 200 keV. Further high voltage modifications and tests will be performed during installation to investigate extension of the energy range to 500 keV for more reliable measurements of ion temperatures and for α-particle simulation experiments. Since accurate measurements of pulse delays on nanosecond time-scale is important, extensive testing and calibration of the long cables between the NPA in the Torus Hall and data recording instrumentation is in progress. The neutral particle analyzer will be operational when JET restarts in 1990.

Interferometry and Polarimetry

The multi-chord far-infrared system has continued to provide routine measurements of line-integrated electron density. New reinforcing rings around the inside of the vacuum vessel have reduced the displacements of retro-reflectors mounted on the inner wall from ≈10mm down to <1mm, thereby considerably improving the performance of the lateral chords.

Work on polarimetry has concentrated on determination of the safety factor on axis, q_0, and on assessment of systematic errors in this parameter due to (a) birefringence, (b) toroidal field pick-up, and (c) uncertainties in the flux-surface geometry. Taking measurements of these effects into account has confirmed previous conclusions that q_0 reaches values significantly below unity in sawtoothing plasmas, $q_0 = 0.75 \pm 0.15$:

- Plasma birefringence gives rise to deviations from linear polarization of the transmitted beam, which corrupts the Faraday rotation measurement. By measuring the phase as well as the amplitude of the beat signal between the transmitted and reference beams on a single chord, the error due to birefringence can be estimated. This is found to be <3%. Nevertheless, a routine measurement of birefringence will be introduced on all chords in 1990;
- Parasitic effects due to misalignment of the probing beam with respect to the toroidal field were assessed by making Faraday rotation measurements with normal and then reversed toroidal field, leaving other plasma parameters unchanged. Errors due to toroidal field pick-up were shown to be insignificant;
- The uncertainty in the assumed elongation of the central flux surfaces is a source of error in the inferred q_0. The requirement of consistency of Faraday rotation measurements made simultaneously on the vertical and lateral chords and the IDENTC equilibrium identification constrains the elongation

K_0 to within ~4%. A corresponding error of ~8% is deduced in the inferred q_0.

An equilibrium identification code, IDENTD, has been developed to satisfy the magnetic and polarimetric measurements simultaneously. This further constrains the inferred current density profile and the deduced q_0. This procedure is routinely applied, and confirms the above conclusions about the value of q_0.

The change in the q-profile when a sawtooth occurs has been studied by Abel inversion of the difference in the density and Faraday rotation signals before and after the collapse. From these studies, it is inferred that $\Delta q_0(max) \approx 0.03$, that the reduction in q_0 during the recovery between sawteeth is linear in time, and that $\Delta q > 0$ at $r(q=1)$. This implies that this surface moves inwards during a sawtooth, confirming an observation made using the 'snake' oscillation [8].

References

[1] M Forrest, P Carolan and N J Peacock. Nature, Vol 271, 718-722 (1978).

[2] T P Hughes, D A Boyd, A E Costley, J A Hoekzema, S Smith, E Westerhof, Proc. 16th European Conf. on Controlled Fusion and Plasma Physics, Vol 13B part IV, 1509-1512, Venice , Italy (1989)

[3] T P Hughes and S R P Smith, J Plasma Physics, 42, 215-240 (1989)

[4] M. Fleischmann and S. Pons, Journal of Electroanalytical Chemistry 261 (1989) 301 and 263 (1989) 187.

[5] S.E. Jones, E.P. Palmer, J.B. Czirr, D.L. Deglaur, G.L. Jensen, J.M. Thorne, S.F. Taylor and J. Rafelski, Nautre 338 (1989) 737.

[6] A. De Ninno, A. Frattiolillo, G. Lollobatista, L. Martinis, M. Martone, L. Mori, S. Podda and F. Scaramuzzi, Europhysics Letters 9 (1989) 221.

[7] G.M. McCracken, M. Bailey, S. Croft, D.S. Findlay, A. Gibson, R.P. Govier, O.N. Jarvis, H.J. Milton, B.A. Powell, G. Sadler, M.R. Sene, D.R. Sweetman, P. van Belle and H.H. Watson, "Experimental Search for 'Cold Fusion' in the Deuterium-Titanium System", CLP-P864.

[8] A Weller et al., Physics Review Letters, 59 (1987) 2303.

Summary of Machine Operation

During 1989, JET operations were essentially made up of three main periods:

a) The First Period (Weeks 4 to 21)

This period included the following activities:

- Extensive CODAS and Power Supplies commissioning (Weeks 4 to 11) which were carried out as normal or extended day operation;
- Further Power Supplies recommissioning in Weeks 12 to 14 (one shift in a double-shift day with the other shift devoted to vacuum leak checking and repairs);
- Difficulties in re-establishing clean ultra-high vacuum conditions in the torus required further vessel washing, cleaning and baking extending to the end of Week 17;
- Restoration of plasma operation (Weeks 18-19). This was more difficult than usual because the new in-vessel geometry required modifications of the position control. Wall conditioning and the commissioning of diagnostics, additional heating and plasma control systems, also took some time. Long-pulse operation tests were carried out ($B_T = 1.7$ T for 60 s and 3 MA for 33 s). In addition 10s duration X-point plasmas were produced;
- Operation (Weeks 20 and 21) with carbon tiles were carried out in this period to obtain results for comparison with those using Be-coated walls (following evaporation), and then Be limiter tiles and Be-coated walls in the two later periods. Operation with belt-limiter, inner wall and X-point plasmas was pursued. A new mode of operation was successfully introduced, that of sweeping the X-point position back and forth in front of the X-point tiles to reduce this heat load which typically terminated a discharge disruptively (the carbon "bloom"). This was undertaken for the double-null X-point configuration. First signs of a possible toroidal field (TF) coil irregularity were noted.

b) The Second Period (Weeks 22 to 29)

In this period, the in-vessel surfaces were coated with a layer of beryllium. This period included one week of scheduled maintenance (Week 24), during which repairs were carried out to the neutral beam heating system. This restored operation of one ion source and thereby make available the full NB heating capability, including two 140 kV beam lines. Throughout this period there was a significant amount of time devoted to studying the suspected TF coil faults.

The evaporation of beryllium produced outstanding performance and improvements which are detailed in the section on Scientific Achievements. Extensive high power operation resulted in in-vessel overloading of protection tiles and their supports. This led to the termination of operation in Week 29 to effect repairs and to prepare for the next phase in the assessment of beryllium as a first wall material.

c) The Third Period (Weeks 37 to 40)

This period was preceded by 7 weeks of in-vessel work in which wall damage was repaired and the

graphite tiles on the belt limiter and on one RF antenna were replaced by beryllium tiles. This work was made more difficult by the fact that the vessel interior was coated with beryllium and therefore in-vessel staff had to wear pressurised suits. After a certain learning period, an effective routine for such work was established, including the precautions necessary and the safe handling of beryllium waste.

Week 37 was devoted to recommissioning the power supplies and restoring plasma operation. Following intensive study of the TF coil in operation and during local tests, the performance of the toroidal field was limited both in voltage applied and in the maximum current drawn.

Weeks 38 to 40 were then devoted to an assessment of the new in-vessel situation : beryllium tiles and a layer of beryllium were evaporated onto in-vessel surfaces. This proved to be even more successful than the previous period, resulting in new record plasma performance. Machine systems functioned well for a three week (6 days per week) period of high power operation without remedial or maintenance work.

The TF coil fault which was noticed in Week 21 and which led to a limitation in toroidal field system performance meant that one TF coil will be exchanged during the 1989/90 shutdown which started in Week 41.

The machine was operated for 90 days during the February - October period. A significant number of these days were required for commissioning of power supplies and for recommissioning of plasma operation. This latter activity was significantly time-consuming in 1989, following:

- In-vessel modifications (to strengthen the vessel to withstand disruptions at 7 MA); and changes in

the radial position control power supplies (to improve the vertical field performance) which were carried out in the 1989/90 Shutdown. Other work carried out in this shutdown which required commissioning time included: the installation of Be evaporators; fibre reinforced upper X-point tiles; two 140 kV NB lines at Octant No 4; and continued upgrading of the ICRF generators from 1.5 to 2 MW each;

- The first beryllium evaporations;
- The vessel entry in which the graphite limiter tiles and the graphite tiles for one antennae were replaced by beryllium ones.

This resulted in only 56.5 double-shift days during which the experimental programme could be carried out. The distribution of these operation days among the different heating programmes was as follows:

11.5%	Ohmic (OH) heating
20.4%	Radio-Frequency (RF) heating only
23.9%	Neutral-Beam (NB) heating only
44.2%	Combined (NB and RF) heating

The allocation of time to the different activities and the number of days in the various heating programmes is shown in Fig.57. The experimental programme was carried out within four Task Forces and the 56.5 double-shift operation days in which they were involved were distributed as follows:

Task Force A (Performance Optimisation in Limiter Plasmas)	25.2%
Task Force B (Performance Optimisation in X-point Plasmas)	26.1%
Task Force C (Reduction of Impurities and Fuel Enrichment)	30.4%
Task Force D (Physics Issues)	18.3%
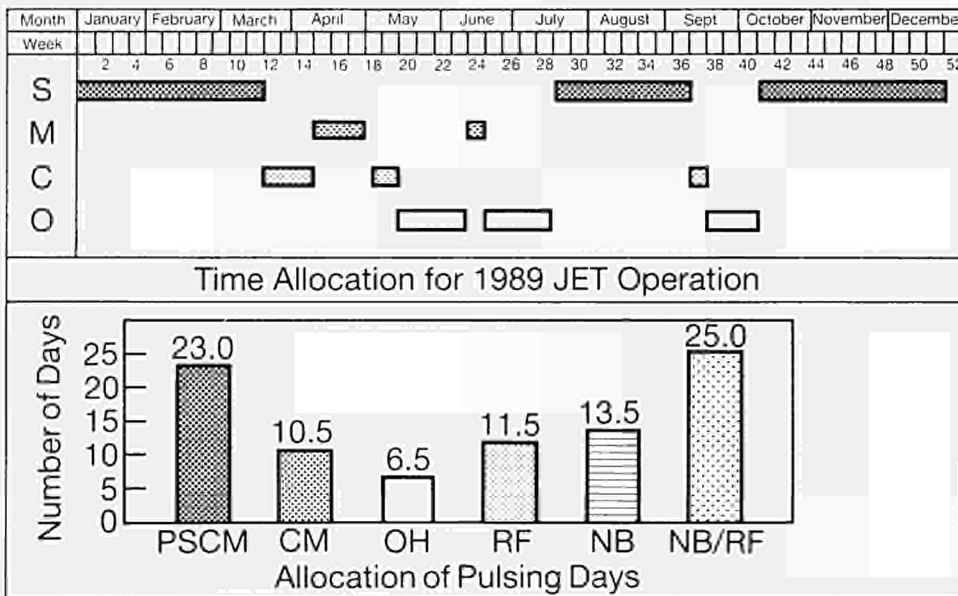
Fig. 57 Allocation of days in which machine pulses were performed during 1989. S = shutdown. M = maintenance and repair. C = commissioning. O = operation; PSCM = power supplies commissioning. CM = integrated commissioning (not specifically power supplies). OH = ohmic heating. RF = radio-frequency heating. NB = neutral beam heating. NB/RF = combined (NB and RF) heating.

The organisation of operation time was altered from 1988 in that a significant amount of commissioning was undertaken in double-shift days, and Saturday double-shift operation was extensively used (13 times). Further, considerable CODAS and Power Supply Commissioning was carried out in early 1989 in parallel with shutdown work.

The number of pulses in 1989 was 2244, bringing the total number of cumulative JET pulses to 21030. The relative number of commissioning pulses continues to decrease (Fig.58). Even more significant is the increasing number of discharges with plasma current exceeding 3 MA, which for 1989 brought the cumulative total to about 5800. A comparison between the current pulse distributions for 1988 and 1989 is shown in Fig. 59 and reflects a continued movement to operation at higher current values in 1989 and a reduction in the number of low current (<1 MA) values.

In spite of the limited time available for operation and hence the smaller number of pulses, 1989 was a year in which considerable technical advances were made and progress achieved in plasma performance was outstanding.
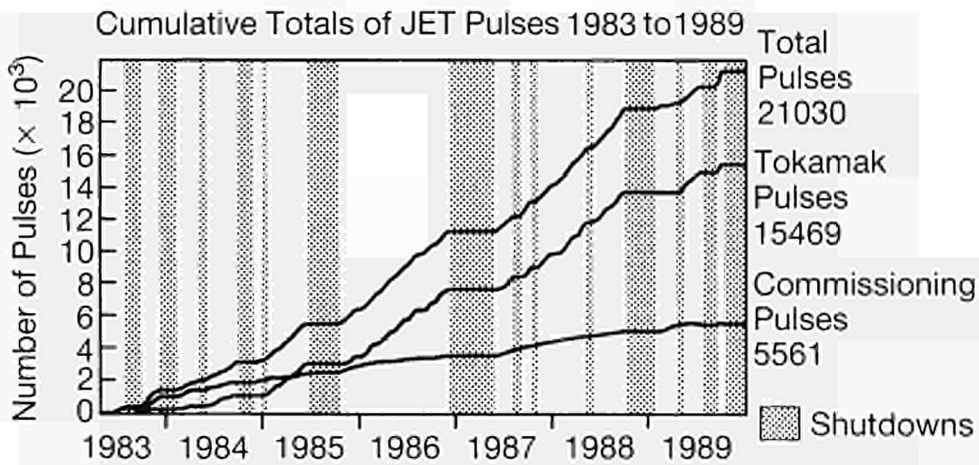
Fig. 58 Cumulative total of JET pulses.
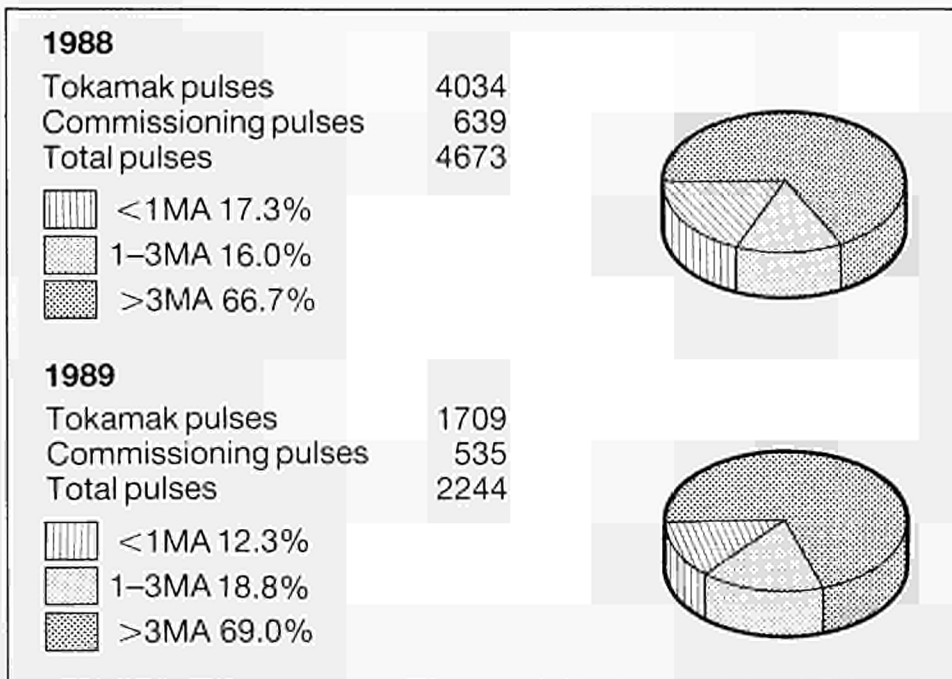
Fig. 59 Relative plasma current distribution for 1988 and 1989.

Summary of Technical Achievements

During the early part of 1989, the machine was in a scheduled shutdown period. The two main tasks during the shutdown were to reinforce the vacuum vessel and to inspect and, if required, repair the ohmic heating coil.

The vessel reinforcement had been planned in early 1988 and work started in October 1988. It consisted of welding inconel rings inside the vessel at the inboard wall to strengthen the vessel against disruption forces. This work which involved a large amount of accurate fitting and heavy welding inside the vessel was successfully completed early in 1989. This work was followed by a careful realignment of the wall protection tiles at both the inboard walls and upper X-point region, to distribute better the heat flux on these tiles where plasma contacted them. After closure, operation restarted but an unusually high impurity level soon revealed that a foreign object was trapped inside the vessel. After inspection, an overlooked cable was located behind the belt limiter tiles. It was then necessary to thoroughly clean the vessel with mild detergent before operation restarted. This unfortunate mishap demonstrated the need for a tighter control of the work and equipment brought inside the vacuum vessel and necessary measures have now been implemented.

Inspection of the ohmic heating coils showed that the problem of coil rotation which had been discovered in 1987 had not recurred. The modifications carried out at the end of 1988 seemed to have been effective.

The salient feature of 1989 operation was the use of beryllium as a first-wall material. For initial beryllium operation up to July 1989, the first-wall design was unchanged. In particular, graphite tiles were still used for the belt limiter, ICRF antennae and wall protections, but all surfaces were coated with a thick layer of evaporated beryllium. Beryllium coating was achieved by means of four beryllium evaporators located at the outboard wall near the equatorial plane. Operation of the evaporators was highly successful and led the way to important results. Some minor technical problems with the evaporators were rectified in July 1989 and this allowed fault free operation until October 1989.

In July-August 1989, the graphite tiles on the belt limiters and ICRH antennae were replaced with beryllium tiles. This operation was not difficult but for the first time, required personnel access to a beryllium contaminated vessel. The first intervention inside a beryllium contaminated vessel proved more difficult than expected. A major effort was required to provide manpower support related to the use of air ventilated suits. Operations such as the dressing and undressing of personnel and the cleaning of the suits required more personnel than anticipated. As a result, this shutdown for the installation of the beryllium belt limiter and antennae tiles took longer than planned. However all operations were carried out in safe conditions, beryllium contamination was well contained and considerable experience was gained in the use of the Torus Access Cabin, the use of suits, and the Health Physics requirements for beryllium monitoring. The smooth running of the subsequent late-1989 shutdown demonstrated that beryllium operation and technical support for intervention in beryllium contaminated areas was well under control.

Operation with beryllium tiles has been successful but as expected local melting of tiles cannot be avoided. Damage on the belt limiter tiles was minor but on some of the ICRF antennae protection tiles, bulk melting occurred at tiles adjacent to the neutral beam injection port. The cause of the melting seemed to be due to a local plasma-beam interaction leading to a significant fraction of the beam energy falling on the protection tiles. Although 1989 operation time was short (no more than 11 weeks), operation was a great success due to the use of beryllium and to the excellent reliability of all other systems. Neutral beam operation was highly reliable and included for the first time two injectors at 140kV (30A deuterium). A major improvement to the ICRH system was the successful operation of the real time automatic tuning system which allowed fast changes of the plasma parameters to be followed, and in particular, transitions from L- to H-mode.

In late May 1989, an electrical fault was detected by the toroidal field fault detection system. Investigation showed that one coil exhibited low turn-to-turn insulation resistance between a number of turns. The fault did not prevent operation but was potentially a threat to the machine since it was not possible to predict its evolution. It was decided to replace this faulty coil with one of the spare coils. The shutdown foreseen in November 1989 was brought forward to start in October 1989 and extended to allow for the coil replacement.

Other important activities during the shutdown were the installation of the ICRH antennae beryllium screens, the assembly of the prototype lower hybrid launcher and the installation of the fast single-shot pellet injector gun. The removal of a toroidal field coil is a major operation requiring a large effort in terms of organisation, preparation of work procedures and planning. By the end of December 1989, the in-vessel work required to separate one machine octant was complete and Octant No.3 containing the faulty coil was ready to be lifted out of the machine.

Scientific Achievements during 1989

Introduction

For 1989, the system of operation of the scientific programme was the same as that in 1988. The programme operated for a series of campaign periods, the standard being of eight weeks duration (composed of six weeks tokamak operation and two weeks of maintenance/commissioning). Two Programme Leaders were nominated with responsibility for formulating near programme proposals (one campaign ahead) and outline plans (two campaign periods ahead). These proposals were presented to the JET Experiments Committee for discussion and approval. These proposals were within the broad outline of the JET Development Plan and subject to guidelines provided by the Experiments Committee.

Programme Leaders for 1988 were:
K.J. Dietz and J.G. Cordey

Four Task Forces carried through the programme, as follows:

Task Force	Task Force Leader
A) *Optimisation of Performance in Limiter Plasmas* (including progression to the highest fusion product, long pulse operation, investigating high confinement regimes, α-particle simulations, etc.);	P. Lomas
B) *Optimisation of Performance in X-Point Plasmas* (including progression to the highest NB and RF powers and attempts at quasi-steady-state operation);	A. Tanga
C) *Reduction of Impurities and Fuel Enrichment* (exploring methods of reducing impurity production by developing wall conditioning and appropriate operational procedures, including beryllium operation, density control experiments, pellets, fuelling with beams, gas puffing, etc);	P.R. Thomas

D) *Physics Issues* (studying physics issues particularly relevant to next-step devices, including disruption control, sawtooth stabilisation, particle and energy transport studies, current drive (NB, RF, LHCD, etc.), operational scenarios for next-step devices, etc);   J. Jacquinot

Task Force Leaders were appointed with responsibility for (i) interacting with and advising Programme Leaders on programme requirements within that task area; (ii) devising and setting out a detailed programme for allocated time within a campaign period; (iii) driving through that task programme (including acting as Control Room representative); (iv) analysing data (in conjunction with Topic Leaders, if appropriate); (v) disseminating information in the task area through internal meetings and publications (in conjunction with Topic Leaders, if appropriate).

In addition, Topic Groups were formed, as follows:

Topic Group	Topic Leader
(a) Energy and Particle Transport;	M.L. Watkins
(b) Plasma Edge Phenomena and Impurity Production (including fuelling and recycling);	L. de Kock
(c) MHD and Disruptions (including sawteeth);	D.J. Campbell
(d) Next-Step Scenarios and Implications for JET	P.P. Lallia

Topic Group subjects are of longer term interest than the immediate tasks undertaken by the Task Force Groups. The Topic Groups are responsible for analysis of results within many areas across the Task Force spectrum, but they also have responsibility for advising Programme Leaders on programme requirements which are topical and relevant to the Groups areas of activity. In addition, the Groups disseminate information through internal meetings and in external publications.

Programme Objectives

JET operation during 1989 was devoted to the assessment of beryllium as a first-wall material. The

reason for the introduction of a new first-wall material was that impurity control in JET, as for other long-pulse high power tokamaks, is of fundamental importance.

Plasma facing materials must be selected so that impurity influxes and their impact on the plasma are minimised. Therefore, these materials should have very low atomic number (low-Z), low chemical interaction with hydrogen, high melting point or sublimation temperature, good thermal conductivity and shock resistance, low erosion through sputtering and should preferably be a getter for oxygen.

The main advantages of beryllium are its low-Z value, which leads to reduced radiation, its strong getter action and its strong wall pumping properties. The main disadvantage its its low melting point of 1280°C. However, for graphite, the temperature of surfaces in contact with the plasma is limited to 1000-1200°C due to self-sputtering, but in contrast to beryllium it can reach much higher temperatures before being damaged.

Beryllium was introduced into JET in two different ways: initially as a thin evaporated layer on the graphite walls and limiters; and later, in addition as a limiter material. Operations under these conditions were compared with results with graphite.

Operations were carried out consisting of three phases:

Phase I: Start-up as a graphite machine after a prolonged shut-down, to re-establish conditions and provide a reference set of parameters in this configuration;

Phase II: Beryllium evaporated on all internal surfaces: ~300A average thickness for each evaporation, about 240g of beryllium were evaporated in 26 evaporations;

Phase III: Operation with beryllium tiles on the belt limiter, and around certain RF antennae: installation took place in full biological protection.

The scientific achievements for 1989 in these phases are described in the following sections, within the Task Force and Topic Group headings.

Optimisation of Performance in Limiter Plasmas

Introduction

The major goal of the task force was to prepare for and undertake high power heating studies in **optimised** plasmas in the limiter configuration with plasma currents up to 7MA. As a result of earlier heating

studies at 5-6MA[1], sawteeth, broad profiles, lack of density control and poor fuel concentration were identified as factors which limited the performance of such discharges. Thus, experiments in these areas were undertaken in scenarios directly relevant at 7MA, including assessment of beryllium as a first wall material. In addition, the subsidiary goals of fusion yield optimisation and α particle simulations were addressed.

Major results included the suppression of sawteeth well into the flat-top of 5MA discharges and peaked density profiles established at 5MA by pellet injection. In the former case, $T_e \leq 12.5$keV was demonstrated with modest ICRH power. In the latter case, central densities $n_{e0} \leq 2.8 \times 10^{20}$m^{-3} were achieved and successfully reheated, showing the transient pellet enhanced phase. The fusion yield of 5MA plasmas has been enhanced by a factor ~ x2 by the density control provided by beryllium walls and the ion temperature increased to 14keV. The fusion performance of belt limiter plasmas at 3MA was improved from $Q_{DD} \sim 5 \times 10^{-4}$ to 9×10^{-4} by the use of beryllium tiles and is now comparable to the best conditioned inner wall limiter plasmas. In addition, the record D-D reaction rate of 4.2×10^{-4}s^{-1} for a limiter plasma has been achieved using Beryllium tiles together with a new scenario for density profile control in the low density regime utilising pellet injection to provide a peaked profile with $n_{e0} \sim 7 \times 10^{19}$m^{-3}. In this case, NB/RF synergism provided a substantial improvement ($\geq 25\%$) in yield due to RF accelerated deuterons with energies above the injection energy. D-He^3 fusion yield optimisation experiments increased the fusion yield from 60 to 100kW. The understanding of the behaviour of fast MeV ions in these and related experiments increases our confidence in α particle behaviour in future JET experiments.

Development of High Current Scenarios

Optimisation of Current Ramp Phase

In 1988, a current ramp rate of 0.75MAs^{-1} was demonstrated up to 7MA using simultaneous B_t/I_p ramp to hold q_ψ constant and thereby avoid the unstable regions of the l_i-q_ψ diagram. At that time, current ramps at constant B_t were limited to 0.25MA/s at high current (5-6MA) by MHD instabilities at rational $q_\psi \simeq 3$ or 4 surfaces. During 1989, a new scenario was developed varying only minor radius and elongation to hold q_ψ constant during the current rise at constant toroidal field. Holding the toroidal field constant permits RF heating and is more relevant to ITER. At $q_\psi \simeq 3.5$, a ramp of 1MAs^{-1} was demonstrated up to 5MA as shown in Fig 60. The time evolution of the equilibrium is shown in Fig 61. Compared with earlier scenarios using aperture expansion[2], this evolution was unusual in keeping both minor radius and elongation small until $q_\psi \simeq 4$ was passed ~1.8s after discharge initiation and whilst the current was less than 2MA.

Although Fig 60 shows rotating MHD modes, which

Fig.60 Time traces of 1MAs⁻¹ ramp to 5MA. (Pulse No: 20360)

Fig.61 Evolution of equilibrium during fast ramp (Pulse No: 20360)

example in Fig 62. The reason for the difference between early and late MHD is associated with small differences in the current profile. Current ramps >1MAs⁻¹ were not attempted but there is no reason to expect any difficulty provided q_ψ is held constant at a non-rational value. This scenario has been used for sawtooth suppression and density profile control experiments and could easily be extended to 7MA with $q_\psi \simeq 3$. The resistive consumption (on-axis) to reach 5MA was 2-3 V-s, which is economical in V-s compared to the 1988 7MA scenario, which consumed 6.9-7.5 V-s resistive on-axis to reach the flat-top. This scenario offers an increase in the flat-top time at 7MA from 2 to ≥ 5 s.
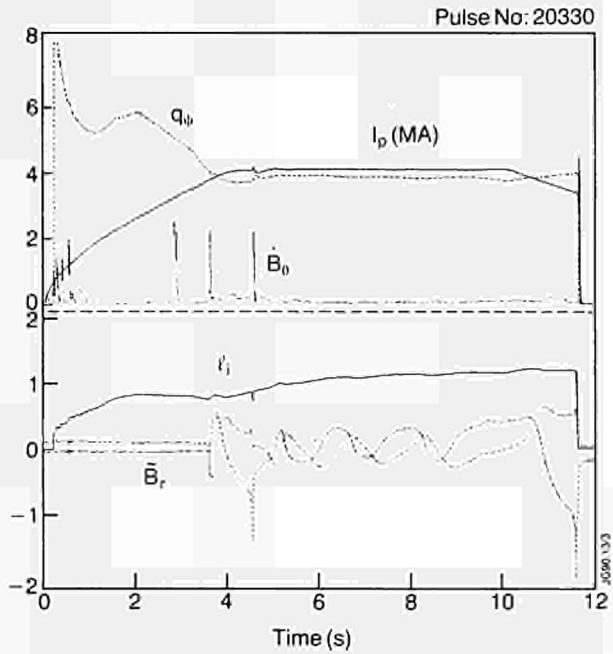
Fig.62 Unsuccessful fast ramp showing persistent quasi-sationary mode (QSM) (Pulse No: 20330)

Effects of Be Gettering and Be Limiters at 5MA

5MA flat-top sawtoothing plasmas were heated at high power (≤ 30MW) during both beryllium evaporation and beryllium belt limiter phases. This data can be compared with previous carbon belt limiter data. Fig 63 shows that global confinement is not affected and is still in line with the predictions of Goldston scaling or Rebut-Lallia scaling. Fig 64 shows the fuel concentration calculated from visible bremsstrahlung radiation plotted versus $P_{tot}/<n_e>$ for the different cases. The fuel concentrations are broadly comparable for the cases of carbon conditioned by either many helium plasma pulses or fresh beryllium evaporation and the case of the beryllium limiter. The fuel concentration is improved for the beryllium limiter case, if strong gas puffing is used. Note that high values of P_{tot}/n_e were obtained with beryllium gettering, but that n_D/n_e was only ~0.6. (Low density operation at 5MA during the beryllium limiter phase was restricted by MHD stability

became quasi-stationary at q = 4 in the unstable region of the l_i - q_ψ diagram, these modes decayed away. During the remainder of the ramp, q_ψ was held between 3 and 4. However, if $q_\psi \simeq 3$ or 4 was touched at higher currents the quasi-stationary mode arising from this rational q activity persisted through the remainder of the current rise and the flat-top and grew to disruption shortly after ramp down was commenced, as shown for

Fig.63 5MA confinement for carbon belt, beryllium evaporation and beryllium belt.
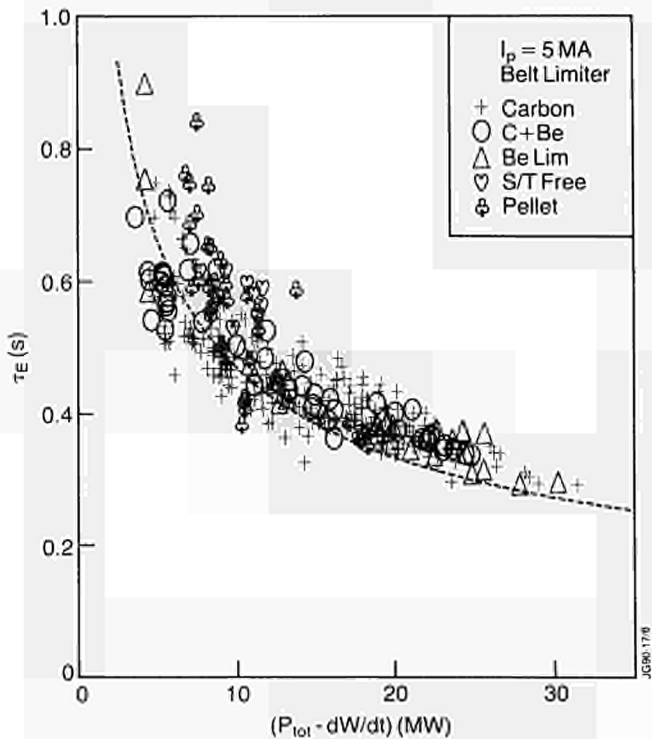
Fig.64 Deuterium concentration for 5MA limiter plasmas for carbon belt, beryllium evaporation and beryllium belt.

consistent with the improved P_{NB}/n_{e0} found with Beryllium as a result of better density control, as shown in Fig 65.

Sawtooth Stabilisation and Density Profile Control
High current (≥5MA) plasmas in JET have safety factors, q_ψ, in the range 2.5-3.5 and therefore, are directly relevant for reactor studies. These plasmas normally feature broad profiles of current, density and temperature as a result of sawteeth having a large inversion radius, and this reduces fusion performance. Experiments in 1988[3] have demonstrated that application of high power ICRF heating during the current rise phase to 5-6MA can stabilise the sawteeth for periods ≤3.5s, and results in an enhancement of all key plasma parameters. In these experiments, RF was applied before or shortly after the onset of sawtooth activity but normal sawtoothing resumed from about the time of the start of the flat-top and before the end of the RF.
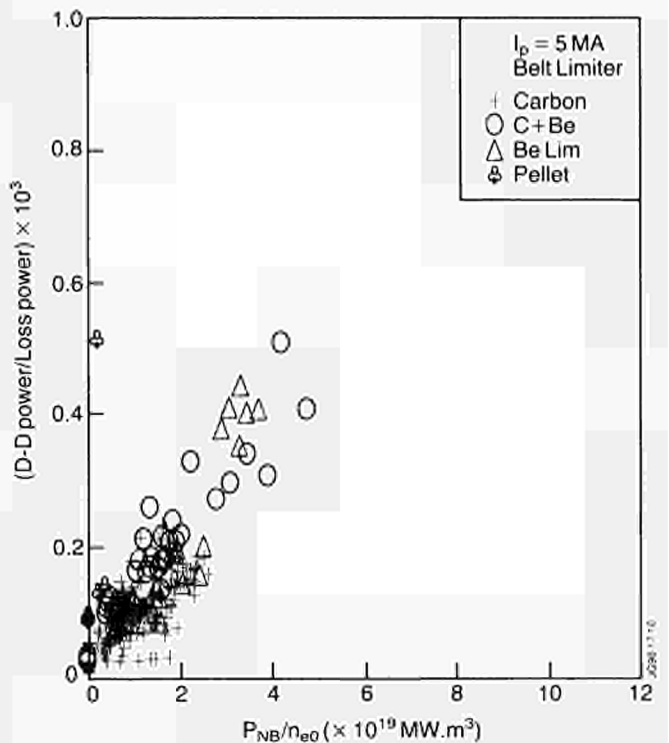
Fig.65 D-D fusion gain for 5MA limiter data comparing bare carbon, beryllium evaporation and solid beryllium.

Three types of new experiment have been carried out during the period when the carbon belt limiter was conditioned by beryllium evaporation (giving enhanced pumping and a better density control as previously described) and which utilised the fast current ramp scenario.

The first type has ICRF heating applied during the current rise phase but after the first sawteeth appear. As shown in Fig 66, sawteeth are suppressed for periods

as a result of the toroidal field limitation and not by the pumping effects of the limiter). The D-D fusion rate is improved by a factor ~x2 comparing either Be or Be evaporation phases with bare carbon. This gain is
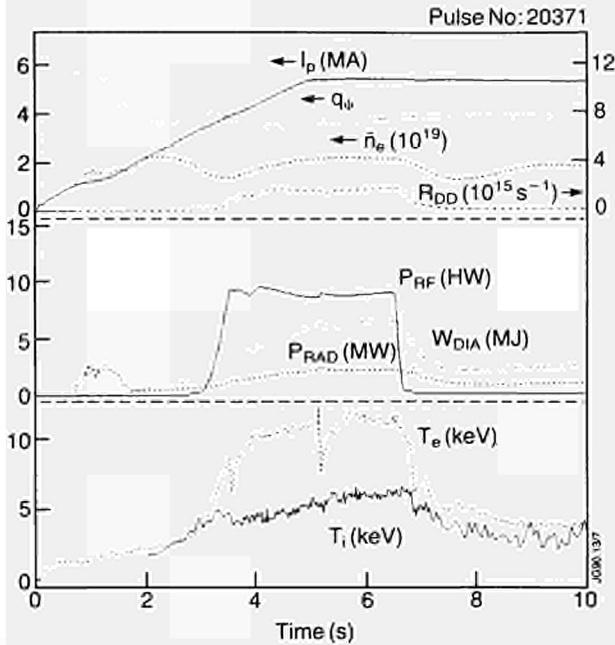
Fig.66 Time traces for Pulse No: 20371 showing sawtooth suppression during flat top of 5MA plasma following current rise heating.

Fig.67 Time traces for Pulse No: 20376 where a strongly peaked density profile is generated early in the current rise by pellets, and is then reheated by ICRF during the remainder of the current rise.

lasting several confinement times and well into the 5MA flat-top, normal sawtooth behaviour resuming after the RF is switched off. There are a few sawtooth crashes during the RF and during this time the radius of the q=1 surface grows to ~ 0.5m as shown by polarimeter and soft X-ray data[4]. Clearly, sawteeth are being transiently stabilised rather than q(0) being raised above unity. The axial electron temperature T_{e0} during the ICRF heating quickly reaches a steady value ≥12keV although current, density and ion temperature evolve with time. At 5MA, T_i is ~ 6 keV so the fusion performance is modest. The high electron temperature gives a long slowing down time and hence stored energy in fast particles builds up to ~2.4MJ. Nevertheless, there is a 10% improvement in global confinement of thermal particles and the incremental confinement reaches 0.5s. Ion heating in such discharges would be most interesting.

In the second type of experiment, a string of pellets was injected even before the start of RF to build up a strongly peaked density profile with n_{e0} ~ 1.8 x 10^{20}m^{-3} (Fig 67). During the current rise heating, sawteeth were absent and polarimeter data showed q_o > 1. During the first second of heating, both T_e and T_i rose to ~7keV and by 1.5s, T_e had reached 10keV, but T_i had fallen to 6keV, and LIDAR showed the density profile was broad with n_{e0} ~ 4 x 10^{19} m^{-3}. Soft X-ray data suggested that the profile broadening was progressive and probably associated with internal MHD activity. Whilst there are some similarities to the 'pellet enhanced plasmas'[5], this feature had disappeared by the time 5MA was reached, and sawteeth resumed shortly after. In the third type of experiment, pellets were injected at intervals throughout the current rise to
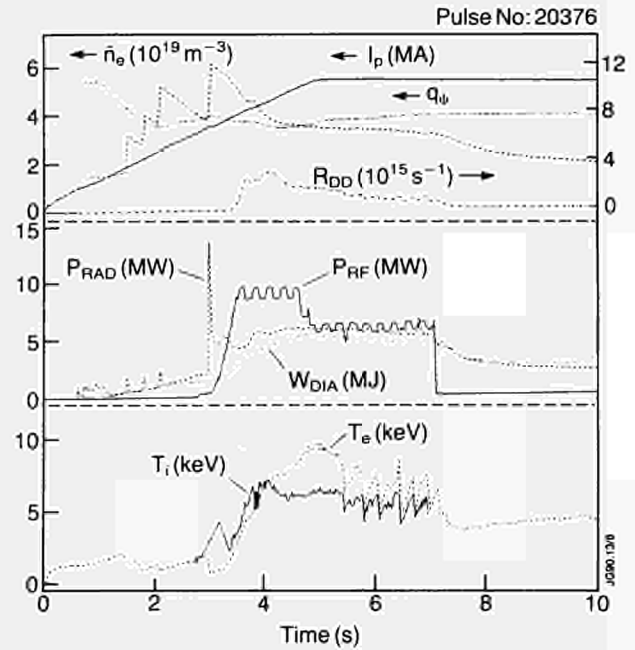
build up a peaked density profile with n_{e0} ~ 2.3 x 10^{20}m^{-3} and q_o > 1 by the time 5MA was reached. The RF was then switched on during the flat-top following the last pellet. An enhanced neutron feature was produced, as in the pellet enhanced plasmas[5], with the D-D reaction rate peaking at 7 x 10^{15} s^{-1}. Thereafter, this rate decayed but 1.5 s after the start of RF, a vestigial remainder of the peaked profile with n_{e0} ~ 6 x 10^{19}m^{-3} could still be seen on the LIDAR data. The time history of such a shot is shown in Fig 68. T_{e0} is much lower than in the other experiments and the profile is not so strongly peaked. Although sawteeth were absent, the soft X-ray data showed MHD activity 'eating away' at the gradient regions.

In a variant of this type of experiment, the last pellet was a large one (6mm) producing a record n_{e0} ~ 2.8 x 10^{20}m^{-3} (for a limiter plasma) which was successfully reheated with RF. A substantial improvement in thermal stored energy (8MJ for only 10MW RF) was obtained transiently. The temperatures were low (~3keV) and the density profile evolved to become very flat after about 1.5 s with n_{e0}~ 8 x 10^{19}m^{-3}.

These new experiments have demonstrated that in low q discharges, it is possible to suppress sawteeth (and thereby reach T_e ≤ 12.5keV) and that it is possible to produce and reheat peaked density profiles with n_{e0} ~ 2.8 x 10^{20}m^{-3}. It still remains to perform ion heating experiments using NB injection in the former scenario to realise full fusion potential.

Fusion Yield Optimisation

Assessment of Limiter Materials in High Yield Regimes
Limiter performance has been assessed for 3MA NB and combined NB/RF heated plasmas in the low density
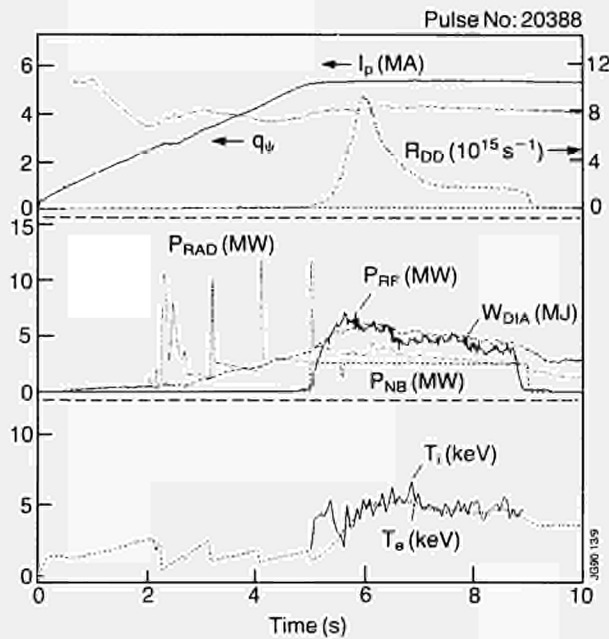
Pulse No: 20388

Fig.68 Pellet fuelling during the current rise to produce a peaked density profile at 5MA, which is then reheated by ICRF during the flat top (Pulse No: 20388)

regime, where fusion performance is greatest. Higher density regimes were covered by the Task Force on Impurities and Density Control (see later). The assessment has been performed for plasmas limited by the belt or the inner-wall tiles for the bare carbon and carbon with beryllium evaporation phases and for the beryllium belt limiter case. The tiles were poorly conditioned (after the major shutdown) for the bare carbon case and the 1988 carbon results provide a better baseline for comparison.

For the inner-wall after beryllium evaporation, a sudden strong carbon influx was seen in a time typically ≤ 1s for 18MW NBI (Fig 69) corresponding to an
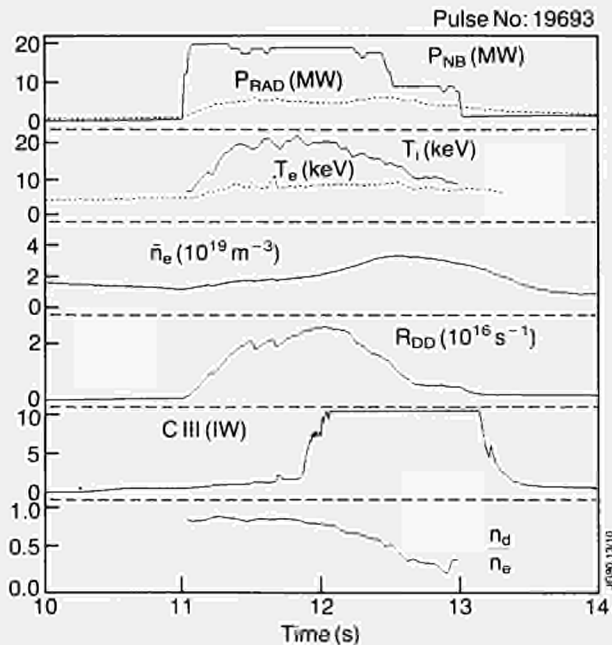
energy limit of 10-20MJ, similar to bare carbon results in both 1988 and 1989. The realignment of inner-wall tiles which was attempted before plasma operation in 1989 had no effect, and, indeed, the CCD camera shows that some tile edges reached 3000°C and were severely eroded. The higher energy limits were obtained after some tile edge erosion had already occurred and with the plasma curvature matching that of the inner-wall. In Fig 69, it can be seen that this carbon bloom caused a rapid increase in Z_{eff} and reduction in central n_D/n_e to a low value and was followed by an increase in density and a drop in temperature and neutron yield.

A similar 'bloom' effect was seen for belt limiter discharges which were too close to the RF antenna tiles, and occurred with a threshold of ~15MJ. This was caused by neutral beam particles ionised in the scrape-off layer whose orbits intercepted the antenna tiles, and was probably the cause of disappointing Z_{eff} values in 1988 for discharges closer than ~1cm to the antennae tiles.

Increasing the plasma-antenna separation for belt limiter plasmas increased the threshold for the 'bloom', until for a separation ~3cm, no sudden influx was observed even for 90MJ of additional heating energy. Instead the fuel concentration fell more slowly to ~50% and then remained steady (Fig 70). The ion temperature and neutron yield reached a peak and then fell before the central fuel concentration had changed significantly, as discussed in the next section. This result was obtained after beryllium evaporation, but experiments on the bare carbon belt did not show any sudden influx of carbon for similar large plasma-antenna separation, though in this case it was only tested up to 43MJ.

For beryllium belt limiter tiles, a sudden influx of beryllium occurred after 5-15MJ of additional heating

Pulse No: 19693

Fig.69 Low density inner wall shot with NBI heating after beryllium evaporation. (Pulse No: 19693).
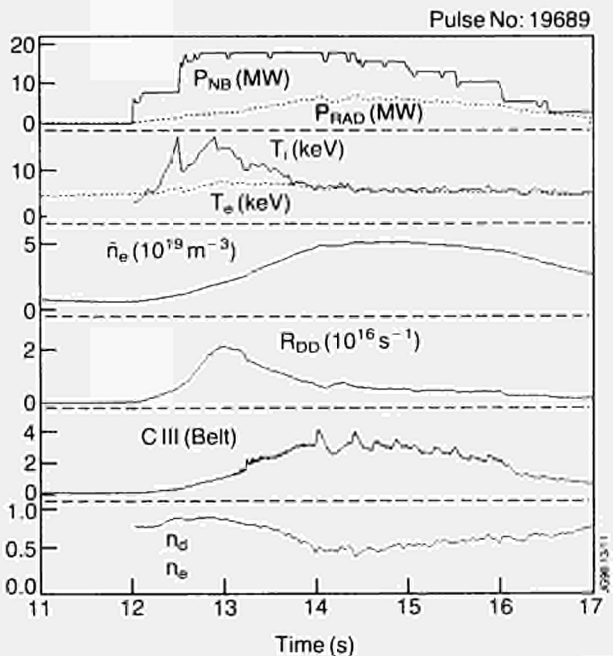
Pulse No: 19689

Fig.70 Low density belt limiter shot with NBI heating after beryllium evaporation. (Pulse No: 19689)
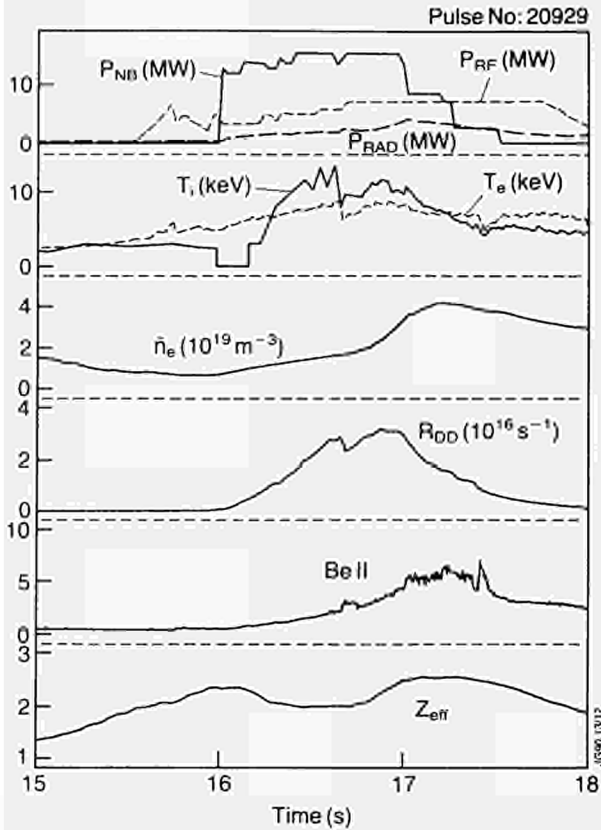
Fig.71 Low density beryllium belt limiter shot with NB and ICRF heating. (Pulse No: 20929)

for low density plasmas (Fig 71) and shortly thereafter n_D/n_e, ion temperature and neutron yield fell. Whilst the beryllium antenna tiles showed severe damage from plasmas where the plasma-antenna separation was too small, increasing this separation did not increase the threshold for the beryllium influx, as shown in Fig 72, suggesting that hot spots on the belt itself led to degradation in plasma purity. In a similar manner to carbon cases, the beryllium antennae damage led rapidly
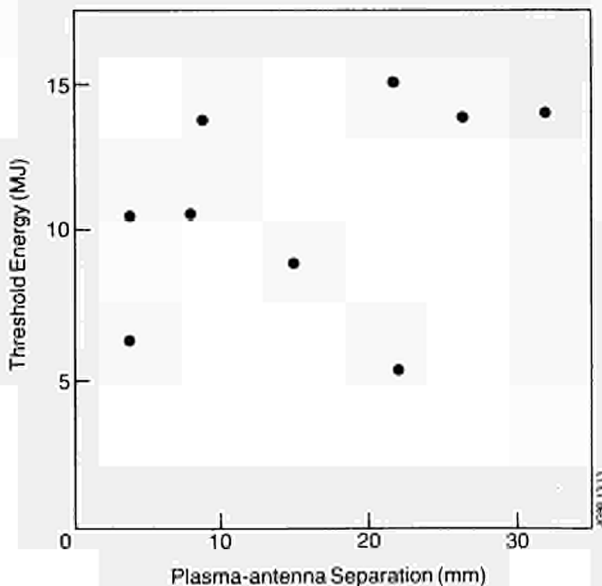
to plasmas with $n_D/n_e \leq 0.25$, but the beryllium belt damage led to $n_D/n_e \sim 0.5$ after 20MW for 2 s for example. By this time, Z_{eff}, n_e, total radiation and beryllium light signals could be approximately steady. Unfortunately, it was not known whether there was any further drift for longer heating pulses. Strong gas puffing can prevent the beryllium source from contaminating the core plasma, but the fusion yield is degraded.

These results are summarised in Fig 73, which shows n_D/n_e obtained from Bremsstrahlung data (taken close to the maximum neutron yield) plotted against $P_{tot}/<n_e>$. For clarity, inner-wall shots, plasmas too close to the RF antennae and pellet shots are omitted from this figure. At moderate values of P_{tot}/n_e, more favourable values of n_D/n_e were obtained for the solid Be limiters, but at high values of P_{tot}/n_e, the fuel concentration was similar for the best data obtained with carbon conditioned by Be gettering or He discharges or with the beryllium limiter.
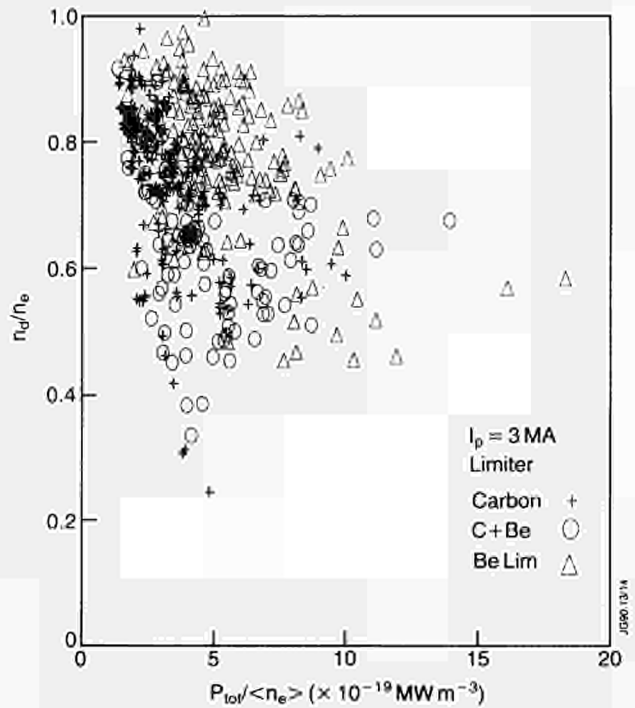
Fig.73 Deuterium concentration for 3MA limiter data comparing bare carbon, beryllium evaporation and solid beryllium.

Fusion Performance

Fusion yield optimisation experiments were performed with plasmas limited by the inner wall and by the belt limiter, with beryllium evaporation and with belt limiter tiles made from solid beryllium. Compared with previous bare carbon surfaces, the most notable gain occurred for plasmas on the belt limiter, where improvements both in $(n_D T_i \tau_E)$ and Q_{DD} of about a factor x2 have been demonstrated. The influence of the limiter on plasma purity in these regimes has already been covered in the previous section. This section shows that density profile shape and density control are also important.

Fig.72 Threshold for beryllium influx.

For plasmas in contact with bare graphite surfaces, it was shown previously that the best performance was obtained in low density inner-wall limited plasmas with high power NB heating, resulting in substantial beam-plasma D-D reaction rates and high central temperatures, with peaked density profiles from the effect of beam refuelling[6]. The necessary density control was achieved in these experiments by intensive He discharge conditioning whose effect was relatively short lived (~ few discharges in D). The high yield regime terminated following the carbon bloom. Similar experiments performed in 1989 showed that this high yield regime could be entered without further conditioning after evaporation of a fresh layer of beryllium. As shown in Fig 74, central beam refuelling created a peaked density profile and the pumping effect of the beryllium maintained a low average density (see Fig 69) and high ion temperature ~20keV for ~1s. The ion temperatures and neutron yields in these experiments were very similar to the best 1988 He conditioned results, and, in both cases, the regime terminated as the core plasma was swamped by carbon following the 'bloom'.
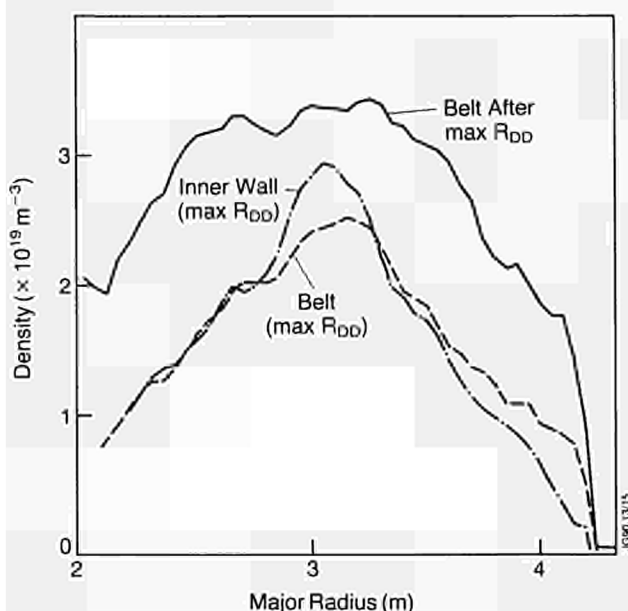
Fig.74 Density profiles for low density beam fuelled plasmas on inner wall, on carbon belt limiter and on carbon belt after fall in neutron yield. All cases with beryllium evaporation.

Following Beryllium evaporation, ion temperatures in the range 14-18keV were achieved for the first time in a belt limiter plasma, as shown in Fig 70. Here the pumping effect of the beryllium was not as strong as for the inner-wall case (compare Fig. 69 and 70), but nevertheless the density rise followed the beam particle source rather than being substantially larger. As shown in Fig 74, the central beam fuelling produces a peaked density profile similar to the inner-wall case. ($n_D T_i \tau_E$) and Q_{DD} were doubled compared with the best bare carbon belt limiter data and were comparable to the best

inner-wall values. The high yield regime was still transient, but for the belt limiter, the decay of the neutron yield was rather less dramatic than for the inner wall and could not be explained by impurity influxes alone. Fig 74 shows the density profile at the peak neutron yield is much more peaked than during the decay of the yield, where the profile is more typical of limiter plasmas. This profile broadening reduced the beam power and particle density sources by a factor ~x2 on axis, and this allowed the central ion temperature to relax. The beam slowing down time was also shorter and this reduced the beam-plasma fusion yield.

For beryllium limiters, it proved difficult to produce strongly peaked density profiles by beam fuelling alone, despite strong pumping. For this reason, the fusion yield in the initial experiments was modest. It is possible that the sawteeth played a stronger role here because the toroidal field was limited to 2.4T (3.1T was used in the earlier experiments). Also beryllium influxes from the RF antennae tiles might have contributed to the higher edge densities. However, when ICRF heating was applied together with the neutral beams, neutron yields exceeding the best carbon results were obtained as shown in Fig 71. Although this lengthened the sawteeth period, the density profile was still rather flat, and the improvement in yield was partly a result of more 140keV beams being used, but was also a result of coupling of the ICRH power to beam injected deuterons. Neutron spectra indicated that deuterons with energies above the injection energy contributed $\geq$ 25% to the yield, and in addition, the time behaviour of the enhancements correlated well with the fast-ion anisotropy. This high yield phase was terminated by an influx of beryllium from the RF antennae tiles and a subsequent rapid rise in density ~1s after the start of the heating pulse.

New Regime with Density Profile Control by Pellet Injection

A further improvement in the yield with beryllium limiter was obtained by using pellet injection to create a peaked density profile rather than relying on beam fuelling. Although the density decayed during the heating, the density profile remained peaked as shown in Fig 75. Using this scenario, the highest fusion gain, $Q_{DD} \sim 9 \times 10^{-4}$, and the highest D-D rate, $R_{DD} \sim 4.2 \times 10^{16} s^{-1}$, yet achieved in a materially limited plasma were obtained, as shown in Fig 76. Also in this discharge, RF accelerated deuterons contributed significantly to the yield. Unlike the previous discharges, the high yield regime was not terminated by a beryllium influx but rather the ion temperature and neutron yield decayed as the peaked density feature disappeared.

Summary of Fusion Yield Optimisation

Q_{DD} scaled with P_{NB}/n_{e0} in a similar manner in the 3MA cases shown in Fig 77, and in the 5MA cases shown in
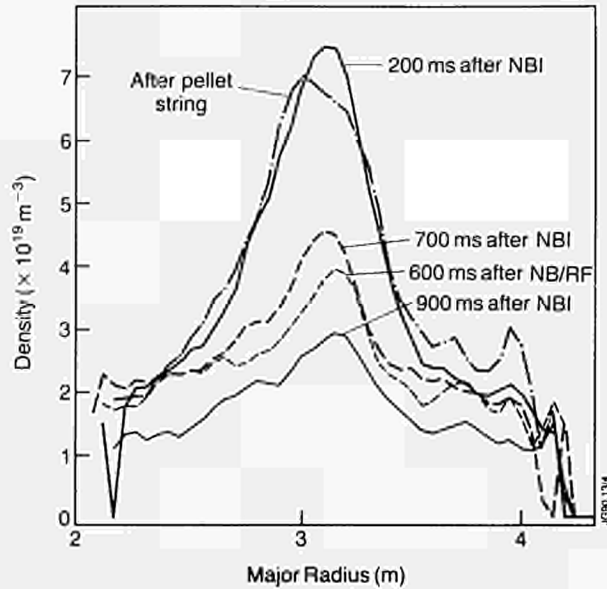
Fig.75 Density profiles evolution during hot-ion phase with NBI and ICRH following pellet injection.

In the figure (Fig.75): Density ($\times 10^{19}$ m^{-3}) vs Major Radius (m). Labels: "After pellet string", "200 ms after NBI", "700 ms after NBI", "600 ms after NB/RF", "900 ms after NBI". JG90.13/4

Pulse No: 20934

P_{NB} (MW), P_{RF} (MW), P_{RAD} (MW), T_i (keV), T_e (keV), $\bar{n}_e$ (10^{19} m^{-3}), R_{DD} (10^{16} s^{-1}), Be II, Z_{eff} (Brem), Z_{eff} (cx), Time (s). JG90.13/5

Fig.76 Time traces for record limiter shot (Pulse No: 20934) with pellet fuelled peaked profile target heated by NBI abd RF.

(D-D power/Loss power) $\times 10^3$ vs P_{NB}/n_{e0} ($\times 10^{19}$ MW m^3). Legend: Carbon +, C+Be ○, Be Lim △, Be+Pellet. JG90.13/6

Fig.77 D-D fusion gain for 3MA limiter data comparing bare carbon, beryllium evaporation and solid beryllium.

carbon (solid symbols), whereas Fig 78(b) compares the beryllium limiter results (open symbols) with the same bare carbon data (solid symbols) at 3 and 5MA. A significant improvement in the equivalent D-T thermonuclear gain can be seen for both beryllium evaporation and beryllium limiter data.

Alpha-particle Simulations

D-He^3 High Fusion Yield Experiments

ICRF heating accelerates ions to ~MeV energies, as shown by nuclear measurements[7], and the behaviour of these fast ions simulates most aspects of α-particles in a fusion reactor[8]. One way of diagnosing these fast particles is to monitor the γ-rays produced in the weaker second branch of the reaction:

$$^3\text{He} + \text{D} \rightarrow \alpha + p + 18.3\text{MeV}$$
$$\rightarrow {}^5\text{Li} + \gamma + 16.6\text{MeV}$$
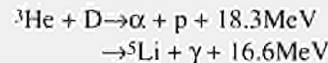
during ^{3}He minority ICRF heating. During a 5s monster sawtooth produced by 10MW of ICRF (monopole) a reaction rate for the D + ^{3}He reaction of ~ 4 x 10^{16} s^{-1} was inferred from the measured 16.6MeV γ yield. This corresponds to $\geq$ 100kW of fusion power[7,9]. Compared to similar experiments in the past, a gain ~ x2 was obtained as a result of the effect of beryllium evaporation which improved n_D/n_e from 0.3 to 0.7. Experiments were also performed scanning the ICRF resonance position and the ^{3}He minority density. Theory predicts that the reaction rate should be sensitive to both these parameters by changing the energy of the fast particles. Such experiments allow refinements to the RF model [8].

Fig 65, indicating that beam-plasma reactions are dominant, in agreement with simulations, and suggesting that density control is the most significant determinant of the yield. The vertical scatter arises because of variations in purity, density profile peakedness and RF acceleration of deuterons. Fig 78 summarises these results for the belt limiter in the $(n_D T_i \tau_E)$ versus T_i plane. Fig 78(a) compares the beryllium evaporation results (open symbols) with bare

Fig.78(a) Fusion performance of 3MA and 5MA limiter plasmas with beryllium evaporation (open symbols) compared to bare carbon (solid symbols).
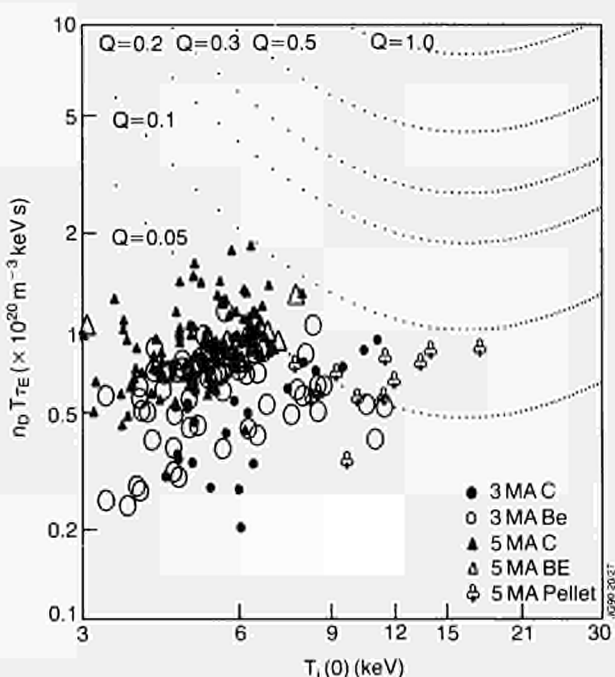
Fig.78(b) Fusion performance of 3MA and 5MA limiter plasmas with solid beryllium limiters (open symbols) compared to bare carbon (solid symbols).

Other Fast Particle Studies

The low density, high electron temperature 5MA plasmas already discussed have a large fast ion energy content - up to 2.5MJ of ~MeV H ions accelerated by ICRF power. The classical slowing down time in the centre of such discharges is ~1.5s, i.e. longer than the thermal energy confinement time. The effective slowing down time $\tau_{eff} = 2W_{fast}/P_{RF}$ is ~ 0.5s. Such

values are expected from a model[8,9], where (a) 65% of the ICRF power is absorbed by the minority ions, (b) the ICRF power deposition profile is calculated by ray tracing and (c) a Stix model is used to calculate the minority distribution on each flux surface. This model is also supported by modulation experiments. The analysis[9] implies a lower limit of ~2s on any other fast particle loss time or a fast particle diffusion coefficient $D_{fast} \leq 0.2 m^2 s^{-1}$. This is certainly a promising result for reactors. However, during the large inversion radius sawtooth crash, which followed the ICRF power switch-off in these discharges, ~0.5MJ of fast ions were expelled from the core, though the remaining fast ions continued to slow down at approximately the classical rate. Loss of fast ions for other monster sawtooth crashes has been demonstrated by nuclear measurements[7]. Clearly, it will be necessary to suppress such sawteeth in order to get efficient α-particle heating.

Conclusions and Summary

These results show that beryllium is an effective limiter material either in solid limiter tiles or thin films deposited on carbon. The main advantage is the density control which it affords. This allows the density to be optimised to permit high electron and ion temperatures and thereby high fusion yields. At high densities, clean plasmas can be made with $Z_{eff} \sim 1$ by strong gas puffing for both 3 and 5MA. It has been shown that it is important to establish a peaked density profile to obtain good beam penetration and high central ion temperatures, and this has been demonstrated both with beam fuelling and with pellet fuelling. Unfortunately, in the cases which optimised the fusion yield, typical values of n_D/n_e were found to be ~0.6, which is only marginally improved over the carbon case. It has been shown that sawteeth can be reliably suppressed at 5MA and that peaked density profiles can be established with pellet fuelling at 5MA. These scenarios can readily be extended to 7MA. In conclusion, the preparatory studies for 7MA are now complete and it only remains to apply these scenarios at 7MA in order to fully optimise JET performance in the limiter configuration.

References

[1] P.J.Lomas and the JET Team, Plasma Physics and Controlled Fusion **31** (1989) p1481(and JET P(89)36)

[2] A.Tanga, P.R.Thomas et al, in Tokamak Start Up, ed H.Knoepfel, Ettore Majorana International Science Series-Physical Sciences. **26** (1985) p159

[3] M.Bures et al, Plasma Physics and Controlled Fusion. **31** (1989) p1843 (and JET-P(89)03p77)

[4] D.J.Campbell et al, American Physical Society Meeting (Anaheim,U.S.A., 1989) (and JET P(89)80 p137).

[5] P.Kupschus et al, JET-P(88)15, p 157, and G.L.Schmidt and the JET Team, Plasma Physics and Controlled Nuclear Fusion Research, Proceedings 12th IAEA Conference, Nice, Vol 1 (1988) p215.

[6] T.T.C.Jones et al, American Physical Society Meeting (Anaheim, U.S.A., 1989) (and JET P(89)80 p75).

[7] G.Sadler et al, Proc IAEA Technical Committee Meeting on Alpha Particles in Fusion Research, Kiev USSR, 1989.

[8] D.F.H.Start et al, Proc IAEA Technical Committee Meeting on Alpha Particles in Fusion Research, Kiev, USSR, 1989.

[9] G.Cottrell et al, American Physical Society Meeting (Anaheim, U.S.A.,1989) (and JET-P(89)80 p207)

Optimization of Plasma Performance in X-Point Plasmas

Summary

The 1989 experimental programme in X-point configuration has been mainly devoted to the study of JET H-modes with high power additional heating. Plasma purity was improved by the use of beryllium gettering, and central values of the ratio of deuterium to electron densities were in the range 0.7 to 0.9. Use of beryllium gettering also improved the control of plasma density, with deuterium pumping rates up to 10^{22} particles s^{-1}. In the double-null configuration, it was possible to achieve low radiated power with ICRF heating, making possible the achievement of H-modes with RF alone. H-mode confinement has also been studied with higher additional heating power. The global confinement time scaled with power, P, as P$^{-0.5}$, with both ICRF and NB heating in the range 4 - 20 MW, confirming earlier results. Extension of the domain of H-mode operation to low values of q ($q_{95} > 2.0$) has shown that global confinement time did not degrade appreciably by decreasing q_{95}. (Here q_{95} is the safety factor value q, at the flux surface which embraces 95% of the magnetic flux).

High values of thermonuclear parameters ($n_D \tau_E T_i$) = 8 x 10^{20} m^{-3}keVs and of Q_{DD} = 2.5 x10^{-3} were achieved in deuterium plasmas with deuterium beams in H-mode discharges at 4 - 4.5 MA. At low density (3 - 4 x 10^{19} m^{-3}keVs), high values of T_i ($T_i(0)$ = 20 - 27 keV) have been achieved in the hot-ion mode with ($T_i(0)/T_{eo}$) = 2-3). At higher densities and with pellet injection (T_i = 9 keV, T_e = 7 keV), a value of the product ($n_D\tau_E T_i$) of 6x10^{20} m^{-3} keVs was also achieved.

With additional power in excess of 10 MW, the termination of the H-mode was suddenly created by an influx of carbon caused by overheating of the graphite tiles. By sweeping the position of the X-point radially and vertically, it was possible to extend the duration of the H-mode by 50%.

The termination of the H-phase, for powers below 10 MW, was caused by excessive radiation losses at high plasma densities, corresponding practically to a density limit. The effect of strong gas puffing during the H-mode was to reduce radiation losses and Z_{eff}, achieving an ELM-free H-phase for longer than 5 s. Very high density regimes were produced by using repetitive pellet injection in the H-mode (n = 3.8.x 10^{20}m^{-3}).

Impurity Sources and Effects of Beryllium Gettering

The gettering of the torus with beryllium , including the target tiles, not only produced a reduction in impurity content, but also provided a means to investigate impurity sources on the graphite target tiles.

The main effect of gettering with beryllium was to reduce oxygen to insignificant concentrations and to reduce the carbon concentration as a consequence of reduced sputtering. These reductions allowed the ratio n_D/n_e to increase from ~0.6, (typical of ungettered cases) to ~0.9, with a reduction in Z_{eff} by x2 and reduced P_{rad}/n_e at the start of the H-phase. Not only were longer H-phases obtained, but the H-mode was achieved with the plasma much closer to material surfaces (limiters, antennas, inner wall) than was possible without gettering.

The beryllium coating on the divertor tiles did not suppress the emission of carbon: even in the first discharges after the deposition of beryllium on the target by overnight evaporation carbon remained in the discharge. The rate of emission of carbon and beryllium at the divertor target tiles was investigated spectroscopically to determine any variation with time after evaporation and also to find the variation with tile temperature. There was no variation of carbon with time, but the beryllium emission was greatest immediately after evaporation and decreased exponentially with a characteristic period of about 10 discharges. Fig 79 illustrates this effect in terms of a decrease in the ratio of BeII and D_γ at the target, measured over the course of a day. Lending support to the idea of gradual removal of the Be coating from the target, was the observation that the rate of pumping of deuterium due to gettering by the Beryllium also showed a decrease from discharge to discharge. The emission variation of carbon and beryllium with temperature of the target tiles showed a different tendency. The carbon emission was almost entirely a function of temperature of the tiles, whereas the emission of Be increased initially as the tile temperature increased during a discharge, but then decreased slowly even though the tile temperature might be fairly constant or even still increasing. Fig 80 shows the
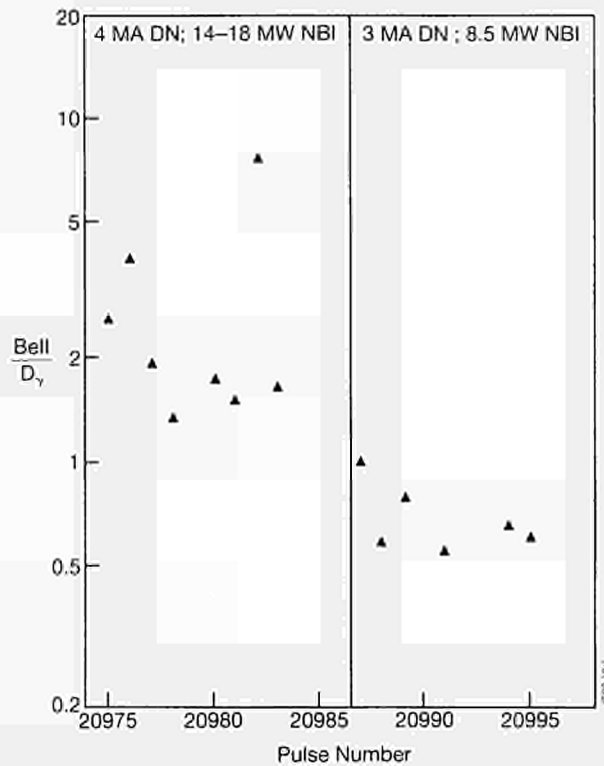
*Fig.79: Deterioration of concentration of beryllium in the divertor plasma during a day of X-point discharges following evaporation. BeII and D_γ were measured at the outer strikepoint when the target was hottest. At a nearby **cooler** region, CCD measurements with a BeI filter showed no such deterioration.*
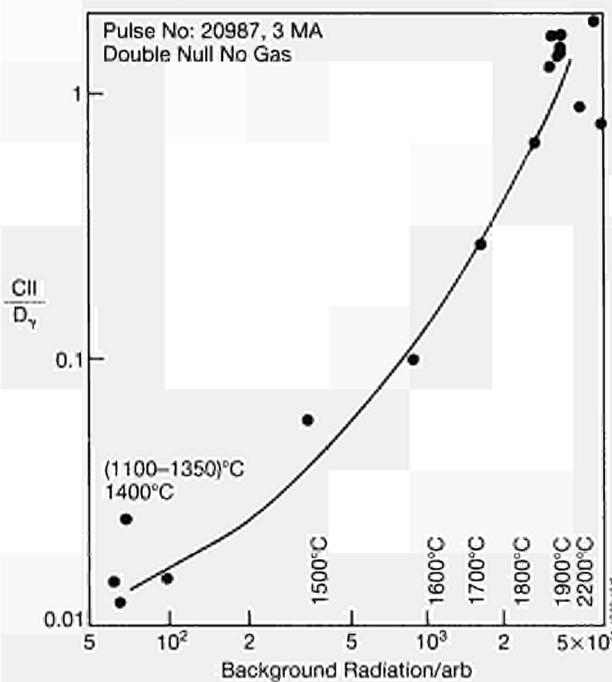
Fig.80: Carbon concentration at the outer divertor target plotted versus background radiation (equivalent to surface temperature). Temperatures are from observations with a CCD camera. Note that the carbon concentration increased by two orders of magnitude over the range of observation.

carbon concentration at the divertor target plotted versus the background radiation, which is equivalent to surface temperature. Data for all discharges are similar,

regardless of the time since evaporation. The only variation for different discharges was in the amount of temperature rise and the corresponding increase in CII/D which depended on the power and duration of the discharge.

Impurity Control
Impurities, once sputtered from the divertor tiles, can be retained in the divertor provided that

(a) they are ionised in the divertor, a condition which is generally realised in JET,
(b) the frictional force between the impurity ions and the flowing deuterium plasma is sufficiently strong and
(c) the thermal force is not too strong.

The friction between plasma and impurities must be sufficiently strong that the impurity density outside the divertor is much lower than at the target. The scale length for decay of impurities is $\lambda_F = (T_z\tau_z)/(mv_H)$, where T_z is the temperature, τ_z is the collision time and m_z is the mass of the impurity species of charge Z, while v_H is the speed of the deuterium plasma flowing through the divertor. For impurity control, $\lambda_F \ll L_d$, where L_d is the length along the magnetic field in the divertor.

The condition on the scale length for friction, λ_F, requires that the plasma in the divertor should be collisional (low T, high n) and have moderate flow. When one combines a model for the flow with one for the relationship between temperature and density at various powers, one finds that impurity control is obtainable in JET only if the plasma temperature in the divertor is fairly low, typically below about 30 eV. Fig 81 shows the temperature criterion for impurity control, plotted as a function of density, for several values of the recycling coefficient.
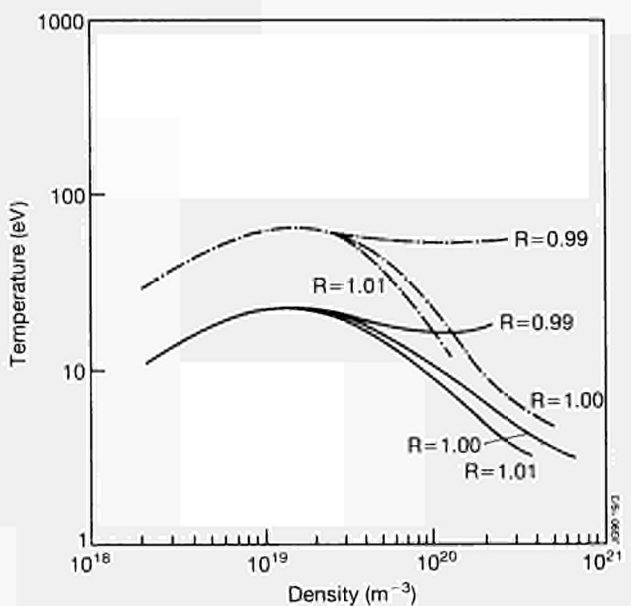
Fig.81: Temperature criterion for impurity control plotted versus density.

Behaviour of Impurities at Moderate Power

For 1988 JET H-modes before beryllium gettering, at moderate NB power, oxygen was the main radiating impurity as shown in Fig 82. Nickel accounted normally for less than 10% of radiated power; an important source of nickel was the RF antennae screens.
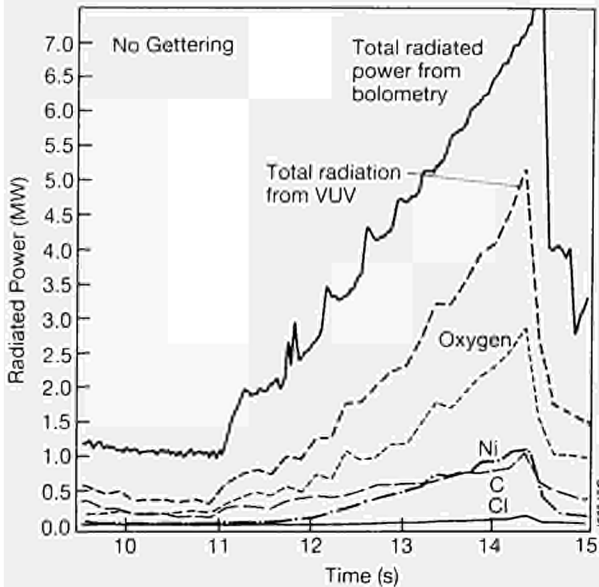
Fig.82: Total radiated power and fraction radiated by Oxygen, Nickel, Carbon, Chlorine, for typical H-mode without Be gettering. NB power = 6.5 MW, I_p = 3.0 MA. (Pulse No: 17909).

Fig.83: Total radiated power and fraction radiated by various impurities, Nickel, Chlorine, Oxygen, Carbon, and H-mode with Be gettering. NB power = 5.5 MW, I_p = 3.0 MA (Pulse No: 20970).

Therefore, it was possible, to find relatively higher levels of nickel in discharges with RF heating or immediately following discharges heated with high power ICRF heating. Routine beryllium gettering substantially reduced the concentration of oxygen in the H-mode as shown, for example, in Fig 82. The comparison of Fig 82 and 83 compares two NB heated discharges with similar total input power (~ 7 MW).

It is evident that with beryllium gettering, the power radiated by oxygen becomes negligible while the power radiated by nickel and carbon is little affected and depends on vessel conditioning. By contrast, the power radiated by chlorine is somewhat higher (0.7 MW) and this depends on vessel conditioning. The gettering effect of beryllium on oxygen is similar in X-point and limiter discharges.

The effects that beryllium gettering had on H-modes can be shown by statistical analysis of plasma parameters. In particular, the trend of Z_{eff} measured by visible Bremsstrahlung versus total loss power (total input power minus the time derivative of plasma energy) is shown in Fig 84. The values of Z_{eff} obtained in a series of 3MA H-modes in 1988 without beryllium gettering are compared with similar discharges with Beryllium gettering. Fig 84 shows an average reduction of Z_{eff} of x2 in the discharges with beryllium gettering.

Fig 85 shows the comparison of total radiated power for gettered and ungettered discharges at the start of H-modes; it is evident that the total radiated power is lower for the Be gettered discharges.

Fig.84: Comparison of values of Z_{eff} from horizontal Bremsstrahlung between Carbon and Beryllium gettering for 3MA H-modes.

H-Modes with ICRH

In 1988 experiments in JET, it had been found that coupling ICRF heating to H-modes generated with NB heating led to relatively strong impurity influxes, a high rise rate of the radiated power losses, and a short duration of the H-mode. The generation of H-modes with ICRF heating alone was not successful in the 1988 experiments, with up to 7.5 MW of ICRF heating power coupled to the plasma.

In the 1989 experiments, H-modes with ICRF heating alone were successfully obtained in JET[1]. This was due to two important enhancements of the JET system. First, the ICRF heating subsystem was equipped with automatic tuning[2], which automatically maintained the impedance matching to antennae despite

77
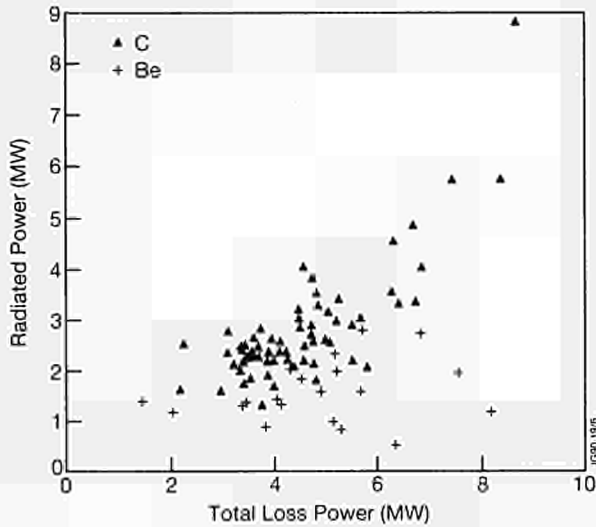
Fig.85: Comparison of total radiated power for Carbon and Beryllium gettering at the start of 3 MA H-modes.

Fig.86: Time traces of the relevant signals for an H mode with ICRH alone. Shown are: the ICRH power, the radiated power, the vertical D_α emission, the kinetic stored energy, the volume average density, the central electron temperature and the central ion temperature.

a rapidly changing coupling resistance. This system allowed coupling of higher ICRF heating powers with the antennae in the dipole phasing configuration. In dipole phasing, the currents in the two active conductors of the antennas are in anti-phase, as opposed to monopole phasing where they are in-phase. In addition, beryllium gettering of the interior of the JET vacuum vessel, including the antennae screens produced lower level of impurities. The previous 1988 experiments were carried out with a carbon vessel interior, nickel antennae screens and monopole phasing.

The experiments were performed in a double-null magnetic separatrix configuration. The dominant power load was on the top X-point (there is a very slight upward vertical displacement), which provided drift of ions directed towards the target area. The X-point target area consisted of carbon tiles. The distance from the X-point to the tiles was typically a few cms. A high triangularity of the discharge was required for the separatrix to match the curvature of the ICRF heating antenna. This was essential for good ICRH coupling. For all experiments, the toroidal field was 2.8T, the plasma current 3MA, the elongation 1.8 and $q_{95}=3.8$ at the horizontal minor radius.

The nominal thickness of the beryllium layer, after multiple evaporations, in places not touched by the plasma, was about 250nm. Fig 86 shows the time evolution of the relevant signals for an H-mode with ICRF heating alone. The variation of the ICRF heating power was due to a variation of the distance between the separatrix and the antenna screen, which changed the coupling resistance. At 49.8s, a 4mm frozen deuterium pellet was injected, which ied to the consecutive transient. The D_α emission signal shown is from a detector with a line of sight near, but not at the X-point. The D_α signal shows a clear L to H transition at 10.4s, followed by an ELM-free H-mode until 12.0s. During
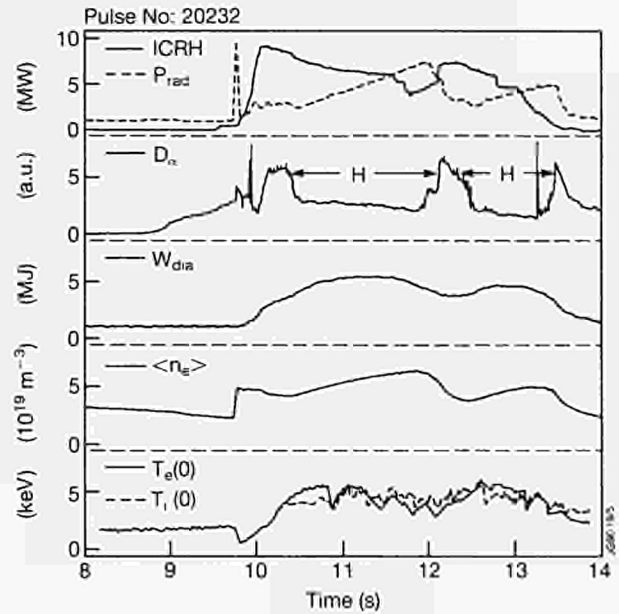
the H-mode, the density and the radiated power increased. The H-mode was terminated when the radiated power becomes higher than the input power; this is a common observation for H-modes. During the subsequent L-phase, the density and the radiated power decreased and from 12.5 to 13.3s, there was a second H-phase.

The maximum stored energy was 5.4MJ at 6.3MW total input power. This gave $\tau_c = 0.85$s, corresponding to $\sim$ x 2 Goldston L mode scaling[6] for these discharges. The electron density at 11.0s was about $5.0 \times 10^{19} m^{-3}$ and had a very flat profile. The density of deuterium increased throughout the H-phase, without additional gas fuelling, showing that there was a source of deuterium probably in the X-point tiles. T_e was about 6keV, and the T_i about 5keV. Characteristic of the H-modes with ICRF heating was the occurrence of long periods during which the sawtooth instability was suppressed. Sawtooth free periods of over 1s were observed, sometimes lasting as long as the H mode.

Fig 87 shows an overview of the confinement of the H modes with ICRF heating alone, in comparison to H-modes with NB alone, at the same plasma current (3MA). Clearly, the confinement of the H-modes with ICRF heating was similar to those of the NB cases, typically corresponding to x2 Goldston L-mode scaling confinement times. For comparison, 3MA L-mode limiter discharges are shown, which have a confinement time slightly in excess of Goldston scaling values. The power threshold for the H-modes with ICRF power is similar to that of the H-modes with NB. For these discharges, at a toroidal field of 2.8T, the threshold was about 8MW.
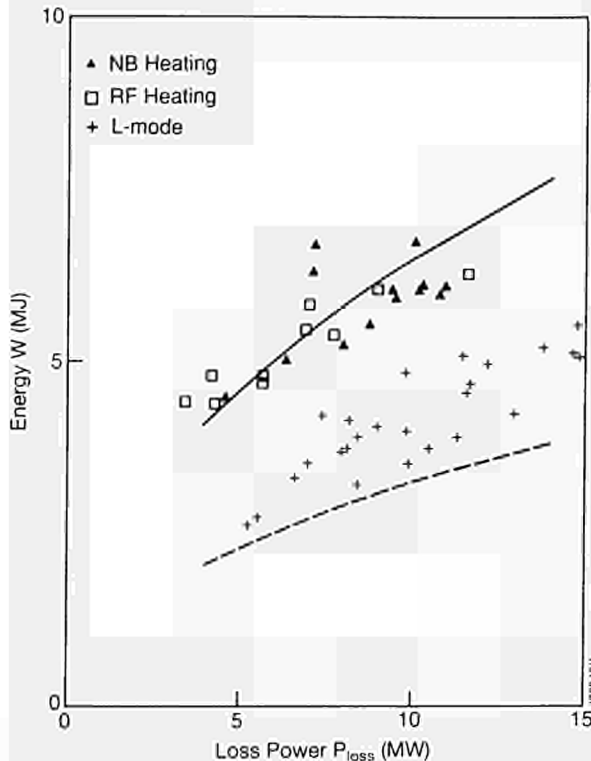
Fig.87: Confinement of H-modes with ICRF power alone, compared with H-modes with neutral beam injection and with L-mode limiter discharges. The plot shows the kinetic stored energy versus the net input power (P_{tot} - dW/dt). All discharges have a plasma current of 3MA. The dashed and the solid line indicate x1 and x2 Goldston L-mode scaling, respectively.

Sweeping of the X-point Position

To increase the effective area of the X-point target, the position of the X-points was modulated, both radially and vertically. The surface temperature of the carbon tiles was monitored with an infrared CCD camera. With a radial sweep at an amplitude of 5cm and a frequency of 1Hz at low (4MW, 5s duration) NB power, a reduction of the peak surface temperature of about 10% was measured. Although increasing the sweep amplitude should improve this number, there was a limitation on the sweep amplitude imposed by considerations of vertical stability of the X-point discharge.

Vertical sweeping of discharges in the double-null X-point configuration was performed to make the best possible use of the total (top and bottom) available target area. For a stationary discharge, it was difficult in practice to balance the heat loads on top and bottom target areas. A combination of a slow radial sweep with a fast vertical motion (100ms) from top to bottom target area just before the predicted time of the strong carbon influx from the top area, delayed the onset of the carbon influx by as much as 0.4s. This was essential in obtaining H-modes with the highest performance.

Long Pulse H-mode

With added gas puffing, long nearly ELM free H-modes were achieved (up to 5.3 s). In these discharges, the carbon catastrophe was significantly delayed and impurity build up was retarded. A comparison of the time evolution of such a Long Pulse H-mode (LPHM) discharge with one at the same input power but without added gas is shown in Fig 88(a) and (b).

During the high gas-puff period, the Z_{eff} rise was seen to be arrested and during the latter part of the H-phase, Z_{eff} was consistently reducing. CCD camera data taken viewing the X-point strike zones showed that the carbon tile temperature was reduced ~ 400°C by the gas-puff enhancing the radiation. However, the tiles still reached 1900 - 2000°C, and thus contributed a considerable source of carbon which did not appear in the bulk of the plasma. Detailed Langmuir probe measurements of the X-point scrape-off layer (SOL) were not possible in these discharges but will be made in 1990. It is known that the SOL collisionality changes by a factor ~x5 (single point probe measurement) but whether this is enough for flow-reversal of impurities to occur is an open question.

In summary, the LPHM represented a significant improvement in radiation build-up over previous JET discharges. Radiation and Z_{eff} profiles remained very hollow throughout the H-phase and for most of the H-phase both the square of the electron density (n_e^2) and the radiation (P_{rad}) increased linearly with time [dn_e/dt=b; (dP_{rad}/dt)=a]. The ratio of these linear rises is a measure of plasma purity and this is shown relative to both the no gas-puff discharge and to earlier JET discharges in Table XII.

Comparison of H-Mode Global Confinement between JET and D-III-D

The energy confinement predictions for H-mode operation in Next Step tokamaks are normally based on the use of a scaling law for L-mode confinement, with an overall multiplier of ~x2 to represent the H-mode character. It is not clear a priori that this is a correct procedure, given the observation that the H-mode enhancement over L-mode confinement involves different physics than the L-mode transport itself. Up to now, a scaling for H-mode confinement, based on data from more than one machine, does not exist. An initial attempt to create such a scaling was made with data from the JET and the DIII-D tokamaks. H-modes, with deuterium NB injection into deuterium plasmas, and free of ELMs, were compared over a range of plasma current (JET for 2-4.5MA; DIII - D for 0.8-2.0MA) and heating power (4.0-13.0MW for both machines). The DIII - D discharges were designed to have the same shape as the JET single-null X-point discharges. Since JET and DIII - D have the same aspect ratio, the separate dependencies on major and minor radius could not be established. To obtain the thermal energy confinement, the fast ion contribution due to the injected NB ions was excluded. The resulting scaling was:

Fig.88: Comparison of long pulse H-mode (Pulse No: 21022) with (a) added gas, and (b) a discharge with same plasma and similar NBI power with no added gas. The early carbon concentrate in the no gas shot can be clearly seen.
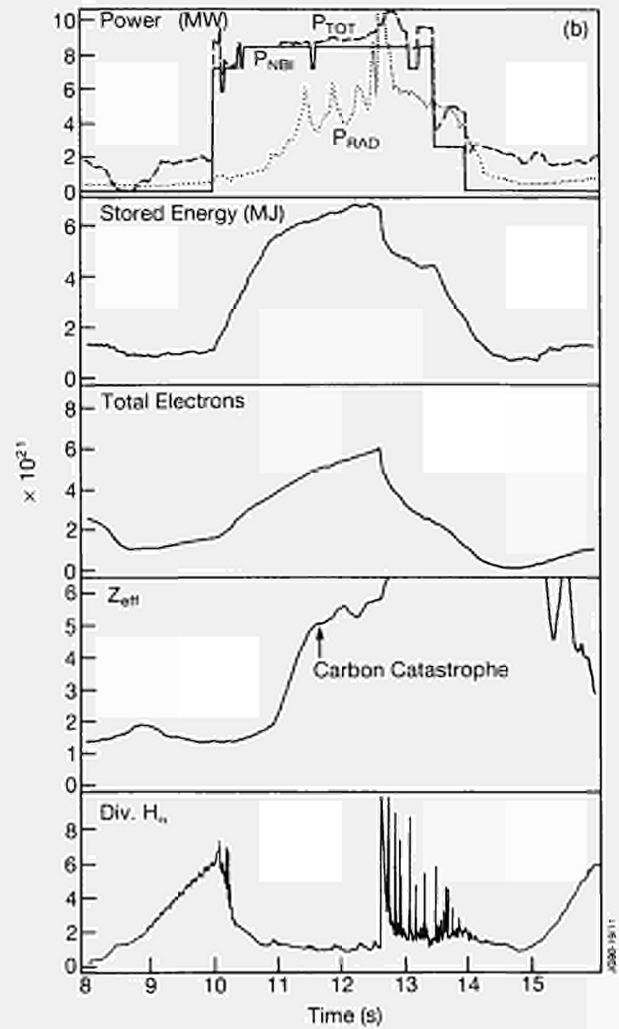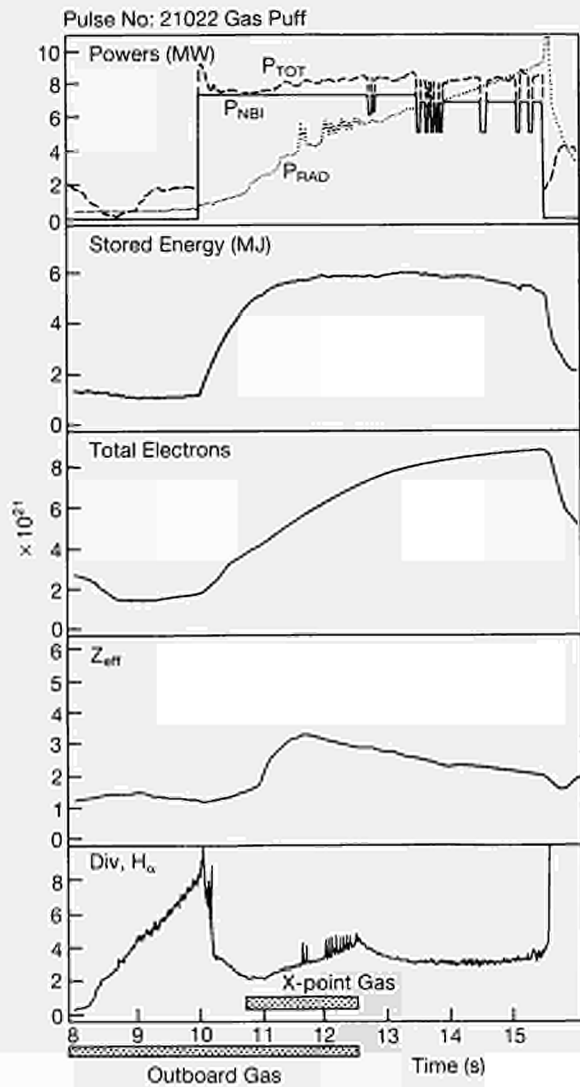
$$\tau_{th} = (0.11 \pm 0.01) \, I_p^{\, 0.98 \pm 0.06} \, P_L^{\, -0.43 \pm 0.07} \, R^{\, 1.44 \pm 0.08},$$

where τ_{th} [s] is the thermal energy confinement time, I_p [MA] is the plasma current, P_L [MW] is the loss power [P_{tot} - dW/dt] (W is the plasma kinetic stored energy) and R [m] is the major radius.

Table XII
Relative radiation and density rises in quasi-linear phase of JET H-modes

Pulse No.	a=dP/dt (MW s⁻¹)	b=d(n²ₑ)/dt (×10³⁸ m⁻⁶ s⁻¹)	a/b (×10⁻³⁸ MW m⁶)	X-Point Tile Configuration
10854	1.7	7.9	0.21	Carbon
14101	2.35	9.4	0.25	Carbon Fibre
17909	2.0	9.5	0.21	Carbon Fibre
18607	1.42	10.0	0.14	Be Gettered (no gas-puff)
21022	1.25	15.0	0.08	Be Gettered (during gas-puff)

Low q Operation

The operation of H-modes in JET has been extended to values of safety factor $q_{95} = 2.0$. The behaviour of H-modes in deuterium at low q in JET is not different from other normal JET H-mode discharges, but it generally has a much less pronounced ELMs activity than observed in DIII-D.

In limiter discharges, the pressure peaking parameter $p(0)/<p>$ has been observed to decrease with decreasing q_{95} and H-modes have been characterised, so far, by generally flatter profiles. However, in typical low-q H-modes, peaking parameters as high as 3 were obtained at high electron and ion temperature. For instance, in Pulse No: 19814 at $I_p = 3$ MA and $B = 1.7$ T, an ion temperature $T_i = 13$ keV was obtained with 8 MW of NB power. With the values of $T_e(0)/<T_e> \approx 3$, $n(0)/<n> \approx 2.1$ and an average density $n = 3 \times 10^{19} m^{-3}$, this discharge reached a value of $(nT\tau) = 2.8 \times 10^{20}$ $m^{-3}keVs$, which scales favourably with the best values achieved at higher currents. (i.e. $I_p = 4.5$ MA, $B_T = 3.4$ T).

Confinement Scaling at Low q

Previous statistical analysis of H-mode experiments in JET, in the range $q_{95} \geq 2.8$, showed a global confinement scaling for the H-mode of the type $\tau_E \propto I_p^{2/3} B_T^{1/3} P_{tot}^{-1/2}$. This scaling, weakly dependent on B_T, favoured the approach to the limiting value $\beta_{tr} = gI_p/aB_t$ by operating at lower values of toroidal field for a given power and plasma current. At lower values of q in DIII-D, a rapid deterioration of confinement was found. Previous analyses of low q confinement in JET ICRF heated discharges showed that the deterioration of confinement was related to the expansion of the inversion radius according to $r_s/a \sim 1.35/q_{95}$. By analogy, it was expected that operating in JET at low B_t, a degradation in confinement should occur.

The main result, shown in Fig 89, is that the global energy confinement time, τ_E did not degrade with decreasing q_{95}. An offset linear fit, $\tau_E = A + B q_{95}$ of this set of data gives the over optimistic result $A = 1.0 \pm 0.2$ and $B = -0.06 \pm 0.05$. Considering the error bars
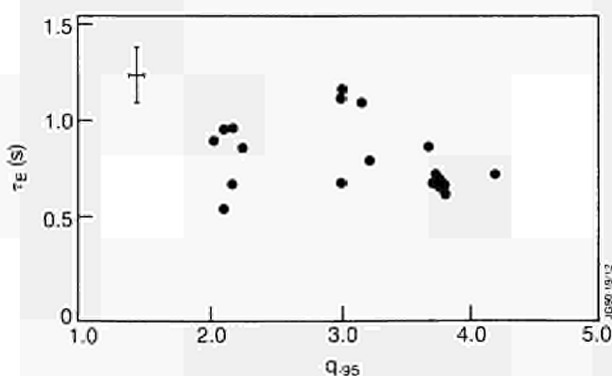
shown in Fig 80, the conclusion was that τ_E did not vary with q_{95} in contrast with the known cases of both limiter and divertor discharges[3,6]. H-mode discharges never reach a rigorous steady state but the confinement time is calculated taking into account the rate of change of the plasma stored energy W_p: ie $\tau_E = W_p/(P_{tot} - dW_p/dt)$.

To understand the behaviour of τ_E versus q_{95}, shown in Fig 89, compared with the results of DIII-D and JET limiter discharges, the scaling of the sawtooth inversion radius r_s should be considered. According to Callen et al.[5], proposed to evaluate the effect of sawteeth on confinement, the fractional change in the incremental energy confinement time $\Delta\tau_E/\tau_E$ is related to the fractional area affected by sawteeth, $\sim(r_s/a)^2$. In Fig 90, the behaviour measured by soft X-ray emission inversion radius r_s versus q_{95} for the H-modes is compared with the result of a fit on JET limiter discharges in the same range of field, current and power. In the low-q H-mode case, the radius of the sawtoothing region, where severe confinement degradation is expected, remains constant within the error bars, in contrast with the limiter cases.
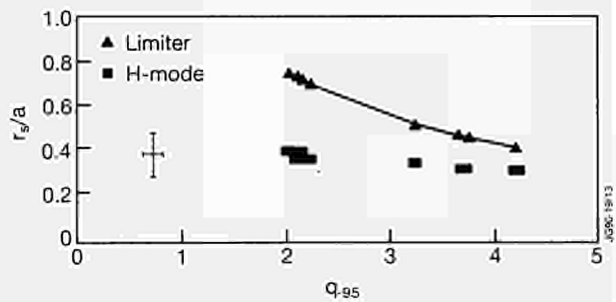
Fig.90: Soft X-ray inversion radius r_s versus q_{95} in limiter and X-point discharges. It is apparent that within the error bars, in the H-mode cases, r_s is constant.

The physical reason of the nearly constant behaviour of r_s versus q_{95} for this set of discharges can be attributed to the broadening of the current profile due to the bootstrap current, appearing as a high β effect linked to low q operation. In this way, $r_s \approx r_q = 1$ does not necessarily increase at lower q, thereby limiting the energy losses from the sawtoothing region.

High β Effects

It appears that the range of β values obtained in JET has been considerably extended, and that high β is naturally related to low-q operation. Experimental results which comprise a large number of JET H-mode discharges, in addition to the data of Fig 89 are shown in Fig 91. The experimental β values are plotted versus β_{tr} (with the conventional coefficient $g = 2.8$). The points close to the boundary do not necessarily imply that a stability limit has been reached, but rather an operational one, due to limitations on the available NB power input at this current, to prevent shine-through of beams to the vessel wall.
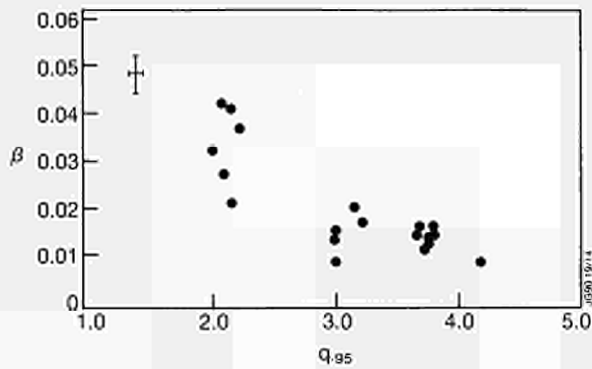
Fig.91: β versus q₉₅. The data refer to a set of 3 MA discharges in deuterium with additional heating in a narrow power range around 9 MW. The range of toroidal field is 1.2<B_T<2.4 T.

Confinement and Transport Analysis

The dependence of global energy confinement time on heating power for ELM-free H-mode in double-null configuration is discussed. Fig 92 features the global energy confinement time τ_E [= $W/(P_{tot} - dW/dt)$] as measured by the diamagnetic loop as a function of the total loss power ($P_{tot} - dW/dt$) for plasma currents of 3 and 4 - 4.5 MA. The data in Fig 92 show a continuing degradation of confinement time, with power scaling approximately as $P^{-0.5}$ as found previously in single-null discharges and at lower power.
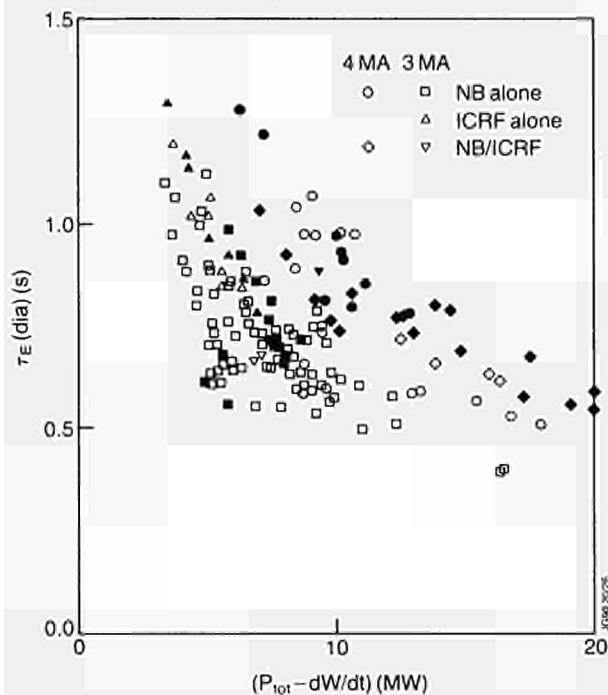
Fig.92: Energy confinement time (diamagnetic) versus input power from ELM free H-mode periods obtained in 3 and 4MA discharges. Solid symbols indicate discharges with pellet injection.

The data shown includes NB as well as ICRF heated H-mode discharges; the average plasma density ranged from 0.3-1.5 x 10²⁰m⁻³, including gas-puff as well as pellet fuelled discharges. The narrow bands of confinement time values sorted per plasma current suggests a weak dependence of global confinement time

on heating and fuelling method and confirms a previously found weak dependence on plasma density.

A limited number of H-modes with hydrogen gas were obtained. Global confinement values did not show a strong effect of mass dependence whilst there was tendency to frequent ELMy behaviour.

Analysis of local transport focussed on selected pulses. The radial dependence of the values of local ion and electro-thermal conductivity as calculated by TRANSP code analysis is shown in Fig 93 for Pulse No: 20981 towards the end of the H-phase. The relatively large error bars mainly reflect uncertainty on profile measurements. In hot-ion H-mode, such as Pulse No: 20981 ($T_i \sim 22$ kW, $P_{NB} = 16$ MW), the ion heat flux was dominant on a large part of the radial profile whilst the electron/equipartition term was comparatively small.
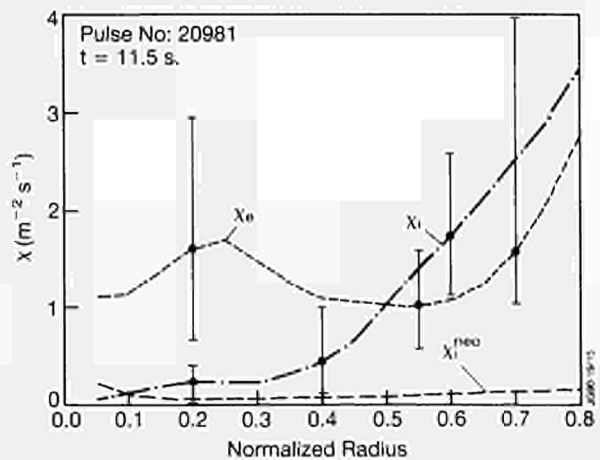
Fig.93: Values of χ_e, χ_i from neoclassical theory versus normalized plasma radius for Pulse No: 20981 at t = 11.5s at the end of the H-phase.
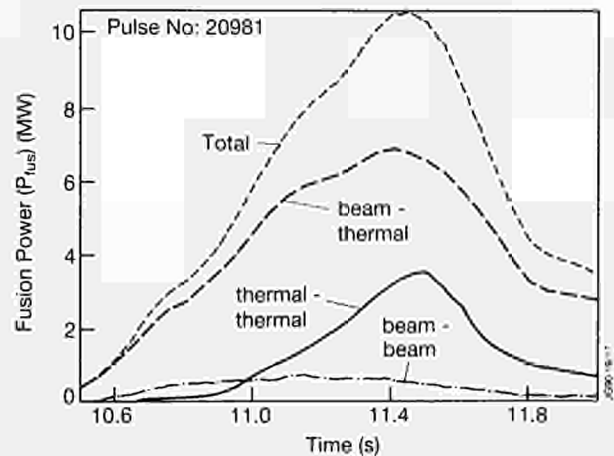
Fig.94: TRANSP simulation of D-T version for Pulse No: 20981 obtained by using the same set of experimental measurements which are a good representation of the D-D case. Only changes are the species mix and the injection energy. This figure features total fusion power, thermal and beam-thermal contributions, assuming 15 MW of 140 keV NB injected into a tritium plasma.

TRANSP code analysis of possible D-T versions of the same pulse are shown in Fig. 94 and 95. Here, the time evolution of total fusion power and the beam
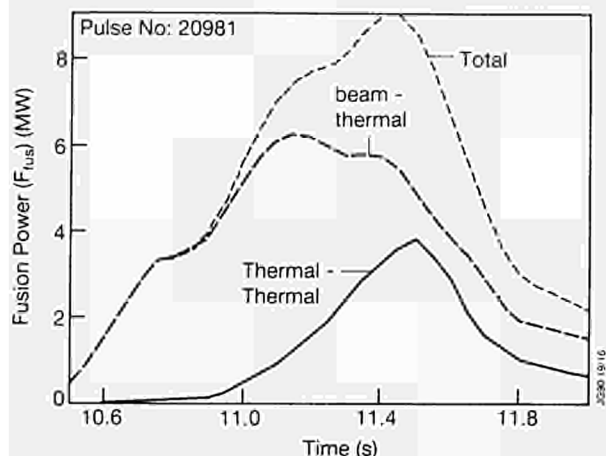
Fig.95: As for previous figure except that the target is an equal mixture of D-T and the injected power is produced by equal NB amounts of D injection at E = 140 kV and T injection at E = 160 kV. Only D-T reactions have been considered.

plasma and thermal components are shown assuming 140 kW deuterium beam injection in tritium target plasma and Deuterium and Tritium injection in a D-T target plasma, respectively. In both cases, the ratio P_{fus}/P_{in} or $P_{fus}/(P_{in} - dW/dt)$ is above 0.5 for about 0.5s.

References

[1] Tubbing, B J D et al, Nucl. Fus. **29** 1953 (1989)

[2] Bosia G et al, Fus. Eng. Des., **11** 458 (1988)

[3] Stambaugh R et al, Plasma Phys. and Controlled Fus., **30** 1585 (1988)

[4] Bhatnagar V P et al, 15th EPS Conference on Plasma Physics and Controlled Fusion, (Dubrovnik, Yugoslavia, 1988) Vol. 12B, part 5, p.358.

[5] Callen J D, Cheng Z., 16th EPS Conference on Plasma Physics and Controlled Fusion (Venice, Italy, 1989) Vol 13B, Part I, p. 427.

Reduction of Impurities and Fuel Enrichment

Introduction

By 1988, it had become apparent that impurities and density control were the main obstacles to the improvement of JET performance. Graphite components had been improved so that they were mechanically able to withstand the power loads encountered inside the vacuum chamber. However, the interaction of the plasma with these components, even under quiescent conditions, was causing unacceptable dilution of the plasma fuel. Still worse, imperfections in the positioning of the plasma facing components led to localised heating during high power pulses which caused enhanced impurity influxes. The enhanced

influxes produced a condition called the "carbon catastrophe" (or alternatively the "carbon bloom" because of the appearance of the hot spots observed by the CCD cameras), in which the deuteron concentration, plasma temperature and neutron yield collapsed.

The graphite surfaces retained a reservoir of deuterium which was easily released by plasma contact. This meant that density control was impossible unless the deuterium was removed by a tedious process of conditioning with helium plasmas. Even then, the improvement of recycling characteristics only lasted for a few pulses. Furthermore, a significant proportion (~50%) of the deuterium fuel was not released after tokamak discharges and this was a cause of some concern about the tritium inventory during the JET active phase. (However, subsequently, a means has been found to force the release of absorbed deuterium and tritium).

In the longer term, as yet, there is no viable scheme for mounting graphite tiles to cooling manifolds in such a way that they can transmit the heat flux anticipated for next step devices such as NET or ITER. Ideally, brazing to copper backing plates would be used but this degrades the otherwise excellent thermo-mechanical properties of graphite. Work on this problem is being carried out on a large scale throughout the world.

These considerations led to the proposal[1], that beryllium should be used as a plasma facing material in JET instead of graphite. Apart from its low atomic number, which makes the radiation cooling per atom smaller than carbon, it has a small sputtering rate, good thermal shock characteristics and a tolerably high melting temperature (1278°C). Although this figure is much lower than the sublimation temperature of carbon, it is considerably offset by beryllium's greater thermal conductivity and the onset of radiation enhanced sublimation in graphite. Preparatory experiments conducted in the ISX-B[2] and UNITOR[3] tokamaks showed that beryllium was a viable limiter material.

Beryllium forms a tightly bound stable oxide so that is is highly effective as a getter to oxygen. In order to separate the effect of the gettering from that due to the plasma interaction with the beryllium, 1989 operation was broken up into three phases: a carbon only phase of a few weeks to re-commission the tokamak and all its systems, a phase where beryllium gettering was used on graphite surfaces and finally a phase with the beryllium belt-limiter tiles installed.

Care was taken, particularly during the first gettering experiments, to monitor the amount of beryllium deposited by the evaporators. Generally the thickness and surface condition were as anticipated from laboratory experiments. However, conditions were encountered, particularly after venting of the vessel, where the beryllium heads were temporarily poisoned so that the evaporation rate was low and where the beryllium surface was blackened and less effective as a getter.

An experiment was performed to measure directly the impurity production from the plasma interaction with graphite as a function of surface temperature. This employed the reciprocating probe as a "Probe Limiter" together with spectroscopic measurements of the deuterium and carbon fluxes. The resulting effective sputtering yield was then compared with model calculations and used as a benchmark for observations of the belt limiters. The results of this experiment are described later.

Impurity Influxes From Beryllium and Graphite

Particle influxes from the limiter and walls were measured for conditions of C-wall/C-limiter, Be-wall/C-limiter (i.e. Be-gettering), and Be-wall/Belimiter. The most notable change to the influxes came with the Be-evaporation: the oxygen was strongly gettered, giving a 20-fold reduction in the oxygen influx, the carbon influx dropped by a factor of ~2 (see Fig. 96(a)&(b)), and Z_{eff} reduced by 0.5 - 1. The fall in Z_{eff} was accounted for mainly by a reduction in the carbon concentration, due to the virtual elimination of the sputtering of carbon by oxygen. Similar levels of plasma purity had been
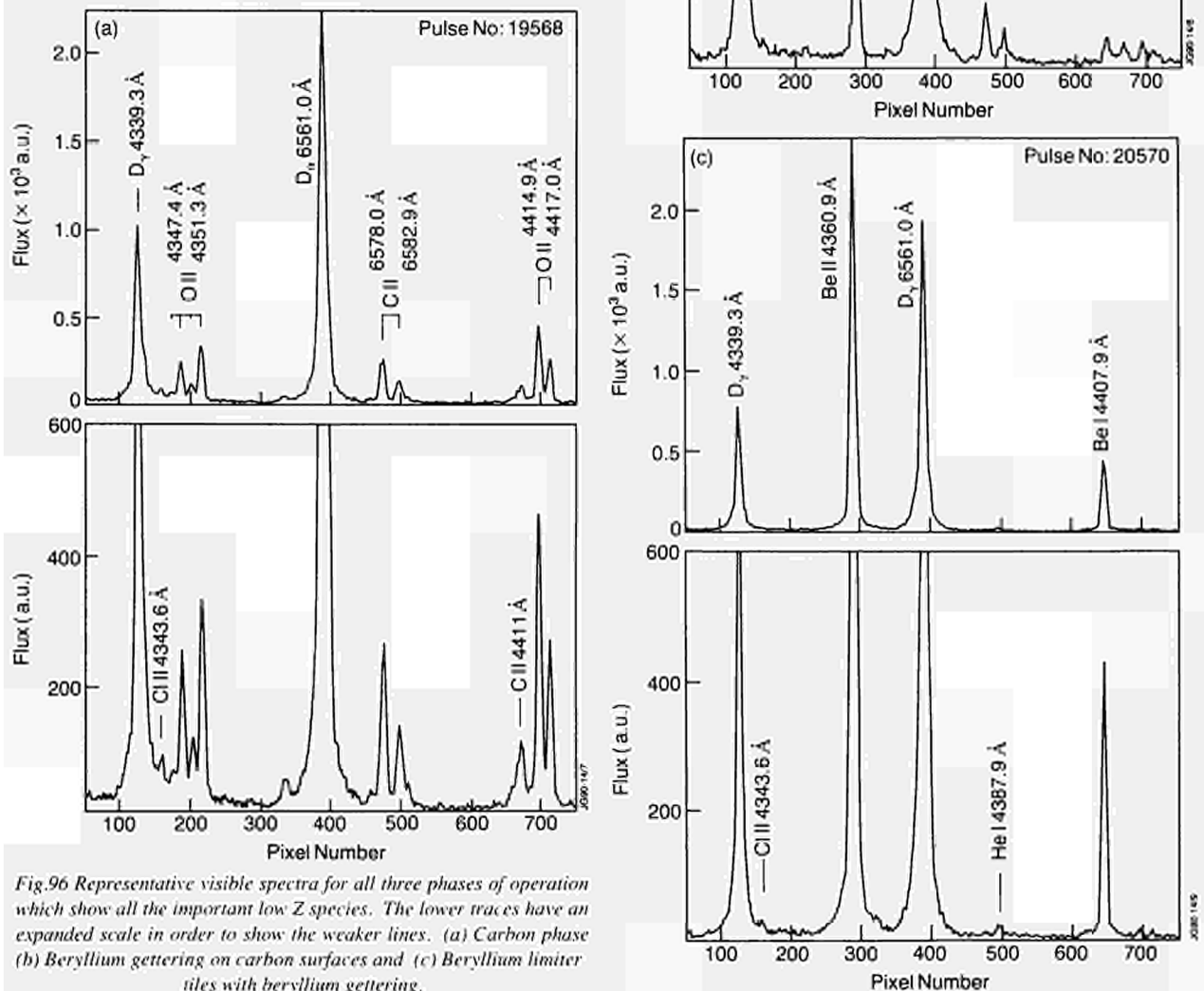
Fig.96 Representative visible spectra for all three phases of operation which show all the important low Z species. The lower traces have an expanded scale in order to show the weaker lines. (a) Carbon phase (b) Beryllium gettering on carbon surfaces and (c) Beryllium limiter tiles with beryllium gettering.

obtained in the past, but only after long periods of machine conditioning.

After Be-evaporation, the Be-coating on the limiters was quickly eroded (in 4 - 20 pulses, depending on input power), but the limiter Be source did not fall to zero (see Fig. 97); charge exchange neutrals from the plasma sputtered beryllium from the walls, which was then ionised and swept onto the limiters.
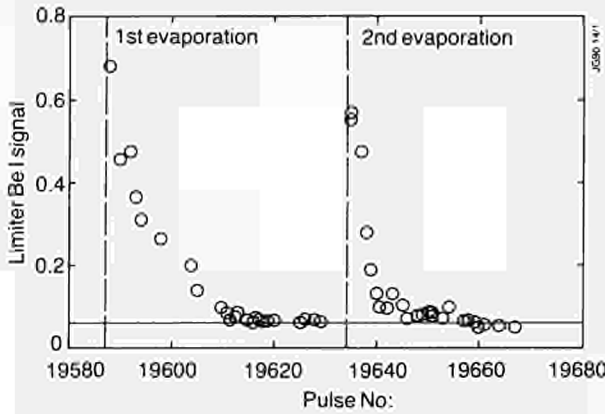
Fig.97 The strength of BeI light emitted from the limiter against pulse number around the first and second beryllium evaporations. The period after the second evaporation marked the start of additional heating experiments so that the erosion rate of the beryllium film was increased.

In the final machine state, Be-limiter/Be-wall, the dominant impurity influx was the beryllium influx (see Fig 96(c)). Very little carbon was observed unless the plasma was limited on the carbon X-point tiles or inner wall tiles.

By simultaneously measuring the impurity and deuterium influxes from the limiter (Γ_i, Γ_D respectively), the effective sputtering yields, Γ_i/Γ_D were determined. For C-limiter/Be-wall, Γ_C/Γ_D had a maximum of ~0.08 (limiter surface temperature < 1200°C) whilst for Be-limiter/Be-wall, Γ_{Be}/Γ_D had a maximum of ~0.35, (see Fig 98). However, at the highest densities, and therefore lowest plasma edge electron temperatures, Γ_{Be}/Γ_D - Γ_C/Γ_D.
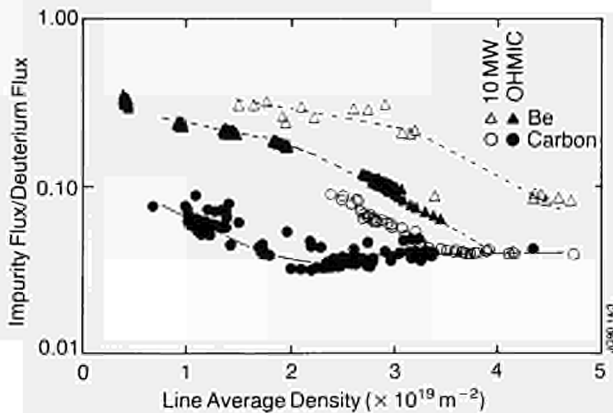
Fig.98 The spectroscopically determined effective sputtering rate for ohmically heated and 10MW ICRF heating discharges against line average density during the graphite and beryllium limiter phases.

At present, the values of the beryllium effective sputtering rate, as shown in Fig.98, cannot be accounted for. The experimental sputtering rates are approximately 3-4 times those reported by Roth[4] for normal incidence of deuterons on beryllium. Whilst a model for the beryllium observations can be constructed, which includes beryllium self sputtering and ion temperatures higher than those of the electrons in the boundary, it is not consistent with the carbon results. Further work will be carried out to try to understand both sputtering rates.

A strong correlation has been seen between Γ_i/Γ_D and $n_i(0)/n_D(0)$ or Z_{eff}. This is illustrated in Fig.99. Pulse No.19642 has a gas puff during the additional heating, such that Γ_C/Γ_D is approximately constant. This suggest that the plasma edge conditions (which determine the sputtering yields of the impurities) determine the purity of the central plasma. Particle transport changes with density, additional heating, etc, but it must be changing in a similar way for the fuel and the low Z impurities.
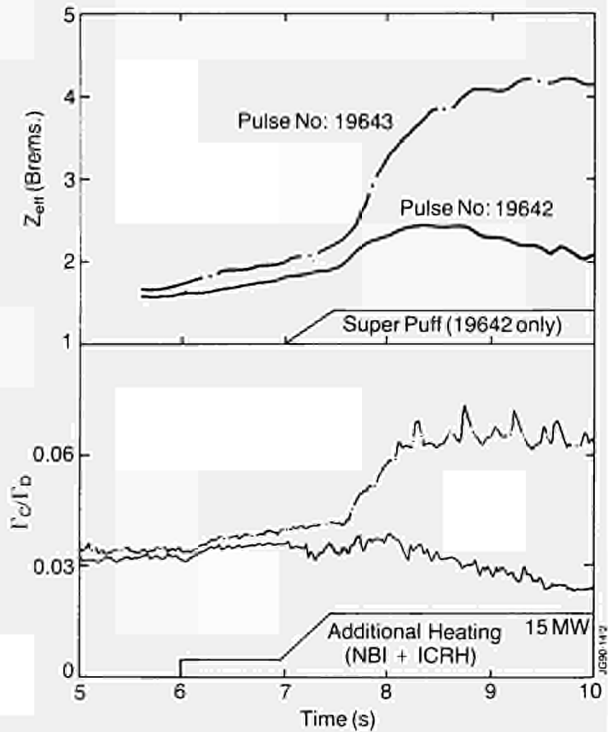
Fig.99 The Z_{eff} and effective sputtering rates for two ICRF heated plasmas with different rates of deuterium gas fuelling.

Impurity Radiation with Beryllium and Carbon Plasma Facing Surfaces

The introduction of Be into the JET machine has resulted in significant changes both in the total impurity content as indicated by Z_{eff} and the relative concentrations of the impurities with their corresponding radiated powers.

With C limiters, the dominant impurity was C, its concentration varying widely from 3 - 10% depending on conditions. Oxygen, with typical concentrations of between 0.2 - 2% showed an anticorrelation with Ni

whose concentration was generally less than 0.1%. The Cl spectrum was only observed when the O spectral lines were intense, both being released from the vessel walls by chemical sputtering. The power radiated by the different impurities in a C limiter discharge is well illustrated by Pulse No.18459, shown in Fig.100.
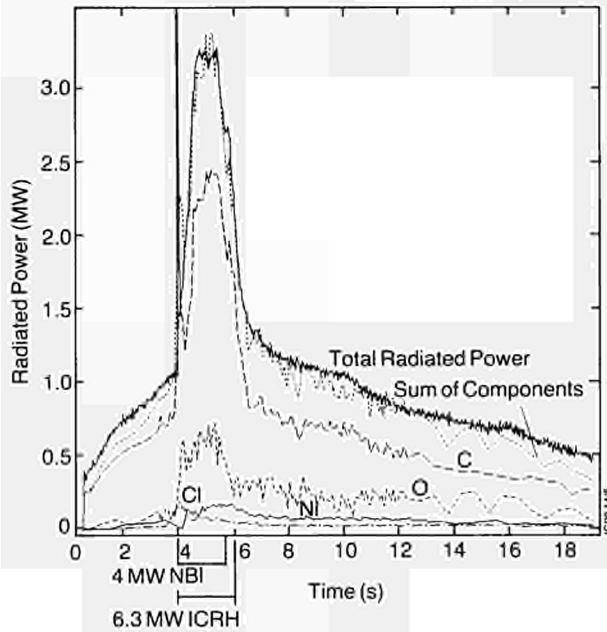
Fig.100 The contributions to the radiated power from different species during the carbon phase.
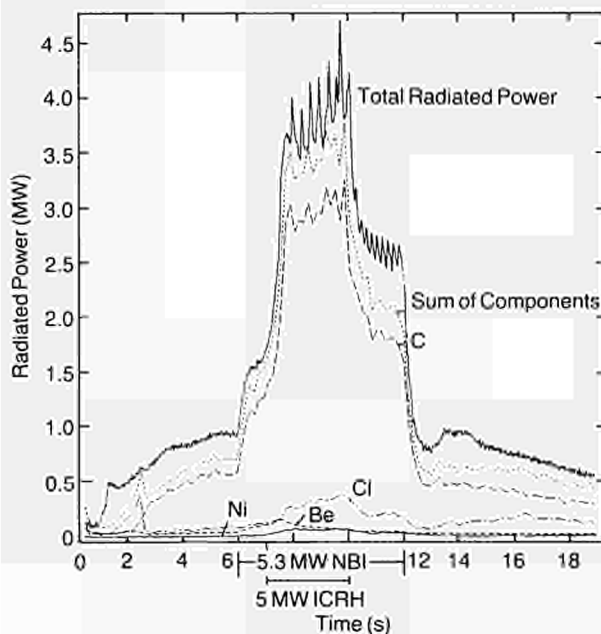
Fig.101 The contributions to the radiated power from different species during the beryllium gettering phase. Note that carbon is still the most important impurity.

After conditioning, the Z_{eff} could be reduced to values of between 1.5 and 3, varying inversely with density. However, such values of Z_{eff} could be achieved immediately after Be evaporation. The Be gettering of

O reduced its concentration by typically an order of magnitude. Although Be was the dominant impurity immediately after an evaporation with a concentration of up to 4%, its level fell rapidly to $\leq 0.5\%$, leaving C as the main impurity. Cl was generally present in these discharges, but at low concentrations (<0.05%). During ICRF heating, Ni was released into the plasma and at times was significant (0.01-0.1% concentration). The radiated power contributions are shown for Pulse No.19641 which illustrates a typical limiter discharge during this phase (Fig.101).

The use of Be limiters allowed lower Z_{eff} values from 1.2 to 2.5 to be achieved routinely. Be with a typical concentration of 3-8% replaced C as the dominant impurity. In the early part of this programme, Cl was found to contribute strongly to the radiated power when n_e was high as is illustrated by the density limit Pulse No.20538 (Fig.102). Conditioning reduced the Cl content from its initial level (~0.1%) and the concentration of C rose to ~1% after X-point operation. Fig.103 shows the radiated power contributions for a limiter pulse during this campaign.
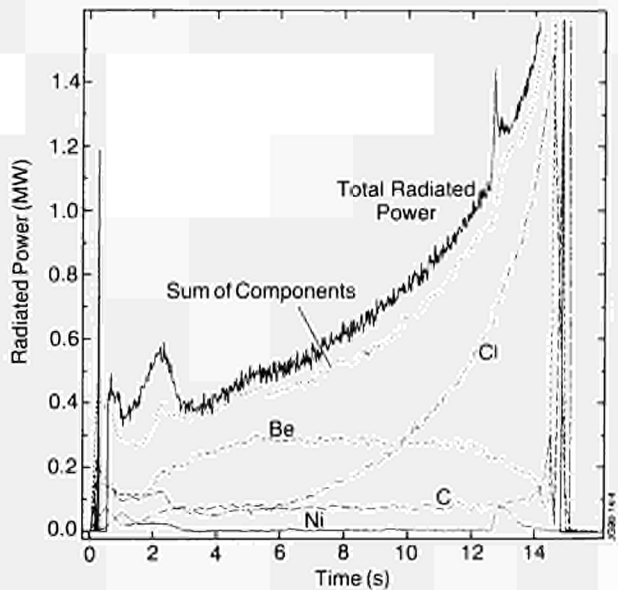
Fig.102 The contributions to the radiated power for a discharge going to the density limit during the beryllium limiter phase. Note the growth in chlorine radiation towards the end of the discharge when the density is highest.

Impurity Control in JET Using Fuelling

Repetitive pellet injection and gas injection, simultaneously with additional heating, were employed to explore the feasibility of inhibiting impurity influx during high power ICRF and NB heating. A prerequisite for such explorations is that recycling is small so that plasma density does not increase uncontrollably due to the fuelling. This requirement is met in JET during Be-gettered and Be-limiter operation in which strong pumping of deuterium is observed, making such investigations feasible.
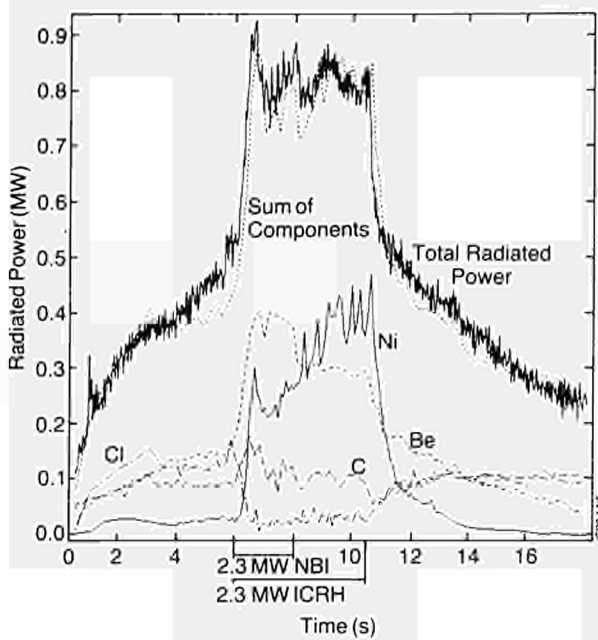
Fig.103 The contributions to the radiated power during the beryllium limiter phase for an additional heating plasma. Note that beryllium is dominant during the ohmic phase and that although nickel comes up during heating the proportion of input power radiated is much smaller than the carbon and beryllium gettered phases.

Injection of superficially penetrating ($r_p/a \geq 0.7$) deuterium pellets (9×10^{20} atoms) has been employed to reduce impurity influx and to flush impurities out of the plasma. Target plasmas on the outer belt-limiters with $I_p = 3MA$, $n_e \approx 3 \times 10^{19}$ m^{-3}, $T_e(0) \approx 3$ keV, $Z_{eff} \approx 1.6$, and $T_e(a) \approx 30$ eV have been studied. On application of 10MW of ICRF heating, $\Delta T_e(0) \approx +5$ keV, $\Delta T_e(a) \approx +40$ eV, and $\Delta Z_{eff} \approx +1.7$ were observed. Rapid (1 - 4 Hz) pellet injection during ICRF heating reduces the ΔZ_{eff}. Such operation is cumbersome, irreproducible, and often $\Delta T_e(0)$ is reduced.

On the other hand, gas injection during high power heating was more consistently effective in reducing ΔZ_{eff} and inhibiting impurity density increase in the plasma core. By careful choice of the amount of gas injected, the associated increase in plasma density and reduction in central temperature can be made negligible. In both Be-gettered (carbon is the main impurity), and Be-limiter (Be is the main impurity) experiments, with the above target plasmas and around 20MW of combined heating, gas injection during heating caused a reduction, by nearly a factor of two, in central impurity density while the plasma electron density and central electron temperature remained nearly constant and the impurity influx at the plasma edge remained unchanged or even increased (see Fig.99 for an example of such behaviour).

Conventional mechanisms of increased shielding due to reduction in neutral penetration are not sufficient to account for the large decrease in both $n_z(0)/\Phi_z$ and $n_D(0)/\Phi_D$. Crudely speaking, the deuterium and impurity confinement times are both reduced by the gas

fuelling. Measurements of the particle transport near the plasma boundary have not yet been made so the source of the confinement time change is not yet clear. A conjecture under investigation is that the increased flow in the scrape-off layer (SOL) induced by gas injection gives rise to the observed large increase in impurity shielding and reduction of effective particle confinement time for impurities as well as deuterium. Impurity control in the high flow-rate pumped divertor phase of JET calls for such a process. If the above conjecture is valid, then the mechanisms invoked seem already to be working in JET.

Effects of Be Gettering and Be Limiters on Impurity Behaviour During ICRF Heating

During ICRF heating, influxes of neutral gas and impurities generally increase. The RF induced influxes have two main sources: the global influx from the limiters and wall due to the additional power flow in the SOL; and from the interaction of RF waves with the antennae Faraday screens (categorized as "RF specific".)

The two stage beryllium programme (Be gettering and installation of Be limiters) resulted in markedly reduced levels of influxes during RF heating.

With Be Gettering
Global Influxes
The density, Z_{eff} and radiated power are dominated by the global influxes. During the ohmic and NBI heated discharges, the main gain was the elimination of oxygen and the subsequent reduction of carbon, which was the dominant impurity. $Z_{eff} = 1.5 - 2$ at $P_{RF} = 10MW$ was routinely achieved. Z_{eff} was inversely proportional to density and scaled weakly with RF power, e.g., $(Z_{eff}^{-1}) \approx P_{RF}^{0.4}$. At the same density, the fraction P_{rad}/P_{tot} is typically 20 - 50% lower than observed previously. Except at the onset of the RF power, the deuterium recycling $R_D < 1$ during the entire RF pulse. This allowed for the density control.

Influx From Antenna Screens
The Be coverage of the antenna screens resulted in a reduction of nickel influx. The Be influx, mainly from the front face of the screen, was estimated to be in the range $\Phi_{Be}^{screen} = 1.1 - 1.2 \times 10^{19}$ atoms MW^{-1} s^{-1} in monopole configuration ($k_{\parallel} = 0$ m). In the dipole configuration ($k_{\parallel} = 7$ m^{-1}), the influxes were reduced by more than a factor x3. In general, the Be influx from the screens scaled with the edge density and the antenna voltage. The contribution of antenna influxes to Z_{eff} was small, $\Delta Z_{eff}^{Be} = (0.015 - 0.02)$ P(MW) and $\Delta Z_{eff}^{Ni} = 0.01$ P(MW). The nickel influx originated at the surfaces in the gaps between the elements of the antenna screen.

Results With Be Limiters
Global Influxes
The installation of beryllium limiters resulted in replacing the carbon influxes by beryllium. The overall

behaviour of Z_{eff} and P_{rad} as a function of RF power and plasma density was similar to the Be gettered case. However, the absolute values were even more favourable. $Z_{eff} = 1 - 2$ at moderate to high densities ($<n_e> \geq 2 \times 10^{19}$ m^{-3}) and P_{rad}/P_{tot} did not exceed 0.3 at $P_{RF} = 15$MW. Deuterium was strongly pumped during the entire RF pulse ($R_D < 1$) and the density could be sustained only by additional gas puffing.

Influx From Antenna Screens
Be influx from the screen, during operation with Be limiters, was reduced by more than a factor x2 compared to the case with carbon limiters and Be gettering. This reduction was attributed to elimination of carbon. Carbon played an important role in sputtering of the screen.

The reduction of influxes in the Be environment allowed an extension of the operation régime for ICRF heating in terms of the density limit, density control and deuterium dilution. Also the H-modes with RF heating alone can now be routinely achieved.

Fig.104 The effective decay times for deuterons and electrons after interruption of the external gas feed for representative conditions during the three phases of operation.

Effect of Carbon and Beryllium First Wall Materials on the Plasma Density

Until the middle of 1989, the JET first wall employed carbon in areas where high particle ($> 10^{21}$/m^2) and heat fluxes (> 0.5 MW/m^2) occurred, such as limiters and divertor target plates. The rest of the vessel wall was inconel. The inconel was covered by nm-μm thick carbon layer due to earlier carbonisation as well as redeposition of carbon eroded from limiters and divertors. Under these conditions, control of the plasma density depended strongly on operational history as carbon was an effective and permanent collector of hydrogenic isotopes. After operational scenarios like glow discharge cleaning in hydrogen or carbonisation, which loaded up the carbon with deuterium, the plasma electron density was almost entirely (>80%) determined by hydrogen and carbon release from limiters and walls. Little external gas was needed to sustain the density throughout the discharge. Access to the low density ($< 10^{19}$ m^{-3}) régime was prevented. Only time consuming (hours) conditioning (by either glow discharges with helium or by helium tokamak discharges) could temporarily remedy this situation.

The use of beryllium evaporation in June 1989 (first of all to getter oxygen) brought about a significant and lasting improvement. For one, the plasma density could only be built up by external gas supply. Any interruption of this supply caused a rapid decay of the plasma deuteron content. Fig.104 shows a comparison of decay times for limiter discharges under various wall and limiter conditions. The decay times were measured at the time when the external gas supply was interrupted and indicate the capacity of the walls/limiters to pump deuterium. Beryllium evaporation reduced the decay time to values which had only been achieved in all
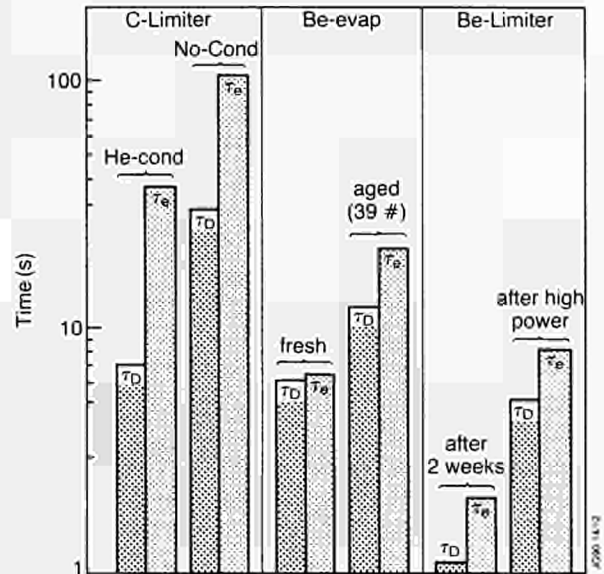
carbon conditions after helium conditioning. There was an ageing process to be observed (possibly due to beryllium erosion at the limiters) but the decay times did not increase to values characteristic for unconditioned carbon.

A further reduction of the decay time was observed after installation of the solid beryllium belt limiter used together with beryllium evaporation. Ageing effects were even weaker. The effect of improved deuterium pumping by beryllium and the lack of strong release of deuterium from material surfaces at the start of the discharges indicates that the deuterium stored during the discharge in the walls/limiters must have been largely released after the discharge. Indeed this has been observed experimentally by measuring the particle balance during and after the discharge. In terms of deuterium recycling, beryllium in JET proved to behave qualitatively similar in a fashion as an all metal first wall, where density control is eased compared to an all carbon wall due to stronger and, in principle, unsaturable pumping. Also the proportion of long term trapping of deuterium has been reduced. However the total inventory is about the same as the carbon phase because the deuterium input is larger.

Density Limits

An important indicator of the plasma impurity content is the density limit and its variation with plasma conditions. There were dramatic changes in the density limit from carbon limiters through the evaporation phase to beryllium limiters. The most significant change was that in both beryllium phases the limit was usually non-disruptive. In the evaporation phase, the limiting density was unchanged except for the cases with ICRF heating where the limit was now the same as

for similar NB power levels. In the beryllium limiter phase, the density limit doubled over the previous limit once the chlorine levels had been reduced by operation.

With beryllium, there was a clear linear dependence of the limit on the square root of input power and it was shown that pellet and gas fuelled discharges had the same limit, if the edge density was considered. These results are consistent with a model for the density limit[5] in which radiative collapse of the boundary to the q = 2 surface causes MHD instability and then disruption.

Limiter and Wall Observations

The achievement of high plasma temperatures using high power auxiliary heating has been accompanied by rapid increases in impurity influxes, principally carbon. In these circumstances, Z_{eff} increases and the effectiveness of the auxiliary heating is reduced.

In plasmas bounded by the inner wall, observations of the carbon protection tiles showed that almost all tile surfaces remained below 600°C. A small number were heated to much higher values, sometimes to ~3000°C. Substantial carbon sublimation then occurred, often leading to a plasma disruption. Inputs of ~15MJ were enough to cause this effect.

In-vessel examination of these tiles confirmed that considerable material had been lost from these areas, and also from a small number of belt limiter tile edges. Thus it appears that the sudden increase in carbon influx is associated with excessive localised heating rather than modest heating of large areas.

Plasma shaping investigations showed that it was possible to distribute the limiter flux over a much larger area of the belt, and in this configuration up to 90MJ of auxiliary heating was applied without these impurity influx increases.

During the Be-gettering phase, a carbon probe was used to investigate the plasma near the limiter. Spectroscopic observations of this probe showed that the effective carbon sputtering yield remained low until the probe surface temperature reached ~1100°C, at which point the yield increased as a strong function of temperature as had been observed in laboratory simulation experiments. These results are compared with the laboratory values for a number of processes in Fig.105. The increase in all sputtering rates above 1200°C is due to a process known as radiation induced sublimation. The measured effective sputtering rate has been satisfactorily modelled by taking account of edge plasma conditions and laboratory sputtering rates.

During beryllium limiter experiments, the edges of some Be tiles were heated to temperatures above the melting point (1278°C) during additional heating periods, despite the use of optimum plasma shaping. The threshold for this was ~15MJ. In extreme cases, droplets were ejected from the melted zones which condensed elsewhere on the limiter, forming areas of enhanced flux deposition which had not previously
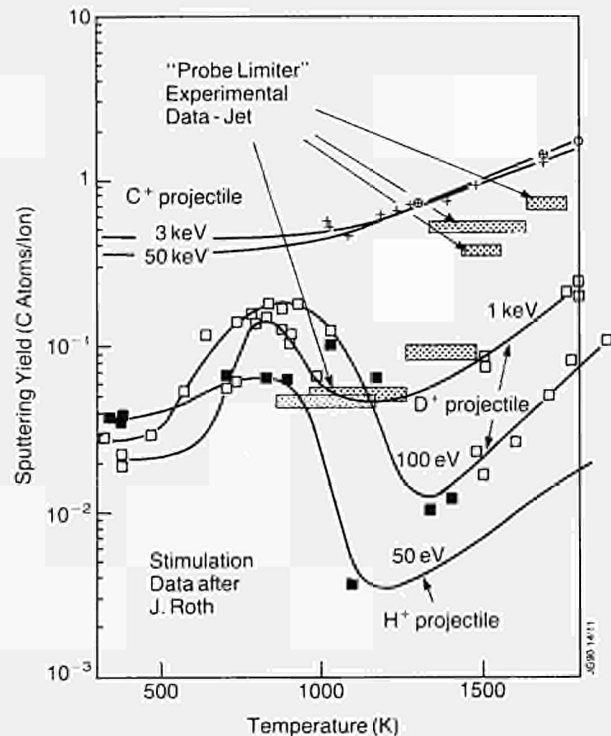
Fig.105 The effective sputtering rate for carbon against surface temperature as measured in the "Probe Limiter" experiment compared with laboratory simulation values for different processes.

existed. It was subsequently found that the melt zones were most often located in areas of maximum toroidal field ripple, but evidence of melting was also found in other areas.

Probe measurements repeated during this operating period showed that the carbon probe had rapidly become coated with beryllium, indicating that a substantial flow of Be could be present in the plasma boundary region. Although strong emission of Be was observed even at 300°C, carbon emission from the probe remained very low until the surface reached ~1700°C. Thus, the Be deposition on the probe resulted in a reduction in the carbon sputter yield and delayed the onset of enhanced yield by increasing the threshold temperature. It is not clear whether the coating consisted of pure beryllium which was evaporated from the probe during the measurement period, exposing the carbon, or that the probe coating was beryllium carbide, which may have a higher threshold temperature.

Enhanced Carbon Erosion and Beryllium Melting During High Power Operation in JET

The highest values for the D-D reaction rate and fusion parameter $(n_D(0)\, T_i(0)\, \tau_E)$ were achieved by heating low density plasmas with neutral beams at high power. During these experiments, a sudden and large increase in the flux of impurities (carbon or beryllium) was continously observed entering the discharge shortly after the start of additional heating. This, in turn, led to a degradation of the plasma performance due to an

impurity concentration, reduced beam penetration and associated reduction in ion temperature.

This phenomenon occurred for the three different plasma configurations; belt limiter; inner-wall; and X-point. During the carbon and Be-gettered phase of operation, the influxes were predominantly carbon. After the installation of the solid Be belt limiters, similar behaviour was observed with Be when heating low density plasma at high power. There was good evidence that these influxes resulted from a small fraction of the total area of the carbon surfaces or beryllium surfaces in contact with the plasma (tile edges particularly) reaching temperatures at which substantial sublimation/melting occurred. Tiles with eroded/melted edges were found on the inner-wall, at the X-point, on the belt limiters and on the RF protection guards. On the belt limiters, these tiles were mainly located at segment joints where they might project inward by up to 1mm due to pressurisation of the cooling circuit.

Limiter Damage

The damage to the beryllium belt limiter tiles was assessed after three weeks of operation. Three types of damage were seen:

- Melting at the edges of the tiles and at the edges of the surface cuts present to reduce stress.
- Melting and cracking of the front face of the tiles.
- Localised areas of strong melting caused by the reionisation of the injected neutral beams.

Examination of damage showed a correlation between surface damage and toroidal field ripple (Fig.106).
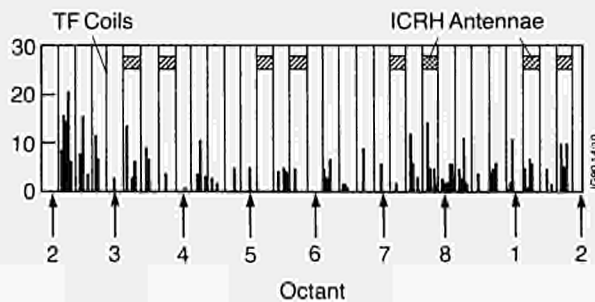
Fig.106 The toroidal distribution of damage to the beryllium belt limiter tiles. The damage was quantified by counting the number of tesselations which had substantial melting in groups of four tiles. The vertical bars are TF coils. The bias to the damaged coil between the positions marked Octant No: 2 and Octant No: 3 is also apparent.

Although the surface damage affected the largest area, only 4% of the segments were damaged in this way, compared to 15-19% which had edge melting. An important point about the positioning accuracy required of plasma-facing components is underlined by these results. The radial variation in the position of the plasma due to field ripple is estimated to be 1.5mm at the face of the belt-limiter. Where the magnetic field was at grazing incidence on the surface, this variation was sufficient to cause localisation of the damage. It is

important that future configurations avoid this condition.

The power level at which melting started was consistent with calculations of the penetration of plasma into the gaps between tiles. The surface melting, however, could not be explained in such simple terms. There was evidence from the camera viewing the limiter to suggest that surface damage was initiated by droplets from edge melting falling onto the surface. The cracking in these areas would have required a substantially higher heat load, and it has been speculated that these could be a result of disruptions.

Summary of Results

The bulk of the work conducted by this Task Force was associated with the evaluation of beryllium as a plasma facing material. The most dramatic effects of beryllium were its gettering of oxygen and the pumping of the plasma. The oxygen gettering had a direct effect on plasma impurity content and an indirect one because oxygen sputtering of carbon was eliminated. The plasma pumping allowed improved density control and this had an important effect on all discharge régimes. Low plasma densities were accessible on the belt limiter for the first time and have permitted high ion temperature operation. On the other hand, at high density, heavy gas fuelling was employed to control impurities without a corresponding increase in the core plasma density.

The effective beryllium sputtering rate turned out to be somewhat higher than expected. The beryllium concentration in the plasma could be correspondingly higher unless gas fuelling was employed. In this respect, beryllium did not live up to its promise. Nevertheless, the beryllium radiative cooling rate was less that that of carbon so that the density limit was increased. Even more impressive was the improvement in ICRF heating operation. The beryllium coating of the Faraday shield all but eliminated the impurity effects associated with ICRF heating and brought its performance to that of NBI.

The "Probe Limiter" experiment demonstrated the increase in carbon sputtering from graphite surfaces above 1200°C which was anticipated from laboratory simulation experiments. A satisfactory model of the observed behaviour has been constructed although that cannot yet be said of beryllium surfaces. Further work must be carried out to investigate whether radiation enhanced sublimation of carbon has the same effect on the plasma as physical sputtering. The carbon atoms produced by the former have considerably lower energy than the latter and so should not penetrate the plasma as well.

The beryllium belt limiters were damaged by melting at the points of tangential contact with the plasma. This is an effective demonstration of the extreme positional accuracy that is required to avoid localisation of power in such circumstances. Plasma facing surfaces must

have a non-zero angle to the magnetic field lines at all points of contact with the plasma and the mechanical accuracy made consistent with this. Such self-consistent solutions are being sought for the pumped divertor design.

References

[1]   P H Rebut et al., JET Report R(89)03.

[2]   R C Isler et al., Nuclear Fusion **25** (1985) p1635.

[3]   J Hackmann and J Uhlenbusch, J.Nucl.Mater. **128-129** (1984) p418.

[4]   J Roth, IPP Garching, FRG, private communication.

[5]   D J Campbell et al., Proceedings of 11th IAEA Conference on Plasma Physics and Controlled Nuclear Fusion Research, (1986) Nuclear Fusion Supplement Vol I, p441.

Physics Issues

The objective of this Task Force was to study physics issues which were particularly relevant to both JET and Next Step Devices. The programme concentrated on four main areas:

- high β regimes;
- fast wave current drive;
- density limits;
- sawtooth stabilisation.

In addition, transport studies were carried out using off-axis modulated ICRH as well as a preliminary investigation of minority ion current drive. The most significant achievements of these experiments were, as follows:

a)   The attainment of 5.5% β in double-null H-mode plasmas and the observation of a soft β-saturation at the Troyon limit corresponding to kink mode activity;

b)   A clear demonstration of collisionless electron damping of the fast magnetosonic wave in high-β plasmas where transit time magnetic pumping is expected to be a major component in the electron wave interaction;

c)   Strong supporting evidence for the theory that fast ions provide the sawtooth stabilisation mechanism which leads to the formation of monster sawteeth;

d)   An improvement in the density limit by up to a factor x4 in discharges with beryllium gettering of the torus and beryllium limiters. The limit is the same for ICRF heating and neutral beam injection, depending only on the input power, and is characterised by the appearance of a stable Marfe. In general there was no disruption.

The detailed results obtained in the principal areas of activity are described in the following sections.

High Beta Experiments in Double-Null X-Point Discharges

These experiments were carried out in H-mode hydrogen plasmas with a plasma current (I_p) of 2 MA and a toroidal magnetic field (B_T) of 1.2T. A combination of deuterium neutral beam, injection and second harmonic hydrogen ICRF heating provided auxiliary heating with total power levels up to 16 MW. The time evolution of the discharge parameters are shown in Fig 107 for a case in which the toroidal field was ramped down from 1.2T to 0.9T. The toroidal beta (β_o) rises during the heating pulse until it reaches the Troyon limit when a crash occurs. This process was repeated giving a sawtooth-like appearance, until, by the end of the heating, a maximum value $\beta_o = 5.5\%$ was reached. Note the low value of the radiated power fraction (30%) which is consistent with the high purity of these plasmas ($Z_{eff} \leq 2$). A summary of the beta
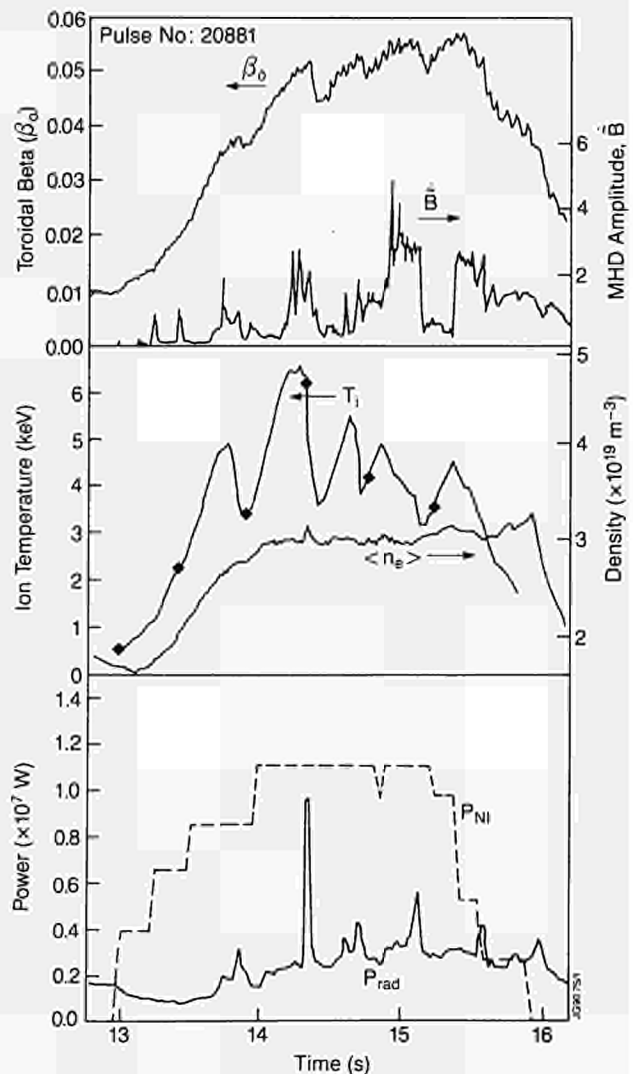
Fig.107 Evolutions of toroidal beta β_o, MHD mode amplitude $\tilde{B}$, ion temperature T_i, volume average density $<n_e>$, injected power P_{NI}, and radiated power P_{rad}

values obtained in all discharges between 1986 and 1989, with a poloidal beta greater than 0.4, is shown in Fig 108. These values are plotted against normalised current $I_p(MA)/a(m)B_T(T)$ and reach the Troyon-Gruber limit for kink modes[1] when saturation occurs.
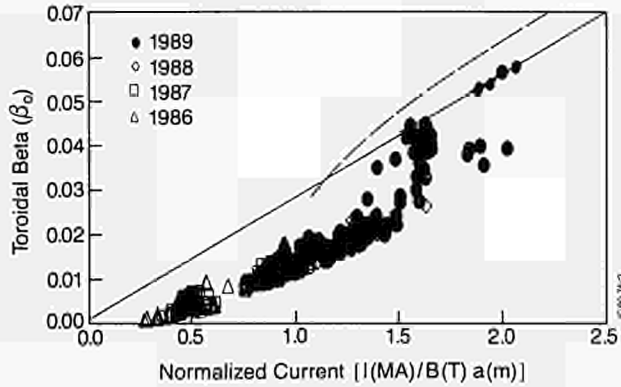
Fig.108 Toroidal beta β_o versus normalised current $I(MA)/B(T)a(m)$ for all 1986-1989 discharges, with $\beta_o > 0.4$. The solid line is the Troyon-Gruber limit $\beta_o = 2.76 I(MA)/B(T)a(m)$. The broken line is the first prediction for JET by Wesson. The highest beta values were obtained in Pulse No: 20881 where the field was ramped down and the beta closely followed the Troyon line.

The β limit is enforced in most discharges by the fast relaxations shown in Fig 107. The MHD behaviour accompanying the crash is complex. The main component in the pre-and post-cursor oscillations has an $m=1$, $n=1$ structure, although there are other phase coupled structures at large major radius out to the plasma edge. The extent of this structure has been observed from tomographic reconstructions of soft X-ray data recorded shortly after the crash. The connected structures appear to allow strongly enhanced energy transport as is evident from the extremely fast heat wave that occurs at the crash. The crash has a marked effect on the plasma parameters[2]. It causes a flattening of the pressure profile, a 40% reduction in central temperatures and plasma rotation and a drop of 70% in the central neutron emission. The neutron emission profiles before and after a crash are shown in Fig 109. In this case, the total fusion reaction rate is reduced by about 30%.

Various stability codes have been used to calculate the kink and ballooning stability of the measured pressure profiles and deduced q profiles[2]. These studies conclude that the β-limit is most likely due to kink modes although infernal modes with $n=2,3$ could be dominant in some cases.

Electron Damping of the Fast Wave by Transit Time Magnetic Pumping

The fast magnetosonic wave in the ion cyclotron frequency range is a major candidate for non-inductive current generation in reactor grade plasmas, where the direct electron damping occurs mainly through transit
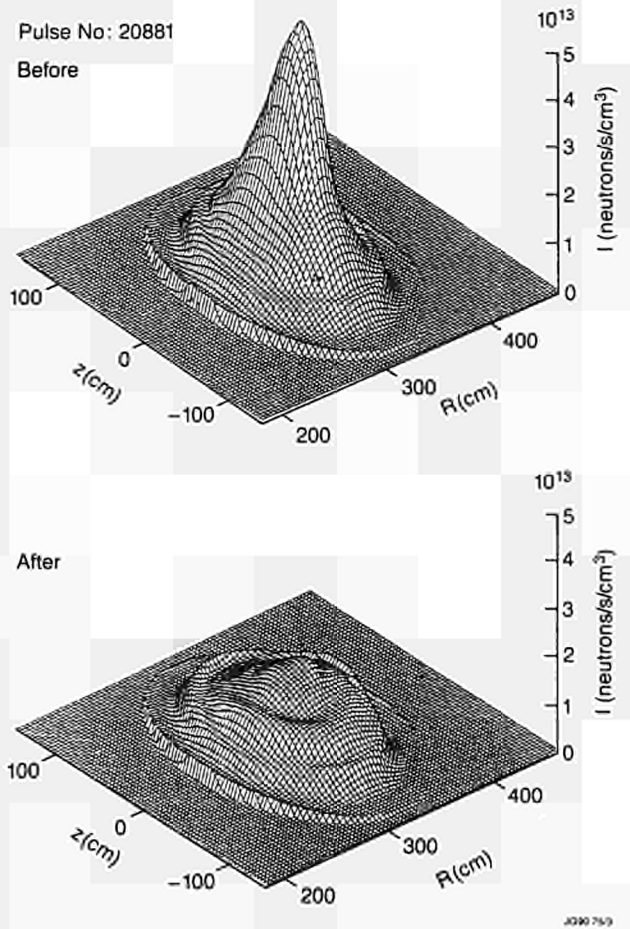
Fig.109 Profiles of the neutron emissivity before and after β crash. The central emission drops by 70%

time magnetic pumping (TTMP). Significant damping by TTMP requires high performance plasmas (high β) so that JET is ideally suited to make such studies. Experiments to demonstrate this mechanism of electron damping were carried out in double-null X-point hydrogen plasmas with $I_p=2MA$ using both NBI and ICRH. The toroidal magnetic field was 1.3T and the volume average β for these discharges was typically 1.4% which is approximately 30% of the Troyon limit for kink modes. The ICRF heating frequency was tuned to the second harmonic resonance of hydrogen at a major radius 0.4m to the high field side of the magnetic axis. This allowed a considerable central volume to be free from ion cyclotron or mode conversion layers, as can be seen from the poloidal cross-section shown in Fig 110. Thus central absorption could only occur through TTMP and this was observed by modulating the ICRH power at 4Hz. The signal from the central channel of the electron cyclotron emission (ECE) diagnostic shows the response of the electron temperature (T_e) to this modulation in Fig 111. The change in dT_e/dt at the RF power transition reveals the presence of direct electron heating and allows the power deposition profile to be deduced.

The electron heating profile obtained from the ECE
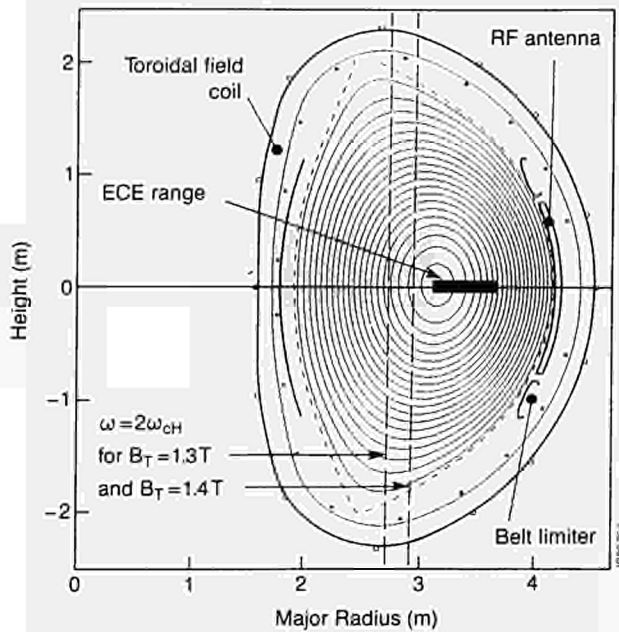
Fig.110 Double-null X-point configuration in JET. The second harmonic ICRH resonance locations for toroidal fields of 1.3T and 1.4T are shown together with the corresponding operating ranges of the ECE diagnostic.
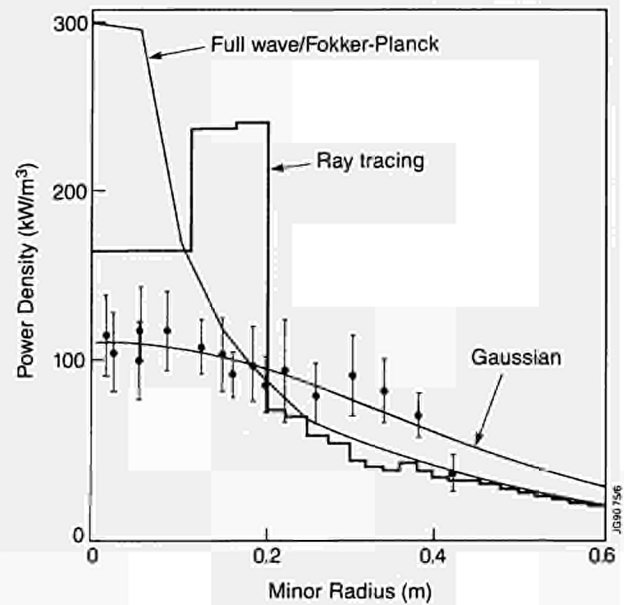
Fig.112 Comparison of the observed direct electron heating power density distribution with theoretical profiles from ray tracing and PION code calculations.
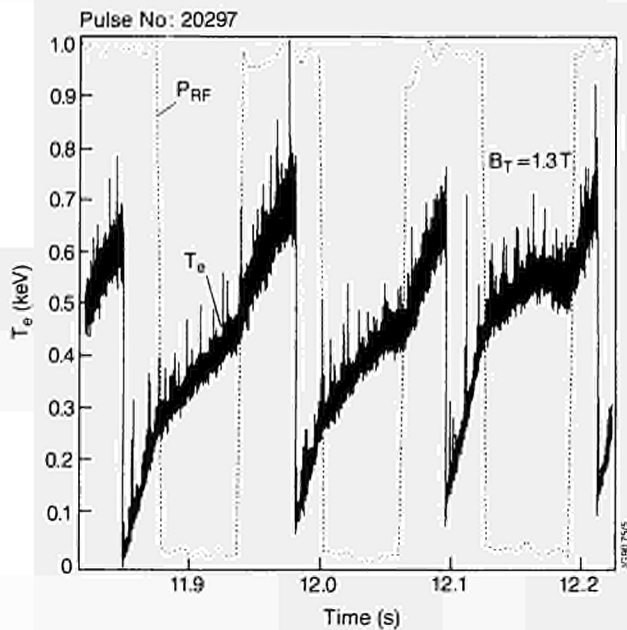
Fig.111 Electron temperature response to modulated RF power measured with the central ECE channel. Note the change in the time derivative of T_e at each RF power step showing the presence of direct electron heating.

measurements is shown in Fig 112. The data include measurements made at $B_0 = 1.4T$ to extend the radial range of the ECE diagnostic. The power density is a maximum on-axis as expected since the TTMP absorption is proportional to the electron pressure which is also centrally peaked. The average electron beta inside the measurement region was 1.5%. The central peaking of the power absorption was also confirmed by

soft X-ray tomography[3]. The total power deposited within the 0.4m minor radius is 22±5% of the input power.

Comparisons with theoretical profiles based on ray tracing[4] and a self consistent treatment of power absorption and velocity distribution using the PION code[5] are also shown in Fig 112. Both calculations predict a more strongly peaked profile that is observed. In the PION code, this could be due to the assumption of an idealised antennae current which over-estimates the electric field in the plasma centre. However, both calculations give excellent agreement with experiment for the total power absorbed by the electrons.

Density Limits with Beryllium Limiters

Density limit experiments were carried out to assess whether beryllium was more effective than carbon as a limiter material. The experiments were performed at several values of the plasma current between 1 MA and 4 MA. Both NBI and on-axis ICRF additional heating methods were used and plasma fuelling was provided by gas or pellet injection. In general, the limit was characterised by the appearance of a stable MARFE (see Fig 113), as was the case with carbon limiters coated by evaporated beryllium. In general, there was no disruption at the density limit which is in contrast to the behaviour with the uncoated carbon limiters. The results are shown on the Hugill diagram in Fig 114, which compares the present data for gas injection with those obtained with carbon walls and limiters (the dashed lines) and with beryllium evaporation. The new operating region is considerably extended, with enhancements of the density limit by up to a factor x 4. Moreover, the usual proportionality between normalized
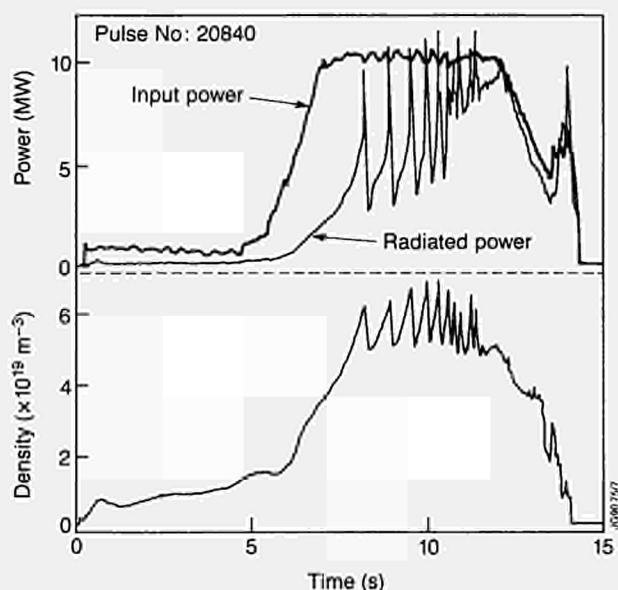
Fig.113 Time evolution of the radiated power fraction and central line averaged density during a typical beryllium MARFE.
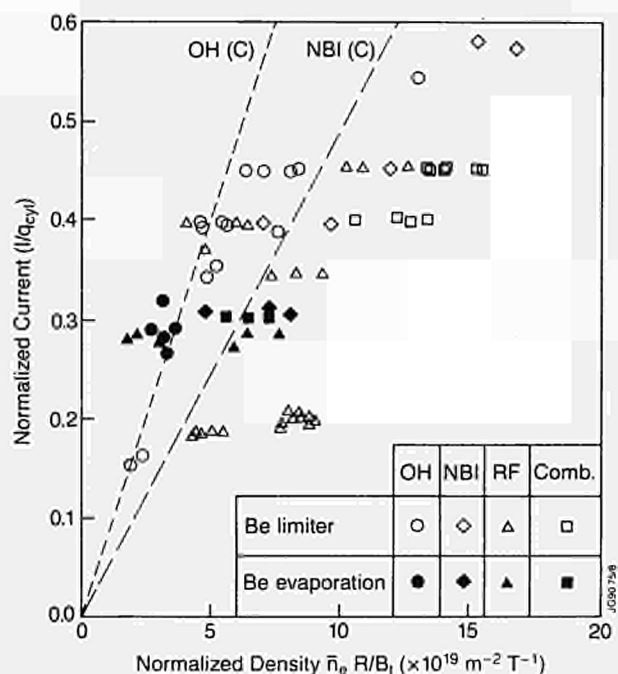
Fig.114 A comparison of density limits due to plasma disruptions with carbon limiters (lines). MARFES after beryllium evaporation (solid points) and MARFES with beryllium limiters (open points).

current (q^{-1}) and $n_e(lim).R/B_0$ appears to be absent, except perhaps for the ohmic heating case. There is no difference between ICRH and NBI additional heating nor between monopole and dipole phasing of the ICRF antennae.

The density at which a MARFE appears is proportional to the square root of the input power, implying that the density limit is actually a radiation limit. Since the edge region produces most of the radiation, it may be more appropriate to plot the edge density rather than the line average density. Such a plot

of normalised edge density against input power is shown in Fig 115. The striking features are that all the points corresponding to MARFES occur at the edge of this existence diagram and this limit is the same for both gas fuelled and pellet fuelled plasmas. The latter effect contrasts with the line average density limit which is up to 50% higher in the case of pellet injection compared with gas injection at the same power level[6]. Thus the relationship between the radiation and the edge density means that considerably improved central and live average densities can be achieved with suitable fuelling techniques.
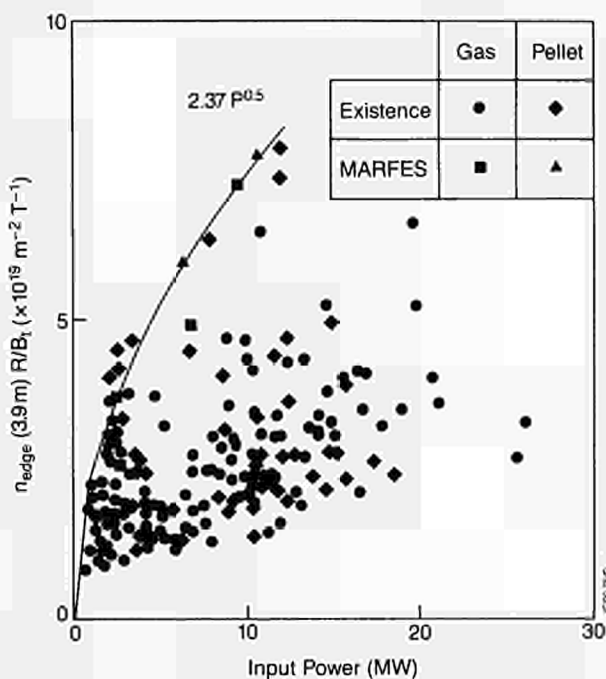
Fig.115 The normalised edge density versus input power showing all MARFES to occur along the edge of a common region of existence.

Sawtooth Stabilization Experiments

Plasma fuelling by repeated pellet injection prior to ICRF heating has been found to stabilise sawteeth for a period of several seconds into the heating pulse. Fig 116 shows an example in which four pellets were injected before the application of 10 MW of ICRH. In this particular discharge, the plasma current was 3 MA and the volume average density was $2.2 \times 10^{19} m^{-3}$. Several measurements indicate that the pellet cooling of the plasma leads to a broadening of the current profile and a value of q(0) above unity. For example, polarimetric measurements give q(0)>1 during the stable period (see Fig 116), and MHD activity with (m,n) = (3,2) or (2,1) is often detected in the plasma core[7].

Experiments have also been carried out to test the theory[8] that fast ions can stabilise sawteeth even when q(0) is less than unity, as appears to be the case in monster sawteeth[9]. The first series of measurements
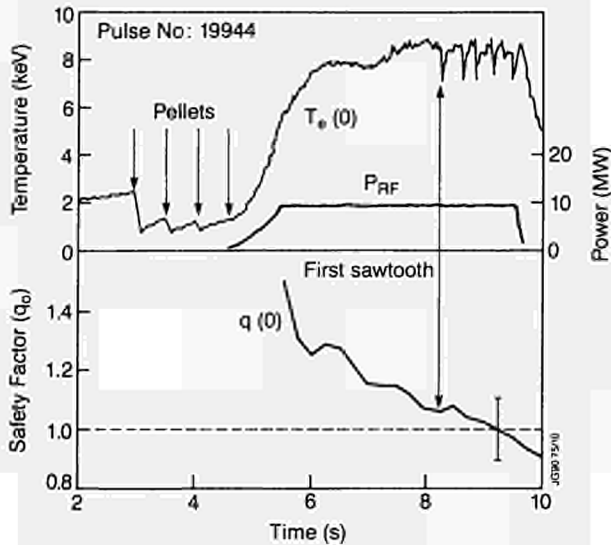
Fig.116 Sawtooth stabilization after repetitive pellet injection. The central safety factor q(0) is greater than unity during the sawtooth free period according to polarimetry.

Fig.118 Fast ion energy content for different minority concentrations.

involved varying the ^{3}He minority concentration concentration during on-axis ICRH in ^{4}He plasmas. Although some problems occurred at high ^{3}He concentrations (less than optimal RF coupling and ^{3}He pump-out during the heating pulse), it was clear that the duration of the sawtooth free period increased with decreasing minority concentration as shown in Fig 117.

Fig.117 Monster sawtooth behaviour for various ICRF minority concentrations. At the higher values of n_{min}/n_i the minority concentration decreases during the heating pulse.

At low ^{3}He density, the fast ion energy content is a maximum (see Fig 118) so that the longest monster sawteeth occur for the greatest fast ion energy content.

An important parameter in the stabilisation theory[9] is the fast ion beta inside the q=1 surface. This aspect

was studied by varying the ICRF resonance position using several toroidal magnetic field values between 2.6T and 3.4T. The results are shown in Fig. 119 and 120 from which it is clear that heating within the sawtooth inversion radius is neccessary for stabilization and that the longest monster sawteeth occur for heating on axis. In addition, the large increase of the inversion reduces at the crash of the monster suggests that the stabilization is terminated when the volume inside the q=1 surface exceeds a critical value.

Quantitative comparisons between theory and experiment are at an early stage. However, a few monster sawteeth pulses have been analysed in terms of a model[7] which considers the relaxation to be initiated by a resistive kink instability and so far the results are in support of this theory.

Summary and Conclusions

The high beta experiments have found a soft non-disruptive limit at the Troyon-Gruber limit for kink modes and have achieved a maximum toroidal beta of 5.5%. The pressure profile at this limit is peaked, which is favourable for a fusion reactor but, less desirably, the fast particles seem to be strongly redistributed by the beta crashes. A clear demonstration of electron damping of fast magnetosonic waves has been achieved in the ion cyclotron range of frequencies and in high beta plasmas where TTMP is expected to be a major component in the absorption process. This result is encouraging for fast wave current drive studies on JET when the ICRF antennae have been modified to give good directivity. The nature of the density limit with beryllium limiters is considerably different from that with carbon limiters. In particular, there is no contraction of the current, usually no disruption and the
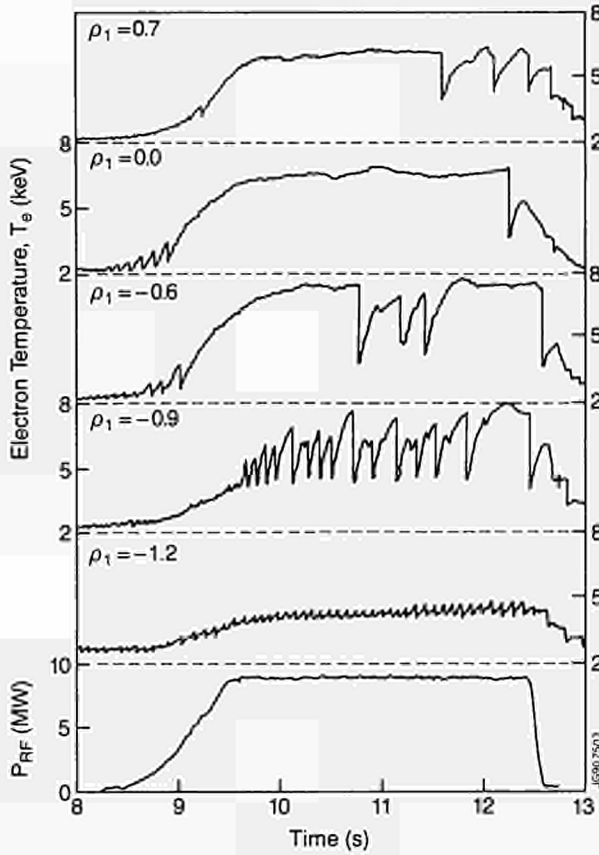
Fig.119 Monster sawtooth behaviour as the ICRF heating resonance position is varied.
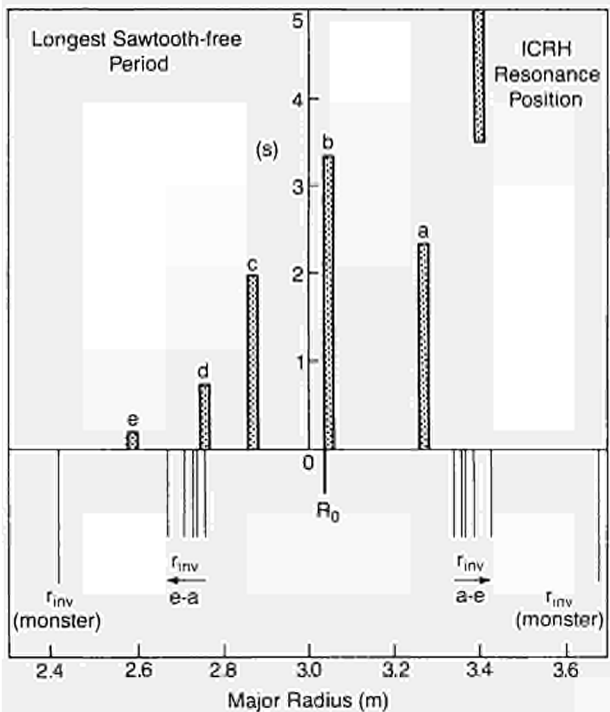
Fig.120 Monster sawtooth duration as a function of resonance position.

density rise is curtailed by a MARFE. The limit depends mainly on the input power, scaling in proportion to the square root of the power, and appears to be governed by the intensity of the edge radiation. Sawteeth have been stabilized by pellet injection which rases q(0) above unity. Strong evidence in support of the theory of monster sawteeth, which invokes stabilization by fast ions, has been obtained from studying the effects of varying the ICRH minority ion concentration and the ICRH resonance location.

References

[1] F Troyon, R Gruber et al Plasma Physics and Controlled Fusion, **26** (1984) 209.

[2] P Smeulders et al, 31st Meeting of the Plasma Physics Division of the American Physical Society, Anaheim, USA, (1989).

[3] D F H Start et al, to be published in Nuclear Fusion.

[4] V P Bhatnagar et al, Nuclear Fusion, **24** (1984) 955.

[5] L-G Eriksson and T Hellsten, JET Report JET P(89)65

[6] C Lowry and the JET Team, 31st Meeting of the Plasma Physics Division of the American Physical Society, Anaheim, USA, (1989).

[7] D J Campbell et al 31st Meeting of the Plasma Physics Division of the American Physical Society, Anaheim, USA, (1989).

[8] F Pegararo et al, Proc. 12th Int. Conf. on Plasma Physics and Contr. Fus. Res. Nice, France (1988) paper IAEA-CN-50/D-IV-6.

[9] D J Campbell et al Phys. Rev Letters, **60** (1988) 2148.

Energy and Particle Transport

Introduction

During 1989, attention has been devoted to specific themes which included:

- the obtention of valid and consistent sets of JET experimental data, that allow a reliable prediction of the equivalent operation with a deuterium and tritium mixture;

- the analysis of these data to determine local transport coefficients, including the assessment of the uncertainties in, for example, the ratio of the electron and ion heat diffusivities, χ_e and χ_i, due to the propagation of experimental errors;

- the use of transient perturbation methods (following the injection of laser-produced impurities and sawtooth collapse) to study particle and energy transport;

- the further development of theoretical models for energy confinement and their comparison with experiment.

Data Validation and Consistency

Establishing sufficient sets of internally consistent data
For several discharges, including standard L-modes and H-modes and others exhibiting strongly peaked profiles of density or temperature, sets of internally consistent data, sufficient for transport analysis, have been established. Particular attention has been devoted to the temperature data (ECE and LIDAR) and density data (LIDAR and FIR interferometer) which are consistent within their error bars, with the calculated magnetic equilibrium and with other independent constraints such as the total plasma energy, the surface voltage and the neutron yield. In many cases, apparent inconsistencies in the data arise, but these have been identified, discussed and, in many cases, resolved. Following discussions in the JET Data Coordination Committee, a Second Processing Chain for JET data will be introduced in the Spring of 1990 and this will facilitate a more routine identification of inconsistencies.

Predictions for DT Fusion Power
On the basis of these sets of consistent data the transport analysis code, TRANSP, has been used to simulate the equivalent JET operation in a deuterium and tritium mixture. The plasma and beam species, beam energy and power mix have to be changed.

For example, the D-T simulation of JET Pulse No: 20981 with all the NB injection at 140kV and a tritium target plasma indicates that the total fusion power is greater than 10MW for 0.5s (Fig 121(a)),[11]. The nominal input power is 18MW (Fig 121(b)) and, at the time of the peak fusion power of 12MW, the discharge has still not reached a steady state.

Local Transport Analysis

Energy transport
During 1989, particular attention has been given to the analysis of specific discharges that exhibit extremes in density and temperature profile and the best overall confinement properties obtained so far in JET[1-5]. These studies include high density pellet-fuelled and ICRF-heated discharges, medium density NBI-heated H-mode discharges, and low density high temperature NB-heated H-mode discharges.

The total heat flux, q, across a surface has been calculated from the heat and particle deposition profiles, the density and temperature profiles and their time rate of change. These heat fluxes may be interpreted in terms of an effective heat diffusivity, χ_{eff}, having subtracted convective energy losses. Of particular interest in 1989 was the availability of ion temperature
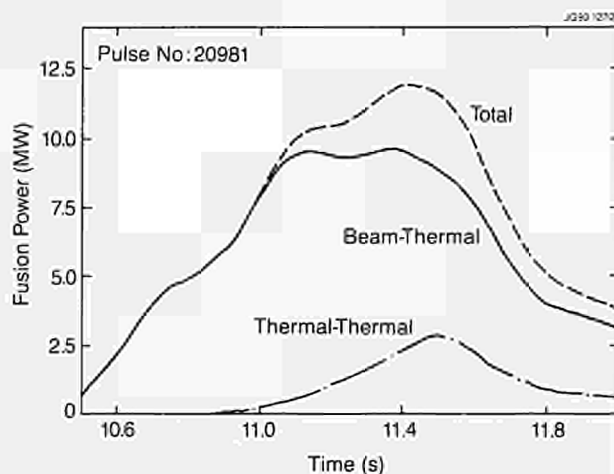
Fig.121 (a) Time behaviour of the total fusion power, beam-thermal fusion power and thermal-thermal fusion power for JET Pulse No: 20981.
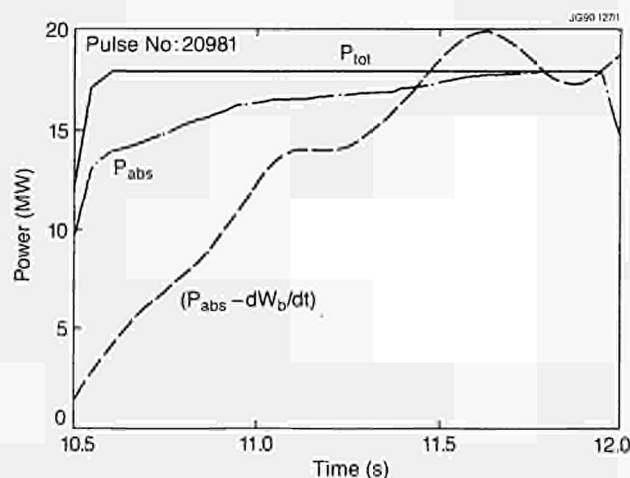
(b) Time behaviour of the total heating power, absorbed power and net absorbed power (after allowing for dW/dt) for JET Pulse No: 20981.

profiles from charge exchange spectroscopy between plasma ions and the neutral beam. This allowed the separation of χ_{eff} into electron and ion components, χ_e and χ_i, to be considered.

Error analysis
Techniques have also been developed to take account, in a well-defined way, of random and systematic errors in the data and their propagation through to the heat diffusivities. Of particular interest has been the error associated with energy equipartition, since this is crucial to the separation of χ_e and χ_i.

High density pellet-fuelled ICRF-heated discharges
Following the injection of deuterium pellets that penetrate to the centre of the discharge and the application of 6-9MW of hydrogen minority ICRH, the overall energy confinement is some 20% better, but the observed highly peaked profiles suggest considerably improved central confinement. The behaviour of χ_e and
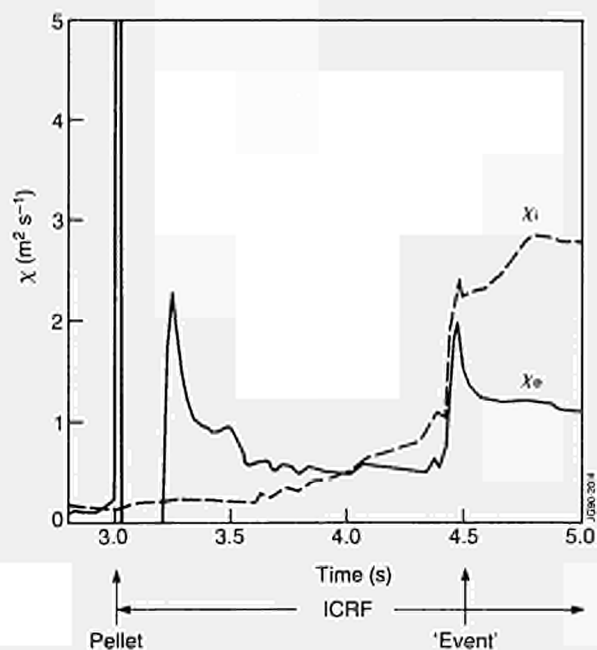
Fig.122 (a) Time behaviour of the effective heat diffusivities for ions, χ_i, and electrons, χ_e, for JET Pulse No: 16211.

χ_i with time in the central core shows low values ($1 m^2 s^{-1}$, or less, see Fig 122(a)) during much of the phase of improved confinement. Subsequently, both χ_e and χ_i increase by more than a factor of two. The spatial profiles of χ_e and χ_i Fig.122 (b)) show that χ is higher further out during the improved confinement phase. Later in the discharge, these values have not changed significantly, but the central values have increased and become comparable to those further out. The relative magnitude of χ_e and χ_i should be considered as only indicative since ion temperatures are not available for this discharge and energy equipartition and the models for ICRF power deposition are significant sources of uncertainty in the separation of χ_e and χ_i.
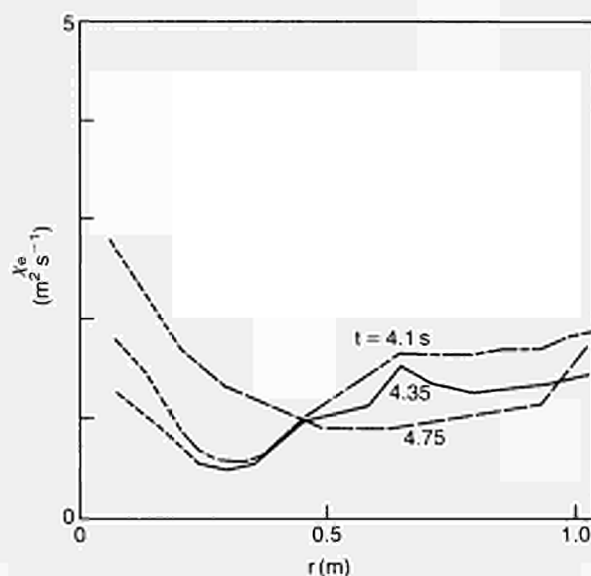
Medium density NBI-heated H-mode discharges
In medium density H-modes, the effective heat diffusivity, χ_{eff} increases to above its ohmic level at the start of neutral beam heating and then decreases progressively throughout the L- and H-phases. There is no obvious abrupt change at the transition. This behaviour is reflected by the ion heat diffusivity (obtained on the basis of the measured ion temperature profile) which decreases in time, ultimately becoming low (~$1 m^2 s^{-1}$) and within a factor of 2-3·$\chi_{i,neo}$ (Fig 123). χ_e on the other hand, is low (<$1 m^2 s^{-1}$) and is subject to large uncertainties.

Low density high temperature NBI-heated L- and H-mode discharges
The increase in density has been limited in JET by extensive ^3He discharge cleaning prior to operation in

(b) Spatial profiles of the effective heat diffusivities for ions, χ_i, and electrons, χ_e, for JET Pulse No: 16211.
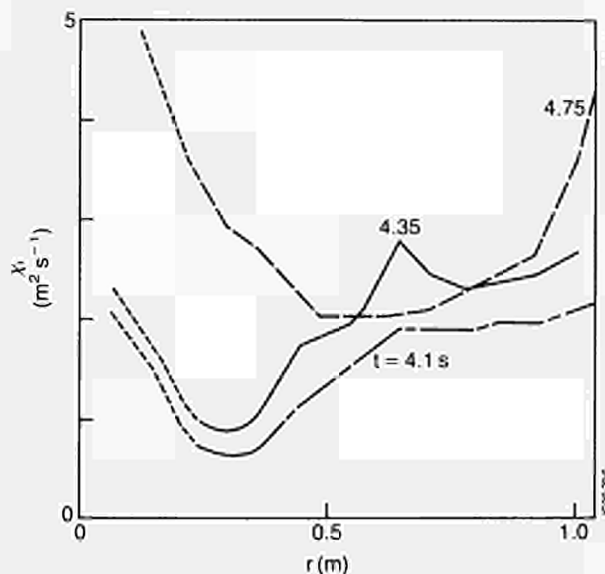
Fig.123 Time behaviour of the effective heat diffusitivity for ions, χ_i, for JET Pulse No: 15894.

deuterium, resulting in lower density, higher temperature, L- and H-modes with well separated ion and electron temperatures and low equipartition of energy over the central half of the plasma. The temporal and spatial behaviour of the heat diffusivities
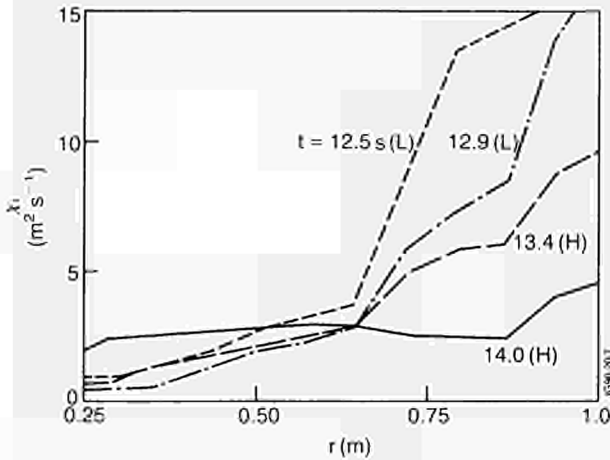
Fig.124 (a) Spatial profiles of the effective heat diffusivity for ions, χ_i, for JET Pulse No: 18757.
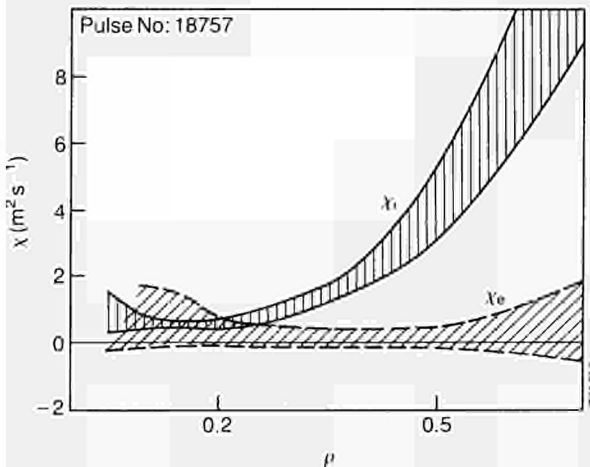
(c) Range of uncertainty, due to errors on T_e, T_i and also Z_{eff}, n_e and P_{rad}, on the spatial profiles of the effective heat diffusivities for ions, χ_i, and electrons, χ_e, at the end of the hot-ion, L-phase of JET Pulse No: 18757.

(b) Range of uncertainty, due to errors on T_e and T_i alone, on the spatial profiles of the effective heat diffusivities for ions, χ_i, and electrons, χ_e, at the end of the hot-ion, L-phase of JET Pulse No: 18757.
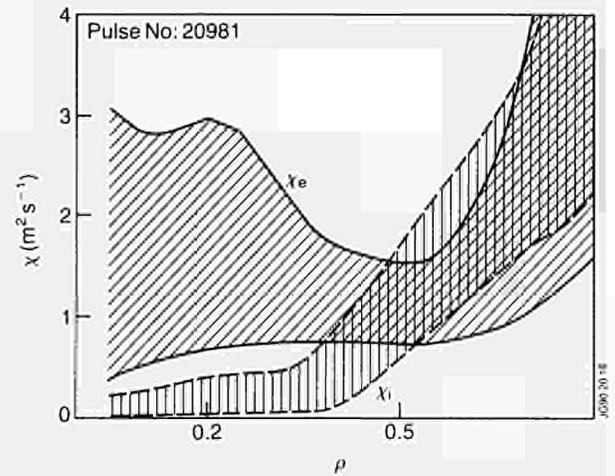
Fig.125 Range of uncertainty, due to errors on T_e and T_i alone, on the spatial profiles of the effective heat diffusivities for ions, χ_i, and electrons, χ_e, during the hot-ion, H-phase of JET Pulse No: 20981.

are similar to those for the medium density H-mode with χ_i flattening progressively as the density increases and broadens with time (Fig 124(a)). At the end of the L-phase, χ_i appears to be significantly larger than χ_e, even when account is taken of the errors in the measurements of T_e and T_i (Fig 124(b)). When errors in the measurement of Z_{eff}, n_e and P_{rad} are also taken into account χ_i and χ_e remain separated but their bands of uncertainty increase (Fig 124(c)). Operation at somewhat higher densities and with some NBI at 140kV leads to more electron heating and in this case χ_e is

higher and comparable to χ_i. However, energy equipartition is more important in these discharges and the introduction of errors in the measurements of T_e and T_i alone results in a wide band of uncertainty (Fig 125).

Particle transport

The relaxation of the peaked density profiles which follow pellet injection in ohmic and good confinement, auxiliary heated discharges has been modelled with an effective particle diffusivity, $D_{eff}(OH)$, found to be lower in the central plasma than further out (Fig 126). No large anomalous inward convection in the central plasma is required[6]. Under conditions of poor confinement, that is, auxiliary heated discharges with enhanced MHD activity, the diffusivity has to be

(a)

(b)

(c)
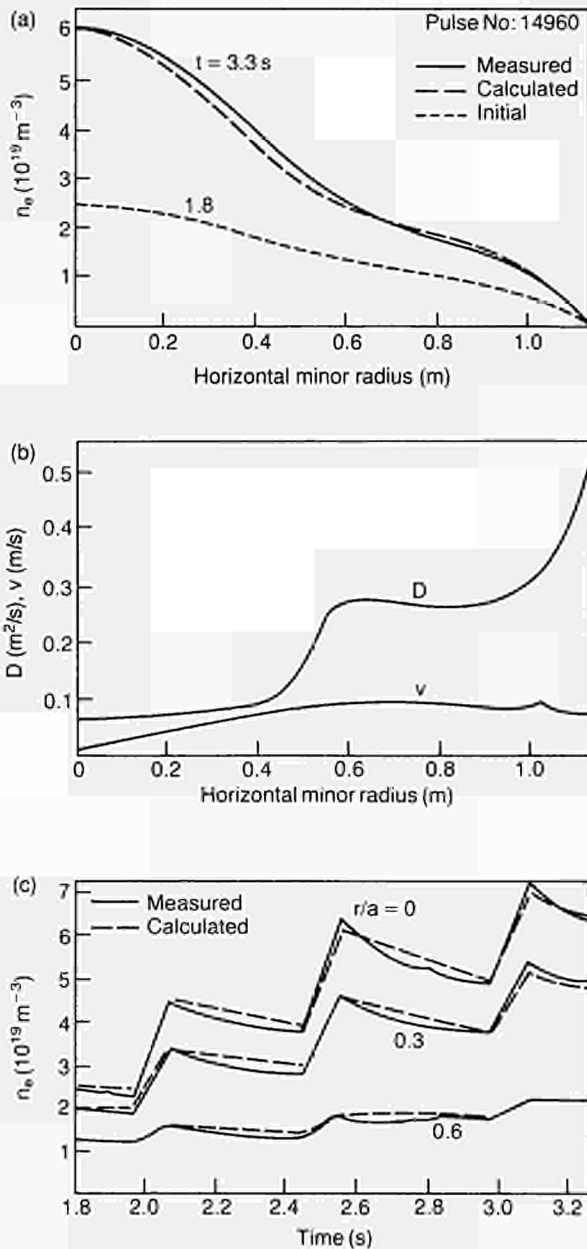
Fig.126 Comparison of the measured and calculated evolution of the electron density during the ohmic heated current rise with multiple 2.7 mm pellet fuelling. Shown are (a) the density profiles; (b) the transport coefficients used for the modelling; and (c) the temporal evolution of the density.

modified by a term dependent on the electron temperature, T_e:

$$D_{eff} = D_{eff}(OH)\left[1 + C \cdot T_e^\alpha\right] \ , \ \text{with} \ \ \alpha \sim 1.3$$

Again there is no need for an anomalous convection.

Furthermore, as shown in Fig 127, D_{eff} decreases with increased profile peakedness (although this correlation may be due to an increase in density rather than profile peakedness). The comparison of D_{eff} with theory (particularly those relating to η_i-mode driven turbulence) shows some qualitative agreement for a

typical pellet-fuelled peaked density profile discharge (Fig 128), but in general the existing models and theories of particle transport do not predict adequately the observed density evolution.
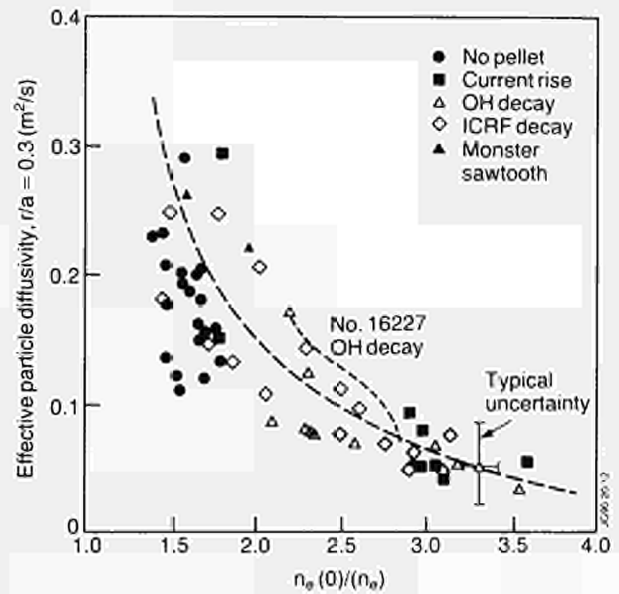
Fig.127 Effective particle diffusivity (electron) at r/a=0.3 as a function of density profile peakedness. The particle diffusivity is derived from a particle balance calculation assuming no anomalous inward particle convection. Values are averaged over 0.4s during a discharge and each point represents a different discharge. The time history of ohmic Pulse No: 16227 is also shown.
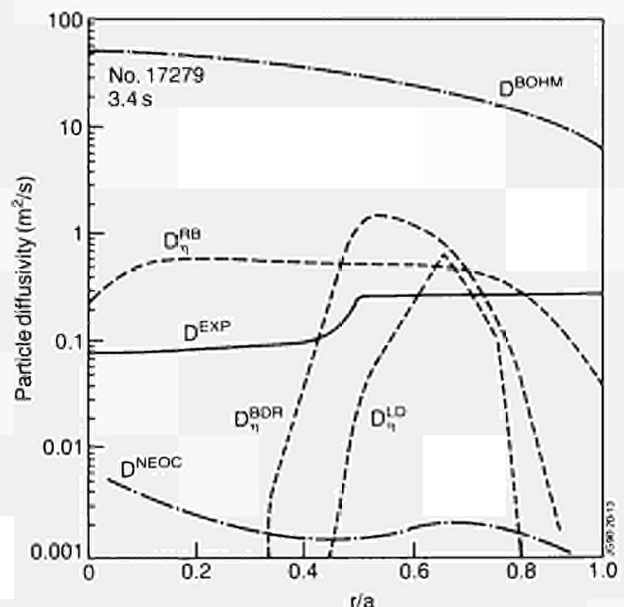
Fig.128 The experimentally determined particle diffusivity for a peaked density profile, pellet-fuelled discharge is compared with the diffusivities obtained on the basis of various theories for η_i-mode driven turbulence (Lee G S and Diamond P H, Phys. Fluids 29, 3291 (1986), Romanelli and Briguglio, JET-P (88)31, and Biglari, Diamond and Rosenbluth, Phys. Fluids B 1, 109 (1989)). The neoclassical and Bohm diffusivities are also shown for reference.

Impurity transport

Impurity transport has been measured in ohmic, ICRF-heated and H-mode plasmas. Following the injection of laser-produced, high-Z impurities, the temporal evolution of the emissivity profiles are obtained with
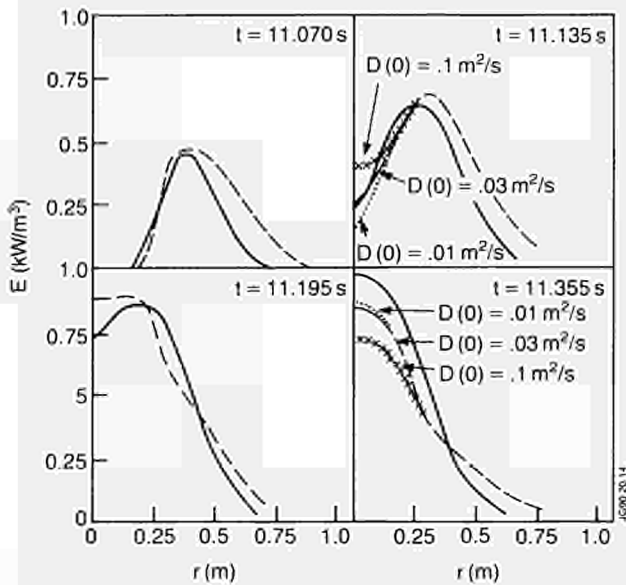
Fig.129 (a) Experimental (solid line) and simulated (dashed line) profiles, respectively, at t = 11.070s, 11.135s, 11.195s and 11.355s for Ni injection, using D and V as shown in the following figure. The effect of varying the central value of the diffusion coefficient is shown for the profiles at t = 11.135s and t = 11.355s.
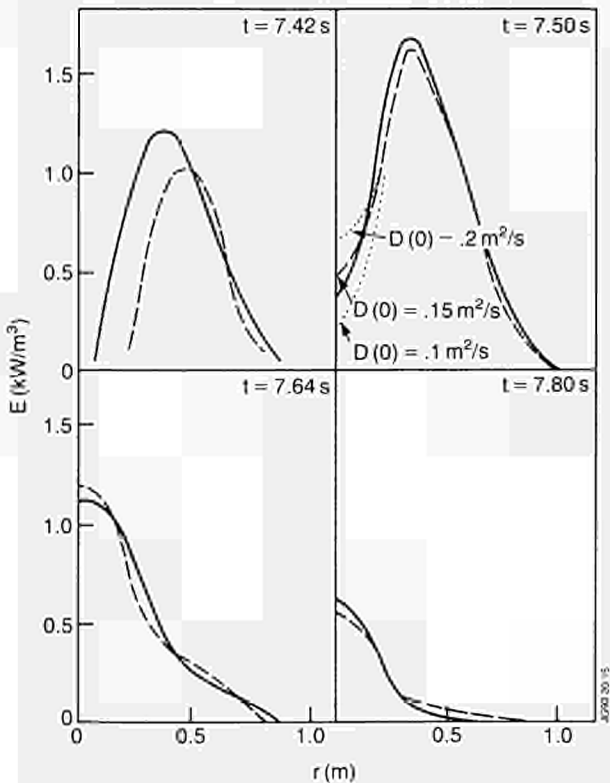
(b) Experimental (solid line) and simulated (dashed line) profiles, respectively at t = 7.42s, 7.50s, 7.64s and 7.80s for Mo injection, using D and V as shown in the following figure. The effect of varying the central value of the diffusion coefficient is shown for the profile at 7.50s.

good spatial and temporal resolution by the soft X-ray cameras diagnostic. Impurity transport codes have been used to model this evolution and allows radially dependent particle transport coefficients, D_Z and V_Z, to be determined.

For both ohmic and ICRF-heated discharges, experimental X-ray profiles are well simulated (Fig 129,[7]) with an impurity transport model in which D_Z and V_Z within the central plasma are significantly reduced from their values elsewhere (Fig 130). The transport is generally increased for the ICRF-heated discharge and also during the sawtooth collapse when impurities leave or enter the central plasma. These results are consistent with the observation of strongly peaked electron density profiles with central fuelling and the faster decay of these profiles with ICRF heating. The results are also consistent with a previous model[8]. Diffusion coefficients are a factor 2-5 higher than those for neoclassical transport in the centre, increasing to a factor 60-300 further out.
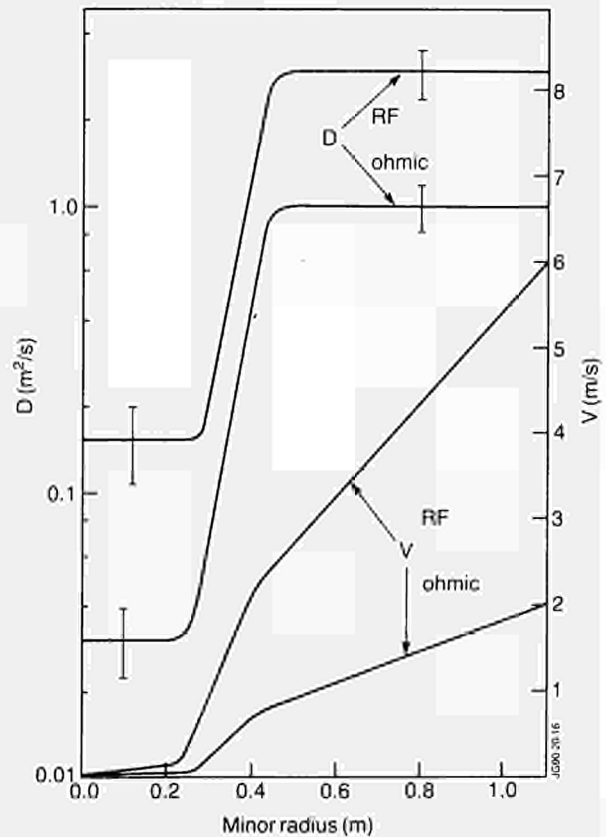
Fig.130 The radial profiles of D (logarithmic scale on the left) and of V (linear scale on the right) used to simulate the injection of Ni into an ohmic plasma and the injection of Mo into a RF heated plasma.

The emission from the lower ionisation stages of cobalt, injected some 0.5s after the start of an H-mode, rises rapidly (within 0.1s) to a steady value which persists to the end of the H-mode (Fig 131(a),[9]). The emission from the higher ionisation stages of intrinsic impurities (such as nickel and oxygen), on the other hand, increase continuously during the H-mode. The
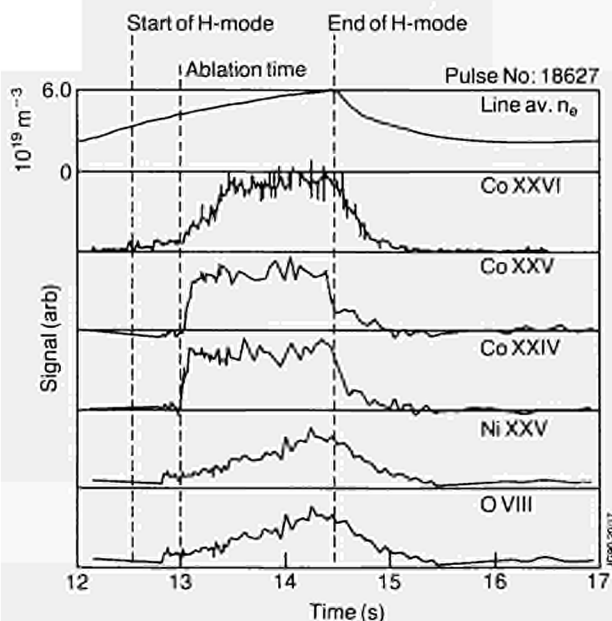
Fig.131 (a) The experimental time development of injected Co and intrinsic Ni and O during an H-mode (JET Pulse No: 18627).
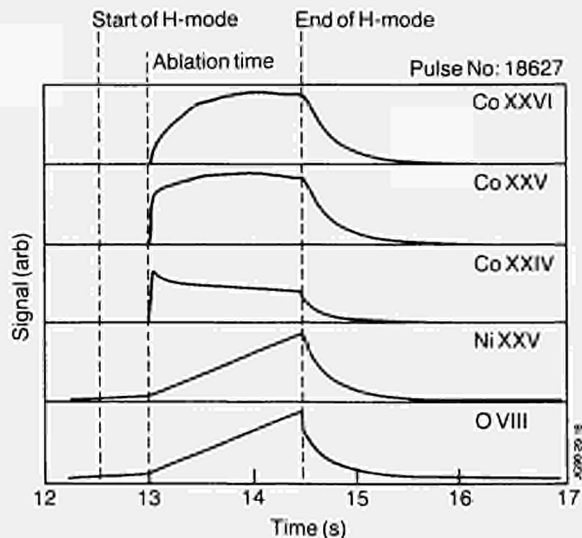
(b) The results of modelling the time development of injected Co and intrinsic Ni and O during an H-mode (JET Pulse No: 18627).

bulk plasma acts, therefore, as a "slightly leaky integrator" of impurities which have confinement times considerably longer than that for plasma energy. Transport modelling (Fig 131(b)) indicates that this behaviour requires a strong inward convection (V_Z / D_Z ~ 50m^{-1}) at the edge of the plasma (Fig 132).

Measurements of χ_e and D_e Following Sawtooth Collapse

The measurement of energy and particle transport coefficients during transient plasma conditions[10,11] has progressed considerably with the modelling of the propagation of temperature perturbations (determined from the electron cyclotron polychromator) and density perturbations (determined from the multichannel reflectometer) following the collapse of a sawtooth.
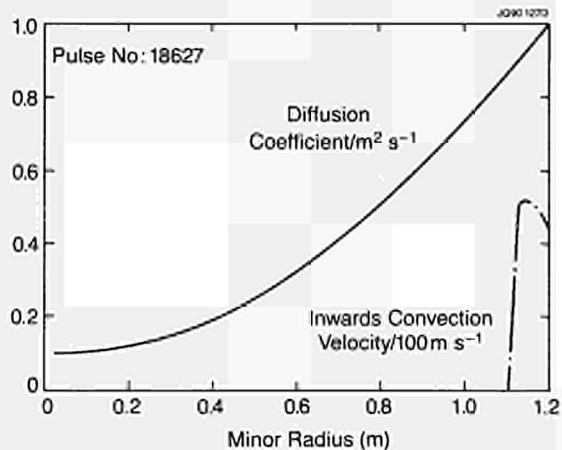
Fig.132 The radial profiles of the diffusion coefficient and the inwards convection velocity used to simulate the time development of injected Co and intrinsic Ni and O during an H-mode (JET Pulse No: 18627).

Temperature perturbation

The propagation characteristics of the temperature perturbation have been determined for a wide range of JET discharges. Using the speed and damping of the perturbation, an effective electron heat diffusivity, χ_{hpp}, has been found[12] to have little or no dependence on the input power and may be represented (Fig 133) by the empirical scaling law:

$$\chi_{hpp} = (2.2 \pm 0.3)\left(\frac{r}{a}\right)^{1.4 \pm 0.2} Z_{eff}^{0.5 \pm 0.1} T_{c.av}^{0.5 \pm 0.1}$$

Furthermore, 1-1/2 D transport modelling indicates that the propagation is better simulated by a transport model that produces confinement degradation via a transport threshold at a critical value of the electron temperature gradient[8], rather than via a non-linear dependence of the heat flux on the pressure gradient[13].
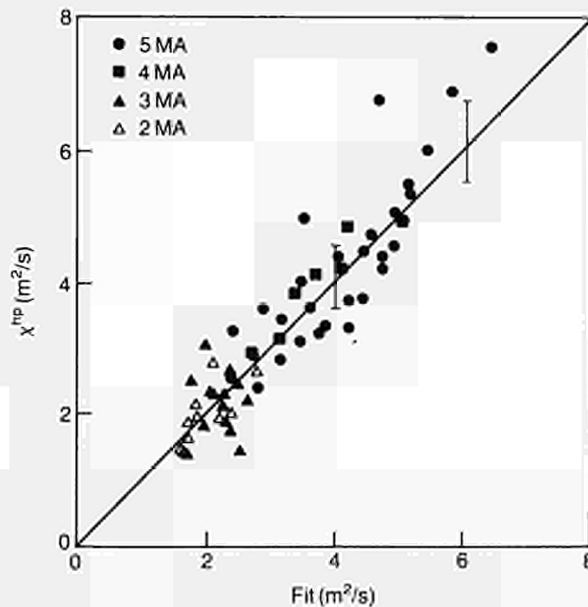
Fig.133 The effective electron heat diffusivity obtained from heat pulse propagation measurements, χ_{hpp}, versus the empirical fit given in the text.

Density perturbation

The propagation characteristics of the density perturbation[14,15] indicate that the density pulse is slower than the temperature pulse, that the density pulse (Fig 134) is comprised of both an outward and inward propagating perturbation (the latter resulting from the earlier interaction of the temperature pulse with the limiters) and that a temporary decrease appears on the reflectometer signal as the temperature pulse passes some 10-20ms after the crash of a large sawtooth.
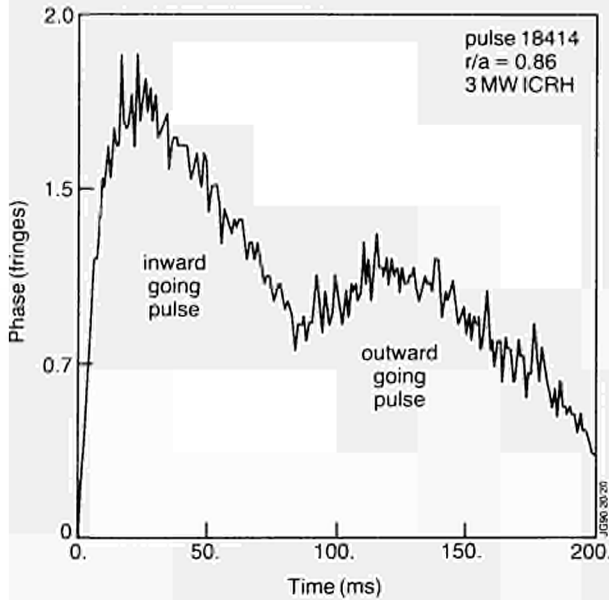
Fig.134 Example of the measured phase change during a sawtooth period on which the two density pulses are clearly visible (Probing frequency is 39 GHz, $n_c = 1.92 \times 10^{19} m^{-3}$ and r/a = 0.86)

Simultaneous measurements of temperature and density perturbations

When simultaneous measurements of the temperature and density perturbations are available, it has been possible not only to compare directly the ratio χ_e/D_e but also to assess the degree of coupling between the perturbations[15] by analysing carefully the full temporal behaviour of the perturbation and the solution of the linearised equations for both perturbations and including diffusion, convection, damping and sources. Typically:

$$\frac{\chi_e}{D_e} = 12 \pm 4$$

and coupling terms allow the simulation of the temporary decrease in density as the temperature pulse passes (Fig 135).

Theoretical Progress

A unified global scaling law for energy transport

Progress has been made in representing global energy confinement in a way that unifies the numerous empirical and theoretical scaling laws of tokamak transport and offers the possibility of better understanding.
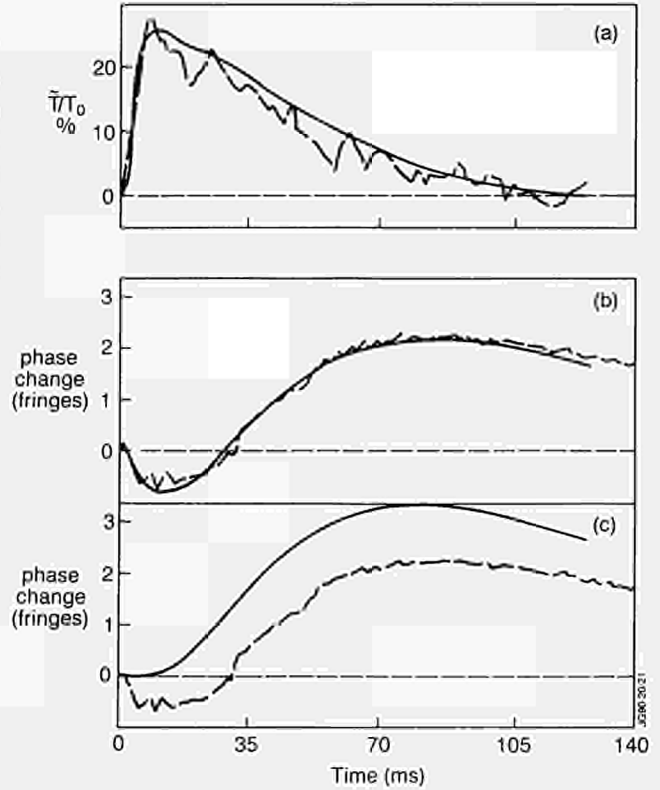
Fig.135 Example of the observed dip in the density as the heat pulse passes for JET Pulse No: 19596 at radial position r/a = 0.66. Dashed lines are data from ECE and reflectometer, respectively; solid lines are the result of simulations.
(a) shows the normalized electron temperature perturbation;
(b) gives the phase change simulated with coupling;
(c) the phase change simulated without coupling.

The scaling of the local heat diffusivity, χ, may be derived with minimal assumptions from the non-linear gyro-kinetic equations of plasma physics and can be cast into two limiting forms[16], corresponding to short and long wavelength turbulence. Furthermore, these scalings may be represented as the product of two terms which for short wavelength turbulence (corresponding to scale lengths, $\lambda \sim \rho_i$ (the ion Larmor radius) $\ll$ L (a typical scale length)) may be written as:

$$\chi_s = D_B(\rho_i/L) \, F_s \, (\nu^*, \beta, q .....)$$

This comprises a leading term with the dependences of gyro-reduced Bohm diffusion, $D_B = kT/eB$, and a function, F_s, the form of which is defined by the specific physical mechanism involved and is dependent largely on the normalised collisionality, ν^*, and the normalised plasma pressure, β (as shown in Table XIII for various theoretical models).

The scaling of the global energy confinement time, τ_E, may be expressed formally in terms of χ and, for short wavelength turbulence, may be written as:

$$\tau_E = \frac{3a^2}{4\overline{\chi}} = \tau_{E_s} F_s^{-2/5}, \quad \text{where } \tau_{E_s} = C_x a I^{4/5} \left(\frac{naR\kappa}{P} \right)^{3/5}$$

$$\text{and } F_s = F_s \left(\nu^*, \beta, q ... \right)$$

103

Table XIII
Theoretical scaling laws for the confinement time τ_E, with the function F_s given as $F_s = v^{*\alpha}\beta\gamma$.

Theory	α	γ
Collisional drift wave	0,1/3,2/3,1	0
Collisionless trapped electron mode	0	0
Dissipative trapped electron mode	-1,-2	0
Dissipative trapped ion mode	-1	0
η_i mode	0	0
Overlapping islands	0	0
Resistive fluid turbulence	1	-1
Res. fluid turbulence (electrostatic)	1	0
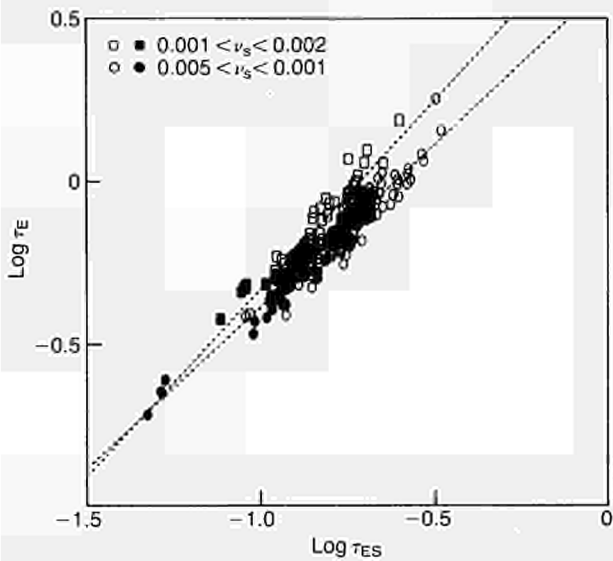
Fig.136 (a) JET H-mode data on confinement time versus the short wavelength scaling of τ_E. Open symbols correspond to $0.3 <\beta<0.5$ and full symbols to $0.5 <\beta< 1.1$.
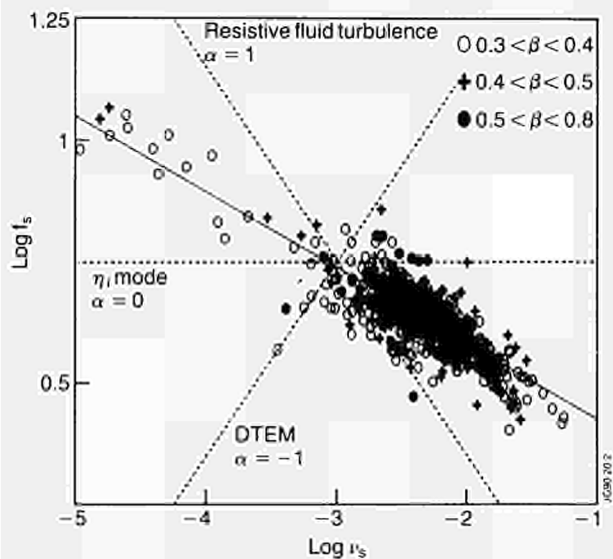
(b) Variation of τ_E/τ_{ES} with v^* for three ranges of β (H-mode data) and three theoretical scalings. Collisional drift waves have $1/3 <\alpha< 1$. The solid line arises from a linear fit to the data.

JET data can be well-fitted to this form (Fig 136(a) shows the fit for the short wavelength model). The spread of data in Fig 136(a) is primarily due to the variation of F with v^*. As pointed out previously[8], it is not possible to draw firm conclusions about the β dependence of F since there is little variation in β for the JET data. However, it is possible to discard some theoretical models (eg. those based on the dissipative trapped electron mode, see Fig 136(b)) but not others (eg. those based on the ion temperature gradient instability (η_i-modes), but see below).

Furthermore, it has been shown that most of the empirical scaling laws purporting to describe tokamak confinement can be cast into the gyro-reduced Bohm form by appropriate choice of F (see Table XIV). The different forms of F reflect the largest uncertainty (about a factor of 4) when extrapolating to future devices, but this uncertainty can be reduced to about 30% if v^* and β are kept constant for the extrapolation. There remains, however, an uncertainty in the scaling with plasma size and this is being addressed by international collaboration and the establishment of an ITER H-mode database.

Table XIV

The tokamak scaling laws for auxiliary heated tokamaks recast to match the short wavelength scaling. The parameter, δ, is the residual in the exponents required to make scaling laws dimensionally correct.

Scaling law	α	γ	δ
Ref.[16]	0.4	-0.4 to 0.4	0
Rebut-Lallia	0.5	-0.5	0
ASDEX	0.54	-0.49	0.056
Mirnov	0.54	-0.49	0.056
Shimomura	0.54	-0.49	0.056
Odajima	0.42	-0.8	0.108
Kaye big	0.47	0.13	0.068
Kaye all	0.49	0.25	0.132
Kaye-Goldston	0.28	0.58	0.132
Goldston	0.44	0.2	0.1
Neo Kaye	0.37	0.55	0.08
Resistive MHD	-	-	-
Lackner	0	0	0
T-10	-0.02	-0.82	0.044
Merezhkin	0	-1	0
Alcator	0.19	-1.18	0.072

Objective of local transport properties from global confinement data

The formulae for interpreting auxiliary heating data for global energy confinement in terms of local transport has been extended [17] to include non-stationary

plasmas with non-zero edge temperatures. Consider the simplified total energy balance equation:

$$3\frac{d}{dt}(nT) = -\nabla.Q + p$$

p is the net heating rate and the total heat flux, Q, is assumed to comprise a diffusive term proportional to the temperature gradient, ∇T, and a negative, non-diffusive flow term which could be a heat pinch or a critical electron temperature gradient threshold for transport. Integrating this equation three times gives the equation for the total stored energy:

$$W = W_p + W_o + \tau_\chi \left[\eta_Q P_{in} - \eta_{nT} \frac{dW}{dt} \right]$$

The pedestal energy, W_p, appears naturally in this formulation, as does the usual off-set term, W_o. The ideal incremental confinement time, τ_χ, depends on the radial profile of the heat diffusivity, χ, as do the heating effectiveness parameters, η_Q and η_{nT}. The pedestal energies evaluated at the 95% flux surface during the H-phase of 3MA single null X-point discharges are plotted in Fig 137 against the net input power. A pedestal energy of up to 4MJ contributes substantially to the total stored energy. Furthermore, there is no pronounced degradation of W_p with input power. This interpretation confirms, for two models of the heat diffusivity, that the main improvement in confinement in H-mode plasmas arises in the edge with the establishment of the pedestal. The form of W_p depends in detail not only on the energy equation but also on the particle equation used.

Global energy confinement also appears to depend on the current profile[18] (rather than the current alone)

since current profile broadening (probably due to the development of a bootstrap current in the edge[19]) has been observed unambiguously in H-modes and correlates with good confinement (Fig 138), perhaps due to the suppression of ballooning modes[20] or tearing modes[21]. However, the causal relationship between current profile broadening and confinement has not been established.
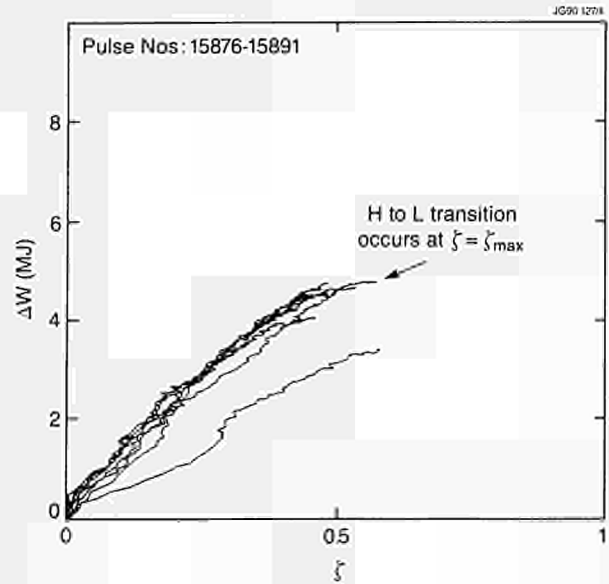
Fig.138 The increase in total stored energy is seen to be proportional to the current profile broadening parameter, ζ, for seven JET pulses exhibiting H-mode confinement.
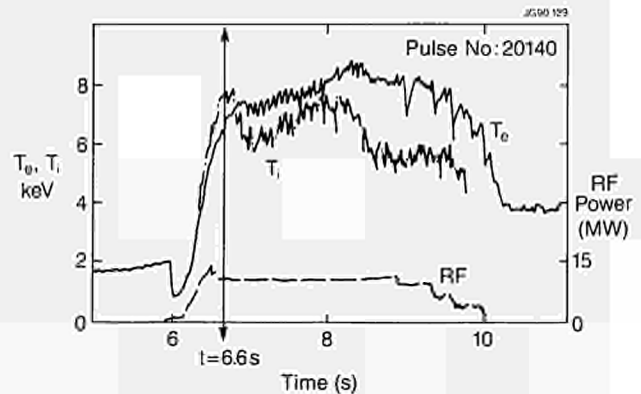
Fig.139 The time behaviour of the central electron and ion temperatures for JET Pulse No: 20140 shows a sudden change in the slope of T_i at 6.6s, indicating, perhaps, the on-set of some additional loss mechanism. The time behaviour of the total applied ICRF heating power is also shown.

η_i-mode transport

Energy transport predicted to result from turbulence induced by the ion temperature gradient instability (η_i-mode) has been compared with that deduced experimentally.

Good confinement has sometimes been observed when the density profile is sufficiently peaked (eg pellet-fuelled, ICRF-heated discharges[3]) for the η_i-mode to be stable. An apparent increase in transport has even been observed at a later time (Fig 139,[22]) when

Fig.137 Total stored energy, W, and the pedestal energy, W_p (evaluated at the radius of the 95% flux surface), as a function of net input power during the H-phase of 3MA JET single null X-point discharges.

the density profile is less peaked. However, the difference between χ_{eff} and that predicted by theory increases as η_i (=$n\nabla T/T\nabla n$) increases above η_{crit} (Fig 140). Furthermore, for a large number of L-mode NBI and ICRF-heated "monster" and long sawtooth-period discharges, a comparison between the experimental total heat flux and that predicted by some of the more plausible models for η_i-mode driven turbulence indicate that η_i-mode transport is often far in excess of even the total heat flux at high temperature while it is insufficient to account for the losses at low temperature (Fig 141,[23]). The lack of accurate measurements of many parameters in the η_i-mode theory introduces many uncertainties into the assessment of a theory that is still evolving.
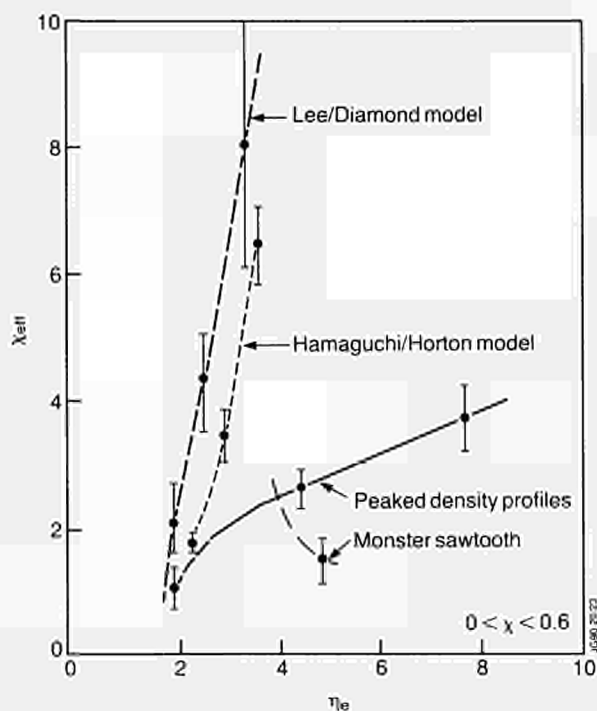
Fig.140 *The effective heat diffusivity, χ_{eff} determined for peaked density profile and "monster" sawtooth discharges, versus the η_e parameter, obtained from LIDAR measurements, together with the corresponding functional dependence for two different theories of η_i mode driven turbulence (Lee G S and Diamond P H, Phys. Fluids 29, 3291 (1986), Hamaguchi S and Horton W, Institute for Fusion Studies, University of Texas Report, IFSR 383).*

Effect of magnetic turbulence on the diffusion of charged particles

The non-linear diffusion of charged particles due to stochastic electromagnetic fields has also been studied[24] using the exact equations of motion to derive a general expression for the diffusion coefficient and to study the consequences in both the quasi-linear and non-linear regimes for fast particles which, it is found, remain neoclassical for arbitrary turbulence.

Diffusion of chaotic magnetic field lines

The statistical properties of chaotic magnetic field lines have been analytically studied and numerically
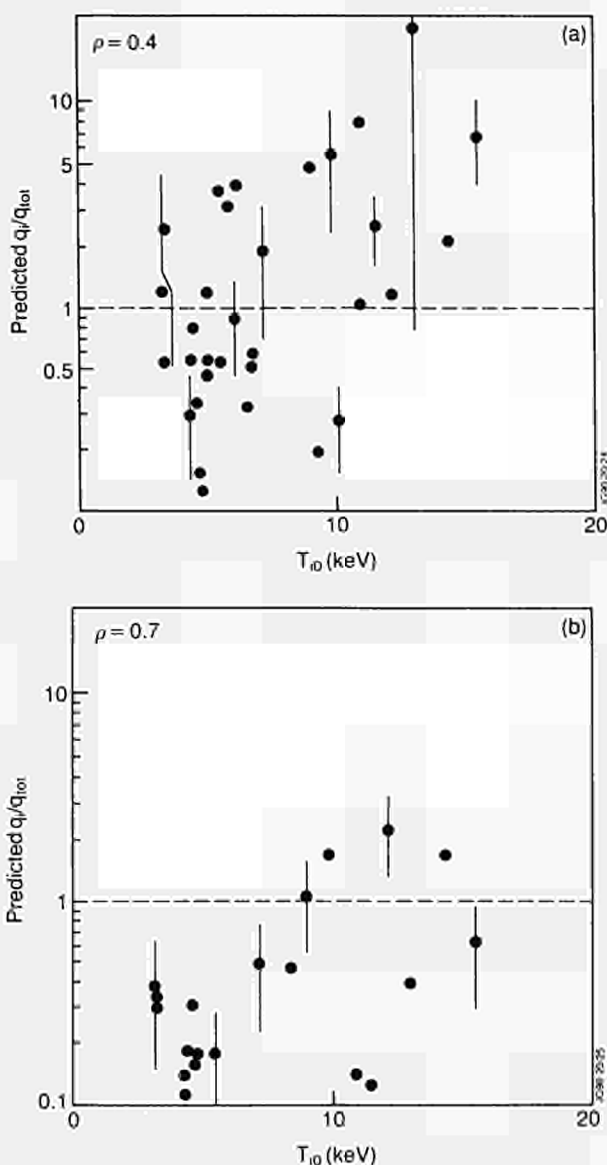
Fig.141 *The ratio of the theoretical ion heat flux, as predicted for η_i mode driven turbulence by Lee G S and Diamond P H, Phys. Fluids 29, 3291 (1986), and the experimentally determined total heat flux as a function of the ion temperature at a normalised minor radius of (a) 0.4 and (b) 0.7.*

determined from the integration of the field line equations[25]. The chaotic field lines are found to follow a diffusion-propagation process through the island chains:

$$\alpha\frac{\partial^2 F}{\partial n^2} - 2(1-\alpha)\frac{\partial F}{\partial p} - (2\alpha-1)\frac{\partial^2 F}{\partial p^2} = 0$$

where F(n,p) is the distribution of chaotic field lines at chain n associated with the initial distribution F(n,0) after covering the distance p toroidally and α is the fraction of chaotic field lines progressing from one chain to the next. α=0 corresponds to the existence of laminar surfaces between island chains; α=1/2 corresponds to a mixture of island chains and chaotic regions; α=1 corresponds to predominantly chaotic behaviour.

Specifically, when islands coexist in equilibrium with a chaotic region ($\alpha=1/2$), the behaviour of the chaotic field lines is close to diffusion, with an associated diffusion coefficient, D_c, defined as the inverse of the average number of toroidal turns made by the field lines to cross one island chain. An approximation to the values computed for D_c, valid for $0.75 \leq \gamma \leq 2$, is given by:

$$D_c = 1.25(\gamma - 0.75)^{2.1}$$

Anomalous energy transport

The above result on the diffusion of chaotic field lines provides a better understanding of the basis for the Rebut-Lallia-Watkins model for local confinement[8], which relies on turbulence in the magnetic topology as the underlying phenomenon for tokamak transport. With this assumption, together with heuristic and dimensional arguments, specific expressions for the electron and ion heat fluxes have been derived[8, 26]:

$$F_e = -n_e\chi_{an,e}\nabla kT_e\left(1 - \frac{\left|(\nabla kT_e)_{cr}\right|}{\nabla kT_e}\right)$$

$$x\,H(\nabla q)H\left(1 - \frac{\left|(\nabla kT_e)_{cr}\right|}{\nabla kT_e}\right) + F_{e,neo}$$

$$F_i = -n_i\chi_{an,i}\nabla kT_i\left(1 - \frac{\left|(\nabla kT_e)_{cr}\right|}{\nabla kT_e}\right)$$

$$x\,H(\nabla q)H\left(1 - \frac{\left|(\nabla kT_e)_{cr}\right|}{\nabla kT_e}\right) + F_{i,neo}$$

$$\chi_{an,e} = 0.5c^2(\mu_o m_i)^{1/2}\left(1 - \sqrt{\frac{r}{R}}\right)(1 + Z_{eff})^{1/2}$$

$$x\left|\frac{\nabla T_e}{T_e} + \frac{2\nabla n_e}{n_e}\right|\frac{q^2}{\nabla q}\frac{1}{B_t\sqrt{R}}\sqrt{\frac{T_e}{T_i}}$$

$$and \quad \chi_{an,i} = 2\chi_{an,e}\frac{Z_i}{\sqrt{1+Z_{eff}}}\sqrt{\frac{T_e}{T_i}}$$

$$with \quad (\nabla kT_e)_{cr} = 0.06\left(\frac{e^2}{\mu_o m_e^{1/2}}\right)^{1/2}\frac{1}{q}\left(\frac{\eta j B_t^3}{n_e(kT_e)^{1/2}}\right)^{1/2}$$

These expressions give rather satisfactory simulations of experimental results, and predictions for the expected performance of JET at full planned power and in the new pumped divertor configuration (Table XV, [26]) and provide also an indication of the implications for next step tokamaks.

References

[1] "Local Confinement Properties of JET-Plasmas and Extrapolation to D-T Operation" Bull. Am. Phys. Soc. **34(9)**, 2055 (1989) and JET Preprint JET P(89)80, 33 (1989), Balet B *et al*

[2] "Confinement Properties of JET Plasmas with Different Temperature and Density Profiles" Plasma Physics and Controlled Fusion **31**, 1713 (1989) and JET Preprint JET-P(89)46, Watkins M L *et al*

[3] "Transport Analysis of Pellet-Enhanced ICRH Plasmas in JET" in "Controlled Fusion and Plasma Physics" (Proc. 16th Europ. Conf. Venice, 1989) **13B(I)**, 131 (1989), Hammett G W *et al*

[4] "Ion Thermal Conductivity and Convective Energy Transport in JET Hot-Ion Regimes and H-modes" in "Controlled Fusion and Plasma Physics" (Proc. 16th Europ. Conf. Venice, 1989) **13B(I)**, 283 (1989), Tibone F *et al*

[5] "High Temperature L- and H-mode Confinement in JET" Submitted for publication in Nuclear Fusion (1990), Balet B *et al* .

[6] "Particle Confinement and Transport in Pellet Fuelled JET Plasmas" Bull. Am. Phys. Soc. **34(9)**, 2057 (1989) and JET Preprint JET-P(89)80, 155 (1989), Baylor L *et al*

[7] "Impurity Transport in JET Using Laser-injected High-Z Impurities in Ohmic and RF-heated Plasmas" JET Preprint JET-P(90)01 Submitted for publication in Nuclear Fusion (1990), Pasini D *et al*

[8] "The Critical Temperature Gradient Model of Plasma Transport: Applications to JET and Future Tokamaks" in "Plasma Physics and Controlled Nuclear Fusion Research 1988" (Proc. 12th Int Conf. Nice 1988) **2**, 191, IAEA, Vienna (1989), Rebut P-H *et al*

Table XV

Predicted plasma performance[26] on the basis of the critical electron temperature gradient model for heat transport with 35MW of additional heating and different JET configurations: Type (a) new pumped divertor, . H-mode, 'monster' sawtooth; Type (b) full aperture, H-mode, 'monster' sawtooth; Type (c) fall-back, L-mode, 'monster' sawtooth; and Type (d) fall-back, L-mode, flattened profiles.

Z_{eff}	$T_e(0)$ (keV)	$n_i(0)$ (10^{19} m^{-3})	$T_i(0)$ (keV)	τ_E (s)	β_t (%)	P_α (MW)	Q_{th}	Type
2.0	8.5	13.0	7.8	0.67	3.2	2.4	0.34	(a)
2.0	12.0	10.0	10.0	0.73	3.0	3.2	0.45	(b)
2.0	7.20	10.0	6.3	0.35	1.9	0.6	0.09	(c)
2.0	3.6	10.0	3.5	0.25	1.4	0.2	0.03	(d)

[9] "Transport Studies During Sawteeth and H-modes on JET Using Laser Ablation" in "Controlled Fusion and Plasma Physics" (Proc. 16th Europ. Conf. Venice, 1989) **13B(I)**, 79 (1989), Hawkes N *et al*

[10] "Measurement of Correlations between Thermal and Particle Transport in JET" in "Plasma Physics and Controlled Nuclear Fusion Research 1988" (Proc. 12th Int Conf. Nice 1988) **1**, 483, IAEA, Vienna (1989), Cheetham A D *et al*

[11] "Correlation of Heat and Particle Transport in JET" in "Proc. IAEA Tech. Com. Mtg on Pellet Injection and Toroidal Confinement, Gut Ising, FRG, October 1988" Report IAEA-TECDOC-534, 113 (1989) and JET Preprint JET-P(88)60, Gondhalekar A *et al*

[12] "Heat Pulse Analysis in JET and Relation To Local Energy Transport Models" in "Controlled Fusion and Plasma Physics" (Proc. 16th Europ. Conf. Venice, 1989) **13B(I)**, 279 (1989), de Haas J C M *et al*

[13] "Local Heat Transport in JET Plasmas" in "Controlled Fusion and Plasma Heating" (Proc. 15th Europ. Conf. Dubrovnik, 1988) **12B(I)**, 115 (1988), Christiansen J P *et al*

[14] "Measurements of the Electron Particle Diffusion Coefficient with the JET Multichannel Reflectometer" in "Controlled Fusion and Plasma Physics" (Proc. 16th Europ. Conf. Venice, 1989) **13B(I)**, 99 (1989), Sips A C C *et al*

[15] "Simultaneous Measurements of Thermal Conductivity and Particle Diffusivity in JET and Their Interpretation" Bull. Am. Phys. Soc. **34(9)**, 2055 (1989) and JET Preprint JET-P(89)80, 123 (1989), Sips A C C *et al*

[16] "A Unified Physical Scaling Law for Tokamak Energy Confinement" Submitted for publication in Nuclear Fusion (1990), Christiansen J P, Cordey J G and Thomsen K

[17] "Offset-Linear Description of H-mode Confinement" in "Controlled Fusion and Plasma Physics" (Proc. 16th Europ. Conf. Venice, 1989) **13B(I)**, 233 (1989), Thomsen K *et al*

[18] "The Role of Current Profile Broadening in L- and H-mode Plasmas" JET Preprint JET-P(89)56 To be published in Nuclear Fusion (1990), Christiansen J P and Cordey J G

[19] "Current Density Profile Evolution in JET" in "Controlled Fusion and Plasma Physics" (Proc. 16th Europ. Conf. Venice, 1989) **13B(IV)**, 1255 (1989), Stubberfield P M *et al*

[20] "Ballooning Stability Analysis of JET H-modes" in "Controlled Fusion and Plasma Physics" (Proc. 16th Europ. Conf. Venice, 1989) **13B(I)**, 229 (1989), O'Brien D P *et al*

[21] "An Interpretation of the Structure of ELMS and the H to L Transition on JET" in "Controlled Fusion and Plasma Physics" (Proc. 16th Europ.

Conf. Venice, 1989) **13B(I)**, 225 (1989), Cripwell P *et al*

[22] "Measurements of Local Features in T_e and n_e Profiles Observed on JET" Bull. Am. Phys. Soc. **34(9)**, 2056 (1989) and JET Preprint JET-P(89)80, 117(1989), Gowers C *et al*

[23] "A Quantitative Assessment of Ion Temperature Gradient Theory Based on JET Experimental Results" Submitted to EPS Conference, Amsterdam (1990), Tibone F *et al*

[24] "Non-linear Diffusion of Charged Particles due to Stochastic Electromagnetic Fields" To be published (1990), Martins A M *et al*

[25] "Behaviour of Chaotic Magnetic Field Lines in a Periodic System (Tokamak)" C. R. Acad. Sci. Paris, **t. 308, Series II**, 1319 (1989), Hugon M *et al*

[26] "Performance Expectations in the New Configuration" in "JET Contributions to the Workshop on the NEW Phase for JET: The Pumped Divertor Proposal (25th-26th September 1989)" JET Report JET-R(89)16, 184 (1989), Rebut P-H *et al*

Plasma Boundary Phenomena and Impurity Production

Effort has been devoted to coordinating the physics understanding of essential phenomena of plasma-wall interaction and providing necessary diagnostics. The use of beryllium as getter and limiter material has lead to a greater involvement in the experimental programme and has focussed attention on processes taking place in the scrape-off layer such as: recycling of hydrogen isotopes, the plasma parameters and their scaling with global plasma parameters, the mechanisms of the impurity release and transport, and the damage to limiter surfaces.

Cooperation took place with the Task Force on Reduction of Impurities and Fuel Enrichment, and the operational aspects and consequences of the use of beryllium are covered in that section of the Report. In particular, this includes the impurity influx measurements with OH, RF and various fuelling scenarios, and the changes in recycling after introduction of beryllium. This section reports in detail the scaling of the parameters of the scrape-off layer, observations of plasma-wall contact from the CCD-cameras; interaction of neutrals with the beryllium layers through the study of gas throughput; and the study of the evolution of the typical beryllium layers found on the wall and other carbon structures.

The presence of beryllium, in the evaporation and in the limiter phases, was expected to remove oxygen by gettering and to replace carbon leading to a reduction in Z_{eff} and radiated power and giving rise to higher density limits. Less expected was the ability of fresh beryllium layers to absorb deuterium which led to a number of other beneficial effects : easy recovery after disruptions, and better density control by means of heavy gas puffing and pellet fuelling leading to effective impurity control.

Edge parameters

The edge parameters have been measured by means of single Langmuir probes embedded in various components such as limiters, divertor target plates, protection tiles of the RF antenna and even in the metal of the Faraday screen. Similar probes have also been inserted on the front of the Fast Transfer System train, also used for the exposure of time resolving collector probes (near the outer midplane) and on the fast reciprocating probe (near the top of the plasma: RCP).

Fig.142(a): Edge density $n_e(a)$ as a function of volume average density $<n_e>$, for $T_i=T_e$ and for $T_i \neq T_e$ derived from the power balance

The Limiter Case

The scaling of the edge density and temperature parameters $n_e(a)$ and $T_e(a)$ with volume average density $<n_e>$ for a Be limiter is shown in Fig 142(a) and (b). $n_e(a)$ has been calculated from the measured saturation current $I_{sat} = n_i e c_s$ and $T_e(a)$ using the assumption $T_i = T_e$. The data for ohmic heated (OH) discharges are from limiter probes and the RCP. The range of accessible $<n_e>$ is much larger than for the carbon limiters as indicated in Fig. 142(a). It is remarkable that $T_e(a)$ seems to be limited at lower densities.

The scrape-off thickness λ_n is about 10mm and does not show large variations with power or density. The various values for $I_p = 3$ and 5MA in OH and mixed additional heating are shown in Table XVI.

In constructing the overall power balance, the power conducted to the limiter, $P_c = P_{tot} - P_{rad}$, was found between 5 - 10 times larger than the power calculated from the integral of I_{sat} and T_e over the radial profile.

(b): Edge temperature $T_e(a)$ as a function of volume average density $<n_e>$

Table XVI

		P_{TOT} (MW)	$P_{TOT}-P_{RAD}$ (MW)	λ_η (mm)	λ_τ (mm)	λ_p (mm)	Pulse No:
$I_p=$ 3MA	OH	2	1.57	28	32	12.1	20583
	P_{NB} 2.6MW P_{RF} ~8MW	~13	10.5	33	26	11.3	20717
$I_p=$ 5MA	OH	4	3.3	21	30	10.2	20899/20901
	P_{NB} ~3.5MW P_{RF} ~6MW	~13	10.6	25	33	11.7	20905/20906

taking $T_i = T_e$. From thermocouple measurements, 60% P_C appeared to be depositied on the limiters and this power was used to force agreement by letting T_i be higher than T_e. The result of this calculation is shown in Fig 143. T_i can be as large as 10 x T_e and as high as 1000 eV. Supporting measurements have been found from the cold component of Be IV and from the hot component of D_α light (which both originate from a location close to the plasma edge). These measurements are also shown in Fig 143. The higher T_i yields lower values of $n_e(a)$ as shown in Fig 142. This observation has consequences for sputtering and power deposition. In this density range for n_e (a), equipartition is too weak to force the ion and electron temperature together. It is believed that the extremely high T_i derived in this way in the lower range of $<n_e>$ for OH (much higher than suggested from the observations of BeIV) and for additional heating must have other causes (i.e. T_i is not so high in these cases).
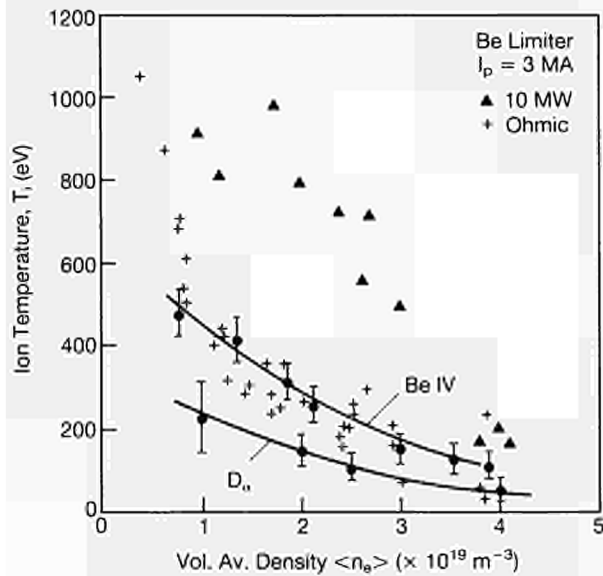
Fig.143: Edge ion temperature $T_i(a)$ as a function of volume average density $<n_e>$ derived from the power balance. For comparison. T_i derived from Doppler broadening of Be IV and D_α lines as shown

Fig.144: The density behaviour during pump-out and heavy gas fuelling. The edge density $n_e(a)$ shows different behaviour during the two phases

Heavy gas puffing during additional heating lead to a suppression of the increase in Z_{eff}. In these cases, the edge density $n_e(a)$ was up to x3 higher than in a discharge with gentle gas fuelling. In Fig 144, the density dropped immediately after pellet injection was stopped until the gas puff started to raise the density. The edge density profiles were different although $<n_e>$ was the same.

The Divertor (X-Point) Case

In divertor discharges measurements have been made to local flux density (I_{sat} A.cm^{-2}) and electron temperature (T_e eV) using an array of 11 fixed Langmuir probes in the divertor target tiles which straddle the X-point position. Due to the high heat loads, many of these probes did not survive to the end of the campaign. Nevertheless they provided more information on the

edge parameters during single and double null operation, particularly during the L-H transition. It is now clearly established that the X-point moves radially inward in many discharges at the onset of NB heating and again at the L-H transition. This movement is confirmed by CCD camera measurements. Although the flux is observed to fall and remain low during the H-mode on the low field side of the X-point (Langmuir and D_α data), the integrated flux across the strike zone shows an initial fall then an exponential rise back to its L-mode value (Fig 145). This behaviour has been interpreted in terms of a confinement time (τ_p^*) which is typically 0.3 - 0.9 s. The edge temperature does not show such a large change. The result suggests that the power to the tiles after establishment of the H-mode is little different from that in the L-mode.
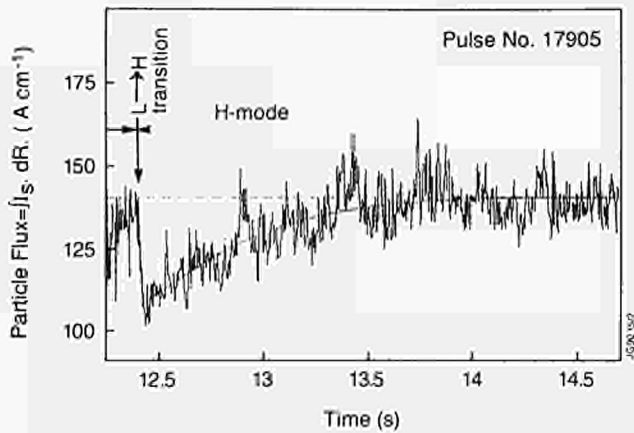
Fig.145: Total particle flux to the divertor target plates during the L-H transition

The rise in flux (and edge density) on the low field side of the X-point is illustrated in the results obtained from the RCP which captured an H-L transition in mid travel (Fig 146(a), (b), (c)). The transient rises during ELMS are also displayed and these are confirmed by the D_α signals. T_e also shows similar rises (less clear) and the results are consistent with radial movements of the X-point. In this example,the probe just reaches the separatrix. It has been observed previously that the floating potential, V_f, falls sharply to negative values just inside the separatrix.

Impurity influx

Although impurity influxes and net yields are extensively covered in earlier contributions, the detailed analysis of a number of cases are reported where Marfes and simultaneous detachment are observed in high power limiter discharges. In these discharges, the surfaces in contact with the plasma heat up to high temperature and the impurity influx and the resultant radiation is observed to increase rapidly - the so called 'carbon bloom'. This effect has been observed in limiter, inner wall and X-point discharges.

If the additional heating power exceeds a critical value for sufficient time at high density, (typically > 20 MW for 1.5s), there is a transition to a MARFE-like state, with the plasma detached from the limiters. Evidence of this condition is obtained from the radiation profile, from local probes at the limiters and from the CCD cameras observing the limiter. Results are shown in Fig 147. The neutral beam heating comes on at 6s, and the ICRF (dipole configuration) at about 7.5s. At each of these states, the impurity influx and the total radiation increase. At 8.6s while the input power and density remain constant, Fig 147(a) and (b), the particle flux to the upper and lower limiters and the antenna begins to decrease, Phase II, Fig 147(c), (d), and (e). The visible spectroscopy shows a similar reduction, the intensities of CII, BeII and H_α lines decreasing by factors of between 3 and 6. This is the start of the detached phase. At 9.1s, there is an abrupt formation of a MARFE, Phase III, and further evidence of detachment comes from the reduction of the coupling resistance of the ICRF antennae, Fig147(f), indicating a

Fig.146(a): Radial profiles of I_{sat}.
(b): Radial profiles of T_e for H and L mode. H mode showing ELM's.
(c): Radial profiles of D_α from the edge region during probe reciprocation showing corresponding ELM's.
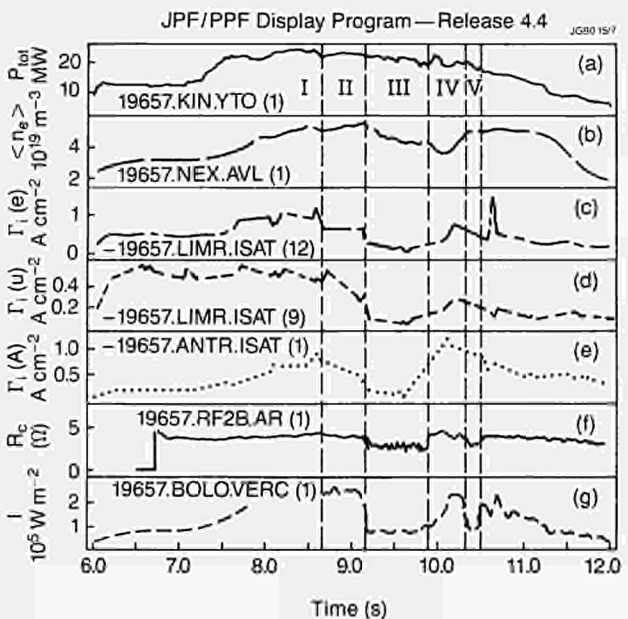
Fig.147: Observation of detachment and MARFE formation during high power heating in Pulse No: 19657:
(a) Total input power (NBI and ICRH)
(b) Volume average density
(c) Ion flux to lower belt limiter from Langmuir probes
(d) Ion flux to upper belt limiter
(e) Ion flux to ICRF antenna
(f) Coupling resistance to antenna 2B (dipole configuration)
(g) Channel 1 of bolometer vertical camera

local reduction in density and from the bolometer channels looking at the low field side of the plasma, Fig 147(g).

The duration of the detached MARFE appears to depend on the additional heating power. During the MARFE phase, the average plasma density, Fig 147(b), and the impurity density both drop, due to the reduction of the impurity source. After typically 1s, the plasma suddenly relaxes to the attached state, the radiated power decreases and the power to the limiters increases again. In one case where the heating pulse was long enough, a second MARFE formed after a recovery phase, Phase V.

The detachment may be considered as the removal of most of the particle and power flux to the limiter. Such an effect has been routinely observed in ohmic discharges but has not previously been observed at such high input powers. In principle, we might hope to use detachment to reduce the impurity concentration, but in the present case such a high impurity content is necessary to induce detachment that no advantage is obtained.

This response of the plasma boundary to large impurity influxes is to be expected on simple power balance considerations. However, it is interesting that the detached state is stable with such high power additional heating. Due to non-uniformities in the limiter interaction and lack of direct observation of the whole interaction area, the precise mechanism for the increased impurity production has not yet been definitively determined.

Limiter Viewing

Emission from the belt limiter and X point target tiles was studied using CCD cameras fitted with carousels of interference filters. Observations of the belt limiter showed the poloidal distribution of impurities, and allowed the plasma contact position to be determined.

During investigations into the "carbon bloom", the plasma shaping was arranged so that the boundary of the plasma was defined near the geometric centre of the limiter poloidal section, to distribute the flux in the scrape-off layer over a larger area of limiter surface. Fig. 148 shows poloidal scans across the image of the lower Carbon belt limiter in CI light. In Fig 148(a), the plasma touches the upper part of the limiter, whereas Fig 148(b) shows a similar scan when the contact is close to the centre of the tile section, and it may be seen that in (b) there is an intensity minimum near the centre, with peaks or either side. Thus, in this case, the particle flux is distributed over a much greater area of the limiter surface. With this form of limiter contact, it was possible to apply ~90 MJ supplementary heating to the plasma without having a carbon bloom. Operations with the beryllium belt limiter were conducted with this optimum shaping.

Surface temperatures ~2500°C were often measured at the strike zones after auxiliary heating. Measurements
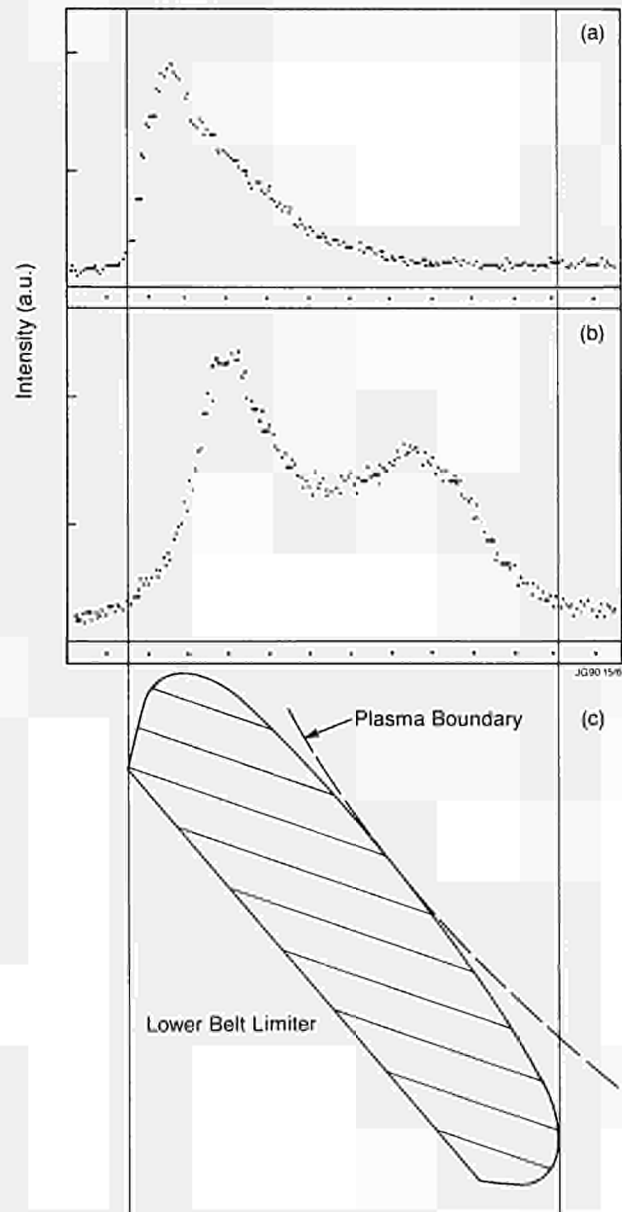

Fig.148: The plasma footprint on the belt limiter
(a) not optimised;
(b) optimised, as used during Be-operation.
(c) Belt Limiter.

of the toroidal flow of carbon, made at a position between bands of tiles, gave values of $10^{20} m^{-3} s^{-1}$ in the scrape-off layer near the strike zone radii.

Sweeping the radial position of the X-point during discharges produced a corresponding sweep of the strike zone positions, and by this means the peak surface temperature could be reduced. However, the observed reduction (<15%) was less than that predicted using simple modelling. A more detailed model, including the measured radial profile of the strike zones predicted reductions closer to those observed.

Sweeping in the vertical direction changed the position of the inner strike zone but produced only a very small movement of the outer zone. However, this type of sweeping caused an alternating loading at the top and bottom of the vessel, thus reducing the

temperature at the top very efficiently. Highest neutron yields were obtained during discharges in which a combination of vertical and radial sweeping was used.

X-point operations after the installation of the beryllium belt limiter produced much more rapid increases in surface temperatures at the strike zones, indicating higher initial power deposition onto the tiles. Often the measured value was ~ 2.2kWcm⁻² compared with ~ 1.4kWcm⁻² measured with carbon belt limiters. This is consistent with the low values of Z_{eff} and total radiated power found during this period, implying that energy conducted to the SOL and, therefore, to the target had become greater.

By injecting additional deuterium into the divertor region, the development and profile of the power deposition was substantially modified. The most
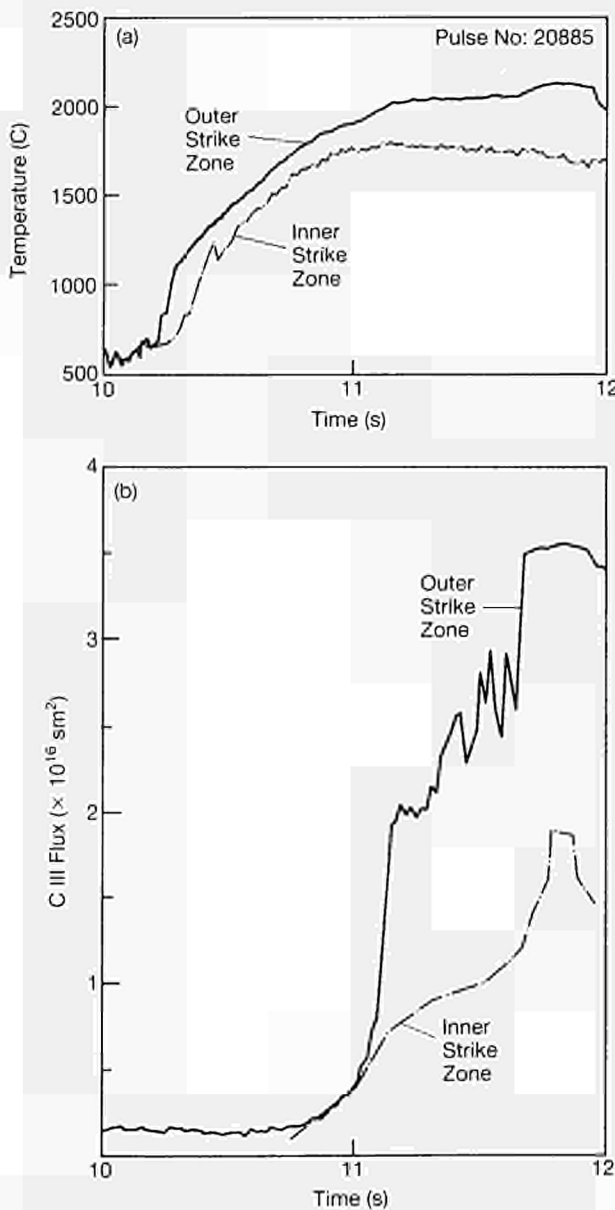

Fig.149: (a) Temperature at the outer strike zone on band 5DE. Temperatures up to 1700°C are directly measured; higher temperatures are extrapolated from adjacent points. (b) CIII intensity at=464.9 nm at the outer strike zone on band 6BC

noticable effect was the reduction in the initial value of deposited power, which resulted in a more gradual rise in surface temperature. Impurity influxes were effectively postponed and the longest duration H-modes were achieved using this technique.

Generally, the impurity influxes correlated with the temperature at the surfaces of the target tiles. However, changes in position of the strike zones occurred at the onset of NB and H-modes. During these periods, additional impurity influxes were observed near the inner strike zone.

Fig.149 shows the temperature and Carbon influx from the outer strike zone during such a pulse. Neutral beam heating is applied at t=0 and approximately 1s later, a rapid increase in CIII flux occurs when the target temperature reaches ~1900°C and a further increase occurs at t≈11.75s when the H-mode collapses.

Neutral gas behaviour and density control

The main effect of the introduction of beryllium is that much less hydrogen is trapped in beryllium and that there is an unsaturable pumping effect. This is discussed in detail in the section on Reduction of Impurities and Fuel Enrichment.

The decrease in percentage of gas permanently trapped is confirmed in the measurements of the recovery of working gas. These measurements were started in the carbon conditions and were continued under beryllium conditions. From Fig.150, it can be seen that a smaller fraction of the working gas remains in the vessel in the beryllium condition. The experimental situation is complicated because parts of the wall and also the inner wall/layer tiles are still carbon and therefore this should not be considered as a 100% beryllium wall.

Measurements have been performed on a shot-by-shot basis as well as integrated over a period covering many shots. The results indicate that, even if the
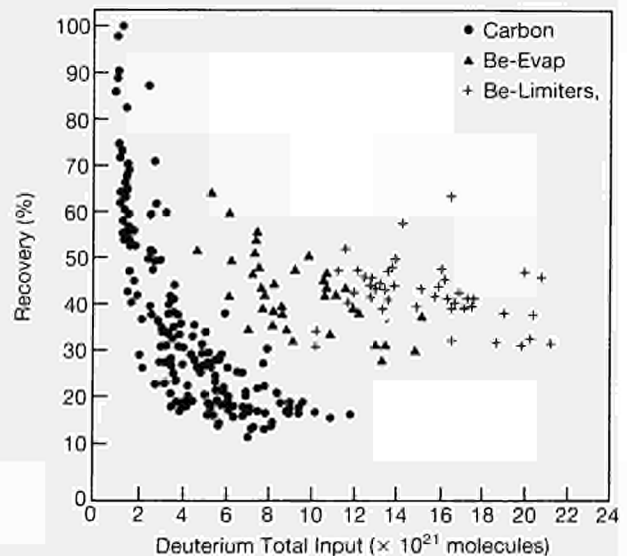

Fig.150: Fractional gas recovery for the C-Be/C and Be phases of operation

fuelling of the discharge by cold gas requires up to twice as much gas as in the carbon phase, higher outgassing is observed within 600s after the discharge. The fractional recovery increased from 20% of the input (high density C shot) to 40-50%. Up to 80% of the input gas was recovered over longer periods (60% with C). In absolute terms, the amount of gas trapped in the vessel is not changed very much compared with carbon walls (for 50 m^2 of relevant surface, 1.2×10^{20} at/m^2/shot was recovered).

Since tritium is produced as a branch of the D-D fusion reaction and the production rate is accurately known from the neutron reactions rate, tritium has been analysed in the exhaust gas, first integrated over a number of shots and later on a shot-by-shot basis, in discharges with high fusion reactivity. The gas samples were converted into tritiated water for analysis by scintillator techniques. This method proved to be sensitive enough to make measurements of individual shots. The integrated samples show a tritium recovery of 20% for the graphite phase of JET increasing to ~40% for both beryllium phases. However, in all cases, the recovery of tritium was half the deuterium value. For samples of individual shots taken 600 s after the discharge, recoveries were observed ranging from 12 to 35%, with an average value again half the deuterium recovery. No correlation has yet been found between the recovery and the local or global plasma parameters. At present, there is also no explanation for the higher retention for tritium compared with deuterium, but this may be due to the differences in the spatial origin and energy of the two isotopes.

The exhaust gas consists of 99% of D$_2$, instead of the typical 90% measured in the carbon phase : the total hydrocarbon content is now $\leq$ 2%, and CO and CO$_2$ are negligible.

Surface analysis

An important aspect of the surface analysis work at JET through the years has been the post-mortem analysis of first-wall components such as protection and limiter tiles and special sample monitoring of the state of the vessel wall. The analyses have provided data on impurity transport mechanisms, sources of in-vessel contamination and the in-vessel deuterium inventory. The retention of deuterium in the vessel is important for pumping and density control characteristics of the machine, and is important for predictions of tritium behaviour in the D-T phase of JET. At the start of 1989, the accumulated inventory of deuterium in the machine following the previous all-carbon phases was estimated to be 1.6×10^{24} atoms, which would imply a retention of 4 gm of tritium if the operations had been in a 1:1 tritium/deuterium mixture .

In 1989, Be was introduced into the machine first as an evaporated layer and then by replacing the graphite belt limiter tiles with beryllium ones. This use of Be is likely to have changed the deuterium retention

characteristics of the JET machine, as was apparent from gas throughout behaviour, so post-mortem analysis will again be important. However, Be-contaminated surfaces must be carefully handled and the analysis equipment has been modified to allow complete limiter or protection tiles to be analysed safely in a non-destructive manner. This analysis facility will provide important data in 1990 and the coming years.

Be was evaporated from four heads introduced near the outer midplane. Although the relative coverage on the vessel wall could be calculated, the absolute amount had to be measured since the efficiency of the evaporator heads changed rapidly with time and conditions. The evaporated thickness was measured by inserting special probes by means of the Fast Transfer System (FTS) and analysing the deposited amount using NRA with a D$^+$ beam after transfer under vacuum to the Surface Analysis Station (SAS). About ten such measurements were performed showing a local deposition in the range 1250-2300Å on the probe which is equivalent to an average coverage of the vessel of 200-400 Å

Since an important function of Be was to getter oxygen, the gettering action was monitored by leaving coated probes in the vessel and observing the build-up of oxygen in the films by means of X-ray Photoelectron Spectroscopy (XPS) between shots. An example is shown in Fig.151 Analyses have been taken at five points along a probe which were at distances 13 to 77mm behind the line of the RF antenna tiles for the series of Pulse Nos: 19587 to 19592. The graphite probe had previously been exposed to the first Be evaporation in JET and covered with a layer of ~2300Å of pure Be at the same time as the surrounding parts of the torus. At the furthest point from the plasma (77mm behind the tiles), oxygen (as beryllium oxide) was found throughout the thickness of the Be layer, though there is a maximum at the outer surface (which corresponds to oxidation of 5 - 10% of the Be in this region). Closer to the plasma, deposition has occurred of impurities from
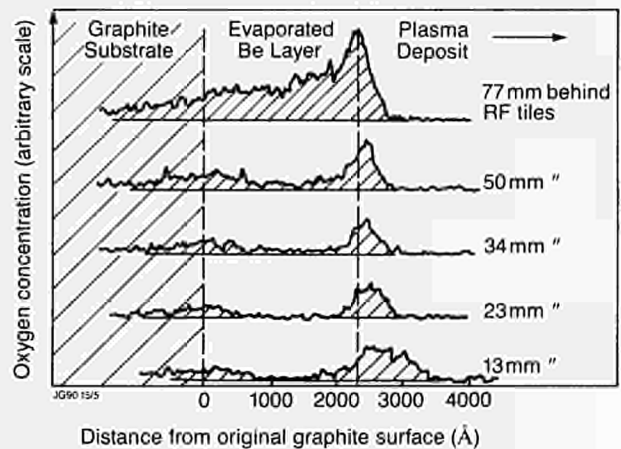

Fig.151: Evolution of oxygen content of fresh Be layers on a carbon substrate as a function of depth in the SOL five pulses after an evaporation

the plasma. This deposit, which was ~1000Å thick at the point 13mm behind the tiles, inhibited oxide formation within the evaporated Be layer, but some oxide still accumulated at the graphite/Be layer interface and at the outer surface.

The composition of the plasma-deposit 13mm behind the RF tiles following these five pulses was 56.2% Be, 28.8%C, 14.6%D, with Cl(0.28%) and Ni (0.17%) the largest of the minor impurites. Oxygen which is incorporated within this deposit is shown by X-ray Photoelectron Spectroscopy (XPS) to be associated with some of the Be, whilst the rest of the Be appeared to be bound to carbon.

The appearance of carbon in the boundary within the first few shots after the heavy Be evaporation was consistent with spectroscopic measurements of the plasma core, which showed that carbon became the dominant impurity, with the Be dropping to ~6% of its original level (which then remains approximately constant) in 4 - 20 discharges. In fact, the decay in the Be level was slower following the first evaporation (see Fig 151) than for any subsequent evaporation.

Fig. 152 shows the ratio C/Be found in the SOL for each of the first six pulses following an evaporation overnight in which the thickness deposited was ~60% of that deposited in the first evaporation. In this case, the amount of carbon deposited per pulse was ~5 times greater than the amount of beryllium by the sixth pulse following the evaporation.
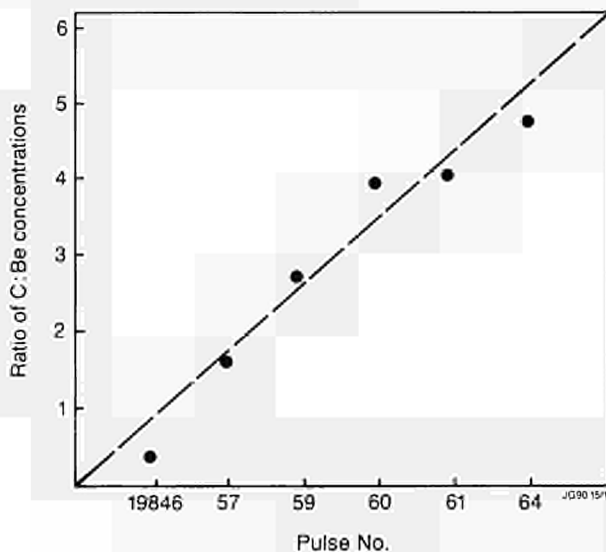
Fig.152: Ratio of C/Be collected 10mm behind the edge of the protection tiles of the RF antenna as a function of Pulse No

Relatively large amounts of carbon were also observed as a deposit deep in the SOL for discharges on the Be belt limiters. This is thought to be related to the presence of the carbon tiles protecting the RF antenna which is near the position of the probe. However, it is remarkable that even for pulses where the carbon content was high on the probe, the carbon impurity content of the plasma remained low indicating a high degree of screening of this particular source.

Magnetic Diagnostics

An important aspect of magnetic measurements in 1989 was the fault in a toroidal field coil. Although small, this became a significant source of error in the diamagnetic flux measurements, and was also detected by the saddle coils. Using these measurements, the time history of the coil fault over the last two years has been reconstructed (see Fig.153). At its most severe, the flux error from the coil fault was less than 1 part in 10^3 of the total toroidal field flux.
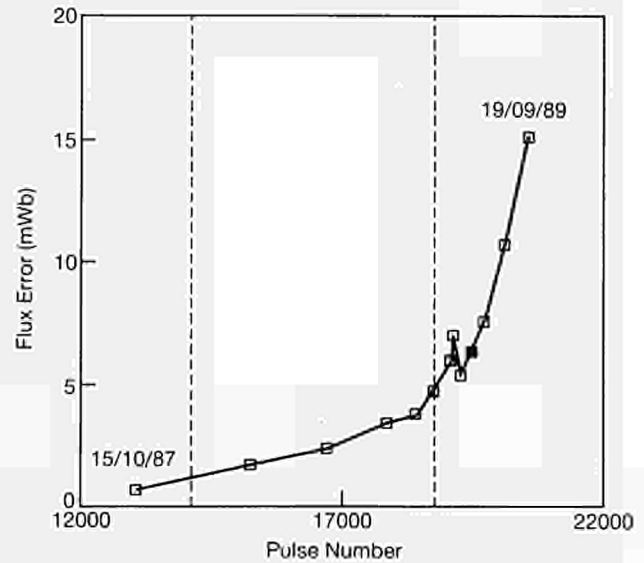

Fig.153: The time development of the flux error caused by the TF fault derived from the set of saddles coils on Octant No: 4

A hard-wire combination of B_{pol} and B_n was successfully installed and commissioned that gives a direct measurement of the horizontal and vertical movement of the current channel during disruptions. This is specially important for divertor discharges where more conventional means would fail. Signals of these combinations are routinely available for all disruptions.

Fast sampled measurements (125 kHz) of Edge Localized Modes (ELMs) near the H to L transition have been taken at the plasma edge by magnetic pick-up-coils. The detailed analysis of these has revealed that the ELM spike is preceded and followed by regular oscillations (Fig 154). Toroidal and poloidal correlations show respectively an n=1 component and an m=5 to 10 depending on the discharges. These structures originate near the edge (q = 5 to 10) in the high shear region of the H-mode, and rotate opposite to the co-injected neutral beam direction with a frequency ($\approx$10 kHz) close to the electron diamagnetic drift frequency. The measured growth rate of the precursors to the ELMs ($\approx 10^4$ s^{-1}) has been found close to the value
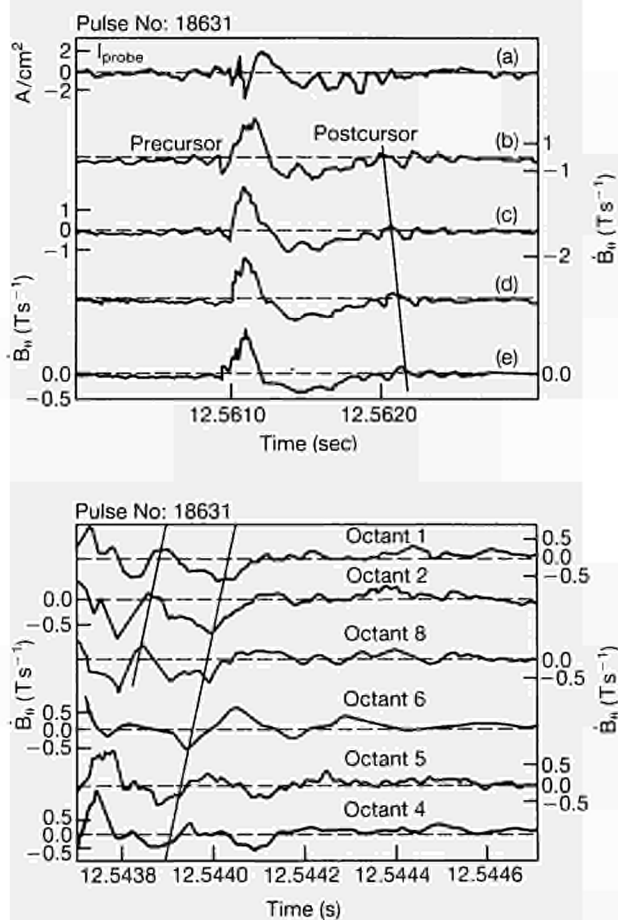
115

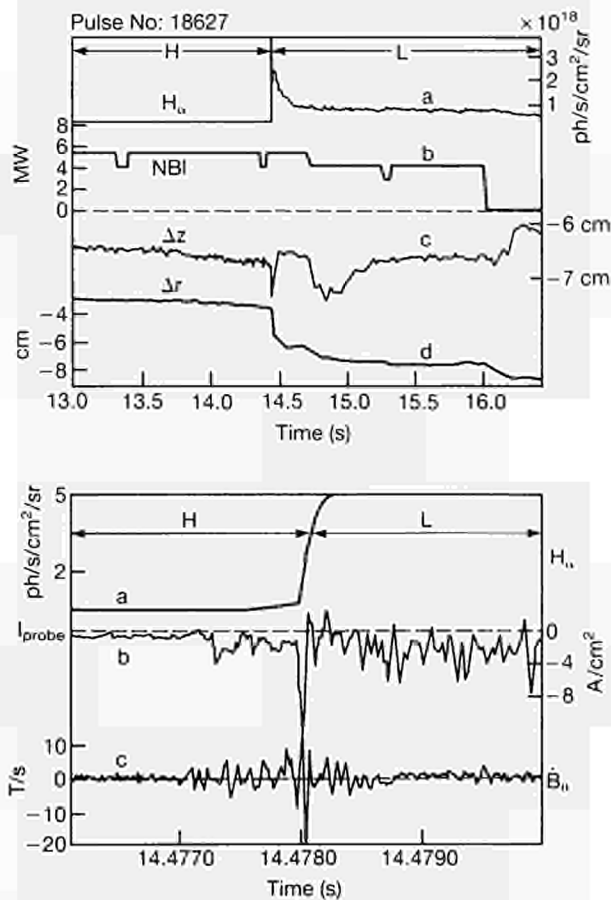Fig.154: Pre-and post cursor MHD oscillations around the ELM spikes

Fig.155: MHD oscillations related to the H-L transition.

predicted by the tearing mode theory ($1 - 3 \times 10^4$ s^{-1}). These results suggest that the observed oscillations could be driven by tearing modes destabilized by the strong current density gradient ($\nabla J/J = 10$m^{-1}) at the plasma edge.

The ELM spike is correlated with strong particle transport ($\approx 3 \times 10^{19}$ particles per ELM) and heat transport (≈ 10 kJ per ELM). Assuming a tearing mode model for the precursors, and given the magnetic fluctuation level during the ELM spike ($\dot{B}_o)/B_o = 4 \times 10^{-4}$), the island width Δ is calculated for two neighbouring rational q surfaces. Within the uncertainties, $\Delta \approx 3$ cm is larger than the distance between the two neighbouring resonances: 2 ± 1 cm. Thus, overlap of islands appears possible, leading to stochastic field topology and to the enhanced edge transport observed during the ELM spike.

A similar magnetic analysis has been carried out for the H to L transition. The spike of the transition is preceded by the same n = 1, m = 5-10 magnetic structures (Fig 155). This result suggests that the ELMs and the H to L transition may both have the same underlying cause, and emphasizes the importance of plasma edge physics in the confinement of H-mode discharges.

MHD Behaviour

During 1989, effort on MHD behaviour was devoted in the areas of: the analysis of disruptions and the influence of large amplitude MHD modes on plasma performance; investigation of the influence on density limits of the introduction of beryllium as a first-wall material; studies of the sawtooth instability and its stabilization; the exploration of the properties of high-β plasmas; and analysis of the plasma current profile. These items are discussed in the following sections.

Disruptions

Analysis of the causes and the mechanism of major disruptions has been a key area of work throughout JET's life. As a result, a detailed understanding of disruptions at the density limit and low-q boundaries has been developed[1]. In addition, operational techniques have been developed for minimising the occurrence of disruptions resulting from the evolution of unstable current profiles during the current rise[1,2]. However, the causes of another class of disruptions, which usually occur at high current, are not so well understood.

The evolution towards disruption in these cases follows the normal evolution in JET: the growth and

locking of an m=2, n=1 mode, followed after some delay (perhaps as long as 1s) by a major disruption. A crucial aspect, which has not been fully elucidated and which is central to the development of techniques for avoiding such disruptions, is the identification of the trigger for the growth of the m=2 mode.

Recent analysis[3] has revealed that these disruptions can be understood when the plasma parameters just before the growth of the m=2 mode are plotted in the l_i-q_ψ plane (where l_i is the plasma inductance and q_ψ the plasma safety factor). The upper and lower boundary lines in this plane, which have been defined empirically for JET[2] based on operational experience, correspond to the density limit and current rise (surface kink mode) disruption boundaries, respectively. High current disruptions which do not correspond either to density limit or current rise disruptions nevertheless cluster along the upper boundary (Fig 156).
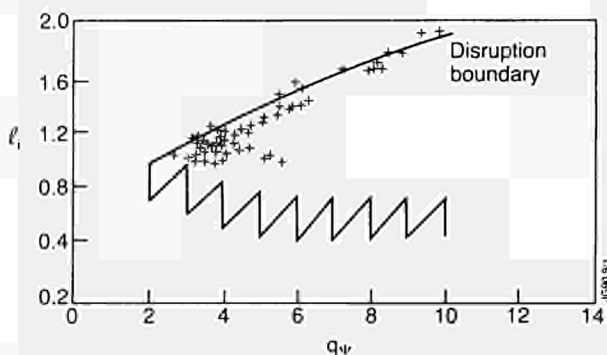
Fig.156: *Parameters in the l_i-q_ψ plane from high current pulses ($I_p \geq$ 5MA) which disrupted, but could not be associated with density limit or current rise disruptions. The points, taken just before the growth of the m=2 disruption precursor, cluster along the high-l_i disruption boundary.*

In the case of density limit disruptions, this boundary is understood to correspond to values of l_i for which the total plasma current flows inside the q_ψ = 2 surface. A possible explanation of the high current disruptions, therefore, is that the current profile becomes too narrow, which leads to the creation of a steep gradient at q_ψ = 2 and hence to the destabilization of an m=2 mode. An important question, as yet unanswered, is what is responsible for the peaking of the current profile and whether means can be developed to avoid such disruptions.

n=1 Modes

Large amplitude n=1 modes (usually with m=2) can develop in JET under various conditions:

- before major disruptions at the density limit, the q_ψ = 2 boundary and at high current;
- following the collapse of a 'monster' sawtooth;
- after pellet injection; during the current rise, if the current profile is too broad;
- and during the transition to the X-point configuration.

In the last four cases a disruption is not inevitable - the mode can saturate at a large amplitude $[(dB_\theta/dt)/B_\theta \leq 1\%]$, following which it usually locks to the wall or rotates at very low frequency (~ 1Hz). Hence, it is commonly called a 'locked-mode'.

(i) Energy Confinement - The most serious consequence for JET operation resulting from the growth of these modes is the occurrence of a major disruption. Thus, a feedback stabilization system is under construction for their control. However, even when a disruption does not occur, such large amplitude modes can have a deleterious effect on the plasma performance: they depress central temperatures (due to toroidal coupling to the m=1 mode), degrade energy and particle confinement (including the confinement of fast particles and impurities), and they significantly reduce fusion reactivity. Toroidal momentum confinement is usually reduced to zero.

The degradation of energy confinement has been analysed[4] in terms of a model[5] which proposes that the flattening of the plasma profiles across magnetic islands accounts for for the loss of stored energy. When the effect of both the m=2 and m=1 (toroidally coupled) islands are included, it is found that the experimental results are in good agreement with calculations based on the model (see Fig 157).
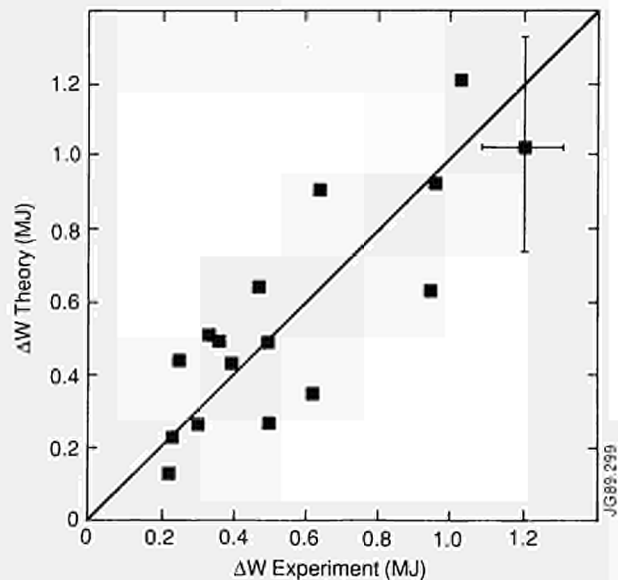

Fig.157: *Plot of observed versus calculated reduction in stored energy during large amplitude MHD activity. The results of the calculation, based on the model of Chang and Callen[5], are in good agreement with experimental results.*

(ii) X-Point Transition - If the plasma density falls too low during the formation of an internal separatrix (or X-point configuration), it is found that a large n=1 mode can grow and lock and that the plasma may disrupt. As the problem is most severe at low-q (and hence high current), this could represent a serious operational limit. However, the problem can be overcome by careful control of the plasma density using

gas puffing or neutral beam injection. Nevertheless, in order to to understand the causes of the growth of the mode, the parameters of such discharges have been mapped into the l_i-q_{95} plane. Here q_{95} is the safety factor of the flux surface enclosing 95% of the poloidal flux and is used as an effective q_ψ for X-point plasmas. The experimental points cluster along the high-l_i boundary (Fig 158), suggesting that, as in the case of high current disruptions, peaking of the plasma current destabilizes the n=1 mode.
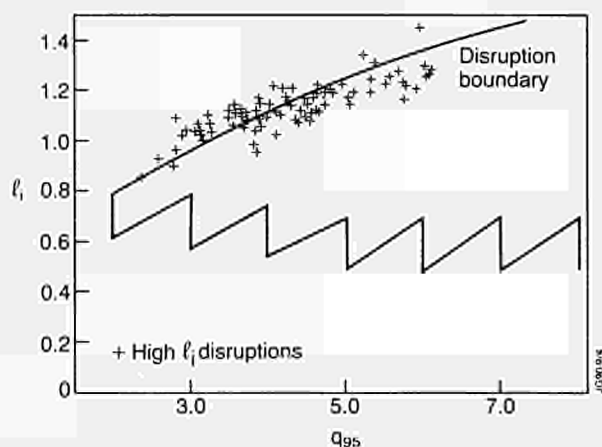
Fig.158: Parameters in l_i-q_{95} plane from discharges which formed large amplitude n=1 modes during the transition to the X-point configuration. The points cluster along the high-l_i disruption boundary.

Density Limit

The introduction of beryllium into the vacuum vessel as a plasma facing material was expected to improve plasma performance by increasing the density limit. Beryllium was introduced firstly as a gettering material and, later, as a limiter. Experiments were carried out to investigate the change in the density limit in the two phases and to study the mechanism for the limit[6].

(i) Beryllium Gettering Phase - During this phase, it was observed that, for gas fuelled discharges with ohmic or NB heating, the density limit was approximately the same as in the carbon-only phase. However, ICRF heated plasmas reached the same limiting density as those heated with a similar level of NB power, whereas in carbon-only cases ICRF heating extended the density limit very little beyond that obtained in ohmic plasmas. In addition, a comparison of gas and pellet fuelling showed that pellet fuelling could be used to extend the density limit, even during high power NB heating. On the other hand, with ICRF heating, gas and pellet fuelled plasmas reached the same density limit. A comparison of density profiles showed that the limiting edge density in these cases was very similar. Although this result was not entirely surprising, these experiments gave the first clear evidence in JET that the density limit should be interpreted in terms of the edge density rather than the central or average density.

One of the most significant aspects of these experiments was that the nature of the density limit differed considerably from that observed in carbon-only plasmas[1]. In the latter case, increasing density led to increasing radiation which produced a transient 'marfe' - a poloidally asymmetric radiating structure located on the inner-wall. Eventually the radiated power reached 100% of the input power, which caused a contraction of the temperature and current profiles. This triggered the growth of an m=2, n=1 mode and resulted, almost invariably, in a major disruption. With beryllium gettering, however, although increasing radiation again led to the formation of a 'marfe', this often persisted for several seconds and the plasma survived without disrupting.
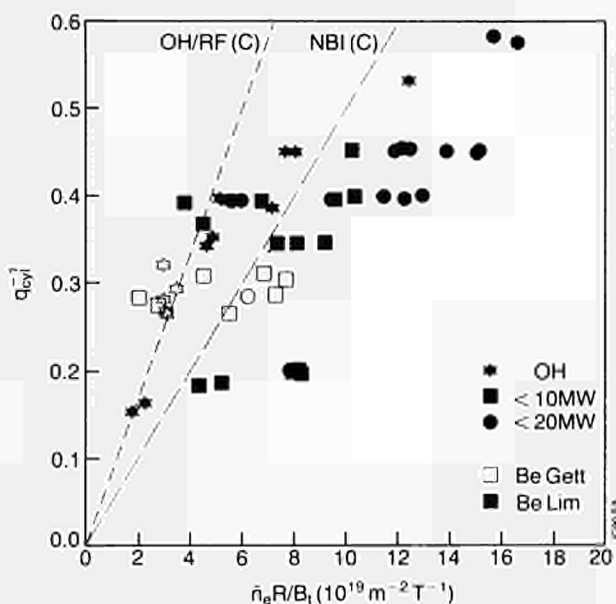

Fig.159. Hugill diagram (operating regime) of pulses which reached the density limit in the beryllium gettered and beryllium limiter phases. The substantial improvement achieved relative to the performance in carbon limiter plasmas is clear.

(ii) Beryllium Limiter Phase - The trends observed in the beryllium gettered phase were more pronounced. In particular, a substantial increase in the density limit was obtained under all heating conditions, and values of $n_e R q_{cyl}/B_\phi > 40$ (the Murakami parameter) were achieved in gas fuelled discharges at total input power levels of 10-15MW. This is approximately twice the value of this parameter which was observed in plasmas with a carbon limiter. The maximum density obtained under various conditions is plotted in the Hugill diagram of Fig 159. The limiting density increased as $\sim P^{0.5}$ for powers up to ~20MW (Fig 160), with only a weak dependence on q_{cyl} and B_ϕ. In addition, these experiments confirmed that the edge density was the critical parameter characterising the density limit, as illustrated in Fig.161, which shows the limiting edge density as a function of total input power.

As in the beryllium gettered phase, the density limit occurred as a 'marfe' when the radiated power fraction
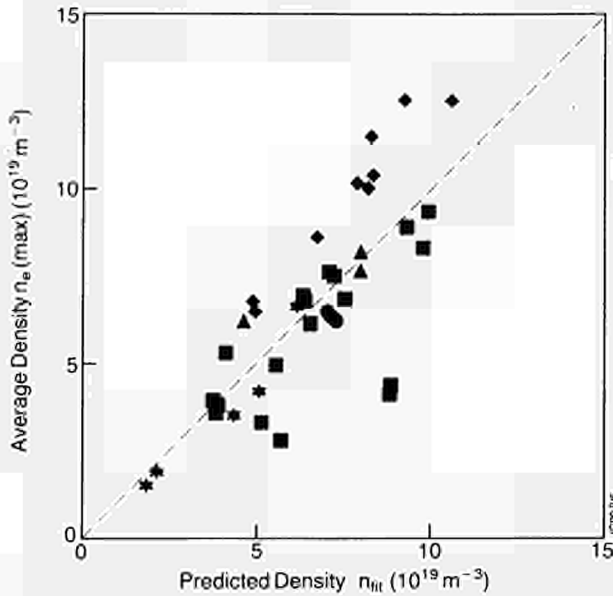
Fig.160: Scaling of the density limit, for gas fuelled discharges, with total power in the beryllium limiter phase. The maximum density increases as ~ $P^{0.5}$
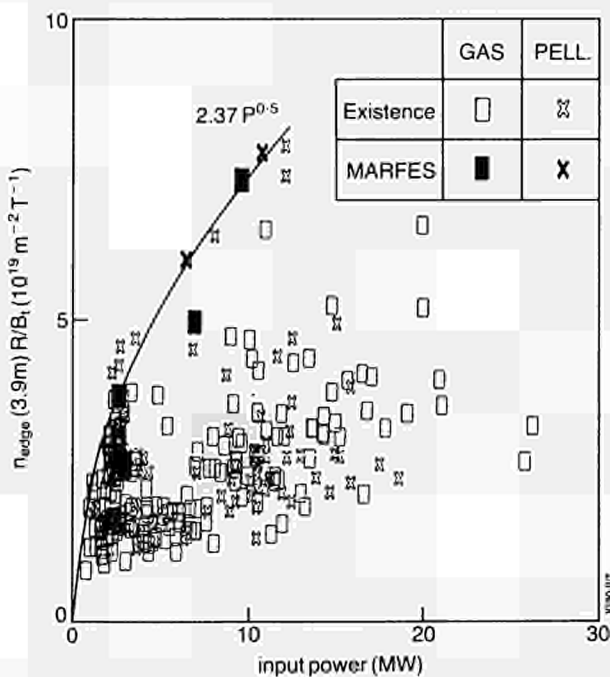
play a significant role in the density limit. Fig 162 illustrates this in the case of a 4MA/2.6T plasma with 11 MW of additional heating. The density limit is reached at 12s and again at 12.8s, when a sharp spike in the radiated power indicates that a 'marfe' has formed. In both cases, however, the density falls and the 'marfe' quenches. At the first density limit, no MHD activity is detected by any of the coil combinations sensitive to rotating n=1,2,3 activity, nor does the 'locked mode' signal indicate a significant level of activity (note that the sudden rise in this signal at 12s is coincidental and due to pick-up from the toroidal field circuit as the toroidal field begins to decay at this time). At the second density limit, a burst of rotating n=1 activity is observed, but this rapidly decays. Such observations are typical of the density limit experiments performed in this phase of operations.
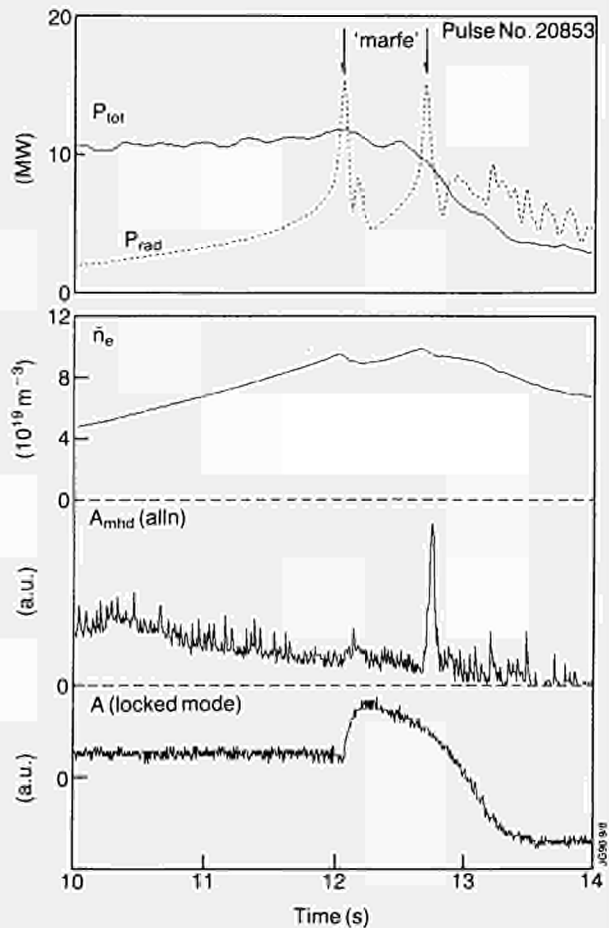

Fig.161: Analysis of the density limit in terms of the edge density for the beryllium gettered and beryllium limiter phases, including both gas and pellet fuelled discharges. Gas and pellet discharges reach a common limit, which follows the ~ $P^{0.5}$ scaling noted previously.

was near unity. Formation of the 'marfe' usually reduced the plasma density, most probably by reducing the edge density, the 'marfe' then quenched and the plasma recovered. Continued gas-puffing again increased the density and the cycle was repeated. Thus, the 'marfe' could occur as a repetitive relaxation, and usually the plasma did not disrupt, if at all, until the auxiliary heating and the plasma current were reduced.

In these discharges, and in contrast to the case for carbon limiters, low m,n number MHD activity did not

Fig.162: Overview of the plasma parameters during a density limit experiment in a 4MA/2.6T plasma with MW of total input power. Note that the density limit is reached twice, occurring as a 'marfe' (arrowed). There is only MHD activity associated with density limit in the second case.

In summary, several aspects of these results are significant. Perhaps most importantly, these experiments indicate that the density limit should be considered rather as a fuelling limit, since, by appropriate refuelling techniques, it might be possible to maintain a peaked density profile, holding the edge density below the limit

while increasing the core plasma density. The observation that the edge density limit can be increased as the square root of the input power is of considerable significance both for the future JET programme and for next step devices. It is worth noting that JET has now reached values of the Murakami parameter required for ITER. Operationally, the observation that the density limit usually occurs as a soft, rather than a disruptive limit, is a key result. In addition, it was found that in cases in which a disruption did occur, the rate of current decay was perhaps an order of magnitude smaller than in carbon-limiter plasmas. Finally, the central issue which requires elucidation is the cycle involved in the formation and quench of the 'marfe' and how this limits the density.

Sawteeth

Detailed analysis of the sawtooth instability has continued with the aim of clarifying some of the many questions which surround this problem. Two dimensional tomographic analysis of soft X-ray emission measurements of the sawtooth collapse[7] have previously shown that the topology of the collapse in JET in not in agreement with that expected from the full reconnection model of the collapse, but resembles a convective behaviour such as that predicted by the 'quasi-interchange' model[8]. Detailed comparisons of reconstructions obtained from electron cyclotron emission (ECE) measurements of electron temperature with those deduced from soft X-ray analysis confirmed this interpretation[9]. However, this interpretation of the sawtooth collapse has been challenged by results obtained from other tokamaks and this has stimulated further work within JET to re-examine the original results.

Two-dimensional tomographic analysis based on two orthogonal cameras has inherent limitations on the poloidal resolution which can be achieved. This has been recognised for many years and the major issue in this investigation is the ability of this technique to resolve the expected differences between the two most common classes of phenomena which could be responsible for the sawtooth collapse.

To clarify this, a simulation has been performed in which contour models of the two principal theoretical forms of the collapse were passed through the tomographic analysis. It was found that for the case previously studied in most detail in JET (in which the hot core of the plasma is displaced horizontally along the major radius) there was no ambiguity in the results: as shown in Fig 163, the tomographic analysis produced accurate reconstructions of the input contours and clear differences were observed between the reconstructions of the reconnection model and of the convective cell which enabled the two to be unambiguously distinguished. Further investigations have also revealed the circumstances under which ambiguity can occur and
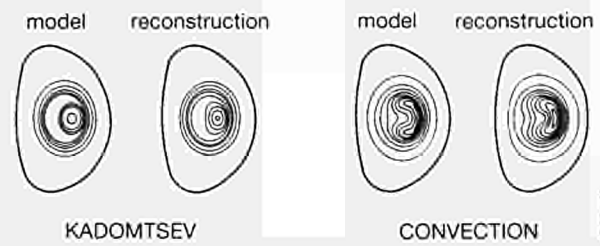

Fig.163: Comparison of simulated X-ray observations of the two most common models for the sawtooth collapse: (a) full reconnection; (b) 'quasi-interchange' mode. For the cases considered the soft X-ray tomographic analysis provides an accurate reconstruction of both models.

these results will provide an important guide for future analysis.

The m=1 activity associated with the sawtooth cycle has long been studied to gain insight into what role, if any, it plays in the sawtooth instability. It has been observed, for example, that a magnetic island-like structure can occur during the successor oscillations to sawteeth and, more especially, partial sawteeth[10]. This raised the question of how such structures are involved in the sawtooth collapse itself. Further analysis[9] suggested that these islands are not directly involved in the collapse since they are frequently absent from the plasma at that time. Furthermore, they can, when present, survive the sawtooth collapse, undergoing a change in radial location in a manner first identified for the 'snake' oscillation[11]. Unfortunately, it has not yet been possible to reconstruct the behaviour of the island during the collapse, so that the nature of its interaction with the sawtooth instability remains open.

The growth and decay of these island-like structures during the sawtooth cycle has been followed in detail and their behaviour reconstructed from ECE measurements of electron temperature. In a case such as that shown in Fig 164, it is found that the island gradually decays on a timescale of order 50ms, leaving an annular shoulder in the temperature profile in the region of the sawtooth inversion radius, which presumably represents the location of the q=1 surface. A remarkable aspect of this evolution is that, as the annulus forms, a second highly localised island emerges at the poloidal position corresponding to the X-point of the original island and the cycle is repeated.

There are several points to note:
- the cycle of growth and decay of the islands is out of phase with the sawtooth cycle and, indeed, the sawtooth collapse does not appear to be related to a particular island amplitude.
- In the cases studied, the evolution of the island is restricted to an annular region about the plasma centre and full reconnection across the plasma centre is not observed - as noted, the island can often survive the sawtooth collapse.
- Although this behaviour is common, it is not universal, and so the presence of such islands is not required for the sawtooth collapse.
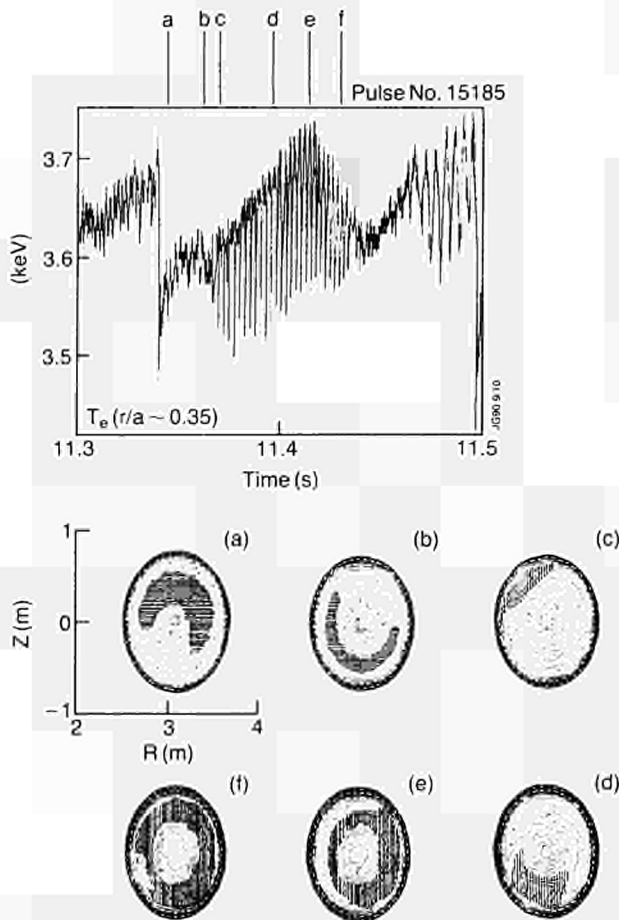
Pulse No. 15185

T_e (r/a ~ 0.35)

Fig.164: Reconstructions, of the evolution of m=1 islands during the sawtooth cycle in JET using ECE measurements of electron temperature. Though common, this phenomenon is not universally observed in JET.
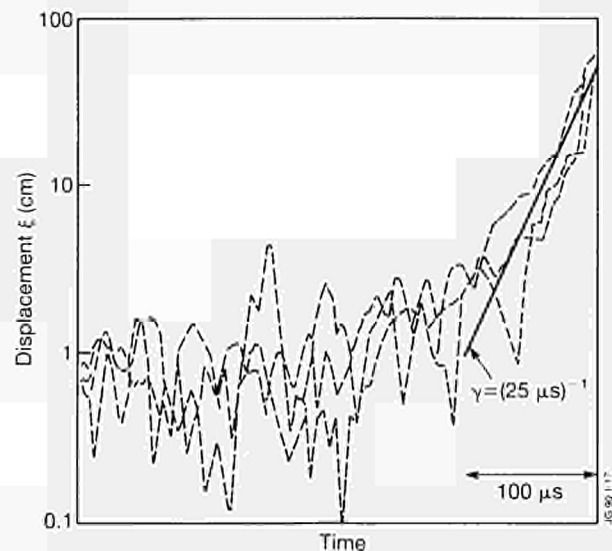

$\gamma = (25\ \mu s)^{-1}$

100 μs

Fig.165: The displacement of the peak of the soft X-ray emission, derived from two dimensional tomographic reconstructions, during the fast sawtooth collapse in JET. Experimental results for three cases are shown which illustrate that a growth rate of ~ 25μs⁻¹ is achieved even before the displacement is large enough to be detected above the experimental noise.

- The existence of such islands through the sawtooth cycle suggests that a q=1 surface survives throughout the cycle, which generalises and confirms the results obtained from analysis of the 'snake' modulation.

The rapid collapse of the sawtooth in JET was, perhaps, the first observation which suggested the existence of a major problem in the understanding of JET sawteeth[12] and it was in response to this that the 'quasi-interchange' model was first proposed[7]. However, it was later realised that the problem of timescale in the sawtooth collapse phase was much deeper[13] in that the 'switch-on' of the instability was much too rapid to be explained, even by the 'quasi-interchange' model.

This question has been reanalysed recently[14] and the nature of the problem clarified. Using soft X-ray tomographic analysis of the sawtooth collapse, it has been shown that the growth rate of the core displacement caused by the the m=n=1 instability is γ ~ $25\mu s^{-1}$ from the time that the displacement can be measured above the noise in the analysis (Fig 165), i.e. the fast growth rate arises suddenly, on a timescale comparable to γ^{-1} rather than the timescale required for the magnetic equilibrium to change. Thus, the instability cannot be understood in terms of simple linear theory.

A possible explanation is that the rapid growth does result from the release of energy arising from an ideal or resistive mode, but that the onset of the rapid growth does not correspond to the equilibrium passing through marginal stability for that mode. It is suggested that a weak stabilizing mechanism exists (of unknown origin) which suppresses the growth of the mode until a second stability boundary is crossed. The energy accumulated in the period between marginal stability and the crossing of this second boundary might then be suddenly released to drive the fast instability.

Sawtooth Stabilization and the Influence of Fast Ions
(i) Sawtooth stabilization - Sawtooth stabilization has been achieved in JET by several means[15]:

(i) on-axis heating during the current 'flat-top' (ICRF and/or NB heating: 'monster' sawteeth[16];

(ii) at the highest currents, on-axis heating during the current-rise significantly delays the onset of saweeth[17];

(iii) pellet injection with or without additional heating suppresses sawtooth activity.

By using these techniques, particularly (i) and (iii), it has been possible to suppress sawteeth for up to 5s in the presence of high power additional heating.

The sawtooth stabilization mechanism in these cases is still the subject of active investigation. In the case of pellet injection, polarimetric measurements of the behaviour of the central value of the safety factor q(0) show that it remains above unity during the sawtooth-free period. This is consistent with the identification of MHD modes having mode numbers m=3, n=2 and m=2, n=1 near the plasma centre. As discussed in previous

reports, 'monster' sawteeth present a considerable problem. Polarimetric measurements show that q(0) can reach values as low as 0.6 during these periods and it has been suggested that the stabilization of the m=1 mode in these cases can be attributed to the influence of a population of fast ions[19].

Heating during the current rise was investigated as a means of stabilizing sawteeth at high currents, $I_p >$ 5MA, where 'monster' sawteeth were irreproducible. Although the original intention was to prevent q(0) falling below unity by raising the electron temperature (and polarimetric measurements do indicate that q(0) ~ 1 during the stable periods), there is evidence that q(0) is, in fact, below unity and that a stabilizing mechanism similar to that which produces 'monster' sawteeth is responsible.

Fig 166 shows a case where ICRF heating was used to produce long sawtooth-free periods at 5MA.
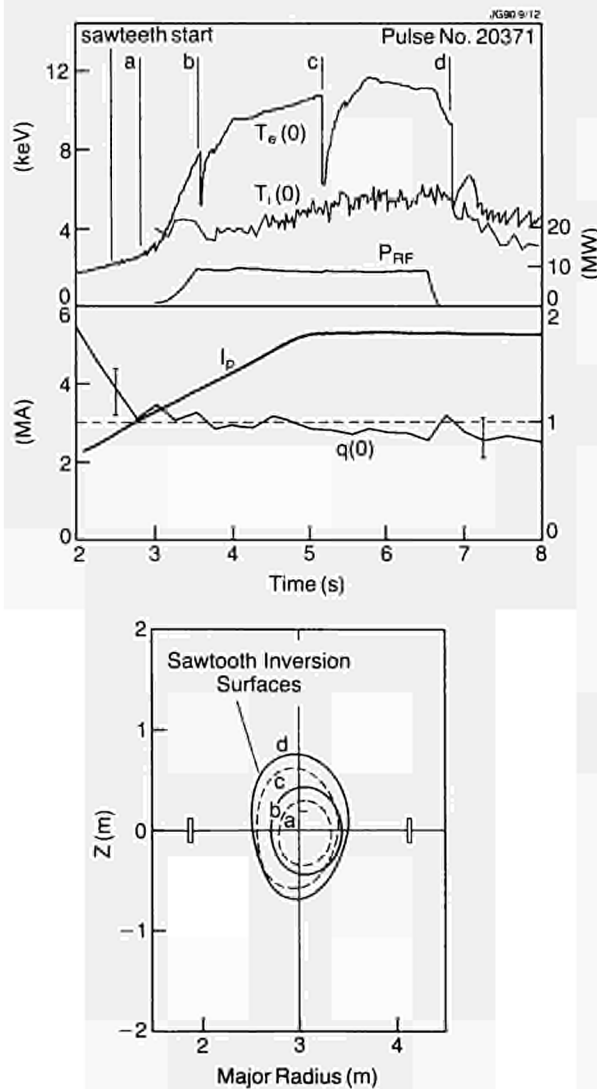
Fig.166: (a) Overview of long sawtooth-free periods produced at 5MA by current-rise heating;
(b) Behaviour of the sawtooth inversion surface, as deduced from two-dimensional tomographic analysis of soft X-ray emission, during the heating phase. The expansion of the inversion surface during this time is clear.

Sawteeth started early in the current rise, at I_p ~ 3MA, before the heating was applied. Nevertheless, several sawtooth-free periods of gradually increasing duration were produced. While q(0) deduced from polarimetric measurements remained close to unity, the sawtooth inversion radius, derived from the tomographic analysis of soft X-ray emission, gradually expanded in the course of the heating phase, suggesting that the q=1 surface was expanding throughout this time. Thus, while the evolution of the currency profile may be influenced by additional heating, a similar stabilization mechanism to that responsible for 'monster' sawteeth may be involved.

(ii) Fast Ion Stabilization of the m=1 - A theoretical model has been developed which proposes that an energetic ion population, accelerated by RF fields or produced by neutral beam injection, can stabilize the m=1 mode[18]. Several aspects of the behaviour of the monster sawteeth are consistent with this theory. In particular, the longest sawtooth-free periods are produced with on-axis heating, while stabilization becomes progressively more difficult as the power deposition is moved further off-axis. This is in agreement with the prediction that the stabilizing effect, resulting from the fast ion pressure β_{ph}, is strongest when the fast ion pressure profile is centrally peaked. In addition, the observation that stabilization becomes more difficult as the q=1 radius expands is expected from the theorectical considerations on the instability growth rate. This also offers a possible explanation for the final termination of the sawtooth-free period since a large expansion of the inversion radius occurs during this period. Finally ICRF heating, 'switch-off' experiments have shown that the delay between the end of heating and the collapse of the monster sawtooth is too small to be explained by equilibrium changes, but consistent with the slowing down time of the fast ions.

By making certain simplifying assumptions, essentially that local quantities may be replaced by global parameters, a quantitative comparison between theory and experiment has been performed[15]. In this analysis, the sawtooth instability is assumed to be initiated by a resistive kink mode, a q-profile with q(0) ~ 0.6-0.9 is employed and the fast ion distribution is calculated by a code which integrates the Fokker-Planck equation after computing the power deposition profile.

The results of this analysis are shown in Fig 167 where computed parameters from a range of discharges, the majority of which had sawtooth-free periods, are plotted in the stability diagram derived from the theory. In the figure,

$$\Gamma = \frac{\gamma_{mhd}}{\omega_{Dh}^{max}} \qquad H = \frac{\varepsilon_o}{s_o} \frac{\omega_A}{\omega_{DH}^{max}} <\beta_{ph}>_a$$

γ_{mhd} is the MHD growth rate in the absence of fast ions, ω_{Dh}^{max} the maximum value of the bounce-average procession frequency of the trapped fast ions, ε_o the
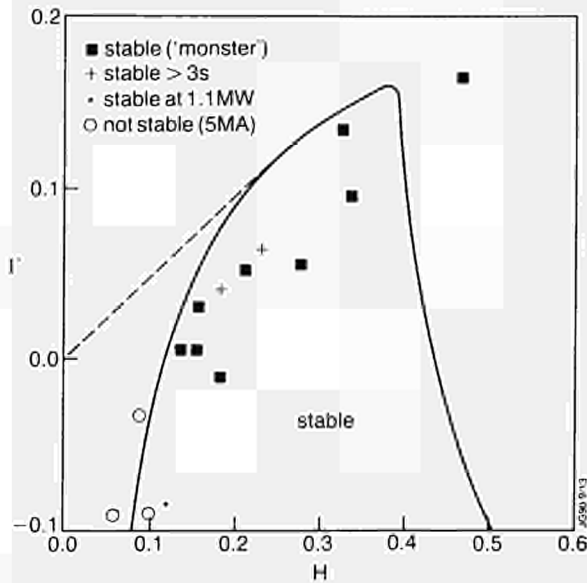
Fig.167: Analysis of a set of discharges, the majority of which had 'monster' sawteeth, in terms of the fast ion theory of stabilization. The parameters are explained in the text. Although the experimental uncertainties are large, most discharges with 'monster' sawteeth fall in the 'stable' region.

aspect ratio of the $q=1$ surface, s_0 the shear at that surface, ω_A the Alfvén frequency, and $<\beta_{ph}>_a$ the poloidal beta associated with the perpendicular fast ion pressure.

It is found that virtually all pulses exhibiting monster sawteeth fall into the stable region, whereas sawtoothing discharges analysed, the large (unquantifiable) error bars and the simplifying assumptions made, the results must, of course, be treated with extreme caution. However, together with the qualitative observations noted above, this first quantitative comparison between theory and experiment is encouraging.

(iii) 'Fishbones' - 'Fishbone'-like bursts are observed in both ICRF and NB heated discharges in JET[19]. They are believed to be destabilized by fast particle populations produced by these heating methods and, indeed, they are described by the same theory which accounts for the stabilization of sawteeth via fast ions - they are predicted to occur in the region outside of the stable boundary in Fig.167. They are observed at rather low values of β_p, but a detailed comparison with theory is difficult due to a lack of diagnostic information on the central fast ion distribution. They do not appear to affect plasma performance until much higher values of β_p and β_ϕ are achieved, but in high β_ϕ experiments, they may play a role in limiting β_ϕ.

Although these are believed to be caused by an interaction with fast particles, until recently no evidence has been obtained in JET of this interaction - in particular, there is no evidence of fast ion losses from the plasma resulting from such bursts. Now, however some indirect evidence of this interaction has been

obtained. Fig 168 shows the correlation between the modulation of the neutron emission from the plasma and the occurrence of such bursts during a high-β_ϕ discharge in JET. Although the modulation of the neutron emission amounts to only a few percent, neutron production is dominated by beam-plasma reactions in these discharges and a modulation of the fast ion population in the plasma centre is thought to be the most likely explanation for this effect.
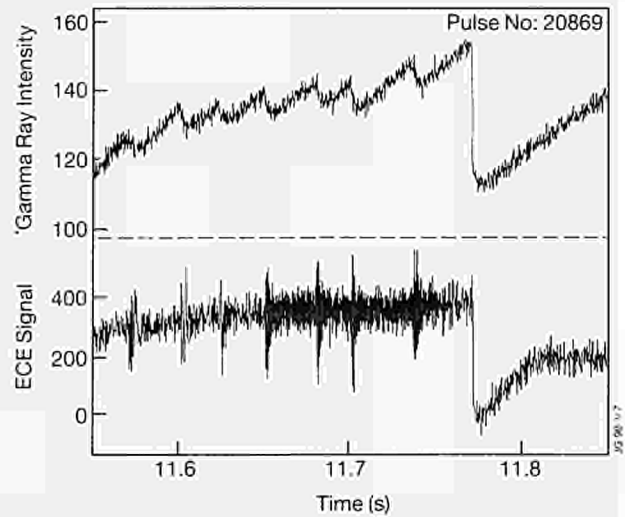

Fig.168: Correlation between 'fishbone'-like bursts observed in the electron temperature near the plasma centre and modulation of the total neutron emission during a high-β discharge. This is the first evidence in JET that such bursts affect the fast ion population.

High Beta Plasmas

During the most recent experimental campaign, a regime of high toroidal beta β_ϕ has been explored[20]. These discharges exploited the double-null X-point configuration to achieve the H-mode, which permitted high values of β_ϕ to be obtained at low toroidal fields B_ϕ ~ 1 - 1.4T. In this regime, values of β_ϕ of up to 5.5% have been achieved, as shown in Fig 169, corresponding to the so-called 'Troyon Limit', $\beta_c(\%) = 2.8 I_p$ (MA)/a(m)B_ϕ(T).

A central issue in the analysis of these discharges has been the nature of the β limiting mechanism. At the highest β achieved in JET, the observed limit is 'soft' rather than disruptive and appears to be associated with internal MHD modes having low poloidal and toroidal mode numbers. Fig.170 illustrates the behaviour during the highest value of bf, which was obtained by ramping down the toroidal field during the heating pulse. Sawtooth-like events in the bf trace can clearly be seen and, soft X-ray emission showed that these are interspersed with 'fishbone'-like bursts. In addition, 'ELMS' were observed at the plasma edge. This range of MHD activity is typical of such discharges.

Detailed comparisons of the influence of sawteeth and 'fishbones' have been performed in these discharges. It is found that both are accompanied by dominantly m=n=1 activity. However, the plasma
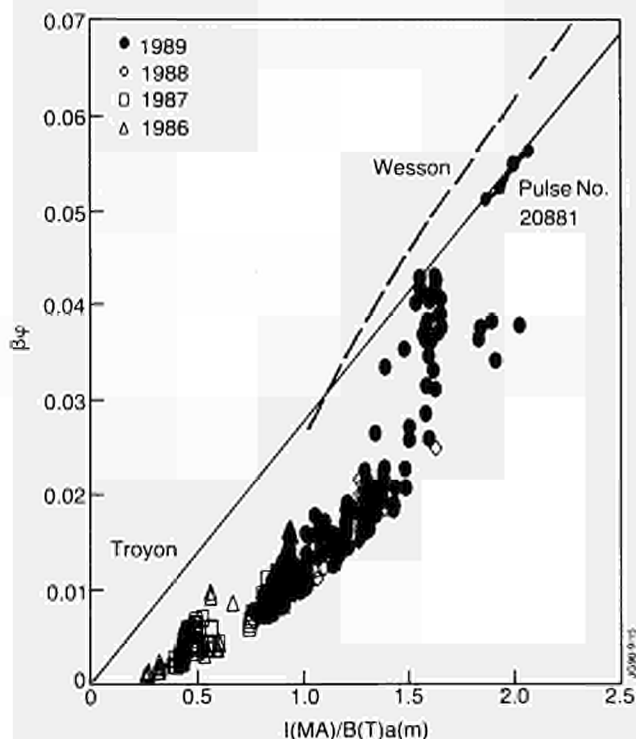
Fig.169: β_ϕ for high-β discharges plotted against normalised current. The solid line represents the 'Troyon Limit' and the dashed line the first prediction of the β-limit in JET (calculated by J. Wesson).

Fig.170: Overview of the JET plasma pulse which achieved the highest value of β_ϕ. The modulation of β_ϕ by sawtooth-like events is clear.

displacement associated with the sawtooth-like event is significantly larger (perhaps by a factor of 2) and the effect on β_ϕ is much greater than that of the 'fishbone'. In addition, a very rapid heat pulse, with a timescale of ~ 100µs, follows the sawtooth-like event and often this appears to trigger an ELM at the plasma edge.

In a number of cases, other beta-limiting mechanisms have been observed. In several discharges, it is found that β_ϕ decays towards the end of the heating pulse. In such cases a large n=2 mode is observed. Analysis of soft X-ray emission indicates that the mode exhibits a range of poloidal mode numbers, m=2, 3, 4, but the dominant component is not clear. While no direct evidence for high m,n ballooning mode activity has been obtained to date, this is due to the difficulty of obtaining such evidence from the diagnostic information available.

Various stability codes have been used to analyse the kink and ballooning stability of these plasmas using the measured pressure and (where possible) q-profiles. Uncertainties in the latter may represent a significant limitation on the results. In addition, no explicit treatment of fast particles has been included. However, within these restrictions a number of conclusions have been reached. Perhaps the most interesting of these is that, in general, the central region of the plasma is marginally stable to high m,n ballooning modes, with the core being unstable, as illustrated in Fig 171. In addition, calculations with the FAR code suggest that the n=2 modes observed to be responsible for beta decay in several cases could be explained by 'infernal' modes[21] if the shear in the central region of the plasma is small.
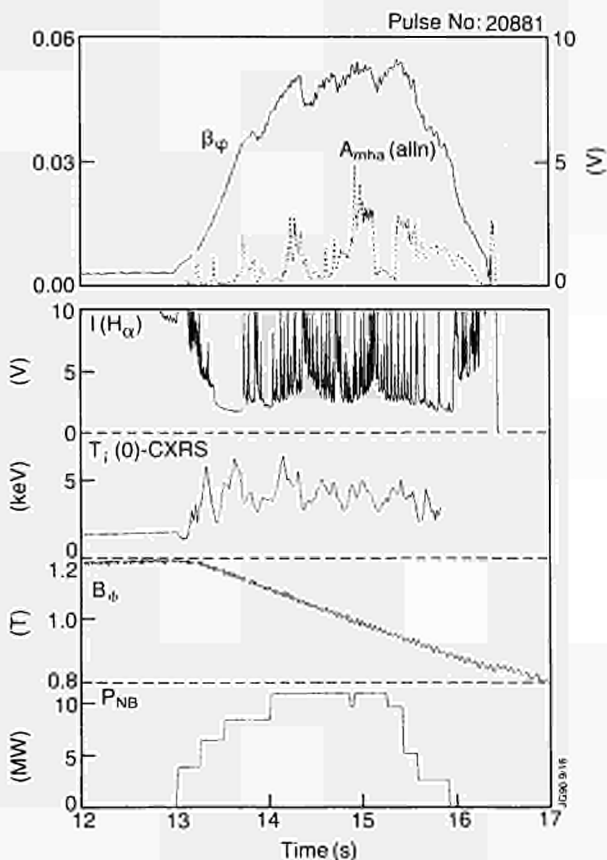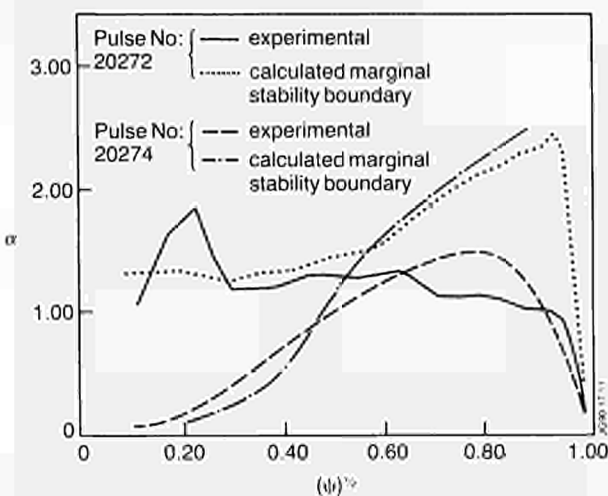

Fig.171: Stability analysis of a high-β_ϕ plasma in JET. The core of the central region of the plasma is found to be marginally stable to ballooning modes.

Current Profiles

Analysis during the year has concentrated on improving the accuracy with which the current and q profiles can be obtained. Particular attention has been given to the

determination of q(0) due to its of role in interpretation of the sawtooth instability. Development has continued of an analysis technique for the self-consistent calculation of magnetic equilibria using the IDENTC code to solve the Grad-Shafranov equation, but utilising constraints from both external magnetic signals and the polarimetric measurements. A systematic study of the propagation of experimental errors through this analysis routine is underway and, to date, the main conclusion is that the previously reported results[22] that q(0) ~ 0.7 in normal sawtoothing discharges has been confirmed.

A new analysis of combinations of signals from the far-infrared interferometer/polarimeter has produced the first estimate of the change in q(0) during the sawtooth cycle in JET. As shown in Fig 172, the deduced change $\Delta q(0)$ is < 0.05 for the range of shots analysed. In addition, there is a gradual increase in $\Delta q(0)$ as the sawtooth period τ_s increases. These results, together with the measurement that q(0) ~ 0.7 in sawtoothing discharges, is consistent with other observations in JET that a q=1 surface exists throughout the sawtooth period. First results from a new measurement of q(0) using the Motional Stark Effect[23] are also consistent with this conclusion.
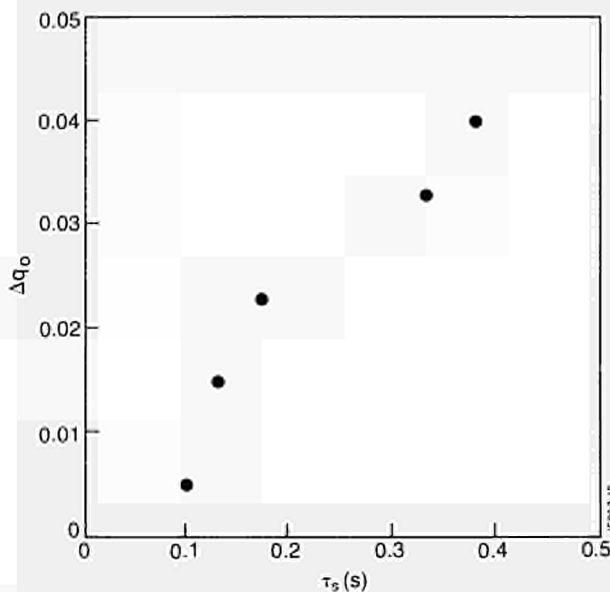

Fig.172: Plot of $\Delta q(0)$, the change in central value of the safety factor, versus the sawtooth period τ_s, as derived from the far-infrared interferometer/polarimeter. $\Delta q(0)$ is very small, suggesting that q(0) remains below unity throughout the sawtooth cycle.

Observations of Magnetic Islands

Analysis of the structure of magnetic perturbations in JET plasmas is a major research activity. Recently the high resolution of the LIDAR Thomson Scattering system, which measures temperature and density profiles, has been exploited to provide evidence of the existence of low m,n magnetic islands during various phases of JET plasmas[24]. As shown in Fig 173, the LIDAR system can identify the extent of the flattening
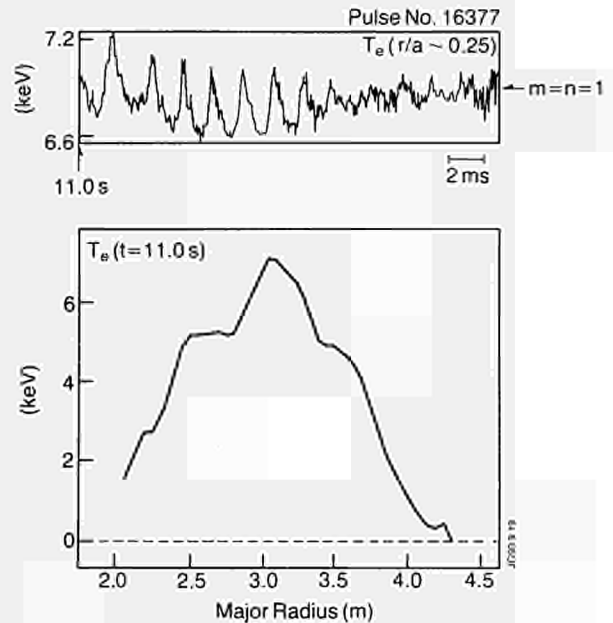

Fig.173: Electron temperature profile, measured by the LIDAR Thomson Scattering diagnostic, which shows a broad feature correlated with the m=1 activity in the plasma centre.

in the electron temperature profile due to m=1 magnetic islands generated by partial sawteeth. More generally, good correlation is found between the occurrence of m=1 oscillations in the soft X-ray and ECE diagnostics and the observation of such structures in the T_e profiles obtained by the LIDAR system.

However, as the dominant source of errors in the LIDAR measurement technique is due to statistical fluctuations in the photoelectric detection system, a more systematic investigation has been undertaken to ascertain which of the structures observed in the T_e profiles are real and which are due to random errors in the measurement. It appears that there is strong evidence, under well-defined plasma conditions, for the existence of m=3, n=2 and m=2, n=1 modes. A particularly interesting result of this analysis is that an anti-correlation is found between the occurrence of structures on the inside (outside) q=1 surface and on the outside (inside) q=2 surface. The result is not entirely understood, but does appear to indicate a phase coupling between the m=1 and m=2 modes.

References

[1] J.A. Wesson et al, Nucl. Fus. **29** 641 (1989).

[2] P.J.Lomas et al, 29th Annual Meeting of the Plasma Physics Division of the American Physical Society, San Diego, USA, (1987).

[3] A. Vannucci and R.D. Gill, JET Report JET IR(89)25 (1989).

[4] J.A. Snipes et al, JET Report JET-P(89)64 (to be publ. in Nucl. Fus. (1990)).

[5] Z. Chang and J.D. Callen, University of Wisconsin Report UWPR 89-1 (1989).

[6] C.G. Lowry et al, 31st Annual Meeting of the

Plasma Physics Division of the American Physical Society, Anaheim, November 1989.

[7] A.W. Edwards et al, Phys. Rev. Lett. **57** 210 (1986).

[8] J.A. Wesson, Plasma Phys. and Contr. Fus. **28(1A)** 243 (1986).

[9] D.J. Campbell et al, Proc. 16th European Conference on Controlled Fusion and Plasma Physics (Venice, Italy, 1989) **2**, 509.

[10] E. Westerhof and P. Smeulders, Nucl. Fus. **29** 1056 (1989).

[11] A. Weller et al, Phys. Rev. Lett. **59** 2303 (1988).

[12] D.J. Campbell et al, Nucl. Fus. **26** 1085 (1986).

[13] J.A. Wesson et al, Proc. 11th International Conference on Plasma Physics and Controlled Fusion (Kyoto, Japan, 1986) **2** 3 (1987).

[14] J.A. Wesson et al, JET Report JET-P(90)03 (1990).

[15] D.J. Campbell et al, 31st Annual Meeting of the Plasma Physics Division of the American Physical Society, Anaheim, USA (1989).

[16] D.J. Campbell et al, Phys. Rev. Lett. **60** 2148 (1988).

[17] M. Bures et al, Proc. 16th European Conference on Controlled Fusion and Plasma Physics (Venice, Italy, 1989) **1**, 3.

[18] F. Pegoraro et al, Proc. 12th International Conference on Plasma Physics and Controlled Fusion (Nice, France, 1988) **2** 243 (1989).

[19] B. Coppi et al, Phys. Rev. Lett. **63** 2733 (1989).

[20] B. Coppi et al, Phys. Rev. Lett. **57** 2272 (1986).

[21] L. Chen et al, Phys. Rev. Lett. **52** 1122 (1984).

[22] M.F.F. Nave et al, Proc. 16th European Conference on Controlled Fusion and Plasma Physics (Venice, Italy, 1989) **2** 505.

[23] P. Smeulders et al, 31st Annual Meeting of the Plasma Physics Division of the American Physical Society, Anaheim, USA (1989).

[24] J. Manickam et al, Nucl. Fus. **27** 1461 (1987).

[25] J. O'Rourke et al, Proc. 15th European Conference on Controlled Fusion and Plasma Physics (Dubrovnik, Yugoslavia, 1988) **1** 155.

[26] A. Boileau et al, J. Phys. B: At. Mol. Opt. Phys. **22** L145 (1989).

[27] C.W. Gowers et al, 31st Annual Meeting of the Plasma Physics Division of the American Physical Society, Anaheim, USA (1989).

Next Step Scenarios and Implications for JET

The JET programme must be viewed as one constituent in the chain of devices leading to a demonstration fusion reactor. It is only in this context that it has its full meaning. It must provide the data necessary to proceed with a Next Step device, an ignited tokamak with long burn capability. Since the beginning of its operational phase, JET has made much progress and major achievements, as has been reported in previous JET Progress Reports. However, further advances must be accomplished to provide a secure basis for the Next Step.

Plasma temperature, density and confinement values already achieved, but not simultaneously, individually meet the requirements of a Next Step device. JET results have allowed some of the parameters of a reactor to be specified. In particular, the plasma current capability of a Next Step tokamak is now foreseen to be about 25 MA for a magnetic field ~ 3-5T, compared to less than 10MA when JET started operation in 1983. However, the highest performance in JET, (such as an equivalent Q_{DT} close to breakeven) has been achieved in a transient state. Even so, a large carbon influx, originating from the target plates, enters the plasma less than 1s after the application of the full beam-power, as illustrated in Fig 174. Carbon impurity prevents the beams reaching the plasma axis and caused a rapid drop in the ion temperature from 27 to 10 keV. The deuterium plasma is continuously diluted and the neutron production falls continuously up to the end of the beam pulse. It is clear that control of impurity influx and exhaust is still inadequate relative to what will be required in the Next Step. To demonstrate effective methods of impurity control in operating conditions close to those of the Next Step tokamak is the aim of a New Phase of JET, recently endorsed by the JET Council. Considerable effort has already been devoted to design and plans for the new phase and these are reported in the section on Developments and Future Plans.
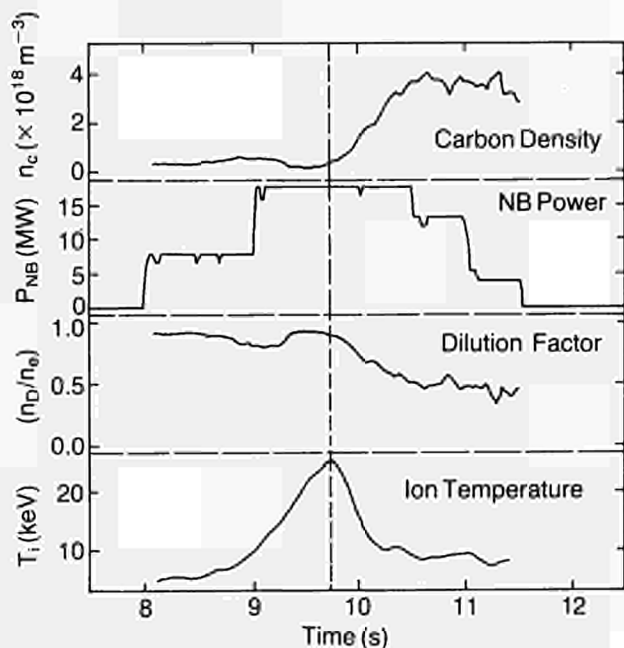
Fig.174: The 'Carbon Bloom' in JET with a beryllium first-wall.

The main areas in which the new phase of JET is expected to provide information for a Next Step device are:

- Control of impurity content, with full additional power for long times, approaching steady-state;

- Improved understanding of particle and impurity transport, prediction of pumping requirements and simulation of transport of fusion ashes;

- Achieving full steady-state in enhanced confinement regimes (i.e. H-modes, peaked density profiles, etc.);

- Test lifetime of divertor plates and assess first-wall materials to be used;

- Fuelling methods, (in particular, a high-speed pellet injection system);

- Perform technology tests and assess systems for the Next Step such as: tritium plant and remote handling, heating and current drive.

In addition JET will contribute to specific topics of the ITER-related Physics R&D Programme, to be carried out during the ITER conceptual design. The ITER tasks which will be addressed by JET are:

PH01   Power and helium exhaust conditions;

PH02   Helium radial distribution in high-temperature tokamak discharges;

PH05   Characterization of low-Z materials for plasma facing components;

PH07   Characterization of disruptions;

PH11   Scaling of V-s consumption during current ramp-up in large tokamaks;

PH14   Steady-state operation in enhanced confinement regimes;

PH15   Comparison of theoretical transport models with experimental data;

PH16   Control of MHD activity;

PH17   Density limits;

PH19   Alpha-particle simulation experiments;

PH21   Ion cyclotron frequency current drive.

Reports on most of these tasks are due in October 1990. Progress reports on tasks PH05, PH11, PH17 and PH21 were already submitted in October 1989.

Theory

The scope and resources of the theory programme are strictly bound to the direct support of the JET experiment. A review at the beginning of 1989 confirmed the research priorities within certain imposed boundary conditions. Even more than in previous years the work concentrated on *Interpretation* of JET data in the areas of local energy and particle transport, of ion cyclotron heating, and MHD phenomena.

Much of the *Predictive* theoretical effort was devoted to calculations of magnetic field structure and impurity

transport for the planned pumped divertor of JET. The actual development of theoretical models from first principles, *Analytic Theory*, has succeeded in providing a description of stabilising sawtooth oscillations by fast particles, and in explaining details of RF wave absorption. Major steps have been taken towards a model for anomalous transport caused by small field asymmetries, and towards a wider class of plasma equilibria including stationary flows.

The continuing assessment of new theory *from the literature* for JET and other tokamak plasmas, has lead to a review on the influence of fluctuations on transport processes. Also the build-up of *data banks* whose derivation requires more elaborate theoretical and computational procedures and care has continued, resulting in a greatly extended number of experimental local thermal and particle flux profiles, both for electrons and ions.

The bank of validated magnetic flux surface configuration, which is basic for many other diagnostics, has been maintained and considerably extended. A new bank of validated ICRH deposition profiles applying wave propagation theory rather than ray tracing has been started.

Due to circumstances, the development of the main theory goal, i.e. the development of a consistent and quantitative overall tokamak plasma model which would reflect all the important plasma physics effects with sufficient accuracy, has unfortunately slowed down.

The lack of in-house manpower has been offset to some extent by wide and lively collaboration through contracts with Institutes in Austria, The Netherlands, France, Poland, and Sweden, and Euratom Associations on models for α-particles, stability, tokamak equilibria, sawtooth oscillations, micro-instabilities and transport data evaluation; and through task agreements with ENEA-Frascati, Italy and AEA-Culham, UK both on plasma transport modelling. In addition, the presence of short-term visitors and Associated Staff was beneficial.

Data Banks and Evaluation Codes

One of the main difficulties in deriving experimental energy and particle fluxes lies in the consistency and accuracy of the measured input data such as temperature, density, radiation profiles, etc. A set of check programmes has been developed and run as initial step of the FALCON (Fast Analysis of Local Confinement) code. For about 1000 time points in 150 JET discharges individually checked heat flux profiles are now available with estimated errors resulting from systematic error propagation studies.

A new version of equilibrium magnetic surface identification code (IDENTD) has been implemented. In addition to the magnetic signals and pressure profiles from laser scattering this code also uses Faraday rotation measurements from a multichannel interferometer as input to determine magnetic flux

surface configuration and current density profiles. The configuration bank now contains 10 to 20 configurations for each of about 600 JET discharges.

Out of the full wave propagation codes for ICRF heating, a simplified version for routine usage has been produced. This code PION calculates power deposition and velocity distribution of resonating ions in steady state in a self-consistent way. A data bank with, initially, about 40 spatial profiles for 19 RF discharges should grow rapidly.

Theoretical Models

Any localised perturbation to the toroidally symmetric field of a tokamak may break up magnetic surfaces and so increase the plasma loss. The momentum absorbed from an injected neutral beam produces such a perturbation. Its 3-dimensional structure in JET has been computed, using a Hamiltonian description which greatly reduces the computing time. Although in JET conditions the magnetic perturbation is appreciable, the resulting magnetic stochasticity is found not to be as extensive as might be expected, and of a different nature.

A review of the correlation between transport and fluctuations showed some qualitative differences between the energy flux and that predicted for the measured fluctuation level. This has motivated further study of neoclassical transport theory. Inclusion of a poloidally varying electrostatic potential increases the electron energy transport in the plateau regime by a large factor, though still not enough to account for that measured.

The absence of sawtooth activity during "monster sawteeth" in JET can be explained by the stabilisation of the m = 1 internal kink instability by energetic ions. The energetic ions are produced by RF heating. The stabilisation persists when resistivity is included. If the fast ions are not sufficiently energetic they may instead excite fishbone oscillations.

Description and Interpretation of the Plasma Behaviour

The evaluation of the local energy transport, using the FALCON code, and its comparison with different theoretical predictions, continues to be an important activity. Detailed comparison between the experimental energy flux and the predicted fluxes from the ion temperature gradient (or η_i) instability show significant discrepancies.

The ICRF heat deposition codes have been used to study various JET phenomena, such as second harmonic heating, the observed non-thermal fusion rate, and changes in toroidal rotation induced by ICRF. The large ion orbit widths are found to significantly broaden the heat deposition profile. The absorption of RF energy at the plasma edge by excitation of Bernstein waves and by parametric decay, has been analysed.

Predictive Computations

The design of the proposed pumped divertor for JET has required extensive modelling and computations. Magnetic equilibrium computations have been done to find the optimum coil currents to produce a magnetic configuration of the type required. This has been matched by transport computations to simulate the flow of plasma and impurities into and out of the divertor region. These must include a Monte-Carlo code for the neutral hydrogen penetration. The objective is to establish the parameter range over which the plasma flow towards the limiter is sufficient to prevent significant inflow of impurities.

The predictive transport computations for the bulk plasma, to test different transport models against JET measurement or to predict the performance in new operating regimes or proposed new tokamaks, has continued. Particular attention has been given to the Rebut-Lallia critical temperature gradient model, though micro-instability based models have also been used. The predicted performance in Ignitor has been studied intensively.

A rather different application of the predictive transport code is to simulate the evolution of the temperature perturbation following a sawtooth crash. Different transport models have again been used, and the predicted heat pulse propagation compared with JET measurements. The Rebut-Lallia model appears to give best agreement.

Summary of Scientific Progress and Perspective

This section sets out a summary of the global results obtained during operation with berylliated walls and with the beryllium limiter and describes specific results addressing topics of physics investigation.

Impurity Fluxes and Concentrations

During the initial graphite phase, carbon was the dominant impurity with typical concentrations of 4 - 7% and with Oxygen at ~ 0.5 - 2%. At high additional heating power, Z_{eff} values were about 3 and little deuterium was left in the plasma (high dilution).

During the beryllium evaporation phase, carbon remained the dominant impurity, but influxes were reduced by a factor of two. Oxygen was reduced to a negligible level. The reduction in carbon influxes was attributed to the absence of oxygen sputtering. The lifetime of the evaporated layers was short and about 5 - 20 discharges depending on applied power, but the reduction in oxygen remained and so did the reduced carbon influx.

During the beryllium limiter phase, beryllium was

the dominant impurity (~ 3%). The carbon content was low (~0.5%) and oxygen was negligible.

Power Handling Capability of the Beryllium Limiter

The power handling capability of the high heat flux components was always higher than the power at which useful discharges could be sustained. For example, the inner wall was able to survive loads of up to 400 MJ, whereas at low densities, useful plasmas could only be produced for levels up to 17 MJ. At higher loads, the plasma became contaminated by graphite to such an extent that starting with a dilution n_D/n_e of 0.7 (n_D deuterium density, n_e electron density) at the start of additional heating, virtually no deuterium was retained in the plasma ($n_D/n_e \sim 0$) after about one second. This catastrophic effect occurred as soon as the graphite reached temperatures in excess of 1200°C when radiation induced sublimation and self-sputtering became important. Self-sputtering is a non-linear process and can increase the carbon influx in an avalanche-like process. The resulting plasma contamination is called the 'carbon bloom' and its occurrence limited the fusion performance of JET. In low density ($n_D \sim 3 \times 10^{19}$ m^{-3}) high temperature ($T_i \sim$ 20 keV) discharges as soon as the carbon entered the plasma, the density increased, the temperature dropped and the neutron output strongly decreased.

The high surface temperatures of the tiles resulted mainly from misalignment of individual high heat flux components, so that power loads were intercepted only by small surface areas. Improving the alignment did not result in better plasma performance. For example, reducing the deviation from circularity at the inner wall from ± 10 mm to ± 2 mm did not suppress the carbon bloom; there was no substantial change either in the loads or in time delay between applying additional heating and the occurrence of carbon influx. Be evaporation did not change this behaviour.

For the beryllium limiter, low density, and high ion temperature plasmas with high neutron output were established. In comparison with the graphite belt limiter, the corresponding Q_{DD} values were increased by a factor x3. The high performance was terminated by the influx of beryllium from hot-spots at the limiter surface. These may result from misalignment of less than 0.3 mm between adjacent limiter tiles. Hot spots led to surface damage on about 30% of the limiter. At high densities, by tailoring the gas-feed during discharges, high power long duration discharges with Z_{eff} values about 1.5 were sustained. In such cases, 30 MW power was fed into the plasma for 6s.

Effective Charge and Dilution

It was found that, especially with the beryllium limiter, a strong gas puff during the start of the additional heating period, could reduce Z_{eff} values to ~ 1.5, even with heating powers of up to 30 MW. The strong gas puff ('Superpuff') was typically ten times larger (a few

hundred mbar s^{-1}) than was possible with the graphite limiter. The Superpuff did not reduce the beryllium influx, but increased the deuterium influx by a factor x2 without increasing the central density compared with a discharge without a Superpuff. In addition, the central electron temperature did not change, indicating the same energy confinement times for both cases. To explain this behaviour, impurity screening must be assumed in a way which cannot be explained by the normal impurity screening model.

Z_{eff} values now depend to a large degree on the method of setting up the discharge and can be strongly influenced by gas influx. It is not possible to use this procedure with a graphite limiter because strong wall pumping is required to avoid disruptions and even with the helium conditioning of the graphite walls the pumping rate was not sufficient.

Z_{eff} values ≤ 1.5 achieved with a Superpuff at high heating power are comparable to the best obtained for a well-conditioned graphite limiter for ohmic discharges. With dilution reduced to $0.7 > n_D/n_e > 0.55$, higher on-axis deuteron densities were achieved. This did not lead to a higher neutron output, because, in contrast to low-density hot-ion discharges, electron and ion temperatures were comparable at the higher densities normally obtained with the Superpuff. In the temperature range considered, the neutron output Q_{DD} scaled as

$$Q_{DD} \sim n_i^2 \, T_i^2$$

where higher ion density was partially offset by lower ion temperatures.

For discharges with beryllium evaporation of with beryllium limiter, higher powers per particle or lower dilution obtained compared with operation with the graphite limiter at the same Z_{eff} values.

Wall Pumping and Hydrogen Retention

Wall pumping has always been observed in JET and it was used to terminate discharges without creating disruptions during the current ramp down. Pumping with graphite walls can be increased by conditioning with beryllium discharges. One measure of the pumping capability of the wall is the characteristic time τ_p^* for density pump-out after the gas supply is switched off:

$$\tau_p^* = \left[N_D \left(\frac{dN_D}{dt} \right)^{-1} \right]_{\phi_{gas} = 0}$$

where N_D = number of deuterium atoms in the machine, and ϕ_{gas} = gas influx due to fuelling. Typical values for τ_p^* range from 20 s for an unconditioned graphite machine to below 1s for a conditioned beryllium limiter.

To maintain a preset density, a larger amount of deuterium must be introduced into the plasma if the wall pumping is increased, as is the case for the belt limiter. This effect poses the question of the hydrogen retention in the wall, which must be seen in the context of the tritium inventory for JET.

Wall pumping experiments indicate that, for graphite limiters, ~ 80% of the deuterium is retained in the vessel, compared with about 10 - 20% for the beryllium limiter or where beryllium is evaporated onto the graphite limiter. Taking into account the larger amount of gas which must be used to obtain similar densities for the graphite and the beryllium limiter, the total retention (number of particles) is about equal in both cases.

The introduction of beryllium has transformed the recycling characteristic of the walls in such a way that they now resemble that of a metal wall (i.e. strong wall pumping is obtained). As a result, density control was greatly improved. The recycling coefficient (~ 0.99 for a non-conditioned C-limiter) decreased to ~ 0.9 for the beryllium limiter. One additional benefit was obtained due to the fact that the vacuum vessel was no longer deconditioned after a high current disruption, and the number of useful discharges was considerably increased.

Density Limit

In a carbon vessel, the density limit occurred as a radiation limit. It was invariably a disruption limit. When the radiation reaches the level of the input power, the plasma edge cools, an $m = 2$ instability grows and is de-stabilised by the radiative contraction of the temperature and current profile.

For a berylliated vessel and for the beryllium limiter, the density limit occurred when about 50% of the input power was radiated. An assymmetric radiating structure - a Marfe - appeared. This limit was not necessarily disruptive and appeared to be a refuelling rather than a radiative limit.

For disruptions (locked modes) which still occurred with the beryllium limiter, the current decay was about a factor x10 slower than for a graphite limiter or beryllium evaporated onto a graphite limiter.

The density limit in ohmic plasmas for carbonised and beryllium gettered vessels were similar:

$$\bar{n}Rq/B \sim 24 \times 10^{19} \ m^{-2} \ T^{-1}$$

With a berylliated vessel or beryllium belt limiter, there was no difference in the limit (Marfing limit) for RF and neutral beam heating in contrast to operation with the graphite limiter when the RF density limit was identical to the ohmic case. Furthermore, it was observed that the density limit depended on the heating power. For an input power of 12 - 15 MW, a value of the density limit $\bar{n}Rq/B < 40 \times 10^{19} \ m^{-2} \ T^{-1}$ was obtained.

The density (Marfing) limit for the berylliated vessel or the beryllium limiter depended on the power input, P, and scaled as $\bar{n} \sim P^{1/2}$ where a very good fit was obtained when the edge density was used instead of the average density .

The density profiles obtained during the density limit experiments were generally flat, and even hollow for high gas feeds. Peaked profiles were obtained with pellets with the highest central density reaching $n_e \sim 4 \times 10^{20} \ m^{-3}.$

Specific Results

Hot Ion Plasmas for Belt Limiter Discharges

For the carbon limiter, the high ion temperature region was not accessible due to poor density control. Deuterium dilution, n_D/n_e, ranged from 0.4 - 0.8, depending on conditioning. Maximum Q_{DD} values of 2.5×10^{-4} were obtained.

With beryllium evaporated on the belt limiter, high power per particle and high ion temperatures were obtained. Peaked density profiles, which increased the neutron output were obtained by beam fuelling. The carbon influx from the belt limiter gave n_D/n_e of about 0.6, and the Q_{DD} values increased to about 6.5×10^{-4}.

The beryllium limiter behaved similarly to beryllium evaporation conditions with respect to power per particle, ion temperature and dilution. However, the density profiles were flat. Pellet fuelled target plasmas resulted in peaked profile hot ion discharges. The maximum fusion yield obtained was $Q_{DD} \sim 8 \times 10^{-4}$. The neutron yield increased when applying ICRF power. In many cases, the neutron output was reduced after the influx of beryllium.

Sawtooth Stabilisation

Sawtooth stabilisation was achieved by on-axis heating during a sawtooth free period (monster sawtooth). This phenomenon is observed over a wide parameter range. RF heating, as well as neutral beam heating were effective. However, the former was more suited due to its better defined on-axis power deposition. The longest sawtooth-free period obtained lasted for more than 5s. During the sawteeth free periods, the on-axis q value can be as low as 0.6 and does not reach values ≥ 1 after the sawtooth crash.

To explain the stabilisation, a model of fast ions has been used which attributes the sawtooth relaxation to the initiation of a resistive internal kink. The stability diagram obtained with this model is in reasonable agreement with the measurements. In addition, to stabilisation by on-axis heating, two other methods appear to be possible, namely by suppressing the onset of sawteeth during the current rise by additional heating, or by injection of pellets into the plasma during the current rise without additional heating.

Alpha Particle Simulation

During sawtooth free periods ICRF heating has been used to produced ^3He ions in the MeV region. The energy of the fast particles reached 2.4 MJ (50% of the total plasma energy). The parameters for the energetic helium ions produced by the ICRF heating are similar to those expected from D-T fusion reactions in JET or NET. The main difference is the ratio of parallel to perpendicular pressure, which is highly anisotropic in the case of the ^3He ICRF heating.

The main findings were that the particles slow down classically as predicted theoretically. Exceptions found for low currents (≤ 2 MA) could be explained by large

D-shaped trapped ion orbits which reduced the slowing down time by allowing the ions to explore cooler plasma regions. The termination of a sawtooth free period leads to a reduction in the fast ion content. Typically 50% is expelled during a sawtooth crash.

The ^{3}He-D fusion reactions with on-axis heating are in good agreement with RF power deposition and fast ion calculations. With beryllium gettering, the fusion yield increased to 100 kW resulting in Q values of about 1%, approximately twice the value obtained with carbon walls and limiter.

The Beta Limit

For thermal plasmas, the maximum β is determined by MHD phenomena: either by resistive kinks (Troyon limit) or by ballooning modes. In the latter case, the limit is higher by about 50%. In JET, the Troyon limit (soft limit) was observed for the maximum beta, whereas DIII and DIII-D observe higher limits which result in disruptions. The reason for this different behaviour may be found in the higher plasma inductance (l_i) in these experiments.

In JET, the beta limit is a soft limit, characterised by β-clipping, ie a relaxation in density and temperature, which can occur periodically while trying to exceed the Troyon limit. The maximum β-values obtained (only after beryllium operation) were between 5 and 6 % in good agreement with the prediction for JET performance.

H-mode with RF only

Initially the application of ICRF heating to neutral beam generated H-modes terminated the H-modes. This was attributed to strong impurity influxes during ICRF heating and difficult coupling conditions. With improvement in the phasing and the coupling, ICRF power was coupled to H-modes but the radiated power increased due to oxygen and nickel radiation.

After beryllium gettering and with the use of a RF dipole configuration, H-modes of up to 1.5s duration were obtained at power levels of up to 12 MW. Threshold power, edge behaviour and confinement was similar to those H-modes obtained with neutral beams only. Energy confinement times were similar to NB cases and reached twice the Goldston L-mode scaling.

Maximum Fusion Performance

Improvements in the fusion parameter ($n_D \tau_E T_i$) were obtained in X-point discharges by using the techniques of beryllium evaporation, 6 MW of 140 keV beams (+ 11 MW at 80 keV) and X-point sweeping to reduce the temperature of the target tiles and then to delay the carbon bloom. Under these conditions, the dilution at the maximum neutron output reached values of $n_D/n_e \sim$ 0.9 and with the strong wall pumping in the resulting low density plasmas, ion temperatures reached $\sim$ 30 keV. The confinement times did not change compared with previous operation with graphite.

Combined radial and vertical X-point sweeping resulted in the following performance:

- neutron yield reached 3.7 x 10^{16} s^{-1}, corresponding to $Q_{DD} \sim$ 2.5 x10^{-3};
- fusion parameter was increased to 8 - 9 x 10^{20} m^{-3} keVs;
- equivalent total $Q_{DD} \sim$ 0.8, with about 25% thermal-thermal and the rest beam-thermal. The resulting equivalent fusion power would be 13 MW.

These best conditions were only obtained transiently ($\sim$0.2 s) before the carbon influx terminated the good performance.

Future Perspective

From the beryllium experiments completed in 1989, it can be concluded that both high plasma purity levels (n_D/n_e) and higher densities can be achieved with beryllium limiters than was possible with carbon. These improvements stem from the elimination of oxygen impurity and the fact that the improved pumping capability of beryllium permitted very strong gas puffing which, in turn, screened the impurity fluxes from the plasma centre. One further operational advantage of using beryllium was that the limiters did not need reconditioning after a disruption as was the case with carbon limiters.

Despite very accurate alignment of the tiles on the belt limiter, there were problems with hot spots and local melting of the tile surface. This implies that, in the future, the limiter and its plasma facing components should be designed in such a manner that the alignment of the plasma facing components system for sweeping the power loading of the limiter surfaces would also help in preventing local melting.

The high Q ($\sim$0.8) H-mode performance achieved in 1989 was a considerable improvement. However, this mode of operation was prevented from reaching its full potential by a strong influx of carbon about one second after commencement of the high power heating. Without this influx, calculations show that a Q value greater than unity would have been achieved.

Progress towards a Reactor

During 1989, substantial progress was made towards reaching reactor conditions in that very high values of the fusion product ($n_i(0) \tau_E T_i(0)$) of 8-9 x 10^{20} m^{-3} keVs were achieved (see Fig 175). This exceeded the 1988 record by more than a factor of x3. These high values were obtained within an H-mode X-point configuration: the X-point was swept across the upper and lower limiting surfaces to delay the onset of the impurity influx (carbon bloom).
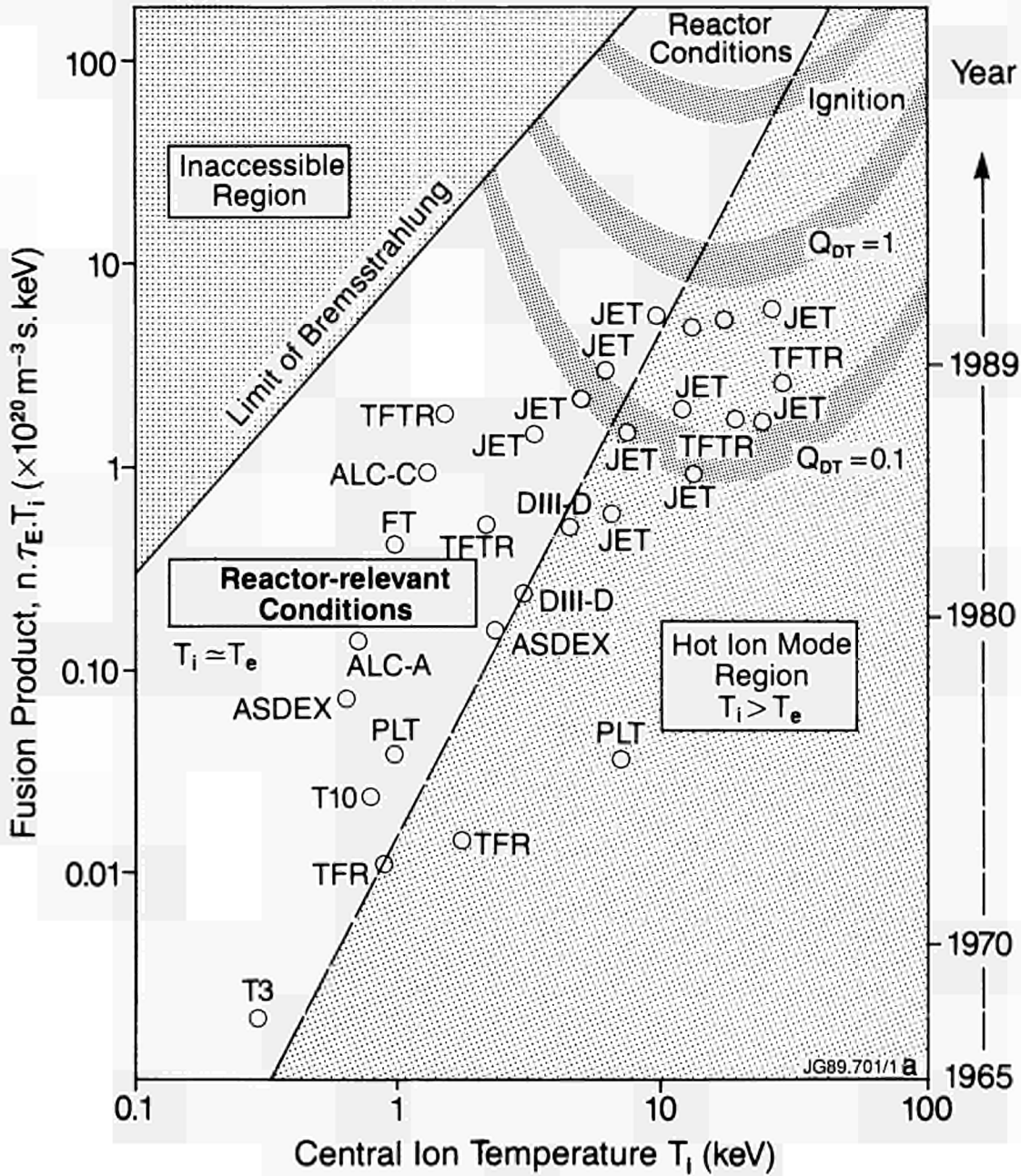
Fig.175: *Fusion parameter as a function of central ion temperature for various fusion devices. The mode of operation relevant for a reactor is where the electron and ion temperatures are nearly equal at values between 15 and 50 keV. The high density/low temperature region is forbidden due to radiation losses*

The neutron yield for this discharge was also the highest ever achieved on JET at 3.7×10^{16} ns^{-1}, with a $Q_{DD} = 3.1 \times 10^{-3}$. A full D-T simulation of this pulse showed that ~ 13MW of fusion power could have been obtained transiently with the 16MW of injected NB power, giving a fusion product value of $(n_i \tau_e T_i)$ which would be within a factor of 5-10 of that required in a reactor.

Significant improvements were also achieved in the limiter configuration due to the improved pumping with beryllium tiles. Higher ion temperatures (>20 keV) and higher values of the fusion product $(n_i \tau T_i) = 1.5 \times 10^{20}$ m^{-3} keVs were obtained. The highest achieved values of the fusion product in the various configurations are listed in Table XVII.

Table XVII

Maximum Values of $<n_i (0)\ \tau_E\ T_i (0)>$

Experimental Programme	Peak Density $n_i (0)$ $(\times 10^{19}\ m^{-3})$	Energy Confinement τ_E (s)	Ion Temperature $T_i (0)$ (keV)	Fusion Product $<n_i (0)\ \tau_E\ T_i (0)>$ $(\times 10^{20}\ m^{-3}.s\ keV)$	Q_{DT} Equivalent	Plasma Current I_p (MA)
Ohmic (4.6MW)	4.0	1.0	3.1	1.2	0.010	5
ICRF (16MW)	3.8	0.4	8.0	1.2	0.025	3
Pellet +(12MW) ICRF	5.4	0.5	7.2	2.0	0.10	3
NBI (20MW) Low n:	2.3	0.3	20	1.5	0.33*	4
Combined NBI+RF (22MW)	4.5	0.5	8.1	2.0	0.30*	3.5
X-point (NB-16MW)	3.7	1.1	22	8-9	0.8*	4

*Beam Plasma reactions are dominant

Developments and Future Plans

In 1978, the original objectives of JET were set out in the JET Design Proposal, EUR-JET-R5, as follows:

'The essential objective of JET is to obtain and study a plasma in conditions and dimensions approaching those needed in a thermo-nuclear reactor. These studies will be aimed at defining the parameters, the size and the working conditions of a Tokamak reactor. The realisation of this objective involves four main areas of work:

    i)   the scaling of plasma behaviour as parameters approach the reactor range;

    ii) the plasma-wall interaction in these conditions;

    iii) the study of plasma heating; and

    iv) the study of α-particle production, confinement and consequent plasma heating.

The problems of plasma-wall interaction and of heating the plasma must, in any case, be solved in order to approach the conditions of interest.

An important part of the experimental programme will be to use JET to extend to a reactor-like plasma, results obtained and innovations made in smaller apparatus as a part of the general tokamak programme. These would include: various additional heating methods, first wall materials, the control of the plasma profiles and plasma formation.'

These objectives still remain valid and continue to provide the focus of the Project's plans. In addition, the JET Project, as a central part of the European Fusion Programme, is directed towards the objectives of that Programme, agreed by the Council of Ministers in the following terms:

'The main objectives of the programme are: to establish the physics and technology basis necessary for the detailed design of NET: in the field of physics and plasma engineering this implies the full exploitation of JET and of several medium-sized specialised tokamaks in existence or in construction...'

At the start of 1989 the JET Project entered its planned Phase III - Full Power Studies. The original design specifications of JET had been achieved and in many cases exceeded. Two of the main programme objectives of the JET programme - the study of plasma heating and of the confinement of plasma - had to a large extent been met in that the results from JET have made it possible to define with confidence the main parameters of a Next Step device. Some aspects of α-particle heating had also been studied in simulation experiments.

During 1989, emphasis within the programme was directed towards the fourth area of study, that of plasma-wall interactions, particularly the control of impurities in high performance plasmas. The Project has now demonstrated clearly the benefits to be derived (albeit transiently) from passive impurity control by the use of beryllium as a first-wall material for plasma-facing components.

In parallel, preparations for D-T operations have continued; after some delays in the construction work and in plant manufacture, the Active Gas Handling building is nearing completion and installation of the major subsystems has started. The planned commissioning programme in this area has been slightly revised, but it is still consistent with a period of tritium operation during 1992.

The most recent experiments on JET achieved plasma parameters approaching breakeven values for about a second, resulting in a large burst of neutrons. These neutrons indicate that fusion D-D reactions are taking place. However, in spite of the plasma pulse continuing for many seconds after reaching peak plasma values, the neutron count fell away rapidly as impurities entered the plasma and lowered its performance. This limitation on the time for which the near-breakeven conditions could be maintained is due to the poisoning of the plasma by impurities. This has further emphasised the need to devise a scheme of impurity control suitable for a next step device.

The JET aims clearly state that JET is an experimental device and that, to achieve its objectives, the latest developments in Tokamak physics must be allowed to influence its programme. However, within a JET programme to 1992, it would not be possible to tackle thoroughly problems associated with impurities. In view of the central importance of impurity control for the success of a Next Step device, the JET Council unanimously supported in October 1989 a proposal to add a new phase to the JET programme, the objective of which would be to establish effective control of impurities in operating conditions close to those of the Next Step. This involves providing JET with a new magnetic configuration, including principally the installation of a pumped divertor. A prolongation of four years from the current end date of 31 December 1992 is needed to carry out the changes and then to allow sufficient experimental time to demonstrate the effectiveness of the new configuration in controlling impurities. This would provide for deuterium operation up to the end of 1994, followed by tritium operations in 1995 and 1996.

In October 1989, the JET Council agreed to the proposed prolongation and invited the Commission to make a proposal to the Council of the European Communities for amending the JET Statutes to allow this prolongation. The JET Council also authorised preliminary expenditure on the New Phase Programme, within a limit on commitment, on items necessary to maintain the schedule of the proposed programme. The possible prolongation of JET was explicitly referred to in the European Commission's proposal for a revised Framework Programme for the period 1990-94.

The current status of the JET programme is that, subject to Decisions of the Council of Ministers on budgets, programmes and statutes, the Project is planning to pursue the New Phase Programme, on the presumption of a prolongation until the end of 1996 but is also, for the present, in a position to proceed towards completion of the programme with D-T operation by the end of 1992.

While present achievements show that the main objectives of JET are being actively addressed and substantial progress is being made, the strategy for JET can be summarised as a strategy 'to optimise the fusion product $(n_i\ T_i\tau_E)$'. For the energy confinement time, τ_E, this involves maintaining, with full additional heating, the values that have already been reached with ohmic heating and in the H-mode with the X-point configuration. For the density and ion temperature, it means increasing their central values $n_i(0)$ and $T_i(0)$ to such an extent that D-T operation would produce α-particles in sufficient quantity to be able to analyse their effects on the plasma.

The enhancements to JET aim to build up a high density and high temperature plasma in the centre of the discharge (with minimum impurity levels) where α-

particles could be observed, while maintaining an acceptably high global energy confinement time, τ_E. The mechanisms involved are to decouple the temperature profile from the current density profile through the use of lower hybrid current drive and neutral beam injection to ensure that, at higher central temperatures, the current density in the centre does not reach the critical value that causes sawteeth oscillations.

This will involve the following:

a) Increase the Central Deuterium Density $n_D(0)$ by:
   • injecting high speed deuterium pellets and higher energy deuterium neutral beams to fuel the plasma centre and dilute impurities;
   • injecting pellets to control the influx of edge material;
   • stabilising the m=2, n=1 magnetic oscillations present at the onset of a disruption with magnetic perturbations produced from a set of internal saddle coils which will be feedback controlled;

b) Increase the Central Ion Temperature, $T_i(0)$ by:
   • trying to lengthen the sawtooth period;
   • controlling the current profile (by lower hybrid current drive in the other region, and by counter neutral beam injection near the centre) to flatten the profile;
   • on-axis heating using the full NB and ICRF additional heating power (24MW, ICRH, and 20MW, NB)

c) Increase the Energy Confinement Time τ_E by:
   • increasing up to 7MA the plasma current in L-mode operation;
   • increasing up to 6MA the plasma current in the full power, H-mode operation in the X-point configuration.

d) Reduce the impurity content, by:
   • using beryllium (Be) evaporators, Be tiles on the belt limiters, and Be antennae screens to decrease the impurity content;
   • Controlling new edge material by using the pumped divertor configuration.

In parallel, preparations for D-T operation are proceeding at full speed to ensure that the necessary systems for gas processing, remote handling, radiological protection, active handling and operational waste management are fully commissioned and operating satisfactorily in good time before the introduction of trtium into the JET device. In addition, the tritium neutral injection system at 160kV and α-particle diagnostics are being developed for this phase.

The following sections describe various developments which are underway on JET to implement these systems.

Stabilization of Disruptions and Large Amplitude MHD Modes

Disruptions limit the operating ranges of current and density in all tokamaks and similar limits have been reached in JET. Disruptions at high plasma currents impose large electromagnetic forces on the machines structure and considerable care has to be exercised in programming the operation of JET to keep to an absolute minimum the number of disruptions at 7MA. Forces increase approximately as the square of the current and consequently serious problems are foreseen for larger tokamaks such as NET and ITER.

Detailed studies of disruptions in JET have stimulated considerable progress in understanding the physical processes involved. The disruption at the density limit is a complex sequence of events that is initiated by a cooling of the plasma edge due to increasing radiation. This destabilises a magnetohydramic (MHD) oscillation, usually with the mode numbers $m = 2, n = 1$. This growing mode can be detected using diagnostic coils placed inside the torus vacuum vessel when it is still only about 0.001% of the equilibrium field of the tokamak. Combinations of signals from these coils will be amplified and used as input to a feedback control circuit that will drive a set of large saddle coils also inside the vessel. Through a sophisticated feedback control system the amplitude and phase of the corrective magnetic fields produced by the saddle coils will be used to cancel the growing instability.

The feasibility of this control method has now been demonstrated by a series of experiments on the DITE tokamak at UKAEA Culham Laboratory carried out under an Article 14 Contract.. These experiments were successfully concluded at the end of April 1989. Using saddle and diagnostic coils similar to those that will be used in JET connected by a linear feedback loop, the DITE experiments have demonstrated the feasibility of substantially reducing the amplitude of saturated $m = 2$, $n = 1$ modes, delaying the onset of disruptions and increasing the maximum plasma density by a modest amount. These results, provide valuable experimental data to stimulate and guide the theoretical studies of disruptions and feedback control that are continuing at UKAEA Culham Laboratory and at JET. They also provide the proof of principle for the JET feedback system. In particular, the DITE experiments investigated the so-called phase instability and have shown that it is less damaging than some theoretical models had predicted.

The diagnostic coils for the JET feedback experiment were installed in the torus during 1989 and have been tested successfully. The saddle coils have been manufactured and are awaiting installation which is scheduled for late 1990. A contract has been placed for two of the eight modules of the power amplifiers and following the success of the DITE experiment, this has been extended to include the full set of eight modules. Delivery will be made during the latter part of 1990 permitting feedback experiments starting during 1991.

As well as appearing as precursors to disruptions, locked modes have been observed in JET to cause degradation of confinement and to degrade discharges with pellet injection. Therefore, the ability to stabilize and control the amplitude of locked modes, as demonstrated by the DITE experiment, may have beneficial effects in JET in improving confinement and pellet refuelled discharges as well as delaying the onset of disruptions and extending the working density range.

Current Drive and Profile Control

The main objectives of current drive and profile control remain:
- to suppress sawtooth activity and to benefit from higher core reactivity by sustaining peaked profiles of both density and temperature;
- to modify local values of the current gradient and improve energy confinement in the plasma centre;
- to assess the current required for non-inductive operation of large tokamaks.

The main tool which is being prepared to control the plasma current profile in JET is the generation of non-inductive current by means of Lower Hybrid Waves. It is also planned to use a high directivity ICRH antenna capable of driving a substantial amount of non-inductive current drive by means of Transit Time Magnetic Pumping (TTMP). This antenna should be installed in 1992, if the pump divertor phase is implemented. The other schemes which can be used for controlling the current profile are neutral beam (NB) current drive and the bootstrap current.

Lower Hybrid Current Drive

The main characteristics of the JET LHCD system are shown in Table XVIII. This will be installed in two stages. The first stage will be fitted during the 1989/90 shutdown. It has the technical features of the complete system which will be installed during the 1990 shutdown. The technical aspects of the LHCD system were presented in the section "Technical achievements with the LHCD system". In this section, discussion is limited to the physics aspects of the LHCD system.

The Lower Hybrid deposition profile has been simulated by using a ray tracing code in a flux surface space coupled to a 1D Fokker-Planck code. The plasma magnetic configuration is provided by the JET magnetic data analysis system and measured temperature and

137

Table XVIII
The JET LHCD System

Frequency	3.7GHz
Power (launched)	10MW
Launcher	Multijunction type
Fixed phasing in the multijunction	90 degrees
Central $N_{//}$	1.8
Range of $N_{//}$	1.4 to 2.4
No. of waveguides in a horizontal row	32
Phase accuracy	10 degrees
Width of the $N_{//}$ spectrum	0.2
Directivity	80%
Density limit	8×10^{20} m^{-3}
Power handling	4-5kW cm^{-3}
Estimated driven current at $n_e=2\times10^{19}$ m^{-3}	3-5MA
at $n_e=5\times10^{19}$ m^{-3}	1.2MA

density profiles are taken into account. Simulations have been carried out on a variety of JET plasmas including H-modes, pellet fuelled discharges, monster sawtooth and hot-ion modes[2]. The JET-RAY code has allowed the production of the expected dependences with the electron temperature, plasma density and parallel wave spectrum.

In Fig.176, the change in the RF driven current density absorption profile is shown for different values of electron density. The simulation was undertaken for a B_T = 3.4 T, I_p = 3.5 MA monster sawtooth discharge with central electron temperature of 9keV.
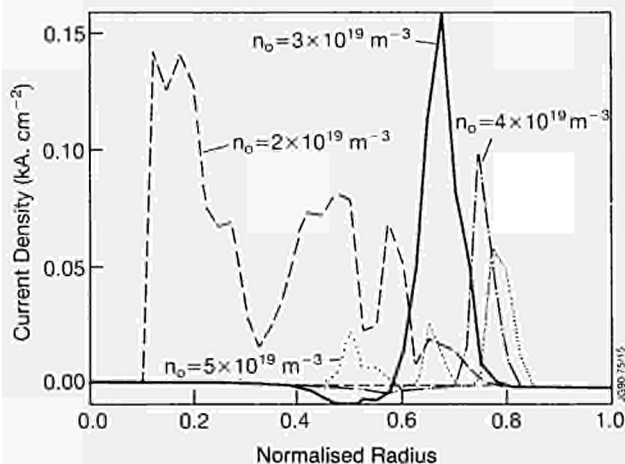
Fig.176: Lower Hybrid current density versus normalized radius for central densities of 5, 4, 3 and 2 x 10^{19}m^{-3}.

From this simulation study, the best target plasmas for LHCD are those with a peaked density profile. This result has been obtained without taking into account fast electron diffusion. An application of the JET-RAY code to other LHCD data has shown that this diffusion may

play a very important role in the control of the current profile. Both experimental and theoretical work will be needed to assess this diffusion process.

Other physics problems such as coupling of LH waves to the fast ion population or induced parametric waves have been studied under Article 14 Contracts with ENEA Frascati, Italy, and UKAEA, Culham Laboratory.

Ion Cyclotron Resonance Current Drive
Ion cyclotron waves can induce non-inductive current drive either by asymmetric heating of minority ions or by direct interaction between the fast wave and electrons. The minority ion current drive scheme has a low efficiency but is capable of producing a highly localized toroidal current. Therefore, local current density control can be obtained, resulting in a flattening of the current profile. During the year, preliminary experiments were carried out but more experimental time is needed to assess the capability of the method.

The interaction between fast wave and electrons can induce current drive from a combination of transit time magnetic pumping (TTMP) and electron Landau damping. In the second process the driving force is the parallel electric field and is similar to LHCD. For TTMP, the driving force is a product of the electron magnetic moment and of the magnetic field gradient. It results in acceleration of electrons along the magnetic field line. The TTMP current drive efficiency is comparable to that of LHCD.

Electron Landau damping and TTMP produce currents in the opposite direction. However, the TTMP component is dominant, when the electron beta of the plasma is large or at low frequency ($\omega<\omega_{LD}$). Therefore, TTMP current drive will occur at the plasma centre, where the beta is maximum. High current drive efficiency requires fast waves with high directivity.

The advantage of TTMP current drive compared to LHCD is the absence of a density limit. Therefore, profile control in a reactor can best be obtained with TTMP current drive in the centre and LH current drive in the plasma periphery.

Operation of JET at high beta values has allowed a study of direct electron HF absorption by TTMP. Experimental conditions were such that there was no competing mode conversion or ion cyclotron absorption within a 0.4 minor radius. The main parameters of the experiment were:
- H-mode plasmas
- B_T = 2T
- f = 48 MHz
- Power = 9MW
- Dipole phasing
- β = 1.4%

Outside this region, power was absorbed by the ions at the first harmonic resonance.

The electron heating profile was deduced from the response to RF power modulation. As expected the

maximum power density occurred on-axis. The discontinuity in the time derivative of the soft X-ray emissivity caused by the RF power transition is plotted against the magnetic flux normalised at the boundary in Fig 177. It can be seen that the electron heating is peaked on-axis with a secondary peak located approximately at the second harmonic layer. The estimated power directly absorbed by the electrons is 1.2 MW, in good agreement with theoretical predictions[3].
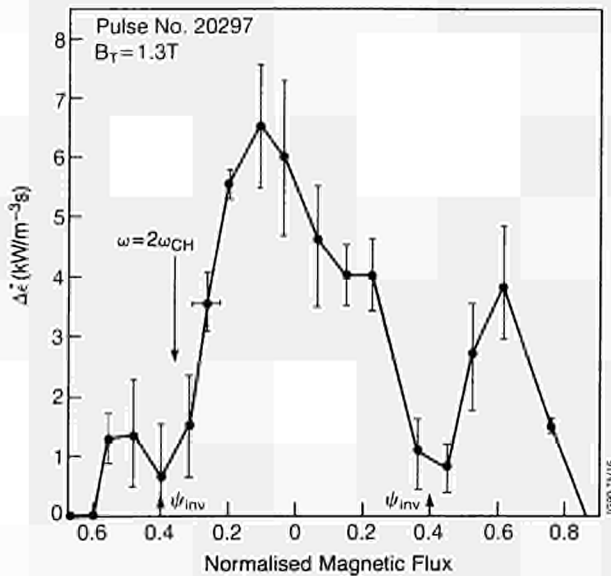

Fig.177: Discontinuity in time derivative of soft X-ray sensitivity caused by the RF power transitions versus magnetic flux normalized at the boundary.

This result confirms the theoretical background for such a scheme. The present ICRH antennae system, where the two central conductors are strongly coupled and cannot be phased, does not allow high directivity to be obtained. However, the new antennae array which has to be designed for the New Phase of JET should significantly improve directivity. The proposed new antennae pairs have four central conductors equally spaced in an integrated structure of two antenna boxes each with a septum that decouples adjacent conductors. A directivity of 80% can be expected in contrast with the maximum 20% directivity for the present arrangement.

Theoretical predictions indicate that a non-inductive current exceeding 1 MA should be achieved. These calculations assume that fast electrons are already present. If a "gap" problem exists, it may be overcome by using a combination of LH waves and of IC waves.

Synergistic current drive experiments combining central TTMP current drive and off-axis LHCD current drive can be carried out. In addition, appropriate use of NB current drive and of bootstrap current might allow the current profile to be controlled. Neutral beam current drive up to 0.5 MA has already been obtained in low density discharges. Large bootstrap induced

currents of ~0.8 MA at the plasma periphery in H-mode plasmas and of ~0.2 MA close to the plasma centre in monster sawtooth plasmas have already been observed.

References

[1] M Pain, et al, The 15 MW microwave generator and launcher of the LHCD experiment on JET, 13th Symposium on Fusion Engineering (SOFE), Knoxville, U.S.A. (1989), to be published;

[2] M Brusati, C Gormezano, S Knowlton, M Lorenz Gottardi, F Rimini, "Simulation of propagation, absorption and current drive efficiency of Lower Hybrid Waves in reactor relevant JET discharges", Eight Topical Conference on RF Power in Plasmas, Irvine, U.S.A. (1989), to be published;

[3] D F H Start, et al, Electron Absorption of Fast Magnetosonic Waves by TTMP in the JET Tokamak, to be published in Nuclear Fusion.

Pellet Injection

Introduction
One of the important requirements for the successful operation of future fusion plasmas is that of fuelling and density control systems. The injection of frozen hydrogen pellets at high velocity is one of the tools to facilitate this :

- by delivering the particles more centrally to the plasma;
- by reducing recycling of gas at the wall (compared with conventional gas puffing);
- by performing this task (unlike neutral injection), without simultaneously applying an excessive amount of additional heating (disproportionate to the number of particles delivered to the plasma).

Experiments using pellet injection with pellet sizes from 2 to 6mm and speeds up to ~ 1350 ms^{-1} have been performed on JET during the last four years. The dependence of pellet penetration into the plasma on pellet size and velocity is well established over this limited range. In particular, it is known that the centre of the JET plasma can only be reached by a high fraction of the pellet for central electron temperatures of $T_{e0} < 1$ - 4 keV (depending on pellet size). The only parameter relevant for reaching plasmas of higher temperatures is the (increasing) pellet velocity. Consequently, JET initiated a programme in 1986 for the development of injectors aimed at pellet speeds approaching 10kms^{-1}, to have the means of investigating penetration depth scaling as well as resulting plasma performance.

Development has progressed to the state where it is now foreseen to employ in the 1990 experimental period a single-shot, high speed (~ 4 kms^{-1}) pellet launcher.

This is a two-stage light gas gun (pneumatic gun employing adiabatic compression heating of the driver gas). It will be operated in parallel with the repetitive (conventional) pneumatic gun launcher (ORNL launcher) jointly operated under the JET - USDoE Pellet Agreement. Both launchers use the common launcher-torus interface (Pellet Interface), described in previous JET Progress Reports. The largest part of the Interface is the pellet injector box (PIB) with its cryopump. The outcome of the development to date and the upgrading of the pellet injector to include the new high-speed feature has been detailed previously[1]. Therefore, only a few highlights and some recent results are covered in this section.

Testbed Results

From earlier results, it was evident that bare solid deuterium pellets, accelerated in a pneumatic gun to high speeds, suffered serious erosion in interaction with the barrel wall. This erosion effect was then catastrophically enhanced by the driver gas by-passing the pellet in the opening gap between pellet and wall. As a consequence, bare pellets could not be brought up to speeds beyond ~3 kms^{-1}. Accordingly, pellets had to be supported by light cartridges ("sabots") made from polyimide or polyethene plastic, which in turn had to be separated in the flight path and prevented from reaching the plasma. The deuterium ice was cryocondensed into operational for the 1990 experimental programme. The launcher consists of a two-stage gun as the driver gas production section, and a cryostat containing all the elements for sabot loading, pellet formation and charging and discharging of the barrel breech. For functional reasons, the barrel belongs to the latter unit as well and so its aiming facilities are referred to the cryostat support frame. For operation on the torus, the launcher needs to be fully commissioned on the Testbed and has to be remotely controlled and monitored. Due to the tight schedule, the control and monitoring systems on the Testbed and JET, respectively, are identical to a high degree (controller hardware and software, cabling jumpers and connectors). This is expected to permit the re-installation and re-commissioning of a launcher at the torus already commissioned at the testbed, with a minimum of time and effort.

For the torus gun, a pumptube, made from high-strength martensitic stainless steel, 3m long and 60mm I.D. bore, was chosen with a front end which during the adiabatic compression heating permitted pressure surges to 5000 bar. Three fast valves allow precise timing of the actuation of the titanium piston by the release of the reservoir pressure (3.5l up to 300 bar), the filling and discharging of the volume in front of the piston, and the discharge of the driver gas. Despite the fact that this gun will only be used at present in single-shot mode (i.e. once per tokamak pulse), provisions for later modification to repetitive mode have been considered.

The first gun is now assembled and being prepared for commissioning on the Testbed.

On the Testbed, these investigations have been performed using a cryostat developed by collaboration with and built by CEN Grenoble, France. It's principle is based on a wheel indexing by 120° and thus transporting a bushing/bursting disc/sabot combination, being loaded in the first and filled with ice in the second position, into the breech position for firing. For the torus launcher, the wheel is replaced by a chain with 12 positions, allowing the filling and storage of up to 10 pellets (two positions are needed again for breech and sabot loading port). The chain can store (though not filled with ice) a further 10 bushings, so that the total number should be ample supply for one operational day. A bushing storage drum with 100 bushings allows reloading of the chain and provides a sufficient number to assure about one week of operation before manual intervention is needed to re-supply the drum. During a shot, the hot high-pressure driver gas is sealed against the cold storage box with its prepared pellets by pneumatically (aided by the pumptube pressure) pressing the upstream and downstream barrel sections tightly (hard seal) against the chain bushing. Here again, although fast repetition is not called for at present, elements to further develop this scheme have always been considered. The gun and cryostat sections of the launcher are joined in such a way that the upstream barrel is pushed with very narrow radial tolerances into the compression head of the gun without axial fixing it, so that the cryostat is largely prevented from absorbing the huge axial momentum of such guns (several 100 tonne force for about 10^{-3}s act on the compression head during the piston reversal). The cryostat has been designed and is under manufacture to be assembled in early 1990. Thereafter, cryostat commissioning immediately followed by integrated launcher commissioning is planned.

Torus Site Preparation

The geometry of the launcher configuration at the PIB is shown Fig 178. The two main items needed for the implementation of the prototype are: the support structure for the two-stage gun; and the modification to the rear insert into the PIB to house the sabot separation and pellet qualification diagnostics, while maintaining the vacuum and diagnostic interface services for the ORNL Launcher.

The two-stage gun support consists of a 1.5 m high and ~ 8 m long wedge-shaped beam suited for carrying up to ten guns. It is anchored into the concrete wall of the Torus Hall by a secondary steel structure to take impact forces of up to 400 tonnes. This steel structure also supports the trunnion bearings attached to the beam which allows the raising of the beam with its guns in place. This is lifted in the manner of a drawbridge freeing the pathway for large equipment to be moved around the torus. The support system was designed for
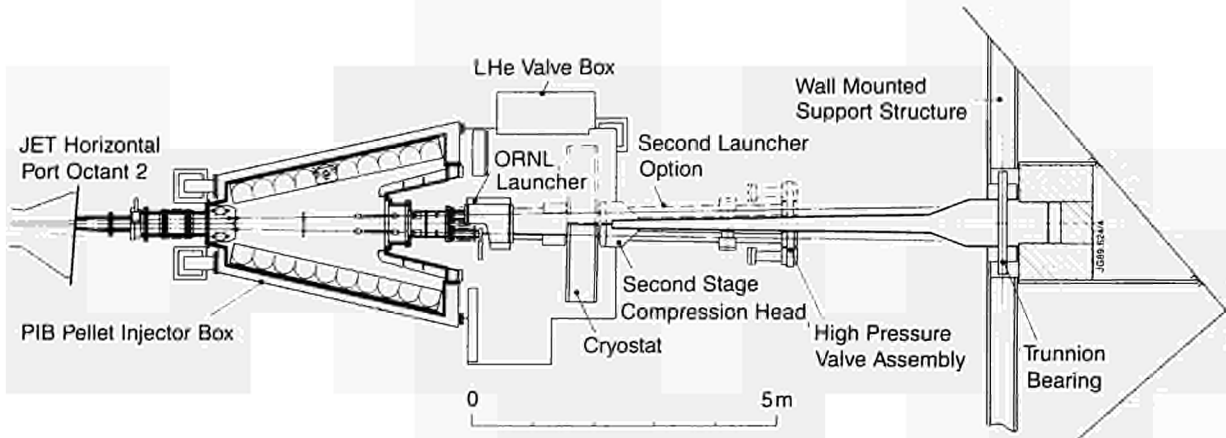
Fig.178: The Pellet Injection Box (PIB) launcher configuration.

later use with an advanced gun system. At present, restrictions on the rear panel allows only the use of two injection lines beneath the ORNL Launcher. The wall support has been installed and the support beam is delivered and ready for further assembly.

Whereas the gun is mainly supported from the wall, the cryostat is supported from the PIB platform. Its 1.5 m long barrel enters a vacuum pocket, attached to the rear insert, which is to contain most of the debris generated in the sabot separation. It is here that the sabot and pellet combination is intercepted in the commissioning by a first material target (bed of titanium pins) until correct aiming is assured when viewed in the virtual target. The latter consists of two orthogonal curtains of light spectrally dependent on position in the curtain. This new (non-destructive) wavelength encoded position indicator needs two light fibres only and has due to the two arrays of 32 diodes each a spatial resolution of ~1mm. After this first check in the aiming procedure, the first target is removed and the pellet will enter the main PIB through a hole in the shear cone which removed the sabot halves. The pellet mass and its velocity will then be measured while the pellet traverses the two microwave cavities of the same interferometer, the other arm of which is used by an ORNL Launcher gun line. Provisions are also being made to photograph the bare deuterium pellet when leaving the interferometer. In case access to the torus is not free, a second target in the PIB intercepts the pellet.

On the control side, hardware and software have been upgraded to be capable of coping with the requirements of an advanced gun system. The firing sequencer and related control system can now handle up to 256 either reprogrammed pellets and/or pellets in time windows which can be triggered by an "intelligent" device following an algorithm to call for pellets for certain plasma states (fuelling feedback application). The sequencer and the subsequent devices such as data cylindrical cup or beaker sabots, which split along the axis into two halves. These halves were separated by using the residual driving gas flow at high pressure (>

100 bar) from the muzzle (the only method successful operated so far). Two main problems were encountered (for the 6mm ID barrel gun):

- The ice does not reproducibly condense into a plastic sabot with low thermal conductivity walls to produce reliable mechanically sound pellets capable of withstanding the required high accelerations (up to 10^7 ms^{-2}) (measured by the in-flight photography of the pellets after leaving the barrel). Later compacting the ice by externally applied pressure did not apparently heal defects effected in the early phase of the condensation process;

- Also, these sabots suffered fracture of their thin walls (0.2 to 1mm) with and without deuterium ice (a mechanical phenomenon not yet understood), in contrast to non-split sabots (for which a separation method is lacked). It was also difficult - during the acceleration in the barrel as well as in the above separation process - to keep the driver gas from penetrating the gap in the bottom of the split sabot and thereby destroying the ice pellet;

- Both findings were backed by similar experience gained at CEA Grenoble, France, in a complementary development effort.

As a result of tedious unravelling of interlinked effects - most of the detailed investigations performed in 1989 in ~ 600 shots, JET decided to adopt an intermediate solution for the launcher prototype, which would yield experimental evidence of high-speed pellets in the torus, before continuing to solve the ice production and sabot flight dynamics problems needed for higher speeds. This intermediate solution employed split sabots which constituted only the bottom of the beaker sabot; thus this plastic cylinder, inserted behind the pellet, shielded the pellet, which is in contact with the barrel wall and so shows only a limited amount of erosion, from the hot driver gas. The ice production for this scheme now uses metal bushings which have the same inner diameter, D, as the barrel and eliminated

141

difficulties in the condensation process. The resulting disadvantage was that the wide experimental choice of pellet (diameter d) was lost (in beaker sabots d can be chosen freely as long as d < D). Employing a 3m long pump tube of 80mm I.D. with a 0.9kg titanium piston, which has now achieved a lifetime of 400 shots without refurbishments, and a 1.5m long barrel several series of shots (~30) at pellet velocities between 3.7 and 4.3 kms^{-1} have been performed on a testbed launcher with this kind of pellet-pusher sabot arrangement. This obtained a pellet angular aiming divergence $< \pm 0.15°$ with simultaneously the divergence of the two sabot halves being clearly $> \pm 0.35°$. This is sufficient for a safe shear-off by a cone as provided in the Pellet Interface.

Prototype Launcher

Two prototype launchers are currently under preparation, of which the first one is scheduled to be acquisition system, plasma protection system, fuelling application as well as the software are capable of handling up to 14 different launchers.

Due to the importance of understanding the mechanism governing pellet penetration, the periscope, which looks upwards onto the plasma midplane and monitors the light plume generated by the pellet when entering the plasma, is being enhanced in several respects. Its sensitivity is stretched by image intensifier techniques to cover a range greater than 10^6, which should enable it to see the plume in the D_α to D_γ radiation (depending on filter wheel settings). Fast switching of one of the intensifier stages (pulse width $\geq$ 10^{-7}s and frequencies $\leq$ 1 MHz) will freeze instant pellet cloud pictures along the pellet track onto a CCD frame. A zoom lens will allow imaging of the torus midplane in a total field on view of 2.3m (minor diameter) x2.0m which can be magnified up to 14 times, whereby a double prism arrangement will scan the particular field of view. The recording of the total light intensity (D_α diode monitoring), thought to be an instant measure of the pellet ablation rate, will be improved. The design for this has been worked out and the components are under procurement.

Future Plans

Experiments to date have shown that pellet injection with the present technology is a valuable tool - so far not yet fully exploited - for plasma fuelling and probing. Assuming that the high-speed option will also add its own contribution to new plasma scenarios, JET will need an advanced launcher system combining the flexibility of the present ORNL multi-pellet launcher (which for technical reason is not suitable for the Active Phase) with the high-speed option. From the above description of the two-stage gun, of its support system and of the cryostat, it is clear that JET has already paid attention in the design of the prototype to the requirement that further modifications and additions

should lead to a repetitive tritium and remote handling compatible advanced launcher system, one the prototype has been brought into operation.

Meanwhile, in collaboration with CENG (Centre d'Etudes Nuclaires, Grenoble, France), the elements of a repetitive high-speed launcher are being investigated. This follows a similar route to that adopted by JET, but deviates in detail to provide back-up solutions. CENG have constructed a testbed with a two-stage gun which has reached similar performance to that of JET. However, they have demonstrated, for single shots, that the gun in principle, can be made repetitive on a 2Hz time scale. They have also designed a repetitive cryostat following alternative routes by employing a linear feed, sliding rod magazines with narrow gap sealing (rather than hard sealing at the breech) and they have demonstrated under relevant shot conditions in a non-cryogenic mock-up that the narrow gap sealing works as expected. CENG has also assisted in investigating difficulties encountered with ice formation into sabots. The contract with CENG is continuing to provide elements for required design decisions before the end of 1991.

References

[1] Kupschus P., et al: Invited Paper at the 13th Symposium on Fusion Engineering (SOFE), Knoxville, USA, (1989). (JET Report JET P(89) 79)

Tritium Handling

The planning for tritium handling requirements is still based on the introduction of tritium into JET in May 1992. During 1989, the design of the Active Gas Handling System (AGHS) was almost completed and procurement proceeded for most subsystems. The construction of the Gas Handling Building (J25) was nearing completion at the end of 1989. The preliminary Safety Analysis Report (PSAR) for the torus and its subsystems was submitted to the UKAEA Safety and Reliability Directorate (SRD) and a comprehensive package of Radiological Protection Instrumentation (RPI) was ordered. In parallel, detailed design safety analysis reports of components have been prepared and submitted to SRD for review.

The objective for 1990 is to install and test components and sub-systems in the Gas Handling Building and to prepare commissioning documents as well as to prepare the remaining detailed safety analysis reports and Final Safety Analysis Reports (FSAR) for the Active Gas Handling System and torus systems. This schedule leaves ~16 months for final commissioning of the AGHS including connection to the torus and auxiliary systems.

Active Gas Handling System (AGHS)
Progress during 1989 and the status at the end of 1989 is summarised below:

Mechanical Forevacuum
The design was completed and all major components including valves and large mechanical pumps were delivered on site and are ready for installation following completion of the Active Gas Handling Building. Buffer tanks are on site and already installed in the Gas Handling Building.

Cryogenic Forevacuum
The contract for the main units containing the major process elements such as LN_2 coldtraps, Charcoal Absorbers, Accumulation Panels, Cryotransfer Pumps and reservoirs in five modules was placed in 1988. Start of manufacture was delayed and delivery is now scheduled from July to November 1990.

A test of the performance of an Accumulation Panel (combined Cryocondensation/Cryosorption pump) identical with the final design was successfully undertaken. At the pump inlet, a pumping speed of $15000ls^{-1}$ was measured for a mixture consisting of 95% D_2 with 5% He at a mass flow rate of 150 mbar ls^{-1}. The major auxiliary components - distribution systems for LN_2 and LH_2 - are on site and ready for installation. The manufacture of cryogenic transfer lines is in progress.

Impurity Processing
The main component - an assembly consisting of eight processing modules - will be delivered in mid-1990. Two recirculation and vacuum pumps and an associated mixing tank are on site, a valve assembly in double containment and a vacuum/leak test box is expected in March 1990.

Intermediate Storage
This transfer and buffer system for hydrogen isotopes is located between Cryogenic Forevacuum and Isotope Separation Systems. It consists of a storage module containing four Uranium Beds and an associated double-contained valve assembly; delivery is expected in early 1990.

Gas Chromatography Isotope Separation
The separation column packing - Palladium on Al_2O_3 substrate, produced by CEA, France - is on site. The plant equipment, a module with four separation columns and an associated valve box, will be delivered in March 1990. Final instrumentation tests were completed; a system detects the arrival of the hydride front at the column exit on the basis of temperature rise in the packing due to the reaction heat of hydride formation. This is now ready for incorporation in the plant. Auxiliary systems for heating/cooling by means of a heat transfer fluid have been delivered.

Cryodistillation Isotope Separation
Parts of the system - Helium compressors, Helium refrigerator instrumentation rack and electronics cubicles have been placed in the building. Delivery and installation of the main plant components - process cold box, valve box, instrumentation box - is imminent. This system features novel recirculation pumps for hydrogen isotopes that permits generation of pressure against the surface tension of liquid soaked up by a sinter filter tube. The final production units were successfully tested with liquid deuterium and generated stagnation pressures up to 30 mbar and operating pressures in excess of 10 mbar at full throughput of $6l(STP) min^{-1}$.

Product Storage
Since the tritium concentration in the protium product stream of the cryodistillation system is expected to be acceptably low for disposal to the stack, it was decided to abandon the storage of protium (this would have had a capacity of $\sim 10m^3$ and would have been rather bulky and expensive). Product storage is now limited to storage of deuterium and tritium in modular units each containing four uranium beds and associated valve assemblies. This system together with a vacuum pump/leak test box is due for delivery in April 1990.

Gas Introduction
This is a distribution system for D_2 and T_2 featuring the necessary accounting facilities, connecting the Product Storage System with the torus, neutral injectors and pellet injectors. At end-1989, its design was nearly completed and procurement was soon to start. A prototype multi-tube test section of the gas transfer liner was successfully tested (see Fig.179).
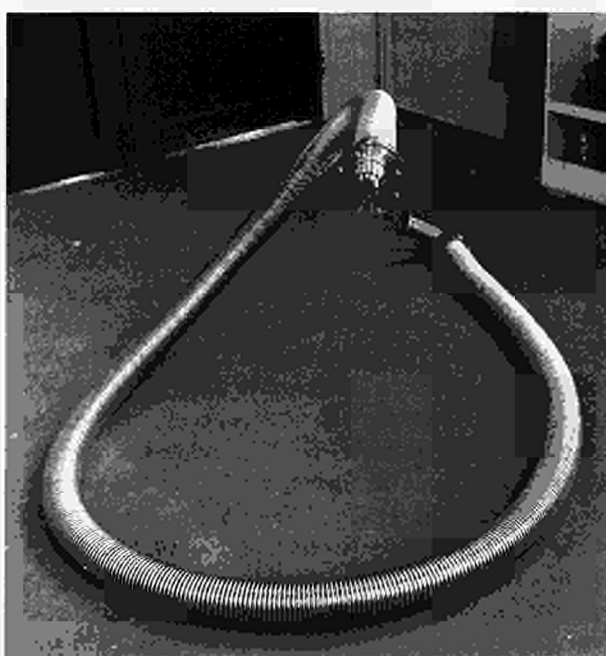

Fig.179: Prototype 5m long multi-tube gas transfer lines for T_2 and D_2.

Analytical Glove Box

To analyse the various active gas handling process streams, sampling lines connect to a central facility featuring the following equipment:

- Quadrupole mass spectrometer
- Omegatron mass spectrometer
- Analytical gas chromatograph.

These components are located in a common glove box, in which a separate compartment contains further equipment for on-line purity monitoring of cryodistillation product streams (based on thermal conductivity for protium and deuterium and on density for tritium). The same compartment also contains the tritium make-up facility with suitable lock and valve arrangements for connection of tritium transport containers. Vacuum pumping equipment and a buffer tank for collection of gas samples after analysis will be installed in a third compartment. This mixture will be periodically reprocessed by the IP System.

Exhaust Detritiation System

Procurement is underway with delivery projected for May 1990. Manufacture is well advanced and factory acceptance tests are scheduled to start in April 1990.

General Systems

In addition to the individual subsystems, the following major features have been either designed or selected and are being procured.

Control System

Operation and control of this complex plant will be performed by a Distributed Control System, which was selected and ordered in 1989 and will be installed beginning March 1990. Procurement and assembly of hardware is well advanced. The contract includes provision of the basic operating software : mimics for all subsystems are defined and specifications for most of the operation sequences are written.

Instrumentation

All instrumentation for plant parameters (pressure, temperature, mass flow, tritium concentration) was defined. Most transducers are on site or handed over to subsystem manufacturers for incorporation, and procurement of ionisation chambers is in progress. A special instrument was developed and successfully tested. To avoid the hazard of pumping and compressing explosive air/hydrogen mixtures, it was necessary to monitor the presence of combustible mixtures at the inlet of the Cryogenic Forevacuum System (all other plant components from this point on are fully protected by inert gas or high vacuum double containment). It was found that commercial oxygen monitors did not operate reliably at low pressure and information supplied by tritium laboratories indicated that the presence of tritium would lead to further ambiguities. Mass spectrometry with residual gas analysers in the presence of all three hydrogen isotopes is also too complex for reliable automatic detection of free oxygen. A special device based on conversion of oxygen to water by reaction on a hot platinum wire with hydrogen isotopes in a LN_2-cooled closed chamber allowing accurate measurement of the resulting pressure drop, was designed and successfully tested[1]. This monitor will now be incorporated in the design of the Mechanical Forevacuum System.

Other Developments

Work on the Accumulation Panel led to a novel vacuum pump, the Cryogenic Diffusion Pump[2] which has potential applications for plasma exhaust pumping in a Next Step device: hydrogen mixed with a few percent helium is cryopumped in a "dip-stick" cold trap geometry with a second outlet; the helium entrained in the hydrogen, is compressed to nearly the total inlet pressure of the mixture.

Progress in Obtaining Official Approvals for Tritium Operation

JET is required under the Host Agreement to satisfy the United Kingdom Atomic Energy Authority (UKAEA) in advance of arrangements for tritium operation. Formal permission is also needed from Her Majesty's Inspectorate of Pollution (HMIP) and JET must comply with various statutory requirements monitored by the UK Health and Safety Executive (HSE). Progress is as follows:

UKAEA Requirements

The UKAEA is now subject to licensing by the Nuclear Installations Inspectorate (NII) under the Nuclear Installations Act and has been required to revise its safety cases and internal procedures. However, the UKAEA has been verbally advised by the NII that the operation of JET will not be required to be licenced and so the existing arrangement continues whereby SRD must be satisfied of the safety case for JET. The design safety justification documentation is being produced to the satisfaction of SRD and, providing the design safety issues already recognised by JET are resolved, there does not appear to be any significant obstacle to obtaining endorsement of the JET design.

However, a change in emphasis has been brought about by UKAEA licensing which requires more thorough operational quality assurance and documentation. As JET is obliged to follow the same safety standards as UKAEA, this will mean more effort will be required to produce documentation for the D-T phase. Work has now started to identify what is required to comply with the NII model licence conditions and UKAEA implementation.

HMIP Requirements

JET already possesses authorisations to dispose of radionuclides to the atmosphere and the River Thames.

These have recently been updated to permit operation with enhanced neutron production in the D-D phase.

An assessment has been made of the upper bound of discharges likely in the D-T phase and the corresponding population doses, which are well within NRPB recommended limits. This assessment has been presented to HMIP and a formal response is awaited.

A programme of background radiation and radionuclide sampling is being undertaken around the site which includes bore-hole and River Thames monitoring and air sampling. At the request of HMIP, this has been extended to include grass sampling and work is in hand to include standing water sampling. This will enable JET to demonstrate that the environmental impact during the tritium phase is minimal.

HSE Requirements
As JET is already registered under the Ionising Radiations Regulations and uses an Approved Dosimetry Service, no changes are required for the D-T phase. However these requirements include a requirement to agree appropriate limits for detection of losses with the HSE Inspector. Discussions have been held with HSE and the proposed JET RPI and accountancy arrangements appear to be acceptable.

Active Gas Handling System
Safety analysis has continued in parallel with its design to ensure that proposed designs are capable of meeting safety criteria and requirements equivalent to those of a licenced site. Particular attention has been given to: the control and protection systems concept; to containment and venting philosophy; and to operation of the analytical laboratory.

There are two major safety issues with the control system which JET has had to resolve to the satisfaction of SRD:

- the need to design essential safety systems in a way which is capable of being analysed for reliability. As a result of the current UK requirements, this can only be achieved using "hard-wired" circuits as the failure modes of software based systems, unless specifically designed for and dedicated to safety systems, cannot be satisfactorily analysed;
- the requirement to provide assurance that inadvertent maloperation of the plant will be minimised has meant that a control system with a proven industrial application was selected and that all software must be properly specified, tested, and documented.

Design Safety Reviews for the majority of AGHS subsystems have been completed and endorsed by SRD and the procedure for keeping track of SRD recommendations has worked to the satisfaction of both parties. One major recommendation was a review of interconnections between systems. This has now been completed as the first part of the Final Safety Analysis Report. It shows that inadvertent connection of any systems under any operating mode does not result in an event which has not already been identified and assessed in the sub-system Design Safety Reviews and shown to be within the design targets.

Torus Safety Assessment
SRD has required a Preliminary Safety Analysis Report to be prepared by JET to enable them to assess at an early stage, before designs are finalised, whether there are any major radiological safety concerns. The first draft of this document has been discussed with SRD and in view of the novel nature of some of the processes they have recommended that Hazard and Operability (HAZOP) studies should be carried out on critical areas. A HAZOP study has been undertaken on the High Speed Pellet Injector and has shown that no major design changes were necessary.

The Preliminary Report considers all torus systems including building ventilation, active drainage and fire suppression. In connection with the latter, a method of passively inhibiting fire spread within the Torus Hall is being pursued. This uses the cryogenic systems boil-off nitrogen to dilute the air in the Torus Hall to a level where it cannot effectively support combustion[3]. The review of compatibility of diagnostics with tritium operation has shown that the main issue is that of window failure. Complete failure of a 100 mm diameter quartz window assembly would cause the torus to fill with air in about two minutes.

One of the design roles of the Exhaust Detritiation System (EDS) of the AGHS is to counter accidental air inleakage by maintaining a slightly sub-atmospheric pressure within the breached vacuum enclosure (by mechanical pumping) and routing the inleakage air to AGHS for detritiation prior to stack discharge[4]. Failure on demand of the EDS during such an air inleakage accident could result in the release in a significant proportion of the tokamak tritium inventory into the Torus Hall, due to heating of the inleaked air by the hot first wall.

If an air inleakage occurred while in-vessel graphite protection were at elevated temperature, the potential could exist for a self-sustaining graphite-air reaction. A preliminary study[5] has shown that for the JET situation, graphite-air reaction rates would be low, having only a minor influence on the venting characteristics. Further studies are in hand to confirm this.

To date there have been no catastrophic window failures during operation but they cannot be ruled out with the current window design. Further work is required to develop a window which will meet the SRD release/frequency target.

Analysis of the gas feed system from the AGHS to the torus against the above limit has shown that the lines in the Torus Hall do not require double containment,

which simplifies remote maintenance. Design safety analysis of all tritium-containing systems, for example baking plant, Neutral Beam System and Gas Introduction is being carried out as detailed designs become available.

Radiological Protection Instrumentation

Following a competitive tendering exercise, a contract was placed with UKAEA Harwell Laboratory for area monitors, discharge stack samplers/monitors and environmental samplers required for the detection of tritium during the D-T phase. A prototype unit of the latter is being used to collect information on the tritium content in the torus exhaust gas during D-D operation.

Tritium Procurement

A specification was prepared for the supply of tritium in a phased manner to meet the JET programme requirements. The results of a full international tender exercise are awaited.

References

[1] J L Hemmerich et al, "Development of a Recombination Detector to Measure Oxygen Concentration in Plasma Exhaust Gas", JET Report JET-IR(89)13.

[2] J L Hemmerich, E Küssel, "The Cryogenic Diffusion Pump and its Implementation in a Complete Fusion Reactor Forevacuum System", JET Report JET-P(89)43.

[3] C J Caldwell-Nichols et al, "A Fire Suppression System for the JET Torus Hall during Active Phase Operations", JET Report JET-IR(89)07.

[4] A Dombra et al, "Exhaust Detritiation System for JET", Proceedings of the 15th Symposium on Fusion Technology, Utrecht, The Netherlands (1988), North-Holland Publishing Co.

[5] M Wykes, "Safety Analysis of Potential Loss of Vacuum Incident in JET", Proceedings of the 13th International Symposium on Fusion Engineering, Knoxville, USA, 1989, to be published.

New Phase for JET

Motivation and Status

Since the beginning of its operational phase, JET has made major achievements but further advances must be accomplished to provide a secure basis for a Next Step Tokamak. Plasma temperature, density and confinement values already achieved, but not simultaneously, are individually close to the requirements of NET. JET results have allowed some of the parameters of a reactor to be specified. In particular, the plasma current capability of a next step Tokamak is now foreseen to be

in the range 25-30MA for a machine with a toroidal magnetic field of ~ 3-5T, compared with 6-10MA predicted when JET started operation in 1983.

However, the control of impurity influx and exhaust which can be achieved without a divertor is still inadequate. This contributes to the limitations of present JET performance. The level of impurity control which might ultimately be achieved has a direct consequence on the size of the Next Step. It also precludes starting the construction of components of the Next Step device before the specifications for the divertor and its associated pumps can be defined.

Based largely on JET results, the present studies to define a next step Tokamak clearly emphasize the need for obtaining additional information not only on impurity control and plasma-wall interaction but also on modes of operation, such as those avoiding plasma disruptions and enhanced confinement regimes.

By virtue of its size, its already demonstrated plasma performance and its long pulse capability, JET is in the best position to address these problems in the basic geometry considered for the next step. Such studies are the original *raison d'etre* of JET and represent a natural development of its presently agreed programme.

Consequently, a New Phase was proposed for JET, with the aim:

To demonstrate effective methods of impurity control in operating conditions close to these of the next step Tokamak; that is in a stationary plasma of "thermonuclear grade" in an axi-symmetric pumped divertor configuration.

The expected results of this new phase are:

- demonstration of a concept of impurity control in JET;
- provide the size and the geometry needed to realize this concept in the next step;
- allow a choice of materials for the plasma facing components;
- provide information on the operational domain for the Next Step, including the impact of particle and impurity control on enhanced confinement regimes.

This objective could be achieved on JET by means of an axisymmetric pump divertor configuration. The proposal is based on experience at JET with X-point operation and on experience with divertor operation on other machines.

The basic concept and engineering features of the JET divertor were discussed at several meetings of the JET Scientific Council and JET Council in 1989. A Workshop dedicated to the presentation and discussion of the JET divertor was also held at JET on 25th-26th September 1989[1]. The JET Scientific Council and JET Council have both strongly supported the JET proposal and recommendations have been made to extend the duration of the JET Project to the end of 1996 in order to allow adequate time for the JET divertor experiment.

Pending a future decision of the Council of European Ministers on prolongation of the Project, the JET Council has allowed the project to proceed with the procurement of long-term delivery items for the divertor.

In order to allow the work to proceed swiftly, a Divertor Task Force was created. This Task Force includes members from most JET Departments and Divisions and thus ensures a strong coordination of the work. Regular progress meetings together with design reviews are held. Responsibilities have been defined and interfaces between the various Divisions or Groups involved have been delineated.

Key Concepts

The key concept of the proposed JET pumped divertor is that since sputtering of impurities cannot be suppressed at the target plate of a divertor, those impurities should be confined in the vicinity of the target plate itself. This confinement can be achieved by maintaining a strong directed flow of plasma particles along the divertor channel towards the target plates, to prevent back diffusion of impurities by the action of a frictional force. A most important feature of the configuration is the connection length, along the magnetic field lines, between the X-point region and the target plates. This distance should be long (~10m) to achieve effective screening effect of the impurities. In other words, the X-point should be well separated from the target plates and in JET this can only be achieved by a **coil which is internal to the vessel.** The proposed configuration shown in Fig.180 consists of a single additional poloidal field coil, inside the vessel and at the bottom.
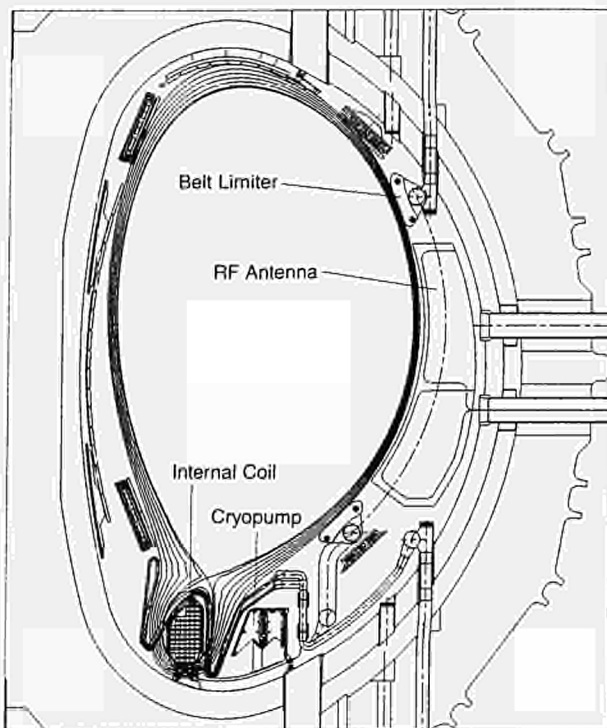
Fig.180: The Proposed Pumped Divertor Configuration;

The formation of a **target plasma** in the divertor channels is another essential feature of the pumped divertor. The cold (radiatively cooled) and dense plasma, which is expected to form in front of the target plates, plays a number of key roles:

- It should radiate a significant fraction of the plasma input power, thus reducing the heat load on the target plates;
- It should reduce the impurity production by screening the target plates;
- It should reduce the probability of the impurities diffusing back to the plasma.

In the vicinity of the outer target plate, a pumping chamber with a cryogenic pumping system is planned to **control the main plasma density.** It should be noted that only a small fraction (~5%) of the hydrogenic neutrals generated at the target plate are expected to be pumped. Some of these neutrals will be able to recycle towards the X-point region (there is a gap between the coil casing and the water cooled elements which defines the divertor channel), re-enter the scrape-off plasma there and enhance the plasma flow to the target plate. This local recirculation of hydrogenic particles should improve the impurity confinement. If required, gas can also be injected near the X-point to further increase the particle flow in the divertor channels.

Physics Aspects

The satisfactory performance of the pumped divertor depends on ensuring that certain paramters of the flow in the Divertor Plasma Channel (DPC) are correctly calculated and considerable effort has been devoted to studies of the DPC. The approach has been to elucidate models of divertor performance using analytical and numerical methods for solving the equations of the models and also to compare the predictions of the models with experiments in JET and elsewhere to validate the models.

Using two fluid models of the plasma, it has been found so far that the frictional force between the flowing plasma and the impurities in the DPC sets quite severe constraints. The frictional force depends on the Mach number of the flow and on the degree of collisionality of the plasma. This leads to a requirement for high density (~10^{20}m^{-3}) and low temperature (~10 eV) plasma for resonable collisionality, and to a moderate Mach number (~10^{-1}) for the flow. Together these can prevent the impurities from escaping from the divertor, provided the thermal force is not too large. The latter can also be controlled with a moderate flow provided the temperature gradients are not too strong. Thus, it appears possible to retain impurities in the DPC by inducing a deuterium flow of ~10^{23} s^{-1} towards the target plates. Impurity radiation (eg ~5% C or O) is effective in reducing the electron temperature at the target plates. The main problem is the relatively high ion temperature and temperature gradients involved, but this would be alleviated at higher density.

The plasma flow in the DPC may be set up either by extracting a fraction (~5%) of the plasma incident on the target and by recirculating it into the DPC near the X-point, or else by additional fuelling at the X-point, which would require additional pumping. However, this addition should be within the capability of the cryopump. The extraction problem and the related injection of gas at or near the X-point are subjects of current work. It would appear that extraction is at its most efficient at even lower temperatures than considered so far and at somewhat higher densities, and it may be that a combination of recirculation and additional fuelling will be required.

There is still a need to demonstrate a consistent model of the system which takes into account the additional impurity sources associated with the recirculation and addition of fuel, and which deals with the asymmetries between the inner and outer divertor. It will also be necessary to optimise the details of the fuelling source at the X-point and these, together with validation of the models, are the main aims of the continuing physics programme.

Engineering Aspects

Fig.180 shows a typical single-null configuration obtained at a plasma current of 6 MA and a divertor coil current of 800 kA-turns. The configuration fills the vessel volume well, while keeping clear of all internal vessel features by at least three e-folding scrape-off lengths. The connection length along magnetic field lines between the X-point and the target plate has been calculated to be ~10m and preliminary calculations indicate that this is sufficient to screen impurities.

The **divertor coil** is a conventional copper, water-cooled coil with 29 turns and able to carry 1 MA-turn for 20s. The coil will be wound inside the vacuum vessel. It is enclosed in a thin (0.8mm) stainless steel casing which will also be used during manufacture for vacuum impregnation with epoxy resin. Magnetic forces on the coil could reach 600-900 tonnes and are restrained by hinged supports which allow differential expansion between the coil and the vacuum vessel.

Although the **target plates** are expected to be shielded by the target plasma they are being designed with the capability to dissipate a large fraction of the plasma input power (40MW) in stationary conditions. The present design uses water-cooled hypervapotrons similar to those used at JET for the high heat flux elements of the JET Neutral Beam systems. Hypervapotrons can easily cope with power densities of $10MWm^{-2}$ and it is estimated that the divertor target plates should cope with 40MW power in steady-state conditions. This estimate includes the benefit expected from sweeping the impact line by about ±100 mm. Sweeping is achieved by a modulation of the divertor coil current between 750 kA and 1 MA. The surfaces facing the plasma will be clad with 2 mm thick beryllium plates brazed onto the hypervapotron. The

choice of beryllium is not ideal since beryllium impurities will not radiate sufficient power. However, the choice of an alternative material could lead to migration of this material onto beryllium tiles elsewhere in the vacuum vessel and ultimately jeopardise the benefits from using beryllium.

For the pumping system, a **cryopump** has been selected because it avoids problems with hydrogen retention and its technology is well known to JET. The pump includes a water cooled entrance baffle, inner liquid nitrogen cooled baffles and liquid helium (LHe) cooled pumping pipes. During plasma pulses, the heat load on the LHe cooled pipes is due to particles and radiation from the target plasma in the divertor channels, whereby the latter predominates. In case the total 40MW input power to the plasma is radiated by the target plasma, then the radiative heat load on the LHe cooled pipes could reach 1 kW. However, the most severe load is due to the neutrons and gamma rays expected during deuterium-tritium operation. In case of operation at Q~1 with a neutron production rate of $10^{19}ns^{-1}$ power in excess of 5 kW would be absorbed by the liquid helium and the stainless steel conduits. This has led to a design with thin walled conduits and a large liquid helium inventory. Of course, aluminium conduits rather than stainless steel would reduce the nuclear heating but eddy currents and associated mechanical forces become prohibitive. It is expected that sub-cooling of the LHe before a pulse together with partial boiling during the pulse, would allow several seconds (3-5s) of operation at Q=1.

Most neutrals produced at the target plate will be re-ionised before reaching the entrance of the cryopump and, therefore, only a few percent (~5%) would be pumped. This should be sufficient to provide a pumping rate of a few $x10^{21}s^{-1}$ which is adequate for density control of the main plasma.

In addition to components which are specific to the pumped divertor, other in-vessel components must be modified to match the new magnetic configuration.

- New ICRH antennae are being designed to match more closely the new plasma magnetic surfaces in the divertor configuration. The new antennae will be deeper and wider than the existing ones and it is expected that the coupling between antennae and plasma will be improved and less sensitive to the distance between the plasma and the RF conductor. New beryllium screens will be provided for these antennae;

- The front end of the lower hybrid launcher must be modified to match better the plasma shape;

- A new belt limiter must be provided. It will comprise two new belts on a smaller major radius than at present and also vertical sections to protect the new ICRH antennae. It is expected that the existing beryllium tiles can be reused for the new belt limiter;

Table XIX
Main Parameters of Divertor Coil

Perfromance	
Nominal ampere turns	1MA
Number of turns	29
Current	34.5kA
Pulse length	20 seconds
Dimensions	
Mean radius	2392mm
Copper cross-section	59mmx30.5mm
Cooling hole diameter	17mm
Conductor and Insulation	
Conductor material	copper-half hard
Weight of copper	5.35 tonnes
Joints in copper	Induction brazed Silfos shim
Insulation material	Glass and Kapton tape vacuum impregnated with epoxy resin
Insulation thickness	3mm interturn, 5mm ground wrap
Electrical terminals	2 rigid conductors passing through lower vertical port
Voltage per turn	0.5kV in operation, 1.0kV test
Voltage to ground	15kV in operation, 30kV test
Cooling	
Cooling by	Forced flow water
Parallel channels	3
Water pressure	10 bars
Flow rate	2.25 ls^{-1}
Casing and Supports	
Case material	1.2mm thick Inconel 625
Case construction	Fully welded enclosing coil, electrical terminals and water connections, connected to vacuum vessel by bellows at base of lower vertical point
Coil supports	At 32 non equi-spaced points- the supports are welded to the limiter and joint rigid sectors of the vacuum vessel but there is no support at main port sector
Coil clamps	The supports are connected to the coil by clamps encircling the exterior of the case with pinned joints to allow assembly
Hinged joints	Vacuum vessel radial expansion is allowed by hinged parallel links between coil clamps and support bases welded to vacuum vessel
Support materials	Base in Inconel 600 and links, pins and clamps in Inconel 625

- The saddle coils at the bottom of the vessel must be raised towards the plasma to produce sufficient perturbation field at the plasma boundary. The saddle coils themselves require no modification since they are translated along the vertical axis of the machine but new supports and busbar sections must be provided.

Further details of components are described below:

Divertor Coil

Technical Characteristics

The design of the coil for the pumped divertor has been completed The coil will be of conventional construction - water cooled copper, epoxy glass insulation - and will be contained in a thin inconel steel case. The coil will be assembled, insulated and encased inside the JET vacuum vessel. The main parameters and features of the coil are given in Table XIX, and are shown in Fig 180.

Forces and Cooling

The forces acting on the divertor coil depend on the magnetic configuration, and have been calculated using the INVERSX or PROTEUS codes for equilibria and disruptions, respectively[1,2]. Some typical cases are listed in the Table XX.

Table XX
Forces on Divertor Coil

Description	Plasma Current (MA)	Divertor Coil Current (MA)	Vertical Force* (tonnes)	Radial Force (tonnes)
Divertor plasma in equilibrium	6.0	1.0	300	100
Disrupted plasma (max values given)	6.0	1.6	-300	-500
Vertically unstable plasma (max values given)	6.0	1.6	-600	-1400
Divertor coil only	1.0	0	-120	380

* +ve vertical force is upwards and +ve radial force is downwards

The maximum forces occur in vertical disruption cases. The estimated maximum stresses are:

Von Mises stress in copper   51MPa
Shear stress in winding   5MPa

These maximum stresses are considerably less than the acceptance test levels, which are 180MPa for brazed joints in copper and 20MPa for shear stress in epoxy glass insulation.

Forces Acting on a Vacuum Vessel

The vertical forces acting on the divertor coil are transmitted to the vacuum vessel via the 32 supports. However, there is no support at the main vertical port sector. This is because the vessel support legs are attached to the main vertical ports. A support at this sector would therefore be much more rigid than supports at other sectors, would take a large proportion of the load and would lead to unacceptable stresses in the vessel.

The position of the supports on the other vacuum vessel rigid sectors has been optimised to minimise stresses. For a 600 tonne vertical load, the reactions and stresses are:

Reaction at octant joint sector   16 tonnes
Reaction at limiter sector   21 tonnes
Maximum stress in vessel (at base of lower main vertical port)   160MPa

During plasma disruptions and vertical instabilities, forces act directly on the vacuum vessel due to eddy currents, in addition to the forces transmitted through the divertor coil. The worst case from a number of simulations (with the Proteus code) gives the following values:

Maximum force on the vacuum vessel
900tonnes(upwards)
Force on divertor coil at same time
200 tonnes (downwards)
Net force on the vacuum vessel
700 tonnes (upwards)

When the new vacuum vessel damper system is installed, the vacuum vessel should withstand a net vertical force of 1000 tonnes with a maximum stress at the base of the upper main vertical port of 255MPa (0.3% strain). The fatigue life of the vessel material at this stress is more than 10,000 cycles. Thus, the vessel has a safety factor of 1.5 relative to forces calculated by the PROTEUS code.

If a normal cooling system is used, in which the cooling water enters the coil at a constant temperature of 20°C, then a wave of cooling travels through the coil causing thermal stresses. Therefore, it will be necessary to use a recirculatory cooling scheme to limit the temperature difference across the coil and thus reduce these stresses. The cooling time depends on the acceptable temperature difference across the coil. If the temperature difference across the coil is limited to 18°C, the coil cools in about 20 minutes.

Manufacturing Methods

The coil must be assembled inside the JET vacuum vessel. It is envisaged that coil manufacture, including winding, insulation and tool design, will be carried out by a specialist manufacturer. Manufacturing methods have been studied by two coil companies under contract to JET. These studies have shown the following manufacturing methods to be entirely practicable and have assisted JET in finalising design details.

Work to be completed by the manufacturer before reaching the JET site includes tool design, tool manufacture, ordering of all materials, and manufacture of all parts. All tools and manufacture methods would be tested before use. Equipment and procedures to be tested include:

● winding - by winding approximately one layer plus one turn on the next layer;
● impregnation - to ensure strong void free insulation;
● brazing - to ensure that it produces joints of the required quality;
● welding of case - to ensure that the coil insulation is not damaged.

As the coil must be assembled inside the vacuum vessel, all parts and tools have to enter the vacuum vessel through ports. Any equipment too large to pass through the ports (430mm wide by 940mm high) must be assembled inside the vessel. Special clean conditions are required not only to safeguard the coil winding but also to protect the vacuum vessel from contamination.

Three methods are considered for forming the conductor

- rolling in the vacuum vessel
- tension winding in the vessel
- brazing of preformed conductors in the vessel

In the case of rolling or winding processes, the coil would be on the median plane of the vacuum vessel so that the conductor being wound can pass out through a vessel port. The conductor lengths will be joined to form a continuous bar by brazing outside the vacuum vessel. A winding machine would be built in the vacuum vessel. The winding forces would be self contained within the winding machine and not reacted on the vacuum vessel. Where possible, other operations would be outside the vacuum vessel.

All three forming methods are feasible. The final choice will be made on the basis of time spent in the vacuum vessel, cost and quality of the final coil. When the winding process is completed the ground insulation will be applied. The coil will be vacuum impregnated with epoxy resin using its case as a mould. When the coil and its connections are finally impregnated in the case, the coil will be electrically tested and will be ready for lowering into its final position.

The design and specifications for manufacture have been completed and the Call for Tender was issued at end-1989. The manufacturing contract will be placed in May 1990 to wind the coil in February 1992.

Plasma Control

The expected disruption behaviour of the divertor plasma has been studied with the PROTEUS evolution code and also with a reduced parameter model of the magnetic system. It is concluded that vertical forces up to 7MN can appear at the vessel/divertor coil system in a 6MA vertical instability.

The first assessment of the control system and of the vertical stabilisation has been performed. A new fast radial field amplifier (FRFA) with enhanced VA rating (25MVA) is required and use made of the passive stabilisation capability of the divertor coil. These studies will continue to define the required extensions of the PPCC. For this purpose, the PROTEUS code and the JACOB electromagnetic code will be further developed.

The Fast Radial Field Amplifier (FRFA)

The control of the vertical position in a Tokamak, with elongated cross-section and with iron magnetic circuit, is rather complex and particularly in JET with the new divertor configuration. The existing Radial Field Amplifier (PRFA) has been able to cope but the experience, gained in operation, has shown that, in a non-symmetric configuration (single X-point), the margin of stability has been progressively eroded.

Vertical stability has been reconsidered and the need for a new fast amplifier has been established for the divertor phase. A modular system has been conceived based on an H-bridge in which each arm consists of two Gate Turn Off (GTO) Thyristors, connected in parallel.

The Fast Radial Field Amplifier (FRFA) will consist of two identical units each supplied by a circuit breaker. Two units will be connected in series so that each can be by-passed by a bipolar thyristor; each unit is made up of two modules that can be connected either in series (Configuration S) or in parallel (Configuration P). The main elements of the Fast Radial Field Amplifier are described, per unit, in the following: a Rectifier Transformer with two secondaries reduces the voltage from 36kV to approximately 1kV, to supply two Thyristor Convertor Units; filters are foreseen in front of each Module, which is a DC/AC power convertor, capable of four quadrant operation (invertor).

ICRF Antennae

The existing ICRF antennae system would be too far away from the separatrix of the plasma in the pumped divertor to provide any significant wave coupling to the plasma and a new set of antenna must be designed, procured and tested before mid-1992. In 1989, the design of the new antennae was well advaned and the contract for the beryllium screen bars, a long delivery item, had been placed. The design philosophy involves:

- Keeping modifications of ICRF systems to a minimum other than the antennae. All elements of generators, main transmission lines, vacuum transmission lines up to the antenna connection and vacuum feedthroughs, etc, will remain unchanged as far as possible to keep costs to a minimum;
- Improve the coupling properties of the new antennae (A2) to H-mode plasmas. This will be done by increasing the depth and the toroidal extent of the antennae system so that the scale length of the RF exciting field becomes larger than the distance to the separatrix. These antennae are optimised for dipole phasing (0, π) which provides the best performance with H mode plasmas;
- Incorporate, if possible, ICRF current drive features. This requires arbitrary phasing between the antennae elements (central conductors) which, in turn, requires decoupling them by the use of spectrums. These are essentially slotted side screens separating the two central conductors of an antenna box. A wave directivity of about 80% is expected and a meaningful test of fast wave current drive should be possible;

● The electrostatic screen facing the plasma will be made of beryllium and it will be aligned, as far as possible, to the vertically asymmetric last closed surface of the divertor configuration to minimise ICRF edge effects.

A larger antenna-plasma distance, that might be required in the pump divertor configuration, could be accepted if the width of the central conductor and the distance to the back wall could be simultaneously increased. This appears to be feasible, as the plasma size will be smaller and more space will be available to increase the back wall distance. Also, the coupling in the dipole mode could be increased if the toroidal distance separating the elements could be increased from the present value. This is achieved, practically, by using four central conductors (each a double loop) equally spaced by 0.4 m (mid-point to mid-point) in the space available between two horizontal ports of the tokamak. The existing coaxial feeds are reused and as before, no viewing ports are blocked. These four antennae elements wil be both capacitively and inductively decoupled from each other by appropriate septums. Only two side protections will be used for this set of four elements. Coupling calculations give a plasma-antenna loading which is about twice the value obtained with the present antennae system.

The new antennae system should be able to couple more than 20MW of ICRF power for a duration of 20s to the plasma in the single-null pumped divertor configuration, where the plasma is kept 5 cm at most from the antenna protection tiles (assuming H-mode operation). Significant ($\approx$1 MA) current drive capability is also predicted. The proposed antennae system will lead to a significant step closer to the design of ICRF launchers for Next Step decies. In particular, it incorporates several conceptual aspects of an in-blanket antenna design for a reactor.

Diagnostic Measurements

Efforts have been devoted to definition of the measurement objectives; to choosing plasma diagnostic techniques appropriate to conditions in JET and defining their deployment; to coordinating the engineering integration of the proposed measurements into the divertor design; and to assessing the personnel and budgetary requirements.

The scope of diagnostic capability needed for the pumped divertor plasma is determined by the measurement objectives. These are:

● to demonstrate feasibility of impurity control using a high flow rate divertor;
● to validate a model of divertor action;
● to optimize pumped divertor performance in JET.

Measurements are required to determine:

● the plasma geometry in the diveror region;
● the electron temperature and density profiles in the divertor plasma;
● the sharing of power between radiative and conductive power loss channels;
● the plasma-surface interactions, erosion/ redeposition in the divertor region;
● the behaviour of impurities, ie. impurity influxes, principal ionization stages, impurity density, temperature and flow, and identification of impurity charge state distribution;
● the behaviour of neutrals in the divertor region.

The feasibility of the following set of diagnostics, with spatial resolution along the separatrix in the divertor region between the X-point and the target plates, and of their integration in the divertor design is under study:

● magnetic pickup coils for determination of plasma geometry;
● Thomson scattering, microwave interferometry and reflectometry, and electron cyclotron absorption measurements for determination of electron density and temperature profiles;
● Bolometry and calorimetry for measurements of power balance;
● Fixed and scanning Langmuir probes, views of the divertor surfaces using cameras in the visible and infrared for determination of plasma-surface interaction;

1989	1990	1991	1992	1993	1994	1995	1996
Full Power Studies		New Additions in Limiter Configuration	Optimization in X-point Configuration & Next Step Oriented Studies			Tritium Phase	

• Pumped Divertor & RF Modifications

• Pumped Divertor Modifications
• Other System Enhancements

• Final Modifications for Tritium Operations

• 1 beam line to 160kV-T
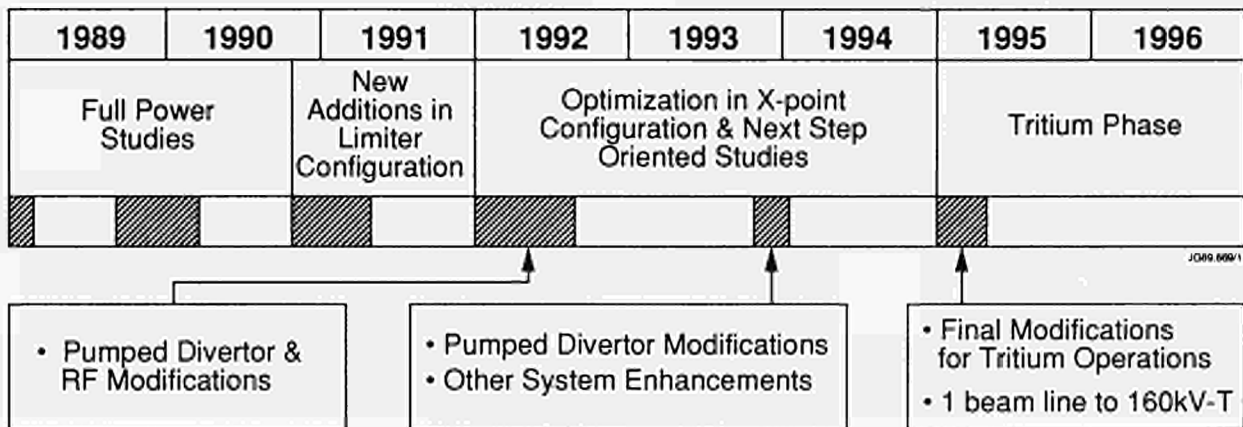
Fig.181: Overall Plan for the JET New Phase.

152

- Spectroscopy in the VUV and visible regions for measurements of impurity behaviour;
- Pressure probes in the divertor and cryopump regions to determine neutral flows.

Planning

The overall pumped divertor planning calls for a start of installation inside the JET vessel, early in 1992. This tight schedule requires that all major manufacturing contracts for long term delivery components should be placed in May-June 1990. By end - 1989, the beryllium screen elements of the new ICRF antennae had been ordered. The overall plan for the New Phase of JET is shown in Fig.181.

In addition, Calls-for-Tender had been issued or were being finalised for the divertor coil and coil case, the target plate elements, the cryopump, the ICRH antenna housing and the belt limiter.

References

[1] JET Contributions to the Workshop on the New Phase for JET: The Pumped Divertor Proposal; JET Report JET-R(89)16.

Future Plans

The JET programme was divided into phases governed by the availability of new equipment and fitting within the accepted lifetime of the Project. At the beginning of 1989, the planned programme was as set out in Table XXI Taking account of the adjustments to the shutdown schedule and the need to allow for sensible periods of operation to establish high reliability in preparation for the active phase of operation, the period remaining for D-T operation was no more than eight months. However, with the advent of the proposal for a New Phase for JET until the end of 1996, the proposed programme is now as set out in Fig. 181.

On the JET programme, Phase I, the Ohmic Heating Phase, was completed in September 1984, and Phase II (Additional Heating Studies) was completed in October 1988. The present Phase IIIA (Full Power Optimization Studies) is underway and future phases are as follows:

Full Power Studies–Phase IIIA (Oct 1989 - Sept 1990)

The current shutdown at the start of this phase includes the following:

- replacement of a toroidal coil;
- installation of beryllium RF antennae screens;

Table XXI
JET PROGRAMME TO 1992

PHASE I	PHASE IIA	PHASE IIB	PHASE IIIA	PHASE IIIB	PHASE IV
Ohmic Heating Studies	Additional Heating Studies		Full Power Optimisation Studies		Tritium Phase
1983 1984	1985 1986	1987 1988	1989 1990	1991	1992

Ohmic Systems	5MA	Vessel restraints and improved volt-seconds for 7MA operation	Vessel reinforcements			
Separatrix		Additional P1 Coils	Separatrix dump plate supports		Cooled separatrix dump plates	
Limiters	Eight carbon mid-plane limiters	Carbon belt limiters	Beryllium belt limiters			
Pellets	Single pellet injector	ORNL multiple pellet injector (1.5km s⁻¹)		Prototype high speed pellet injector (>3km s⁻¹)	Multiple high speed pellet injector	
NBI	First NBI line (80kV)	Second NBI line (2×80kV)	One line modified to 140kV D		Second line modified to 140kV D	One line modified to 160kV T
ICRH	Three A₀ antennae	Eight A₁ antennae		Be antennae Screens		
LHCD			Install Vacuum Chamber	Prototype system	Full system	
Disruption control					Saddle coils	
Tritium and Remote handling					Tritium plant and main RH modifications	Final modifications

JG90 72 (rev 20/3/90)

- installation of prototype LHCD system;
- installation of prototype High Speed Pellet Launcher;
- installation of beryllium tiles as lower X-point dump plates.

During the operational phase that follows, the second neutral beam box will be progressively brought up to 140kV (deuterium).

The main aims of the experimental programme in 1990 will be to improve plasma performance operating with high reliability, in limiter configuration with currents up to 7MA with high energy content and at up to 6MA in X-point plasmas, in order to exploit the H-mode regime of operations. Profile effects and related physics issues will also be studied using the prototype LHCD, RF, and Neutral Beam systems and High Speed Pellet injection (eg particle and energy transport in transient conditions, disruption and sawtooth stabilisation).

Installation and initial commissioning of Tritium Plant components will also be taking place throughout 1990.

New Additions in Limiter Configuration—Phase IIIB (Oct 1990-Dec 1991)

After the shutdown at the start of this phase the following are planned to be operational:

- cooled separatrix dump plates (with beryllium protection);
- full LHCD system for profile control;
- disruption control system using internal saddle coils.

A multiple high speed pellet gun would also be installed at this time (or during a break in subsequent operations) as soon as it is available.

The scientific aims of the following operation period will be to exploit these new additions fully, in order to:

- obtain maximum performance in limiter configuration with high reliability;
- control disruptions by feedback system and control sawteeth through full power LHCD;
- optimise transient performance in X-point operation.

Preparations for D-T operations will also continue during his period, including active commissioning of the tritium plant (subject to consent by the approving bodies).

The New Phase Programme—Phase IVA (Jan 1992-Sept 1993)

At the start of 1992 the Project will enter an extended (~9 months) shutdown in order to install equipment for the New Phase Programme. This will involve intensive in-vessel work to install:

- divertor structure;
- pumping chamber and cryopump;
- internal poloidal coil;
- modified belt limiter;

- A2 ICRH antennae and modified protection;
- modified LHCD grill and protection;
- divertor diagnostics.

The single-null X-point pumped divertor configuration should enable JET to progress towards quasi-steady state high power operation - at 6MA for up to 10s; at 3MA for up to 20s (B=3.4T); and at 3MA for up to one minute (B=2.1T).

The first operating period of the new phase should focus initially on establishing reliable operation in this configuration. Subsequently, attention should be devoted to the study of the performance and effects of the pumped divertor in controlling impurities, plasma density and exhaust and of power loading on the target plates.

New Phase Programme—Phase IVB (Oct 1993 - Dec 1994)

The proposed shutdown (~4 months) in late 1993 would be to provide an opportunity, in the light of information from the experimental programme and elsewhere, to install modifications to the pumped divertor (eg enhanced divertor geometry). In addition, it would be possible to install other enhancements aimed at improving performance in the new configuration or for the Tritium Phase (eg enhanced pellet injection or fuelling system, modifications to LHCD or additional heating systems).

The primary objective of the following operating period would be to provide information necessary to establish with confidence the key design features of the Next Step in relation to:

- impurity control;
- fuelling;
- helium transport and exhaust of ashes.

With regard to JET's own requirements, the objective will be to optimise reliability and plasma performance in the divertor configuration in anticipation of D-T operations. A two-fold increase in potential α- particle power has been estimated for the new configuration. In parallel, active commissioning of the Tritium Plant and Remote Handling preparation should have been completed.

D-T Operations—Phase V (Jan 1995 - Dec 1996)

Subject to the approval of the JET Council and to necessary official consents, and when it is clear that the results in deuterium and general levels of system reliability justify it, the D-T phase would start in 1995 after a short shutdown for final pre-tritium modifications.

During tritium operations, it would be possible to study in depth the physics of α-particle production, confinement and heating and thermal excursions. In addition, the real experience of tritium operation in a relevant scale tokamak (ie tritium handling and recovery, fuel mixture control, confinement properties of D-T plasmas, remote maintenance and plasma

diagnostics with large neutron and gamma backgrounds) should provide essential information for the detailed design and operational planning for the Next Step.

Cessation of Operations
As noted, the Project is for the present proceeding in a manner compatible both with pursuing the New Phase programme towards 1996 and with completing its experimental life with D-T operations in 1992. In terms strictly of the experimental programme, the two paths diverge at the end of 1991. However, as the JET Council recognised, it is becoming increasingly difficult to maintain both options within the constraints on staff, money and time available. By the end of 1990, the Project will be forced, in the absence of a decision on extension for the New Phase, into making choices which will adversely affect at least one of the possible paths.

Appendix I

JET Task Agreements 1989

Title	Associations (JET Responsible Officer)	Duration of Agreement
RF HEATING DIVISION		
LOWER HYBRID CURRENT DRIVE ON JET– • Exchange of knowledge • Design and construction of special item • High power tests	EUR-CEA CADARACHE (CEA/TA4) (J.Jacquinot)	Started January 1987
PHYSICS OF LOWER HYBRID CURRENT DRIVE ON JET •set-up predictive and interpretive codes •participation in the LHCD programme at JET	UNIVERSIDAD DI LISBOA (UTL/TAI) (J.Jacquinot)	Oct. 1987-Oct. 1990
LH AND ICRF EFFECTS ON JET •CD efficiency including transport •Synergistic effects between FWCD and LHCD •Modulated heating modelling •Minority CD experiments •Effect of RF CD on MHD stability	EUR-UKAEA Culham (J Jacquinot)	Jan. 1989-Dec. 1992
EXPERIMENTAL DIVISION I		
PHYSICS OF SHAPED CROSS-SECTIONS	CULHAM UK (CUL/TA4) (P.E. Stott)	Being reviewed
EDGE PLASMAS & PLASMA SURFACE INTERACTIONS	CULHAM UK (CUL/TA4) (P.E. Stott)	June 1983-Dec. 1992
PLASMA WALL INTERACTIONS	GARCHING, FRG (IPP/TA2) (P.E. Stott)	Jan. 1984-June 1991
NEUTRON PRODUCTION,RELATED PHYSICS AND ASSOCIATED DIAGNOSTICS	SWEDEN (NFR/TA1) (P.E. Stott)	Jan. 1984-Dec 1992
PLASMA SURFACE INTERACTIONS	SWEDEN (NFR/TA2) (P.E. Stott)	July 1987-July 1990
NEUTRON PRODUCTION RELATED PHYSICS	HARWELL UK (HAR/TA1) (P.E. Stott)	Aug 1985-Dec 1992
NEUTRON PRODUCTION RELATED PHYSICS AND ASSOCIATED	FRASCATI,ITALY (ENEA/TA3) (P.E. Stott)	Jan. 1986-Jan. 1992
PHYSICS OF TURBULENT AND CONVECTIVE TRANSPORT, MHD AND RELATED DIAGNOSTICS	FOM, NETHERLANDS (FOM/TA2) (P.E. Stott)	Nov. 1987-Oct 1990
EXPERIMENTAL DIVISION II		
BULK IMPURITY PHYSICS AND IMPURITY RELATED DIAGNOSTICS	EUR-IPP FRG (P.R. Thomas)	Started Feb. 1983
SPECTROSCOPIC MEASUREMENTS: INTERPRETATION AND IMPURITY ANALYSIS	EUR-CEA Cadarache, FRANCE (P.R. Thomas)	Started July 1984
PHYSICS OF ION AND ELECTRON ENERGY TRANSPORT AND RELATED DIAGNOSTICS	EUR-ENEA CREF (P.R. Thomas)	Started Oct. 1983

Title	Associations (JET Responsible Officer)	Duration of Agreement
CHARGE EXCHANGE RECOMBINATION SPECTROSCOPY	FOM. NETHERLANDS (M. von Hellerman)	Started June 1983
IMPURITY ANALYSIS AND PLASMA DIAGNOSTICS USING SPECTROSCOPIC MEASUREMENTS	EUR-NFR SWEDEN (NFR/TA3) (P.R. Thomas)	Started Jan.1988
THEORY DIVISION		
TESTING THEORETICAL TRANSPORT MODELS AGAINST JET DATA	EUR-UKAEA CULHAM LAB (CUL/TA5) (T.E. Stringer)	Started Dec. 1986
THEORY AND MODELS OF ANOMALOUS TRANSPORT	EUR-ENEA FRASCATI,ITALY (D.F. Duchs)	Started Jan. 1988

Appendix II

Articles, Reports and Conference Papers Published in 1989

1. Radial profiles of neutron emission from ohmic
    discharges in JET.
    Adams J M, Cheetham A, Conroy S, Gorini G,
    Gottardi N, Iguchi T, Jarvis O N, Sadler G,
    Smeulders P, Watkins N, Van Belle P.
    Controlled Fusion and Plasma Physics. 16th Euro.
    Conf., Venice, 13–17 March 1989.
    Contributed papers. Part I of IV. European
    Physical Society, 1989. pp.I–63 – I–66.
    Report JET–P(89)03, pp.9–12.

2. Analysis of vertical instability in the JET
    experiment.
    Albanese R, Bertolini E, Bobbio S, Martone R,
    Miano G, Noll P.
    Procs. 15th Symp. on Fusion Technology, Utrecht,
    The Netherlands, 19–23 September 1988.
    Amsterdam, North–Holland. 1989.
    Vol.1, pp.694–699. Report JET–P(88)69,
    pp.133–138.

3. Diagnostics for the JET multi–pellet injector.
    Bailey W, Kupschus P, Gadeberg M, Szabo T,
    Cracknell D, Adams M J, Mills B.
    Procs. 15th Symp. on Fusion Technology, Utrecht,
    The Netherlands, 19–23 September 1988.
    Amsterdam, North–Holland. 1989. Vol.1,
    pp.720–723.

4. Local confinement properties of JET plasmas.
    Balet B, Cordey J G, Stubberfield P M.
    American Physical Society. Bulletin.vol.34 No.9
    October 1989 (Programme of the 31st Annual
    Meeting of the Division of Plasma Physics, Anaheim,
    Calif., 13–17 November 1989). p.2055.

5. Transport analysis using the TRANSP code.
    Balet B, Stubberfield P M,
    Joint European Torus JET. 1989. 52p.
    Report JET–R(89)05

6. High Temperature L and H-mode Confinement
    in JET.
    Balet B et al.
    Report JET-P(89)81.

7. Radiation–shielded double crystal X–ray
    monochromator for JET.
    Barnsley R, Schumacher U, Kallne E, Morsi H,
    Rupprecht G.
    Controlled Fusion and Plasma Physics. 16th Euro.
    Conf., Venice, 13–17 March 1989.
    Contributed papers. Part IV.European Physical
    Society, 1989. pp.IV–1557 – IV–1560.

8. Integrated electron temperature and density
    measurements on JET.
    Bartlett DV, Campbell D J, Costley A E,
    Gottardi N, Gowers C W, Kirsch K, Kissel S E,
    Nielsen P, Nowak S, O'Rourke J, Salzmann H.
    Controlled Fusion and Plasma Heating. 15th Euro.
    Conf., Dubrovnik, 16–20 May 1988.
    Contributed papers.Geneva, European Physical
    Society, 1988. Part III, pp.1119–1122.

9. JET impurity results in helium plasmas.
    Behringer K, Denne B, Morgan P D, Stamp M F,
    Forrest M J
    Journal of Nuclear Materials vols.162–164 April
    (I) 1989 (Procs. 8th Int. Conf. on Plasma–Surface
    Interactions in Controlled Fusion Devices,
    Julich, FRG, 2–6 May 1988) pp.398–403.

10. Neoclassical transport calculations using the
    impurity transport code 'Strahl".
    Behringer K.
    Joint European Torus JET. February 1989.47p.
    Report JET–R(89)03

11. Spectroscopic determination of impurity influx from
    localized surfaces.
    Behringer K, Summers H P, Denne B, Forrest M,
    Stamp M.
    Plasma Physics and Controlled Fusion vol.31 no.14
    December 1989 pp.2059–2099.
    Report JET–P(89)05

12. Space resolved measurement of impurity radiation
    on the JET tokamak.
    Behringer K H, Breton C, de Michelis C,
    Denne B, Magyar G, Ramette J, Saoutic B.
    Basic and Advanced Diagnostic Techniques for
    Fusion Plasmas. Course and Workshop, Villa
    Monastero, Varenna, 3–13 September 1986. 3 vols.
    Edited by P E Stott and others.

Luxembourg, Commission of the European Communities, and Citta di Castello, Monotypia Franchi. 1987. Vol.I, pp.305–311.

13. Probes for the assessment of plasma–limiter interaction in JET.
Behrisch R, Coad J P, Ehrenberg J, De Kock L, Roth J, Wielunski M, Tagle J A.
Journal of Nuclear Materials vols.162–164 April (I) 1989 (Procs. 8th Int.Conf. on Plasma–Surface Interactions in Controlled Fusion Devices, Julich, FRG, 2–6 May 1988) pp.598–603.

14. Preparation for D–T operation at JET.
Bell A C, Caldwell–Nichols C, Campbell J, Chuilon P, Gordon C, Newbert G, Wykes M E P.
Procs. 15th Symp. on Fusion Technology, Utrecht, The Netherlands, 19–23 September 1988.
Amsterdam, North–Holland. 1989.
Vol.1, pp.209–218. Also in Fusion Engineering and Design, vol.11 nos.1&2 June/July 1989 (Invited papers of the 15th SOFT, Utrecht, 1988). pp.209–218.

15. Rotation and mode locking in tokamaks.
Berge G, Sandal L K, Wesson J A.
Physica Scripta vol.40 no.2 August 1989 pp.173–187.

16. JET Design, Construction and Performance
Bertolini E.
Report JET-P(89)58 - paper submitted to Nuclear Energy Journal

17. Effect of sawteeth, safety factor and current on confinement during ICRF heating of JET.
Bhatnagar V P, Cordey J G, Jacquinot J, Start D F H.
Plasma Physics and Controlled Fusion vol.31 no.3 March 1989 pp.333–344.
Report JET-P(88)51

18 ICRF power deposition profiles and heating in monster sawtooth and peaked - density profile discharges in JET.
Bhatnagar V P, Taroni A, Ellis J J, Jacquinot J, Start D F H.
Controlled Fusion and Plasma Physics. 16th Euro. Conf., Venice, 13–17 March 1989. Contributed papers. Part I of IV. European Physical Society, 1989. pp.I–127 – I–130.
Report JET-P(89)03, pp.53-56.

19. ICRF power–deposition profiles, heating and confinement of monster sawtooth and peaked–density profile discharges in JET.
Bhatnagar V P, Taroni A, Ellis J J, Jacquinot J, Start D F H.
Plasma Physics and Controlled Fusion vol.31 no.14 December 1989 pp.2111–2126.
Report JET-P(89)38

20. Latest JET results and future prospects.
Bickerton R J (presenter) and JET Team
Plasma Physics and Controlled Nuclear Fusion Research.
12th Int. Conf., Nice, 12–19 October 1988. Vol.1. Vienna, IAEA. 1989. pp.41–65.
Report JET–P(88)78, pp.1–23.

21. Latest results from JET.
Bickerton R J and the JET Team Europhysics News. European Physical Society Bulletin vol.20 no.1 January 1989 pp.1–5.

22. Tokamak experiments.
Bickerton R J, Keen B E.
Basic Physical Processes of Toroidal Fusion Plasmas. Course and Workshop, Villa Monastero, Varenna, 26 August–3 September 1985. 2 vols. Luxembourg, Commission of the European Communities, and Citta di Castello, Monotypia Franchi. 1986. Vol.I, pp.19–64.

23. A general method for measuring the scattering matrices of N–port systems.
Bizarro J P, Pain M.
Joint European Torus JET. 1989. 17p.
Report JET–R(89)11

24. One electron and two electron–one photon electric dipole transitions in the Mg like argon spectrum.
Bliman S, Indelicato P, Hitz D, Marseille P, Desclaux J P.
Joint European Torus JET. April 1989. 17p.
Report JET–P(89)19
Paper submitted to Journal of Physics B.

25. Spectroscopic study of doubly excited Na–like argon ions.
Bliman S, Suraud M G, Hitz D, Rubensson J E, Nordgren J, Cornille M, Indelicato P, Knystautas E J.
Joint European Torus JET. June 1989. 16p.
Report JET–P(89)44
Paper submitted to J. Phys. B: At Mol. Opt. Phys.

26. Problems and Methods of Self-consistent Reconstructions of Tokamak Equilibrium Profiles from Magnetic and Polorimetric Measurements.
Blum J, Lazzaro E et al
Report JET-P(89)63

27. Analysis of low–Z impurity behaviour in JET by charge exchange spectroscopy measurements.
Boileau A, von Hellerman M, Horton L D, Summers H P, Morgan P D.
Nuclear Fusion vol.29 no.9 September 1989 pp.1449–1458.

28. The deduction of low–Z ion temperature and densities in the JET tokamak using charge exchange

recombination spectsocopy.
Boileau A, von Hellermann M, Horton L D,
Spence J, Summers H P.
Plasma Physics and Controlled Fusion vol.31 no.5
May 1989 pp.779–804. Report JET–P(89)18

29. Observations of motional Stark features in the Balmer
spectrum of deuterium in the JET plasma.
Boileau A, von Hellermann M, Mandl W,
Summers H P, Weisen H, Zinoviev A.
Journal of Physics B. Atomic and Molecular Physics
vol.22 no.7 14 April 1989 pp.L145–L152.
Report JET–P(89)04

30. Ion temperature measurement from Doppler
broadening of He–like nickel lines.
Bombarda F, Giannella R, Kallne E, Tallents G J.
Journal of Quantitative Spectroscopy and Radiative
Transfer vol.41 no.4 April 1989. pp.323–333.

31. Management of operational active wastes on JET.
Booth S J.
Joint European Torus JET. 1989. 13p.
Report JET–P(89)21
Paper submitted to IAEA Technical Committee
Meeting on Fusion Reactor Safety, Jackson Hole,
Wyoming, 4–7 April 1989.

32. 32MW ICRH plant operation experience on JET.
Bosia G, Schmid M, Farthing J, Knowlton S,
Sibley A, Wade T, Negro E.
Procs. 15th Symp. on Fusion Technology, Utrecht,
The Netherlands, 19-23 September 1988.
Amsterdam, North-Holland. 1989. Vol.1,
pp.459-463. Report JET-P(88)69, pp.113-117.

33. Dynamics of Rotating Tearing Modes under
Phase Locked Feedback Control
Bosia G, Lazzaro E.
Report JET-P(89)71

34. ³He-d fusion reaction rate measurements during
ICRH heating experiments in JET.
Boyd D A, Campbell D J, Cordey J G, Core W G F,
Christiansen J P, Cottrell G A, Eriksson L–G,
Hellsten T, Jacquinot J J, Jarvis O N, Kissel S E,
Lowry C, Nielsen P, Sadler G, Start D F H,
Thomas P R, Van Belle P, Wesson J A.
Nuclear Fusion vol.29 no.4 April 1989 pp.593–604.

35. JET polari–interferometer.
Braithwaite G, Gottardi N, Magyar G, O'Rourke J,
Ryan J, Veron D.
Review of Scientific Instruments vol.60 no.9
September 1989 pp.2825–2834.
Report JET–P(89)15

36. A model for calculating room air and surface
tritium concentration.
Brereton S J, Gordon C W.
Joint European Torus JET. 23p.
Report JET–R(89)06

37. MHD modes near the X–line of a magnetic
configuration.
Bulanov S V, Pegoraro F, Shasharina S G.
Joint European Torus JET. August 1989. 20p.
Report JET–P(89)52
Paper submitted to Plasma Physics and
Controlled Fusion.

38. Enhanced performance of high current discharges
in JET produced by ICRF heating during the
current rise.
Bures M, Bhatnagar V, Cottrell G, Corti S,
Christiansen J P, Eriksson L G, Hellsten T,
Jacquinot J, Lallia P, Lomas P, O'Rourke J,
Taroni A, Tibone F, Start D F H.
Controlled Fusion and Plasma Physics. 16th Euro.
Conf., Venice, 13–17 March 1989. Contributed
papers. Part I of IV. European Physical Society,
1989. pp.I–3–I–6. Report JET–P(89)03, pp.77–80.

39. Enhanced performance of high current discharges
in JET produced by ICRF heating during the
current rise.
Bures M, Bhatnagar V, Christiansen J P, Cottrell G,
Corti S, Eriksson L–G, Hellsten T, Jacquinot J,
Jarvis O N, Lallia P, Lomas P, O'Rourke J,
Taroni A, Sack C, Start D F H.
Plasma Physics and Controlled Fusion vol.31 no.12
October 1989 pp.1843–1862. Report JET–P(89)26

40. ICRF Heating Plasma Edge Interaction in JET with
Beryllium Gettering
Bures M et al
Report JET-P(89)72

41. The JET high temperature in–vessel inspection
system.
Businaro T, Cusack R, Galbiati L, Raimondi T.
Procs. 15th Symp. on Fusion Technology, Utrecht,
The Netherlands, 19–23 September 1988.
Amsterdam, North–Holland. 1989. Vol.2,
pp.1401–1405. Report JET–P(88)69, pp.26–30.

42. Sawteeth and the m=1 mode in JET.
Campbell D J, Edwards A W, Pearson D.
Controlled Fusion and Plasma Physics. 16th Euro.
Conf., Venice, 13–17 March 1989. Contributed
papers. Part II. European Physical Society, 1989.
pp.II–509–II–512. Report JET–P(89)03, pp.17–20.

43. Sawtooth activity and current density profiles in JET.
Campbell D J, Cordey J G, Edwards A W, Gill R D,
Lazzaro E, Magyar G, McCarthy A L, O'Rourke J,

Pegoraro F, Porcelli F, Smeulders P, Start D F H, Stubberfield P, Wesson J A, Westerhof E, Zasche D.
Plasma Physics and Controlled Nuclear Fusion Research. 12th Int. Conf., Nice, 12–19 October 1988.
Vol.1. Vienna, IAEA. 1989. pp.377–385.
Report JET–P(88)78, pp.101–110.

44. Sawtooth stabilization experiments in JET.
Campbell D J, Cheetham A D, Cordey J G, Eriksson L G, Gill R D, Jacquinot J J, Lallia P P, Nave M F F, O'Rourke J, Pearson D, Pegoraro F, Porcelli F, Start D F H, Stubberfield P, Schmidt G, Taroni A, Tibone F.
American Physical Society. Bulletin. vol.34 no.9 October 1989 (Program of the 31st Annual Meeting of the Division of Plasma Physics, Anaheim, Calif., 13–17 November 1989). p.2056.

45. Testing of divertor samples for NET at the JET NBI test bed.
Cardella A, Libin B, Coulon M, Evans D, Falter H D, Faron R, Hemsworth R S, Martin D, Moons F, Tivey R, Vassiliadis M.
Procs. 15th Symp. on Fusion Technology, Utrecht, The Netherlands, 19–23 September, 1988.
Amsterdam, North–Holland. 1989. Vol.1, pp.854–858.

46. Space and time–resolved diagnostic of line emission from the separatrix region in JET X–point plasmas.
Chabert P, Breton C, De Michelis C, Denne B, Giannella R, Gottardi N, Magyar G, Mattioli M, Ramette J, Saoutic B.
Controlled Fusion and Plasma Physics. 16th Euro. Conf., Venice, 13–17 March 1989. Contributed papers. Part IV. European Physical Society, 1989. pp.IV–1505 – IV–1508.
Report JET–P(89)03, pp.81–84.

47. Non–inductively driven currents in JET.
Challis C D, Cordey J G, Hamnen H, Stubberfield P M, Christiansen J P, Lazzaro E, Muir D G, Stork D, Thompson E.
Nuclear Fusion vol.29 no.4 April 1989 pp.563–570.
Report JET–P(88)38.

48. Measurements of correlations between thermal and particle transport in JET.
Cheetham A D, Gondhalekar A, De Haas J C M, Jarvis O N, Morgan P D, O'Rourke J, Sadler G, Watkins M L.
Plasma Physics and Controlled Nuclear Fusion Research. 12th Int. Conf., Nice, 12–19 October 1988.
Vol.1. Vienna, IAEA. 1989. pp.483–493.
Report JET–P(88)78, pp.142–154.

49. Determination of current distribution in JET from soft X–ray measurements.
Christiansen J P, Callen J D, Ellis J J, Granetz R S.
Nuclear Fusion vol.29 no.5 May 1989 pp.703–711.
Report JET–P(88)66.

50. Local transport in sawtooth–free JET discharges with ion cyclotron resonance heating.
Christiansen J P, Cordey J G, Muir D G.
Nuclear Fusion vol.29 no.9 September 1989 pp.1505–1513. Report JET–P(89)12

51. Design of the protection crowbar for the LHCD klystrons in JET.
Christodoulopoulos C, Cross D, Hrabal H, Bertolini E, Claesen R, Weigand W.
Procs. 15th Symp. on Fusion Technology, Utrecht, The Netherlands, 19–23 September 1988.
Amsterdam, North–Holland. 1989. Vol.1, pp.337–341. Report JET–P(88)69, pp.103–107.

52. Poloidal electric field and variation of radial transport during ICRF heating in the JET scrape–off layer.
Clement S, Tagle J A, Laux M, Erents S K, Bures M , Stangeby P C, Vince J , de Kock L.
Controlled Fusion and Plasma Physics. 16th Euro. Conf., Venice, 13–17 March 1989. Contributed Papers. Part III. European Physical Society, 1989. pp.III–935–III–938. Report JET–P(89)03,pp.93–96.

53. Gas release on venting the JET torus.
Coad J P.
Joint European Torus JET. 1989. 13p.
Report JET–R(89)15

54. The retained deuterium inventory in JET and implications for tritium operation.
Coad J P, Behrisch R, Bergsaker H, Ehrenberg J, Emmoth B, Partridge J, Saibene G, Sartori R, Simpson J C B, Wang W–M.
Journal of Nuclear Materials vols.162–164 April (I) 1989 (Procs. 8th Int. Conf. on Plasma–Surface Interactions in Controlled Fusion Devices, Julich, FRG, 2–6 May 1988) pp.533–541.

55. Performance of a pneumatic hydrogen–pellet injection system on the Joint European Torus.
Combs S K, Jernigan T C, Baylor L R, Milora S L, Foust C R, Kupschus P, Gadeberg M, Bailey W.
Review of Scientific Instruments vol.60 no.8 August 1989 pp.2697–2700.

56. Time resolved measurements of triton burnup in JET plasmas.
Conroy S, Jarvis O N, Sadler G, Huxtable G B.
Nuclear Fusion vol.28 no.12 December 1988 pp.2127–2134. Report JET–P(88)16.

57. Triton burnup in JET.
Conroy S, Argyle J P, Batistoni P, Clipsham E,
Huxtable G B, Jarvis O N, Pillon M, Podda S,
Rapisarda M, Sadler G, Van Belle P.
Controlled Fusion and Plasma Physics. 16th Euro.
Conf., Venice, 13–17 March 1989. Contributed
papers. Part I of IV. European Physical
Society,1989. pp.I–67 – I–70.
Report JET–P(89)03, pp.5–8.

58. Global modes and high energy particles in
ignited plasmas.
Coppi B, Migliuolo S, Pegoraro F, Porcelli F.
Joint European Torus JET. 1989. 61p.
Report JET–P(89)22

59. Quiescent window for global plasma modes.
Coppi B, Detragiache P, Migliuolo S, Pegoraro F,
Porcelli F.
Physical Review Letters vol.63 no.25
18 December 1989 pp.2733–2736.
Report JET–P(89)49

60. Unification of ohmic and additionally heated energy
confinement scaling laws.
Cordey J G.
Basic Physical Processes of Toroidal Fusion
Plasmas. Course and Workshop, Villa Monastero,
Varenna, 26 August–3 September 1985. 2vols.
Luxembourg, Commission of the European
Communities, and Citta di Castello, Monotypia
Franchi. 1986. Vol.I, pp.209–216.
Report JET–P(85)28.

61. Influence of neutral injection on the velocity
distribution of excited atoms in a plasma.
Core W G F, Cowern N.
Joint European Torus JET. March 1989. 7p.
Report JET–P(89)11
Paper submitted for publication as a Letter in
Nuclear Fusion.

62. A model for the calculation of 2–D neutral transport
in non–circular tokamak plasmas.
Core W G F.
Joint European Torus JET. 1989. 19p.
Report JET–R(89)04

63. Wave induced ion transport in ICRH tokamak
plasmas.
Core W G F.
Nuclear Fusion vol.29 no.7 July 1989 pp.1101–1111.
Report JET–P(89)42.

64. Correlation reflectometry: a possible new technique
for diagnosing density microturbulence.
Costley A, Cripwell P.
Proc. Cadarache Workshop on Electrostatic
Turbulence, 4–6 October 1989. Euratom–CEA.
Departement de Recherches sur la Fusion Controlee
1989. pp.89–96. Report EUR–CEA–FC–1381 and
Report JET–P(89)82.

65. Papers presented at Joint Workshop on ECE and
ECRH (EC7), Hefei, China, May 1989.
Costley A E and others
Joint European Torus JET. 1989. 27p.
Report JET–P(89)53

66. A High Power 140GHz Collective Scattering
Diagnostic to Measure Fast Ion and a-Particle
Distributions in JET: Physics Aspects and Technical
Aspects
Costley A et al.
Report JET-P(89)53.

67. Alpha particle simulation experiments in JET.
Cottrell G A, Cordey J G, Jacquinot J, Jarvis O N,
Lomas P J, Sadler G, Start D F H.
American Physical Society. Bulletin. vol.34 no.9
October 1989 (Program of the 31st Annual Meeting
of the Division of Plasma Physics, Anaheim, Calif.,
13–17 November 1989). p.2057.

68. Non–thermal DT yield with (D)T ICRH
heating in JET.
Cottrell G A, Bhatnagar V P, Bures M,
Eriksson L G, Hellsten T, Jacquinot J, Start D F H.
Plasma Physics and Controlled Fusion vol.31 no.11
October 1989 pp.1727–1740. Report JET–P(89)35.
(Expanded version of contributed paper presented at
16th Eur. Conf. on Controlled Fusion and Plasma
Physics, Venice, 13–17 March 1989).

69. Non–thermal DT yield with (D)T ICRH
heating in JET.
Cottrell G A, Bhatnagar V P, Bures M,
Eriksson L G, Hellsten T, Jacquinot J, Start DFH .
Controlled Fusion and Plasma Physics. 16th Euro.
Conf., Venice, 13–17 March 1989. Contributed
papers. Part I of IV. European Physical Society,
1989.pp.I–71 – I–74.
Report JET–P(89)03, pp.101–104.

70. Correlation reflectometry.
Cripwell P, Costley A E, Hubbard A E.
Controlled Fusion and Plasma Physics. 16th Euro.
Conf., Venice, 13–17 March 1989.
Contributed papers. Part I of IV. European Physical
Society, 1989. pp.I–75 – I–78. Report JET–P(89)03,
pp.133–136.

71. An interpretation of the structure of ELMS and the
H to L transition on JET.
Cripwell P, Edwards A, Galvao R, Gottardi N,
Harbour P, Haynes P, Hender T C, Joffrin E H,

Malacarne M, Mantica P, Salmon N, Snipes J A,
Tagle A, Zasche D.
Controlled Fusion and Plasma Physics. 16th Euro.
Conf., Venice, 13–17 March 1989. Contributed
papers. Part I of IV. European Physical Society,
1989. pp.I–225 – I–228.
Report JET–P(89)03, pp.125–128.

72. Heat pulse analysis in JET and relation to local
energy transport models.
de Haas J C M, Han W, Lopes–Cardozo N J,
Sack C, Taroni A
Controlled Fusion and Plasma Physics. 16th Euro.
Conf., Venice, 13–17 March 1989. Contributed
papers. Part I of IV. European Physical Society,
1989. pp.I–279 – I–282.
Report JET–P(89)03, pp.61–64.

73. Performance of carbon tiles and in situ carbon
coatings in JET and TEXTOR.
de Kock L.
Fusion Technology vol.15 no.1 January 1989
pp.89–101. Report JET–P(88)22.

74. The plasma boundary in JET.
de Kock L, Stott P E, Clement S, Erents S K,
Harbour P J, Laux M, McCracken G M,
Pitcher C S, Stamp M F, Stangeby P C,
Summers D D R, Tagle A J.
Plasma Physics and Controlled Nuclear Fusion
Research. 12th Int. Conf., Nice, 12–19 October
1988. Vol.1. Vienna, IAEA. 1989. pp.467–475.
Report JET–P(88)78, pp.89–100.

75. Beryllium-like Mo XXXIX and lithium-like Mo XL
observed in the Joint European Torus tokamak.
Denne B, Magyar G, Jacquinot J.
Physical Review A. General Physics vol.40 no.7
1 October 1989 pp.3702–3705. Report JET–P(89)31

76. The role of atomic spectroscopy in fusion research.
Denne B.
Physica Scripta vol.T26 1989 (Meeting of Group for
Atomic Spectroscopy, Technical University Graz,
Austria, 12–15 July 1988) pp.42–50.

77. Spectrum lines of KrXXVIII–KrXXXIV observed
in the JET tokamak.
Denne B, Hinnov E, Ramette J, Saoutic B.
Physical Review A. General Physics vol.40 no.3
1 August 1989 pp.1488–1496. Report JET–P(88)74

78. JET neutral beam species measurements by
Doppler–shift spectroscopy.
Deschamps G H, Falter H D, Hemsworth R S,
Massmann P.
Procs. 15th Symp. on Fusion Technology, Utrecht,
The Netherlands, 19–23 September 1988.

Amsterdam,North–Holland. 1989. Vol.1,
pp.588–592. Report JET–P(88)69, pp.98–102.

79. From JET to NET: design steps in tritium and
vacuum systems.
Dinner P, Hemmerich J L.
Procs. 15th Symp. on Fusion Technology, Utrecht,
The Netherlands, 19–23 September 1988.
Amsterdam, North–Holland. 1989. Vol.2,
pp.1330–1339.

80. Design of JET lower hybrid current drive generator
and operation of high power test bed.
Dobbing J A, Bosia G, Brandon M, Gammelin M,
Gormezano C, Jacquinot J, Jessop G, Lennholm M,
Pain M, Sibley A, Wade T.
Procs. 15th Symp. on Fusion Technology, Utrecht,
The Netherlands, 19–23 September 1988.
Amsterdam, North–Holland. 1989. Vol.1,
pp.454–458. Report JET–P(88)69, pp.123–127.

81. Exhaust detritiation system for JET.
Dombra A H, Wykes M E P, Hemmerich J L,
Haange R, Bell A C.
Procs. 15th Symp. on Fusion Technology, Utrecht,
The Netherlands, 19–23 September 1988.
Amsterdam, North–Holland. 1989. Vol.2,
pp.1301–1305. Report JET–P(88)69, pp.118–122.

82. 3/2 or 5/2 for convective thermal transport?
Duchs D F.
Joint European Torus JET. July 1989. 13p.
Report JET–R(89)13

83. Impurity generation by ICRF antennas.
D'Ippolito D A, Myra J R, Bures M, Stamp M,
Jacquinot J.
American Physical Society. Bulletin. vol.34 no.9
October 1989 (Program of the 31st Annual Meeting
of the Division of Plasma Physics, Anaheim, Calif.,
13-17 November 1989). p.2035.

84. Hydrogen and helium recycling in tokamaks with
carbon walls.
Ehrenberg J.
Journal of Nuclear Materials vols.162 164 April (I)
1989 (Procs. 8th Int. Conf. on Plasma Surface
Interactions in Controlled Fusion Devices,
Julich, FRG, 2 6 May 1988) pp.63 79.
Report JET- P(88)57.

85. Wall pumping in JET.
Ehrenberg J.
JET Team American Physical Society. Bulletin.
vol.34 no.9 October 1989 (Program of the 31st
Annual Meeting of the Division of Plasma Physics,
Anaheim, Calif., 13-17 November 1989). p.2056.

86. The JET Neutron Time of Flight Spectometer.
Elevant T et al.
Report JET-P(89)76

87. The behaviour of the scrape off layer in JET with
toroidal belt limiters.
Erents S K, Tagle J A, McCracken G M, Israel G,
Brinkschulte H W, de Kock L.
Journal of Nuclear Materials vols.162-164 April (I)
1989 (Procs. 8th Int. Conf. on Plasma Surface
Interactions in Controlled Fusion Devices, Julich,
FRG, 2-6 May 1988) pp.226-230.

88. The scaling of edge parameters in JET with plasma
input power.
Erents S K, Harbour P J, Clement S,
Summers D D R, McCracken G M, Tagle J A,
de Kock L.
Controlled Fusion and Plasma Physics. 16th Euro.
Conf., Venice, 13 17 March 1989. Contributed
Papers. Part III. European Physical Society, 1989.
pp.939- 942. Report JET-P(89)03, pp.137-140.

89. A method to study electron heating during ICRH.
Eriksson L G, Hellsten T.
Controlled Fusion and Plasma Physics. 16th Euro.
Conf., Venice, 13-17 March 1989. Contributed
Papers. Part III. European Physical Society, 1989.
pp.1077 -1080. Report JET-P(89)03, pp.21-24.

90. Electron heating during ion cyclotron resonance
heating in JET.
Eriksson L–G, Hellsten T.
Nuclear Fusion vol.29 no.6 June 1989 pp.875–883.
Report JET–P(88)47

91. Self–consistent calculations of ICRH power
deposition and velocity distribution.
Eriksson L–G, Hellsten T.
Joint European Torus JET. September 1989. 65p.
Report JET–P(89)65
Paper submitted to Nuclear Fusion.

92. Conditioning of the JET neutral beam sources.
Falter H D, Deschamps G H, Hemsworth R S,
Massmann P.
Procs. 15th Symp. on Fusion Technology, Utrecht,
The Netherlands, 19–23 September 1988.
Amsterdam,North–Holland. 1989. Vol.1,
pp.583–587.

93. Comments on ICRH current drive in JET.
Fried B, Hellsten T, Moreau D.
Plasma Physics and Controlled Fusion vol.31 no.11
October 1989 pp.1785–1795.

94. The JET remotely controlled welding system.
Galetsas A, Wykes M.

Procs. 15th Symp. on Fusion Technology, Utrecht,
The Netherlands, 19–23 September 1988.
Amsterdam, North–Holland. 1989. Vol.2,
pp.1411–1415.

95. Ideal ballooning stability of JET discharges.
Galvao R M O, Goedbloed J P, Huysmans G,
Lazzaro E, O'Rourke J, Schmidt G, Smeulders P.
Controlled Fusion and Plasma Physics. 16th Euro.
Conf., Venice, 13–17 March 1989. Contributed
papers. Part II.
European Physical Society, 1989. pp.II–501 –II–504.
Report JET–P(89)03, pp.41–44.

96. A dual system for the stabilisation of the vertical
plasma position of the JET experiment.
Garribba M, Ciscato D, Browne M, Dorling S,
Noll P.
Procs. 15th Symp. on Fusion Technology, Utrecht,
The Netherlands, 19–23 September 1988.
Amsterdam, North–Holland. 1989. Vol.2,
pp.1658–1662. Report JET–P(88)69, pp.93–97.

97. Behaviour of impurities during H–mode in JET.
Giannella R, Behringer K, Denne B, Gottardi N,
Hawkes N C, von Hellermann M, Lawson K,
Morgan P D, Pasini D, Stamp M F.
Controlled Fusion and Plasma Physics. 16th Euro.
Conf., Venice, 13–17 March 1989. Contributed
papers. Part I of IV. European Physical Society,
1989. pp.I–209 – I–212.

98. Determination of the shear on the q = 1 surface of
the JET tokamak.
Gill R A, Edwards A W, Weller A.
Nuclear Fusion vol.29 no.5 May 1989 pp.821–825.

99. Q–profiles in JET.
Gill R D, Edwards A W, Keegan B, Lazzaro E,
O'Rourke J, Weller A, Zasche D.
Controlled Fusion and Plasma Physics. 16th Euro.
Conf., Venice, 13–17 March 1989. Contributed
papers. Part II.
European Physical Society, 1989. pp.II–469–II–472.
Report JET–P(89)03, pp.97–100.

100. X–ray emission during pellet injection into JET.
Gill R D.
Nuclear Fusion vol.29 no.3 March 1989 pp.397–403.

101. Magnetic deflection of intense ion beams in the JET
neutral injection system.
Goede A P H, Falter H D.
Beams '88. 7th Int. Conf. on High–Power Particle
Beams, Karlsruhe, 4–8 July 1988. 2 vols.
Kernforschungszentrum, Karlsruhe. 1988.
pp.747–754.

102. Control of impurity influx into JET by repetitive pellet injection.
Gondhalekar A, Cheetham A, Erents S K, Gottardi N, Mast K F, Morgan P D, Pasini D, Stamp M F, Tagle J A, Thomas P R, von Hellermann M.
American Physical Society. Bulletin. vol.34 no.9 October 1989 (Program of the 31st Annual Meeting of the Division of Plasma Physics, Anaheim, Calif., 13–17 November 1989). p.2056.

103. Correlation of heat and particle transport in JET.
Gondhalekar A, Cheetham A D, de Haas J C M, Jarvis O N, Morgan P D, O'Rourke J, Sadler G, Watkins M L.
Joint European Torus JET. 1988. 10p.
Report JET–P(88)60
Paper submitted to the IAEA Technical Committee Meeting on Pellet Injection and Toroidal Confinement,Gut Ising, W. Germany, 24–26 October 1988.

104. Simultaneous measurements of electron thermal and particle transport in JET.
Gondhalekar A, Cheetham A D, de Haas J C M, Hubbard A, O'Rourke J, Watkins M L.
Plasma Physics and Controlled Fusion vol.31 no.5 May 1989 pp.805–811.
Report JET–P(88)50

105. Measurement of tritium distribution in JET.
Goodall D H J, McCracken G M, Coad J P, Causey R A, Sadler G, Jarvis O N.
Journal of Nuclear Materials vols.162–164 April (I) 1989 (Procs. 8th Int. Conf. on Plasma–Surface Interactions in Controlled Fusion Devices, Julich, FRG, 2–6 May 1988) pp.1059–1064.
Report JET–P(88)70, pp.1–11.

106. Measurements of local gradient variations observed on JET T_e and n_e profiles.
Gowers C, Cordey J G, Edwards A, Lazzaro E, Nave F, Nielsen P, Salzmann H.
American Physical Society. Bulletin. vol.34 no.9 October 1989 (Program of the 31st Annual Meeting of the Division of Plasma Physics, Anaheim, Calif., 13–17 November 1989). p.2056.

107. JET experimental results.
Green B J.
Joint European Torus JET. August 1989. 26p.
Report JET–P(89)59.
Paper submitted to Nuclear Energy Journal.

108. Machine utilisation and operation experience with JET from 1983.
Green B J, Chuilon P, Noble B, Saunders R, Webberley D.

Procs. 15th Symp. on Fusion Technology, Utrecht, The Netherlands, 19–23 September 1988.
Amsterdam, North–Holland. 1989. Vol.2, pp.1633–1637. Report JET–P(88)69, pp.69–73.

109. Experiments with high voltage insulators in the presence of tritium.
Grisham L R, Stevenson T, Wright K, Falter H D, Causey R, Chrisman W.
American Physical Society. Bulletin. Vol. 34, No.9 October 1989 (Program of the 31st Annual Meeting of the Division of Plasma Physics, Anaheim, Calif., 13–17 November 1989). p.2066.

110. Extracted beam composition with a mixed sotope feed.
Grisham L R, Falter H D, Hemsworth R, Deschamps G.
Joint European Torus JET. May 1989.
Report JET–P(89)24
Review of Scientific Instruments.Vol.60, No 12, pp 3730-3733, (1989).

111. A predictive equilibrium code for JET.
Guo W K, Micozzi P.
Joint European Torus JET. 1989. 24p.
Report JET–R(89)12

112. Transport analysis of pellet–enhanced ICRH plasmas in JET.
Hammett G W, Colestock P L, Granetz R S, Kupschus P, McCune D C, Phillips C K, Schmidt G L, Smithe D N.
Members of JET/USDOE Pellet Collaboration Controlled Fusion and Plasma Physics. 16th Euro. Conf., Venice, 13–17 March 1989. Contributed papers. Part I of IV.
European Physical Society, 1989. pp.I–131 – I–134.

113. Operational experience of JET surface physics diagnostics.
Hancock C J, Jakob D, Neill G F, Prior P, Nicholson C, Stevens A L, Vince J.
Procs. 15th Symp. on Fusion Technology, Utrecht, The Netherlands, 19–23 September 1988.
Amsterdam, North–Holland. 1989. Vol.1, pp.309–313. Report JET–P(88)69, pp.31–35.

114. Analysis of effect of Be gettering on X–point plasmas.
Harbour P J, Denne B, Erents S K, Gottardi N, Mast K, Morgan P D, Reichle R, Stamp M F, Summers D D R, Tagle J A, Tanga A.
American Physical Society. Bulletin. vol.34 no.9 October 1989 (Program of the 31st Annual Meeting of the Division of Plasma Physics, Anaheim, Calif., 13–17 November 1989). p.2054.

115. The X–point scrape–off plasma in JET with

beryllium evaporation.
Hawkes N C, Barnsley R, Denne B,
Giannella R, von Hellermann M, Lawson K,
Morgan P, Peacock N, Stamp M, Thomas P,
Weisen H.
American Physical Society. Bulletin. vol.34 no.9
October 1989 (Program of the 31st Annual
Meeting of the Division of Plasma Physics,
Anaheim, Calif., 13 17 November 1989). p.1980.

117.Transport studies during sawteeth and H-modes
on JET using laser ablation.
Hawkes N C, Wang Z, Barnsley R, Behringer K,
Cohen S, Denne B, Edwards A, Giannella R,
Gill R, Magyar G, Pasini D, Peacock N J,
Schumacher U, Vieider C, Zasche D.
Controlled Fusion and Plasma Physics. 16th Euro.
Conf., Venice, 13 17 March 1989. Contributed
papers. Part I of IV. European Physical Society,
1989. pp.I 79 I 82.
Report JET P(89)03, pp.85 88.

118.Fast wave antenna coupling to slow waves and ion
L- and H-modes.
Harbour P J, Summers D D R, Clement S, Coad J P,
de Kock L, Ehrenberg J, Erents S K, Gottardi N,
Hubbard A, Keilhacker M, Morgan P D, Snipes J A,
Stamp M F, Tagle J E, Tanga A, Behrisch R,
Wang W-M.
Journal of Nuclear Materials vols.162–164 April (I)
1989 (Procs. 8th Int. Conf. on Plasma–Surface
Interactions in Controlled Fusion Devices,
Julich, FRG, 2–6 May 1988) pp.236–244.
Report JET-P(88)70, pp.138–159.

116. Impurity behaviour and transport in JET following
Bernstein waves during ICRF heating of tokamak
plasmas.
Heikkinen J A, Bures M.
Joint European Torus JET. May 1989. 25p.
Report JET-P(89)40 Paper submitted to Plasma
Physics and Controlled Fusion.

119. Non–linear power conversion by non–resonant
parametric decay of the fast wave
during ICRF heating.
Heikkinen J A, Avinash K.
Nuclear Fusion vol.29 no.8 August 1989
pp.1307–1317. Report JET-P(89)29

120. Electrostatic Wave Generation by the Faraday
Shield in ICRF Heating
Heikkinen J A.
Report JET-P(89)74

121. A modelling scheme for the direct electron heating
profiles during ion cyclotron resonance heating.
Hellsten T, Eriksson L–G.

Nuclear Fusion vol.29 no.12 December 1989
pp.2165–2173.
Report JET-P(89)28

122. Resonant ion diffusion in ICRF–heated tokamak
plasmas.
Hellsten T.
Plasma Physics and Controlled Fusion vol.31 no.9
August 1989 pp.1391–1406. Report JET-P(88)41

123. The cryogenic diffusion pump and its
implementation in a complete fusion reactor fore
vacuum system.
Hemmerich J L, Kussel E.
Joint European Torus JET. June 1989. 13p.
Report JET-P(89)43 Paper submitted to J. Vac. Sci.
Technol. A.

124. Key components of the JET active gas handling
system– experimental programme and test results.
Hemmerich J L, Dombra A H, Gowman J,
Groskopfs E, Haange R, Konstantellos A, Kussel E,
Lasser R, Milverton P, Walker K, Walter K.
Procs. 15th Symp. on Fusion Technology, Utrecht,
The Netherlands, 19–23 September 1988.
Amsterdam, North–Holland. 1989. Vol.1, pp.93–100.
Also in Fusion Engineering and Design, vol.11
nos.1&2 June/July 1989 (Invited papers of the 15th
SOFT, Utrecht, 1988). pp.93–100.
Report JET-P(88)63.

125. A study of the seizure problem with high– current
filament feedthroughs in plasma generators.
Hemsworth R S, Altman H, Hurford D.
Review of Scientific Instruments vol.60 no.4
April 1989 pp.588–591.

Report JET-P(88)25

126. Empirical evaluation of three–electron
quantum–electrodynamics effects from lithiumlike
resonance lines of elements Z = 22–42 in the
Tokamak Fusion Test Reactor and Joint European
Torus tokamaks.
Hinnov E, Denne B.
Physical Review A. General Physics vol.40 no.8
15 October 1989 pp.4357–4360.
Report JET-P(89)30

127. Design of a Thomson scattering diagnostic system to
measure fast ion– and alpha–particle distributions
in JET.
Hoekzema J A, Costley A E, Hughes T P,
Hammond N P, Barkley H J, Kasparek W,
Muller G A, Rebuffi L, Schuller P G, Thumm M.
Procs. 15th Symp. on Fusion Technology, Utrecht,
The Netherlands, 19–23 September 1988.
Amsterdam, North–Holland. 1989. Vol.1,
pp.314–318. Report JET-P(88)69, pp.83–87.

128. The design, construction, installation and testing
of a boost amplifier for the vertical field power
supply of JET.
Huart M, Basile G L, Ciscato D, Buc O, Goff J K.
Procs. 15th Symp. on Fusion Technology, Utrecht,
The Netherlands, 19–23 September 1988.
Amsterdam, North–Holland. 1989. Vol.1,
pp.330–336. Report JET–P(88)69, pp.52–58.

129. Effects of plasma dielectric properties on Thomson
scattering of millimetre waves in tokamak plasmas.
Hughes T P, Smith S R P.
Joint European Torus JET. 1989. 42p.
Report JET–P(89)13, Journal of Plasma Physics
Vol. 42, pp. 215–240, (1989).

130. Physics aspects of a Thomson scattering diagnostic
for fast ion and alpha particle velocity
distributions in JET.
Hughes T P, Boyd D A, Costley A E,
Hoekzema J A, Smith S R P, Westerhof E.
Controlled Fusion and Plasma Physics. 16th Euro.
Conf., Venice, 13–17 March 1989. Contributed
papers. Part IV. European Physical Society, 1989.
pp.IV–1509 – IV–1512.
Report JET–P(89)03, pp.73–76.

131. Behaviour of chaotic magnetic field lines in a
periodic system (Tokamak).
Hugon M, Mendonca J T, Rebut P–H.
Comptes Rendus. Series II. In French vol.308 1989
pp.1319–1325.
Report JET–P(89)14

132. A comparison between beryllium and graphite as
materials for JET limiters and wall surfaces.
Hugon M, Lallia P P, Rebut P H.
Joint European Torus JET. 1989. 22p.
Report JET–R(89)14

133. Study of the behaviour of chaotic magnetic field lines
in a tokamak.
Hugon M, Mendonca J T, Rebut P H.
Controlled Fusion and Plasma Physics. 16th Euro.
Conf., Venice, 13–17 March 1989. Contributed
papers. Part I of IV. European Physical Society,1989.
pp.I–271 – I–274. Report JET–P(89)03, pp.37–40.

134. JET progress towards D–T operation.
Huguet M, Bertolini E.
JET Team Fusion Technology vol.15 no.2 pt.2A
March 1989 (Procs. 8th Topical Meeting on the
Technology of Fusion Energy, Salt Lake City, Utah,
9–13 October 1988) pp.245–258.

135. Ballooning stability of JET discharges.
Huysmans G T A, Galvao R M O, Goedbloed J P,
Lazzaro E, Smeulders P.

Plasma Physics and Controlled Fusion vol.31 no.14
December 1989 pp.2101–2110. Report JET–P(89)34.

136. Effect of Beryllium Evaporation on the performance
of ICRN on JET,
by J. Jacquinot et al.
Report JET-P(89)85

137. Enhanced JET performance after beryllium
evaporation.
Jacquinot J
Plasma Physics and Controlled Fusion. News Sheet
no.14 September 1989 p.1.

138. Determination of deuterium concentrations in JET
plasmas from fusion reaction rate measurements.
Jarvis O N, Adams J M, Balet B, Conroy S,
Cordey J G, Elevant T, Morgan P D, Sadler G,
Watkins N, Van Belle P
Controlled Fusion and Plasma Physics. 16th Euro.
Conf., Venice, 13–17 March 1989. Contributed
papers. Part I of IV. European Physical Society,
1989. pp.I–15 – I–18.
Report JET–P(89)03, pp.1–4.

139. Determination of deuterium concentrations in
JET plasmas.
Jarvis O N, Adams J M, Balet B, Conroy S,
Cordey J G, Elevant T, Gill R D, Loughlin M J,
Mandl W, Morgan P D, Pasini D, Salder G,
Watkins N, van Belle P, von Hellermann M,
Weisen H.
Joint European Torus JET. 1989. 15p.
Report JET–P(89)55
Paper submitted to Nuclear Fusion.

140. Photoneutron production accompanying plasma
disruptions in JET.
Jarvis O N, Sadler G, Thompson J L.
Nuclear Fusion vol.28 no.11 November 1988
pp.1981–1993.

141. High performance neutral beam heated plasmas in
JET with beryllium gettering.
Jones T T C, Bickley A, Challis C, de Esch H,
Lomas P, Stork D, Thompson E.
American Physical Society. Bulletin. vol.34 no.9
October 1989 (Program of the 31st Annual Meeting
of the Division of Plasma Physics, Anaheim, Calif.,
13–17 November 1989). p.2054.

142. Experimental determination of plasma–surface
interactions in JET in respect of recycling, pumping
and fuelling efficiency.
Jones T T C, Cuthbertson J W, Ehrenberg J ,
Gondhalekar A, Morgan P D, Tagle T A.
Journal of Nuclear Materials vols.162–164 April (I)
1989 (Procs. 8th Int. Conf. on Plasma–Surface
Interactions in Controlled Fusion Devices,

Julich, FRG, 2–6 May 1988) pp.503–508.
Report JET–P(88)70, pp.118–137.

143. Improved confinement in L–mode JET plasmas.
Jones T T C, Balet B, Bhatnagar V, Boyd D,
Bures M, Campbell D J, Christiansen J P,
Cordey J G, Core W F, Corti S, Costley A E,
Cottrell G A, Edwards A, Ehrenberg J, Jacquinot J,
Lallia P, Lomas P J, Lowry C, Malacarne M,
Muir D G, Nave M F, Nielsen P, Sack C, Sadler G,
Start D F H, Taroni A, Thomas P R, Thomsen K.
Controlled Fusion and Plasma Physics. 16th Euro.
Conf., Venice, 13–17 March 1989. Contributed
papers.
Part I of IV. European Physical Society, 1989.
pp.I–11 –I–14. Report JET–P(89)03, pp.141–144.

144. On global H–mode scaling laws for JET.
Kardaun O, Thomsen K, Christiansen J, Cordey J,
Gottardi N, Keilhacker M, Lackner K, Smeulders P,
JET Team.
Controlled Fusion and Plasma Physics. 16th Euro.
Conf., Venice, 13–17 March 1989. Contributed
papers. Part I of IV. European Physical Society,
1989. pp.I–253 – I–256.

145. The design of the JET lower hybrid launcher.
Kaye A S, Brinkschulte H, Evans G, Gormezano C,
Jacquinot J, Knowlton S, Litaudon X, Moreau D,
Pain M, Plancoulaine J, Walker C, Wilson G.
Procs. 15th Symp. on Fusion Technology, Utrecht,
The Netherlands, 19–23 September 1988.
Amsterdam, North–Holland. 1989. Vol.1,
pp.449–453.

146. The JET H–mode at high current and power levels.
Keilhacker M (presenter) and JET Team
Plasma Physics and Controlled Nuclear Fusion
Research. 12th Int. Conf., Nice, 12–19 October 1988.
Vol.1. Vienna, IAEA. 1989. pp.159–181.

147. Overview of JET results using a beryllium first wall.
Keilhacker M and the JET Team
American Physical Society. Bulletin. vol.34 no.9
October 1989 (Program of the 31st Annual Meeting
of the Division of Plasma Physics, Anaheim, Calif.,
13–17 November 1989).
Report JET-P(89)83

148. Ion optics calculations for tritium injection into JET.
Kirby P, Goede A P H, Papastergiou S.
Nuclear Instruments and Methods in Physics
Research. Section A: Accelerators, Spectrometers,
Detectors, and Associated Equipment vol.A281 no.1
20 August 1989 pp.176–183.
Report CLM–P 860.

149. The JET multi–pellet injector and its
future upgrades.
Kupschus P, Sonnenberg K, Bailey W,
Gadeberg M, Hardaker J, Hedley L, Helm J,
Flory D, Twynam P, Szabo T, Zacchia F.
Joint European Torus JET. April 1989. 6p.
Report JET–P(89)16
Paper submitted for publication in Procs. of IAEA
Technical Committee Meeting on Pellet Injection
and Toroidal Confinement, Gut Ising, FRG,
24–26 October 1988.

150. Three papers presented at the Course and Workshop
on Tritium and Advanced Fuels in Fusion Reactors,
Varenna, 6–15 September 1989.
Kupschus P, Haange R, Dombra A, and others
Joint European Torus JET. 1989. 87p.
Report JET–P(89)66

151. Upgrading the JET magnet systems for 7MA plasma.
Last J R, Bertolini E, Huguet M, Mondino P L,
Noll P, Sonnerup L, Bell C, Molyneaux T.
Fusion Technology vol.15 no.2 pt.2A March 1989
(Procs. 8th Topical Meeting on the Technology of
Fusion Energy, Salt Lake City, Utah, 9–13 October
1988) pp.267–274.
Report JET–P(88)43, pp.23–30.

152. Bifurcated tokamak equilibria with vanishing edge
current density.
Lazzaro E, Shchepetov S V.
Joint European Torus JET. April 1989. 13p.
Report JET–P(89)17 Paper submitted for
publication in Physics Letters.

153. Relaxation model of H–modes in JET.
Lazzaro E, Avinash K, Gottardi N, Smeulders P.
Plasma Physics and Controlled Fusion vol.31 no.8
July 1989 pp.1199–1214.

154. Coupling of slow waves near the lower hybrid
frequency in JET: implications for the
launcher design.
Litaudon X, Moreau D.
Joint European Torus JET. 1989. 23p.
Report JET–R(89)02

155. The swan coupling code: user's guide.
Litaudon X, Moreau D.
Joint European Torus JET. November 1988. 46p.
Report JET–R(89)01

156. JET latest results.
Lomas P J (presenter) and JET Team
Joint European Torus JET. February 1989. 8p.
Report JET–P(89)09 Paper submitted for
publication in Plasma Physics and Controlled
Fusion.

157. An overview of JET results.
Lomas P J (presenter) and JET Team

Plasma Physics and Controlled Fusion vol.31 no.10 August 1989 (Controlled Fusion and Plasma Physics: 16th European Physical Society Plasma Physics Division Conf., Venice, 13–17 March 1989.) pp.1481–1496. Report JET–P(89)36

158. Heat Pulse Analysis in Jet Limiter and X-Point Plasmas.
Lopez-Cardoza N J and de Haas J C M.
Report JET-P(89(78

159. Consequences of trapped beam ions on the analysis of neutron emission data.
Loughlin M J, Adams J M, Hawkes N, Hone M, Jarvis O N, Laundy B, Sadler G, Syme D B, Watkins N, Van Belle P
Controlled Fusion and Plasma Physics. 16th Euro. Conf., Venice, 13–17 March 1989. Contributed papers. Part I of IV. European Physical Society, 1989. pp.I–83 – I–86.
Report JET–P(89)03, pp.13–16.

160. Measurement of the fractional thermonuclear neutron yield during deuterium neutral–beam injection into deuterium plasmas.
Loughlin M J, Van Belle P, Hawkes N P, Jarvis O N , Sadler G, Syme D B.
Nuclear Instruments and Methods in Physics Research.
Section A: Accelerators, Spectrometers, Detectors, and Associated Equipment vol.A281 no.1 20 August 1989 pp.184–191.
Report JET–P(89)10.

161. Measurement of the Response Function of an³He Ionization Chamber to Monoenergetic Neutrons in the Energy Range 2-3MeV.
Loughlin M J et al.
Report JET-P(89)73

162. Density limits in JET with evaporated beryllium. ()
Lowry C G, de Kock L, Ehrenberg J, Gondhalekar A, Gottardi N, Lomas P J, Mast F, Tanga A, Thomas P R, Tubbing B
American Physical Society. Bulletin. vol.34 no.9 October 1989 (Program of the 31st Annual Meeting of the Division of Plasma Physics, Anaheim, Calif., 13–17 November 1989). p.2054.

163. The hot ion mode of small bore plasmas in JET.
Lowry C G, Boyd D A, Challis C D, Christiansen J P, Cordey J G, Cottrell G A, Edwards A W, Jones T T C, Lallia P P, Nielsen P, Sadler G, Schmidt G, Start D F H, Stork D, Thomas P R, Tubbing B.
Controlled Fusion and Plasma Physics. 16th Euro. Conf., Venice, 13–17 March 1989. Contributed papers. Part I of IV. European Physical Society,

1989. pp.I–87 – I–90.
Report JET–P(89)03, pp.65–68.

164. Plasma surface interactions at the JET X–point tiles.
Martinelli A P, Behrisch R, Coad J P, de Kock L.
Controlled Fusion and Plasma Physics. 16th Euro. Conf., Venice, 13–17 March 1989. Contributed Papers. Part III. European Physical Society, 1989. pp.III–943 – III–946.
Report JET–P(89)03, pp.161–164.

165. Alignment of the JET high power particle beams.
Massmann P, Deschamps G H, Falter H D, Hemsworth R S, Meinberger A.
Procs. 15th Symp. on Fusion Technology, Utrecht, The Netherlands, 19–23 September 1988. Amsterdam, North–Holland. 1989. Vol.1, pp.578–582. Report JET–P(88)69, pp.59–63.

166. Contributions from ion–atom charge–exchange collisions to the C VI Lyman–series intensities in the Joint European Torus tokamak.
Mattioli M, Peacock N J, Summers H P, Denne B, Hawkes N C.
Physical Review A. General Physics vol.40 no.7 1 October 1989 pp.3886–3897. Report JET–P(89)06

167. Distribution of erosion and deposition on the JET belt limiters.
McCracken G M, Behrisch R, Coad J P, Goodall D H J, Harbour P, de Kock L, Pick M A, Pitcher C S, Roth J, Stangeby P C
Controlled Fusion and Plasma Physics. 16th Euro. Conf., Venice, 13–17 March 1989. Contributed Papers. Part III. European Physical Society, 1989. pp.III–947 – III–950.
Report JET–P(89)03, pp.129–132.

168. Erosion and deposition processes in tokamaks.
McCracken G M, Stangeby P C, Goodall D H J, Pitcher C S.
Fusion Engineering and Design vol.11 nos.1&2 June/July 1989 (Invited papers of the 15th Symp. on Fusion Technology (SOFT), Utrecht, The Netherlands, 19–23 September 1988). pp.151–166.

169. Erosion and redeposition at the JET limiters.
McCracken G M, Goodall D H J, Stangeby P C, Coad J P, Roth J, Denne B, Behrisch R.
Journal of Nuclear Materials vols.162–164 April (I) 1989 (Procs. 8th Int. Conf. on Plasma–Surface Interactions in Controlled Fusion Devices, Julich, FRG, 2–6 May 1988) pp.356–362.
Report JET–P(88)70, pp.31–46.

170. Experimental search for 'cold fusion' in the deuterium–titanium system.

McCracken G M, Croft S, Gibson A, Jarvis O N,
Powell B A, Sene M, R van Belle P, Bailey M,
Findlay D J S, Govier R P, Milton H J, Sadler G,
Sweetman D R, Watson H H H.
Culham Laboratory. 1989. 13p.
Report CLM–P864.

171. Thermal effects in drift–tearing modes.
Mendonca J T
Joint European Torus JET. May 1989. 13p.
Report JET–P(89)37 Submitted to Plasma Physics
and Controlled Fusion.

172. Stability of $m_0=1$ modes in the reconnecting regime.
Migliuolo S, Coppi B, Pegoraro F, Porcelli F.
American Physical Society. Bulletin. vol.34 no.9
October 1989 (Program of the 31st Annual Meeting
of the Division of Plasma Physics, Anaheim, Calif.,
13–17 November 1989). p.2162.

173. Summary of energy and particle confinement in
pellet–fuelled, auxiliary–heated discharges on JET.
Milora S L, Bartlett D V, Baylor L R, Behringer K,
Campbell D J, Charlton L, Cheetham A, Cordey J G,
Corti S, Gadeberg M, Galvao R, Gondhalekar A,
Gottardi N A, Granetz R, Hammett G,
von Hellermann M, Hirsch K, Hogan J T,
Houlberg W A, Jarvis O N, Jennigan T C,
Kupschus P, Lee G S, Morgan P, Phillips C K,
O'Rourke J, Sadler G, Schmidt G L, Snipes J,
Stubberfield D, Taroni A, Tubbing B, Weisen H.
Controlled Fusion and Plasma Physics. 16th Euro.
Conf., Venice, 13–17 March 1989. Contributed
papers. Part I of IV. European Physical Society,
1989. pp.I–91 – I–94.
Report JET–P(89)03, pp.153–156.

174. Maximum entropy tokamak configurations.
Minardi E, Lampis G.
Joint European Torus JET. 1989. 18p. Report
JET–R(89)10.

175. Thresholds for H–transitions.
Minardi E
Joint European Torus JET. July 1989. 21p.
Report JET–P(89)50 Paper submitted to Plasma
Physics and Controlled Fusion.

176. Fluid Flow-like Order-Disorder Transition in Non-
Integrable Hamiltonian Systems.
Montvai A and Düchs D F
Report JET-R(89)75

177. Studies of visible impurity radiation from JET
plasmas during heating and fuelling experiments.
Morgan P D, Boileau A, Forrest M J,
von Hellermann M, Horton L, Mandl W,
Stamp M F, Summers H P, Weisen H, Zinoview A.
Controlled Fusion and Plasma Physics. 16th Euro.
Conf., Venice, 13–17 March 1989. Contributed
papers. Part I of IV. European Physical Society,
1989. pp.I–95 – I–98.
Report JET–P(89)03, pp.105–108.

178. Fishbone–like events in JET.
Nave M F F, Campbell D, Joffrin E, Pegoraro F,
Porcelli F, Smeulders P, Thomsen K.
Controlled Fusion and Plasma Physics. 16th Euro.
Conf., Venice, 13–17 March 1989. Contributed
papers. Part II. European Physical Society, 1989.
pp.II–505 – II–508.
Report JET–P(89)03, pp.149–152.

179. Forces on the JET vacuum vessel during disruptions
and consequent operational limits.
Noll P, Sonnerup L, Froger C, Huguet M, Last J.
Fusion Technology vol.15 no.2 pt.2A March 1989
(Procs. 8th Topical Meeting on the Technology of
Fusion Energy, Salt Lake City, Utah, 9–13 October
1988) pp.259–266.

180. Conceptual design of plasma exhaust cryopumping
in NET.
Obert W, Perinic D.
Procs. 15th Symp. on Fusion Technology, Utrecht,
The Netherlands, 19–23 September 1988.
Amsterdam, North–Holland. 1989. Vo 181.

181. Cryopumping in the active (D/T) phase of JET.
Obert W.
Procs. 15th Symp. on Fusion Technology, Utrecht,
The Netherlands, 19–23 September 1988.
Amsterdam, North–Holland. 1989. Vol.1,
pp.781–785.

182. Performance of the cold ejector of the JET cryoplant.
Obert W, Mayaux C, Hemsworth R, Jones A,
Parfitt A, Peel T, Ziegler B.
Joint European Torus JET. July 1989. 8p.
Report JET–P(89)54
Paper submitted to Advances in Cryogenic
Engineering, Procs. of CEC Conf.

183. Studies of neutron source fractions from NBI–heated
discharges in JET.
Olsson M, von Belle P, Elevant T, Sadler G.
American Physical Society. Bulletin. vol.34 no.9
October 1989 (Program of the 31st Annual Meeting
of the Division of Plasma Physics, Anaheim, Calif.,
13–17 November 1989). p.2057.

184. Ballooning stability analysis of JET
H–modes discharges.
O'Brien D P, Bishop C M, Galvao R, Keilhacker M,
Lazzaro E, Watkins M L.
Controlled Fusion and Plasma Physics. 16th Euro.
Conf., Venice, 13–17 March 1989. Contributed

papers. Part I of IV. European Physical Society,
1989. pp.I–229 – I–232.
Report JET–P(89)03, pp.145–148.

185. Extended variable representations.
Pegoraro F.
American Physical Society. Bulletin. vol.34 no.9
October 1989 (Program of the 31st Annual Meeting
of the Division of Plasma Physics, Anaheim, Calif.,
13–17 November 1989). p.1976.

186. Extended variable representation.
Pegoraro F
Physics Letters A vol.142 nos.6,7 18 December
1989 pp.384–388. Report JET–P(89)47

187. Limit on beta(sub p) due to global modes in ignited
plasmas.
Pegoraro F, Porcelli F, Coppi B, Migliuolo S.
Controlled Fusion and Plasma Physics. 16th Euro.
Conf., Venice, 13–17 March 1989. Contributed
papers. Part I of IV. European Physical Society,
1989. pp.I–275 – I–278.
Report JET–P(89)03, pp.33–36.

188. Plasma modes, periodicity and symplectic structure.
Pegoraro F.
Joint European Torus JET. May 1989. 22p.
Report JET–P(89)41 Paper submitted for
publication in Festschrift Volume in Honour of Prof.
L A Radicati, Scuola Normale Superiore, 1989.

189. Theory of sawtooth stabilisation in the presence of
energetic ions.
Pegoraro F, Porcelli F, Coppi B, Detragiache P,
Migliuolo S.
Plasma Physics and Controlled Nuclear Fusion
Research. 12th Int. Conf., Nice, 12–19 October 1988.
Vol.1. Vienna, IAEA. 1989. pp.243–250.
Report JET–P(88)78, pp.122–129.

190. Detailed structure of the q profile around q=1 in JET.
Pegourie B, Dubois M A, Gill R D.
Controlled Fusion and Plasma Physics. 16th Euro.
Conf., Venice, 13–17 March 1989. Contributed
papers. Part II. European Physical Society, 1989.
pp.II–533 – II–536.

191. Full power operation at JET: consequences for
in–vessel components.
Pick M A, Celentano G, Deksnis E, Dietz K J,
Froger C, Hugon M, Huguet M, Rebut P H,
Shaw R, Sonnerup L, Stott P.
Procs. 15th Symp. on Fusion Technology, Utrecht,
The Netherlands, 19–23 September 1988.
Amsterdam, North–Holland. 1989. Vol.1,
pp.776–780. Report JET–P(88)69, pp.36–40.

192. Integrated engineering design of new in–vessel

components.
Pick M A, Celentano G, Dietz K J, Froger C,
Rossi L, Shaw R, Sonnerup L.
Procs. 15th Symp. on Fusion Technology, Utrecht,
The Netherlands, 19–23 September 1988.
Amsterdam, North–Holland. 1989. Vol.1,
pp.771–775. Report JET–P(88)69, pp.41–45.

193. Calibration of neutron yield activation measurements
at Joint European Torus.
Pillon M, Martone M, Jarvis O N, Kallne J.
Fusion Technology vol.15 no.3 May 1989
pp.1420–1429.

194. Calibration of neutron yield activation measurement
at JET using MCNP and furnace neutron
transport codes.
Pillon M , Verschuur K A, Jarvis O N, Kallne J,
Martone M.
Fusion Engineering and Design vol.9 May 1989
(Procs. 1st Int. Symp. on Fusion Nuclear
Technology, ,Tokyo, 10–19 April 1988. Part B).
pp.347–352.

195. Neutron energy spectrum determination near the
surface of the JET vacuum vessel using the multifoil
activation technique.
Pillon M, Jarvis O N, Conroy S.
Joint European Torus JET. 1989. 13p.
Report JET–P(89)25 Submitted to Fusion
Technology.

196. Impurity production and transport at the
JET belt limiter.
Pitcher C S, McCracken G M, Stangeby P C,
Summers D D R.
Controlled Fusion and Plasma Physics. 16th Euro.
Conf., Venice, 13–17 March 1989. Contributed
Papers. Part III. European Physical Society, 1989.
pp.III–879 – III–882.
Report JET–P(89)03, pp.121–124.

197. Impurity production and transport at limiters in JET.
Pitcher C S, McCracken G M, Stangeby P C,
Summers D D R.
American Physical Society. Bulletin. vol.34 no.9
October 1989 (Program of the 31st Annual Meeting
of the Division of Plasma Physics, Anaheim, Calif.,
13–17 November 1989). p.2030.

198. Automatic welding and cutting of JET standard joint
configuration.
Presle P, Galbiati L, Raimondi T.
Procs. 15th Symp. on Fusion Technology, Utrecht,
The Netherlands, 19–23 September 1988.
Amsterdam, North–Holland. 1989. Vol.2,
pp.1406–1410. Report JET–P(88)69, pp.88–92.

199. The JET remote maintenance system.
Raimondi T.
Robotics and remote maintenance concepts for
fusion machines. Technical Committee meeting, held
in Karlsruhe, 22–24 February 1988. Vienna, IAEA.
1989. pp.63–74. Report JET–P(88)13, pp.1–12.

200. The JET experience with remote handling equipment
and future prospects.
Raimondi T.
Procs. 15th Symp. on Fusion Technology, Utrecht,
The Netherlands, 19–23 September 1988.
Amsterdam, North–Holland. 1989. Vol.1,
pp.197–208.
Also in Fusion Engineering and Design, vol.11
nos.1&2 June/July 1989 (Invited papers of the 15th
SOFT, Utrecht, 1988). pp.197–208.
Report JET–P(88)64

201. Use of teleoperators and transporters in JET.
Raimondi T, Galbiati L, Jones L P D F.
Robotics and remote maintenance concepts for
fusion machines. Technical Committee meeting, held
in Karlsruhe, 22–24 February 1988. Vienna, IAEA.
1989. pp.115–127.

202. The critical temperature gradient model of plasma
transport: Applications to JET and future tokamaks.
Rebut P H, Lallia P P, Watkins M L.
Plasma Physics and Controlled Nuclear Fusion
Research. 12th Int. Conf., Nice, 12–19 October 1988.
Vol.1. Vienna, IAEA. 1989. pp.191–200.

203. Experience with wall materials in JET and
implications for a future ignited tokamak.
Rebut P H, Dietz K J, Lallia P P.
Journal of Nuclear Materials vols.162–164 April (I)
1989 (Procs. 8th Int. Conf. on Plasma–Surface
Interactions in Controlled Fusion Devices,
Julich, FRG, 2–6 May 1988)
pp.172–183.

204. Future plans for JET and ideas for a
post–JET machine.
Rebut P–H
Joint European Torus JET. August 1989. 30p.
Report JET–P(89)60
Paper submitted to Nuclear Energy Journal.

205. Implications of fusion results for a reactor: a
proposed next step device – JIT.
Rebut P H
Contributed papers presented at 12th Int. Conf. on
Plasma Physics and Controlled Nuclear Fusion
Research, Nice, France, 12–19 October 1988.
Joint European Torus JET. 1988. pp.155–168.

206. JET results and the prospects for fusion.

Rebut P H, Lallia P P.
Procs. 15th Symp. on Fusion Technology, Utrecht,
The Netherlands, 19–23 September 1988.
Amsterdam, North–Holland. 1989. Vol.1, pp.1–21.
Also in Fusion Engineering and Design, vol.11
nos.1&2 June/July 1989 (Invited papers of the 15th
SOFT, Utrecht, 1988). pp.1–21.
Report JET–P(88)58

207. The JET project and its impact on nuclear
fusion research.
Rebut P H.
Joint European Torus JET. 1989. 6p.
Report JET–P(89)20 Invited paper presented to 4th
Euro Physical Society Seminar on International
Research Facilities, Zagreb, Yugoslavia,
17–19 March 1989.

208. A pumped divertor for JET.
Rebut P H and JET Team
American Physical Society. Bulletin. vol.34 no.9
October 1989 (Program of the 31st Annual Meeting
of the Division of Plasma Physics, Anaheim, Calif.,
13–17 November 1989). p.2057.

209. Remote handling in thermonuclear fusion research.
Removille J.
Joint European Torus JET. 1989. 15p.
Report JET–R(89)08 Paper presented at Forum de
Robotique et de Telemanipulation "La Suisse dans
l'Europe" au "Club 44" a la Chaux de Fonds,
18 April 1989. In French.

210. The integration, control and operation of JET remote
handling equipment.
Rolfe A C,
Robotics and remote maintenance concepts for
fusion machines. Technical Committee meeting, held
in Karlsruhe, 22–24 February 1988. Vienna, IAEA.
1989. pp.201–213.

211. Operational aspects of the JET remote
handling system.
Rolfe A C,
Fusion Engineering and Design vol.10 June 1989
(Procs. 1st Int. Symp. on Fusion Nuclear
Technology, Tokyo, 10–19 April 1988. Part C).
pp.501–507. Report JET–P(88)12.

212. A numerical model of the JET poloidal circuit.
Rutter P, Bonicelli T, Santagiustina A, Thomas P R,
Tubbing B.
Procs. 15th Symp. on Fusion Technology, Utrecht,
The Netherlands, 19–23 September 1988.
Amsterdam, North–Holland. 1989. Vol.1,
pp.319–323. Report JET–P(88)69, pp.64–68.

213. Investigations of Fast Particle Behaviour in JET
Plasmas using Nuclear Techniques Sadler G et al
Report JET–P(89)77

214. The Lidar Thomson scattering diagnostic on JET.
Salzmann H, Bundgaard J, Gadd A, Gowers C,
Gusev V, Hansen K B, Hirsch K, Nielsen P,
Reed K, Schrodter C, Weisberg K.
Joint European Torus JET. 1989. 41p.
Report JET-R(89)07

215. The performance of JET PF system for 7MA material
limiter and 5MA magnetic limiter operation.
Santagiustina A, Bertolini E, Bonicelli T, Huart M,
Last J, Lomas P, Marchese V, Mondino P L,
Noll P, Petree F, Raymond C, Tanga A.
Procs. 15th Symp. on Fusion Technology, Utrecht,
The Netherlands, 19–23 September 1988.
Amsterdam, North–Holland. 1989. Vol.1,
pp.324–329. Report JET–P(88)69, pp.46–51.

216. Gas balance measurements at JET.
Sartori R, Saibene G, Hemmerich J L, Pick M A.
Controlled Fusion and Plasma Physics. 16th Euro.
Conf., Venice, 13–17 March 1989. Contributed
Papers. Part III. European Physical Society, 1989.
pp.III–963 – III–966.
Report JET–P(89)03, pp.49–52.

217. Nonlinear analysis of Coulomb relaxation of
anisotropic distributions.
Schamel H, Hamnen H, Duchs D F, Stringer T E,
O'Brien M R.
Physics of Fluids B: Plasma Physics vol.1 no.1
January 1989 pp.76–86.

218. Internal modes in large gyroradii plasma regimes.
Schep T J, Pegoraro F, Porcelli F.
American Physical Society. Bulletin. vol.34 no.9
October 1989 (Program of the 31st Annual Meeting
of the Division of Plasma Physics, Anaheim, Calif.,
13–17 November 1989). p.2060.

219. Sawtooth oscillations in ion cyclotron
emission from JET.
Schild P, Cottrell G A, Dendy R O.
Nuclear Fusion vol.29 no.5 May 1989 pp.834–839.
Report JET–P(88)62.

220. An investigation of the relationship between plasma
size and H–mode energy confinement.
Schissel D P, DeBoo J C, Burrell K H,
Stambaugh R D, Keilhacker M, Stork D, Tanga A,
Thomsen K, Tubbing B J.
American Physical Society. Bulletin. vol.34 no.9
October 1989 (Program of the 31st Annual Meeting
of the Division of Plasma Physics, Anaheim, Calif.,
13–17 November 1989). p.1940.

221. Heating of peaked density profiles produced by
pellet injection in JET.
Schmidt G (presenter) and JET Team
Plasma Physics and Controlled Nuclear Fusion

Research. 12th Int. Conf., Nice, 12–19 October 1988.
Vol.1. Vienna, IAEA. 1989. pp.215–228.

222. Continuously space–resolved X–ray
spectroscopy at JET.
Schumacher U, Kallne E, Morsi H W, Rupprecht G.
Review of Scientific Instruments vol.60 no.4 April
1989 pp.562–566.

223. Simulation of JET boundary plasma in single– null
magnetic configurations.
Simonini R, Taroni A, Harbour P J, Keilhacker M,
Spence J, Rebut P H, Watkins M L.
American Physical Society. Bulletin. vol.34 no.9
October 1989 (Program of the 31st Annual Meeting
of the Division of Plasma Physics, Anaheim, Calif.,
13–17 November 1989). p.2056.

224. Measurements of the electron particle diffusion
coefficient with the JET multichannel reflectometer.
Sips A C C, Costley A E, de Haas J C M,
Prentice R.
Controlled Fusion and Plasma Physics. 16th Euro.
Conf., Venice, 13–17 March 1989. Contributed
papers. Part I of IV. European Physical Society,
1989. pp.I–99 – I–102. Report
JET–P(89)03, pp.89–92.

225. Simultaneous measurements of thermal condictivity
and particle diffusion in JET and their interpretation.
Sips A C C, de Haas J C M, Hogeweij G M D,
Prentice R, Costley A E.
American Physical Society. Bulletin. vol.34 no.9
October 1989 (Program of the 31st Annual Meeting
of the Division of Plasma Physics, Anaheim, Calif.,
13–17 November 1989). p.2055.

226. Density profile determination by function fit with
possibility of hollow and peaked profiles.
Smeulders P, Kardaun O, Christiansen J P, Ellis J,
Gottardi N.
Joint European Torus JET. 1989. 10p.
Report JET–R(89)09

227. High–beta regimes in JET.
Smeulders P, Campbell D, Cheetham A, Gottardi N,
Hender T, Huysmans G, Jacquinot J, Lazzaro E,
Nave F, O'Brien D, Salmon N, Tanga A, Ward D.
American Physical Society. Bulletin. vol.34 no.9
October 1989 (Program of the 31st Annual Meeting
of the Division of Plasma Physics, Anaheim, Calif.,
13–17 November 1989). p.2055.

228. An analysis of plasma ion toroidal rotation during
large amplitude MHD activity in JET.
Snipes J A, Weisen H, de Esch H P L, Galvao R,
Hender T C, Lazzaro E, Stork D,
von Hellermann, Zasche D.
Controlled Fusion and Plasma Physics. 16th Euro.

Conf., Venice, 13–17 March 1989. Contributed
papers. Part II. European Physical Society, 1989.
pp.II–513 – II–516.
Report JET–P(89)03, pp.109–112.

229. Plasma Stored Energy and Momentum Losses
during Large MHD Activity.
Snipes J A et al,
Report JET-P(89)64

230. JET pump limiter.
Sonnenberg K, Deksnis E, Shaw R, Watson R,
Croessmann D, Watkins J, Koski J, Reiter D.
Journal of Nuclear Materials vols.162–164 April (I)
1989 (Procs. 8th Int. Conf. on Plasma–Surface
Interactions in Controlled Fusion Devices,
Julich, FRG, 2–6 May 1988) pp.674–679.

231. Prototype of a high speed pellet launcher for JET.
Sonnenberg K, Kupschus P, Helm J, Flory D,
Zacchia F.
Procs. 15th Symp. on Fusion Technology, Utrecht,
The Netherlands, 19–23 September 1988.
Amsterdam, North–Holland. 1989. Vol.1,
pp.715–719.

232. Particle influx measurements in JET helium plasmas
using a multichannel visible spectrometer.
Stamp M F, Behringer K H, Forrest M J,
Morgan P D, Summers H P.
Journal of Nuclear Materials vols.162–164 April (I)
1989 (Procs. 8th Int. Conf. on Plasma–Surface
Interactions in Controlled Fusion Devices,
Julich, FRG, 2–6 May 1988) pp.404–408.

233. Sputtering measurements on JET using a
multichannel visible spectrometer.
Stamp M F, Forrest M J, Morgan P D,
Summers H P.
Controlled Fusion and Plasma Physics. 16th Euro.
Conf., Venice, 13–17 March 1989. Contributed
papers. Part IV. European Physical Society, 1989.
pp.IV–1513 – IV–1516.
Report JET–P(89)03, pp.45–48.

234. Experimental and theoretical studies of ion cyclotron
heating on JET.
Start D F H, Bhatnagar V P, Boyd D A, Bures M,
Campbell D J, Christiansen J P, Colestock P L,
Cordey J G, Core W, Cottrell G A, Eriksson L G,
Evrard M P, Hellsten T, Jacquinot J, Jarvis O N,
Kissel S, Knowlton S, Lean H W, Lomas P J,
Lowry C, McCarthy A L, Nielsen P, O'Rourke J,
Sadler G, Tanga A, Thomas P R, Thomsen K,
Tubbing B, Van Belle P, Wesson J A.
Plasma Physics and Controlled Nuclear Fusion
Research. 12th Int. Conf., Nice, 12–19 October 1988.

Vol.1. Vienna, IAEA. 1989. pp.593–603.

235. Physics of high power ICRH on JET.
Start D F H, Bhatnagar V P, Bosia G, Boyd D A,
Bures M, Campbell D J, Christiansen J P,
Cordey J G, Cottrell G A, Devillers G,
Eriksson L G, Evrard M P, Heikkinen J A,
Hellsten T, Jacquinot J, Jarvis O N, Knowlton S,
Kupschus P, Lean H, Lomas P J, Lowry C,
Nielsen P, O'Rourke J, Sadler G, Schmidt G L,
Tanga A, Taroni A, Thomas P R, Thomsen K,
Tubbing B, von Hellermann M, Willen U.
Joint European Torus JET. May 1989. 9p.
Report JET–P(89)32
Paper presented at 8th Topical Conf. on Radio
Frequency Power in Plasmas, Irvine, USA,
1–3 May 1989.

236. Confinement of MeV Ions in JET created by ICRN,
Start D F et al.
pp.25–28.

237. Progress towards long pulse steady state
H-modes on JET.
Stork D, Tanga A, Tubbing B, Giannella R,
Gottardi N, Harbour P J, Hawkes N,
Summers D D R.
American Physical Society. Bulletin. vol.34 no.9
October 1989 (Program of the 31st Annual Meeting
of the Division of Plasma Physics, Anaheim, Calif.,
13-17 November 1989). p.2055.

238. Diagnostics for experimental fusion reactors.
Stott P E, Costley A E.
Joint European Torus JET. October 1989. 22p.
Report JET-P(89)68
Lecture presented to Int. School of Plasma Physics,
Varenna, September 1989.

239. Effects of ELMs and impurities on confinement in
DIII D and JET.
Stott P E, DeBoo J C, Petrie T W, St John H,
Schissel D P.
American Physical Society. Bulletin. vol.34 no.9
October 1989 (Program of the 31st Annual Meeting
of the Division of Plasma Physics, Anaheim, Calif.,
13-17 November 1989). p.1940.

240. The JET plasma boundary with limiter and
X-point discharges.
Stott P E (presenter) and JET Team
Journal of Nuclear Materials vols.162-164 April (I)
1989 (Procs. 8th Int. Conf. on Plasma Surface
Interactions in Controlled Fusion Devices, Julich,
FRG, 2-6 May 1988) pp.3-13. Report JET-P(88)34.

241. The Plasma Contamination Efficiency of different
Impurity Generation Mechanisms in Tokamaks.

Strangeby P C and Farrell C.
Report JET-P(89)70.

242. Comparison of predicted and measured heat
transport in JET.
Stringer T E.
Joint European Torus, JET. January 1989. 21p.
Report JET-P(89)01
Paper submitted to the Lausanne Workshop on
Fusion Theory.

243. Current density profile evolution in JET.
Stubberfield P M, Balet B, Campbell D, Challis C D,
Cordey J G, Hammett G, O'Rourke J, Schmidt G L.
Controlled Fusion and Plasma Physics. 16th Euro.
Conf., Venice, 13 17 March 1989. Contributed
papers. Part IV. European Physical Society, 1989.
pp.IV-1255 - IV-1258.
Report JET-P(89)03, pp.25-28.

244. The effect of He and D(sub 2) discharges on the
electron temperature and impurity production in JET.
Tagle J A, Erents S K, McCracken G M, de Kock L,
Stamp M F
JET papers presented at the 8th Int. Conf. on Plasma
Surface Interactions in Controlled Fusion Devices,
Julich, 2-6 May 1988. Joint European Torus JET.
1989. pp.94-117.

245. The effect of different ICRH heating scenarios on the
JET scrape-off layer.
Tagle J A, Erents S K, Bures M, Brinkschulte H,
McCracken G M, de Kock L, Coad J P, Simpson J.
Journal of Nuclear Materials vols.162-164 April (I)
1989 (Procs. 8th Int. Conf. on Plasma-Surface
Interactions in Controlled Fusion Devices, Julich,
FRG, 2-6 May 1988) pp.282-287.

246. Operation at high plasma current in JET.
Tanga A, Bures M, Garribba M, Green B J,
How J, Jacquinot J, Last J, Lomas P, Lowry C G,
Malacarne M, Mantica P, Mondino P L, Noll P,
Rebut P H, Santagiustina A, Schueller F C,
Snipes J, Thomas P R, Tubbing B.
Controlled Fusion and Plasma Physics. 16th Euro.
Conf., Venice, 13-17 March 1989. Contributed
papers. Part I of IV. European Physical Society,
1989. pp.I-103 - I-106.

247. Plasma characteristics of H-mode in JET
with Be gettering.
Tanga A, Bartlett D, Gowers C, Gottardi N,
Jacquinot J, Harbour P, Lazzaro E, Morgan P,
Stork D, Thomsen K, Tubbing B.
American Physical Society. Bulletin. vol.34 no.9
October 1989 (Program of the 31st Annual Meeting
of the Division of Plasma Physics, Anaheim, Calif.,
13-17 November 1989). p.2055.

248. Global power balance and local heat transport in JET.
Taroni A, Balet B, Betello G, Bhatnagar V P,
Christiansen J P, Cordey J G, Corrigan G, Corti S,
Duchs D F, Galvao R, Gorini G, Gottardi N,
von Hellerman M, Han W, Jacquinot J, Kardaun O,
Lallia P P, Lauro-Taroni L, Lomas P J, Muir D,
Rebut P H, Sack C, Schmidt G L, Smeulders P,
Start D F H, Stringer T E, Thomas P R, Thomsen K,
Tibone K, Watkins M L, Weisen H.
Plasma Physics and Controlled Nuclear Fusion
Research. 12th Int. Conf., Nice, 12-19 October 1988.
Vol.1. Vienna, IAEA. 1989. pp.367-376.
Report JET-P(88)78, pp.111-121.

249. Fixed points behaviour in truncated two-
dimensional Navier-Stokes equations.
Tebaldi C.
Joint European Torus JET. January 1989. 11p.
Report JET-P(89)02
Paper submitted for publication in Non Linear
Dynamics.

250. Fast particles in plasma and alpha-particle physics.
Thomas P R.
Joint European Torus JET. May 1989. 17p.
Report JET-P(89)39
Submitted to Plasma Physics and Controlled Fusion.

251. High temperature experiments and fusion
product measurements in JET.
Thomas P R (presenter) and JET Team
Plasma Physics and Controlled Nuclear Fusion
Research. 12th Int. Conf., Nice, 12-19 October 1988.
Vol.1. Vienna, IAEA. 1989. pp.247-255.

252. Offset-linear description of H-mode confinement.
Thomsen K, Callen J D, Christiansen J P,
Cordey J G, Keilhacker M, Muir D G, Watkins M.
Controlled Fusion and Plasma Physics. 16th Euro.
Conf., Venice, 13-17 March 1989. Contributed
papers. Part I of IV. European Physical Society,
1989. pp.I-233 - I-236.
Report JET-P(89)03, pp.69-72.

253. Ion thermal conductivity and convectiveenergy
transport in JET hot-ion regimes and H-modes.
Tibone E, Balet B, Cordey J G, Corrigan G,
Duchs D F, Galway A, Hamnen H, Maddison G,
Sadler G, Stacey W, Stringer T, Stubberfield F,
Watkins M L.
Controlled Fusion and Plasma Physics. 16th Euro.
Conf., Venice, 13-17 March 1989. Contributed
papers. Part I of IV. European Physical Society,
1989. pp.I-283 - I-286.

254. Double null x-point operation in JET with NBI and
ICRH heating.
Tubbing B, Bhatnagar V, Boyd D, Bures M,
Campbell D, Christiansen J, Cordey J, Cottrell G,

Edwards A, Giannella R, Jacquinot J, Keilhacker M,
Lowry C, Lallia P, Muir D, Nielsen P, Start D,
Tanga A, Thomas P, Tibone F.
Controlled Fusion and Plasma Physics. 16th Euro.
Conf., Venice, 13–17 March 1989. Contributed
papers. Part I of IV. European Physical Society,
1989. pp.I-237 – I-240.
Report JET–P(89)03, pp.117–120.

255. H modes in JET with ICRF.
Tubbing B, Bartlett D, Jacquinot J, Lazzaro E,
Stork D, Thomsen K, Tanga A.
American Physical Society. Bulletin. vol.34 no.9
October 1989 (Program of the 31st Annual Meeting
of the Division of Plasma Physics, Anaheim, Calif.,
13–17 November 1989). p.2055.

256. H–mode in JET with ion cyclotron
resonance heating alone.
Tubbing B J D, Jacquinot J J, Stork D, Tanga A.
Nuclear Fusion vol.29 no.11 November 1989
pp.1953–1957.
Report JET–P(89)61

257. Experimental set–up for gas balance
measurement at JET.
Usselmann E, Hemmerich J L, Holland D,
Grobusch L, Schargitz U, Sartori R, Saibene G.
Joint European Torus JET. August 1989. 14p.
Report JET–P(89)51
Lecture presented at 11th Int. Vacuum Congress,
Cologne, 25–29 September 1989.

258. New piezo driven gas inlet valve for
fusion experiments.
Usselmann E, Hemmerich J L, How J, Holland D,
Orchard J, Winkel T, Grobusch L, Schargitz U,
Pocheim N
Procs. 15th Symp. on Fusion Technology, Utrecht,
The Netherlands, 19–23 September 1988.
Amsterdam, North–Holland, 1989. Vol.1,
pp.738–742. Report JET–P(88)69, pp.78–82.

259. Data acquisition at JET - experience and progress.
van der Beken H, Clarke H, Herzog R, Jones E,
Saffert J, Shu Y, Steed C, Wheatley M.
IEEE Transactions on Nuclear Science Vol.36 no.5
October 1989 (6th Conf. on Real-Time Computer
Applications in Nuclear, Particle, and Plasma
Physics, Williamsburg VA, 15-19 May 1989)
pp.1639-1646 Report JET-P(89)27

260. Real time application of transputers for soft X-ray
tomography in nuclear fusion research
van der Goot E, Edwards A W, Holm J.
Joint European Torus JET. June 1989 6p
Report JET-P(89)45
Paper submitted for publication in Procs. of Int.

Conf. on the Application of Transputers, Liverpool
University, 23-25 August 1989

261. Ion temperature profiles in JET
von Hellermann M, Boileau A, Horton L, Mandl W,
Summers H P, Weisen H.
Controlled Fusion and Plasma Physics. 16th Euro.
Conf., Venice, 13-17 March 1989. Contributed
papers. Part I of IV. European Physical Society, 1989
pp.I-107 - I-110. Report JET-P(89)03, pp.113-116

262. Study of light impurities in the JET tokamak
using visible spectroscopy.
von Hellermann M, Boileau A, Hackman J,
Mandl W, Morgan P D, Summers H P, Stamp M F,
Thomas P R, Weisen H.
American Physical Society. Bulletin. Vol.34 no.9
October 1989 (Program of the 31st Annual Meeting
of the Division of Plasma Physics, Anaheim, Calif.,
13-17 November 1989) p.2056

263. The JET ICRF antennae screen: Experience with the
actively cooled nickel screen and design of a
new beryllium screen.
Walker C I, Brinkschulte H, Bures M, Dragomelo N,
Coad J P, Kaye A S, Knowlton S, Plancoulaine J.
Procs. 15th Symp. on Fusion Technology, Utrecht,
The Netherlands, 19-23 September 1988
Amsterdam, North- Holland 1989 Vol.1,
pp.444—448 Report JET-P(88)69, pp.128-132

264. Confinement properties of JET plasmas with
different temperature and density profiles.
Watkins M L, Balet B, Bhatnagar V P, Cordey J G,
Hammett G W, Hellsten T, Keilhacker M,
Milora S L, Morgan P D, Sack C, Schmidt G L,
Taroni A, Thomas P R, Thomsen K, Tibeone F,
von Hellermann M, Weisen H.
Plasma Physics and Controlled Fusion vol.31 no.10
August 1989 (Controlled Fusion and Plasma
Physics: 16th Euro. Phys. Society Plasma Physics
Division Conf., Venice, 13-17 March 1989)
pp.1713-1724 Report JET-P(89)46

265. Some theoretical aspects of diffusion in
cylindrical plasmas
Weenink M P H.
Joint European Torus, JET. September 1988 28p
Report JET-R(88)07

266. Charge exchange spectroscopy measurements of ion
temperature and toroidal rotation in JET
Weisen H , von Hellermann M, Boileau A,
Horton L D, Mandl W, Summers H P.
Nuclear Fusion vol.29 no.12 December 1989
pp.2187-2197 Report JET-P(89)48

267. Disruptions in JET
Wesson J A, Gill R D, Hugon M, Schuller F C,

Snipes J A, Ward D J, Bartlett D V, Campbell D J,
Duperrex P A, Edwards A W, Granetz R S,
Gottardi N A O, Hender T C, Lazzaro E,
Lomas P J, Lopes Cardozo N, Mast K F,
Nave M F F, Salmon N A, Smeulders P,
Thomas P R, Tubbing B J D, Turner M F,
Weller A.
Nuclear Fusion vol.29 no.4 April 1989 pp.641-666
Report JET-P(88)44

268. The sawtooth mystery.
Wesson J A.
Physical Today. Vol. 42., No1. January 1989.
(Plasma Physics reports 1988) pp.s-60 - s -63

269. Leak evaluation in JET and its consequences for
future fusion machines.
Winkle T, Orchard J.
Joint European Torus JET. August 1989. 24p.
Report JET-P(89)57
Paper submitted to Vacuum Journal.

270. Joint European Torus - The building design
and construction.
Woodward C.
Joint European Torus JET. May 1989.33p.
Report JET-P(89)62.
Paper submitted to the Procs. of the Institution
of Civil Engineers, Part II, Research and Theory.

271. Measurement and comparison with theory of
the temperature dependence of satilite to resonance
line ratios of helium-like nickel from JET tokamak.
Zastrow K-D, Kaline E, Summers H P.
Joint European Torus JET. September 1989.20p.
Report JET-P(89)67
Paper submitted to Phys. Rev. A.

272. JET Annual Report, 1988.
JET Joint Undertaking, 1989.
Edited by B.E. Keen, G.W. O'Hara, and A. Stone
EUR-12322-EN,(EUR-JET-ARII)

273. JET Progress Report 1988.
JET Joint Undertaking, 1989.
Edited and compiled by B.E. Keen
EUR 12323-EN(EUR-JET-PR6)

JET
JOINT
UNDERTAKING

PROGRESS
REPORT 1989
Volume II

JET
JOINT
UNDERTAKING
PROGRESS
REPORT 1989
Volume II

Contents

Appendix III

Reprints of JET Papers

A I

Contributed papers to
16th European Conference on Controlled
Fusion and Plasma Physics,
Venice, Italy, 13th–17th March 1989

Many Authors

JET CONTRIBUTED PAPERS TO

16TH EUROPEAN CONFERENCE ON CONTROLLED FUSION AND PLASMA PHYSICS,
VENICE, 13TH-17TH MARCH 1989

DETERMINATION OF DEUTERIUM CONCENTRATIONS IN JET PLASMAS FROM FUSION
REACTION RATE MEASUREMENTS

O N Jarvis, J M Adams[1], B Balet, S Conroy[3], J G Cordey, T Elevant[4],
P D Morgan, G Sadler, N Watkins[1] and P van Belle

JET Joint Undertaking, Abingdon, Oxon, OX14 3EA, UK
[1] Harwell Laboratory, UKAEA, Oxon, OX11 ORA, UK
[4] Imperial College of Science and Technology, London, SW7 2BZ, UK
[1] Royal Institute of Technology, Stockholm, Sweden

ABSTRACT

The concentration of deuterium in the central regions of JET plasmas,
expressed as a fraction of the electron concentration (n_d/n_e), has been
determined using four different methods involving neutron detection. These
measurements are found to be consistent and agree within experimental
errors with values deduced from Z_{eff} measurements using visible
bremsstrahlung radiation.

1.   INTRODUCTION

Fusion reaction rates are determined by the velocity distributions and
densities of the interacting ions. In the case of plasmas in thermal
equilibrium, the velocity distributions are Maxwellian and are determined
by the ion temperature which, in JET, is routinely measured using a variety
of techniques. For the other cases of current interest, involving neutral
deuterium beam injection and the study of the tritons emitted from d-d
fusion reactions, the source velocity distributions are known and the
slowing down distributions are determined by classical Coulomb collisions.
Thus, measurements of the t-d and d-d fusion reaction rates determine the
effective deuterium density. Since the fusion reaction rates are strongly
peaked at the centre of the plasma, the density measured will be
essentially the central density.

2.   DIAGNOSTIC TECHNIQUES

The nuclear measurements can be divided into four classes: studies of
ohmic and ICRF heating, Neutral Beam Heating, Neutral Beam Injection
transient analysis and examination of triton burnup. These various neutron
techniques have to be applied with some circumspection with regard to
plasma operating conditions. For example, high power ICRF heating tuned to
hydrogen may give rise to energetic deuterons through second harmonic
acceleration; the presence of these high energy deuterons is not taken into
account in the analysis, as yet.

1)   Ohmic and ICRF Heating - For this case, the plasma is assumed to be
in thermal equilibrium with the fusion-reaction-rate radial profiles being
described in terms of the magnetic flux surfaces. The central ion
temperature is obtained from several diagnostics including Neutron
Spectrometry [1], Ni x-ray crystal spectrometry [2] and Neutral Particle
Analysis [3]. According to availability, a suitable average of these
measurements is taken. The 2.5 MeV neutron emission profiles are routinely
recorded with the 19 channel profile monitor [4]. A computer code (ORION)
is used to reproduce the experimental line-integrated count-rates by
adjusting a parametrized neutron source profile to the data using a maximum
likelihood technique, assuming a given deuterium density. This density is
then iterated until the central temperature reproduces the independently
measured value. In this way, $n_d(o)/n_e(o)$ is derived.

11)   Neutral Beam Heating - The 2.5 MeV neutron energy spectra from the
central region of the JET plasma are measured using a double-interaction
Time-of-Flight neutron spectrometer [5]. The neutron energy spectra
contain two components, the contribution from thermal (plasma-plasma)
reactions and that from beam-plasma reactions. The thermal contribution is
well-known to be Gaussian with width proportional to $T_i^{1/2}$. The beam-plasma
contribution is more complicated with a shape which depends on geometry and
beam injection energy; it is calculated using the kinematics code FPS [6].
With the shapes of the two contributions known, it is a relatively
straightforward matter to adjust their relative proportions so as to obtain
a good fit to the measured spectrum [7]. In this manner we obtain the
thermal to total neutron production ratio. At this point, we have
sufficient information to be able to invoke the code ORION and to deduce
the central density ratio as was done for Ohmic discharges. It should be
noted that this derivation is but an approximation because (inter alia) the
magnetic flux surfaces are not precise contours of neutron emission in the
case of strong neutral beam heating (beam trapping effects).

111)   Neutral Injection Transient Analysis - This technique exploits the
fact that the slope of the neutron emission rate at beam switch-on (which
is abrupt) is almost entirely due to beam-plasma interactions and is
principally dependent on the beam power, energy and deuterium concentration
n_d/n_e, and only weakly dependent on the electron temperature. The
time-dependent transport code TRANSP [8] is used to enforce agreement
between measurement and prediction at switch-on time by adjusting the
n_d/n_e value. This provides a normalization factor for the Z_{eff} value
obtained from measurements of the visible bremsstrahlung. The adjusted
Z_{eff} is found to have the correct time evolution to provide excellent
agreement between calculated and measured neutron yields for all later
times in the discharge. Only selected discharges have been studied with
TRANSP so far.

1v)   Triton Burnup - The 14 MeV neutron emission from JET plasma is
measured by a combination of techniques; an activation technique provides
the absolute magnitude of the emission whilst a silicon diode technique
provides the time evolution [9,10]. In the present application it is
assumed that the triton burnup is described perfectly by the standard
formulae and any deviations are ascribed to a correction factor to be
applied to Z_{eff}.

v) Z_{eff} from Visible Bremsstrahlung - The results from the neutron
measurements have been compared with the n_d/n_e ratios derived from visible

bremsstrahlung measurements of Z_{eff} for a variety of plasma conditions.
The bremsstrahlung determination involves electron density and temperature
profile information and a knowledge of the plasma geometry. A horizontal
chord through the plasma is used for the standard measurement of Z_{eff}. A
15 chord array is also used to provide a Z_{eff} profile [11]. An n_d/n_e ratio
can be derived from $Z_{eff}(o)$ on the assumption that the major impurities are
carbon and oxygen in the ratio 3:1. However, helium is occasionally
employed for operational reasons but the helium content is not measured.
Furthermore, the hydrogen content is uncertain. Thus the visible
bremsstrahlung measurement really provides the ratio of the sum of
hydrogen, deuterium and helium densities to the electron density and
consequently may overestimate the n_d/n_e ratio. The neutron measurements
provide n_d/n_e ratios to an accuracy of about 20%. The Z_{eff} measurement has
an absolute accuracy of ± 25% but this implies decreasing accuracy for
n_d/n_e as Z_{eff} rises.

3.   CONCLUSION

The various measurements of Z_{eff} and n_d/n_e are presented in Table I
for a list of representative discharges from the operation of JET in 1988.
The time intervals under investigation were those corresponding to the
maximum neutron emission intensities. It is important to note that H-mode
discharges are unusual in having hollow Z_{eff} profiles. Flat profiles were
assumed for the H-mode neutron values quoted within parentheses, in Table
I; these correspond to neutron-weighted rather than central values of
n_d/n_e. The following conclusions can be drawn:

(i)   The neutron measurements agree within their respective errors.
(ii)   The visible bremsstrahlung estimate of n_d/n_e is in broad agreement
with the neutron assessment. A comparison is provided in figure 2.
(iii)   The deuterium concentration is found to vary over the range 0.3 to
1.0, depending on discharge conditions.

REFERENCES

[1]   O N Jarvis et al, Rev Sci Instr 57 (1986) 1717.
[2]   R Bartiromo et al, "The JET High Resolution Bent Crystal
      Spectrometer", JET-P(88)11.
[3]   R Bartiromo et al, Rev Sci Instr 58 (1987) 788.
[4]   J M Adams et al, this conference.
[5]   T Elevant et al, Bull Am Phys Soc 32 (1987) 1870.
[6]   P V Belle and G Sadler, in Basic and Advanced Diagnostic Techniques
      for Fusion Plasmas (Proc Course and Workshop, Varenna 1986), Vol III,
      Rep EUR 10797 EN, CEC (1987) 767.
[7]   M J Loughlin, PhD Thesis, Harwell Laboratory Report HL/1382.
[8]   R J Goldston et al, J Comput Phys 43 (1981) 61.
[9]   S Conroy et al, "Time-Resolved Measurements of Triton Burn-Up in JET
      Plasmas", JET-P(88)16.
[10]   S Conroy et al, this conference.
[11]   P D Morgan, 15th European Conference on Controlled Fusion and Plasma
      Heating, 1988. Europhys. Conf. Abstracts, Vol 12B, Part 1, p139.

TABLE I

| Discharge		Vis. Brem.			Neutron (n_d/n_e)			
Class	Number	$\bar{Z}_{eff}$	$Z_{eff}(o)$	n_h/n_e	Spectra	Tritons	TRANSP	Average
6 and 7MA	17793	3.7	4.6	0.35	0.3	0.4		0.35
Ohmic	17796	3.9	4.9	0.3	0.3	0.35		0.3
He prefill	17797	3.7	4.6	0.35	0.3	0.4		0.35
High T_i	17836	4.2	4.8	0.3	0.4	0.25		0.3
P_{RF}>10MW	17838	4.7	5.4	0.2	0.35	0.25		0.3
High Power	16370	2.6	3.3	0.6	0.4	0.4		0.4
5MA	16382	3.5	4.0	0.45	0.35	0.3		0.3
High T_i	16041	3.0	3.6	0.55	0.35	0.4	0.5	0.45
	16066	4.5	5.2	0.25	≤0.5	-	0.3	0.3
H-Mode	15894	2.1	1.9	0.8	0.65	(0.55)	0.55	0.6
3MA	16259	1.9	2.1	0.8	0.8	(0.55)	(0.35)	0.8
	16268	2.7	3.4	0.75	0.7	(0.45)	(0.35)	0.7
	17933	3.2	2.8	0.7	0.5			0.5
Pellets	16211	1.4	1.7	0.85	0.85			0.85
3MA	16228	1.4	1.7	0.85	1.0			1.0
	16235	1.6	1.9	0.8	0.65			0.65
	17279	1.9	2.3	0.8	0.7			0.7
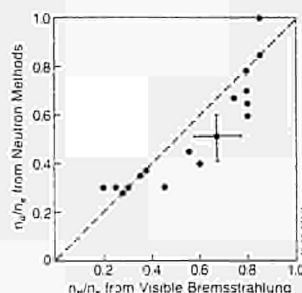
Fig. 1: Comparison of
deuterium concentration
from neutron measurements
with estimates from
Bremsstrahlung
measurements.

Triton burnup in JET

S Conroy¹, J P Argyle², P Batistoni³, E Clipsham, G B Huxtable²
O N Jarvis¹, M Pillon³, S Podda³, M Rapisarda³, G Sadler, P van Belle

JET Joint Undertaking, Abingdon, Oxfordshire OX14 3EA, UK
¹Imperial College of Science, Technology and Medicine, London, SW7 2SZ, UK
²Harwell Laboratory, UKAEA, Oxfordshire OX11 0RA, UK
³ENEA, CRE Frascati, Italy

Abstract

Triton burnup measurements have been made at JET using time-integrated copper activation and time-resolved silicon detector techniques. The results confirm the classical nature of both the confinement and the slowing down of the 1 MeV tritons in a plasma.

Introduction

D-D fusion reactions produce approximately equal quantities of 2.5 MeV neutrons and 1.0 MeV tritons. The 1.0 MeV tritons slow down over a period of order 0.5 second and whilst doing so may undergo a D-T fusion reaction, emitting a 14 MeV neutron. Measurements of both 2.5 MeV and 14 MeV neutrons have been made at JET and are used here to analyse the confinement and thermalisation properties of fast tritons.

Neutron detection

The 2.5 MeV neutron emission is measured with a fission chamber system (1) which is calibrated by direct (ie not activation) techniques to an accuracy of better than ±10%. The time-integrated 14 MeV neutron flux at a point just outside the vacuum vessel is measured through the induced activation of copper foils (2). Neutron transport codes are used to relate the flux to the total yield, with an estimated error of ±15% (3). These codes are also used to relate the induced activation of Indium foils to the 2.5 MeV neutron yields and good agreement is found with the fission chamber results, giving confidence in the accuracy of the codes. Time-resolved 14 MeV neutron emission rates are measured using (n,p) and (n,α) reactions in a 450mm³ silicon diode positioned outside the vacuum vessel. The charged reaction products slow down in the diode generating an output pulse-height spectrum proportional to the energy deposited. By counting only pulses corresponding to an energy of greater than 6 MeV deposited in the diode, a signal proportional to the 14 MeV neutron emission rate is obtained. Finally, cross calibration with the activation system provides an absolute measurement (±20% accuracy).

Previously, one of the main experimental limitations with the silicon diode was the appearance of a breakthrough signal at very high count rates, believed to be due to pile-up of individual signals due to neutrons and gamma-rays (4). In the present apparatus, this effect has been reduced by increasing the maximum count-rate capability of the diode electronics and removing the diode from the immediate vicinity of the plasma, thereby increasing the maximum 2.5 MeV rate at which the diode operates reliably by approximately a factor of 10. This limit now corresponds to a total neutron emission strength of 10¹⁶ n/s.

Data analysis

Analysis of the data is performed by comparison with a simple time-dependent classical model of the 14 MeV neutron emission rate (4). The model uses 10 nested flux surfaces to model the plasma. Each surface has its own triton source rate, electron temperature, electron density and deuterium density which are taken from other diagnostics. Tritons are slowed down on each surface and the 14 MeV neutron emission calculated for each time point, taking into account the temporal variations in the background plasma parameters. When run for stationary (time-independent) problems, the code provides results which are almost indistinguishable from those obtained with the more sophisticated full orbit codes HECTOR and SOCRATE (5,6), demonstrating that the departures of the fast ions from their birth flux surfaces are insignificant for the JET plasmas of interest. The model does not include triton diffusion or sawtooth effects, although these are not thought to be large effects for most of the plasmas studied here.

Results

Fig 1 shows a typical neutral beam heated discharge. The delay in the 14 MeV neutron emission relative to the 2.5 MeV neutron emission agrees well with the model. In order to optimise the fit over a wide range of shots, the energy loss rate has been enhanced by 15% in the model, which is smaller than the estimated error of ±20-25%. This factor is reduced if the ECE temperature data is normalised to the LIDAR electron temperature data, as previously reported (2), however the ECE data are preferred for the time-dependent calculation as they are available with good time resolution. From this we deduce that the triton slowing down process in JET is classical, within experimental errors.

Fig 2 shows the comparison of the time-integrated silicon diode data with the model (including the 15% enhanced energy loss) over a wide range of plasma discharges with $I_p > 3$ MA and $Z_{eff} < 3$. The agreement is good apart from a systematic overestimate by the model of 40%. This is thought to be due in part to errors in the derivation of the deuterium density from Z_{eff} measurements; the same conclusion is obtained from fusion reaction product measurements in general (7). If the absolute 14 MeV neutron emission rates and the model are assumed to be correct then triton burnup may be used to determine the

deuterium density with an accuracy of approximately 20% by dividing the experimentally observed 14 MeV neutron emission rate by the calculated 14 MeV neutron emission rate for a pure deuterium plasma. The technique is of use mainly when $Z_{eff} > 4$ as the errors on the Z_{eff} measurement cause errors of >50% in the n_D/n_e ratio deduced from it. The results of this technique are reported elsewhere at this conference (7).

The confinement of fast tritons during major MHD events has also been investigated. At a normal sawtooth crash, no evidence of triton losses has been found, implying these losses to be <10%. The large crash associated with many pellet shots usually causes no significant losses of tritons. For monster sawteeth just one case has been found where the 14 MeV neutron emission fell abruptly at the crash (fig. 3). For this 3MA combined heating discharge the 2.5 MeV neutron profile monitor (8) shows unusually large inverted sawteeth in the outer regions of the plasma after the crash, indicative of the transport of high energy deuterium ions from the centre of the plasma. A similar movement of tritons could give rise to the observed drop in the 14 MeV neutron emission rate, either due to the loss of tritons from the plasma or by relocation of tritons to regions of lower deuterium dilution.

Conclusions

The combination of the absolutely calibrated activation system and the time-resolved silicon diode provides an accurate measurement of the time-resolved 14 MeV neutron emission rates at JET. The slowing down and burnup of the tritons agrees with a simple classical code, within errors. The confinement of tritons appears very good at JET for plasmas with $I_p > 3$ MA.

References

1. O N Jarvis et al, 'Further calibrations of the time-resolved neutron yield monitor', JET IR(85)06
2. P Batistoni et al, Proc. 15th European Conference on Controlled Fusion and Plasma Physics, Dubrovnik 1988, vol 12B part 1 (1988) 135 et loc cit
3. M Pillon et al, 'Calibration of neutron yield activation measurements at JET using MCNP and FURNACE neutron transport codes ', JET P(88)10
4. S Conroy et al, 'Time-resolved measurements of triton burnup in JET plasmas', JET P(88)16
5. M Kovanen et al, 'HECTOR: a code for the study of high energy charged particles in axisymmetric tokamak plasmas', JET R(88)01
6. G Gorini et al, 'Calculation of the classical triton burnup in JET deuterium plasmas', JET P(87)35
7. O N Jarvis et al, these proceedings
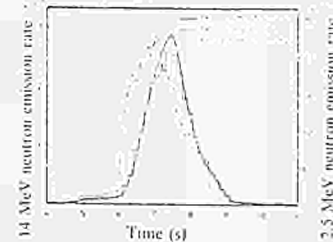8. J M Adams et al, these proceedings

Figure 1. Comparison of calculated 14 MeV neutron emission rates with the experimentally observed rates. The calculation has been normalised to the experimental neutron yield to show the temporal agreement.
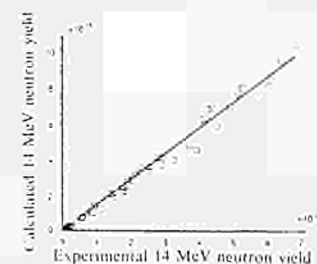

Figure 2. Comparison of experimental and calculated 14 MeV neutron yields for a variety of shots. The straight line is the best fit passing through the origin and has a gradient of 1.4. This discrepancy is thought to be due to an overestimation of the n_D/n_e ratio derived from Z_{eff} measurements.
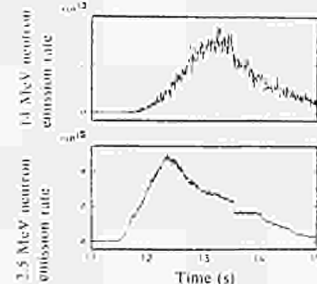

Figure 3. Comparison of experimental 2.5 and 14 MeV neutron emission rates for a discharge with a monster sawtooth at 3.5 seconds. This is the only observation of a sawtooth causing an abrupt drop in the 14 MeV neutron emission rate.

RADIAL PROFILES OF NEUTRON EMISSION FROM OHMIC DISCHARGES IN JET

J M Adams[1], A Cheetham, S Conroy[2], G Gorini[3], N Gottardi, T Iguchi[4],
O N Jarvis, G Sadler, P Smeulders, N Watkins[1] and P van Belle

JET Joint Undertaking, Abingdon, Oxon, OX14 3EA, UK
[1] Harwell Laboratory, UKAEA, Oxon, OX11 ORA, UK
[2] Imperial College of Science and Technology, London, SW7 2BZ, UK
[3] Scuola Normale Superiore, Pisa, Italy
[4] University of Tokyo, Tokyo 113, Japan

ABSTRACT

Neutron emission profiles from several ohmically heated discharges
have been studied using a variety of analytical techniques to extract the
ion temperature profiles which are found to agree well, both in shape and
magnitude, with the electron temperature profiles as measured by the LIDAR
Thomson scattering diagnostic.

INSTRUMENTAL DETAILS

The neutron emission profile measurement diagnostic at JET [1] has
been in routine operation for the past 18 months. It measures the spatial
neutron emission, as a function of time, in a poloidal section through the
JET plasma. The instrument comprises a total of 19 lines-of-sight, with 10
horizontal channels measuring the vertical profile and 9 vertical channels
measuring the horizontal profile. The associated 19 NE213 liquid organic
scintillator detectors, suitably shielded against the high magnetic fields
around JET, are housed in 2 'heavy' concrete fan-shaped multi-collimator
arrays, (or cameras), at a distance 5.5-5.8 m from the centre of the vacuum
vessel. The detector lines-of-sight are shown schematically in figure 1.
An indication of the spatial resolution of the instrument can be given by
considering the individual channel separations at the centre of the plasma;
for the vertical profile this is 22 cm, and for the horizontal profile 18
cm.

Pulse shape discrimination techniques are employed to distinguish
between neutron and γ-ray events in the liquid scintillators. In order to
reduce the backscattered neutron contribution from the vessel walls, a
lower neutron energy bias of 2 MeV is employed. Based on the FURNACE
calculations of Verschuur [2], this results in the backscattered neutron
contribution being $\sim$ 3% of the direct neutron yield in the central channels
of the horizontal camera. A strong ^{252}Cf source placed at the collimator
entrance has been used to show that the "cross-talk" between adjacent
channels is negligible.

The neutron emission data recorded in the individual channel line
integrals were all corrected for the backscattered neutron contribution,
live time, absolute neutron detection efficiency, neutron attenuation and
collimator scattering, and the known collimator solid angles.

Considerable effort has been expended in validating the overall
performance of the instrument, including independent measurements of the
absolute response of the individual detectors. No instrumental defects
were discovered and it is now considered that the experimental data are
essentially correct for the D-D plasma 2.45 MeV neutron emission from ohmic
discharges. The total neutron yields from the time-dependent neutron yield
and neutron profile monitor diagnostics agree to within ± 20%, which is
within the absolute errors of these instruments. Summation of the
measurements over several weeks of operation has been compared with the
integrated profiles obtained with small solid state track detectors located
in the collimators; good agreement between the profile shapes was obtained,
affording a test of the diagnostic for high power additionally heated
discharges.

As a first application of the instrument, a series of ohmic
discharges, with plasma currents between 3 and 6 MA, have been analysed
using several techniques. The objective of this exercise was to compare
the ion temperature profile as derived from the neutron emission data with
the electron temperature profiles provided by the ECE and LIDAR
diagnostics. For these discharges, the neutron data were integrated over
several seconds in order to obtain good statistics and were normalised, in
absolute terms, to the time dependent total neutron yield monitor
diagnostic.

ANALYSIS OF RADIAL PROFILE DATA

Four analytical techniques have been applied to these discharges with
the objective of determining the optimum technique for the particular
circumstances under study. One technique is a forward calculation which
relies on flux surface symmetry and assumes a given neutron emission radial
dependence with parameters optimised by straightforward least squares
fitting of predictions to experimental data. The other three are inversion
techniques: (i) Cormack tomography [3] which makes no assumptions about
the plasma geometry, (ii) Generalised Abel inversion [4] which assumes flux
surface symmetry, and (iii) Constrained Tomography [3] using near-elliptic
contours described by a 4-term polynomial expansion. The results obtained
using these codes were in agreement in all the essential quantities.

(a) Forward Calculations - An example of a fit using this approach is
given in figure 1, showing the deviation between the fit and measurement.
Typically, the deviation from a particular channel is ± 20% which is
greater than the expected channel to channel uncertainty of ± 10%. An
axial ion temperature of $\sim$ 2 keV is obtained for a range of different
source profiles which fit the data equally well.

(b) Cormack Tomography - This method fits the data perfectly because of
the large number of coefficients used, but is very sensitive to
experimental uncertainties. For this reason the other techniques are
preferred for the present instrument which has rather few lines-of-sight.

(c) Generalised Abel Inversion and Constrained Tomography - Figures 2
and 3, respectively, show the reconstructed neutron emission and deduced
ion temperature profiles for a typical ohmic discharge, obtained using both
techniques; the results from the forward calculations are also shown.

These independent analyses lead to a number of interesting
observations: (1) within the uncertainties, the neutron emission is indeed
constrained to the magnetic flux surfaces, (2) the neutron emission
centroid is displaced $\sim$ 5 cm outwards from the magnetic centre (the
accuracy with which the latter is known is ± 7 cm), (3) the deduced neutron
emission profiles are well determined in regions of strong gradient, but
are subject to large uncertainties in the centre (as would be expected for
line-of-sight integrated data), (4) the deduced ion temperature profiles
are more precisely determined, with an absolute uncertainty of up to ± 20%
(mainly due to the n_d/n_e uncertainty as obtained from Z_{eff} determinations),
and (5) the constrained tomography gives ellipticities in good agreement
with the magnetic flux surfaces at large radii.

More generally the central ion temperature obtained from these
neutron measurements is typically 5 to 10% lower than those obtained by the
large crystal X-ray spectrometer [5], but still within the experimental
errors. As shown in figure 3, the ion temperature profiles fall close to
the electron temperature profiles as measured by the LIDAR [6] diagnostic,
at least out to 3.7 m, after which the neutron emission data becomes too
weak to be usable. On the other hand, the ECE [7] temperature profile
seems to be 40% higher, and rather broader. For these ohmic discharges,
the ion-electron equipartition time is much shorter than the energy
confinement time so the temperature difference between electrons and ions
would be expected to be small.

REFERENCES

[1] J M Adams, O N Jarvis, J Källne et al, Controlled Fusion and Plasma
    Heating, (Proc 14th Europ Conf Madrid, 1987), Vol 11D, Part III,
    European Physical Society (1987) 1224.
[2] K A Verschuur, "Furnace Calculations for JET Neutron Diagnostics", ECN
    Report 146 (1983), and private communication.
[3] R S Granetz and P Smeulders, Nuclear Fusion 28 (1988) 457.
[4] N Gottardi, H Krause and K F Mast, Controlled Fusion and Plasma
    Heating (Proc 12th Europ Conf, Budapest, 1985), Vol 9F, Part I,
    European Physical Society (1985) 30.
[5] R Bartiromo et al, "The JET High Resolution Bent Crystal
    Spectrometer", JET-P(88)11.
[6] H Salzmann et al, Nuclear Fusion 27 (1987) 1925.
[7] D V Bartlett et al, Electron Cyclotron Emission and Electron Cyclotron
    Resonance Heating, (Proc. 6th Joint Workshop, Oxford, 1987),
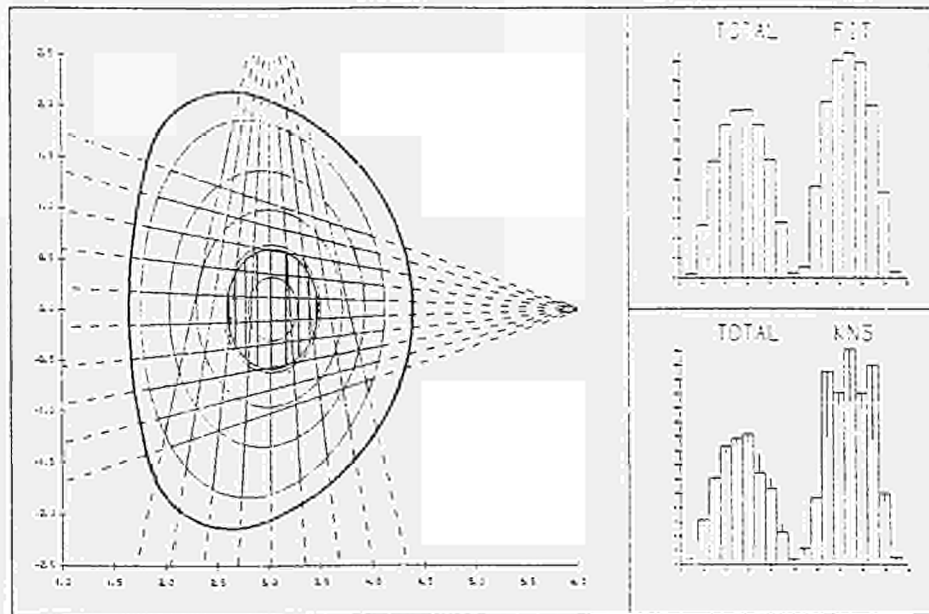   CLM-ECR(1987)137.

Fig.1. Showing the magnetic flux surfaces in the JET tokamak for discharge number 15149 and the 19 lines-of-sight of the profile monitor. The half-width of the neutron emission profile is indicated by the shading. The figures to the right show the predicted best-fit signals in the 19 channels (upper) and the measured signals (lower), where the mismatch is indicated by the vertical bars.
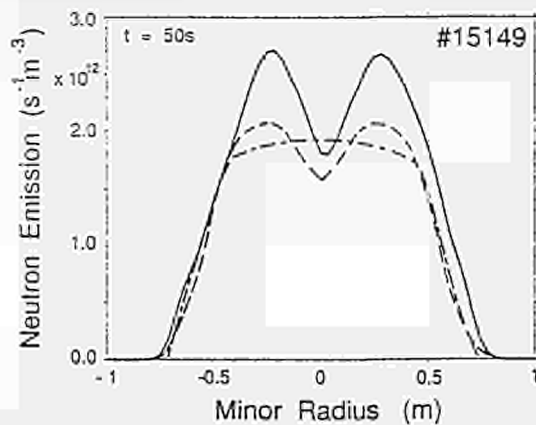

Fig.2. Neutron emission profiles deduced from Generalized Abel Inversion (solid curve), constrained tomography (dashed) and the forward calculation (dot-dashed).
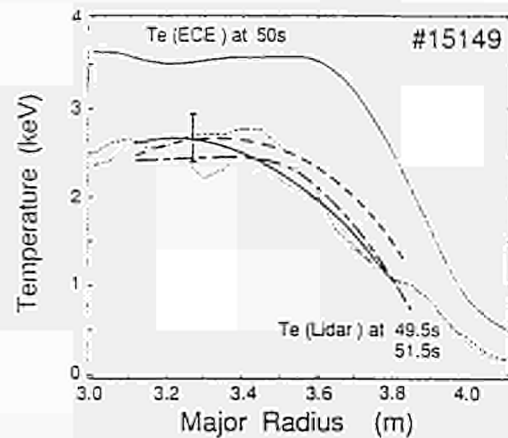
Fig.3. Comparing the three ion temperature profiles deduced from the neutron emission profiles of fig.2 with the electron temperature profiles provided by LIDAR and ECE diagnostics.

A8

CONSEQUENCES OF TRAPPED BEAM IONS ON THE ANALYSIS OF NEUTRON EMISSION DATA

M J Loughlin, J M Adams*, N Hawkes*, M Hone, O N Jarvis, B Laundy,
G Sadler, D B Syme*, N Watkins* and P van Belle

JET Joint Undertaking, Abingdon, Oxon, OX14 3EA, UK
* Harwell Laboratory, Didcot, Oxon, OX11 ORA, UK

ABSTRACT

Neutron energy spectra have been measured during D* neutral beam
heating of deuterium plasmas. The thermonuclear to beam-plasma neutron
production ratios are deduced. For a non-radial spectrometer
line-of-sight, the trapped beam-ion fraction must be considered.

INTRODUCTION

The neutron spectrum from a pure thermonuclear plasma is a gaussian
whose width is determined by Doppler broadening which arises from the
thermal motion of the ions. For a deuterium plasma, the full width at half
maximum (fwhm) of the neutron energy distribution can be related to the ion
temperature T_i according to the equation fwhm = c $\sqrt{T_i}$, (T_i and fwhm in keV)
[1]. The parameter c is weakly dependent on T_i and is approximately equal
to 82.5. This equation is only valid during pure ohmic or low power RF
heating when the ion energy distribution is Maxwellian. This is clearly
not the case during neutral beam injection (NBI). Under these
circumstances the neutron spectrum is very broad ($\sim$ 400 keV) and distinctly
non-gaussian. The detailed shape of the neutron spectrum depends primarily
on the neutral-beam energy and the injection angle, the angle of the
neutron emission and, as will be seen later, the proportion of beam ions in
trapped orbits. At JET, neutron spectra are measured using two
lines-of-sight using two high resolution neutron spectrometers. The first
spectrometer, a ^{3}He ionisation chamber, is positioned in the roof
laboratory, directly above the torus, with a line-of-sight perpendicular to
the magnetic field [2]. The second, a nominally identical detector, is
positioned in the torus hall, inside a massive hydrogenous shield, with a
well collimated line-of-sight in the vessel mid-plane and at approximately
60 degrees to the magnetic field. These spectrometers have been used to
measure the neutron spectra produced during NBI.

NEUTRON SPECTRA DURING NBI

Calculations of neutron spectra have been made for the lines-of-sight
used at JET using the code FSPEC [1]. These show that there are four
distinct spectra which need to be considered (figure 1); (i) the
thermonuclear spectrum which is a gaussian centred at 2.45 MeV with width
of the order of 100-200 keV, (ii) the beam-plasma spectrum emitted in a
direction perpendicular to the magnetic field, also centred at about 2.45
MeV but considerably broader and showing a 'double humped' shape, (iii) the
beam-plasma spectrum produced by beam ions in passing orbits which move
towards the spectrometer, this is similar to that emitted perpendicularly
but shifted up in energy, and (iv) the spectrum which arises from the
trapped beam ions which oscillate towards and away from the detector. This
spectrum is noticeably broader and is peaked at 2.45 MeV.

The spectrometer in the roof laboratory is insensitive to the motion
of the beam ions in the toroidal direction, and is therefore insensitive to
the trapped particles. The observed neutron spectrum is the sum of the
thermonuclear spectrum and the beam-plasma spectrum. The spectrometer in
the torus hall, however, is sensitive to the direction of the toroidal
motion of the beam ions and therefore to the presence of neutrons produced
from trapped ions.

MEASUREMENTS

Both spectrometers have been operated at JET since November 1986. A
series of spectra are accumulated for each JET discharge during 'time
slices' of 1.0 second and adjustable pre-collimators are used to ensure
that the count-rates in the detectors are optimized for good statistics
whilst avoiding pile up distortion.

The response of a ^{3}He chamber is complex because there are a number of
reactions in the detector which can lead to pulse production. It is only
the full energy peak, produced by the ^{3}He(n,p)T reaction, which is useful
in determining the incident neutron spectrum. In order to maximise the
number of 'useful' counts, a great deal of attention has been paid to the
shielding for the spectrometers. The position in the roof laboratory is
ideal; the detector was simply placed over a penetration in the 2 m thick
floor, which provides an excellent neutron shield. To operate a
spectrometer in the torus hall required the construction of a massive
enclosure with 60 to 100 cm of lithiated paraffin wax walls to shield the
detector from the thermal neutrons to which it is very sensitive. The
spectrometer itself is further shielded by lead to reduce the number of
counts due to gamma-rays. The total weight of the shield is approximately
17 tonnes.

ANALYSIS AND RESULTS

A survey of NBI heated discharges during the 1988 campaign has been
made. Those shots in which the detector count-rate was in excess of 5 kHz
or with too few counts (< 500 counts) were eliminated.

We consider first the simpler case of the spectrum emitted normally to
the magnetic field, ie. towards the roof laboratory. The measured pulse
height spectrum is a convolution of the incident neutron spectrum and the
detector response function (the noise introduced by the processing
electronics is negligible, as indicated by the width of a pulser). The
incident neutron spectrum consists of the sum of the thermonuclear spectrum
and the beam-plasma spectrum. The ion temperature is obtained from either
the large crystal X-ray spectrometer [3] or from the active charge-exchange
diagnostic [4]. The ratio of the neutron emission from these two processes
was determined by summing the two spectra, folding with the detector
response function and comparing the result with the data. By adjusting the
area of each spectrum, the fit of the resultant spectrum to the measured
data was optimised using the method of least squares; then the
thermonuclear (plasma-plasma) fraction was determined.

The thermonuclear fraction was determined in the same way using the
data obtained with the torus hall spectrometer. However, in this case
the beam-plasma spectrum due to trapped ions must also be considered. If
the spectrum due to trapped ions is not taken into account, good fits are
not possible and large systematic errors in the value obtained for the
plasma-plasma fraction are introduced (figs. 2 and 3). With the trapped
ions taken into account, the values of the plasma-plasma fraction obtained
with each spectrometer are consistent, to within the estimated errors
(figure 3).

The presence of trapped beam particles has implications for other
neutron diagnostics. Since the orbits of trapped particles are
predominantly on the outboard side of the plasma, their presence indicates
that the 'centre of gravity' of the neutron emission has a tendency to
become displaced outwardly from the toroidal magnetic axis. This deduction
is supported by the measurements obtained from the neutron emission profile
monitor [5]. Figure 4 shows the neutron emission profiles for discharges
18618 and 18620, the latter having a higher electron density. The neutron
spectrometer indicated that the trapped fraction for these was 12% and 71%
respectively. Figure 4 shows the neutron emission profile as viewed from a
vertical direction. The increased asymmetry of the emission in 18620
relative to 18618 is clear. This provides an indication that the neutron
emissivity from deuterium beam-heated plasma is not constant around the
magnetic flux surfaces. Therefore the interpretation of neutron emission
data becomes considerably more complex.

REFERENCES

[1] P van Belle and G Sadler, in Basic and Advanced Diagnostic Techniques
    for Fusion Plasmas, (Proc Course and Workshop, Varenna 1986), Vol III,
    Rep EUR 10797 EN, CEC (1987) 767, Varenna 1986.
[2] O N Jarvis et al, Rev Sci Instr, 57 (1986) 1717.
[3] R Bartiromo et al, "The JET High Resolution Bent Crystal
    Spectrometer", JET-P(88)11
[4] M G Von Hellerman et al, "Charge Exchange Recombination Spectroscopy
    on JET", JET-P(86)45.
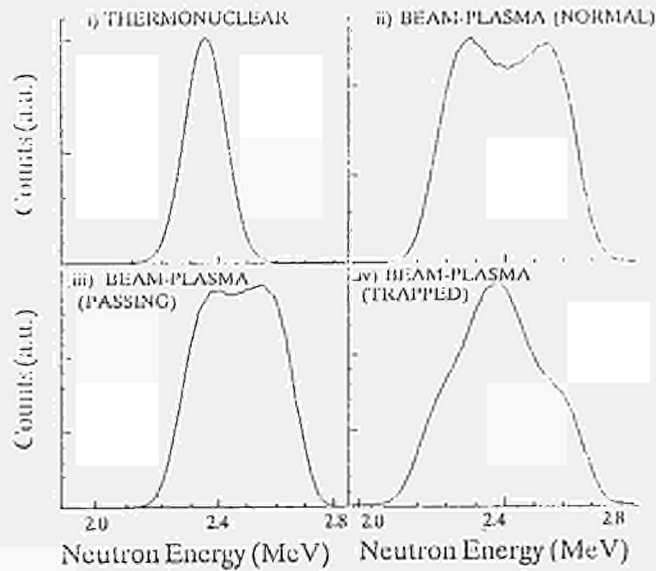[5] J M Adams et al, this conference

Figure 1: Neutron spectra produced during NBI
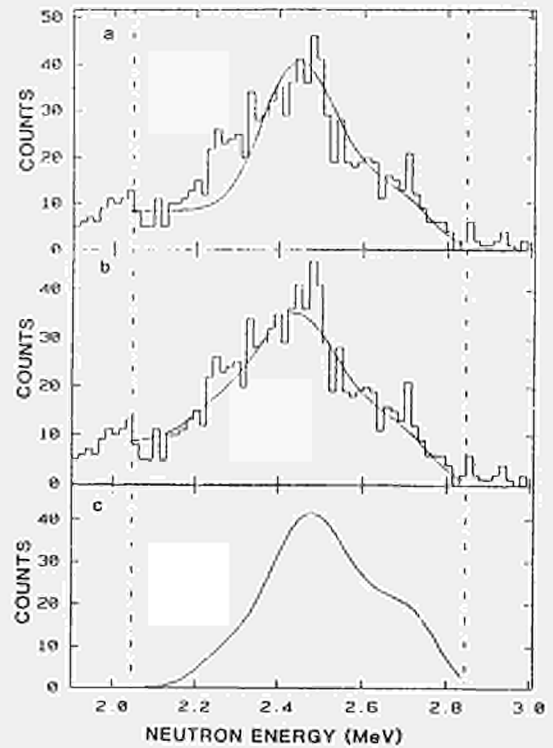

Figure 2: a) Experimental data (histogram) and fit (curve) assuming no trapped fraction.
          b) Experimental data and fit, trapped fraction included.
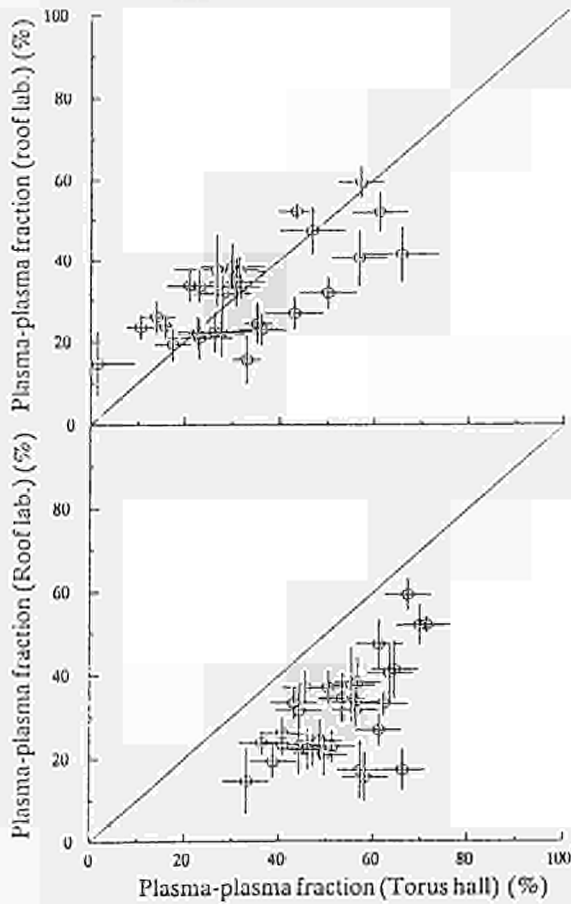   c) Incident neutron spectrum which gave fit (b).

Figure 3: Comparison of results of determination of plasma-plasma fraction from the two spectrometers with (upper) and without (lower) trapped fraction.
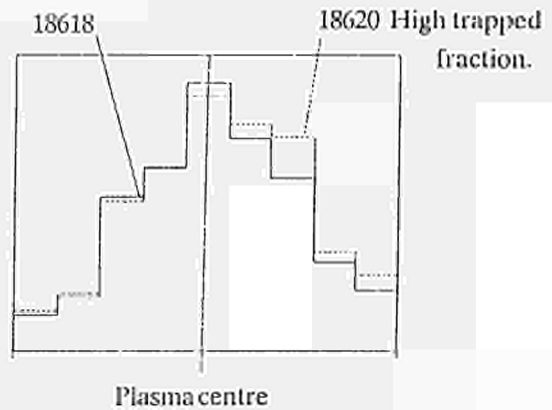

Figure 4: Radial neutron emission profiles for two discharges 18618 - trapped fraction 12%, 18620 - trapped fraction 71%. The latter discharge shows greater neutron emission on the outboard side of the plasma.

SAWTEETH AND THE m=1 MODE IN JET

D J Campbell, A W Edwards and D Pearson[1]

JET Joint Undertaking, Abingdon, Oxon, OX14 3EA, U K
[1] *Imperial College of Science and Technology, University of London, U K*

Introduction — Sawtooth activity in JET exhibits considerable complexity, the sawtooth cycle being interrupted by a variety of mhd phenomena: subordinate relaxations, 'fishbones' and quasi–continuous mhd oscillations. However, detailed experimental investigations of the sawtooth collapse in JET have shown that the instability is not directly related to this activity, but occurs as a rapidly growing m=1 instability which leads to a convective flow in the plasma core and a rapid loss of energy from the central region[1]. Here we consider the relationship between the m=1 activity observed during the sawtooth cycle and the sawtooth collapse and discuss the implications of this relationship for theories of the sawtooth instability.

Observations — To investigate the detailed evolution of mhd structures in JET, soft X–ray tomography and ECE reconstructions have been used to analyse the evolution of the plasma during a sawtooth cycle. Two perpendicular soft X–ray diode arrays permit the reconstruction of the contours of X–ray emission from the plasma with a time resolution of 10 μs[1]. In addition, localised ECE measurements from a calibrated 12–channel grating polychromator are used to reconstruct two–dimensional contours of electron temperature by exploiting the rotation of mhd structures in the plasma and by using assumptions about the rotational symmetry of these structures[2] (in cases considered here, it is assumed that m=n). This effectively limits the time resolution of the technique to the rotational period of the structure in question, which, in JET, is usually 100 μs – 5 ms. While this allows slowly growing and decaying mhd activity (eg successor oscillations) to be analysed, the timescale of the sawtooth collapse (~100 μs) limits the application of the ECE technique during the collapse to plasmas with very high power NBI heating, where rotational frequencies ~20 kHz can be produced.

As reported previously[3-4], sawtooth activity in JET varies greatly, depending upon such factors as plasma density, current and heating regime. Nevertheless, the sawtooth collapse mechanism is independent of this variation[4-5] and, in particular appears to be independent of the presence or absence of precursor oscillations. The collapse leads to the formation of a hot crescent, as the plasma centre is displaced by a cold 'bubble', behaviour which closely resembles the model due to Wesson[6], which postulates that $|1 - q_0| \lesssim 10^{-2}$. This remains true even in cases where $q_0 \sim 0.7$, as is observed during sawtooth stabilization in JET[7-8]. Although it is rapidly cooled, the crescent may persist for tens of milliseconds after the collapse, causing successor oscillations. This behaviour is illustrated in figure 1, where, for the first time, it has been possible to compare the details of the collapse of sawteeth by two independent diagnostics. The dynamics of the collapse reconstructed from ECE are in striking agreement with that deduced using the soft X–ray tomography, and are a confirmation of the fact that the soft X–ray emission predominantly reflects the evolution of the electron temperature and, it is reasonable to conclude, that of the magnetic surfaces (as argued in [9]).

In some cases a structure resembling a magnetic island is observed in reconstructions of successor oscillations to sawteeth and partial sawteeth[2]. This raises the question of what role, if any, is played by magnetic islands in the sawtooth instability. Figure 2 compares ECE reconstructions of successor oscillations for two sawtooth collapses. As indicated in the figure, these reconstructions are carried out for the first successor oscillation after the collapse. In case (i), the successor has the form discussed above, ie it is a warm crescent–shaped object. However, in (ii) the crescent–shaped object is cooler than the plasma core, resembling a magnetic island, and it is surrounded by a ring of warmer plasma which is the residue of the hot crescent formed by the displacement of the core.

Further investigation of cases such as (ii) suggests that the 'island–like' object is not involved in the collapse, but is simply the residue of a pre–existing island which has survived the collapse. Evidence for this can be deduced from figure 2(ii), where large precursor oscillation to the sawtooth collapse can be observed and where, furthermore, the successor oscillation to the collapse is in–phase with the precursor oscillation. ECE reconstructions of the precursors show the island–like structures in the plasma when difference techniques are used to 'enhance' the images. Although it has not yet been possible to follow the evolution of such an island through the sawtooth collapse, the fact that many sawtooth collapses occur without such structures strongly suggests that they

are not an essential component of the sawtooth instability. Further evidence for such an interpretation comes from observations of the 'snake' perturbation in JET[10]. This phenomenon, believed to be caused by a magnetic island on the q=1 surface, is observed to persist through many sawtooth collapses. As in the cases considered here, it has not yet been possible to analyse the detailed evolution of the 'snake' through the collapse, and the nature of its interaction with the sawtooth instability remains open.

The growth and decay of these magnetic islands during the sawtooth cycle can, however, be followed in detail, and figure 3 illustrates such a case. This shows that the island observed in the successor oscillation gradually reconnects in an annulus about the plasma centre on a timescale of ~50 ms, resulting in the formation of a flat shoulder in the electron temperature profile in the region of the sawtooth inversion radius, which presumably represents the location of the q=1 surface. Although the island does not reconnect the plasma centre, a small drop in the central temperature is often observed during this time. A remarkable aspect of the time development shown in figure 3 is that, as the annular reconnection approaches completion, a second, highly localised, island emerges at the X–point of the old island (timeslices (c) to (f)). This new structure grows and again reconnects in a ring about the plasma centre. Once this reconnection is complete, the cycle recommences. There are several points to note here: firstly, that the cycle of island growth and reconnection is out of phase with the sawtooth cycle and, indeed, the sawtooth collapse does not appear to be related to a particular island amplitude; secondly, that the reconnection is always observed to occur in an annular region, and has never been observed to involve the plasma centre; thirdly, that although this behaviour is very common (it has previously been referred to as a 'slow' partial sawtooth[8]), it is not always present and, therefore, does not appear to be a necessary feature of the sawtooth cycle; finally, the existence of such islands throughout the sawtooth cycle suggests that a q=1 surface exists throughout the sawtooth cycle, a result which generalizes and confirms that obtained from observations of the 'snake'.

Discussion — While the results presented here clarify the phenomenology of the sawtooth cycle in JET, the fundamental problem, ie the nature of the sawtooth instability, remains unsolved. The striking agreement between soft X–ray and ECE reconstructions of the sawtooth collapse confirms the remarkable similarity reported previously between the observed behaviour and that ' predicted by the quasi–interchange model[6]. Nevertheless, this agreement appears paradoxical if a q=1 surface exists throughout the sawtooth cycle and if, indeed, $q_0 \sim 0.7$ in at least some cases. It is clear, however, that the experimental results are not in agreement with Kadomtsev–like models which are based on full reconnection[11]. This is also true for more recent models[12-13], although the observed growth time of the instability remains the more fundamental objection to these (and indeed all existing) theories. While it is impossible to exclude the possibility that a very small amplitude tearing mode (width ~1 cm say) is present at the start of the sawtooth collapse, it is clear from the JET results that it is the geometric rearrangement of the plasma core which is responsible for the observed collapse rather than a reconnection of the core. The cause of the subsequent loss of energy from the core also remains problematic, however.

These results may have wider implications for the evolution of the q–profile. As noted above, the observation of cycles of reconnecting islands throughout the sawtooth period generalizes the deduction from 'snake' observations that a q=1 surface exists throughout the sawtooth cycle. In addition, such cycles of islands may contribute to the maintenance of localised regions of very low shear in the q–profile[14], which may have important consequences for theories of the stability of the m=1 mode.

References
[1] A W Edwards et al, Phys Rev Lett 57 210 (1986).
[2] E Westerhof and P Smeulders, to be published.
[3] D J Campbell et al, Nucl Fus 26 1085 (1986).
[4] D J Campbell et al, Proc 11th IAEA Conf, Kyoto, 1986, 1 433.
[5] R D Gill et al, Proc 15th EPS Conf, Dubrovnik, 1988, 1 350.
[6] J A Wesson et al, Proc 11th IAEA Conf, Kyoto, 1986, 2 3.
[7] J O'Rourke et al, Proc 15th EPS Conf, Dubrovnik, 1988, 1 155.
[8] D J Campbell et al, Proc 12th IAEA Conf, Nice, 1988, Paper IAEA–CN–50/A–7–2.
[9] P A Duperrex et al Proc 15th EPS Conf, Dubrovnik, 1 362.
[10] A Weller et al, Phys Rev Lett 59 2303 (1987).
[11] B B Kadomtsev Fiz Plazmy 1 710 (1975).
[12] T Sato et al, Proc 12th IAEA Conf, Nice, 1988, Paper IAEA–CN–50/D–3–2.
[13] A Y Aydemir et al, Proc 12th IAEA Conf, Nice, 1988, Paper IAEA–CN–50/D–3–1.
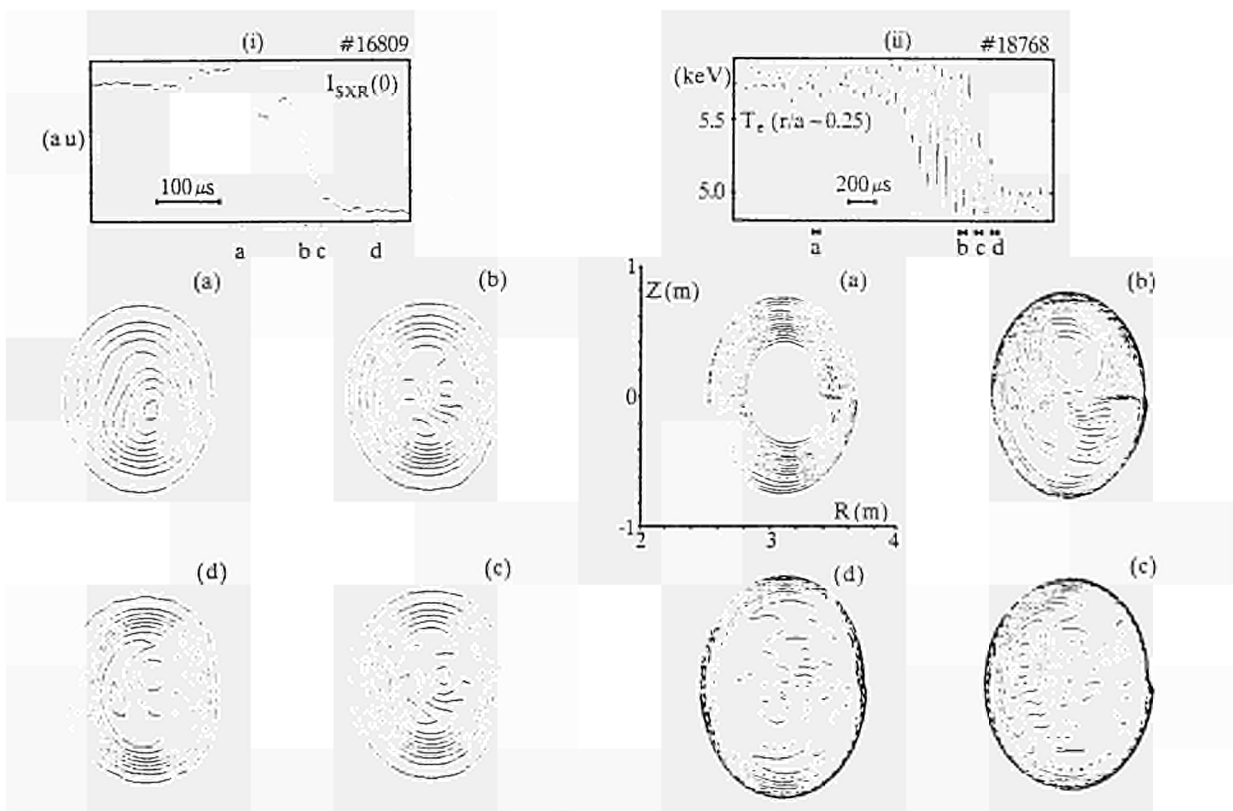[14] R D Gill et al, JET Preprint JET–P(88)59, to be published.

Fig 1 : (i) Reconstruction of sawtooth collapse using soft X−ray tomography.
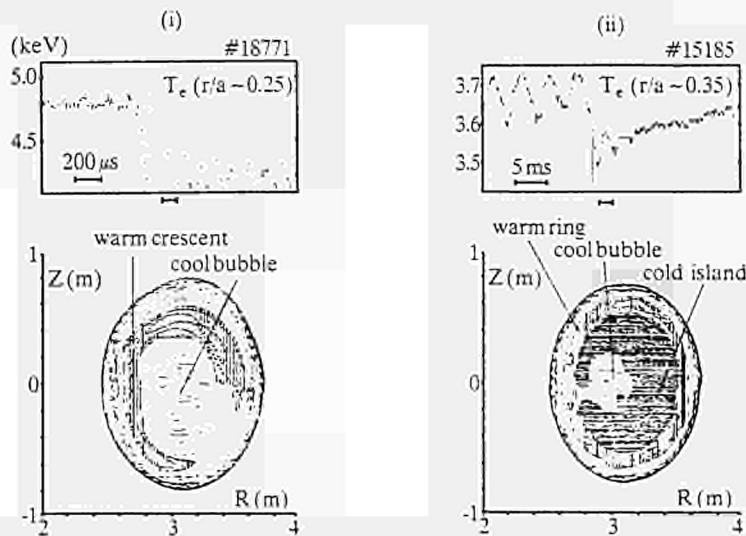(ii) Reconstruction of sawtooth collapse using ECE.

Fig 2 : (i) ECE reconstruction of successor oscillation showing warm crescent structure.
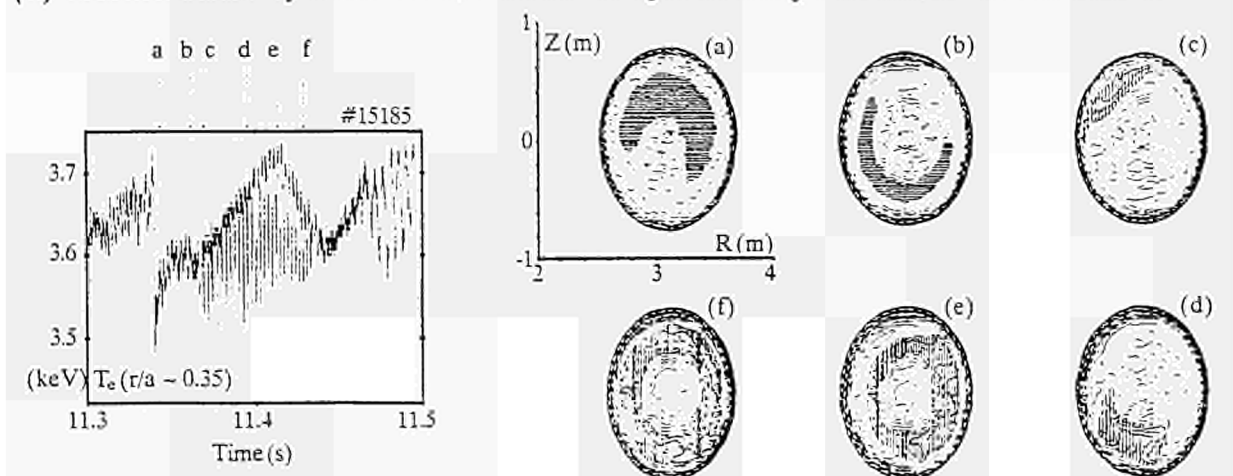(ii) reconstruction of successor to another collapse showing cool island−like structure.

Fig 3 : ECE reconstructions of mhd oscillations during sawtooth ramp phase showing
cycles of island growth and reconnection in annulus about plasma core.

A METHOD TO STUDY ELECTRON HEATING DURING ICRH

L.-G. Eriksson* and T. Hellsten

JET Joint Undertaking, Abingdon, Oxon., OX14 3EA, UK.
*Chalmers University of Technology, S-41296 Göteborg, Sweden.

INTRODUCTION - Collisionless absorption of ICRF waves occurs either by ion cyclotron absorption or by electron Landau (ELD) and transit damping (TTMP). Both ion cyclotron absorption, and direct electron absorption results in electron heating. Electron heating by minority ions occurs after a high energy tail of the resonating ions has been formed i.e. typically after 0.2-1s in present JET experiments. Electron heating through ELD, and TTMP, takes place on the timescale given by electron-electron collisions which is typically of the order of ms. This difference in the timescales can be used to separate the two damping mechanisms. This can be done by measuring the time derivatives of the electron temperature after sawtooth crashes during ramp-up and ramp-down of the RF-power.

After a sawtooth crash, the electron temperature profile becomes almost flat in the centre and hence resulting in a small energy conduction The electron energy balance equation can therefore be approximated by

$$\frac{d}{dt} (\frac{3}{2} nkT_e) = \eta j^2 - \frac{1}{\tau_{ie}} nk(T_e - T_i) - P_{rad} + P_{RFD} + P_{RFI} \quad (1)$$

where η denotes the resistivity, j the current density, τ_{ie} the energy transfer time between ions and electrons, P_{rad} the radiation losses, P_{RFD} the direct RF-power density going to the electrons and P_{RFI} the power density due to power transfer from the heated minority ions.

The l.h.s. of Eq. (1) can be obtained from the experiment by measuring the slope of the electron temperature, vs time, after a sawtooth crash and from the electron density. The electron temperature is measured by the 12-channel grating polychromator [1], which measures the temperature at 12 positions. The density is measured with a 2mm microwave interferometer [2]. The main contributions to the r.h.s. of Eq. (1) comes from the ohmic and the RF-heating terms. Thus, if direct heating dominates over indirect heating, and the ohmic heating stays roughly constant, one would expect to see a linear relation between the coupled power and the electron heating after sawtooth crashes during power ramps. The power density due to direct electron heating by ICRH can then be obtained from the slope of the curve of the local electron heating (i.e. l.h.s. of Eq. (1)) vs the coupled power. Hence, the power deposition can be found by measuring this slope for different radii. If indirect heating dominates, the local heating becomes a nonlinear function of coupled power. In particular, the indirect heating should be delayed by the order of a slowing down time for ion electron collisions, t_s. To get a qualitative understanding of the indirect heating, we study the following simplified Fokker-Planck equation

$$\frac{\partial f}{\partial t} = Q_{RF}(f) + \frac{1}{v^2} \frac{\partial}{\partial v} [\frac{v^3 f}{t_s}] + \frac{f}{t_1} \quad (2)$$

where f is the distribution function, Q_{RF} is the RF-operator [3], and t_1 is an equivalent loss time. Multiplying by $\frac{1}{2}mv^2$ and integrating yields

$$W_f = exp[-\int_0^t (\frac{2}{t_s} + \frac{1}{t_1})dt'](\int_0^t P_{RF}(t) exp[\int_0^t (\frac{2}{t_s} + \frac{1}{t_1})dt''] dt' + W_f(t=0)\} \quad (4)$$

where W_f is the energy of the resonating ions. The indirect electron heating is then obtained as $p_e = 2W_f/t_s$. It is possible to obtain some insight into the indirect heating by taking the experimental data for the electron temperature and the coupled power and integrate Eq. (4) numerically using different t_1 to model losses during a sawtooth crash.

ANALYSIS OF EXPERIMENT - A series of ICRH experiments were performed in ^{4}He-plasmas with ^{3}He as the minority species. The RF-frequency was equal to 33.9MHz chosen such that the cyclotron resonance of ^{3}He passed close to the magnetic axis. Toroidal dipole phasing of the antennae was used, which peaks the spectrum around toroidal mode numbers n = 30. The axial electron density was about $n_e(0) = 4$-4.5×10^{13} cm^{-3}, $B_o = 3.4T$, $T_e = 5$-$10keV$, $T_i = 4$-$8keV$ and $Z_{eff} = 4$-4.5. The filling pressure of the minority ions, ^{3}He, varied between 5-120mbar.

The discharges #13683, 13684, 13687 and 13692 all showed a linear relation between the electron heating, p_e, and the coupled power, P_{RF}, indicating that direct electron heating dominated. The direct RF-power deposition profiles are shown in Fig.1. For the lower filling pressures (15-30mbar, 30mbar corresponds to $n_{3He}/n_e = 0.05$) the deposition profiles are broad and almost identical whereas the 120mbar discharge gave a more peaked profile.

We have compared the measured power deposition profiles for direct electron heating with profiles calculated with a modified version of the LION code, which includes ELD and TTMP [4]. Two calculated power deposition profiles due to TTMP and ELD are shown in Fig.1, with $n_{3He}/n_e = 0.025$ and 0.05. The power deposition has been obtained by approximating the coupling spectrum with six toroidal modes. There is a rough agreement between the calculated and measured deposition profiles. Both show broad profiles which become more peaked at higher minority concentration.

Fig.2 shows p_e, P_{RF}, for discharges #13684, 13688 and 13689. Only the discharge with the lowest filling pressure (5mbar) gives a nonlinear relation between p_e and P_{RF} consistent with indirect electron heating. Discharge #13689, with filling pressure 60mbar, shows a non-linear relation between p_e and P_{RF} which is different from what one would expect from indirect heating. As mentioned before, discharge #13684, (30mbar), gives a linear relation between p_e and P_{RF} consistent with dominating direct electron heating.

Further information can be obtained by studying the energy content of the minority ions. For indirect electron heating the energy content of the minority ions should be large whereas it is expected to be small for direct electron heating. The energy content in the perpendicular minority ion tail, W_f, can be obtained as: $W_f = 3/4(\delta W_{DIA} - \delta W_{MHD})$, where W_{DIA} and W_{MHD} measures the plasma energy content based on the diamagnetic effect and equilibrium calculations, respectively ($W_{DIA} = 3/2 W_{\parallel}$, $W_{MHD} = 3/4 W_{\perp} + 3/2 W_{\parallel}$). Fig.3 shows the estimated fast ion energy contents for discharge #13688, (8mbar) and 13692, (120mbar), the fast ion energy content increases only significantly for discharge #13688, which is in agreement with the analysis above. Both discharges #13688 and 13692 gave rise to sawtooth-free periods, whereas the discharges in the 15-30mbar range did not. Thus, it appears to be possible to create sawtooth-free periods with both dominating indirect electron heating or with dominating direct electron heating.

We now analyse discharge #7220 in which hydrogen minority heating in a deuterium was performed, $n_H/n_D = 0.03$. It was dominated by indirect electron heating. A prominent feature of this discharge is the hysteresis effect seen when the coupled power is ramped up and down, Fig. 4. A numerical solution of Eq. (5) using the experimental data for the electron temperature, RF-power etc. is also shown in Fig. 4. The theoretical curve has been normalised at $P_{RF} = 4.38MW$. The qualitative features, i.e. the shape of the curves, are in good agreement. It is interesting to note that the shape of the theoretical curve is almost unchanged if one assumes losses up to 50% of the fast ion energy content during a sawtooth crash. It is therefore difficult to determine the fast ion losses from this analysis.

DISCUSSIONS - For intermediate minority concentrations with the dipole phasing of the antennae a broad power deposition profile is obtained for the direct electron heating. Due to the large toroidal mode number no linear mode conversion should take place. TTMP and ELD are then the most likely absorption mechanisms. For the highest concentration of minority ions the direct deposition profile becomes more peaked. Comparison between the power deposition profile due to TTMP and ELD as calculated with the LION-code shows rough agreement with the measured profiles. Sawtooth-free periods were obtained for both the high and low minority concentrations, but not for the intermediate concentrations.

When indirect electron heating dominates, the electron heating increases on the time scale of high energy ions slowing down on electrons. Theoretical calculations of the electron heating are in good qualitative agreement with the measured values. The results indicate that indirect electron heating dominates for low minority concentrations and that a non-negligible part of the ions are being confined near the centre after sawtooth crashes.

REFERENCES
[1] Tubbing, B.J.D. et al., in Contr. Fusion and Plasma Physics, Proc.
     12th European Conf, Budapest 1985, 9F-I (1985) 215.
[2] Fessey, J.A. et al., J. Phys. E: Sci. Instrum. 20 (1987) 169.
[3] Stix, T., Nucl. Fusion 15 (1975) 737.
[4] Llobet, X. et al., Proc. Joint Varenna-Lausanne Int. Workshop on
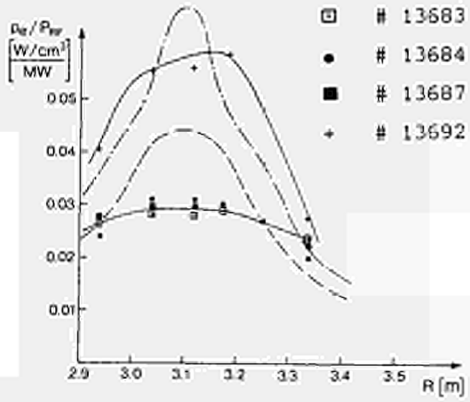   "Theory of Fusion Plasmas", Chexbres, 1988.

Fig. 1: Measured and calculated
direct electron heating profiles
calculated for
$n_{^3He}/n_e = 0.025$ (- - -),
$n_{^3He}/n_e = 0.05$ (-.-.-)
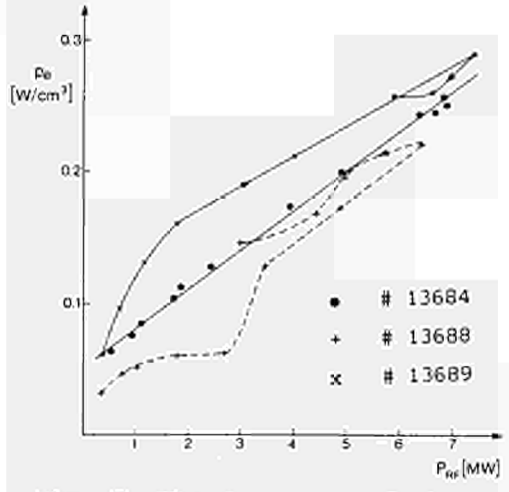
Fig. 2: The increase of the
electron energy after a sawtooth
crash, p_e vs coupled RF-power.
The arrows show the time sequence.
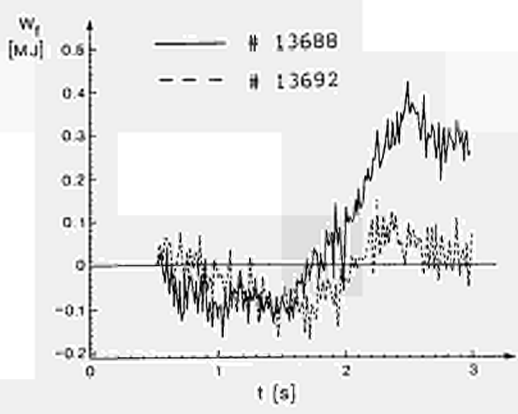
Fig. 3: Fast ion energy content.
The RF-power is ramped during
t = 2s to t = 3s and then reaches
a flat top.
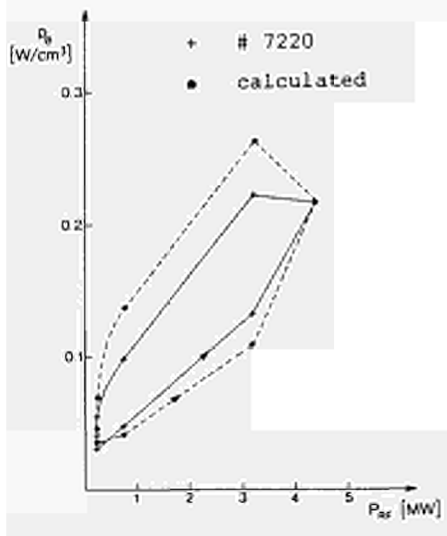
Fig. 4: The increase of electron
energy after a sawtooth crash.

CURRENT DENSITY PROFILE EVOLUTION IN JET

P M Stubberfield, B Balet, D Campbell, C D Challis,
J G Cordey, G Hammett*, J O'Rourke, G L Schmidt*.

JET Joint Undertaking, Abingdon, Oxon, OX14 3EA, UK
*Princeton Plasma Physics Laboratory, Princeton, New Jersey, USA

ABSTRACT

Simulation studies have been made of the current density profile
evolution in discharges where the bootstrap current is expected to be
significant. The changes predicted in the total current profile have been
confirmed by comparison with experimental results.

1. __Introduction__ The evolution of current profile has been followed
using the TRANSP code [1] in three very different JET discharges with
strong auxiliary heating, (1) H-mode, (2) extended sawteeth (monster) and
(3) pellet fuelled ICRH discharges. The input parameters to the TRANSP
code, which solves the poloidal field diffusion and equilibrium equations,
include profiles of electron temperature, density and Z_{eff} from visible
Bremsstrahlung. To check the accuracy of the simulation the time
development of the simulated and measured loop voltage, the second
Shafranov current moment [2] and the six polarimeter channels are compared.
The three cases are discussed in detail below.

2. __H-modes__ In previous papers [3][4] it has been shown that in
H-modes the bootstrap current had to be included to explain the loop
voltage behaviour in these discharges. A typical example is shown in
Fig.1. In this 3 MA discharge the predicted bootstrap current reached
0.8 MA at the end of the H-mode phase. The bootstrap current profile is
strongly peaked in the outer radial region (see Fig.3) due to the sharp
density gradient. To confirm that the total current density profile was
indeed being broadened the measured second Shafranov moment Y2S (from the
external pick-up coils) has been compared with that predicted by the code
(Fig.2). Clearly a much better fit is obtained when the bootstrap current
is included in the analysis.

The broadening of the current profile may eventually lead to the
safety factor q on axis exceeding unity and the stabilisation of the saw-
teeth. The timescale for the current to diffuse from the central region
however, is very long (~ 10 seconds) and exceeds the duration of the H-mode
phase. This explains why sawteeth continue throughout the H-mode. The
inversion radius, nevertheless, is seen to slowly contract indicating some
broadening of the current profile.

3. __Discharges with an extended sawtooth-free period (Monsters)__ The
main characteristics of these extended sawtooth free discharges (monsters)
have been extensively reported elsewhere [5] and a mechanism has been
proposed for the stabilisation of the sawteeth [6]. Here we examine how
the presence of the bootstrap current and a peaked Z_{eff} profile affect the
evolution of the current profile.

In Fig.4 the time development of the central electron temperature is
shown for a discharge with a long sawtooth free period at the end of the
current ramp. The time behaviour of q on axis from TRANSP is also shown
for four different assumptions. Curve (a) is the development of q on axis
for a flat Z_{eff} profile and no bootstrap current, showing q falling
throughout the monster phase. Curve (b) is a flat Z_{eff} profile but
includes the bootstrap current and in this case the reduction in q during
the monster phase is reduced. Recent multichord measurements [7] of the
visible Bremsstrahlung have shown that the Z_{eff} profile is peaked on axis,
typically the peak to edge ratio is 2:1, in this type of discharge, and
using the measured Z_{eff} profile (curve c) we find that q on axis is
approximately constant in the first second of the sawtooth free period. To
further ascertain the sensitivity of the q behaviour to the Z_{eff} profile in
curve (d) the peaking factor (peak to edge ratio) was increased by 50%
above the measured value. In this case the q axis increases slightly
during the initial phase of the extended sawtooth free period. Results of
TRANSP, calculations of polarimeter and Y2S are consistent within the
systematic experimental errors. It is therefore not yet possible to
determine which is the appropriate model for TRANSP.

4. __Pellets fuelled pulses with intense ICRH__ These are 3 MA shots in
which a pellet is injected in the current rise and this is then followed by
intense ICRH [8], throughout this whole period there are no sawteeth. The
intense ICRH produces a very strong pressure gradient close to the magnetic
axis and hence a very large bootstrap current (~ 0.8 MA) which is peaked
off-axis (see Fig.3). The development of the current profile in these
discharges has been followed by TRANSP and the time development of the
q at various radii is shown in Fig.5. Prior to pellet injection q is
falling at all radii as the current is being increased, following pellet
injection the centre of the plasma is cooled and the current profile
broadens and q on axis rises (point A). At point B the bootstrap current
has become significant and the total current profile becomes hollow with q
double valued. Comparison with the polarimetry (Fig.6) suggests that this
is indeed a reasonable interpretation of the profile behaviour, but the
sensitivity of the data is not sufficient to confirm this result entirely.

SUMMARY

It is shown that the bootstrap current plays a key role in changing
the current profile in H-modes, monster and pellet fuelled ICRH discharges.
In discharges with monster sawteeth it is found that q on axis initially
increases due to to the bootstrap current and the peaking of the Z_{eff} pro-
file and that this may influence the duration of the sawtooth free period.
In the ICRH pellet fuelled discharges the current profile becomes hollow.

REFERENCES

[1] Goldston, R.J., et al., J. Comput. Phys. 43 (1981) 61.
[2] Zakharov, L.E., Shafranov, V.D., Sov. Phys. Tech. Phys., 18 (1973)
    151.
[3] Cordey, J.G., Challis, C.D., Stubberfield, P.M., Plas. Phys. and
    Contr. Fus., 30 (1988) 1625.
[4] Challis, C.D. et al., to be published in Nuclear Fusion.
[5] Campbell, D.J. et al., 12th Int. Conf. on Plas. Phys. and Contr. Nucl.
    Fus. Res., Nice (1988) A-7-2.
[6] Pegoraro, F. et al., ibid [5] D-4-6.
[7] Morgan, P.D., Proc., EPS Conf. Cont. Fus. & Plas. Htg. (1988) 139.
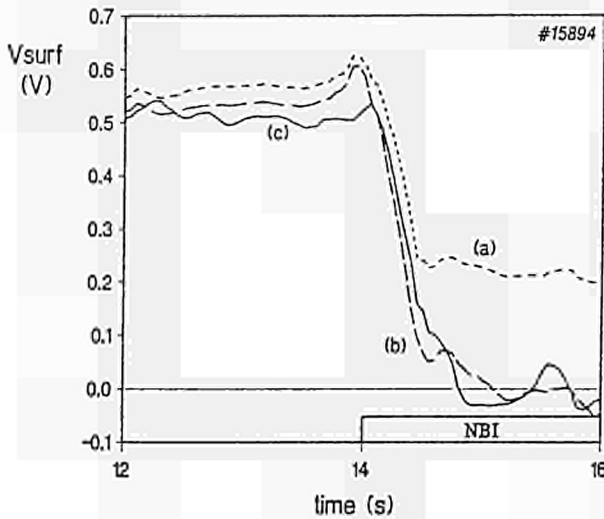[8] Schmidt, G.L. et al., ibid [5] A-4-1.

Figure 1: Evolution of voltage vs.time
(a)Simulation including only changes
in conductivity
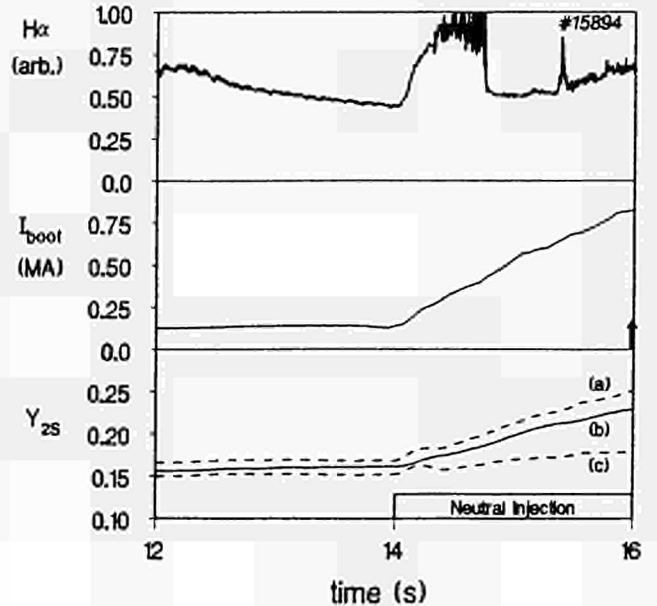(b)with addition of bootstrap current
(c)measured value

Figure 2: (i)H-α signal
(ii)Total bootstrap current vs.time
(iii)Evolution of Y2S
(a)with bootstrap current
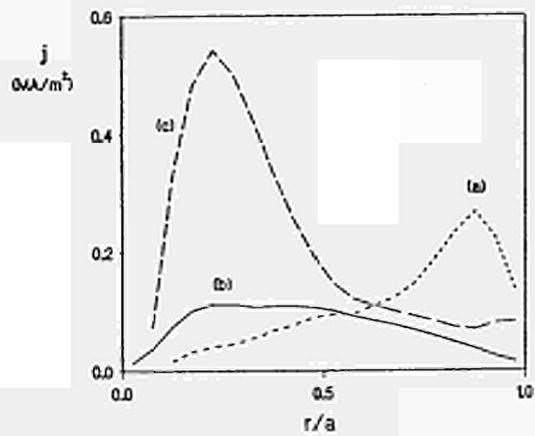(b)measured value
(c)without bootstrap current

Figure 3: Current density profiles for
(a)H-mode pulse at time shown by
arrow in Figure 2
(b)Monster pulse at time shown by
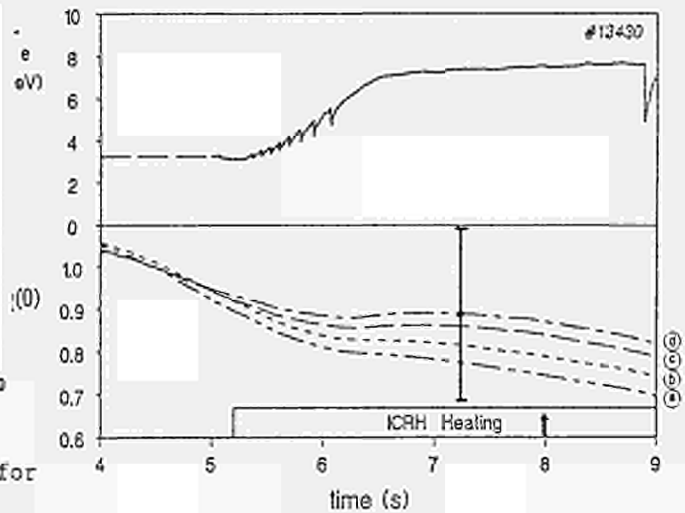arrow in Figure 4
(c)Pellet pulse at time C in figure 5

Figure 4: (i)Evolution of T_e(central) vs.time
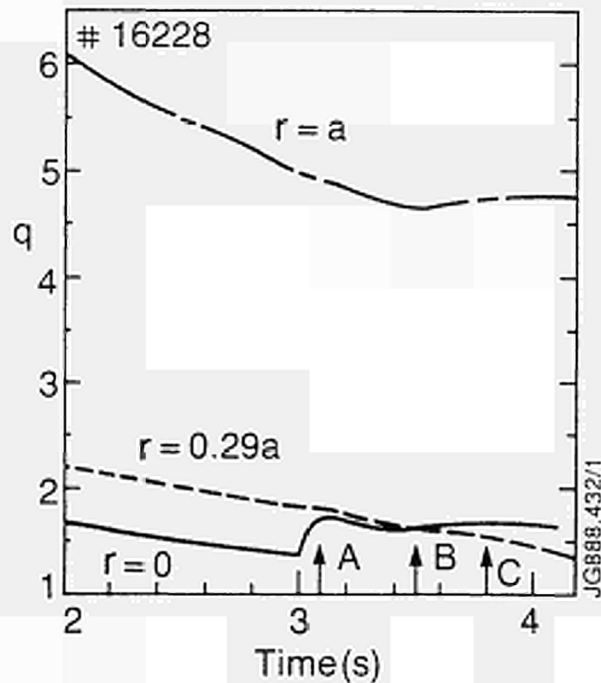(ii)Evolution of q vs. time

Figure 5: Evolution of q vs. time
at 3 different radii
A and B are described in text
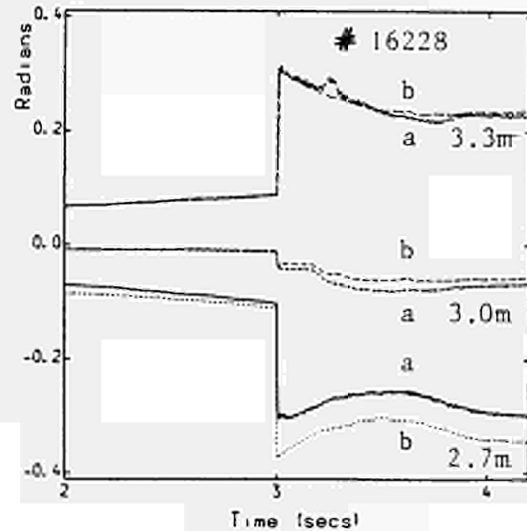C is time for the profile shown in Figure 3

Figure 6: Comparison of predicted and
measured values for 3 central
polarimetry channels (a) measured values
(b) simulated

ION THERMAL CONDUCTIVITY AND CONVECTIVE ENERGY TRANSPORT IN JET HOT-ION REGIMES AND H-MODES

F.Tibone, B.Balet, J.G.Cordey, G.Corrigan, D.F.Düchs, A.Galway, H.Hamnén, G.Maddison[2], G.Sadler, W.Stacey[3], T.Stringer, P.Stubberfield, M.L.Watkins

JET Joint Undertaking, Abingdon, Oxon., OX14 3EA, UK
[1] Chalmers University of Technology, Gothenburg, Sweden
[2] UKAEA, Culham Laboratory, Abingdon, Oxon. UK
[3] Georgia Institute of Technology, Atlanta, Georgia 30332, USA

INTRODUCTION

Local transport in a recent series of JET experiments has been studied using interpretive codes. Auxiliary heating, mainly via neutral beam injection (80keV $D^\circ \to D^+$), was applied on low-density target plasmas confined in the double-null (DN) X-point configuration ($I_p = 3$-3.5MA, $B_t = 2.5$-3.2T). This has produced two-component plasmas with high ion temperature and neutron yield and, above a threshold density, H-modes characterised by peaked density and power deposition profiles. H-mode confinement was also obtained for the first time with 25MW auxiliary power, of which 10MW was from ion cyclotron resonance heating. Operational aspects and global performance of these experiments are discussed in [1].

We have used profile measurements of electron temperature T_e from electron cyclotron emission and LIDAR Thomson scattering, ion temperature T_i from charge-exchange recombination spectroscopy (during NBI), electron density n_e from LIDAR and Abel-inverted interferometer measurements. Only sparse information is, however, available to date concerning radial profiles of effective ionic charge and radiation losses. Deuterium depletion due to high impurity levels is an important effect in these discharges, and our interpretation of thermal ion energy content, neutron yield and ion particle fluxes needs to be confirmed using measured Z_{eff}-profiles.

Electron and ion energy balances can be separated at these low plasma densities, thereby allowing a reliable estimate of the ion thermal conductivity χ_i. Bulk plasma radiation amounts to 30-40% of the total input power; the uncertainty on its radial distribution strongly affects the determination of χ_e when ion heating is dominant.

HOT-ION REGIME

A peak ion temperature of 18keV and D-D neutron rates of 10^{16}/s are produced by 20MW NBI into a low-density target plasma ($\langle n_e \rangle = 0.5 \ 10^{19} m^{-3}$, $Z_{eff} = 4$). Excellent beam penetration leads to a centrally peaked density profile ($n_{eo}/\langle n_e \rangle = 2$), and an even more strongly peaked ion temperature profile (Fig.1A; the large central value of $n_i \equiv \nabla \ell n T_i / \nabla \ell n n_i$ is shown in Fig.1C).

The transient hot-ion phase is dominated by fast ion dynamics. TRANSP calculations involving sophisticated treatment of beam-plasma interaction [2] show that W_{fast} accounts for half of the total stored energy, with a nearly isotropic fast ion velocity distribution. The observed time evolution of D-D neutron yield is well reproduced (Fig.1B), showing that 90% of the neutrons come from beam-beam and beam-plasma reactions.

The strongly peaked ion source predicted is found to be compatible with the measured electron density only if the Z_{eff}-profile is significantly hollow, with $Z_{eff} \le 2$ near the plasma center (where $n_{fast} > 0.5 \ n_e$ during the first 0.5 sec of NBI).

Low density and high temperature make thermal exchange between electrons and ions a minor effect, and the two energy balances can be unambiguously separated. Main transport losses for the thermal plasma are through the ion channel: χ_i (Fig. 1C) increases with radius and is larger than χ_e by an order of magnitude. For $\rho > 1/4$ ($\rho \equiv$ normalised radial coordinate) χ_i is larger than the neoclassical prediction by at least a factor 20. For both electrons and ions, the convective heat flux (here $q_{cv}=3/2\Gamma T$, Γ being the particle flux) accounts for more than half of the net heat flux near the plasma center. Viscous energy transport associated with the damping of toroidal rotation is a small fraction (<10%) of the ion losses.

HIGH- AND LOW-DENSITY H-MODES WITH 10 MW NBI

Analysis of ELM-free JET H-modes at medium/high density ($\langle n_e \rangle > 2.5 \ 10^{19} m^{-3}$) in the DN configuration yields similar results to those obtained for single-null cases [3]. Beam deposition and plasma density profiles are flat or even hollow, and W_{fast} is a minor fraction ($\le 10\%$) of the total stored energy. Although the e-i thermal exchange term is uncertain, the observation that at medium density $T_i(\rho) = T_e(\rho)$ while ion heating is predominant implies $\chi_i \ge \chi_e$. The "effective" thermal conductivity $\chi_{eff} \equiv -q_{cd}/n_e\nabla T_e$, q_{cd} being the total conductive heat flux, is ~ 1-$1.5m^2/s$ for $\rho < 0.8$ (Fig.2). This is approximately a factor of 2 lower

than in comparable limiter L-mode conditions.

In recently obtained low-density H-modes [1] the beam deposition profiles remain centrally peaked throughout the H-phase, T_i / T_e and the L/H transition is significantly delayed until the plasma density has built up. The phase preceding the transition is a hot-ion regime of the type discussed, dominated by fast ions and with $\chi_i \ge 2 \chi_e$ for the thermal plasma. χ_{eff} appears to be decreasing in time during the L-phase, and settles on an H-mode value $\sim 1 \ m^2/s$ (Fig.2).

Quiescent H-modes are characterized by significantly improved particle confinement. The electron flux Γ_e, which is outwards throughout the plasma in L-regimes, remains such near the edge (where the recycling source dominates) but is reversed in the inner plasma, corresponding to the formation of a shoulder in the density profile (Fig.3). In the low-density H-mode, Γ_e remains positive also near the plasma center.

The corresponding reversal of convective heat flux may have a bearing on the interpretation of the improved energy confinement at the L-H transition. If $\Gamma_i \equiv \Gamma_D + \Gamma_{imp} \sim \Gamma_e$, the effect on the total energy balance could be significant, with q_{cv}/q_{tot} up to +25% in L-modes and down to -10% in H-modes. However, with the impurity concentrations typical of these plasmas ($n_{imp}/n_e \sim 5\%$) such effect is very sensitive to Γ_{imp}: if Γ_e is mostly a consequence of impurity flows, then Γ_i may well be opposite to Γ_e, and dominant. On the other hand, the effect would be enhanced if impurities were counterflowing with respect to electrons. Profile measurements of Z_{eff} are necessary in order to resolve this issue.

H-MODE WITH STRONG COMBINED AUXILIARY HEATING

The pulse shown in Fig. 4 is so far a unique example of H-mode obtained with 15MW NBI and 10MW ICRH heating a target plasma fuelled by multiple pellet injection. Power deposition is predicted to be mostly on ions for NBI and mostly on electrons for ICRH. The measured electron density profile is only moderately peaked, and $T_e \sim T_i$. Estimated fast ion energy content is $\sim \frac{1}{2} W_{tot}$ initially, then decreases but still contributing significantly to the global energy confinement. The electron convective heat flux is again found to be inwards over most of the plasma, and $\sim 15\%$ of the net electron heat flux. The effective thermal conductivity for the background plasma is $\chi_{eff} \sim 3 \ m^2/s$ (Fig.2), supporting the conclusion that confinement is degrading with increasing input power [3].

CONCLUSIONS

Non-thermal ions play a dominant role in the hot-ion regime in JET. 90% of the observed neutron yield is due to beam-beam and beam-plasma reactions. The background plasma is characterized by $\chi_i \gg \chi_e$.

Low-density H-modes (featuring peaked density profiles) appear to have transport properties similar to higher density ones. The reversal of local particle fluxes during H-phases, associated with increased particle confinement, may influence the energy balance and could explain part of the improvement in energy confinement with respect to L-modes. Thermal plasma confinement in the H-mode appears to degrade with increasing input power.

The anomalous nature of ion energy transport [4] is confirmed, and $\chi_i \ge \chi_e$ is found in all cases where the energy balances can be decoupled.

REFERENCES
[1] B.J. Tubbing et al., this conference.
[2] R.J. Goldston et al., Journal Comp. Physics 43 (1981) 61.
[3] M. Keilhacker et al., IAEA-CN-50/A-III-2, Nice 1988.
[4] A. Taroni et al., Proc. EPS Conf., Madrid 1987, 11D (Pt. I) 97.

FIGURE CAPTIONS

Fig. 1 Hot-ion regime:
A) density and temperature profiles
B) time evolution of measured and computed D-D neutron yield
C) $T_{io}(\bullet)$, χ_i (solid line) and n_i (dashed, assuming similar profile shapes for n_i and n_e) at (a) $\rho=1/3$, (b) $\rho=1/2$ vs time:
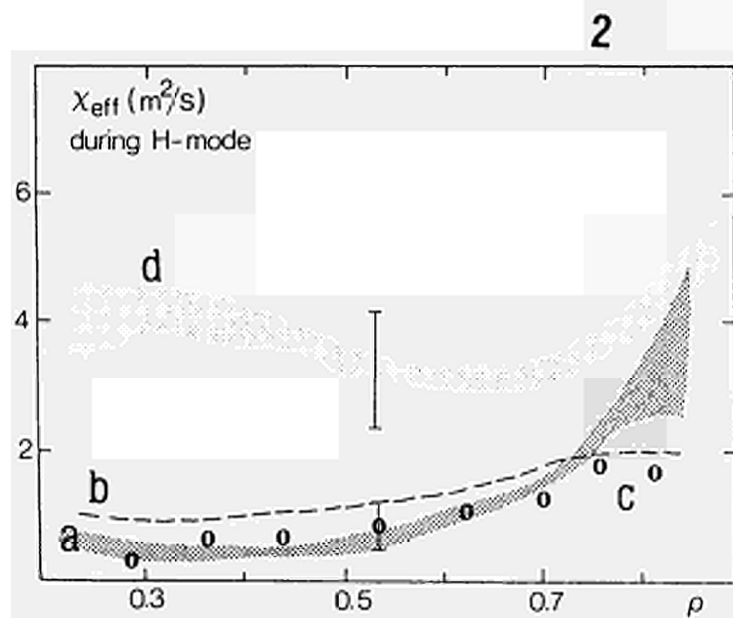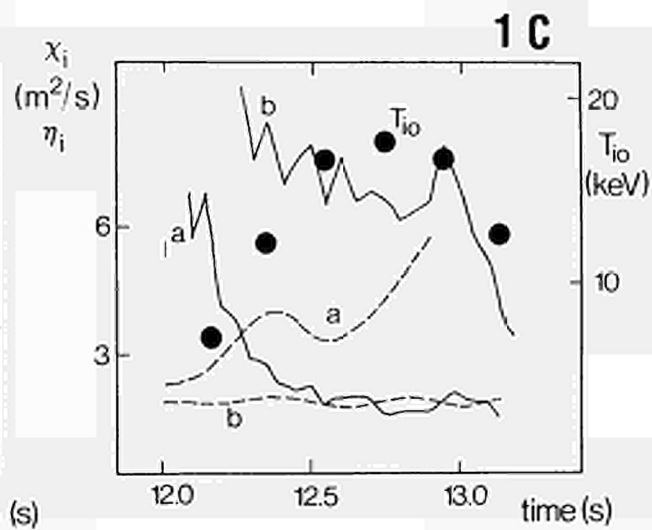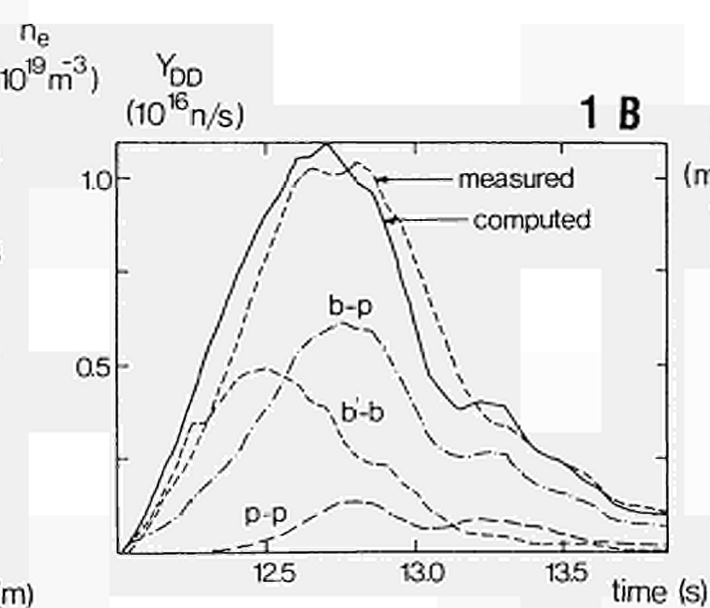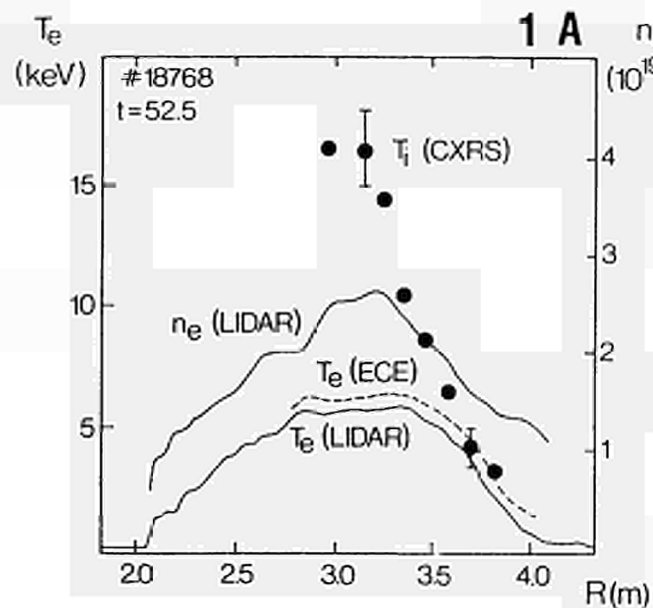
Fig. 2 "Effective" thermal conductivity for various JET H-modes:
(a) medium n, SN 8MW NBI (#14832/15894); (b) high n, DN 10MW NBI (#17386);
(c) low n, DN 10MW NBI (#18757); (d) medium n, DN 25MW NBI+ICRH (#18773).

Fig. 3 Measured dn_e/dt and predicted electron source S_e for:
(a/b) low density plasma (L/H-phase); (c) high density H-mode

Fig. 4 Overview of H-mode with $P_{aux} \sim 25$MW, pulse #18773 (open circles = computed kinetic energy)

1 A

T_e (keV) n_e (10^{19}m^{-3})

#18768
t=52.5

T_i (CXRS)

n_e (LIDAR)

T_e (ECE)

T_e (LIDAR)

R(m)

1 B

Y_{DD} (10^{16}n/s)

measured
computed

b-p

b'-b

p-p

time (s)

1 C

χ_i (m^2/s) η_i

T_{io} (keV)

b

T_{io}

a

a

b

time (s)

2

χ_{eff} (m^2/s)
during H-mode

d

b

a

c

ρ

3

(10^{19}m^{-3}/s^{-1})

S_e
d n_e/dt

a

b

c

b

c

a

ρ

4

T_{eo} (ECE)

T_{io} (CXRS)

keV

MJ

W_{dia}

W_{mhd}

10^{19}m^{-3}

$\langle n_e \rangle$

MW

P_{input}

P_{rad}

time(s)
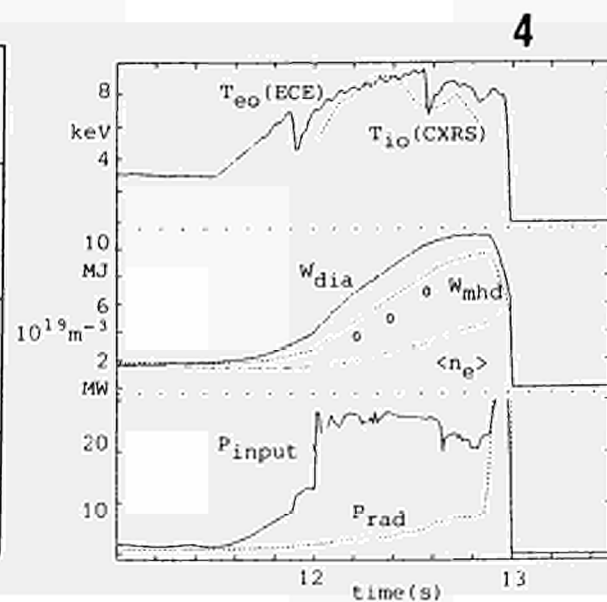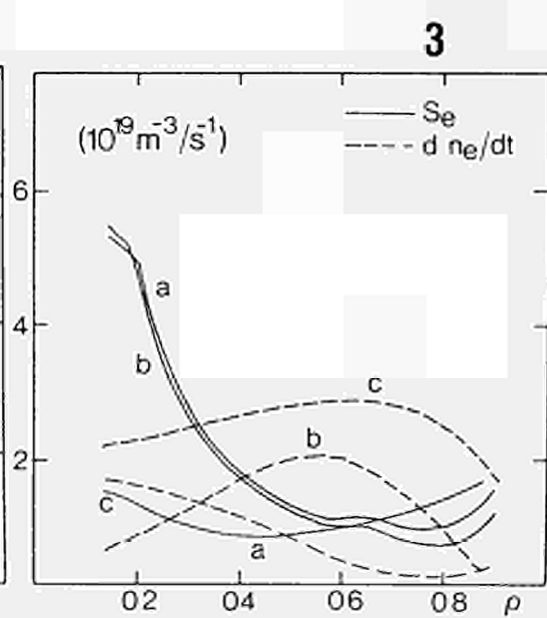
LIMIT ON β_p DUE TO GLOBAL MODES IN IGNITED PLASMAS

F. Pegoraro and F. Porcelli

JET Joint Undertaking, Abingdon, Oxon., OX14 3EA, UK

B. Coppi and S. Migliuolo

MIT, Cambridge, Mass. 02139, USA

ABSTRACT

It is shown that fusion produced α-particles can lead to stable values of β_p that are considerably larger than those predicted by the ideal MHD theory. The stabilising mechanism is effective if a combined criterion is met, involving among others, the area of the plasma cross-section where q is below unity and the ignition temperature. The implications of this criterion are discussed in terms of envisaged ignition scenarios.

INTRODUCTION

Internal MHD modes, such as sawteeth and fishbone oscillations, affect the central hottest part of the plasma column and can damage the plasma performance, hindering the achievement of ignition conditions. These modes cause a repetitive failure of the central plasma confinement leading to a spatial redistribution of the plasma energy. In addition, these modes spread, and possibly expel from the plasma, the α-particles which are produced at the centre of an ignited D-T plasma. On the other hand this loss of confinement can also be beneficial, e.g. in avoiding ^{4}He ash accumulation at the plasma centre once the plasma is ignited, or in preventing the fusion thermal runaway. Control over the onset of the internal modes becomes particularly important for plasmas where the magnetic winding parameters q is expected to fall below unity over a sizeable portion of the poloidal cross-section.

In this paper we show, along the analysis of Refs. [1,2] that the α-particles produced by the fusion reactions, naturally exert a controlling influence. This can enhance the stable values of the poloidal beta β_p of the bulk plasma by as much as three times its threshold value, as determined within the ideal MHD approximation. However, this control turns out to be ineffective if the area where q is below one is large (say $r_0/a \gtrsim 1/2$, with $q(r_0) = 1$ and a the mean radius of the plasma column). Besides r_0/a, key parameters are the ratio between the magnetic curvature $\ast$ ∇B drift frequency of the α-particles and the Alfvén frequency, which scales as $n^{1/2}/(r_0 B)$, and the central ignition temperature T_0 ($T_{e0} = T_{i0}$ is assumed). The latter controls the ratio between the α-particle $\beta_{p\alpha}$ at ignition and β_p. If ignition is to be achieved at high values of T_0 (say $T_0 \gtrsim 20$-25keV) the effect of the α- particles on internal modes may turn from stabilising to destabilising. This resurgent instability [3] interacts with the newly born, fully energetic α's, and can thus affect the ignition energy balance severely.

STABILITY DOMAIN

The relevant dispersion relation, which governs internal $m = 1$ modes in the presence of energetic particles, as derived e.g. in [1], reads

$$[\omega(\omega - \omega_{di})]^{1/2} = i\omega_A[\lambda_H + \lambda_K(\omega)] \qquad (1)$$

where $\omega_{di} = [(k_\theta c/e n B)(dp_i/dr)]_0$ is the bulk ion diamagnetic frequency at $r = r_0$, $\lambda_H = \gamma_{mhd}/\omega_A \sim O(\epsilon_0^3 \beta_p^2)$ is the ideal driving term, $\epsilon_0 = r_0/R_0$ and $\omega_A = V_A/R_0\sqrt{3}$ is the Alfvén frequency. The complex function $\lambda_K(\omega) \sim O(\epsilon_0^{3/2} \beta_{p\alpha})$ gives the contribution of the α-particles and can be approximated by

$$\lambda_K(\omega) = (\epsilon_0^{3/2} \beta_{p\alpha}/s_0) \, \hat{\lambda}_K(\omega/\bar{\omega}_{D\alpha}). \qquad (2)$$

where $s_0 = d \ln q/d \ln r|_{r=r_0}$, $\beta_{p\alpha}^* = -[8\pi/B_p^2(r_0)] \int_0^1 dx \, x^{3/2} (dp_\alpha/dx)$. $\bar{\omega}_{D\alpha}$ is the bounce averaged magnetic drift frequency at $r = r_0$ of deeply trapped α-particles with energy $\epsilon = 3.5$Mev, and the form factor $\hat{\lambda}_K$ which is shown in Fig. 1, is largely independent of the plasma parameters. An isotropic slowing down distribution function has been assumed.

Solving (1) for $\omega = \omega_R \equiv \text{Re } \omega$, we obtain the marginal stability curve in the $\lambda_H - \hat{\beta}_{p\alpha}$ plane where

$$\hat{\lambda}_H = (\omega_A \lambda_H/\bar{\omega}_{D\alpha}) \equiv \gamma_{mhd}/\bar{\omega}_{D\alpha}, \quad \hat{\beta}_{p\alpha} = (\omega_A \epsilon_0^{3/2}/\bar{\omega}_{D\alpha} s_0) \beta_{p\alpha}^* \qquad (3)$$

This curve is plotted in Fig. 2 for $\omega_{di}/\bar{\omega}_{D\alpha} = 5 \times 10^{-2}$. The portion of the unstable domain, immediately above the stability curve to the left of its maximum, corresponds to fishbone oscillations [4] with $\omega \sim \omega_{di}$ which resonate with slowed down α-particles. The portion to the right of the
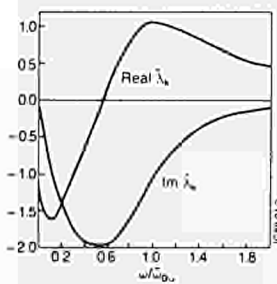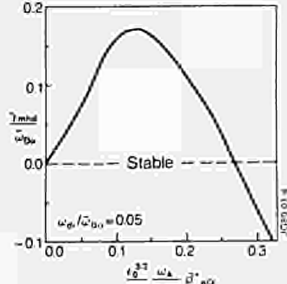
maximum corresponds to fishbone oscillations [3] with $\omega \sim \bar{\omega}_{D\alpha}$, driven by the precessional motion of the α-particles. Further within the unstable domain, almost purely growing internal $m = 1$ modes occur. The stability curve in the $(\omega_{di}/\bar{\omega}_{D\alpha}) - \hat{\beta}_{p\alpha}$ plane is shown in Fig. 3 for $\gamma_{mhd}/\bar{\omega}_{D\alpha} = 0.05$ and 0.1. These curves indicate that above a maximum value of $\gamma_{mhd}/\bar{\omega}_{D\alpha}$, and/or of $\omega_{di}/\bar{\omega}_{D\alpha}$ no stabilisation is possible.

The stability domain in the $\lambda_H - \hat{\beta}_{p\alpha}$ plane [5] is essentially independent of the plasma parameters, once the ratio $\omega_{di}/\bar{\omega}_{D\alpha}$ is fixed. In an ignited plasma the latter is characteristically $\gtrsim 10^{-1}$. A more explicit form of the stability criterion can be obtained by expressing λ_H and $\beta_{p\alpha}$ in terms of β_p, for chosen values of the geometrical and profile plasma parameters and of the central ignition temperature T_0.

For convenience, we adopt the simplified, even though rough, model

$$\lambda_H = (3\pi/2) \, \epsilon_0^3 [\beta_p^2 - \beta_{p,mhd}^2] \qquad (4)$$

where

$$\beta_p = [8\pi/B_p^2(r_0)][\langle p(r_0) \rangle - p(r_0)]. \qquad (5)$$

with $\langle p(r_0) \rangle$ the average of p inside the q = 1 surface. The ideal mhd threshold $\beta_{p,mhd}$ varies characteristically between 0.1 and 0.3, being smallest for elongated configurations and for large r_0/a. This leads to the following estimate of the maximum stable value $\beta_{p,max}$

$$\beta_{p,max}^2 - \beta_{p,mhd}^2 = 5.6 \times 10^{-2} \, \frac{\bar{\omega}_{D\alpha}}{\omega_A} \left(\frac{R_0}{r_0}\right)^2 (1 - 5.5 \frac{\omega_{di}}{\bar{\omega}_{D\alpha}}) \qquad (6)$$
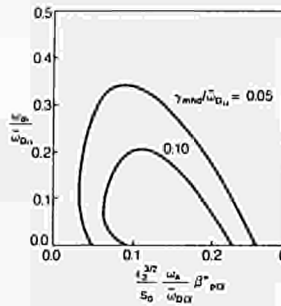
Fig. 3: Stability domain in the $(\omega_{di}/\bar{\omega}_{D\alpha}) - \hat{\beta}_{p\alpha}$ plane.
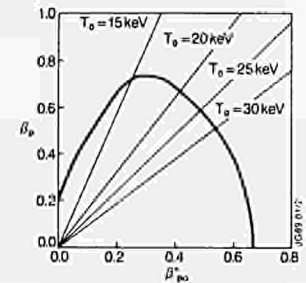
Fig. 4: Stability domain in the $\hat{\beta}_p - \hat{\beta}_{p\alpha}$ plane (see definition below Eq. (2)).

where the r.h.s. decreases approximately as r_0^{-3}. For $\beta_{p,max} \gg \beta_{p,mhd}$, $\beta_{p,max}$ scales approximately as

$$\beta_{p,max} = 0.5 \, \frac{[n_i(r_0)/10^{14} \text{ cm}^{-3}]^{1-4}}{(9 \, r_0/R_0)(r_0/50\text{cm})^{1/2}(B/10\text{T})} \qquad (7)$$

The stability domain in the $\hat{\beta}_p - \hat{\beta}_{p\alpha}$ plane is shown in Fig. 4 where we have chosen $\beta_{p,mhd} = 0.2$. An increase of r_0 from $r_0/a = 0.36$, shown in Fig. 4, to $r_0/a = 0.6$ brings $\hat{\beta}_{p,max}$ down from approximately 0.7 to 0.35, while the largest value of $\hat{\beta}_{p\alpha}^*$ on the stability curve decreases from 0.67 to 0.2.

At ignition, the ratio $\beta_{p\alpha}^*/\beta_p$ is determined by the central plasma temperature T_0 and by a profile factor. For fixed profiles, the rapidly increasing temperature dependence is shown by the slopes of the straight lines in Fig. 4, corresponding to the ratio $\hat{\beta}_p/\hat{\beta}_{p\alpha}^*$ (T_0). This ratio has been evaluated for the following profiles: $p \propto p_0(1 - r^2/a^2)^\sigma$, with $\sigma = 2$ for the thermal plasma and $\sigma = 6$ for the alphas. These lines indicate that the largest stabilisation is obtained at relatively low ignition temperature. If ignition is sought at higher values of T_0, the enhanced stability is largely lost and, as r_0/a is increased above the value shown, the instability threshold may fall below its ideal mhd value, as fishbones with $\omega = \bar{\omega}_{D\alpha}$ can be excited.

CONCLUSIONS

These results indicate that fusion α-particles can indeed help in controlling the onset of internal modes in an ignited plasma. However, this control is most effective when the area where $q < 1$ is not too large, i.e. when the consequences of these modes would be less damaging. The most effective strategy, besides keeping β_p small, is to approach ignition conditions at relatively low temperatures and large values of $n^{1/2}/(r_0 B)$. Higher temperatures can be expected to lead to fishbone oscillations with $\omega \sim \bar{\omega}_{D\alpha}$ and, consequently, to scattering of fully energetic α-particles. Fishbone oscillations with $\omega \sim \omega_{di}$ can occur if ignition is approached at $\beta_p \gtrsim \beta_{p,mhd}$, but $\gamma_{mhd} < \omega_{di}/2$, and $\beta_{p\alpha}$ is still small. However, these oscillations resonate with slowed down α's and are not expected [6] to affect the energy balance significantly. In fact they may even be beneficial in easing the problem of ash accumulation.

REFERENCES

[1] B. Coppi, J. Hastie, S. Migliuolo, F. Pegoraro and F. Porcelli, Phys. Lett. A132, 267 (1988).
[2] F. Pegoraro, F. Porcelli, B. Coppi, P. Detragiache and S. Migliuolo, XII Int. Conf. Plasma Phys. & Contr. Fus., Nice, (1988) paper IAEA-CN-50/D-4-6.
[3] L. Chen, R.B. White, M.N. Rosenbluth, Phys. Rev. Lett. 52, 1122 (1984)
[4] B. Coppi, F. Porcelli, Phys. Rev. Lett. 57, 2272 (1986).
[5] B. Coppi, S. Migliuolo, F. Pegoraro and F. Porcelli, "Global modes and high-energy particles in ignited plasmas", to be published.
[6] B. Coppi, F. Porcelli, Fusion Tech. 13, 448 (1988).

Fig. 1: Real and imaginary parts of $\hat{\lambda}_K$ defined in Eq. (2).

Fig. 2: Stability domain in the $\hat{\lambda}_H - \hat{\beta}_{p\alpha}$ plane (see Eq. (3)).

STUDY OF THE BEHAVIOUR OF CHAOTIC MAGNETIC FIELD LINES IN A TOKAMAK

M. Hugon, J.T. Mendonça and P.H. Rebut

JET Joint Undertaking, Abingdon, Oxon, OX14 3EA, UK

1. INTRODUCTION

One plausible explanation for the observed anomalous energy losses in tokamaks is the existence of a confinement region in the plasma, where magnetic islands coexist with stochastic magnetic field lines [1]. It is the purpose of the present work to elucidate the statistical behaviour of the stochastic field lines. This is done by numerically integrating the field line equations. Assuming $2N_0 + 1$ magnetic island chains centered at radial positions $x_N = N/m$, where m is the poloidal mode number, the field line equations are:

$$\frac{dx}{dz} = \frac{B_x}{B_z} = \frac{\gamma^2}{16m} \sum_{N=-N_0}^{+N_0} \sin(Nz - my + \phi_N); \quad \frac{dy}{dz} = \frac{B_y}{B_z} = x \qquad (1)$$

γ is the overlapping parameter and ϕ_N are the phase shifts, which are assumed to be randomly distributed among the island chains. In Eqs. (1), x is normalised to $\Delta = 1/m$ and the poloidal and toroidal variables, y and z, are in radians. Note that, in the limit $N_0 \rightarrow \infty$ and for $\phi_0 = \ldots = \phi_N = $ const, Eqs. (1) exactly reduce to the standard map [2].

2. CROSS SECTION OF STOCHASTIC FLUX TUBES

Let us call o(N) the normalised cross section of the flux tubes associated with the stochastic field lines which leave the 0th island chain and attain the Nth island chain. It is defined by the expression [1]:

$$o(N) = \frac{2}{S} \iint \frac{B_x(\gamma)}{B_z} H(B_x) \, H_{cross}^N \, dydz; \qquad S = \iint dxdy \qquad (2)$$

where $H(B_x)$ is the Heaviside function and H_{cross}^N is equal to 1 if the field line attains the Nth island chain and zero otherwise. The numerical results obtained from Eqs. (1) and (2) with 9 island chains can be described by:

$$o(1) = A(\gamma - \gamma_C)^B \qquad (3)$$

where $A = 0.47 \pm 0.13$, $B = 2.50 \pm 0.23$ and $\gamma_C = 0.75 \pm 0.05$ for $\gamma_C \leq \gamma \leq 2$. The error bars are not due to numerical errors but to deviations induced by the particular choices of ϕ_N.

Using a recurrence analysis, it is possible to show that:

$$o(N) = o(1) \{1 + (N - 1)(1 - \alpha)\}^{-1} \qquad (4)$$

where α is the fraction of the stochastic field lines which cross one island chain. Eq. (4) was checked numerically, using for α the arithmetical mean of the values $\alpha(N) = N(N - 1)^{-1} - [o(1)/o(N)]^{cal}(N-1)^{-1}$. The results are summarised in Table I, which shows that the recurrence relation is very well satisfied.

3. STOCHASTIC VOLUME

The normalised volume filled by the stochastic field lines, V_s, and the normalised volume occupied by the magnetic islands, V_i, is defined by:

$$V_{s,i} = \frac{1}{S} \iint \frac{B_x(\gamma)}{B_z} H(B_x) \, L_{s,i} \, dydz \qquad (5)$$

where the lengths $L_{s,i}$ are:

$$L_s = 2H_{cross}^1 [z(x=1)-z_0(x=0)]/2\pi + 2H_{cross}^{0,-1} [z_1(x=0)-z_0(x=0)]/2\pi$$
$$+ H_{cross}^{0,-1} [z_2(x=0)-z_0(x=0)]/2\pi$$
$$L_i = [1 - (H_{cross}^1 + H_{cross}^{0,-1} + H_{cross}^{1,-1})] [z_2(x=0)-z_0(x=0)]/2\pi$$

$H_{cross}^{0,-1}$ (resp. $H_{cross}^{1,-1}$) is equal to 1, if the field line attains the island chain -1, (resp. +1 or -1) after having crossed the plane x = 0 once (resp. more than once), and zero otherwise. $z(x = 1)$ is the toroidal coordinate of the field line in the plane of the chain +1 and $z_i(x = 0)$ are the toroidal coordinates of the field line in the plane of the chain 0 after i crossings of this plane.

The computation of Eqs. (5) using Eqs. (1) indicates that the relation $V_s + V_i = 1$ is verified. For $\gamma < \gamma_C$, the island volume V_i is shown to increase with γ according to $2\gamma/\pi$, as expected. For $\gamma > \gamma_C$, the magnetic surfaces of the island are destroyed by stochasticity and V_i decreases until it reaches 0, when γ is close to 1.5.

4. DIFFUSION COEFFICIENT

The mean number of turns in the toroidal direction to cross N island chains is determined by $T(N) = V(N)/o(N)$, where $V(N)$ is defined by an expression formally identical to Eqs. (5), but with $L(N) = 2H_{cross}^N [z(x = N)-z_0(x = 0)]/2\pi$. The numerical results for $T(N)/T(1)$ are represented in figure 1 as a function of N, for different values of γ. $T(N)$ is very close to $N^2T(1)$ for $\gamma = 1.3$ and 1.35, which is characteristic of a diffusion process across the island chains. However, for $\gamma \geq 1.8$, there is a slight deviation from the diffusion, since $N < T(N)/T(1) < N^2$. These effects are described by a kinetic equation for the field lines containing a diffusion and a propagation term [3].

The diffusion coefficient is defined as $D = 1/T(1)$. The average of the numerical values obtained for D from Eqs. (1) with different phases ϕ_N is given in figure 2 as a function of γ. Also shown is a fit of the computed results valid for $\gamma_C \leq \gamma \leq 2$:

$$D = A'(\gamma - \gamma_C)^{B'} \qquad (6)$$

where $A' = 1.25 \pm 0.30$ and $B' = 2.10 \pm 0.40$. Figure 2 shows that Eq. (6) is in good agreement with the data obtained for $D = 1/T(1)$ using the standard map, D^{SM}, for $\gamma_C \leq \gamma \leq 1.1$, indicating that the standard map provides a good approximation of the exact field line calculation for values of γ close to γ_C. However, D^{SM} departs from Eq. (6) for larger values of γ and follows the quasi-linear diffusion coefficient $D^{QL} = \pi^2\gamma^4/128$ before starting to saturate for $\gamma \geq 1.75$. The saturation is due to the fact that, for the standard map, $T(1)$ can never be less than 1. A proper definition of D prevents the well known strong oscillations of D^{SM} around D^{QL} [4].

5. CONCLUSION

The recurrence relation (4) on o(N) has been numerically tested by integrating the field line equations. The same computation has shown that the behaviour of the stochastic field lines is close to a diffusion process, when islands are in equilibrium with a stochastic region. The diffusion coefficient for the stochastic field lines D is defined as the inverse of the average number of toroidal turns to cross one island chain. The computation of D from Eqs. (1) is valid for values of γ up to 5. The island and stochastic volumes have been also defined and computed, ensuring that the equality $V_i + V_s = 1$ is satisfied.

Table I

Comparison between the numerical results $[o(N)/o(1)]^{cal}$ and those obtained through Eq. (4), $[o(N)/o(1)]^{rec}$, using for α the arithmetical mean α^{av} of $\alpha(N) = N(N-1)^{-1} - [o(1)/o(N)]^{cal}(N-1)^{-1}$.

γ	1.30		1.35		1.80		3.00	
α^{av}	0.461		0.438		0.524		0.629	
$\frac{o(N)}{o(1)}$	cal	rec	cal	rec	cal	rec	cal	rec
N = 2	0.651	0.650	0.642	0.640	0.679	0.678	0.671	0.729
3	0.473	0.481	0.465	0.471	0.497	0.512	0.589	0.574
4	0.390	0.382	0.376	0.372	0.425	0.412	0.496	0.473
5							0.448	0.402

REFERENCES

[1] P.H. Rebut et al, in Plasma Physics and Controlled Nuclear Fusion Research (Proc. 11th Int. Conf. Kyoto, 1986), Vol.2, IAEA, Vienna, 187(1987).
[2] B.V. Chirikov, Phys. Reports 52, 265 (1979).
[3] M. Hugon, J.T. Mendonça and P.H. Rebut (1989) - to be published.
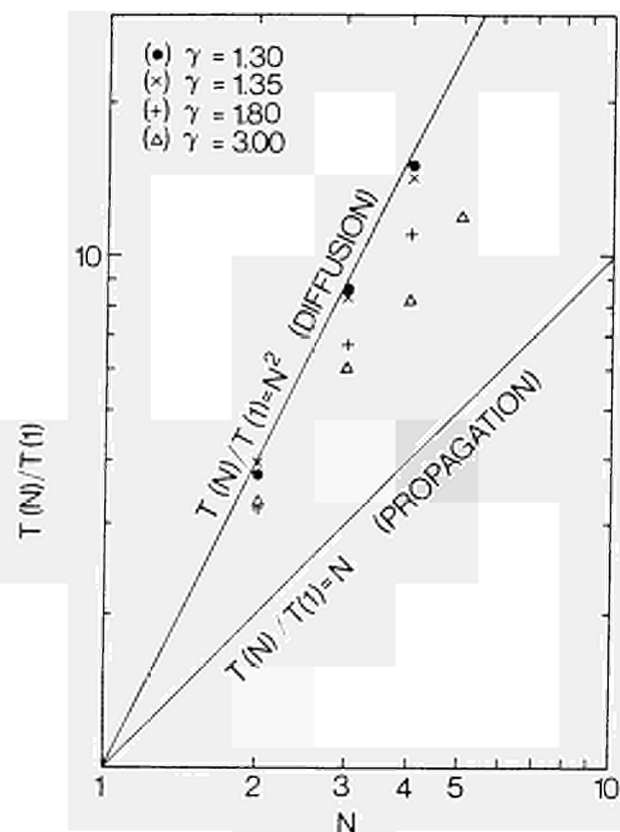[4] Y.H. Ichikawa, T. Kamimura and T. Hatori, Physica 29D, 247 (1987).

Fig. 1

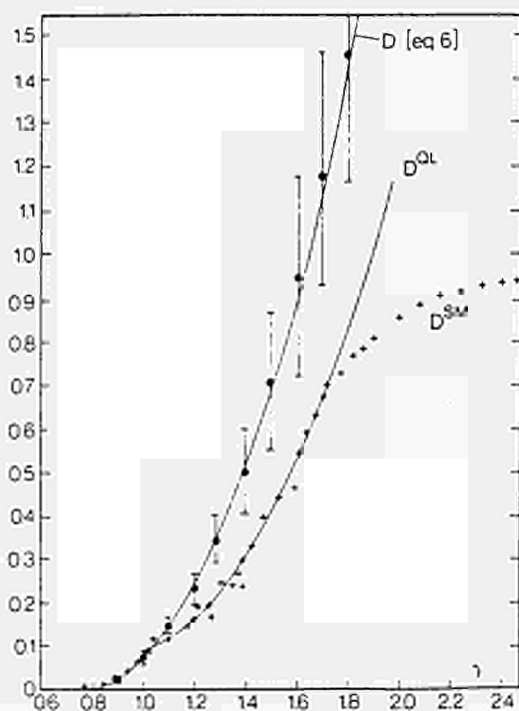Mean number of turns T(N) in the toroidal direction for a stochastic field line to cross N island chains.

Fig. 2

Diffusion coefficient. The numerical results (●) computed from eq. (1) are compared with eq. (6) with the quasi-linear curve D^{QL} and with those obtained from the standard map, D^{SM}.

IDEAL BALLOONING STABILITY OF JET DISCHARGES

R.M.O. Galvão[1], J.P. Goedbloed[2], G. Huysmans[2], E. Lazzaro,
J. O'Rourke, G. Schmidt[3], P. Smeulders.

JET Joint Undertaking, Abingdon, Oxon., OX14 3EA, UK.
[1]Instituto de Pesquisas Espaciais and Universidade de São Paulo, Brazil
[2]FOM-Instituut voor Plasmafysica, Nieuwegein, The Netherlands
[3]Princeton Plasma Physics Laboratory, Princeton, New Jersey, USA

INTRODUCTION

Conditions under which ballooning modes are expected to be excited have recently been obtained in two different types of discharges in JET. In the first type, discharges with β approaching the Troyon-Sykes-Wesson critical value β_c for optimised pressure profiles have been produced at low toroidal fields ($B_T = 1.5T$). In the second type, extremely high pressure gradients have been produced in the plasma core through pellet injection in the current rise phase of the discharge followed by strong additional heating [1]. The stability of these discharges has been studied with the stability code HBT [2] coupled to the equilibrium identification code IDENTC [3].

The equilibrium pressure and diamagnetic function profiles are determined in IDENTC by an optimisation procedure to fit the external magnetic measurements. The resulting pressure profile in the equatorial plane is then compared with the profile derived from 'direct' measurements, i.e., electron density and temperature profiles measured by the LIDAR diagnostic system [4], ion-temperature profile measured by the charge-exchange diagnostic system [5], and ion density profile calculated from the Z_{eff} and electron density profiles. Furthermore, the value of the safety factor q on axis is compared with that determined from polarimetry [6]. When good agreement is found, the output data from IDENTC is passed directly to HBT to carry out the stability analysis. When there is not a good agreement, as in the case of pellet discharges with highly peaked pressure profiles, the equilibrium is reevaluated using the 'experimental' profile and the data from polarimetry.

HIGH-β DISCHARGES

A series of discharges at low plasma current and low toroidal field ($I_p = 1.5MA$ and $B_T = 1.5T$) with strong ion cyclotron heating have been produced in JET to attempt reaching the critical value $\beta_c = 0.028\, I_p(MA)/a(m)\, B_T(T)$ of β for ideal MHD stability. In Fig.1 we show the experimental data for shot 14729 which has one of the highest values of the ratio β/β_c obtained so far, viz., $\beta/\beta_c = 0.6$. We note that after $t = 47s$ the central electron temperature starts to show some spikes superimposed on the usual sawtooth. These spikes are well correlated with the MHD activity measured by external coils. Furthermore, the activity after $t = 47.5s$ seems to increase for larger values of the toroidal mode number n. To investigate a possible role of ballooning modes, we have carried out a stability analysis at $t = 48.0s$, when LIDAR data are available. In Fig. 2 we show the pressure profile determined by IDENTC normalised by the maximum electron pressure determined by LIDAR. There is no ion temperature profile available for this shot and for the stability calculations the magnitude of the total pressure is determined by the value of the poloidal beta, $\beta_I = 8\pi S\langle p\rangle/\mu_0 I_p^2$, where S is the area of the cross-section of the plasma column and $\langle p\rangle$ the plasma average pressure. The plasma is found unstable in the central region indicated in the figure and becomes unstable by crossing the boundary of the first stability region. The unstable region is localised inside the $q = 1$ surface and thus the consequence of the instability is probably to help trigger the sawtooth crash.
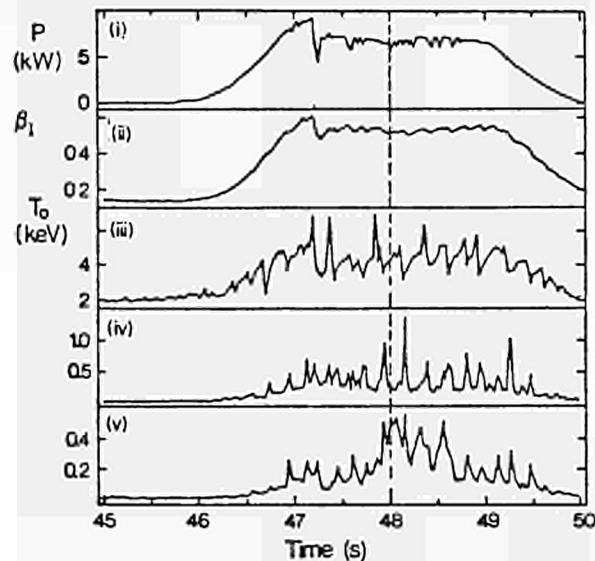
DISCHARGES WITH PELLET FUELLING

Discharges with strong pressure gradients (dp/dr > 300kPa/m) have been produced in JET with pellet injection followed by strong additional heating. In Fig. 3 we show the experimental data for shot 17749. The pellet is injected at t = 42s, during current rise, followed one second later by strong heating. We notice that the value of β saturates at a constant value $\beta_I = 0.4$ and that at $t = 44.2s$ it starts to drop although the total heating power is approximately constant. This drop in the value of β_I is strongly correlated with an initial increase in the n = 4 MHD activity followed by a sharp increase in the n = 2 coupled with the n = 3 activity, whereas there is no n = 1 activity. Analysis of the fast X-ray emission indicates that the n = 2 activity is related to an odd poloidal mode number $m \geq 3$. In Fig. 3a, iv we show also the trace of β_I for shot 17747. In this shot there was no pellet injection but the level of heating power was the same as in shot 17749. The pressure profile is much broader for the no pellet shot (Fig. 4a) and there is no drop in the value of β_I at constant heating power.

The stability of these discharges has been analysed using the experimental profiles and the value of $q_0 = 1.2$, determined by IDENTC from polarimetry data. Shot 17749 is found unstable around the regions of maximum pressure gradient, but stable at the centre. The discharge without pellet injection 17747 is stable. The unstable region in the shear vs pressure gradient diagram has been determined by increasing β_I while keeping constant the values of q_0 and q_1 ($q_0 = 1.2$; $q_1 = 4.07$ for shot 17747 and $q_1 = 3.83$ for shot 17749). Again the plasma becomes unstable by crossing the boundary of the first stability region. Because the unstable magnetic surfaces are localised in the middle of the plasma, one expects that the consequence of the ballooning instability to be just an enhanced transport in this region. The rate of decay towards a stable profile, is however, constrained by transport from the centre of the plasma and to the plasma boundary. This leads to the somewhat slow relaxation of the value of β observed experimentally.

CONCLUSIONS

High-β discharges have been shown to be ballooning unstable at the centre of the discharge although β is below the critical value given by the Troyon-Sykes-Wesson limit. The pellet discharge 17749 has been found to approach the unstable region for ballooning modes from the first stable region. Access to the second stability region would require a larger pressure gradient and current profile control to keep $q_0 > 1.2$.

REFERENCES

[1] The JET Team, 12th International Conference on Plasma Physics and Controlled Nuclear Fusion Research, Nice, France, 1988. Paper IAEA-CN-50/A-IV-).

[2] J.P. Goedbloed, G.M.D. Hogweij, R. Kleibergen, J. Rem, R.M.O. Galvão and F.H. Sakanaka, Proceedings of the 10th International Conference on Plasma Physics and Controlled Nuclear Fusion Research, London, 1986, (IAEA, Vienna, 1987), Vol. II, p. 165.

[3] E. Lazzaro and P. Mantica, Plasma Physics and Controlled Fusion 30, 1735 (1988).

[4] H. Salzmann, J. Bundgaard, A. Gadd, C. Govers, et al., Rev. Sci. Instrum. 59, 1451 (1988).

[5] M. von Hellermann, et al., Ion Temperature Profiles in JET, this conference, paper P4 A1 12.

[6] J. O'Rourke, J. Blum, J. Cordey, A. Edwards et al., Proceedings of the 15th Conference on Controlled Fusion and Plasma Heating, Dubrovnik, 1988, Europhysics Conference Abstracts 12B, Part 1, p. 155.
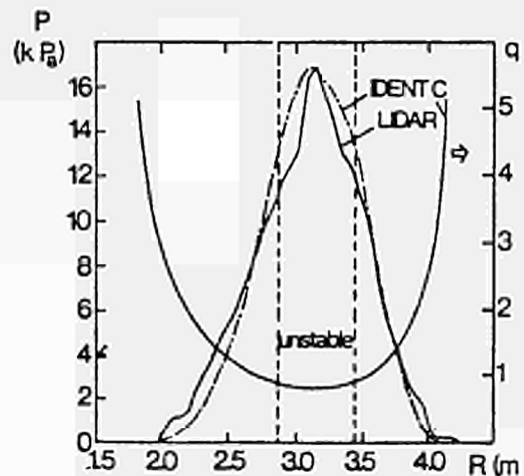
Fig. 1: Experimental data for #14729:
i) total radio-frequency power;
ii) Shafranov's poloidal beta;
iii) central electron temperature from electron cyclotron emission;
iv) n = 1 and
v) n = 3 MHD activity in arbitrary units.

Fig. 2: Electron pressure profile measured by the LIDAR diagnostic system (full line) at t = 48s and corresponding renormalised total pressure and q profiles determined by the equilibrium code IDENTC. The indicated region is unstable to ballooning modes.
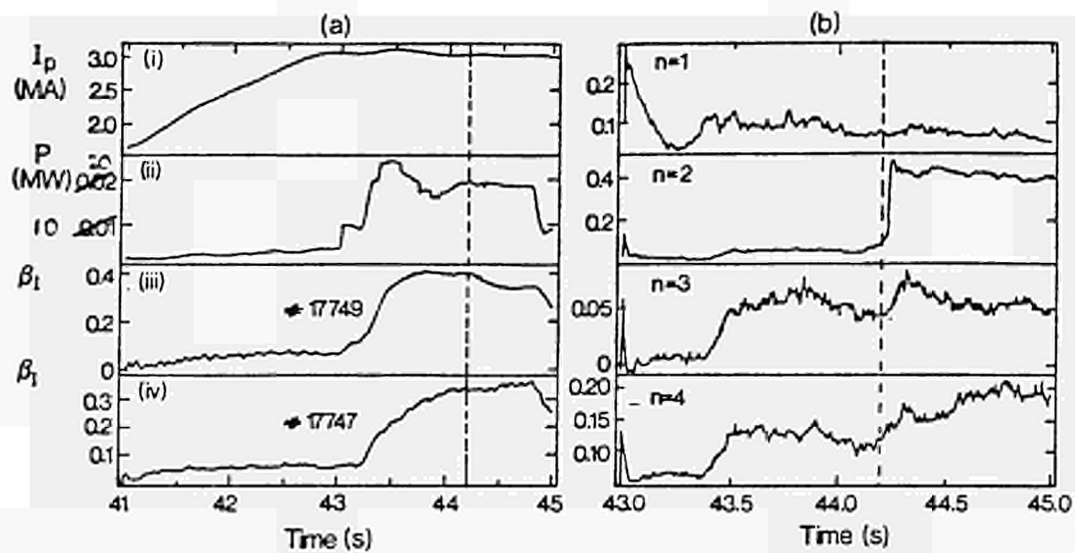
Fig.3(a): Experimental data for #17749: i) plasma current; ii) total heating power (NBI + ICRF + OHMIC); iii) & iv) Shafranov's poloidal beta (including trace for #17747). A 4mm pellet is injected at t = 42s in #17749; (b) MHD activity for #17749 (arbitrary units).
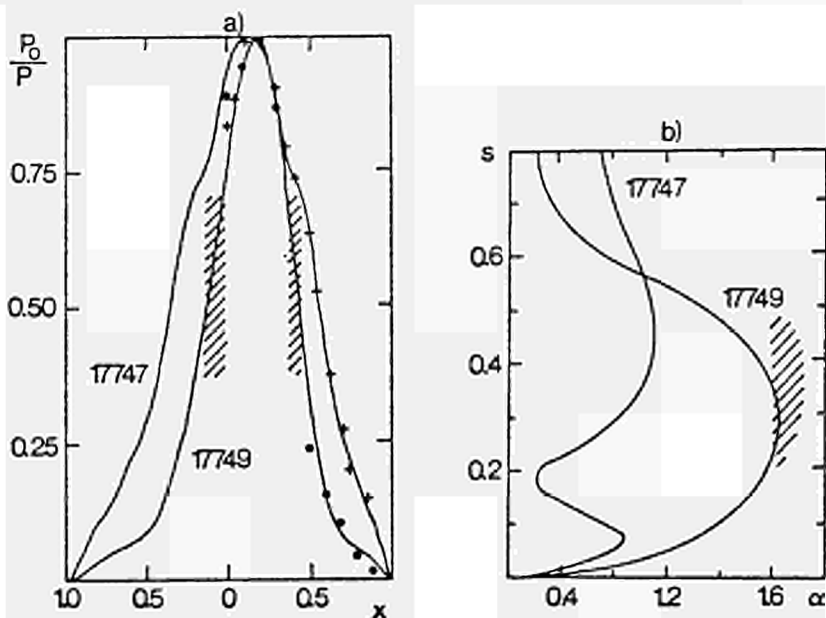

Fig.4(a): Normalised total pressure profiles for #17747 and 17749 used in the stability calculations. The horizontal axis is the radial position in the equatorial plane normalised to the half-width of the plasma cross-sections (a ≈ 1.18m). The crosses and dots represent the experimental pressure profiles for #17747 and 17749, respectively. The maximum pressures are approximately 75kPa for #17747 and 156kPa for #17749. The shaded region for shot 17749 is unstable to ballooning modes; (b) Corresponding $s = 2(\psi/q)(dq/d\psi)$ vs $\alpha = - (4q^{*2}/\epsilon B^{2})\sqrt{\psi}\, dp/d\psi$ stability diagram, where $q^* = \epsilon B \int d\ell/\mu_o I_p$.

SPUTTERING MEASUREMENTS ON JET USING A MULTICHANNEL VISIBLE SPECTROMETER

M F Stamp, M J Forrest*, P D Morgan, and H P Summers

JET Joint Undertaking, Abingdon, Oxon., OX14 3EA, UK
* UKAEA Association, Culham Laboratory, Abingdon, Oxon., OX14 3DB, UK

1. INTRODUCTION

A multichannel visible spectrometer has been used on JET to simultaneously observe the emission from D, H, He, C and O atoms and ions in the proximity of a belt limiter. The absolute intensity of the line emission, along with a Langmuir probe measurement of the edge electron temperature and an atomic physics model, allows us to calculate the influxes of these species.

Under steady-state conditions the influxes of D and He are the same as the effluxes, so the ratio of impurity to fuel fluxes, eg. carbon to deuterium, is the apparent sputtering yield of deuterium on carbon in the tokamak environment.

The measured flux ratio Γ_c/Γ_D is also indicative of the central carbon impurity concentration in JET, because the limiters are the main source of impurities. For similar particle transport, $\Gamma_c/\Gamma_D = n_c(o)/n_D(o)$, so for a 10% flux ratio, $n_c/n_e \approx 6.6\%$, $Z_{eff} \approx 3$.

2. INSTRUMENTATION

Visible light, emitted by atoms and ions in front of the JET belt limiter is collected by a telescope and focused onto one end of a 1mm dia quartz optic fibre. Aperture matching optics focus the other end of the optic fibre onto the entrance slit of a 1-m Czerny-Turner monochromator that has been modified to accept an intensified linear diode array on its focal plane.

The active area of the detector is 25mm, covering approximately 20nm for a typical reciprocal linear dispersion of 0.8nm/mm. The spectrometer is equipped with a 600 ℓ/mm ruled grating of blaze wavelength 1.25µm. Spectral lines of D_γ, O II and C IV are seen in the third order of diffraction, and D_α, He I and C II in the second order of diffraction, when the spectrometer is set to a wavelength of 1.2µm (fig.1).

3. DATA INTERPRETATION

We use the standard interpretation [1-3], where the observed line intensities are proportional to the influxes of the observed ions:

$$\text{Particle Influx} \quad , \quad \Gamma = 4\pi \left(\frac{S}{XB}\right) I$$

where I is the measured intensity of a line of excitation rate X and branching ratio B, and S is the ionisation rate for that ion (atom).

It is important to note that the ratio S/XB is essentially density independent for JET electron edge densities, and varies approximately linearly with electron temperature for most low Z impurity lines [4]. (For D_α, this ratio is essentially constant for $20 < T_e < 1000$ eV and $n_e < 5\times10^{18}$ m^{-1}).

4. RESULTS

The carbon influx has been measured in JET deuterium and helium discharges, over a range of electron density, plasma current and additional heating power.

Figure 2 shows the carbon flux as a function of line-average electron density for two sets of consecutive 3 MA discharges, one in helium and the other deuterium. The flux is constant or slowly falling with density, and is higher in helium discharges. This is in contrast to the deuterium and helium fluxes, which increase with density squared and linearly with density, respectively [4].

The apparent sputtering yield $(\Gamma_c/\Gamma_{D,He})$ is shown in fig.3. For He plasmas this has a minimum of ~ 7% $(T_e(a) ~ 20$ eV) and for D plasmas, ~ 4.5% $(T_e(a) ~ 30$ eV). These low values are close to those expected from physical sputtering, including self-sputtering, of room temperature graphite [5]. At surface temperatures above 1000°C, radiation-enhanced sublimation should become important and may dramatically increase the sputtering yield [6]. The carbon self-sputtering yield also increases above 1000°C. Figure 3 shows that at low density and high edge electron temperature the sputtering yield is over 50% in the helium discharges, and nearly 20% for the deuterium, though higher values have been observed in other lower density deuterium plasmas. However, observation of the belt limiters with a CCD camera [7] showed that in the D plasmas the limiter temperature was less than 1000°C, and in the helium plasmas there were some 'hot-spots' with a maximum temperature of 700-750°C.

Figure 4 shows Z_{eff} plotted against the measured flux ratio for the previous deuterium data. The dashed curve assumes $\Gamma_c/\Gamma_D = n_c(o)/n_D(o)$. The general agreement is very good, suggesting that the main impurity is carbon, and that the transport of deuterium and carbon is similar.

Figure 5 shows the carbon flux plotted against the total input power to the plasma, for several plasma currents and additional heating powers. The data at different plasma currents are for similar shaped plasmas (though the 5 MA discharges were only 3 cm from the inner wall) that were nominally 'balanced' on the upper and lower belt limiters. The toroidal fields were different such that q~9 for $I_p = 2$ MA, q~5 for $I_p = 3$-4 MA and q~3.5 for $I_p = 5$ MA. Most of the additional heating was ICRH, but data points for upto 8 MW of NBI are included. The radiated power fraction was approximately constant at 0.4 (± 0.1).

Figure 5 clearly shows that the carbon influx is proportional to the total input power, and although the gradient is different for different plasma currents, it is within the error bars of the absolute measurements and the uncertainty with which the top-bottom belt limiters were 'equally' loaded.

In contrast the deuterium flux is independent of the additional heating, being approximately proportional to the line-average electron density squared.

5. SUMMARY

Simultaneous measurement of C, He, D lines emitted in front of the JET belt limiter allows an evaluation of the particle fluxes, and of the carbon sputtering yield.

At high electron density the sputtering yield is ~4% for D on carbon and ~7% for He on carbon, in agreement with physical sputtering calculations. At low electron density the sputtering yields can be very high (>50%), consistent with very high Z_{eff} values (>5), and this cannot be explained by sputtering calculations for the measured limiter temperatures of <800°C.

Such large experimental sputtering yields suggest that the carbon self-sputtering yield is higher than reported in ion-beam experiments [5], perhaps because of non-normal angle of incidence.

The carbon influx from the limiter seems to depend only on the input power to the plasma, whether it be ohmic, ICRF or NBI, at a measured rate of ~6×10^{20} atoms/s/MW. Consequently, the 'cleanest' plasmas are obtained at high electron densities when the deuterium (or helium) influxes are largest. Conversely, operation in D at low density, and with He conditioning (in order to reduce the recycling and the deuterium influx) will produce carbon dominated plasmas.

6. REFERENCES

[1] M F Stamp et al., Proc. 12th European Conf. on Controlled Fusion and Plasma Physics, Budapest, Vol.9F, Part II (1985), p.539.
[2] W Engelhardt, Proc. of Course on Diagnostics for Fusion Reactor Conditions, Villa Monastero, Varenna, Vol.1, (1982) p.11, (Report EUR 8351-I EN).
[3] A Pospieszczyk et al., J. Nucl. Mat. 145-147 (1987), p.574.
[4] M F Stamp, K H Behringer, M J Forrest, P D Morgan, and H P Summers, J. Nucl. Mat. 162-164 (1989), in press.
[5] J Roth, J Bohdansby and W Ottenberger, Report IPP 9/26 (1979).
[6] J Roth, J. Nucl. Mat. 145-147 (1987) p.87.
[7] D D R Summers, private communication.

Fig.1 Survey spectrum from the limiter viewing OMA spectrometer, showing lines of D, He, O and C.
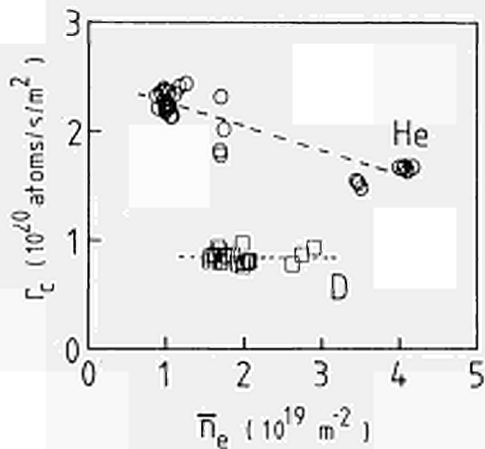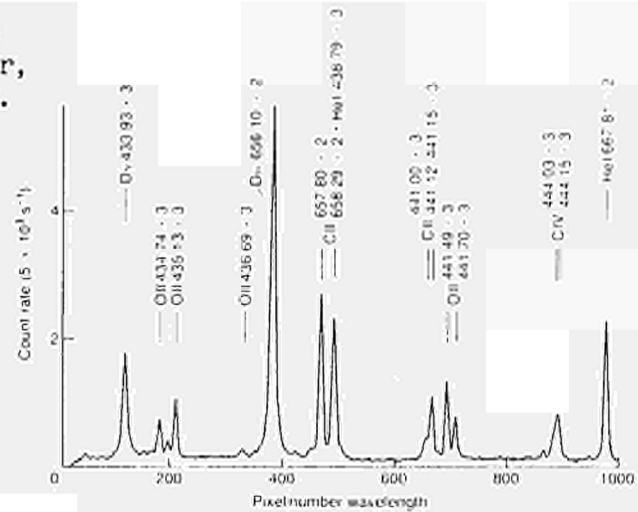
Fig.2 The variation of carbon influx with line-average density in ohmic 3 MA He and D discharges.
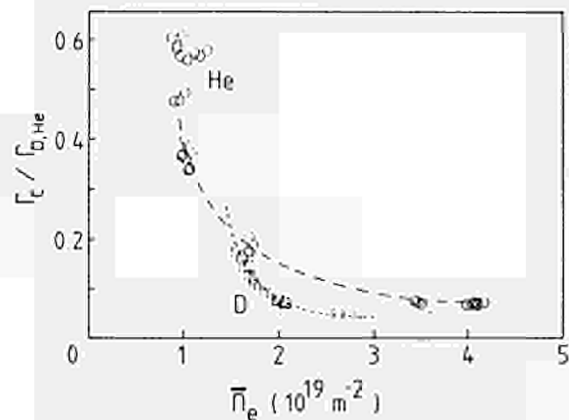
Fig.3 The variation of carbon sputtering yield with line-average density in ohmic 3 MA He and D plasmas.
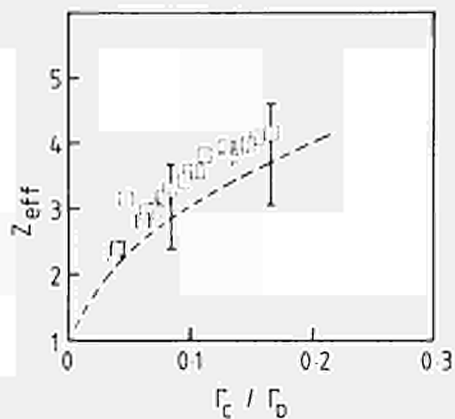
Fig.4 Z_{eff}(bremsstrahlung) vs carbon sputtering yield. The dashed line assumes i) $\Gamma_C/\Gamma_D = n_C(0)/n_D(0)$ and ii) carbon is the only impurity.
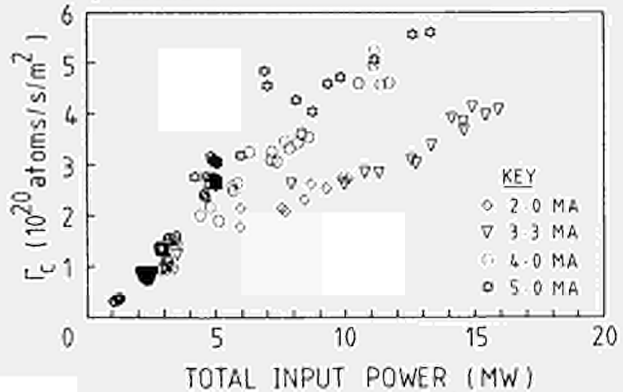
Fig.5 The variation of carbon influx with total input power for several plasma currents. The radiated power fraction is approximately constant.

A25

GAS BALANCE MEASUREMENTS AT JET

R. Sartori, G. Saibene, J.L. Hemmerich, M.A. Pick

JET Joint Undertaking, Abingdon, Oxon OX14 3EA, England.

1. Introduction

The inventory of gas in the walls of the JET machine is of concern for future operation, in particular during the DT phase. A diagnostic system which allows one to quantify the amount of gas released after each JET discharge as well as over a longer period has been operated since December 1987. Gas balance calculations have been carried out by comparing the amount of gas released to the total number of molecules fuelled into the plasma as cold gas, pellets and neutral beams. In addition, all the gas released during a period of operation, ranging from a few discharges to a few days, was collected and chemically analysed.

2. Experimental set-up and procedure

The experimental data presented were collected over a period of 9 months of JET operation. The in-vessel configuration was as described in [1]. The experimental set-up is shown in Fig. 1. During the measurements the main roughing pumps are disconnected (VA closed) and replaced by the helium cryopump CR. At the start of a discharge VB is closed. During the discharge gas is pumped from the vessel by the main turbo pumps and the pressure in V_1, measured by the capacitive gauge 2 , increases. After 600 seconds VB opens and the gas is collected in CR. Subsequently CR is heated and the collected gas is transferred to the reservoir R. Samples are taken to be chemically analysed by gas chromatography. The number of molecules collected after one shot or a series of shots is calculated from the pressure increase in the calibrated volumes V_1 and R respectively. The chemical composition of the collected gas is used to determine a correction factor for the number of deuterium molecules in the gas collected.

Deuterium (and/or He) is introduced into JET either as cold gas (initial puff followed by a density feedback system control inlet), as pellets or as neutral beams [2]. We estimate the error of the amount of gas input to be ± 5% (± 10% for pellet fuelled discharges). The error on the output measurements is estimated to be ≤ 5%.

3. Results

Data were collected for more than 500 discharges in a wide range of operational conditions. Fig. 2 shows the ratio P between the number of molecules released within 600 s after the discharge and the total number injected N_i, as a function of N_i, for successful plasma shots only. All these discharges have deuterium as main input gas. For a typical input of $N_i \gtrsim x \, 10^{21}$ molecules only a fraction of N_i varying from 10% to 40% is recovered within 600 s. In fact a variation of an order of magnitude in the total input results in only a factor of two variation in the total output. Values above 50% are normally observed only for very low density shots. These results are in good agreement with gas balance measurements for ohmic shots with deuterium in TFTR [3].

The percentage of gas recovered (Fig. 2) decreases with increasing input indicating that the total amount of deuterium trapped in the walls increases with the number of molecules injected. The fraction of gas released is independent of whether the shot is ohmic, additionally heated and/or pellet fuelled. The increase in the fraction released observed in TFTR after NB heated discharges is not found in JET. The fraction of deuterium released shows no significant dependence on plasma current (from 3 to 7 MA), current flat-top duration (1-10s), total power (up to 20 MW) or plasma configuration. Measurements carried out in JET operating at higher wall temperature (350°C versus 300°C) showed only a marginally higher recovery. After a He-cleaning pulse (i.e. a very low density, long current flat-top He discharge) the percentage of gas recovered varies from ~ 100% up to 900% of the input. Assuming that all the He is recovered, an average value of 0.8 x 10^{21} molecules of deuterium are released after such a discharge. Under these conditions at least 10 He discharges would be required to recover all the gas trapped in the walls during a high density deuterium shot (input ~ 10 x 10^{21} molecules). However, other experiments in JET show a decreasing in the deuterium release rate over a sequence of cleaning shots [4]. The amount of deuterium recovered after a plasma shot ending in a disruption varies from 2 x 10^{21} to 1 x 10^{22} molecules, i.e. up to 10 times the release measured after a shot with soft landing. The percentage of gas recovered varies from 50% to 500% of the deuterium injected, being around 80% for most of the disruptions. The total number of molecules recovered is always greater than the plasma inventory at the time t_D of the disruption. No clear relationship has been found between the measured fractional release and the plasma current or power at the time

t_D. This could indicate that the induced outgassing depends on the dynamics of each particular disruption, including in particular the local power deposition.

Taking account of the deuterium released during a whole day of operation (not only during the first 600 s after each shot), the average amount of gas recovered is ~<50%. We measured the long term outgassing of the vessel for 8-12 hrs after the last shot of the day with the wall and the limiters remaining at operation temperature. The decreasing deuterium release rate R was determined as a function of time. This further outgassing, however, contributes to the overall gas balance only by a few percent. The main impurities detected in the collected gas are hydrocarbons of various orders, the most abundant being CD_4 (~ 2% of the molecules); the relative amounts are fairly constant for different JET operating conditions. The resulting average correction on the total number of deuterium molecules is around +8%. With this correction the amount of deuterium that is left in the vessel walls is estimated to be around 40% of the input. This result is in good agreement with preliminary in-vessel deuterium retention measurements for the 1987 campaign [5].

Further understanding in the wall pumping phenomena during a plasma discharge can be gained by relating the fuelling and outgassing characteristics of a discharge to the actual plasma inventory. The fuelling efficiency F, the fraction of input gas which ends up in the plasma, is defined as the ratio between the plasma electron inventory I (corrected for Z_{eff}) and the gas input N_{io}. Both quantities are taken at time t_o, defined as the time when the fuelling due to density feedback stops. For $N_{io} > 2 \times 10^{21}$ molecules, F varies from 10% to 60% (Fig. 3). A large fraction of the input gas molecules is therefore already lost in the early phase of the discharge during or at the end of the density ramp-up, which is in many cases coincident with the end of the current ramp-up. In particular for ohmic shots with no fuelling after the density ramp-up the number of molecules recovered is equal or slightly less than the maximum inventory (Fig. 4). For additionally heated or pellet fuelled discharges the ramp-up pumping does not account for all the gas lost, since in this case the recovery is lower than the maximum inventory. For all but pellet fuelled discharges, where there is a large additional fuelling, this early pumping does, however, represent the major contribution to the total wall pumping. F is, similar to the percentage recovered, a decreasing function of N_{io} [6].

4. Conclusions

Particle balance measurements on a shot-by-shot basis show a high deuterium retention in the JET vessel walls. The fraction of input gas trapped into the walls at 600 s varies from 60% to 90% of the injected deuterium, the latter value being the most representative for high density shots. On this basis a direct prediction of the tritium inventory during the future DT operation can be done. Correcting for hydrocarbon content and taking into account overnight outgassing, it is shown that still up to 70% of the input gas is likely to be trapped in the walls. For example, for 100 high density plasma discharges requiring a total fuelling of 7.5 g of tritium, the maximum total tritium retention would be around 4.9 g. However, it has to be pointed out that this estimate does not take into account any physical or chemical process (e.g. thermal outgassing, He glow discharge cleaning) which could be exploited to enhance tritium release.

For ohmic shots the trapping of deuterium by the walls takes place mostly during the density ramp-up. Two phenomena are likely to contribute to the deuterium trapping into the JET walls: prompt implantation and co-deposition. Co-deposition of deuterium-rich carbon layers is related to the sputtering of carbon during the plasma discharge. This phenomenon, although it cannot account for the large early pumping observed, is likely to contribute to the 'further pumping'. The same considerations apply in general to additionally heated discharges. For pellet fuelled shots a stronger further pumping is observed. A more detailed analysis of the observed effects will be published.

References
[1] M. Pick et al, Proc. of 12th Symp. on Fusion Engineering, Monterey (CA) 1987, p. 137
[2] B.J. Green, Spring College on Plasma Physics, Trieste (Italy) 1987 (JET-R(87)06)
[3] K.L. Wilson, H.F. Dylla, Joint Report SAND88-8212 and PPPL-2523, October 1988
[4] G. McCracken, private communication
[5] M.P. Coad et al, 8th PSI, Jülich May 1988. To be published in J. Nucl. Mat.
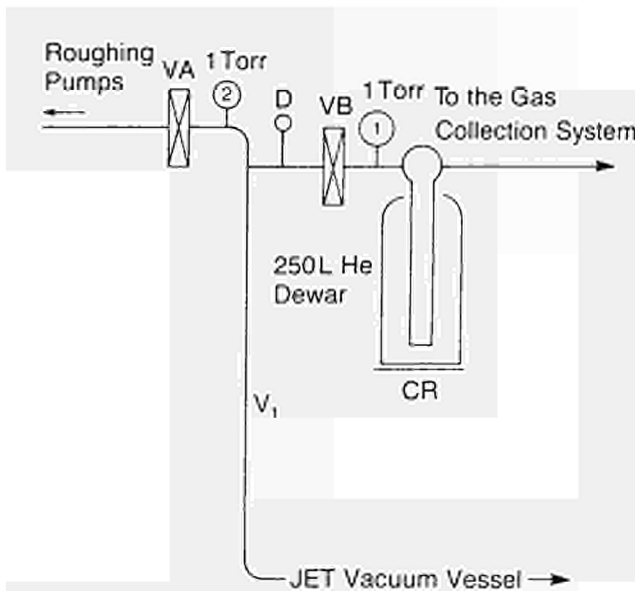[6] J. Ehrenberg, 8th PSI, Jülich May 1988. To be published in J. Nucl. Mat.
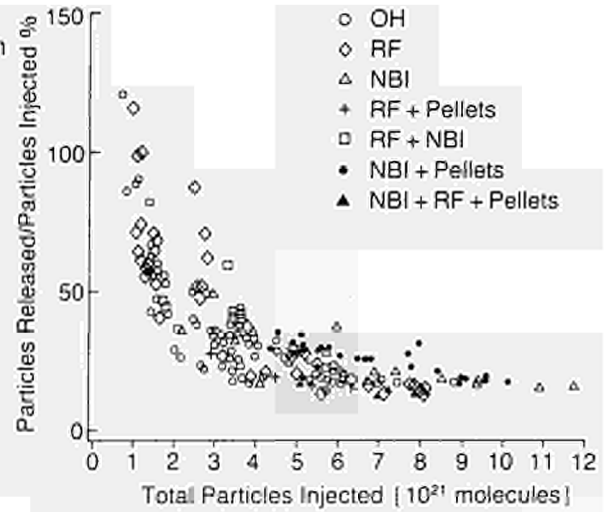
Fig. 1: Experimental set-up

Fig. 2: The fraction of gas released P in 600 s after the end of a discharge as a function of the number of molecules injected N_i
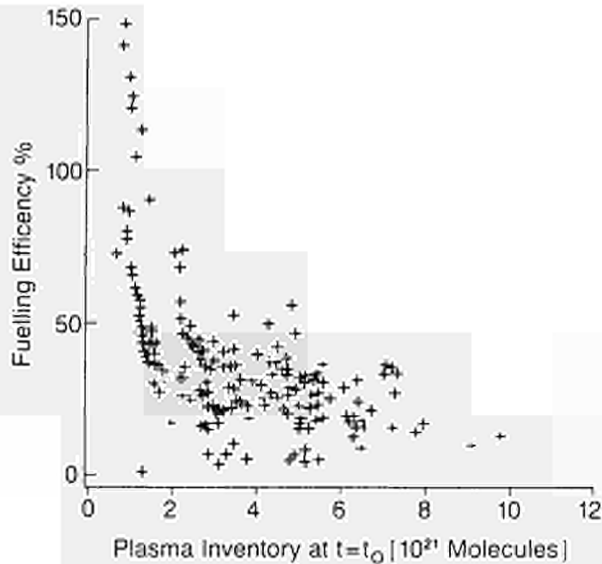

Fig. 3: The fuelling efficiency F as a function of the number of molecules injected N_{io}, for the same set of data as Fig. 1.
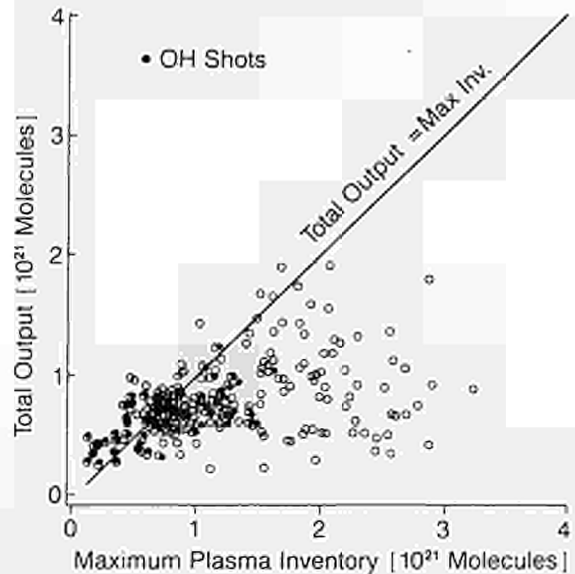

Fig. 4: The total output as a function of the maximum plasma inventory, for the same set of data as Fig. 1.

ICRF POWER-DEPOSITION PROFILES AND HEATING IN MONSTER SAWTOOTH AND PEAKED-DENSITY PROFILE DISCHARGES IN JET

V.P. Bhatnagar, A.Taroni, J.J. Ellis, J. Jacquinot, D.F.H. Start

JET Joint Undertaking, Abingdon, Oxfordshire, England OX14 3EA

1. INTRODUCTION :

The ion-cyclotron resonance heating (ICRH) of JET tokamak has demonstrated, among other results, (a) that the plasma can undergo a transition to a new regime, the so called 'monster sawtooth' [1] in which the plasma enjoys long quiescent periods where there is little coherent MHD activity and the sawtooth instability is suppressed for durations of up to 3 s and, (b) that the pellet-produced peaked-density profiles can be reheated [2] and sustained for up to 1.2 s resulting in high values of central electron and ion temperatures simultaneously and leading to an increased nuclear reactivity of the plasma. In this paper, we compare experimental results of electron and ion-heating in discharges that feature monster sawtooth with those in pellet-produced peaked-density profile discharges which were heated with ICRF.

Also we carry out a comprehensive analysis of ICRF-heated peaked-density profile discharges by a transport code to simulate the evolution of JET discharges and to provide an insight into the improved heating and confinement found in these discharges. In this analysis, the ICRF power-deposition profile in the minority-heating scenario is computed by the ray-tracing code BRAYCO [4] that self-consistently takes the finite antenna geometry, its radiation spectrum and the hot-plasma damping into account. The power delivered to ions and electrons is calculated based on Stix model [5].

2. RESULTS :

(a) Monster Sawtooth: The ICRF minority heating generally produces 'giant' sawteeth where $T_{e0}(\max)/T_{e0}(\min) \simeq 2$ compared to 1.1-1.2 in the ohmic phase and the sawtooth period is also increased by a factor of 2-3. The strong electron heating is related to the fact that during ICRH, a long minority-ion tail is produced which relaxes on the electrons and heats them predominantly. When the ICRF power is centrally deposited and exceeds a certain threshold (minimum $\simeq 3$ MW), monster sawteeth are produced generally when $q_{00} \simeq 3.3$ and the stabilisation is believed to be due to the presence of fast ions. [6] During the stable period, density and stored energy rise slowly but T_e saturates and the T_i-profile peaks which would lead to higher reactivity.

For limiter ICRH discharges, in Fig. 1 and 2, we plot T_{e0} and T_{i0} as a function of P_{tot}/n_{e0} for a range of plasma currents $I_p = 2$-6 MA, where 0 refers to the central values. The data for 2-3 MA is mostly of monster sawtooth whereas for 5-6 MA, it refers to the usual giant sawtooth. For a given central confinement volume, the data in Fig. 1 and 2 can be directly related to central electron and ion kinetic-energy confinement times respectively. A clear off-set linear behaviour is seen in the T_{i0}-plot whereas the T_{e0}-plot tend to saturate. This behaviour is a general characteristic of the ICRF minority-heating and will be compared to the particularly interesting case of peaked-density profile heating (see below). We note that within the scatter of the data there is little difference in the central incremental confinement time for 2-6 MA which has been independently verified by a local analysis. [7]

(b) Peaked-Density Profile Heating : We present results of peaked-density profiles that are produced by pellet fuelling in the current ramp-up phase and are followed by ICRH in JET limiter discharges. In Fig. 3, we present time traces of RF-power launched, DD-reaction rate, T_{e0}, T_{i0} and $\langle n_e \rangle$ of a 3 MA shot in which a 4 mm pellet penetrates deep inside the plasma and produces $n_{e0} \simeq 1 \times 10^{20}$ m^{-3} which slowly decays but the peaked-density is maintained for 1.2 s (see Fig. 13 of Ref. 2). Due to cooling by the pellet, T_{e0} initially drops but the immediate application of ICRH heats electrons steadily. Initially the T_e-profile is flat but becomes more and more peaked as time evolves. Note that T_{e0}-rise initially steepens but T_e then saturates. There is a crash at which time the peaked profile disappears and R_{DD}, T_{i0}, T_{e0} all drop though P_{RF} is still maintained. RF power delivered to electrons ($P_{e\,RF}$) and ions ($P_{i\,RF}$) and their profiles calculated by ray-tracing [4] for a peaked-profile discharge are shown in Fig. 4, where the symbol ∞ refers to the steady-state when the minority tail has been fully formed. Note that, due to higher density, a significant fraction of the minority power goes to background ions. Such a calculation made at a few time slices of this shot is plotted in Fig. 3. The steady-state calculation overestimates P_e and P_i. For electrons, the steady-state is reached in about a Spitzer time [5] τ_s and for ions it is even quicker. Generally, the error is largest at the start of the RF pulse but, decreases as time progresses. However, in the present case, $\tau_s \simeq 30$ ms at $t = 43.2$ s and increases to 0.6 s at $t = 44.2$ s. Relative to charateristic time of the variation $\simeq 0.35$ s, the error in P_e is small but, P_i is moderately

overestimated. Note that initially a larger fraction of power is delivered to ions which is consistent with the rapid rise of T_{i0} which then saturates. The steady rise of T_e is related to the continuously increasing P_e. In these calculations peaking of T_i, T_e and n_e-profiles is appropriately taken into account. For central heating there is little difference in the (H)-minority power-deposition profile, but, the redistribution of power among electrons and deuterons depends sensitively on the local plasma parameters.

In Fig. 1 and 2, we compare the electron and ion heating of peaked-density profile discharges heated with ICRF with the heating of broad-density profiles obtained both in monster and non-monster sawtooth discharges. We note that T_{e0} is improved by about 35% but, the most important gain is obtained in the ion temperature which is increased by a factor of 2 and allows high T_{e0} and T_{i0} simultaneously which is not achieved otherwise. Also on a similar comparison (not presented), the neutron production rate is found to be higher by a factor of 4. The comparison shown in Fig. 1 and 2 demonstrates that the central confinement has improved significantly. But, there is only a small improvement when $\langle T_e \rangle$ is compared at a fixed $P_{tot}/\langle n_e \rangle$. By another analysis, we find that with peaked-density profile heating, the global electron kinetic-energy confinement is about 20% better.

(c) Transport-Code Simulations : We use the Rebut-Lallia model [9] in our 1-D transport code that solves the electron and ion energy-balance equations and the poloidal-field diffusion equation with neo-classical resistivity. The density profiles, the radiated-power profiles and Z_{eff} are taken from the JET experimental data base. The deposition profiles of the RF-power imparted to electrons and ions are computed by ray-tracing [4]. This permits the evaluation of χ_e and χ_i seperately and supplements the analysis presented in Ref. (10). The time evolution of T_e and T_i for several shots has been simulated but, for illustration here, results of T_e and T_i-profiles at two time-points before and after the 'crash' when the peaked profiles are lost (see Fig. 3) are presented. The temperature profiles after the crash are similar to the standard monster-like discharges and are simulated in the usual way [10] giving good agreement with experimental profiles as shown in Fig. 5(a). However, to reproduce the temperature profiles in the 'good confinement-phase' (before the crash) where the density profile is peaked in the central region ($\rho/a \le 0.5$), the values of the electron and ion heat-conductivities are required to be reduced by a factor of 2 and 4.5 respectively in the inner-half radius. With such a prescription the characteristic profiles of improved confinement are well reproduced as shown in Fig. 5 (b). We note that though the values of χ_e and χ_i were reduced from the normal monster-like values based on the ray-tracing calculations of power deposition, these values, however, remain 'anomalous' in the region $0.2 < \rho/a < 0.8$. The coefficients can be calculated with confidence in this region as most of input power is deposited here whereas the radiation takes place outside this region.

3. CONCLUSIONS :

In the ICRF heating of peaked-density profile in JET limiter discharges, we find typically that T_{i0} is higher roughly by a factor of 2 and T_{e0} roughly by 35 % at a fixed P_{tot}/n_{e0} when compared to non-peaked profile cases. Also, on a similar comparison, the neutron production rate is found to be higher roughly by a factor of 4. The central confinement improves significantly whereas there is about 20% improvement in global electron kinetic-energy confinement. For central heating, the power-deposition profile changes little with the peaking factor but ion heating is improved in the pellet case due to a higher collisionality between the background ions and the energetic minority. Full ray-tracing calculations of power transferred to electrons and ions are consistent with the rate of rise of T_{e0} and T_{i0} in peaked-profile cases. The transport-code simulation of these discharges reveals that there is a reduction of both χ_e and χ_i in the central region of the plasma in ICRF heated peaked-profile discharges. However, identification of the physical mechanism(s) that play a role in this improvement must await further evaluation.

REFERENCES :
(1) D.J. CAMPBELL et al, Phys. Rev. Letters, 60, (1988) 2148.
(2) J. JACQUINOT et al, Plasma Phys Contr. Fusion, 30 (1988) 1467.
(3) G. SCHMIDT et al, IAEA Conf., Nice, France, (1988) CN-50/A-4-1.
(4) V.P. BHATNAGAR et al, Nuclear Fusion, 24, (1984) 955.
(5) T.H. STIX, Nuclear Fusion, 15, (1975) 737.
(6) F. PEGORARO et al, IAEA Conf., Nice, France, (1988) CN-50/D-4-6.
(7) J.P. CHRISTIANSEN et al, Bull. American Phys Society 33 (1988) 2030
(8) V.P. BHATNAGAR et al, JET Joint Undertaking, (1988) JET-P(88)51.
(9) P.H. REBUT et al, IAEA Conf., Nice, France, (1988) CN-50/D-4-1.
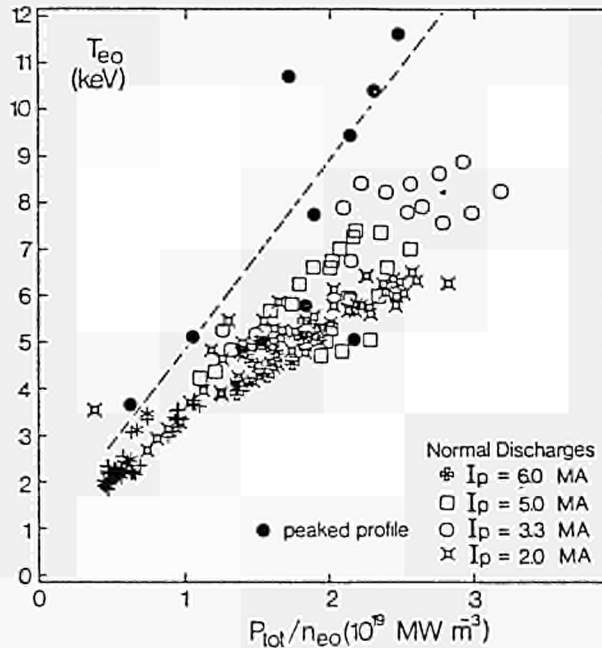(10) A. TARONI et al, IAEA Conf., Nice, France, (1988) CN-50/A-7-1.

FIG. 1. A plot of T_{e0} vs P_{tot}/n_{e0} for peaked profile and normal discharges. Macroscopic data analysis does not reveal any insight as to why two peaked-profile shots performed poorly.
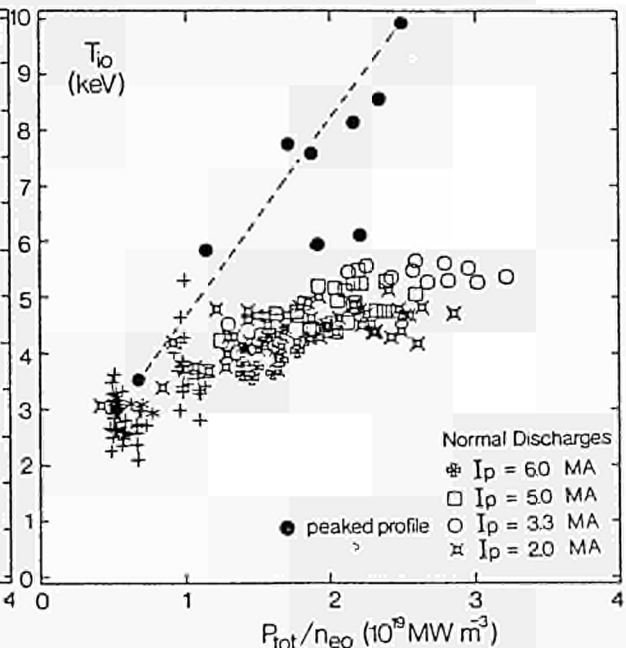
FIG. 2. A plot of T_{i0} vs P_{tot}/n_{e0} for peaked profile and normal discharges. See remark in Fig. 1.
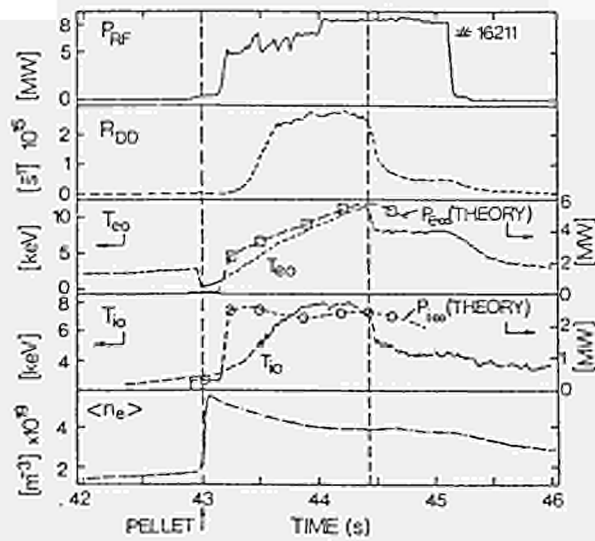
FIG. 3. Time traces of P_{RF}, R_{DD}, T_{e0}, T_{i0} and $<n_{e0}>$. Theory refers to ray-tracing.
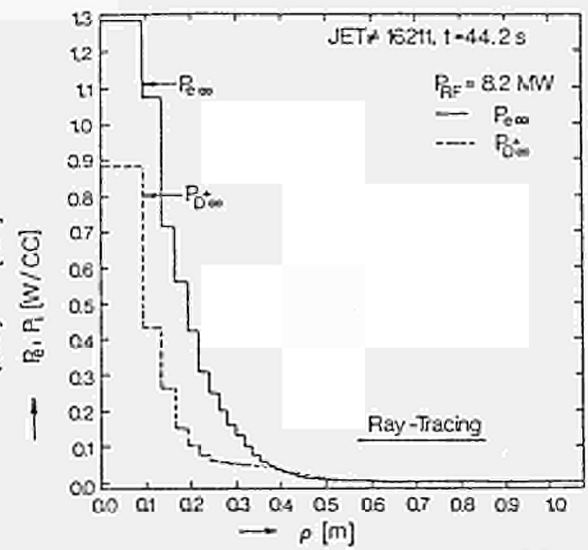

FIG. 4. Steady-state power-deposition profile of electrons and ions.
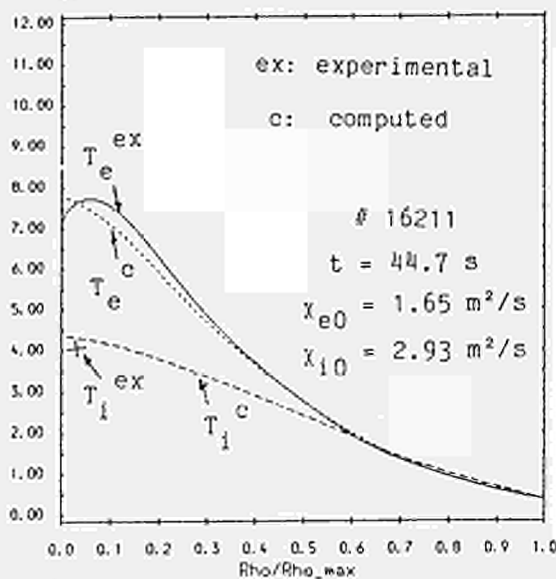

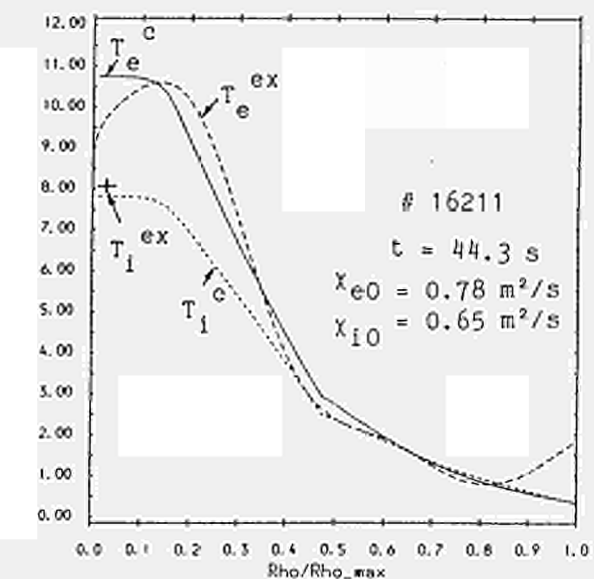FIG. 5 (a) Experimental and computed temperature profiles after crash.

FIG. 5 (b) Experimental and computed temperature profiles before crash.

BEHAVIOUR OF IMPURITIES DURING THE H-MODE IN JET

R. Giannella , K. Behringer, B. Denne, N. Gottardi, N.C. Hawkes* , M. von Hellermann,
K. Lawson* , P.D. Morgan, D. Pasini, M.F. Stamp

JET Joint Undertaking, Abingdon, Oxon, U.K.

*UKAEA/Euratom Association Culham Laboratory, Abingdon, Oxon, U.K.

INTRODUCTION

In additionally-heated tokamak discharges, the H-mode phases are reported to display, together with a better energy confinement, a longer global containment time for particles. In particular, steep gradients of electron density and temperature are sustained in the outer region of the plasma column. This enhanced performance is observed especially in discharges in which the activity of edge localized modes (ELMs) is low or absent. High confinement and accumulation of metallic impurities, which quickly give rise to terminal disruptions have been described under similar conditions /1/. In JET H-modes very long impurity confinement times are also observed. However the experimental condition is somewhat more favourable since quiescent H-modes are obtained lasting much longer than the energy confinement times and the radiation from metals is generally negligible. The dominant impurities are normally carbon and oxygen, the latter generally accounting for half or more of the power radiated from the bulk plasma. During the X-point operation the effective influx of carbon into the discharge, which is normally in close correlation with that of deuterium /2/, is substantially reduced while the influx of oxygen, whose production mechanism is believed to be of a chemical nature, does not show significant variations.

EXPERIMENTAL EVIDENCE

Long duration (< 4 sec) H-mode phases that are free from ELMs are easily obtained at JET. An example of such discharges is illustrated by fig. 1. During these phases the power radiated from the bulk plasma is observed to increase at a rate which is constant or slightly increasing with time. A similar time behaviour is also shown by the intensities of lines emitted by the hydrogen-like ions of oxygen and carbon while for the lower ionization stages of these impurities, whose radiation is localized outside the magnetic separatrix, no important intensity variations are observed. Nickel lines emitted at various radii inside the separatrix are also seen to increase continuously during these phases, but the contribution of metals to the radiated power is usually marginal (< 10%). Their concentration, estimated from the absolute intensities of lines radiated by different ionization states, is generally lower than 10⁴ of the electron densities.

The bolometric measurements indicate that the radiation is emitted during these phases in very thick (0.4 to 0.6 m) external layers with substantial emission from regions with very high electron temperature (1 to 2 keV) where the typical coronal emissivity of light impurities is very much reduced with respect to its maxima. The soft X-ray emission profiles (fig. 2) indicate rather uniform distributions of the light impurities within a radius of 0.5 m from the magnetic axis. Measurement from charge-exchange recombination spectroscopy also give hollow profiles of carbon density (fig. 3) steadily increasing with time while conserving the shape during the whole ELM free phase. These results are in agreement with the Z_{eff} profiles deduced from the bremsstrahlung measurement in the visible spectrum.

The evidence of very long confinement times for impurities is confirmed by experiments involving the injection of impurities /3/. The results of these tests also indicate the rapid formation, after the injection of metal impurities, of a hollow profile of their concentration whose decay time appears to be much longer than the few seconds available before the collapse of the high confinement plasma configuration.

The ELM-free H-mode terminates when the power radiated from the bulk plasma reaches a substantial fraction (≈ 60%) of the input power P_{inp} or when the total radiation (including radiation from the X-point region) exceeds P_{inp}: at the present levels of impurity influxes, this limits this phase to durations shorter than 4 secs. However, longer lasting H-modes or trains of H-modes are achieved if a mechanism sets in that may result in a quenching of the radiation. Intermittent short phases of i) ELM activity or ii) L-mode can substantially extend the duration or improve the performance of H-modes. These two mechanisms are different in several respects including the particle transport and their efficiency in depleting the plasma of impurities. In the first case while the plasma makes a transition from the quiescent H-mode to a phase of frequent ELMs the radiated power from the bulk plasma rapidly stops increasing and begins to decrease at a comparable rate. The line radiation from the metal ions emitting in the central plasma, however, keeps increasing for several hundred milliseconds at the same rate as during the ELM-free phase: the ELM activity only affects the plasma outer regions while their transport in the inner plasma is not varied. This is interpreted as evidence of a reduced diffusivity for impurities in the inner plasma during the H-mode with respect to the L-mode values. The second case is also illustrated in fig 1. The H-L transition is generally marked by a very strong spike in the radiated power from the X-point region followed by a very fast decrease of the radiation from all the plasma while the average density is only slightly reduced. In both cases, due to the reduction of the radiated power, the ELM-free H-mode is often resumed after a short (0.3 to 0.5 sec) interruption but with an important difference. While in the ELM phase the impurity content is only reduced in the plasma periphery and the transport of impurities in the centre continues unperturbed, in this second case an effective depletion of the impurities all over the plasma has taken place allowing, in the subsequent ELM-free phase, lower levels of radiation at the same values of electron density and temperature.

Very long quasi stationary H-modes can also be produced by provoking a continuous ELM activity. Such discharges are obtained when the clearance between the separatrix and the inner wall or the belt limiters is small. In these cases the influx of carbon into the discharge is higher and the relative contribution of this element to the radiation is of greater importance but the oxygen contribution is also much reduced. In these circumstances the impurity confinement times are smaller and a moderate increase of the radiation (as well as of the density) can be achieved. In those cases where the electron density reaches a stationary level, the radiation level also is seen to settle or slowly decrease. The radiation pattern during these phases displays thin (< 20 cm) emitting layers at the extreme periphery of the plasma column. In these cases there is no apparent increase in the total content of impurities in the discharge.

TRANSPORT ANALYSIS

The very long temporal scale of the radiation signals originating inside the separatrix from intrinsic and injected impurity ions is clear evidence that the impurity containment time is much longer than the global energy confinement time (≤ 1 sec) in JET quiescent H-modes. This has the practical implication that in the present experimental conditions it is not possible to observe the stationary distribution of impurities (a reduction of a factor of five or larger in the effective impurity influxes would be required with respect to the present values to run quiescent H-mode discharges). In particular it is not possible to clarify at present whether the hollowness of the impurity distribution across the discharge is simply a transient feature or if there is any active mechanism sustaining the positive gradients of their densities. Neoclassical effects connected to the positive gradients of the background plasma density, or to the exchange of momentum between the plasma and the co-injected neutral beams /4-5/, could in fact justify an outward-directed convection in the internal regions of the discharge.

In order to account for the bolometric profiles observed, displaying a very substantial shift of the light impurities total emission from its natural 'locus' (T_e = 100 to 300 eV for oxygen) to a region of the plasma with temperature much higher, a strong ratio is required between the total impurity density at ≈ 20 cm inside the magnetic separatrix and at the scrape-off region. Such a pronounced shaping of density profile cannot be described by diffusion, but requires a dominant convective mechanism localized at the plasma periphery, just inside the separatrix itself. This inward convection zone has to be restricted to a rather limited region in order to allow for the experimental hollow profiles of radiation and impurity densities. A strong ratio between the inward convective velocity v and the particle diffusivity D in this outer zone is also required by the observed long confinement times. Values of v/D of 0.5 cm⁻¹ or larger are needed if the thickness of this convective zone is about 20 cm. In fig. 4 a

velocity profile used to simulate these data is shown. The impurity density profile obtained after 2 sec of transport using this velocity and uniform diffusion coefficient D = 1500 cm² sec is also shown. The corresponding computed bolometric radiation and soft X-ray emission profiles for the case of oxygen are also shown and compared with the experimental data for the JET pulse illustrated in fig. 1 at t = 13 sec. The neoclassical convective velocity profiles computed from the experimental density and temperature are generally quite similar both in shape and absolute values to the one assumed shown in the figure. It should be observed, however, that a detailed quantitative comparison is not justified in this case because of the large experimental uncertainties in the gradients of T_e and n_e and on the q profile.

A very similar convection and diffusion scheme also describes the time behaviour of different ionization stages of a metallic impurities, both injected /3/ and intrinsic, under similar experimental circumstances.

CONCLUSIONS

Enhanced confinement of the impurities is observed during quiescent H-mode phases in JET neutral-beam heated discharges. This effect is due to the formation of a convective layer at the plasma periphery. The shape and absolute value of the convective velocity are comparable to those expected from the neoclassical theory. The diffusion coefficient also appears to be reduced during these phases. Spontaneous or provoked ELM activity can stop (and reverse) the continuous buil-up of impurities in the plasma periphery that, at the present level of the impurity influxes, leads to a termination of the quiescent phase after a few seconds.

REFERENCES

/1/ E.R. Müller, G. Janeschitz, P. Smeulders, G. Fussmann, Nucl. Fus. 27 (1987) 96.

/2/ B. Denne et al. 14th Europ. Conf. on Contr. Fus. and Plasma Phys. (Madrid, Spain, 1987) vol. 11D,I 109.

/3/ N.C. Hawkes et al. this conference.

/4/ W.M. Stacey, D.J. Sigmar Nucl. Fus. 19 (1979) 1665.

/5/ R.C. Isler et al. Nucl. Fus. 23 (1983) 1017.

Fig. 1   # 17909
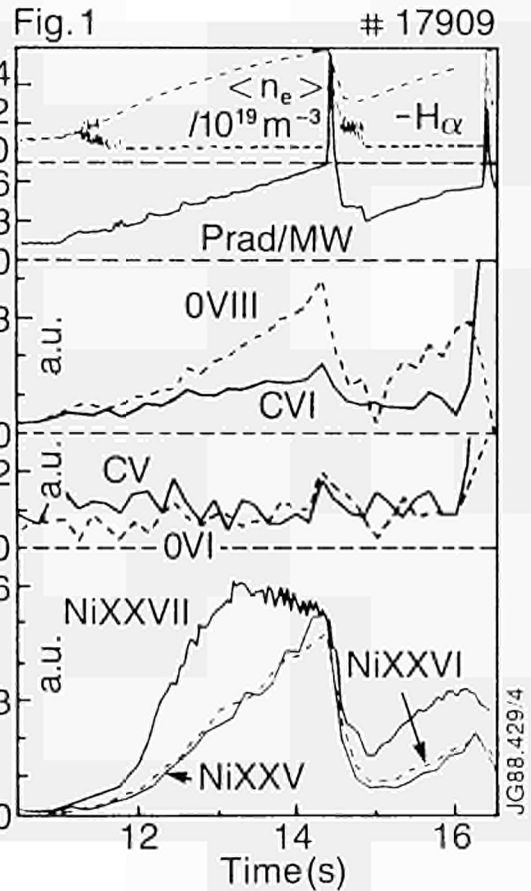
fig. 1   Time evolution of the average electron density, Hα intensity, total radiated power P_{rad} and of the radiation from different ionization stages of carbon, oxygen and nickel. Two quiescent H-mode phases are separated by a short L-mode phase.
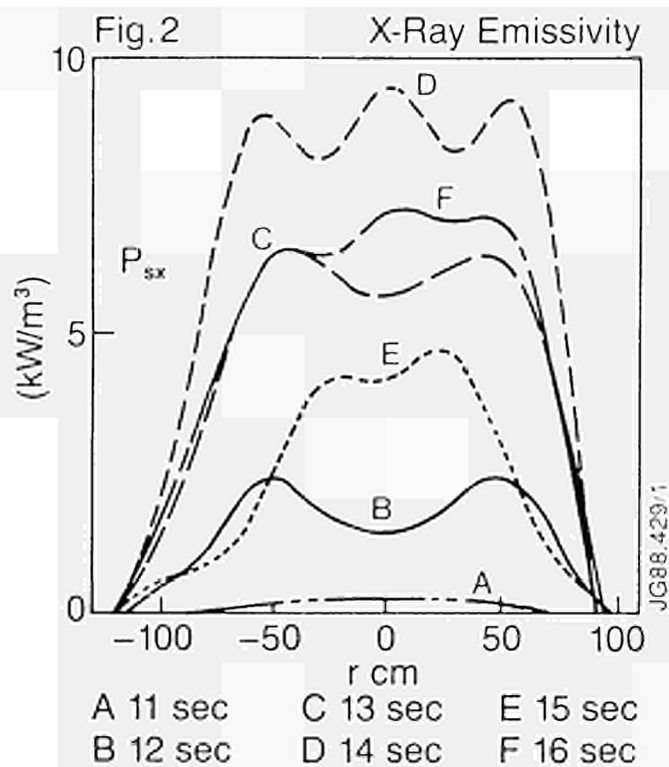
Fig. 2

X-Ray Emissivity

A 11 sec   C 13 sec   E 15 sec
B 12 sec   D 14 sec   F 16 sec

fig. 2   Soft X-ray emission profiles at different times during the the pulse displayed in figure 1.
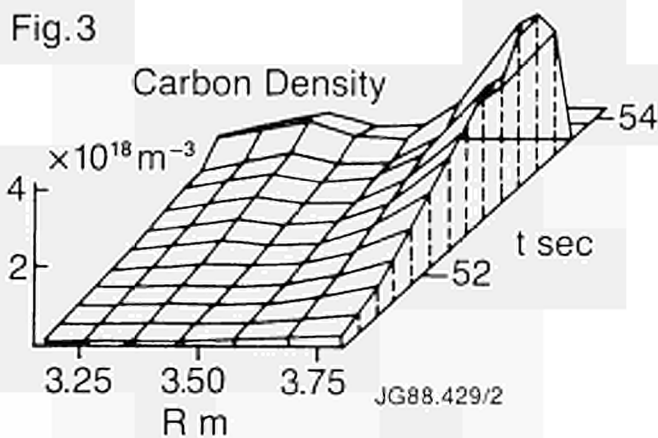
Fig. 3

Carbon Density

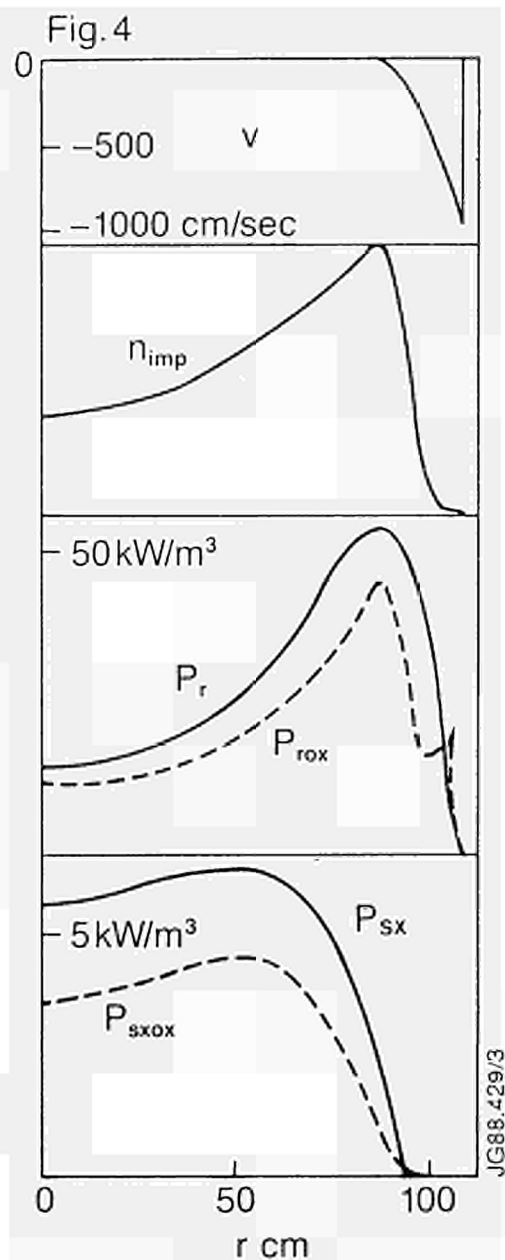fig. 3   Carbon density measured by charge exchange recombination spectroscopy in the pulse displayed in figure 1.

Fig. 4

fig. 4   Shape of the convective velocity assumed for the simulation of the pulse displayed in fugure 1 and profile of the impurity density after 2 sec of transport. The corresponding computed total radiation and soft X-ray emission profiles for the case of oxygen (4% of the electron density at the plasma centre) are also shown and compared with the experimental profiles.

HEAT PULSE ANALYSIS IN JET AND RELATION TO LOCAL ENERGY TRANSPORT MODELS

J.C.M. de Haas*, W. Han, N.J. Lopes Cardozo*, C. Sack, A. Taroni

JET Joint Undertaking, Abingdon, Oxon., OX14 3EA, UK
*FOM, "Rijnhuizen", The Netherlands

INTRODUCTION

The evolution of a perturbation $\tilde{T}_e$ of the electron temperature depends on the linearised expression of the heat flux q_e and may be not simply related to the local value of the electron heat conductivity χ_e [1]. It is possible that local heat transport models predicting similar temperature profiles and global energy confinement properties, imply a different propagation of heat pulses.

We investigate here this possibility for the case of two models developed at JET [2,3]. We also present experimental results obtained at JET on a set of discharges covering the range of currents from 2 to 5MA. Only L-modes, limiter discharges are considered here. Experimental results on the scaling of χ^{HP}, the value of χ_e related to heat pulse propagation, are compared with those of χ^{HP} derived from the models.

DERIVATION OF χ^{HP} AND EXPERIMENTAL RESULTS

The value of χ^{HP} is derived from the electron temperature traces following [4]. The velocity of the heat pulse and the radial attenuation are given by:

$$v = (d(\tau_p)/dR)^{-1} \qquad (1)$$

$$\alpha = - 10a \frac{d}{dR} (\log_{10} A) \qquad (2)$$

Here R is the major radius where the time τ_{pq} at which the peak of $\tilde{T}_e$ is reached, is measured; A is the amplitude of $\tilde{T}_e$. The corresponding "cylindrical" quantities, used in [4], are given in first approximation by $v_{CYL} = \sqrt{\kappa} \frac{a}{a-s} v$ and $\alpha_{CYL} = \frac{a-s}{a} \alpha$, a being the horizontal minor radius, s the Shafranov shift and κ the plasma elongation.

The analysis in [4] shows that an approximate heat pulse diffusion coefficient

$$\chi^{HP} = 4.3 \ a_{CYL} \ v_{CYL}/\alpha_{CYL} \qquad (3)$$

can be introduced for the description of the heat pulse propagation in JET. Here $a_{CYL} = \sqrt{\kappa} \ a$.

The JET discharges in the period 1986-1988 for which χ_{exp}^{HP} has been derived following Eqs.(1-3) are summarised in Table 1. The geometry was practically the same for all analysed discharges: major radius $R_o = 3m$, horizontal minor radius $a = 1-1.2m$ and elongation $\kappa = 1.3-1.5$. The analysis has been performed only in high field discharges because the signal to noise ratio of the signal from the diagnostic, a 12-channel ECE grating polychromator [5], is proportional to B^2. The remaining discharge parameters, current I, total input power P_{tot}, effective charge Z_{eff}, volume average density $\langle n_e \rangle$ and peak temperature T_{eo} cover a wide range. The dependence of χ_{exp}^{HP} on these parameters is investigated. The main problem is related to the non-complete independence of the parameters. For example one expects some internal relationship among n_e, P_{tot} and Z_{eff} or n_e, T_e, P_{tot} and I. A study of the correlation matrix shows that the correlation between pairs of the parameters is not too strong and that a regression analysis is carried out. There is a coupling between the radial position $x = r^{HP}/a$ where χ^{HP} is measured and the mixing radius $r_{mix} \propto a/q_a$, q_a being the cylindrical safety factor at the boundary. This implies that one cannot distinguish between variations of I and x^{HP}. Here it is assumed that any effect is related to variations of x^{HP} and not of I; a dependence of χ^{HP} I can be introduced by a correspondent variation in the dependence on x^{HP}. Fitting a power law model for χ^{HP} to the data yields:

$$\chi_{exp}^{HP} = (2\pm0.5)(\chi^{HP})^{2.1\pm0.2} Z_{eff}^{0.6\pm0.1} T_e^{0.5\pm0.2} P_{tot}^{0.0\pm0.1} \langle n_e \rangle^{0.0\pm0.1} \qquad (4)$$

The mean square root of the fit (Fig. 1) is 0.328m²/s which is comparable to the estimated error on χ_{exp}^{HP}. The correlation coefficient with the largest value (-0.84) is that between the constant and T_e. Fits with less variables show that the main dependences are those shown in Eq. 4. The dependence on Z_{eff} has been checked separately for the subsets of discharges with I = 2-4MA and with I = 5MA (which shows the largest

variation in Z_{eff}). The fits yield the same results within error bars.

Keeping in mind its limitations, this analysis confirms [1] that the dependence of χ_{exp}^{HP} on P_{tot} is either absent or weak (possibly via T_e) and shows a rather strong dependence on Z_{eff}. A separate dependence on I and x cannot be derived.

RESULTS OF TRANSPORT CODE SIMULATIONS

The space and time evolution of T_e following sawtooth crashes has been computed by means of the full 1½ D transport code JETTO [6]. We consider here two local energy transport models proposed at JET: the so-called Rebut-Lallia (or critical electron temperature gradient) model [2] and the critical pressure gradient model related to resistive instabilities proposed by P. Thomas [3]. The velocity of the heat pulse and its attenuation have been derived from the computed results, (Fig.2) using Eqs.(1) and (2). The coefficients χ_{RL}^{HP} and χ_{PT}^{HP} have been evaluated using Eq.(3). Discharges at 2 and 5MA have been studied so far.

An example of results obtained with the code is given in Table 2. Here the first line refers to a JET discharge at 2MA, with 4MW of ICRF additional power. The other lines are the results of computational experiments corresponding to variations of the input power, Z_{eff} and the position at which χ^{HP} was evaluated. The numerical results are consistent with those expected from the study of the linearised expressions of the heat fluxes. This confirms the validity of Eq.(3), even in the case of highly nonlinear models such as those considered here. As shown in Table 2, one finds $\chi_{PT}^{HP} = \gamma \chi_{PT}$, with $\gamma = 1.5$, consistent with $\chi_{PT} \propto \nabla p$ and $p_e \gtrsim p_i$, where p indicates the pressure. This implies that χ_{PT}^{HP} is too low for ohmic discharges (see lines 3 and 4 in Table 2 and Fig. 2). The dependence of χ_{RL}^{HP} is weaker and compatible with the experimental results also in the ohmic cases. Table 2 also shows that χ_{RL}^{HP} does not depend on Z_{eff}, contrary to experimental indications. This could indicate that a factor $(1 + Z_{eff})^{1/2}$ has been neglected in the expressions of χ_{RL} derived so far [7]. Some increase of χ_{PT}^{HP} with Z_{eff} is observed. It is, however, weaker than observed experimentally.

Both models predict an inverse dependence of χ^{HP} on the current I. They also predict that χ^{HP} depends weakly on x in the region $x \lesssim .8$ and increases sharply in the boundary region. This is qualitatively consistent with the experimental results but quantitative comparisons have not been possible so far.

CONCLUSIONS

We have shown that the numerical simulation of heat pulse propagation with a full 1½D transport code can be used to assess local energy transport models. The experimental results obtained so far in JET plasmas indicate that χ^{HP} has a weak or no dependence on the input power. This important feature is better simulated by a transport model producing confinement degradation through a transport threshold at a critical value of the electron temperature gradient [2] than by a model producing degradation via a nonlinear dependence of the heat flux on the pressure gradient [3]. The relatively strong dependence of χ^{HP} on Z_{eff} implied by the analysis of the experimental data, seems to indicate a stronger dependence of the local χ on Z_{eff} than predicted, showing a possible line of improvement for the models.

More work is required for a quantitative comparison of predicted and experimental results on the dependence of χ^{HP} on the plasma current and the radial position, possibly extending the study to "controlled" heat pulses, generated by the time modulation of auxiliary power deposited at chosen values of x in a set of reference discharges.

REFERENCES

[1] B.J.D. Tubbing, et al., Nucl. Fusion 27 (1987) 1843.
[2] P.H. Rebut, et al., 12th IAEA Conf., Nice, France (1988), CN50/D-4-1.
[3] P. Thomas, et al., Proc. XV EPS Conference, Dubrovnik, 1988, Vol.1, p.127.
[4] N.J. Lopes Cardozo, et al., Nucl. Fus. 28 (1988) 1173.
[5] B.J.D. Tubbing, et al., Proc XII EPS Conference, Budapest, 1985, Vol.9F-I, p.215.
[6] G. Cenacchi and A. Taroni, JET-IR(88)03.
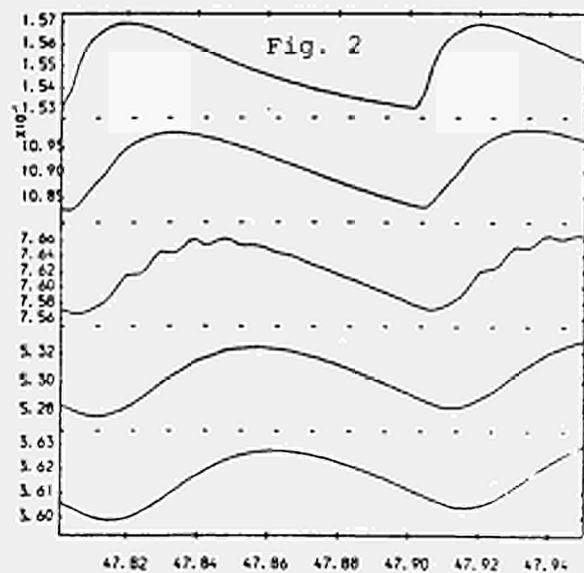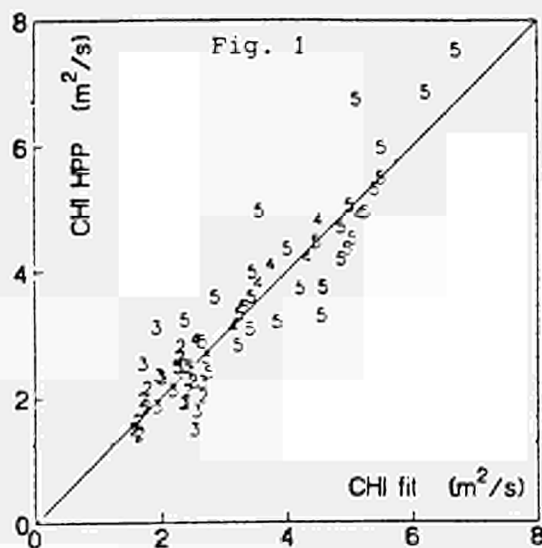[7] P.H. Rebut, Private communication.

Fig. 1: Plot of the measured χ^{HP} vs the fitted χ^{HP} according to Eq. 4 for the full data set.

Fig. 2: Time (sec) evolution of $\hat{T}_e$(keV) computed with the RL model. Channels corresponding to ρ/ρ_{max} = 0.5, 0.6 ... 0.9 are shown. The parameter of the discharges are I = 2MA, P_{tot} = P_{OH} = 1MW, Z_{eff} = 2.2, $\langle n_e \rangle$ = 2.1×10^{19}m⁻³, $T_{eo} \approx 3.6$keV. One derives χ^{HP}_{RL} = 1.6 at R = 3.7. Equation 4 gives χ^{HP} = 1.8

TABLE 1

I(MA)	B_t(T)	$\langle n_e \rangle$(m⁻³)	P_{tot}(MW)	Z_{eff}	x = r/a	T_{eo}(keV)	N° of Pulses
2.0	3.5	2.0±0.2	2.5-5.0	2.2-3.5	0.52	4.1-5.5	12
3.0	2.9-3.5	1.8-4.0	2-14	2.6±0.2	0.6-0.7	3.1-4.3	16
4.0	2.9	1.9-3.3	3.2-6.7	2.0-3.5	0.8	3.2-5.0	7
5.0	3.5	1.6-4.0	4.0-16.0	1.5-5.0	0.78	3.1-5.3	31

TABLE 2 - Values of χ^{HP}_{RL} and χ^{HP}_{PT} derived from numerical "experiments" simulating heat pulse propagation at I = 2MA and different values of P_{tot}, Z_{eff} and R. The first line in the table corresponds to JET pulse 15020 for which χ^{HP} = 1.95 was determined experimentally at R = 3.65. Values of $\chi = q_e/n_e \nabla T_e$ are also given.

I(MA)	Z_{eff}	P_{tot}(MW)	R(m)	χ^{HP}_{RL}(m²/s)	χ_{RL}(m²/s)	χ^{HP}_{PT}(m²/s)	χ_{PT}(m²/s)
2	2.2	4.6	3.68	1.9	1.0	1.8	1.1
2	2.2	4.6	3.9	3.0	1.5	2.1	1.4
2	2.2	1	3.68	1.6	0.5	1	0.6
2	2.2	1	3.9	3.1	0.7	1.2	0.8
2	2.2	16	3.68	2.3	1.3	2.3	1.5
2	2.2	16	3.9	3.2	2.3	3.2	2
2	1	4.3	3.68	2.0	1.0	1.5	1.0
2	4	4.8	3.68	1.8	1.0	2.0	1.3

THE HOT ION MODE OF SMALL BORE PLASMAS IN JET

C.G.Lowry , D.A.Boyd[1], C.D.Challis, J.P.Christiansen, J.G.Cordey, G.A.Cottrell,
A.W.Edwards, T.T.C.Jones, P.P.Lallia, P.Nielsen, G.Sadler, G.Schmidt[2], D.F.H.Start,
D.Stork, P.R.Thomas, B.Tubbing

JET Joint Undertaking, Abingdon, Oxon. OX11 3EA, England
1 University of Maryland, College Park, MD20742, USA.
2 Princeton Plasma Physics Laboratory, New Jersey, USA.

ABSTRACT

Ion temperatures in excess of 20 keV and high D-D neutron rates have been achieved in
JET, by the injection of 80 keV neutral beams into low density, low volume plasmas. Two
small bore configurations were tried, one limited on the inner wall and the other on the belt
limiters (low field side). Both configurations had plasma current of 3 MA and toroidal field
of 3.4T at the vessel axis. The small plasma minor radius aids the beam penetration while the
low density increases the power per particle and beam slowing down time. The inner wall
configuration has several advantages; it can have a smaller volume because of the lower
major radius and higher toroidal field, the neutral beams are closer to tangential, and the
inner wall is known to pump deuterium effectively. The limiter configuration, however,
allows the use of combined RF and NBI heating systems and could benefit from geometrical
scaling of confinement.

OPERATING PROCEDURE

Extensive helium conditioning of the limiting surfaces was required to obtain the low
density target plasma. During these conditioning discharges the ability of the wall to pump
was monitored by the decay rate of neutron production after a small deuterium puff. In
subsequent deuterium discharges the increase in the target density was slow, but the
pumping ability of the wall deteriorated after only a few pulses, and disruptions caused
instant de-conditioning. For the inner wall pulses the plasma was initially full bore and
limited on the belt limiter it was then pushed to the inner wall over a period of 1.5 to 2
seconds. The reverse procedure was used to produce the small bore limiter plasmas.

NEUTRAL BEAM HEATING AND FUELING

The objectives of operating such small bore plasmas was to increase the peak neutron
production rate by entering the hot-ion mode and to achieve axially peaked beam
deposition. The achievement of 23 keV ion temperature is consistent with the high ratio of
NBI power to the total number of plasma electrons. With an electron temperature of only 9
keV these plasmas can clearly be regarded as being in the hot-ion mode. Both inner wall and
limiter pulses had axially peaked beam deposition, figure 1, in the inner wall case this lead to
strong peaking of the density within the half radius, figure 2. However, in the limiter case
wall pumping was insufficient to maintain the low edge density. Between 400 ms and 800 ms
into the beam pulse the carbon influx from the limiting surface was observed to increase
dramatically for a period of a few hundred milliseconds, which had the effect of creating a
density pedestal. Even at the higher density the beam source was strongly peaked, and when
switched off the rapid edge pumping of the inner wall pulses produced almost triangular
density profiles.

The carbon event or 'catastrophe' has not only been observed in such small bore
configurations but has become a characteristic of high power heating in JET. After the start
of the beam pulse the CIII emission from the limiting surface begins to increase in
proportion to the D-alpha emission, followed by a burst of CIII emission which saturates the
detector for some 200 ms and returns to a level which can be extrapolated from before the
burst, see figure 3. Up to three such bursts have been seen in one pulse, the first seem to be
accompanied by a decrease in D-alpha emission although subsequent bursts show no such
correlation. The delay of the first burst after beam-on decreases with increasing beam

power, this favours a surface temperature dependant mechanism. However, the return to a
similar level of emission suggests some form of bifurcation.

CONFINEMENT

These small bore plasmas provide two opportunites to examine confinement scaling.
First we have the largest variation in major radius possible for JET, and secondly the inner
wall plasmas are close in geometry to the TFTR configuration. Figure 4 summarises the
results of both comparisons. The limiter pulses show confinement similar to that for the
inner wall indicating no major radius dependance of confinement. If compared to the
Goldston confinement scaling an enhancement of 1.7 is observed for the inner wall plasmas,
but the enhancement is less for the limiter discharges. Using TRANSP[1] to analyse one
discharge of each of these configurations it can be seen that fast ions account for 25 % of the
stored energy in the inner wall case, and 15 % on the limiter. The fast ions therefore account
for half of the measured enhancement. Also shown in figure 4 are some of the first TFTR
'supershots'[2], with co-injection, for these pulses the stored energy has been multiplied by a
factor of 3 to allow for the different plasma current. With such an adjustment the results
from the two machines are in good agreement.

NEUTRON PRODUCTION

The maximum neutron rate is observed to depend only on the NBI power and the
pumping ability of the wall. TRANSP runs show that for both small bore configurations 60%
of the peak neutron production is from beam-beam reactions with only 4 % from thermal
reactions. The beam-thermal reaction rate is similar to that for beam-beam but peaks a few
hundred milliseconds later, by which time the beam-beam contribution is significantly less.
Large bore double null x-point plasmas show the beam-thermal reactions to dominate the
peak neutron rate. It is thus surprising that the peak total rate is a similar function of the
NBI power in both configurations, Figure 5. Methods which were tried in order to deviate
from the curve included the use of RF heating and pellet injection. RF heating in monopole
has been used in double null x-point plasmas and showed an enhancement in neutron rate of
typically 30 %. However, in the small bore limiter plasmas no such enhancement was
observed. A 10 % improvement was achieved by injecting 2.7 mm pellets into the plasma
just before the expected peak in the neutron rate. Although the onset of the carbon
catastrophe was delayed in some cases, the 10 % improvement seemed to be due to a
reduced ratio between carbon and deuterium release prior to the event. Pellets injected
before beam-on reduced the maximum neutron rate due to an associated increase in the
target density.

SUMMARY

Small bore plasmas on JET have shown strongly peaked density profiles and
confinement 1.7 times the Goldston scaling. The enhanced confinement is partially
accounted for by the fast ion content of the plasma and is in line with observations under
similar conditions on TFTR. The neutron production in these plasmas lie on a similar curve
as a function of NBI power as for other JET configurations, with a small improvement
possible by injecting pellets during the beam pulse. Attempts to purify the target plasma
using pellets failed due to the associated density increase, a situation which can be resolved
only by reducing the carbon level in the plasma.

REFERENCES

1. R.J.Goldston et al, J. Comput. Phys. 43 61 (1981).
2. R.J.Hawryluk et al, in Plasma Physics and Controlled Nuclear Fusion Research 1986
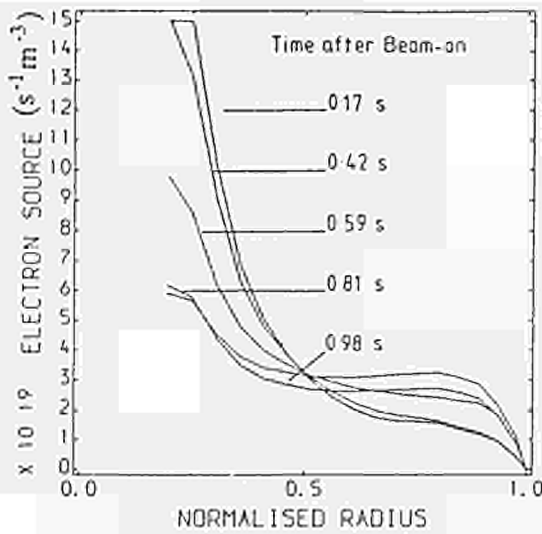,(Proc. 11th Int. Conf. Kyoto, 1986), Vol. 1, 51.
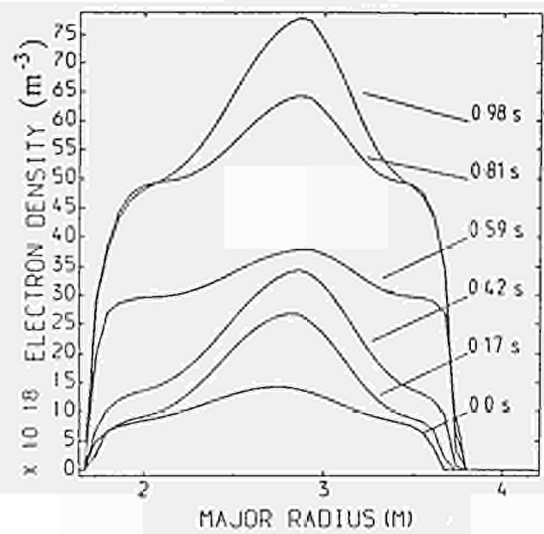
Figure 1

Figure 2
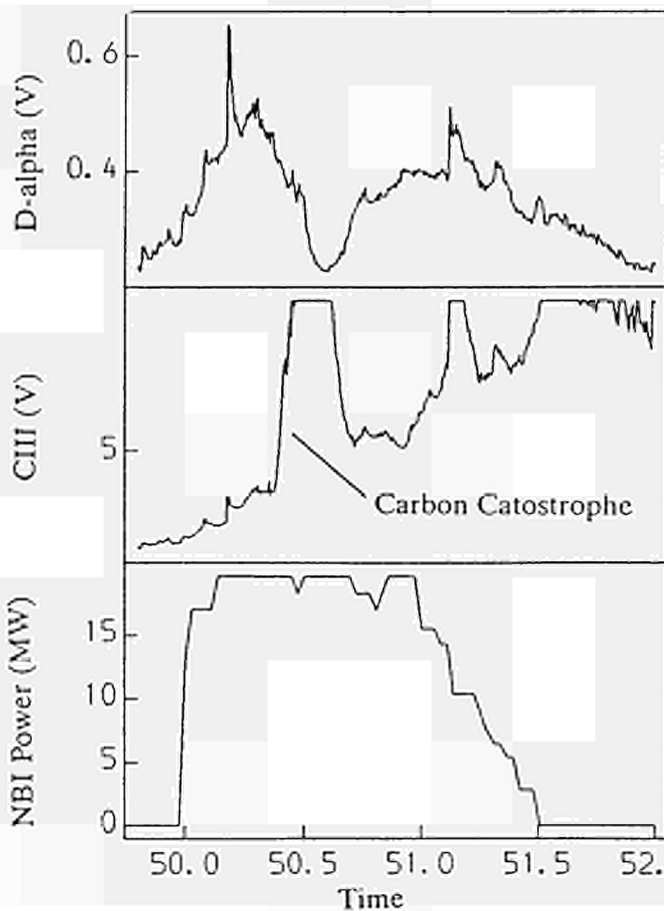

Figure 3

Carbon Catostrophe

Figure 1 shows the electron source due to the neutral beam injection as a function of the normalised minor radius at ∽ 200 ms intervals.

Figure 2 shows the electron density profile as a function of the major radius, for the same times as figure 1.

Figure 3 shows the CIII and H-alpha emission during the heating phase of an inner wall plasma. The 'carbon catostrophe' is seen to last for only 200 ms and is accompanied by a reduction in the H-alpha emission.
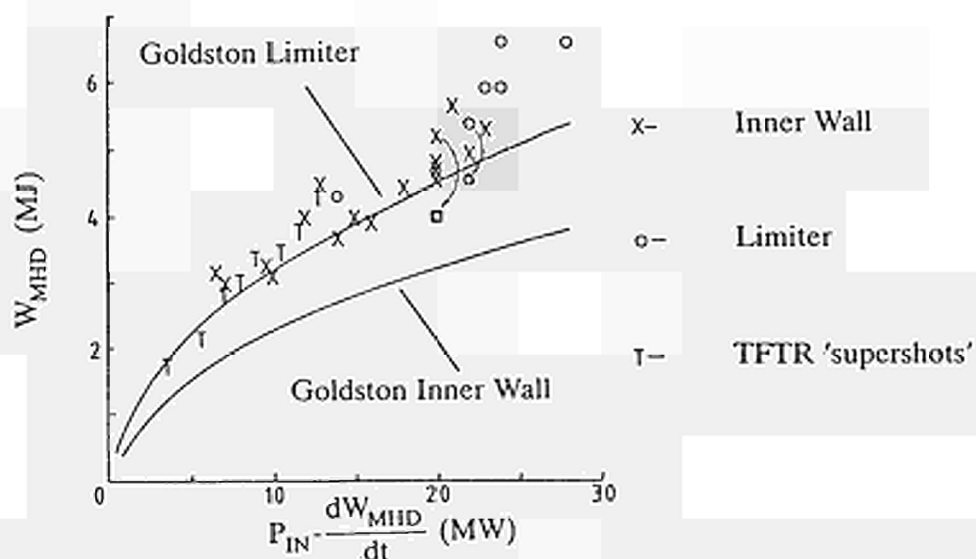
Figure 4 This shows the stored energy, W_{MHD}, versus the total input power taken when $\dfrac{dW_{MHD}}{dt} = 0$, for the inner wall and limiter configurations, and for some TFTR 'supershots'. The two shaded points show the stored thermal energy as calculated by TRANSP. For comparison the Goldston scaling is shown for the two JET configurations.
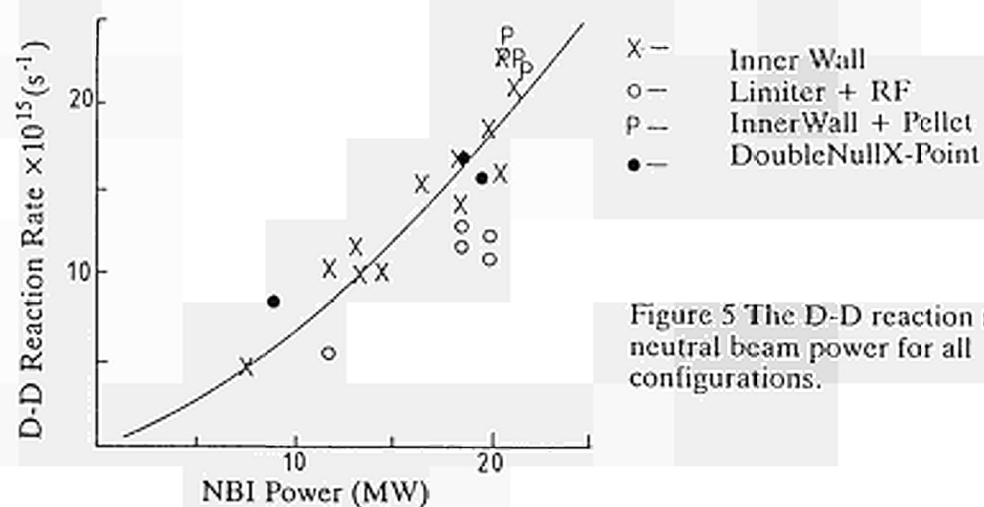
Figure 5 The D-D reaction rate versus neutral beam power for all configurations.

OFFSET-LINEAR DESCRIPTION OF H-MODE CONFINEMENT

K Thomsen, J D Callen*, J P Christiansen, J G Cordey,
H Keilhacker, D G Muir, M L Watkins

JET Joint Undertaking, Abingdon, Oxon, OX14 3EA, UK
*University of Wisconsin, Madison, WI 53706, USA

1. Introduction

The formulas for interpreting auxiliary heating data in terms of local transport models [1] apply to steady state plasmas with negligible edge temperatures. However, in JET H-mode discharges, edge temperatures above 500eV are observed and the plasma does not normally reach a steady state [2]. An energy evolution equation for plasmas with non-zero edge temperatures based on local transport models is proposed in Section 2. Analysis of JET discharges with the time dependent energy balance code TRANSP [2] suggest that the best models for the total heat diffusion coefficient χ correspond to $\chi(r) = \chi_0$ during the H-mode phase and $\chi(r) = \chi_0/(1-\alpha r^2/a^2)$ during the L-mode phase; this result is in agreement with previous results [1]. Section 3 presents results obtained by applying the energy evolution equation to JET L-H mode data; two models for heat diffusibility χ are used. The conclusions are given in Section 4.

2. Energy Evolution Equation

The local power balance equation for plasmas with density $n = n_e = n_i$ and temperature $T = T_e = T_i$ is $3\frac{\partial}{\partial t}nT = -\nabla\cdot\vec{q} + Q$, where Q is the net heating rate. The total heat flux $\vec{q}$ is assumed to be well represented by a diffusive term proportional to the temperature gradient ∇T and a negative non-diffusive flow term which represents a heat pinch or a critical temperature gradient, ie. $\vec{q} = -n\chi\nabla T - \vec{q}_{pinch}$. The flux surface averaged power balance equation is integrated 3 times (see [1] for details) to give the following equation for the time evolution of total stored energy $W = 3\int d^3x$:

$$\tau_\chi \, \eta_{nT} \frac{d}{dt} W = -W + W_p + \tau_\chi \, \eta_Q \, P_{in} + W_0 \qquad (1)$$

The pedestal energy W_p appears naturally in this formalism for plasmas with non-zero edge temperatures $T(a) \neq 0$, ie. $W_p = 3T(a)\int d^3x \, n$. The power P_{in} represents a simple volume integration $\int d^3x$ of Q and W_0 is the usual offset term [1]. The remaining quantities depend on the radial profile of $\chi(r)$ as described in [1] with τ_χ denoting the 'ideal' incremental confinement time and η_Q the heating effectiveness. The effectiveness η_{nT} for the pressure profile is calculated in a way similar to that of η_Q. For rapidly changing pressure profiles the effectiveness of the $\frac{\partial}{\partial t}nT$ profile should be used instead of η_{nT} in Eq.(1).

3. Results

The aim of the analysis is to establish if eq. 1 can adequately represent JET L and H-mode data obtained for plasmas with X-point configurations and currents of 3 to 5 MA. This JET data shows that at fixed current and power the total energy W in the L and H-mode can differ by a factor 2 or 3. Our analysis suggests that the confinement in the central plasma region is the same in L and H-modes; the difference is therefore mainly due to different confinement properties in the outer region, i.e. for $\rho > 0.9$, where ρ denotes a normalised flux surface label $0 \leq \rho \leq 1$. We have carried out calculations of the various terms of (1) using JET L and H mode data as follows.

W and dW/dt are measured by the diamagnetic loop; W_p is derived from kinetic measurements of T_e and n_e assuming $T_i = T_e$ ($\rho=0.95$), $n_e = 2n_i$. The effectiveness's η_Q and η_{nT} are evaluated following the prescription in [1];

for simplicity we assume a flat density profile $n_{(\rho)} = n_0$; two types of heat diffusivity profiles $\chi_{1(\rho)} = \chi_0$, the second with $\chi_2(\rho) = \chi_0/(1-\rho^2)$. The results from our calculations are shown in Figures 1-4.

The effectiveness η_{nT} associated with non-steady state plasmas is found to be systematically higher for H than for L-mode data. Fig. 1 shows that η_{nT} does not vary with power P, current I and toroidal field; the values for the entire H mode data are approximately 20% above the L mode values. The 20% difference in η_{nT} arises mainly because χ_1 has been used for H mode data and χ_2 for L-mode data. A similar difference in η_Q is found between H and L mode values. Figure 2 demonstrates that for NBI heated plasmas η_Q depends mainly on the absolute value of density which determines beam penetration and thus the beam power deposition profile. There is an implicit variation of η_Q which beam power and current which both indirectly determine the plasma density. Thus when we combine the terms of (1) both L and H mode data can be represented by

$$P_{eff} = \eta_Q \, P_{in} - \eta_{nT} \frac{dW}{dt} \approx 0.5 \left(P_{in} - \frac{dW}{dt} \right). \qquad (2)$$

Figures 1 and 2 therefore serve to illustrate how the effectiveness's η_Q and η_{nT} depend upon the models χ_1 or χ_2 for heat diffusivity profiles.

The calculated values of W_p from H mode data are shown in Figure 3 against the net total input power $P_{in} - dW/dt$. There is a pronounced dependence for the H-mode values of the pedestal energy W_p upon power which may be expressed as

$$W_p(\text{H-mode}) = \tau_{edge} \, (P_{in} - dW/dt), \quad \tau_{edge} = 0.4s. \qquad (3)$$

The L-mode values of W_p are scattered in the 0 - 1 MJ range with no dependence upon power and hence they are not included in Figure 3.

The difference in W_p between L and H mode suggests that the improved H-mode confinement, i.e. $W(\text{H-mode}) \sim 2-3$ times $W(\text{L-mode})$ at a given P_{in} is associated with the relationship (3) while confinement in the central region is similar for L and H modes. The latter is confirmed by Figure 4 which shows the energy difference $W-W_p$ against P_{eff} defined by eq. 2. The difference $W-W_p$ and its variation with P_{eff} is almost the same for L and H mode. The scatter is caused by several assumptions:

1) The choice of a fixed value $\rho = 0.95$ used to estimate W_p; 2) experimental uncertainties in determining edge values of T_e, T_i, n_e, n_i etc. The slopes $d(W-W_p)/dP_{eff}$ derived for L and H mode data from Figure 4 and representative of t_χ in (1) should differ by a factor 2 in accordance with the choices χ_1 and χ_2 (see [1]). Presently our L-mode data is insufficient to substantiate this point.

4. Conclusions

The interpretation methods in (1) have been extended to nonstationary plasmas with nonzero edge temperatures. This has led to a new form of a time dependent energy equation which is suitable for analysis of the 2 confinement regions observed in H-mode plasmas. The new interpretation method has been applied to JET data obtained in X-point configuration using 2 models for heat diffusivity. Presently the results from the analysis suggest that the improvement for confinement obtained in the H-mode is associated with the pedestal energy W_p which increases with effective power.

References

[1] Callen, J.D. et.al. Nucl.Fus.27 (1987) 1857.
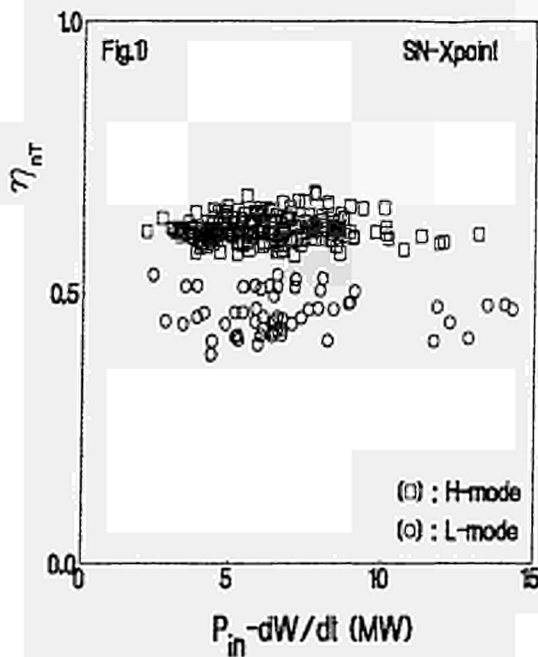
[2] JET team H. Keilhacker. IAEA-CN-50/A-111-2 (1988)

Fig. 1 Effectiveness of pressure profile η_{nT} versus net total input power for SN-X-point plasmas with I_p=3-5MA and B_T=2-3.4T (□) H-mode, (○) L-mode.
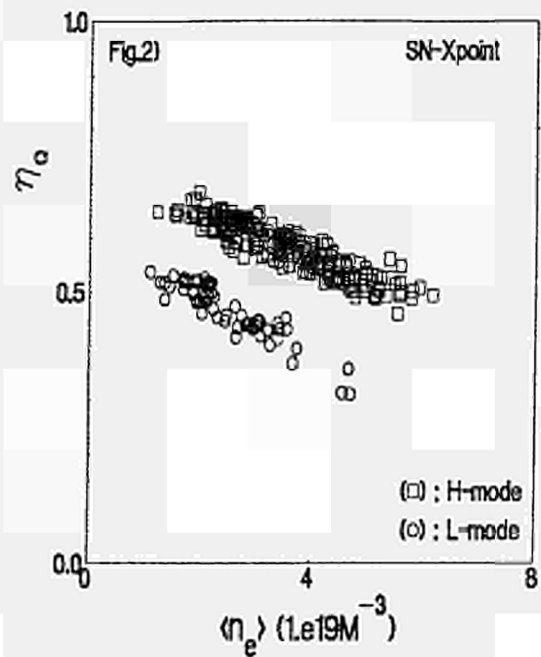

Fig. 2 Heating effectivness η_Q (without radiation correction) versus volume average electron density $\langle n_e \rangle$ for SN-X-point plasmas with I_p=3-5MA and B_T=2-3.4T. (□) H-mode. (○) L-mode.

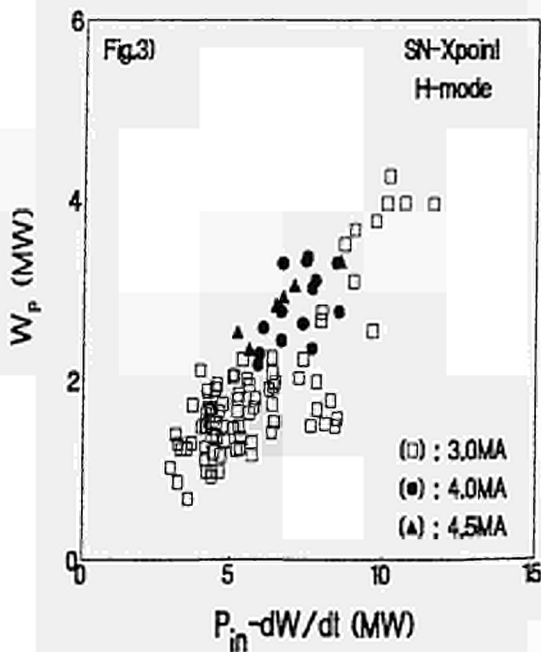Fig. 3 Pedestal energy W_p(ρ=0.95) versus net total input power for H-mode in SN-X-point plasmas. (□) I_p=3MA, (●) I_p=4MA, (▲)I_p=4.5MA.
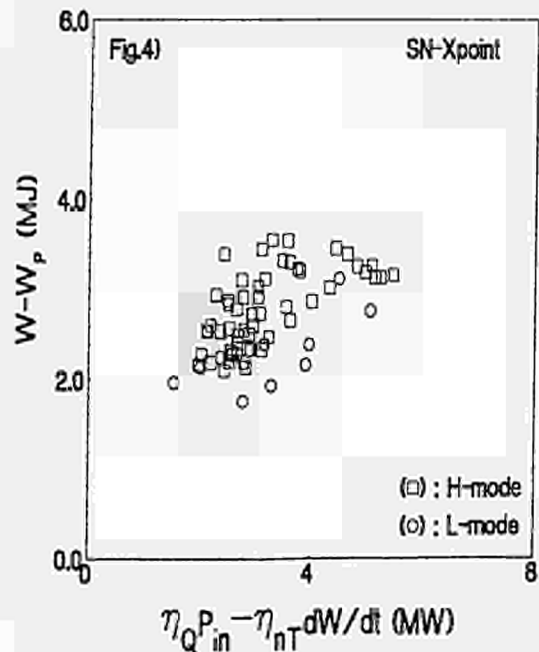
Fig. 4 Core energy W-W_p(ρ=0.95) versus net effective input power in SN-X-point plasmas with I_p=3MA; B_T=2-2.2T. (□) H-mode, (○) L-mode.

PHYSICS ASPECTS OF A THOMSON SCATTERING DIAGNOSTIC FOR FAST ION AND ALPHA PARTICLE VELOCITY DISTRIBUTIONS IN JET

T P Hughes*, D A Boyd**, A E Costley, J A Hoekzema,
S R P Smith* and E Westerhof**

JET Joint Undertaking, Abingdon, Oxon, OX14 3EA, UK
* Permanent address: University of Essex, Colchester, CO4 3SQ, UK
**Permanent address: University of Maryland, College Park,
Maryland 20742, USA
* University of Essex, Colchester, CO4 3SQ, UK
** FOM-Instituut voor Plasmafysica, Rijnhuizen, The Netherlands

1. INTRODUCTION

A diagnostic system to measure the velocity and spatial distributions of fast ions in JET is being designed, based on collective scattering of microwaves from a high power (up to 1 MW), modulated, long pulse (up to CW) gyrotron. Several of the simplifying assumptions usually made for scattering in the visible or infrared will not be valid. Following a brief description of the diagnostic, we discuss aspects of the relevant physics and present some results of detailed calculations.

2. THE DIAGNOSTIC SYSTEM

For incident radiation with frequency ω_I and wave vector k_I the scattered radiation with ω_S and k_S at an angle θ to k_I is due to density fluctuations with $\omega = \omega_S - \omega_I$ and $k = k_S - k_I$. If $\alpha \stackrel{\sim}{=} 1/|k| \lambda_D \gtrsim 1$, the shielding electrons moving with each ion scatter collectively and the scattered spectrum contains features dependent on the ion velocity distributions. The spectral function S is the sum of contributions from all particle species, including contributions from the various thermal plasma ions, from DT reaction product alpha particles slowing down from their birth energy of 3.5 MeV and from fast ion populations created by neutral beam injection or RF heating. The ion velocities along k are mapped on to the frequency shift of the scattered radiation: $\Delta\nu_i = k \cdot v_i / 2\pi$.

The gyrotron frequency is selected to minimize noise due to electron cyclotron emission while ensuring access to the plasma centre. There is a minimum in the ECE spectrum between ν_{ce} and $2\nu_{ce}$, near 140 GHz at B = 3.4 T. At this frequency the plasma is accessible for 'O' mode radiation up to the cut-off density of 2.4×10^{20} m^{-3}.

To measure the expected alpha particle contribution to the scattered spectrum under JET conditions we need $\alpha \gtrsim 2$. For JET plasmas this requires $\theta \lesssim 60°$. If θ is reduced the signal-to-noise ratio improves but the spatial resolution deteriorates: the optimum will probably be in the range $20° \lesssim \theta \lesssim 40°$. To simplify interpretation the angle ϕ between k and B will normally be restricted to $\phi < 80°$, to avoid severe magnetic field effects.

Modulated radiation from the gyrotron is injected via a steerable mirror. Scattered radiation is collected in the similar, steerable antenna pattern of the receiver. The antennas will be located symmetrically about the horizontal midplane of the torus (for details see Costley et al, JET-R(88)08, 1988).

3. EFFECTS OF REFRACTION

The refractive index of the plasma, μ, is given by the Appleton-Hartree formula. In the proposed system the injected beam will be 'O' mode and the scattered 'O' mode will be detected. Refraction can be substantial: typically, $0.7 < \mu('O') < 1$ in JET.

The refractive index has an important direct effect on the scattered spectrum, because $k = k_S - k_I = \frac{\omega_S}{c} \mu_I k_I - \frac{\omega_S}{c} \mu_S k_S$, so the frequency shift corresponding to a given ion velocity depends on μ_I and μ_S.

Refraction also modifies the paths of the incident and scattered beams. We have used a modified TORAY code (Kritz et al, PPPL-1980, 1983) as follows: (a) for given position and orientation of the injector, follow the central ray into the plasma and find the point P of intersection with a specified plane (eg. the horizontal mid-plane). (b) for given position of the receiver, find by iteration the orientation which brings the central ray of its antenna pattern to P. (c) find k_I, k_S, B, n_e, T_e at P-, remembering that the ray direction is not in general the same as k.

The diagnostic will use focused, near-Gaussian beams with $w_0 \sim 3$ cm. We have devised an approximate method of calculating the behaviour of simple Gaussian beams based on the fact that the hyperboloid which defines the beam may be generated from a set of straight lines. We take several generators spaced around the axis of each beam and we follow them through the plasma. Figure 1 shows the intersections with three horizontal planes. The generators do not accurately represent the direction of propagation, but the patterns they create are well centred on the axes of the beams and indicate the shape of the scattering volume.

Effects of density fluctuations on the patterns are being studied.

4. THE SCATTERING CROSS-SECTION

It will be shown elsewhere that for similar incident and scattered antenna patterns with Gaussian radius w, the scattered power detectable by a heterodyne receiver in a resolving bandwidth $\Delta\nu$ Hz is

$$P_S = P_I\, n_e\, \Delta\nu\, r_0^2\, \lambda_S^2\, S(k,\omega)\, G/(\pi^{\frac{1}{2}} w\, \sin\theta_r) \qquad (1)$$

where G is a function of the incident and scattered polarization vectors, the dielectric tensors and the scattering geometry, and $r_0^2 = 7.94 \times 10^{-30}$ m^2. 'O' to 'X' scattering can be strong just above the upper hybrid frequency but is unlikely to affect the detection of 'O' to 'O' scattering.

5. SIGNAL-TO-NOISE RATIO

The noise power received by a heterodyne detector in bandwidth $\Delta\nu$ Hz may be characterised by an effective temperature T_N(eV):

$$P_N = 1.6 \times 10^{-19}\, T_N\, \Delta\nu\, W \qquad (2)$$

For JET plasmas a typical value for T_N at 140 GHz is about 500 eV. This is expected to be the main source of statistical noise.

Although the gyrotron beam path never takes it near a zone where it approaches the rest mass cyclotron resonance, in hot JET plasmas there is still some significant cyclotron absorption. The absorbed power will cause increased electron cyclotron emission; as this extra emission is in phase with the modulated gyrotron power it will not be distinguishable from the scattered signal. The cyclotron resonance condition for the second harmonic (the significant resonance in this case) is

$k - k_{||} \beta_{||} - 2k_{co}\,(1-\beta^2)^{\frac{1}{2}} = 0$, where k is the free space wavenumber of the gyrotron radiation, $k_{||}$ is its component parallel to the magnetic field, k_{co} the wavenumber associated with the rest mass cyclotron resonance, β the velocity of the resonant electrons normalized to c and $\beta_{||}$ its component parallel to the magnetic field. This condition determines the surface in velocity space on which the gyrotron power is absorbed (see Figure 2). The same equation with slightly different parameters stipulates the condition for cyclotron emission to be detected by a receiver channel. The differences arise because the receiver is tuned to a frequency different from the gyrotron and its antenna points in a different direction which produces a different Doppler shift. For these resonance curves see the figure. At the intersection of the two curves are those few electrons which both absorb gyrotron power and emit power which can be detected by the receiver. Calculations suggest that the extra modulated power received as a result of this process is negligible.

With phase sensitive detection and an integrating time τ, the final signal-to-noise ratio of the system is

$$s/n = (P_S/P_N)\,(1 + \tau\Delta\nu)^{\frac{1}{2}}/(1 + P_S/P_N) \simeq (P_S/P_N)\,(\tau\Delta\nu)^{\frac{1}{2}} \qquad (3)$$

for $P_S/P_N \ll 1$ and $\tau\Delta\nu \gg 1$. Then from (1), (2) and (3) with $\nu_S = 140$ GHz

$$\frac{S}{n} = 3.4 \times 10^{11}\; SG\; \frac{(n_e/10^{19}\mathrm{m}^{-3})\,(P_{inc}/300\mathrm{kW})\,(\tau/200\mathrm{ms})^{\frac{1}{2}}(\Delta\nu/100\mathrm{MHz})^{\frac{1}{2}}}{(w/3\mathrm{cm})\,(T_N/500\mathrm{eV})\,(\sin\theta/\sin20°)} \qquad (4)$$

6. CALCULATIONS FOR TYPICAL JET PLASMAS

In the pre-DT phase fast ions will be created by ion cyclotron heating of minority ions with RF power, and also by neutral beam injection.

ICRF Heating. We have assumed that ICRH on ^{3}He minority ions in a deuterium plasma (+ 10% hydrogen) absorbs half the 25 MW of available RF power and creates anisotropic Maxwellian minority velocity distributions with $T_\perp$ perpendicular and parallel to B. It is assumed that $\theta = 20°$, and $\phi = 60°$, with B = 3.4 T. The effective minority temperature is taken to be $T_{m_{eff}} = T_\perp \sin^2\phi + T_{||} \cos^2\phi$

The plasma conditions assumed for Figures 3(a) and (b) are:

	$n_e(10^{19}\mathrm{m}^{-3})$	T_e(keV)	T_i(keV)	$n_{min}(10^{17}\mathrm{m}^{-3})$	$T_{m_{eff}}$(keV)
a	2	10	10	14	1,010
b	10	5	5	10	282

Best-fit Maxwellians for the wings have been added, together with the spectra with no RF heating (all ions at T_i). The Maxwellian half-intensity widths are within 5% of the expected values after allowing for the refractive index effects. Signal-to-noise ratios are given for the channel widths shown (1/5 of half intensity half width). Satisfactory measurements of $T_{m_{eff}}$ should be possible.

Neutral Beam Injection. In Figure 3(c) it is assumed that a beam of 140 keV deuterons is injected into a deuterium (+ 10% hydrogen) plasma. The fast particles slow down classically with an isotropic distribution function $f(v)$ α $1/(v_c^3 + v^3)$ where $v_c \sim 0.1\, v_e$ (thermal). The calculated scattered spectrum is shown for $\theta = 20°$, $\phi = 0$, with $n_e = 2 \times 10^{19}$ m^{-3}, $T_e = 10$ keV, $T_i = 30$ keV, $n_{fast} = 2 \times 10^{18}$ m^{-3}. The background curve is calculated with all deuterons at T_i. It is clear that it will not be possible to deduce reliable information about the fast deuterons.

The feasibility of measuring the alpha particle distribution in the DT phase of JET has already been discussed (Costley et al, 1988). More detailed calculations allowing for refractive effects confirm that it should be possible to measure velocity distributions of the expected alpha populations in the energy range 0.5 to 3.5 MeV. A calculated scattering spectrum is shown in Figure 3(d), with predicted signal-to-noise ratios.

7. CONCLUSION

The diagnostic should provide valuable information about the velocity distributions of alpha particles and fast RF-heated minority ions in JET.
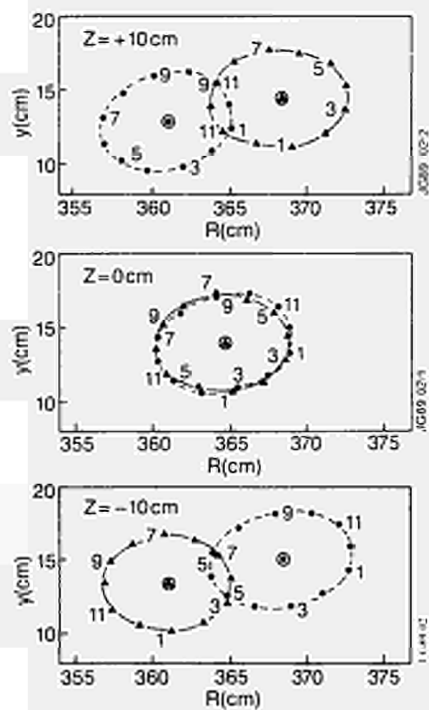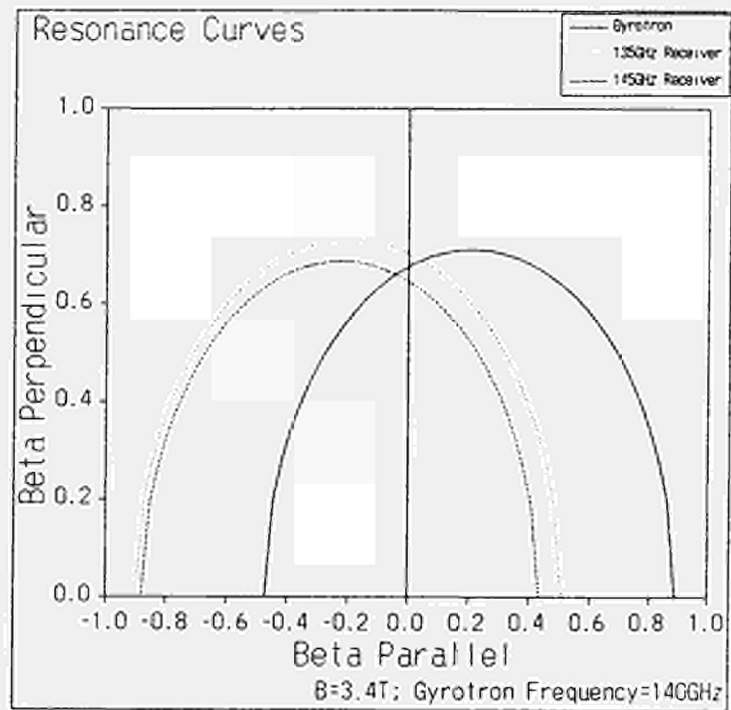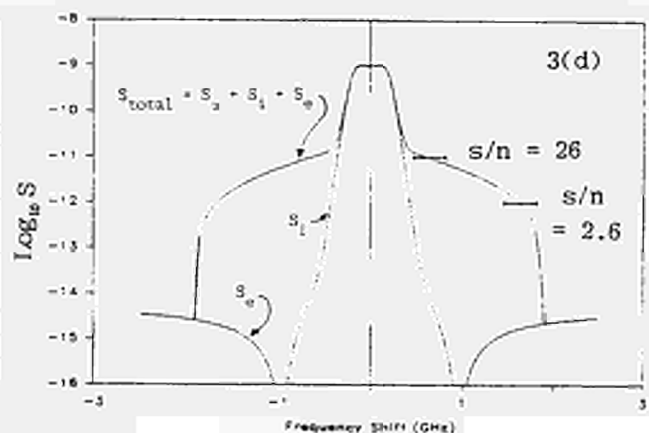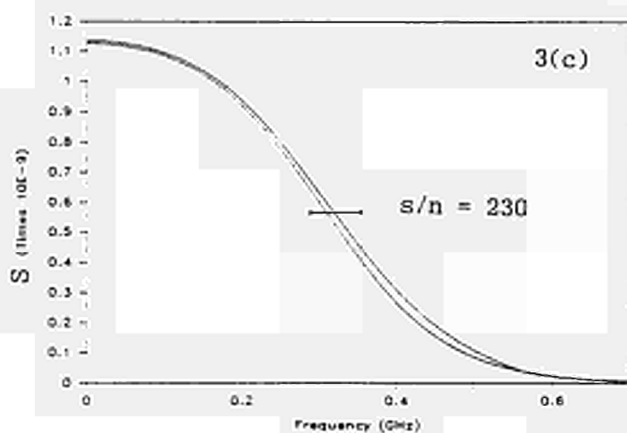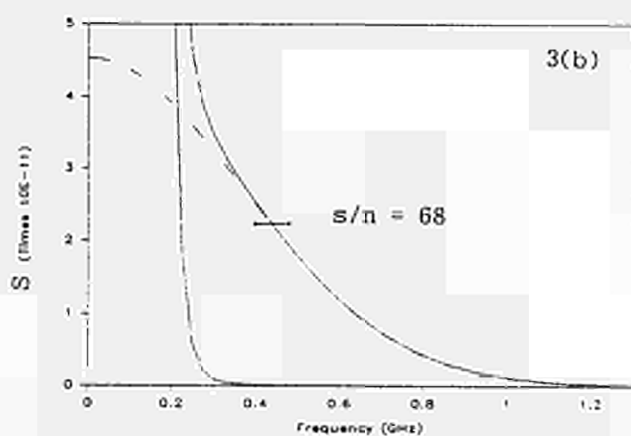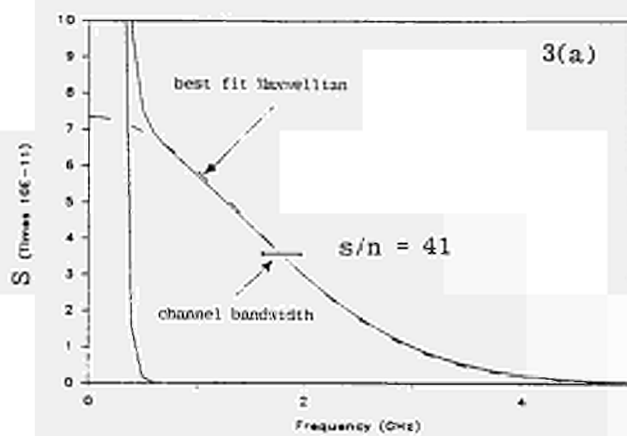
FIGURE 1

FIGURE 2

FIGURE 3

ENHANCED PERFORMANCE OF HIGH CURRENT DISCHARGES IN JET PRODUCED BY ICRF HEATING DURING THE CURRENT RISE.

M.Bures, V.Bhatnagar, G.Cottrell, S.Corti, J.P.Christiansen, L.-G.Eriksson*, T.Hellsten, J.Jacquinot, P.Lallia, P.Lomas, J.O'Rourke, A.Taroni, F.Tibone, and D.F.H.Start.

JET Joint Undertaking, Abingdon, Oxon, OX14 3EA, UK.
*Chalmers University of Technology, Gothenburg, Sweden.

Abstract. The performance of high current discharges can be increased by applying central ICRF heating before or shortly after the onset of sawtooth activity in the plasma current rise phase. Sawtooth-free periods have been obtained resulting in the enhanced discharge performance. High $T_e(0) = 9 - 10.5$ keV with peaked profiles $T_e(0)/<T_e> = 3 - 4$ were obtained giving values of $n_e(0)T_e(0)$ up to $6 \cdot 10^{20}$ (keV m^{-3}). Improvements in $T_i(0)$ and neutron production are observed. A 60% enhancement in D-D reaction rate from 2nd harmonic deuterium ($2\omega_{cD}$) heating appears to be present. In all current rise(CR) discharges radiation amounts to 25-50% of total power.

Introduction. ICRF heating experiments at 5 and 6 MA during the current rise were carried out in the D(H) heating scheme at 48 MHz. The RF antennae were phased as dipoles with maximum power emitted at $k_{\parallel} = 7$ m^{-1}. During the 5 MA discharges the RF power was applied at the level of $I_p = 3.7$ to 3.9 MA and ramped up during 0.5 sec to reach the full value at $I_p = 4$ to 4.2 MA. During the 6 MA discharges the corresponding current levels were 4.45 and 4.75 MA. The CR heating data are compared to the flat-top(FT) heating data performed for each plasma current during the same day and therefore with the same conditions of the tokamak. Typical FT target density and Z_{eff} were $<n> = 2.3 - 3 \cdot 10^{19}$ m^{-3}, $Z_{eff} = 1.6 - 2.5$ for 5 MA discharges and $<n> = 2 \cdot 10^{19}$ m^{-3}, $Z_{eff} = 4$ for 6 MA.

Current penetration and sawtooth behaviour. During the 5 MA discharges the sawtooth activity starts when the plasma current reaches the value $4.6 - 4.7$ MA. The application of RF heating delays the onset of sawteeth, the delay increasing with RF power. Fig.1 compares the evolution of the central electron temperature during RF heating to that of the ohmic discharge. A measure of current penetration is shown by polarimetric measurement of the central safety factor q(0). The first sawtooth crash occurs when q(0) is close to unity. While in the ohmic phase the reduction in $T_e(0)$ is ≈ 200eV, it reaches 3 to 3.5 keV in the case of RF heating. It implies that q is ≈ 1 over a substantial part of the plasma core. This is supported by the T_e profile measurements shown in Fig.2a. The inversion radius of the first crash is roughly 40 cm compared to 15 cm in the ohmic case. During the FT heating the corresponding value is ≈ 60 cm. In 6 MA discharges the sawtooth activity starts when the plasma current reaches 4 MA, clearly much earlier than during 5 MA discharges. The difference may be due to higher resistivity from a higher Z_{eff}. By application of RF power the sawtoothfree period was obtained following the normal sawtooth activity. Thus, as demonstrated by 6 MA results, the dominant physical mechanism responsible for the delay of sawteeth is similar to that of the Monster sawtooth stabilisation. As indicated by polarimetric measurements, the delay of current penetration also contributes.

Enhanced performance during CR heating. The main observed improvements over heating during the current flat-top can be summarised: 1) factor 1.4 (5MA discharges) and 1.5 - 2 (6 MA discharges) increase in a, where a is defined by $\Delta T_e(0) = aP_{RF}/n_e(0)$; 2) 10-20% increase in $T_e(0)$ in both 5 and 6 MA discharges; 3) 10-20% increase in $\Delta W/\Delta P_{tot}$; 4) factor 2 increase in D-D reaction rate for 5 MA discharges. The relatively high gain in $T_e(0)$ during 6 MA discharges (shown in Fig.3)

is explained by the low $T_e(0)$ values obtained in the FT phase. Such low values are consequence of a large plasma volume within the $q = 1$ surface affected by losses associated with sawtooth instability (Fig.2b). The rate of increase of $T_i(0)$ with $P_{RF}/n_e(0)$ is roughly the same in all cases of FT and CR heating, but the absolute values are systematically higher in the current rise. Presently it is not clear if the $\Delta W/\Delta P_{tot}$ is conserved at higher powers than those achieved, i.e., above $P_{RF} + P_{ei} = 15$ MW. In Fig.4 the value of $n_e(0)T_i(0)$ is plotted for two 5 MA discharges during current FT and CR, with $P_{RF} = 11$ MW. A value of $6 \cdot 10^{20}$ (keV m^{-3}) has been reached during both CR and more recently with combined RF heating and pellet injection into a 3 MA discharge[1,2]. The electron temperature peaking ratio $T_e(0)/<T_e>$ reaches values $3.5 - 4.2$ during 5 MA CR compared to 3 in 6 MA CR. Density peaking ratios in CR and FT are similar $n_e(0)/<n_e> = 1.4 - 1.6$. The D-D reaction rate data is shown in Fig.5. As explained below, a significant contribution to the neutron enhancement results from the creation of high energy deuterium tail. The reason why the 6 MA discharges did not produce a comparable improvement is the relatively high Z_{eff}.

$2\omega_{cD}$ heating. The neutral particle spectra measurements indicate that the fast hydrogen and deuterium tails are formed after the application of RF power. During the 5 MA CR discharge with 11 MW of RF power the hydrogen spectrum develops a tail with a "temperature" ≈ 45 keV. A substantial fraction of particles is in the high energy range. Similarly deuterium spectra indicate a tail formation with a "temperature" $\approx 30 - 35$ keV. In this case the majority of particles is in the bulk of the distribution fuction. The neutral particle analyser measures the energy of hydrogen neutrals up to 65 keV and deuterium up to 45 keV. Thus the information is of qualitative nature and the true tail temperature is certainly much higher. The correlation between the fluxes of high energy neutrals and neutrons also suggests that $2\omega_{cD}$ heating is present. The low energy channels do not exhibit such a correlation. To estimate the importance of the $2\omega_{cD}$ heating for the neutron yield, a self-consistent full wave RF power deposition calculation[3] in conjuction with Fokker-Planck calculations of the hydrogen and deuterium distribution functions were carried out. The complete spectrum of the dipole antenna was used. Fig.6 shows the results from the calculations which are compared with the measured neutron yield. The open circles represent the simulation of the thermal part of the yield. An agreement with the measured values can be obtained if we assume Z_{eff} 30% higher than the measured one(2.6 instead of 2). The 60% contribution from the fast deuterons is also indicated. The power deposition calculation does not include electron Landau and TTMP damping. Estimates suggest that 10 - 20% of the power can be directly damped by electrons. This will slightly decrease the calculated enhancement, bringing it even closer to the measured value.

Conclusions. Elimination of sawtooth activity by application of high power ICRF heating during the plasma current rise phase of 5 and 6 MA discharges results in an enhanced performance in terms of all major plasma parameters. In particular high value of $n_e(0)T_i(0) = 6 \cdot 10^{20}$ (keV m^{-3}) has been reached together with enhanced neutron yield by $2\omega_{cD}$ heating. The peaking $T_e(0)/<T_e>$ reaches the value 4.2 which is a factor 2 higher than in the flat-top phase. The density peaking $n_e(0)/<n_e> = 1.5$ remains unchanged. Current rise heating appears to be one of the candidates for T(D) operation[4] in JET, eventually combined with pellet injection. It also provides an interesting target for NBI heating. The possibility of extending this mode of operation for longer period will be a subject of future experiments.

References.

1. G.Hammet et al., this conference.
2. V.Bhatnagar et al., this conference.
3. L.-G.Erikson et al., to be published in Nuclear Fusion.
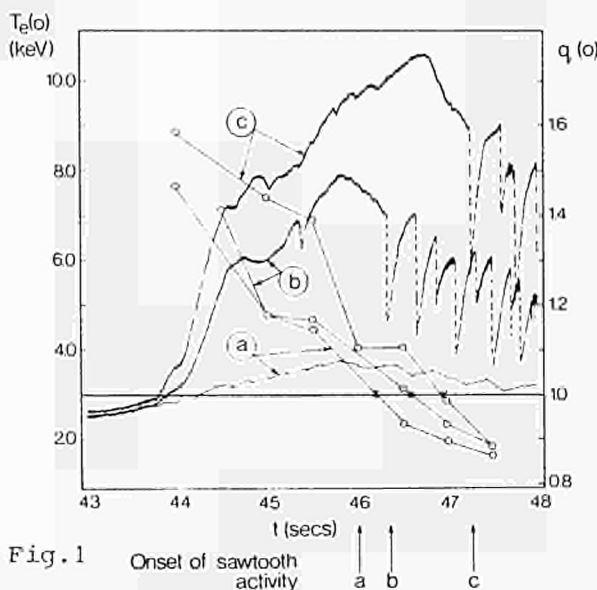4. J.Jacquinot et al., Plasma Phys. and Contr. Fus., Vol.30, no.11, p.1467.

Fig.1 Central electron temperature and q(0) time evolution in a)ohmic, b)$P_{RF} = 4.3$ MW and c)$P_{RF} = 11$ MW discharges.
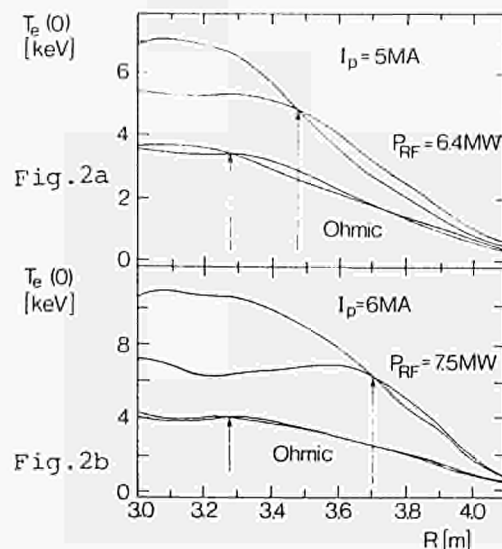
Fig.2a,b Electron temperature profiles associated with the first sawtooth colapses(just before and after) in ohmic and RF heated discharges in CR. The arrows indicate the inversion radii.
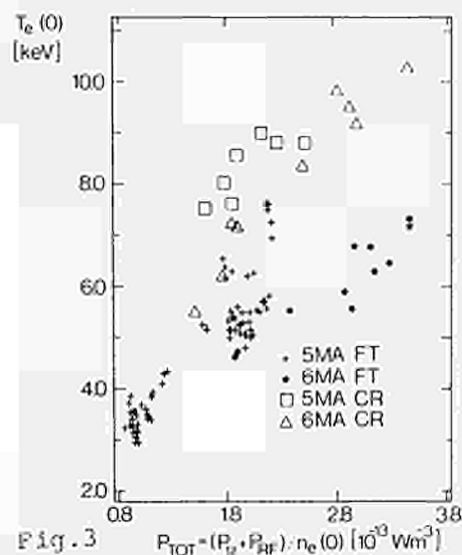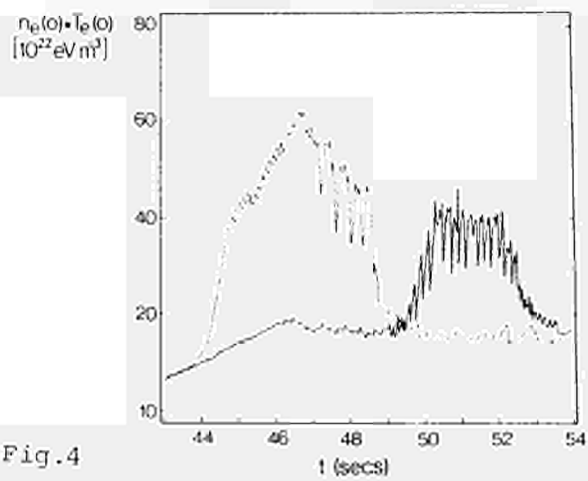
Fig.3

Fig.4

Fig.3 Central electron temperature versus total power per particle.
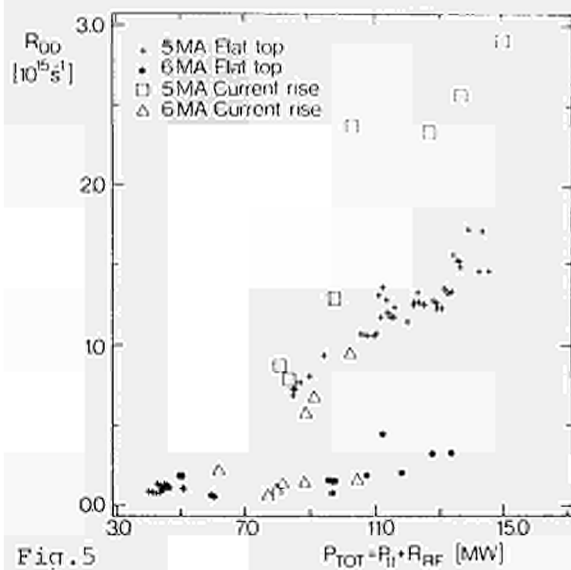*Fig.4* $n_e(0)T_e(0)$ during CR and FT 5 MA discharges, $P_{RF} = 11$ MW.
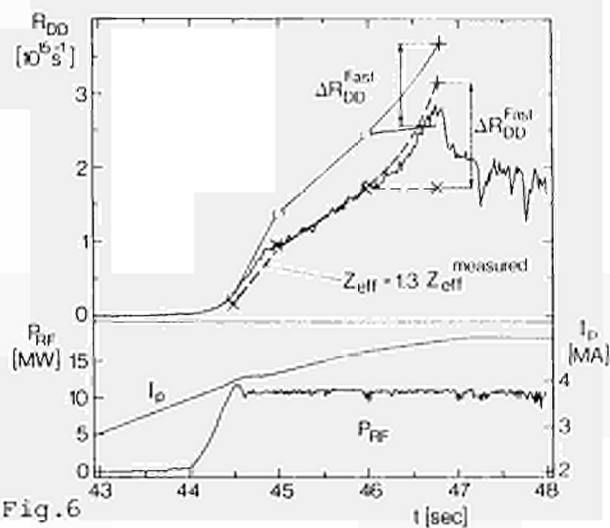

Fig.5

Fig.6

Fig.5 Neutron yield as a function of power input.
Fig.6 Time evolution of measured and calculated neutron yield. ΔR_{DD} represents the contribution from the $2\omega_{CD}$ heating. Plasma current and RF power are also shown.

SPACE- AND TIME-RESOLVED DIAGNOSTIC OF LINE EMISSION FROM
THE SEPARATRIX REGION IN JET X-POINT PLASMAS

P Chabert*, C Breton*, C DeMichelis*, B Denne, R Giannella, N Gottardi,
G Magyar, M Mattioli*, J Ramette*, and B Saoutic*

JET Joint Undertaking, Abingdon, Oxon., OX14 3EA, UK
* EURATOM-CEA Association, Cadarache 13108 St Paul lez Durance, FRANCE

1.   INTRODUCTION The SPEX GISMO VUV spectrometer installed on JET has
appeared to be appropriate to study the impurities radiation during
X-point operation [1]. Preliminary results have been obtained with 2 of
the 3 spectrometers. They concern mainly the light impurities emission,
C III, O VI in the vicinity of the X-point during the transition from L to
H mode. The results are reported for both single X and double X
discharges and future prospects are assessed.

2.   INSTRUMENTATION As described in more detail in ref.[1] the
diagnostic is made up of 3 spectrometers, 2 viewing in the horizontal
direction, one viewing vertically. Each of them scans the plasma by means
of a rotating mirror providing typically one angular profile in 10 msec
every 100 msec. Furthermore, each mirror can be stopped at any
predetermined position so as to obtain time evolution along fixed chords.
The light is diffracted by a grazing incidence grating, and 3 wavelength
can be monitored simultaneously. The 2 UV detectors cover the wavelength
range from 100 A to 2500 A. The auxiliary slit of the spectrometers
defines a spatial resolution of a few cm in the X-point region.

A poloidal cross-section of the JET machine and the port of the
diagnostic can be seen in Fig.1, together with the mirrors of the
horizontal spectrometers. The spectrometers are referred as UH (upper
horizontal), LH (lower horizontal) and scan respectively the lower and
upper halves of the plasma.

The plot of the poloidal magnetic surfaces for a typical single
X-point discharge shows that the X-point corresponds to a mirror angle
between 12 and 14°.

3.   RESULTS Figure 2 shows the time evolution of the C III line
integrated signal observed by UH and LH at an angle of 14°. The formation
of the X-point give rise to a strong signal at the top of the plasma while
the corresponding signal at the bottom decreases. This is consistent with
the bolometer data.

The H-mode transition causes a sudden fall in the carbon signal for
both UH and LH.

Figure 3 is an example of fast fluctuation commonly observed on O VI
signal, along the line-of-sight between 10° and 14°, after the injection
of neutral beam. As they are correlated with the spikes observed on
Dα and poloidal coils, they are considered to be due to ELM instabilities
[2]. The sudden drop in the frequency at the L-H transition preceeds the
termination of the ELMS, as observed previously [3].

Figure 4(a) shows a typical example of the angular profile evolution
of O VI emission in single null discharges. The X-point establishment
phase shows clearly a rise in the emission at 14°. The resulting profile
is quite consistent with what is commonly observed by bolometry [4]. The
start of NBI can cause ELM fluctuations to occur for a short time, chang-
ing the profile in an artificial way, the period of the fluctuations being
smaller than the scanning time.

The profile eventually stabilises to the one shown in dotted line in
Fig.4(b) which is quite similar to those before NBI. The L-H transition
(as seen by the drop in D_α) shows a shrinking of the profile, with the
appearance of a new peak apparently located on the inner side of the
X-point which last until the end of the H-mode. Without the vertical line
it is not possible to know the direction in which the maximum of radiation
has moved.

Figure 4(a) has to be compared with fig.5 (L mode case) where the
neutral beam injection causes a sudden burst of O VI radiation. (The
small bumps observed are due to ELM fluctuations and are not spatial
variations for the reasons given above.)

Figure 6 shows the time behaviour of O VI emission profile in double
null H-mode discharge for the upper and lower spectrometers. It should be
noted that the profiles are narrower than in the single null case. The
H-mode causes a slight decrease in both the upper and lower signals.

4.   CONCLUSION AND FUTURE PLANS A preliminary study of the impurities
radiation from the X-point region during H-mode discharges has been under-
taken. Further investigations, carried out in 1989 will require the
implementation of the vertical line, to localise more accurately the
bright region near the X-point, as well as an absolute calibration of the
detector so as to give an estimate of the radiated power.

REFERENCES
[1]   K H Behringer et al., Course and Workshop on basic and advanced
       diagnostic techniques for fusions plasma, Varenna 1986, Vol.1,
       p.305.
[2]   P Cripwell et al., This conference.
[3]   A Hubbard et al., Proc. 15th EPS Dubrovnik, May 1988.
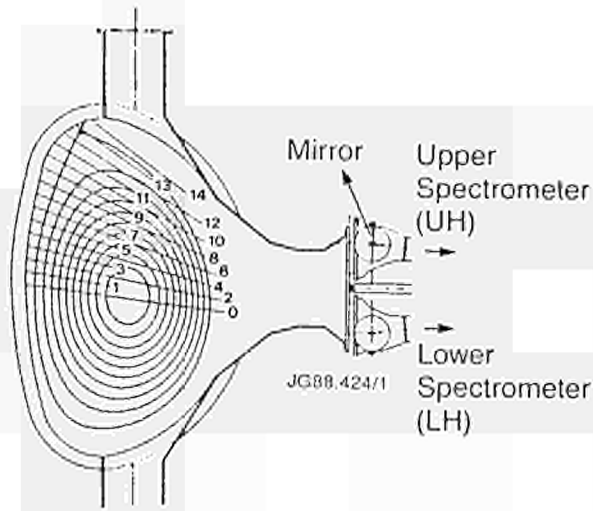[4]   H J Jaeckel et al., Proc. 14th EPS Madrid, June 1987.

Fig.1:   JET vacuum vessel octant 6
         showing 2 rotating mirrors
of the horizontal spectrometers.
Also shown are several lines-of-
sight for various angles of the
lower mirror together with a
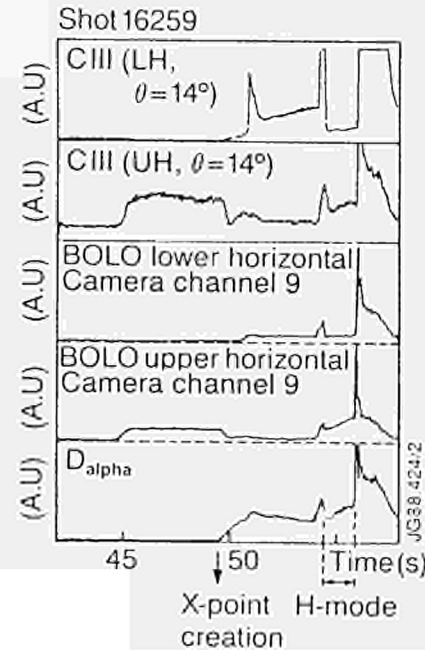typical poloidal flux plot in
upper single X-point discharge.

Shot 16259

CIII (LH, $\theta=14°$)

CIII (UH, $\theta=14°$)

BOLO lower horizontal
Camera channel 9

BOLO upper horizontal
Camera channel 9

D_{alpha}

45   50   Time(s)

X-point   H-mode
creation

Fig.2:   Time evolution of C III line
         integrated intensity ($\lambda=977$ Å)
together with bolometer and D_α signals
in upper single null H-mode. The chords
of the bolometers correspond roughly to
those of the spectrometers.
(NBI at 54 sec)

Shot 17378
OVI Intensity

L-mode   H-mode

52.04   52.06   52.08   52.10
(Secs)
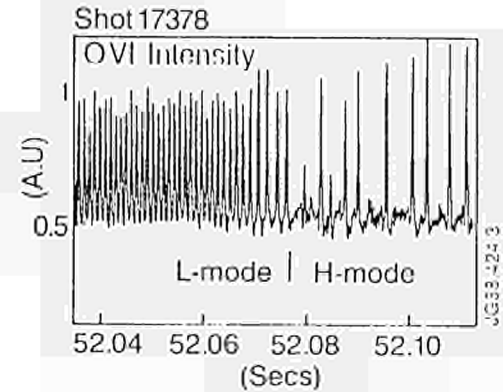
Fig.3:   Edge fluctuations on
         O VI signal ($\lambda=1032$ Å)
during an L-H transition, in
upper single null discharge.
Signal viewed by LH with $\theta=12°$.

Shot 17061

OVI
Intensity
(A.U)

JG88.424/4

H
-mode

Time(s)

Mirror angle

(a)

JG88.424/5

t=54.9
(H-mode)

t=54.7
(L-mode)

Degr

(b)

Shot 17087

OVI
Intensity
(A.U)

JG88.424/6

Time(s)

Mirror angle
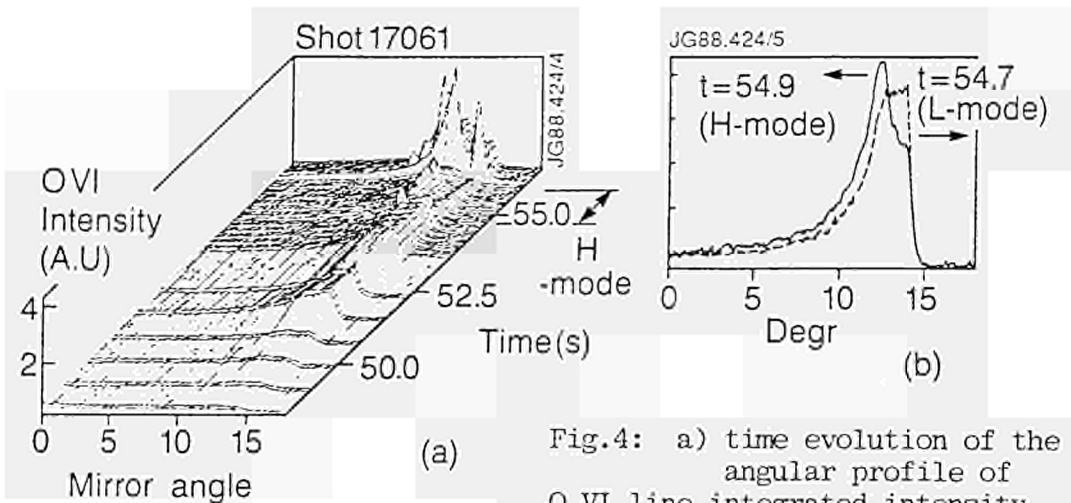
Fig.4: a) time evolution of the
angular profile of
O VI line integrated intensity
(λ=1032 Å) seen by LH. H-mode in
upper single X-point. I_p=3 MA,
B_T=2.2T, NBI power = 12 MW,
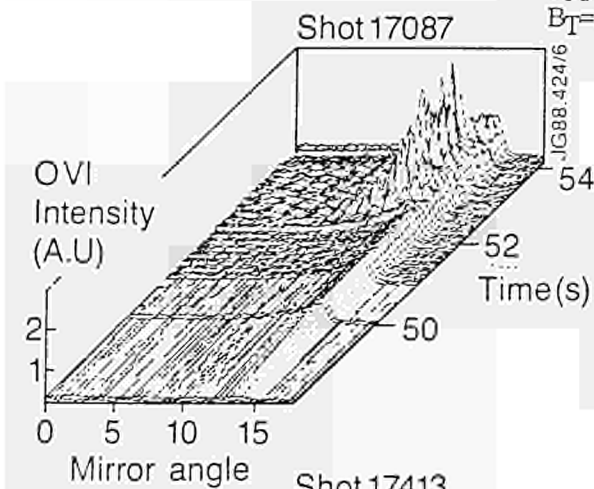NBI starts at 54.5 sec.

b) detail of the L-H
transition.

Fig.5: Same parameters as
fig.4 for an L-mode
in upper single X-point.
I_p=3 MA, B_T=2.2T, NBI power =
8 MW, NBI starts at 52 sec.

Shot 17413

(a)
OVI
Intensity
(A.U)

JG88.424/7

Time(s)

Mirror angle

Shot 17413

(b)
OVI
Intensity
(A.U)

JG88.424/8

H
-mode

Time(s)

Mirror angle
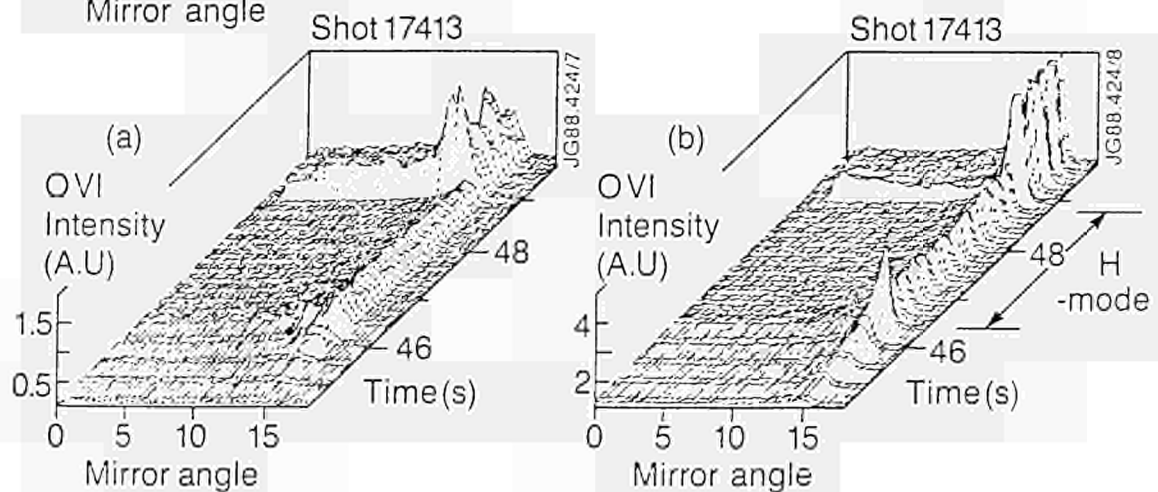
Fig.6: Time evolution of O VI intensity profile in double X-point
H-mode. NBI power = 6 MW, NBI starts at 46 sec.
a) LH   b) UH.

TRANSPORT STUDIES DURING SAWTEETH AND H-MODES ON JET USING LASER ABLATION.

N Hawkes[a], Z Wang, R Barnsley, K Behringer[b], S Cohen[c], B Denne,
A Edwards, R Giannella, R Gill, G Magyar, D Pasini, N Peacock[a],
U Schumacher[b], C Vieider[d] and D Zasche[b]

JET Joint Undertaking. Abingdon. Oxon, OX14 3EA, UK
[a] *UKAEA Culham Lab.. Abingdon, Oxon, OX14 3DB*, UK
[b] *Max-Planck-Institut fur Plasmaphysik, D-8046, Garching*, FRG
[c] *Plasr ⁊ Physics Laboratory, Princeton Univ., Princeton, NJ 08544*, USA
[d] *Uppsala Institute of Technology*, SWEDEN

A system for the controlled injection of trace impurities by laser ablation has recently been commissioned on JET. Small amounts of metallic impurities have been injected in order to study transport phenomena. In all cases the amounts, corresponding to an injected quantity of a few 10^{18} atoms (an impurity concentration of 0.01% of n_e), were sufficiently small to avoid perturbing any plasma parameter apart from the radiation ($\Delta P_{rad} < 0.5$ MW). We report here on measurements of impurity confinement time (τ_{imp}) and observations of impurity transport effects using this technique.

A suite of spectrometers viewing fixed lines of sight was used to gather information on the time behaviour of a range of ionisation stages. In addition measurements of the soft X-ray emission were obtained with good spatial and temporal resolution from two X-ray cameras.

Sawteeth observations - The soft X-ray cameras show inverted sawteeth during the rise phase of radiation from injected impurities. Figure 1 shows the time development of the central chord soft X-ray signal and central electron temperature (T_e) illustrating the inversion of the first sawtooth after impurity injection.

Clearly the increase in radiation due to the influx of impurities into the central region of the plasma at the time of the sawtooth crash overcompensates the drop in T_e. In most cases the inverted sawtooth is accompanied by a large amplitude $m = 1$ oscillation. This oscillation usually disappears within less than half a sawtooth period. During this time the amplitude of the oscillation decays gradually. Their frequency also decreases, from 500 Hz immediately after the sawtooth crash to 400 Hz as the oscillation disappears. A clear understanding of these oscillations is still lacking.

Tomographic reconstruction of the plasma emissivity reveals that impurity transport within the central region (inside the $q = 1$ surface) is profoundly different from that in the rest of the plasma. Figure 2 shows a sequence of radial emission profiles from the same discharge for times after the ablation. Background radiation, present before ablation, has been subtracted out. Immediately after ablation the radiation profile builds up at mid radius, with no growth in radiation from the centre. This central region, inside $q = 1$, only fills in when a sawtooth crash occurs, time t_2 in the figure. The filling is incomplete even after the first crash, it taking typically two to three sawtooth cycles for the intially hollow profile to become peaked on axis. The radiation profiles indicate that rather than a transport barrier at $q = 1$, impurity transport inside the $q = 1$ region is reduced, there being only a slow evolution of the radiation profile in this zone between sawtooth crashes. During the decay phase the reverse situation applies in that impurities linger in the central region, again only crossing $q = 1$ at the time of the sawtooth crash.

Scaling studies - Scaling studies were performed in ohmic L-mode shots of the decay time of XUV radiation intensity from high ionization stages (ionisation energies typically > 1 KeV) of the injected metals. Such radiation is emitted from the outer 1/3rd of the plasma radius. At this radius the decay time of the intensity is representative of the global impurity containment time (τ_{imp}). The decay curves of the intensity were corrected for variations in T_e and n_e with the application of an empirical correction formula derived from modelling calculations performed with an impurity transport code. The corrected decay curves were then fitted by an exponential to give the decay time and the resulting times stored in a database. The X-ray observations indicate that diffusion of impurities inside $q = 1$ is much lower than in the outer regions but since transport is effectivly enhanced during the sawtooth crash and the decay times span many sawtooth cycles the times we measure are governed by the transport in the region outside $q = 1$.

No dependence of τ_{imp} with charge of the ablated ions was detected, thus simplifying the further analysis of the data. An apparent scaling of τ_{imp} with density was

observed in the data (figure 3) with the form $.09(n_e/10^{19})^4/q_L$. However with the parameter range explored it is not yet possible to rule out other dependencies. τ_{imp} and the energy confinement time, τ_L, were found to be uncorrelated. In particular no reduction in τ_{imp} with auxilliary heating was detected (up to $P_{tot} < 15$ MW) although the number of heated shots studied was limited. During H-mode, however, the impurity confinement time became much longer than under any other operating condition, exceeding τ_L.

Transport in H-mode - Our dataset includes two observations of impurity transport during H-mode which we have modelled using an impurity transport code. In a 4MA shot, 18627, cobalt was injected into the discharge a: 12s, 0.5s after the start of the H-mode. Figure 4 shows the time traces of the injected Co as well as the time traces of the intrinsic impurities nickel and oxygen.

The emission from the lower ionisation stages of Co rises rapidly (within 0.1s) to a steady value which persists up to the end of the H-mode. The lower stages of C and O show little effect of the H-mode whereas OVIII and CVI (ionisation energies 870 and 490 eV) behave like the nickel lines [1] (ionisation energies > 2000 eV) and ramp up during the H-mode. The bulk plasma therefore behaves as an almost ideal 'integrator' of impurities. Adjustment of the raw signal intensities to take account of the changing n_e and T_e modifies the near rectangular Co XXIV and Co XXV time traces, giving them a slow decay with time, leading to the plasma being described better as a slightly 'leaky' integrator with confinement time of 4s (> τ_L).

A transport model describing the behaviour of intrinsic impurities during H-mode had previously been proposed [2]. This model accounted for the time development of radiation from iron injected near the H-mode transition of a 3MA shot (17068) (giving an impurity decay time of 0.8s - nearly equal to τ_L). To account for the data in figure 4, however, it is necessary to include a stronger inwards convection (Γ) at the very edge of the plasma. The profiles of diffusion (D) and Γ adopted for the modelling are shown in figure 5 and the resulting time evolution of Co, Ni and O radiation in figure 6 which well describe the experimental observations. The lower ionisation stages of oxygen lie in the scrape off (or in the region of inwards convection) and hence do not see the impurity build up of the bulk plasma.

The neoclassical transport description of Hirshman and Sigmar [3] as evaluated by Fussmann 4 is implemented in the transport code allowing comparisons to be made with our coefficients. The crucial feature in our model is the ratio of Γ/D (~50 m⁻¹) at the plasma edge. Whilst the ∇n, n, terms of the drift (arising out of the steep edge density gradients) are of approximately the correct shape the ∇T_e/T_e screening terms are hard to estimate from the T_e profiles. The neoclassical ratio Γ/D is plausibly comparable with our model ratio. The D profile is not a sensitive parameter in the model and the profile selected is greater than the neoclassical diffusion by a factor varying between 3 in the centre and 50 at the edge. The choice of a lower D value leads to a slower penetration by impurities of the core plasma and thus gives a slower rate of rise of emission from (particuarly) Co XXVI. The effect of sawteeth has not been included, however, in this model and will act to mitigate this slower rise.

Conclusions - Laser ablation of test impurities into JET plasmas has demonstrated a significant reduction of transport within the $q = 1$ surface as well as the expected increase in transport during a sawtooth crash. Studies of the variation of τ_{imp} with plasma parameters have yielded a scaling model but it cannot yet be regarded as complete.

Studies of H-mode plasmas extend observations of intrinsic impurity behaviour and confirm the significance of the edge (within 0.2m of the separatrix) with respect to the retention of impurities. Whilst not adequately described by neoclassical transport there are enough similarities to encourage further investigation in this direction. The particular effects of the neutral beam driven momentum source and the non circularity of the minor cross-section are not included in the neoclassical description adopted here.

References
[1] Giannella R. *et al.* this conference.
[2] Behringer K *et al.* EPS Dubrovnik in Europhys. Conf. Abs. 12B 1 p338.
[3] Hirshman S.P. and Sigmar D.J. Nucl. Fus 21 (1981) 1079
[4] Fussmann G. *et al.* J. Nucl. Mater. in print (1988) (8th PSI, Jülich 1988)
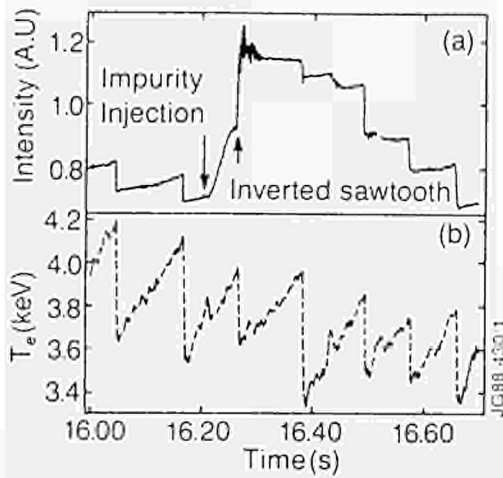
Figure 1. Time evolution of central chord soft X-ray signal (a) and electron temperature (b) during a discharge with Mo injection.
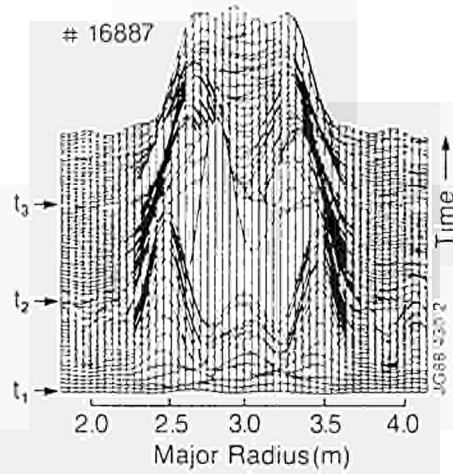

Figure 2. Time evolution of the injected impurity X-ray emission distribution along the horizontal central chord: t_1, impurity injection, t_2, t_3 sawtooth crashes (Shot 16887).
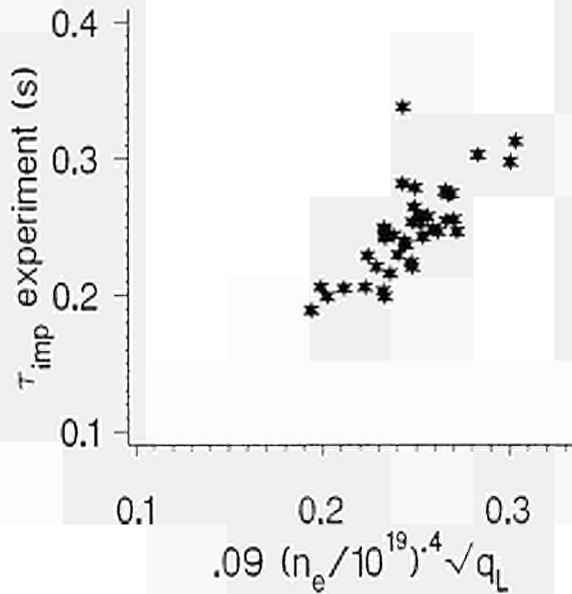

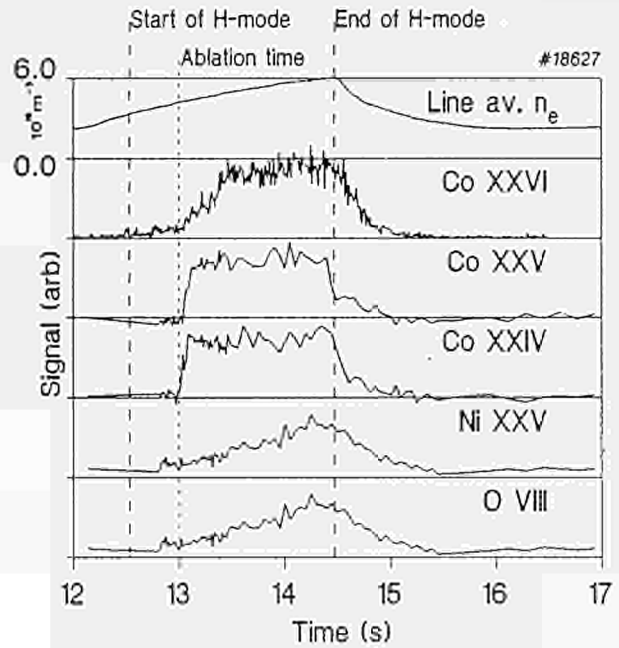Figure 3. Scaling of t_{imp} with volume average electron density and safety factor.

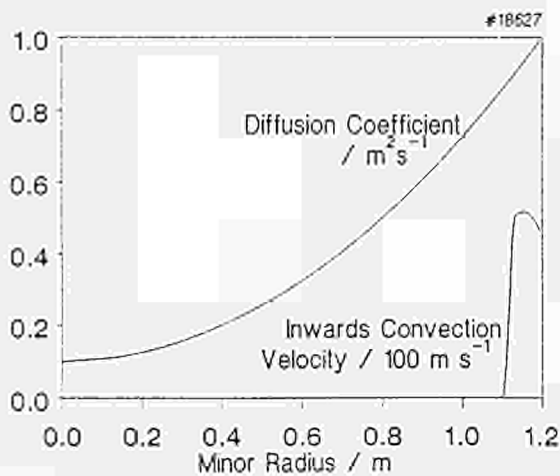Figure 4. Time development of injected Co and intrinsic Ni, C and O during an H-mode (Shot 18627).

Figure 5. Transport parameters used in modelling.
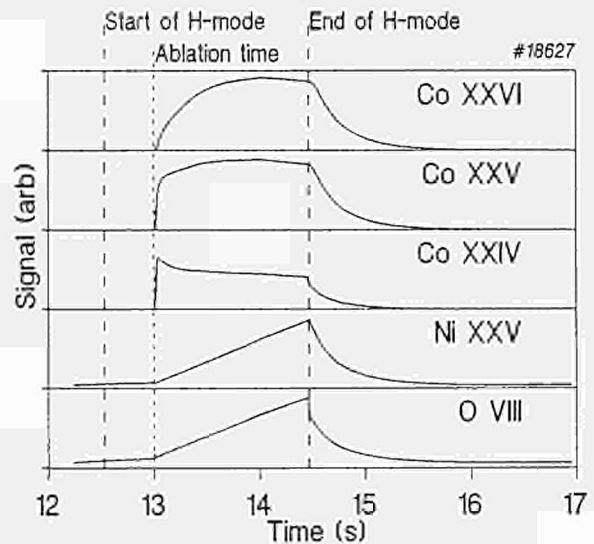
Figure 6. Results of modelling. A correction for density variation has been applied.

MEASUREMENTS OF THE ELECTRON PARTICLE DIFFUSION COEFFICIENT WITH THE JET MULTICHANNEL REFLECTOMETER

A C C Sips*, A E Costley, J C M de Haas* and R Prentice

JET Joint Undertaking, Abingdon, Oxon, OX14 3EA, UK
* FOM "Rijnhuizen", The Netherlands

INTRODUCTION

Experimental determinations of the cross-field particle diffusion coefficient (D_p) are important in studies of transport in tokamak plasmas [1,2]. D_p has been determined from measurements of density perturbations following a sawtooth collapse [2,3], oscillating gas puff [4], and injected high velocity pellets [2]. In each case the density changes have been measured using multichord interferometry and D_p is obtained with an accuracy of typically 20%.

At JET, D_p has been determined by using microwave reflectometry to measure changes in the density profile following a sawtooth collapse. Reflectometry provides relatively localized information on the electron density and so offers the promise of providing accurate measurements of the radial dependence of D_p. Initially, a single channel reflectometer was used to measure an outward propagating density pulse following a sawtooth collapse [5]. More recently, a multichannel reflectometer [6] has been used to study a dominant inward propagating density pulse following the collapse of a monster sawtooth [7]. The inward going pulse is thought to be generated by the faster heat pulse reaching the plasma limiter in advance of the density pulse. These studies demonstrate that, in general, simultaneous inward and outward propagating pulses have to be taken into account in determinations of D_p using the sawtooth collapse.

In this paper, we present our most recent measurements of D_p. The experimental data are compared with the prediction of a comprehensive numerical transport model which includes both outward going and inward going density pulses.

THE MULTICHANNEL REFLECTOMETER

The reflectometer at JET has 12 probing frequencies in the range 18-80 GHz. It operates in the ordinary mode and so probes electron densities in the range $0.4 - 8.0 \times 10^{19}$ m^{-3}. It can be operated either with the source frequencies fixed, or swept over a narrow range. In the former mode it provides the magnitude and direction of rapid movements of the density layers. The sensitivity of the system is such that movements of 1.0 mm of the 0.4×10^{19} m^{-3} density layer, and 0.2 mm of the 8.0×10^{19} m^{-3} density layer, can be clearly resolved. In the narrow band swept mode, the positions of the different density layers are determined.

The data presented in this paper are obtained with the seven channels which probe the density layers $0.4 - 4.0 \times 10^{19}$ m^{-3}. The reflectometer is operated in the fixed frequency mode. The data are recorded with a bandwidth of 700 Hz, at a sampling rate of 1-2 kHz and 3-4 seconds of a JET discharge are monitored.

DENSITY PULSES FOLLOWING A SAWTOOTH COLLAPSE

For the discharges investigated, typically five of the probed density layers lie outside the mixing radius, figure 1. Following a sawtooth collapse, the phase change measured on these channels rises and falls, figure 2. The time interval between the sawtooth collapse and the peak of the phase change is termed the delay time. This time is observed to decrease with increasing radius, figure 3, demonstrating the existence of an inward propagating pulse. This pulse originates at the plasma edge 10-40 ms after the sawtooth collapse.

NUMERICAL MODEL

Our model is a 1-D numerical transport model in which diffusive and convective terms are included. The model is outlined in figure 4.

First an equilibrium electron density profile is established assuming a radially dependent particle diffusion coefficient of the form $D_p(r) = D_p(1 + \alpha r^2/a^2)$ and an anomalous pinch velocity $v_p(r) = CD_p(r) r/a^2$. The coefficient C is adjusted, keeping the total number of particles constant,

until the predicted central density is the same as that measured by the JET multichord interferometer.

Next the sawtooth oscillations, and the consequential density pulses, are simulated. The outward propagating pulse is simulated by collapsing the density profile inside the mixing radius, while the inward propagating pulse is simulated by changing the edge recycling coefficient (R) during the sawtooth period (figure 5). The recycling coefficient is temporarily raised above 1 by an amount A_r. This gives the influx of particles from the edge and increases the total number of particles in the plasma. After time τ_r, R is decreased to a value below 1 to restore the total number of particles to the initial value (at the crash). The particle diffusion time is comparable with the sawtooth period at JET and so it is necessary to simulate a sequence of density pulses.

The computed phase changes on each channel are compared with the measured phase changes. D_p, A_r, τ_r, and α are adjusted to give the best fit to the measurements. A typical fit is shown in figure 2.

RESULTS

Thus far we have analysed sawteeth measured on seven different plasma pulses. In all cases the pulses had a current of 5 MA, toroidal field of 3.1 T, and were limited on the belt limiters. The plasmas were heated with ICRH in the range 0 to 7 MW. A total of sixteen sawteeth (an average of two per discharge) have been compared with the model predictions. The best fit to all the measurements is obtained with $\alpha = 2$ but α values in the range 1-4 cannot be excluded. Typically we find D_p equal to 0.16 ± 0.02 m^2/s and the best fitted value for all the data lies in the range 0.16 ± 0.04 m^2/s. D_p is independent of the amount of ICRH coupled into the plasma.

Further, we have examined the relationship between A_r and the drop in the electron temperature at the crash $\delta T_e(0)$ (as measured by ECE). We observe that A_r is proportional to $\delta T_e(0)$, figure 6. This supports the suggestion that the inward propagating density pulse is due to the increased energy flow to the limiters resulting from the heat pulse associated with the sawtooth collapse. We have also observed that the predicted maximum increase in the total number of particles in the plasma during the sawtooth period agrees well with that calculated from independent D_p measurements.

CONCLUSIONS

A radially dependent electron particle diffusion coefficient is derived by modelling the changes in the electron density profile after a sawtooth collapse as measured with a multichannel reflectometer at different radial positions outside the mixing radius. An important feature of the numerical model is that it contains outward and inward propagating density pulses. The inward propagating pulse is simulated by changing the edge recycling coefficient during the sawtooth period. Comparing the data from the reflectometer with the model predictions for several plasma shots, the value for D_p is found to be $[0.16 \pm 0.04] (1 + \alpha r^2/a^2)$ m^2/s with $\alpha = 2$. This agrees with values obtained by other methods at JET [2]. The value for χ_e for these plasma conditions lies typically in the range of 3-5 m^2/s at r/a = 0.8 [8]. This confirms the large value for χ_e/D_p found in recent transport studies at JET [2].

REFERENCES

[1] J Callen et al, Nuclear Fusion 27 (1987) p1857.
[2] A Cheetham et al, 12th International Conference on Plasma Physics and Controlled Nuclear Fusion Research, Nice, October 1988, IAEA-CN-50/I-2-2.
[3] S K Rin et al, 15th European Conference on Controlled Fusion and Plasma Heating, Dubrovnik, May 1988. Vol 12B, Part I, p187.
[4] O Gehre et al, 15th European Conference on Controlled Fusion and Plasma Heating, Dubrovnik, May 1988. Vol 12B, Part I, p7.
[5] A E Hubbard et al, 13th European Conference on Controlled Fusion and Plasma Heating, Schliersee, April 1986. Vol 10C, Part I, p193.
[6] R Prentice et al, 15th European Conference on Controlled Fusion and Plasma Heating, Dubrovnik, May 1988. Vol 12B, Part III, p1115.
[7] R Prentice et al, 30th Annual Meeting of APS, Hollywood, November 1988, Poster paper.
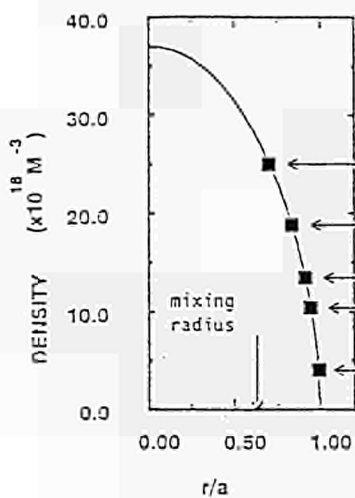[8] J C M de Haas et al, this conference.

Figure 1: Example of an electron density profile with the position of the reflectometer channels outside the mixing radius (squares).
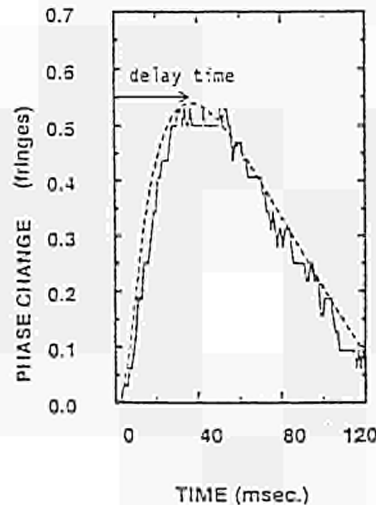
Figure 2: Signal on reflectometer channel (F=39 GHz, r/a=0.83) during sawtooth period (solid line) and best fit model prediction (dashed line).
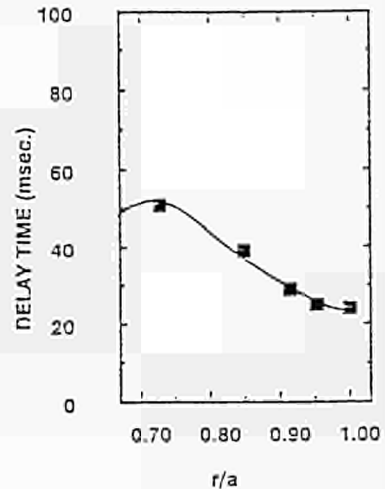
Figure 3: The observed delay time at different radial positions (squares) compared with model prediction (best fit, solid line).
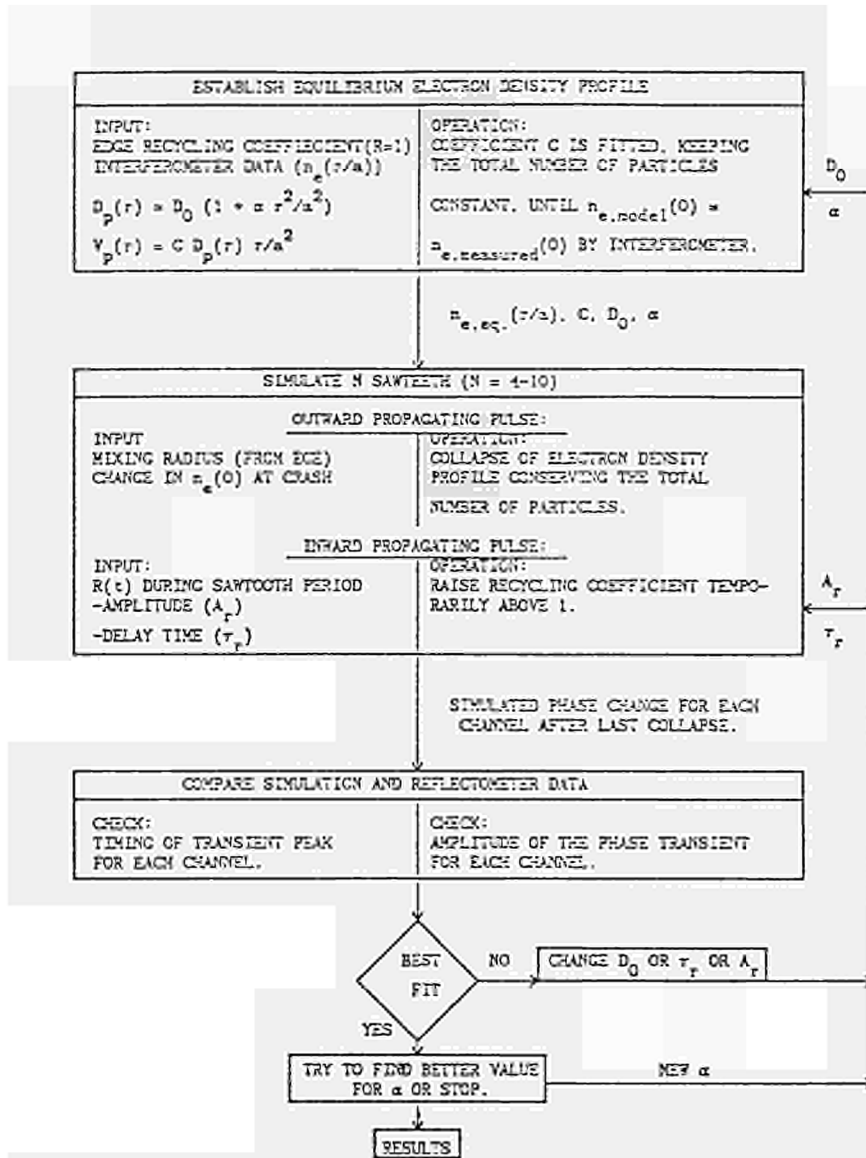
```
┌─────────────────────────────────────────────────────────────────────┐
│              ESTABLISH EQUILIBRIUM ELECTRON DENSITY PROFILE           │
├──────────────────────────────────┬──────────────────────────────────┤
│ INPUT:                           │ OPERATION:                       │
│ EDGE RECYCLING COEFFICIENT(R=1)  │ COEFFICIENT C IS FITTED, KEEPING │
│ INTERFEROMETER DATA (n_e(r/a))   │ THE TOTAL NUMBER OF PARTICLES    │
│                                  │                                  │
│ D_p(r) = D_0 (1 + α r²/a²)       │ CONSTANT, UNTIL n_e,model(0) =   │
│                                  │                                  │
│ V_p(r) = C D_p(r) r/a²           │ n_e,measured(0) BY INTERFEROMETER.│
└──────────────────────────────────┴──────────────────────────────────┘
```

$n_{e,eq.}(r/a)$, C, D_0, α

```
┌─────────────────────────────────────────────────────────────────────┐
│                    SIMULATE N SAWTEETH (N = 4-10)                     │
│                  OUTWARD PROPAGATING PULSE:                           │
├──────────────────────────────────┬──────────────────────────────────┤
│ INPUT                            │ OPERATION:                       │
│ MIXING RADIUS (FROM EDGE)        │ COLLAPSE OF ELECTRON DENSITY     │
│ CHANGE IN n_e(0) AT CRASH        │ PROFILE CONSERVING THE TOTAL     │
│                                  │ NUMBER OF PARTICLES.             │
│          INWARD PROPAGATING PULSE:                                   │
│ INPUT:                           │ OPERATION:                       │
│ R(t) DURING SAWTOOTH PERIOD      │ RAISE RECYCLING COEFFICIENT TEMPO-│
│ -AMPLITUDE (A_r)                 │ RARILY ABOVE 1.                  │
│ -DELAY TIME (τ_r)                │                                  │
└──────────────────────────────────┴──────────────────────────────────┘
```

SIMULATED PHASE CHANGE FOR EACH
CHANNEL AFTER LAST COLLAPSE.

```
┌─────────────────────────────────────────────────────────────────────┐
│              COMPARE SIMULATION AND REFLECTOMETER DATA                │
├──────────────────────────────────┬──────────────────────────────────┤
│ CHECK:                           │ CHECK:                           │
│ TIMING OF TRANSIENT PEAK         │ AMPLITUDE OF THE PHASE TRANSIENT │
│ FOR EACH CHANNEL.                │ FOR EACH CHANNEL.                │
└──────────────────────────────────┴──────────────────────────────────┘
```

BEST FIT — NO → CHANGE D_0 OR $τ_r$ OR A_r

YES

TRY TO FIND BETTER VALUE FOR α OR STOP. — NEW α

RESULTS

Figure 4: Description of numerical model used to simulate the observed density pulses after a sawtooth collapse.
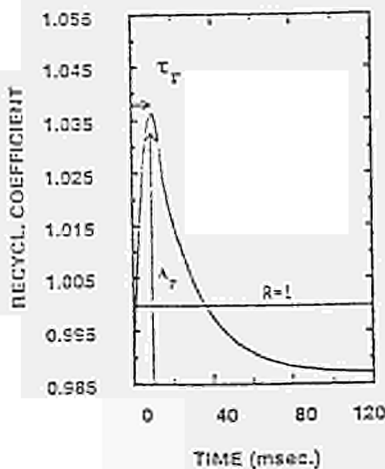
Figure 5: Time dependent recycling coeffient used by the model to simulate the inward propagating density pulse.
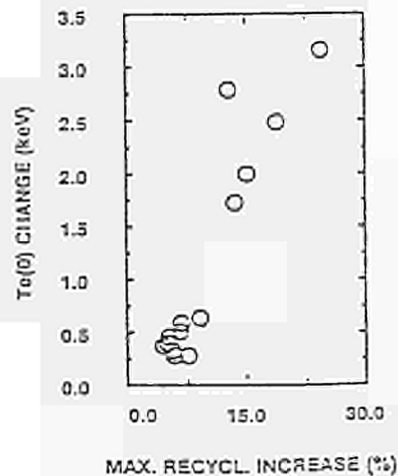
Figures 6: Comparison of simulated maximum increase in the edge recycling (A_r) and the change in central electron temperature at the sawtooth crash.

POLOIDAL ELECTRIC FIELD AND VARIATION OF RADIAL TRANSPORT
DURING ICRF HEATING IN THE JET SCRAPE-OFF LAYER

S Clement*, J A Tagle, M Laux*, S K Erents*, M Bures
P C Stangeby^, J Vince and L de Kock

JET Joint Undertaking, Abingdon, Oxon OX14 3EA, UK
* Zentral Institut für Elektronenphysik, AdW der DDR, 1086 Berlin, DDR
° Association CIEMAT/EURATOM, Madrid, Spain
· Culham Laboratory, Association UKAEA/EURATOM, Abingdon, Oxon, UK
Δ Institute for Aerospace Studies, University of Toronto, Canada

1. INTRODUCTION

The highly anomalous perpendicular transport in the plasma edge of a
tokamak is generally attributed to plasma turbulence, primarily to density
and electrostatic potential fluctuations. The edge transport could be
modified by changing the geometry of objects in contact with the plasma
(limiters, radio frequency antennae ...) and during additional heating
experiments. Poloidal asymmetries in the scrape-off layer (SOL) in
tokamaks using poloidal limiters (eg. ALCATOR-C) have been recently
reported [1], indicating a poloidal asymmetry in cross-field transport. A
poloidal ring limiter obstructs communications between different flux tubes
in the SOL, thus permitting poloidal asymmetries in n_e and T_e to develop if
$D_\perp$ is θ-dependent. When JET was operated with discrete limiters,
equivalent to a single toroidal limiter at the outside mid-plane, little
poloidal variation in the SOL plasma properties was observed [2].
Currently JET is operated with two complete toroidal belt limiters located
approximately one meter above and below the outside mid-plane. This
configuration breaks the SOL into two regions: the low field side SOL
(LFS), between the limiters, and the rest of the SOL on the high field side
(HFS). Differences on the scrape-off lengths in the two SOLs are reported
here, indicating that cross-field transport is faster in the LFS-SOL, in
agreement with observations made on ASDEX [3] and T-10 [4]. The
cross-field transport will also be influenced by the presence of a poloidal
electric field (E_θ) in the SOL plasmas, through $E\times B/B_T^2$ drifts. As a
consequence of the field, the ions, accelerated by the field, will strike the surfaces of
the limiters, wall and antennae and enhance the neutral and impurity
influxes. These effects have been observed during ICRF heating in several
tokamaks [5]. If E_θ varies poloidally then this would also result in
poloidal variation in transport. E_θ was measured in the JET SOL using a
triple Langmuir probe during ICRF heating. Strong radial drifts are
deduced at the (single) observation point employed, which may also
contribute to enhanced sputtering.

2. DENSITY SOL LENGTHS IN JET BELT LIMITER CONFIGURATION

In the discrete limiter configuration each flux tube traces out at
least one complete poloidal transit, and any poloidal variation in $D_\perp$ would
not be expected to manifest itself as a variation in plasma properties, due
to the rapid transport along B. In contrast, in the belt limiter
configuration, any poloidal variation in $D_\perp$ would be expected to manifest
itself as different SOL lengths in the SOLs (LFS and HFS). Figure 1 shows
a density profile measured with two fixed Langmuir probes on one of the
ICRF antenna protection tile located in the LFS-SOL, and the density
profile measured with a reciprocating probe (RCP) at the top of the vessel
in the HFS. Also presented is the correction of the density profile from
the RCP after the compression of field lines (∼ 2.5) has been taken into
account. Figure 2 shows the SOL length (λ_n) for discharges with $I_p = 3$ MA,
$B_T = 3.4$ T and additional ICRF heating up to 17 MW. It can be seen that
$\lambda_n^{LFS} > \lambda_n^{HFS}$ independently of the power applied. Although the connection
length in the LFS-SOL is shorter than for the HFS-SOL, when the toroidal
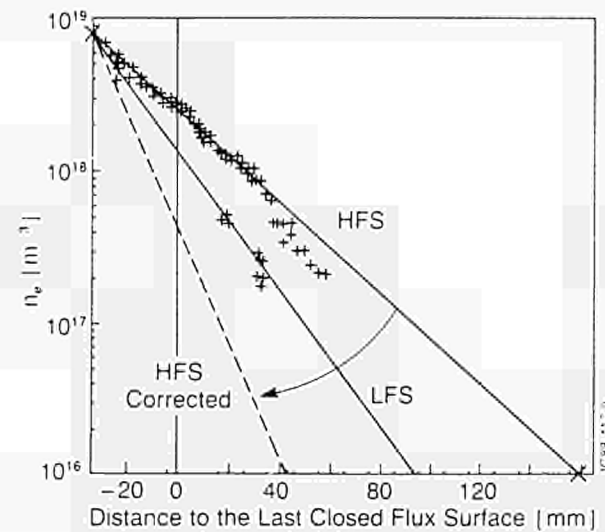plasma geometry is taken into account, then one expects $\lambda_n^{LFS} = \lambda_n^{HFS}$.

provided $D_\perp$ does not vary poloidally. Since the results show that, in
fact, $\lambda_n^{LFS} > \lambda_n^{HFS}$, it is concluded that $D_\perp^{LFS} > D_\perp^{HFS}$. No strong variation
with ICRF power was found except a slight flattening of profiles at high
current and high power. The ion saturation current values (I_{sat}) at the
Last Closed Flux Surface, LCFS, measured from RCP and antenna probes are
shown in figure 3. Since the LCFS cannot be precisely determined at the
RCP location, the difference of a factor of two in the I_{sat} values is
within experimental uncertainty. It is also found that edge temperatures
are lower (LFS-SOL) for the belt limiter configuration than for the
discrete limiters. Inference of average values of $D_\perp$ for the LCFS and HFS
SOLs will be carried out taking into account the difference in the
temperature and the geometries of the two SOLs; present results indicate
that the plasma outflux is higher in the outer midplane.

3. EDGE POLOIDAL ELECTRIC FIELD DURING ICRF HEATING

During a number of discharges with RF in JET the three tips of a
triple probe were allowed to float and very large differences of potential
were measured between the tips during the RF pulse. The probe tips are
located at the same radius, in different poloidal position (30 mm apart)
and in different flux tubes [6]. The potentials between the tips range
from 2V/cm during the ohmic part of the discharges up to around 40 V/cm
during the RF pulse, and are interpreted as an electric field. Two
dependent but not orthogonal components of the field give the strength as
well as the orientation. Figure 4 shows the total electric field during a
5 MW RF heating discharge ($I_p = 3.1$ MA, $B_T = 3.4$ T) in D gas with ^{3}He (33
MHz) as a minority heating gas. The field is oriented downwards (angle ∼
-60°) with respect to the plasma current. The voltage signals were
measured at a low sampling rate (< 10 kHz) and without filtering.
Rectifying effects on the probe during RF were found to be negligible
in previous experiments at low RF powers (≤ 4 MW) [7]. Measurements were
made with the probe located 10 mm behind the RF antenna protection tiles
and 15 mm behind the LCFS. Owing to the change of plasma conditions in
consecutive discharges, where the probe was moved radially, we could not
measure any radial dependence of these potentials. However, for a fixed
radial position, the variation of the electric field with RF power and
different gas minority heating has been studied. Figure 5 shows
the electric field for a 3.1 MA, 3.4 T discharge in D with H minority (44
MHz). It is worth noting that the electric field is much lower in high
power discharges H than for ^{3}He minority heating. The antenna
configuration was dipole in both cases and the field dependence with total
RF power and minority gas is shown in figure 6. The small field found
during H minority heating is consistent with the more efficient wave
damping when compared with the ^{3}He minority case. It agrees with the
measurements of the oscillating magnetic fields in the plasma edge in JET
[8]. The electric field was found to exist during ICRF, independently on
whether the antenna closest to the probes was powered or not, implying a
significant toroidal extent of the field. This field causes a radial drift
of $E_\theta/B_\phi = 1500/3.4 = 400$ m/s which is comparable to the diffusive velocity
$D_\perp/\lambda_n = 2.5/0.015 = 170$ m/s. Such drifts could therefore change the SOL
particle balance locally, and strong local outflows may occur, implying
enhanced ion sputtering and impurity production during ICRH.

REFERENCES

[1] B La Bombard and D Lipschultz, Nuclear Fusion 27 (1987) 81-89.
[2] P C Stangeby, J A Tagle, S K Erents and C Lowry, Plasma Physics and
    Controlled Fusion, to be published.
[3] M Keilhacker and B Doybelge, Nuclear Fusion 21 (1981) 1497.
[4] V A Vershkov et al, J Nuclear Material 145-147 (1987) 611.
[5] R J Taylor et al, 9th IAEA Conference, Baltimore, Plasma Physics and
    Controlled Fusion (1982), Vol III, 251-256.
[6] M Laux and J A Tagle (to be published).
[7] S K Erents et al, J Nucl Mater 145-147 (1987) 231.
[8] M Bures et al, Bull American Physics Soc 33 No 10 (1988).

Fig 1: Density profile in the SOL
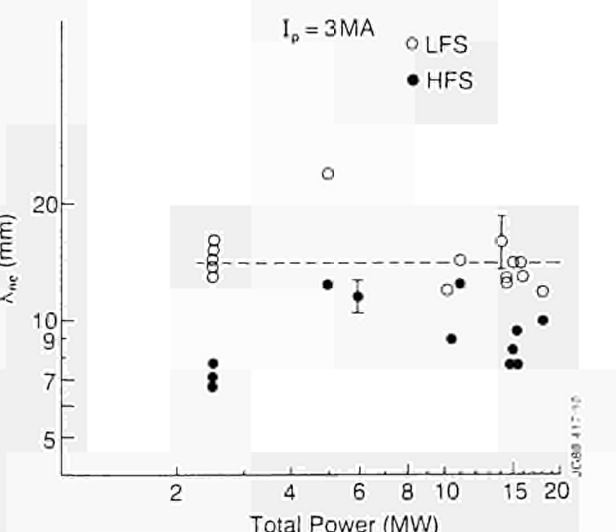at the HFS and the LFS.

Fig 2: Density scrape-off SOL
length vs total applied power
for 3 MA discharges.
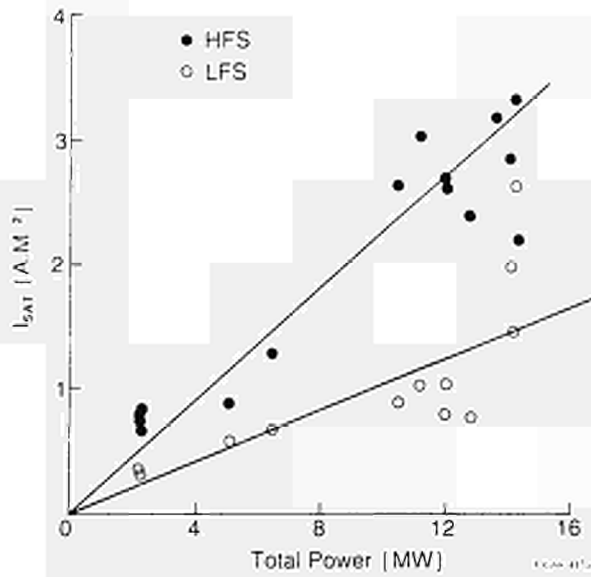
Fig 3:   Ion saturation current
         at the LCFS vs total applied
         power in LFS and HFS.
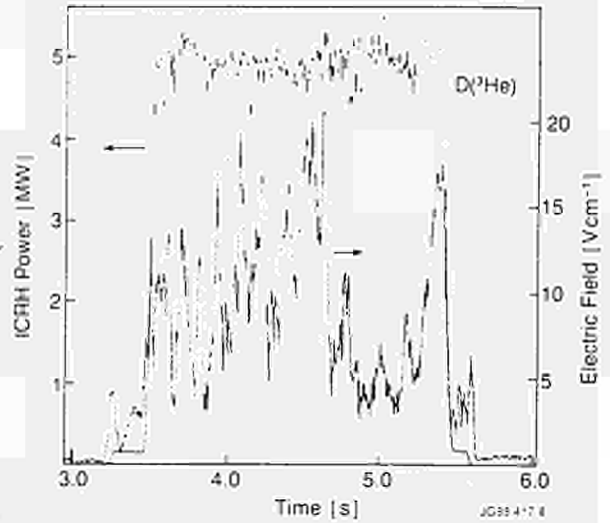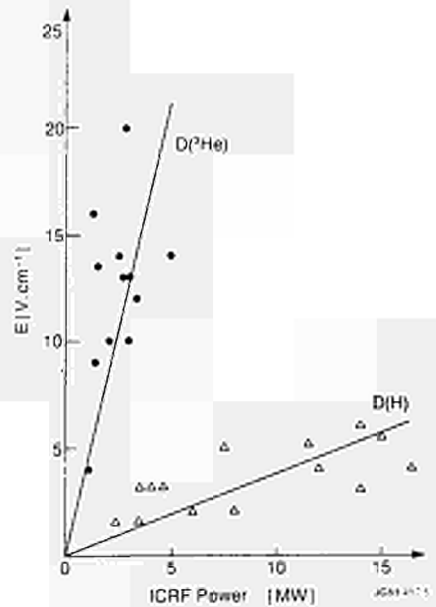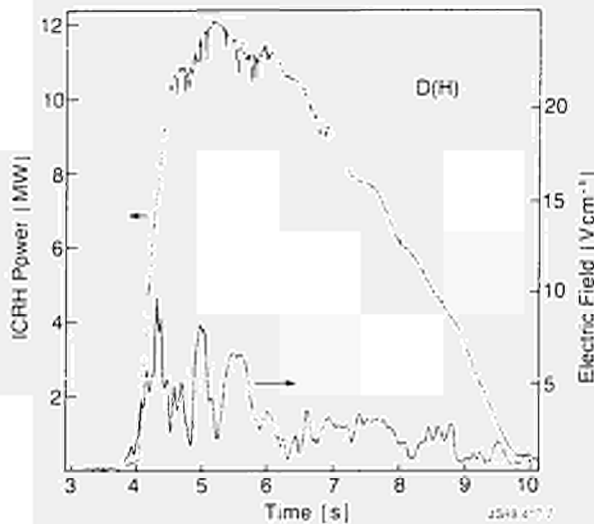

Fig 4:   Electric field
         measured during ICRF
         heating, with ³He as
         minority gas.

Fig 5:   Same as Fig 4, but with H
         as minority gas.

Fig 6:   Strength of the
         electric field vs ICRF
         power for ³He and H
         minority gases.

Q-PROFILES IN JET

R D Gill, A W Edwards, B Keegan, E Lazzaro, J O'Rourke,
A Weller and D Zasche

JET Joint Undertaking, Abingdon, Oxon., OX14 3EA, UK

1.   INTRODUCTION Tokamak q-profiles play a central role in the determination of plasma stability and $q(r)$ towards the plasma centre is particularly important for the sawtooth instability. On JET, $q(r)$ has been determined from magnetic measurements and Faraday rotation. Further information about the position of the q=1 surface has been found from the sawtooth inversion radius, the position of the snake and the resonance effect observed on visible light and X-ray emission during pellet injection. In addition the shear at the q=1 surface has been measured from pellet ablation [1]. This result is supported by the movement of the snake caused by a sawtooth crash. A summary of these data will be made after presenting the new results from pellet ablation.

2.   PELLET ABLATION EFFECTS During the injection of solid D_2 pellets into JET a large drop in the soft X-ray and visible light emission has been observed as the pellet crosses the q=1 surface (fig.1). The minor radius (r_1) of the minimum of the emission has been found to be very well correlated with the sawtooth inversion radius (r_{1X}) determined from tomographically reconstructed soft X-ray camera data. The position of the q=1 surface within a sawtooth cycle has been established in a plot (fig.2)
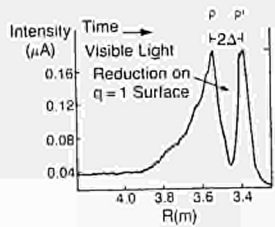
Fig.1 Visible light emission during pellet ablation.
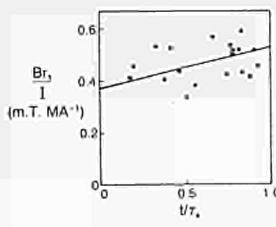
Fig.2 Correlation plot for q=1 surface.

of normalised radius (r_1 B/I) versus normalised time t/τ_s with τ_s the sawtooth period. The normalised radius is used as it has been previously observed that $r_{INV} \propto I/B$. Despite considerable scatter, the data is consistent with a previous observation [2] on the movement of the snake oscillation which showed that r_1 moved outwards during the sawtooth cycle by ~30%. r_{1X} corresponds to the value of r_1 at the start of the sawtooth cycle.

3.   DETERMINATION OF dq/dr The physics of pellet ablation is well understood: the plasma electrons move along their magnetic field lines and lose energy in the ablation cloud which surrounds the pellet (of radius r_p) and protects it from direct heating (fig.3). The ablated
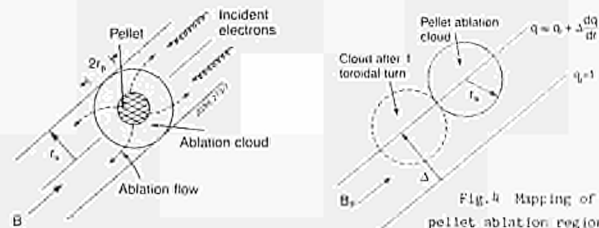

Fig.3 Pellet ablation processes.

Fig.4 Mapping of pellet ablation region after 1 toroidal transit.

material expands radially up to a critical radius [3] ($r_a \approx 3.5 r_p$ for JET) and then flows along the field lines. The relative velocities are such that the plasma electrons can make many (~10) toroidal transits of the torus while the pellet ablation cloud crosses a flux surface. On a non-rational q-surface electrons from many parts of the flux surface can interact with the pellet. However, for integer q, the flux tube closes on itself thereby reducing the reservoir of available electrons. The cold ablated electrons cool the plasma slowly compared with the time for the cloud to cross the magnetic surface and q is not expected to be modified on this timescale. On integer q-surfaces the effects of shear must also be considered and it can be shown that in order to have an appreciable reduction in ablation rate $dq/dr < q/\pi r$, ie., the shear must be small. If $q=q_0(1+\alpha r^2)$ the condition becomes $(q-q_0)/q<1/\pi s$ and this condition is only likely to be satisfied on the q=1 surface. This provides an explanation for the lack of observation of a dip in ablation rate on surfaces other than q=1. It can also be shown that large effects would not be expected on rational non-integer surfaces either.

Values of dq/dr on the q=1 surface may be found by considering the degree of overlap of the pellet ablation cloud with electrons which have made one toroidal transit of the machine (fig.4). Some overlap will occur, corresponding to points P and P' of fig.1 when

$$\frac{dq}{dr} = \frac{r_{a1}}{\pi r \Delta}$$

where $2\Delta = PP'$ and r_{a1} is the radius of the pellet cloud when it reaches q=1 and is determined from pellet ablation rate calculations and a knowledge of the plasma density and temperature profiles. Putting typical values into the equation above gives $dq/dr \approx 5 \times 10^{-2}$ m^{-1} and for a parabolic profile (s=2) $(1-q_0) \approx 10^{-2}$ showing a q_0 extremely close to one. Similar calculations for a number of different shots (fig.5) show some scatter but suggest that dq/dr does not change appreciably throughout the sawtooth cycle.
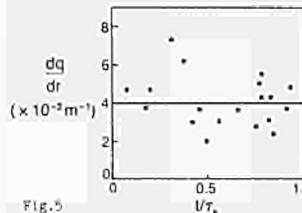

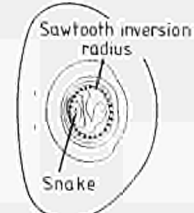Fig.5   Fig.6
dq/dr deduced from pellet ablation. Tomographically reconstructed snake.

4.   THE SNAKE The snake is also clearly associated with the q=1 surface and makes an inward step in minor radius of ~30% coincident with a sawtooth crash. During the slow ramp phase of the sawtooth the change in central q caused by diffusion can only be about $\Delta q \approx 0.02$ and therefore to provide the required shift of the snake the q-profile must be very flat. For a parabolic profile, a central q-value very close to 1 results ($q_0 \approx 0.97$).

Detailed tomographic analysis of the snake shows that although it is clearly associated with the q=1 surface it lies to the inside of the sawtooth inversion radius determined just before pellet injection (fig.6).

5.   FARADAY ROTATION Direct measurements of $q(r)$ have been made on JET using a 6 channel far-infrared polarimeter [4] which determines line integrals of $(n_e B_\parallel)$. Inversion of the experimental data requires knowledge of the flux surface shapes and these are calculated from an equilibrium code which uses data from magnetic measurements at the plasma periphery; this information is supplemented in the central regions by the soft X-ray tomographically determined iso-emissivity surfaces and sawtooth inversion surfaces. For ohmic discharges the q-profiles determined have central q values of $q_0 \approx 0.7$-0.9 and these are significantly below 1 even when the known errors of ~15% are taken into account. The measurements also determine the position of the q=1 surface in good agreement with the sawtooth inversion radius (fig.7).
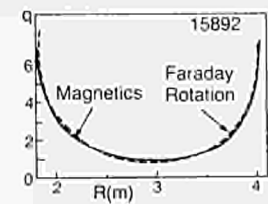

Fig.7 Position of q=1 from FR.

Fig.8 q(r) from magnetics and FR.

6.   MAGNETICS RECONSTRUCTIONS Information provided by a variety of measurements can be used to define a sequence of nested reconstructions of the pressure profile and $q(r)$ which satisfy the equilibrium equation $R^2 \nabla \cdot (R^{-2} \nabla \psi) = -\mu_0 R_0 J(\psi, p)$ with ψ the magnetic flux function [5]. In the simplest approach only the external magnetic fields are used and the solutions are insensitive to the central value of q. Further restriction of the problem by the imposition of integral constraints improves the determination of internal characteristics. For example, a self consistent analysis of the polarimeter measurements can be made by requiring that the solution of the GS equation also gives the best fit to the measured values of the Faraday rotation (FR) angles. The analysis gives q(r) with an accuracy varying from 3% at the edge to 20% at the centre. Generally the analysis done independently of the FR data shows q(r) dropping below 1 at the onset of sawteeth and good overall agreement on the shape of q(r) (fig.8). Adding the FR data gives lower values of q_0.

7.   DISCUSSION Overall q(r) in JET is well determined, but on the critical issue of the value of q_0 the information falls into two categories: the data obtained by indirect means from the snake, pellet ablation etc., points to q_0 very close to 1; whereas the more direct determinations from magnetics and FR give values significantly below 1 even if the errors (15-20%) are taken into consideration. Compatibility between these data can be obtained if it is assumed that q(r) has a rather complicated behaviour with a local flattening at q=1 and a more rapid drop towards the plasma centre. This profile shape would have many implications for theories of the sawtooth instability mechanism.

We would like to thank J Peters for his computational assistance.

REFERENCES
[1] R D Gill et al., JET P(88)59
[2] A Weller et al., Phys.Rev.Lett. 59(1987)2303
[3] P B Parks, Nucl.Fus. 20(1980)311
[4] J O'Rourke et al., Contr.Fus. & Plas.Heat. (Dubrovnik) 12B(1988)155
[5] E Lazzaro and P Mantica, Plas.Phys. & Contr.Fus. 30(1988)1735

NON-THERMAL DT YIELD WITH (D)T ICRH HEATING IN JET

G.A.Cottrell, V.P.Bhatnagar, M.Bures, L.G.Eriksson[+], T.Hellsten,
J.Jacquinot and D.F.H.Start.
JET Joint Undertaking, Abingdon, Oxon., OX14 3EA, United Kingdom.
[+]Chalmers University, Sweden.

Abstract. We present projections of the (D)T fusion yield expected during fundamental ICRH heating of D in JET plasmas. To obtain high Q, one needs to use a relatively high plasma density ($n_{e_0} > 5 \times 10^{19}$ m^{-3}) and dipole antenna ($k_\parallel \approx 7 m^{-1}$) to reduce mode conversion. For high minority concentration ($n_D/n_e \approx 10\%-30\%$), we have used ray-tracing and global wave ICRH codes to estimate cyclotron damping on deuterium ($\approx 80\%$) and the rf power coupled directly to electrons ($\approx 17\%$) via TTMP and Landau damping. With launched rf power $P_{rf}=12$MW deposited ≈ 0.3m off-axis, we predict fusion powers P_{fus} up to ≈ 8MW for a range of JET plasmas with achieved plasma pressure $n_{e_0}T_{e_0} = 6 \times 10^{20}$keV m^{-3} and $Z_{eff}=2$. Projecting to $P_c=20$MW, P_{fus} increases to 17MW with $Z_{eff}=2$.

Introduction. In a two-ion component plasma, the fast wave can be damped on a minority ion species at its fundamental cyclotron resonance causing the minority ion distribution function to develop a non-Maxwellian velocity distribution with a high energy tail. The tail will also enhance the fusion reaction rate with the background ion species [1]. Earlier JET experiments [2,3] in the ($^3He)D$ minority scheme have produced <1MJ of fast ^3He ions in the plasma (with particle energies up to a few MeV) and a ^3He-D reaction rate R<2$\times 10^{16}$ s^{-1} ($\approx$ 60kW of fusion power). Measured fast ion energy content and fusion reactivity in these experiments have been modelled in detail [3,4] using Fokker-Planck and global wave codes. Good agreement between experiment and theory was found, consistent with i) classical slowing down of fast ions and ii) correct prediction of the cyclotron damping on the ^3He. The possibility of using the deuterium cyclotron resonance (D)T scheme has been considered [5] for the JET active phase. This paper discusses its optimisation.

Modelling. We have used experimental data to predict the (D)T performance. Measured temperature and density profiles for three types of ICRH heated discharge [6] were studied and used as the basis for predictions. These were: a) 3MA peaked profile (pellet) cases [7,8], b) 5MA current-rise heating cases [9] and c) 3MA 'monster' sawtooth cases. For the pellet cases the plasma profiles, taken from laser scattering (LIDAR) data, were peaked and were parameterised by: $y(x)= y_0+(y_0-y_a).(1-x^2)^\gamma$ where $x=r/a$. For electron temperature profiles $y_a/y_0 =0.1$ and $\gamma=2$ and for electron density profiles $y_a/y_0 =0.2$ and $\gamma=4$. To obtain high projected Q values, it was found necessary to use higher ($n_D/n_e \approx 10\%-30\%$) minority concentrations than have been used in previous JET experiments. In the absence of experimental data in these conditions, we have estimated wave damping in simulated (D)T plasmas using both global wave and ray-tracing codes. The result of a ray-tracing calculation [10] for the full $k_\parallel$ spectrum of the toroidal dipole antenna is shown in Fig.1. Of the launched rf power, 80% was damped in a single pass on the D minority, 17% was deposited on the electrons via TTMP and Landau damping and 3% was unabsorbed.
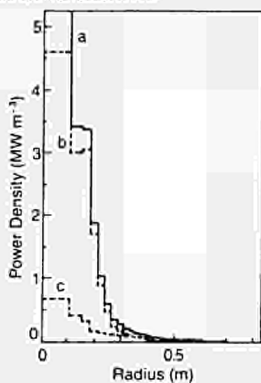

Figure 1 Calculated ICRH deposition profiles of: a) total, b) deuterium and c) electron power densities for the case of central heating (f=25MHz, $B_\varphi(0)=3.55T$) in simulated (D)T plasma based on experimental conditions of peaked-profile (pellet) discharge (case a, see text) but with assumed values $n_D/n_e = 30\%$ and $P_c=20$MW.

To estimate the fusion yield we used a gaussian radial power deposition profile and the Stix solution ($k_\perp=0$) for the tail [3]. Inclusion of finite ion Larmor radius effects and, in particular, the E_- component of the rf electric field in the Fokker-Planck calculations results in a more energetic tail which tends to reduce the fusion yield compared with the Stix model. For high D minority concentration (n_D/n_e <30%), $|E_-|/|E_+| \approx 12$, and the reduction is typically 20%. The Stix model was applied (Fig.2) to data for case a) assuming, for simplicity, $T_i=T_e$ and $Z_{eff}=1$. To project the model to higher rf power heating cases it was necessary to predict the plasma temperatures expected for the new conditions. In doing this (Fig.4), we have extrapolated measured empirical temperature scaling laws based on existing JET results. Each of the datasets for cases a)-c) could be well described by the offset-linear relation: $T_{j_0}(keV) = \alpha_j+\beta_j [P_t(MW)/n_{e_0}(10^{19}m^{-3})]$ where j = electrons or ions and P_t the input power. In making these extrapolations, we have assumed no degradation in heating efficiency (i.e the coefficients β_j are independent of power). The coefficients are, for case a) $\alpha_e=0.8$, $\beta_e=4.1$, $\alpha_i=1.1$, $\beta_i=3.6$; case b) $\alpha_e=0.8$, $\beta_e=4.1$, $\alpha_i=1.1$, $\beta_i=2.6$; and case c) $\alpha_e=0.7$, $\beta_e=2.7$, $\alpha_i=2.3$, $\beta_i=1.2$. The higher power cases (Fig.4) show optimal Q values at central densities typically $n_{e_0} \approx 1 \times 10^{20}$m^{-2}.

Figure 2 Stix code results for the ICRH driven DT fusion power with fixed $n_{e_0}T_{e_0}= 6 \times 10^{20}$ keV m^{-3} and coupled rf power $P_c =10$MW. Off-axis ($r_{oa}=0.3m$) rf heating was modelled with gaussian deposition width $r_d =0.2m$.
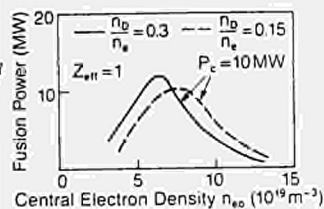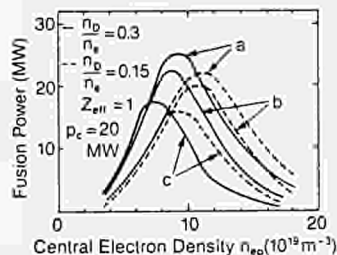

Figure 3 Stix code results for three projected cases; a) peaked profiles (pellet injection), b) current-rise heating and c) 'monster' sawtooth cases. Off-axis ($r_{oa}=0.3m$) rf heating was modelled with gaussian deposition width: $r_d =0.2m$.

Sensitivity analysis and impurity dilution effects. To illustrate the sensitivity of the ICRH-driven fusion yield with resonance location, we examine a test case A with parameters: $n_D/n_e = 0.3$, $P_c=10$MW, $n_{e_0}=6 \times 10^{19}$ m^{-3}, $T_{e_0}=T_{i_0}=10$keV, rf deposition gaussian width $r_d =0.2$m and off-axis heating distance $r_{oa} =0.3$m (corresponding to the distance between the cyclotron resonance and the magnetic axis). Variations with respect to r_{oa} and Z_{eff} are shown in Fig.4. A maximum in the fusion yield occurs at $r_{oa} \approx 0.3$m where the maximum deuterium tail temperature [3] $T_{tail} \approx 140$keV. If the ICRH power is deposited too centrally, the minority ions are driven to energies beyond the maximum in the DT cross-section. Conversely, if the ICRH power is deposited too far off-axis, the tail energy is too low and the tail is generated in a low temperature region of the plasma where the collision time is smaller. We have neglected any variations in the heating efficiency with r_{oa}. In the scan with respect to variations in Z_{eff}, carbon impurities were assumed. In the peaked profile case a), the volume average Z_{eff} falls to ≈ 1 immediately following pellet injection but then rises to approximately 3 1s later; impurities are known to accumulate on the axis after pellet injection. For the current-rise heating case b), $Z_{eff} \approx 2$ and, in the 'monster' sawtooth case c), Z_{eff} values range between 4.0-2.5. Fig.4 shows that the fusion power has degradation factors, f,

Figure 4 Sensitivity analysis (case A) of the variation of a) DT fusion power and minority tail temperature with rf power off-axis displacement and, b) DT fusion power and carbon impurity density with Z_{eff}
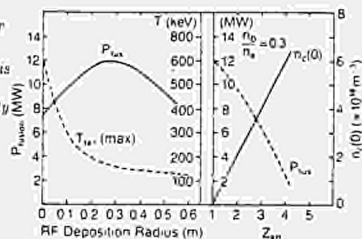
equal to a) 50%, b) 75% and c) 20%-66% respectively of the values calculated for $Z_{eff}=1$. The lower limit corresponds to the upper limit of Z_{eff}. In case b), analysis of the central neutron emissivity (from the neutron profile monitor) and T_i (from neutron spectroscopy and doppler broadening of Ni impurity lines) gave a central concentration ratio $n_D/n_e=90\% \approx 10\%$. If the dilution is identical when $P_c=20$MW, the optimum fusion powers (for $n_D/n_e=30\%$) are: a) $P_{fus} \approx 13$MW ($Q_{rf} \approx 50\%$), b) $P_{fus} \approx 17$MW ($Q_{rf} \approx 67\%$) and c) $P_{fus} \approx (4-12)$MW ($Q_{rf} \approx 14\%-46\%$). Extrapolation of the experimental scaling: $Z_{eff} \alpha 1/n_e$ to the optimum density ($n_{e_0} \approx 1 \times 10^{20}$ m^{-3}) of Fig.3 then gives degradation factors, f, of a) 81%, b) 96% and c) 67%-92% respectively. We note that both the peaked-profile (pellet) and the current-rise cases were not in steady-state conditions. Detailed analyses of these discharge types can be found in references [8] and [9] respectively.

Conclusion. A study of ICRF-driven DT fusion reactivity of projected JET plasmas shows the possibility of reaching Q_{rf} ($\equiv P_{fus}/P_{rf}) \approx 70\%$ provided impurity dilution can be kept to a reasonable level. Particularly encouraging is the DT projection based on the 5MA current-rise heating case (at density $n_{e_0} = 6 \times 10^{19}$m^{-3}) where values $n_{e_0}T_{e_0} = 6 \times 10^{20}$ keV m^{-3} and $Z_{eff} \approx 2.0$ have been obtained simultaneously.

References
[1] Stix, T.H. Nuc.Fusion, 15, 737. (1975)
[2] Cottrell, G.A., et al., Bull.Amer.Phys.Soc. 33, 2032 (1988)
[3] Boyd, D.A., et al. Nuc.Fusion(1989) to be published.
[4] Eriksson, L.G., et al. Nuc.Fusion Lett. (1989) to be published.
[5] JET Team, Plas.Phys. and Contr.Fus. 30, 1467 (1988)
[6] Jacquinot, J., et al. Bull.Amer.Phys.Soc. 33, 2031 (1988)
[7] Bhatnagar, V.P. et al. this conference
[8] Hammett, G. et al. this conference
[9] Bures, M. et al. this conference
[10] Bhatnagar, V.P., et al. Nuc Fusion 24, 955 (1984)

STUDIES OF VISIBLE IMPURITY RADIATION FROM JET PLASMAS DURING HEATING AND FUELLING EXPERIMENTS

P D Morgan, A Boileau[1], M J Forrest[2], M von Hellermann, L Horton[3],
W Mandl, M F Stamp, H P Summers, H Weisen and A Zinoviev[4]

JET Joint Undertaking, Abingdon, Oxon OX14 3EA, UK / [1] Tokamak de Varennes,
Varennes, CANADA / [2] UKAEA Culham Laboratory , Abingdon, Oxon OX14 3DB, UK
/ [3] ORNL ,Oak Ridge, Tennessee 37830, USA / [4] Joffe Inst., Leningrad, USSR

1.   INTRODUCTION

At JET extensive use is made of visible spectroscopy in the study of plasma impurities, [1]. Measurements of absolute line intensities from such species as O II, C III and D I are used to deduce the influxes of light impurities as well as deuterium at the plasma periphery. The absolute continuum emission at 523.5nm, measured using a 15-telescope poloidal array, is used to determine $Z_{eff}(r)$ and its temporal evolution. Charge-exchange recombination spectroscopy (CXRS) has proved to be a powerful technique during NBI to measure, amongst other parameters, the density of C and O at up to 15 separate points on the plasma minor radius.

The combination of these diagnostic techniques permits the global impurity behaviour in the plasma to be followed. In this paper, results are reported pertaining to studies of plasmas heated by NBI and ICRF, and fuelled by the injection of D_2 pellets.

2.   APPARATUS AND ANALYSIS

The apparatus is described in detail elsewhere, [2,3,4]. Using a spectrometer equipped with an OMA, line emissions at the plasma edge from the light impurity and fuel species are measured absolutely. For a given atom or ion the measured intensity I can be used to deduce the influx Γ of that species, since $\Gamma = 4\pi IS/XB$,where S is the ionisation rate, X is the excitation rate and B is the branching ratio, [2].

Each channel in the poloidal array measures the line integral of the continuum emissivity, or the brightness, along a chord through the plasma. Using the technique of Abel inversion the brightnesses are transformed into the radial profile of emissivity, $\epsilon(r)$. Knowledge of $n_e(r)$ and $T_e(r)$ permits the radial profile of Z_{eff} to be determined, [3], since $\epsilon(r) \propto Z_{eff}(r).n_e^2(r).g_{ff}(r)/T_e^{1/2}(r)$ - g_{ff} being the free-free Gaunt factor.

The CX spectra are recorded using 3 spectrometers equipped with OMAs. The path through the plasma of the octant 8 neutral beam is observed using a fan of 15 sight-lines. These are almost horizontal and intersect the beam at various radial positions, [4]. The intensities of the C^{5+} and O^{7+} lines recorded are proportional to the neutral beam density and to the density of the appropriate fully-stripped ion, permitting the densities of these impurities to be derived. A novel diagnostic method is being developed at JET, based on the analysis of Balmer-Alpha light emitted by fast injected D atoms colliding with deuterons and fully-stripped impurity ions, [5]. Local values of Z_{eff} can be derived from the measured intensity ratio of the spectrum representing the 80 keV neutrals and that of the thermal CX D_α feature. The latter directly gives the deuteron density.

3.   RESULTS AND DISCUSSION

(a)   H-Mode Discharges   In the case of discharges limited by a single-null magnetic separatrix, following NBI and the establishment of an H mode, throughout its life there is a steady increase in $\bar{Z}_{eff}$. In Fig 1, a selection of radial profiles of Z_{eff} are shown at various times during the X-point and H-mode phases of a discharge. The maximum value of $Z_{eff}(r)$ does not occur on axis, rather it is situated at R $\approx$ 3.6 m (r $\approx$ a/2) which is approximately the location of the q=1 surface. As time evolves the profile becomes more hollow and $\bar{Z}_{eff}$ increases from ~ 2.2 at 8.9s to ~ 3.1 at 14.3s. At 15s, following an H to L transition, the profile of $Z_{eff}(r)$ is no longer hollow but has a rather flat form.

From a spectroscopic survey it is seen that the dominant impurity is C with O being the next most important. The metallic impurities make a negligible contribution to Z_{eff}. Fig 2 shows a time sequence of C radial density profiles, derived from CXRS. The carbon density increases throughout the H mode and exhibits a rather flat radial dependence, with a tendency to peak at around 3.7m. Following the H to L transition, the $n_c(r)$ profile is rearranged to give a steady decrease in C density from the centre to the edge, with a substantial reduction in total carbon content.

The increase in the fuel and impurity densities during the life of the

---

H mode can be understood in terms of an improved particle confinement - by a factor ranging from 3 to 5, [3]. This is confirmed by measurements of the C influx at the plasma periphery. At the onset of the H mode the influx deduced from the intensity of C III drops by a factor of 2. Thereafter, the influx increases by ~ 30 % during the life of the H mode, in which time $\bar{n}_e$ has increased by over a factor of 3. At the end of the H-mode phase, on transition to the L mode there is an abrupt increase in the C influx by more than 100 % - as the barrier to good particle and thermal transport suddenly collapses and $\bar{n}_e$ and n_c drop by almost a factor of 2.

(b)   Discharges Fuelled By Pellet Injection   Pellet injection has a dramatic effect on the temporal evolution of $Z_{eff}(r)$. Where substantial density is deposited on axis , values of $Z_{eff}(0)$ close to 1 can be transiently achieved, through dilution of the core impurities by D ions from the pellet. However, on a time scale of 2 to 3s, which is several particle containment times, recycling establishes a higher $\bar{Z}_{eff}$, consistent with edge fuelling.

On the application of additional heating to plasmas with highly-peaked electron density profiles, impurity accumulation has been observed in the plasma centre. Because of the higher charge of the impurity ions, their density profiles are more strongly peaked on axis than that of the plasma deuterons. In Fig 3 a time sequence of $Z_{eff}(r)$ profiles is presented for a discharge into which a 4 mm D_2 pellet was injected at 3s, during the current-ramp phase. Subsequently, a combination of ICRF and NBI was applied beginning at 3.25 and 3.65s, respectively.

Prior to pellet injection the profile of $Z_{eff}(r)$ is almost flat, exhibiting a slight drop towards the plasma edge. The average value $\bar{Z}_{eff}$ is $\approx$ 2.4. The whole profile has been substantially depressed 0.1s after injection, with $Z_{eff}(0) \leq 1.4$ and $\bar{Z}_{eff} \approx 1.6$. The profile is hollow on axis, with $Z_{eff}(r)$ rising towards the plasma edge. At 3.9s, following the application of ICRF and NBI, the profile has changed dramatically to exhibit a plateau extending from ~ 3.6m to the plasma edge and a peak rising to a maximum at the plasma centre. At this time $\bar{Z}_{eff}$ has risen to ~ 2.4. Finally at 4.2s, shortly before the peaked density profile flattens due to a sawtooth crash, the profile of $Z_{eff}(r)$ is even more pronounced in its division into a central peak and an outer plateau. The average value $\bar{Z}_{eff}$ has risen to ~ 2.7 with $Z_{eff}(0)/Z_{eff}(a/2) \approx 2$.

In Fig 4 the radial C density profiles measured by CXRS are presented. At 3.7s, shortly after the application of NBI, the C density is ~ 1.2×10^{18} m^{-3} on axis, and roughly half this value for r $\gtrsim$ a/2. As time progresses, the density both on axis and over the outer half of the minor radius increases steadily, until at ~ 4.2s $n_c(0)$ is about 2.2×10^{18} m^{-3} with an edge density around half this value. The general form of the $n_c(r)$ profiles is in good agreement with that of the $Z_{eff}(r)$ profiles, showing a relatively-narrow peaked central density and a pedestal for r $\gtrsim$ a/2. However, at 4.8s, after the sawtooth crash the profile of $n_c(r)$ is essentially flat, the carbon density having redistributed itself.

4.   SUMMARY

The global impurity behaviour in JET has been studied using visible spectroscopy. From absolute measurements of line and continuum emission, repectively, the influxes of light impurities at the plasma edge and the profile of $Z_{eff}(r)$ have been derived. Also, CXRS permits the radial density profiles of C and O to be measured during NBI.

In the case of X-point plasmas, at the onset of an H mode following NBI, the influxes of the hydrogenic and light impurity species are seen to decrease sharply, corresponding to an improved particle confinement. Throughout the life of the H mode, $\bar{Z}_{eff}$ increases steadily. The $Z_{eff}(r)$ profile becomes hollow on axis and peaks at around half the minor radius. CXRS measurements show a steady increase in the C density during the H mode with the profile tending to peak at r $\approx$ a/2.

The injection of a D_2 pellet into the plasma produces a highly-peaked profile of $n_e(r)$ and an abrupt reduction of $Z_{eff}(0)$, provided deep penetration is achieved. On the application of NBI and ICRF, from CXRS the density of C is seen to increase substantially on axis and to exhibit significant peaking. This indication of an accumulation of light impurities at the plasma centre is supported by the peaked profile of $Z_{eff}(r)$, with $Z_{eff}(0)/Z_{eff}(a/2) \approx 2$.

5.   REFERENCES

[1] K H Behringer et al., Proc. 13th Symposium on Phys. Ionised Gases,
     Sibenik, p.241, (1987).
[2] M F Stamp et al., this conference, (1989).
[3] P D Morgan and J J O'Rourke, Proc. 14th Europ. Conf. on Controlled
     Fusion and Plasma Physics, 11D, (pt.3), p.1240, (1987).
[4] M von Hellermann et al., this conference, (1989).
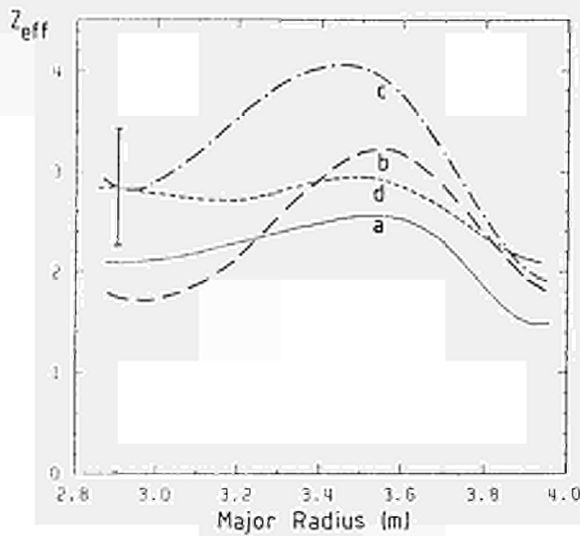[5] A Boileau et al., Research Note, J. Phys. B, to be published, (1989).

FIG.1: $Z_{eff}(r)$ profiles for pulse #18663. (a) t=8.9s, during X-point phase. (b) t=12.3s, (c) t=14.3s; during H-mode phase. H mode starts at 11.6s. (d) t=15s, 0.6s after H to L transition. P_{NBI}=7.5 MW.
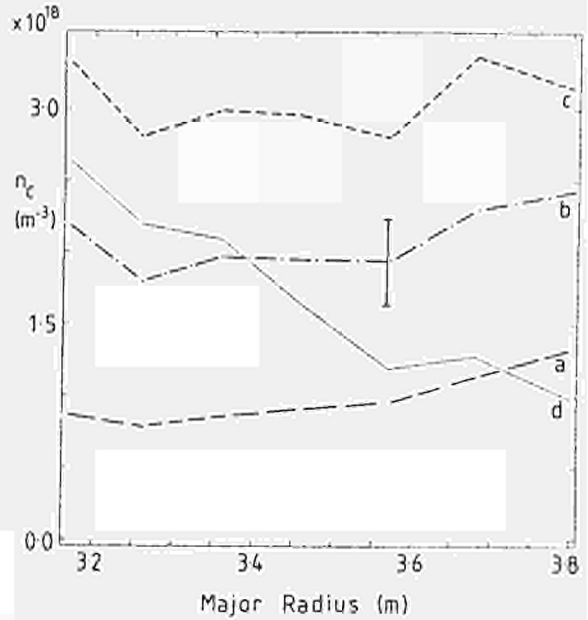

FIG.2: Radial profiles of carbon density for pulse #18663. (a) t= 12.3s, (b) t=13.2s, (c) t=14.1s; during H-mode phase. (d) t=14.8s, 0.4s after H to L transition. I_p=3.1 MA.
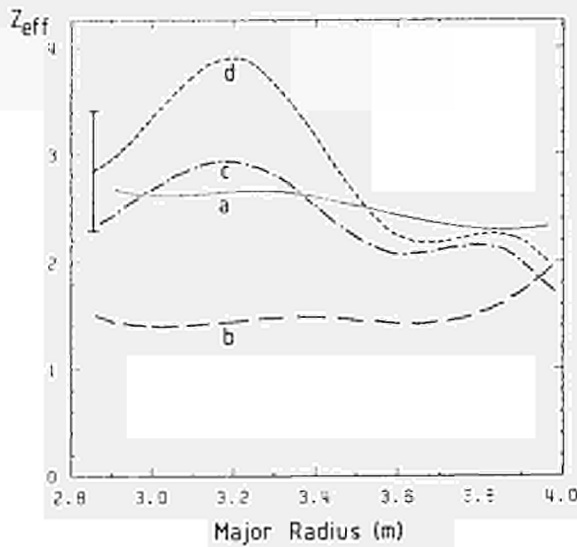
FIG.3: $Z_{eff}(r)$ profiles for pulse #17279. (a) t=2.8s, OH phase. (b) t=3.1s, 0.1s after pellet injected. (c) t=3.9s, (d) t=4.2s; during NBI and ICRH. P_{NBI}=2.8 MW. P_{ICRH}=7.3 MW.
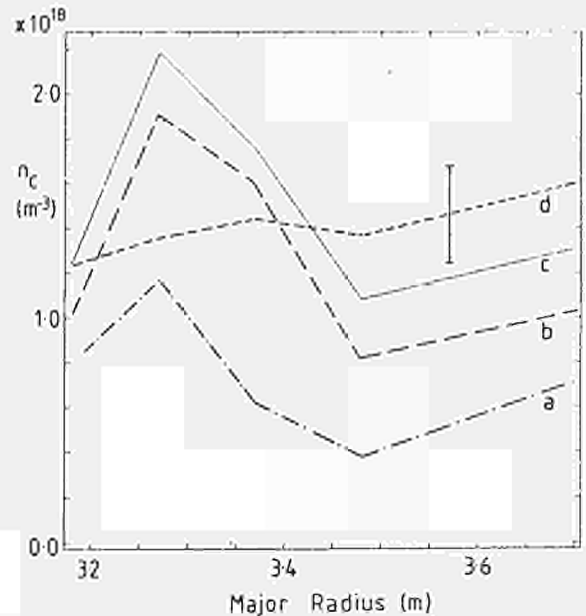
FIG.4: Radial profiles of carbon density for pulse #17279. (a) t= 3.7s, (b) t=3.9s, (c) t=4.2s; during NBI and ICRH. (d) t=4.8s, 0.4s after collapse of peaked $n_e(r)$ profile. I_p=3.1 MA.

AN ANALYSIS OF PLASMA ION TOROIDAL ROTATION DURING
LARGE AMPLITUDE MHD ACTIVITY IN JET

J A Snipes, H Weisen[1], H P L de Esch, R Galvao[2],
T C Hender[3], E Lazzaro, D Stork,
M von Hellermann, D Zasche[4]

JET Joint Undertaking, Abingdon, Oxon, OX14 3EA, UK
[1] CRPP/EPFL, 21, Av. des Bains, CH-1007 Lausanne, Switzerland
[2] Instituto de Pesquisas Espaciais and the Universidade de Sao Paulo, Brazil
[3] UKAEA, Culham Laboratory, Abingdon, Oxon OX14 3DB, UK
[4] Max-Planck-Institut fur Plasmaphysik, D-8046 Garching, FRG

Introduction A detailed study of plasma ion toroidal rotation in JET during large amplitude MHD activity has revealed a strong viscous force that couples plasma ions to MHD modes. Depending on the MHD modes present, this force can couple across all of the plasma cross section, across only the central region, roughly within the q=1 surface, or across only the outer region outside the q=1.5 surface. The force acts to flatten the ion toroidal rotation frequency profile, measured by the JET active charge exchange spectroscopy diagnostic [1], across the coupled region of plasma. The frequency of rotation in this region agrees with the MHD oscillation frequency measured by magnetic pick-up coils at the wall. The strength of the force between the ions and modes becomes evident during high power NBI when the mode locks [2] and drags the ion toroidal rotation frequency to zero, within the errors of the measurements. The present theories of plasma rotation either ignore MHD effects entirely [3], consider only moderate n toroidal field ripple [4], or low n ripple effects [5].

Sawtooth Related MHD Modes As observed previously on JET [6] and on ISX-B [7], the measured MHD frequency of m=1, n=1 modes agrees well with the central plasma ion toroidal rotation frequency. Sawtooth precursor and postcursor oscillations driven by m=1, n=1 modes at the q=1 surface are toroidally coupled to n=1 modes near the plasma boundary with higher m numbers also with n=1. These coupled modes maintain the same oscillation frequency as the m=1, n=1 mode, but have $m/n \approx q_\psi(a)$. That is, modes at the plasma edge take on the rotation frequency of the driving mode from the q=1 surface. Thus, even for very peaked ion toroidal rotation profiles, the measured MHD oscillation frequency at the edge agrees with the plasma ion rotation frequency measured in the center during NBI.

Figure 1a shows an example of a reasonably peaked ion toroidal rotation frequency profile during sawtooth related MHD activity. Note that, during sawtoothing, the ion rotation profile is always flat across the central region, which is roughly the extent of the q=1 radius. In the top traces, the central ion rotation frequency closely follows the peaks of the MHD oscillation frequency. The measurement of the MHD frequency is made by a zero crossing frequency to voltage converter with an n=1 combination of poloidal field pick-up coils as input. The rapid collapses in the MHD frequency are partly real changes in the oscillation frequency (that are to rapid to be observed by the charge exchange diagnostic due to its 50 msec integration time and 50 msec dead time) and partly due to the MHD signal dropping below the threshold of the frequency to voltage converter.

Persistent Rotating MHD Modes When the MHD oscillations persist for more than about 300 msec, the ion toroidal rotation frequency profile flattens over an even larger region than the q=1 radius, sometimes flattening as much as 70% of the plasma cross section. Figure 1b shows an example with an oscillating predominantly n=2 mode that persists for about 5 sec. The discharge begins much like the previous one in Figure 1a with a peaked rotation profile during sawtooth related activity, then during the persistent n=2 mode, the rotation profile flattens out to roughly the q=1.5 radius. The spacing between channels of the charge exchange diagnostic is about 10 - 15 cm. The measured m number at the edge was found to be a mixture of 4 and 5, so linear toroidal coupling to the m=3, n=2 mode is

expected. Note that the profile begins to peak up again as the n=2 mode decays away after about 19 sec. Similar rotation profile flattening is also observed during persistent n=1 or n=3 oscillations. Note, however, that while the MHD frequency increases proportional to n, the ion rotation frequency agrees with the n=1 oscillation frequency.

Rotation During Quasi-Stationary Modes (QSM) The agreement between the ion rotation frequency and the n=1 frequency becomes particularly apparent during high power NBI when mode locking occurs, which brings the mode to rest. Under most conditions, the ion toroidal rotation profile collapses to zero, within the errors of the measurements, within 100 - 300 msec of mode locking. Figure 2 shows an example of mode locking during NBI combined with ICRH. A monster sawtooth collapse at about 13.5 sec drives a large predominantly n=1 mode unstable. Almost immediately, the central rotation frequency begins to drop as the mode frequency slows down. The mode locks at about 13.79 sec and the entire ion toroidal rotation profile comes to rest, within the errors of about ± 5 krad/sec, in about 200 msec. This time lag is believed to be due to the inertia of the ions. Note, however, that the Ni XXVII ion toroidal rotation from the central region of the plasma, which has a sampling rate of 20 msec, comes to rest in about 120 msec, indicating that the 100 msec sampling rate of the charge exchange diagnostic is artificially increasing the time delay.

While the behavior in Figure 2 is what normally happens, there are special cases with NBI after pellet injection in the current rise where the outer region of the plasma is locked by the QSM, but the inner region, roughly within the q=1.5 surface, is allowed to rotate (Figure 3). A pellet injected at 3 sec drove an oscillating mode, which becomes a QSM at about 4 sec with a dominant mode number of m=2, n=1. The ion rotation continues within the q=1.5 surface despite the presence of the QSM, until a q=1 surface emerges in the plasma at about 6.5 sec, according to equilibrium code calculations, after which time the rotation profile remains flat at approximately zero despite continued NBI.

Conclusion and Comparison with Theory Plasma ion toroidal rotation is strongly coupled to MHD activity through a viscous force between the ions and the modes that equilibrates the plasma rotation and MHD oscillation frequencies. Sawtooth related modes flatten the ion rotation profile within the q=1 surface. Persistent modes lasting for more than about 300 msec can flatten the ion rotation profile across more than 70% of the plasma cross-section. Quasi-stationary modes that come to rest can also bring the plasma rotation to rest, within the errors of the measurements, in 100 - 300 msec despite NBI. Nonetheless, central plasma rotation can occur during QSM's near the plasma boundary when q(0) > 1.

These results indicate that MHD effects should be taken into account in theories of plasma rotation to obtain a more accurate description of the rotation. The observed time required for the ions to lock to the mode is 100 - 300 msec, and appears to be independent of the mode amplitude for the cases studied, suggesting that it may be fundamentally due to the plasma inertia. The extent of flattening of the ion rotation profile, however, seems to be well correlated with rational q surfaces, indicating that toroidally coupled MHD modes are indeed responsible for flattening the rotation profile.

References
[1] A Boileau, et al, to appear in Plasma Physics and Cont Fusion.
[2] Snipes, J A, et al, Nuclear Fusion, 28 (1988) 1085.
[3] Stacey, W M, et al, Nuclear Fusion, 26 (1986) 293.
[4] Boozer, A H, Physics of Fluids, 23 (1980) 2203.
[5] Mynick, H E, Nuclear Fusion, 26 (1986) 491.
[6] Stork, D, et al, 14th EPS Conf on Plasma Phys and Cont Fusion, Madrid, Vol I, (1987) 306.
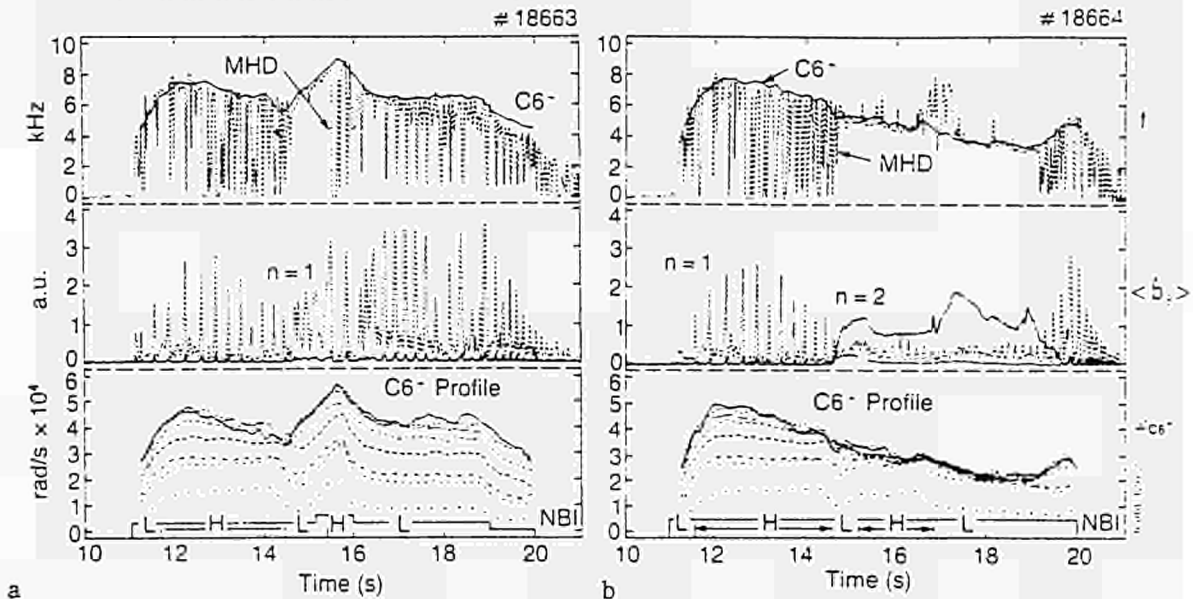[7] Isler, R C, et al, Nuclear Fusion, 26 (1986) 391.

Figure 1. a) A discharge with sawtooth related MHD activity showing good agreement between the central charge exchange toroidal rotation frequency and the n=1 MHD frequency at the edge, together with the n=1, 2 and 3 rectified and smoothed MHD amplitudes and the C 6+ rotation profile. b) A similar discharge but with a large n=2 mode that flattens most of the C 6+ rotation profile. The times during H and L mode are indicated during the NBI. The spacing between the charge exchange channels is 10 - 15 cm.
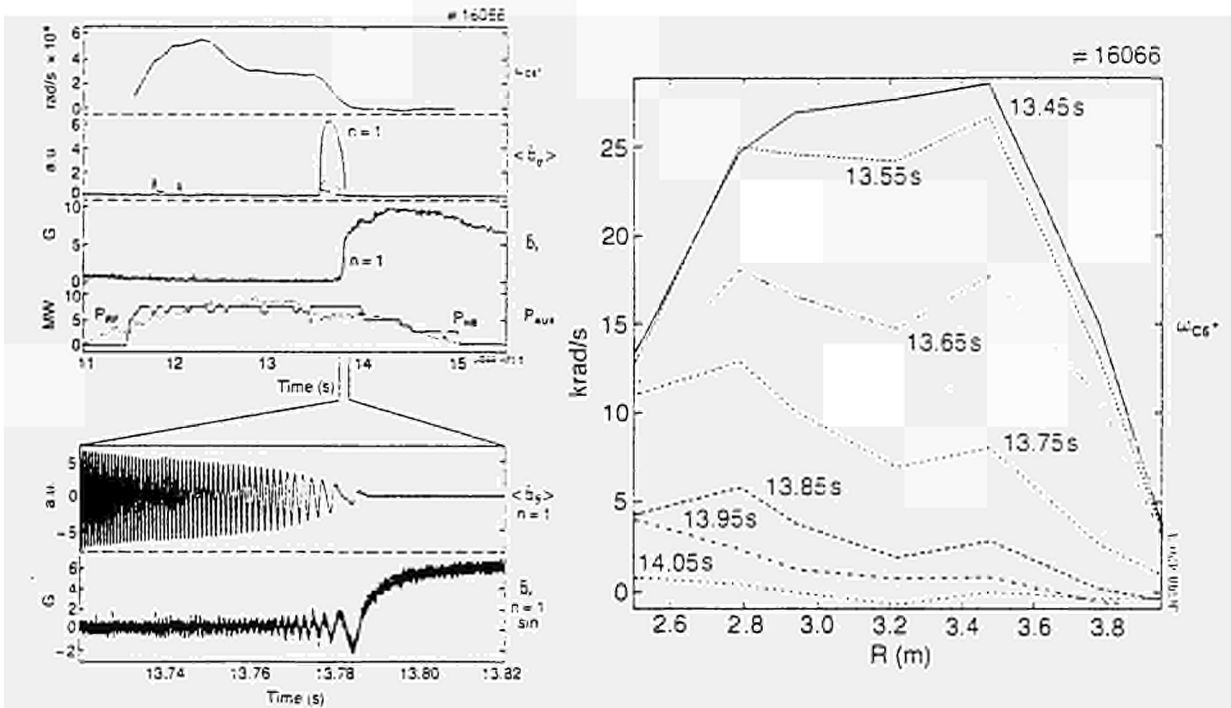
Figure 2. Mode locking during NBI + ICRH showing the subsequent collapse of the C 6^+ ion toroidal rotation profile. The time traces are the ion rotation near the center; the rectified amplitude of the n=1, 2 and 3 oscillations; followed by the locked mode radial field amplitude; and the NB and ICRH power. The expanded time traces show the n=1 oscillations slowing down and locking together with the sine component of the QSM.
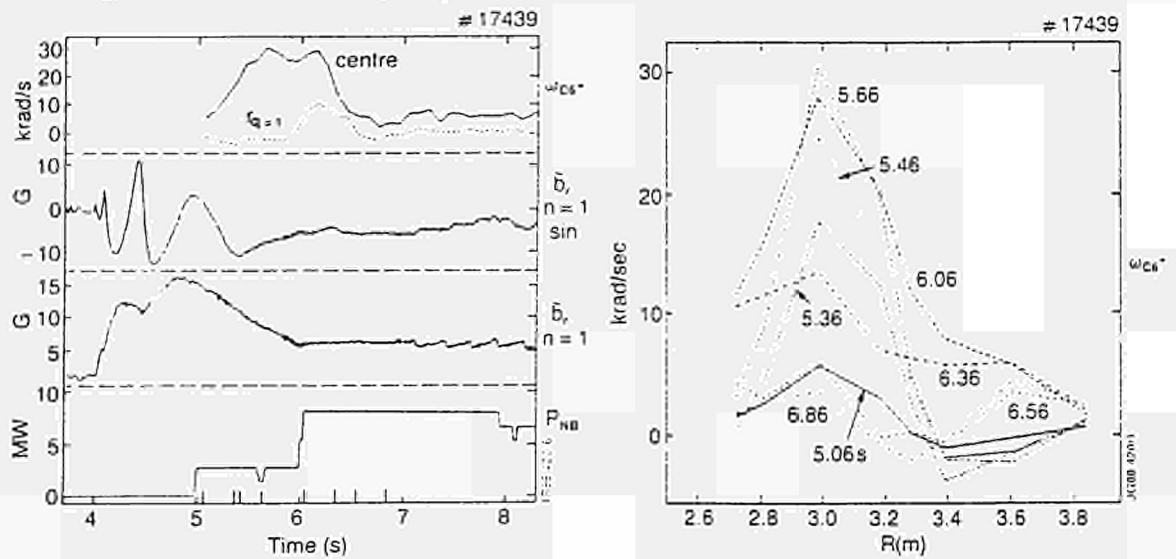

Figure 3. Pellet injection at 3 sec during the current rise drives an MHD mode that becomes a QSM at 4 sec and remains locked during NBI. Plasma ion rotation occurs within the q=1.5 surface despite the QSM at the boundary until a q=1 surface emerges in the plasma at about 6.5 sec, after which the central rotation also comes to rest, within the errors of the measurements.

M von Hellermann, A. Boileau *, L. Horton*, W. Mandl, H. P. Summers, H. Weisen

*JET Joint Undertaking , Abingdon Oxon OX14 3EA, UK
*IREQ, Tokamak de Varennes, Canada, ORNL , Oak Ridge, USA

Introduction:Radially and temporally resolved ion temperature profiles in auxiliary-heated and pellet-fuelled JET plasmas are obtained routinely from the observation of charge exchange line spectra of fully stripped carbon and oxygen. In addition the Doppler width of the x-ray emission spectrum of highly ionized nickel provides a measurement of the on-axis ion temperature. Analysis of the CX deuterium Balmer alpha spectrum shows that the deuteron temperatures are in close agreement to simultaneously measured carbon and oxygen temperatures. First results of this novel technique are reported in [1].

Results and Discussions : In   this paper we describe characteristic features of ion temperature profiles for   different JET operation modes such as low-density high-temperature plasmas, high-density pellet-fuelled plasmas, and high-density high-confinement H-mode plasmas.

The JET charge-exchange diagnostic employs one vertical line of sight and a horizontal multichord array (Fig.1), which intersects the heating neutral beams at 15 points along the minor radius. The spatial resolution defined by the intersection of the pencil like viewing lines and neutral beam is +/- 2cm , that is less than 1% of the major tokamak radius. The collected light is transferred by optical fibres to a set of 3 remote spectrometers and is recorded by multi channel detector arrays. The time evolution of ion temperature profiles can be monitored with a temporal resolution varying typically between 12 to 100 msec.

The development of the ion temperature profile was investigated in the extreme cases of high-ion-temperature, but low-density plasmas ($T_i = 23$ keV, $T_e = 10$keV, $n_D = 1.5 \, 10^{19} m^{-3}$) and in high-density, but moderate temperature , pellet-fuelled discharges ($T_e = T_i = 11$ keV, $n_D = 4 \, 10^{19} m^{-3}$). In the first case, an input of 19 Mwatts of NB heating power has led to very peaked profiles of ion temperature , toroidal plasma rotation and ion pressure .

accompanied by a simultaneous increase in the neutron reaction rate . Fig. 2a and 2b show the radial profiles of ion temperature and ion pressure . The deuteron density in this example has been derived from   electron and CX carbon densities [2] . The collapse of ion temperature and neutron rate coincides with a sharp increase in density , both of electrons and impurities, approximately 0.6 sec after the onset of neutral beam heating and fuelling. Fig.3 shows the temporal development of central ion temperature, electron and carbon density and neutron reaction rate .

In pellet-fuelled ICRH-heated plasmas, comparable high peaking factors are observed with almost identical radial profiles of ion and electron temperatures (Fig.4). Only 2 neutral beams with a power of 1.3 MWatt each were switched on in this example, to provide a minimum of neutral particle density required for the operation of the CX diagnostic.

Rather broad ion temperature profiles are observed during high confinement modes in the magnetic limiter configuration. Figs.5 and 6 show the evolution of ion temperature during a long neutral beam pulse, displaying an extended H-mode phase, followed by a brief L-mode and then a second H-mode phase. Minute details of the transition L to H and H to L can be recorded by the very intense outer channels of the CX diagnostic which enable an integration time as short as 12 msec (Fig.7). The transition from L- to H-mode and vice versa is typically accompanied by a distinctive change in temperature and density near the plasma boundary. The signals in Fig.7 (H_α-plasma-boundary and T_i at 3.82m) start with a back-transition from H- to L-mode , illustrated by a sudden drop of ion temperature from 1.4 keV down to 0.7 keV. The change occurs in a time scale of 10 msec. The second H-mode following an L-mode period of approximately 300 msec displays an increase in ion temperature to an almost constant level of approx. 1.1 keV. The end of the H-mode is associated with a drop to 0.6 keV 1 2 sec later.

Summary:The results presented in this paper have shown some extreme cases of ion temperature profiles illustrating the different operation modes of the JET tokamak. In the three examples of low-density high temperature, high-density moderate temperature and high-density high-confinement plasmas comparable values of a maximum fusion product $n_d T_i \tau_E$ in the order of 10^{20} keV m^{-3} sec are achieved.

References: [1] A. Boileau et al. " Observations of Motional Stark Features in the Balmer Alpha Spectrum of Deuterium in the JET Plasma", submitted to J.Phys.B, [2] P.D.Morgan et al., this conference, [3] G.Schmidt et al., IAEA-CN-50/A-IV-1, Nice, Oct. 88
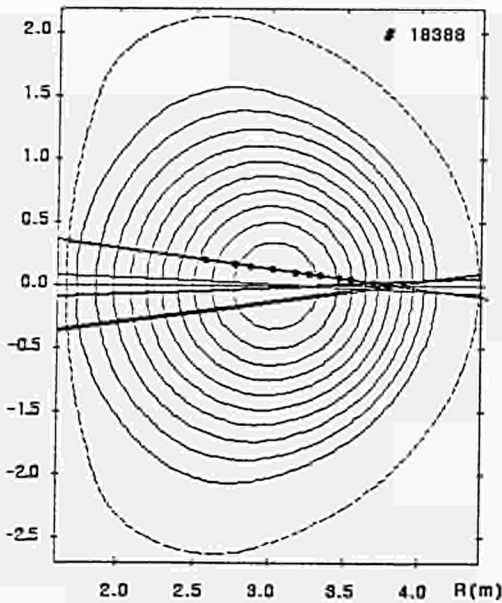

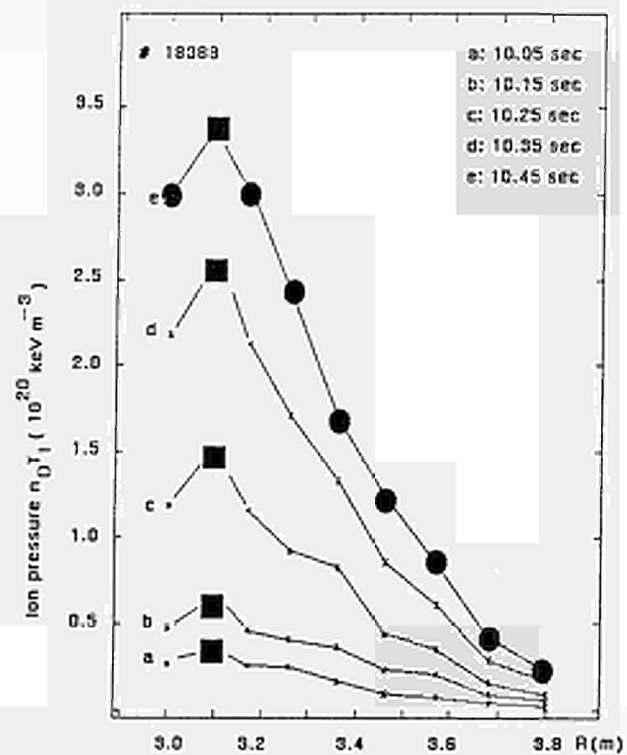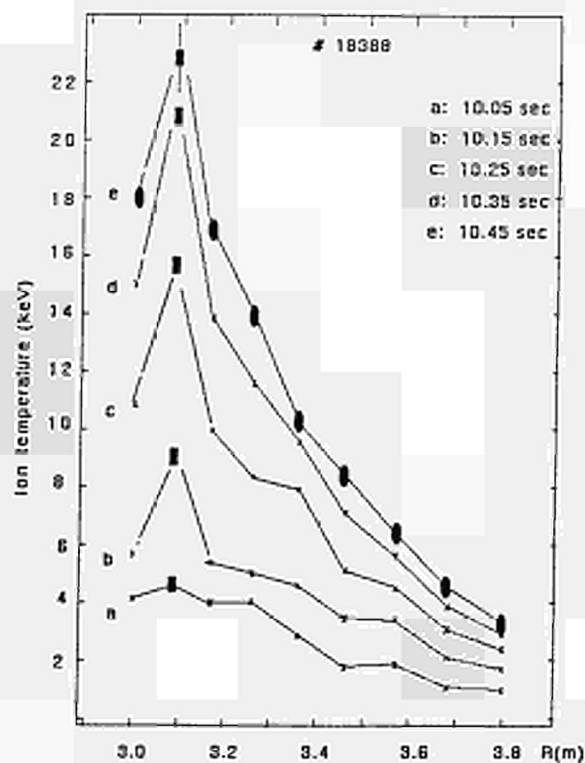Fig.1 Poloidal view of the JET heating neutral beams and intersection points with the CX multichord array (octant 8) .

Fig.2a
Fig.2b
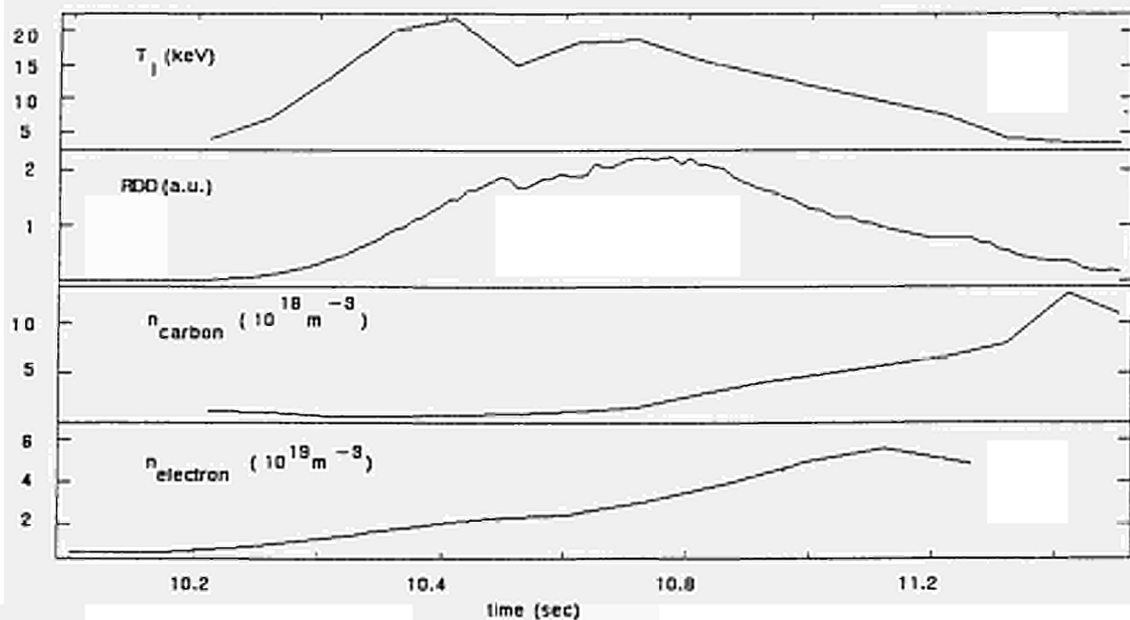Radial profiles of ion temperature and ion pressure. JET pulse 18388

Fig.3
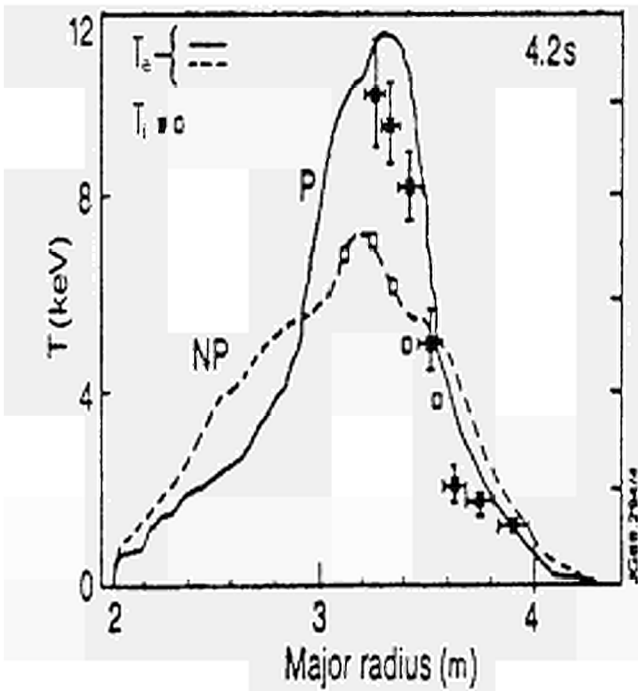Survey of T_i, n_e, n_C, RDD in a hot-ion-mode plasma

Fig.4 Profiles of electron and ion temperature in comparable pellet (P) and non-pellet (NP) plasmas , cf. [3]
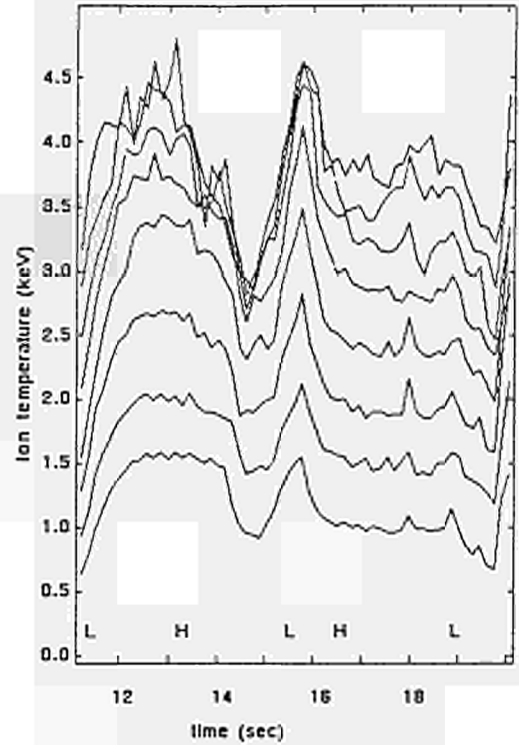

Fig.5 Ion temperature traces at 8 radial chords during a long NB pulse, with several transitions from L- to H-mode
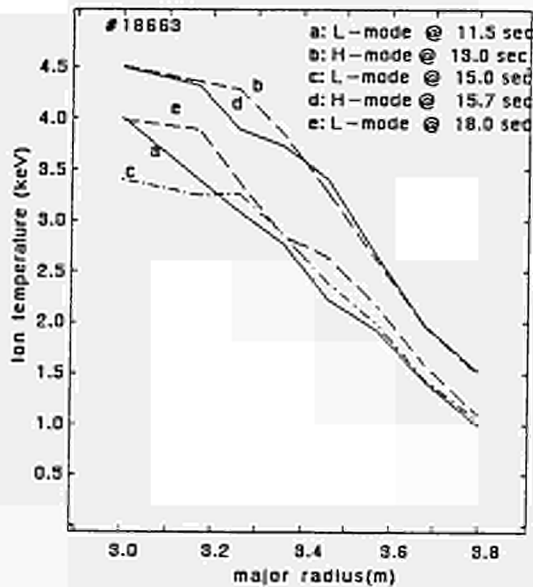

Fig.6 Radial ion temperature profiles in L- and H-mode phases of the same pulse
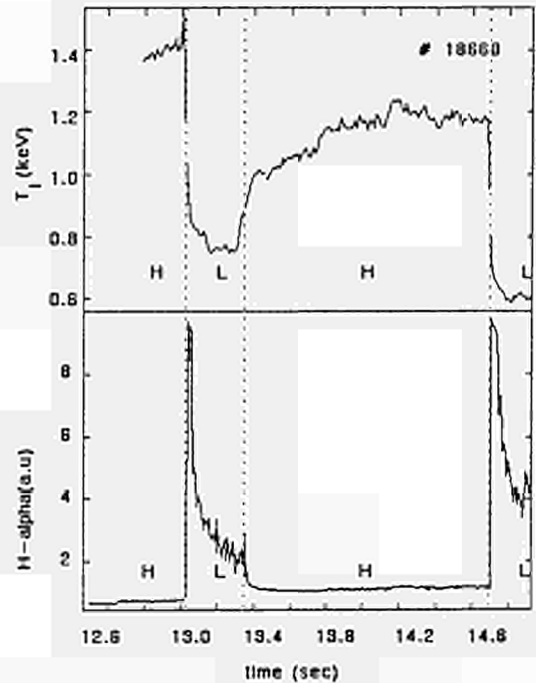

Fig.7 H-alpha, plasma boundary and Ti at R=3.82m, showing details at high sampling rate

DOUBLE NULL X-POINT OPERATION IN JET WITH NBI AND ICRH HEATING

H. Tubbing, V. Bhatnagar, D. Boyd[1], M. Bures, D. Campbell,
J. Christiansen, J. Cordey, G. Cottrell, A. Edwards, R. Giannella,
J. Jacquinot, M. Keilhacker, C. Lowry, P. Lallia, D. Muir, P. Nielsen,
D. Start, A. Tanga, P. Thomas, F. Tibone

JET Joint Undertaking, Abingdon, Oxon, OX14 3EA, UK
[1]University of Maryland, College Park, MD20742, USA

1. **INTRODUCTION** In this paper we report on a selection of experiments on H-modes, in 3 and 3.5MA discharges, in the double null X-point configuration. The first experiment, section 2, is an attempt to couple ICRH power to H-modes. Here we also report on a rather unique H-mode with a smaller than usual distance between plasma and limiter. The second experiment, section 3, is on H-modes in the low density, hot ion regime.

2. **ICRH COUPLING TO MEDIUM DENSITY H-MODES** The aim of the experiment is to increase central temperature by central ICRH deposition. Further, an attempt was made at generating an H-mode with ICRH only [1]. The magnetic configuration is a double null X-point, in a deuterium plasma, with $I_p \approx 3MA$, $B_t \approx 2.45T$, elongation $K \approx 1.8$, and volume average density $\langle n \rangle \approx 2 \cdot 10^{19} m^{-3}$ before the L-H transition. The distance to the belt limiter is about 30mm, to the antennae about 85mm. The ICRH details are: monopole antenna phasing, at a frequency of 33.5MHz, using hydrogen minority. ICRH coupling resistances of 4Ω were obtained.

With ICRH heating only, weak H-mode signatures were observed on the H_α and edge magnetic fluctuations. However, we did not observe 'H' confinement (see figure 1), nor the characteristic enhanced density increase rate. Before excluding the option of ICRH only H-modes in JET, however, we will have to operate the ICRH at power
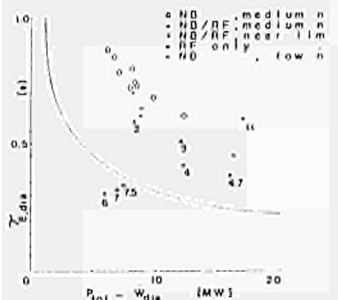

Figure 1: comparison between H-modes with NBI only (#17386, solid line) and an H-mode with combined NBI/ICRH heating (#17391, dashed line).
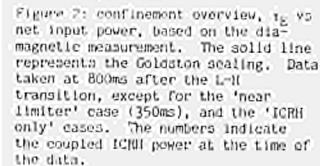

Figure 2: confinement overview, τ_E vs net input power, based on the diamagnetic measurement. The solid line represents the Goldston scaling. Data taken at 800ms after the L-H transition, except for the 'near limiter' case (350ms), and the 'ICRH only' cases. The numbers indicate the coupled ICRH power at the time of the data.

significant increase. The primary sources of Ni are the ICRH antenna screens. It is expected that future installation of Beryllium screens on the ICRH antennae will alleviate the problem.

The confinement overview is shown in figure 2. It is apparent that the combined heating cases have somewhat lower confinement times than comparable NBI only cases. However, this can, to the first order, be accounted for by the difference in radiated power.

Central electron and ion temperatures are not increased by the ICRH, as is illustrated in figure 1. The results are an important improvement over earlier (1986) attempts to couple ICRH to 3MA, single null X-point, H-modes.

Recently a 3.5MA, 3.2T H-mode was obtained in the double null X-point configuration but with a distance between plasma and limiter of only 10mm. This discharge (#18773) has excellent ICRH coupling properties. Hitherto, it was believed that the limiter clearance should be at least 30mm [2]. The pre-heating target was pellet fuelled (3 × 2.7mm pellet, before beam-on) and a 3 to 3.5MA current ramp was executed. The pre-heating target density is $\langle n \rangle \approx 1.4 \cdot 10^{19} m^{-3}$. 10MW of ICRH is coupled, on top of 15MW NBI, with a coupling resistance of 6Ω (monopole phasing, 48MHz, H minority). The rate of increase of P_{rad} is low (5MW/s), indicating that the Ni influx is negligible. The confinement time (diamagnetic)

levels which are more clearly above the L-H power threshold.

With combined NBI/ICRH power, elm free H-modes were obtained. During these the density, the effective ion charge Z_{eff}, and the radiated power increase with time. The H-modes are terminated when the total radiated power (appr. 70% of which is from the bulk plasma and 30% from the X-points) equals the input power. In figure 1 we compare an H-mode with 8MW NBI and 7MW ICRH to a similar case with 10MW NBI only. The increase of the radiated power P_{rad} is 5MW/s for the NBI case, vs 10MW/s for the NBI/ICRH case (up to 18MW/s in a bad case).

The enhanced radiation is dominantly due to nickel contamination, as is apparent from an analysis of Ni line intensities. It is further confirmed by the observation that Z_{eff} shows no

is about 600ms, the D-D reaction rate is $1.9 \cdot 10^{16} s^{-1}$. Both electron and ion temperatures are about 10keV. The peculiarities of this discharge are not understood, (see also [5]) but clearly this scenario looks very promising and deserves further investigation.

3. **H-MODES IN THE HOT ION REGIME** The primary aim of the experiments described here was the study of hot ion modes [3][4], using the double null configuration to obtain low density. Figure 3 shows a comparison between a low density and a medium density discharge, in similar plasma conditions, both with 10MW NBI. In the low density discharge there is a delay between beam-on (52s) and the L-H transition (53s). During this delay the plasma is in the hot ion regime (the density is below the L-H transition density threshold, see below) Concentrating on the H phase of the two shots, it is apparent that the low density case has desirable characteristics; while it has almost the same $n_D T_i \tau_E$ product, it has a 50% higher D-D reaction rate [5] because of the higher ion temperature and the longer slowing down time.

Figure 3: comparison between an H-mode at medium density (#17386, solid line) and one at low density (#18757, dashed line). Both discharges have 10MW NBI from 52s. Note that the H_α signal for the low density case is multiplied by 10.

The rate of increase of the density is lower in the low density discharge: $\langle \dot{n} \rangle \approx 1.3 \cdot 10^{19} m^{-3} s^{-1}$ vs $\langle \dot{n} \rangle \approx 2.6 \cdot 10^{19} m^{-3} s^{-1}$, averaged from 100 to 600ms after L-H). Note that the beam fuelling accounts for $0.8 \cdot 10^{19} m^{-3} s^{-1}$. The rate of rise of the radiated power is also lower ($P_{rad} \approx 3.0MWs^{-1}$ vs $P_{rad} \approx 4.5MWs^{-1}$). The lower density increase rate is probably associated with the deuterium inventory of the X-point tiles rather than with the low density as such.

Penetration of the NBI (80keV D) is much improved and the density profiles remain more peaked. The rate of increase of Z_{eff} is higher in the low density discharge. In fact, it appears that the carbon influxes are approximately of equal magnitude, $\langle \dot{n}_C \rangle \approx 2 \cdot 10^{18} m^{-3} s^{-1}$. The problem of deuterium dilution is thus more severe.

The low density target discharges also provide information on the L-H transition density threshold. It is observed that for discharges with a pre-heating density below $\langle n \rangle \leq 1 \cdot 10^{19} m^{-3}$, the L-H transition is delayed
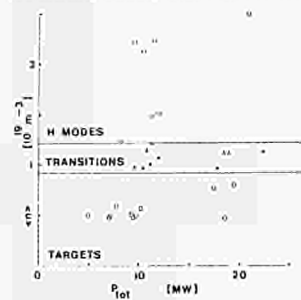

Figure 4: Illustration of the L-H transition threshold density. This threshold is independent of input power P_{TOT}.

with respect to beam-on (up to 1s, see fig. 3, while for normal medium density H-modes this is ≤ 200ms). During the delay time, the beam fuelling increases the target density to the density threshold of about $1 \cdot 10^{19} m^{-3}$. This is illustrated in figure 4, where we plot the pre-heating target density and the density at the transition vs the total input power. It appears that the density threshold is rather independent of the input power. A similar plot of electron temperature (at r/a ≈ 0.7) vs input power shows appreciably more scatter.

The potential of the low density H-modes lies in the benefits of the hot ion regime. With the present 80keV NBI system, the window for the hot ion regime is between $\langle n \rangle \approx 0.5 \cdot 10^{19}$ and $1.5 \cdot 10^{19} m^{-3}$. This allows only a small overlap with the H-mode density window, $\langle n \rangle \geq 1 \cdot 10^{19} m^{-3}$. With the near future upgrade of the NBI to 140keV, this overlap should be appreciably wider.

4. **CONCLUSIONS** On the ICRH coupling experiments: significant ICRH power has been coupled to H-modes generated with NBI and a plasma to limiter distance of 30mm. In these discharges, there is a Ni influx problem. The increased radiated power limits the confinement, and the central temperatures. No H-modes have yet been observed with ICRH only, although weak H-mode signatures have been observed. More recently an H-mode has been observed with a plasma limiter separation of about 10mm. This configuration allowed excellent ICRH coupling, and showed no significant Ni influxes. 11MJ stored energy was obtained in a 3.5MA plasma with 25MW input power.

On the low density H-modes: H-modes have been obtained at low densities $\langle n \rangle \geq 10^{19} m^{-3}$ where there is an overlap with the hot ion regime. These discharges have several desirable properties. The low density H-modes have similar $n_e T_E T_i$, but a higher D-D rate than medium density ones.

[1] D. Start et al, proc. 12th IAEA conference, Nice, 1988.
[2] M. Keilhacker and JET team, proc. 12th IAEA conference, Nice, 1988. See also report IAEA-CN-50/A-111-2.
[3] P. Thomas et al, proc. 12th IAEA conf. Nice, 1988.
[4] C. Lowry et al, this conference.
[5] F. Tibone et al., this conference.

IMPURITY PRODUCTION AND TRANSPORT AT THE JET BELT LIMITER

C S Pitcher*, G M McCracken***, P C Stangeby** and D D R Summers

Joint European Torus, Abingdon, Oxon OX14 3EA, UK

*   Canadian Fusion Fuels Technology Project, Toronto, Canada
** JET and University of Toronto Institute for Aerospace Studies, Canada
*** Culham Laboratory UKAEA, Abingdon, UK

1 Introduction

Under certain operating conditions in JET the impurity content of the discharge can be high, thus reducing the fusion reaction rate through the dilution of the hydrogenic fuel. The dilution in most discharges is predominantly due to carbon impurities [1]. In order to understand how carbon impurities are produced and transported into the plasma, detailed measurements have been made with a CCD camera looking at the graphite limiter with interference filters centered on intense spectral lines of the low ionization states of carbon (C I, C II, C III) as well as the fuel species ($D\alpha$) and helium (He I).

2 Experiment

The viewing geometry is sketched in the upper portion of Fig. 1. The CCD camera is mounted at the top of the torus and looks at the bottom belt limiter. The boundary plasma conditions are determined with Langmuir probes built into the belt limiter and with a fast reciprocating probe (RP) at the top of the torus [2]. The built-in probes give the time dependence of the electron density and temperature in the edge plasma while the RP provides radial profiles from the wall to several centimetres inside the last closed flux surface (LCFS). The boundary plasma conditions obtained with the probes are essential in the interpretation of the spectral emission observed around the limiter.

3 Spatial Distributions

Figure 1 shows the spatial distributions of C I, C II, C III, $D\alpha$ and He I observed in a discharge with Ohmic heating only, a plasma current $I_p = 3.1 MA$, toroidal magnetic field $B_T = 2.3T$ and volume-average density $\bar{n}_e = 1.5 \times 10^{19} m^{-3}$. In this discharge the plasma is limited by the lower belt only and helium is present as a trace impurity. In general, all of the emissions are centered about the magnetic field tangency point. The $D\alpha$ and He I distributions appear strikingly similar with both having their maxima at the tangency point. This is in contrast to the C I distribution which has its maximum shifted away from the tangency point to the ion drift side. The C II and C III distributions show a progressive broadening and shift in the ion drift direction.

The transport of the carbon atoms and ions originating from the limiter has been modelled using the two-dimensional impurity transport code LIM [3]. Carbon atoms are assumed to be produced by physical sputtering and are launched from the limiter surface into a plasma grid. The plasma density ($n_e(r)$) and temperature ($T_e(r)$) profiles in the boundary plasma are specified in the code from probe measurements and are approximated by exponential functions.

Once ionized, the C^+ ion is heated by the background plasma and starts to disperse. The code tracks the dispersal of the ions along and across the magnetic field lines, taking into account the effects of ionization to higher stages, heating, classical parallel diffusion and anomalous cross-field diffusion. When the impurity ion densities in the vicinity of the limiter are determined, the line of sight integrations of the emitted radiation are calculated using the radiating efficiencies of the atoms and ions [4].

Results from the code appear in Fig. 2. The following SOL parameters are assumed by the code; $\lambda_T = 17mm$, $\lambda_n = 6mm$, $T_e(a) = 60eV$ and $n_e(1) = 2n_e(a) = 1.5 \times 10^{18} m^{-3}$. These values are consistent with the RP measurements allowing for the compression of the magnetic surfaces from the probe position to the limiter. The higher density on the ion drift side of the limiter is required to reproduce the asymmetric C I distribution obtained experimentally. Further, to obtain the observed drift of the C II and C III, the background plasma is assumed to have a flow velocity of $10^4 m/s$ (Mach number ~ 0.1) in the ion drift direction. The carbon ions thus appear to be swept in the ion direction by friction associated with a background plasma flow.

4 Particle Fluxes

The experimental photon fluxes for the above conditions have been converted with the aid of theoretical photon efficiencies at $T_e \sim 50eV$ into total particle influxes. The error in this conversion is estimated to be a factor of ~ 2. Within this uncertainty, the C I, C II and C III influxes are similar and are approximately $\sim 4 \times 10^{20} carbons^{-1}$, compared with the total

deuteron influx of $\sim 4 \times 10^{21} Ds^{-1}$. The LIM simulation gives C I, C II and C III influxes that are in reasonable agreement with these values. The observed effective yield appears to be high $\Gamma_C/\Gamma_D \sim 0.1$ but, within experimental error, can be explained by deuteron and carbon physical sputtering.

The fact that the fluxes of the low ionization states of carbon are similar means that negligible scrape-off layer screening is occurring for these ionization states resulting in little prompt redeposition of impurities. This is predicted by the code and to be expected, since the SOL in low density (Ohmic) boundary plasma conditions is nearly transparent to sputtered carbon atoms.

5 ICRH Power Scaling

As the input power is increased through the application of ICRH the central density of the plasma increases without external gas puffing. This behaviour is shown in Fig. 3 for well-conditioned 3.3 MA, 3.4 T discharges. The resulting edge density rise is somewhat greater, being roughly proportional to the total input power. The increase in density is such that the electron temperature in the boundary remains constant at $T_e(a) \sim 55eV$. Similarly, λ_n (22 mm) remains approximately constant as measured by the RP, as does Z_{eff} (2.3), and the radiated power fraction ($P_{rad}/P_{tot} \sim 0.4$). The carbon sputtered from the limiter, as measured by the C I, increases roughly in proportion to the edge density (Fig. 3). This is expected since a constant electron temperature implies a constant sputtering yield and a constant photon efficiency for the radiating atoms. Similar results are obtained in reference [5].

6 High Power Operation

As shown by Fig. 3, the power scaling of impurity production at the limiter is relatively simple, the sputtered carbon flux is proportional to the edge density which is proportional to the total input power. During high power operation, however, this scaling breaks down as enhanced carbon erosion occurs at "hot spots" that appear at the limiter tile edges, typically with an area of $\sim 10cm^2$. In Fig. 4 the C III emission associated with a single hot spot on the lower belt limiter and the edge plasma conditions as measured by the built-in Langmuir probes are shown as a function of time. On the application of ~ 28 MW of combined ICRH and NBI heating the edge density rises and the electron temperature remains constant, as observed at lower powers. The C III emission rises in proportion to the edge density up to a point, ~ 0.5 s after the start of the heating, where the signal abruptly rises and saturates. The temperature of the hot spot at this time had risen to approximately 1600 C as estimated from the black-body emission measured with the CCD camera. As a result of the massive influx of carbon from this and other locations, the discharge detaches, the total radiation abruptly jumps from ~ 40% to ~ 100%, and the edge density and temperature drop significantly. Once the heating power is reduced the discharge re-attaches and the edge signals and radiated power revert to more typical values. These observations taken in limiter discharges are consistent with measurements in high-power X-point and inner wall discharges.

From the C III observation it appears that enhanced erosion is occurring at ~ 1600 C probably due to radiation-enhanced sublimation [6]. Unfortunately, the majority of the limiter surface is not observed and it may be that some spots are hot enough for thermal sublimation to be important.

7 Conclusions

Dilution in JET plasmas can be serious and thus the production and transport from a major source of these impurities, the limiter, has been studied. The spatial distributions of the C I, C II and C III have been modelled with a two-dimensional Monte Carlo code and are in reasonable agreement with experiment. Little prompt redeposition at the limiter appears to be occurring in Ohmic discharges with most of the atoms being ionized on closed field lines and thus free to disperse and contaminate the plasma. The application of auxiliary heating has little effect on the boundary except to increase the density and thus the limiter sputtering in proportion; this results in a constant Z_{eff} in the centre of the discharge. During high power operation, isolated "hot spots" on the limiter reach temperatures of > 1600 C and appear to emit carbon at an enhanced rate, consistent with radiation enhanced sublimation.

References

1. K Behringer et al, J N Mat 163-165 (1989) to be published.
2. S K Erents et al, J N Mat 163-165 (1989) to be published.
3. P C Stangeby et al, JET-P(87)61 and Nucl Fusion (to be published).
4. K Behringer, J N Mat 145-147 (1987) 145.
5. M F Stamp et al, these proceedings.
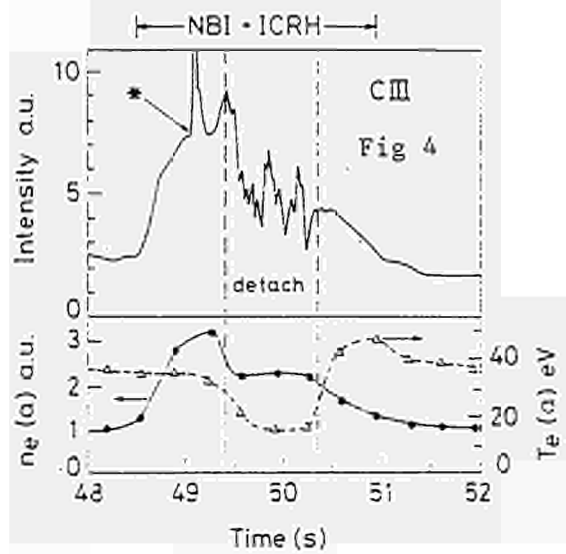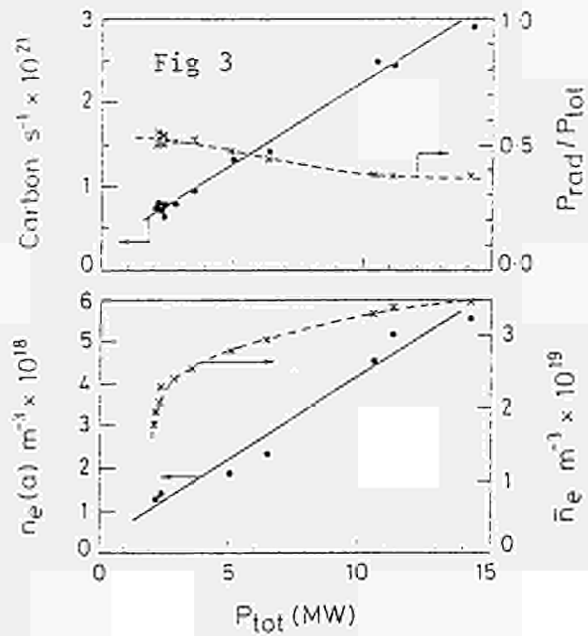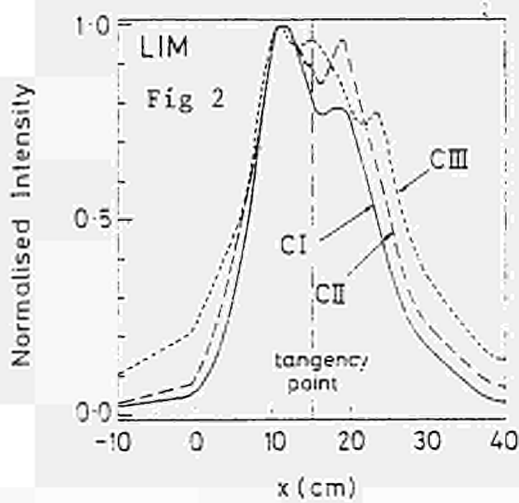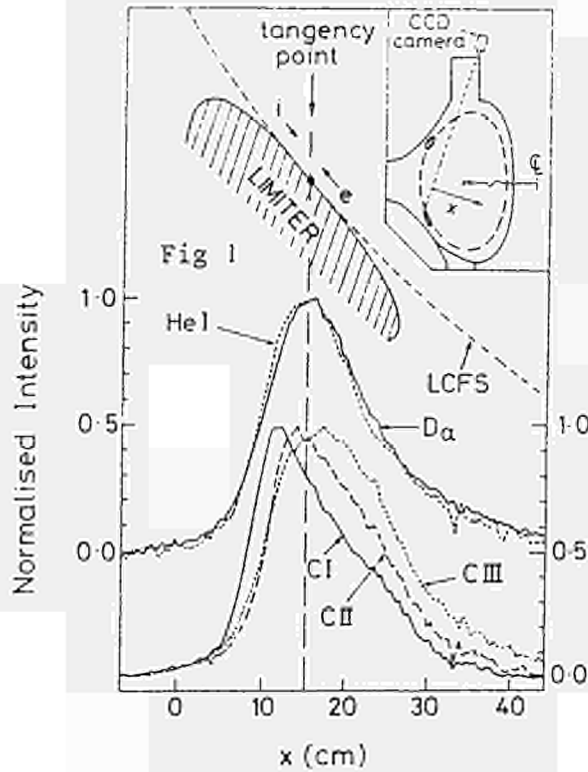6. J Roth, J N Mat 145-147 (1987) 87 and private communication.

Fig. 1 Spatial distributions of the low ionization states.

Fig. 2 Spatial distributions of C I, C II and C III as predicted by the LIM code.

Fig. 3 The ICRH power scaling of the carbon influx, the radiated power fraction P_{rad}/P_{tot}, the edge density $n_e(a)$ and the volume-averaged density $\bar{n}_e$.

Fig. 4 The C III intensity associated with a hot spot on the lower belt limiter and the edge plasma conditions during ~ 28 MW combined heating. $I_p = 5MA$, $B_t = 3.2T$, discharge balanced between upper and lower limiters. "*" denotes hot spot temperature ~ 1600 C.

AN INTERPRETATION OF THE STRUCTURE OF ELMS AND THE H TO L TRANSITION ON JET

P Cripwell*,A Edwards,R Galvao,N Gottardi,P Harbour,P Haynes@,T C Hender= ,
E H Joffrin,M Malacarne,P Mantica#,N Salmon,
J A Snipes,A Tagle,D Zasche +

JET Joint undertaking,Abingdon,Oxon,OX14 3EA,U.K.
* Imperial College of Science,Technology,and Medicine,University of London,U.K.
@ UKAEA Culham Laboratory,Abingdon,Oxon,U.K.
= Istituto di Fisica del Plasma,EURATOM,ENEA-CNR Ass.,Milano,Italy
+ Max-Planck Institut fur Plasmaphysik,D-8046,Garching,F.R.G.

Introduction

Edge localised modes play an important role in H-mode confinement and stability [1]. Recent studies have identified precursors to the H to L transition rotating in the opposite direction to co-injected neutral beams [2], and proposed that the H to L transition is triggered by a giant ELM [3]. Tearing modes driven by edge current density and ballooning modes driven by pressure gradient have been put forward as possible explanations for these precursors.

Initial studies on JET [4], have described the characteristics of edge fluctuations in X-point plasmas and their effects on energy and particle confinement.

In this paper we perform a detailed magnetic analysis of ELMs and their precursors, and make a comparison with the H to L transition. These magnetics results correlate with those of other diagnostics such as the microwave reflectometer and X-point langmuir probes. Localization of ELMs and H to L transition spike is determined with the soft X-ray camera, and particle transport estimated by an H-alpha detector. Finally possible theoretical explanations for ELMs are discussed.

Structure of ELMs and precursors

The ELM structure is examined poloidally by two sets of coils (10kHz cut-off, 6dB roll-off) near the X-points and toroidally by lower frequency response coils (10kHz cut-off, 12dB roll-off).

Typical ELMs during an H-mode are presented fig(1a). ELMs are visible by all the diagnostics mentioned above. In addition a significant magnetic fluctuating toroidal component was observed (typically, larger than one tenth of the fluctuating poloidal component : $\tilde{B}_{\phi}/B_{\phi\theta} \cong 5.10^{-4}$). The ELM spike has predominantly an n=0 component with an n=1 contribution of typically 30%. The poloidal component is predominantly m=1, with a phase inversion about the X-point for both single null and double null plasmas. In the single null case, the second phase inversion does not occur in a reproducible location.

ELMs are preceded by precursors and also often followed by postcursors (fig(1b)). Typically precursors start at about 0.5ms before the ELM, and postcursors stop 1ms after. Both are identical except that the amplitude of postcursors ($\tilde{B}_{\phi}/B_{\phi\theta} \cong 5.1^{-6}$) is often two or three times higher than the amplitude of precursors.

Because of this small amplitude they are only detected by the magnetics and the langmuir probe. Toroidal correlations show an n=1 component rotating opposite to the co-injected neutral beam direction with a frequency of about 6 to 8kHz. The frequency of precursors has been found to be close to the electron diamagnetic drift frequency calculated in the high shear region (≈10kHz). Poloidal mode numbers in the range of 5 to 10 have been estimated for the ELM precursors. Such high m (n=1) modes are resonant very near the separatrix in the high shear boundary region.

Soft X-rays have verified [4] that ELMs originate near the edge, and also exhibit an inversion radius at about 5 to 10 cm inside the plasma indicating the enhanced

particle and energy transport in this region when ELMs occur. To explain this large transport during the ELMs the island width has been calculated in the high shear region for two neighbouring surfaces, assuming a tearing mode model for the precursors. Within the range of uncertainties over the edge shear and poloidal mode number of the precursors, overlap appears possible for the measured amplitude of ELM ($\tilde{b}/B_{\phi\theta} \cong 5.10^{-4}$), thus leading to a stochastic field topology and enhanced transport. To support this interpretation, reflectometry measurements of n_e near the inversion radius have been made during and in between ELMs. Preliminary results show at all frequencies an increased level of density fluctuations (by a factor two or three) during ELMs.

Differences have also been noticed on toroidal correlations, but more complete analysis is required.

Comparison with the H to L transition

A similar magnetic analysis has been carried out for the H to L transition (fig(2)). Unlike ELMs, the spike that occurs at the H to L transition has dominantly an n=1 structure with a strong n=0 contribution of about 40%. The poloidal structure is also m=1 predominantly but the phase inversion does not occur at the X-point. However this n=0 m=1 component is probably due to the fast displacement of the plasma (≈1cm radially,≈2cm vertically) when the transition occurs.

In addition, the H to L transition is also often preceded by precursors for about 1ms. They again rotate in the electron diamagnetic drift direction with a frequency of 6 to 8 kHz, and exhibit a predominantly n=1, and m=5 to 10, structure, indicating that they are localized near the separatrix.

The edge localization of the H to L transition is corroborated by the soft X-ray reconstruction shown fig(3). The spike of the transition does not affect the center of the plasma, and is a much faster phenomenon (≈100 µs) than the ELM spike (≈0.5 ms).

Given the identical precursors observed before the ELMs and the H to L transition, it seems that they may both have the same underlying cause. However, a decisive conclusion cannot be drawn due to differences in the modes structure and the duration.

Interpretation and conclusion

As the ELMs during H-modes are accompanied by n=1 m=5 to 10 precursor structures, high n ballooning activity would seem to be precluded as an explanation of their origin. It seems likely that in the high shear edge region, n=1 instabilities with a broad spectrum of coupled poloidal harmonics are destabilized. The observed rotation of the precursors in the electron diamagnetic drift direction with approximately the electron diamagnetic drift frequency is in agreement with the tearing theory [5].

The magnetic fluctuation level during ELM spikes may be sufficient to give island overlap in the high shear region. This overlapping could lead to ergodization of field lines and enhanced edge transport [4], reducing the edge pressure gradients. Thus, tearing modes are a possible candidate to explain the precursors and would lead to stochastic transport during ELMs.

The H to L transition spike is preceded by similar precursors, but its different mode structure and shorter duration make it difficult to identify the transition as a giant ELM.

References

1. M. Malacarne et al, Plasma Physics and Controlled Fusion 29 (12) (1987) 1675-1686.
2. K. Toi et al, IPP III 135, May 1988.
3. N. Ohyabu et al, Proc of the XV EPS conf on Contr Fus and Pl Heat, Dubrovnik, May 1988, Vol I, p 227-230.
4. A. Hubbard et al, Proc of the XV EPS conf on Contr Fus and Pl Heat, Dubrovnik, May 1988, Vol II, p 651-654.
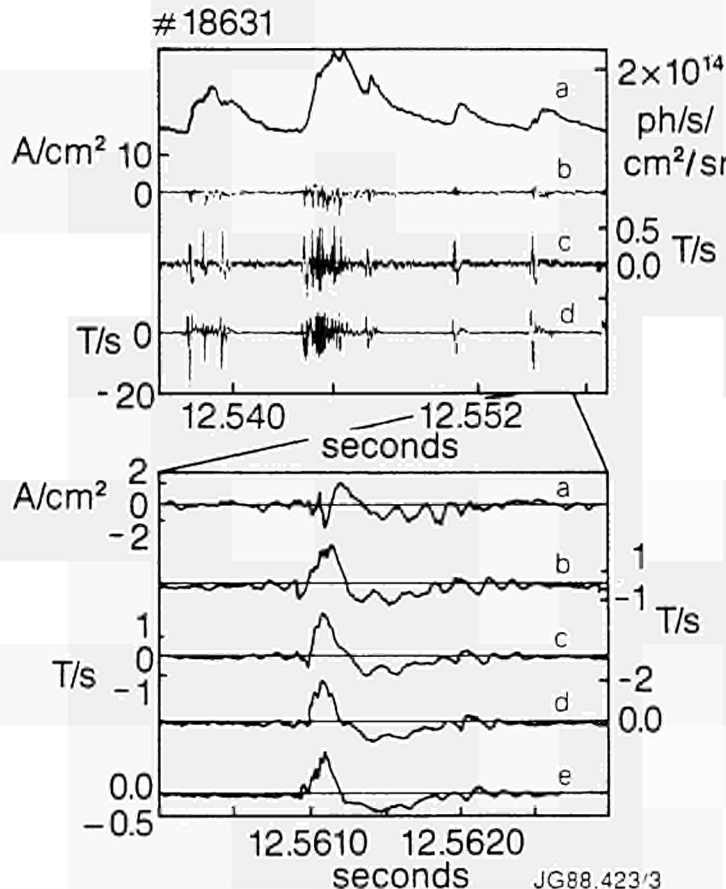5. R. D. Hazeltine, D. Dobrott, and T. S. Wang, Phys Fl. 18 (75) 1978.

Fig 1a : ELMS for pulse 18631 (q at the edge : 9)
a) H-alpha channel viewing the X-point.
b) Langmuir probe signal.
c) Toroidal magnetic component near the X-point.
d) Magnetic coil near the X-point.

Fig 1b : Poloidal correlation of coils showing the propagation (m=9) of the oscillations before and after an ELM.
a) Langmuir probe.
b to e) poloidal array of coils near the X-point.
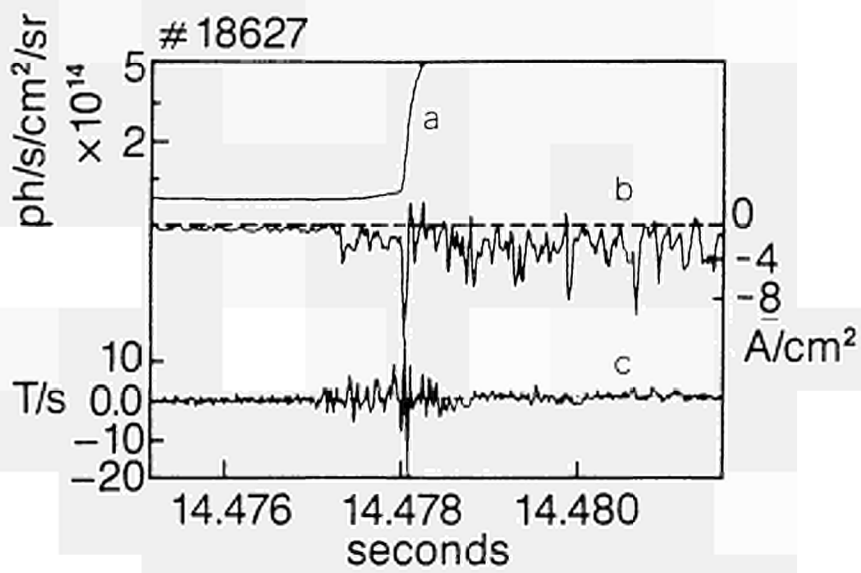
JG88.423/3

Fig 2 : H to L transition showing the precursors.
a) H-alpha channel viewing the X-point.
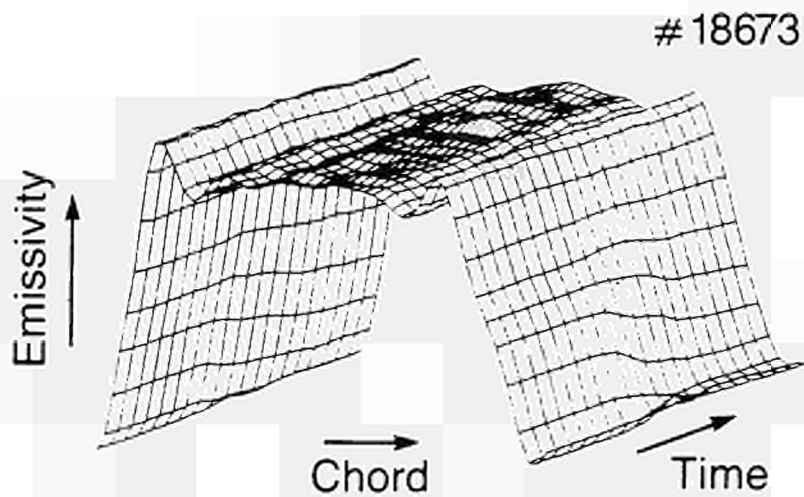b) Langmuir probe signal near the X-point.
c) coil near the X-point.

Fig 3 : Reconstructed X-ray emissivity of an
H to L transition spike over 0.5ms along
the vertical chord (Z = -1.6 to Z = 1.6).

DISTRIBUTION OF EROSION AND DEPOSITION ON THE JET BELT LIMITERS

G M McCracken*, R Behrisch**, J P Coad, D H J Goodall*, P Harbour,
L de Kock, M A Pick, C S Pitcher*, J Roth**, P C Stangeby**,

JET Joint Undertaking, Abingdon, Oxon OX14 3EA, UK

* UKAEA Culham Laboratory, Abingdon, OX14 3DB, UK, (Culham/Euratom
  Association)
** Institute for Aerospace Studies, University of Toronto, Canada, M3H 5T6
* Canadian Fusion Fuels Technology Project, Ontario, Canada
** Max-Planck-Institut fur Plasmaphysik, 8046 Garching bei Munchen, FRG

1. Introduction

The distribution of erosion and deposition of limiter material is of
importance both for extrapolating to the next generation of fusion
machines and for understanding impurity transport in the boundary layers
of present day tokamaks. Erosion patterns have previously been reported
for the JET discrete graphite limiters used up to 1986 [1]. We have now
made measurements on the belt limiters used in 1987-88. These
measurements show that although the pattern of net erosion is
qualitatively similar to the earlier results the new maximum erosion
($\sim$40μm) is reduced by about a factor 5, consistent with the larger
limiter surface area.

2. Experimental Observations: Belt Limiters

The two toroidal belt limiters were installed in JET in 1987 on the
low field side of the vacuum vessel, above and below the midplane [2].
These limiters consist of a large number of graphite tiles on water
cooled inconel mounting plates. The physical dimension of a number of
tiles were carefully measured before installation. Two tiles were
removed in August 1987 after about two months operation, $\sim$ 470
discharges. A further 8 tiles were removed in May 1988 after $\sim$ 4000
discharges. They were then remeasured. The difference between two sets
of measurements is plotted in fig 1 as a function of the distances along
the centre-line of the tile. The erosion is 20-50μm, which compares with
the much larger erosion of 150μm at the discrete limiter tiles exposed to
2800 discharges in 1986. The lower erosion rate is expected because the
belt limiter area is about ten times larger than the discrete limiters,
and the total particle outflux is similar. The tiles are mounted in
adjacent pairs and generally reproducible results are obtained for each
pair. The pair exposed for only 2 months have erosion/deposition values
less than 10μm. The tiles from the bottom limiter and from 2 toroidal
positions on the top limiter have quantatively similar results with
erosion/deposition changes $\sim$ 20-40 μm. This indicates reasonable
toroidal uniformity, consistent with Langmuir probe results [3]. A
cross-check on the absolute deposition was carried out by sectioning the
tiles. Typical results are also shown in fig 1. Where deposition is
indicated by the physical measurements it is clearly observed in the
sectioning; where erosion is indicated by the measurements no deposition
can be seen. The results obtained for deposition show the
erosion/deposition transition in good agreement with the mechanical
measurements.

A series of depth profile measurements were then carried out using
SIMS. Samples from different positions on the tile were measured to
obtain the nickel, chromium, hydrogen and deuterium depth distribution.
Some of the results are shown in fig 2. Nickel was the dominant metal
with concentrations up to 10^{21} atoms cm^{-3} (1% of graphite density).
Chromium and iron were present at levels $\le$ 15% of the nickel. In the
samples from the deposition region (fig 2, position A) the metal and
hydrogen distributions extends into > 10μm. In the region E where net
erosion was measured, the depth of the metals is < 2μm with a peak at
0.3μm. At positions M & P the depth of the metals is 3-4μm. The
hydrogen and deuterium depth profiles show similar behaviour to the
metals. One surprising result is that the amount of hydrogen in the
surface is typically 10-20 times higher than the deuterium, despite the
fact that plasma operation and glow discharge cleaning over most of the
exposure period was in either deuterium or helium. Sample E, where there
is net erosion is an exception. The hydrogen may be due to adsorption of
water vapour by the deposited film on exposure to atmosphere.

3. Discussion

The experimental results were first compared with a simple
analytical model which neglects ionization in the SOL [1]. The
theoretical change in limiter dimension (Δh) has been plotted in fig 2 as
a function of position on the tile. We have taken typical experimental
values of the ion flux density (2A/cm^2) and electron temperature (50eV)
at the LCFS and have assumed an exposure time of 5×10^4 seconds,
corresponding roughly to the integrated duration of the plasma
discharges. We have also taken the e-folding distances for the fuel and
impurity particle fluxes to be equal (λ_Γ) and the electron temperature
e-folding distance, $\lambda_T = 2\lambda_\Gamma$. It has been found that the distributions
of net erosion/redeposition are insensitive to the value of λ_T, when $\lambda_T >$
λ_Γ, which is always observed. Similarly, the predicted distributions are
insensitive in the range 30 eV < T_e (a) < 100
eV, which encompasses most operating conditions in JET.

Reasonable agreement is obtained between the experimental curves
and the theoretical results in fig 1, both in the relative shape of the
erosion pattern and the absolute level. One striking disagreement occurs
in the region of the tangency point, where in the model the
erosion/redeposition approaches a null since the field lines are parallel
to the surface at this point. In contrast, the experimental results show
significant net deposition in this region which may result from
ionisation of impurities in the SOL. Net deposition near the LCFS for
the belt limiters is also in contrast with those from the discrete
limiter case, where there was net erosion at the limiter surface closest
to the plasma [1]. To assess the effect of ionisation in the SOL we have
used the Monte Carlo code, LIM [4]. Earlier calculations have shown that
ionisation in the SOL becomes significant ($\ge$ 25% of total ionisation),
when the edge density reaches a value = 3×10^{18} m^{-3}. This leads to
redeposition near the LCFS where the ionisation rate is high [5]. The
results are shown in fig 1. It is seen that net deposition does occur
near the tangency point. The reason for the difference between the belt
limiter results and the earlier discrete limiter data is probably the
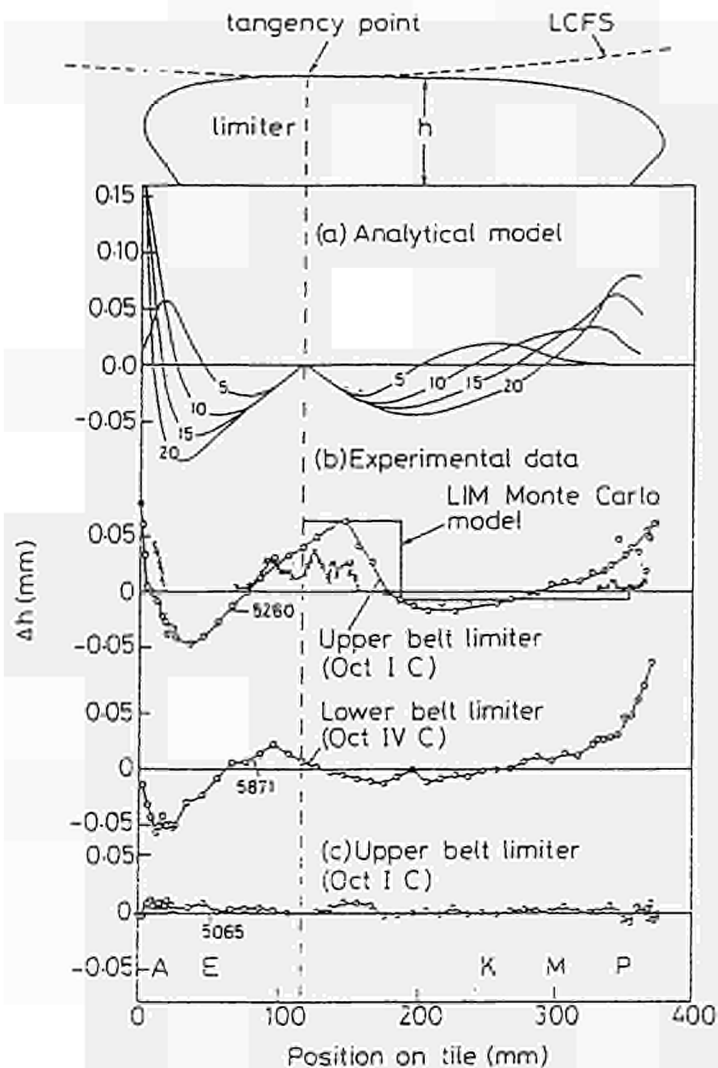higher operating density associated with high power additional heating.

No direct measurements have yet been made of erosion and deposition
on the divertor target plates. However, the spatial distribution of
deuterium, hydrogen and metal concentrations on the plates has been
studied by Martinelli [6]. Comparison of the results with present
measurements indicates that there is net erosion at the ion and electron
side separatrix with deposition elsewhere. A similar picture emerges
from the recent β back-scattering measurements [7].

Conclusions

An erosion and redeposition pattern has been observed on the JET
belt limiters. The effect is toroidally symmetric. The radial
distribution is similar to that observed for the earlier discrete
limiters, except that there is now some net deposition near the LCFS,
where previously there was net erosion. This effect is probably due to
the higher operating densities leading to ionisation in the SOL. The
effect has been modelled with the Monte Carlo code LIM and moderately
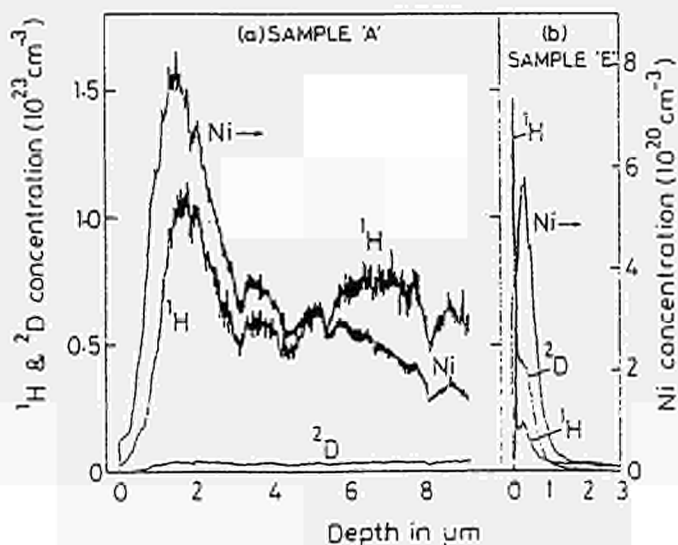good agreement with the spatial distribution has been obtained.

References

[1] G M M McCracken, O H J Goodall, P C Stangeby et al. J Nucl Mat
    163-165 (1989) to be published.
[2] K J Dietz. J Nucl Mat 155-157 (1988)8.
[3] Erents et al. J Nucl Mat 163-165 (1989) to be published.
[4] P C Stangeby, C Farrell and L Wood Contributions to Plasma Physics
    28 (1988)501.
[5] G M McCracken, P C Stangeby and C S Pitcher. Contributions to
    Plasma Physics 28 (1988) 447
[6] A P Martinelli. 16th EPS Venice 1989
[7] B Mills and D Buchenauer. Private communication. December 1988.

Figure 1. tangency point / LCFS / limiter / h
(a) Analytical model
Δh (mm)
0·15, 0·10, 0·05, 0·0, -0·05
5, 10, 15, 20
(b) Experimental data
LIM Monte Carlo model
5260
Upper belt limiter (Oct I C)
Lower belt limiter (Oct IV C)
5871
(c) Upper belt limiter (Oct I C)
5065
A E K M P
0   100   200   300   400
Position on tile (mm)

1a Calculated erosion of limiter tile using analytical model [1] which neglects ionisation in the SOL. Ion current density 2A cm^{-2} deuterons, $T_e(a)$ = 50 eV, exposure times 5 x 10^{4}s, for different λ_Γ and $\lambda_T = 2\lambda_\Gamma$.

b. Spatial distribution of erosion and redeposition on the JET belt limiter after exposure to ~ 4000 discharges in 1987-88. Physical measurements ooooo, measurements of deposition obtained by sectioning xxxx. Monte Carlo calculation using LIM code for $T_e(a)$ = 50eV λ_Γ = 20mm λ_T = 40mm $D_\perp$ = 1m^{2}s^{-1} $n_e(a)$ = 3 x 10^{18}m^{-3}

c. Distribution on belt limiter after 470 discharges; physical measurements.

Figure 2. (a) SAMPLE 'A' (b) SAMPLE 'E'
^{1}H & ^{2}D concentration (10^{23}cm^{-3})
Ni concentration (10^{20}cm^{-3})
Ni, ^{1}H, ^{2}D
Depth in μm

2. Depth distribution of nickel, hydrogen and deuterium measured on two samples; 'A' from a region of deposition; 'E' from an erosion region, see fig 1. The distributions were obtained by SIMS using a 15keV O^{2+} beam.

CORRELATION REFLECTOMETRY

P Cripwell*, A E Costley and A E Hubbard#

JET Joint Undertaking,Abingdon,Oxon,OX14 3EA,U.K.
* Imperial College of Science,Technology and Medicine, University of London,U.K.
# Centre Canadien de Fusion Magnetique, Varennes, Quebec,Canada

Introduction

The diagnosis of density microturbulence is important in the experimental investigation of the mechanisms underlying energy transport in tokamak plasmas. Scattering of coherent electromagnetic radiation (microwaves and laser light) is used to determine the power spectrum of the fluctuations at discrete values of the wavenumber k /1/. However, scattering techniques do not usually distinguish between radially and poloidally propagating waves and they do not determine the coherence length of the waves.

In this paper, we present a new technique based on microwave reflectometry for diagnosing density microturbulence /2/. We believe that the technique will provide, within certain limits, the dispersion relation and coherence length of the waves characterising the turbulence. Since the technique involves the correlation of signals from two or more reflectometers, we have termed it *correlation reflectometry*. We have constructed a preliminary correlation reflectometer and we present the first results of measurements on JET.

Principle

Two independent reflectometers operating with radiation of slightly different frequencies, f_1 and f_2, are arranged to probe the plasma along the same line of sight. The reflectometers probe density layers at R_1 and R_2, separated by a small amount Δx.

Turbulent fluctuations in the electron density give rise to rapid changes in the optical path length of the plasma arms of both reflectometers and therefore to changes in the phase of the reflected radiation. These phase changes are caused by (a) variations in the refractive index in the propagation region and (b) movement of the reflecting layer. Calculations, relevant to tokamak plasmas, have shown that (b) dominates (a) by a large factor (typically several orders of magnitude) /3/.

The fluctuations can be represented as a broadband spectrum of electrostatic waves. Each wave has a frequency ω, wavenumber k, and a finite coherence length l_c which can be defined as the length of the coherent wavetrain to the e^{-1} amplitude points. The magnitude of the fluctuating phase measured by the reflectometer operating at f_1 will therefore be:

$$\Delta\phi_1(t) = \mu \cdot \frac{4\pi f_1}{c} \sum_m \Delta L_{m1} \sin(\omega t + \delta_{m1})$$

where ΔL_{m1} is the amplitude of movement of the layer at R_1 caused by the wave m and δ_{m1} is the phase of the wave. $\mu^* = (1/2\Delta L)\int_{2\lambda_L}\mu(R) \, dR$ is the average refractive index over ΔL and, for smoothly varying density profiles, is a constant for different values of ΔL. A similar expression exists for $\Delta\phi_2$ by replacing the subscript 1 with 2.

The relative power at each frequency ω is given by the autopower spectrum denoted $G_1(\omega)$ while the power that is common to both signals is given by the crosspower spectrum $G_{1,2}(\omega)$. The full expressions for $G_1(\omega)$ and $G_{1,2}(\omega)$ are given in standard texts on spectral analysis /4/. $G_{1,2}(\omega)$ may be expressed as a complex number:

$$G_{1,2} = C_{1,2} + i.Q_{1,2}$$

where $C_{1,2}$ is the in-phase power that is common to both signals while $Q_{1,2}$ is the $\pi/2$ out of phase common power. At any given frequency the phase difference between signals common to both sets of data is given by:

$$\Theta_{1,2}(\omega) = \tan^{-1}(Q_{1,2}(\omega) / C_{1,2}(\omega))$$

The phase difference between the signals common to both sets of data is due to the propagation of the wave between R_1 and R_2 and so :

$$\Theta_{1,2}(\omega) = k(\omega).\Delta x$$

Hence, from a measurement of $\Theta_{1,2}(\omega)$ and a knowledge of Δx, we can determine k at a range of frequencies, i.e. we can determine the *dispersion relation* for the waves describing the density fluctuations. Strictly, we measure the dispersion relation of the component of k along the line of sight of the reflectometer.

In the above we have implicitly assumed that $\Delta x < l_c$, however, this may not always be the case. In fact, if f_2 is changed so as to increase Δx, then the power common to both signals will decrease as Δx becomes greater than $l_c(\omega)$. This effect may be quantified using the coherence function $\gamma^2_{1,2}$ which is a measure of the power common to both signals normalised to the total power in both signals:

$$\gamma^2_{1,2}(\omega) = \frac{|G_{1,2}(\omega)|^2}{|G_1(\omega)| \, |G_2(\omega)|}.$$

$|G_{1,2}|$ is the magnitude of the crosspower spectrum. The correlation length $l_c(\omega)$ is found by analysing the variation of $\gamma^2_{1,2}(\omega)$ with increasing Δx.

Limitations

Several effects can limit the information that can be obtained by this technique. First, the reflection does not in practice take place at a single plane but occurs over a layer of finite thickness, ΔR. This is a consequence of the fact that the refractive index goes to zero over a finite distance. It means that the technique can only be used to examine waves with $l_c \gtrsim \Delta R$.

Second, because the sets of data are finite, there will be a lower limit to the coherence which is significant. Such a limit is a statistical factor and it may be calculated accordingly. The other limits of reflectometry, for example limits of accessibility due to electron cyclotron absorption, will also apply /2/.

Preliminary Implementation

A correlation reflectometer has been constructed on JET to examine the feasibility of the technique. The reflectometer operates in the extraordinary mode and probes the plasma along a major radius in the midplane. In the experiment, the frequency of one beam was fixed at 49 GHz whilst the frequency of the second was varied in steps from 51 - 57 GHz. Signals at the two frequencies were separated using a purpose built diplexer which ensured an isolation of > 20 dB, between the channels. The fluctuating signals were detected with Schottky diode detectors and digitised with a video bandwidth of 20kHz.

A limited amount of data has been obtained on ohmic and additionally heated plasmas. Figures 1 through 4 show the crosspower spectrum, the coherence, the crossphase spectrum, and the derived dispersion curve obtained on an ohmic pulse with $B_t = 2.1$ T and $I_p = 3$ MA. For these data $f_1 = 49$ GHz, $f_2 = 51.3$ GHz, $\Delta R \cong 2$ cm, $\Delta x \cong 2$ cm and the reflectometers probed the region r/a = 0.8 where $n_e = 1.5 \, 10^{19}$ m^{-3} and $T_e = 1.2$ keV. Clear evidence for correlation is seen and we note from figure 4 that the wave phase velocity is $\cong 6.10^4$ cm.s^{-1}. When f_2 was changed to 53 GHz the correlation was significantly less, indicating that over most of the frequency range examined the correlation length for the radially going waves is in the range $2 < l_c < 4$ cm.

Conclusions

A new diagnostic technique for probing density microturbulence using microwave reflectometry appears feasible. The technique should provide the dispersion relation of radially propagating waves and, within certain limits, give an estimation of the wave correlation length. Preliminary measurements on JET under one specific ohmic plasma condition gives a wave phase velocity of 6.10^4 cm.s^{-1} and a correlation length in the range $2 < l_c < 4$ cm.

Acknowlegements

References

1. Liewer P. Nucl Fusion 25, 543,1985
2. Costley. A.E. Proc Course and Workshop, Basic and Advanced Diagnostic Techniques for Fusion Plasmas, EUR 10797, Vol 2 379 - 396, Varenna, 1986
3. Simonet F. These de Doctorat D'Etat, Universite de Nancy I : Etude de la Reflectometrie Hyperfrequence, 1985
4. Bendat and Piersol - Random Data: Analysis and Measurement Techniques, Wiley, 1971
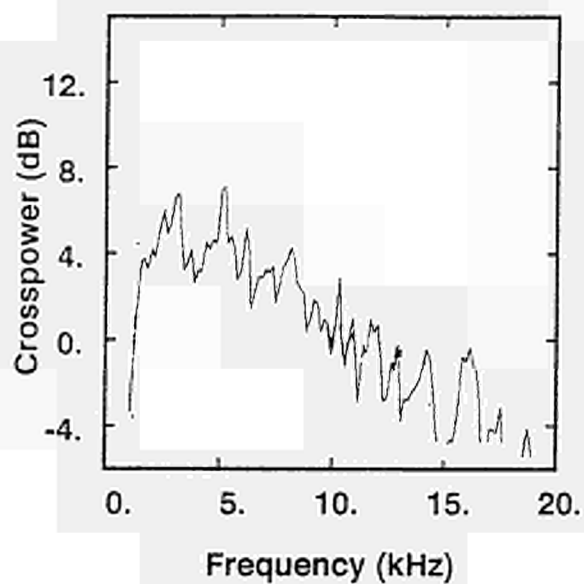
Fig 1: The crosspower spectrum of two signals when the reflectometers were tuned with their reflection layers approx 2cm apart
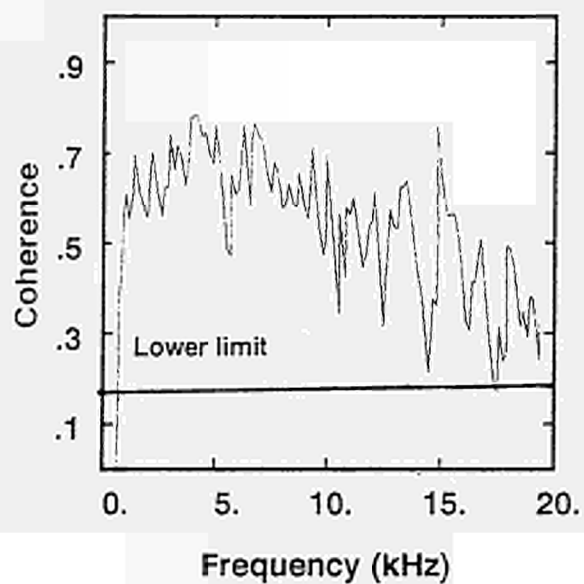

Fig 2: The derived coherence function corresponding to the the crosspower in fig 1.
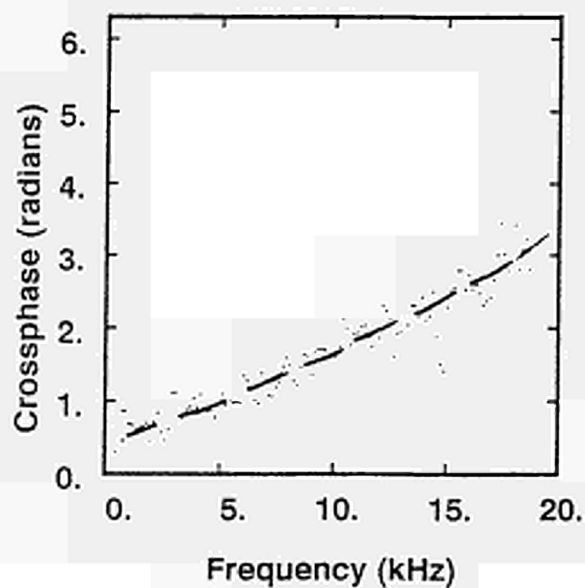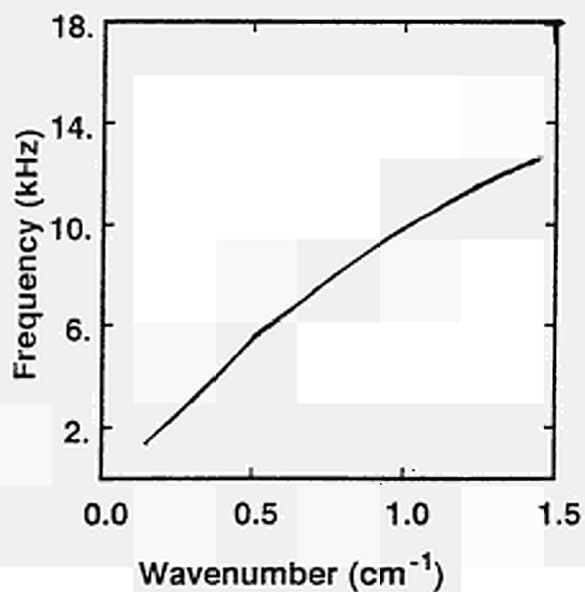

Fig 3: The crossphase spectrum

Fig4: The derived dispersion relation.

THE SCALING OF EDGE PARAMETERS IN JET WITH PLASMA INPUT POWER

* S K Erents, P J Harbour, S Clement, D D R Summers
* G M McCracken, J A Tagle and L de Kock

JET Joint Undertaking, Abingdon, Oxon, OX14 3EA, UK
* Culham Laboratory, Association UKAEA/EURATOM, Abingdon, Oxon, UK

1. Introduction

The scaling of edge parameters of density and temperature with central density and ohmic power in JET has been presented previously for the discrete limiter geometry (1) and more recently for the new belt limiter configuration, (2). However, the scaling with plasma current (I_p) is difficult to interpret because varying I_p does not only change the input power but also the safety factor qs and consequently the SOL thickness. The use of additional heating at constant current allows more direct observation of the effects of changing heating power.

In this paper we present data in which the plasma input power is increased by ICRH, (Pt < 20MW), using a 3MA target plasma, and compare data for different plasma currents using discrete and belt limiter geometries. Edge data is presented from Langmuir probes in tiles at the top of the torus, when the tokamak is operated in single null magnetic separatrix (divertor) mode, as well as for probes in the main plasma boundary to contrast these date with limiter data.

2. Diagnostics

Edge measurements are made using a reciprocating Langmuir probe at the top of the vessel, about half between X-point tile and upper belt limiter, which can cross the last closed flux surface (LCFS), defined by the limiters even in high power discharges. Details of the diagnostic are reported in (2). For measuring conditions at the target tiles during divertor operation, a poloidal array of 8 Langmuir probes, separated by ~70mm, is used, (3).

3. Limiter Fluxes

For the discrete limiter configuration, it was found that the ion saturation current I_s at the LCFS was almost independent of central density $\langle N_e \rangle$, but increased as the square of plasma current, I_p, (1). This result contrasts with belt limiter data, in which it is found that $I_s \propto I_p$. The results are illustrated in figure 1. However, the total flux to the limiters $\Gamma = I_s.A_w$ (A_w = wetted are of limiter) in both configurations is similar in both scaling and magnitude, as might be expected since it should be determined by global plasma parameters. The fact that total flux Γ scaling is similar while the flux density I_s is different is because the two configurations have different wetted areas. For the discrete limiters Aw = 2.8 λ hw (m²) where hw is the wetted height. For the belt limiters Aw = 52 λ sinθ (m2) where θ is the angle the field lines make with the limiters. For both configurations, $\lambda \propto 1/I$, but $\theta \propto 1/qs$, ie $\theta \propto I_p$. Hence for the belt limiters the wetted area is almost constant, (0.2 m²). An empirical scaling Γ = 2.4E21 I_p s-1 is found.

4. Densities and temperatures in limiter discharges

The problem of changing qs is eliminated when power is put in by means other than ohmic heating. Neutral beam heating results in a steep change in central density, and internal plasma energy, W, with Pt. This is not the case for ICRF heating in a well conditioned torus, when also a sufficiently long steady state is obtained, figure 2. For Pt = Pohm + Picrh > 5MW, $\langle Ne \rangle$ shows only a slow rise with Pt. The density at the LCFS Ne(a) on the other hand rises linearly with Pt. At low ICRH powers there is a rise in $\langle Ne \rangle$, and this is reflected in a fall in edge temperature T_e(a). However, at higher powers Te(a) also rises with Pt. The low edge temperatures (< 90eV even at 20MW) and high edge densities, are indicative of rapid re-cycling in the edge – a feedback mechanism keeping edge temperatures low.

5. Edge temperature scaling with power to the edge

The global power balance/transport model (1) predicts the approximate scaling that T_e(a) α $P_c^{\cdot \cdot \cdot}$/$\langle N_e \rangle^{\cdot \cdot}$. Experimentally for belt limiter plasmas, edge temperatures scale as T_e(a) α $\langle N_e \rangle^{\cdot \cdot}$, (2) but are generally lower than those for discrete limiter operation reported in (1). To investigate the scaling of T_e(a) with power to the edge, P_c= Pohm + Pirch.- Prad, we plot T_e(a). $\langle N_e \rangle$ versus P_c. to eliminate changes in $\langle N_e \rangle$. The results are shown in figure 3. A scaling of Te(a) α Pc$^{\cdot \cdot}$ (fitted line) is obtained for the belt limiter data. The divertor (X-point tile) 3MA ohmic data is lower, and more scattered, however scaling with P_c is inconclusive. Agreement with the simple theory is very good for these constant q_s, (I_p = 3MA) belt limiter data.

6. Power to the divertor tiles

Total power to the divertor tiles has been plotted as a function of P_c for ohmic single null discharges in figure 4. Two data sets are illustrated, the upper when the separatrix was clearly on probe 5 of the 8 probes. The power SOL thickness λ_p refers to the outer (low field side) SOL. The inner SOL has shorter λ_p, and in general a much lower fraction of the total power falls on the tiles in this region. When the null is moved poloidally to the high field side of the torus, the separatrix falls close to probe 4 or even 3, and the total power to the tiles appears to fall, (lower data set). A small error (< factor 2) may exist in absolute values of P_t due to an uncertainty in the position of the separatrix, and the collecting area of the probes. Clearly, however, for both data sets there is a shortfall of a factor 2 or more in the power to the tiles. This is consistent with both discrete and belt limiter discharge data when only 40% of available power to the edge was accounted for. The SOL thickness (110 mm) agrees well with reciprocating probe data for divertor discharges when the field line compression is taken into account in moving ~1m poloidally round the torus.

7. Conclusions

1. Total particle fluxes to limiters are similar for both discrete and belt limiter configurations, and scale linearly with plasma current.

2. Both edge density and and temperature increase as power is input to the plasma by ICRH. The linear increase in edge density due to extra influx of neutrals directly released from the wall holds temperatures to < 90 eV even at 20MW input power.

3. A temperature scaling with power close to that predicted by global power balance/transport (1) is obtained when the plasma is heated by ICRH, (T_e α $P_c^{\cdot \cdot}$).

4. Power to divertor tiles in divertor plasmas increases linearly with power to the edge, but only 50% of the power is accounted for, as in limiter discharges.

References

1. S K Erents, J A Tagle, G M McCracken, P C Stangeby and L de Kock, Nuclear Fusion 28 (1988) 1209

2. S K Erents, J A Tagle, G M McCracken, G Israel, H W Brinkschulte and L de Kock, 'The behaviour of the scrape-off layer in JET with toroidal belt limiters', J Nucl Mat 163-165 (1989 to be published.

3. P J Harbour et al, 'The behaviour of the scrape-off plasma during X-point discharges in JET with L- and H-modes'. J Nucl Mat 163-165 (1989) to be published.
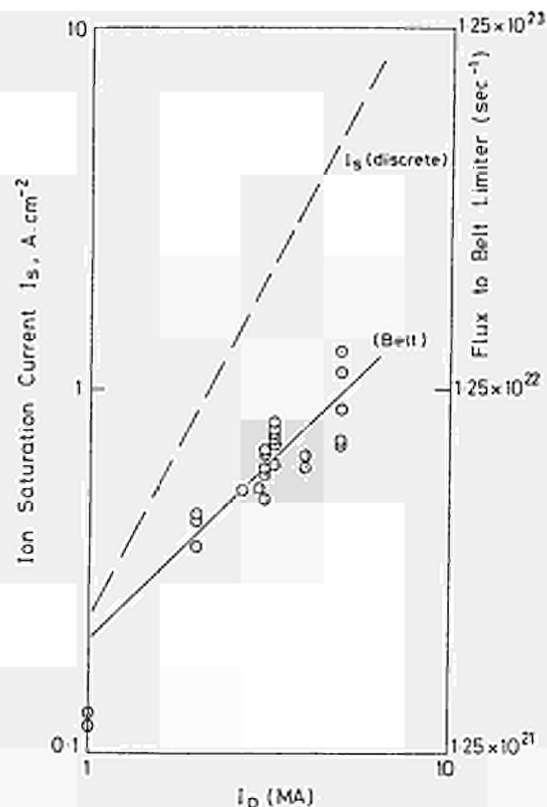
FIGURE 1. SCALING OF ION SATURATION CURRENT WITH PLASMA CURRENT FOR DISCRETE AND BELT LIMITERS.
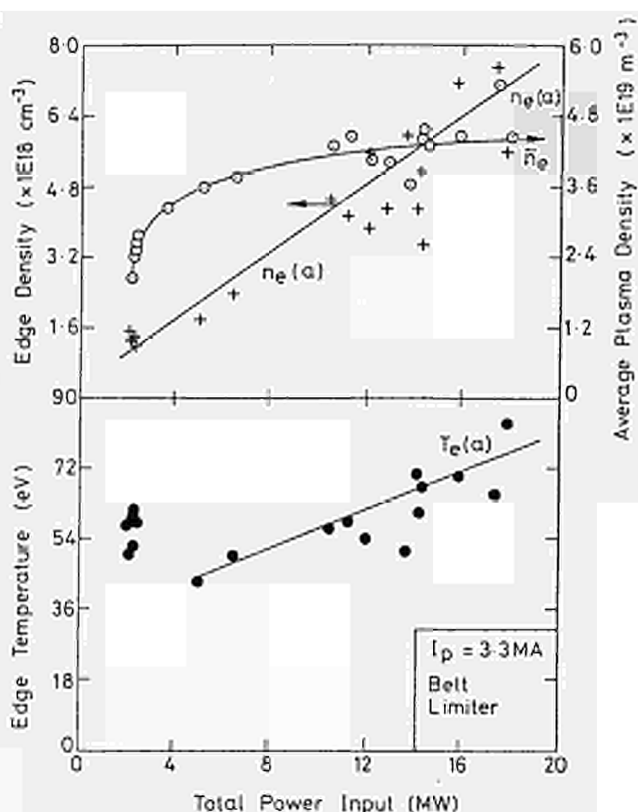

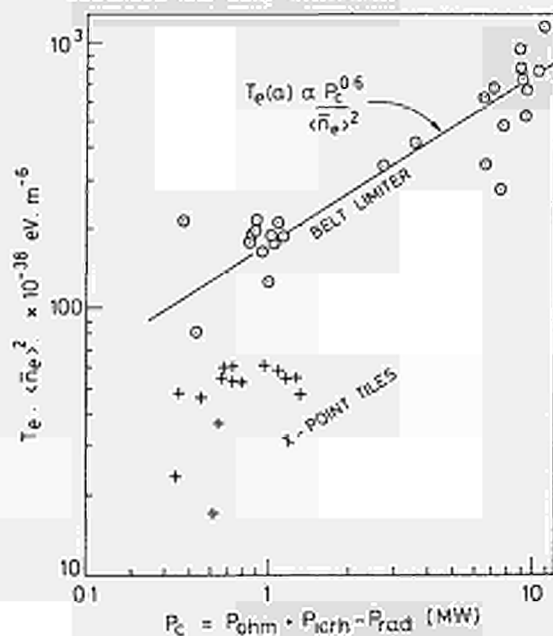FIGURE 2. EFFECT OF ICRH POWER ON EDGE DENSITY AND TEMPERATURE.

FIGURE 3. SCALING OF EDGE TEMPERATURE WITH POWER TO THE EDGE FOR LIMITER AND DIVERTOR (X-POINT) PLASMAS.
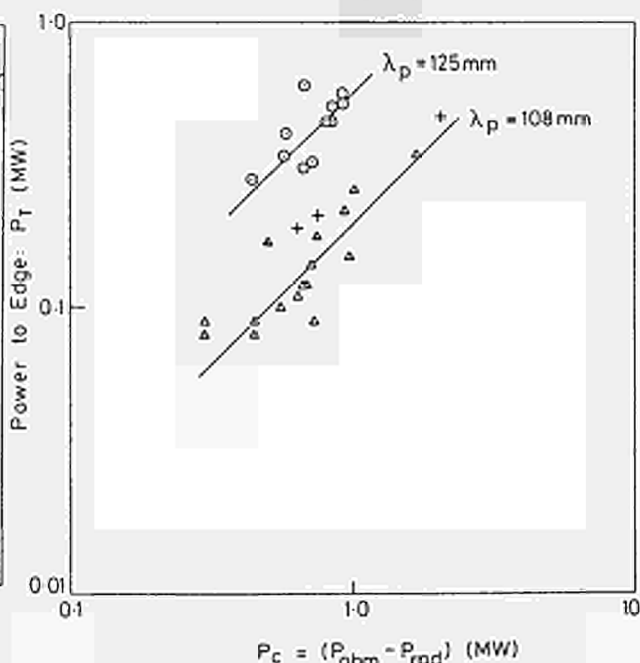

FIGURE 4. POWER SCALING TO DIVERTOR TILES DURING SINGLE NULL DIVERTOR OPERATION.

IMPROVED CONFINEMENT IN L-MODE JET PLASMAS

T T C Jones, B Balet, V Bhatnagar, D Boyd[1], M Bures, D J Campbell,
J P Christiansen, J G Cordey, W F Core, S Corti, A E Costley,
G A Cottrell, A Edwards, J Ehrenberg, J Jacquinot, P Lallia, P J Lomas,
C Lowry, M Malacarne, D G Muir, M F Nave, P Nielsen, C Sack, G Sadler,
D F H Start, A Taroni, P R Thomas, K Thomsen

JET Joint Undertaking, Abingdon, Oxon, OX14 3EA, UK
[1]University of Maryland, College Park, MD20742, USA

1. Introduction

The JET confinement data show considerable variations of stored plasma energy W (thermal + fast ions) at fixed input power P, plasma current I, toroidal field B and plasma configuration C. The data on confinement properties, e.g. the confinement time τ_E or its incremental value $\tau_E(inc)$, derived from variations of P at fixed I, B, C thus exhibit scatter which makes the scaling of τ_E with P, I, B, C difficult to establish. The effects from sawteeth, from variations in the power deposition profiles and from plasma edge physics on confinement do not depend on P, I, B, C in any simple way which would permit a deduced scaling law to be identified with a single (or more) physics loss mechanism(s). In this paper we examine the response of confinement to variations in plasma configuration at fixed I and B (3 MA and 3 T). Results from global and local transport analysis are discussed in sections 2 and 3; section 4 describes the role of fast ions produced by ICRF and NBI heating. High confinement in the L-mode regime at increased plasma currents up to 6 MA is also studied, in particular the effects from sawteeth on stored energy W. Such effects increase with current and presently only predictive transport studies (section 5) can estimate what may be achieved at high current without sawteeth effects. The predictive studies also assess the benefits which may arise from an increase of the neutral beam energy at high plasma currents (section 6). The conclusions are based on an extensive study of data from JET pulses with up to 14 MW of ICRH, 21 MW of NBI and 6 MW of ohmic power. None of the pulses included in the study show the sudden reduction of D_α emission characteristic of the L to H mode transition of confinement.

2. JET plasma configurations

At fixed current (3 MA) and field (3 T) JET has been operated with several plasma configurations which are labelled as follows: LIM, a plasma attached to one or both of the belt limiters; IWL, a plasma attached to the inner vessel wall; DN, an up-down symmetric plasma with a separatrix inside the vessel. Up to 21 MW of NBI power has been applied to all configurations while only the DN and LIM configurations have had more than 10 MW of ICRH either alone or combined with NBI. Fig.1 presents a subset of the JET confinement data at 3 MA; the subset includes data from power scans in which the ICRH power does not exceed 50% of the total input power. Each data point in Fig.1 corresponds to the value of confinement time τ_E and power P measured at the maximum of W (inferred from the diamagnetic loop diagnostic). When $W = W_{max}$, dW/dt is small such that the data in Fig.1 should represent steady state values. The various symbols refer to the different configurations described above. The solid line shows the variation of τ_{EG} with P derived from the Goldston scaling law [1]. In general the highest τ_E values occur in the DN configuration in which sawteeth are suppressed by ICRH; such high values are comparable with those obtained in JET H-mode plasmas [2].

3. Local transport calculations

Those JET pulses which exhibit L-mode high confinement, are studied by predictive transport calculations. The calculations employ electron and ion heat fluxes represented either by the Rebut-Lallia model [3] or a modified model appropriate to H-mode confinement [4]. The profiles of electron and ion heating rates from NBI and ICRH are calculated by the PENCIL and QFLUX codes; the profile of radiated power is obtained by Abel inversion of bolometer data. In order to match the predicted to the measured temperature profile, when $\tau_E > \tau_{EG}$, it is necessary to employ the H-mode model for the heat flux.

4. Fast ion energy

High values of τ_E are reached usually in the DN configuration if the initial (target) density is low (of order $10^{19}/m^3$). Application of ICRH to such a target establishes a population of high perpendicular energy (~ 1 Mev) minority H ions which heat the electrons to temperatures in excess of 10 keV. This population exists for several confinement times in the centre of the plasma (where the ICRF resonance position is located); the absence of sawtooth crashes maintains this population. A second population of fast D ions is generated by neutral beam injection. While the energy content of the anisotropic H minority ions can be estimated from two magnetic energy measurements, that of the nearly isotropic NBI generated D ions can not. In order to evaluate the total fast ion energy content full transport calculations with the TRANSP interpretation code have been performed for a few high τ_E pulses. The calculations confirm that the thermal energy content $W_{th} = W - W_{fast}$ is still above the value W_G obtained from the Goldston scaling law [1]. Fig.2 shows values of W_{kin} vs P. W_{kin} is the plasma thermal energy content derived from kinetic measurements of ion and electron temperature and electron density. Fig.2 also confirms that the 3 MA DN data shows an improvement in confinement over the Goldston scaling.

5. Sawteeth effects at 3, 5, 6 MA

Fig.3 shows variations of W with P for selected 3, 5 and 6 MA pulses. It can be seen that doubling I from 3 to 6 MA does not double W as suggested in earlier scalings [5]. The stored energy W at 5 and 6 MA is affected more strongly by sawteeth than at 3 MA. The stored energy W increases with current I since the field is fixed at ~ 3 T. A sawtooth collapse reduces the thermal energy content inside the inversion radius and it also reduces the fast ion energy [6]. The reduced performance due to sawteeth can be modelled by predictive transport calculations. The sawtooth effects are taken into account by enhancing the heat transport coefficient in the sawtooth region to a Bohm-like value. The heat fluxes are otherwise given by the Rebut-Lallia model [3]. Fig.4 demonstrates how the time evolution of total stored energy W for a 6 MA JET discharge would improve if sawteeth were stabilised. The increase in W that would arise at 5, 6 and 7 MA is likely to restore the dependence of W (or τ_E) upon I previously reported [5]; presently such an improvement remains however a conjecture.

6. Beam deposition profiles and the effect of radiated power

The efficiency of NBI heating as defined in [7] reduces with increasing plasma density n, due to poorer beam penetration. The efficiency at a fixed beam energy of 80 keV is lower at 6 MA than at 3 MA due to the increased density associated with high plasma current. Calculations show that increasing the D° beam energy to 140 keV would be sufficient to yield a peaked deposition profile in a 6 MA plasma provided the density can be controlled during injection. However, local transport calculations at 6 MA indicate that a more peaked power deposition profile will be beneficial only if the deleterious effects of sawteeth can be eliminated. The importance of power radiated from the plasma core has also been examined for high current discharges; local transport calculations indicate that it does not contribute more than $\sim 10\%$ to the confinement degradation.

7. Conclusions

The DN configuration at 3 MA is found to exhibit confinement properties better than those predicted by the scaling law proposed in [1]. The favourable current dependence implied in the Goldston scaling is however not established by the present data from JET high current discharges. The departure from the scaling law is attributed to sawteeth effects; elimination of sawteeth at high current should yield high confinement as demonstrated by the predictive calculations.

References
[1] R J Goldston, Plasma Physics and Controlled Fusion 126 p87 (1984).
[2] M Keilhacker, IAEA-CN-5D/A-III-2, Nice (1988).
[3] P-H Rebut et al, IAEA-CN-5O/D-4-1, Nice (1988).
[4] P-H Rebut et al, Proc XV EPS Conf. on Controlled Fusion and Plasma Physics, Vol I p247, Dubrovnik (1988).
[5] J G Cordey et al, IAEA-CN-47/A-II-3, Kyoto (1986)
[6] V Bhatnagar et al, this Conference.
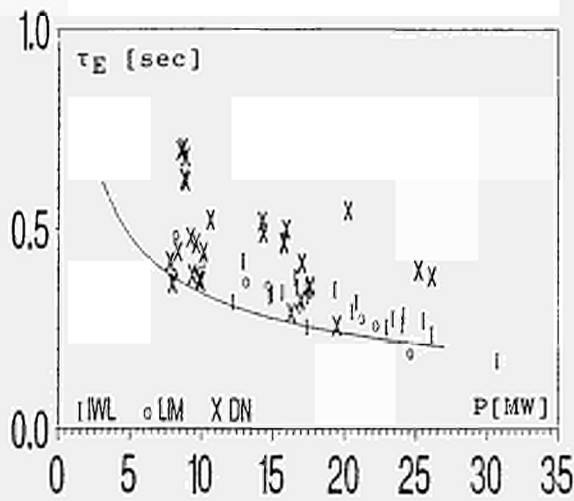[7] J D Callen et al, Nucl. Fusion 27 p 1857 (1987).

Fig.1 Confinement time τ_E vs P at various 3 MA configurations.   Solid line represents Goldston scaling [1].
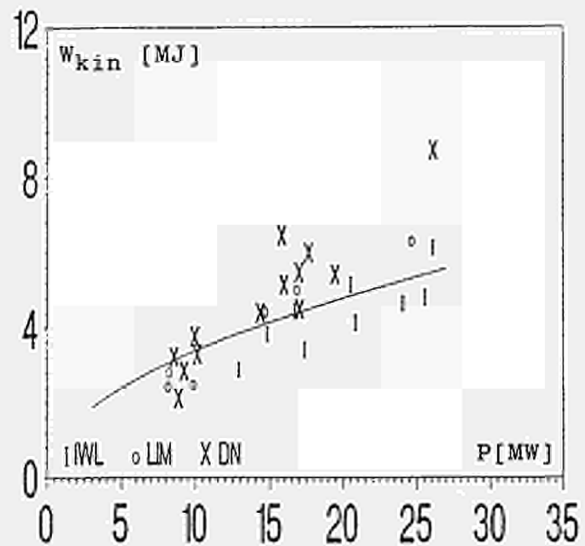

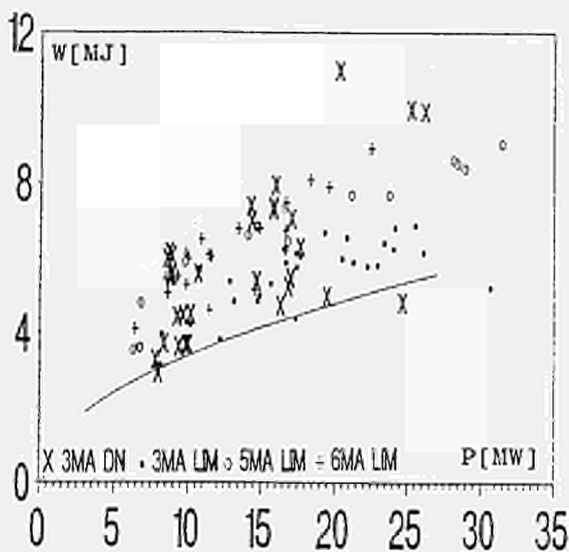Fig.2 W_{kin} vs P at various 3 MA configurations. Solid line as in Fig.1.

Fig.3 Total energy W vs P for selected 3, 5 and 6 MA pulses. Solid line represents Goldston scaling [1] at I = 3 MA, broken line at I = 6 MA.
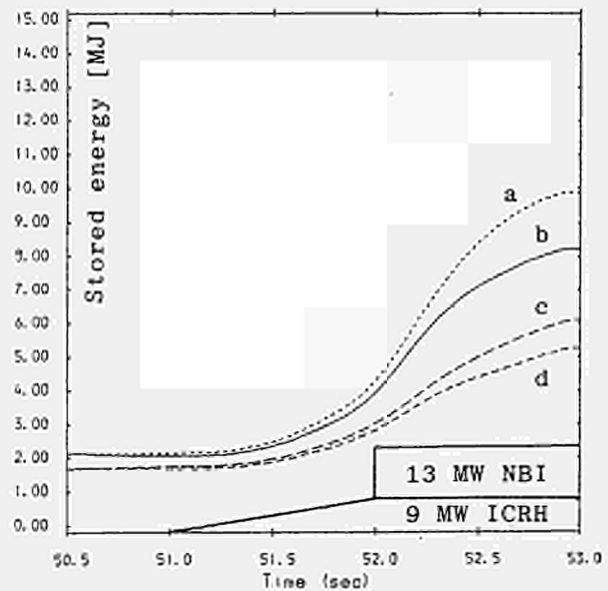

Fig.4 Calculated stored energies vs time from predictive simulations based on Rebut-Lallia transport model [3] in a 6 MA pulse: a, total stored energy without sawteeth; b, as a with sawteeth effects; c, electron stored energy without sawteeth; d, as c with sawteeth effects.

BALLOONING STABILITY ANALYSIS OF JET H-MODE DISCHARGES

D.P. O'Brien, C.M. Bishop#, R. Galvao,
M. Keilhacker, E. Lazzaro, M.L. Watkins

JET Joint Undertaking, Abingdon, Oxon. OX14 3EA, UK
#UKAEA Culham Laboratory, Abingdon, Oxon. OX14 3DB, UK

1. Introduction

Previous studies [1] of the stability of a large aspect ratio model equilibrium to ideal MHD ballooning modes have shown that across the bulk of the plasma there exist two marginally stable values of the pressure gradient parameter α. These define an unstable zone which separates the first (small α) stable region from the second (large α) stable region. Close to the separatrix, however, the first and second regions can coalesce when the surface averaged current density, Λ, exceeds a critical value. The plasma in this region is then stable to ballooning modes at all values of the pressure gradient. In this paper we extend these results to JET H-mode equilibria using a finite aspect ratio ballooning formalism, and assess the relevance of ideal ballooning stability in these discharges. In particular we analyse shot 15894 at time 56 sec. which is 1.3 s into the H-phase.

2. Equilibrium and Stability

Stability information is obtained by solving the ballooning equation separately on each flux surface. The geometry of the surface, and the distribution of poloidal field, are obtained from an equilibrium reconstruction using the IDENTC code. This code generates a best fit to the experimental magnetic and kinetic data, subject to the constraints of MHD equilibrium [2]. However, since the reconstruction procedure requires zero current density of the boundary, values for Λ have been taken from transport calculations performed by the TRANSP code [3]. This gives a profile of current density J from which Λ can be calculated using

$$\Lambda = 2J/\langle J \rangle$$

where J is the surface average of J, and $\langle J \rangle$ is the average of J over the enclosed volume. A plot of Λ against minor radius for shot 15894 is shown in Figure 1. In the edge region of an H-mode plasma the dominant contribution comes from the bootstrap current due to the presence of a steep density gradient [4]. The corresponding steep edge gradient in the electron pressure is clearly seen from the ECE and FIR interferometer data, and LIDAR data (Figure 2). In the ballooning equation the pressure gradient parameter α is treated as an eigenvalue for each flux surface, and the equation solved to give the marginally stable value of α.

3. Results of the stability analysis

Figure 2 shows a plot of α versus minor radius for the H-mode discharge #15,894. In the interior of the plasma we see the existence of first and second stable regions separated by an unstable zone, while close to the separatrix the first and second regions coalesce. It is important to note that this graph has been plotted using the experimental value of Λ on each flux surface, as given by Figure 1. The second stability boundary is very sensitive both to Λ and to the modulation of the poloidal field around the flux surface. For increasing values of the flux surface label ψ the second marginally stable α increases initially as Λ falls. Closer to the edge, however, the combined effects of poloidal field modulation (due to proximity to the separatrix), together with an increasing Λ, cause the second stable α to fall sharply, so that coalescence occurs in the edge region.

The effects of varying Λ (while retaining the flux surface shape and poloidal field) are shown in the α-Λ diagram of Figure 4. The vertical line shows the experimental value of Λ in the H-mode. At smaller values of Λ, as would occur in L-mode plasmas (which do not exhibit the steep edge density gradient) there is no coalescence, and the first and second regions are separated by a large unstable zone.

4. Comparison with experimental pressure profiles

These results have been compared with experimental values of the pressure gradient determined from the LIDAR Thomson scattering diagnostic, with electron pressures scaled by a factor 2 to account for the ion pressure contribution. Over the bulk of the plasma these give values of α = 0.2 which lie, as expected, in the first region of stability. Near the separatrix, however, the steep pressure gradients (electron pressure gradients = 150 kPa m⁻¹) lead to experimental values of α which increase sharply towards those determined for the first stability boundary, so that at r = 0.9m we obtain α = 0.75. This shows the relevance of ideal ballooning stability in H-mode discharges. Although these results do not show edge gradients in the coalesced region, as considered in ref.[1], it should be noted that because of limited spatial resolution (0.09 m using the convolution technique), the LIDAR diagnostic may be unable to measure the very short gradient scale lengths which appear to be characteristic of the edge region of an H-mode plasma. In particular the edge gradient of the LIDAR profile shown in Figure 2 has a scale length of about 0.1 m. The experimental values of pressure gradient in the edge region should therefore be regarded as lower bounds on the true values. Furthermore, the values of Λ close to the edge are determined by the bootstrap current, and hence by the density gradient, and so may also have been underestimated.

Conclusions

We have analysed the ballooning stability properties of JET H-mode shot 15894. Across the bulk of the plasma there exist two stable regions separated by an unstable zone. Close to the separatrix, however, we have found that the current density exceeds the critical value required for coalescence of the first and second stable regions. It has been suggested [1] that this coalescence phenomenon is associated with the transition from L-mode into H-mode. Experimentally determined values of the pressure gradient in the edge region lie somewhat below the coalesced region. However, these values may have been underestimated due to the limited spatial resolution of the LIDAR diagnostic.

REFERENCES

[1] C.M. Bishop, Nucl. Fusion 26 (1986) 1063.
[2] J. Blum, J. Gilbert, B. Thooris, JET contract JT3/9008 (1985).
[3] P. Stubberfield et al., This Conference.
[4] J.G. Cordey et al., Plas. Phys. and Contr. Fus., 30 (1988) 1625.

Figure Captions

Fig. 1 Current density parameter Λ as a function of normalized flux from centre to edge of plasma.

Fig. 2 Comparison of electron pressure profiles from ECE (used as input for TRANSP) and from the LIDAR diagnostic (upper curve) for shot 15894.

Fig. 3 Pressure gradient parameter α as a function of normalized flux from ψ = .5 to ψ = 1 (plasma edge).

Fig. 4 Sensitivity analysis of α as a function of Λ on a surface approximately 1 cm from edge of plasma.
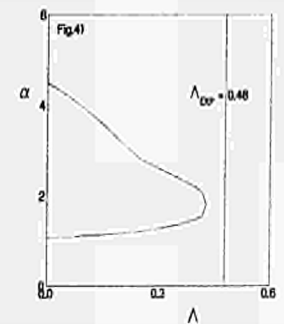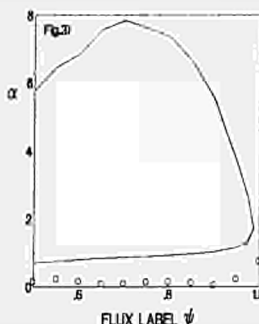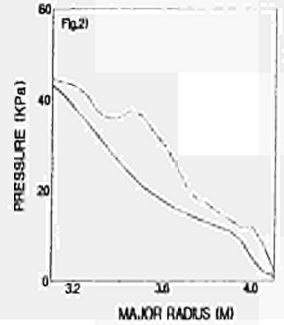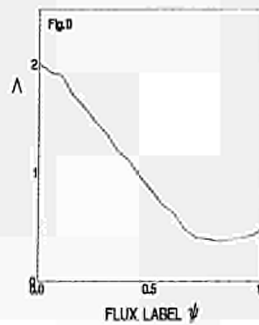
M.F.F.Nave¹, D.Campbell,E.Joffrin,F.Pegoraro,F.Porcelli,
P.Smeulders,K.Thomsen

JET Joint Undertaking, Abingdon, Oxon, U.K.
¹ Laboratorio Nacional de Engenharia e Tecnologia Industrial, Sacavem, Portugal

Introduction

A variety of MHD activity has been observed in JET during auxiliary heating experiments. In particular, periodic bursts of oscillations detected in several diagnostics show signatures similar to that of the 'fishbone' instabilities [1]. Here we describe the characteristics of these instabilities, discuss the operating conditions under which they are observed, and compare these with the predictions of theory.

Observations

Additional heating experiments in JET have been carried out at total powers of up to 34MW. Two methods of auxiliary heating are employed: (co-directional) neutral beam injection (NBI), with up to 21MW of 80keV deuterons, and ion cyclotron resonance heating (ICRH) using (mainly) first harmonic heating of a minority species (H or ³He) at powers up to 18MW. Both types of heating produce fishbone-like bursts. We believe that this is the first observation of such bursts in radio frequency heated plasmas.

'Fishbones' in JET occur as repetitive bursts lasting a few milliseconds, with a repetition time of ~ 10ms and are observed in electron cyclotron emission (ECE), soft X-rays (SXR) and magnetics diagnostics (figure 1). Sometimes continuous MHD oscillations are observed instead (figure 1). Both forms of activity are usually superimposed on sawtooth oscillations, although in a few cases bursts have been observed during the sawteeth-free periods [2].

The frequency of the observed oscillations lies typically in the range 6-10 kHz for both ICRH and NBI discharges.(There are however exceptions of ICRH discharges with very low frequencies of ~ 1kHz and NBI discharges with frequencies as high as 20kHz). A typical burst and its frequency spectrum are shown in figure 2. For the NBI discharges, the frequency of the oscillations is of the order of the bulk rotation frequency, as determined by X-ray spectroscopy of Doppler-shifted impurity emission lines. However, such high frequency in the ICRH case is difficult to explain by the plasma rotation velocity. In these discharges it has also been observed that the frequency of the fishbone-like oscillation is ~ 3 times higher than the frequency of sawtooth precursor activity which is usually of the same order as the bulk rotation frequency [3]. Perhaps the closest similarity between our observations and those reported from PDX [1] lies in the observed slowing down of the frequency of the MHD oscillation during a burst. It is found that the the decrease in frequency is faster when the the plasma current is higher. Magnetic mode analysis in ICRH and NBI discharges reveals an n = 1 toroidal component rotating in the direction of the plasma current, which is also in the direction of the ion diamagnetic drift. Magnetic poloidal structure cannot be precisely estimated, but tomographic reconstruction of soft X-rays (figure 3) and ECE signals shows an m = 1 kink centered on the sawtooth inversion radius. An m = 2, n = 1 component has also been observed outside the sawtooth inversion radius.

While the MHD characteristics of this activity exhibit similarities with those observed in PDX discharges, analysis of the effects of these bursts on fast particle populations in JET plasmas reveals no significant modification of the high energy plasma component which could be associated with the bursts (figure 4). The two principal diagnostics of fast particle distributions in JET are the neutral particle analyser (NPA) and the total neutron yield. Both show the influence of sawteeth and subordinate relaxations, the former by an enhanced level of charge exchange neutral losses following a sawtooth collapse, and the latter through a sawtooth modulation of the total neutron emission. However, no such effects are observed during fishbone-like bursts, at least not within the time resolution of the relevant diagnostics. It is possible that the larger size of the JET plasma leads to confinement of the fast particles which are predicted to be resonantly scattered by the instability [4,5]. An alternative explanation migth be the low amplitude of the poloidal field fluctuation associated with the bursts ($b_p/B_p \sim 10^4 - 3 \times 10^4$). It should be noted that a fall in neutron

production is observed during continuous MHD activity. However, this can probably be explained as a result of the observed decrease in temperature associated with such activity.

Fishbone-like bursts are observed over a wide range of the JET operating space. They occur in both the I and II confinement regimes and are more common at low values of the edge safety factor q (or high values of plasma current). Since $\beta_p \propto I_p^{-2}$, the rather unexpected result is that this activity is often observed at low rather than high values of β_p, though there appear to be a threshold value of $\beta_p \sim 0.1$ for their occurrence (figure 5). It has also been observed that the fishbone-like activity occurs at low β_p compared to that of sawtooth-free regimes. The influence of the bursts on plasma confinement is still being assessed. While, in certain regimes, high current discharges are found to have lower confinement than that predicted by the Goldston L-mode scaling, it is not clear that this should be associated with enhanced levels of MHD activity, rather than, say, heating deposition profile effects.

Theoretical considerations

Theory models [4,5] suggest that the fishbone instability is caused by the resonance between an m = 1, n = 1 mode and trapped energetic ions inside the q = 1 surface. These trapped energetic ions can be either produced by neutral beam injection or can be accelerated by ICRH waves.

It has been recently shown [6] that fishbones and sawtooth supression in the presence of energetic ions are intrinsically related as both phenomena can be explained in terms of a single dispersion relation encompassing the resonant and non-resonant fast ion contributions. This is illustrated by fig.6, representing the stability plane identified by the parameters

$$ \beta_p^* = -8\pi \; (r_0^2 \; B_0^2 \; (r_0))\int_0^{r_n} dr \; r^2 \; dp \; dr \quad , \quad \beta_{ph}^* = -8\pi \; .(r_0^2 \; B_0^2 \; (r_0))\int_0^{r_n} dr \; r^{1.2} \; d(r^{1.2} \; p) \; dr $$

where β_p^* is the beta poloidal of the bulk plasma , and β_{ph}^* is the beta poloidal of the hot ions, both calculated at the position of the q = 1 surface, $q(r_0) = 1$. The stable regime lies below the solid line,extending to values of β_p^* as high as three times the ideal MHD m = 1 instability threshold, β_p^{mhd} .7 (in fig.6 we have assumed $\beta_p^{mhd} = 0.2$). Fishbone oscillations are excited just outside the stable domain. The fishbone frequency in the plasma rest frame is predicted to range between the ion diamagnetic frequency, $\omega_{*i} = (cT_i \; (eBr_p \; p))$ dp dr ,for low values of β_{ph}^* .5 , and the fast trapped ion precession frequency, $\overline{\omega}_{Dh} = c \; E_h \; (eBr_0 \; R_0)$ with E_h the average fast ion energy, for high values of β_{ph}^* .4". Further away from the stable domain (i.e. outside of the dashed lines in fig.6) ideal MHD internal kink are unstable. (Values of r_0 ,a = 0.4 and of $\omega_{*i} \; \overline{\omega}_{Dh} = 0.2$ have been assumed in fig.6.) The stable domain shrinks considerably as the q = 1 radius is increased. In addition β_p^{mhd} is lower at large r_0 ,7. These considerations may account for the increasing difficulty in stabilishg sawteeth and for the more likely occurrence of fishbones at high currents, as roughly $r_0 \propto 1$ q. Also, for comparable values of β_{ph}^* , fishbones on the high frequency side of the spectrum can be expected to be more easily excited at high currents. The stable domain disappears as ω_{*i} becomes comparable to $\overline{\omega}_{Dh}$. Then, the fishbone frequency becomes tied to ω_{*i} (The conditions for fishbones excitation in this regime have been discussed in Ref.5.).

Comparison between the theory and the experimental results is complex because of the difficulties associated with the determination of the fast ion profiles (entering β_{ph}^* ; note that the pressure of the fast ions can be slightly hollow near the axis for the minority ions, specially during off-axis ICRH heating), and the plasma gradients at the q = 1 surface. In addition, the plasma rotation frequency ,which accounts for a Doppler shift in the predicted mode frequency, is estimated with uncertainties. Here we shall mention three examples:

(i) a slow frequency ICRH pulse (#14010, $P_{RF} \approx 7MW$, $I_p \approx 3MA$),
where $\omega_{*i} \approx 3 \times 10^3 \; s^{-1}$, $\overline{\omega}_{Dh} \approx 5 \times 10^4 \; s^{-1}$ (assuming $E_h \approx 0.5 \; MeV$) and $\omega \approx 2.5 \times 10^3 \; s^{-1}$;

(ii) a combined ICRH + NBI pulse (#15750, $P_{RF} \approx 8MW$, $P_{NBI} \approx 5MW$, $I_p \approx 6MA$),
where $\omega_{*i} \approx 0.8 \times 10^3 \; s^{-1}$, $\overline{\omega}_{Dh} \approx 7 \times 10^4 \; s^{-1}$ (assuming $E_h \approx 0.5 \; MeV$) and $\omega \approx 1.6 \times 10^4 \; s^{-1}$; and

(iii) an NBI pulse (#16883, $P_{NBI} \approx 13MW$, $I_p \approx 4MA$),
where $\omega_{*i} \approx 7 \times 10^3 \; s^{-1}$, $\overline{\omega}_{Dh} \approx 1 \times 10^4 \; s^{-1}$ (assuming $E_h \approx 40 \; keV$) and $\omega \approx 5.6 \times 10^4 \; s^{-1}$

In example (i) we have an ICRH discharge consistent with values of β_p^* and β_{ph}^* to the left of the stable domain, where the predicted frequency is $\omega \sim \omega_{*i}$ .In the NBI examples (ii) and (iii), ω is of the order of the plasma rotation frequency, so the corresponding mode frequency in the plasma rest frame is difficult to determine. The second example shows an intermediate frequency, $\omega_{*i} < \omega < \omega_{Dh}$ .In the third case, the frequency is higher than the characteristic frequencies. However since $\overline{\omega}_{Dh} \sim \omega_{Dh}$, the expected rest frame frequency is also of the same order.

References

/1/ K. McGuire et al., Phys. Rev. Lett. 50,891 (1983)
/2/ D.J. Campbell et al., Phys. Rev. Lett. 60, 2148 (1988)
/3/ D. Stork et al., Procc. 14th EPS Conference vol.I, p.306 (1987)
/4/ L.Chen, L.B. White and M.N.Rosenbluth, Phys. Rev. Lett. 52, 1122 (1984)
/5/ B. Coppi and F. Porcelli, Phys. Rev. Lett. 57, 2722 (1986)
/6/ F. Pegoraro et al., IAEA-CN-50/D-4-6 (Nice, 12-19 October 1988)
/7/ M.N.Bussac et al., Phys. Rev.Lett. 35, 1638 (1975)

Figure captions

Figure 1 - Temperature and ICRH power versus time for a discharge showing both bursts and continuous oscillations. Both types of activity are out of phase on each side of the centre indicating an m = 1 mode.

Figure 2 - Magnetic signal of a fishbone-like event and its power spectrum showing a peak frequency at 9kHz.

Figure 3 - Soft X-ray emission reconstruction showing an m = 1 structure associated with a fishbone-like oscillation.

Figure 4 - Neutron flux and temperature versus time. No change in Φ_n is observed associated to the bursts seen in the T_c trace.

Figure 5 - Total diamagnetic beta poloidal versus the total input power for fishbone-like events observed during the first 6 months of 1988.

Figure 6 - Stability regimes in the β_p^* - β_{ph}^* plane (see definitions in the text). The 'stable' area corresponds to the sawtooth-free domain, outside of which the fishbone domains are indicated.
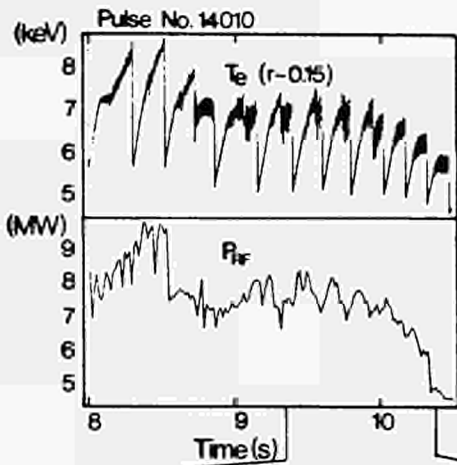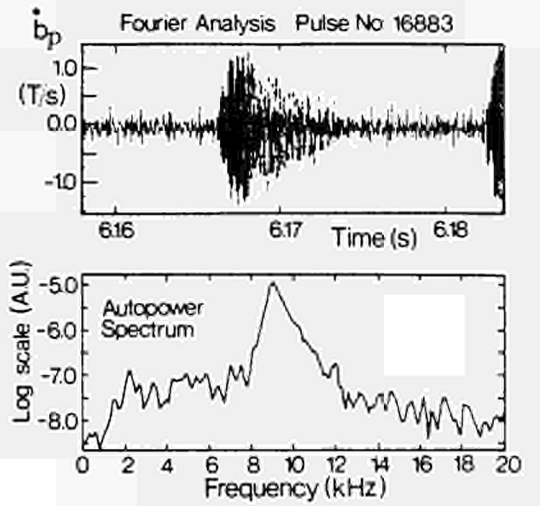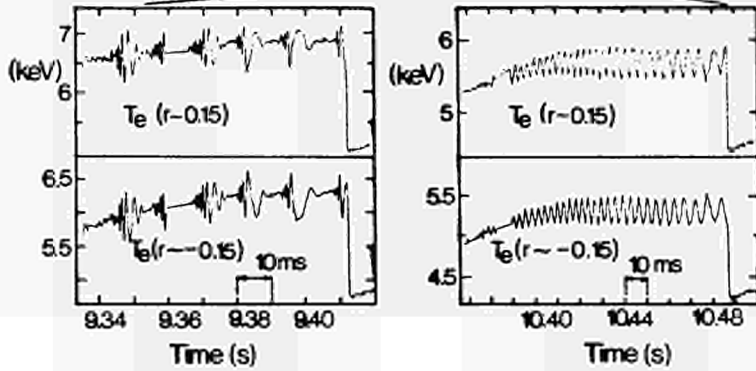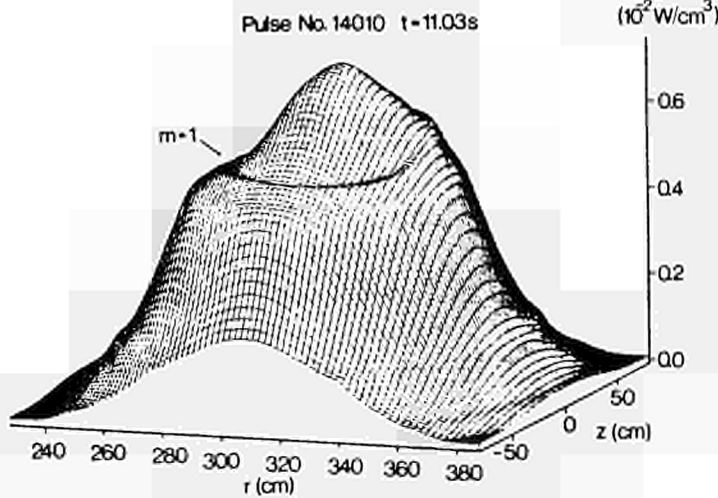
Figure 1

Pulse No. 14010

(keV)
T_e (r~0.15)
8
7
6
5

(MW)
P_{RF}
9
8
7
6
5

8   9   10
Time (s)

(keV)
7
6
T_e (r~0.15)

6.5
5.5
T_e(r~-0.15)   10ms

9.34   9.36   9.38   9.40
Time (s)

(keV)
6
5
T_e (r~0.15)

5.5
4.5
T_e (r~-0.15)   10ms

10.40   10.44   10.48
Time (s)

$\dot{b}_p$ Fourier Analysis   Pulse No 16883

(T/s)
1.0
0.0
-1.0

6.16   6.17   Time (s)   6.18

-5.0   Autopower
-6.0   Spectrum
-7.0
-8.0

Log scale (A.U.)

0   2   4   6   8   10   12   14   16   18   20
Frequency (kHz)

Figure 2

Pulse No. 14010   t=11.03s

I
$(10^2 W/cm^3)$
0.6
0.4
0.2
0.0

m=1

240   260   280   300   320   340   360   380
r (cm)

50
0
-50
z (cm)

Figure 3

(A.U.)   Pulse No 14055
0.10
0.08
0.06

Φ_n (r~0.15m)

(keV)
7
6
5

T_e (r~0.15m)

10.7   10.8
Time (s)

Figure 4

β_p
0.5
0.4
0.3
0.2
0.1
0.0

* NB
◇ NBRF
× RF

0   5   10   15   20   25   30
P_{total} Figure 5

β_p^*
0.6
0.4
0.2

fishbones with $\omega \sim \omega_{*i}$

Stable

fishbones with $\omega \sim \omega_{Di}$

0   0.02   0.04   0.06   0.08   0.10
β_{ph}^* Figure 6
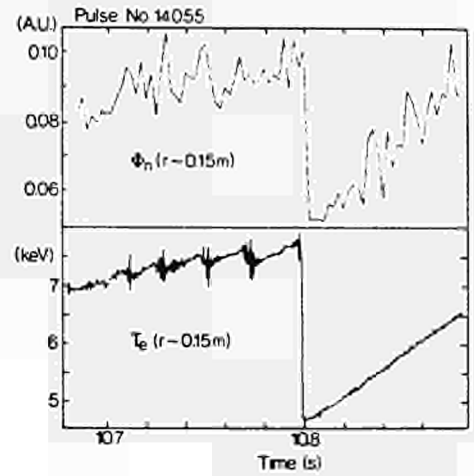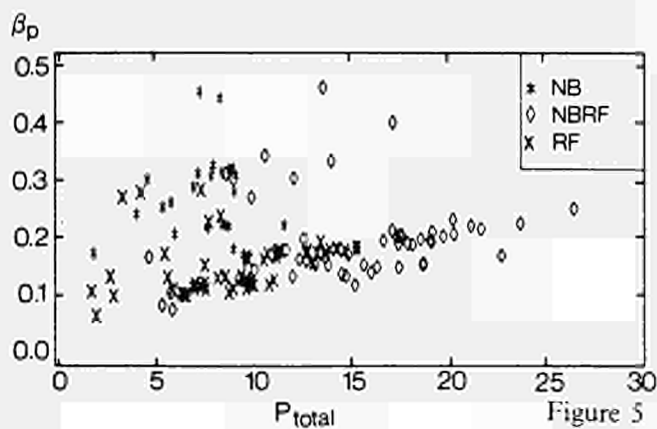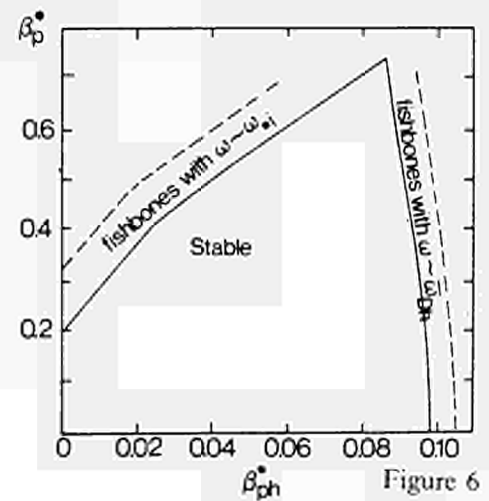
A76

SUMMARY OF ENERGY AND PARTICLE CONFINEMENT IN PELLET-FUELLED, AUXILIARY-HEATED DISCHARGES ON JET*

S.L. Milora[1], D.V. Bartlett, L.R. Baylor[1], K. Behringer, D.J. Campbell,
L. Charlton[1], A. Cheetham, J.G. Cordey, S. Corti, M. Gadeberg, R. Galvão,
A. Gondhalekar, N.A. Gottardi, R. Granetz[3], G. Hammett[2], M. von Hellermann,
K. Hirsch, J.T. Hogan[1], W.A. Houlberg[1], O.N. Jarvis, T.C. Jennigan[1],
P. Kupschus, G.S. Lee[1], P. Morgan, C.K. Phillips[2], J. O'Rourke, G. Sadler,
G.L. Schmidt[2], J. Snipes, D. Stubberfield, A. Taroni, B. Tubbing, H. Weisen

JET Joint Undertaking, Abingdon, Oxon. OX14 3EA, U.K.
[1]Oak Ridge National Laboratory, Oak Ridge, Tennessee, U.S.A.
[2]Princeton Plasma Physics Laboratory, Princeton, New Jersey, U.S.A.
[3]Massachusetts Institute of Technology, Cambridge, Massachusetts, U.S.A.

INTRODUCTION

A transient improvement in plasma performance and central confinement has been observed in auxiliary heated JET limiter plasmas associated with a peaking of the plasma density profile and strong centralized heating[1,2]. Suitable target plasmas for ICRF and NBI heating experiments are created by deuterium pellet injection with a multi pellet injector system developed jointly by ORNL and JET[3]. Two types of discharge conditions have been observed. In the first (type A), the density profiles decay gradually during the first 1.3s of the heating pulse while maintaining an elevated density core plasma inside r/a < 0.6 superimposed on a flat density pedestal as shown in Figs. 1b and 2a. During this phase the central electron and ion temperatures increase rapidly (up to 12 keV and 10 keV respectively in the best discharges). This results in an increase in the central plasma pressure by approximately a factor of three ($\beta(0) \approx 5\%$) above gas fuelled discharges and gives rise to sharply increased pressure gradients in the plasma core. As shown in Fig. 1, an abrupt collapse of the central electron and ion temperatures terminates the enhanced phase at 1.3 s and leads eventually to a 20% decrease in plasma stored energy. While these discharges are predicted to be stable to kink modes, they approach the first stability boundary for ballooning modes in the region of steepest pressure gradient[2,4]. The pressure and q profiles inferred from transport analysis are also close to those for which 'infernal' (intermediate-n) mode instability is predicted. This phenomenon, which does not occur in all cases, relaxes the discharge parameters to the less peaked standard profile shapes. Under conditions for which the temperature collapse does not occur (type B), the core plasma parameters also improve initially; but, in the latter phase of the decay of the density perturbation, the central ion temperature is observed to decrease while the electron temperature remains elevated. Ion thermal diffusivities inferred in this phase are comparable to those predicted by η_i mode turbulence theory[5].

---

*This work has been performed under a collaboration agreement between the JET Joint Undertaking and the U.S. Department of Energy.

PARTICLE TRANSPORT

Particle transport in pellet fuelled discharges has been evaluated by interpretative and predictive 1-1/2 D radial transport codes (PTRANS[6] and WHIST[7] respectively) using density measurements from the 6-channel interferometer and H_α detectors to infer the edge particle source strength. Particle diffusivity in the core of the plasma is found to depend on the profile shape. Particle balance calculations for peaked density profiles $(n_e(0)/\langle n_e \rangle > 2)$ give D $\approx$ 0.08 m²/s while for non pellet-fuelled plasmas with $n_e(0)/\langle n_e \rangle \approx 1.5$, D is in the range of 0.2 - 0.3 m²/s. The time evolution of the electron density profile for the shot shown in Fig. 1 was modelled with the PTRANS code using a neoclassical pinch velocity and a time dependent diffusion coefficient which is uniform inside the central plasma core and increases abruptly at the radius where the density pedestal forms as shown in Fig. 2b. The shape of D is found to be similar in both ohmic discharges and rf heated discharges up to the point where the temperature collapse takes place. Afterward, the density profile broadens and the central value of D increases abruptly to the value found in the density pedestal region. A similar diffusion model used in the predictive WHIST code ($D^{an} \approx$ 0.08 m²/s in the core, rising sharply to 0.2 m²/s at r/a $\approx$ 0.4, and then increasing as r² to 0.4 m²/s at the edge) gives good agreement with the density profile evolution and central density decay rate (Fig. 1b).

ENERGY CONFINEMENT AND TRANSPORT

The global energy confinement times evaluated during stationary conditions (dW/dt $\approx$ 0) are compared in Fig. 3 with Goldston scaling[8]. The best discharges show an improvement relative to L-mode scaling of up to 50%.

For type A cases, the open symbols indicate the confinement time measured after the enhanced phase. A single fluid transport analysis indicates that the 20-30% improvement in global confinement observed in the enhanced phase is due to a local improvement in confinement inside r < 0.5 m which is associated with a factor of 2-3 reduction in thermal diffusivities[9].

Time dependent details of energy transport in type A cases have also been analyzed with WHIST[7] and the interpretative transport analysis code TRANSP[10]. In both analyses, a constant H minority species concentration was assumed. For concentrations in the range of 1-2.5% the resulting ion and electron heating rates are approximately equal as is observed experimentally. The WHIST results are shown in Fig. 1 for a heat transport model in which the anomalous electron heat diffusivity is assumed not to vary in time and is taken to be proportional to the particle diffusivity as determined from the above analysis (ie. $\chi_e^{an} \approx 13 \cdot D^{an}/4$) and for the anomalous ion contribution given by $\chi_i^{an} \approx \chi_e^{an}$. This model, which was chosen because of the similarity in the measured ion and electron temperature profiles, adequately reproduces the plasma response $(T_e(r), T_e(0)$ and $T_i(0))$ in the ohmic phase and during the first 1 s of auxiliary heating. The improvement in global energy confinement at the start of rf heating (Fig. 1e) is a consequence of the assumption that the transport is constant in time (ie. no degradation relative to the ohmic levels) and that the heating profile becomes more peaked compared to the broader ohmic profile[11]. Experimentally the global confinement time follows this increase initially but eventually decreases to 60% of the WHIST value. This discrepancy is partly due to an increase in total radiated power (which affects the power balance only in the plasma edge) observed experimentally but not predicted by WHIST which assumes a constant impurity concentration. The TRANSP analysis of this discharge also indicates that the core plasma confinement is not strongly degraded in the first 1s of heating; but, subsequent to that, χ_i in particular increases up to the time of the temperature collapse where an abrupt increase in both χ_i and χ_e takes place[10].

The TRANSP code has also been used to study type B discharges in which the ion temperature gradually decreases in the latter phase of the density decay as shown in Fig. 4. The ion and electron thermal diffusivities shown in Fig. 4 were inferred for a model that assumes $\chi_i \approx \alpha(t)\chi_e$. The TRANSP results indicate an increase in χ_i during the phase in which $T_i(0)$ decreases. While χ_i on axis is approximately equal to the neoclassical (Chang-Hinton) level during this period, the values at the half radius and beyond are more than an order of magnitude larger. However, within r $\approx$ 0.6m, χ_i calculated by TRANSP and the predicted values from the theory of η_i mode turbulence extended to account for the weak density gradient seen in the discharge[5] are in reasonable agreement. Immediately after pellet injection and during the early enhanced phase, $n_e \approx d \ln T_0/d \ln n_0 \approx n_i \leq 2$ within r/a $\approx$ 0.5 because of the steep internal density gradients. As the density decreases and the plasma reheats, η increases beyond the threshold value for instability and this could be responsible for a decrease in confinement within the core plasma. Outside r/a $\approx$ 2/3 where the density profiles are relatively flat even after pellet injection, η_i mode turbulence alone cannot explain the anomalous ion transport.

CONCLUSIONS

Several predictive and interpretive transport codes have been used to study the transient enhanced confinement regime observed on JET when a core plasma densified by pellet injection is heated by high power ICRF heating. Particle and heat transport coefficients within the region where the density gradient is pronounced (r $\leq$ 0.5 m) are reduced by factors of 2-3 relative to standard rf heated limiter discharges. The enhanced confinement appears to be correlated with density profile peaking and can be terminated abruptly by an expulsion of energy from the core caused by steep pressure gradients[4], or more gradually by an increase in transport coefficients which may be associated with η_i mode turbulence.

REFERENCES

[1] P. Kupschus et al., Proc. 15th Eur. Conf. on Contr. Fus. and Plasma Heating, Dubrovnik, 1988, Vol.1, p.143. S.L. Milora et al., ibid, p.147.
[2] G.L. Schmidt et al., Proc. 12th Int. Conf. Plasma Phys. and Contr. Nucl. Fusion Res. (Nice, 1988) IAEA-CN-50A-IV-1.
[3] S.L. Milora et al., in Proc. 12th Symp. on Fusion Eng. (Monterey 1987), IEEE Vol.2, p.734 (1987). P. Kupschus et al., ibid, p. 781.
[4] R. Galvão et al., this conference.
[5] G.S. Lee and P.H. Diamond, Phys. Fluids 29, 3291 (1986) and G.S. Lee in preparation.
[6] L.R. Baylor et al., presented at the IAEA Technical Committee Meeting on Pellet Injection and Toroidal Confinement, Gut Ising, FRG, Oct. 1988.
[7] W.A. Houlberg et al., ibid.
[8] R.J. Goldston, Plasma Phys. Controlled Fusion 26, p.87 (1984).
[9] A. Taroni et al., Proc. 12th Int. Conf. Plasma Phys. and Contr. Nucl. Fusion Res. (Nice, 1988) IAEA-CN-50A-7-1.
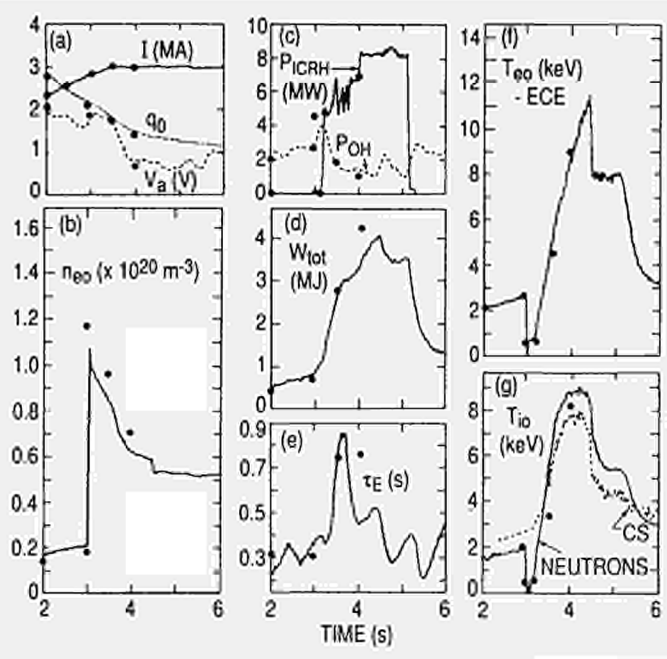
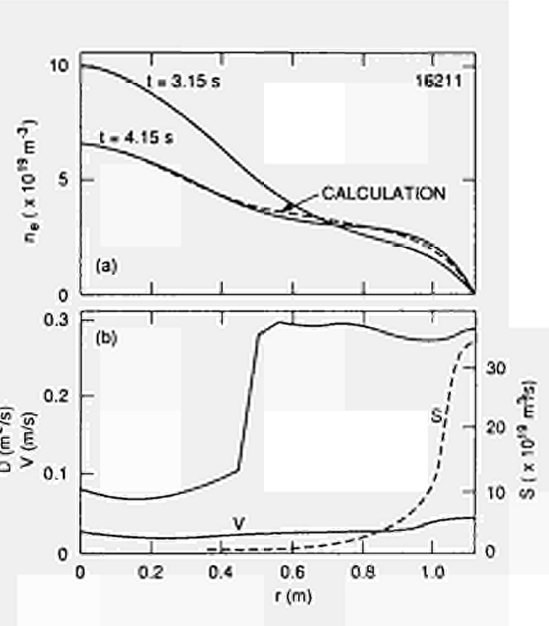Fig.1 Summary for shot 16211 and comparison with WHIST code results(·)

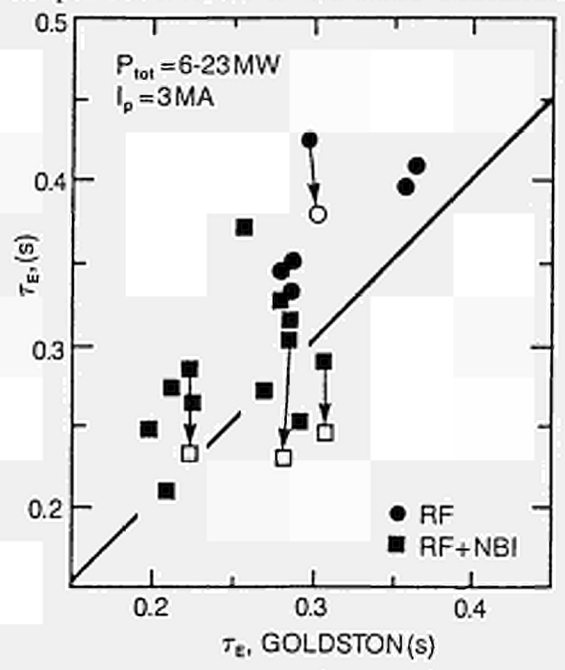Fig.2 Comparison of measured and calculated n_e profile evolution for shot 16211.

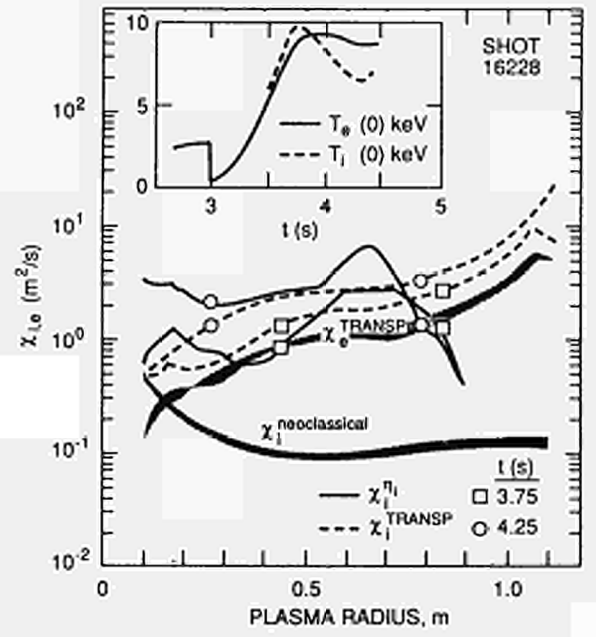Fig.3 Comparison of global τ_E with Goldston scaling for pellet fuelled auxiliary heated plasmas.

Fig.4 Thermal diffusivity profiles obtained from TRANSP compared with predictions from η_i mode theory. Heating power = 11 MW.

RADIATION-SHIELDED DOUBLE CRYSTAL
X-RAY MONOCHROMATOR FOR JET

R. Barnsley, U. Schumacher[1], E. Källne[2], H.W. Morsi, G. Rupprecht[3]

JET Joint Undertaking, Abingdon, Oxon OX14 3EA, UK
[1] MPI für Plasmaphysik, Ass. EURATOM-IPP, D-8046 Garching, Fed. Rep. of Germany
[2] Fysik 1, Kungl. Tekniska Högskolan, S-10044 Stockholm, Schweden
[3] Now at Eur. Southern Observatory (ESO), D-8046 Garching, Fed. Rep. of Germany

Abstract

A double crystal X-ray monochromator for absolute wavelength and intensity measurements with very effective shielding of its detector against neutrons and hard X-rays was brought into operation at JET. Fast wavelength scans were taken of impurity line radiation in the wavelength region from about 0.1 nm to 2.3 nm, and monochromatic as well as spectral line scans, for different operational modes of JET.

1. Introduction

Soft X-ray plasma spectroscopy is a well established technique which provides a range of diagnostic information relating to the concentration, transport and temperature of impurity ions [1,2]. A high temperature plasma, producing a significant rate of DT fusion reactions, as anticipated in the latter phases of JET operation (active phase) will produce high fluxes of neutrons and γ-rays. The need to provide good shielding of the detector while covering a wide spectral range, places severe constraints on the design of an active phase crystal spectrometer. This required the development of a new high precision crystal-drive mechanism, and special techniques to evaluate the suitability of crystal diffraction properties over a larger surface area [3,4]. Shielding is achieved by placing the instrument outside the JET torus hall and by using two crystals in the parallel (non-dispersive) mode. For this device input and output beams are fixed for all wavelengths, allowing a labyrinth radiation shield to be built around the optical path between the small penetration in the JET biological shield and the detector (Fig. 1).

2. The active phase double crystal monochromator

The crystals are mounted via rotary tables to linear displacement tables, and their trajectories necessary to maintain the Bragg condition are controlled by a fast digital servo system [3]. It is necessary that the crystals be kept parallel to well within their diffraction profiles, which is achieved by the control system to about 6 arc sec. in the full Bragg angle range from 26° to 60°. The resolving power is $\lambda/\Delta\lambda = (1/\Delta\Theta) \cdot tan\Theta$ where the angular width $\Delta\Theta$ is defined mainly by remotely interchangeable coarse $(1/\Delta\Theta = 600)$ and fine $(1/\Delta\Theta = 5000)$ gridded collimators. The sight-line contains a
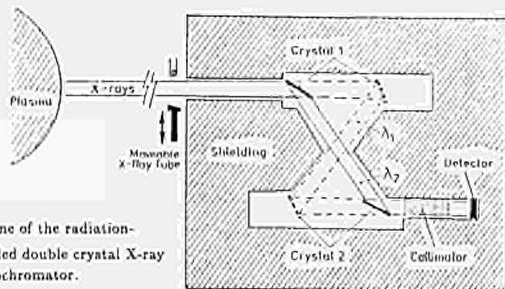

Fig. 1 Scheme of the radiation-shielded double crystal X-ray monochromator.

remotely deployable calibration source which, together with the high resolution angle encoders and the fine collimator, allows absolute wavelength calibration and Doppler line-profile and line-shift measurements.

Absolute intensity measurements are performed using the throughput relation:
$N = IF_c \chi \Delta\Theta R_{cc} P_{cc} n/\omega$, where N is the counts integrated in a spectral line of intensity I (photons $m^{-2}s^{-1}sr^{-1}$), F_c the projected crystal area, χ the acceptance angle perpendicular to the plane of dispersion, $\Delta\Theta$ the collimator acceptance angle, R_{cc}, P_{cc} the double crystal integrated and peak reflectivities, respectively, ω the crystal rotational velocity and η the combined efficiency of detector and windows. The luminosity of the system is typically about $10^{-9} sr \cdot m^2$.

The detector is a multiwire gas proportional counter (MWPC) with thin polymer window for which the gas pressure, high voltage, and pulse height window can be controlled automatically to suit the observed wavelength range. This gives a high quantum detection efficiency (QDE) and allows background rejection and selection of the desired diffraction order by pulse height analysis. The 48 anodes are connected into 8 groups, each with its own signal processing chain, which allows signal-plus-background count rates of $\sim 10^7 s^{-1}$ without serious pile-up. All instrument and vacuum system functions can be controlled automatically by the JET control and data acquisition system (CODAS).

3. Examples for the operational modes of the active phase double crystal monochromator

The double crystal monochromator can be operated in different modes: Broad band spectra can be taken covering the Bragg angle range from about 26° to 60° in a time of about one second. With crystals like Topaz(303), LiF(220), Gypsum, TℓAP and KAP, as applied so far, the wavelength range from about 0.12 nm to about 2.3 nm was covered. An example of such a broad-band spectrum taken with TℓAP crystals is given in Fig. 2, showing some Ne-like Ni lines and some members of the oxygen Lyman
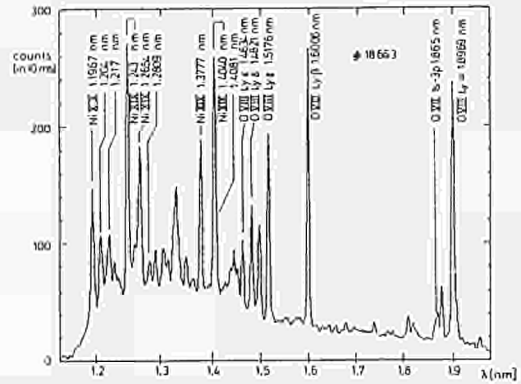

Fig. 2 Broad band spectrum obtained using TℓAP crystals covering the wavelength range from 1.13 nm to 1.95 nm with Ne-like Ni lines and the Lyman series of oxygen

series. Since the absorption in the thin foil (which separates the monochromator from the torus vacuum) increases with wavelength the count rate ratios do not directly reflect the line intensity ratios. Another mode is the repetitive scan of a smaller wavelength interval. An example of a line scan is given in Fig. 3. It is a scan of the profile of a certain spectral line performed many times throughout the discharge in order to follow the time behaviour of the line width and its intensity. This figure shows that the sensitivity of the monochromator is good enough to reveal the different behaviour of O and Ni. Fig. 4 gives as an example for the fourth operational mode, the monochromatic time behaviour of the Fe XXV line obtained from laser ablation of Fe into the JET discharge [5].

Acknowledgements

References

/1/ E. Källne et al., Physica Scripta 31, 551 (1985,
   and J. de Physique 48, C9/335 (1987)
/2/ R. Barnsley et al., Rev. Sci. Instrum. 57, 2159 (1986)
/3/ C. Andelfinger et al., MPI für Plasmaphysik, Garching, Report IPP 1/226 (1984)
/4/ U. Schumacher, Nucl. Instr. and Meth. A 251, 564 (1986) and A 259, 538 (1987)
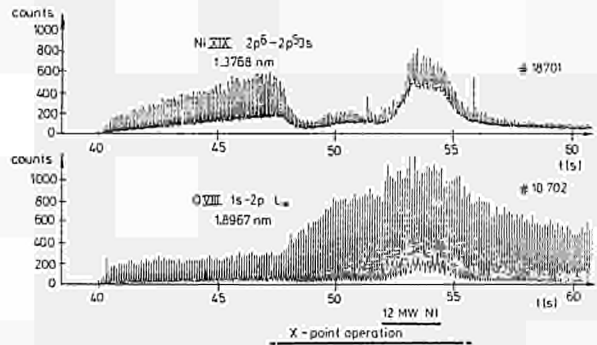/5/ N. Hawkes, Z. Wang et al., this conference

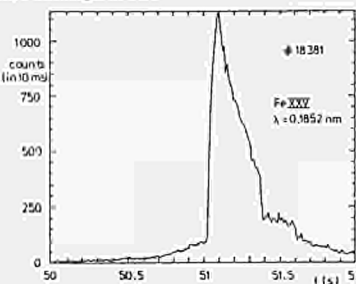Fig. 3 Line scans for Ne-like Ni (above) and Oxygen Lyman α throughout two consecutive discharges at JET

Fig. 4 Time behaviour of He-like Fe line from laser ablation of Fe.

PLASMA SURFACE INTERACTIONS AT THE JET X-POINT TILES

A.P. Martinelli*, R. Behrisch*, J.P. Coad, and L. de Kock

JET Joint Undertaking, Abingdon, Oxon OX14 3EA, UK
*Max-Planck-Institut für Plasmaphysik, EURATOM Association
D-8046 Garching/München, FRG

Introduction

Operation with a magnetic divertor, which leads to a zero poloidal field inside the volume of the discharge vessel (the X-point) has led to substantial improvements in confinement time in JET. In this mode the diverted plasma is conducted to a large number of graphite tiles (X-point tiles) near the top of the vessel. The power handling capability of these tiles limits the maximum additional heating power to the discharge.

The study of the surface modifications of the X-point tiles of JET is therefore of interest both to correlate the magnetic configuration and plasma particle and energy fluxes with the surface modifications, and also to get information about the erosion and deposition at these wall areas.

Figure 1 shows the geometry of the X-point tiles and the separatrix in JET [1]. Two bands of graphite target tiles with scrape off layer impinging on the slope of the tiles are shown; the analysis of one such band of (four) tiles is described here.

Experimental and Results

The set of four carbon tiles with an area of $(540 \times 184 \times \sin 70°)$ mm^2 were removed from the vessel wall close to the plasma X-point of Octant VIII b/c. A view of the tiles (as seen from below) and their relative position to Oct. I and VII as well as to the inner and outer wall are schematically shown in Fig. 2.

The tiles had been in use in the June 1987 to May 1988 experimental period of about 4300 discharges, of which ca. 1000 were X-point discharges, and they were removed in May 1988. Carbon strips as indicated in Fig. 2 were cut (about 2 mm thick, 8 mm wide) along the lines HH, KK (from 0 to 540 mm) and along LL, MM, NN, 00 (from 0 to 184 mm). The tiles are ridged, so that for strips LL, MM, NN and 00 the surface from 0-92 mm faces the electron-drift direction and from 92-184 mm faces the ion-drift direction with in each case the point at 92 mm being nearest the plasma centre. The strips were analysed each 5mm by nuclear reaction analysis (NRA) using the $^3He(D,p)$ ^4He reaction with 790 keV $^3He^+$-ions in order to determine deuterium collected in a surface layer of about 0.5 /um and by proton induced x-ray emission (PIXE) using 1.5 MeV H^+ to detect the metals (Ni, Cr, Fe) in a surface layer of about 8 /um.

The results of the NRA and PIXE analysis along line HH are shown in Fig. 3. The D concentration ranges from a maximum of about 10^{18} D/cm^2 down to a minimum of about 10^{17} D/cm^2 at coordinates between 80 and 240 mm, then reaches a value of about 6 10^{17} D/cm^2 from about 240 to 540 mm. The metal (Ni, Cr, Fe) concentrations are lower, but they show a lateral distribution similar to the D deposition. This observation is similar to results of earlier analysis of limiters from JET [2,3] and other plasma experiments [4]. The relative concentrations of Ni, Cr, Fe agree well with their concentration in Inconel.

Figure 4 shows the D and Ni, Cr, Fe concentrations along line MM (0 to 184 mm). The D and metal depositions are much lower from ca. 30 mm to the ridge at 92 mm, by factors of 10 to 20. The cut-off at ca. 30 mm probably represents the shadow cast by the next set of poloidal tiles at Octant VIII a/b. The D and metal depositions are also reduced on the electron-drift side of the tiles on slices NN and 00, but by smaller factors (ca. 2 and 12, respectively), whilst on slice LL there is only a slight decrease in the level. The results show strong erosion on the electron-drift side of the tiles, centred near the strip MM and tailing off away from this area (e.g. Fig. 3).

At several representative spots the depth profiles of the depositions have been measured by SIMS (Secondary Ion Mass Spectroscopy). These profiles show that the major part of the deposition is carbon with a D concentration of about 0.4 and a metal concentration in the range of 1 %. The deposited layers have a total thickness mostly 1.5 to 2 /um and up to 5 /um in the areas of large deposition. With the NRA only a layer of 0.5 /um is analysed, and the total deposition of D in the areas of large deposition is a factor 3 to 5 higher, as observed in the SIMS measurements.

A systematic SEM (Secondary Electron Microscopy) investigation of the cut strips shows layers of deposited material all over the strips. The deposited layers appear to have suffered erosion, to a larger extent in the dotted-region, where low deposition was measured, to a lesser extent in the hatched and cross-hatched regions with higher deposition as shown in Fig. 2.

Discussion

From the poloidal and toroidal strips of the analysed set of tiles an average value of about 3.3 x 10^{18} D/cm^2 for the D deposit can be attributed to these areas, and a D inventory D = 3 x 10^{21} per set of four X-point tiles.

Since there are 40 bands of X-point tiles they contribute 1.2 x 10^{23} D atoms to the total inventory, which is ca. 4 times more than reported for tiles exposed in June/August 1987 [5], but perhaps to be expected after the vastly increased number of X-point discharges.

The much lower levels of D and metals (ca. 10^{17} D/cm^2 and 2 x 10^{16} metal atoms/cm^2) on sections of MM (Fig. 4) are consistent with an area where erosion dominates during X-point discharges, but where deposition may occur at other times as observed previously on limiters [2,3] and the polished visual appearance of the tile in this region is consistent with this hypothesis. It appears, therefore, that the electron-side separatrix intersects the band of tiles in the neighbourhood of strip MM, so that NN and 00 are deeper into the SOL and thus receive progressively lower flux of less energetic ions. The position of the separatrix is known to move by ca. 150 mm during a single X-point discharge, which agrees well with the width of the minimum in D along HH shown in Fig. 3. There will also have been some variation in X-point position from shot to shot and during the operational campaign.

At the separatrix strong erosion occurs. Away from the separatrix, i.e. on the ion-drift side of the tiles and in the area LL on the electron-drift side, deposition as the dominant mechanism is more evident. The deposition levels well away from the separatrix are similar to those observed on the sides of limiters, where deposition occurs (ca. 10^{18} D cm^{-2} and ca. 2 x 10^{17} Ni cm^{-2}) [2,3].

By considering codeposition of C and D on the tile surface one finds on the average C = D/0.4 = 3.3 $10^{18}/0.4$ = 8.2 x 10^{18} C/cm^2. This corresponds to an average thickness of about 1.4 /um (ca. 4000 monolayers of C), which is also close to the value observed by the SIMS measurements in the hatched and cross-hatched regions of Fig. 2.

Similarly, a deposit of carbon 2.5 x 10^{17} C/cm^2 can be calculated on the dotted area of low concentration in Fig. 2 (ca.100 monolayers of C or more). Evidence of erosion (or no erosion) of the graphite substrate at the dotted (or the other regions of Fig. 2) cannot be given, therefore, strictly speaking, the measured concentrations of D, Ni, Fe, Cr, and C cannot be considered as "net" deposition.

However, by extrapolating linearly the average carbon deposition C = 8.2 x 10^{18} C/cm^2 after 2 x 10^4 s (1000 discharges x 20 s) to a year operation, an average C deposition of about 1 mm thickness with local variations by a factor 10 is calculated on the surface of the tiles.

The following table summarizes some main results:

	D	C	Ni
Average Deposit/set of tiles (D/cm^2)	3.3 x 10^{18}	8.2 x 10^{18}	2.0 x 10^{17}
Total Deposit (D, C, Ni)	3.0 x 10^{21}	7.7 x 10^{21}	1.9 x 10^{20}
Average Deposit/sec (D/cm^2 s)	1.7 x 10^{14}	4.0 x 10^{14}	1.0 x 10^{13}

References

/1/ P.J.Harbour, L. de Kock, S.Clement,
Procs. 15th Europ. Conf. Controlled Fusion and Plasma heating,
Eds. S. Pesic, J. Jacquinot, Duhrovnik 1988, EPS, Geneva, 12 B, Part II, p. 655.

/2/ R.Behrisch, J.Ehrenberg, H.Bergsaker, J.P.Coad, L.de Kock, B.Emmoth, H.Kukral, A.P.Martinelli, G.M.McCracken, and J.W.Partridge,
J. of Nucl. Mater. 145-147 731-735 (1987).

/3/ H.Bergsaker, R.Behrisch, J.P.Coad, J.Ehrenberg, B.Emmoth, S.K.Erents, G.M.McCracken, A.P.Martinelli and J.W.Partridge,
J. of Nucl. Mater. 145-147 727-730 (1987).

/4/ TFR Group, A.P.Martinelli, R.Behrisch, and W.Englert,J. of Nucl. Mater. 145-147 681-685 (1987).

/5/ J.P.Coad, R.Behrisch, H.Bergsaker, J.Ehrenberg, B.Emmoth, J.Partridge, G.Saibene, R.Sartori, J.C.B.Simpson and W.M.Wang,,
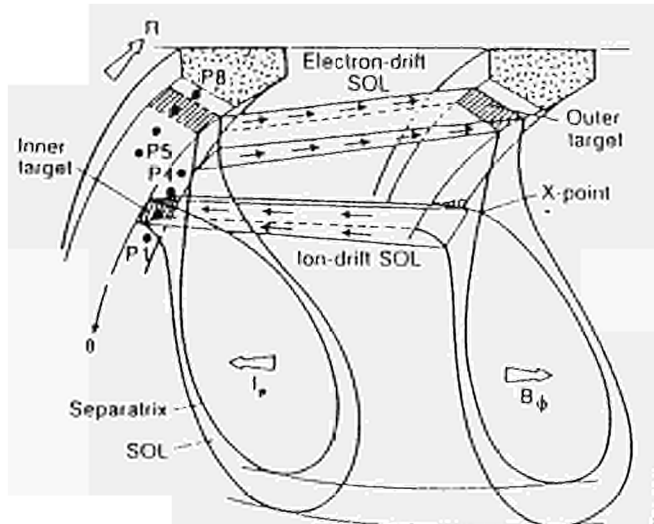PSI Conf. Jülich, to be published in J. of Nucl. Mater. (1989).

Fig. 1. Geometry of the X-point divertor in JET.
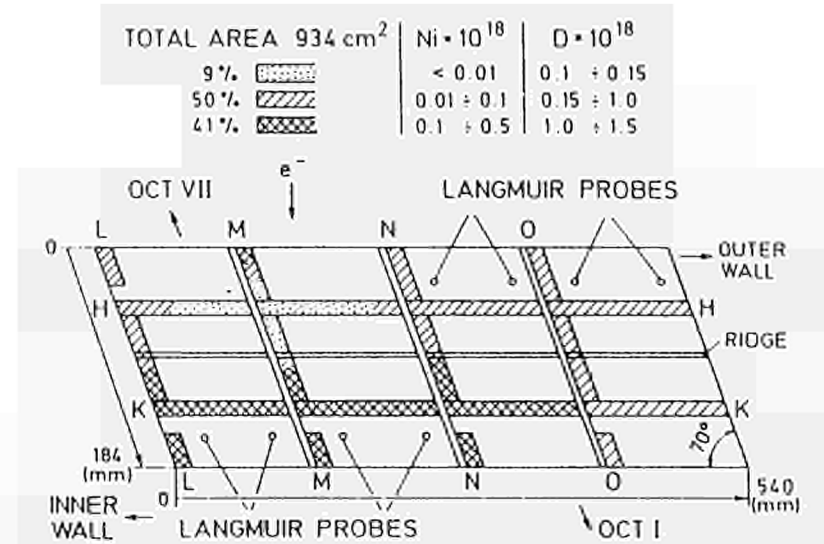
Fig. 2. Set of four plasma X-point carbon tiles of octant VIIIb/c of JET. Indicated are the strips analysed by NRA and PIXE as well as the analysis results.

Fig. 3. NRA and PIXE analysis along line HH of the X-point carbon tiles.

Fig. 4. NRA and PIXE analysis along line MM of the X-point carbon tiles.

An Overview of JET Results

The JET Team
(presented by P J Lomas)

Invited Paper presented at the 16th European Conference on
Controlled Fusion and Plasma Physics, Venice, Italy.
13th−17th March 1989.

AN OVERVIEW OF JET RESULTS

The JET Team ★

Presented by P.J.Lomas

JET Joint Undertaking,Abingdon,Oxfordshire,OX14 3EA,UK

ABSTRACT

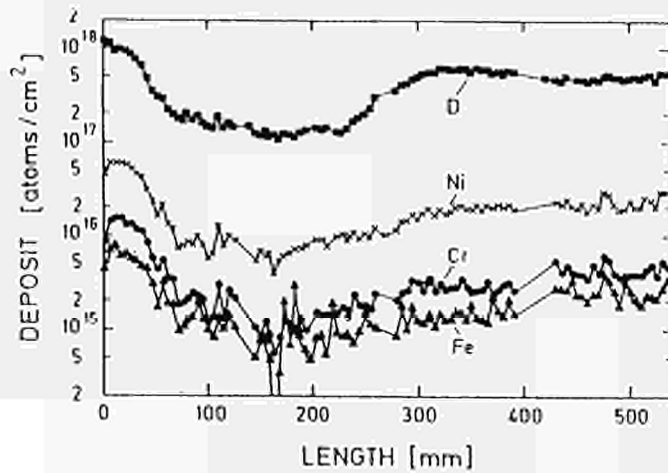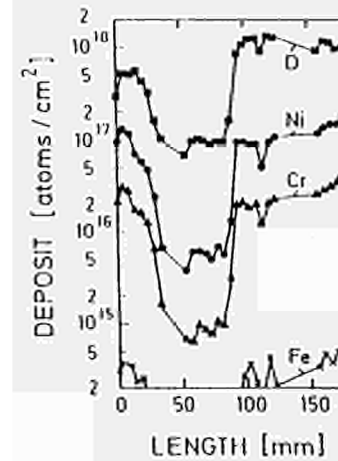An overview is given of experimental results obtained on JET during 1988, and in particular of results at high total power input into plasmas with various configurations. An account is given of the various interpretations of these results and some of the difficulties encountered are related. The progress is summarised in terms of the projected D-T performance.

KEYWORDS

Fusion, Tokamak, Magnetic Confinement

1. INTRODUCTION

A number of improvements to the JET machine performance have been made possible by the major enhancements (Bertolini et al, 1987) made to JET itself in 1987. Some of the benefits realised have already been described at the Dubrovnik meeting, (Gibson, 1988) but since then the plasma current has been increased to 7MA in the limiter configuration and to 5.3MA in the single null magnetic separatrix configuration. The neutral beam power was increased to 21MW and the ICRH power coupled to the plasma reached 16MW (Bickerton et al, 1988). The maximum power input to a plasma was 35MW including the Ohmic input. The flat top pulse length at 7MA was 2 seconds but at lower current 10 seconds was typical. The heating pulse lengths were typically 2-5 seconds. However, at 3MA and with 6MW of ICRH, flat tops exceeding 20 seconds were demonstrated. In addition the multiple pellet injector, (Kupschus et al, 1988a) which first became operational in late 1987, was used extensively during 1988.

The main experimental studies on JET during 1988 concerned high power heating at high plasma current (up to 6MA), H mode studies at high plasma current (up to 5MA), the hot ion and improved confinement regimes, the heating of pellet fuelled plasmas and lastly beam and RF driven high fusion yield.

Important results were obtained on the behaviour of fast particles (both tritons and high energy minority ions accelerated by ICRH) which are encouraging for alpha heating. These are discussed elsewhere (Thomas et al, 1988, Conroy et al, 1989). The current and projected fusion performance of JET was reviewed in (Gibson, 1988) and the following critical areas identified:-

(a) the extrapolation of presently observed confinement scaling (particularly with plasma current).
(b) the peakedness of the plasma profiles
(c) the control of impurities and fuel depletion.

In the remainder of this paper the JET results are described bearing these points in mind. The main sections reflect the experimental studies as listed above. However, as we shall see, sawteeth play a significant role and therefore a section is dedicated to this topic.

2. HIGH POWER HEATING OF LIMITER PLASMAS

High power heating experiments have been performed for plasma currents of 3-6MA using either the toroidal carbon belts or the inner-wall carbon protection tiles as limiters. The belt limiters are designed to handle high powers and have been used for the higher current experiments. The inner wall gives better density control and has been used at 3MA to obtain higher T_i. However there is no significant difference in confinement according to which is used as the limiter.
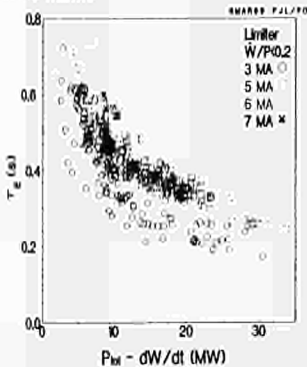

Fig 1. Confinement time versus power input for limiter plasmas at various currents. The curves show the Goldston predictions for 3, 5 and 6MA.

Whereas the confinement of Ohmic (Cordey et al, 1986a) and moderate power cases scales roughly as the square root of density, the confinement at high power has no clear density dependence (Thomsen et al, 1987 and Thompson et al ,1987). Indeed in some cases the confinement decreases with density, although this may be an effect of radiation and/or changes in the fast particle stored energy. The confinement degrades with power as clearly seen in Fig. 1 which shows a degradation similar to that expected from the Goldston auxiliary heating scaling (Goldston, 1984). Typical confinement times are in the range 0.3-0.9sec for Ohmic discharges, 0.3-0.5sec at 15MW and 0.2-0.3sec at 30MW. Some data in this figure show a rapid approach to an asymptotic value of confinement time with increasing power -i.e an incremental confinement behaviour (Cordey, 1986a). However, at the highest powers with combined neutral beams and ICRH, it is not clear whether an asymptotic value has been reached or whether the confinement continues to degrade with power. In other words it is not possible to distinguish unambiguously between power law and incremental type models. The confinement time does increase with current but the dependence is weaker than linear (Bhatnagar et al 1988), and the data suggests that q is the significant parameter.

The global form of the Rebut-Lallia model (Rebut and Lallia, 1988) also fits the data reasonably well as shown in Fig. 2. The 3MA data tends to be better than predicted by either Rebut-Lallia or Goldston whereas the 6MA data is worse. However the local form of the

Rebut-Lallia model describes well the temperature profiles outside the sawtoothing region (Jones et al, 1989) even at high power and high current, provided that the profile is artificially flattened inside the inversion radius. The model therefore does not predict the central temperatures when sawteeth are present, and indeed the temperature excursion over a sawtooth period can be large (Jacquinot, 1986).
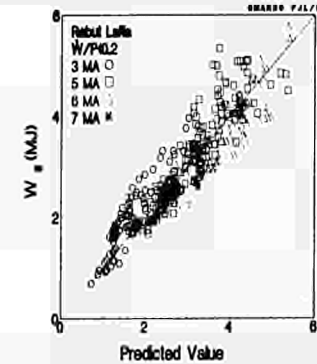

Fig 2. Electron stored energy compared with the prediction of the Rebut Lallia model for limiter plasmas.
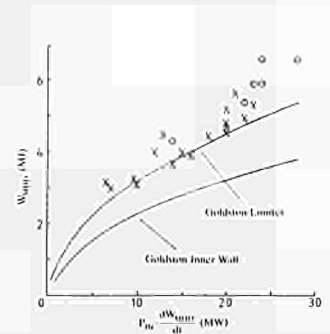

Fig 3. Plasma stored energy as a function of total power for small bore plasmas limited by either belt or inner wall. The curves show the Goldston prediction for the two cases.

○ Belt limiter
X Inner wall

Low density target plasmas and improved density control during additional heating can be achieved with plasmas limited on the inner wall carbon tiles after extensive conditioning with GDC in helium, followed by tokamak discharges in helium. Subsequent discharges with deuterium prefill have a target plasma which is almost entirely carbon with $n_e \approx 5 \cdot 10^{18} \text{m}^{-3}$. With NBI the density rises, and the profile becomes peaked due to deep beam refuelling. The ion temperature rises to 23keV whereas the electron temperature rises to 8-12keV for $P_{tot}/n_e \gtrsim 11$ MW 10^{19}m^3 (Thomas et al, 1988). The D-D fusion rate is high (up to $2 \cdot 10^{16} s^{-1}$) and made up of similar contributions from beam-beam and beam plasma reactions and somewhat less from thermonuclear reactions. Unfortunately, before steady state conditions are reached, these discharges suffer from a large carbon influx and uncontrolled density rise due to local overheating of the tiles. The beam penetration can be improved by reducing the minor radius and this gives strongly peaked density profiles - the so called 'jolly good shots' (Lowry et al, 1989). High ion temperatures 23-25keV are produced. The D-D rates $\approx 2.4 \cdot 10^{16} s^{-1}$ are predominantly beam-beam reactions in this case. Fig. 3 compares data from such small minor radius plasma (a = 1.0 m) limited on the inner wall or-limited by the outboard belt limiters. This data does not show the expected strong major radius dependence (Goldston, 1984) and in fact is similar to the full bore 3MA data already shown in Fig. 3.

It is generally observed in Ohmic discharges in JET that Z_{eff} scales roughly as $1/n$ (Cordey et al, 1986a), and indeed spectroscopic measurements show that the ratio of fluxes of carbon and deuterium scale in a similar manner. At moderate and high density these measurements are consistent with calculations based on physical sputtering of carbon using measured scrape off layer parameters. (de Kock et al, 1988). At low density (i.e with high edge temperatures), particularly with helium plasma, the measured carbon fluxes are significantly higher than expected. With additional heating, Fig. 4 shows the carbon fluxes increase, but this is offset by an increased deuterium flux and consequently the increase in Z_{eff} is small, but the final density is higher. Z_{eff} is then higher than an OH discharge with the same density. An increasing carbon flux is to be expected from the observed changes in the boundary layer (Tagle et al 1989, Stamp et al 1989, Pitcher et al 1989). However at high power the carbon fluxes can
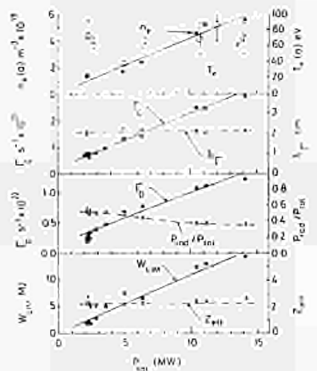
Fig 4. Various edge measurements plotted against total power input for ICRF heated (H minority, dipole) 5MA limiter plasmas. The data includes:
Edge density and temperature, $n_e(a)$ and $T_e(a)$
Fluxes of deuterium and carbon, Γ_D and Γ_C
Scrape off thickness, λ_r, for flux.
Ratio of radiated power to input, P_{rad}/P_{tot}
Total energy to limiter, W_{Lim}
Z_{eff} from visible Bremmstrahlung.
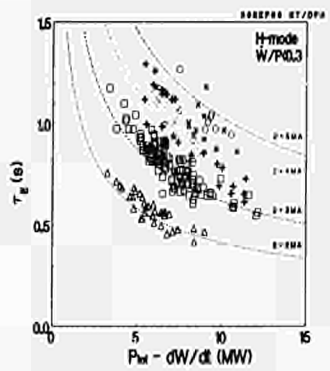
Fig 5. Variation of confinement time with power input for ELM free H mode plasmas at various currents.The curves show twice the Goldston prediction for the indicated currents.

△ 2MA, B < 2.2 Tesla.
□ 3MA, B < 2.7 Tesla.
+ 3MA, B > 2.7 Tesla.
◇ 4MA, B > 2.7 Tesla.
x 4MA, B > 2.7 Tesla.
◇ 5MA, B > 2.5 Tesla.

increase abruptly and cause a deterioration of plasma purity and a strong reduction in the D-D fusion yield, the so called 'carbon catastrophe'. Some tile edges on the belt limiter reach temperatures ~ 1600°C (Pitcher et al,1989) at this time. Subsequent examination has shown severe erosion on these edges and on high spots on the inner wall. At such temperatures the carbon erosion due to radiation enhanced sublimation becomes large (Pitcher et al, 1989) and moreover, as pointed out in (Hugon, Lallia and Rebut, 1989), the carbon flux will increase continuously with time for surface temperatures $\geq$ 1300 °C, where the carbon self sputtering coefficient exceeds unity, and will avalanche for surface temperatures $\geq$ 1600 °C.

3. ELM FREE H MODE RESULTS

The L to H mode transition in JET can be recognised by the characteristic drop in D_α light. During the H mode this light can be spiky (ELMS) or smooth (ELM free). The transition is less obvious on stored energy or density which generally rise throughout the heating pulse. The density rise can be controlled by provoking ELMs but at the expense of confinement. The threshold neutral beam power is typically 5MW at a toroidal field of 2.2 Tesla rising to typically 10MW at 3.2 Tesla. ELM free H modes could be obtained with up to 14MW of NBI. In order to compare like with like this section treats ELM free H modes with neutral beams only. Other results are presented in the next section.

As already demonstrated (Keilhacker et al, 1988b), the profiles of density and temperature exhibit the usual steep gradients at the edge during the H mode, the density profile is otherwise very flat or even hollow and the electron and ion temperature profiles are broad. The current profile broadens after the L-H transition partly because of the reduced edge resistivity but predominantly because of a large bootstrap current (Stubberfield et al, 1989) which arises from the steep gradients at the edge.

In JET the confinement of ELM free H modes shows degradation with increasing power as shown in Fig. 5. It can be seen that the confinement is 2-3 times the Goldston prediction. The confinement scales linearly with plasma current except at low q where some deterioration is observed. The data can also be described by an incremental confinement model where $\tau_{inc} \approx 0.14 * I_p(MA)$ sec (Keilhacker et al, 1988b). The confinement properties of ELM free H modes in single or double null configuration are similar.

It is difficult to distinguish χ_e and χ_i in the H mode since T_e and T_i are tightly coupled. It is useful to define an effective thermal diffusivity $\chi_{eff} = Q/n_e k \nabla T_e S$ where Q is the total heat flux across a surface of area S (Keilhacker et al, 1988b). In the discharge described in this reference, χ_{eff} at half radius increased from 1 m² s⁻¹ in OH to 2 m² s⁻¹ in the L mode but slowly relaxed back to the OH value through the L to H transition. During both L and H, χ_{eff} increased more strongly with radius than during the OH phase. Taking convection into account and assuming $\chi_e = \chi_i$ leads to χ_e decreasing at the extreme edge where the shear is large.More detailed transport analysis results are presented in (Tibone et al, 1989 and Watkins, 1989).

Table 1. χ_{einc} from heat pulse propagation for a 3MA X point plasma (16256). The measurements are made over the range of normalised minor radii, r/a = 0.4-0.75.

time (sec)	P_{beam} (MW)	χ_{einc} m²/s	phase
52-54	0.0	2.6±0.5	OH
54.5	9.0	2.5±0.5	L-H transition
55.8	6.5	3.0±0.6	H phase
57-58	4.0	2.9±0.5	L phase

The incremental electron thermal diffusivity χ_{einc} (at approximately half radius) estimated from sawtooth heat pulse propagation is shown in Table 1 for the OH, L and H phases of a 3MA X point plasma. χ_{einc} remains in the range 2.5-3.0 m² s⁻¹ throughout and, unlike χ_{eff}, certainly does not change by a factor 2. Incremental transport coefficients have in fact been measured by a number of different perturbation methods (Cheetham et al, 1988 and Gondhalekar et al, 1988) and the results for an Ohmically heated limiter plasma and a neutral beam heated H mode plasma are summarised in Table 2. Each row in Table 2 corresponds to simultaneous measurements.The first point to notice is that the transport coefficients measured by the different methods are in agreement. The second is that the transport coefficients are the same for the two very different kinds of discharge. Interestingly similar values of χ_{einc} are found (Start et al, 1988) for a 2MA RF heated limiter discharge, by RF power modulation. These results amplify the conclusions from Table 1 and suggest that the underlying transport mechanism in the plasma core is always the same in limiter and X point discharges with or without additional heating and in L or H mode. Furthermore the large ratio of χ_e/D_e suggests transport by micro-magnetic stochasticity rather than drift waves.

A plot of Q against $n_e k \nabla T_e$ for L and H phases of X point discharges (Keilhacker et al, 1988a) is consistent with a linear relationship of slope $\approx$ 3 m/s⁻¹ as indicated by the perturbation measurements, but different offsets for the two phases. This suggests that the apparent discrepancy between incremental analysis and profile analysis is a consequence of an heat pinch or some threshold behaviour.

Table 2. Transport coefficients from various perturbation methods

3MA OH limiter plasmas

method	χ_e	D_e	χ_i	radius r/a
pellet	2.8±0.3	0.4±0.1	-	0.5-0.6
sawtooth pulse	2.9±0.4	0.4±0.2	-	0.6-0.8
transport analysis		0.3-0.6		0.67

3MA NBI heated H mode plasmas

method	χ_e	D_e	χ_i	radius r/a
pellet	3.0±0.5	0.3-0.6	1-3	0.4-0.6
sawtooth pulse	3.0±0.6	-	-	0.5-0.7
transport analysis	-	0.2-0.4	-	0.67

Probe measurements have been made (Harbour et al, 1988 and Keilhacker et al, 1988b) in the diverted plasma in the vicinity of the target plates and these show, during the H phase, that the outboard plasma has a temperature, $T_e \approx 50eV$, and density, $n_e \approx 2 \times 10^{19} m^{-3}$, whereas the inboard plasma is cooler, $T_e \approx 13eV$, but has a higher density, $n_e \approx 8 \times 10^{19} m^{-3}$. The difference in sheath

potentials leads to significant thermoelectric currents in the scrape off layer. In addition more power flows to the outer divertor target suggesting that the power flow into the scrape off layer is near the outboard mid plane. The high power density gives surface temperatures on the target plates which can exceed 2000 °C which gives rise to large carbon influxes. During the OH phase the diverted plasma is collisional but during the H phase the electron mean free path is comparable to the distance along a field line from target to X point. Close to the separatrix the outboard diverted plasma is opaque to low energy deuterons escaping from the target but far from the separatrix the plasma is transparent in both OH and H phases. Probe measurements in the scrape off layer itself (far from the divertor) indicate that close to the separatrix the particle flow is away from the divertor. At distances more than 30mm from the separatrix the flow is towards the divertor. This intriguing flow pattern may be connected with the density increase in the core plasma.

4. MORE X POINT RESULTS

Whereas the previous section concentrated on ELM free H modes at fairly high density and with NB only, this section deals with X point discharges with ICRH. H mode discharges with combined NB,ICRH, and low density hot ion X point discharges. More care must be taken when comparing data in this section because of the influence of ELM activity on confinement (Keilhacker, 1988b).
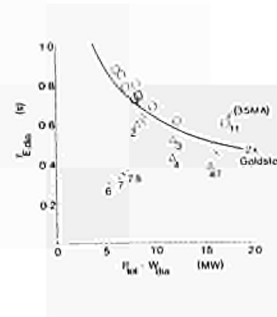
With ICRH alone powers $\approx$ 7.5MW have been coupled into an X point discharge when the antennae were phased as monopoles. In this case, short periods of reduced D_α and fluctuation level were observed. However, as shown in fig 6, the confinement time in these discharges (lozenges) is of order the Goldston prediction, whereas neutral beam H mode data (circles) is of order twice Goldston for the same configuration and similar power levels. With combined NB,ICRH the confinement is of order 1.8 times Goldston as shown in Fig. 6 (triangles) and the D_α is reduced, characteristic of the H mode. However, the radiation increases faster than for the NB only cases, thereby reducing confinement, and the H mode phase is terminated earlier (Tubbing et al, 1989) probably due to the build-up of nickel (from the antenna screens) in the plasma core (Giannella et al, 1989). Impurity injection experiments (Hawkes et al, 1989) show that the impurity confinement time can be as long as 4 seconds or more in such ELM free cases. Note, as yet it has not proved possible to couple significant ICRH power with the antennae phased as dipoles which in limiter discharges produces negligible nickel release.

Fig 6. Confinement time versus power input for 3MA double null X point discharges. The numbers attached to points indicate the ICRH power in MW.

◇ RF only
○ NB only, medium n_e
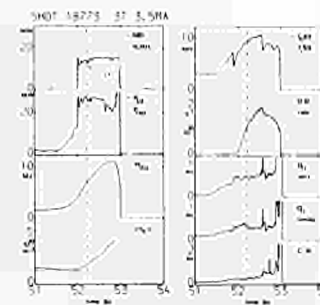△ Combined NB/RF
□ NB/RF, 3.5MA
X NB only, hot ion.

Fig 7. Various time traces for 3.5MA double-null X point shot 18773 with high NB and ICRH power.
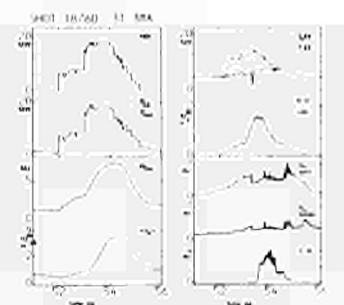
Fig 8. Various time traces for 3.0MA double-null X point shot 18760 with high NB power at low density.

The record stored energy in JET was produced by combined heating in a similar double null configurationbut at a slightly higher current of 3.5MA (the square in Fig. 6). Some time traces of this discharge are shown in fig. 7. Note that at the time marked by the dashed vertical line the confinement is already twice Goldston and although the D_α from the limiter drops, the D_α from the X point region is unchanged. It is not clear in this case whether this marks the L-H transition, but dn_e/dt, τ and the pedestal temperature indicate that subsequently the discharge is in the H mode (Tubbing et al, 1989). Notice also the increased carbon flux at the sawtooth crash (at 52.6 sec) followed by a drop in D_α light from both limiter and X point regions.The confinement is actually degraded at this time and the D-D reaction rate is reduced. Shortly afterwards the radiation increases catastrophically and the discharge disrupts.This discharge is interesting not only because of the high confinement (600ms) at high total power input and high D-D fusion yield, but also because these conditions are found where the limiter clearance is small (only 10mm) and therefore the RF coupling is good, and because the nickel influx is negligible.

Low density target plasmas can be produced in the double null X-point configuration, and with neutral beam heating the H mode transition is delayed until the density is sufficiently high (Tubbing et al, 1989). The confinement during the H mode phase (the Xs in Fig. 6) is almost as good as higher density discharges in the same configuration but the ion temperature, $T_i \approx 18keV$ is much higher, $n_{eff} \tau T_{io}$ is similar in the two cases but because of the higher T_i and longer slowing down time the D-D reaction rate is higher, up to $2.1*10^{16} s^{-1}$. Fig. 8 shows the time traces of such a discharge at high NB power. Here the H mode transition is clearly seen on the D_α light from both limiter and X point regions about 1/4 sec after the step in NB power, and at about this time the ion temperature reaches its maximum and thereafter declines as the

density increases. The D-D reaction rate (predominantly beam-plasma and beam-beam reactions) is still increasing but shortly afterwards begins to decline after the jump in CIII light and subsequent contamination of the plasma.

5. SAWTEETH AND SAWTOOTH SUPPRESSION

It has already been suggested that sawteeth play an important role in confinement during ICRF heating on JET (Bhatnagar et al, 1988) and the data presented in section 2 suggests that the same applies to combined NB/ICRF heating. In this section new results on sawteeth are summarised.

Two dimensional time resolved reconstructions of T_e from ECE measurements during the sawtooth crash (Campbell et al ,1989) show, in confirmation of earlier soft X-ray reconstructions (Edwards et al, 1986), that the displaced hot core residue spreads poloidally in a crescent surrounding the cold bubble on axis. This suggests a broad convective flow rather than the resistive reconnection in a narrow layer proposed by Kadomtsev.

Polarimetric measurements (O'Rourke et al, 1988) show that, in an OH plasma, sawtoothing starts with $q_a \approx 1$ as expected and, as the inversion radius grows, q_a falls to $\approx 0.7 \pm 0.15$. The D_α light from the ablation cloud of an injected pellet shows a characteristic drop in the vicinity of the $q = 1$ surface. This can be explained by the cooling of the plasma on a flux tube which nearly closes on itself leading to a reduction in the ablation rate. The time and space dependencies of the D_α light can be used to estimate dq/dr at the $q = 1$ surface. (Gill et al, 1989). This is found to be small, $\lesssim 4 \cdot 10^{-2}$ (if effects due to possible island formation are neglected) and changes little during the sawtooth period. Pellets can also produce a snake (Weller et al, 1987) which is a localised density perturbation with $m = n = 1$ topology and at the $q = 1$ surface. This snake can survive many sawtooth periods and can move in minor radius ($\Delta r \simeq 30\%a$) during a sawtooth period, suggesting that the $q = 1$ surface moves similarly. Resistive diffusion would allow only a small change in q_a during a sawtooth period and therefore only a small change in the position of the $q = 1$ surface is expected unless the shear at this surface is small. This supports the pellet ablation result that the shear is small at the $q = 1$ surface. Taken together with the polarimetric measurements, these results suggest a local flattening of the q profile in the vicinity of $q = 1$.

Under certain conditions with additional heating the sawtooth can be suppressed for several seconds (Campbell et al, 1988). These periods without sawteeth are called 'monster sawteeth'. Monster sawteeth can occur over a wide range of parameter space with ICRH. They are ubiquitous at moderate and high q particularly at low density and moderate heating power, and have been seen with combined NB/ICRH heating even in the H mode (see for example fig. 5). They occur more rarely at high current (low q) and high density or with NB heating only. Polarimetry finds $q_a \approx 0.7 \pm 0.2$, suggesting that the sawtooth instability has been stabilised rather than q_a raised above 1. This can be explained by the effects of energetic ions produced by NBI or ICRH (Pegoraro et al, 1988). Compared with a sawtoothing discharge or the sawtoothing phase of the same discharge monsters show confinement times the greater by up to 20%. However the profiles of T_i and T_e are much more peaked than the time average profiles during sawtoothing phases giving an important improvement in the fusion yield.

Sawteeth can also be avoided by heating the electrons whilst q_a is well above 1, during the current rise (Start et al, 1988). Polarimetry (Bures et al, 1989) shows that the current penetration is slower, as expected, and the time at which q_a falls below 1 is delayed. However the first sawtooth crash after $q_a = 1$ is reached has a large inversion radius suggesting $q_a < 1$ and hints that a sawtooth stabilisation mechanism is at work in a similar manner to the monster sawtooth case. Practically speaking current rise heating is a way of extending the favourable properties of monsters to higher currents (up to 5MA) and lower q_a (down to ~3.3) in a reproducible way. At the highest value of P_{tot}/n_e the central value of T_e is increased from 7keV (during the flat top at 6MA) to 10keV (at 5MA during the current rise to 6MA). With ICRH only, T_i is also increased from 5 to 7keV. Higher ion temperatures are obtained if NBI is also used (up to 9.5keV) but unfortunately at high NBI powers the sawteeth restart. The global confinement is typically 10-20% better than the values obtained during the flat top with sawteeth present. Interestingly the confinement reaches an asymptotic value very quickly as the power is increased and does not degrade further.

6. PEAKED DENSITY PROFILES WITH PELLET INJECTION

Earlier sections describe enhanced values of $n_{i0}\tau_E T_i$ obtained by increasing τ_E (H modes), and by increasing T_i (hot ion regime).This section discusses enhanced performance obtained by increasing n_{i0} using pellet injection. As will be shown the peaked density profiles obtained also produced improved T_{e0}, T_{i0} and τ_E with additional heating.

Strongly peaked density profiles have been obtained only with pellets which penetrate to or beyond the magnetic axis. This is arranged by the injection of either a sequence of small pellets or fewer small pellets followed by a single larger pellet. These scenarios are chosen to optimise the electron temperature for good penetration (Milora et al, 1988). During the flat top, sawteeth are often suppressed by deep pellet injection and a peaked density profile, with $n_{e0} \approx 1.3 \cdot 10^{20} m^{-3}$ can be formed (Kupschus et al, 1988b), which decays rather slowly to $0.9 \cdot 10^{20} m^{-3}$ over 2 seconds. High central densities, $n_{e0} \lesssim 2.0 \cdot 10^{20} m^{-3}$, and peaked density profiles, $n_{e0}/\langle n_e \rangle \approx 3$, have been produced by deep pellet fuelling during the current rise before the onset of sawteeth where the decay of the density profile is slow. Furthermore, ICRH heating can be successfully applied (Kupschus et al, 1988a). Despite the high density, high central electron temperatures up to 11.5keV are produced with only 8-10MW of ICRH power. Fig. 9 shows central electron temperature against normalised heating rate P_{tot}/n_e for these peaked profile results (solid circles) compared with current rise heating results (solid squares) and normal monster and sawtoothing discharges at various currents (Bhatnagar et al, 1989). The improvement compared with other 3MA data is clear and is comparable to the current rise heating result at a higher current. The electron temperature profile is very peaked, $T_{e0}/\langle T_e \rangle \approx 4$, more so than a typical monster. Fig. 10 shows the companion plot of central ion temperature against normalised heating power. Whereas normally with ICRH alone T_i saturates at 5-6keV, in these pellet shots T_i follows T_e and can reach 10.5keV. Shortly after pellet injection Z_{eff} is low, ~1.4, but subsequently the central impurities build up (Morgan et al, 1989).

D-D fusion rates $\approx 9 \cdot 10^{15} s^{-1}$ are obtained, a factor 4-6 higher than otherwise obtained with ICRH alone. This yield is almost entirely thermonuclear in origin. The contribution from tail deuterons produced by second harmonic heating must be small since similar yields are found with both H and ^{3}He minorities.

The global energy confinement time is only 10-20% higher than in a comparable discharge without the pellet but the central confinement is enhanced by a factor ~2 (Schmidt et al, 1988, Bhatnagar et al, 1989, Hammet et al, 1989, Watkins 1989) within the regions of steep density gradient. η_i and η_e are low ($\lesssim 1$) immediately after pellet injection and rise above the threshold for η_i modes before the end of the enhanced confinement phase. χ_e values inferred from transport analysis are comparable with the predictions of η_i mode turbulence (Milora et al, 1989). However the uncertainties are large, particularly because the radial profile of n_{i0}/n_e is poorly known. Such turbulence does not explain the transport outside the region of steep gradients. An alternative explanation of the enhancement might arise from possible negative
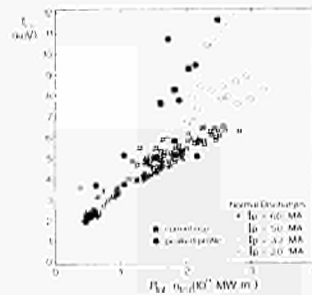

Fig 9. Central electon temperature against normalised power for various discharges heated by ICRF including current rise heating and peaked density profiles.
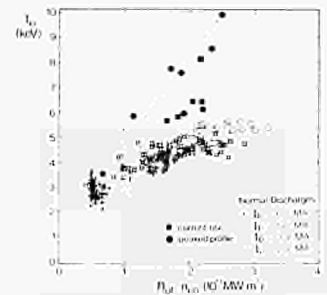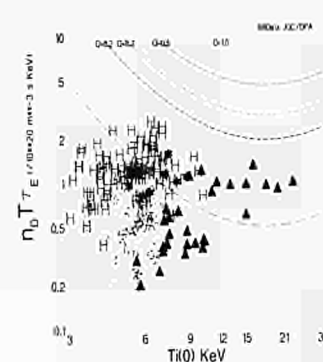

Fig 10. Central ion temperature against normalised power for various discharges heated by ICRF including current rise heating and peaked density profiles.

dq/dr in the centre caused by bootstrap currents (Stubberfield et al, 1989) which would be expected to impede the formation of small islands (Rebut et al, 1986 and Rebut et al, 1988).

7. FUSION PERFORMANCE

The maximum values of $n_{i0}\tau_E T_i$ obtained in JET lie in the range $1-2.4 \cdot 10^{20} m^{-3}$.s.keV as shown in fig. 11. The higher values are obtained in the H mode where $T_i \approx 6-8$keV, and the lower values in the hot ion regimes where $T_i \approx 12-23$keV. The peaked profile regime with pellets is intermediate between these extremes. Fig. 11 also shows contours of thermonuclear gain Q_{DT} for a 50:50 deuterium-tritium mixture for a pure plasma with a pressure profile peaking factor of 3 and $T_i = T_e$ (or equivalently $n_{i0}/n_e = 0.5$ for $T_i = 2T_e$). Despite the variations in Z_{eff}, profiles and T_i, T_e in the JET data, these contours can be used to predict the JET D-T thermonuclear performance for the best discharges in Fig. 11 to within 15%. It can be seen that the best cases extrapolate to $Q_{DT} \lesssim 0.1$.

For typical limiter plasmas the extrapolation is somewhat less favourable, even at high current, and $Q_{DT} \approx 0.05-0.07$ is expected. Calculations taking actual parameters and profiles for typical discharges and simply replacing the measured deuterium density by a 50:50 deuterium-tritium mixture and increasing the beam energy to 140keV give $Q_{TOTAL} \approx 0.3$, including non thermal reactions. It was already shown in section 4 that it is possible to move horizontally in fig. 11 by increasing P_{tot}/n_e to produce an hot ion H mode plasma. If it were possible to control the density of high current H modes and maintain $n_{i0}\tau_E T_i \approx 2.4 \cdot 10^{20} m^{-3}$.s.keV at $T_i \approx 15$keV then $Q_{DT} \approx 0.25$ is obtained. In addition, a substantial improvement would accrue from improved n_{i0}/n_e. When beam driven reactions are taken into account (Cordey et al, 1986b) the prospects for $Q_{TOTAL} \approx 1$ appear good. A similar conclusion can be drawn by using scaling laws to extrapolate existing results with current and power (Gibson, 1988).

Fig 11. Measured values of $n_{i0}\tau_E T_i$ as a function of T_{i0}.

H H mode data.
* pellet shots.
▲ low density (hot ion)
○ other limiter data.

The curves show contours of Q_{DT}.

Studies of ICRF heated deuterium in a tritium plasma suggest that the enhanced reactivity from the deuteron tail could give $Q_{TOTAL} \approx 0.7$ (Cottrell et al, 1989). Such calculations are supported by the observation of a ^{3}He-D reaction rate $\approx 2 \cdot 10^{16} s^{-1}$ (equivalent to 60kW of fusion power) with ^{3}He minority heating in a deuterium plasma (Boyd et al, 1989), where good agreement was found with theoretical prediction. These experiments reveal no surprises concerning the behaviour of energetic ^{3}He ions, and apart from the perpendicular velocity distribution, represent an α simulation relevant to JET with $Q_{TOTAL} \sim 1$ or an ignited ITER (Bickerton et al, 1988).

8. SUMMARY AND CONCLUSIONS

During 1988 JET operated with plasma currents up to 7MA and total additional heating power up to 35MW.The plasma performance included $\tau_E \lesssim 1.3$ sec, $T_i \lesssim 23$ keV, $T_e \lesssim 12$ keV, and $n_{e0} \lesssim 2.0 \cdot 10^{20} m^{-3}$ (highest values obtained on different discharges). A range of configurations were explored including limiter and X point, L and H mode, sawtoothing and sawtooth free discharges and discharges with strongly peaked density profiles. In both limiter and H mode the confinement behaves broadly as expected, namely improving with current and degrading with power with the usual multipliers compared with Goldston scaling, for example. However in both cases the confinement deteriorates at low q (i.e at high current). Apart from the H mode, improved performance was found at low density, in sawtooth free discharges and in discharges with peaked density profiles. Unfortunately all these regimes suffer to some extent from unacceptable carbon influxes particularly at high power input (the so called carbon catastrophe) and in improved confinement cases from impurity build up. The confinement results in general continue to behave in an offset linear manner as described by Rebut-Lallia and in particular transport coefficients measured by perturbation methods appear to be independent of heating scheme or confinement mode suggesting either a threshold behaviour or heat pinch. The exception is the peaked profile regime where transport coefficients are reduced markedly where the density gradient is large, whereupon the transport may be determined by η_i mode turbulence. Alternatively this result might be explained by a possible negative dq/dr.

Encouraging results have been obtained coupling large ICRF powers to H modes produced by NBI which show promise for very high power combined heating of H modes in the near future. Other encouraging results include the high ion temperature regimes (now established for both inner wall and H mode plasmas), the current rise heating scheme which extends the favourable properties of monsters to lower q and finally the results on density profile control with pellets.

As far as fusion performance is concerned, it has been shown that JET is approaching the desired plasma conditions on a broad front with these different regimes, and whilst plasmas already demonstrated have modest Q_{DT}, there is scope for significant improvement. Perhaps the most challenging obstacle yet to be overcome remains the control both of density and of impurities.

9. ACKNOWLEDGEMENTS.

It is a pleasure to acknowledge the contributions from the following- V.Bhatnagar, M.Bures, D.J.Campbell, J.G.Cordey, J.P.Christiansen, C.D.Challis, J.C.M.de Haas, L.de Kock, R.Giannella, R.D.Gill, A.Gondhalekar, P.J.Harbour, T.T.C.Jones, J.Jacquinot, M.Keilhacker, P.Kupschus, C.G.Lowry, C.S.Pitcher, J.O'Rourke, M.Stamp, D.Start, J.A.Tagle, A.Taroni, F.Tibone, P.R.Thomas, K.Thomsen, B.Tubbing, M.von Hellermann and M.L.Watkins for their efforts in sifting vast quantities of data, without which this summary would have been the poorer. The pellet injection results were obtained during work performed under a collaboration agreement between the JET Joint Undertaking and the US. Department of Energy (USDOE).

10. REFERENCES

Bickerton,R.J. et al, (1988) Latest JET Results and Future Prospects.
Plasma Physics and Controlled Fusion Research (Proc. 12ᵗʰ
Int Conf. Nice) IAEA-CN-50/A-VII-2

Bertolini,E. et al, (1987) in Proc. 12ᵗʰSymp. on Fusion Engineering. (Monterey, USA)

Bhatnagar,V. et al, (1988) Effect of Sawteeth, Safety Factor and Current
on Confinement during ICRF Heating of JET, JET-P(88)51.
To be published in Plasma Physics and Controlled Fusion.

Bhatnagar,V. et al, (1989) ICRF Power Deposition Profiles and Heating
in Monster Sawteeth and Peaked Density Profile Discharges in JET.
Europhysics Conference Abstracts 13B, p127. ★

Boyd,D.A. et al, (1988) ³He-D Fusion Reaction Rate Measurements During
ICRH Expriments in JET. To be submitted for publication.

Bures,M. et al, (1989) Enhanced Performance of High Current
Discharges in JET produced by ICRF Heating during the Current Rise.
Europhysics Conference Abstracts 13B, p3. ★

Campbell,D.J. et al, (1988) Stabilisation of Sawteeth with
Additional Heating in the JET Tokamak.Phys. Rev. Lett. 60, 2148.

Campbell,D.J. Edwards,A.W and Pearson,D.(1989) Sawteeth and the m = 1 Mode in JET.
Europhysics Conference Abstracts 13B, p509. ★ ,

Cheetham,A.D. et al, (1988) Measurements of Correlations Between Thermal
and Particle Transport in JET. Plasma Physics and Controlled Fusion
Research (Proc. 12ᵗʰInt. Conf. Nice, 1988) IAEA-CN-50/I-2-2

Conroy,S. et al, (1989) Triton Burnup in JET.
Europhysics Conference Abstracts 13B, 67. ★

Cordey,J.G. et al, (1986a) Energy Confinement with Ohmic and Strong
Auxiliary Heating in JET. Plasma Physics and Controlled Fusion
Research (Proc. 11ᵗʰInt. Conf. Kyoto, 1986) Vol 1 p99, IAEA, Vienna.

Cordey,J.G. et al, (1986b) Prospects for Alpha Particle Heating in JET
in the Hot Ion Regime. JET-P(86)38

Cottrell,G.A. et al, (1989)Non Thermal DT Yield with (D)T ICRH in JET.
Europhysics Conference Abstracts 13B, 71. ★

de Haas,J.C.M and Lopes Cardozo,N.J. (1988) χₑ from Heat pulse
Propagation during JET H-mode. 30th Annual meeting of the Plasma
Physics Division of the APS, Hollywood, Florida. Bull.APS, 33 no 9 p2030.

de Kock,L. et al, (1988) The Plasma Boundary in JET. Plasma Physics and
Controlled Fusion Research (Proc. 12ᵗʰInt. Conf. Nice, 1988)
IAEA-CN-50 A-7-12.1/2

Edwards,A.W et al. (1986) Rapid Collapse of a Plasma Sawtooth Oscilation
in the JET Tokamak. Phys. Rev. Lett. 57 p210.

Giannella,R. et al, (1989) Behaviour of Impurities During the H mode in
JET. Europhysics Conference Abstracts 13B, 209. ★

Gill,R.D. et al, (1989) q Profiles in JET.
Europhysics Conference Abstracts 13B, 469. ★

Gibson,A. (1988) Plasma Performance in JET.
Plasma Physics and Controlled Fusion 30,1390.

Goldston,R (1984)Plasma Physics and Controlled Fusion 26, 87.

Gondhalekar,A. et al (1988)Simultaneous Measurements of Electron Thermal
and Particle Transport in JET.
To be published in Plasma Physics and Controlled Fusion.

Hammet,G.W. et al, (1989)Transport Analysis of Pellet Enhanced ICRH
Plasmas in JET.Europhysics Conference Abstracts13B,131. ★

Harbour,P.J. et al (1988) Workshop on Plasma Edge Theory in Fusion
Devices, Augustusburg, GDR, in 'Contributions to Plasma Physics',
Akademie-Verlag, 28 (1988) 4/5 pp417-419, Berlin, GDR

Hawkes,N. et al, (1989) Transport Studies during Sawteeth and H modes
on JET using Laser Ablation.Europhysics Conference Abstracts 13B, 79. ★

Hugon,M. Lallia,P. and Rebut,P.H (1989)Comparison Between Beryllium and
Graphite as Materials for JET Limiters and Wall Surfaces. To be submitted for publication.

Jacquinot,J. (1986) RF Heating on JET.
Plasma Physics and Controlled Fusion Research (Proc. 11ᵗʰInt. Conf. Kyoto)
Vol. 1 p449, IAEA, Vienna.

Jones,T.T.C. et al, (1989) Europhysics Conference Abstracts 13B, 11. ★

Keilhacker,M. et al, (1988a) Studies of Energy Transport in JET H modes.
Europhysics Conference Abstracts 12B, p231. ○

Keilhacker,M. et al, (1988b)The JET H Mode at High Current and Power
Levels. Plasma Physics and Controlled Fusion Research (Proc. 12ᵗʰ
Int. Conf. Nice, 1988) IAEA-CN-50 A-III-2.

Kupschus,P. et al, (1988a) Multipellet Injection on JET
Europhysics Conference Abstracts 12B, 143. ○

Kupschus,P. et al, (1988b) JET Multipellet Injection Experiments.
IAEA Techn Comm. Meeting, Gut Ising,Oct 1988.

Lowry,C.G. et al, (1989) The Hot Ion Mode of Small Bore Plasmas in JET.
Europhysics Conference Abstracts 13B, 87. ★

Milora,S.L. et al, (1988) The JET Multipellet Launcher and Fuelling of
JET Plasmas by Multipellet Injection.
Europhysics Conference Abstracts 12B, 147. ○

Milora,S.L et al, (1989) Summary of Energy and Particle Confinement
in Pellet Fuelled Auxiliary Heated Discharges on JET.
Europhysics Conference Abstracts 13B, 91. ★

Morgan,P.D et al, (1989) Studies of Visible Impurity Radiation from
JET during Heating and Fuelling Experiments.
Europhysics Conference Abstracts 13B, p95. ★

O'Rourke,J. et al, (1988)Europhysics Conference Abstracts 12B, 155. ○

Pegoraro,F. et al, (1988) Theory of Sawtooth Stabilisation
in the Presence of Energetic Ions.
Plasma Physics and Controlled Fusion Research (Proc. 12ᵗʰ
Int. Conf. Nice, 1988) IAEA-CN-50 D-4-6

Pitcher,C.S. et al, (1989) Impurity Production and Transport at the JET
Belt Limiter.Europhysics Conference Abstracts 13B, 879. ★

Rebut,P.H. Brusati,M. Hugon,M. and Lallia,P. (1986) Magnetic Islands
and Chaos Induced by Heat Flow. Plasma Physics and Controlled
Fusion Research (Proc. 11ᵗʰInt. Conf. Nice, 1988) Vol 2, p187, IAEA, Vienna.

Rebut,P.H. ,Lallia,P. and Watkins,M.L, (1988) The Critical Temperature
Gradient Model of Plasma Transport. Plasma Physics and Controlled
Fusion Research (Proc. 12ᵗʰInt. Conf. Nice, 1988) IAEA-CN-50/D-4-1.

Schmidt,G.L et al, (1988) Heating of Peaked Density Profiles Produced by
Pellet Injection in JET. Plasma Physics and Controlled Fusion
Research (Proc. 12ᵗʰInt. Conf. Nice, 1988) IAEA-CN-50/A-IV-1.

Stamp,M.F. et al, (1989) Sputtering Measurements on JET using a
Multichannel Visible Spectrometer.
Europhysics Conference Abstracts 13B, 1513. ★

Start,D.F.H et al, (1988) Experimental and Theoretical Studies
of Ion Cyclotron Heating on JET.
Plasma Physics and Controlled Fusion Research (Proc. 12ᵗʰ
Int. Conf. Nice, 1988) IAEA-CN-50/E-II-3

Stubberfield,P.M. et al, (1989) Current Density Profile Evolution in JET
Europhysics Conference Abstracts 13B, 1255. ★

Tagle,J.A et al, (1989) The Effect of Different ICRF Heating Scenarios on
the JET Scrape-Off Layer.To be published in Journal of Nuclear Materials.

Tibone,F. et al, (1989)Ion Thermal Conductivity and
Convective Energy Transport in JET Hot Ion Regimes and H modes.
Europhysics Conference Abstracts 13B, 283. ★

Thomas,P. et al, (1988) High Temperature Experiments and Fusion Product
Measurement on JET.Plasma Physics and Controlled Fusion Research
(Proc. 12ᵗʰInt. Conf. Nice, 1988) IAEA-CN-50 A-4-4

Thomsen,K. et al, (1987) Confinement Analysis of Auxiliary Heated JET
Discharges. Europhysics Conference Abstracts 11D, 168. ▲

Thomson,E. et al, (1987) Phenomenological and Predictive Studies of
Confinement and Global Heating in JET Neutral Beam Heated Limiter
Discharges. Europhysics Conference Abstracts 11D, 310. ▲

Tubbing,B. et al, (1989) Double Null X point Operation in JET with
NBI and ICRH.Europhysics Conference Abstracts 13B, 237. ★

Watkins,M.L (1989) Confinement Properties of JET Plasmas with Different
Density and Temperature Profiles. ibid.

Weller,A. (1987) Persistent Density Perturbations at Rational q Surfaces
Following Pellet Injection in JET.Phys. Rev. Lett. 50, 2303.

★ Proc. 16ᵗʰ European Conf. on Controlled Fusion and Plasma Physics, Venice, 1989.
○ Proc. 15ᵗʰ European Conf. on Controlled Fusion and Plasma Heating, Dubrovnik, 1988.
▲ Proc. 14ᵗʰ European Conf. on Controlled Fusion and Plasma Physics, Madrid 1987.

APPENDIX 1.

THE JET TEAM

JET Joint Undertaking, Abingdon, Oxon, OX14 3EA, U.K.

J.M.Adams[1], F.Alladio[4], H.Altmann, R.J.Anderson, G.Appruzzese, W.Bailey, B.Balet, D.V.Bartlett, L.R.Baylor[24], K.Behringer, A.C.Bell, P.Bertoldi, E.Bertolini, V.Bhatnagar, R.J.Bickerton, A.Boileau[1], T.Bonicelli, S.J.Booth, G.Bosia, M.Botman, D.Boyd[11], H.Brelen, H.Brinkschulte, M.Brusati, T.Budd,M.Bures, T.Businaro[4], H.Buttgereit, D.Cacaut, C.Caldwell-Nichols, D.J.Campbell, P.Card, J.Carwardine, G.Celentano, P.Chabert[27], C.D.Challis, A.Cheetham, J.Christiansen, C.Christodoulopoulos, P.Chuilon, R.Claesen, S.Clement[10], J.P.Coad, P.Colestock[6], S.Conroy[1], M.Cooke, S.Cooper, J.G.Cordey, W.Core, S.Corti, A.E.Costley, G.Cottrell, M.Cox[1], P.Cripwell[13], F.Crisanti[4], D.Cross, H.de Blank[16], J.de Haas[18], L.de Kock, E.Deksnis, G.B.Denne, G.Deschamps, G.Devilars, K.J.Dietz, J.Dobbing, S.E.Dorling, P.G.Doyle, D.F.Duchs, H.Duquenoy, A.Edwards, J.Ehrenberg[14], T.Elevant[12], W.Engelhardt, S.K.Erents[3], L.G.Eriksonn[3], M.Evrard[2], H.Falter, D.Flory, M.Forrest[3], C.Froger, K.Fullard, M.Gadeberg[11], A.Galetsas, R.Galvao[8], A.Gibson, R.D.Gill, A.Gondhalekar, C.Gordon, G.Gorini, C.Gormezano, N.A.Gottardi, C.Gowers, B.J.Green, F.S.Griph, M.Gryzinski[26], R.Haange, G.Hammett[6], W.Han[9], C.J.Hancock, P.J.Harbour, N.C.Hawkes[3], P.Haynes[1], T.Hellsten, J.L.Hemmerich, R.Hemsworth, R.F.Herzog, K.Hirsch[14], J.Hoekzema, W.A.Houlberg[24], J.How, M.Huart, A.Hubbard, T.P.Hughes[13], M.Hugon, M.Huguet, J.Jacquinot, O.N.Jarvis, T.C.Jernigan[24], E.Joffrin, E.M.Jones, L.P.D.F.Jones, T.T.C.Jones, J.Kallne, A.Kaye, B.E.Keen, M.Keilhacker, G.J.Kelly, A.Khare[15], S.Knowlton, A.Konstantellos, M.Kovanen[21], P.Kupschus, P.Lallia, J.R.Last, L.Lauro-Taroni, M.Laux[15], K.Lawson[3], E.Lazzaro, M.Lennholm, X.Litaudon, P.Lomas, M.Lorentz-Gottardi[2], C.Lowry, G.Magyar, D.Maisonnier, M.Malacarne, V.Marchese, P.Massmann, L.McCarthy[28], G.McCracken[3], P.Mendonca, P.Meriguet, P.Micozzi[4], S.F.Mills, P.Millward, S.L.Milora[24], A.Moissonnier, P.L.Mondino, D.Moreau[17], P.Morgan, H.Morsi[14], G.Murphy, M.F.Nave, M.Newman, L.Nickesson, P.Nielsen, P.Noll, W.Obert, D.O'Brien, J.O'Rourke, M.G.Pacco-Duchs, M.Pain, S.Papastergiou, D.Pasini[20], M.Paume[17], N.Peacock[3], D.Pearson[1], F.Pegoraro, M.Pick, S.Pitcher[1], J.Plancoulaine, J-P.Poffé, F.Porcelli, R.Prentice, T.Raimondi, J.Ramette[17], J.M.Rax[27], C.Raymond, P.H.Rebut, J.Removille, F.Rimini, D.Robinson[3], A.Rolfe, R.T.Ross, L.Rossi, G.Rupprecht[14], R.Rushton, P.Rutter, H.C.Sack, G.Sadler, N.Salmon[13], H.Salzmann[14], A.Santagiustina, D.Schissel[25], P.H.Schild, M.Schmid, G.Schmidt[8], R.L.Shaw, A.Sibley, R.Simonini, J.Sips[16], P.Smeulders, J.Snipes, S.Sommers, L.Sonnerup, K.Sonnenberg, M.Stamp, P.Stangeby[19], D.Start, C.A.Steed, D.Stork, P.E.Stott, T.E.Stringer, D.Stubberfield, T.Sugie[18], D.Summers, H.Summers[20], J.Taboda-Duarte[22], J.Tagle[10], H.Tamnen, A.Tanga, A.Taroni, C.Tebaldi[23], A.Tesini, P.R.Thomas, E.Thompson, K.Thomsen[11], P.Trevalion, M.Tschudin, B.Tubbing, K.Uchino[29], E.Usselmann, H.van der Beken, M.von Hellermann, T.Wade, C.Walker, B.A.Wallander, M.Walravens, K.Walter, D.Ward, M.L.Watkins, J.Wesson, D.H.Wheeler, J.Wilks, U.Willen[12], D.Wilson, T.Winkel, C.Woodward, M.Wykes, I.D.Young, L.Zannelli, M.Zarnstorff[8], D.Zasche[14], J.W.Zwart.

PERMANENT ADDRESS

1 UKAEA, Harwell, Oxon, UK
2 EUR/EB Association, LPP-ERM-KMS, B-1040 Brussels, Belgium
3 Institute National des Recherches Scientifique, Quebec, Canada
4 ENEA CENTRO Di Frascati, I-00044 Frascati, Roma, Italy
5 Chalmers University of Technology, Goteborg, Sweden
6 Princeton Plasma Physics Laboratory, New Jersey, USA
7 UKAEA Culham Laboratory, Abingdon, Oxon UK
8 Plasma Physics Laboratory, Space Research Institute, Sao Jose dos Campos, Brazil
9 Institute of Mathematics, University of Oxford, UK
10 CRPP/EPFL, 21 Avenue des Bains, CH-1007 Lausanne, Switzerland
11 Riso National Laboratory, DK-4000 Roskilde, Denmark
12 Swedish Energy Research Commission, S-10072 Stockholm, Sweden
13 Imperial College of Science and Technology, University of London, UK
14 Max Planck Institut für Plasmaphysik, D-8046 Garching bei München, FRG
15 Institute for Plasma Research, Gandhinagar Bhat Gujat, India
16 FOM Instituut voor Plasmafysica, 3430 Be Nieuwegein, The Netherlands

17 Commissariat a l'Energie Atomique, F-92260 Fontenay-aux-Roses, France
18 JAERI, Tokai Research Establishment, Tokai-Mura, Naka-Gun, Japan
19 Institute for Aerospace Studies, University of Toronto, Downsview, Ontario, Canada
20 University of Strathclyde, Glasgow, G4 0NG, UK
21 Nuclear Engineering Laboratory, Laperanta University, Finland
22 JNICT, Lisboa, Portugal
23 Department of Mathematics, University of Bologna, Italy
24 Oak Ridge National Laboratory, Oak Ridge, Tenn., USA
25 G.A. Technologies, San Diego, California, USA
26 Institute for Nuclear Studies, Swierk, Poland
27 Commissariat a l'Energie Atomique, Cadarache, France
28 School of Physical Sciences, Flinders University of South Australia, South Australia SO42
29 Kyushu University, Kasagu Fukuoka, Japan
30 Centro de Investigaciones Energeticas Medioambientales y Techalogicas, Spain
31 University of Maryland, College Park, Maryland, USA
32 University of Essex, Colchester, UK
33 Akademie der Wissenschaften, Berlin, DDR

CR 88 49 1A

Confinement Properties of JET Plasmas with Different Temperature and Density Profiles

M L Watkins et al

Invited Paper at the 16th European Conference on Controlled Fusion and Plasma Physics, Venice, Italy. 13th—17th March 1989.

CONFINEMENT PROPERTIES OF JET PLASMAS WITH DIFFERENT
TEMPERATURE AND DENSITY PROFILES

M. L. Watkins, B. Balet, V. P. Bhatnagar, J. G. Cordey, G. W. Hammett, T. Hellsten,
M. Keilhacker, S. L. Milora, P. D. Morgan, C. Sack, G. L. Schmidt, A. Taroni,
P. R. Thomas, K. Thomsen, F. Tibone, M. von Hellermann, H. Weisen
and
the JET Team[1]

JET Joint Undertaking, Abingdon, Oxon., OX14 3EA, UK

ABSTRACT

The confinement properties of plasmas with substantially different temperature and density profiles
have been analysed. The effects of fast particles and energy pedestals on the overall confinement of
plasma energy in limiter (L-mode) and X-point (L- and H-modes) discharges heated by NBI or ICRF
or both are determined. The importance of the bootstrap current when such energy pedestals are
formed is noted. Using sets of consistent experimental data, including ion temperature profile
measurements, the local transport properties are compared in the L- and H-phases of a single null X-
point medium density NBI heated discharge, the "enhanced" confinement phase of a limiter high den-
sity pellet-fuelled and ICRF heated discharge, the hot-ion phase of a double null X-point low density
NBI heated discharge and the hot-ion and H-phases of a double null X-point low density high tem-
perature NBI heated discharge.

KEYWORDS

Confinement; H-mode; hot-ion mode; interpretation; JET; pellet; plasma; tokamak; transport.

INTRODUCTION

The flexibility of the JET apparatus and its systems has allowed plasmas with substantially different
temperature and density profiles (Bickerton and the JET Team, 1989). In a single null X-point con-
figuration deuterium neutral beam injection (NBI) at 80kV has been used to heat medium/high den-
sity plasmas; very flat, and even hollow, density profiles develop during the H-phase (Keilhacker and
the JET Team, 1989). In a double null X-point configuration lower density, higher temperature H-
mode discharges have been achieved with NBI alone (Balet et al., 1989) and in combination with ion
cyclotron resonance heating (ICRH) (Tubbing et al., 1989); these tend to have mildly peaked density
profiles. In such a configuration NBI has also heated low density plasmas with highly peaked tempera-
ture and density profiles, reminiscent of the TFTR "supershot" regime (Strachan et al., 1987). The
central ion temperature, $T_i(0)$, reaches 23keV with a central electron density, $T_e(0) \sim 8$keV and
a central electron density, $n_e(0) \sim 2.10^{19}$m^{-3} (Thomas and the JET Team, 1989; Tibone et al., 1989).
In a limiter configuration ICRH has been used to obtain hot electron plasmas with $T_e(0)$ up to 12keV
and $T_i(0) \sim 7$keV at $n_e(0) \sim 3.510^{19}$m^{-3} (Start et al., 1989). In combination with the injection of deute-
rium pellets very peaked density and temperature profiles have been obtained with $n_e \sim 10^{20}$m^{-3},
$T_e \sim 10$keV and $T_i \sim 8$keV (Schmidt and the JET Team, 1989). Using NBI and ICRH together, high
$T_i(0)$ and $T_e(0)$ have been obtained simultaneously.

In this paper, the confinement of a number of these different types of discharges is discussed. Fir-
stly, the overall confinement properties are compared. Particular emphasis is placed on identifying
the contribution of fast ions (Thomas and the JET Team, 1989) and energy pedestals (Keilhacker and
the JET Team, 1989; Thomsen et al., 1989) to the confinement of the bulk plasma. The importance
of the bootstrap current (Cordey et al., 1988; Stubberfield et al., 1989) and its effect on the stability
of ballooning modes (O'Brien et al., 1989) when such energy pedestals form is also noted.

Secondly, the JET experimental data and the interpretive and predictive methods used to describe
the local transport properties of the bulk plasma are summarised. A substantial diagnostic capability
is complemented by a suite of analysis codes, which includes the time dependent energy balance code,
TRANSP (Hawryluk, 1980; Goldston et al., 1981), the timeslice energy balance code, FALCON (Ti-
bone et al., 1989) and the predictive transport code, JETTO (Taroni et al., 1989).

Thirdly, these methods are applied to consistent sets of data for four specific discharges that exhibit
the extremes of profiles and the best confinement properties observed in JET. These studies com-
prise: a 3MA/3.1T single null X-point, medium density, H-mode discharge heated by 8MW of NBI;
a 3MA/3T limiter discharge of high density, pellet-fuelled and ICRF heated; a 3MA/3.4T double null
X-point, low density, hot ion discharge heated with 21MW of NBI; and a 3MA/3.4T double null X-
point, low density, high temperature H-mode discharge heated by 10.5MW of NBI.

GLOBAL CONFINEMENT PROPERTIES

For limiter (L-mode) discharges Thomas and the JET Team (1989) pointed out that the overall con-
finement of plasma energy is apparently insensitive to variations in the central temperature, or den-
sity, by a factor two. This is shown in Fig. 1(a) for a data set comprising discharges at 3MA/2.8-3.4T
and distinguished according to whether $T_e(0)$, $T_i(0)$, $T_e(0)$ and $T_i(0)$ or $n_e(0)$ is high (Fig. 1(b)). This
result does not preclude the possibility of better central confinement, where the temperatures and
densities are high, but, for these discharges, the central volume is relatively small and contributes little
to the average temperature or density. In fact, even when pellets are injected deep into an ohmic plas-
ma and subsequently heated by ICRF, the density and temperature profiles remain very peaked, but,
during a phase of "enhanced" confinement, the overall confinement is only some 20% better than after
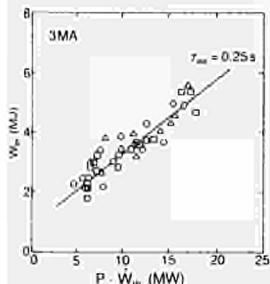this phase (Milora et al., 1989).

Fig. 1(a) Total plasma energy, W_{th}, as a function of Fig. 1(b). Characterisation of the 3MA JET limiter discharges
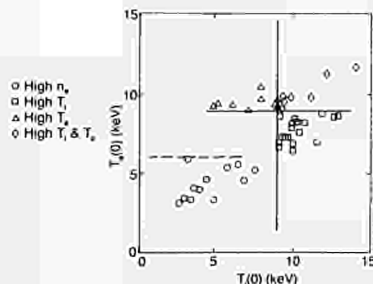net input power for 3MA JET limiter discharges   according to $T_e(0)$ and $T_i(0)$

For a list of the JET Team members, see Lomas and the JET Team, 1989.

The L-mode data of Fig. 1(a) have been characterised by an off-set linear scaling law for the total
plasma energy, W_{th}:

$$W_{th} = W_{oi} + \tau_{inc} (P - dW_{th}/dt) \qquad (1)$$

where $\tau_{inc} = 0.25$s is the incremental confinement time (Callen et al., 1987).

In the single null X-point configuration at the same
plasma current, the overall energy confinement is
somewhat better during the L-phase (Tanga and the
JET Team, 1987). In the H-phase, however, the den-
sity and temperature profiles are broader and the con-
finement is better by a factor of 2. This is shown by the
diamagnetic measurement of the stored energy, W, as
a function of net input power for a dataset of 3MA/2.8T
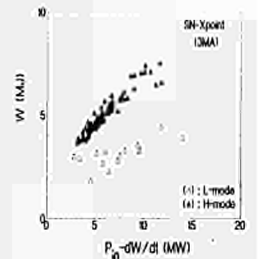single null X-point discharges (Fig. 2).

Much of the improvement in the overall energy con-
finement in the H-phase can be attributed to the de-
velopment of pedestals in energy, as seen by the
LIDAR Thomson scattering system in the steep edge
gradients in the electron density, and sometimes the
electron temperature also (Fig. 3). The contribution of
these pedestals to the overall energy confinement must
be extracted before the intrinsic confinement of the
bulk plasma can be established (Keilhacker and the
JET Team, 1989; Thomsen et al., 1989).

Fig 2. Total stored energy, W, as a function of net
input power for 3MA JET single null X-point
discharges in L- and H-modes.

Consider the simplified total energy balance equation:

$$3 d(nT)/dt = -\nabla.Q + p \qquad (2)$$

p is the net heating rate and the total heat flux, Q, is assumed to comprise a diffusive term propor-
tional to the temperature gradient, ∇T, and a negative, non-diffusive flow term which could be a heat
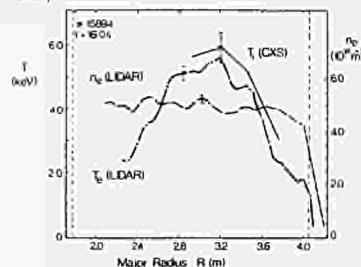pinch (Callen et al., 1987) or a critical electron temperature gradient (Rebut, Lallia and Watkins,
1989).

Fig. 3. Radial profiles of electron density, n_e, electron
temperature, T_e, and ion temperature, T_i, during the H-phase
of a 3MA JET single null X-point discharge. The dashed line
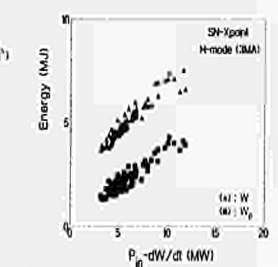indicates the radius of the 95% flux surface

Fig. 4. Total stored energy, W, and the pedestal
energy, W_p (evaluated at the radius of the 95% flux
surface), as a function of net input power during the
H-phase of a 3MA JET single null X-point discharges

Integrating eq. (2) three times gives an equation for the total stored energy, $W_{th} = \int nTdV$:

$$W_{th} = W_p + W_o + \tau_\chi \{ \eta_Q P_{in} - \eta_{nT} (dW_{th}/dt) \} \qquad (3)$$

The pedestal energy, W_p, appears naturally in this formulation, as does the usual off-set term, W_0.
The "ideal" incremental confinement time, τ_χ, depends on the radial profile of the thermal diffusiv-
ity, χ, as do the heating effectiveness parameters, η_Q and η_{nT}. The pedestal energies, evaluated at the
radius of the 95% flux surface during the H-phase of 3MA single null X-point discharges, are plotted
in Fig. 4 against the net input power. A pedestal energy of up to 4MJ contributes substantially to the
total stored energy. Furthermore, there is no pronounced degradation of W_p with input power. The
values of W_p obtained in the L-phases which precede the H-phases are scattered in a range up to 1MJ
and also apparently show no degradation with input power. The energy differences, $W-W_p$, for the
H- and L-phases of the discharges are similar. However, to compare in detail the confinement proper-
ties of the bulk plasma in the L- and H-phases requires a full local transport analysis, as reported in
later sections of the paper.

The confinement properties in the edge which might allow such energy pedestals are not discussed in
this paper. None-the-less, it is worth noting that the experimentally determined pressure gradients,
though large (15CkPa.m^{-1}), lie somewhat below the critical values for the threshold for ballooning in-
stabilities, which have been calculated on the basis of JET H-mode equilibria and a finite aspect ratio
ballooning formalism (O'Brien et al., 1989). However, the experimental values may have been under-
estimated due to the limited spatial resolution of the LIDAR diagnostic (0.08m). Furthermore, close
to the separatrix, coalescence of the first and second stable regions occurs since the total current den-
sity (resistive, beam-driven and bootstrap) exceeds the calculated critical value. The dominant con-
tribution to the current density in the edge of an H-mode plasma is the bootstrap current which arises
from the steep edge density gradient (Cordey et al., 1988; Stubberfield et al., 1989).

LOCAL TRANSPORT ANALYSIS

The experimental data input to the interpretive codes (TRANSP and FALCON) comprise the time
dependence of the magnetic flux surface geometry and the plasma current, the electron density profile
(inverted data from a six channel FIR interferometer and LIDAR when available), the electron
temperature profile (ECE data and LIDAR data when available), the ion temperature profile (charge
exchange spectroscopy (CXS) of fully stripped carbon and oxygen when available (von Hellermann
et al., 1989)), the radiated power profile (inverted bolometer data), the Z_{eff} profile (visible bremss-
trahlung, checked against CXS and neutron yield estimates of the deuterium to electron density ratio)
and the edge particle confinement time (D_α monitors).

The CXS measurement of the ion temperature profile is not available for the pellet-fuelled ICRF-
heated discharge considered here. The profile has been modelled, therefore, with an ion thermal dif-
fusivity, χ_i, proportional to the electron thermal diffusivity, χ_e, the constant of proportionality, $n(t)$,
being adjusted in time so that the calculated central ion temperature, $T_i(0)$, matches that obtained
from doppler broadening of the He-like nickel line observed with an X-ray crystal spectrometer.

Neutral beam heating and fuelling is calculated using either monte carlo (Goldston et al., 1981) or
multiple pencil beam methods (Cordey, Keilhacker and Watkins, 1987). Ion cyclotron resonance heat-
ing is calculated using either a 3-D poloidal mode expansion code (Smithe et al., 1987) or a ray trac-
ing code (Bhatnagar et al., 1984).

The predictive code (JETTO) uses much of the above experimental data as input, except that the elec-
tron and ion temperatures are calculated with a model based on the critical temperature gradient
model of Rebut, Lallia and Watkins (1989) and then compared with the experimental data.

Local transport analyses use the energy and particle conservation equations (Hawryluk, 1980) to pro-
vide, in the first instance, the total heat flux through magnetic surfaces in the interior of the plasma.

An "effective" thermal diffusivity may be defined, such as that obtained from power balance, $\chi_{eff} = Q/n_e \nabla k T_e S$ (where the total heat flux, Q, including the contributions from energy equipartition and convection, across a surface of area, S, is assumed to be proportional to $n_e \nabla k T_e$). In principle, it is possible to proceed further, separating the convective energy losses and, if ion temperature profile data is available, separating the electron and ion conductive energy losses and defining "effective" heat diffusivities, χ_e and χ_i:

$$q_e = -n_e \chi_e \nabla k T_e \; ; \qquad q_i = -n_i \chi_i \nabla k T_i \qquad (4)$$

The "effective" diffusivities shown in this paper are from TRANSP. Similar results are obtained with FALCON and JETTO. Flux surfaces are labelled with either a normalised coordinate, ρ ($0 < \rho < 1$) or the equivalent circular radius, r ($0 < r(m) < 1.5$). The range of interest is usually limited to $0.25 < r(m) < 1.0$. Outside this range the errors become substantial.

The data used for the analyses in this paper are consistent in the sense that the calculated total stored energy, surface voltage (including the contributions from the resistive, beam-driven and bootstrap currents) and total neutron yield (including the contributions from beam-beam, beam-plasma and plasma-plasma reactions) are within the experimental uncertainties on the measurements. None-the less, varying the experimental data within their individual levels of accuracy can introduce a large uncertainty in, for example, the equipartition of energy between electrons and ions and hence in χ_e and χ_i. The errors on χ_e and χ_i are presently estimated at $\pm 50\%$, except when χ_e is apparently much lower than χ_i and the error on χ_e can increase to a factor of 2-3.

MEDIUM DENSITY H-MODE DISCHARGE

The time behaviour of various parameters in the single null X-point JET discharge #15894 is shown in Fig. 5. The L-phase, which lasts for ~0.7s from the start of 8MW of NBI at a time of 14s, is followed by a transition to the H-phase (as indicated by the abrupt fall in the intensity of the D_α emission and the subsequent low level activity). The plasma density, the total stored energy and the neutron reaction rate increase until the H-phase terminates as the NBI power is reduced at 17s. $T_e(0)$ remains roughly constant, or even falls slightly, in time.

The radial profiles of n_e, T_e and T_i are shown in Fig. 4 at a time of 16s, well into the H-phase. In the bulk of the plasma the most characteristic feature is the flat density profile, which changes little as the density increases. The electron temperature also changes little with time. Within the accuracy of the measurements the electron and ion temperatures are the same.

Fig. 5. Time behaviour of electron temperature on axis, $T_e(0)$, volume averaged electron density, $<n_e>$, total stored energy, W, neutron reaction rate, R_{DD}, neutral beam power, P_{NB}, D_α intensity, $I(D_\alpha)$, bulk radiation, P_{rad}(bulk) and X-point radiation, P_{rad}(X-pt) for a 3MA/3.1T JET single null X-point discharge

During the L-phase of the discharge the neutral beam deposition profile is reasonably peaked. The ion power balance is between NBI and ion thermal conduction. In the electron power balance similar levels of NBI and ohmic power are lost mainly by electron heat conduction. The stored energy increases throughout the L-phase, largely due to the increasing density from beam fuelling and recycling. The higher densities achieved during the H-phase of the discharge lead to poor penetration of the NBI with deposition profiles becoming peaked outwardly. Energy equipartition can increase in importance, particularly in the outer regions shown but, since the electron and ion temperatures are the same, within their errors, this is a source of considerable uncertainty, particularly in the electron power balance.

The "effective" thermal diffusivity, χ_{eff}, increases to above its ohmic level at the start of neutral beam heating (Keilhacker and the JET Team, 1988). It then decreases progressively throughout the L- and H-phases. There is no obvious abrupt change in χ_{eff} at the transition. The present analysis, using the measured ion temperature profiles, indicates that this behaviour in time is reflected by the ion heat conductivity, χ_i (Fig. 6). There is apparently little change in the electron heat conductivity, χ_e, but these low values ($< 1m^2 s^{-1}$) are subject to large uncertainties from energy equipartition.

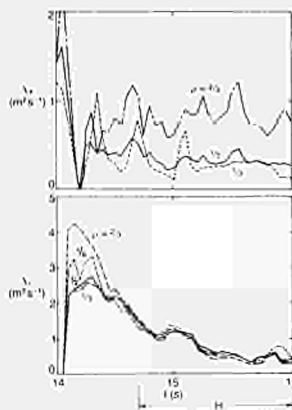Fig. 6. Time behaviour of the effective heat diffusivities for electrons, χ_e, and ions, χ_i, for JET pulse 15894

Fig. 7. Spatial profiles of the effective heat diffusivities for electrons, χ_e, and ions, χ_i, for JET pulse 15894

The spatial profiles of χ_e and χ_i at selected times throughout the discharge (Fig. 7) are rather flat over much of the region shown; further out, the formation of an energy pedestal and losses associated with particle recycling and convection dominate in the H-phase. It is to be noted that although χ_i is initially larger than χ_e, χ_i becomes comparable to χ_e, and within 2-3 $\approx \chi_{i,neo}$, by the end of the H-phase.

HIGH DENSITY PELLET-FUELLED, ICRF-HEATED DISCHARGE

The time behaviour of various parameters of pellet-fuelled, ICRF heated JET discharge #16211 is shown in Fig. 8. A 4mm diameter deuterium pellet is injected at a time of 3s with a multipellet injector developed jointly by ORNL and JET (Kupschus et al., 1987; Milora et al., 1987). The pellet penetrates deep into a deuterium ohmic plasma, reducing T_e and T_i considerably. With up to 8MW of

ICRH both T_e and T_i recover to well in excess of their ohmic values during a phase of "enhanced" confinement and high deuterium neutron yields ($>10^{15}$n/s).

During this phase the overall energy confinement is some 20% better than after, but the highly peaked density and temperature profiles suggest considerably improved central confinement. At a time of 4.8s there is an abrupt collapse of the central temperatures, density and neutron yield and the overall confinement is reduced.

The different ICRF models tend to agree that heating occurs, predominantly within 0.35m of the magnetic axis and with up to 50% of the input power heating the ions (Bhatnagar et al., 1989; Hammett et al., 1989). On the basis of these results the present transport calculations assume for the ICRF heating a gaussian deposition profile, centred on the magnetic axis and with 50% of the total power heating the electrons and 50% the ions.

Fig. 8. Time behaviour of ICRF power, P_{RF}, neutron reaction rate, R_{DD}, central electron temperature, $T_e(0)$, central ion temperature, $T_i(0)$ and volume averaged electron density, $<n_e>$ for JET pulse 16211

During the enhanced confinement phase, at a time of 4.1s, the ion power balance is between ICRF and ion heat conduction. In the electron power balance, the ICRF power to the electrons is comparable to electron heat conduction and the lower ohmic power to the total radiated power. Following the enhanced confinement phase, at a time of 4.75s, the power balances are somewhat more complicated with energy equipartition contributing some 25% extra (less) power to the ions (electrons), which is taken up by additional (lower) ion (electron) heat conduction losses.

The behaviour of χ_e and χ_i with time at a radius of 0.35m, in the central core of the plasma, is shown in Fig. 9. During much of the enhanced confinement phase (prior to the 'Event') χ_e and χ_i are comparable and low ($< 1m^2 s^{-1}$). Following this phase both χ_i and χ_e increase by more than a factor of two.

The spatial profiles of χ_e and χ_i at different times throughout the discharge are similar (Fig. 10). During the enhanced confinement phase (4.1s and 4.35s) χ_e and χ_i are significantly lower in the central region than further out. The central values are comparable to $\chi_{i,neo}$. Following this phase, at the later time of 4.75s, the central values of χ_i and χ_e have increased to levels at least comparable to those further out, which have not changed significantly from 4.1-4.75s.
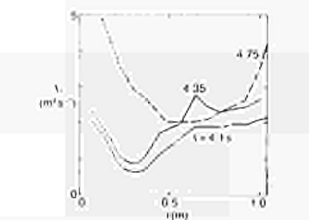

Fig. 9. Time behaviour of the effective heat diffusivities for ions, χ_i, and electrons, χ_e, for JET pulse 16211

Fig. 10. Spatial profiles of the effective heat diffusivities for ions, χ_i, and electrons, χ_e, for JET pulse 16211

LOW DENSITY HOT ION MODE

The time behaviour of various parameters in the double null X-point JET discharge #18768 is shown in Fig. 11. The increase in density following up to 21MW of NBI is limited by extensive ^{3}He discharge cleaning prior to operation in deuterium. As a result the NBI profile is very peaked. Heating is predominantly to the ions, with $T_i(0)$, obtained from a fast sampling central channel of the CXS diagnostic, increasing to more than 18keV after 0.5s of heating. $T_e(0) \approx 9$keV is considerably lower. The deuterium neutron yield ($>10^{16}$n/s) also reaches a maximum at this time, prior to a large influx of carbon (Lowry et al., 1989).
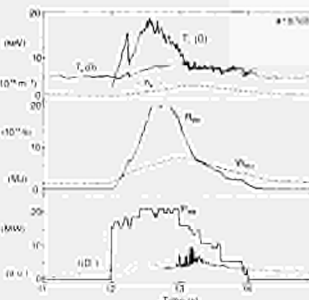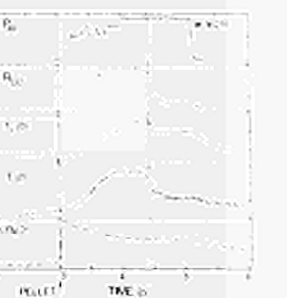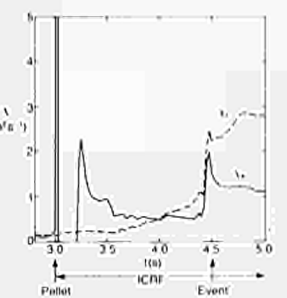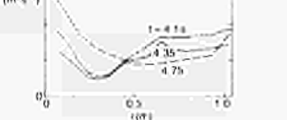

Fig. 11. Time behaviour of central electron temperature, $T_e(0)$, central ion temperature, $T_i(0)$, volume averaged electron density, $<n_e>$, total stored energy, W_{dia}, neutron reaction rate, R_{DD}, neutral beam power, P_{NB} and D_α intensity, $I(D_\alpha)$, for JET pulse 18768
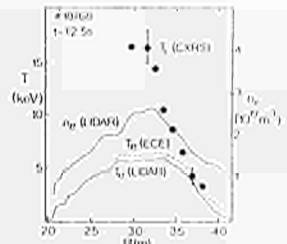

Fig. 12. Radial profiles of electron density, n_e, electron temperature, T_e, and ion temperature, T_i, during the hot ion phase of JET pulse 18768

The radial profiles of n_e, T_e and T_i are shown in Fig. 12 at the time of maximum neutron yield. The most characteristic feature are the extremely peaked ion temperature profiles and the well peaked density profiles. The electron temperature, determined by both the ECE and LIDAR measurements

is considerably lower than the ion temperature in the central region, but in the outer regions the electron and ion temperatures are the same, to within their error bars.

Over most of the radius the ion power balance is largely between NBI and ion heat conduction. Convective energy losses begin to contribute in the central region. The electron power balance is rather more complicated, with energy equipartition and ohmic heating becoming important, but still less than NBI. In the central region the power loss is shared, approximately equally, by electron heat conduction and convection. In the outer region, the power loss is mainly through radiation and electron heat conduction. The plasma energy is increasing rapidly.

The behaviour of χ_i with time at various radii is shown in Fig. 13 to change little for 1s after NBI begins. The spatial profile of χ_i at a time of 12.5s shows an increase from low central values ($\sim 1 m^2 s^{-1}$, within a factor 2-3 $\times \chi_{i,neo}$) to high values ($\sim 10 m^2 s^{-1}$) in the outer region (Fig. 14). χ_e is low and comparable to the central value of χ_i, but is, however, subject to large uncertainty.
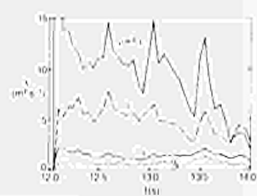
Fig. 13 Time behaviour of the effective ion heat diffusivity, χ_i for JET pulse 18768
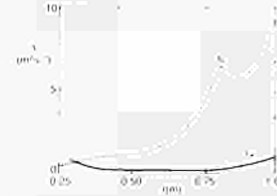
Fig. 14 Spatial profiles of the effective heat diffusivities for ions, χ_i, and electrons, χ_e, for JET pulse 18768

LOW DENSITY H-MODE DISCHARGE

The time behaviour of various parameters in the double-null X-point JET discharge #18757 is shown in Fig. 15. The increase in density following 10.5MW of NBI is again limited by extensive ^{3}He discharge cleaning prior to operation in deuterium. The NBI profile is very peaked. Heating is predominantly to the ions with $T_i(0)$ increasing to more than 15keV after 0.7s of heating. $T_e(0) \sim 6keV$ is considerably lower. The deuterium neutron yield reaches a maximum ($\sim 5 10^{15}$n/s) at this time. Shortly after, following the collapse of a sawtooth, this hot ion plasma makes a transition at constant power to an H-phase (as indicated by the abrupt changes in both the intensity of the D_α emission and the slope of the W_{dia} measurement). During this phase the plasma density and energy increase, $T_i(0)$ decreases and the neutron yield falls slightly.

The radial profiles of n_e, T_e and T_i are shown in Fig. 16, during the hot-ion phase of the discharge. The most characteristic features are the extremely peaked ion temperature and electron density profiles. The electron temperature, determined by both the ECE and LIDAR measurements is considerably lower than the ion temperature in the central region, but in the outer regions the electron and ion temperatures are the same, to within their error bars. Following the transition to the H-phase the density profile, determined from the interferometer data, broadens.

As in the case of the low density hot-ion discharge, in this phase of the present discharge the ion power balance is between NBI and ion thermal conduction. Near the very centre of the plasma, convection is as important as conduction. The electron power balance is again more complicated: convective energy losses are dominant in the central plasma, and comparable to both conduction and radiation further out. The plasma energy increases throughout this phase. During the H-phase of the discharge,
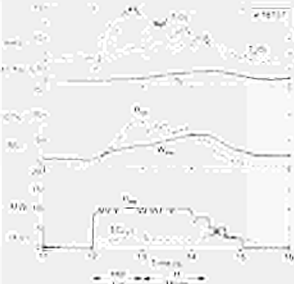

Fig. 15 Time behaviour of central electron temperature, $T_e(0)$, central ion temperature, $T_i(0)$, volume averaged electron density, $<n_e>$, total stored energy, W_{dia}, neutron reaction rate, R_{DD}, neutral beam power, P_{NB} and D_α intensity, $I(D_\alpha)$ for JET pulse 18757

Fig. 16 Radial profiles of electron density, n_e, electron temperature, T_e, and ion temperature, T_i, during the hot ion phase of JET pulse 18757

conduction remains the dominant loss in the ion power balance. In the electron power balance conduction and radiation remain comparable, but convective energy losses are reduced as a result of the flatter density profiles that develop.

The behaviour of χ_i with time at various radii shows a progressive decrease in the outer region of the discharge, but little change in the centre of the discharge (Fig. 17). As for the medium/high density H-mode discharge there is again no obvious abrupt change in χ_i at the transition from the L-phase to the H-phase at the time of 13s. The spatial profiles of χ_i (Fig. 18) also show low central values, within 2-3 $\times \chi_{i,neo}$, and the initially very high value of χ_i in the outer region is reduced in time. Apparently low values of χ_e ($< 1m^2 s^{-1}$) are obtained, but, again, these are subject to large uncertainty.
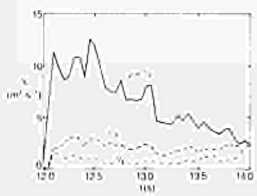

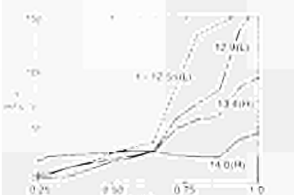Fig. 17 Time behaviour of the effective ion heat diffusivity, χ_i for JET pulse 18757

Fig. 18 Spatial profiles of the effective heat diffusivities for ions, χ_i, and electrons, χ_e for JET pulse 18757

SUMMARY

The wide variety of diagnostic and analysis facilities available at JET has allowed a study of the confinement properties of plasmas with substantially different temperature and density profiles.

The overall confinement of plasma energy for limiter (L-mode) discharges heated with NBI or ICRF or both is very similar and insensitive to variations by a factor of two in the central temperature and density when the effects of fast particles are taken into account. When strongly peaked density profiles are heated with ICRF the overall confinement is somewhat better ($\sim 20\%$). On the other hand, the overall confinement during the H-phases of X-point discharges is substantially better ($\times 2$) than during the preceding L-phases. However, when the contribution of an energy pedestal is taken into account the confinement of the bulk plasma in L- and H-phases is similar. The importance of bootstrap currents and their effect on the stability of ballooning modes when such energy pedestals form is noted.

Local transport analyses, using interpretive and predictive codes and sets of consistent experimental data, provide a better description of confinement. Such analyses have been reported for: a single null X-point medium density, NBI heated H-mode discharge; a limiter, high density, pellet-fuelled and ICRF heated discharge; a double null X-point, low density, NBI heated hot ion discharge; and a double null X-point, low density, high temperature, NBI heated H-mode discharge.

The confinement is described in terms of "effective" heat diffusivities, χ_i and χ_e, having already subtracted convective energy losses which are important only in the extreme hot ion regime and then only near the plasma centre. χ_i can be significantly larger than χ_e for these discharges, in which the ions receive more than 50% of the input power. With peaked density profiles (due to either pellet injection and ICRF heating or NBI heating at low density), the central values of χ_i and χ_e are low ($\sim 1m^2 s^{-1}$, or less). Further out χ_i increases to $\sim 2m^2 s^{-1}$, or more. In H-mode discharges, χ_i decreases and flattens progressively, as the density increases and broadens with time, ultimately becoming low ($\sim 1m^2 s^{-1}$). There is no obvious abrupt change at the transition from the L-phase to the H-phase. In all cases, the lowest values of χ_i are within a factor of 2-3 $\times \chi_{i,neo}$.

The "effective" diffusivities might appear meaningful for comparison with theory. However, it should be stressed that a specific, purely diffusive, form for the heat flux has been assumed: no attempt has been made, for example, to extract a heat pinch, or similar term, or to separate contributions from different ion species. Furthermore, errors in the experimental data can introduce large uncertainties, particularly in χ_e. None-the-less, low values of χ_e ($\sim 1m^2 s^{-1}$, or less) could be reconciled with heat pulse propagation measurements ($\chi_{HPP} \sim 3m^2 s^{-1}$, Lomas and the JET Team, 1989) through a heat pinch and since χ_i decreases with increasing density, particle and ion heat transport might be related.

REFERENCES

Balet, B. et al. (1989). High Temperature L- and H-mode Confinement in JET. To be submitted to Nuclear Fusion.
Bhatnagar, V. P. et al. (1984). Ray Tracing Modelling of the ICRF Heating of Large Tokamaks. Nuclear Fus., 24, 955.
Bhatnagar, V. P. et al. (1989). ICRF Power-Deposition Profiles and Heating in Monster Sawtooth and Peaked Density Profile Discharges in JET. Proc. 16th Eur. Conf. on Cont. Fusion and Plasma Physics, Venice, 1989, 13B(I), 127, EPS.
Bickerton, R J. and the JET Team. (1989). Latest JET Results and Future Prospects. In: Plasma Physics and Controlled Fusion Research (Proc. 12th Int. Conf., Nice, 1988), Paper IAEA-CN-50/A-1-3, IAEA, Vienna.
Callen, J. D. et al. (1987). Modelling of Temperature Profiles and Transport Scaling in Auxiliary Heated Tokamaks. Nucl. Fusion, 27, 1857.
Cordey, J. G. Keilhacker, M. and Watkins, M. L. (1987). Prospects for Alpha Particle Heating in JET in the Hot Ion Regime. Physica Scripta, T16, 127.
Cordey, J. G. et al. (1988). Bootstrap Current Theory and Experimental Evidence. Plasma Physics and Controlled Fusion, 30, 1625.
Goldston, R. J. et al. (1981). New Techniques for Calculating Heat and Particle Source Rates due to Neutral Beam Injection in Axisymmetric Tokamaks. J. Comput. Phys., 43, 61.
Hammett, G. W. et al. (1989). Transport Analysis of Pellet-Enhanced ICRH Plasmas in JET. Proc. 16th Eur. Conf. on Cont. Fusion and Plasma Physics, Venice, 1989, 13B(I), 131, EPS.
Hawryluk, R. J. (1980). An Empirical Approach to Tokamak Transport. Proc. Course and Workshop, Varenna, 1979, 19.
Keilhacker, M. and the JET Team. (1989). The JET H-mode at High Current and Power Levels. In: Plasma Physics and Controlled Fusion Research (Proc. 12th Int. Conf., Nice, 1988), Paper IAEA-CN-50/A-III-2, IAEA, Vienna.
Kupschus, P. et al. (1987). The JET Multipellet Injector Launcher-Machine Interface. Proc. 12th Symp. on Fusion Eng., Monterey, 1987, 2, 781, IEEE.
Lomas, P. J. and the JET Team. (1989). An Overview of JET Results. Plasma Physics and Controlled Fusion. This Volume.
Lowry, C. G. et al. (1989). The Hot Ion Mode of Small Bore Plasmas in JET. Proc. 16th Eur. Conf. on Cont. Fusion and Plasma Physics, Venice, 1989, 13B(I), 87, EPS.
Milora, S. L. et al. (1987). Design of a Repeating Pneumatic Pellet Injector for the Joint European Torus. Proc. 12th Symp. on Fusion Eng., Monterey, 1987, 2, 784, IEEE.
Milora, S. L. et al. (1989). Summary of Energy and Particle Confinement in Pellet-Fuelled, Auxiliary-Heated Discharges on JET. Proc. 16th Eur. Conf. on Cont. Fusion and Plasma Physics, Venice, 1989, 13B(I), 91, EPS.
O' Brien, D. P. et al. (1989). Ballooning Stability Analysis of JET H-mode Discharges. Proc. 16th Eur. Conf. on Cont. Fusion and Plasma Physics, Venice, 1989, 13B(I), 229, EPS.
Rebut, P. H., Lallia, P. P. and Watkins, M. L. (1989). The Critical Temperature Gradient Model of Plasma Transport: Applications to JET and Future Tokamaks. In: Plasma Physics and Controlled Fusion Research (Proc. 12th Int. Conf., Nice, 1988), Paper IAEA-CN-50/D-4-1, IAEA, Vienna.
Schmidt, G. L. and the JET Team. (1989). Heating of Peaked Density Profiles Produced by Pellet Injection in JET. In: Plasma Physics and Controlled Fusion Research (Proc. 12th Int. Conf., Nice, 1988), Paper IAEA-CN-50/A-IV-1, IAEA, Vienna.
Smithe, D. N. et al. (1987). An Algorithm for the Calculation of Three-dimensional ICRF Fields in Tokamak Geometry, Nuclear Fus., 27, 1319.
Start, D. F. et al. (1989). Experimental and Theoretical Studies of Ion Cyclotron Heating on JET. In: Plasma Physics and Controlled Fusion Research (Proc. 12th Int. Conf., Nice, 1988), Paper IAEA-CN-50/E-II-3, IAEA, Vienna.
Strachan, J. D. et al. (1987). High-temperature Plasmas in the Tokamak Fusion Test Reactor. Phys. Rev. Lett., 58, 1004.
Stubberfield, P. M. et al. (1989). Current Density Profile Evolution in JET. Proc. 16th Eur. Conf. on Cont. Fusion and Plasma Physics, Venice, 1989, 13B(IV), 1255, EPS.
Tanga, A. et al. (1987). Experimental Studies in JET with Magnetic Separatrix. In: Plasma Physics and Controlled Fusion Research 1986 (Proc. 11th Int. Conf., Kyoto, 1986), 1, 65, IAEA, Vienna.
Taroni, A. et al. (1989). Global Power Balance and Local Heat Transport in JET. In: Plasma Physics and Controlled Fusion Research (Proc. 12th Int. Conf., Nice, 1988), Paper IAEA-CN-50/A-7-1, IAEA, Vienna.
Thomas, P. R. and the JET Team. (1989). High Temperature Experiments and Fusion Product Measurements in JET. In: Plasma Physics and Controlled Fusion Research (Proc. 12th Int. Conf., Nice, 1988), Paper IAEA-CN-50/A-4-4, IAEA, Vienna.
Thomsen, K. et al. (1989). Offset-linear Description of H-mode Confinement. Proc. 16th Eur. Conf. on Cont. Fusion and Plasma Physics, Venice, 1989, 13B(I), 233, EPS.
Tibone, F. et al. (1989). Ion Thermal Conductivity and Convective Energy Transport in JET Hot-ion Regimes and H-modes. Proc. 16th Eur. Conf. on Cont. Fusion and Plasma Physics, Venice, 1989, 13B(I), 253, EPS.
Tubbing, B. et al. (1989). Double Null X-point Operation in JET with NBI and ICRH Heating. Proc. 16th Eur. Conf. on Cont. Fusion and Plasma Physics, Venice, 1989, 13B(I), 237, EPS.
von Hellermann, M. et al. (1989). Ion Temperature Profiles in JET. Proc. 16th Eur. Conf. on Cont. Fusion and Plasma Physics, Venice, 1989, 13B(I), 107, EPS.

The JET Project and its Impact on Nuclear Fusion Research

P-H Rebut

THE JET PROJECT AND ITS IMPACT ON NUCLEAR FUSION RESEARCH

P.H. Rebut

JET Joint Undertaking, Abingdon, Oxon, OX14 3EA, U.K.

INTRODUCTION

The Joint European Torus (JET), situated near Abingdon, UK, is the largest project in the co-ordinated programme of the European Atomic Energy Community (EURATOM). The EURATOM Fusion Programme is designed to lead ultimately to the construction of an energy producing reactor. Its strategy is based on the sequential construction of major apparatus such as JET, the Next European Torus (NET), and DEMO (a demonstration reactor), supported by medium sized specialized Tokamaks.

BASIC PRINCIPLES

The basic principle of the fusion process is the fusing or joining together of light nuclei to form heavier ones and in so doing a small quantity of mass is converted into a large amount of energy. Fusion is the process occurring in the sun where light atoms, heated to temperatures of about 15M°C (~13keV) fuse together. The rate at which fusion occurs in the sun is relatively slow; for a fusion reactor on earth, a higher rate is required and hence much higher temperatures are needed - typically in the range of 100-200 M°C (10-20keV), which is 10 times greater than the temperature in the centre of the Sun. In addition, in a reactor, a high enough concentration (or density) of fuel must be maintained at these temperatures for sufficient periods. For a reactor, there are several possible fusion reactions, but the one that is easiest to achieve is that between the two isotopes of hydrogen - deuterium and tritium. Deuterium can be easily and cheaply obtained from water and tritium can be manufactured in a fusion reactor from the light metal lithium. The reactions involved are:

Fusion Reaction	$D + T \rightarrow {}^4He + n$
Tritium Breeding Reactions	${}^6Li + n \rightarrow T + {}^3He$
	${}^7Li + n \rightarrow T + {}^4He + n$

The sun uses gravitation forces to hold the high temperature nuclei (or plasma) together but on earth this force would be much too small. Since plasma is made up of a mixture of charged particles (nuclei and electrons), magnetic fields can be used to contain the plasma. The most effective magnetic configuration used to hold the high temperature plasma is toroidal in shape. In a reactor, there must be sufficient fuel present and the energy losses must be kept low to ensure that more energy is released from the fusion reaction than is needed to heat the fuel and run the system. The effectiveness of the magnetic field in containing plasma and minimising losses can be measured by the time taken for the plasma to cool down. This is called the energy confinement time and needs to be between one and two seconds in a reactor - although the plasma will be contained for considerably longer times. The power output depends on the amount (or density) of fuel present, but there is a limit on the amount that can be held by the magnetic field. This needs to be only a few thousandths of a gram per cubic metre, but this is sufficient to yield vast amounts of energy. Thus a fusion reactor must produce very high temperature plasmas of sufficient density and long enough energy confinement time to generate a net output of power.

In a fusion reactor, the values of temperature, (T_i) density (n_i) and energy confinement time (τ_E) must be such that the product $(n_i.\tau_E.T_i)$ exceeds $5 \times 10^{21} m^{-3} skeV$. Typical values for the parameters that must be attained simultaneously for a reactor are:

Central ion temperature, T_i	10-20keV
Central ion density, n_i	$2.5 \times 10^{20} m^{-3}$
Global energy confinement time, τ_E	1 - 2s

The principal advantages of fusion as a new energy source are, essentially:-

- it is a vast new energy source;
- fuels are plentiful and widely available and these avoid the environmental problems associated with the burning of fossil fuels;
- a fusion reactor will be an inherently safe system;
- there will be no radioactive waste from reaction products, although the reactor structure itself becomes radioactive.

THE JET PROJECT

In Europe, there are several national fusion research laboratories which together form a well-integrated programme co-ordinated and partly funded by Euratom. During the early 1970s a consistent set of encouraging results emerged from a number of small-scale experiments around the world. It was then clear that to achieve near-reactor conditions much larger experiments were required which were likely to be beyond the resources of any individual country. In 1973, it was decided in Europe that one such large device would be built as a joint venture, the Joint European Torus (JET) and a Design Team was set up to prepare a design. Approval to proceed with the Project was given at the end of 1977. On 1st June 1978, the formal organisation for the Project - the JET Joint Undertaking - was set up. The Project Team is drawn from Euratom and the fourteen member nations - the twelve EEC countries, together with Switzerland and Sweden. Funding - currently at about 100M ECU per year - is provided 80% by Euratom, 10% by the U.K. as host country and the remaining 10% by members roughly in proportion to the size of their national fusion research programme. The construction of JET, its power supplies and buildings, were completed, on schedule and broadly to budget by mid-1983 and the research programme started.

The objective of JET is to obtain and study a plasma in conditions and dimensions approaching those needed in a thermonuclear reactor. This involves four main areas of work:

- (i) to study various methods of heating plasma up to the thermonuclear regime;
- (ii) to study the scaling of plasma behaviour as parameters approach the reactor range (that is to understand how the plasma temperature, density and confinement vary with dimensions, shape, magnetic field, plasma current etc., so that we can accurately define the parameters for a reactor);
- (iii) to study the interaction of plasma with the vessel walls and how to continuously fuel and exhaust the plasma;
- (iv) to study the production of alpha-particles generated in the fusion of deuterium and tritium atoms and the consequent heating of plasma by these alpha-particles.

THE JET MACHINE

The plasma in JET is heated and contained in a very large toroidal or ring-shaped vessel known as a torus [1]. The plasma is confined away from the walls of the vessel by a complex set of magnetic fields. The detailed shape of the magnetic field is described as a Tokamak, a name used by the Russians who pioneered this particular form of magnetic device for high temperature plasma. There are many tokamaks in the world, principally in Europe, the United States, the Soviet Union and Japan, but JET is by far the largest and most powerful. The main dimensions of the machine are given in Table I.

Table I: JET Parameters

Parameter	Design Values	Achieved Values
Plasma Major Radius (R_0)	2.96m	2.5 - 3.4m
Plasma Minor Radius (hor.)(a)	1.25m	0.8 - 1.2m
Plasma Minor Radius (vert.)(b)	2.1m	0.8 - 2.1m
Toroidal Field at R_0	3.45T	3.45T
Plasma Current	4.8MA	7.0MA
Neutral Beam Power	20MW	21MW
ICRF Heating Power	15MW	18MW

Plasma is heated in JET by a very large electric current - up to 7 Million amperes (MA) - together with two other additional heating methods. These are radio frequency (RF) heating (up to 20MW), and neutral beam (NB) injection heating (up to 21MW) which involves injecting beams of energetic atoms into the plasma. When the plasma is sufficiently hot and well confined abundant fusion reactions will take place turning the deuterium and tritium nuclei into helium nuclei (alpha-particles) and neutrons. The alpha-particles remain in the magnetic confinement region and their high energy continuous to heat new plasma to keep the reactions going.

Although this will not take place in JET, when sufficient reactions are taking place in a reactor the external heating systems can be turned off as the plasma will continue to heat itself. The neutrons will escape from the plasma and, in a reactor, will be slowed down in a surrounding blanket of moderator causing the blanket to heat up to a few hundred degrees Celsius. This heat will be removed to raise steam to drive turbines to generate electricity in the conventional way. By making the blanket of a lithium compound, the neutrons will also combine with lithium to produce tritium for fuelling the plasma.

A basic objective of JET is to study the self heating of plasmas by the alpha-particles, but the production of tritium and heating by neutrons will be the major objectives of the NET experimental device.

JET's plasma current is generated by a massive 2700 tonne transformer in which the plasma is the transformer's secondary winding. The magnetic confinement configuration is made by combining two magnetic fields, one produced by the plasma current itself and the other by a set of electromagnetic coils surrounding the torus. Finally a set of horizontal hoop coils encircling the apparatus ensures that the plasma remains centrally in the torus.

JET RESULTS

JET is now about midway through its programme and results achieved in JET so far are most impressive [2]. The technical design specifications of JET have been achieved in all parameters and exceeded in several cases (see Table 1). The plasma current of 7MA and the current duration of up to 30 seconds are world records and are over twice the values achieved in any other fusion experiment. The neutral beam injection system has been brought up to full power (21MW) exceeding the design value. In addition, the ICRF heating system has taken advantage of improvements in technology to increase its power level to ~18MW in the plasma. In combination, these heating systems have provided 35MW power to the plasma, and this is likely to increase in the near future.

So far, plasma temperatures up to 250M°C (23keV) have been reached and the plasma densities (up to ~$1.8 \times 10^{20} m^{-3}$) and energy confinement times (up to 1.5s) are within the range required in a reactor (see Table II). Although these values have been achieved in individual experiments, they have not all been reached simultaneously. There are two regimes of energy confinement observed in a special magnetic configuration (the X-point configuration). One of these, a higher confinement regime (called the H-mode) has energy confinement times about twice the lower values (called the L-mode). In both regimes, confinement degradation occurs in that the plasma thermal energy does not increase proportionally to the heating power. Therefore considerably more power is needed to increase the plasma temperature and energy. This problem is presently being investigated.

Fig.1 presents a plot of the fusion product $(n_i.\tau_E.T_i)$ versus central ion temperature T_i for a series of experimental devices developed over the last 20 years. It is seen that considerable progress has been achieved in 20 years and JET has now reached a fusion
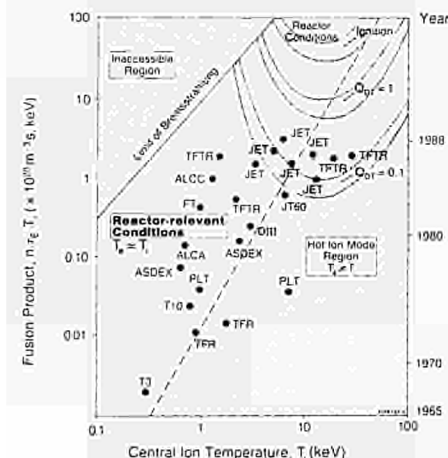

Fig.1: Plot of fusion product $(n_i.\tau_E.T_i)$ versus central ion temperature T_i for a series of experimental devices

product value of $3 \times 10^{20} m^{-3} skeV$, which is only about a factor of 20 below the value of $5 \times 10^{21} m^{-3} skeV$ required in a reactor. In particular,JET has shown that plasmas of thermonuclear grade may be contained in a controlled way in a terrestrial device. These latest results put JET on the top of the fusion league table - a position it is likely to maintain for the rest of its operating life.

These experiments are currently being carried out in hydrogen or deuterium plasmas and plans for using the tritium are scheduled to come into operation in 1991. The forward programme up to 1992 include a number of these enhancements and innovations intended to enable JET to create abundant fusion reactions and thereby achieve its objective of producing "plasmas of dimensions and parameters close to those in a fusion reactor".

Table II: JET Results

	Best Achieved	Achieved Simultaneously	Reactor Values
Temperature,T			
(M°C)	250	70	120 -240
(keV)	23	6	10 - 20
Energy Confine-			
ment Time, τ_E (s)	1.5	0.9	1 - 2
Density, n,			
$(x10^{20} m^{-3})$	1.8	0.5	2 - 3

IMPACT ON NEXT STEP

Plasma temperature, density and confinement values already achieved, but not simultaneously, are individually close to the requirements of NET. In addition, JET results on scaling of these parameters have allowed some of the requirements of a reactor to be specified. In particular, the next step Tokamak must be about 2.5 times the linear dimensions of JET, have a plasma current of 25-30MA, and an output of several GW. The plasma must be maintained for very long times, such as 1 hour, rather than the 20-30 second bursts presently used in JET. Sufficient knowledge now exists to design such a device, but a number of plasma engineering problems remain to be solved.

These relate mainly to the interaction of the plasma with the vessel walls - eg, control of impurities, fuelling and exhaust. JET has the capability of studying these problems and will be doing so in the second half of its programme. JET will operate with deuterium/tritium plasmas, rather than pure deuterium ones, so that the production of alpha-particles in a true thermonuclear plasma can be studied. This will require a tritium fuelling system and, since JET will become radioactive, remote handling equipment will be used.

There are several teams working on designs for a Next Step. These include NET (Next European Torus) and ITER (International Thermonuclear Experimental Reactor),

involving groups from the US, USSR, Japan and Europe. The results from JET are very important from a reactor point of view. Both design teams are taking JET results into account and are adopting the same design philosophy as JET, that is a large non-circular cross-section and a large plasma current.

Based largely on JET results, the present studies to define ITER, NET or any other next step Tokamak clearly emphasize the need for obtaining additional information not only on impurity control and plasma-wall interaction but also on modes of operation, such as those avoiding plasma disruptions and enhance confinement regimes.By virtue of its size, its already demonstrated plasma performance and its long pulse capability, JET is in the best position to address these problems in the basic geometry considered for a Next Step.

CONCLUSIONS

In summary:

(a) JET is a successful example of European collaboration involving fourteen countries;
(b) This advanced technology machine was constructed on time and broadly to budget;
(c) On the technical side, JET has met all its design parameters and in many cases, has substantially exceeded the values. In particular, it has reached a record plasma current of 7MA;
(d) On the scientific side, JET has achieved plasmas with ion temperatures of 250M°C (23keV) and simultaneously ion and electron temperatures have exceeded 12M°C (10keV). In addition, JET has reached record plasma energy confinement times in excess of 1s;
(e) Individually, the parameters required for a fusion reactor had been achieved, and simultaneously the fusion product is within a factor of 20 of the reactor value. JET overall performance is closer than any other machine to required reactor conditions;
(f) JET has successfully achieved and contained plasmas of thermonuclear grade;
(g) JET technical and scientific achievements give confidence that a fully ignited experimental reactor could be built, as soon as control of particles is achieved;
(h) JET results show that a Tokamak with a plasma current of 30MA in a machine of 2-3 times the size of JET is required to produce ignition;
(i) Energy confinement would no longer be the dominant problem. However, scientific difficulties remain in the areas of:
   - plasma wall interactions and impurities
   - plasma fuelling and exhaust
   - quasi-continuous operation
(j) JET is the largest and most powerful fusion experiment in the world. It has the capability for studying these reactor relevant problems and providing important information required in designing and planning the Next Step device;
(k) JET results will continue to be of crucial importance in the development of Fusion research.

REFERENCES

[1] The JET Project - Design Proposal: EUR-JET-R5
[2] Latest JET Results and Future Prospects, The JET Team, Proc. of 12th Int. Conf. on Plasma Phys. and Contr. Nuc. Fus.Res., (Nice, France, 1988) (to be published in Nuclear Fusion Supplement)

Diagnostics for
Experimental Fusion Reactors

P E Stott, A E Costley

Diagnostics for Experimental Fusion Reactors

P E Stott and A E Costley

ABSTRACT

The diagnostic requirements for an experimental fusion reactor are outlined. The JET diagnostics are described briefly and their possible extrapolation to a typical Next Step fusion device (ITER) is considered. Key areas where developments are necessary are identified and possible ways of implementing the diagnostics are discussed. It is concluded that it should be possible to measure most plasma quantities using extrapolations of established techniques, but new approaches may be needed for some important quantities.

INTRODUCTION

It will be an extremely difficult task to optimize the performance of the next generation of fusion experiments in order to achieve and sustain ignition. Learning how to control the purity, stability, confinement and power balance of an ignited fusion plasma will involve an experimental programme more extensive and challenging than any that has been carried out so far in the fusion programme. This will require a comprehensive set of diagnostics capable of measuring all the plasma quantities that characterize an ignited plasma. These diagnostic systems will have to operate with high accuracy, stability and reliability for long periods in an extremely hostile environment. Particularly high standards of reliability will be required for those diagnostics that are incorporated in plasma control loops.

Measurements in high temperature fusion plasmas are difficult. Methods involving physical contact with the plasma can be used only at the extreme edge of the discharge and non-invasive methods must be used in the hot plasma core. Some techniques are passive and utilize particles or radiation that have been emitted spontaneously by the plasma, other techniques are active and use beams of particles or radiation from external sources as probes. Some of these techniques work only over a limited range of plasma conditions and thus several independent diagnostic systems may be needed to cover the complete range of conditions encountered in a single experiment. Almost all plasma measurements depend on complex plasma effects whose interpretation or calibration may have uncertainties, particularly in some ranges of plasma conditions, and it is very desirable to be able to measure the most important quantities by several independent techniques.

Considerable development work will be needed before the detailed design and construction of the diagnostic systems for the Next Step fusion device can begin. Some developments are specific to certain diagnostic methods whilst others are of a more general application. In order to identify some of the areas where development work will be needed, we attempt in this paper to summarize the diagnostic requirements and to identify some possible contenders. We will base our discussion on our experience with the JET diagnostics since this is the most extensive set that has been constructed for a large tokamak experiment with tritium compatibility as an integral part of the specification.

Device	Major Radius m	Minor Radius m	Elongation	Toroidal Field T	Plasma Current MA
JET	3.0	1.2	1.7	3.4	7
ITER	5.8	2.0	2.2	5.1	20
NET	6.0	2.2	2.2	5.4	27
JIT	7.5	3.0	2.0	4.1	30
CIT	2.1	0.65	2.0	10	11
Ignitor	1.2	0.43	1.8	12	12

Table I: Parameters of JET and some proposed Next Step Experiments

DIAGNOSTIC REQUIREMENTS FOR NEXT STEP EXPERIMENTS

Table I compares the main parameters of JET with some of the Next Step fusion experiments presently being studied. These fall into two groups; NET, ITER and JIT have plasma currents in the range 20 - 30 MA and their physical dimensions would be roughly twice the size of JET, whereas CIT and Ignitor are somewhat smaller with currents of 9 - 13 MA. The diagnostics for these various experiments will share many common features but some of the problems will be device specific and so for reference we will consider ITER as a typical Next Step experiment.

The objectives of ITER are to demonstrate a steady-state ignited plasma with pulse length > 200s in the *physics phase* and up to 2 weeks in the *technology phase* in order to establish the physics and technological data base for designing a demonstration power reactor. During the physics phase of the experiment, a full set of diagnostics will be needed to guide the experimental program of the largest and most important machine in the world fusion program through the exploration of the different modes of operation. The aims will be to reach ignition and subsequently to provide the data necessary to understand the physics of an ignited plasma. The magnitude of this task should not be underestimated. Experience on JET and TFTR has shown that the physics of large tokamaks differs in many important ways from smaller experiments. It is reasonable to suppose that the step to a fusion reactor will produce a similar number of challenges to our understanding of tokamak physics. It is difficult to contemplate trying to operate or optimise the performance of a fusion reactor working in new and unexplored regimes without adequate measurements. During the physics phase an important task will be to establish effective control methods for maintaining the ignited plasma in safe and optimum conditions. During the technology phase a reduced set of diagnostics will suffice to provide the plasma data base needed for the technology experimental program. However during this phase the routine and reliable operation of those diagnostics which form part of the plasma control systems will be particularly important.

The simultaneous measurement of all the main plasma quantities is desirable in order to ensure maximum consistency between the different measurements and to maximize the utilisation of discharges. For the reasons mentioned earlier, it is desirable to have several independent methods for measuring the most important plasma quantities. To make measurements in the edge and divertor plasma regions where temperatures are lower and better spatial resolution is needed (Figure 1), it may also be necessary to use different techniques to those that are most suitable for the main plasma. Similar considerations apply to the different phases of the discharge since plasma conditions and time scales will change considerably during a single discharge. Good measurement accuracy is very important as measurement errors tend to accumulate as they propagate down the analysis chain.
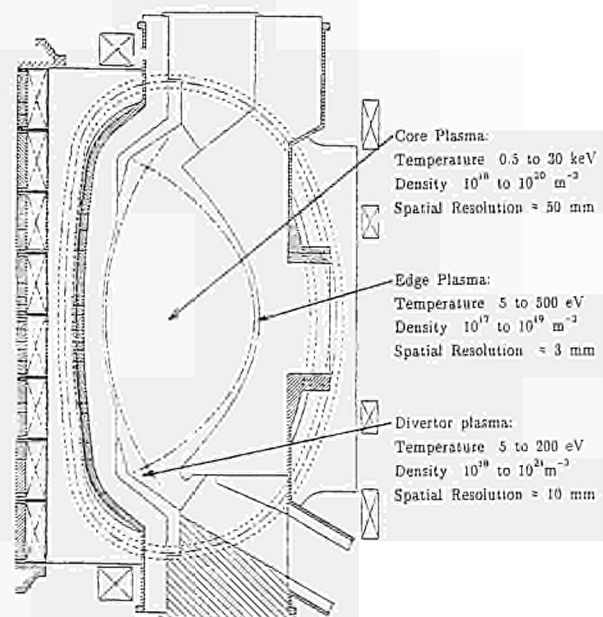

Core Plasma:
Temperature 0.5 to 30 keV
Density 10^{18} to 10^{20} m^{-3}
Spatial Resolution ≈ 50 mm

Edge Plasma:
Temperature 5 to 500 eV
Density 10^{17} to 10^{19} m^{-3}
Spatial Resolution ≈ 3 mm

Divertor plasma:
Temperature 5 to 200 eV
Density 10^{19} to 10^{21} m^{-3}
Spatial Resolution ≈ 10 mm

Figure 1 A simplified poloidal cross-section of ITER indicating diagnostic access and typical plasma parameters in different regions.

A wide range of diagnostic techniques [1,2] has been developed on present day confinement experiments and some, but not all, of these will be applicable with further development to the Next Step experiments. Problems of access to the plasma through the blanket, magnets and mechanical structures are particularly difficult as is the provision of windows and other optical components near to the plasma. Other general issues that need development include remote maintenance, operation in a hostile environment, real-time data processing, reliability and assessing the consequences of failure. Experience of some of these issues has been gained on JET and forms a useful starting point.

JET DIAGNOSTICS AND POSSIBLE EXTENSIONS

The Joint European Torus (JET) is the largest tokamak in the world and came into operation in 1983. JET's main objective is to obtain and study plasmas in conditions and with dimensions approaching those needed for a fusion reactor. JET has about 50 separate diagnostic systems [3,4]. About half of these are major installations that involved substantial effort to design and implement. Some of the others are extensions or variants of one of the major systems making use of the same infra-structure, and some are temporary or experimental diagnostics. Some plasma quantities are measured by different diagnostics and some diagnostics measure several different plasma quantities, and so a systematic classification either by measured quantity or by diagnostic technique is difficult. Rather than describe each of these systems, it is more informative to review the main areas of plasma measurements and to consider the possible extrapolation of some of the present techniques to ITER.

Plasma Position and Shape, Plasma Current and Energy

The shape and position of the plasma boundary is determined by measuring the components of the poloidal magnetic field through voltages induced in coils located outside the plasma. In JET the component parallel to the vacuum vessel wall is measured with multiturn, solenoidal coils inside the vacuum vessel. These coils are wound out of inconel-sheathed, coaxial cable with a ceramic (MgO) insulator and are enclosed in a secondary inconel vacuum container as a precaution against leaks (so far none have occurred). The perpendicular field components are measured with single-turn loops, also wound from ceramic coaxial cable, on the outside of the vessel. There is considerable redundancy with identical sets of coils installed on each octant. Software checks for data consistency are made and if errors in the data are detected, data from a back-up coil set can be substituted. Two coil sets are dedicated to the plasma shape and position feedback control systems. The same coils measure the total plasma current, loop volts and magnetic fluctuations (up to 10 kHz for the standard internal coils and up to 500 kHz for some special coils). The total plasma energy and pressure can be determined from measurements of the poloidal and toroidal fields.

The JET magnetic diagnostics have proved to be extremely robust and reliable. This is important because these measurements are used for plasma control and are therefore essential to JET's operation. The extrapolation to the inductive phase of the Next Step should present no serious problems, but new methods will need to be developed to measure the steady-state magnetic fields during the technology phase.

Electron Density Profiles

The main methods that are used to measure electron density profiles in JET are Thomson scattering and transmission interferometry. Thomson scattering will be considered later in the section on electron temperature diagnostics.

Transmission interferometry is one of the longest established diagnostic methods and has evolved into a sophisticated technique with a very large, multi-channel, far infra-red system installed on JET. However this diagnostic method has two serious disadvantages for further extrapolation to larger fusion devices. Multiple lines of sight through the plasma would be required in order to measure plasma density profiles and these appear to be extremely difficult to implement in a device like ITER. Indeed even in JET there are insufficient lines of sight (5 vertical and 3 horizontal) to yield density profiles with good spatial resolution. A further problem is caused by the sensitivity of interferometric measurements to mechanical vibrations In JET the interferometer is mounted on a large, independently supported frame in order to de-couple it from the tokamak, but an equivalent frame for ITER would be impracticably large. For these reasons it seems unlikely that transmission interferometry will be used as a major diagnostic for density profile measurements in the plasma core, but there may be a need for a few channels as a monitor of the line integrated density.

Reflectometry is a promising new diagnostic method that appears to have considerable potential for future large devices because the density profile can be measured by probing the plasma along a single line of sight. The probing frequency is in the microwave region and can be conveniently transmitted along metal waveguides over long distances so that sources and detectors can be remote from the tokamak. Reflectometry was attempted in some early tokamaks but substantial developments did not occur until quite recently. Advances in microwave technology have stimulated renewed interest in this technique and reflectometers have been developed on TFR, JET, Asdex and Tor-Supra. The basic principle is simple. A beam of microwave radiation is directed into the plasma and reflected at the density layer where the local electron density is equal to the cut-off density which is a function of the wave frequency. If the source frequency is swept, the position of the different density layers can be located to build-up a density profile. A key question, that is the focus of present research, is whether it is possible to measure the density profile in the presence of density fluctuations.

Electron Temperature Profiles

Thomson scattering and electron cyclotron emission (ECE) are the two main methods used in JET for measurements of electron temperature profiles. Thomson scattering is also used to measure densities and therefore has the advantage that both density and temperature can be measured simultaneously which is desirable when these two parameters are combined to calculate the plasma kinetic energy. Laser light is directed into the plasma and scattered off the electrons. The scattered light is Doppler shifted by the movement of the electrons and thus the spectrum yields the electron velocity distribution and the temperature, whilst the intensity of the scattered light yields the electron density. The scattering cross-section is extremely small and a laser with high energy output is necessary, ruby and neodymium lasers are commonly used.

JET has developed a new type of Thomson scattering system based on the LIDAR principle. This uses a laser pulse whose duration ($\approx 3 \times 10^{-10}$ s) is much shorter than the transit time of the laser light across the plasma ($\approx 1.3 \times 10^{-8}$ s) so that time can be related to spatial position. The back-scattered light is collected and spectrally analyzed to determine the electron velocity distribution. The spatial resolution, which is determined by the laser pulse duration and the detector response time ($\approx 3 \times 10^{-10}$ s), is typically 80mm. JET presently uses a ruby laser with a repetition rate of 0.5 Hz and this is being upgraded to an alexandrite laser with a repetition rate of 10 Hz. Further development of alexandrite or other types of laser could give higher repetition rates. The LIDAR technique requires only a single line of sight access to the plasma, whereas other types of spatial scan Thomson scattering systems (for example the imaging system developed for TFTR) require at least two approximately orthogonal views, one of which has to be wide angle. The LIDAR method appears to be best suited to measurements of the core profiles in ITER but lacks sufficient spatial resolution for the edge. An imaging system may be more suitable for the edge and divertor regions. The implementation of Thomson scattering systems will require the development of windows and mirrors that are compatible with the reactor environment.

ECE is well developed as a temperature diagnostic. Electrons gyrating in the tokamak magnetic field emit radiation at harmonics of the characteristic electron cyclotron frequency. The electron temperature is determined by the intensity of the emitted radiation and the spatial position is determined by the frequency. Instrumentation has been developed to measure the temperature at a fixed point with fast time resolution or to scan the plasma to measure temperature profiles. ECE is well suited for measurements in a hostile environment because the emission is primarily at microwave frequencies which can be readily transmitted along waveguides and around corners to the sensitive detectors outside the radiation shield wall. Limitations can arise from the phenomenon of harmonic overlap (emission from different locations in the plasma in different harmonics at the same frequency) and the interpretation can be ambiguous in plasmas with significant numbers of non-thermal electrons. In addition to its capability to diagnose core plasma profiles, ECE has potential to measure temperatures in the edge and divertor plasmas.

Ion Temperature Profiles

Several techniques are used to measure ion temperatures in JET including charge-exchange neutral particle analyzers, charge-exchange recombination spectroscopy, X-ray crystal spectroscopy and neutron diagnostics. All of these techniques have some limitations and in general ion temperature measurements have more difficulties than electron temperature measurements.

Charge-exchange neutral particle analyzers need to have a direct view of the plasma and consequently they are difficult to shield against neutrons. The system presently installed on JET uses channel multipliers and was not designed for the tritium phase. A radiation resistant detector based on the time of flight principle is being developed. The incident neutral will be ionized in a thin foil and the resulting secondary electron will start a coincidence timing circuit. The ion will be momentum analyzed in a magnetic field and its energy determined by the flight time to a second detector which will be gated open for a window appropriate to the neutral energy in order to eliminate spurious counts due to neutrons and gammas. This system will be tested on JET and could form the basis for development of future systems.

Plasma ion temperatures and macroscopic rotation velocities are measured spectroscopically from the Doppler broadening and shifting of spectral line emission from impurity ions. Although the temperature that is measured is actually that of the impurity rather than the hydrogen ion there is usually, though not always, good coupling between the ion species so that the temperatures are similar. Measurements can be made in the visible region of the spectrum using fiber optic light relay systems or in the soft X-ray region using double crystal spectrometers in a periscope-like arrangement to traverse a neutron shield wall. Both methods offer potential for extrapolation to future machines provided radiation resistant fibers and crystals can be developed.

In large, hot tokamaks high Z impurities are undesirable and low Z impurities are fully ionized in the core and therefore do not emit line radiation. Emission can be observed with the technique of charge-exchange recombination spectroscopy which uses an injected neutral beam to convert (via charge-exchange collisions) some of the fully ionized impurities into a less ionized state that can emit. Passive neutral particle analyzer measurements also become difficult in large, dense tokamaks because the neutral density in the plasma core is small and insufficient neutrals are produced. Moreover these are strongly attenuated before they reach the plasma edge. An energetic neutral beam is needed to penetrate the core and provide an active source. JET utilizes the heating neutral beams for these diagnostics but in many other tokamaks there are special diagnostic neutral beams. The extrapolation of these techniques to future, larger experiments would require the development of neutral beams with MeV energies and currents of several Amperes.

Ion temperatures can be determined from both the neutron yield and the neutron energy spectrum. The total yield is strongly dependent on the central ion temperature and relatively insensitive to profile shape. Ion temperature profiles can be measured with collimated arrays of neutron counters. However yield measurements are extremely sensitive to non-thermal ion distributions. Neutron spectroscopy is a more reliable way of determining the ion temperature in plasmas where the temperatures are high enough to produce a measurable broadening of the neutron energy spectrum. High resolution spectrometers for 2.4 and 14 MeV neutrons are being developed on JET and will obviously be important for ITER.

Plasma Current Density

Measurement of the spatial distribution of the plasma current in JET has used the Faraday rotation technique as an extension of the multi-channel far infra-red interferometer and is also applying a Thomson scattering method. In ITER the number of vertical sight lines is limited and it will be difficult to measure the current density profile over the complete plasma cross-section with the Faraday rotation technique although measurements of the current density on axis may be possible with a few sight lines. Measurements of the current density profile will be particularly important in ITER and other Next Step experiments which will use non-inductive current drive and the development of other diagnostic methods is important. Several techniques have been proposed including the motional Stark effect in charge-exchange recombination spectroscopy but none have been demonstrated in a large tokamak.

Impurity Identification and Densities

Spectroscopy is an important diagnostic for the identification of impurities and measurements of their concentrations. Different types of spectroscopic instrumentation are needed to cover the wide region of spectral interest from the visible to soft X-rays. Many of the most important emission lines from impurities are in the ultra violet at wavelengths where there are no suitable window materials or efficient mirrors so that the spectroscopic instruments and detectors must be connected by vacuum to the tokamak and must be in a direct line of sight of the plasma. Clearly these instruments will not be compatible with the ITER environment. To overcome these problems on JET, visible and X-ray spectrometers that can be placed remote from the plasma

behind the radiation shielding wall have been developed. Visible light is easily relayed via fiber optics, but radiation resistant fibers or other light relay systems will be needed for ITER. These visible light systems can also be used with charge-exchange spectroscopy. In the soft X-ray region of the spectrum JET is developing double crystal spectrometers where the two crystals act as the dispersing and reflecting elements in a light relay system to allow the sensitive detector to be placed behind the radiation shielding wall. The application of this method to ITER will require the development of radiation resistant crystals.

Radiated Power

The total power lost from the plasma by impurity radiation is measured with metal resistance bolometers that have a relatively flat response over a wide spectral range including the soft X-ray and ultra violet regions that contain the strongest emission lines. The bolometers consist of a thin plastic foil that has a thin metal absorber layer (usually gold) evaporated onto the plasma-facing side and a metal resistor labyrinth on the reverse side. The foil is heated by the plasma radiation and the temperature rise is determined from the change in resistance. Profiles of the radiated power density are measured with large arrays of these bolometers viewing the plasma through small apertures so as to make a pin-hole camera. Radiation resistant versions of the bolometers need development. Heating by the neutron and gamma radiation can be subtracted in principle by using a pair of identical detectors, one of which is shielded from the plasma light, in order to measure only the nuclear heating.

Neutrons and Fusion Products

JET is well equipped with a wide range of instrumentation for studying the neutron and gamma emission from D-D and D-T plasmas and ITER will have similar requirements. Although JET has not yet operated in tritium, some 14 MeV neutrons have been measured already due to the tritium produced and confined in D-D plasmas. The full range of diagnostics includes neutron yield monitors with time and space resolution but no energy discrimination, and neutron spectrometers with varying degrees of spectral resolution. The total neutron emission in JET varies from 10^{10} s^{-1} to 10^{19} s^{-1} and the range in ITER will extend up to 10^{24} s^{-1}. No single instrument is able to cover this wide dynamic range and consequently a range of instruments with different sensitivities and resolutions is needed. Calibration will be a problem in ITER because portable calibration sources are much too weak to lie within the operational range of neutron fluxes. Alternative calibration methods based on foil activation techniques are being developed on JET and will need further development for ITER.

The first tokamaks on which alpha particle diagnostics can be tested are JET and TFTR. The alpha birth profile can be obtained from the neutron yield profile and a variety of methods will be used for the escaping alphas. After an extensive evaluation of possible methods for measuring the energy distribution of the confined alphas, JET is developing two techniques. A collective Thomson scattering diagnostic at a microwave frequency (140 GHz) will be constructed to measure the distribution of energetic (> 0.5 MeV) alphas, and charge-exchange recombination spectroscopy will be used for lower energy alphas. Application of the collective scattering method to ITER will require the development of a powerful source with a wavelength ≈ 200μm.

MHD Instabilities

Information on MHD instabilities (sawteeth, disruptions and ELMs) is provided by many diagnostics including magnetic coils, soft X-rays, ECE, neutrons and emission spectroscopy. The magnetic diagnostics provide useful monitors of MHD activity as well as valuable information on mode numbers. Soft X-ray diode arrays and ECE give two dimensional pictures of the electron temperature fluctuations inside the plasma. Reflectometry has the potential to probe the density fluctuations inside the plasma, but this requires further development. It appears feasible to extend some of these diagnostics (ECE, magnetics, reflectometry and neutrons) to the Next Step but the soft X-ray systems on which MHD studies rely heavily in present day tokamaks do not appear to be feasible because there are no suitable detectors that can withstand the high neutron flux. There may also be problems with spectroscopy if radiation resistant windows and fiber optics cannot be developed.

High Frequency Fluctuations

For many years it has been postulated that high frequency fluctuations in the plasma may be responsible for enhanced transport losses but, despite

extensive efforts, conclusive results have not been achieved. There are considerable difficulties in making diagnostic measurements of the relevant quantities such as density, temperature, electric potential and local magnetic field with sufficient spatial and temporal accuracy. It is unrealistic to attempt to design major diagnostic systems for comprehensive fluctuation measurements in ITER until suitable diagnostic methods have been developed and demonstrated on smaller tokamaks. Nevertheless, much valuable information can be obtained from diagnostics that are installed with a different primary purpose (examples include magnetics, reflectometry and ECE) and it will be important to give adequate consideration to the high frequency capability when these systems are specified and implemented.

Edge Plasma, Divertor and First Wall

In many ways the edge plasma is more difficult to diagnose than the core. Spatial scale lengths are generally much shorter and there are significant toroidal and poloidal asymmetries. Until quite recently the edge plasma has received less attention than the core and consequently edge diagnostics are less well developed. Probes are widely used to measure density, temperature and power flux at the extreme edge where temperatures are sufficiently low. JET uses arrays of fixed probes embedded in the limiters, divertor tiles and ICRH antennas as well as movable probe drives, and experience has shown that these can be made reasonably robust and reliable. Similar systems will need to be developed for ITER. JET is developing high resolution ECE, Thomson scattering and microwave reflectometer diagnostic systems to bridge the difficult gap between the probe measurements and the core profile diagnostics. Further development of these and other methods will be required for the edge and divertor plasma regions in ITER. Infra-red camera measurements of the surface temperatures of the limiters, divertor tiles and antennas have been very valuable in JET for optimising plasma operation and identifying localised hot spots. These infra-red cameras will be much too sensitive to radiation for use in ITER without massive shielding and new detection methods or light relay systems must be developed. Visible light spectroscopy using fiber optic relay systems is used to identify and measure impurity influxes from specific surfaces such as the limiters and divertor tiles. These techniques could be extended to ITER if suitable lines of sight are available and radiation resistant relay optics are developed.

SELECTION OF DIAGNOSTICS

The original feasibility studies for JET identified about 25 diagnostics that were considered essential for the experimental program. There was a deliberate policy to base the selection on methods that had already been demonstrated on other fusion experiments, so that the work could focus on the substantial problems of engineering reliable systems for JET rather than concentrating on developing new and untried ideas. All of these systems have been built and are now operating successfully. A further group of about 10 diagnostics was also identified which needed much more development before the detailed design could start. It is interesting to note that only 3 of these have ultimately been built and the final versions are quite different from the initial concepts. Since JET began operating, a further 15 new systems have been added. Some of these have evolved out of earlier systems, some are in response to changes in JET's requirements and others are completely new diagnostic techniques that have been developed in the past decade. This experience suggests that a good initial survey of requirements is essential to fix the main diagnostic systems, but it is also desirable to maintain the flexibility to respond to new developments and requirements that will certainly emerge during the long life of a major fusion experiment.

A key issue in the selection of diagnostics is the access requirements. In the case of JET, access to the plasma is limited due to the intense competition between diagnostics and machine systems for the available ports. Diagnostic access to the Next Step will be even more difficult because of the blanket and radiation shield and by restrictions on the maximum apertures that can be tolerated through these structures by considerations of nuclear heating in the superconducting magnets. It appears that vertical access, which in JET is inferior to the horizontal access, may be better in ITER due to the large ports that will be provided for divertor pumping and maintenance. Wide angle views will be very hard to realize. Some diagnostic methods inherently need less access than other methods (examples are reflectometry compared to transmission interferometry and LIDAR Thomson scattering compared to imaging systems) and there are obvious attractions in developing these methods. It is important that diagnostic access requirements should be established and discussed together with the requirements for other systems of the experimental fusion reactor during the conceptual design stage. Whilst it is clear that diagnostic access requirements cannot be allowed to make unreasonable demands

on the design of the other reactor systems, it would be equally foolish to design an experimental fusion reactor that cannot be adequately diagnosed.

KEY DEVELOPMENT AREAS

Even though there has been considerable development in the diagnostics for the present large tokamaks, several key developments are necessary before the construction of the diagnostics for the Next Step can begin.

Windows and Plasma-Facing Optical Components

Windows on the vacuum vessel are needed for many diagnostics which view the plasma in the visible, infra-red and microwave regions of the spectrum. JET uses crystal quartz windows bonded with aluminium or gold to an inconel flange. These work well at temperatures up to about 450 C but there have been some failures. Windows on the bottom of the torus are particularly vulnerable as the aluminium bond is easily damaged by water during torus washing or accidental leaks from cooling systems. During plasma operation some of the windows become coated with a partially opaque layer and this can affect the transmission properties of the window creating calibration problems for diagnostics.

For ITER and for fusion reactors, windows will present a very serious problem because of radiation damage and darkening at high neutron fluences. Windows must be extremely reliable. In some cases it may be possible to locate the window out of the direct line of sight of the plasma provided that a suitable reflecting surface can be found, but this will itself have to survive in the direct line of sight of the plasma. The development of suitable windows and reflecting surfaces is an important issue common to the extrapolation of many diagnostics.

Radiation Hardened Optics

Several diagnostics require light relay systems to allow sensitive detectors to be located outside the reactor hall. Fiber optics are particularly convenient but suffer from fluorescence and darkening due to nuclear radiation. ITER will require fibers with improved radiation resistance or the development of optical relay systems using discrete components.

Tritium Compatibility & Radiation Hardening

Preparations are being made to operate JET in tritium during the last 2 years of the experimental programme. For planning purposes a total of 10^4 shots and a total of 10^{24} neutrons in a two year period have been assumed. The tritium compatibility of the diagnostic systems was considered in the initial feasibility studies and about 75% of the systems were identified as being required for the tritium phase and capable of being made compatible by a careful choice of components and by placing all sensitive components outside the torus hall. These systems were also designed to be remotely handled so that modular subsystems of diagnostics could be removed for repair or replacement. Although these provisions increased the initial complexity of the diagnostics they have minimized the work that will be required to make the transition to the tritium phase and there has been the useful bonus that commissioning the diagnostics could proceed whilst JET is operating. Some diagnostics could not be made tritium compatible because they needed sensitive detectors close to the plasma but were needed for the detailed physics studies in the earlier phases of JET. These include the ultra violet spectrometers, X-ray diode arrays, charge-exchange neutral particle analyzers and infra-red cameras used to monitor the temperatures of limiters and other internal structures and will be removed before the tritium phase.

Reliability

It is difficult to quantify accurately the reliability of the diagnostics on JET since discharges can be lost or delayed due to a number of reasons and yet frequently only one is selected as the culprit. A relatively small fraction of the delays to JET operation have been due to major incidents such as vacuum or water leaks in diagnostic equipment connected to the torus, other faults in diagnostics which require access to the torus hall and faults to essential diagnostics which are needed for the safe operation of JET. Faults which invalidate the data are even less easy to quantify since they are not usually recognized immediately and may only invalidate a particular area of interpretation. These are caused by various factors such as drifting calibrations, operator errors, incompatible plasma conditions and incorrect setting of timing windows etc. Further improvements of diagnostic reliability are required for the Next Step experiments where the consequences of failures will be even more serious.

Data Acquisition and Real Time Processing

Good temporal and spatial resolutions are needed and, combined with the large dimensions and discharge duration, these necessitate many measurements per discharge. The raw data from almost all of the JET diagnostics is collected and stored in a central computer system (the few exceptions are one or two new or temporary diagnostics). The JET data acquisition system now records about 10 Mbytes per discharge but this requires that many diagnostics can be operated at their maximum time resolution only during limited time windows that have to be pre-set and therefore some important plasma events may be missed. The total data stored after 6 years of operation (15,000 discharges) is about 150 Gbytes. These diagnostic data files are available to all JET staff within a few minutes of the discharge and greatly facilitate analysis of the data and discussion of results. This open access policy puts considerable pressure on diagnostic physicists to ensure that their data is accurate and validated for use by other users who generally are unfamiliar with the details of particular diagnostic systems.

The larger physical dimensions and longer discharge durations in ITER will increase the data acquisition and storage requirements by several orders of magnitude. Although these demands will no doubt be matched by future developments in data handling and storage technology, it will be desirable to develop data compression methods so that it will be possible to utilise the diagnostic capability more fully. Real time data analysis methods will be particularly important on ITER in view of the need to display plasma information in the control room whilst the discharges are in progress. Real time displays are being developed on JET for some diagnostics (an example is the derivation of the electron temperature profile from ECE) and with the rapid development of powerful microprocessor-based networks it will be feasible to provide real time analysis for most diagnostics.

The plasma control systems presently employed in fusion experiments are rudimentary compared to the systems that will be required in a fusion reactor and considerable development will be needed for the diagnostic sensors and associated data reduction systems. In particular these systems must be extremely reliable and robust and will of course need real time data processing and validation.

IMPLEMENTATION, COSTS AND TIME SCALES

Implementation

The JET team in 1979 was far too small to be able to undertake the design and construction of the complete set of diagnostics entirely in-house. Moreover it was apparent that much valuable diagnostic expertise was available in the fusion laboratories who are partners in JET. Some of the diagnostics which were essential for JET's safety were designed and built in-house, but most of the systems were built by the other European fusion laboratories under contract.

Formally the work was divided into four main phases. The *feasibility design phase* typically lasted for a few months and established the requirements and basic technical specifications. Issues such as access requirements, location, number of sight lines, radiation hardening and need for remote handling were usually established at this stage. Single contracts were awarded for the *detailed design and construction phase* and although this had the advantage of allowing construction of some components to commence before the detailed design of all components was complete, it did lead to difficulties in agreeing fixed prices for the contracts on the basis of an outline design. The final phases of *installation, commissioning, and operation* were merged in many cases with some parts of the diagnostic being brought into operation and used before the entire installation was complete.

It is important to stress that although many separate groups were involved in the design and construction of the JET diagnostic systems, there was close overall supervision and coordination from JET and particular attention was paid to maintaining common standards in areas that interfaced with other JET systems. This is important if the final result is to achieve a coordinated and integrated set of diagnostics. In contrast to earlier fusion experiments where diagnostics had been essentially built by scientists, the JET systems have required substantial engineering due to their large physical dimensions, remote handling requirements and the need to maintain compatibility with the high quality of engineering in other machine systems.

Costs

The overall cost of the JET diagnostics is about 85 MioECU (about 95 M$) in 1989 values. These costs include the external manpower but not that from within the JET team. Design, construction and operation to date have involved about 1000 man years, roughly equally divided between professional and technical support. These figures correspond to about 10% of the overall costs and efforts of JET and, pending a detailed assessment of diagnostic requirements for ITER, this provides a useful indication of the provisions that should be made for diagnostics in the outline design.

Time Scales

Experience on JET has shown that the time scale to design, construct, install and bring into full reliable operation the set of diagnostics needed for a major fusion experiment is typically between three and seven years. The specification and design of the diagnostics for JET began about 4 years before JET started operation and consequently only a few systems were available for the first plasma discharges and the many systems did not come into full operation until one or two years later. Following this experience at least five to seven years should be allowed for the design and construction of diagnostics for the Next Step. There are several important areas of development that need to be addressed before this work can start. During the present conceptual design stages of ITER and the other experiments it is important to identify the main diagnostics in order to identify access and other requirements at a stage when it is still possible to influence the machine design. Furthermore it is essential that diagnostics that have the potential for extrapolation to the Next Step should be fully developed on existing machines.

SUMMARY AND CONCLUSIONS

The overall conclusions to be drawn from the experience on JET is that a comprehensive and integrated set of diagnostics is needed to optimize the operation and guide the progress of a major fusion experiment. It is interesting to note that whilst JET was being built many people doubted the need for so many diagnostics, but once JET began to operate it became increasingly clear that more rather than fewer were required. Adequate provision should be made for diagnostics at an early stage in the design of the Next Step experiment and the diagnostics must be regarded as an integral part of the machine. Good engineering design is needed for reliable operation and to ensure compatibility with other machine systems. Experience on JET has shown that individual diagnostic systems can be built by different fusion laboratories, but it is important to maintain good overall coordination so that the final result is a well integrated diagnostic system rather than a diverse arrangement of instruments built to different standards.

This survey, which is summarised in Table II, has shown that existing techniques to measure plasma shape, position, current, electron density and temperature profiles, and neutron yields appear to be capable of extrapolation to ITER but require a certain amount of development. The extrapolation of existing methods for measuring ion temperature and current density profiles, high frequency fluctuations and some aspects of the edge and divertor plasmas appear more difficult and will probably require substantial development before the detailed design can start. In some cases techniques that have not yet been demonstrated on existing machines are required, for example collective scattering for diagnosing fast ions and alpha particles. A number of key development areas, common to many diagnostics have been identified, especially windows and plasma facing optical components, radiation hardened optical transfer systems, data acquisition and real time data analysis, tritium compatibility and remote handling. It is important to find solutions to these problems at an early stage so that the detailed design of the diagnostics can start in a few years time.

ACKNOWLEDGEMENTS

REFERENCES

1   Equipe TFR (1979) *Tokamak Plasma Diagnostics,* Nuclear Fusion **18** 647.
2   Stott, P.E., et. al. Eds., *Basic and Advanced Diagnostics for Fusion Research,* Proceedings of the Varenna International School of Plasma Physics (1986), EUR 10797 EN, (3 vols) published by the CEC, Brussels.
3   Stott, F.E., *Review of JET Diagnostics and Results,* ibid, vol III, 845.
4   Stott, F.E., *Plasma Measurements for JET,* Phil. Trans. R. Soc. Lond. A **322,** 47, (1987).

Table II—Main JET Diagnostics
and their Possible Extension to Experimental Reactor Conditions

PARAMETER	TECHNIQUE	APPLICABILITY	COMMENT ON POSSIBLE EXTENSION TO EXPERIMENTAL REACTOR DIAGNOSTIC
Plasma position and shape Current and total energy content	Magnetics	✓	Basically suitable but need to establish that suitable materials are available and to develop methods of measuring steady fields.
Electron Density Profiles	Transmission Interferometry	✗	Unlikely to be suitable because of substantial access demands.
	Thomson Scattering	✓	Powerful and accurate technique but requires development of radiation resistant windows and mirrors. For density measurement absolute calibration is also required.
	Reflectometry	✓	Promising technique but a key question is whether the density profile can be measured routinely in the presence of density fluctuations.
Electron Density Profiles	Thomson Scattering	✓	See above.
	Electron Cyclotron Emission	✓	Well suited in principle but limitations can arise from harmonic overlap and problems of interpretation from non-thermal emission.
Ion Temperature	Neutral Particle	◇	Requires the development of detectors compatible Analyzer with high levels of neutron irradiation and high energy diagnostic neutral beams.
	X-Ray Crystal Spectroscopy	◇	Suitable in principle but requires development of radiation resistant crystals and may require high Z seeding of plasma.
	Charge Exchange Recombination Spectroscopy	◇	Suitable in principle but requires development of radiation resistant optical components, fibres etc., and high energy diagnostic neutral beams.
	Neutron Diagnostics	✓	Suitable calibration methods and neutron spectrometers need further development.
Plasma Current Density	Faraday Rotation	◇	Full profile measurements unlikely because of substantial access demands but measurement of current density on axis may be possible using a limited number of sight-lines. Accurate measurements of the density profile are required by other means.
	Thomson Scattering	◇	Yet to be demonstrated on a large plasma and likely to be very difficult to apply to a reactor plasma.
	Charge Exchange Recombination Spectroscopy	◇	Yet to be demonstrated, requires dedicated neutral beam and visible optics.
Impurity Identification and Densities	Visible and Near UV Spectroscopy	✓	Development of radiation resistant optical components (windows, mirrors, light-guides) required.
	VUV Spectroscopy	✗	Severe detector damage probable and no alternative to line of sight.
	X-Ray Spectroscopy	◇	As in ion temperature
	Charge Exchange Recombination Spectroscopy	◇	As in ion temperature

J CR 89 114 1

Table II Contd.

PARAMETER	TECHNIQUE	APPLICABILITY	COMMENT ON POSSIBLE EXTENSION TO EXPERIMENTAL REACTOR DIAGNOSTIC
Radiated Power	Bolometry	✓	Requires development of radiation resistant bolometer and demands wide angle of view.
Neutrons and Fusion Products	Neutron Flux	✓	Possible but development work is required on calibration and to improve life-time of detectors.
	Neutron Yield Profile	✓	Possible but development work is required on calibration and detectors.
	Neutron Activation	✓	Possible but need to select isotopes with long half-life and further develop methods of calibration.
Escaping Alphas	Particle Detector	◇	Requires development of radiation hard detectors.
Confined Alphas	Collective Thomson Scattering	◇	Yet to be demonstrated and requires development of powerful source at $\lambda \sim 200\,\mu$m.
	Charge Exchange Recombination Spectroscopy	◇	Yet to be demonstrated and see comments above on practical problems.
MHD Instabilities	Magnetics	✓	See above.
	Soft X-ray	◇	Detector survival is a major problem. Possibly have extensive system for physics phase and much reduced system for technology phase.
	Neutrons	✓	Possibly complements X-ray approach for use in D-T phase.
	Electron Cyclotron Emission	✓	See above.
	Reflectometry	✓	See above.
	Visible Spectroscopy	◇	See above.
High Frequency Fluctuations (>100kHz)	Magnetics	✓	See above.
	Reflectometry	✓	Suitable in principle but interpretation is difficult.
	Soft X-ray	◇	See above.
Edge Plasma Divertor and First Wall	Langmuir Probes	✗	Unlikely to be suitable because of severe erosion.
	ECE	✓	Suitable in principle but range of plasma conditions is likely to be limited.
	Reflectometry	✓	Should provide information on density fluctuations but measurements of density profile are uncertain.
	Visible Spectroscopy	◇	See above.
	IR Imaging	✗	Unlikely to be suitable because of radiation damage to sensors and optical components.
	Sample Probes	✓	Should be possible but with reduced diagnostic capability.

✓ Probably will be applicable after suitable development.

◇ Needs more extensive development, or may be suitable only for selected phases of ITER programme.

✗ Unlikely to be applicable.

JET Contributions to the Workshop on the New Phase for JET: The Pumped Divertor Proposal

(25th – 26th September 1989)

P-H Rebut, P P Lallia

THE NEW PHASE FOR JET AND ITS OBJECTIVE

P.-H Rebut and P P Lallia

JET Joint Undertaking, Abingdon, Oxon, UK

1. Introduction

The Euratom Fusion Programme is designed to lead ultimately to the construction of an energy producing reactor. Its strategy is based on the sequential construction of major apparatus such as JET, NET and DEMO, supported by medium sized specialized Tokamaks.

Since the beginning of its operational phase, JET has made major achievements but further advances must be accomplished to provide a secure basis for the next step Tokamak. Plasma temperature, density and confinement values already achieved, but not simultaneously, are individually close to the requirements of NET. JET results have allowed some of the parameters of a reactor to be specified. In particular, the plasma current capability of a next step Tokamak is now foreseen to be in the range 25-30MA, compared with 6-10MA predicted when JET started operation in 1983.

On the other hand, the control of impurity influx and exhaust which can be achieved without a divertor is still inadequate. This contributes to the limitations of present JET performance. The level of impurity control which could be achieved has a direct consequence on the size of the next step. It also precludes starting the construction of components of the next step device before the specifications for the divertor and its associated pumps can be defined.

Based largely on JET results, the present studies to define ITER, NET or any other next step Tokamak clearly emphasize the need for obtaining additional information not only on impurity control and plasma-wall interaction but also on modes of operation, such as those avoiding plasma disruptions and enhanced confinement regimes.

By virtue of its size, its already demonstrated plasma performance and its long pulse capability, JET is in the best position to address these problems in the basic geometry considered for the next step. Such studies are the original *raison d'etre* of JET and represent a natural development of its presently agreed programme. They would however imply an additional phase in the JET programme.

The aim of this new phase would be:

> To demonstrate effective methods of impurity control in operating conditions close to those of the next step Tokamak; that is in a stationary plasma of "thermonuclear grade" in an axi-symmetric pumped divertor configuration.

The expected results of this new phase are:

A) • demonstration of a concept of impurity control in JET;
   • the size and the geometry needed to realize this concept in the next step;
   • choice of the material for the plasma facing components;

B) • the operational domain for the next step, including the impact of particle and impurity control on enhanced confinement regimes.

To increase further its relevance to the next step Tokamak, this new phase would also focus the JET programme by optimizing all the JET systems for operation, including those with tritium, in one magnetic configuration, i.e. single null X-point with an axisymmetric pumped divertor.

The progress made in controlling these impurities should improve the α-particle production and heating during the JET tritium phase.

2. Contents

The aim of this paper is to introduce the scientific and technical considerations as the basis of the JET proposal. Section 3 describes the concept of impurity control envisaged for JET and the reasons for a pumped divertor. Section 4 summarises needs to better delineate the operational domain of a future reactor. Section 5 indicates the consequences of the New Phase on the Tritium operation in JET. Section 6 shows the proposed schedule and the conclusions are presented in Section 7.

3. Impurity control

Achieving control of the impurity influx into the plasma is a prerequisite for building a Tokamak reactor. In the case of high Z impurities, radiation losses may prevent attainment of the temperature required for ignition. The presence of low Z impurities, in addition to helium produced by nuclear reactions, dilutes the concentration of reacting ions and therefore reduces the α-particle power. Under present conditions, the lifetime of the plasma facing components would be severely limited. The degree of impurity control which could be achieved has a direct consequence on the size of the next step.

Fig.1 shows, depending on the impurity concentration n_Z/n_D, by which factor the fusion product $n_i T_i \tau_E$ must be increased to reach and sustain ignition. The calculation is made by supposing a peak temperature of 30keV, for various impurities such as Beryllium, Carbon, Iron and Molybdenum. High power discharges in JET with carbon walls and target plates lead to carbon concentrations very close to values above which ignition would be impossible in any machine, i.e. $n_C/n_D \approx 16\%$. The use of lower Z materials allows a higher impurity concentration, but even a Beryllium concentration of 11% requires a doubling of the fusion product required for ignition.

The means of controlling impurities to be considered and tested on JET during the new phase are:

(i) passive, - by reducing the production of impurities at source, i.e. by a proper choice of the target plates;

(ii) active, - by creating an outward flow of deuterium from the bulk of the plasma toward the target plates which prevents by friction impurities reaching the main plasma.

3.1 Passive control

Regarding the plasma facing components, the objective is to define wall protection and X-point tiles for NET, ITER or any other next step device. The present line of approach on JET is directed towards low-Z materials such as beryllium or beryllium carbides, but alternative routes may have to be considered and tested first in the NI test-bed.

A simple model has been used to calculate the influx of the main impurity (of charge Z), at the limiter or target plates. Fig. 2 sketches the cascaded flux of impurity, ϕ_Z, caused by sputtering of the limiter by a flux of deuterium, ϕ_D. ρ is the fraction of ϕ_Z which returns to the limiter without entering the plasma. Including the possible contribution of an oxygen flux, ϕ_O, the ratio ϕ_Z/ϕ_D in steady state is given by:

$$\frac{\phi_Z}{\phi_D} = \frac{(1-\rho)}{F_{ZZ}}\left[F_{DZ} + \frac{\phi_O}{\phi_D}F_{OZ} + \frac{S}{\phi_D}H_{EV}\right] \quad [1]$$

where S is the equivalent area of the limiter. The functions F_{DZ}, F_{ZZ} and H_{EV} are averaged along the limiter surface from the contact point with the plasma over a distance X and are defined as

$$F_{DZ} = \int_0^1 \frac{Y_{DZ}(E_D,T)}{1-\rho Y_{ZZ}(E_Z,T)} dX$$

$$F_{ZZ} = \int_0^1 \frac{1-Y_{ZZ}(E_Z,T)}{1-\rho Y_{ZZ}(E_Z,T)} dX$$

$$H_{EV} = \int_0^1 \frac{W_Z(T)}{1-\rho Y_{ZZ}(E_Z,T)} dX \quad [2]$$

where Y_{DZ} and Y_{ZZ} are the sputtering yields of the material Z with deuterium and self ions, $W_Z(T)$ is the evaporation rate of the material Z. F_{OZ} is given by an equation similar to Eq.[2], but using the sputtering yield for oxygen, Y_{OZ} (E_O,T).

Eqs.[1] and [2] show the importance of the self sputtering coefficient Y_{ZZ}. When $Y_{ZZ} = 1/\rho$, the solutions diverge towards a pure carbon plasma. This could be the explanation of the carbon "bloom" observed in high power discharges on JET.

Assuming carbon tiles and a parabolic distribution of the temperature along x, the relative carbon flux ϕ_C/ϕ_D is plotted in Fig.3 versus the limiter maximum surface temperature for different values of ρ. The edge electron temperature T_e is assumed to be 60eV. The maximum of ϕ_C/ϕ_D around 600°C reflects the "chemical sputtering" of carbon by deuterium. Recent measurements made on JET by using a carbon probe moved near the plasma boundary are plotted on the same figure. It seems to indicate that the model used with $\rho \sim 0.6$ would describe the observations rather well. Sputtering by oxygen was omitted in the calculation to reflect the experimental conditions performed after Beryllium gettering.

Fig 4 shows the ratio ϕ_{Be}/ϕ_D versus the target plate temperature, calculated when Beryllium is the plate material. No experimental data are available as yet, but the model indicates a lower impurity influx than with Carbon for the same limiter temperature.

Whatever the plates are made of, whether Carbon or Beryllium, the critical parameter is the maximum temperature reached by the tiles. It should not exceed 1100°C to avoid an unacceptable impurity influx. Hot spots resulting from tile misalignments are particularly dangerous. To be compatible with practical cooling systems, the heat load must be reduced from present values and a safe design should limit the tile temperature to ~800°C. Methods of achieving this are to sweep the X-point and to create a highly radiative zone in front of the target plates.

3.2 Active impurity control

To allow an active impurity control in JET, it is proposed to install an axi-symmetric pumped divertor, as shown on Figs.5 and 6. A single-null system should keep a plasma current capability of up to 6MA and still provide the required information for the next step.

The objectives of an active impurity control in a reactor are:

    i)   to minimise the impurity content into the plasma

    ii)   to reduce the heat load on divertor plates to values which can be sustained continuously

    iii)   to exhaust the ashes

    iv)   to control the plasma density.

Methods of achieving these objectives are respectively:

    for (i), a strong flow of deuterium in the Divertor Plasma Channel (DPC), to keep the impurities near the target plates;

    for (ii), a sweeping of the intersection of the DPC with the target plates and a high level of impurities of medium or low Z in this area to evacuate the power by radiation;

    for (iii), a moderate flow of deuterium in the Scrape-off layer (SOL) and a pump near the target plates;

    for (iv), a fuelling of the plasma by pellet, neutral beams or gas and pumping in the DPC.

The plasma behaviour in the SOL and the DPC can be understood qualitatively by considering the basic steady-state equations for the flow F and the pressure p in a 1-D model. x is the coordinate along the magnetic field line and S is the particle source term. The equations

$$F_e = F_i = n_e u_e = n_h u_h; \qquad \frac{dF}{dx} = S$$

impose ambipolarity and particle conservation, when the cross-section of the magnetic flux tube is assumed to be constant, i.e. ~1/|B|. n is the density and u the directed velocity of the fluid along the x direction. The indices e, h, and z refer to electron, hydrogen and impurity of charge Z, respectively.

The momentum conservation in steady state can be written:

$$-\frac{dp}{dx} = n_h m_h u_h \frac{du_h}{dx} + m_h u_h S_h \qquad [3]$$

in the absence of external forces and assuming $S_Z = 0$; p is the total pressure of the plasma,

$$p = n_h \left(\frac{Z-1}{Z - Z_{eff}} \right) \left(kT_e + kT_h \frac{Z - Z_{eff} + 1}{Z} \right)$$

Integrating Eq.[3] leads to

$$p \simeq p_0 - m_h \frac{F^2}{n_h} \qquad [4]$$

p_0 is the plasma pressure in the SOL, where the particle flux F is zero. Note that $m_h F^2/n_h = M^2 p$, where M is the Mach number.

Fig.7 shows isothermal and isoflows in a plane p, n_h. In this diagram, isothermal cross isoflow curves in two points, one above and one below $p_0/2$, corresponding to subsonic and supersonic flows respectively. For a given plasma temperature T, the maximum isoflow compatible with Eq.[4] is tangent to the isothermal in $p = p_0/2$. That is the prevailing condition at the target plates which represent a sink for the particles. The heatload to be evacuated there is $P_t \sim F_t (E_i + \delta kT)$ where E_i is the energy of ionisation and $\delta \simeq 6$ takes into account the sheet potential.

The bold line a-b-c-d-t on Fig.7 shows an idealised trajectory between the plasma separatrix and the target plates. In the first approximation, the plasma temperature does not vary at the X-point where the hydrogen is injected. The diagram shows the compression achieved in the DPC, section c-d, where the particle source term is taken to be zero. The length of this section, and therefore the length of the DPC, must be sufficient and this has consequences on the size of a future device. Higher compression ratio would be obtained by having the point c closer to the transonic regime. However, the risk would be to bifurcate to a supersonic flow, like section e-f, resulting in a decompression in the DPC.

In order to increase the friction, hydrogen-impurity and the radiated power in front of the target plates, a low temperature, high density plasma is wanted. This will also limit erosion and

therefore increase the lifetime of the target plates. It is worth noting that these conditions result in a rather high plasma density at the separatrix which is unfavourable to non inductive current drive methods such as neutral beams or Lower Hybrid waves.

A numerical model has been developed to describe quantitatively the plasma behaviour in the SOL and in the DPC. It indicates that a hydrogen flow could stop the flow of impurities toward the X-point in JET. Fig.8 shows the steady state distribution of Beryllium density along the x coordinate with and without a hydrogen flow.

4. Operational domain of the next step

Regimes of enhanced confinement, such as H-modes, peaked density profiles or stabilized sawtooth could permit a reduction in reactor size only if these regimes could be maintained for the duration of the thermonuclear burn. If not, they might still facilitate reaching ignition in the first phase of the burn. As enhanced particle confinement is concomitant with improved energy confinement, helium exhaust in a reactor may justify interrupting the periods of better confinement, i.e. controlling them.

Enhanced regimes of confinement in JET appear to result from either,

(i)   better insulation at the plasma edge in the case of the H-mode; key parameters and methods of control in this area are:

    •   the existence of a magnetic separatrix and the distance separating the X-point from the wall;

    •   the plasma density which will be controlled by the pumped divertor;

    •   the plasma temperature which depends on additional heating power and on radiative losses near the plasma edge; therefore, the use of beryllium tiles and, even more, successive impurity control should be beneficial;

(ii)   reduced heat transport or suppression of instability in the core of the plasma for peaked density profiles and "monster" sawteeth, respectively. Means of control are:

    •   deep fuelling of the plasma by either repetitive injection of high speed pellets or high energy beams to increase the central density;

    •   strong pumping at the edge to maintain the density gradient in steady state conditions;

    •   production of fast ions in the plasma core by either ICRF or NBI to produce conditions relevant to "monster" sawteeth and the control of the current profile by LHCD to prevent the safety factor on axis decreasing to a too low value.

The design of the new step Tokamak is also strongly dependent on the frequency and the severity of major plasma disruptions to be expected during its lifetime. Ability to control the plasma in conditions close to disruptive limits (such as : density limit, locked modes following pellet injection and β-limit) will also influence the operating domain of the next step. Studying these limits and controlling the plasma by use of the active saddle coils is part of the JET programme. The new phase will allow extension of these studies in the most relevant conditions and in the proper geometry.

5. Consequences for the tritium phase and JET performance in the pumped divertor configuration

All JET systems, including ICRF antennae and diagnostics will be made compatible with the single-null configuration to ensure full coherence of the studies. It should correspond to the geometry used in the tritium phase.

Performance of JET in D-T operations has been estimated by using a 1-D transport code and assuming the heat transport described by the critical electron temperature model. Fig.9 shows the α-particle power, excluding the beam-plasma contribution, expected as a function of Z_{eff}, for 6MA discharges with 35MW of additional power. The two lines correspond to H-mode with (solid line) or without (hollow line) the existence of a monster sawteeth in the pumped divertor configuration. The single cross corresponds to an H-mode with the present JET plasma cross-section at $Z_{eff} = 2$. This value of Z_{eff} has been made possible, at least transiently, by the use of Beryllium gettering. With efficient impurity control and Z_{eff} approaching close to 1, a factor greater than 2 could be gained on the expectation of the present JET configuration and breakeven could be approached.

In summarizing the JET performance in the pumped divertor configuration, the capability of JET should allow:

    •   6MA single-null X-point configuration for up to 10s with an axisymmetric pumped divertor in the bottom of the vacuum vessel.

    •   3MA double-null X-point operation could also be performed up to 20s at a magnetic field of 3.4T;

    •   an increase, by more than a factor 2 of the expected α-particle power.

7. Tentative Schedule

A schedule for the JET programme incorporating the new phase is shown in Table I. It can be seen that the earliest date to have a pump limiter in JET is 1992. Further optimization would likely be necessary about 18 months later, in the light of experimental results.

To provide time for the new phase, the use of tritium in JET should be postponed until the end of 1994. At this stage, all the information on particle transport, exhaust and fuelling, first wall requirements and enhanced confinement regimes needed to construct the next step Tokamak, should be available. Final tests with tritium, including the α-particle heating studies could be performed in the two years following, leading to the completion of the JET programme by the end of 1996. During the tritium phase and even later, tests on prototype elements for the next step could be undertaken on the JET site, using the test facilities, tritium plant and power supplies.

8. Conclusions

Plasma performance in JET allows a definition of the plasma current capability of a Tokamak aimed at achieving ignition. As a step towards an energy producing reactor, the next objective of a next step Tokamak is to sustain an ignited state for a period of up to one hour. The control of impurities and the exhaust of helium is an essential condition for maintaining ignition. Techniques of achieving this, together with limits of operation have to be experimentally tested prior to construction of a next step. This can be undertaken on JET and the required data should be available by the end of 1994. Information on tritium operation and α-particle heating would be obtained by the end of 1996.

The present proposal would add a new phase to the JET programme dedicated to the studies of impurity control and operating domain for the next generation of Tokamaks. It would aim at focussing operations along the geometry considered for the next step. It makes the best use of the existing investment on JET, in expertise and equipment, for the preparation of NET and later DEMO.

Table I : JET Programme in the New Phase

1989	1990	1991	1992	1993	1994	1995	1996
Full Power Studies		New Additions in Limiter Configuration	Optimization in X-point Configuration & Next Step Oriented Studies			Tritium Phase	

• Pumped Divertor & RF Modifications

• Pumped Divertor Modifications
• Other System Enhancements

• Final Modifications for Tritium Operations
• 1 beam line to 160kV-T

JG89.669/1

IMPURITY IMPACT ON THE CONFINEMENT TIME REQUIRED FOR IGNITION

$\beta = ct$; $T_{eo} = T_{io} = 30\,keV$
$T_e = T_i = T_{eo}(1-\rho^2)$
$n_e = 10^{20}(1-\rho^2)^{\frac{1}{4}}$ (m^{-3}) without impurity
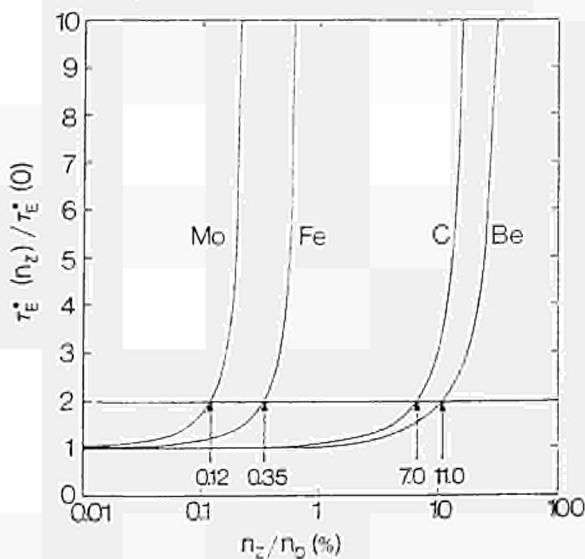
Fig. 1: Enhancement factor on the energy confinement time required to reach ignition versus the impurity concentration. For medium and high Z impurity such as molybdenum and iron, the enhancement is required to compensate the radiation losses. For low Z materials such as carbon and beryllium, dilution is the dominant factor.

Sputtering Model Used
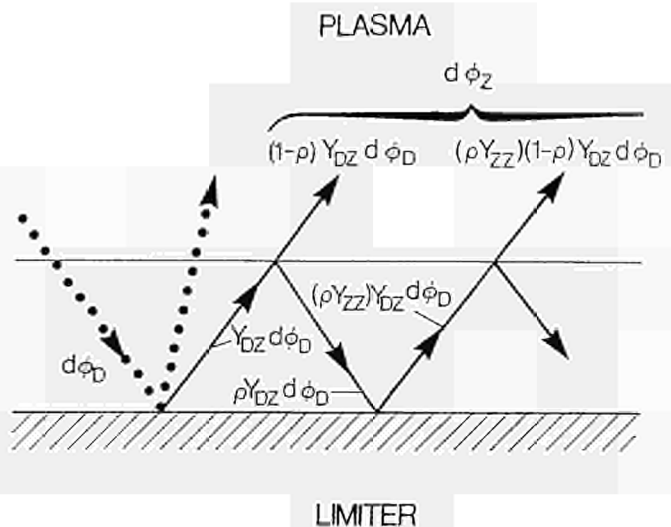
Fig. 2: This schematic diagram shows a flux of only one ion species (deuterium), $d\dot\phi_D$, impinging on a limiter made from a material Z. $d\dot\phi_D$ produces by sputtering Z atoms, which are subsequently ionized. The flux of impurity Z, $d\dot\phi_Z$, entering the plasma results from the series of cascades accomplished by the Z ions returning to the limiter and creating other Z atoms by self-sputtering.

Relative Flux of C as a function of Central Temperature of Limiter or Divertor Tiles
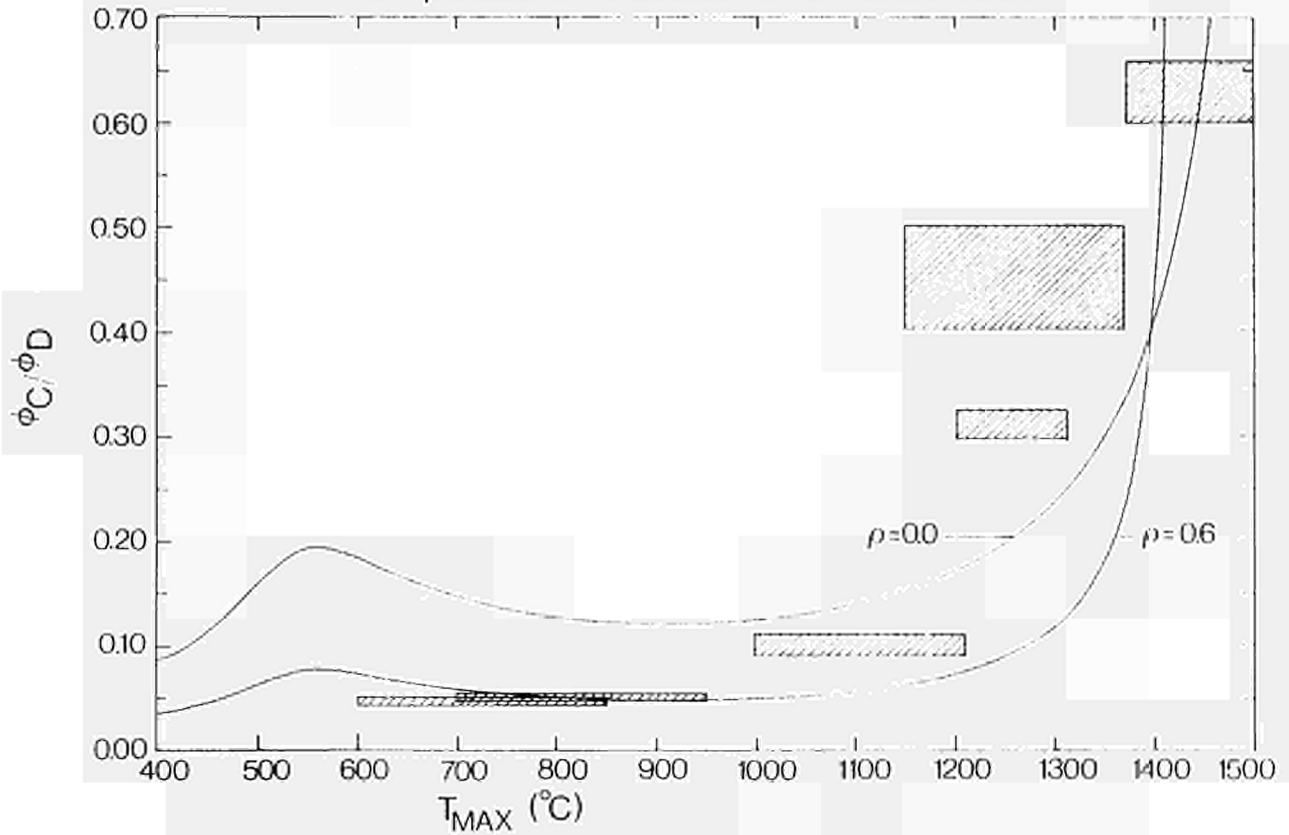
Fig.3: Ratio of carbon to deuterium flux versus maximum target temperature. The curve indicates the result of the simple model described in the text. The shaded boxes indicate the measurements made on JET.

Relative Flux of Be as a function of Central Temperature of Limiter or Divertor Tiles
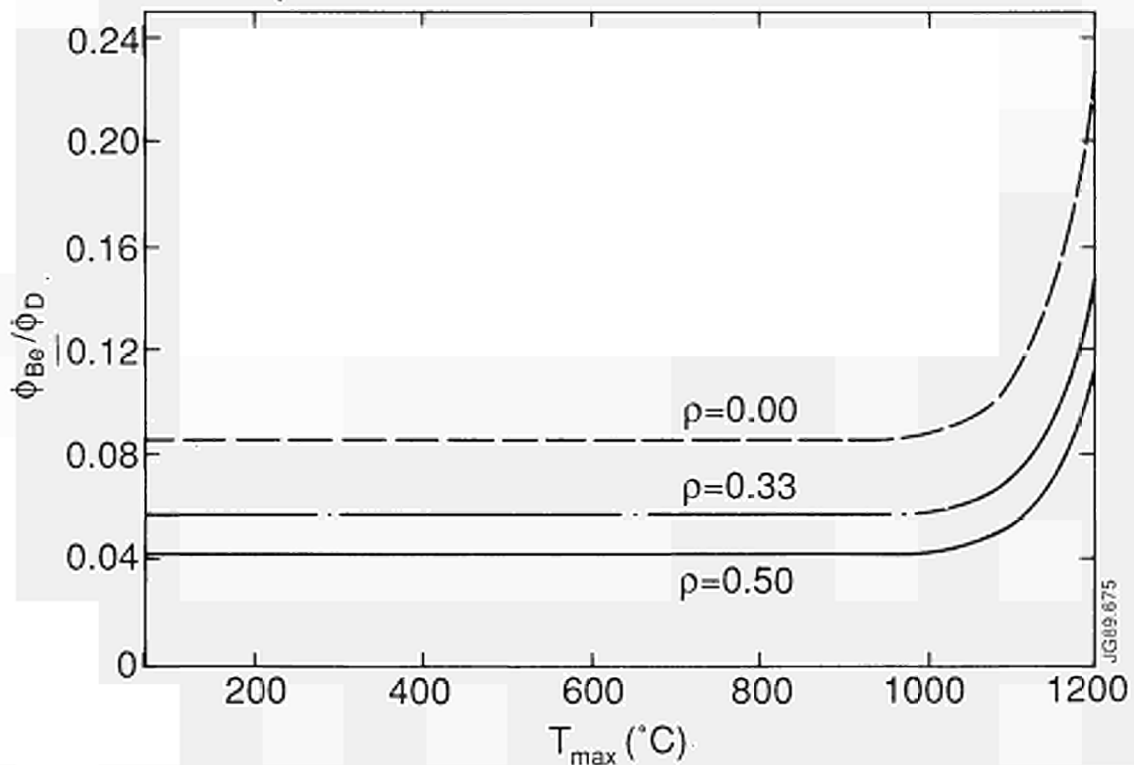
Fig.4: Plot of relative Beryllium to deuterium flux against the limiter maximum surface temperature, T_{max}, for three values of ρ. The sharp increase in the flux with temperature is due to evaporation.
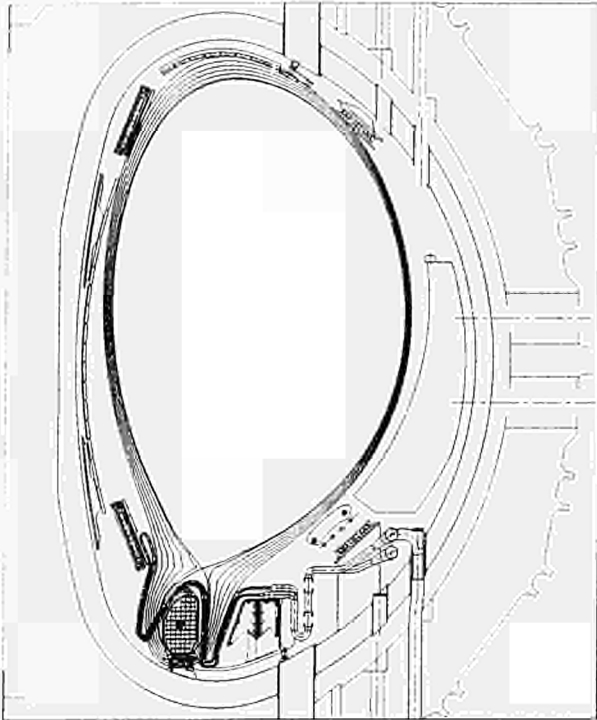
Fig 5: Cross section of JET showing the plasma and the main elements of the proposed pumped divertor.
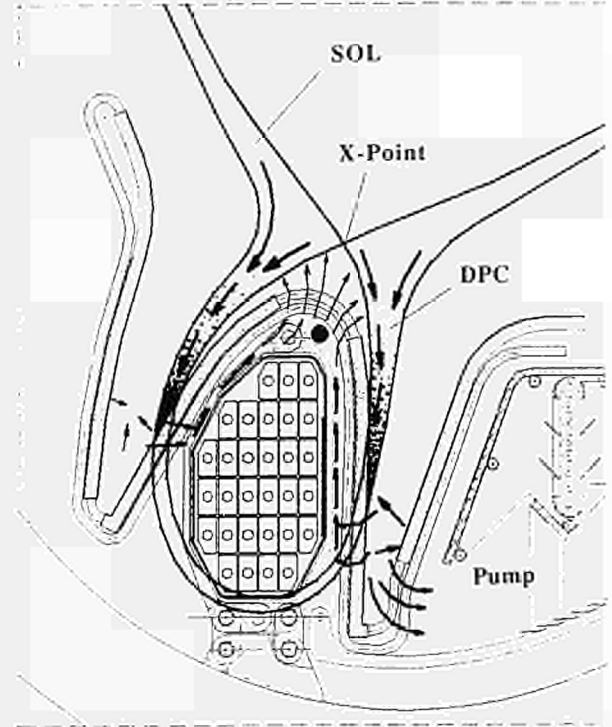
Fig.6: Enlargement of Fig.5, showing some details of the divertor coil and of the pump. The large arrows represent the deuterium flow in the scrape off layer (SOL) and in the divertor plasma channel (DPC). The thinner arrows sketch the flows of neutral particles.
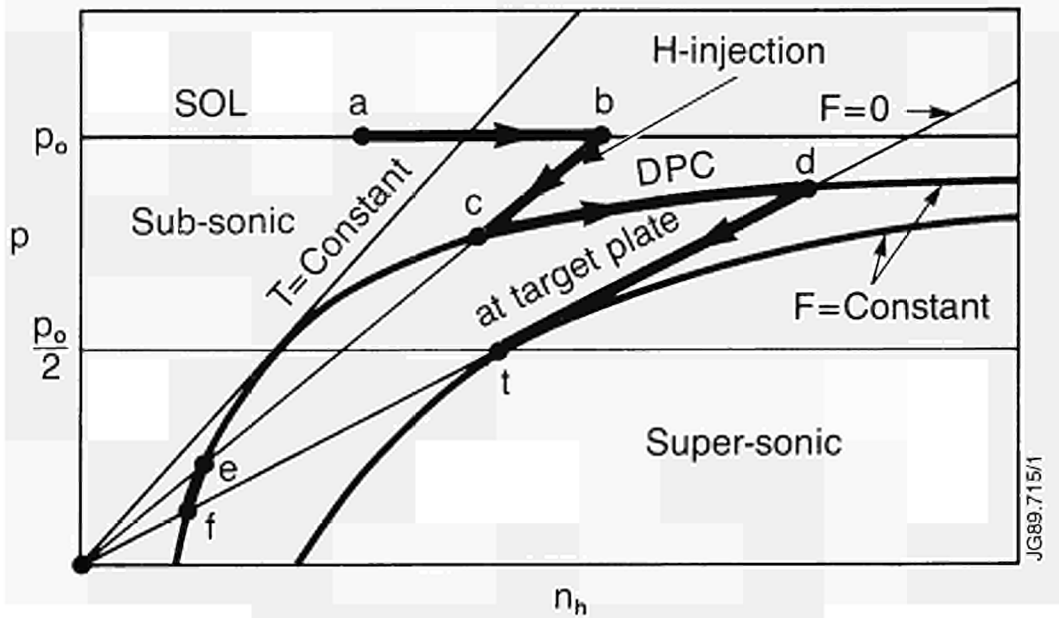
Fig.7. Diagram p,n showing the qualitative space evolution of plasma parameters:
- in the SOL (section a-b where the flow F = 0)
- at the X-point (section b-c)
- in the DPC (section c-d where F = constant)
- just in front of the target plates (section d-t where the flow becomes transonic)

Impurity Density versus Poloidal Distance
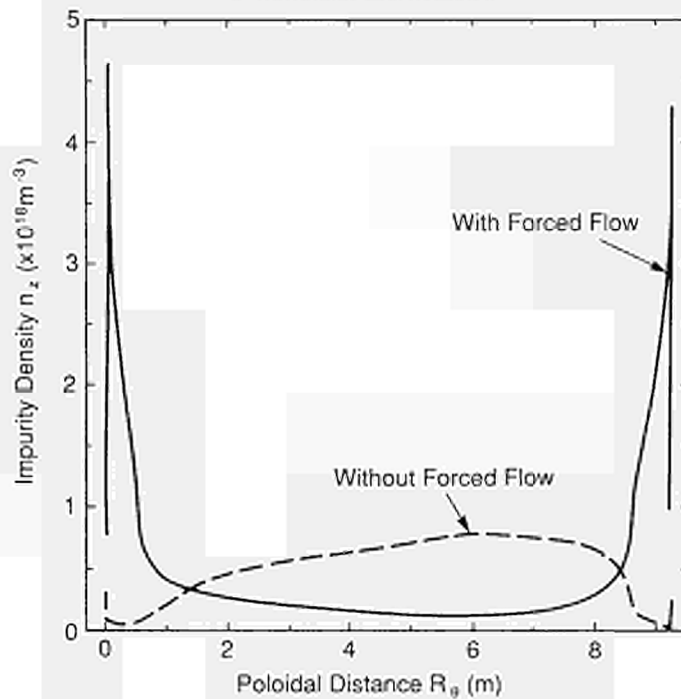
Fig 8: Spatial distribution of the impurity density along the field lines in the SOL and the DPC. The numerical simulation is made for with and without forced deuterium flow. The target plates are at R = 0 and R = 9.1m. The SOL extents approximately from R = 0.6m to 8.5m.

JET performances as simulated by the

the Critical Temperature Gradient Model
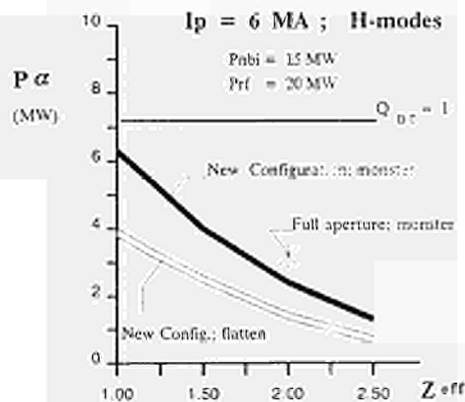
$<ne> = 10 ** 20$ m-3 with new config.

$<ne> = 7.5 \ 10**19$m-3 with full apert.

beam-plasma reactions are not included;

(+ 1 to 2 MW of alpha power.)

Fig 9. Expected JET performance calculated from a 1-D transport code using the critical temperature gradient model for the heat transport. The evolution of the α-particle power is seen versus Z_{eff} in the new configuration with divertor with and without "monster" sawtooth. The single point at $Z_{eff} = 2$ represents the expectation with the presently available plasma cross-section and the transiently achieved impurity content after beryllium evaporation.

JET Papers Presented at 13th Symposium on Fusion Engineering (SOFE)

(Knoxville, Tennessee, USA)

Many Authors

JET PAPERS PRESENTED AT THE 13TH SYMPOSIUM ON FUSION ENGINEERING, KNOXVILLE, TENNESSEE, USA, 2ND – 6TH OCTOBER 1989

IMPURITIES IN JET AND THEIR CONTROL

by

P.H. Rebut, P.P. Lallia, B.E. Keen
and the JET Team*
JET Joint Undertaking, Abingdon, Oxon, OX14 3EA, UK

ABSTRACT

This paper describes the problems of impurities in JET and proposals for their control. The latest results from JET are presented in which beryllium has been used as the first wall material facing the hot plasma. Substantial improvements in plasma purity and corresponding reductions in plasma dilution have been observed. This has allowed a fusion product ($n_D T_i \tau_E$) of $5 \times 10^{20} m^{-3}.s.keV$ to be reached (which is within a factor of 10-15 of that required in a fusion reactor), albeit in a transient situation. Even so, at high heating powers, impurity influx limits the attainment of higher parameters and prevents reaching a steady state situation. A new phase is proposed for JET with an axi-symmetric pumped divertor configuration to address the control of impurities, fuelling and exhaust of helium ashes in operating conditions close to those of a Next-Step Tokamak with a stationary plasma of thermonuclear grade. The latest proposal for the configuration is described which should demonstrate a concept of impurity control; determine the size and geometry needed for this concept in the Next-Step; allow a choice of plasma facing components for the Next-Step and demonstrate the operational domain for the Next-Step. With an efficient axi-symmetric pumped divertor, ignition should occur in a Tokamak reactor about twice the size of JET at $I_p \sim 25-30MA$, $B_T \sim 5T$ and produce a thermal output power, $P_{out}(th)$, $\sim 1-4GW$ (depending on density).

INTRODUCTION

The Joint European Torus (JET) is the central project in the European Fusion programme. This programme is coordinated by the European Atomic Energy Community (EURATOM). The EURATOM Fusion Programme is designed to lead ultimately to the construction of an energy producing reactor. Its strategy is based on the sequential construction of major apparatus such as JET, the next European Torus (NET), and DEMO (a demonstration reactor), supported by medium sized specialized Tokamaks.

The objective of JET is to obtain and study a plasma in conditions and dimensions approaching those needed in a thermonuclear reactor [1,2]. This involves four main areas of work:

(i) to study various methods of heating plasmas to the thermonuclear regime;
(ii) to study the scaling of plasma behaviour as parameters approach the reactor range;
(iii) to study the interaction of plasma with the vessel walls and how to continuously fuel and exhaust the plasma;
(iv) to study the production of alpha-particles generated in the fusion of deuterium and tritium atoms and the consequent heating of plasma by these alpha-particles.

JET is now about midway through its experimental programme. The technical design specifications of JET have been achieved in all parameters and exceeded in several cases (see Table I). The plasma current of 7MA and the current duration of up to 30 seconds are world records and are over twice the values achieved in any other fusion experiment. The neutral beam injection heating system has been brought up to full power (~21MW) and the ICRF heating power has been increased to ~18MW in the plasma. In combination, these heating systems have provided 35MW power to the plasma [3].

Table I
JET Parameters

Parameter	Design Values	Achieved Values
Plasma Major Radius (Ro)	2.96m	2.5 - 3.4m
Plasma Minor Radius (hor.)(a)	1.25m	0.8 - 1.2m
Plasma Minor Radius (vert.)(b)	2.1m	0.8 - 2.1m
Toroidal Field at Ro	3.45T	3.45T
Plasma Current	4.8MA	7.0MA
Neutral Beam Power	20MW	21MW
ICRF Heating Power	15MW	18MW

During 1987/88, the plasma vessel was operated with carbon tiles on the inside of the vacuum vessel walls to provide a low-Z material facing the plasma. In this situation, plasma temperatures up to 23keV were reached and the plasma densities (up to $\sim 2 \times 10^{20} m^{-3}$) and energy confinement times (up to 1.5s) were within the range required in a reactor. Although these values were achieved in individual experiments, they have not all been reached simultaneously [3]. There are two regimes of energy confinement observed in X-point magnetic configuration. With this configuration, a higher confinement regime (H-mode) has energy confinement times about twice the normal values (L-mode). In both regimes, confinement degradation occurs in that the plasma thermal energy does not increase proportionally to the heating power. Therefore, considerably more power is needed to increase the plasma temperature and energy. In these experiments, carbon impurities in the plasma at high power levels became a problem to further enhancing the plasma parameters.

IMPACT OF IMPURITIES ON JET PLASMAS

When JET was operating with all-carbon walls, impurities created the following problems:

- the production of impurities increased with the input power to the plasma. In ohmic discharges, Z_{eff} varied as I_p/n where I_p is the plasma current and n the density;
- at high power, the heat load on the tiles was too high, and the plasma evolution presented a catastrophic behaviour, the so-called "carbon catastrophe" or "carbon bloom". This is shown in Fig.1. About 25 MW of additional power are coupled to the plasma. After 0.2s, the carbon line emission seen on the JET inner wall increases abruptly. Increased plasma dilution, increased power radiation, reduced neutral beam penetration and a threefold fall of the fusion yield resulted from the carbon influx;
- for lower input power with long duration, problems are also, encountered. Without fuelling, deuterium is pumped by the carbon and replaced by impurities, resulting in a large dilution of the plasma. This is
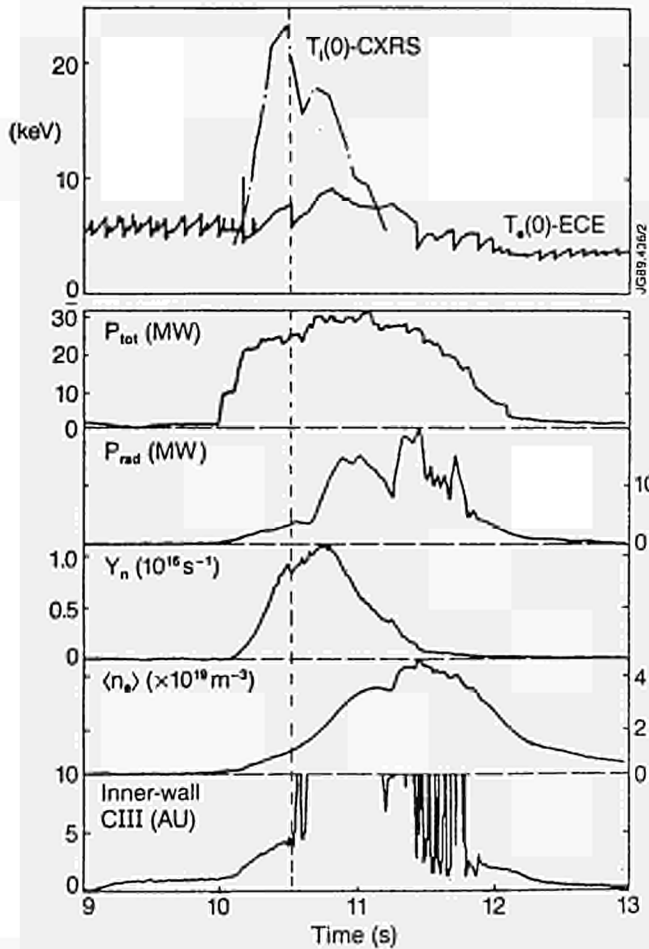
Fig.1: The carbon 'catastrophe' in JET. 25MW of heating are coupled to the plasma. After 0.2s, the C-line emission increases abruptly
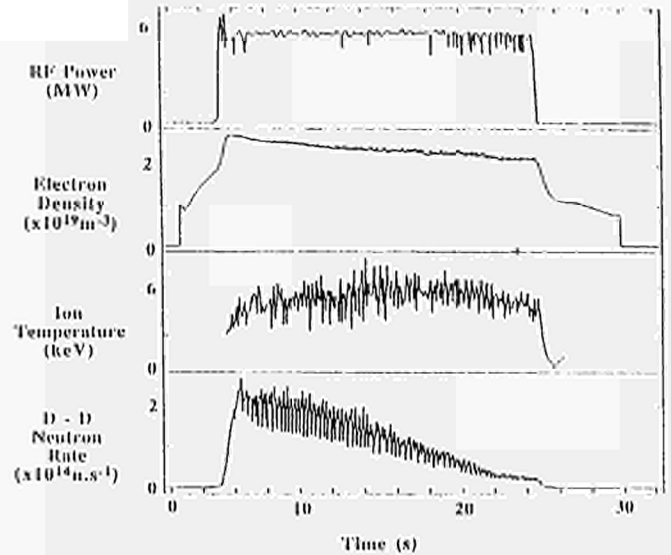

Fig.2: Long pulse operation in JET without fuelling, showing the progressive reduction of neutrons

- a severe carbon influx ('carbon bloom') is still a problem for plasmas located on the inner wall and for plasmas with an X-point, and is a serious limitation in H-mode studies, restricting power level to ~10MW. A typical example is shown in Fig.4, which indicates the rise in carbon density at high power inputs. Correspondingly, the ion temperature falls and the dilution factor (n_D/n_e) falls similarly.

The reduced impurity levels have allowed operation at higher densities and improved the general JET performance. The improved parameters are given, as follows:

- the fusion parameter ($n_D \tau_E T_i$) has been increased to $5 \times 10^{20} m^{-3} skeV$ for both high (20keV) and medium temperatures (9keV). Fig.5 shows a plot o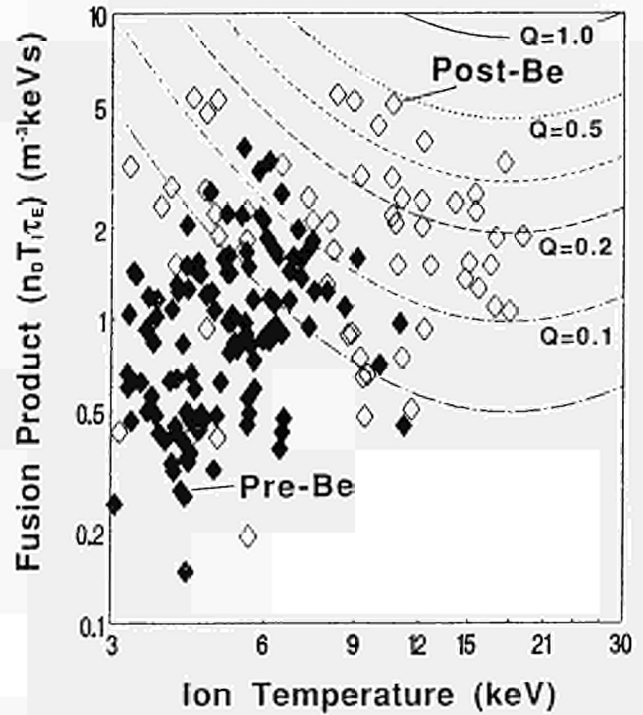f fusion product ($n_D T_i \tau_E$) versus ion temperature, T_i, for H-mode configurations in the pre-Be and post-Be phase of operation;
- the neutron yield has doubled to $1.8 \times 10^{16} ns^{-1}$ and the fusion factor Q_{DD} increased to 1.1×10^{-3}. This is equivalent to $Q_{DT} \sim 0.5$;

illustrated in Fig.2 showing the input ICRF power, the electron density, the ion temperature and the D-D fusion reaction rate during a 3MA pulse of 22s duration. The temperature is unchanged for 20s, the electron density slightly decreases but not enough to explain the progressive reduction of neutrons. In fact, the initial deuterium has been replaced by impurities;

- the maximum density achieved without occurrence of a plasma disruption appears to be limited by edge radiation.

JET RESULTS AND ACHIEVEMENTS WITH BERYLLIUM

To further improve JET results in 1989, the carbon tiles and inside of the vacuum vessel were first covered with evaporated Beryllium, and then later, the belt limiter tiles and RF antennae tiles were replaced by Beryllium tiles.

The effect of Beryllium evaporation on the impurity influxes are as follows:

- Oxygen impurity is essentially eliminated from the plasma;
- Carbon is the main impurity, but its influx is lower by a factor ~2 compared with all-carbon walls;
- the plasma charge Z_{eff} is significantly reduced in ohmic plasmas (down to 1.3) and with strong additional heating (down to ~2). Typical results are shown in Fig.3;

Fig.3: Z_{eff} values versus line average density for pre-Be and post-Be experiments.
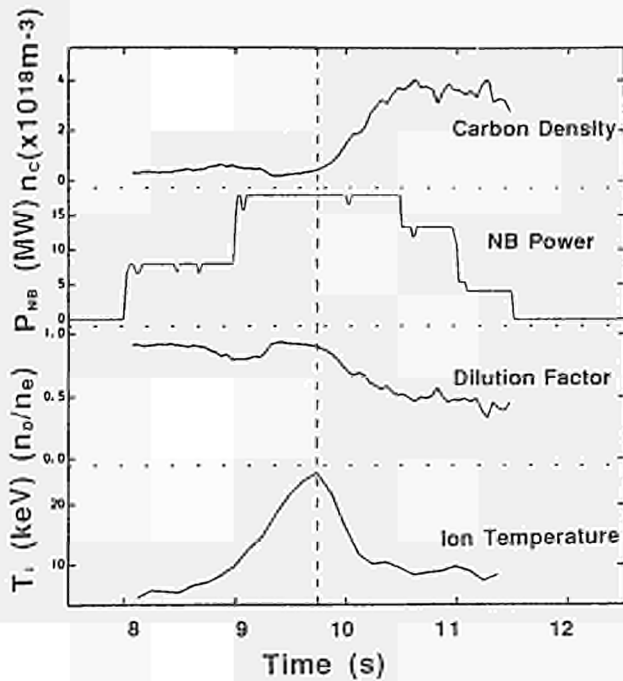
Fig.4: The carbon bloom effect in JET with Beryllium evaporation. At high powers, the carbon density rises and the ion temperature and dilution factor (n_D/n_e) fall, correspondingly.

Fig.5: The fusion product ($n_D T_i t_E$) verus ion temperature, T_i, for H-mode configurations in the pre-Be and post-Be phase of operation.

- the density limit has been increased to a value of (nRq/B) ~ 30 (with a record peak density of $4 \times 10^{20} m^{-3}$ with pellet fuelling). This limit is principally a fuelling limit and not a disruption limit as previously found with the carbon limiters;

- the pumping of the deuterium after Be evaporation is more efficient than with carbon walls. This has permitted low density and high temperature (25keV) operation for times exceeding 1s;

- the vessel is no longer deconditioned by disruptions;

- H-modes have been created with ICRH alone for periods exceeding 1s. Their confinement characteristics are similar to those previously obtained with neutral beam (NB) heating alone;

- values of β up to the Troyon limit have been obtained in low field ($B_T = 1.4T$) double-null X-point plasmas;

- sawtooth free periods exceeding 5s have been achieved, but the stabilisation mechanism is not yet clear.

Initial experiments with Be tiles have shown that they behave in a satisfactory manner, when compared to the Carbon tiles. The main JET parameters for the pre-Be and post-Be phases are summarised in Table II.

PROPOSED NEW PHASE FOR JET

Achieving control of the impurity influx into the plasma is a prerequisite for building a Tokamak reactor. In the case of high Z impurities, radiation losses may prevent attainment of the temperature required for ignition. The presence of low Z impurities, in addition to helium produced by nuclear reactions, dilutes the concentration of reacting ions and therefore reduces the α-particle power. Under present conditions, the lifetime of the plasma facing components would be severely limited. The degree of impurity control which could be achieved has a direct consequence on the size of the next step.

Fig.6 shows, depending on the impurity concentration n_z/n_D, by which factor the fusion product ($n_i T_i \tau_E$) must be increased to reach and sustain ignition. The calculation is made by supposing a peak temperature of 30keV, for various impurities such as Beryllium, Carbon, Iron and Molybdenum. High power discharges in JET
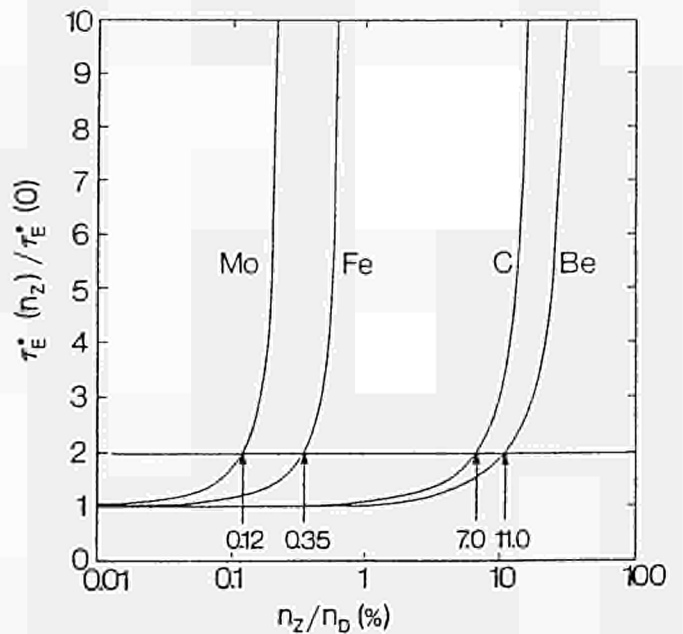
$$\beta = ct; \ T_{eo} = T_{io} = 30 \, keV$$
$$T_e = T_i = T_{eo} \ (1 - \rho^2)$$
$$n_e = 10^{20} \ (1 - \rho^2)^{1/4} \ (m^{-3}) \ \text{without impurity}$$

Fig.6: Enhancement factor on the energy confinement time required to reach ignition versus the impurity concentration. For medium and high Z impurity such as molybdenum and iron, the enhancement is required to compensate the radiation losses. For low Z materials such as carbon and beryllium, dilution is the dominant factor

Table II

MAIN JET PARAMETERS ACHIEVED
(Not necessarily in the same plasma pulse)

		With C	With Be
Electron Density	$n_e (10^{19} m^{-3})$	20	40
Electron Temperature	$T_e (keV)$	13	13
Ion Temperature	$T_i (keV)$	23.0	25
Energy Conf. Time	$\tau_E (s)$	up to 1.3	up to 1.3
Z_{eff}		3.0-7.0	1.3-4
Fusion Product	$n_i T_i \tau_E$ $(10^{19} m^{-3} keVs)$	30	50*
$Q_{DT}(total)$		0.3	0.5*

(* Non-steady state)

with carbon walls and target plates lead to carbon concentrations very close to values above which ignition would be impossible in any machine, i.e. $n_C/n_D \approx 16\%$. The use of lower Z materials allows a higher impurity concentration, but even a Beryllium concentration of 11% requires a doubling of the fusion product required for ignition.

By virtue of its size, its plasma performance and its long pulse capability, JET will address the problem of impurity control in the basic geometry considered for the next step tokamak. A new phase is proposed for JET which aims to:

demonstrate effective methods of impurity control in operating conditions close to those of the next step tokamak; that is in a stationary plasma of "thermonuclear grade" in an axi-symmetric pumped divertor configuration.

The objectives of the pumped divertor in JET are:

* control of impurities in the plasma;
* decrease of the heat load on the target plates;
* control of the plasma density.
* demonstrate exhaust capabilities;

The progress made in controlling these impurities should also improve the α-particle production and heating during the JET tritium phase.

Key concepts of the JET pumped divertor

Since the sputtering of the target plates by the impurities cannot be suppressed, impurities should be confined close to the plates themselves. Such confinement can be achieved by a strong plasma flow, directed along the divertor channel towards the plates. If large enough the frictional force between the plasma and the impurities should prevent impurity diffusion towards the X-point.

The connection length along the magnetic field line between the X-point and the target plates should be long (>10 m) to achieve effective screening of the impurities. This has the consequence of requiring a coil internal to the vacuum vessel.

A high density, low temperature target plasma in the divertor channels is an essential feature as it plays several key roles:

* it radiates a significant proportion of the power to be evacuated from the plasma, spreading the heat load on a larger area and therefore reducing the share of the target plates;
* high collisionality increases the friction with the impurities, therefore reducing their back-diffusion;
* its low temperature reduces the impurity production by sputtering, and therefore erosion of the target plates.

A pumping chamber is introduced in the vicinity of the target plates to provide control of the main plasma density. Fig 7 shows a cross-section of the general arrangement of the JET vacuum vessel with the divertor coil, the divertor channels and the pumping system. Modified ICRF antennae and lower belt limiter are also indicated. Fig.8 shows an enlargement of the divertor coil.
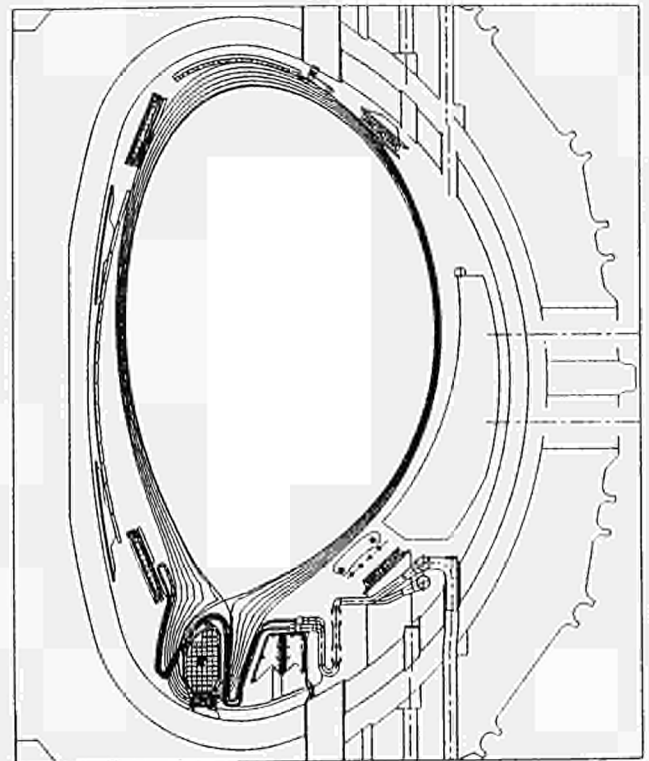

Fig.7: Cross section of JET showing the plasma and the main elements of the proposed pumped divertor.

PHYSICS OF IMPURITY CONTROL

Methods of controlling impurities to be considered and tested on JET during the new phase are either passive or active.

Passive Impurity Control

The objective of passive impurity control is to reduce the production of impurities at source by a proper choice of plasma-facing components. The present line of approach on JET is directed towards low-Z materials such as beryllium or beryllium carbides, but alternative routes may have to be considered and tested.

A simple model has been used to calculate the influx of the main impurity (of charge Z), at the limiter or target plates. Fig.9 sketches the cascaded flux of impurity, ϕ_Z, caused by sputtering of the limiter by a flux of deuterium, ϕ_D. ρ is the fraction of ϕ_Z which
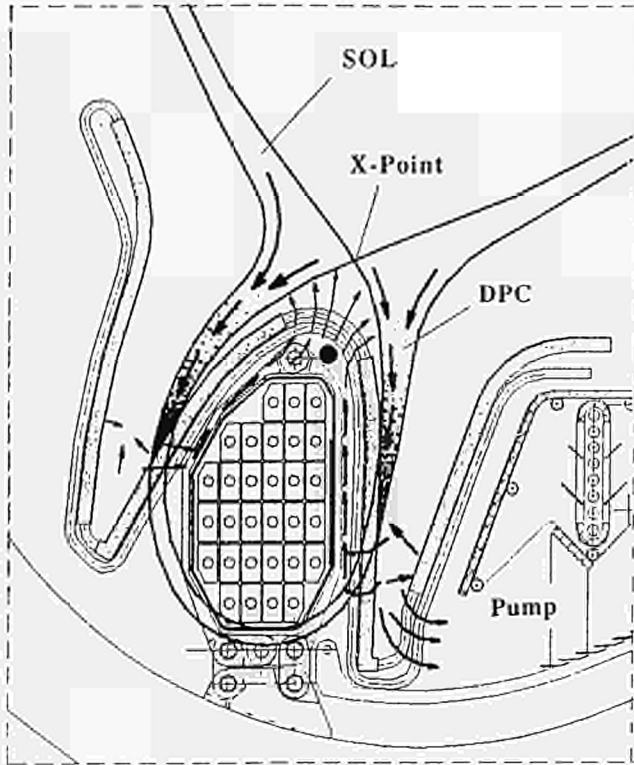
Fig.8: Some details of the divertor coil and of the pump. The large arrows represent the deuterium flow in the scrape off layer (SOL) and in the divertor plasma channel (DPC). The thinner arrows sketch the flow of neutral particles.

returns to the limiter without entering the plasma. Including the possible contribution of an oxygen flux, ϕ_O, the ratio ϕ_Z/ϕ_D in steady state is given by:

$$\frac{\phi_Z}{\phi_D} = \frac{(1-\rho)}{F_{ZZ}}\left[F_{DZ} + \frac{\phi_O}{\phi_D}F_{OZ} + \frac{S}{\phi_D}H_{EV}\right] \quad [1]$$

where S is the equivalent area of the limiter. The functions F_{DZ}, F_{ZZ} and H_{EV} are averaged along the limiter surface from the contact point with the plasma over a distance X and are defined as

$$F_{DZ} = \int_0^1 \frac{Y_{DZ}(E_D,T)}{1-\rho Y_{ZZ}(E_Z,T)}dX$$

$$F_{ZZ} = \int_0^1 \frac{1-Y_{ZZ}(E_Z,T)}{1-\rho Y_{ZZ}(E_Z,T)}dX$$

$$H_{EV} = \int_0^1 \frac{W_Z(T)}{1-\rho Y_{ZZ}(E_Z,T)}dX \quad [2]$$

where Y_{DZ} and Y_{ZZ} are the sputtering yields of the material Z with deuterium and self ions, and $W_Z(T)$ is the evaporation rate of the material Z. F_{OZ} is given by an equation similar to Eq.[2], but using the sputtering yield for oxygen, $Y_{OZ}(E_O,T)$.

Eqs.[1] and [2] show the importance of the self sputtering coefficient Y_{ZZ}. When $Y_{ZZ} = 1/\rho$, the solutions diverge towards a pure carbon plasma. This could be the explanation of the carbon "bloom" observed in high power discharges on JET and TFTR.

Assuming carbon tiles and a parabolic distribution of the temperature along x, the relative carbon flux ϕ_C/ϕ_D is plotted in Fig.10 versus the limiter maximum surface temperature for different values of ρ.
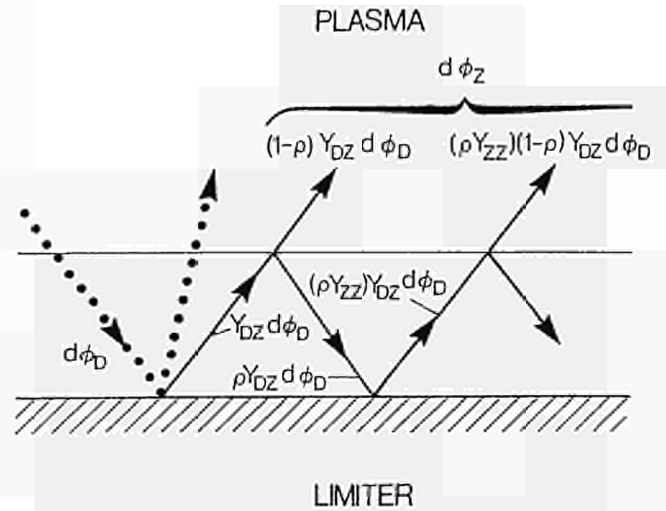
Fig.9: This schematic diagram shows a flux of only one ion species (deuterium), $d\phi_D$, impinging on a limiter made from a material Z. $d\phi_D$ produces by sputtering Z atoms, which are subsequently ionized. The flux of impurity Z, $d\phi_Z$, entering the plasma results from the series of cascades accomplished by the Z ions returning to the limiter and creating other Z atoms by self-sputtering.

The edge electron temperature T_e is assumed to be 60eV. The maximum of ϕ_C/ϕ_D around 600°C reflects the "chemical sputtering" of carbon by deuterium. Recent measurements made on JET by using a carbon probe moved near the plasma boundary are plotted on the same figure. It seems to indicate that the model used with $\rho \approx 0.6$ would describe the observations rather well. Sputtering by oxygen was omitted in the calculation to reflect the experimental conditions performed after Beryllium gettering.

Fig 11 shows the ratio ϕ_{Be}/ϕ_D versus the target plate temperature, calculated when Beryllium is the plate material. No direct experimental data are available as yet, but nevertheless, the Beryllium tiles have been able to tolerate a higher energy load than the carbon tiles.
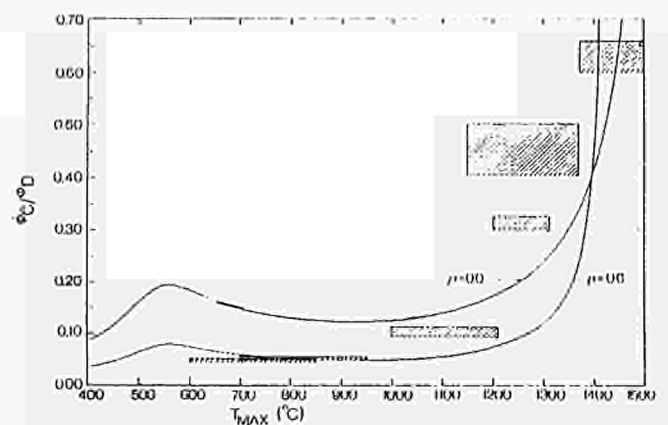

Fig.10: Ratio of carbon to deuterium flux versus maximum target temperature. The curve indicates the result of the simple model described in the text. The shaded boxes indicate the measurements made on JET.
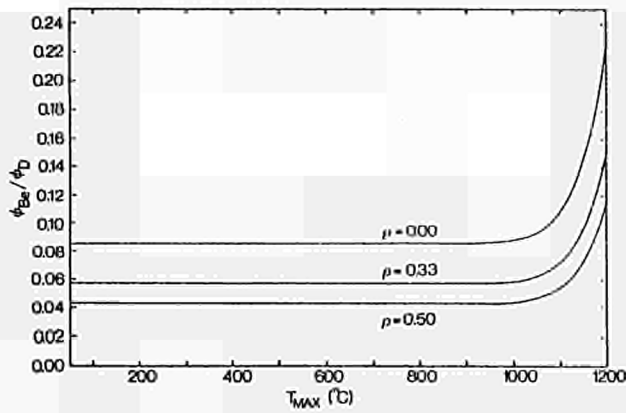
Fig.11: Plot of relative beryllium to deuterium flux against the limiter maximum surface temperature, T_{max}, for three values of ρ. The sharp increase in the flux with temperature is due to evaporation.

Whatever the plates are made of, whether Carbon or Beryllium, the critical parameter is the maximum temperature reached by the tiles. It should not exceed 1100°C to avoid an unacceptable impurity influx. Hot spots resulting from tile misalignments are particularly dangerous. The power load capability will depend strongly on the thermal conductivity of the material used. To be compatible with present values and a safe design should limit the tile temperature to ~800°C. Methods of achieving this are to sweep the X-point and to create a highly radiative zone in front of the target plates.

Active Impurity Control

The objectives of active impurity control are:

    i)   to minimise the impurity content into the plasma;

    ii)   to reduce the heat load on divertor plates to values which can be sustained continuously;

    iii)   to control the plasma density;

    iv)   to exhaust the ashes in a reactor.

Methods of achieving these objectives are, respectively:

    for (i), a strong flow of deuterium in the Divertor Plasma Channel (DPC), to keep the impurities near the target plates;

    for (ii), a sweeping of the intersection of the DPC with the target plates and a high level of impurities of medium or low Z in this area to evacuate the power by radiation;

    for (iii), fuelling of the plasma by pellet, neutral beams or gas and pumping in the DPC;

    for (iv), a moderate flow of deuterium in the scrape-off layer (SOL) and a pump near the target plates.

The plasma behaviour in the SOL and the DPC can be understood qualitatively by considering the basic steady-state equations for the flow F and the pressure p in a 1-D model. x is the coordinate along the magnetic field line and S is the particle source . The equations

$$F_e = F_i = n_e u_e = n,\qquad \frac{dF}{dx} = S$$

impose ambipolarity and particle conservation, when the cross-section of the magnetic flux tube is assumed to be constant, i.e. $\sim 1/|B|$. n is the density and u the directed velocity of the fluid along the x direction. The indices e, h, and z refer to electron, hydrogen and impurity of charge Z, respectively.

The momentum conservation in steady state can be written:

$$-\frac{dp}{dx} = n_h m_h u_h \frac{du_h}{dx} + m_h u_h S_h \qquad [3]$$

in the absence of external forces and assuming $S_Z = 0$; p is the total pressure of the plasma,

$$p = n_h\left(\frac{Z-1}{Z-Z_{eff}}\right)\left(kT_e + kT_h\frac{Z-Z_{eff}+1}{Z}\right)$$

Integrating Eq.[3] leads to

$$p = p_0 - m_h \frac{F^2}{n_h} \qquad [4]$$

p_0 is the plasma pressure in the centre of the SOL, where the particle flux F is zero. Note that $m_h F^2/n_h = M^2 p$, where M is the Mach number.

Fig.12 shows isothermal and isoflows in a plane p, n_h. In this diagram, isothermal cross isoflow curves in two points, one above and one below $p_0/2$, corresponding to subsonic and supersonic flows respectively. For a given plasma temperature T, the maximum isoflow compatible with Eq.[4] is tangent to the isothermal in $p = p_0/2$. That is the prevailing condition at the target plates which represent a sink for the particles. The heat load to be evacuated there is $P_t \sim F_t (E_i + \delta kT)$ where E_i is the energy of ionisation and $\delta \approx 6$ takes into account the sheet potential.

The bold line a-b-c-d-t on Fig.12 shows an idealised trajectory between the plasma separatrix and the target plates. In the first approximation, the plasma temperature does not vary at the X-point where the hydrogen is injected. The diagram shows the compression achieved in the DPC, section c-d, where the particle source term is taken to be zero. The length of this section, and therefore the length of the DPC, must be sufficient and this has consequences on the size of a future device. Higher compression ratio would be obtained by having the point c closer to the transonic regime. However, the risk would be to bifurcate to a supersonic flow, like section e-f, resulting in a decompression in the DPC.

In order to increase the friction, hydrogen-impurity and the radiated power in front of the target plates, a low temperature, high density plasma is needed. This will also limit erosion and therefore increase the lifetime of the target plates. It is worth noting that these conditions result in a rather high plasma density at the separatrix which is unfavourable for non-inductive current drive methods such as neutral beams or Lower Hybrid waves.
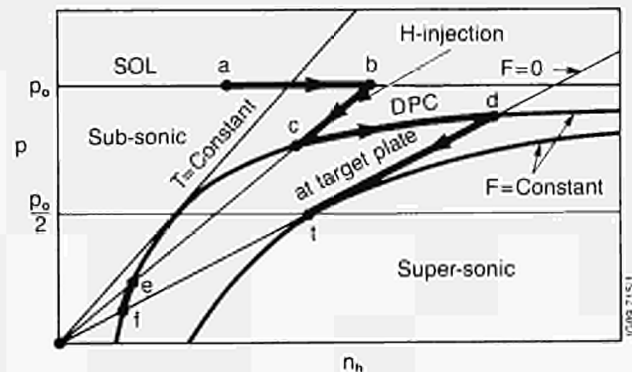

Fig.12: Diagram p, n showing the qualitative space evolution of plasma parameters:
- in the SOL (section a-b where the flow F=0)
- at the X-point (section b-c)
- in the DPC (section c-d where F=constant)
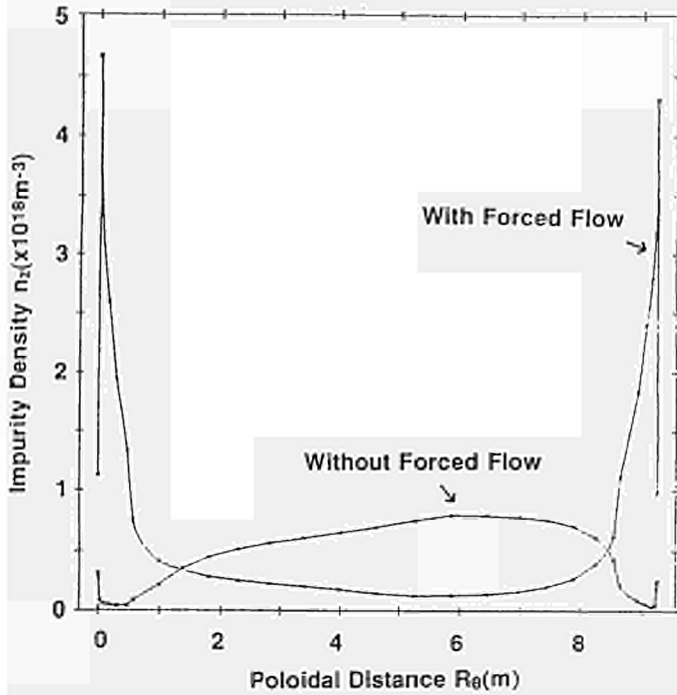- just in front of the target plates (section d-t where the flow becomes transonic)

Fig 13: Spatial distribution of the impurity density along the field lines in the SOL and the DPC. The numerical simulation is made with and without deuterium flow, respectively. The target plates are at R = 0 and R = 9.1m. The SOL extents approximately from R = 0.6m to 8.5m.

A numerical model has been developed to describe quantitatively the plasma behaviour in the SOL and in the DPC. It indicates that a hydrogen flow could stop the flow of impurities toward the X-point in JET. Fig.13 shows the steady state distribution of Beryllium density along the x coordinate with and without hydrogen flow.

ENGINEERING OF THE JET PUMPED DIVERTOR

More detailed descriptions of the system can be found in Ref [4]. Two specific elements are shown in Figs.14 and 15, namely, the target plates and the cryo-pump, respectively.

The present target plates use a two-phase cooling system, water cooled hypervapotrons. They are similar to those used successfully by JET for the high power flux elements of the Neutral Beam Injection system. These are made of copper and are covered by 3 mm. of beryllium, as shown in Fig.14. The Be tiles are designed to leave apertures allowing recirculation of neutrals towards the X-point or their pumping. The angle of incidence with the magnetic field lines will be of several degrees to reduce sensitivity to misalignement, and therefore, reduce the occurrence of "hot spots". The impact position will be swept at 2Hz over ~10cm by modulating the current in the divertor coil by ±200kA-turns. Without radiation from the plasma, the peak load integrated over a cycle should remain <1.5MWm^{-2}.

A cryo-pump solution has been selected because it avoids excessive hydrogen retention and the technology is well known to JET. The water cooled copper shields and the nitrogen cooled baffles should allow the heat load on the LHe-tubes to stay below 1kW in D-D operations. If breakeven is approached during D-T operations, the predominant load for the LHe tubes will be neutron heating and could reach values up to 7 kW. Several seconds in such conditions should still be possible.

All JET systems, including ICRF antennae and diagnostics will be made compatible with the single-null configuration to ensure full coherence of the studies. It should correspond to the geometry used in the tritium phase.
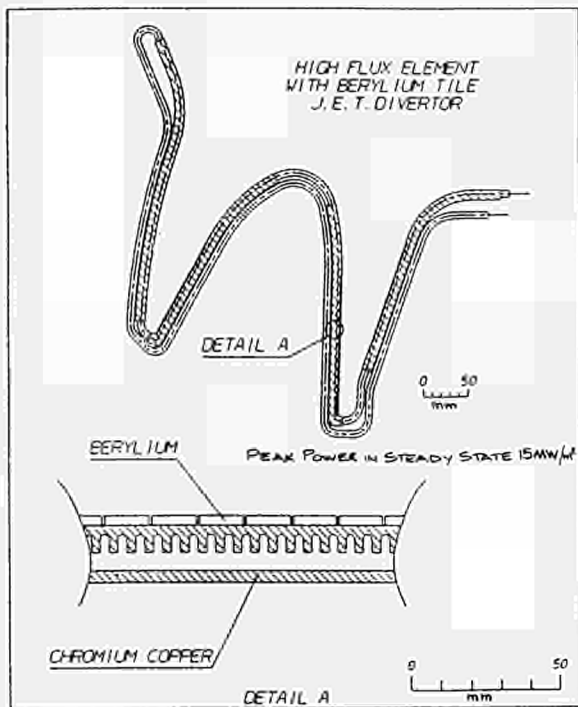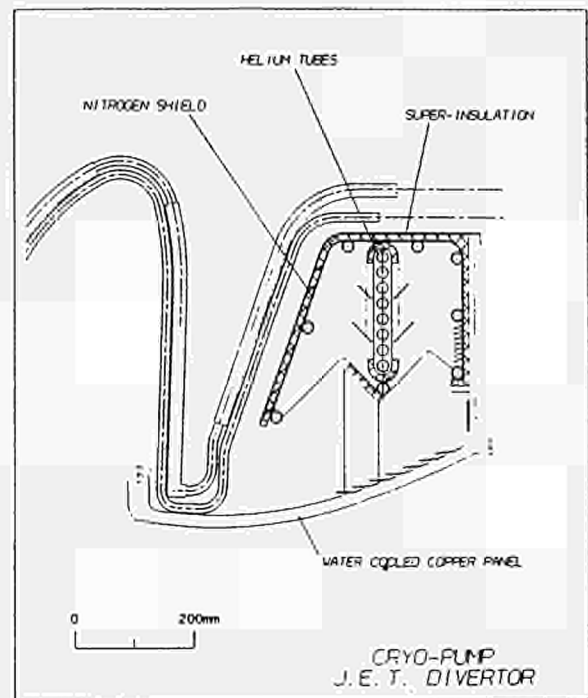

Fig.14: Detail of the target plate of the divertor

Fig.15: Detail of the cryo-pump of the divertor

$I_p = 6MA$: H-mode
$P_{NB} = 15MW$
$P_{RF} = 20MW$

$Q_{DT} = 1$

New Configuration; monster

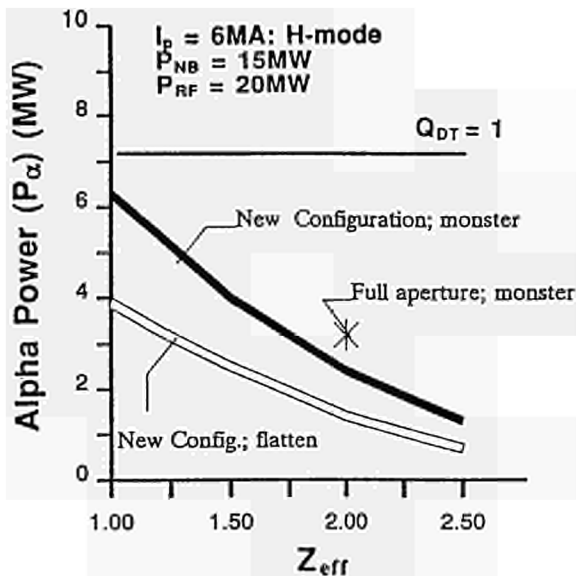Full aperture; monster

New Config.; flatten

Fig 16: Expected JET performance calculated from a 1-D transport code using the critical temperature gradient model for the heat transport. The evolution of the a-particle power is seen versus Z_{eff} in the new configuration with divertor with and without "monster" sawtooth. The single point at $Z_{eff} = 2$ represents the expectation with the presently available plasma cross-section and the transiently achieved impurity content after beryllium evaporation. ($<n_e> = 10^{20}m^{-3}$ with new configuration; $<n_e> = 7.5 \times 10^{19}m^{-3}$ with full aperture; beam plasma reactions are not included)

EXPECTED PERFORMANCE OF JET IN THE TRITIUM PHASE

Performance of JET in D-T operations has been estimated by using a 1-D transport code and assuming the heat transport described by the critical electron temperature model [5]. Fig.16 shows the α-particle power, excluding the beam-plasma contribution, expected as a function of Z_{eff}, for 6MA discharges with 35MW of additional power. The two lines correspond to H-mode with (solid line) or without (hollow line) the existence of a monster sawteeth in the pumped divertor configuration. The single cross corresponds to an H-mode with the present JET plasma cross-section at $Z_{eff} = 2$. This value of Z_{eff} has been made possible, at least transiently, by the use of Beryllium gettering. With efficient impurity control and Z_{eff} approaching close to 1, a factor greater than 2 could be gained on the expectation of the present JET configuration and breakeven could be approached.

In summarizing the JET performance in the pumped divertor configuration, the capability of JET should allow:

- 6MA single-null X-point configuration for up to 10s with an axisymmetric pumped divertor in the bottom of the vacuum vessel.
- 3MA double-null X-point operation could also be performed up to 20s at a magnetic field of 3.4T;
- an increase, by more than a factor 2 of the expected α-particle power.

TENTATIVE SCHEDULE

A schedule for the JET programme incorporating the new phase is shown in Table III. It can be seen that the earliest date to have a pump limiter in JET is 1992. Further optimization would likely be necessary about 18 months later, in the light of experimental results.

To provide time for the new phase, the use of tritium in JET should be postponed until the end of 1994. At this stage, all the information on particle transport, exhaust and fuelling, first wall requirements and enhanced confinement regimes needed to construct the next step Tokamak, should be available. Final tests with tritium, including the α-particle heating studies could be performed in the two years following, leading to the completion of the JET programme by the end of 1996. During the tritium phase and even later, tests on prototype elements for the next step could be undertaken on the JET site, using the test facilities, tritium plant and power supplies.

CONDITIONS TO CONTROL IMPURITIES IN A REACTOR

The conditions to be fulfilled in a reactor should be, as follows:

- the effective charge Z_{eff} of the plasma must stay below 2. This implies the use of a low-Z material for the target plates. Recent experiments in JET have shown that beryllium appears to be a good candidate;

- the target plates must stay at a sufficiently low temperature ($< 800°C$) to limit the sputtering or the evaporation of first-wall material. This requires lowering the mean power density on the target plates. Therefore, sweeping the target plate by 1 - 2m, by moving the X-point at several Hz is a probable solution. The angle of incidence of the magnetic field lines should not be too low in order to reduce the sensitivity to "hot spots";

- the plasma close to the target plates must be at low temperature and high density to limit erosion of the tiles and to increase the radiated power. Typical figures would be $n = 1-2 \times 10^{20}m^{-3}$ and $T = 10eV$. The corresponding density in the scrape off layer is $3-5 \times 10^{19}m^{-3}$. This is unfavourable for non-inductive plasma current drive schemes such as neutral beams or Lower Hybrid waves;

- the volume of the plasma in the divertor channel must be large enough to radiate a good fraction of the α-particle power. This impacts on the size of a reactor.

Once achieved, the previous conditions should ensure an acceptable lifetime of the target plates. The problem of removing the helium ash concentration into the plasma needs still to be solved. This requires a better than present prediction of the particle transport across the plasma. A satisfactory model of particle transport does not yet exist.

With efficient impurity and plasma density controls, ignition should occur in a tokamak equipped with an axi-symmetric pumped divertor similar to the one described in Ref.[6], ie. with the following basic parameters: $I_p = 25-30MA$, $B_T = 5T$, $R_0 = 7.5m$, $a = 3m$ and $b/a = 2$. The thermal power of such a device should be controlled between 1-4GW, depending on operating density.
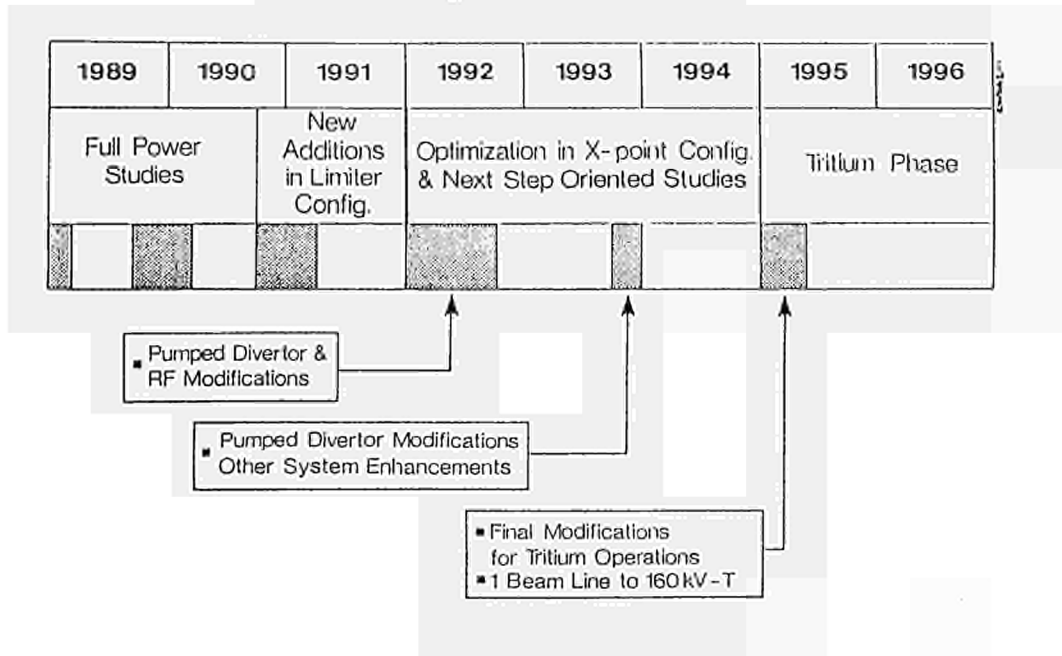
CONCLUSIONS

In summary, the paper sets out the main points, as follows:

- JET has successfully achieved and contained plasmas of thermonuclear grade. Individually, parameters required for a fusion reactor have been achieved, and simultaneously, the fusion product ($n_D T_i \tau_E$) is within a factor ~10-15 of that required in a fusion reactor;

- Latest JET results (using Beryllium in place of Carbon) show:

  - fusion product ($n_D T_i \tau_E$) of $5 \times 10^{20}m^{-3}skeV$ has been obtained for both medium (~9keV) and high (~20keV) temperatures;
  - neutron yield has doubled to $~2 \times 10^{16}ns^{-1}$, which is equivalent to $Q_{DT} \sim 0.5$;

However, these values were in a transient state and could not be sustained in the steady state;

Table III: JET Programme in the New Phase

1989	1990	1991	1992	1993	1994	1995	1996
Full Power Studies		New Additions in Limiter Config.	Optimization in X-point Config. & Next Step Oriented Studies			Tritium Phase	

- Pumped Divertor & RF Modifications
- Pumped Divertor Modifications
  Other System Enhancements
- Final Modifications for Tritium Operations
- 1 Beam Line to 160 kV–T

- the Next Step Tokamak aims to sustain an ignited plasma for periods up to one hour. Therefore, control of impurities, fuelling and exhaust of helium ashes are essential for maintaining ignition;

- techniques of achieving these requirements in **steady-state operation** must be tested prior to construction of a Next Step;

- a new phase is proposed for JET with an axi-symmetric pumped divertor configuration to address these problems in operational conditions close to those of a Next Step Tokamak with a stationary plasma (10s - 1minute) of thermonuclear grade;

- in this new configuration, JET should be able to:

  - demonstrate a concept of impurity control;
  - determine the geometry needed for this concept in the Next Step;
  - allow a choice of material for plasma facing components for the Next Step;
  - demonstrate the operational domain for the Next Step.

- with an efficient axi-symmetric pumped divertor, ignition should occur in a Tokamak reactor with parameters:

$$I_p = 25\text{-}30MA, \quad B_T = 5T, \quad R = 7.5m, \quad a = 3m, \quad \varepsilon = 2,$$

and $P_{out}(th) = 1\text{-}4GW$ (depending on density)

REFERENCES

[1] The JET Project - Design Proposal: EUR-JET-R5;

[2] Rebut, P.H., et al, Fusion Technology, 11, (1987), 13-281;

[3] Latest JET Results and Future Prospects, the JET Team, Proc. of 12th Int. Conf. on Plasma Phys. and Contr. Nucl. Fus. Res., (Nice, France, 1988) (to be published in Nuclear Fusion Supplement);

[4] Technical Status of JET and Future Prospects by The JET Team, Proc. of the 13th Symposium on Fusion Engineering, (Knoxville, USA, 1989), to be published;

[5] Rebut, P.H., Lallia,P.P., and Watkins, M.L.,The Critical Temperature Model of Plasma Transport: Applications to JET and Future Tokamaks,Proc. of 12th Int. Conf. on Plasma Phys. and Contr. Nucl. Fus. Res., (Nice, France, 1988) (to be published in Nuclear Fusion Supplement);

[6] Rebut, P.H., Implications of Fusion Results for a Reactor, Proc. of 12th Int. Conf. on Plasma Phys. and Contr. Nucl. Fus. Res., (Nice, France, 1988) (to be published in Nuclear Fusion Supplement);

TECHNICAL STATUS OF JET AND FUTURE PROSPECTS

THE JET TEAM

Presented by M. Huguet and E. Bertolini
JET Joint Undertaking, Abingdon, Oxon, U.K.

ABSTRACT

A description of the technical status of the JET machine and essential systems during the 1989 experimental campaign is given first. The vacuum vessel has been mechanically reinforced and is now able to resist safely the large disruption forces at plasma currents up to 7 MA. An electrical fault has developed in one of the toroidal field coils and although operation is continuing, coil replacement is planned to take place by the end of 1989. The use of a beryllium first wall has been the salient feature of 1989 operation and the technological and safety aspects of operation with beryllium are reviewed.

In the second part the motivation is explained for a new orientation of the JET development programme with the aim of studying the problem of impurity control. To this end, it is proposed to operate JET in a divertor configuration. Technological aspects of the pumped divertor operation are reviewed and a brief technical description of the major components is given.

I. INTRODUCTION

JET is the central and largest experiment of the fusion programme of the European Community. JET was established with the aim of extending the plasma parameters to values close to those required in a fusion reactor and to operate with deterium-tritium (D-T) mixtures for the study of the production and confinement of α-particles and their heating effect on the plasma. JET operation started in 1983 and in 1985 reached its full design rated value of the plasma current, ie. 5 MA. The physics results established JET at the forefront of fusion research but indicated that the degradation of energy confinement with increasing heating power was an important limitation to JET performance [1].

At this stage a major engineering effort, the so called "7 MA Study" was initiated with the aim of assessing the technological limits of the machine and its power supplies and, as a result, extending the operational domain and, in particular, the plasma current well beyond the original design values [2]. The main findings of this study have already been reported [3, 4, 5]. It was found that the electromagnetic system, ie, coils, mechanical structure and power supplies, would allow operation at plasma current in excess of 7 MA in the limiter (material limiter) and X-point (magnetic limiter) configurations.
It was also found that the main technological limitation was associated with the forces acting on the vacuum vessel during radial disruptions and vertical instabilities of the plasma. Since radial disruptions tend to be frequent, specially when new operation domains near the physics limits (density limit, low q limit) are being explored, it was decided that mechanical reinforcements of the vacuum vessel were necessary to better contain disruption forces [4]. These mechanical reinforcements are described in the section "Status of systems during the 1989 experimental campaign".

Operation in 1988 was very successful. Achievements included operation up to 7 MA plasma current, routine H-mode operation at 5 MA, total heating power to the plasma up to 34 MW, and a record value of the fusion product $(\hat{n}_i . \tau_E . \hat{T}_i)$ of $2.5 \times 10^{20} \mathrm{m}^{-3}.\mathrm{s}.\mathrm{keV}$.

II. STATUS OF SYSTEMS DURING THE 1989 EXPERIMENTAL CAMPAIGN

Vacuum Vessel and First Wall

One of the major findings of the 7 MA study, which was also supported by experimental data, was that radial plasma disruptions result in large deflections of the inboard portion of the vacuum vessel wall. A disruption at a plasma current of 6 MA deflects the wall by 10 mm and this in turn initiates large amplitude ($\sim$ 6-10 mm) radial oscillations of the vertical ports of the vessel. The mechanical analysis revealed that in this case the yield limit of the vessel material (Inconel 600) is exceeded over a significant area at the base of the port, and structural failure could be expected after only a few thousand disruptions at plasma currents in excess of 6 MA.
It was decided to reinforce the vacuum vessel by means of toroidal rings welded onto the inside surface of the inboard wall of the vessel. These rings have been installed during a shutdown from October 1988 to March 1989 and are shown in Figure 1 [7].
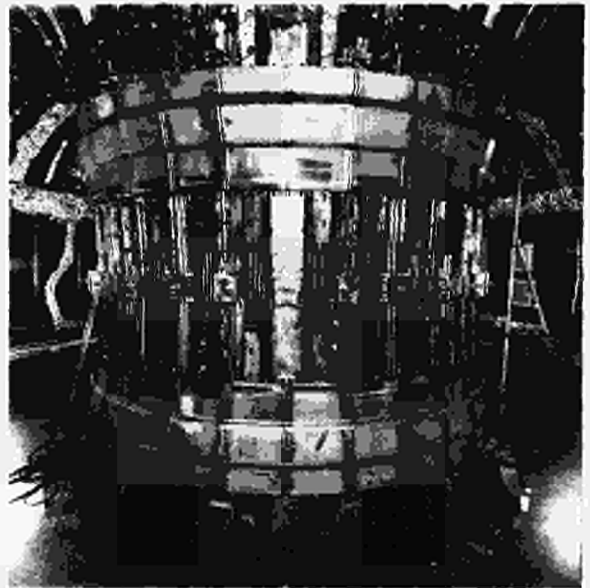

Fig:1 Reinforcing rings welded on the inboard wall of the vessel.

There are two rings, one above and one below the equatorial plane. Each ring is 800 mm high and 12 mm thick and is made up of 32 trapezoidal inconel plates welded together. During a plasma disruption at 7 MA, each ring is compressed by a hoop force of 7000 kN giving a compressive stress of 90 MPa. For this reason, the plates have been shaped so as to increase the buckling strength of the complete ring. The plates are not attached directly to the vessel wall but are

welded onto short inconel pedestals which are them-
selves welded on the rigid sectors of the vessel. With
this arrangement, the electrical resistance of the
rings is fairly high and toroidal eddy currents flowing
in the rings are only 30% of the eddy currents flowing
in the main body of the whole vacuum vessel.
Experience has shown that plasma formation is not
affected by the reinforcing rings.

Following the installation of the reinforcing rings,
the inboard wall has been covered with graphite protec-
tion tiles (Figure 2). Carbon fibre reinforced (CFR)
tiles were already successfully used in 1988 [3] and
more tiles of this type have now been fitted at the
inboard wall. The tiles are also better aligned than
before and they can act as an inboard bumper limiter at
full power.

Figure 2 shows a discontinuity in the wall protection
tiles just above and below the reinforcing rings. This
is due to the fact that the internal saddle coils for
the stabilisation of plasma disruptions [7] have not
been installed yet. Installation of these coils is
planned for 1990.
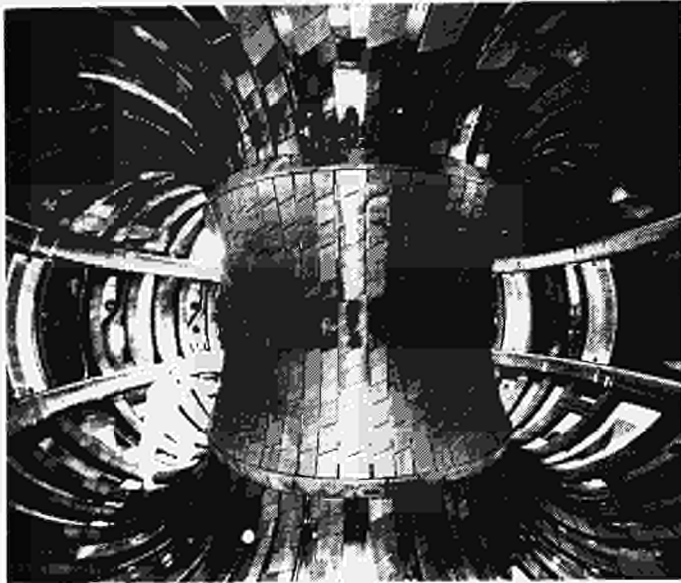
Fig 2: Vessel configuration in 1989

For X-point operation, the wall protection at the top
part of the vessel is provided by CFR tiles which have
been carefully shaped and aligned. In 1989 the energy
deposition on the X-point tiles (single null configura-
tion) has been limited to 30MJ per pulse with X-point
sweeping and 20 MJ per pulse for a stationary X-point.

In the limiter configuration, the plasma leans against
the two outboard belts of the belt limiter. This
limiter, with a power handling capacity of 40 MW for 10
seconds, has been unchanged since its installation in
1986 [8]. In September 1989 however, the graphite
tiles of the limiter have been replaced with beryllium
tiles.

There was no change in 1989 to the eight ion cyclotron
resonance heating (ICRH) antennae except that water
cooling of the electrostatic screens had to be
abandoned due to thermal stress problems resulting in
internal water leaks.

As already mentioned, the salient feature of 1989
operation has been the use of beryllium as a first wall
material. For initial beryllium operation, the first
wall design was unchanged, in particular the graphite
tiles were still used for the belt limiter, ICRH
antennae and wall protections, but all surfaces,
including graphite tiles as well as inconel walls and
nickel electrostatic screens of the ICRH antennae, were

coated with a thin layer of beryllium.

Beryllium coating was achieved by means of 4 beryllium
evaporators located at the outboard wall near the
equatorial plane and equally spaced along the toroidal
direction. The evaporators consist basically of an
electrically heated carbon fibre reinforced graphite
resistance which is covered by a bell-shaped beryllium
head. During plasma operation the beryllium heads are
retracted inside their ports, out of reach of the
plasma. For evaporation, the heads are pushed inside
the vessel and heated up to a temperature close to
1100°C. The evaporation rate was found to decrease
after a few hours of operation but then stabilised at a
value in the range of 0.6g per hour per head giving an
average deposition on the vessel walls of 7.0×10^{-9}
m/hour. The life expectancy of the head is 200-300
hours. Operation of the evaporators has been generally
satisfactory although problems due to the mechanical
stability of the graphite heater and the beryllium head
at high temperatures, differential expansion between
graphite and beryllium, and sintering between graphite
and beryllium, have been identified and will result in
minor design changes [9].

For beryllium operation, evaporation sessions of 1 to 5
hours have been used. Since it was found that the
beneficial effect of the beryllium coat tends to wear
out during operation, evaporation has been repeated
overnight typically every two or three days. The total
amount of beryllium evaporated in June-July 1989 has
been about 240g.

Magnet systems

In May 1989, a fault was detected by the fault detec-
tion of the toroidal field (TF) magnet. Upon investig-
ation it was found that one coil exhibited low turn to
turn insulation resistance between a number of turns.
Further examination using an endoscope revealed that
the ground insulation was cracked at one point near
internal brazed joints and dripping marks where seen
originating from this crack. Analysis of the dripping
marks indicated that copper carbonate was present thus
confirming that an internal water leak had occurred.
At this stage, the nature of the fault is not fully
understood since two groups of turns (numbers 11-16 and
20-21) show a low turn-to-turn insulation resistance
but the turns in between are healthy.

On the JET TF coils, each turn is electrically access-
ible through the water inlet and outlet channels.
Careful DC resistance measurements have revealed that
the turn-to-turn electrical faults are located about
halfway along turns, ie, far away (about 6 metres) from
the water inlet/outlet channels where all the internal
brazed joints are located. There is therefore no clear
correlation between the electrical fault and the
evidence of a water leak.

It should also be noted that the faults have all
developed in what is electrically the first pancake of
the first coil and therefore a failure due to a fast
voltage transient transmitted by the busbars cannot be
excluded.

Operation at full field has nevertheless continued with
this fault, keeping the coil under close scrutiny.

The faulty coil has of course to be replaced with one
of the four spare coils available. This is a major
operation which involves the removal of one octant of
the machine and this intervention is now planned to
take place before the end of 1989 during a planned
shutdown for the installation of the beryllium screens
for the ICRH antennae and the new lower hybrid
launcher.

The ohmic heating (primary) coil stack has been
affected by a problem of coil rotation which was dis-
covered in 1986. The individual sub-coils making up
the stack are rotated around their axis by the twist of
the mechanical structure during plasma pulses.

Friction forces prevent the sub-coils from returning precisely to their initial position and so pulse after pulse this ratcheting effect gives rise to large (several mm) rotational displacements. A first attempt at solving this problem was made in 1987. Interlocking keys were machined at the interfaces between sub-coils and these keys were fitted with springs to restore the sub-coils position after each pulse. This did not fully cure the problem due to the large friction between the coil surfaces. Also relative rotation between the sub-coils proper and their inner support steel rings was observed. Additional modifications including the installation of low friction layers between sub-coils and interlocking keys between sub-coils and inner rings were carried out by the end of 1988. No further rotation of the ohmic heating coil stack has been observed during the 1989 experimental campaign.

In 1989 the ohmic heating coil stack has been operated routinely in the configuration investigated by the "7 MA Study", ie, with a current of 60 kA (original design value of 40 kA) in the six centre coils [5].

Magnet power supplies

There was no change to the configuration of the magnet power supplies compared to that used in 1988 [3] except for the installation of the final booster amplifier in the circuit of the vertical equilibrium field. This new supply was commissioned in March 1989 and has since allowed much improved control of the radial position of the plasma during the early phase of the discharge.

Brief review of fuelling and heating systems

The pellet injector provided by Oak Ridge National Laboratory USA under a JET-US DOE Collaboration Agreement, has continued to contribute significantly to physics results. The injector can delivery 2.6, 4 and 6 mm pellets at a velocity of 1-1.5km/s and with a repetition rate between 5 and 1 Hz [10].

The neutral beam injection system includes two boxes each with 8 injectors. One of the boxes contains 8 x 80 kV, 40A injectors while the other box contains 6 x 80 kV, 40A injectors and 2 x 140 kV, 30A injectors. The 140 kV injectors were previously operated at 80 kV but have been converted to 140 kV operation by replacing the four grid extraction system of the ion sources by a three grid system [11]. The high voltage power supplies have also been upgraded to provide 140 kV [12]. It is planned to convert the eight injectors of one box to 140 kV.

A major improvement to the ICRH (ion cyclotron resonance heating) system, has been the successful operation of the real time automatic tuning system which allows fast changes in the plasma parameters to be followed and in particular transitions from L to H-modes [13]. The maximum ICRH power coupled has reached 18 MW. It is planned to replace the nickel electrostatic screens of the eight antennae by beryllium screens towards the end of 1989.

Beryllium handling

The use of beryllium as a first-wall material has required a major effort in the development of safe handling techniques.

Personnel access to the inside of the vacuum vessel during shutdowns is provided through a specially built Torus Access Cabin (TAC) which includes a stainless steel washable cabin docked onto one of the access port to the vessel (Figure 3). Depending on the contamination level, personnel wear respiratory protection for work inside the vessel. During a shutdown in July-August 1989, the beryllium contamination in air inside the vessel was found to be between 15 and 50 $\mu g/m^3$ ie, well above the statutory limit for respiratory protection (2 $\mu g/m^3$). Work was carried out using full protective suits with an external air supply. The

Torus Access Cabin also features a decontamination shower, a filtered ventilation system and a liquid waste handling system [14].
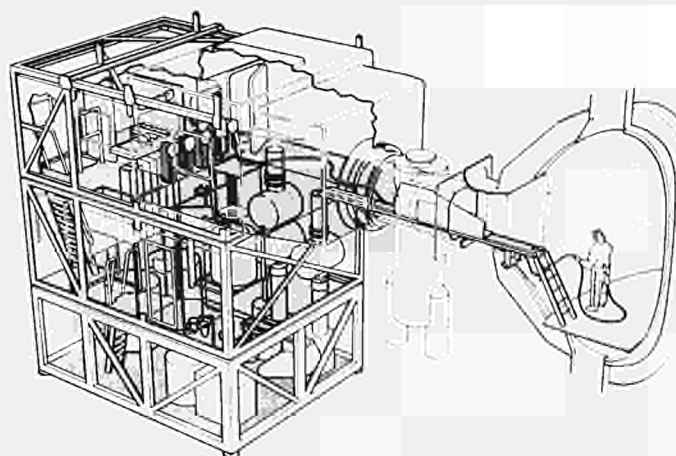

Fig 3: Torus Access Cabin for beryllium interventions.

Many interventions require an opening of the vacuum vessel, but no access inside the vessel. For such interventions JET has developed bagging techniques which ensure that no beryllium dust is spread outside the vessel.

In addition to facilities for work in the vessel, there is also a need for a work area for beryllium components or beryllium contaminated components or equipment. Such a work area has been built in the JET Assembly Hall. The area (10 x 8m³) is fully contained with a filtered ventilation system and is provided with decontamination equipment such as fume hoods and ultrasonic baths. In 1989 the facility has been extensively used for the preparation and cleaning of beryllium tiles before assembly in the machine and also for the cleaning of the air suits before reuse.

One of the difficulties of beryllium handling is the lack of on-line monitoring systems. Beryllium in air or on surfaces is measured by the Atomic Absorption Spectrometric technique, which involves the collection of beryllium on filter paper, the dissolution in acid of filter paper and then the spectral analysis of the solution. Due to the large number of smear samples to be analysed, the turn over time can be long (12 or 24 hours in June-July at JET) and this can seriously impede work progress.

Working with beryllium has also made it necessary to generate a large number of written procedures covering the various types of beryllium interventions. Such procedures include also a "Safety Assessment" which gives a full description of the hazards involved and the precautions to be followed.

The JET experience with beryllium is still too recent to draw general conclusions on the technical and logistics problems associated with the use of beryllium. It was found that work in the beryllium contaminated vessel took about twice as long as the same work in the clean vessel. This was due to restrictions on the number of people able to work simultaneously with full protective suits. The logistics effort required to support work in two shifts is considerable, the major problems being associated with the monitoring of the contamination on components, tools, air suits and with decontamination work.

III. OVERVIEW OF THE JET PROGRAMME: EMERGENCE AND DEFINITION OF A NEW OBJECTIVE

The approved JET experimental programme runs up to the end of 1992 and includes from 1989 to 1991 a phase of full power optimisation studies before the tritium phase in 1992.

The full power optimisation studies feature many new developments or systems to enhance JET performance before operation with deuterium and tritium (D-T operation). These new systems are summarised in Table 1

TABLE I
The Approved JET Programme

Date	Systems coming into operation
1989	Beryllium belt limiter Neutral beam injectors modified to 140 kV(D) (one (NB) of 8 injectors only)
1990	Beryllium antennae screens Prototype lower hybrid system Prototype high speed pellet injector (>3km/s)
1991	Tritium plant (not connected to Torus) Cooled X-point dump plates Internal saddle coils Full power lower hybrid system Multiple high speed pellet injector NB injectors modified to 140 kV(D)
1992	One NB injector box modified to 160 kV(T) (other box 140 kV(D) Tritium plant and remote handling system Tritium operation
End 1992	End of JET experimental programme

The initial success of operation with beryllium as a first wall material indicates that all future JET operation will continue to use beryllium. The belt limiter has been fitted with beryllium tiles in August 1989 and it planned to replace the nickel electrostatic screens of the ICRH antennae by beryllium screens early in 1990.

Other systems shown on Table I include water cooled dump plates for operation in the X-point configuration and internal saddle coils for the stabilisation of plasma disruptions. A high speed (5 km/s) pellet injector is also foreseen for deeper fuelling of the dense hot plasmas together with a lower hybrid current drive system for profile control and stabilisation of sawteeth. Neutral beam systems are to be upgraded to 140 kV for deuterium injection and then one of the two systems will be modified to 160 kV for tritium injection.

The main objective of the programme shown in Table I is the optimisation and enhancement of plasma parameters to maximise the α-particle production, or the Q-factor, during the deuterium-tritium phase of operation. This programme rationale has been very successful so far and has had a profound impact on the design of the ignition devices of the next step such as NET or ITER. It is indeed one of the main achievements of JET that confinement parameters can now be extrapolated to larger devices and that the main design parameters, in particular the size and plasma current of the next step machines, can be confidently chosen so that ignition can be achieved with a reasonable safety margin.

Although confinement parameter are better understood, there is a growing realisation that the problem of impurities, with its associated energy losses and fuel dilution effect, is one of the main outstanding and

unsolved problem on the way towards a fusion reactor. In most JET discharges, the fuel dilution (defined as the ratio of the deuterium density to electronic density) is below 0.5 and values closer to 1 have only been achieved in transient conditions with pellet fuelled discharges [15]. The dramatic improvement of plasma performance with beryllium has illustrated the importance of impurities but new concepts are now required for impurity control during high power stationary plasma discharges.

The next step devices are large divertor devices, about twice the linear size of JET, and operating for long pulses (a few 100s to a few 1000s) at a plasma power in the GW range. The design of the divertor of these machines is a formidable task for which there is insufficient data at present. In particular, the problem of the erosion of the target plates of the divertor and how to control the back flow of impurities generated at the target plate towards the main plasma, has no solution at present.

The need to optimise JET's performance therefore coincides with that of testing an impurity control system relevant for the next step devices. For this reason a new objective has been proposed for JET as follows:

"To demonstrate an effective method of impurity and particle control in enhanced confinement regimes, in the operating domain for the next step with a stationary plasma of thermonuclear grade".

The underlying physics concepts of the pumped divertor are described by Rebut [6] so only a brief qualitative description is given in this paper.

This ambitious objective is proposed to be achieved on JET by means of an axisymmetric divertor configuration. This proposal is based on present experience at JET with X-point operation and on experience with divertor operation on the Asdex machine at Garching, FRG. The proposal is further justified by the fact that the next step designs all use an axisymmetric divertor configuration.

IV. THE PROPOSED JET PUMPED DIVERTOR

The key concept of the proposed JET pumped divertor is that since sputtering of impurities cannot be suppressed at the target plate of a divertor, those impurities should be confined in the vicinity of the target plate itself. This confinement can be achieved by maintaining a strong directed flow of plasma particles along the divertor channel towards the target plates, to prevent back diffusion of impurities by the action of a frictional force. A most important feature of the configuration is the connection length, along the magnetic field lines, between the X-point region and the target plates. This distance should be long (of the order of 10 metres) in order to achieve an effective screening effect of the impurities. In other words, the X-point should be well separated from the target plates and in JET this can only be achieved by a coil which is internal to the vessel. The proposed configuration shown in Figure 4 consists of a single additional poloidal field coil, inside the vessel, at the bottom.

The formation of a target plasma in the divertor channels is another essential feature of the pumped divertor. The cold (radiatively cooled) and dense plasma, which is expected to form in front of the target plates, plays a number of key roles:

   a)   It should radiate a significant fraction of the plasma input power thus reducing the heat load on the target plates.

b) It should reduce the pumpurity production by screening the target plates.

c) It should reduce the probability of the impurities diffusing back to the plasma.
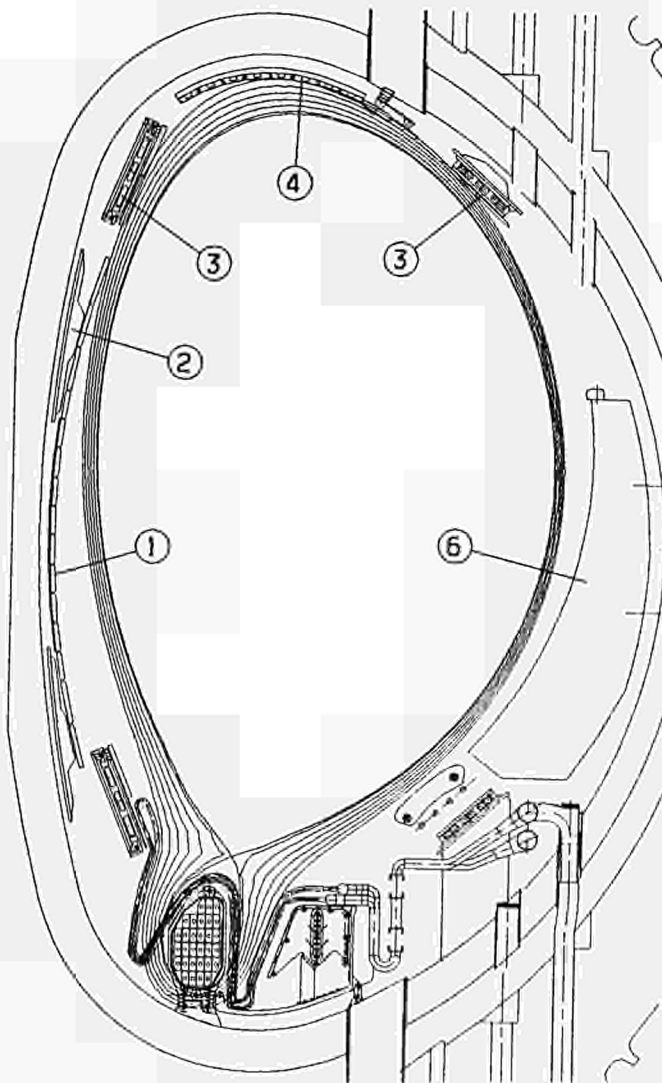
Figure 4: Overall configuration and magnetic field lines. 1. Protection tiles, 2. Reinforcing rings, 3. Saddle coils, 4. X-point dump plate, 6. ICRH antenna.

In the vicinity of the outer target plate, a pumping chamber with a cryogenic pumping system is foreseen to allow the control of the main plasma density. It should be noted that only a small fraction ($\sim$5%) of the hydrogenic neutrals generated at the target plate are expected to be pumped. Some of these neutrals will be able to recycle towards the X-point region (there is a gap between the coil casing and the water cooled elements which define the divertor channel), re-enter the scrape-off plasma there and enhance the plasma flow to the target plate. This local recirculation of hydrogenic particles should improve the impurity confinement. If required, gas can also be injected near the X-point to further increase the particle flow in the divertor channels.

Brief technical description

Figure 4 shows a typical single-null configuration obtained at a plasma current of 6 MA and a divertor coil current of 800 kA.turn. The configuration fills the vessel volume well while keeping clear of all the

internal vessel features by at least three scrape-off e-folding lenths. The connection length along magnetic field lines between the X-point and the target plate has been calculated to be $\sim$10 metres and preliminary calculations indicate that this is sufficient to screen impurities.
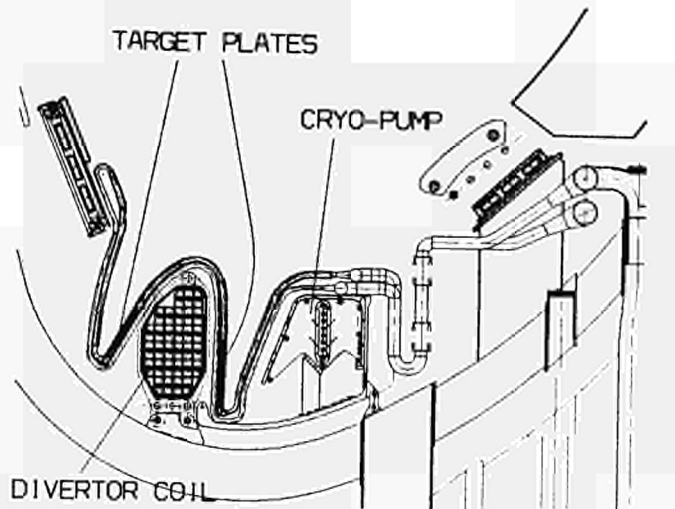
Figure 5: Main components of the pumped divertor.

The divertor coil is a conventional copper, water cooled coil with 29 turns and able to carry 1 MA.turn during 20 seconds. The coil is to be wound inside the vacuum vessel. It is enclosed in a thin (3mm thick) stainless steel casing which will also be used during manufacture for vacuum impregnation with epoxy resin. Magnetic forces on the coil could reach 600-900 tonnes and are restrained by hinged supports which allow differential expansion between the coil and the vacuum vessel.

The divertor channels boundaries consist of water cooled copper elements clad with a 3mm thick beryllium layer. They protect the coil and the cryopump from the power radiated by the target plasma. The elements are detached from the coil to leave a gap behind them through which neutrals generated at the target plate can recycle towards the X-point.

Although the target plates are expected to be shielded by the target plasma they are being designed with the capability to dissipate a large fraction of the plasma input power (40 MW) in stationary conditions. The present design uses water cooled hypervapotrons similar to those used at JET for the high heat flux elements of the JET Neutral Beam systems [16]. Hypervapotrons can easily cope with a power densities of 10 MW/m² and it is estimated that the divertor target plates could cope with a power of 30 MW in steady conditions. This esti-mate includes the benefit expected from sweeping the impact line by about 6-8 cm. Sweeping is easily achieved by a modulation of the divertor coil current between 750 kA and 1 MA. The surfaces facing the plasma will be clad with 3mm thick beryllium plates brazed onto the hypervapotron. The choice of beryllium is not ideal since beryllium impurities will not radiate sufficient power, however the choice of an alternative material could lead to migration of this material onto beryllium tiles elsewhere in the vacuum vessel and ultimately jeopardize the benefits from using beryllium.

For the pumping system, a cryopump has been selected because it avoids problems with hydrogen retention and its technology is well known to JET. The pump includes

an external water cooled copper shield, inner liquid nitrogen cooled baffles and liquid helium (LHe) cooled pumping pipes. During plasma pulses, the heat load on the LHe cooled pipes is due to particles and radiation from the target plasma in the divertor channels, whereby the latter predominates. In case the total input power to the plasma of 40 MW is radiated by the target plasma, then the radiative heat load on the LHe cooled pipes could reach 1 kW. The most severe load however is due to the neutrons and gamma rays expected during deuterium-tritium operation. In the case of operation at $Q \sim 1$ with a neutron production rate of 10^{19}/s a power in excess of 5 kW will be absorbed by the liquid helium and the stainless steel conduits. This has led to a design with thin walled conduits and a large liquid helium inventory. Aluminium conduits rather than stainless steel would of course reduce the nuclear heating but the eddy currents and associated mechanical forces become prohibitive. It is expected that sub cooling of the LHe before a pulse together with partial boiling during the pulse, will allow several 3 to 5 seconds of operation at Q=1.

Most neutrals produced at the target plate will be re-ionised before reaching the entrance of the cryopump and therefore only afew per cent ($\sim 5\%$) will be pumped. This is sufficient to provide a pumping rate of a few times 10^{21}/s which is adequate for density control of the main plasma.

V.CONCLUSIONS

The study of plasma-wall interactions and the control of impurities has been stated as a major objective of the JET project since the very beginning of the design phase, and has also been one of the main motives throughout its experimental programme. Effort has so far concentrated on the development of passive systems such as low Z materials, initially graphite and now beryllium, for the first wall.

There is now a need to step up effort in the area of impurity control, not only to improve JET performance, but also to test an impurity control system relevant for the next step ignition machines. It is proposed that an axisymmetric divertor as envisaged for the NET and ITER designs should be tested on JET.

The construction and operation of a pumped divertor is a major addition to the JET programme and requires a substantial extension to the JET experimental phase. The new proposed timetable foresees that operation with the new divertor configuration would start in 1992 and would go on with deuterium until 1994. Tritium would be introduced in 1994 and the JET experimental programme would be complete by the end of 1996.

The proposed JET pumped divertor includes novel features of active impurity and particle control and will be tested with a quasi stationary plasma of thermonuclear grade. The divertor should therefore provide an indispensable data base for the design of the divertors of the next generation of machines.

REFERENCES:
[1] P. H. Rebut and the JET team, JET latest results and future prospects. Proceedings of the 11th Conference on Plasma Physics and Controlled Nuclear Fusion, Vol. 1, p.31-49, (Kyoto, Japan November 1986)

[2] E. Bertolini, M. Huguet and the JET team, JET project Technical development dictated by the recent scientific results and prospects of extensive D-T plasma studies in break-even conditions. Proceedings of the 12th Symposium on Fusion Engineering, Vol 2. p.978. (Monterey, USA. October 1987).

[3] M. Huguet, E. Bertolini and the JET team. JET Progress towards D-T Operation. Proceedings of the 8th Topical Meeting on the Technology of Fusion Energy, (Salt Lake City, Utah, USA), 9th-13th

October 1988), Vol.15, No.2 Part 2A, p.245-258.

[4] P. Noll, L. Sonnerup, C. Froger, M. Huguet, J. Last, Forces on the JET vacuum vessel during disruptions and consequent operational limits. Proceedings of the 8th Topical Meeting on the Technology of Fusion Energy, (Salt Lake City, Utah, USA, 9th-13th October 1988), Vol.15 No.2 Part 2A, p.259-266.

[5] J. Last, E. Bertolini, M. Huguet, P. L. Mondino, P. Noll, L. Sonnerup, C. Bell, T. Molyneaux, Upgrading of the JET magnet system for 7MA plasma. Proceedings of the 8th Topical Meeting on the Technology of Fusion Energy, (Salt Lake City, Utah, USA, 9th-13th October 1988), Vol. 15, No.2 Part 2A, p.267-274.

[6] P. H. Rebut, The Problem of Impurities in JET and Proposed Control of Plasma Exhaust. 13th Symposium on Fusion Engineering, (Knoxville USA, October 1989).

[7] M. Pick et al, Integrated design of new in-vessel components. Proceedings of the 15th Symposium on Fusion Technology. Vol 1. p.771, (Utrecht Netherlands. September 1988)

[8] G. Celentano et al, The JET Belt Limiter, Proceedings of the 14th Symposium on Fusion Technology, Vol 1. p.581 (Avignon (France). September 1986).

[9] M. Pick, Beryllium in JET - Operational Experience, 13th Symposium on Fusion Engineering, (Knoxville, USA, October 1989)..

[10] P. Kupschus et al, Proceedings of the 12th Symposium on Fusion Engineering. (Monterey USA October 1987). IEEE vol.2 p.781-83 (1987)

[11] R. S. Hemsworth, G. H. Deschamps, H. D. Falter, P. Massmann, Testing of the upgraded JET Neutral Injectors Proceedings of the 12th Symposum on Fusion Engineering. (Monterey USA October 1987) Vol.1 p.276.

[12] P. L. Mondino, R. Claesen, J. A. Dobbing, P. A. Baigger. Design, Commissioning and early operation of the power supply and protection system for the extraction of the JET neutral injectors at 160 kV. Proceeding of the 14th Symposium on Fusion Technology, Vol.1, p.933-939, (Avignon, France, 8th-12th September 1986).

[13] G. Bosia et al, 32 MW ICRH plant experience on JET. Proceedings of the 15th Symposium on Fusion Technology. Vol.1 p.459, (Utrecht, The Netherlands, September 1988).

[14] S. J. Booth Contact Maintenance on JET into the Active Phase. Proceedings of the ENC4/FORATOM IX. Vol.3, p.51-56, (Geneva, Switzerland, June 1986).

[15] The JET Team. Latest JET results and future prospects. Proceedings of 12th International Conference on Plasma Physics and Controlled Nuclear Fusion Research. (Nice, France. 12th-19th October 1988).

[16] R. B. Tivey et al, A Comparison between Hypervapotron and Multitube High Heat Flux Beam Stopping Elements. 13th Symposium on Fusion Technology, (Knoxville, USA, October 1989).

UPGRADING THE JET PELLET INJECTOR WITH A TWO-STAGE LIGHT GAS GUN PROTOTYPE AND FUTURE PLANNING

P. Kupschus, K. Sonnenberg, W. Bailey, M. Gadeberg. J. Hardaker.
L. Hedley, J. Helm, D. Flory, P. McCarthy, A. Nowak, P. Twynam,
T. Szabo, M. Watson

JET Joint Undertaking, Abingdon, Oxon OX14 3EA, UK

Summary

For about two years the Joint European TORUS (JET) has been using a multi-pellet injector jointly built by JET and the Oak Ridge National Laboratory (ORNL). This was and is jointly operated by a JET - US Pellet Team within the Pellet Agreement between JET and the US Department of Energy (USDoE) under the wider umbrella of the EURATOM - USDoE Agreement on collaborative Fusion Research. This injector is composed of the ORNL Launcher, employing three independently firing repetitive (up to 5 s^{-1}) pneumatic guns for pellet speeds of up to 1.5 kms^{-1}, and a JET launcher-torus interface (Pellet Interface) which provides all required services to the launcher and its immediate control system. In particular, it provides the differential pumping to match the high pressures of the gun system to the vacuum pressure and flow requirements of the plasma boundary. The Pellet Interface, in its design from its conception about four years ago, was intended to be equipped with a JET built pellet launcher system employing also high-speed guns at a later date once the ORNL Launcher will have been removed as it is not compatible with the JET requirements for the Active Phase (tritium and remote handling compatibility). As a first step - to learn about the possible plasma physics benefits as well as to gain technical experience concerning the application of advanced gun technology, a JET two-stage light gas gun prototype has been developed and is now being installed in parallel with the ORNL Launcher. This paper reports on the JET pellet injector development programme, its motivation and its results to date. It describes briefly the presently operated pellet injector, continues to outline the design of the prototype in more detail and finally sketches the plans for the near future.

Introduction

The injection of pellets of frozen hydrogen isotopes (i.e. the fuel), is so far the only method of providing a particle source term beyond the recycling boundary layer of the future fusion plasma without simultaneously depositing excessive power. Injection of single particles, i.e. neutral particle injection, requires for sufficient penetration such high energies (in the range of or more than 1 MeV) that they also deliver unreasonable amounts of power to the plasma. Without such source terms, particle inventory and fluxes are solely determined by the plasma particle transport and the properties of limiter/wall and divertor dump plate. It is therefore of vital interest to have a tool to create such a source, whether to facilitate or influence the fuelling and re-fuelling of the plasma; whether to shape and tailor the density profiles in space and time, or to diagnose plasma response behaviour following the sudden deposition of the pellet mass.

To illustrate possible benefits one may be reminded of the discovery of the (transiently) enhanced performance mode of peaked density profiles by central pellet deposition in conjunction with central ion cyclotron radio frequency heating (ICRH) [1,2]. This is a mode with some potential to boost a plasma in start-up to ignition. However, the density build-up could only be facilitated while the plasma was still cold (i.e. less than about 3 keV) due to the penetration law for the pellets. Since the high density decay time after pellet injection and the time for heating the plasma to ignition temperatures (say 10 keV) are similar in magnitude, injection with central deposition at a later time when temperatures are already more elevated would be highly advantageous. It is hoped that higher velocity pellets will enable JET to move in this direction.

As is discussed in [3], the ablation of the pellet mainly by hot plasma electrons through the shield of a gas cloud, formed by the evaporation of the pellet and subsequently after ionisation distributed along the magnetic field lines throughout the plasma, is in detail a rather complex process not yet understood quantitatively. An unknown parameter in the various modifications of theories, the ionisation radius of the emerging cloud, has been benchmarked against the experimental penetration depths (the end of the pellet trajectory), mostly gained in a small speed range up to 1.5 kms^{-1}; thus leaving a large uncertainty in what the speed dependence of penetration should be. Nevertheless, it is likely to be fairly weak $L_p @ v_p * T_e(0)^{-5/3} * r_p^{5/3}$, where L,v,R denote penetration depth, velocity and initial radius of pellet (suffix p) and $T_e(0)$ the central electron temperature of a test plasma with linear (i.e. triangular) profiles, or vanishing altogether as in some variations of the theory. As can be seen from the above formula the penetration depth decreases rapidly with temperature which can in principle be compensated by using larger pellets. In reality, there is a limit for the acceptance of particles by the plasma either by the cooling effect (in the first instance the pellet mixes adiabatically with the plasma and reheating may require considerable amounts of energy/power) or by other plasma phenomena. Although plasmas have survived through pellet events, doubling the plasma particle contents, it is desirable to keep the disturbance as small as possible, and so the velocity should be chosen to vary the penetration depth. The choice between these parameters is the subject of experimental investigations to be performed when the tool becomes available.

The gun technology of accelerating macroscopic pellets calls for a considerable step over and above the velocities relatively easily achievable with present technology: i.e. employing centrifuges (theoretically 1.5 to 2 kms^{-1}, practically $\leq$ 1 kms^{-1}) and pneumatic guns (practically about 1.5 times the sound velocity a_s of the driver gas, which is ca 1.3 kms^{-1} for ambient temperature hydrogen). Development is continuing and reaches from a comparatively modest upgrading of the pneumatic principle by using hot driver gas to the more exotic ones like electromagnetic rail guns and rocket drivers. "Hot" pneumatics are still limited approximately to the $1.5 * a_s \leq 10$ kms^{-1} limit and although the other mentioned principles would permit higher velocities their development state [4] is such that within the limited lifetime of JET there would be little chance of an experimental application. Consequently, it was decided to apply two-stage light gas gun technology in a first step, develop and employ on JET a high-speed gun prototype (pellet speeds around 4 kms^{-1}) and to expand this to a gun system of this type with higher flexibility and enhanced speed capabi-

lity towards 10 kms⁻¹ in the following years. Already this requires a considerable effort because the sound velocity only moderately increases with temperature (a. ~ √T). The two-stage gun technology - through generation of the hot driver gas by adiabatic compression using a fast moving piston, transiently for the acceleration time of the pellet only - poses considerable difficulties with regard to mechanical integrity and low cycle fatigue, as well as heat transfer concerning the high-temperature and cryogenic regimes.

Report on the Injector Development Programme

General Outline

In the earlier phase (1985 - 1987), JET, EMI (Ernst-Mach-Institut der Fraunhofer-Gesellschaft, Freiburg, FRG), CENG (CEA Centre d'Études Nuclaires de Grenoble, France) and Risø National Laboratory (Roskilde, Denmark) have undertaken various collaborative investigations. These have looked at the principles of the "hot" pneumatics as well as at the technology of formation and also tried to assess the thermal and mechanical properties of frozen hydrogen isotope pellets. The results of the merged efforts of JET, EMI and CENG have been reported [5] and can be summarised as follows:

1) Bare 6 mm cylindrical (diameter = length) deuterium pellets have been formed by in-situ condensation (i.e. into the barrel breech); and despite the very low compressional strength in the order of 0.5 MPa these pellets were capable of withstanding driving pressures of about 75 bar leading to a maximum peak acceleration limit of $6*10^6$ ms⁻². A small two-stage gun (cf to gun parameters in Table 1) was capable of accelerating equivalent (i.e. $35*10^{-3}$ g) styro-foam pellets to 4.6 kms⁻¹. Two-stage guns have been in use in military laboratory type installations for the last 25 years for accelerating at about 10^8 ms⁻² heavier loads to almost 10 kms⁻¹. So, the soft pellets required a scale-down of gun performance into a different time domain of the acceleration process. Due to a velocity dependent erosion effect, which the bare deuterium pellet suffered in interacting with the inner barrel surface and/or the driver gas the speed of these pellets was limited to 2.7 kms⁻¹. We concluded that even particular optimisation would not result in speeds significantly in excess of 3 kms⁻¹.

2) Deuterium pellets were subsequently supported by a cup-like cartridge, traditionally called a sabot, and 5 mm deuterium pellets in 6 mm O.D. sabots mostly made from polyimide were reaching now 3.8 kms⁻¹. Due to the higher mass of the pellet/sabot combination (typically now in the region of (0.2 g or beyond) the acceleration limit was now set by the gun performance in yielding only the above mentioned values. At this stage the stringently required removal of the sabot before a pellet can be delivered to the plasma could not yet be facilitated.

In the present phase of the development programme (1988 - 1989/90) the work is now carried out in collaboration between JET and CENG with the following task division:

1) JET will develop, design, construct, install and operate a PROTOTYPE launcher featuring a two-stage gun with a pellet formation cryostat with ten pellet/sabot storage stations. It will be capable of providing one pellet per tokamak pulse at around 4 kms⁻¹, repetitive in the sense that it can be re-armed automatically in less than about 10 minutes. It is on this item that the paper will concentrate.

2) CENG will follow JET in the present line but must take all necessary measures to advance the prototype launcher towards a truly repetitive (about 1 s⁻¹) launcher design, in principle, compatible with the requirements for the Active Phase of JET (i.e. low degree of maintenance, tritium and remote handling compatibility).

In 1990 and the following years the remaining development problems have to be solved and the achieved results - depending somewhat on the outcome of experiments to be conducted with the PROTOTYPE - have to achieve a real design to be implemented in about 1991.

Pellet Injection Test Range and Results

JET has built up two launcher test ranges the basic set-up being sketched in FIG. 1. The two-stage gun on the left consists of a high-pressure reservoir the stored energy of which is used to propel the piston (to the right) once the fast valve has been actuated. The prefilled foreland gas (of about 1 bar) .on the right hand side of the piston will then be adiabatically compressed in a very short time (within some ten milliseconds) and the nozzle pressure will surge into the 1000 bar range for about one millisecond. Under the action of this pressure the pellet will start to move at a certain break-away pressure (to be defined if necessary by a bursting disc) and ride on the crest of the pressure wave down the barrel which for testing is equipped with pressure sensors. The pellet will then in free flight penetrate two light curtain stations each triggering one of two flash-light photographs and finally impinge on a target (usually a soft aluminium disc) in a vacuum tank (sometimes two are used connected to each other) where pellet aiming accuracy and sabot separation data can be taken. The parameter range for the prototype two-stage gun (with the corresponding values for the JET/EMI gun in parallel, + indicating further intended boosting) are:

TABLE 1: Two-stage gun parameters

	JET	JET/EMI	
Pump tube length	3 - 5	0.13 - 1.0	m
Pump tube inner diameter	60 - 100	30	mm
Barrel length	1.5 - 3	1 - 1.5	m
Barrel inner diameter	6 - 10	6	mm
Piston mass	1 - 3	0.2	kg
Reservoir pressure	200 +	300	bar
Reservoir volume	5 - 10	0.7	l
1st stage "energy"	to 2000 +	200	barl
Nozzle pressures	to 4000 +	1000	bar

FIG. 2 shows a picture of the two test ranges. The one in the foreground has been used to investigate ice pellet sabot behaviour using a pellet formation cryostat out of the CENG development; the cryostat features a cold transport wheel (with axis excentric to the barrel) at near liquid helium (LHe) temperatures with a pellet holder which can be brought into three different positions by indexing: pellet formation, barrel firing and sabot loading position. The cryostat was designed with a pellet holder bushing, a copper ring in which the sabot is inserted, which provides the thermal contact to the LHe cell during condensation, and which finally serves in sealing the front and rear end of the breech against the pressure surge preventing it from reaching the pellet condensation area (cf FIG 5, a and b). The fact that in this cryostat design the barrel pressure cannot be raised beyond 1200 bar (and the gun system cannot operate at higher nozzle pres-
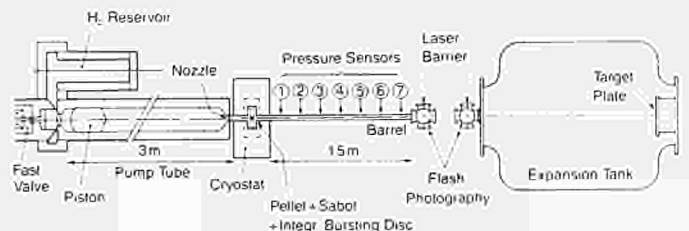

FIG. 1: Basic Sketch of Test Range

barrel pressure cannot be raised beyond 1200 bar (and the gun system cannot operate at higher nozzle pressures than 2000 bars) limited somewhat our ability to perform integral tests for prototype conditions. With the first operating we therefore installed another launcher range (the one in the background of FIG. 2) to develop the elements of repetitiveness, the critical components (like fast valve and piston) and to test barrels differing in material, inner diameter and length as well as a variety of sabots and their separation scenarios; with the breech pressure now going up to 2000 bar (when the nozzle pressure is close to 4000 bar). This gun up to now fired ambient temperature plastic pellets in plastic sabots.
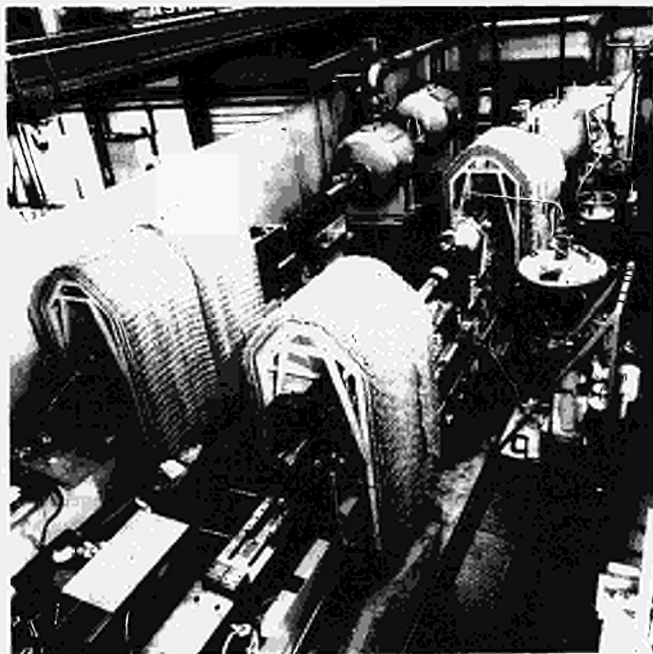
FIG. 2: The Two Launcher Ranges of the JET Pellet Testbed

An example of the performance of the latter gun is given in FIG. 3: the diagram shows the pressure versus time curves for the nozzle position (1) and at further six consecutive barrel pressure sensors locations. The nozzle peak pressure goes up to 3600 bar, typically half of this , i.e. 2000 bar, can be seen as
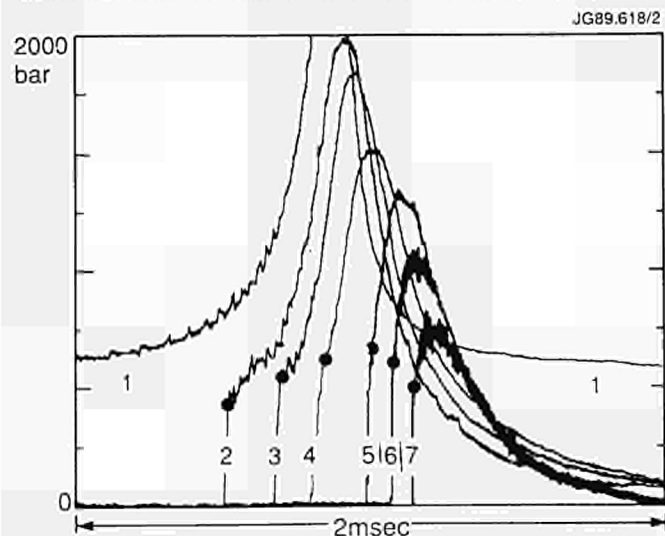
the maximum at the breech. The pressure driving the pellet is the static pressure - marked with a point in the plot - which is 500 to 600 bar over the full length of the barrel, leading e.g. for a 0.2 g load to a constant acceleration of $6*10^8$ ms^{-2}; this in turn would theoretically result in 4.9 kms^{-1}for a 1.5 m barrel (the actually measured pellet speed here was 3.6 kms^{-1} for a 0.4 g pellet consistent with the above data, and the static pressure values are confirmed by the transit time analysis).

Both guns have proven to give reliable operation with pellet speeds around 4 kms^{-1} (the first one though only for smaller pellet/sabot mass). The fast valve to actuate the piston, designed and built by JET, has now performed through some 500 cycles; pistons with PTFE piston rings have exceeded 300 cycles (the piston rings to be renewed every 30 shots) and pure titanium pistons have gone through more than 150 cycles continuously without maintenance, so that we feel very confident that all the elements of automatic gas handling and re-arming are available and that the design incorporating the experience with these two guns will work in the torus environment.

Unexpectedly, the formation of deuterium ice pellets still being intact after acceleration and after (and so far partial) separation from their sabots has turned out to be much more difficult. This is due to a combination of problems:

1) It is apparently difficult to reproduce the conditions of initial condensation of the ice and imperfections introduced in the beginning cannot be mended later on. The condensation process seems to be adversely influenced by low thermal conductivity of the sabot walls made from polyimide or polythene. Despite remarkable overall improvements with respect to the ice quality by various procedural variations including extrusion and compacting of the condensate (by movement of the gas feed plunger in FIG 5,a) pellets with direct ice contact to the bushing wall still exhibit better and more reproducible mechanical ice properties than those with plastic walls throughout.

2) The dynamics of acceleration of a ice pellet/sabot combination where the latter one was initially split in axial direction to facilitate radial separation when leaving the barrel by means of gas pressure developed by the pellet (either through the acceleration process by erosion in slotted sabot walls or by eddy current heating due to magnetic flux swing (FIG. 4b) or by driver gas still emerging from the muzzle (FIG. 4a). The remainder of the sabot then has to be removed by a shear cone (FIG. 4c). These methods already mentioned in [6] looked promising in earlier experiments and the method according to FIG. 4b works well with plastic pellets. But as a result of the splitting of the bottom of a thin-walled sabot the hot propellant gas can jeopardise the ice integrity (FIG.
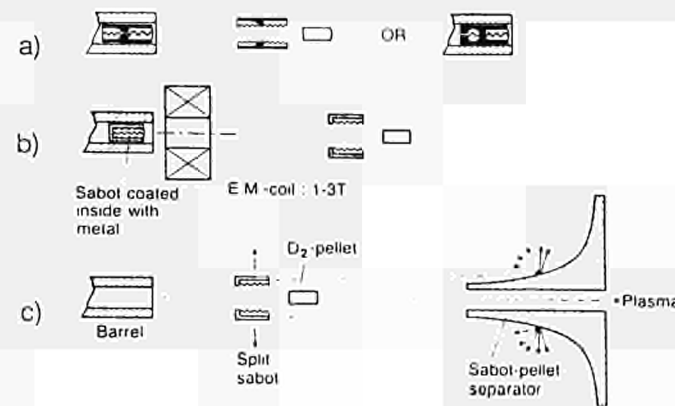

FIG. 3: Pressure versus time plots at nozzle (trace 1) and .1, .3, .55, .8, 1.05, and 1.3 m downstream from the breech (traces 2 to 7).

FIG. 4: Principles of Sabot Separation

A138

5b). A stronger sabot into which the ice was extruded in spherical form improves that situation but suffers from a large mass penalty (FIG. 5c; also again the reproducibility of ice formation was found to be less). The closed bottom of the assymmetric sabot in FIG. 5d provides better protection of ice and more reproducible results (though the occurrence of some ice powder indicates again problems in the ice formation). Finally, the bottom-only sabot of FIG. 5e yields excellent results (the pellet shows erosion but to a
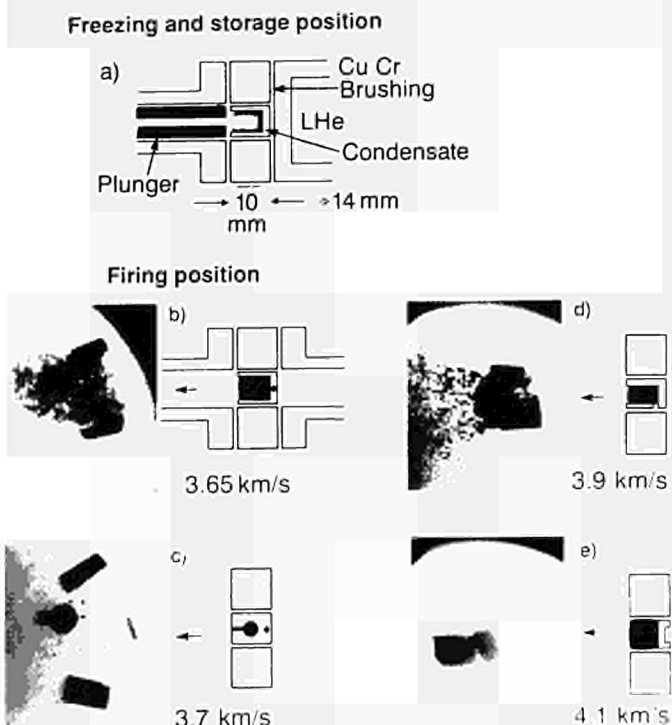
Freezing and storage position

Firing position

3.65 km/s

3.9 km/s

3.7 km/s

4.1 km/s

FIG. 5: Formation Schematics and In-flight Photography of Deuterium Ice Pellets/Sabot Combinations

minor extent since the driver gas is sealed off) but we may expect less directional stability due to this erosion. Separation for the last two types of sabots is more difficult then for the split one. We are currently more systematically investigating sabot removal methods for the latter methods by driver gas pressure or by a blast of explosives as an immediate solution for the PROTOTYPE but will return to and study earlier ideas with stronger metallic sabots which pose friction problems in the barrel.

The new cryostat under construction for the Prototype will enable us to integrally test these ideas and we are confident that a satisfactory solution can be found for the 4 kms⁻¹ problem. The two-stage gun and the cryostat on one of the launcher ranges is now being replaced by the new components of the PROTOTYPE and this is planned to be performed in such a way that after successful testing under experimental conditions as they apply at the torus (using also a duplicate of the JET main control system) these very component will be transfered to the torus and installed and commissioned in the minimum of change-over time.

The Present JET Injector

A detailed description of the presently operating JET Injector can be found in [7] and [8] with regard to the Pellet Interface and the ORNL Launcher, respectively. We will concentrate here mainly on those aspects which bear relevance to the implementation of the PROTOTYPE and will refer to the later FIG. 7 to 9 concerning details.

The ORNL launcher forms its pellets by punching them out of a continuously extruded ice ribbon when the breech closes into the extrudate whereupon they are fired with gas from a fast valve, the whole sequence being performed within milliseconds. The launcher consists of three independently firing guns in a common vacuum housing, and three different sizes of pellets of 2.7, 4 and 6 mm, each with its own respective barrel, can be fired in arbitrarily timed salvoes of up to 32, 16 and 16 pellets, respectively (at present only limited by the control software) with up to 5 pellets/s. The three barrels are arranged in a plane, the two outer ones focussing under 1.4° and this plane is tilted by 1.9° downwards towards the torus in order that all barrels aim at the midpoint of the narrowest aperture in the horizontal port. The pellets are travelling in free flight without the aid of guide tubes, are permitted within a cone of less than 0.5° half angle (defined by the interferometer aperture) and are characterised on their flight to the torus, when they enter the Pellet Interface, by special diagnostics with regard to shape and integrity (CCD camera photography), mass (detuning of a μ-wave cavity of an interferometer), velocity (transit time measurement from light trigger and μ-wave cavity) and D_α-light (CCD photography and total intensity time trace, when the pellet is dissolved in the plasma). In off-line commissioning shots a titanium target can be inserted in a gun line to ultrasonically determine the aiming.

The differential pumping is facilitated by a cryo-condensation pump of ca 8*10⁶ ls⁻¹ pumping speed for hydrogen in the 3.5 m long, 7 m high and 1.5 to 2.5 m wedge shaped pellet injector box (PIB) of 50 m³ volume separated from the torus vacuum (reaching into the duct) by flow restrainer tubes of nominally 60 ls⁻¹
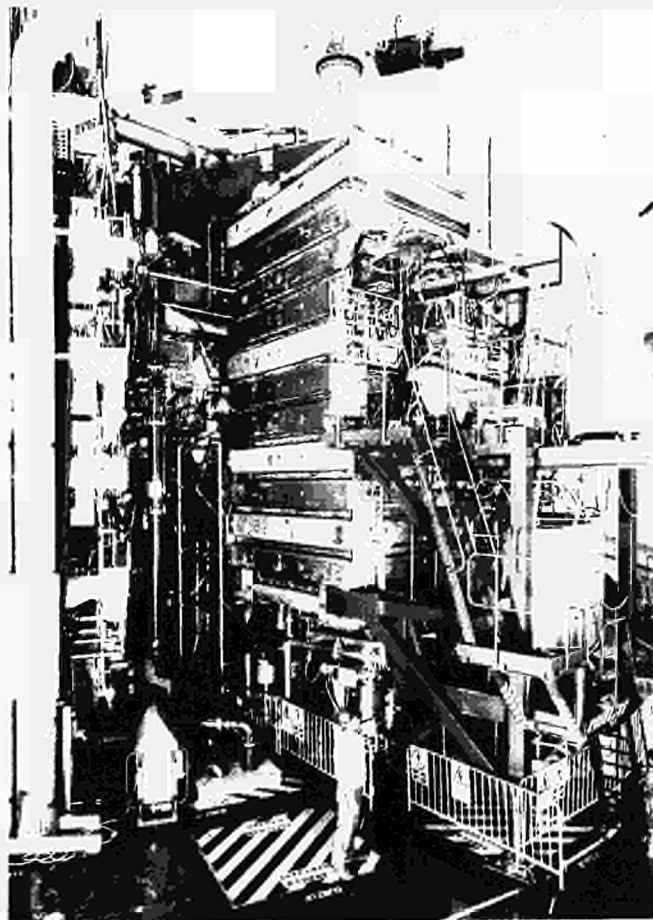

FIG. 6: Photograph of the JET Pellet Injector (the ORNL launcher cube can be seen above the platform)

conductance each; these can be closed by flap valves if the gun line is not needed. Under worst conditions, the 3 barl per pellet of the 6 mm gun propellant surge is pumped away with a time constant of ca $7*10^{-3}$ s, delivering theoretically a maximum of less than $2*10^{-2}$ mbarl of hydrogen to the plasma (corresponding to $1.5*10^{-7}$ mbar torus filling pressure). Since the surge is not being delivered at an instant the actual fraction going into the torus is considerably less and has indeed up to now never been detected by any plasma diagnostic even when more than one of the restrainer tubes were open. The capacity of the cryopump which pumps the propellant as well as the wasted extrudate deuterium (at present ca 70 % of the gas load) is currently 1000 barl, limited by hydrogen safety precautions; this provides at present one to two days of operation between regenerations. The cryopump is estimated to pump up to 5000 barl (and was proven to have a capacity of more than 3000 barl); when the conversion of the PIB into a 3.5 bar absolute pressure vessel will be completed 2500 barl should routinely be possible. This will then provide the capacity for 25 machine pulse per day at 100 barl on aggregate, sufficient for the PROTOTYPE and presumably also without further measures for an advanced gun system. Regeneration of the cryopump can be performed overnight automatically in a 3-4 hour cycle. FIG. 6 shows a picture of the present status of the injector.

The PROTOTYPE High-Speed Launcher

Design and Preparations

The PROTOTYPE Launcher guns (one is optional to be installed perhaps at a later date) will be using the two outer of the three gun lines existing below the torus midplane as a mirror image to ORNL gun lines. The preparations for mounting the PROTOTYPE are done in such a way as to minimise the effort for later upgrades and for the advanced gun system as yet to be defined in detail. In particular, the necessary structural enhancements to provide mountings for the two-stage guns are already well established considering only one gun (assuming that simultaneous firing will not be needed or only performed by selected guns). An ca 8 m long, 1.5 m high carbon steel beam can support up to five two-stage guns up to about 5 m in length on either of its sides; the guns then can have barrel lengths somewhat in excess of 3 m. The PROTOTYPE will have initially a 3 m pump tube and a 1.5 m long barrel. FIG. 7 shows the outline of this arrangement. Since the length of the beam will make use of the available space back to the corner of the torus hall it was decided to take the weight of the beam (fully equipped up to 20 t) by the PIB platform and the wall but to anchor the force transferred to the beam under the momentum of the

reversing piston (ca 80 t for the PROTOTYPE, up to 400 t for upgraded guns) fully in the concrete wall. Since the beam is blocking the peripheral haul passage for a number of larger components it was conceived as a draw bridge allowing us to lift it out of the way with only a minimum of service interruptions; in particular electrical cabling does not have to be disconnected.

The dashed line in FIG. 7 marks the blow-up in FIG.8 which shows in more detail the two-stage gun
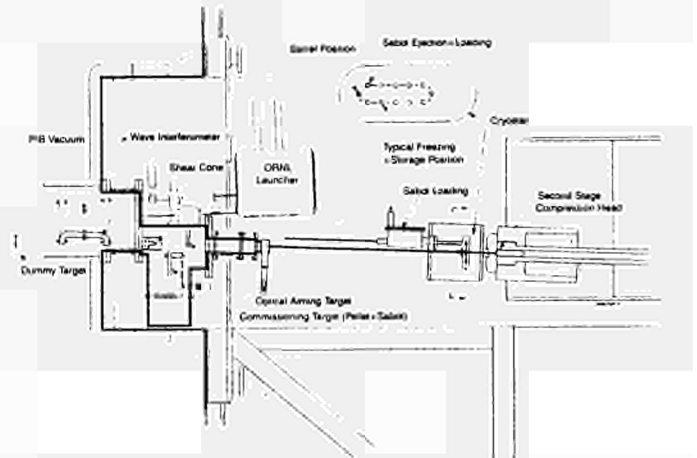
FIG. 8: Close-up of dashed area in FIG. 7

front end (the pump tube inner diameter being initially 60 mm), the cryostat with its chain guiding 10 freezing and storage cells - which can be indexed into the barrel or sabot loading and ejection position - and the barrel entering a very complicated PIB vacuum pocket (this design is a consequence of the parallel operation of the ORNL Launcher). Pellets from the launcher will penetrate curtains of wavelength encoded light at the optical aiming target (this will under all operation conditions provide information about the in-flight position of pellet and sabot at this location) and will impinge on a commissioning target until the correct aiming is achieved by means of barrel flexing. Once this target is removed the pellets will enter the PIB through the centre hole of the shear cone which intercepts the sabot parts. The pellet will be photographed (not shown here) when it leaves the μ-wave interferometer and it will be intercepted by a dummy target again for commissioning purposes when the further path to the plasma is not permitted. The ultrasonic target may still be usable at 4 kms^{-1} but is thereabout in jeopardy of being destroyed. The commissioning and the dummy target will be composed from densely packed titanium needles and no diagnostic will be attached to them. FIG. 9 shows the arrangement in
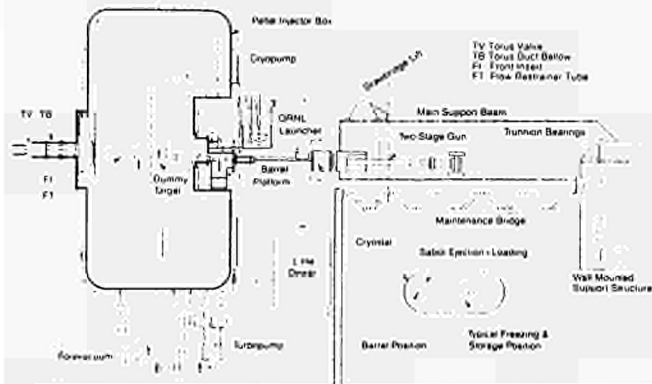

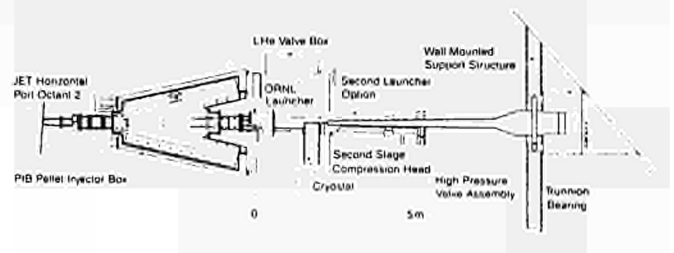FIG. 7: Schematic of injector with PROTOTYPE

FIG. 9: JET High-Speed Injector in Plan View

plan view, FIG.10 presents an artist's view of the beam and support steelwork at the wall and FIG. 11 shows the steelwork already in place (above the support fixed to the wall is the main cabling junction box).

Installation Schedule

The delivery of the support beam is expected in a few weeks time and further structural enhancements are scheduled for the JET shutdown starting right after this conference. The two-stage gun is being delivered in parts now and will be installed on the testbed and commissioned at the end of this year, the cryostat
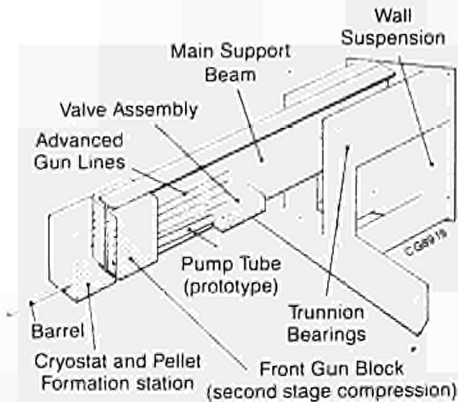

FIG.10: Artist's View of JET High-Speed Injector

FIG. 11: Injector Support Steelwork on Torus Hall Wall

though on parts delivery also in a few weeks time is more of a problem because the consequences of the latest pellet formation and sabot removal tests have still to be implemented but it is hoped that integral commissioning of the launcher on the testbed can commence very early in 1990 with the launcher ready in time for operation in the next operational period of JET starting in spring 1990. During that period we aim at gaining some experimental evidence as to how beneficial high-speed injection can be regarded for fusion plasmas.

Future Plans

Assuming that there will be such benefits the PROTOTYPE launcher is to be expanded into a repetitive (i.e several shots during a tokamak pulse, preferably

with repetition rates approaching 1 s^{-1}) multi-pellet system (e.g. a ten gun system) compatible with the requirements of low- maintenance, remote handling and tritium use. Apart from the necessary two-stage gun and cryostat development, now being performed under collaboration with CENG, a major item to be upgraded will be the gas exhaust system of the remaining second-stage propellant and the first-stage piston driver gas both of which need to be removed fast if the guns are to be made repetitive. There is also the problem of the possible contamination with tritium of the vast amount of first-stage driver gas (possible 1000 barl per pellet shot) which may not be permitted for chimney release, would then have to be re-compressed in a contaminated cycle whereby it can only occasionally be cleaned up by the tritium recovery plant. The required effort, the resources and the time scale for the solution of these problems have to be viewed against the JET overall programme and its priorities but so far it is JET's intention to go ahead in this direction.

Conclusion

The preparation for the implementation of a high-speed pellet launcher prototype is being carried out with the aim of obtaining experimental results in the 1990 operational period of JET. It is hoped that this will provide us with information on what role this method of fuelling and density control will play in future fusion application.

References

[1] P. Kupschus et al., "Multi-Pellet Injection on JET", IAEA Technical Committee Meeting on Pellet Injection and Toroidal Confinement, Gut Ising, FRG, Oct 24-26, 1988, to be published

[2] G.L. Schmidt for the JET TEAM, "Heating of Peaked Density Profiles Produced by Pellet Injection in JET", 12th IAEA Conference on Plasma Physics and Controlled Nuclear Fusion Reseach, Nice, France, October 12-19, 1988, Paper IAEA-CN-50/A-IV-1

[3] W.A. Houlberg et al., "JET Pellet Ablation Studies and Projections for CIT and ITER", ibid [1]

[4] P. Kupschus, "Injector Development - Summary and Review", ibid [1]

[5] K. Sonnenberg et al., "High Speed Pellet Development", IEEE Proceedings of the 12th Symposium on Fusion Engineering, Monterey, CA, Oct 12-16, 1987, Vol 2, pp 1207

[6] K. Sonnenberg et al., "Prototype of a High-Speed Pellet Launcher for JET", Proceedings of the 13th Symposium on Fusion Technology SOFT, Utrecht, NL, Sept 19-20, 1988; North-Holland, Amsterdam, 1989, Vol 1, pp 715

[7] P. Kupschus et al., "The JET Multi-Pellet Injector Launcher - Machine Interface", ibid [5], Vol 2, pp 780

[8] S. Milora et al., "Design of a Repeating Pneumatic Pellet Injector for the Joint European Torus", ibid [5], Vol 2, pp 784

BERYLLIUM IN JET
A Report on the Operational Experience

K. J. Dietz, M. A. Pick, A. T. Peacock, K. Sonnenberg,
J. Ehrenberg, G. Saibene, R. Sartori
JET Joint Undertaking, Abingdon, Oxon, UK

Abstract: Beryllium was introduced as plasma facing material into JET. This paper describes the preparations carried out and the observed improvements in plasma performance.

I. Introduction

The use of beryllium in JET was proposed as early as 1975 [1]. Since the start of operation in 1983 studies were initiated by JET to assess it as an alternative to graphite, the limiter material selected initially. The studies comprised the use of beryllium limiters in small tokamaks, ISX-B [2] and UNITOR [3,4], as well as model investigation on sputtering [5], hydrogen retention [6], and wall-pumping.

In the tokamak experiments it was established that beryllium is a well suited material for limiters which facilitates the conditioning of the respective machine, reduces the oxygen content of the plasma by gettering and allows for increased density limits. Overloading of the limiter i.e. applying loads above the design limit led to surface melting which resulted in increased beryllium content of the plasma even when at a later stage the power density was reduced to values below the design limits.

The model experiments showed that beryllium has a sputtering rate comparable to that of graphite at ambient temperature, but which in contrast to graphite is not temperature dependent. At 600 K its hydrogen retention is by about a factor of three lower than graphite. The mechanism for hydrogen pumping is comparable to a metal which dissolves hydrogen and does not form hydrides.

From these results predictions were made [7,8] which led us to propose the introduction of beryllium into JET with the expectation of an improved plasma performance. In particular:

i) Due to lower effective charge at the same relative impurity content the deuterium dilution should be improved in such a way that the plasma contains more deuterons for a given density. Consequently the fusion parameter $n_D T_i \tau_E$, the product of deuteron density, ion temperature, and energy confinement time, should increase.

ii) The relative impurity concentration for beryllium should be less than that for carbon because the former does not show chemical erosion (hydride formation), radiation induced sputtering or, for perpendicular incidence, self sputtering yields above unity.

iii) Beryllium is a getter for oxygen and therefore it can be expected that the oxygen content of the plasma and the sputtering by oxygen will be decreased and thus reduced edge radiation should lead to increased density limits.

Areas of concern remain the fact that the angular dependence of the self-sputtering rate for beryllium is not known and there is danger of thermally overloading the limiter surface.

It should be noted that due to its higher thermal diffusivity for the same surface temperature beryllium can take about 1.7 times the load of graphite. In fact the maximum permitted surface temperatures for graphite and beryllium are similar and should not exceed 1300 K for beryllium and 1500 K for carbon [8]. For beryllium the surface temperature is limited by the vapour pressure (melting point is 1556 K) and for graphite by radiation enhanced sublimation and self-sputtering.

It was observed on graphite surfaces during discharges in JET that the sputtering yield of graphite rises from 5% for temperatures of 1300 K to unity for 1700 K. This can be understood in terms of self-sputtering and/or radiation enhanced sublimation. It should be noted that this result excludes graphite as a material for high heat flux components if surface temperatures exceeds 1500 K.
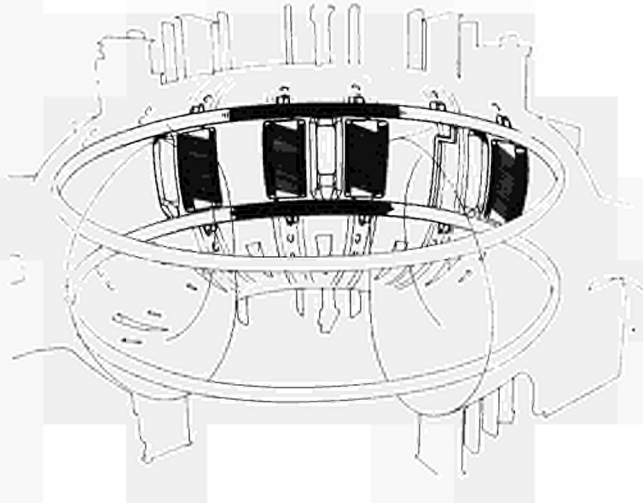

Fig. 1: Sketch of the JET belt limiter and RF antennae

II. Preparation for Operation with Beryllium

In parallel to the experimental investigations into the properties of beryllium with respect to its behaviour in the presence of a tokamak plasma, designs were carried through to introduce into JET a beryllium limiter and at the same time to cover the internal surfaces by a thin evaporated beryllium layer.

The switch of the limiter material from graphite to beryllium was planned to be implemented in connection with the belt limiter [9] which was designed to allow for an easy exchange of materials. A schematic view is shown in Fig. 1. The belt limiter consists of two rings concentric to the magnetic axis at the outboard wall above and below the midplane of JET. It is based on inertia cooling and designed in

such a way that the limiter material is inserted between cooling fins which are welded to the watercooled support structure. The limiter material consists of plates of 20 mm thickness, 70 mm wide and 380 mm high. Any two plates are assembled into one unit. This is held by disk springs which are located in slots in the fins. There is a total of 1200 of such assemblies and it takes four men about 50 hours to exchange the limiter material.

The beryllium employed is S-65B, cold pressed and sintered. The area between the fins is blackened to improve the heat transfer by radiation to the fins. If the power is evenly distributed between the upper and lower ring and hot spots do not develop the total power handling capability should be 40 MW for 10 s. It is assumed that radiation is negligible and that all power is conducted to the limiter. The resulting maximum surface temperature is 1300 K. The corresponding thermal load is 4 MWm^{-2}. For such a load elastic-plastic analysis showed plastic deformation in the near surface regions [10]. This required castellation of the surface and heat load experiments showed that indeed surface cracking could be avoided for several thousand heat cycles.

The second element for the beryllium operation in JET are the evaporators [11]. A schematic diagram is shown in Fig. 2. The hot isostatically pressed beryllium head (3 kg) in the form of a hollow cylinder closed at one end is supported by a tube made of CFC graphite. Two thermocouples are inserted into the beryllium head. Inside the graphite support tube there is a spirally wound CFC heater fired at 2200K. Their resistance is about 1 Ω at operating temperature. The power (up to 180V at 100 A), is supplied through fine grain graphite conductors which are connected to TZM rods. A heat shield consisting of tantalum sheets is inserted into the tube to protect the outer support. Four such evaporators can be inserted into the vessel by 300 mm for evaporation and retracted again for pulse operation.
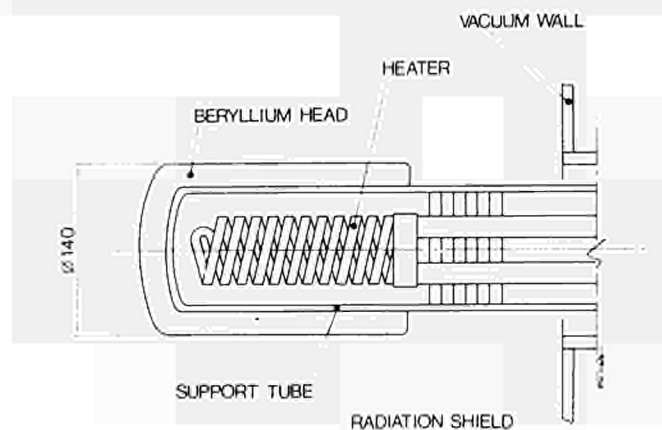
Fig. 2: Schematic of the beryllium evaporator

Reliable values for the emissivity of beryllium at elevated temperatures were not available. Therefore an estimate of 0.2 to 0.4 was made for the design. That resulted in a power requirement of 6.4 kW for a head temperature of 1325 K and corresponds to an evaporation rate of 6.7 x 10^{-7} gcm^{-2}s^{-1}. This is equivalent with the deposition of an average 1 μm thick layer inside the JET vessel within ten hours.

Tests were carried out on these evaporators before their introduction into the JET vessel. Fig. 3 summarizes details of the tests. The head temperatures
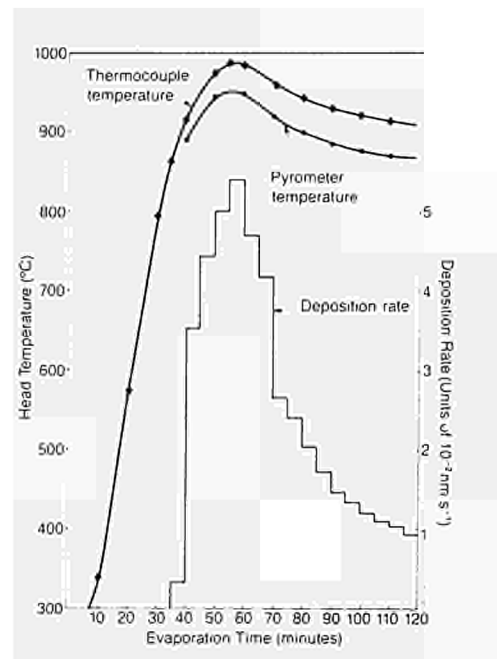
Fig 3: Deposition rate and head temperature as a function of time at 4.8 KW power input

measured by thermocouples and a pyrometer are shown together with the deposition rate at 0.5m from the head. The evaporation was only carried out after the partial pressures of water and oxygen in the UHV test vessel were in the 10^{-10}mbar range.

The temperature in the head reaches a maximum after 55 to 60 minutes; this also corresponds to the evaporation rate maximum. Later the temperature decreases and consequently the evaporation rate. As the input power was held constant this behaviour can only be explained by an increase of emissivity during the initial operation. At later times the evaporation becomes roughly time independent albeit at a largely reduced rate.

Observations in the JET vacuum vessel confirmed this behaviour. After 100 hours of operation it took five hours to obtain an average thickness of 100 Å at the inner wall compared with less than 1 hour initially. The change of emissivity responsible for this degradation is due to the formation of a dust layer on the evaporator heads consisting of beryllium and beryllium oxide (10%). The oxidation occurs during the evaporation by interaction with the residual gases. To minimize this effect a better vacuum or a higher evaporation rate has to be established.

III. Operation with Beryllium

Dilution of the JET plasma by low-Z impurities and the absence of proper density control were the main limitations to the performance during the use of graphite as the limiter and wall material. The introduction of beryllium addressed directly the problem of finding an alternative to graphite.

The operational plan took into account the initial vessel configuration. In particular:
    graphite tiles on the belt limiter
    inner wall graphite tiles
    X-point graphite tiles
    RF-antennae graphite side protection
    RF-antennae nickel screen
A view of the inside of the JET vessel showing all these components has been presented previously [12].

Three phases were foreseen for the evaluation of beryllium.

Phase 1 consisted of a start-up as a graphite machine after some month of shut-down, to establish reference discharges.

Phase 2 saw the start of beryllium evaporation with average thicknesses of the deposited layers of 100 Å. In total 26 evaporations were carried out and 240 g of beryllium were deposited. The layers are very uneven in thickness, up to one mm thick immediately behind the evaporators and only about 1000 Å for the thinnest films at the inner wall. The adhesion on the fine grain graphite is very good even for thicknesses of up to one mm, whereas CFC graphite is not suited as a substrate and shows spallation as can be seen in Fig. 4. The graphite tiles (CFC) immediately behind

IV. Plasma Behaviour

This section deals mainly with the results from Phase 2, the beryllium gettering phase, those from Phase 3 are not yet available. The main observations obtained immediately after the first gettering can be summarized as follows:

· The beryllium layer on the graphite limiter erodes quickly, typically within one to five discharges, a surface coverage of 5 to 10% beryllium remains;

· Carbon remains the dominant impurity but the carbon influx is lower by a factor of about two;

· The oxygen content is reduced by at least a factor of ten from typically 0.5-2% to levels below 0.1%;

· The ratio of radiated to total power input is consistently reduced to values below 30%;
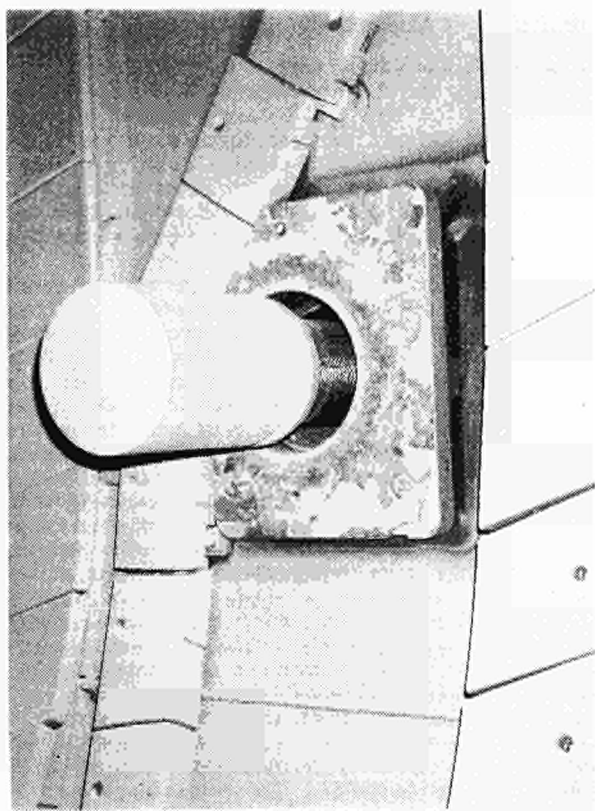
Fig 4: Beryllium layers close to one evaporator head showing spallation on CFC graphite. Thickess of deposited film about 1 mm

Fig. 5: Belt limiter during installation. Note the biological protection

the evaporator head form a heatshield to protect the vacuum vessel. The thickness of the spallated layer is estimated to be about one millimetre.

Phase 3 followed the successful conclusion of Phase 2 and has just started after the introduction of the beryllium tiles into the vessel. The exchange of the limiter material was carried out under full biological protection [13,14]. JET has established a code of practice which is more stringent than that used in the beryllium industry. For levels of airborne dust larger than 0.2 μgm^{-3} (industry 2 μgm^{-3}) respiratory protection is to be worn.

During the installation of the tiles the dust levels in the machine - in stagnant air - varied between 15 and 50 μgm^{-3}. Fig.5 shows part of the belt limiter during installation.

· The effective charge is lowered by about one unit, high density discharges with values close to unity can be achieved in ohmically heated discharges;

· The beryllium layer exhibits strong wall pumping facilitating density control;

· Density limits are no longer characterized by disruptions. Strong poloidal assymmetries in density develop which reject any further density increase. Additional heating (including RF) allows for at least two times higher densities compared to ohmic discharges, density clamping was not only found during Neutral Injection but also during RF-heating. In pellet fuelled discharges peak densities of $4 \times 10^{20} m^{-3}$ could be obtained;

· Dilution of the hydrogen isotopes at the plasma core is reduced ($n_D/n_e \sim 0.8$-0.9), thus increasing the

neutron output to values $\sim 2 \times 10^{16} s^{-1}$. The maximum achieved equivalent Q_{DT}-value, albeit non-stationary approached 0.5.

Generally it can be stated that the beryllium gettering opened up new operation regimes with respect to effective charge, peak and average densities, density and current profiles and led as well to the development of schemes for sawteeth suppression and thus to increases in electron and ion temperature. It is interesting to note that energy confinement times were not changed for comparable discharges in graphite and beryllium surrounding.

V. Wall Pumping

The pumping of hydrogen by graphite walls/limiters [10,15] can be separated into two types: a strong transient pumping where removal rates of $10^{21} s^{-1}$ can be achieved and a continuous pumping effect with rates of around $10^{19} s^{-1}$. The first effect occurs whenever the plasma is brought out of equilibrium with the limiters and walls either by fuelling (gas, beams, pellets) or by moving the plasma from the limiter to the inside wall. The transient pumping lasts for one to two seconds and reduces then to the lower rate of the second pumping type of $10^{19} s^{-1}$ which seems to continue throughout the rest of the discharge. The transient pumping effect is largely responsible for the fact that the ratio of the number of hydrogen ions in the plasma to the number of hydrogen atoms admitted into the tokamak is well below one (the so called fuelling efficiency, see Table 1). The continuous pumping reduces this ratio further during the course of the discharge.

He conditioning of the graphite walls can temporarily increase the pumping, but after about 5 discharges the initial situation is recovered.

Discharges which were performed directly after Be evaporation showed a pumping effect as good as with He-conditioned graphite walls. Indeed within the uncertainties no significant difference can be found to graphite walls even when the beryllium layer has aged (after 40 discharges), see Table 1. Nevertheless more gas is used for a certain density because the hydrogen dilution in the plasma by impurities has been reduced by about a factor of two in Be-gettered discharges.

Density control in Be-gettered discharges with additional heating has improved particularly in discharges with fresh Be-layers. During RF heating the density increase can be almost fully attributed to an influx of impurities, and during neutral beam heating the pumping rate can become as high as the fuelling of the beam so that a so called density clamping occurs.

VI. Hydrogen Retention

Gas balance measurements have been carried out, both for the operation with graphite and with beryllium walls. These measurements were motivated by the concern about the tritium inventory during the D-T phase. A diagnostic system [16] to compare the amount of gas injected into JET with that released after a discharge has been in operation for the last operation periods of JET. It consists of a cryogenic pumping system parallel to the forevacuum system and stores the gas released from the vacuum vessel after each shot. A storage tank takes the collected gas from the cryopanel after a period of operation. This gas can then be analyzed for quantity and chemical composition and compared with the input from gas puffing, pellets and Neutral Injection.

The measurements described were performed for hundreds of discharges for graphite walls under various conditions [17].

Fig. 6 summarizes the results for graphite walls for different discharge conditions. It can be seen that the retention does not depend on the type of
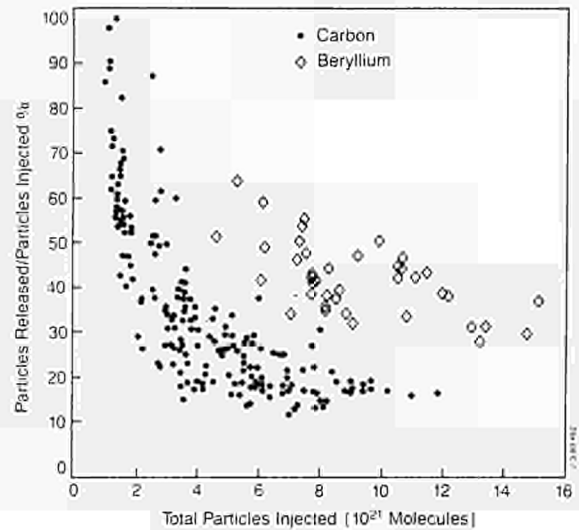

Fig. 6: Fraction of gas released 600s after a discharge as function of the injected molecules

fuelling but only on the amount of particles introduced into the torus. The fraction of gas retained in the vacuum vessel increases with the particle input. At high densities (large amount of particles injected) the retention can approach 90% for graphite walls. The integration time for the gas release measurement is 600 s. Integration times extended over more than 24 hours improved the global recovery to about 50%.

The beryllium gettering not only changed the plasma behaviour and the recycling but also the deuterium retention. Preliminary analysis shows that the retention has decreased from 90% to 70% for 600 s integration time and the recovery rate for a full day of operation was up to 80% by integrating the gas release during a full day of operation. This is in marked contrast to the operation with graphite walls where only about 50% could be recovered under similar conditions.

It should be noted that in spite of the beryllium evaporation, due to the short lifetime of the layers JET was still essentially a graphite machine. Further improvements in the hydrogen retention can only be expected once JET is fully operational with the beryllium belt limiter.

TABLE 1
Fuelling efficiency at the end of the gas puff for different wall conditions

Component	Temp [K]	Condition	Fuelling Efficiency
Graphite wall	570 570	He-conditioned aged	~ 0.1 ~ 0.4
Beryllium wall	570 570	fresh layer aged	~ 0.1 ~ 0.3
Beryllium wall	420 420	fresh layer aged	~ 0.3 ~ 0.4

VII. Summary and Conclusions

The evaporation of beryllium inside JET has changed considerably the behaviour of the machine and the plasma performance. Recovery from disruption was fast and density control was easily achieved. The operational space with respect to Z_{eff}-values, dilution, density and temperature could be considerably extended. The dilution was reduced and consequently the fusion parameter was doubled to 5×10^{20} $m^{-3}keVs$. The equivalent Q_{DT}-value, albeit non-stationary, approaches 0.5.

Beryllium tiles were installed on the belt limiter which required for the first time an intervention into the vessel with full biological protection. The control of the beryllium environment was successful and installation times did not require more manhours for in-vessel work than previously.

Experimental results are not yet available for the operation with the beryllium limiter. Preliminary findings indicate the possibility to obtain very low Z_{eff}-values ($<1.3-1.8$) for additionally heated discharges. Energies of up to 180 MJ were deposited on the limiter. That is twice the amount which can be taken by the graphite limiter before the occurrence of the carbon bloom. At the edges of the beryllium limiter tiles hot spots develop as also observed for the graphite. More work will be required to separate the material properties from design limitations.

The future will see the transition of JET into an even more beryllium based machine. The screens of the RF-antennae, presently nickel, will be exchanged to beryllium ones at the end of 1989. From then on operation will be possible in a machine presenting essentially only beryllium to the plasma.

Acknowledgements

References

[1] P. H. Rebut et.al., The JET Project, EUR-JET-R5

[2] P. K. Mioduszewski et.al., The Beryllium Limiter Experiment in ISX-B. Nuclear Fusion 26(1986), 1171

[3] J. Hackmann and J. Uhlenbusch, Experimental Study of the Compatibility of Beryllium Limiters with a Tokamak Plasma. Nuclear Fusion 24(1984) 640

[4] M. Bessenrodt-Weberpals, J. Hackmann, C. Nieswand and J. Uhlenbusch, The Effect of Beryllium Limiters on the Tokamak Plasma of UNITOR. J. Nucl. Mat, 162-164(1989) 435

[5] J. Bohdansky, J. Roth, W. Ottenberger, Sputtering Measurements of Beryllium. IPP-JET No 31 1985

[6] W. Möller, B.M.U. Scherzer and J. Bohdanski, Retention and Release of Deuterium Implanted into Beryllium. IPP-JET Report No 26, March 1986

[7] P. H. Rebut et.al., Low-Z Material for Limiters and Wall Surfaces in JET: Beryllium and Carbon. JET-R(85)03

[8] M. Hugon, P. P. Lallia and P. H. Rebut, A Comparison between Beryllium and Graphite as Materials for JET Limiters and Walls. JET-R(89)14

[9] G. Celentano et.al., The JET Belt Limiter. Proc. 14th Symp. Fusion Technology 1(1986)581, Avignon (France) 1986

[10] R. D. Watson and J. B. Whitley, Thermal Fatigue Tests of a Prototype Beryllium Limiter for JET. Nucl. Eng. and Design/Fusion 4(1986)49

[11] K. Sonnenberg et.al., Wall Concepts and Density Control in JET. Proc. 14th Symp. Fusion Technology 1(1986).273, Avignon (France) 1986

[12] M. Huguet and the JET Team, Technical Status of JET and Future Prospects, This Conference

[13] S. J. Booth, Contact Maintenance on JET into the Active Phase. Transactions of ENC 86, FORATOM IX, Geneva (Switzerland) 3(1986),51

[14] S. J. Booth, Management of Operational Active Wastes on JET. IAEA Technical Committee Meeting on Fusion Reactor Safety. Jackson Hole, Wyoming, USA, 1989

[15] J. Ehrenberg et.al., Hydrogen and Helium Recycling in Tokamaks with Carbon Walls. J. Nucl. Mat 162-164(1989)

[16] E. Usselmann et.al., Experimental Set-up for Gas Balance Measurement at JET. Proc. 11th Int. Vac. Congress, Cologne (W. Germany), October 1989, in preparation

[17] R. Sartori et.al., Gas Balance Measurements at JET. Proc. 16th Conf. Contr. Fusion and Plasma Physics, Venice (Italy), 3(1989),963

THE 15 MW MICROWAVE GENERATOR AND LAUNCHER OF THE LOWER HYBRID CURRENT DRIVE EXPERIMENT ON JET

M. Pain, H. Brinkschulte, G. Bosia, M. Brusati, J.A. Dobbing, A. Ekedahl, M.Gammelin, C. Gormezano, C. Idelon, J. Jacquinot, G. Jessop, A. Kaye, M. Lenholm, J. Plancoulaine, Ph. Schild, A. Sibley, T. Wade, C. Walker, R. Walton, G. Wilson

JET Joint Undertaking, Abingdon, OXON, OX14 3EA, United Kingdom

The lower hybrid current drive experiment on JET, aimed at generating current in the plasma by launching a wave at 3.7 GHz into the torus, required the building of a large high power microwave generator and antenna. The generator can provide 15 MW for 10 seconds or 12 MW for 20 seconds. This power will be fed to a phased-array antenna consisting of 48 stainless steel modules assembled in an array of 384 waveguides. The antenna position will be controlled in real time in order to optimize the coupling to the plasma. The phasing between different modules can be set so as to vary the $N_{//}$ between 1.8 and 2.4.

1 - INTRODUCTION

The lower hybrid current drive experiment on JET (1) is designed to generate large currents inside the JET plasma in order to study the effects of the modification of the current profile on energy and particle confinement. Broadening of the current profile is a way of supressing internal instabilities (such as sawtooth) linked to excessive peaking of the current profile. It is therefore expected that the profile modification will improve the energy contentand reactivity of plasmas with additional heating. Another use of LHCD current drive is the saving of volts per second in the transformer, which should enable the operation of the JET device for longer flat top pulses.

Installation of the full performance system is scheduled for the mid-1990 shutdown. Installation of a prototype antenna connected to the first two generator modules (total power 5.2 MW) is foreseen in december1989.

The general characteristics of the generator can be seen in table 1. The choice of the frequency is a compromise between physics considerations (which tend to push towards higher frequencies) and technological problems, as well as the availability of large power generating devices. Our final choice was 3.7 GHz. Large amounts of power are required, since the LHCD power injected must be in the same scale as the ohmic power. The total power output of the generator was fixed at 15 MW, and the pulse lenght to 20 seconds. Finally we were asked to include remote handling capabilities and built-in safety systems allowing operation during the tritium phase, as well as high reliability requirements, since any intervention near the JET device will be long and difficult once the tritium phase starts. This means extensive testing of all components to be installed next to the machine (antenna modules, RF windows, waveguide components, loads, etc.). This tests required the building of a test bed generator providing up to 1.3 MW, wich was in the same time used as a test bench for concepts of the main generator.

The system also has an active real time feed-back control of the position of the antenna in order to achieve an optimal power coupling to the plasma, as well as feed-back control of the phasing of the different modules in order to achieve the narrow radiated spectrum required to maximise efficiency. This also allows changing the phasing of the antenna modules in order to modify the current deposition profile.

2 - THE GENERATOR

The LHCD generator (2) will be composed of six modules of 4 klystrons each. A general diagram of such a module is shown in figure 1. Layout problems called for an extremely compact design, providing about 100kW/m2 of floor surface.

The klystrons are manufactured by Thomson-CSF and are capable of delivering 500 kW for a twenty seconds pulse or 650 kW

for a 10 seconds one, with a minimum efficiency of 40%.

The four klystrons of each module share a single high voltage power supply capable of delivering 65 kV and 100 A. The klystrons are protected by a crowbar against accidents like internal arcing.

Each klystron can be connected either to the antenna or to a matched load (for comissioning purposes) by means of a waveguide switch. Each klystron is also protected by an isolator, capable of continuous operation at a VSWR of 1.8 at maximum power, as well as short pulses at a VSWR of 3.

Each klystron is mounted in an oil tank enclosing all the klystron electrodes and components liable to be at high potential,

TABLE 1

GENERATOR		
Frequency	3.7	GHz
N0 of klystrons	24	
Total power (10s pulse)	15	MW
(20s pulse)	12	MW
Duty cycle	1/30	
Efficiency	42	%
Maximum VSWR	1.8	
Waveguide standard	RG284	
TRANSMISSION LINES		
Lenght	40m	(approx)
Losses	8	%
Material	copper	
ANTENNA		
Number of waveguides	384	
$N_{//}$	1.4 - 2.4	
Waveguide Material	Stainless steel	
Coatings	Copper + Carbon	
Maximum temperature	500	^{0}C
Total weight	8	tons
POSITION AND PHASE CONTROL		
Stroke	250	mm
Response	20mm/150ms	
Scan time of the real time controler	<40	ms
Phase accuracy	10	°

Figure 1: Functionnal blocks of a generator module.
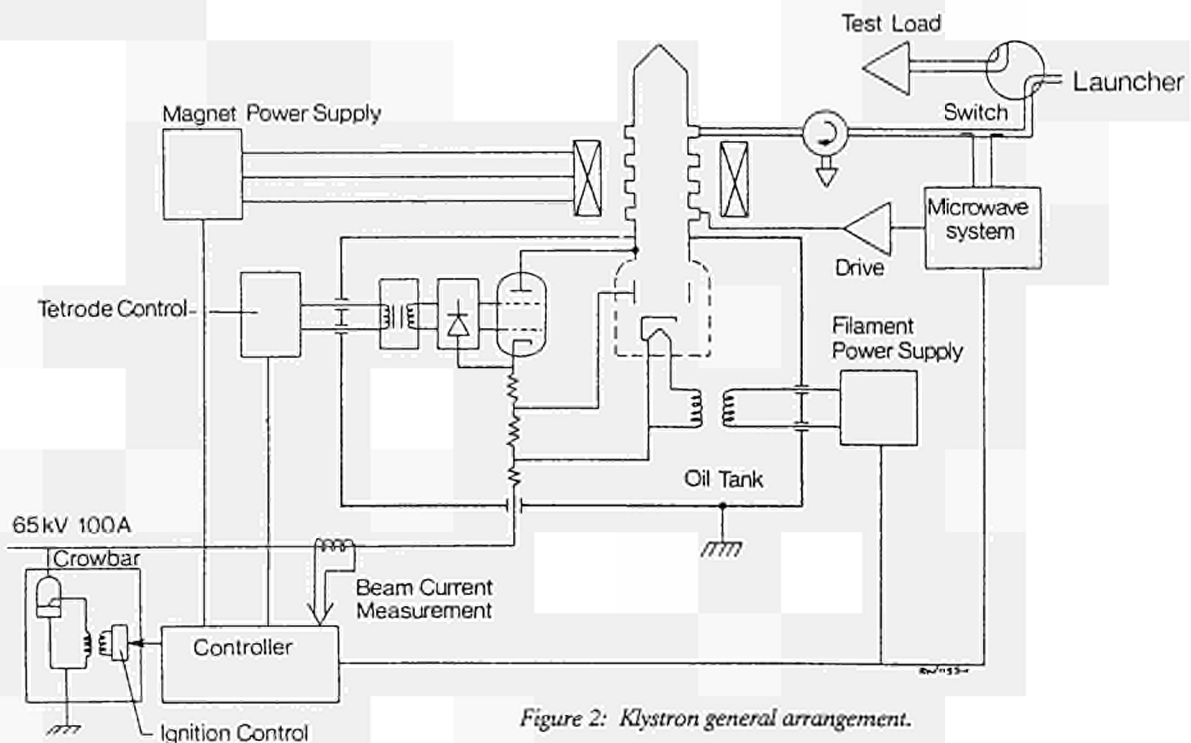
Each module has its independent programmable control logic, responsible for pulse generation and timing and interlocks checking. This logic is divided in three different stages:

- A PLC common to the four klystrons of the module takes care of all the slow interlocks (water flows, water temperature, etc.) as well as the pulse generation and human interface. It can either be operated in local mode for comissionning purposes or in remote mode. In this mode the controller is linked to the JET main computer system allowing all control operations to be executed from the JET central control room.

- Each klystron has a dedicated microprocessor board which takes care of all fast interlocks (temperature at the lips of the output cavity of the klystron, focalising magnets faults, etc.). This board is linked to the PLC which provides the human interface functions.

- Each klystron has a fast state machine, built using the principle of a programmed array having some of its inputs connected to its outputs. The behaviour of the system is summarised in figure 3: The plain arrows show the path for a normal pulse. In this situation, each state has a given lifetime (usually a few tens on miliseconds, with the exception of the RFH state, which stays on for the requested RF pulse lenght). If a fault minor fault is detected, the pulse is aborted following the reverse path. If a major fault is detected, the pulse is aborted and the crowbar fired through the emergency off state. If a high VSWR is detected, the power is turned off (RF interrupt state) and then re-applied. The state machine can make a state transition in as little as 1 microsecond.

The modularity of the generator is an important feature as it has allowed sharing of equipment between klystrons thus reducing costs, while at the same time allowing to divide the generator in reasonable sized units that can be tested and comissioned

such as the klystron filament power supply transformer, the modulating anode power supply (which controls the klystron's electron beam) and the limiting fault resistors. The modulating anode potential is controlled through high frequency isolation transformers followed by rectifiers, thus allowing the control electronics to remain at ground potential. The general arrangement can be seen in figure 2.

Figure 2: Klystron general arrangement.

separately. A prototype of one module containing only two klystrons was built to be used as a high power test facility for microwave components as well as a test bench for the conception of the generators has been in operation since July 1988, and was found to be safe to operate and easy to maintain, once the initial bugs were cleared out.
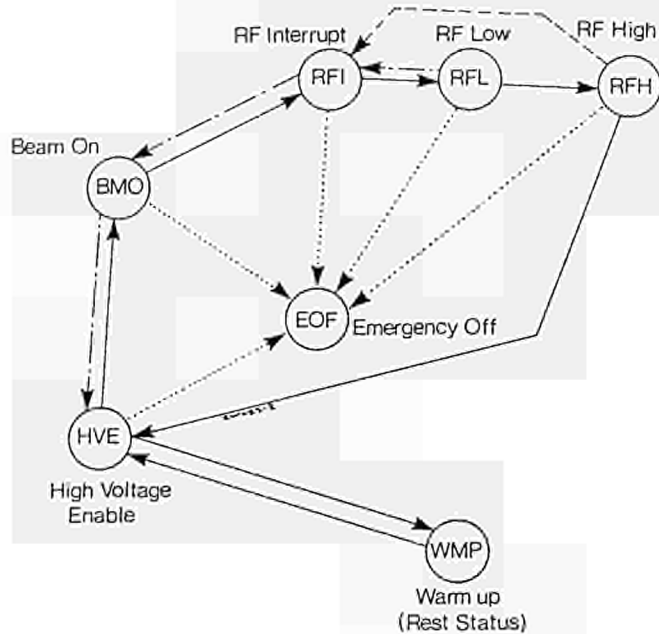
Figure 3: States diagram of the klystron fast logic controller.
——— Normal path during a pulse.
- - - - Transition prompted by high reflection.
— · — · Transition prompted by minor faults.
·········· Transition prompted by a major fault.

3 - TRANSMISSION LINES

The transmission lines running from the klystron to the splitting network are built in copper. Special flanges have been designed to suit remote handling requirements. This flanges are larger than normal UDR32, giving more space for the remote handling robot to work. Special reusable gaskets have been developed. This gaskets do not mark the flanges, which is an advantage over normal knurled ones.

The section of the waveguide going from the klystron to the microwave switch follows the WG284 standard dimensions (72x34mm). This section is water ·cooled, in order to reduce stresses due to thermal expansion.

The section going from the switch to the splitting network starts with a DC break (to isolate the generator from the torus potential) followed by about 30 m of slightly overdimensionned waveguide (77x38.6mm). The lines have been built in such a way as to make all of them of the same lenght. This reduces the dynamic range of the phase control system, as the lines expand by roughly the same amount during the pulse. The phase control system only has to correct the small errors arising from the differences in klystrons power output, cooling speeds or loss coefficients of different lines. This section is cooled by natural convection.

The whole line is pressurised to 1 bar of SF6 in order to improve its power handling capabilities. The lines have a measured loss of about 8% per 30 m.

4 - ANTENNA

The design of the antenna (3) was severely constrained by the particularities of the JET machine, in particular the size of the JET port and the remote handling and tritium containment requirements. The only available location for the antenna was one of the main horizontal ports (0.4 x 1 m). The antenna is a phased array of waveguides 72x9mm each separated by 2mm walls. There is 12 rows x 32 columns of waveguides making a total of 384 waveguides.

The splitting network required to feed this array can be seen in figure 4. First the power coming from each klystron is divided in two by a hybrid junction on the pressurised waveguide side (that is, before the window isolating the transmission line from the toruws vacuum). This first split on the pressurised side simplifies the design of the RF windows, as each one only handles one half of the klystron total power. Convection cooled flexible sections are inserted to allow the movement of the launcher. We use double beryllium oxide windows, in order to provide tritium containment as well as greater protection to the JET vacuum in case of breakdown. The insterspace between those windows is pumped by an ion pump that allows for the vacuum to be monitored. After the window separating the pressurised waveguides from the torus vacuum, each waveguide is split in eight using the "multijunction" arrangement (see Fig 5). Each multijunction uses 6 E-plane junctions and one H-plane junction as well as waveguide phase shifters to provide at the output side a 2 rows x 4 columns array. The full launcher requires then 48 multijunctions. The multijunction concept has also the advantage of reducing the power reflected to the klystron in case of mismatch at the mouth of the antenna. By phasing properly the klystrons that feed different multijunctions the $N_{//}$ of the launched wave can be varied from 1.4 to 2.4.

The material chosen for the multijunctions is stainless steel, in order to be able to bake the launcher at 500 degrees. Stainless steel also reduces the forces due to disruptions as its conductivity is low compared to copper. The main inconvenient is that in order to reduce RF losses it is imperative to coat the multijunction with a high conductivity material, copper in our case. The coating is then carbonised in order to reduce the multipactor effect by baking it in an acethylene athmosphere at 500 degrees. Rough coatings such as gold were tested but found to have unacceptable losses.

The fourth port of the H plane junction is connected to a matched load. This load is made of carbon coated with silicon carbide, and is cooled by radiation in the same way the multijunctions are.

The whole set of multijunctions are kept together by a rigid mechanic structure. As the mouth of the antenna is to be moved in order to seek the optimal coupling, which is very dependent on density, this structure is supported by two hangers (one near the mouth, the other at the rear of the assembly). The inner hanger has been most complicated to design, since it has to sustain the difficult environment existing in the torus vacuum while allowing free movement to the launcher along one axis and keeping it centered inside the frame of the torus port. A flexi-pivot design was preferred to a bearing system in consideration of the environment roughness. The launcher is enclosed in a vacuum vessel linked to the vacuum vessel by a 1.5 m diameter double inconel bellow. A system of hydraulic actuators with a typical response of 20mm in 150 ms and a full stroke of 25 cm will provide
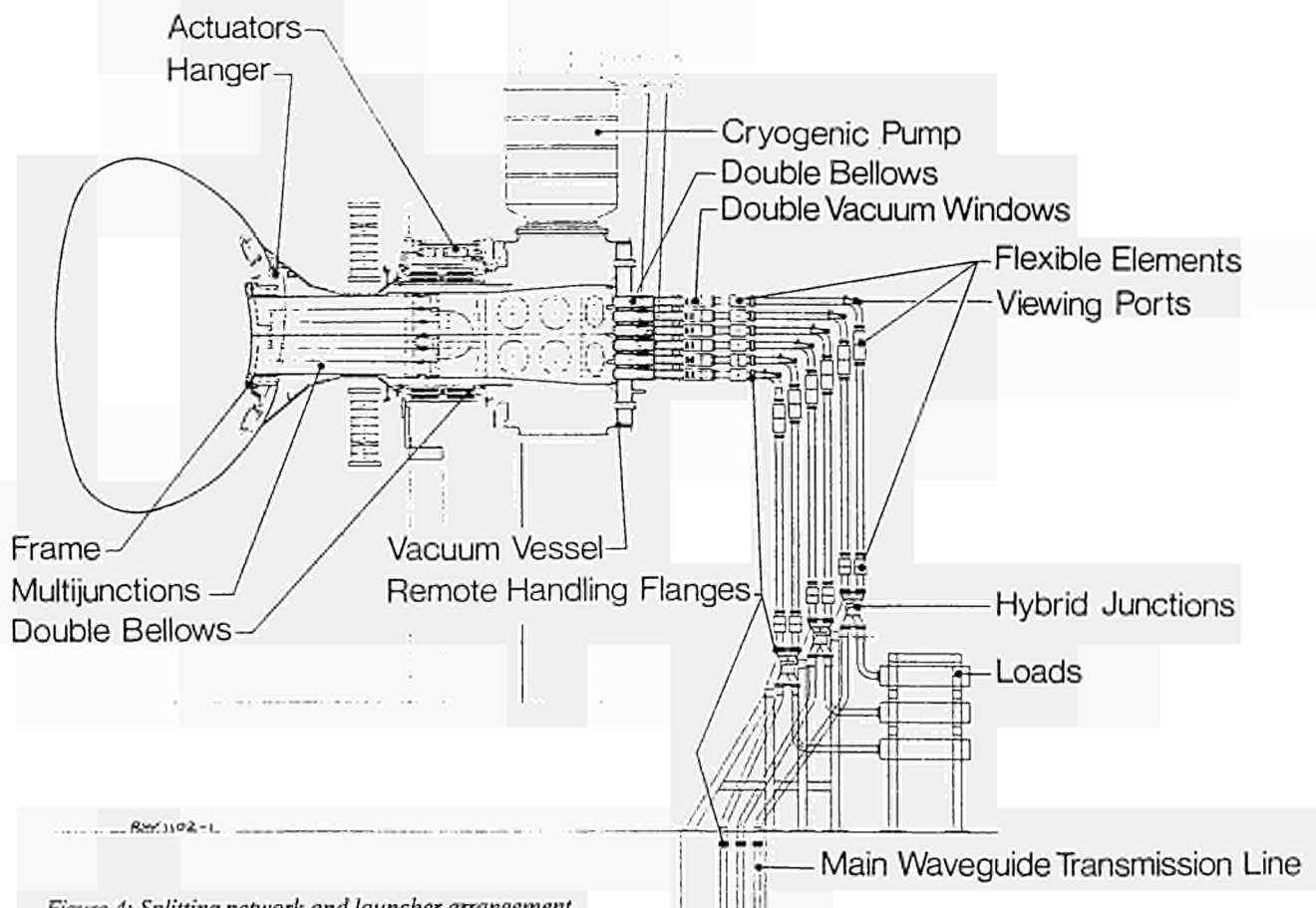
Figure 4: Splitting network and launcher arrangement.

the moving power. To avoid formation of plasma inside the waveguides the vacuum vessel is pumped by a 100.000 l/s cryopump. This type of pump is required in order to comply with the tritium control rules.

The mouth of the launcher is shaped both in the toroidal and poloidal direction. This implies that all the multijunctions have to have slightly different phase shifters as their lenght after shaping is different. The mouth is protected from the plasma by a frame covered with carbon tiles. They might be replaced with beryllium ones if required.

All the components of the prototype launcher have already been tested at high power (including the multijunctions, which required the design of a special eight-inputs matched load), and the assembly of the launcher is now well advanced. Moreover, the multijunctions were tested used a specially developped computer driven test bench, allowing the complete measurement of the scattering matrix at low power.

5 - PHASE CONTROL AND POSITION CONTROL

The phase control system (4) is intended to maintain a constant phase shift between adjacent rows of multijunctions in the antenna: If the phase shift between adjacent waveguides of the same multijunction is defined by the dimensions of the multijunction, the phase relation between contiguous waveguides belonging to two different multijunctions denpends on the phase relation of the klystrons that feed those multijunctions and on the lenght of the transmission lines. The transmission lines have

been designed to be of the same lenght for all klystrons, in order to have the same expansion during the pulse. But in order to keep the klystrons in phase and to compensate any differential dilatation during the pulse, an active compensation system was required. The system acts on the klystron by changing the phase of the drive power fed to it. But the main problem is how to measure the phase at the mouth of the antenna since all equipment installed near the torus has to be neutron resistant, which excludes any semiconductor device and greatly increases the cost of any solution using cables as a measuring intermediary. The chosen system was to use the cross talk between different multijunctions. The power is sent through one of the lines and the power coming back is monitored in the two adjacent lines. This allows to compare the phase error due to differential dilatation between those two lines. This measure cannot be done at 3.7 GHz, because the structure of the multijunction has been studied precisely to send back to the plasma any power coming to its mouth, and also because this would require all the other klystrons to be stopped for the duration of the measurement. By shifting the frequency, the multijunction effect is prevented from working, and the measurement becomes possible whithout perturbating the other klystrons. The system shifts periodically (for about 1 ms every 500 ms) the frequency of each klystron (by about 3 MHz) in turn in order to scan all lines. The system also sets the amplitude of the drive so as to keep the power output equal to the set points provided by the control logic. the system also generates the signals to trip the system in case of high reflection from the antenna.

The position control system is intended as a close loop feeding the actuators system with the position set point calculated by using diagnostics such as the density at the mouth of the antenna (using Langmuir probes) and the power reflected to the klystron in each line. The system will cause the antenna to move in such a way as to minimize the reflected power, as this would mean that the antenna is well matched. The calculations required to convert the input information in the position set point are carried out by a real-time computer, giving maximum flexibility in the choice an parametrisation of the algorithm.

H - plane junction

E - plane junction
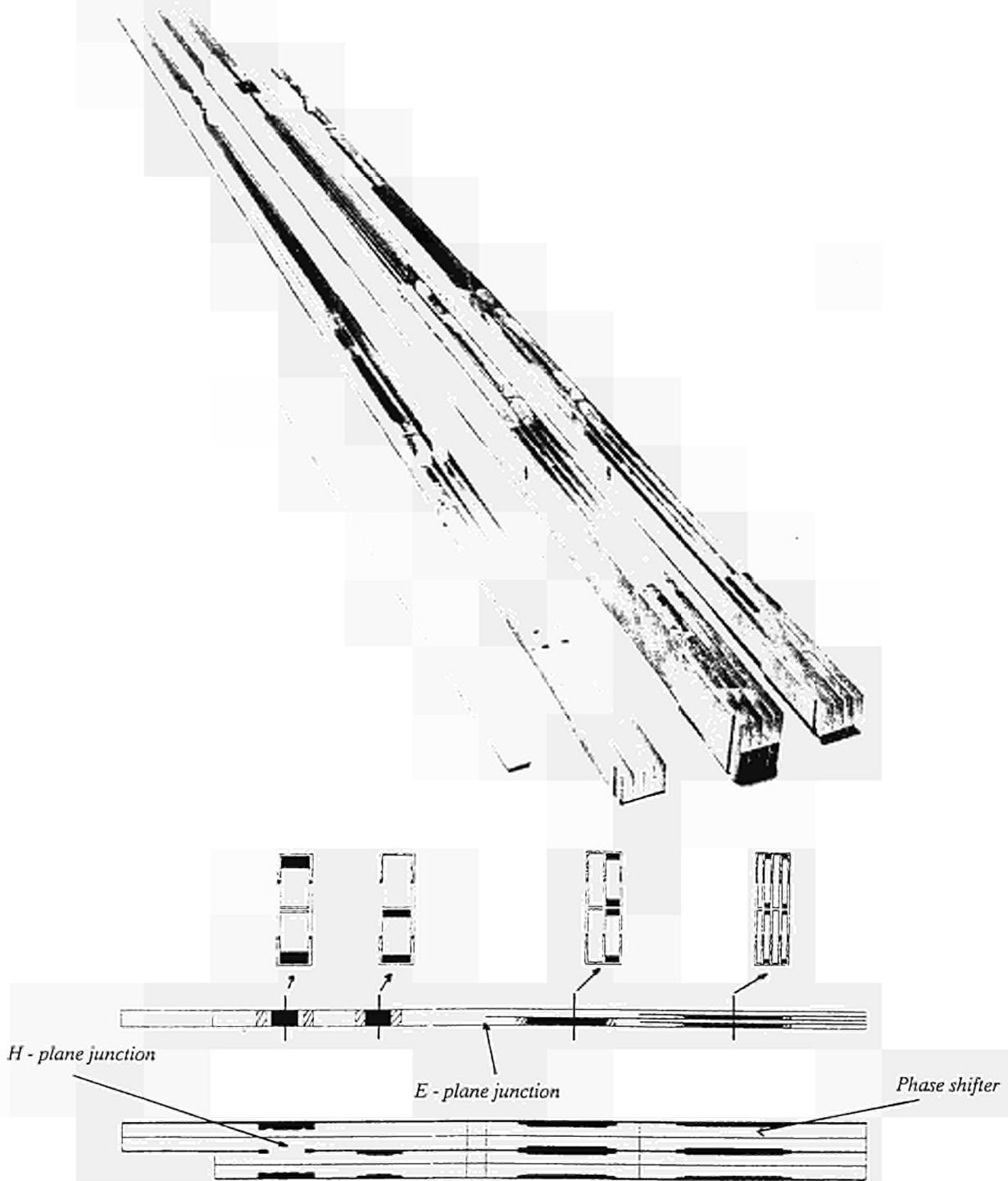
Phase shifter

Figure 5: a) Components of a "multijunction" module before brazing.
b) Diagrams of a multijunction showing the H and E plane
juctions as well as the different phase shifters.

A151

6 - CONCLUSION

In addition to the assesment of the interest of the lower hybrid current drive scheme for the future, the lower hybrid current drive experiment will allow us to analyse the difficulties of such an installation in the perspective of a reactor.

The main difficulty has to do with the coupling to the plasma: The surface of the launcher being important, we will check that it is possible to achieve a good matching in all the waveguides by moving the whole antenna. The development of the real-time position control system will be an essential part of this goal. The distance between the protective frame and the mouth of the grill is another parameter to be tested, since a compromise must be found between the high densities (around 10^{18} cm-3) required to achieve a good coupling and the resitance to erosion by the plasma of the antenna mouth.

We will also check that it is possible to operate such a system with diagnostic methods compatible with high neutron flux environments such as the phase measurements by frequency shifting. Finally, this experiment will highlight the problems linked with this type of antenna concept in order to assess its relevance to a future reactor design.

7 - REFERENCES

(1) C. Gormezano et al., Proceedings 12th Symp. on Fus. Eng., Vol. 1 P. 38 (Monterrey, 1987)

(2) J. A. Dobbing et al., 15th SOFT proceedings, Vol. 1 P. 454, (Utrecht, 1988)

(3) A. Kaye et al., 15th SOFT proceedings, Vol. 1 P. 449 (Utrecht, 1988)

(4) G. Bosia et al., Proceedings 7th Conf. on Appl. of RF Power to Plasmas, P. 139 (Kissimee, 1987)

M E P Wykes
JET Joint Undertaking, Abingdon, Oxfordshire, OX14 3EA, England

Abstract

A considerable area of the JET First Wall will be clad with graphite protection tiles for D-T operation. During plasma discharges, tiles will be subjected to high thermal fluxes and consequent high temperatures. Accidental loss of vacuum through air inleakage in such a situation could cause graphite oxidation and concommitant energy input to the inleaking gas. The JET Exhaust Detritiation System (EDS) is designed to prevent the escape of tritiated gases and activated or toxic dust from the torus by pumping the breached torus to maintain a slightly sub-atmospheric pressure. The objective of the safety analysis presented herein is to validate that the design pumping capacity of the EDS is adequate to cater for the peak graphite oxidation rates envisaged during a potential air inleakage incident with hot graphite in JET.

Introduction

During D-T operation of JET, considerable quantities of frozen tritium will accumulate on the helium panels of the neutral injector, pellet injector and divertor cryopumps. Loss of vacuum by air inleakage could initiate uncontrolled regeneration of the pumps, allowing gaseous tritium to spread throughout the vacuum enclosure. For breaches above a certain size, the possibility would exist of complete loss of vacuum and efflux of tritiated gas out through the breach to the external environment. Such a situation will be safely contained by the EDS.

Analytic Approach

The analysis is guided by the following principles:

* All assumptions should be conservative to produce upper bound values of safety related parameters.

* To formulate as simple a model as possible, consistent with adequately representing the processes involved.

* To obtain closed solutions, i.e. algebraic formulae rather than computer generated numerical data, both to facilitate checking of results and to allow rapid study of parameter variations.
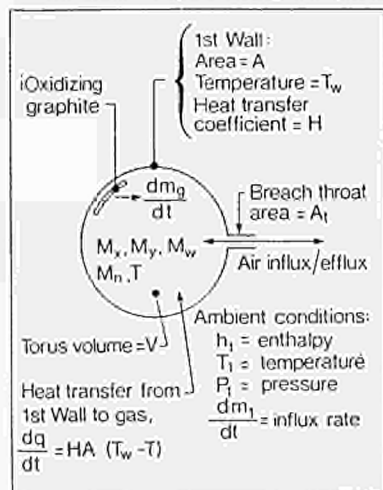
Figure 1: Air Inleakage Model

Figure 1 shows a schematic of a breached torus during a time interval (dt), with air inleakage, oxidizing graphite and heat transfer from the first wall to the influxed gas within the torus. The symbols for Fig 1 and the subsequent analysis are defined as follows:-

|	
A	- first wall heat transfer area
A_t	- breach throat area
$C_{x,y,w,n}$	- Gravimetric constant volume specific heats of O_2, CO, CO_2, N_2
$d( )$	- infintesimal change in process variable during time interval dt
F	- mol fraction of CO in oxidation products
H	- first wall surface to influxed gas heat transfer coefficient
h_1	- influx air stagnation enthalpy
K	- O_2 mass fraction of influx air
$k_{x,y,w,n}$	- gravimetric constant volume specific heats of O_2, CO, CO_2, N_2
$M_{x,y,w,n}$	- instanteous masses of O_2, CO, CO_2 and N_2 at time t after influx start
$dm_{x1,y1,w1,n1}$	- efflux rates of O_2, CO, CO_2, N_2
$\dfrac{dm_g}{dt}$	- gravimetric graphite oxidation rate($= \dot{m}_g$)
$\dfrac{dm_1}{dt}$	- influx air mass flow rate ($= \dot{m}_1$)
$\dot{N}_e$	- total molar efflux rate from torus
P_1	- atmospheric pressure
P_t	- breach throat pressure
R_o	- universal gas constant
$R_{x,y,w,n}$	- characteristic gas constants of O_2, CO, CO_2 and N_2
t	- elapsed time after influx (or efflux) start
T	- mixed mean temperature of gas in torus (absolute)
U	- total internal energy of gases in torus
V	- total torus volume
v_1	- ambient specific volume of influx air
$\Delta U_{y,w}$	- energy of formation of CO and CO_2 (at absolute zero) per kg oxidized graphite
θ_g	- oxidising graphite temperature
θ	- mixed mean efflux temperature

Influx Phase Analysis

Applying the 1st Law of Thermodynamics to the breached torus during a time interval (dt), at time t after influx start, yields:

$$dq = HA(T_w - T) = d(u) - h_1 dm_1 \qquad (1)$$

The total internal energy change, including the incremental oxidation process is:

$$d(u) = \left[M_x C_x + M_y C_y + M_w C_w + M_n C_n \right] dT$$

$$+ \left[C_x dM_x + C_y dM_y + C_w dM_w + C_n dM_n \right] T$$

$$- \left[\Delta U_y F + \Delta U_w (1-F) \right] dm_g \qquad (2)$$

For the oxidizing graphite, the mol and mass balances are:

$$\text{mol: } C + (1-\tfrac{F}{2})O_2 \rightarrow (F)CO + (1-F)CO_2$$
$$\{12\} \quad \{32\} \quad \{28\} \quad \{44\} \tag{3}$$
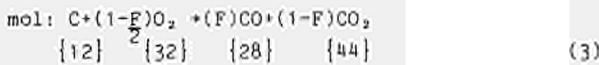
the rounded mol weights are shown bracketed

$$\text{mass: } dm_g + \tfrac{32}{12}(1-\tfrac{F}{2})dM_x \rightarrow \tfrac{28}{12}F dM_y + \tfrac{44}{12}(1-F)dM_w \tag{4}$$

For the influxing gases, the mass balances are:

$$dM_x = K dm_1 - \tfrac{32}{12}(1-\tfrac{F}{2})dm_g \tag{5}$$

$$dM_y = \tfrac{28}{12} F dm_g \tag{6}$$

$$dM_w = \tfrac{44}{12}(1-F)dm_g \tag{7}$$

$$dM_n = (1-K)dm_1 \tag{8}$$

Combining Equs (5),(6),(7) and (8) with Equ (2) and dividing by (dt) gives:

$$\frac{d(u)}{dt} = \left[M_x C_x + M_y C_y + M_w C_w + M_n C_n \right]\frac{dT}{dt}$$
$$+ T\left[\frac{dm_g}{dt}\left\{\tfrac{28}{12}C_y F + \tfrac{44}{12}C_w(1-F) - \tfrac{32}{12}C_x(1-\tfrac{F}{2})\right\} \right.$$
$$\left. + \frac{dm_1}{dt}\left\{K C_x + (1-K)C_n\right\} \right]$$
$$- \left[\Delta U_y F + \Delta U_w(1-F) \right]\frac{dm_g}{dt} \tag{9}$$

The 1st Law differential equation (as given by Equs (1) and (9)) requires the specification of the independant variable input flows dm_1 and $\frac{dm_g}{dt}$ in order to effect a solution. The simplest assumption would be that both flows are constant, but before proceeding in this manner, the validity of this assumption must be checked.

Simplifying Assumptions

The influx through the torus breach may be represented as an isentropic nozzle flow, for which the mass flow equations are (2):

$$\frac{dm_1}{dt} = \frac{A_t}{v_1}\left[\gamma R_1 T_1 \left(\tfrac{2}{\gamma+1}\right)^{\frac{\gamma+1}{\gamma-1}} \right]^{\frac{1}{2}} \quad ; \quad \frac{P_t}{P_1} < \left(\tfrac{2}{\gamma+1}\right)^{\frac{\gamma}{\gamma-1}} \tag{10}$$

$$= \frac{A_t}{v_1}\left[\left(\tfrac{2\gamma}{\gamma-1}\right) R_1 T_1 \left\{ \left(\tfrac{P_2}{P_1}\right)^{\frac{2}{\gamma}} - \left(\tfrac{P_2}{P_1}\right)^{\frac{\gamma+1}{\gamma}} \right\} \right]^{\frac{1}{2}} \quad ; \quad \frac{P_2}{P_1} > \left(\tfrac{2}{\gamma+1}\right)^{\frac{\gamma}{\gamma-1}} \tag{11}$$

Table 1 gives the variation of specific influx flow rate with breach throat pressure ratio for normal air, and demonstrates that for the major portion of the influx the inflow is constant at the choked value.

$\frac{v_1}{A_t}\frac{dm_1}{dt}$	201	201	201	201	201	201	198	187	164	124
$\frac{P_t}{P_1}$	0.1	0.2	0.3	0.4	0.5	0.58	0.6	0.7	0.8	0.9

+ critical pressure ratio

Table 1: Variation of Specific Influx Flow Rate with Breach Throat Pressure Ratio

Moreover the assumption of constant choked flow would tend to underestimate the influx period and also the total quantity of gas entering the torus. Thus it is acceptable for the present analysis and:

$$\frac{dm_1}{dt} = \dot{m}_1 = \text{constant} \tag{12}$$

The graphite oxidation rate can be expressed as an Arrhenius type relationship:-

$$\frac{dm_g}{dt} \propto \exp\left(-\tfrac{1}{\theta_g}\right) \tag{13}$$

The oxidizing graphite temperature θ_g is governed by the tile power balance thus:

$$\frac{d\theta_g}{dt} \propto \Sigma \text{ Power flows to/from graphite}$$
$$\text{(radiation, convection, conduction,)}$$
$$\text{(particles, heat of oxidation)}$$

If the power balance is:-

+ ve ; $\frac{dm_g}{dt}$, θ increase

- ve ; decrease

o ; constant

A study of the JET graphite power balance under air inleakage conditions is being performed. The study is not presently concluded but initial indications are that the power balance will be strongly negative for the highest envisaged plasma power loading of 10 MW/m² (corresponding to a localised hot spot), compared to normal operation plasma loading of 1.2 MW/m². Figure 2 shows a computed average temperature history of a JET CFC

CFC INNER WALL TILE AT 10MW/m²
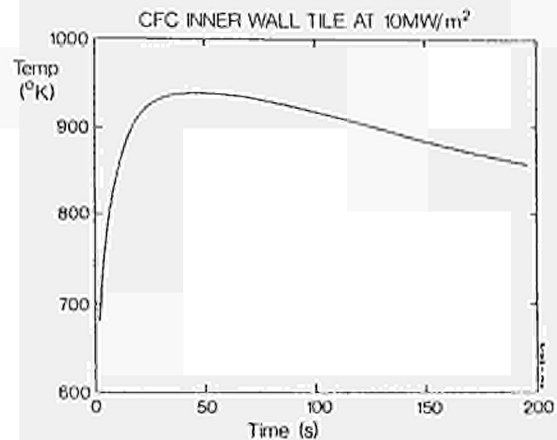
Fig.2 Average temperature of inner wall tile, initial temperature = 670°K

graphite inner wall tile following irradiation at 10MW/m² under UHV conditions (1). The peak average temperature is attained after ~ 45s and the subsequent temperature decay is due to radiative losses only. It is anticipated that the decay will be considerably enhanced during an air inleakage incident by convection and conduction heat transfer. As an upper bound value, it is assumed that the graphite power balance is zero with a constant oxidation rate corresponding to the maximum temperature shown in Fig 2, ie. 950°K.

Simplified Influx Analysis

With the oxidation and influx flow rates constant, the O_2 mass balance (Equ 5) becomes:

$$\frac{dM_x}{dt} = K\dot{m}_i - \frac{32}{12}(1-\frac{F}{2})\dot{m}_g \qquad (14)$$

Integration yields: $M_x = \left[K\dot{m}_i - \frac{32}{12}(1-\frac{F}{2})\dot{m}_g\right]t \qquad (15)$

Similarly for CO, CO_2 and N_2 (Equs (6),(7) and (8)):

$$\frac{dM_y}{dt} = \frac{28}{12}F\dot{m}_g \qquad ; \quad M_y = \frac{28}{12}F\dot{m}_g t \qquad (16)$$

$$\frac{dM_w}{dt} = \frac{44}{12}(1-F)\dot{m}_g \quad ; \quad M_w = \frac{44}{12}(1-F)\dot{m}_g t \qquad (17)$$

$$\frac{dM_n}{dt} = (1-K)\dot{m}_i \quad ; \quad M_n = (1-K)\dot{m}_i t \qquad (18)$$

Substituting Equs (14) to (18) and (9) into (1) gives:

$$HA(T_w-T) = (T+t\frac{dT}{dt})\left[\begin{array}{l}\dot{m}_i\{KC_x+(1-K)C_n\} \\ +\dot{m}_g\{\frac{28}{12}FC_y+\frac{44}{12}(1-F)C_w-\frac{32}{12}(1-\frac{F}{2})C_x\}\end{array}\right]$$

$$- \dot{m}_g\left(\Delta U_y F+\Delta U_w(1-F)\right) \qquad (19)$$

This may be rewritten as:

$$\frac{dT}{dt} + \frac{T}{t}\left(1+\frac{HA}{G}\right) = \frac{L}{Gt} \qquad (20)$$

where:

$$G = \dot{m}_i\{KC_x+(1-K)C_n\}+\dot{m}_g\{\frac{28}{12}FC_y+\frac{44}{12}(1-F)C_w-\frac{32}{12}(1-\frac{F}{2})C_x\}$$

$$L = HAT_w+\dot{m}_g\{\Delta U_y F+\Delta U_w(1-F)\}$$

The Integrating Factor for Equ (20) is (3)

$$I = \exp\left(\int(1+\frac{HA}{G})\frac{dt}{t}\right)= t^{(1+\frac{HA}{G})} \qquad (21)$$

With this Integrating Factor, the general solution to Equ (20) is:

$$T = \left[\frac{L}{G+HA}\right] + J\,t^{-(1+\frac{HA}{G})} \qquad (22)$$

J is a constant of integration and in the present context must be zero if T is to remain finite as t tends towards zero. The influxed gas temperature is then:

$$T= \frac{HAT_w+\dot{m}_g\left(\Delta U_y F+\Delta U_w(1-F)\right)+\dot{m}_i h_i}{HA+\dot{m}_i\left(KC_x+(1-K)C_n\right)+\dot{m}_g\left(\frac{28}{12}FC_y+\frac{44}{12}(1-F)C_w-\frac{32}{12}(1-\frac{F}{2})C_x\right)}$$

$$(23)$$

The influx period τ_i is determined from the condition that at the end of the influx, the sum of the partial pressures of the gases in the torus is equal to atmospheric pressure, ie.

$$P_i = \frac{T}{V}\left(M_x R_x+M_y R_y+M_w R_w+M_n R_n\right) \qquad (24)$$

where M_x, M_y, M_w and M_n are given by Equs (15), (16), (17) and (10) with $t=\tau_i$. Using these equations, and noting that the product of the molecular weight and characteristic gas constant for each of the oxidized product gases is equal to the universal gas constant R_o, the influx period is given by:

$$\tau_i = \frac{V\,P_i}{\dot{m}_i\{KR_x+(1-K)R_n\}+\frac{FR_o}{24}\dot{m}_g\}} \qquad (25)$$

Efflux Phase

At the end of the influx phase, the gases in the breached torus would tend to efflux out of the breach, driven by both the continuing oxidation and heat transfer from the first wall. In this section, expressions for the dynamic efflux temperature (θ) and the molar flow rate from the torus are presented.

By applying the 1st Law of Thermodynamics, gas mass balances and assuming that the sum of the partial pressures of the gases is equal to atmospheric pressure at all times during the efflux, it can be shown (4) that the temperature during efflux is given by:-

$$\theta = \frac{(HAT_w+\Psi)T}{(HAT_w+\Psi)\exp(\frac{-t}{\tau_e})+T(HA+\lambda)(1-\exp(\frac{-t}{\tau_e}))} \qquad (26)$$

where: $\Psi = \dot{m}_g\left(\Delta U_y F+\Delta U_w(1-F)\right) \qquad (27)$

$$\lambda = \dot{m}_g\left(\frac{28}{12}Fk_y+\frac{44}{12}(1-F)k_w-\frac{32}{12}(1-\frac{F}{2})k_x\right) \qquad (28)$$

$$\tau_e = \frac{\gamma P_i V}{(\gamma-1)(HAT_w+\Psi)} \qquad (29)$$

Likewise, it can be shown, with the assumption that the gases have a common isentropic index, that the molar efflux rate is given by:-

$$\dot{N}_e =\left(\frac{(HAT_w+\Psi)-(HA+\lambda)T}{R_o T}\right)\frac{\gamma}{(\gamma-1)} \exp\left(\frac{-t}{\tau_e}\right) \qquad (30)$$

JET Pertinent Parameter Values

The most uncertain parameter is the graphite oxidation rate $\dot{m}_g$. To obtain an upper bound value, it is assumed that:-

* Maximum oxidizing graphite area would be:

$$Area = \frac{total\ inner\ wall\ power\ load}{specific\ inner\ wall\ power\ load} = \frac{40(MW)}{10(\frac{MW}{m^2})} = 4m^2$$

* The graphite oxidation rate data of O'Brien et al(5) is applicable, ie:

$$r = 16\exp\left(\frac{-5710}{\theta_g}\right); \theta_g<1273°K; g/min \qquad (31)$$

Assuming a constant graphite temperature equal to the peak value shown in Fig 2 (ie. zero power balance assumption), the corresponding oxidization rate for the test samples of Ref(5) would be:-

$$r = 0.0392\ g/min$$

Scaling this value by the area ratio of the Ref(5) test samples and the JET upper bound oxidizing area ($4m^2$) yields:-

$$\dot{m}_g = 0.0024\ kg/s \qquad (32)$$

The ambient air influx is assumed to arise from the instantaneous shattering of a 100mm diameter diagnostic window assembly. For normal air (K = 0.23) at a stagnation temperature of 300°K, the choked flow rate, from Equ 10, is:-

$$\dot{m}_i = 1.83\ kg/s \qquad (33)$$

Additional parameter values are:-

$T_i = 300°K; T_w = 573°K; A = 220m^2$

$H = 5W/m^2°K; V = 280m^3$ (torus+1NIB+LHCD)

Thermodynamic data are from Ref(6), in particular:

$\Delta U_y = -9490$ }
$\Delta U_w = -32785$ } kJ/kg oxidized graphite

Numerical Results for Influx and Efflux

To give an overview of the relative influences of the first wall heat transfer and oxidation processes on the influx and efflux characteristics, the salient process variables are evaluated from the derived expressions, using the parameter values outlined in the previous section, for the 4 following cases

H = 0 } with $\dot{m}_g$ = 0 and 0.0024kg/s

H = 5 }   (F = 0 and F = 0.5)

The numerical results are shown Table 2:

Variable		$\dot{m}_g$ = 0		$\dot{m}_g$ = 0.0024 (kg/s)	
		H = 0	H = 5	H = 0	H = 5
T(°K)		420	494	466(487)	514(526)
τ_i(s)		127	107	113(108)	103(100)
Influxed	M_x	48.8	41	42(40.8)	39(38.4)
Gas	M_y	0	0	0.32(0)	0.29(0)
Masses	M_w	0	0	0.5(0.95)	0.45(0.88)
(kg)	M_n	183.6	155	163(156)	149(144)
Energy transfers (MJ)					
First Wall heat transfer		0	9.3	0	6.7(5.2)
Recompression		18.2	15.3	16.1(15.4)	14.7(14.2)
Oxidation		0	0	5.7(7.9)	5.2(7.8)
$\dot{N}_e$} max m³ STP/h		0	488	445(F=0) 296(F=0.5) 134(F=1)	684(F=0) 619(F=0.5) 538(F=1)
τ_e(s)		-	155	1930(1245)	144(138)

Table 2: Numerical results for influx and efflux; normal influx air (F=0 values bracketed)

Discussion of Results

The predicted influx temperatures (Table 2) span the range 420 to 526°K for the selected parameter variations. The lowest value (no first wall heat transfer or oxidation) is the minimum which could obtain with air inleakage. It can be shown (7) that in this limiting case, the influx temperature is given by the product of the ambient temperature (T_1) and the isentropic index (Y) of the influxing gas. The influx temperature increases with both heat transfer and oxidation, the incremental contribution of the two effects being of the same order. The peak temperature of 526°K corresponds to complete oxidation to CO_2.

The influx period (τ_i) reduces with both heat transfer and oxidation, directly reflecting the increase in influx temperatures which reduce the gas masses in the torus at influx end. This effect is shown in the influxed gas mass results, which also indicate the small quantities of CO and CO_2 generated.

The energy transfer results indicate that for all the paramter cases considered the work done by the external atmosphere in recompressing the influxed gases is the dominant term. Even though

the oxidation rate is small, the energy release is of the same order as that due to first wall heat transfer, reflecting the large energies of formation of CO and CO_2.

The peak efflux rate without oxidation (at H=5W/m²°K) is predicted as 488m³STP/h. This is increased somewhat by oxidation, the increase depending on the fraction of Co in the oxidation products (maximum value with 100% CO_2). The efflux time constant is much larger with oxidation at zero heat transfer due to the source term in Equ (29).

The peak efflux rate predicted is 684m³ STP/h. This is somewhat in excess of the design EDS pumping capacity of 600m³/h. However, in practice, the EDS will start pumping before the breached torus attains atmospheric pressure. Moreover, the assumptions used in the analyses are very conservative, particularly that of the graphite zero power balance and it is envisaged that the EDS will cope safely and adequately with the exhaust from such an air inleakage accident.

This aspect will be reviewed following completion of the aforementioned graphite power balance study.

Summary

*   Graphite oxidation will not be a major influence on the influx characteristics during a loss of vacuum by accidental air inleakage in JET.

*   The dominant energy transfer is that due to recompression of the influxed gases by the external atmosphere.

*   In the event of such an air inleakage accident, the EDS will safely pump away the exhaust gases and maintain the breached torus at subatmospheric pressure.

References

(1) E Deksnis, C Earl, "The implementation of TOPAZ, DYNA and NIKE on the JET mainframe computer", JET Report, to be published, 1989

(2) AH Shapiro, "The dynamics and thermodynamics of compressible flow 1 and 2", Ronald Press, 1953 and 1954

(3) HTH Piaggio, "Differential equations", G Bell & Sons, 1960

(4) MEP Wykes, "Graphite oxidation effects on a potential loss of vacuum incident in JET", JET Report, to be published, 1989

(5) MH O'Brien et al, "Combustion testing and thermal modelling of proposed CIT graphite tile materials", Idaho National Engineering Laboratory Informal Report EGG-FSP-8255, Sept 1988

(6) JANAF "Thermochemical Tables", 2nd Edition 1971

(7) MEP Wykes, " Safety analysis of torus vacuum breach", JET-P(88)37,1988

LEVEL 1 SOFTWARE AT JET: A GLOBAL TOOL FOR PHYSICS OPERATION

H van der Beken, BJ Green, CA Steed, JET Joint Undertaking, Abingdon, Oxon OX14 3EA, UK
JW Farthing, PA McCullen, TRASYS, Rue d'Arlon 88-B, Brussels, BELGIUM
J How, TORE SUPRA, CEA, CEN Cadarache, St Paul-lez-Durance, FRANCE

Abstract

The operation of JET is done from a central control room, through a computer assisted COntrol and Data Acquisition System (CODAS). After manual selection of the required parameters and waveforms, the preparation and execution of each pulse is controlled by the computers. As experience was gained in operations, the need became evident for an integrated tool to prepare pulse schedules and to improve the selection of parameters and their monitoring. This led to the development of additional components of the "LEVEL 1" software with the following aims:

* to provide a convenient pulse schedule preparation tool including conversion algorithms from plasma to machine control parameters.
* to improve and integrate the parameter setting tools.
* to provide parameter validation at pulse schedule preparation and parameter setting times
* to allow to recall "old" pulses.

The paper describes the structure of the suite of software developed for this purpose, along with its present status.

Introduction

The Joint European Torus (JET) is a large Tokamak experiment designed to study fusion in conditions approaching those required for a reactor. The COntrol and Data Acquisition System (CODAS) is based on a hierarchical network of some 20 Norsk Data computers. The interface between the computers and the experiment hardware is through CAMAC instrumentation which covers both the control and data acquisition requirements for JET. Before a JET discharge the CODAS computers set up all the control parameters needed to execute the required pulse and perform the acquisition of data from all subsystem computers on completion of the pulse. The design and operation of CODAS and the evolution of the data acquisition, from its initial implementation, have been adequately described elsewhere [1], [2], and will not be covered here. This paper presents the development of additional components of the supervisory (LEVEL 1) software to provide a more general tool to assist in the Physics operation of the JET experiment.

Software Concepts

The organisation of the CODAS computers is shown in Fig 1. From the outset it was decided to split the operational hardware of JET into its main functional components and to assign each component its own subsystem computer. In this way each component can be commissioned and tested independently of other subsystems. Towards this end the software developed for CODAS was also split and distributed on each subsystem, each computer running an identical set of global software components and its own set of local components for control specific to that subsystem.

GENERAL STRUCTURE OF CODAS
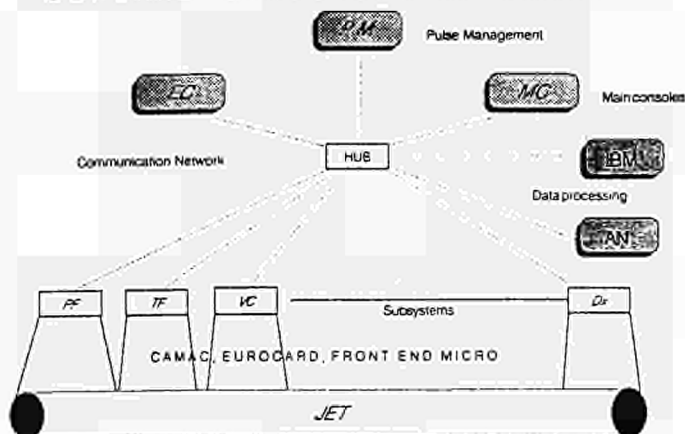
Fig 1

The overall software structure is shown in Fig 2. Three levels of software exist within CODAS these are:

LEVEL 1 is the supervisory level which is responsible for coordinating the operation of all subsystem computers during a JET discharge.

The components of the LEVEL 1 software related to pulse preparation, setting and monitoring are discussed further in this paper.

Level 2 is responsible for:

* the implementation of sequences of actions on individual units, of which there may be many per subsystem.
* the integrated control of these units as required for coordinated operation of the subsystem as a whole, and also as part of the integrated operation of JET.

Level 3, which is the lowest level and essentially corresponds to a direct action on a plant component.

SOFTWARE   HIERARCHY   SCHEMATIC
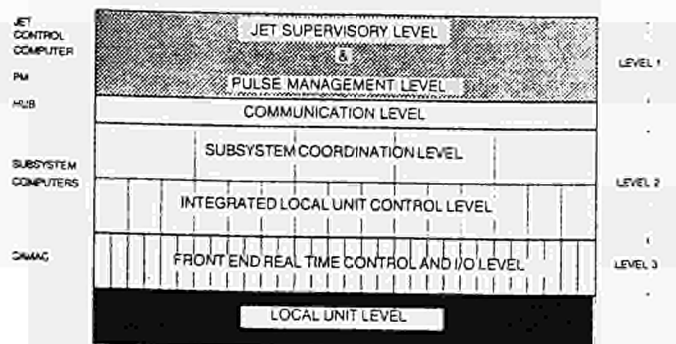
Fig 2

Role of CODAS during a JET Pulse

From the start of countdown during a JET discharge, JET along with all subsystem computers follows the State transition diagram shown in Fig 3.

JET STATE TRANSITION DIAGRAM
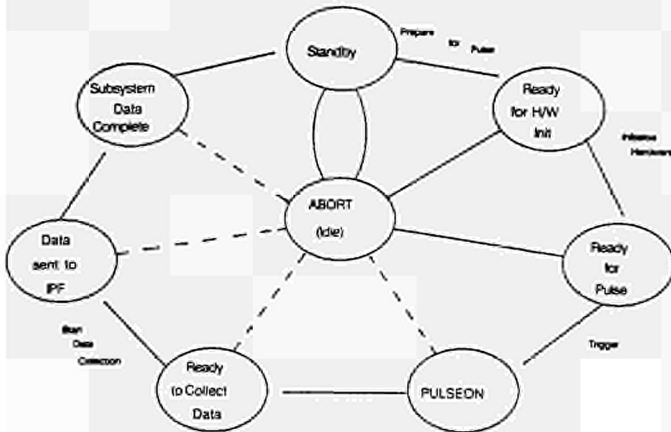
Fig 3

The COUNTDOWN component of the LEVEL 1 software acts in a supervisory role, running on the Machine Control computer (MC), and coordinates the orderly transition of all computers through the various states. The two most important transitions are Preparation for Pulse, and Initialisation of Hardware. During these two transitions, all control parameters and hardware, including timing sequences and waveform generators, are loaded with the values to be used during the ensuing pulse. The General Acquisition Program (GAP) performs most of this setting up under control of parameters loaded into a tree structured database file (GAP-TREE). In the initial operation of JET, virtually all setting of parameter values, timing requirements and set points was performed using ad hoc selection tools, the role of the LEVEL 1 software being simply the coordination of the control software across all CODAS subsystem computers. As more operational components were added to the experiment, however, the number of parameters, set points, and waveforms grew steadily and it became apparent that the role of the LEVEL 1 software should be extended to provide a number of additional features both OFF-LINE and ON-LINE to simplify the task of the Session Leaders, and Engineers in Charge (E-i-C) of Operations.

Expansion of LEVEL 1

It was clear that there were a number of areas in which LEVEL 1 could improve safety and efficiency of operation. These were as follows:

- to provide a convenient tool for Session Leaders in the OFF-LINE preparation of Pulse Schedules also including conversion algorithms to allow Plasma parameters to be translated into corresponding Machine control parameters.
- to allow automatic setting of Machine parameters in accordance with Pulse Schedules when the required Pulse Type is selected by the E-i-C of operations.
- to provide validation of parameters in the Pulse Schedule both OFF-LINE and ON-LINE, to ensure that values selected are consistent and comply with any operational limits in force when the pulse is selected.

- to provide ON-LINE monitoring of parameters included in the Pulse Schedule and indicating any differences between the currently selected Pulse Type and the immediately preceding pulse or any other selected pulse.
- finally on completion of a pulse to read back the actual plant or GAP-TREE parameter values and archive them for subsequent reference.

In order to provide the flexibility required by the changing environment of a facility like JET, the pulse management suite of programs was designed to be data driven and use a central database residing on the Pulse Management computer (PM).

Structure of Pulse Management Software

The main components of the Pulse Management software are shown in Fig 4.

MAIN COMPONENTS OF LEVEL 1
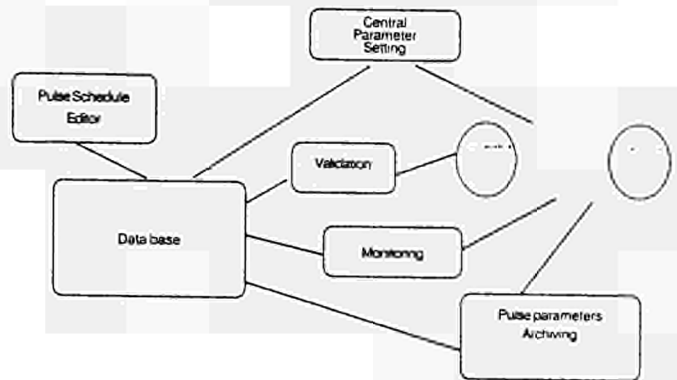
Fig 4

A diagram showing more detail of the database and the components held within it is shown in Fig 5.

DATABASE DETAILS
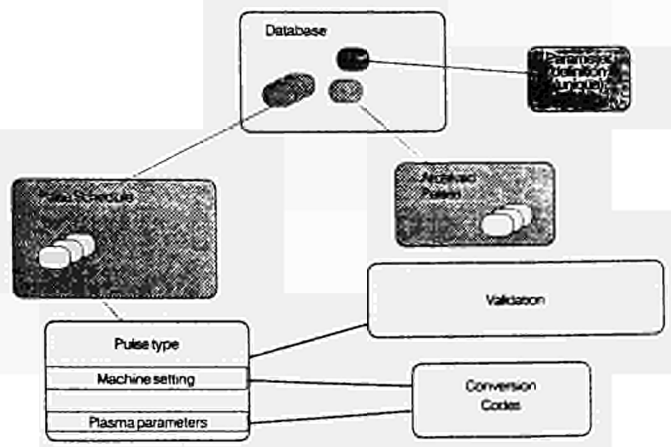
Fig 5

Objects Known to Pulse Management

Parameter (Machine and Physics)

Machine parameters refer to physical points in the
plant and are both readable and settable (eg
set-points, timer settings and control waveforms).
Physics parameters are used to describe requirements
and do not refer to settable items (eg required RF
power). Physics parameters may be converted to
machine parameters via conversion algorithms.
The definition of each parameter (of which there are
more than 500) is held in a centralised database. The
following information is held:

* parameter name.
* parameter description.
* parameter type (Machine/Physics).
* how the parameter may be read.
* how the parameter may be written.
* minimum and maximum permitted value.
* default value.
* threshold for monitoring.

Pulse Types and Schedules

A Pulse Type defines how the machine must be set up
for a specified discharge. It comprises all the
relevant parameters and their associated values
(scalars or waveforms).

A Pulse Schedule is a database file comprising several
Pulse Types. There are 2 types of Schedule -
Operations and Standard.

Operations Schedules are prepared to enable a session,
a given sequence of pulses, to be performed.
Typically there would be 20 or 30 Pulse Types, each
one differing only slightly from the previous one.

Standard Schedules contain Pulse Types which result in
discharges having known characteristics. A standard
Pulse Type may be used directly to set up the machine
or it may be copied into an Operations Schedule.

Pulse Schedules (and their Pulse Types) are created
and maintained with the Pulse Schedule Editor.

Archived Pulses

An archived pulse is essentially the same as a Pulse
Type (in that it comprises a list of parameters and
values) and like standard Pulse Types, it may be used
to set up the machine (in order to attempt to re-run
discharge) or it may be copied into a Pulse Schedule
for running at a later date. The set point values are
those really used during a specified pulse as opposed
to those intended to be used. Archived Pulses are
created automatically by the Pulse Parameter Archiving
System.

Process Components of Pulse Management

Pulse Schedule Editor

The Pulse Schedule Editor is a terminal-based program
which allows for the creation and modification of
Pulse Schedules and Pulse Types. The user is normally
presented with a menu (of commands) and a form
(parameters and values). Since a Pulse Type may
contain 200 user-fillable parameters, several forms
are required. Commands allow the user to move to
another form.

The main features provided include:

* since the program is used by a large number of
  people of differing background and experience, the
  menus and forms can be "tailor-made" to meet any
  individual requirements.
* extensive help facility. The user can obtain
  relevant help information at each stage of the
  program. This is normally presented as a menu from
  which the user can select the desired item.
* printing all or part of the Pulse Schedule. A
  summary of each Pulse Type is printed onto an A4
  sheet showing the values of the most important
  parameters together with a list of the differences
  between this and the previous Pulse Type.
* running conversion algorithms on the Pulse Type.
  The aim of the algorithms is to reduce the number
  of machine parameters that have to be specified by
  the user and to avoid tedious and repetitive "hand"
  calculations.
* validation of the Pulse Type. Where appropriate
  the Pulse Type will be validated to ensure that
  operational limits are not exceeded.

Central Parameter Setting

Central Parameter Setting is the means by which the
machine is set up in preparation for an experiment.
The operator may select either a Pulse Type from a
Schedule or an Archived Pulse as the reference.
After selection, the operator is presented with a list
of all the parameters whose values differ from the
current plant settings. The operator may then load
either a selection or all of these parameters.
The reason for adopting the idea of only displaying
the differences is twofold. Firstly, it is usually
the way that the E-i-C views an experiment (ie how
does it differ from the previous). Secondly, the
loading time is greatly reduced (typically only 10 to
20 parameters have to be loaded).

Pulse Parameter Monitoring

This facility allows the E-i-C to view two parameter
comparisons:

* the parameters (and values) for which the current
  plant settings differ from the settings for the
  previous pulse. the E-i-C can see at a glance the
  differences between this pulse and the last pulse.
  At the end of a pulse this list is empty (because
  this pulse = last pulse). As the setting up for
  the next pulse proceeds the list starts to fill.
* the parameters (and values) for which the current
  plant settings differ from the reference which has
  been selected by the operator using the Central
  Parameter Setting. This allows the E-i-C to see at
  a glance the differences between this pulse and the
  next pulse.

When the reference is first selected this list
contains all the differences. As the setting up for
the next pulse proceeds the list starts to empty.
When there is nothing in the list the E-in-C knows
that the setting up has been completed.

Pulse Parameter Archiving

At the end of each Pulse the list of parameters and
values which were used are archived in the database.
Parameters which were not relevant to the pulse (eg an
excluded subsystem) are also stored but with a special
status. The archiving system allows to refer to
pulses which were actually run.

Conversion Algorithms

The main purpose of conversion algorithms is to convert Physics parameters into machine parameters. This should in turn reduce the number of parameters which have to be specified by the user in a Pulse Type. All conversion algorithms may be run from the Pulse Schedule Editor either on request of the user (via a command) or automatically (when the Pulse Type is stored).

Validation Algorithms

Validation algorithms are used to check the parameter settings for consistency and validity. The process of validation is divided into a small number of independent tasks in order to ease maintenance and to add elements as experience is gained. A validation may produce a result in one of the following classifications:

- Class 1 - Fatal Error.
- Class 2 - Serious Inconsistency.
- Class 3 - Non-serious inconsistency.
- Class 4 - OK.

The validation is applied in two ways:

- a Pulse Type may be validated by the user using the Pulse Schedule Editor either on request or automatically. It is possible to prevent the setting up of Pulse Types which have either not been validated or have failed the tests (one or more validations in Class 1 or 2).
- a Pulse Type is validated after the setting up stage as part of the Countdown process as at this stage it can take into account the status of the plant (eg cooling water temperature) and forms part of the machine protection. The action taken by the Countdown depends on the result of the validation as follows:

  a. the Countdown is aborted if there are one or more validations in Class 1.
  b. the Countdown is suspended if there are one or more validations in Class 2. The E-i-C must decide whether to proceed with the Countdown or not.
  c. the Countdown continues if all the validations result in Class 3 or 4. In this case the E-i-C can view a checklist containing the results of all the validations.

Present Status

Operational Components

Pulse Schedule Editor is being used to produce Pulse Schedules.

Pulse Parameter Monitoring is used by the Engineer-in-Charge.

Pulse Parameter Archiving is being used to store all pulses.

Validation of the expected power dissipation in the Toroidal Field coils.

Components under Commissioning

Central Parameter Setting is being used to set up the Radio Frequency subsystem.

Conversion algorithms are being used on RF to compute generator waveforms. They are also being used to calculate timer settings for the Central Timing System (CTS) and the Gas Introduction System.

Components to be Developed or Expanded

More validation and conversion algorithm codes are to be specified.

The Pulse Schedule Editor will have new features in response to user requests. Currently it is not possible to validate Pulse Types from within the Editor, nor is it possible to copy an archived pulse into a Pulse Schedule.

Conclusion

The modularity and the data driven aspects of the pulse management components of the Level 1 software facilitate its gradual introduction into the daily operation and will allow to adapt easily to the operational requirements. Its development and integration have required a continuous interaction between users and developers. On-going development of conversion and validation algorithms will allow an easier and safer operation of JET.

References

[1] CODAS: The JET Control and Data Acquisition System - H van der Beken, CH Best, K Fullard, RF Herzog, EM Jones, CA Steed - Fusion Technology Journal, January 1987, Vol. 11, No. 1

[2] Data Acquisition at JET - Experience and Progress - H van der Beken, HE Clarke, RF Herzog, EM Jones JJ Saffert, Y Shu, CA Steed, MR Wheatley - Real Time '89 Conference, Williamsburg, USA

DESIGN FEATURES OF THE JET VACUUM ENCLOSURE FOR SAFE OPERATION WITH TRITIUM

C J Caldwell-Nichols, E Usselmann
JET Joint Undertaking, Abingdon, Oxon, OX14 3EA, U.K.

Abstract

The JET machine is intended for eventual operation with tritium-deuterium plasmas to produce very significant fusion reactions. Starting from the initial design concept, its evolution resulting from operational experience and simultaneous theoretical studies a consistent approach has been developed for the preparations needed for safe operation with D-T plasmas. The main machine vacuum components are inherently suitable as they were designed for tritium operation and where necessary are physically very strong. Experience with certain components and appendages are indicating the changes necessary in their detailed design. Fundamental features of all metal construction and double containment on weak points such as bellows create designs which have primary safety built in. Work is in progress on detailed identification of weaknesses in the design and their rectification. In parallel tritium compatibility assessments of all subsystems is being undertaken as part of safety approval programme for the use of tritium in JET.

Introduction

The main features of the JET vacuum vessel have been reported in detail [1]. The vessel itself is very strong and is of double walled construction in a D-shaped cross section toroid with a vacuum tight interspace. The vessel is thus doubly contained for greatly enhanced safety and possible continuation of operation if the inner vessel is punctured. For vacuum conditioning hot helium is passed through the interspace to bake the vessel and during plasma operations the vessel is routinely kept hot using this heating system as a result of the discovery that it improved plasma performance.

The appendages to the main vacuum envelope are designed and constructed with equivalent objectives. These systems are primarily the Torus vacuum system, the Gas Introduction System, the set of Diagnostics, the Active Gas Handling System, the Neutral Beam Injectors, The RF Heating Systems and the Pellet Injector System. The last four are major items and their devel-

opments have been reported in detail [2,3,4,5,6] and are being upgraded for tritium operation where necessary. All other systems are being rationalised as a result of operational experience, some of the major developments are described below.

Mechanical Measures.

Two Inconel restraint rings have been installed on the inner wall above and below the mid-plane of the Torus to give additional strength and reduce excessive distortion of the vessel during tokamak shots and disruptions [7]. The necessity was realised as a result of measurements of vessel distortion and predictions of the effects of high current operations and disruptions at 7MA plasma current. New vessel supports attached to all the upper and lower Main Vertical Ports have improved the distribution of forces on the vessel, and soon dampers are also to be attached to these ports to remove the energy of radial oscillations of the vessel.

Vacuum Measurement

The original concept at JET was for individual subsystems to make their own measurement of the JET vacuum for local control of the subsystem vacuum, including their isolation valves, using programmable vacuum gauge controllers. This had the disadvantage of needing a large number of gauges on the Torus with the increased risk of single failures causing problems for Torus operations. The JET Penning gauges have had several leaks around the central conductor due to physical damage. JET has produced a damage tolerant design (Fig.1) based on the Balzers gauge where the central insulating ceramic is mechanically decoupled from the external electrical socket and the supporting tube is epoxy filled as an additional barrier against leaks.

Using these new gauges and modified Pirani heads it is intended to install up to 3 Master Measuring Stations close to the main pumping chambers to perform all the vacuum measurements of the Torus. These measuring stations will have isolation valves so repairs can be made without venting the Torus. All other individual gauges will be removed from the Torus and the measure-
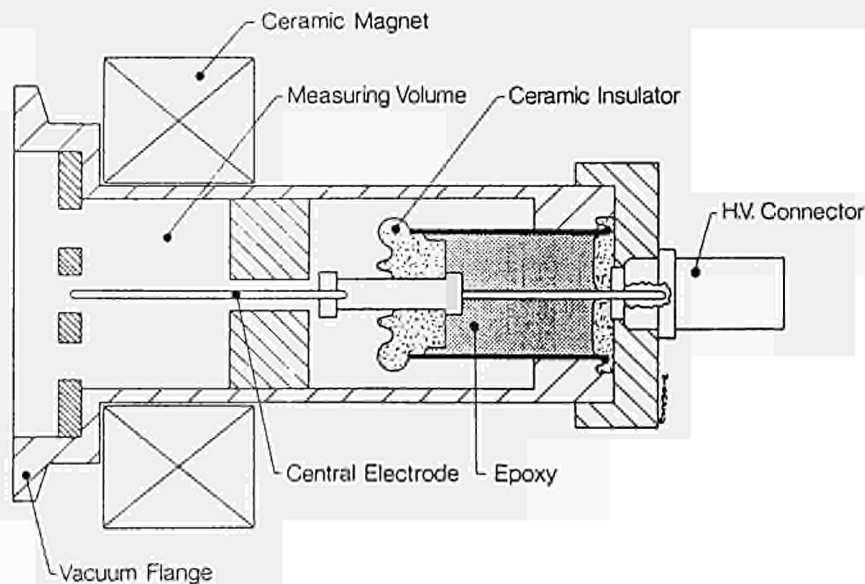
Fig.1 JET Penning Gauge

ments from the master stations will then be distributed to the various subsystem computers and vacuum controllers as required. This is now possible due to enhancements in the intercommunication capability of all the subsystem computers.

Gas Introduction Valves

The present gas introduction modules have had problems and have too many components in them. Failures have occurred on the edge welded bellows sealing the stems of the electrodynamic valves and a redesign was essential for tritium operations. A new design concept for the gas introduction valves based on piezoelectric transducers has been developed and a gas introduction system using a piezo valve has been in use for over a year on JET [8].

Figs 2 and 3 show the design and schematic for use of these valves. The valves are radiation resistant and not affected by magnetic fields.

desirable to keep the outer of a pair of bellows as cool as possible to reduce tritium permeation to atmosphere, such as in the LHDC system on JET, a gas filling will make this difficult to achieve.

Continuous pumping of interspaces to high vacuum or better is impractical as invariably the conductances of the pumping ports available are too low to achieve the required pumping speed, particularly if tritium is also permeating into the interspace. If interspaces are evacuated and sealed off the pressure has a high probabilty to rise to at a poor region on the Paschen curve for electrical breakdown. Electrical feedthroughs have had problems with breakdowns in interspaces and therefore they will all be backfilled with gas (Argon) at about 0.6 Bar. But generally there can be no firm rule on the condition for all interspaces and each will be considered individually. Fig. 4 shows the complex bellows arrangement of the beryllium evaporators on JET.

Fig. 2 Piezo-electric Valve (cross section)

Valve seat — Piezo crystal — Pneumatic piston — Compressed air connection — Hydraulic piston — Closing springs — Electric connection — Clamp — Valve membrane

Fig.3 Piezo Valve Installation Arrangements at Torus (schematic)

V1 = Manual Shut-off Valve
VP = Piezo Valve
R1 = Storage Tank 0.76ℓ
G = 1000 Torr Absolute Gauge
F = Dust Filter
VF = Refill Valve
PR = Pressure Regulator 1 to 6 bar
R2 = Ti-Fe Storage Bottle ~15bar
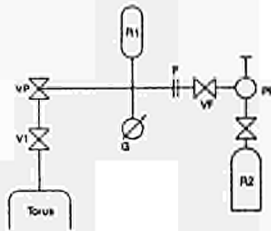
They require compressed air for their operation but only for the opening sequence of the valves, otherwise they are fail safe as if the air fails they shut immediately. The results of the trials of these valves to date is good. If found fully acceptable they will be fully adapted for tritium operations with double containment and remote handling connections. This will most likely be as a complete demountable module containing the other associated components.

Bellows and Interspace Systems

Experience with bellows at JET suggests that they should be avoided if possible and new equipment is following this guideline. Where bellows exist already or are essential, double bellows with a vacuum tight interspace are mandatory. The problem of what to do with interspaces is complex. Each should have a pumping/gauge port otherwise any leak could be virtual and cause serious problems of identification. One solution is to fill with a suitable gas to about 0.6 Bar, chosen so there is always a slight vacuum at the highest temperature. This has the advantage for leak detection and monitoring the interspace pressure will indicate a the leak and the direction, i.e. atmosphere to interspace or interspace to Torus. The correct selection of filling gas, not helium, will indicate that an interspace is leaking by examination of the Torus gas analysis. However in the case where it is highly

Diagnostic Systems

These fall into three group for tritium safety purpose, those that have no vacuum interface, those that have optical windows on the main vacuum vessel and those with direct connection to the Torus vacuum. For diagnostics the source of tritium is that introduced into the vessel for plasmas.

Those with no interface do not have a severe safety problem except where they penetrate the biological shield they have to be sealed to retain the depression system integrity.

Those with optical windows present a particular problem in that a failure of a window is likely to be a severe event. Wykes [9] has studied the effects of a complete window failure to calculate of the mass of air that would enter the vessel immediately after a failure and subsequent quantity of tritium released into the Torus Hall. There are also first estimates of the effects of graphite tiles catching fire if window failure occurred when tiles were at their hottest. The prevention of the ingress of large amounts of air is a high priority.

Diagnostics with direct interface to the Torus vacuum typically have beamlines connected directly to the Torus vacuum and have their own vacuum pumping sys-
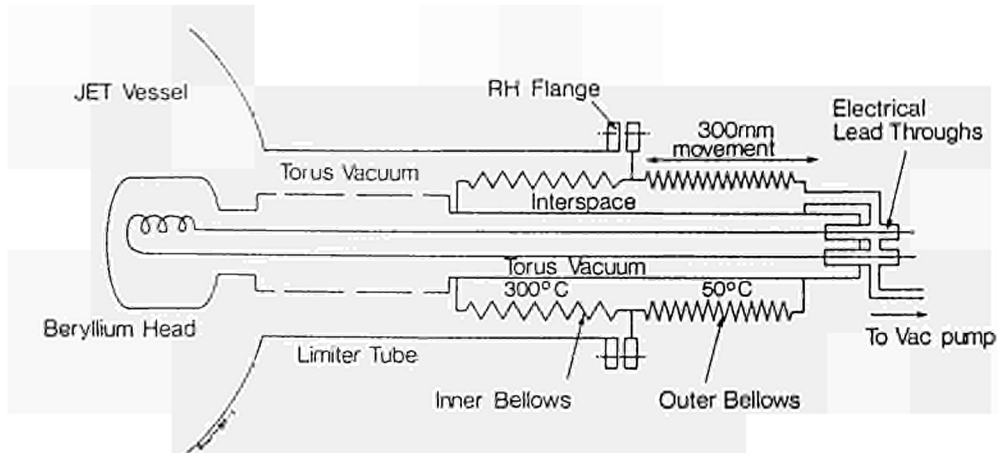
Fig 4.   Schematic – Beryllium Evaporators

tem. At present these comprise of turbomolecular pump and rotary vane backing pump sets. The turbo pumps are tritium sealed but the backing pumps are not suitable, the original plan for a shared backing line connected to a common pump was discarded as too difficult to control safely. Most turbo/backing pump sets are to be replaced with regenerable getter pumps on the diagnostic beamlines except that one mechanical set will be retained on each for pumping down where venting occurs independently of the Torus. Here tritium sealed backing pumps will be used with their exhausts being sent to the Active Gas Handling Plant for detritiation. Those with beamlines have all-metal isolation gate valves (VAT Series 43 or 48) at the Torus port flange. This provides secondary containment and a result of this is that the requirement for all bellows systems to be doubled has been relaxed for systems behind such isolation valves. Further, non-remote handleable but all-metal vacuum flanges can be retained where remote handling is never to be required. These two important concessions mean that several important diagnostic systems can be retained without the need for very extensive and difficult redesign for tritium operation.

Windows

The diagnostic optical windows are made from one of three materials, crystalline quartz, fused silica or synthetic sapphire, according to the requirements of the particular diagnostic. These materials are vacuum sealed to metal and fabricated into demountable assemblies. The windows on JET have proved very, but not totally, resilient to JET conditions and have to be improved for Active Phase operations. It is not conceivable that a window can be designed which will remain intact under all circumstances, particularly for a water leak onto a hot ceramic disc.   Experience to date with thick discs is that the pieces of a thermally cracked disc remain in place resulting in a large vacuum leak but preventing catastrophic venting of the Torus. Hence the concept has evolved for windows to be damage tolerant to the extent that a large hole in the vacuum envelope in the event of damage should be unlikely to appear. However a large vacuum leak would be 'acceptable' in as much as it would allow time for shutdown actions to take place, i.e. warming up of cryopanels, pumping out and venting the Torus etc. Fig. 5 shows a conceptual design of a fault tolerant window assembly which is under consideration at JET. It consists of an inner sacrificial disc with the main sealed disc on the outside. The connecting interspace is vented to the Torus vacuum by a small hole. This hole would allow vacuum pumpdown, making a sealed and pumpable interspace unnecessary, but it would not allow easy access for water from a leak to reach the outer window.

Tritium Safety Analysis

Before tritium can be used in JET various safety authorities will have to be satisfied that the machine is safe. A set of systematic safety analyses for each subsystem (Tritium and Radiation Compatibility Assessments) specifically directed at tritium compatibility has been initiated at JET and the results will form part of the overall safety case for approval for tritium operations. Conventional safety aspects of subsystems is examined elsewhere, this approach is valid as tritium is a radiological hazard with safety problems usually unrelated to others. The aim is to evalu-
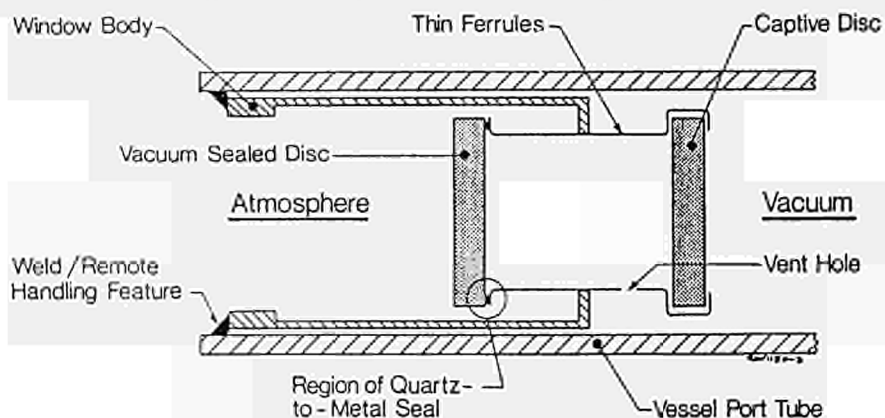
Fig.5 Conceptual Design of Damage Tolerant Window

ate the safety of each system as it is at present and then recommend modifications to the design or modes of operation of a subsystem for use with tritium. An iterative process is envisaged where recommendations are evaluated by the groups responsible for a subsystem, physical changes made to a subsystem and eventually a final assessment is produced for approval to the safety authority.

What is examined in each case is how much tritium is likely to be released during normal operations, due to maintenance operations and accident conditions and how these can be minimised. Permeation of tritium is the largest potential release during normal operations. Maintenance will often involve dismantling vacuum systems that have been exposed to tritium with subsequent release of tritium to air. Accidents such a optical window failure will have effects beyond the particular subsystem and are treated together and not particular to the subsystem. Other potential accidents peculiar to a subsystem are postulated and evaluated for tritium release.

To date of the systems assessed, mostly diagnostics, few are regarded as needing major modifications for tritium primarily because basic rules such as all-metal containment have been followed. Large systems such as the neutral injectors require a different approach and are in the early stages of asssessment.

Permeation.

Systematic evaluations are performed of the maximum amount of tritium per year that could be expected to permeate through the hot metal walls of each subsystem under standard JET tritium conditions. These conditions are the partial pressures and total times in a normal operational year that tritium is expected inside the Torus as a source term for permeation. The equation used for the estimation of permeation is the standard free energy expression:-

$$P(t) = C*\exp(-N/RT)*(A/x)\sqrt{p} \qquad - \qquad (1)$$
C,N are constants, A = area, x = thickness of material

This is a highly temperature dependant function and there are obvious advantages is keeping component temperatures low, particularly on surfaces next to atmosphere.

The square root dependence on partial pressure means that pumping interspaces is not particularly effective in reducing overall permeation as usually the required pumping speed at the very low pressures necessary are not achievable through the small pumping ports available. Oxide layers may reduce permeation on JET, the conditions for this to happen are not well understood and are highly variable. However, apart from some exceptional situations the worst case estimates of the total permeation from JET appear to be acceptable. When tritium operations start the total releases from JET will be monitored for radiological protection reasons. This will give an empirical indication of the global releases that could be expected from the next generation of machines which are likely to be operated under comparable conditions. Bellows are of particular interest as they are weak points having large areas and small thicknesses, the factor A/x of bellows on many systems is considerably larger than the combine A/x of the remainder of the system. The analyses show clearly that double bellows arrangements do not significantly inhibit tritium permeation because an interspace rapidly reaches mean partial pressure and the net effect is due only to the total thickness both bellows. The most important feature of double bellows in respect of tritium release is the second chance they give in the event of a failure.

Failure Modes

Possible failure modes of subsystems are examined and initial estimates on likely effects have been made. A vacuum leak in a metal component is unlikely to be large initially. As the vessel is under high vacuum conditions a leak is readily detected and operations can cease. Tritium is unlikely to pass out of a leak where air at pressure is going in the opposite direction. Timescales are such that other actions can be taken before and event becomes serious, typically for a diagnostic with a beamline the isolation valve can be closed. More crucial would be a failure in the valve itself as that could not be isolated.
For several of the more complex systems full fault tree and event tree analyses will have to be done as part of the final assessment for tritium operations.

Conclusions

The operational experience with the JET subsystems and consideration of theoretical studies has led to a consistent approach to the enhancements required for Active Phase operations at JET. Many are now being proved on the machine, other developments, notably damage tolerant diagnostic windows, have to be thoroughly developed before application.

Complete safety cases for all components of the machine will have to be produced and approved before operations with tritium are permitted. These are well in hand and are expected to be completed in good time.

Acknowledgements

References

[1] M J Walravens, 'The Vacuum Vessel,' presented at a Seminar on The Mechanical Engineering Aspects of JET,' Institution of Mechanical Engineers, November 1988
[2] R Haange et al, 'General Overview Of Active Gas Handling System At JET,' Proceedings 3rd Topical Meeting on Tritium Technology in Fission, Fusion and Isotopic Applications, Toronto, May 1988.
[3] G Duesing et al, 'Neutral Beam Injector System,' Fusion Technology, Volume 11, Number 1, pp163-202.
[4] A Kaye et al, 'Radio-Frequency Heating System,' Fusion Technology, Volume 11, Number 1, pp203-234.
[5] C Gormezano et al, 'The JET 10-MW Lower Hybrid Current Drive System,' Proceedings 12th SOFE, Volume 1, pp38-41.
[6] K Sonnenberg et al, 'Prototype Of A High Speed Pellet Launcher For JET,' Proceedings 15th SOFT, 1988, Volume 1, pp715-719.
[7] M A Pick et al, 'Integrated Engineering Design Of New In-Vessel Components,' Proceedings 15th SOFT, 1988, Volume 1, pp771-775.
[8] E Usselmann et al, 'New Piezo Driven Gas Inlet Valve For Fusion Experiments,' Proceedings 15th SOFT, 1988, Volume 1, pp 738-742.
[9] M E P Wykes, 'Safety Analysis Of Torus Vacuum Breach,' JET-P(88)37.

TRITIUM CONTAMINATION STUDIES
INVOLVING TEST MATERIALS AND JET REMOTE HANDLING TOOLS

A Tesini, R Jalbert*
JET Joint Undertaking, Abingdon, Oxfordshire, OX14 3EA, England
*TSTA, Los Alamos National Laboratory, Los Alamos, New Mexico, 87545, USA

Abstract

To determine the potential contamination of remote cutting and welding tools to be used in the JET torus after the introduction of tritium, experiments were performed using these tools on INCONEL pipe specimens which had been exposed to elemental tritium (HT) at a concentration of 4.6×10^{10} Bq/m³. A maximum tritium release of ~ 15,600 Bq was measured during welding, resulting in a tool's surface contamination of ~ 0.5 Bq/cm². A second series of tests was performed in order to determine the degree of surface contamination of various materials when exposed to HTO as a function of the exposure time and the relative efficacy of different decontamination techniques. Stainless steel, aluminium alloy and PVC rigid were exposed to HTO (liquid) at a concentration of 4.4×10^{10} Bq/l for 1, 24, 120 hours and decontaminated. The decontamination techniques used included a) leaching in water, b) baking at 100°C, c) hot air stream, d) weathering. The maximum levels of tritium surface contamination measured during the test were ~ 12 Bq/cm² for stainless steel, ~ 5 Bq/cm² for aluminium alloy and ~ 1,700 Bq/cm² for PVC. A decontamination factor of about 80% as measured by smears was achieved using a hot air stream at 125°C on stainless steel and aluminium alloy and baking PVC at 100°C.

Introduction

The Joint European Torus (JET) is a large tokamak constructed and operated by the European Community. Located near Abingdon, England, it has been in operation since 1982 first using hydrogen and then deuterium as the fuel gases. It is planned to introduce tritium at the facility and to burn tritium along with deuterium in the torus by early to mid 1992.

The introduction of tritium will cause a number of changes in the operation of the facility. These changes will be required because of the contamination of the plumbing, torus and equipment with which the tritium comes into contact and the activation of the torus and associated nearby equipment and strutural components resulting from the fusion DT neutrons.

Handling of tritium contaminated material is not a new experience nor is that of dealing with activated components. However, the combination of the two coupled with the size of the equipment involved does present a new challenge for the operators of the facility. This will be met in part with sophisticated remote-handling equipment and special maintenance facilities to protect workers from both tritium and penetrating beta/gamma radiation.

Much of the maintenance work will take place on the machine itself. Remote handling equipment for performing some of the associated necessary tasks has already been designed and tested. Among these are the special tools which are the subject of the first part of this paper. These tools, one pipe cutter and two pipe welders, will be used to cut and weld placement tube sections within the torus itself.

It is expected that the tools, when exposed to the contaminated environment of the torus and especially to the outgassing pipes being cut or welded, will themselves become contaminated. The extent of this latter contamination was the subject of a series of tests recently performed in the Experimental Contamination Studies Laboratory of the Tritium Systems Test Assembly at the Los Alamos National Laboratory.

In addition and as part of this study coupons of aluminium, stainless steel, and polyvinyl chloride were exposed to tritiated water (Hereafter: HTO) and experiments performed to determine the relative effectiveness of several simple decontamination techniques. It is important for anyone who expects to handle highly-contaminated equipment to have plans and facilities ready in advance for handling such equipment and in many cases, to reduce the level of contamination so that it can more easily and effectively be handled with minimal protection.

Exposures of Cutting and Welding Tools

In the first phase of the experiment INCONEL 600, pipe specimens of the type and size used in the JET torus were exposed to elemental tritium (HT) concentrations approximating those expected in the torus (4.6×10^{10} Bq/m³ or 1.2 Ci/m³). Following the exposures, the specimens were allowed to outgas for 10 minutes and then smeared for surface contamination; the outgassing rate was then measured for 5-10 minutes, which was also repeated during the cutting or welding operation which followed. Following the operations, the surface contamination of the tool was measured.

The remote handling tools that were involved in the experiment included a 91 mm dia port cutting tool (Fig.1), a 91 mm dia fillet welding tool (Fig.2) and a 55 mm dia orbinal welding tool (Fig.3). The specimens involved were INCONEL 600 pipes, ranging in diameter from 50 to 95 mm and identical to those installed in the JET torus.
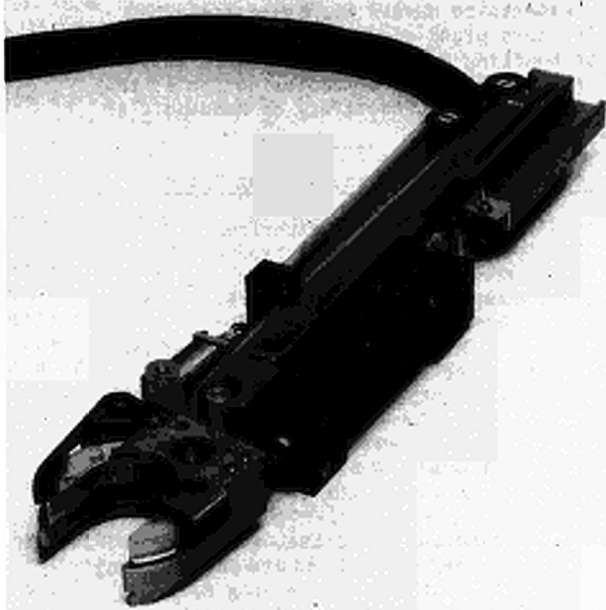

Fig.1

Fig.2

Fig.3

Exposures of the pipe specimens were made in a 10 lt exposure chamber arranged in a closed loop configuration with a pump, flow meter and glycol bubbler to purge the source HT gas of any residual oxide (HTO), (Fig 4).
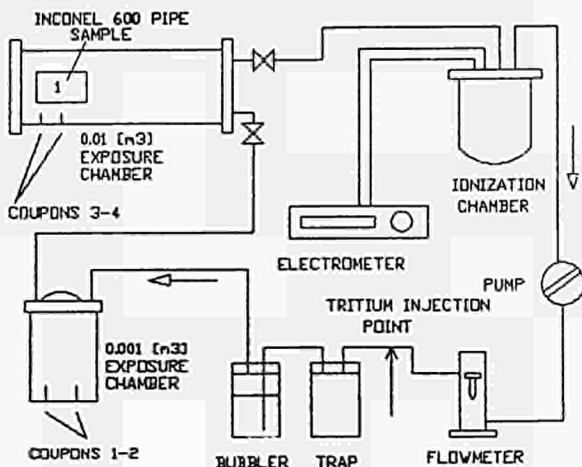

Fig.4
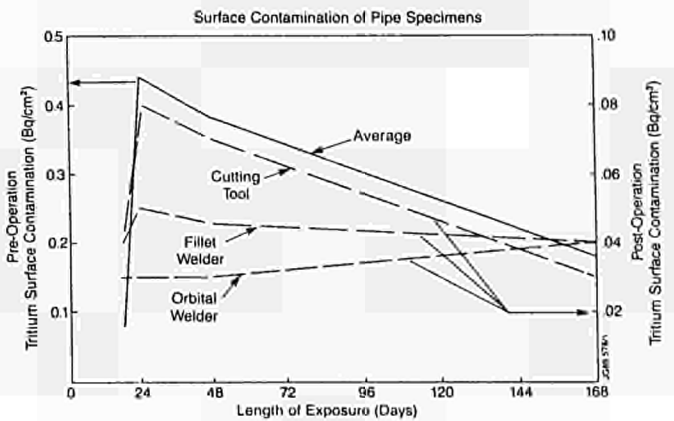
Surface contamination was measured by dry filter papers analyzed by liquid scintillation counting. Outgassing of the specimens was accomplished by placing the specimen in a special aluminium box continuously purged to two water bubblers for measuring outgassing HTO. A tritium monitor ionizaton chamber placed after the bubblers failed to detect any HT, probably because of its lack of sensitivity (1 µCi/m³).

Pipe Specimen Surface Contamination

To study the effect of the length of the exposures on the level of contamination, different exposure times were used: 18,24,48 and 168 hours. The initial surface contamination levels measured after the end of the exposure ranged from about 0.1 Bq/cm² for the 18 hour exposure to a high of 0.44 Bq/cm² following the 24 hour exposure and decreasing for the longer exposures of 48 and 168 hours to ~ 0.2 Bq/cm², perhaps due to oxygen depletion in the metal and loss of surface HTO from the converted HT prior to the end of the longer exposures. After the cutting operations, the levels dropped to about 0.06 Bq/cm² whereas following the welding, the levels dropped to about 0.03-.04 Bq/cm² probably due to the higher temperature involved in the welding operations. Fig.5 illustrates these data.

Fig.5

Outgassing of Pipe Specimens

The outgassing rate of the pipe specimens measured about 10 minutes after the end of the exposure was about 0.2 Bq-min⁻¹cm⁻² and was highest for the 18-hour exposure, (Fig.6).
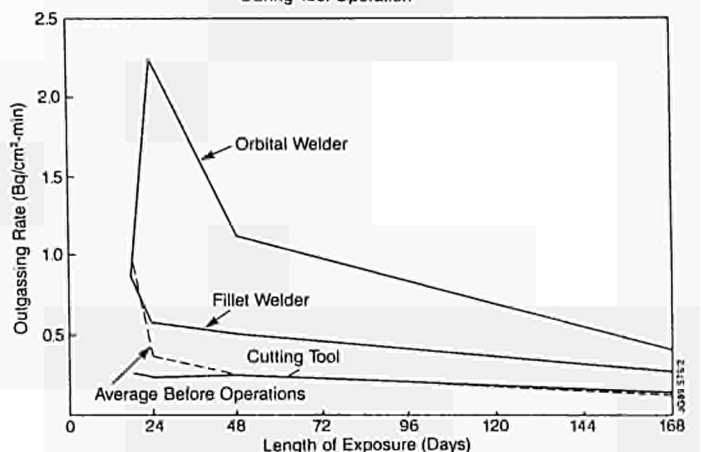
Fig.6

During the cutting operation, the outgassing rates did not change whereas during the welding operation, the rate significantly increased due again to the heat generated during that operation.

Tool Contamination

The contamination of the tools resulting from the cutting and welding operations was measured immediately following the operation. The levels roughly followed the total outgassing rate of the specimen coupled with its surface area and the time required for the operation. Because of the complexity of the tools, however, it was not possible to quantify these numbers since each tool was structurally different and no comparable surface could be used. In any case the levels of resultant contamination were very low, as expected, ranging from about 0.03 Bq/cm² to 0.5 Bq/cm². The highest value was well below any limit at which decontamination or special handling precautions would be required.

Decontamination Experiment

Coupons of aluminium alloys (BS1470), stainless steel (304) and rigid PVC were exposed to tritiated water and decontaminated. Surface and absorbed tritium was measured by smears and leaching. The results of these tests are presented here.

Square coupons 50 x 50 x 1.5 mm were allowed to soak in a bath of tritiated water having a concentration of 4.4×10^7 Bq/ml (1.2 mCi/ml) for 1 hour, 24 hours and 120 hours. (This concentration is equivalent to an air concentration of approximately 9×10^8 Bq/m³ (24 mCi/m³) at 100% relative humidity). Prior to exposure, the samples were washed in acetone and rinsed in alcohol. At the end of each exposure, the coupons were removed from the bath and allowed to air dry for 18 hours. This was followed by smearing one side of each coupon with wet filter paper, which was then counted by liquid scintillation. For each set of parameters three coupons were used and the results averaged.

Following the initial smears, the coupons were decontaminated by one of the following techniques: 24-hour outgassing at room temperature; 24-hour leaching in water at room temperature; 24-hour baking at 100°C; and 1-hour heating in a hot air stream (125°C) followed by 23-hour outgassing in room air.

After the 24-hour decontamination, the coupons were again smeared and then placed in water baths for 24 days to leach out the remaining tritium.

The decontamination efficiency was measured in two ways. One was determined by smearing the coupons before and after the 24-hour decontamination period. The other was calculated from the amount of adsorbed/absorbed tritium in one of the sets of coupons before any decontamination and from the amount of remaining tritium after decontamination. In this case the tritium was measured by leaching.

In order to simplify the presentation of the data, the results for the 1-hour, 24-hour and 120-hour exposures are averaged since in most cases the data are similar and do not form any consistent pattern. Table 1 and Table 2 summarize the results of this experiment.

If the removable surface contamination is the only criterion, there is not much difference among the various techniques used in this study. Leaving

TABLE 1 : DECONTAMINATION EFFICIENCY				
	OUTGASSING	LEACHING	HOT AIR +	BAKING
STAINLESS STEEL				
SURFACE (1) CONTAMINATION	0.71	0.60	0.72	0.68
BULK (2) CONTAMINATION	0.25	0.66	0.61	0.59
ALUMINUM				
SURFACE (1) CONTAMINATION	0.58	0.64	0.81	0.63
BULK (2) CONTAMINATION	0.29	0.76	0.77	0.79
RIGID PVC				
SURFACE (1) CONTAMINATION	0.64	0.38	0.55	0.53
BULK (2) CONTAMINATION	0.27	0.43	0.50	0.82

(1) MEASURED BY SMEARS   (2) MEASURED BY LEACHING

TABLE 2 : CONTAMINATION LEVELS FOLLOWING HTO EXPOSURE AT 4.4×10^{10} Bq/LITRE (Bq/cm²)				
	LENGTH OF EXPOSURE (HR)	STAINLESS STEEL	ALUMINUM ALLOY	RIGID PVC
SURFACE CONTAMINATION (BY SMEARING)	1	1.3	0.30	0.24
	24	0.45	0.51	0.26
	120	0.43	0.73	0.38
TOTAL ABSORBED/ ADSORBED (BY LEACHING)	1	14	6.5	160
	24	4.3	5.9	1900
	120	2.0	5.4	5000

the material simply to outgas, however, is apparently less effective than any of the other methods at least in removing adsorbed tritium.

A combination of heat and moisture is generally considered a fairly effective technique although it wasn't employed here. No method is 100% effective. Any method that speeds up the removal of absorbed tritium will also drive the tritium more deeply into the material, making it more inaccessible for removal.

It is well known that hydro carbons are difficult to decontaminate, largely because of their greater permeability to HT and, especially, to HTO. An ultimate technique to remove tritium that has not penetrated the material too deeply is to resort to destructive techniques such as sanding, grinding or chemical removal. However, these techniques leave the surface rough thereby increasing the actual area and making it more susceptible to further contamination unless polished.

BEAMLINE DUCT GAS RELEASE/CONDITIONING AND THE UPGRADED DUCT WALL PROTECTION SYSTEM OF THE JET NEUTRAL INJECTORS

A J Bickley, T T C Jones, S Papastergiou, C D Challis, J F Davies, H P L de Esch, D Stork, and H Altmann

JET Joint Undertaking, Abingdon, Oxfordshire, OX14 3EA, UK

Abstract: During injection of neutral beams into the JET Tokamak, there have been three occasions when damage to the water cooled duct liner has occurred due to re- ionisation within the duct region. As a result, improved duct protection and direct fast pressure gauges have been installed. The pressure measurements are analysed in terms of a gas re-emission coefficient and results for various surface conditions have been obtained. The mechanical design of a new improved duct protection system is also presented.

1. Introduction

The JET Neutral Beam ducts have a rather restricted geometry dictated by the arrangement of the toroidal field coils. At its throat, the duct cross-section measures only 800mm vertically by 280mm horizontally (Fig.1) yet it transmits >10 MW 80 kV D° neutral beams at power densities >200 MW m^{-2} (60% higher than the original design specification). With such high power densities and small duct dimensions, the duct gas evolution characteristics critically determine the safety with respect to power loadings from beam re-ionisation and the possibility of beam-blocking. During earlier operating periods, the original water-cooled nickel duct liner panels failed due to excessive re-ionisation power loadings associated with pressure excursions in the duct, as determined from the D_α scanner intensity [1]. A graphite tile was installed as a temporary protection measure, but the operating experience with this tile proved unsatisfactory [1]. Subsequently, an improved system of inertial copper protection plates was installed [1], and the ducts fitted with fast-response Penning gauges to monitor the pressure directly and to provide an interlock signal. The pressure evolution has been analysed to yield information on particle-induced gas-release. Results for bare, carbonised and Be coated copper surfaces have been obtained which confirm that the well conditioned duct operates well below the beam-blocking threshold at full power. From the positive results of the improved duct protection, an upgraded, more reliable duct wall system has been designed, based on a copper structure with high thermal capacity.

Fig. 1 Plan of JET Neutral Injection system showing arrangement of Neutral Injector Box (NIB), Rotary High Vacuum Valve (RHVV) and Duct.

2. Conditioning history of clean copper and carbonised duct surfaces

Following installation of Penning gauges in the JET NI ducts, the first measurements during duct conditioning were obtained in December 1987. Following a short period of operation the machine was heavily carbonised in January 1988, and the duct conditioning procedure was repeated. The conditioning history for these two surface states is compared in this section.

The behaviour of the duct surfaces may be described by an ion-induced gas re-emission coefficient; prior to discussing the results the following section explains how the re-emission coefficient may be derived from the experimental pressure measurements.

2.1 Pressure balance in the duct

Let the total rate of gas production in the duct, due to beam bombardment, be Q_{DUCT} (mbcm^3 s^{-1}), with a pump-out speed from the duct of $\overline{C}$ cm^3 s^{-1}. Let the pre-beam duct pressure (largely determined by the neutraliser gas flow into the NIB) be P_0 (mb), and let the pressure during the beam be $P = P_0 + \Delta P$ (mb). For a duct volume V (cm^3) we have:

$$Q_{DUCT} = \Delta P.C + \dot{P} V \quad \text{mbcm}^3 \text{ s}^{-1} \qquad (2.1)$$

Let us assume that the rate of production of D_2 molecules at surfaces under bombardment can be described by a single gas re-emission coefficient (Γ). We may therefore write:

$$Q_{DUCT} = \frac{\phi_B (R+I)\Gamma}{M} \qquad (2.2)$$

where ϕ_B = beam particle current through the duct (number per second)

R = fraction of beam reionised

I = fraction of beam directly intercepted in the duct

M = number of molecules in 1 mbcm^3 at 300 K

For R<<1 the probability of re-ionisation in path length L is given by

$$R = \sigma_{01} n L \qquad (2.3)$$

where n is the gas molecule number density and σ_{01} is the beam ionisation cross-section for collisions with the gas molecules. An approximately flat pressure profile over the re-ionisation path length is assumed. In the case of the JET ducts, most of the contribution to duct re-ionisation power loading comes from ions created over a distance ~3m extending upstream from the stray tokamak vertical field crossover point through the rotary valve back to the NIB (Fig.2). Taking a flux-weighted average over the three energy components present in 80 kV D° injection we have $\sigma_{01} = 12.8 \times 10^{-17}$ cm^2. For L = 300cm this gives (for P in mb):

$$R = 1040 P \qquad (2.4)$$

ie., typically 1-4% for full power injection and standard neutraliser gas flow. It is the value of Γ for reionised particles which determines the maximum beam particle current which may be transmitted before the onset of beam blocking. This latter phenomenon arises when Q_{DUCT} exceeds the rate of pump-out and an equilibrium cannot be established until the pressure has exponentiated to a level at which a substantial
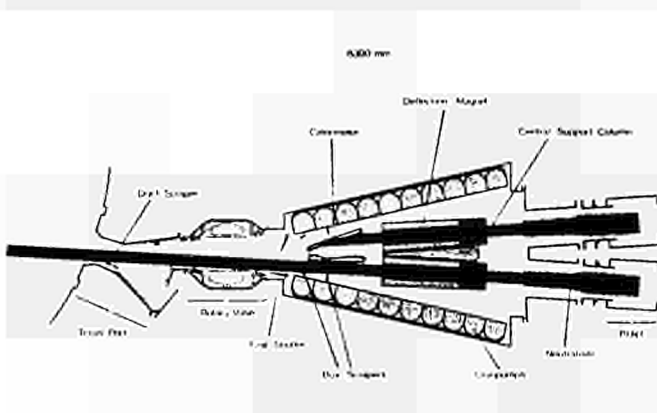
fraction R of the beam becomes reionised [2]. It may be shown that a sufficient condition for beam blocking is when:

$$\Gamma > \frac{C}{\sigma_{01} \, L \, \phi_B} = \Gamma_{CRIT} \qquad (2.5)$$

For values of σ_{01}, L given above, and for the appropriate value of $\phi_B = 1.25 \times 10^{20}$ s^{-1} per beam (80 kv D°) eq.(2.5) becomes:

$$\Gamma_{CRIT} = 32/N \qquad (2.6)$$

where N is the number of beams which traverse the duct (for JET, 1≤N≤8).

Equations (2.1-2.4) may be used to derive a value for Γ from the Penning gauge data. The derivation relies on an estimate of the directly intercepted fraction I, and on the assumption that Γ is the same for the directly intercepted and reionised beam particles. In §3 it is shown how estimates of Γ for the reionised and directly intercepted particles may, in principle, be separately obtained. However, this requires a scan of gas input into the NIB at constant power, and only a small amount of suitable data are available. Moreover, such a scan requires constant duct conditions over several pulses, and therefore cannot be applied to pulses early in the conditioning sequence. Therefore, estimates of Γ given below are based on eqs.(2.1-2.4) with a value I=0.015 assumed. This value is based on results from the neutral beam transmission code ZAP [3] and is supported by calorimetric data (§3).
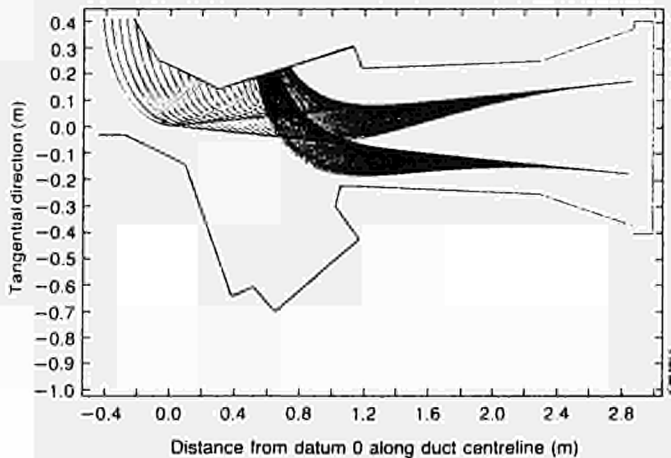
Fig. 2   Simulated re-ionised particle trajectories for 80 keV D° tangential and normal bank beams. The magnetic field corresponds to a 3 MA limiter plasma. Particles dumped in the duct are created over a length L ~3m extending back through the RHVV to the NIB. The simulation is well-supported by thermocouple measurements.

2.2 Conditioning history of uncarbonised copper duct surfaces

The conditioning procedure is always carried out following a machine vent to atmosphere. Prior to operation with plasma the vessel is baked at 300°C and subjected to several hours of glow discharge cleaning (GDC) in D$_2$, then in He. The duct water circuits are then cooled with N$_2$ and filled with water before injection starts.

Fig. 3 shows the Penning gauge traces during injection of a single beam for 0.5s, for the first and second shots in the conditioning sequence of a 'clean' (uncarbonised) duct. The two traces exhibit markedly different features. The first pulse shows clearly a large but finite release of gas within the first ~100ms, followed by an exponential-like pump-out. No significant change in plasma density, radiated power

etc. is observed, and it is assumed that the released gas is D$_2$. On the subsequent pulse, there is no sign of a fast gas release, and the pressure rises towards a limiting or slowly increasing value. The observed behaviour suggests a prompt release of a <u>finite</u> amount of loosely bound gas on the first shot, followed quickly by an approach to approximately steady-state conditions. More insight is gained from evaluation of Γ as described in §2.1. Table I gives the results for the time phases marked in Fig.3; the duct pump-out speed is taken from reference [4]:

Table I   Values of Γ obtained from eqs.(2.1-2.4) for C=150x10⁶cm³s⁻¹, L=300cm and σ_{01} = 12.8x10⁻¹¹ cm³

Phase	Description	Q_{DUCT} (mbcm³s⁻¹)	Γ
I	Prompt release phase	21400	33
II	Subsequent pump-out	16300	25
III	Second pulse, slowly rising P	2100	16
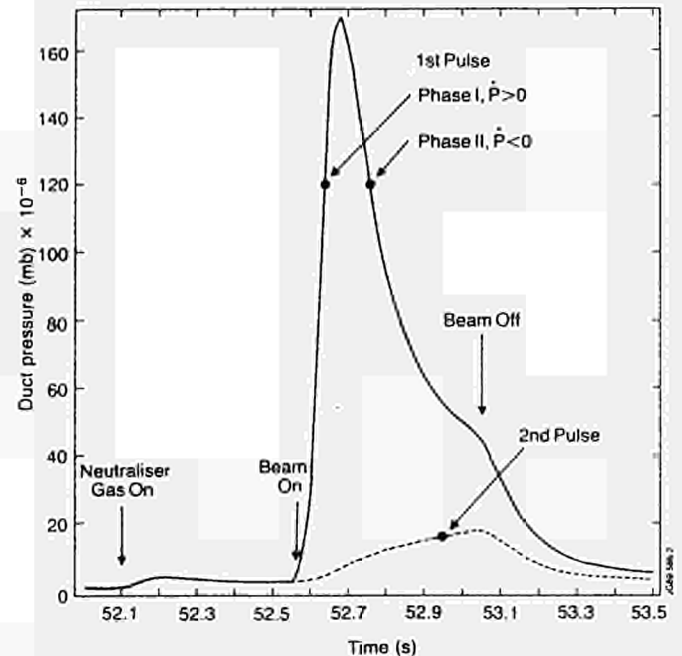
Fig. 3   Duct pressure evolution for the first and second single-beam pulses of 0.5s duration in an unconditioned, uncarbonised duct. The gas re-emission coefficients calculated from this data at each of the phases marked are given in Table I.

According to eq.(2.6), Γ_{CRIT} for 1 beam is ~32. The results in Table I suggest that $\Gamma \geq \Gamma_{CRIT}$ for the prompt release phase, which leads to a substantial pressure developing, corresponding to a reionised fraction R~15%. However, in the subsequent phase the calculation yields $\Gamma < \Gamma_{CRIT}$, whereupon the pressure tends towards a much lower equilibrium value. During the second pulse, a value Γ~16 is obtained, and there is no sign of a prompt release phase.

The above observations indicate that the first beam pulse in the conditioning process should be no longer than that necessary to desorb the loosely bound gas responsible for the prompt release, thus avoiding high reionisation power loadings during phase II while the high pressure generated in phase I is still pumping away. Calculations [5] based on particle trajectory tracing suggest that for a standard 3 MA limiter plasma, the maximum power density on the duct protection is approximately given by:

$$W_0 \text{ (W cm}^{-2}\text{)} = 4 \cdot 3 \, P \, (10^{-6} \text{ mb}) \qquad (2.7)$$

for 1 beam firing, and this result is supported by

measurements from thermocouples installed in the protection plates. Thus we have $W_o \sim 500$ W cm^{-3} during phases I-II of Fig.3, and this leads to temperature gradients and consequent mechanical stresses which approach levels sufficient to cause permanent buckling of the copper plates [1]; the 10-20mm Cu plates were designed originally for ~ 200 W/cm^2 for 10s. As a result of this analysis, the first pulse on each beam source has subsequently been limited to <200ms duration, which is found to be sufficient to desorb all the loosely bound gas. Conditioning continues by applying ~ 20 beam.seconds integrated injection in the form of short individual beam pulses of $\leq$ 1s duration. Up to 4 beams are usually fired sequentially into one discharge. The beams are then successively stacked and the pulse-length extended. The duct pressure is carefully monitored for signs of runaway. In the December 1987 conditioning sequence, $\Gamma \sim 2$ was obtained after ~ 150 beam.seconds. Conditions continue to improve over an operating period however; Fig.4 shows data for a 2 beam and an 8 beam pulse taken in the same session at the end of the first 1989 operating period and after several hundred beam.seconds of accumulated injection. A value of $\Gamma = 0.8$ is obtained in each case. The data of Fig.4 were obtained after Be had been evaporated onto the walls of the torus; no obvious differences in duct behaviour were observed following the introduction of Be. The amount of Be deposited in the duct region during operation up to July 1989 has been determined from sample swabs, and found to be ~ 250 μgm^{-2} which corresponds to an average thickness of 1.35×10^{-10}m.
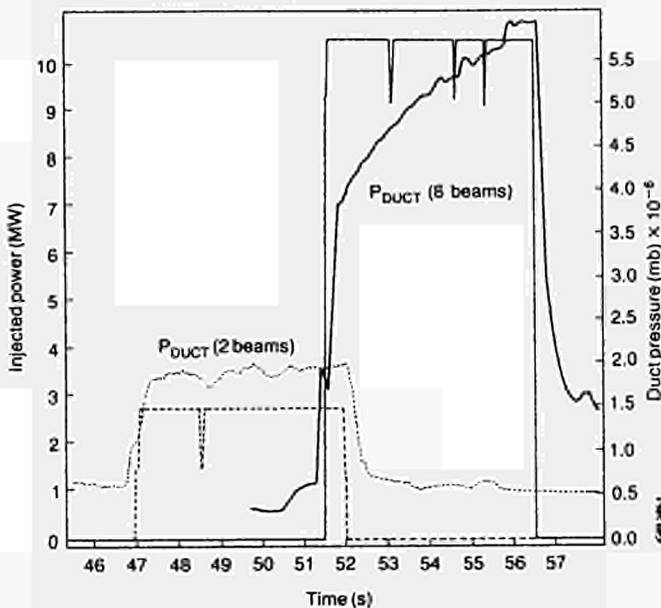
Fig. 4 Injected power and duct pressure evolution for long-pulse (5s) two-beam and eight-beam (10 MW) shots in a well conditioned duct. The data yield $\Gamma = 0.8$ in each case.

2.3 Conditioning History of Carbonised Duct

The JET vacuum vessel has been periodically carbonised in order to reduce Ni influxes from the ICRF antenna screens. This is performed by running a glow discharge in CD$_4$ for several hours with the vessel hot. The actual temperatures of the duct components recorded during the carbonisation were in the range 200-250°C. This section describes the general behaviour observed when attempting to condition the duct following a heavy carbonisation in January 1988. The main result is that duct conditioning was very slow, and the carbon film also appeared to re-absorb D$_2$ between pulses so that a large prompt re-emission pressure spike was generally present. Operation became so difficult that the vessel was eventually opened for mechanical cleaning of the duct surfaces.

2.3.1 Status of duct following carbonisation:
After the vessel opening, the following duct status was observed:

i) All copper surfaces on the duct and RHVV protection plates were covered with a thin layer of amorphous carbon which was easily removable by light rubbing. The depth of this layer increased in the direction away from the torus (towards the RHVV). This layer was also present on the explosion-bonded Nickel coating of the vapotron beam scraping elements.

ii) There was evidence of clean-up due to beam bombardment. This was principally on the side-scraping vapotron elements and in the mid-plane on the duct protection. There was still carbon present but definite lighter patches whose shapes were similar to the probable reionisation 'footprint' were seen.

2.3.2 Phenomena of carbonised duct conditioning:
a) First pulse: For the first pulse on all PINIs a massive pressure rise was seen on the Duct Penning gauge. This pressure rise was $\sim 6-8 \; 10^{-4}$ mbar and lasted until beam turn off (which was after 50-100ms for the first shots). According to eq.(2.7), the resulting maximum power density on the protection plate would have been ~ 2.5 kW cm^{-3}, a gross overloading very likely to have caused buckling of the Cu protection plates which was subsequently observed. At two of the first pulses the tokamak plasma disrupted shortly after the beam switched on. These disruptions were associated with strong carbon influx into the plasma. This influx was correlated with the beams with a delay of some 20-40ms between application of the beam and response of the CIII signal.

b) Subsequent pulses: On subsequent pulses, the pressure rise was substantially reduced (Fig.6) but the effect did not decline as rapidly as during the conditioning of the uncarbonised duct in December 1987.

The comparative figures are:

Clean duct pressure reduction in 3 shots: Factor ~ 80

Carbonised duct pressure reduction
in 3 shots: Factor ~ 20

Most striking is the difference in the pressure evolution after several shots. For the non-carbonised duct, after the first shot, there is no longer a prompt pressure pulse but the duct pressure comes up nearly to equilibrium and then begins a slow rise. After about 4-5 seconds accumulated beam-on time this is in the region of $\sim 1-1.4 \; 10^{-6}$ mbar. For the carbonised duct an initial pressure pulse (lasting ~ 200ms) is present even after several shots (Fig.5). This is then succeeded by a near equilibrium phase which is in the region of $\sim 6 \; 10^{-6}$ mbar at the end of a $\sim 1-2$ sec. pulse after 5.6 seconds accumulated beam-on time.

It is evident that the gas release of the carbonised duct under beam bombardment is characterised by prompt and equilibrium phases, similar to the uncarbonised duct case. However, in comparison with the uncarbonised surface:

i) The prompt gas release is dangerously large, and is observed on successive pulses.

ii) The pressure during the near steady-state phase conditions away more slowly, implying a high value of re-emission coefficient is maintained for longer.

It seems that between NB pulses the carbonised surface of the duct re-absorbs gas in a loosely bound fashion. This is not unreasonable in view of the

discovery on vessel entry that the surface was
amorphous in nature and would offer a large surface
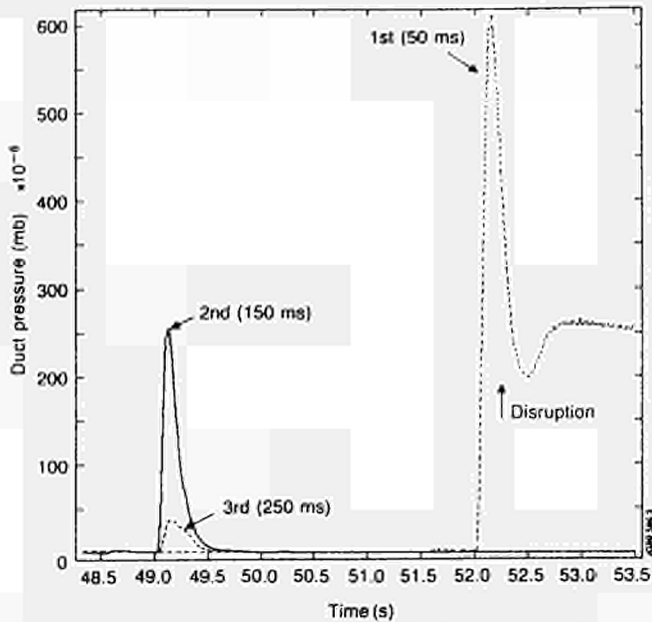area for pumping of tokamak deuterium.

Fig. 5 Duct pressure evolution during successive
initial single beam pulses through the
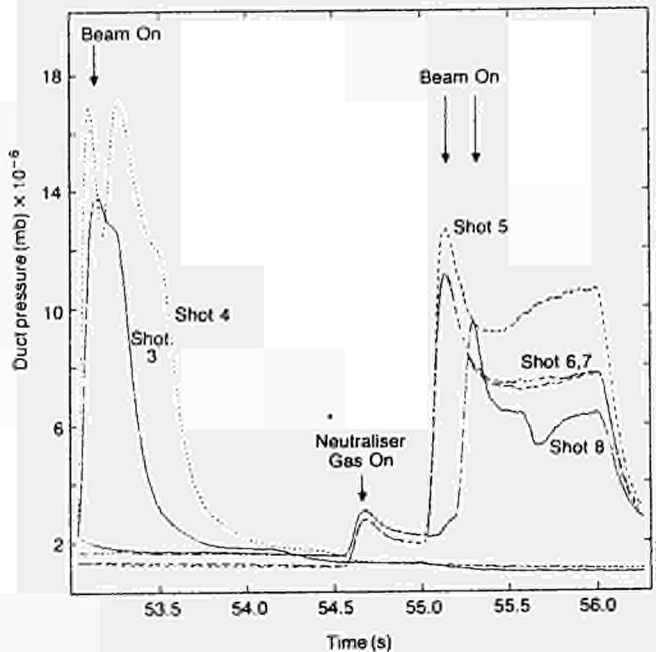carbonised duct. The beam pulse-lengths are
indicated in each case.

Fig. 6 Duct conditioning sequence for a single beam,
shots 3-8, in the post-carbonised duct. The
figure shows the slow reduction of the gas
release in both the prompt and equilibrium
phases.

3. Re-emission coefficient determined from a gas scan at constant power in a well conditioned duct

In this section, the equation for pressure
evolution in the duct region is given, and used in a
steady-state analysis of the pressure measured by the
Penning gauge in a well conditioned duct at different
total gas flows. A previous derivation has been
carried out by Riviere and Sheffield [2]. In the
present work the effect of direct interception is
additionally taken into account.

3.1 Equation for the duct pressure evolution: Pressure
evolution in the duct during injection is described
by the equation:

$$\frac{dP}{dt} = \frac{Q}{V} + \frac{Q_W}{V} - P\left(\frac{C}{V}\right) \qquad (3.1)$$

where P = duct pressure (mb)
V = duct volume (cm^3)
Q = gas input from the NIB and from direct
interception (mbcm^3 s^{-1})
Q_W = gas desorbed from the duct wall by
reionised particles (mbcm^3 s^{-1})
C = duct pumping speed (cm^3 s^{-1})

Q is the sum of net gas input from the NIB in the
absence of beam (Q_O), and gas produced by direct
interception:

$$Q = Q_O + \frac{\alpha \ \phi_B}{M} \quad mbcm^3 \ s^{-1} \qquad (3.2)$$

where ϕ_B = beam particle flux per second
α = coefficient equal to the product of the
fraction I of beam particles directly
intercepted and the associated gas release
coefficient
M = number of molecules in 1mbcm^3 at 300 K.

Q_W is the gas production rate at the duct walls
due to the impact of reionised particles:

$$Q_W = \phi_B \ P \ \Gamma \ L \ \sigma_{01} \ mbcm^3 \ s^{-1} \ . \qquad (3.3)$$

The steady-state solution of eqn.(3.1) is given
by:

$$P* = A \ P_O + B \qquad (3.4)$$

where P_O = pre-beam pressure when the only gas load is
due to the source and neutraliser gas,

$$A = \frac{1}{1 - \Gamma/\Gamma_{CRIT}} \qquad (3.5)$$

and

$$B = A \ \frac{\alpha}{\Gamma_{CRIT} \ \sigma_{01} \ L \ M} \qquad (3.6)$$

The above derivation implicitly makes the
following assumptions:

i) The contributions to the pressure distribution
in the Rotary Valve and duct region arising from each
source of gas are similar in shape, and

ii) The average value of the total pressure
distribution in these regions is adequately represented
by the measured pressure.

iii) Q_O is not significantly affected by the
removal of gas from the NIB by the beam.

iv) $n \ L \ \sigma_{01} \ll 1$

Semi-analytical calculations [5] of the pressure
distribution suggest that assumptions (i) and (ii) are
true to within a factor of 2. For standard operation,
the total gas flow into the NIB is 260 mbls^{-1} D$_2$,
compared with an equivalent neutral beam current of
only 19 mbls^{-1} D$_2$ thus supporting assumption (iii).
Equation (2.4) implies that $n\sigma_{01}L \leq 4\%$ and is generally
~1% for a well conditioned duct, confirming assumption
(iv).

3.2 Data analysis

During 1988 a series of synchronous pulses were
obtained in a well conditioned duct to investigate the
beamline performance at various total gas flows to the
NIB, while maintaining the beam power constant. The
four pulses analysed were all 2-beam shots with 2, 4, 6
and 8 neutraliser gas valves firing respectively
(25 mbls^{-1} D$_2$ flow per valve). The duct pressure
evolution was monitored by the duct Penning gauge.

A graph of P* vs P_0 is given in Fig.7. P_0 is the pressure measured immediately prior to switching on the beam, and P* is the pressure at the end of the beam pulse, taken to be representative of the steady-state value. The main feature of the plot is that the slope is close to unity. This implies, from eq.3.5, that Γ is much less than Γ_{CRIT}, ie. that the system is operating well below the conditions needed for beam blocking to occur. Assuming 1.5% of the beam particles are directly intercepted (consistent with calorimetric data for the same shots, shown in Fig.8) and using eqns. 2.5, 3.4-3.6, the 70% confidence domain of Fig.7 translates to $0.3 < \Gamma < 0.9$ for direct interception, and $0 < \Gamma < 1$ for reionised particles. A value of $\Gamma = 0.5$ would correspond to the ideal steady-state where the hydrogenic content of the near-surface material has attained a constant level. Within errors we are clearly in this position.
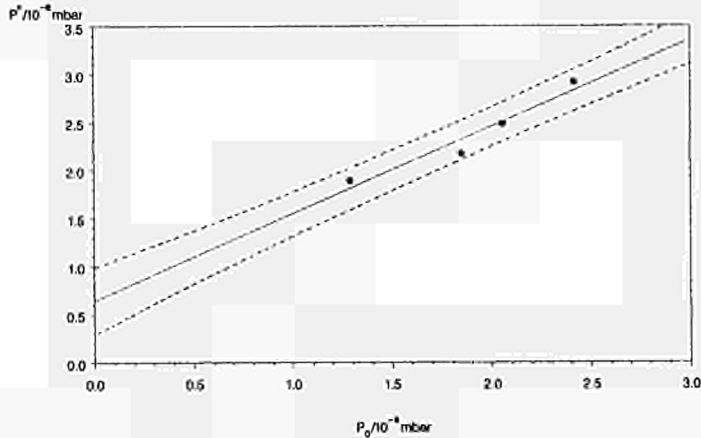
Fig. 7 Equilibrium pressure during beam-on, P*, versus pre-beam pressure P_0. The data were taken during a scan of total NIB gas input at constant beam power of 2.5 MW (two 80 keV D^0 beams). The broken lines define the 70% confidence limits for the straight line fit. The data were obtained in a well-conditioned duct.
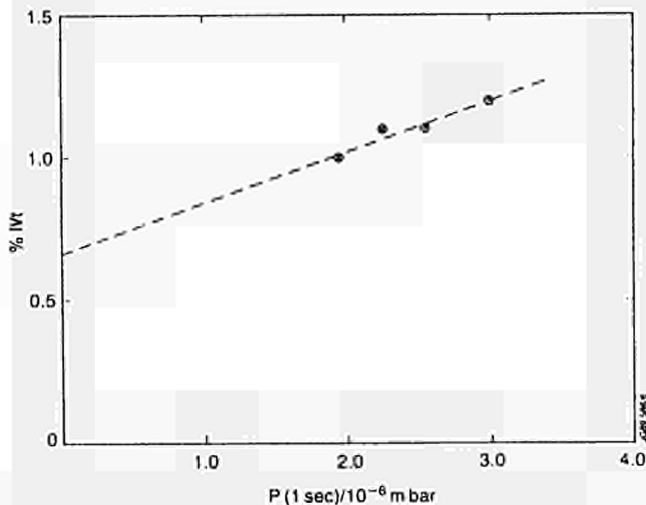
Fig. 8 Total energy deposited in the duct, from waterflow calorimetry, versus duct pressure measured after 1 sec of beam-on, for the same shots illustrated in Fig.7. The energy is expressed as a percentage of the total electrical energy delivered by the HV supplies. Offset of the fitted line gives the directly intercepted fraction I, when divided by the neutralisation efficiency. This yields I~1.5% which is used in the calculations of Γ.

A172

4. "UNLOADING" THE DUCT USING REDUCED GAS FLOWS

Equation (3.4) describes the reduction in reionisation fraction R to be expected from lowering the total NIB gas input Q_{NIB}, since $R \propto P*$ and $Q_{NIB} \propto P_0$. For JET the offset B is small (low direct interception fraction I), so that $R \leq Q_{NIB}$. Thus, a 50% reduction in Q_{NIB} should result in ~50% reduction in the reionised power density. Exploiting this possibility may be important, eg., to permit an extension of the pulse-length.

5. THE UPGRADED DUCT PROTECTION SYSTEM

Owing to the higher neutral power than the original design and unforeseen stray magnetic field effects (depending on the different operating scenarios of JET), high values of re-ionisation power density (> 100-600 W/cm^2) have been observed. This has resulted in a series of failures in the duct. Carbon tiles, that were first introduced to protect the Ni wall, resulted in large D_2 release and beam blocking [1]. Thereafter water cooled copper tiles were installed which have protected successfully the Ni liner to date. It is planned to replace this partially protected Ni liner with a new component which uses only inertially cooled copper tiles to protect the vessel wall. The proposed design as shown in Fig.9 will be more reliable (no bellows or flexible pipes), uses more than ten times less water (no hypervapotrons) and will be also simpler and cheaper. Some restrictions will be experienced however in operations much longer than 10s owing to lack of active cooling. The copper tiles can easily deal with the power densities experienced in the duct while the spacing of the brazed cooling pipes guarantees much faster cooling times than the inter-pulse time of 10 min. Slots are incorporated in the design of the copper tiles to minimise thermal stresses and bending of the tiles towards the beams due to temperature gradients across the tile thickness. The copper tiles have to withstand considerable disruption forces due to changes in the magnetic field of up to 50 T/S for a 7 MA disruption. The maximum aggregate disruption moment M (Nm) on a copper plate which is transmitted to the support structure is calculated using the formula

$$M = 0.12 \frac{\dot{B}t \; BA^{3/2}}{\rho} \qquad (5.1)$$

where $\dot{B}$ = rate of change of magnetic field (T/S)
B = remaining magnetic field perpendicular to surface of plate (T)
t = eddy current skin depth (m)
A = area of plate (m^2)
ρ = electrical resistance of copper

Owing to the method of supporting of the tiles, the actual maximum bending moment on each tile is ~ 10% of the above value. Fig.10 gives the stress distribution on the stainless steel support of the copper components.

In analysing the disruption behaviour of the tiles the time constant of the current decay and of the disruption are compared. These time constants have to be such that the disruption forces have time to develop during the loss of the plasma. Furthermore, no significant mechanical resonance problems are anticipated since the first three natural frequencies are <25Hz, c/f the characteristic disruption frequencies ~ 50-200Hz. A large number of thermocouples have been incorporated to monitor the operation of the component. Provisions have also been made for the pressure measurements (Penning gauges) and D_α-light scanners for checking the beam position (Fig.9).
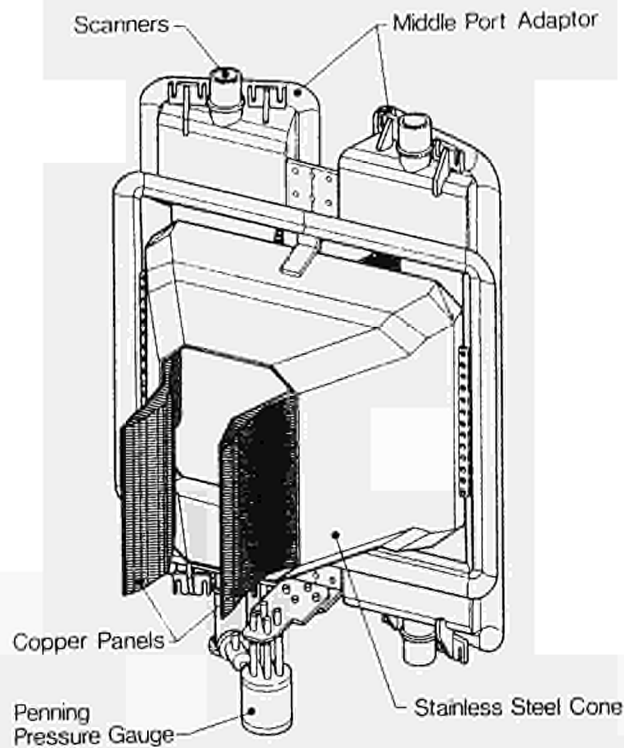
Fig. 9 The upgraded NI Duct Protection system and its instrumentation.

Fig.10 Stress distribution on the stainless steel support cone due to eddy currents.

[4] A P H Goede, JET Divisional Note "Gas flow caluulations for the JET Neutral Injector in the Test Bed and Torus Configurations", JET-DN-C(85)9.

[5] H P L de Esch, JET Divisional Note, "Influence of Magnetic fields on the power loading of the duct", JET-DN-C(89)76.

[6] S Papastergiou, "The NI Duct Protection for the DT Phase of JET", JET Divisional Note, JET-DN-C(88)60.

References

1] A Goede, S Papastergiou, et al, "The Reionised Neutral Beam Fraction and the Duct Wall Protection of the JET Neutral Beam Injectors", Proc. of 12th Symposium on Fusion Engineering, Vol 2, p 1115, Monterey (USA), Oct.87.

2] A C Riviere and J Sheffield, Nucl.Fus. 15 (1975)944.

3] R S Hemsworth et al., 3rd Neutral Beam Heating Workshop, Gatlinburg (1981) p.611.

RELIABILITY ANALYSIS OF THE JET NEUTRAL INJECTION BEAMLINES

S Papastergiou

JET Joint Undertaking, Abingdon, Oxfordshire, OX14 3EA, UK

Abstract

Early operation of the JET Neutral Injection systems was affected adversely by poor reliability in some of the duct protection, electrodeposited components and inconel bellows. A quantitative reliability analysis has been undertaken to highlight necessary design and component improvements.

The analysis is based on a two-stage Markov followed by a Duane model of the system. The Markov model represents the system as having two stages: the working and failure stages. It can go from one stage to the other through failure and repair rates. Expressions for reliability and availability are obtained in terms of these failure and repair rates, which do not change radically for relatively large periods of time. The two stage Markov logic can be also extended to a three stage one.

The Duane model is a curve fitting model for the time evolution of fault occurrences. It can quantify any reliability improvements and, when combined with a confidence statistical analysis (X^2 test), it can predict future failure rates at a certain level of confidence. Such predictions have been verified by the behaviour of both Neutral Injection (NI) systems.

The model has shown that a series of design and component changes has resulted in a many-fold increase in the reliability of the system. Copper electrodeposition has been largely replaced by contact cooling or deep drilling technology. The number of bellows is being minimised and their manufacturing methods are being improved. An upgraded duct protection system is being implemented.

The model quantifies the reliability improvements of each design change, assists in the definition of the spares policy and can predict the reliability of the system during the active phase. It shows that the reliability improvement is adequate since its predicted value during the active phase is compatible with its duration and the spares policy. Moreover, it highlights that the availability of the system during the active phase will depend mainly upon the remote handling repair rates.

Introduction

Several failures in various parts of the mechanical systems of the JET NI Beamlines have affected adversely their reliability and availability [1]. Electrodeposited copper components (magnet liners, neutralisers, calorimeter backpanels) have failed and thus were replaced by deep drilled, brazed (calorimeter backpanels) or contact cooling components. Similarly, thin walled single ply inconel bellows failed and have been mostly replaced by stainless steel multi-ply bellows.

Other failures that have affected the beamlines were: a broken filament stem and filament ceramics in plasma sources, failure of a Helicoflex vacuum seal in the accelerator stack, water freeze-ups in the system, shear of a pin in the drive mechanism of a calorimeter [1], and unreliable behaviour of Rafix water connections.

The protection of the duct wall has been a particularly difficult problem and several failures have been experienced there. These were due mainly to the inability to predict accurately the trajectories and the resultant power densities of the reionised particles in the duct region under the different magnetic fields which are produced from the several JET operational scenarios [2,3].

However recent measurements of the JET stray magnetic fields combined with a particle trajectory tracing code have enhanced our understanding of the problems [5]. Furthermore a new upgraded [3] component will be installed to enhance the reliability of the systems in the duct region.

Definitions - Assumptions

Definitions

Reliability, $r(t)$: probability of no failures in a given interval of time Δt_i.

Availability, $p(t)$: probability of working at a given time.

The reliability depends on the failure rate λ while the availability is a function of both λ and the repair rate μ.

Assumptions

(i)   Only the mechanical system is analysed.

(ii) The time of the analysis is the calendar time, excluding non-operational time such as planned shutdowns and maintenance periods.

(iii) When a component is repaired/replaced through a major design change which aims to remove a common cause failure, the reliability related to this particular fault (only) of the new component is 1. Note that the other possible causes of failure in the component remain (bellows, welds, etc). This assumption has been tested successfully with the replacement of the electrodeposited components, the single ply inconel bellows and the duct protection, over several years of the operation of the beamlines.

(iv) For any reliability predictions, it is assumed that the historic behaviour of a system

determines its future performance, provided that the operating conditions do not alter significantly and the fatigue life of the components is not altered.

Markov Modelling of the NI System

Figure 1 shows a simple model for the repairable NI system. This system can go from the working state W to the failure state F and back through λ and μ respectively. Such a model can be used to calculate approximately the availability p(t) and reliability r(t) of our system through the failure and repair rates [4]. Such a calculation is valid since the failure rates of our systems remain approximately constant for long periods of time (Fig.2):

$$p(t) = \frac{\mu}{\lambda + \mu} \left[1 + \frac{\lambda}{\mu} e^{-(\lambda+\mu)t} \right]$$

$$r(t) = e^{-\lambda t}$$

when $\mu \gg \lambda$ then the unavailability of the system q(t) is

$$q(t) = 1 - p(t) = \frac{\lambda}{\mu}$$

W – Working Stage
F – Failure Stage
λ – Failure Rate
μ – Repair Rate
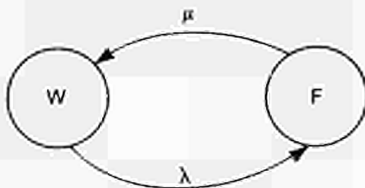
FIG. 1 Two stage model of each NI system

Therefore it is clear that the unavailability of our systems during say the active phase, depends equally on the failure rate and the repair rate. Repair rates through remote handling are unknown at present and thus unavailability predictions cannot be made. Future mock-up tests of the remote handling activities will help in predicting the unavailability of the system during the active phase

The above simple two stage Markov logic can be extended to a three stage one:

Stage	Condition
0	Both Injectors working
1	One Injector working
2	No Injector working

If the failure stage is defined as that with neither injector operating, then the Mean Time Between Failures (MTBF) is [4]:

$$MTBF = \frac{3\lambda + \mu}{2\lambda^2} = \frac{\mu}{2\lambda^2}$$

The values of λ, μ can be obtained from the historic behaviour of the system (Figs. 2, 3, 4).

The Duane Model

Figure 2 shows the bathtub curves for both the Octant 8 (OCT8) and Octant 4 (OCT4) injectors. The

period of infant mortality (which was shorter for the OCT4 system that came into operation later) is clear. Failure rates reduce by a factor of 5 while the reliability of the system in the typical intermaintenance period of 6 weeks increased by 20 times (Fig.5). The experience with the OCT8 system led to design modifications which resulted in faster reliability growth of the OCT4 system. Furthermore, it is also shown that a 50% reduction in the failure rate of the OCT8 system will be obtained through design changes: The manufacture of inconel bellows has been improved so that hardening of the material during manufacture is avoided and all welding can be tested during production. The new duct wall protection system [3] will reduce further the failure rates of both systems. No sign of ageing of either system is present.
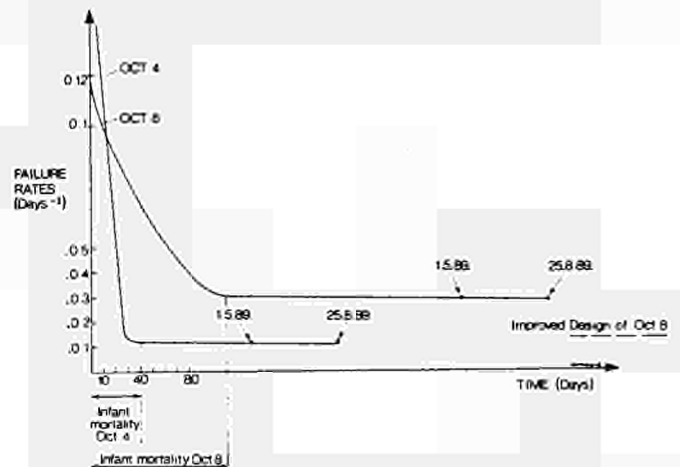
FIG. 2 Bathtub curves of the NI systems

Figures 3, 4 show the number of failures versus time for OCT8 and OCT4 respectively. Figure 3 shows also the improved OCT8 system when the design improvements, together with assumption (iii) mentioned earlier, are applied.

The reliability growth of our systems is apparent in all these graphs.

The behaviour of both systems in Figs. 3, 4 can be represented with the Duane model.

$$N(t) = Kt^{(1-a)},$$

where: N(t) = number of failures; t = time; K, a = parameters quantifying the initial system condition and rate of improvement respectively.
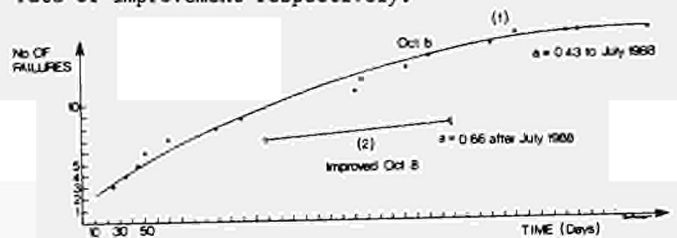
FIG. 3 Reliability growth diagram of the OCT 8 NI system

There is a strong reliability growth, as shown in the value of the parameter a in Figs.3 and 4. It is noted that any value near to 0.6 denotes an excellent reliability improvement, while a value of 0.2 indicates a rather routine improvement.
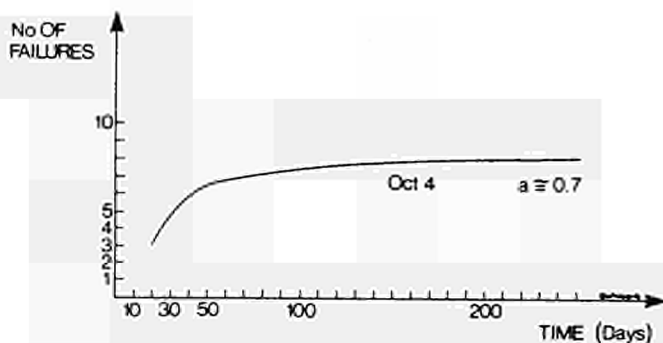
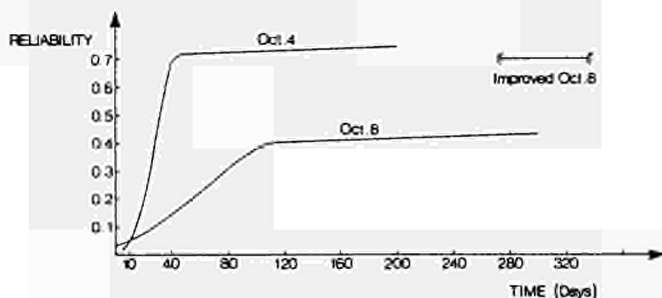FIG. 4 Reliability growth diagram of the OCT 4 NI system

FIG. 5 Reliability of the NI systems during a typical 6 week inter-maintenance period
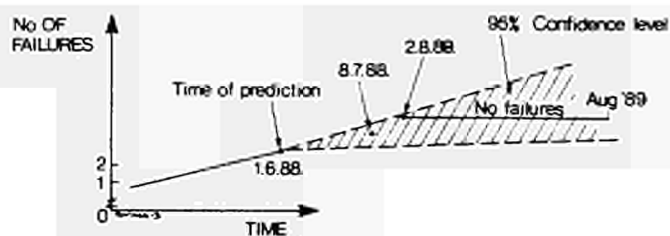

FIG. 6 Reliability prediction for the OCT 8 NI system
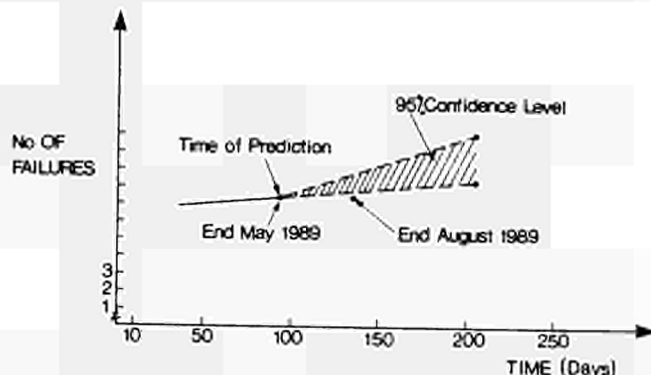
FIG. 7 Reliability prediction for the OCT 4 NI system

Reliability Predictions

The Duane modelling of our system together with the statistical X^2 test [4] can be used for reliability prediction, provided no major operational changes are incurred in the system. Such a prediction is of a probabilistic nature and can determine future values of failure rate Λ for a certain confidence level, say 95%.

The analysis results in

$$\frac{\lambda X_1^2}{2n} \leq \Lambda \leq \frac{\lambda X_2^2}{2n},$$

where: λ = the recent or average historical failure rate of the system provided it does not vary radically with time; n = the number of failures occurring upto the time of the analysis; X_1^2, X_2^2 = confidence values, depending on the confidence level; say 95%:, thus X_1^2 = 6.908, X_2^2 = 28.845 [4].

Confidence levels above 95% are not considered practical in view of the relatively few reliability data that we have. Figure 6 shows such a reliability prediction made in June 1988 and the following behaviour of the OCT8 system. The agreement is rather good. Figure 7 gives a similar analysis for the OCT4 system. At least one failure was predicted during 10 weeks of operation. In fact, no failure was seen in the 3.5 weeks following the time of prediction. Such a reliability prediction has been extended to the active phase of the system and checked successfully for its compatibility with the duration of this phase and the spares policy of JET.

Spares Policy

The above analysis can determine the spares policy of a system. The value of failure rate Λ can be predicted and then it can be shown [4] that a policy of s spares can cover us for a period of time T with the following probability, P(s)

$$P(s) = \sum_{i=1}^{s} \frac{e^{-\Lambda T}(\Lambda T)^i}{i!}$$

In the first half of 1988, electrodeposited neutralisers were failing while the delivery of the new deep-drilled ones was not due before the beginning of 1989. The above analysis gave us confidence that the two spare neutralisers we had for the second half of 1988 were adequate, with a possibility of ∿ 95%.

Maintenance - Replacement Policies

Figures 2, 3 and 4 show that the failure rate of both our systems is almost constant for relatively long periods of time. Their failure follows the exponential distribution with a failure rate $\lambda=0.01$ (days^{-1}). The exponential distribution is one of the Weibull distributions with the shape parameter equal to 1.

Suppose we intend to define a maintenance policy to replace components so that the total 'cost' (time lost) is minimised. The time T_m for such a preventive maintenance policy is [6]:

$$T_m = \mu - z\sigma$$

μ : mean life of our system; $\mu \equiv \frac{1}{\lambda}$ = 100 days
σ : standard deviation of fault occurrences
z : parameter depending, according to the Weibull distribution, on the cost of preventive maintenance, the cost of failure replacement, μ and σ.

However, it can be shown that since our failures follow the exponential distribution, the average service life in standard deviation units is 1. Thus irrespective of the costs of preventive and failure replacements, the policy we should follow is one of "replacement with same components only at failure" [6]. Naturally preventive replacements with components that will introduce design changes aiming to remove common cause failures and improve the failure rate and reliability of the system, should be done as soon as such causes are identified.

The above policy can be deduced also looking at the bathtub curves of Fig.2. It is clear that we are in the period of useful life of our systems with almost constant failure rates and failures of random nature. This random nature of failures justifies the above policy. Therefore, we should never replace a component with a spare one (Central Column, Box Scraper, Calorimeters, etc.), unless a failure occurs or a design improvement is aimed. It is worth noting that such a policy has been applied intuitively at NI Division of JET.

Conclusions

There is strong reliability growth of the JET NI systems, due mainly to well planned interventions to improve the design of the system.

A model has been developed and verified to quantify this reliability growth, predict future reliability and assist with a spares policy.

The reliability improvements of the NI system are compatible with the duration and the spares policy of the JET active phase.

Acknowledgement

References

[1] R S Hemsworth, Failures of the Mechanical Components of the JET Injectors, JET Divisional Note, JET-DN-C(88)62.

[2] A Goede, S Papastergiou, et al., The Reionised Neutral Beam Fraction and the Duct Wall Protection of the JET Neutral Injection Systems, Proc. of 12th Symposium on Fusion Engineering, Vol.2, p.1115, Monterey (USA), Oct. 1987.

[3] H Altmann, A J Bickley, T T C Jones, S Papastergiou, et al., Beamline Duct Gas Release/Conditioning, and the Upgraded Duct Wall Protection System of the JET Neutral Injectors, Proc. of 13th Symposium on Fusion Engineering, Knoxville (USA), Oct. 1989.

[4] D J Smith, Reliability and Maintenability in Perspective, 2nd Edition, MacMillan Publishers Ltd., 1985.

[5] B de Esch, Personal communication, JET, 1989.

[6] National Centre of Systems Reliability, An Introduction to Reliability Assessment, UKAEA, 1988

PUMPING OF GASEOUS HELIUM USING ARGON FROSTED LIQUID HELIUM CRYO- CONDENSATION PUMPS

P Massmann, R Romain, G H Deschamps, H D Falter, R S Hemsworth and W Obert

JET Joint Undertaking, Abingdon, Oxon, OX14 3EA

ABSTRACT

It has been demonstrated in the Neutral Injection Test Bed that the JET neutral injectors are capable of producing 10 s He beams repetitively with a rate of 7 min per shot without a prohibitive pressure rise. This can be achieved without modifications to the JET liquid helium (LHe) cryo-condensation pumps. The He is pumped by cryo-sorption on Ar, which is frosted onto the LHe temperature panels before each pulse. The measured effective pumping speed is about 0.25 times the value for H_2.

The measurements involved 3 cryo-pumps, 2 of the JET open structure type and one with a conventional type of liquid nitrogen (LN$_2$) cooled baffle. The tests show that the Ar/He coverage ratio and the thickness of the Ar layer seem to be important. The sticking coefficients for He on Ar frost derived for the 3 pumps agree with each other within the errors.

INTRODUCTION

It is proposed to inject beams of energetic He atoms into JET to simulate the behaviour of slowed-down α-particles and their subsequent exhaust from the plasma. Such an experiment will require a relatively high He pumping speed, to be achieved preferably without modifications to the LHe cryo-condensation pumps installed in the injectors.

Recent experiments have confirmed that satisfactory pumping speeds can be obtained by cryo-sorption on Ar [1] or SF$_6$ [2], which is frosted onto the LHe temperature panels of a cryopump. To demonstrate the feasibility of the cryo-sorption technique for a JET injector He pumping speed measurements have been made in the Neutral Injection Test Bed. For this purpose Ar was preferred because it combines the properties of a noble gas with a gas suited for cryo-sorption [3].

EXPERIMENT

A schematic of the Test Bed is shown in Fig. 1. The experiment is about 13 m long, the vessel volume 90 m³. Most measurements were taken with the 2 module version (Double Module) of the 20 module JET serial open structure cryopumps. A cross section of this pump is shown in Fig. 2. The height of the pump is 5.8 m. A comprehensive description of the pump is given in [4]. The open structure arrangement gives a transparency of about 50%, which is about twice the value obtained with conventional chevron pumps. Additional data was obtained for the other two cryopumps in the Test Bed, i.e. a prototype of the open structure pumps (OS Prototype) and a pump with circular cross section developed at FAR [5] with a conventional chevron type of LN$_2$ cooled baffle (FAR Chevron).

The conventional vacuum system consists of two turbo pumps of 1400 l/s (H$_2$) each, backed by a Roots blower and a roughing pump. For most of the measurements the turbo pumps were valved off once the cryopumps were cooled down, or it was verified that their influence was negligible.

Helium was introduced through the gas feeds of the second stage neutralisers. The He flows were measured with CHELL flow meters [6]. Argon was introduced in the Target Tank at a fixed rate of typically 40 mbl/s, determined volumetrically.

Generally pressures were measured with MKS Baratrons [6]. Only in the case of very low values BALZER IMR 120 ionisation gauges [7] were used. These had been calibrated against Baratrons, and the calibration was extrapolated to the low pressures measured.
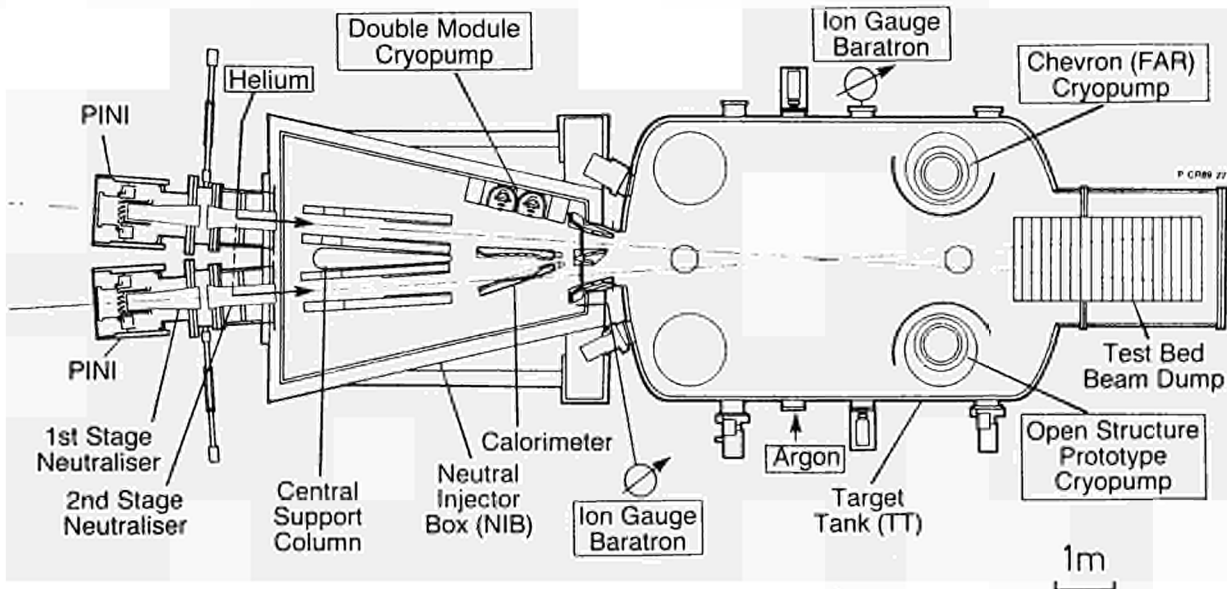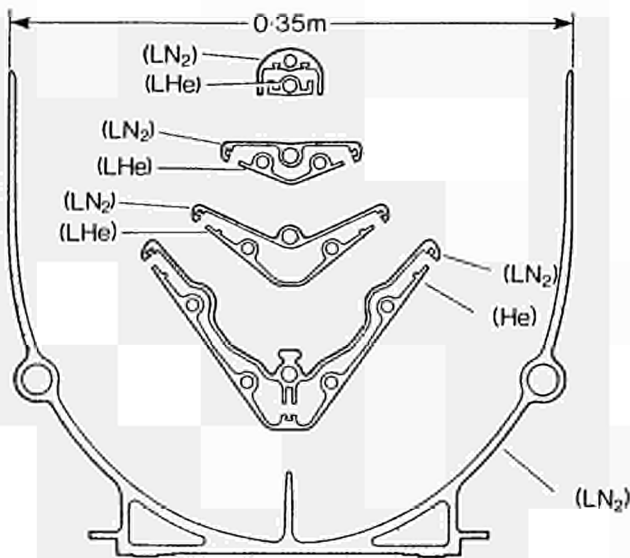

FIGURE 1: Plan View of the Test Bed

FIGURE 2: The JET Open Structure Configuration

RESULTS

Early measurements showed that applying one single Ar coverage with an Ar/He ratio, rated for the total of several subsequent He pulses, results in a continuous shot to shot decrease in the effective He pumping speed, defined by the ratio of the flow over the pressure rise from the start of the pulse. Therefore the desired amount of Ar was injected before each shot for the rest of the experiments.

Characteristic waveforms of the pressure rise during a He puff obtained with the Double Module are compared in Fig. 3. In each case the Ar/He coverage ratio was rated for a 10 s pulse and injected onto a clean LHe temperature surface. Curve (1) combines a relatively low He flow with a high Ar/He ratio. Under these conditions the pressure, after the system time constant, stayed constant for about 20 s and then rose slowly reaching a value of $4\ 10^{-4}$ mb when the pulse was stopped at 75 s.

Reducing the Ar/He ratio led to pressure plateaus of nearly the same height but of decreasing lengths, reaching merely 1 s for the lowest ratio considered (2). In Fig. 4a this dependence is plotted in terms of

the Ar density on the LHe temperature surface, the points corresponding to Ar/He ratios of 20:1, 40:1, 80:1 and 160:1. The effective pumping speed derived from the plateaus is shown in Fig. 4b.

For the case of the high He flow together with the low Ar/He ratio (3) the pressure does not saturate but increases moderately. The pressure drop after the He puff is however substantially steeper than for the case of the lower He flow. This behaviour has been confirmed for the smaller OS Prototype. In this case the transition from waveforms of type (2) to (3) occurs already at He flows of about 1 mbl/s. Unfortunately the pumping speed cannot be derived from the decay since it is governed by the system time constant.
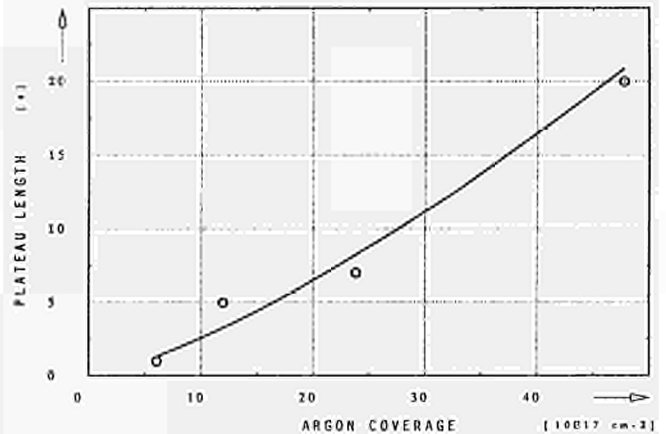
FIGURE 4a: Length of Pressure Plateau vs Ar Coverage
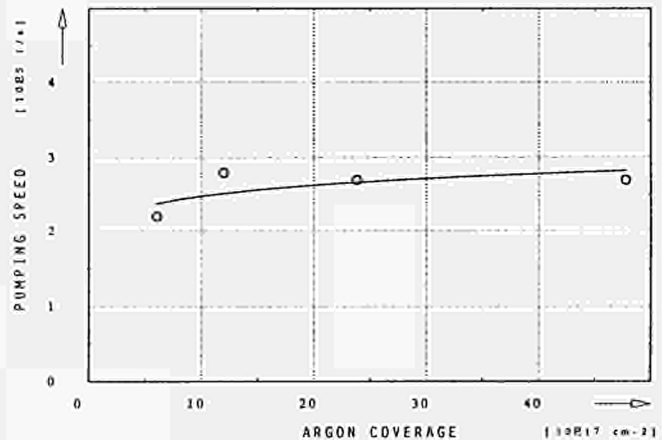
FIGURE 4b: Effective Pumping Speed vs Ar Coverage

Interestingly, the effective pumping speed for the low flow case, as defined by the plateaus of curves (1, 2) in Fig. 3, is approximately equal to that of the mean value (or the value at 6 s) of the high flow case, which shows no saturation.

A demonstration of cryo-sorption He pumping with an injector relevant flow rate of 26 mbl/s has been carried out with the Double Module (Fig. 5a). Twenty one consecutive 10 s He puffs have been injected admitting Ar with a ratio of 20:1 (at 10 s) prior to each shot. The repetition rate was about 7 min. Except from a minor regeneration at shot 16 (with subsequent recovery) the pumping speed as measured at 6 s stays practically constant.

FIGURE 3: Baratron Waveforms
(1) He flow 5 mbl/s, Ar/He = 160:1; (2) He flow 5 mbl/s, Ar/He = 20:1; (3) He flow 26 mbl/s, Ar/He = 20:1
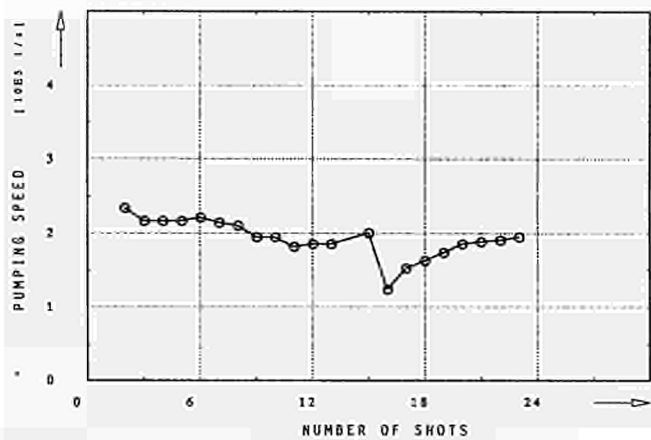
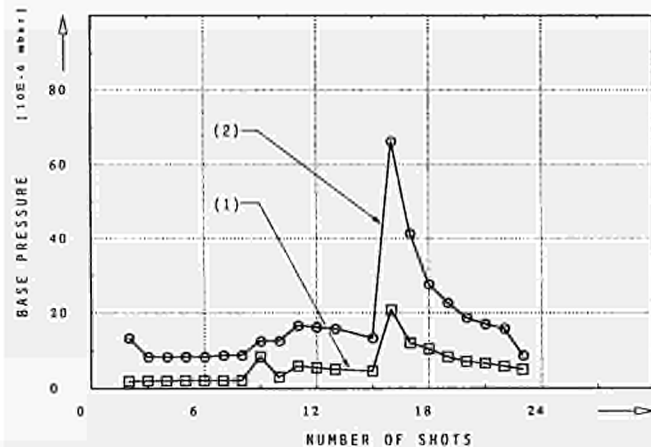FIGURE 5a: Helium Pumping Demonstration

FIGURE 5b: Base Pressures During Demonstration Run
(1) before a shot, after argon coverage; (2) after a
shot, argon not yet injected for the next pulse to come

The base pressures immediately before and after
each He pulse during the demonstration run are shown in
Fig. 5b. It can be seen that the pressure after a pulse
is typically higher than before (see also Fig. 3). The
old pressure can however be recovered, usually by one
new Ar coverage prior to the next shot. The 'acciden-
tal' shot 16 occured when one Ar puff was not suffi-
cient to reduce the base pressure far enough. It has
been verified with the OS Prototype that in such a case
additional Ar injection will bring down the pressure
provided the pump capacity is not exceeded. Generally,
thermal run-away (which nearly happend in shot 16) can
be avoided by allowing more time between shots, permit-
ting the exhaust flow to settle down to its stationary
level. Using the turbo pumps also helps to reduce the
base pressure before a new Ar coverage is applied.

As a part of the normal source conditioning
programme, 5 s He beams have been successfully extrac-
ted from one source with a repetition rate of about 4
min. For a higher shot frequency regeneration after a
couple of shots occured at several occasions.

Effective He pumping speeds have been measured for
the 3 cryopumps. The pumping curves are shown in Fig.
6. It can be seen that the pressure rises taken at 6 s
for the higher flow cases fit well onto a straight line
together with the points at low flows where a plateau
is obtained. The pumping speeds derived from Fig. 6 are
listed in Table 1. The errors in these measurements are
estimated to be about ±10%.

Since a pressure equilibrium is obtained in the
case of the lower He flows, the degree of binding of
the He atoms on the Ar snow has been calculated. The
sticking coefficient σ is given by [3]

$$1/\sigma = 1 + S_{maxHe}/S_{He} - 1/\tau \qquad (1)$$

where S is the measured pumping speed, S_{max} the maximum
pumping speed obtainable with a pump opening A and τ
the transparency of the baffle. For molecular flow
S_{max}/A is equal to 0.25 times the average thermal
velocity, i.e.

$$S_{max}/A = (1/4) (8kT / \pi m)^{1/2} \qquad (2)$$

For $\sigma = 1$ the transparency is given by

$$\tau = S/S_{max} \qquad (3)$$

The transparencies have been determined for the 3
pumps by measuring the pumping speeds for H_2 and
assuming a sticking coefficient of 1. The values
obtained are included in Table 1. Since the 2 pumps in
the Target Tank are equipped with a shield for protec-
tion against the beams and sputtered Cu from the beam
dump the transparency of the OS Prototype is lower than
the one of the Double Module. Similarly the transpa-
rency of the FAR Chevron pump is also lower than
measured at FAR [5].

The sticking coefficients obtained using equation
(1) are listed in Table 1. Since two pumping speed
measurements are involved the errors are estimated to
be $\geq \pm 20\%$.

DISCUSSION

It has been shown that acceptable pumping speeds
for injector relevant He flows can be achieved and
maintained for a large number of consecutive shots.
Fig. 3 confirms that cryo-sorption is a dynamic and
complex process. The explanation of the waveforms Fig.
3 is therefore restricted to some remarks following the
qualitative picture given in [3].

Strictly speaking the pumping speed in a cryo-
sorption process is not completely constant since the
sticking coefficient σ depends, in first instance, on
the (Ar/He) coverage ratio and the temperature of the
adsorbing (Ar) layer. σ decreases with higher tempera-
tures and increases with higher Ar/He ratios. Here the
variation is comparatively little for the high Ar/He
ratios but tends to gets stronger for the small ratios.
Additionally, He diffusion processes along the surface
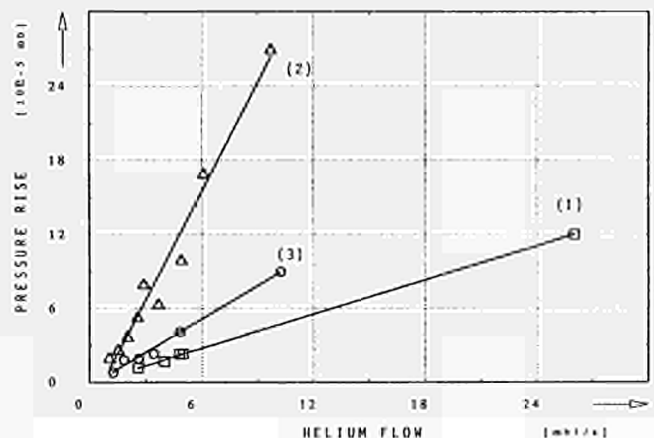and into the bulk of the Ar play a role. The latter is

FIGURE 6:   Pumping Curves
(1) Double Module; (2) OS Prototype; (3) FAR Chevron

TABLE 1
Summary of Pumping Speed Data

PUMP TYPE	Open-ing [m²]	LHe Area [m²]	HYDROGEN				HELIUM			
			Pumping Speed [10⁵ls⁻¹] $[10^5 \text{ls}^{-1}]$	Spec. Pump. Speed $[\text{ls}^{-1}\text{cm}^{-2}]$	Max. Spec. Pump. Speed $[\text{ls}^{-1}\text{cm}^{-2}]$	Transp.	Pumping Speed $[10^5 \text{ls}^{-1}]$	Spec. Pump. Speed $[\text{ls}^{-1}\text{cm}^{-2}]$	Max. Spec. Pump. Speed $[\text{ls}^{-1}\text{cm}^{-2}]$	Stick. Coeff. (± 20%)
DOUBLE MODULE	4.06	12.22	8.50	20.94	44.5	0.47	2.17	5.42	31.5	0.21
OPEN STRUCTURE	0.84	2.53	0.88	10.52	44.5	0.24	0.34	4.05	31.5	0.22
FAR CHEVRON	4.12	2.28	2.05	4.85	44.5	0.11	1.10	2.67	31.5	0.27
	A		S	S/A	Smax/A	τ	S	S/A	Smax/A	σ

again a function of the thickness of the adsorbing layer. With a thick Ar coverage the layers close to the surface, which mainly determine the pumping speed, are occupied longer before the particles can diffuse further into the bulk.

In terms of this qualitative picture curve (1) in Fig. 3 represents a high Ar/He ratio together with a thick layer, i.e. a high σ combined with an expected 'slow' bulk diffusion. These 2 opposite effects would explain why the effective pumping speed does not vary very much when the Ar/He ratio is increased, because the thickness is varied at the same time.

In the case of curve (3) we have a thick layer with an Ar/He ratio decreasing to a relatively low value at the end of the pulse. This would explain why the pressure is ramping up without reaching a plateau. The (with respect to curve (2)) steep decrease at the end of the pulse could then be interpreted as a relaxation effect due to diffusion into the bulk.

Compared to (3) in Fig. 3 the relative Ar/He ratio for curve (2) is the same but the thickness is reduced. This could explain why a plateau, albeit a small one, is reached in the beginning of the pulse where the Ar/He ratio is still high. It is however not obvious why the pressure should rise steeper than in (3) during the later stages of the pulse, unless there are temperature effects involved. Assuming poor heat conduction between the Ar and the LHe panel, it would become plausible that a 'heating up' of the Ar (due to larger heat conduction with increasing pressure) would have more effect on a thinner layer. Temperature rises of the LHe panel could however not be measured with sufficient accuracy.

The explanation of diffusion into the bulk is somehow contradicted by the early measurements with a single thick layer rated for several subsequent shots. Here the effective pumping speed clearly decreased already after the first shot. An alternative explanation could be that the surface of the Ar frost becomes rougher when the thickness of the layer is increased, offering a larger adsorption area per He atom. This could explain the difference between curves (3) and (2), because a thicker and rougher layer would have a higher pumping capacity. In this case it is however difficult to explain why the pumping speed in curve (1) is not higher than in the beginning of curve (2).

The measured sticking coefficients (Table 1) appear to be higher than the 0.14 reported in [8]. Only

a small correction of 5% towards lower σ would be obtained if a H_2 condensation coefficient of 0.85 [3] (instead of 1 assumed) would have been taken for the calculation of the transparencies. On the other hand the σ values for the 3 pumps are in reasonable agreement with each other.

CONCLUSION

The He pumping demonstration run and the experience with He beams gained in the Test Bed suggest that He injection into JET should not cause major operational problems. The technique of cryo-sorption with Ar injection between shots does not demand modifications to the existing cryopumps. The effective pumping speed measured with the Double Module indicates that the average pressure during a pulse will be about three times higher than for D_2 operation at the same flow.

Argon coverage prior to each pulse will require that the injector has to be valved off between shots to prevent flooding of the torus with Ar. This can be achieved with the already existing Fast Shutter. The Ar injection could easily be incorporated into the normal beam pulse schedule. In the Test Bed this is done by operating the Ar valve by means of a timer with an adjustable delay which is triggered by the closure of the neutraliser gas valves. Since the shot frequency of the injectors is considerably lower than in the Test Bed run-away of the cryopumps should also be easy to avoid.

REFERENCES

[1] K SCHAUBEL, J KIM, DIII-D Operations Memo, GA Technologies Inc., Dec. (1988)
[2] K SHIBANUMA et al., J. Vaccum Soc. Japan, 31 (1988), p 311, in Japanese, Figs in English
[3] R A HAEFER, Kryo-Vakuumtechnik, Springer, Berlin, Heidelberg, New York (1981)
[4] W OBERT et al., Proc. 13th SOFT, Varese (1984)
[5] Z SLEDZIEWSKI, Le Vide Supplement 221 (1984), p 47
[6] MKS Instruments Inc., 6 Shattuk Road, ANDOVER, MA 01810, USA, Fax (617)975-0093
[7] BALZERS AG, FL-9496 BALZERS, Liechtenstein, Fax (075)42762
[8] V B YUFEROV, P M KOBZEV, Sov. Phys. Tech. Phys. 14 (1970), p 1261

A COMPARISON BETWEEN HYPERVAPOTRON AND MULTITUBE HIGH HEAT FLUX BEAM STOPPING ELEMENTS

H Altmann, H D Falter, R S Hemsworth, D Martin, S Papastergiou, R B Tivey

JET Joint Undertaking, Abingdon, Oxfordshire, OX14 3EA, UK

Abstract

Structures capable of accepting high heat fluxes ($\geq 10MW/m^2$) in steady state are an important aspect of fusion engineering. The hypervapotron principle has been used successfully in the JET Neutral Beam Injectors at power densities up to 10 MW/m². Tests have been carried out in the JET Neutral Injection Test Bed to assess the safe operating limits of these elements which form the basic sub-unit from which larger components (beam dumps, scrapers, etc.) are assembled.

In addition, a multi-channel water cooled element ('multitube') has been developed and tested as a possible alternative to the hypervapotron.

The results from these tests are reported and a comparison is made between the data obtained from the two types of elements. In particular, the dependence of the peak power density limit as a function of total incident power, coolant flow and pressure are presented. Measured and computed temperature profiles in the elements are used to assess the internal stresses and their subsequent implications for the fatigue life.

Both the hypervapotron and the multitube type of element are shown to be suitable for the 140 kV deuterium and ultimately the 160 kV tritium Neutral Beam Injectors for JET.

Introduction

A series of tests have been performed to assess the safe operating limits of the hypervapotron elements (Fig.1) under varying conditions of flow, peak power density and total intercepted power. Interest in these limits exists because of the restrictions that the elements may impose on the proposed high voltage operation of the JET Beamlines in Deuterium and Tritium.

All JET elements have been constructed of a CuCrZr alloy. This results in a limit on the maximum element temperature of 450°C, imposed to avoid over-precipitation of the chromium in the material. The maximum element temperature is calculated from extrapolated temperatures measured by thermocouples installed 3mm below the front surface.

Tests have also included a 'multitube' element Fig.2 designed as a possible alternative to the hypervapotron. The element uses the same overall geometry, but the twin hypervapotron channels are replaced by manifolds that feed coolant to multiple holes drilled across the element face.

The test elements were instrumented extensively with thermocouples to give an overall thermal profile for use in a NASTRAN finite element analysis in order to obtain better understanding of the mechanical limits of the elements.

As possible improvements have been identified, the elements have been modified and then retested. This has led to a steady improvement in element performance and hence higher specified operational limits for both types of elements.
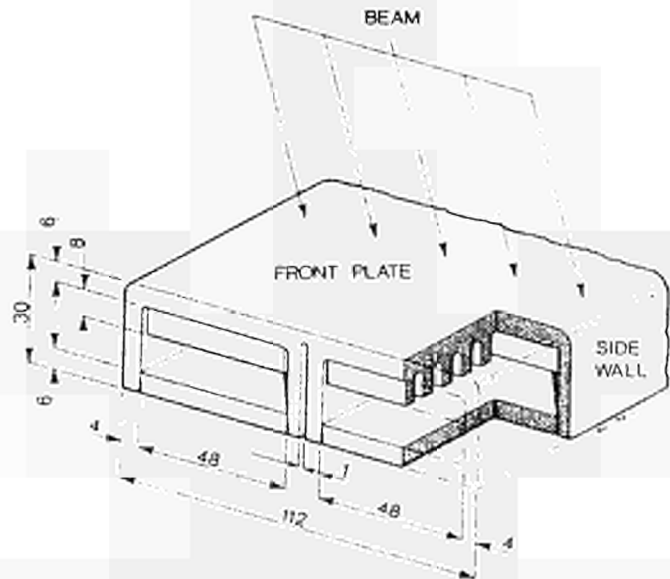
Fig. 1   Modified hypervapotron showing the 1mm slot at the central web.
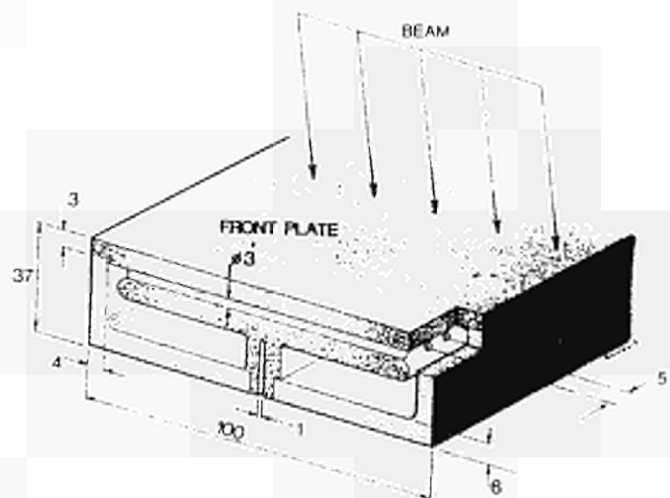
Fig. 2   Modified multitube showing the reduced hole pitch and the profiled cooling channel inlet and outlet.

Figure 3 shows the arrangement of the test elements and inertial strips used for calorimetry. The elements are suspended in the Neutral Injection Testbed target tank. In the most recent test, beams from two adjacent Beam Source positions were used in turn to illuminate the elements. This allowed the ratio of power density to total intercepted power to be varied because of the differing angles of incidence.
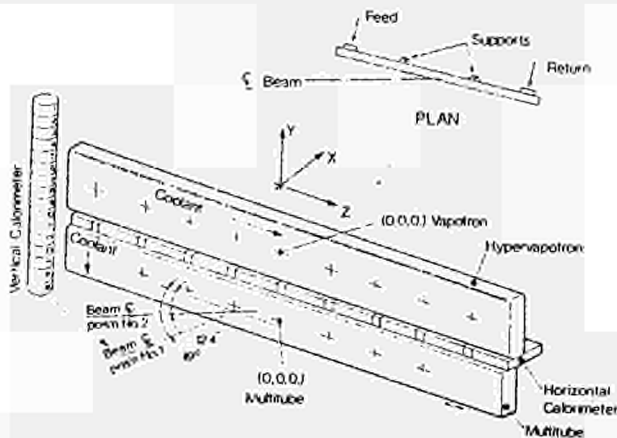
Fig. 3 Arrangement of test elements showing the inerial calorimeters and beam incidence angles from the two adjacent POSITIVE ION NEUTRAL INJECTOR POSITIONS.

Coolant was supplied to the elements via parallel circuits, the returns being led separately through the vacuum enclosure where control valves allowed element flow and internal pressure to be controlled individually.

Instrumentation included >100 thermocouples to monitor element and coolant temperatures, displacement transducers to measure element deflection and pressure transducers to measure pressure drop across elements.

The development and operational/tested limits of the elements are reported.

Results & Developments of Hypervapotron Elements

Examination of the experimentally determined temperature profiles has shown that the hypervapotron sidewall runs substantially cooler than the central web region. Even for shots where beams have been centred over the sidewall, peak temperatures are still recorded in the central web [1]. The temperature difference is >40%. The two regions have similar internal geometries except that there is a 1mm slot at the side wall, but a solid connection between the central web and the finned structure.

An element with a 1mm slot at both sidewall and central web was tested to determine the effect on its power handling capability.

The modified element was subjected to ~900 beam pulses with surface power densities upto 14 MW/m² for 7 seconds and total power upto 0.94 MW with coolant flows ranging from 3.6 to 22m³/hr. Data are shown in Fig.4 which demonstrates that, as expected, although the temperature of central web is reduced it still runs hotter than the sidewall. This difference can be explained by geometric effects and the reduced surface power density at the sidewall due to the Gaussian beam profile.
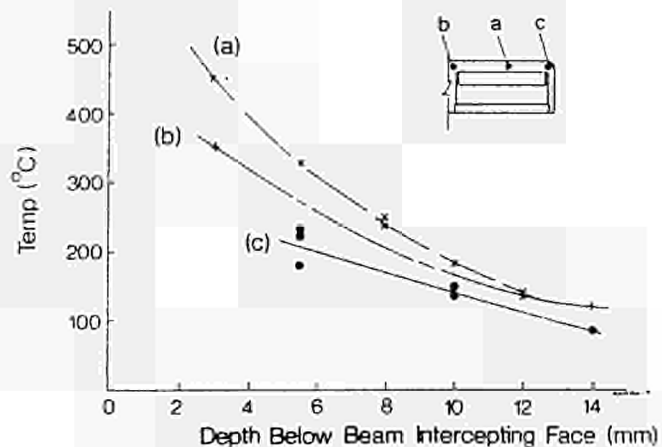
Fig. 4 Temperature gradient through the (a) Fin (b) central web and (c) sidewall for a coolant flow rate of 14.4m³/hr and a total power of 0.9 MW.

The inclusion of the 1mm slot has enhanced the coolant flow in the root of the central web and improved the heat transfer. This has reduced the web temperature without any significant effect on the finned cooling structure temperatures. Figure 5 shows the reduction in temperature of ~100°C for similar pulses on standard and modified hypervapotron geometries.
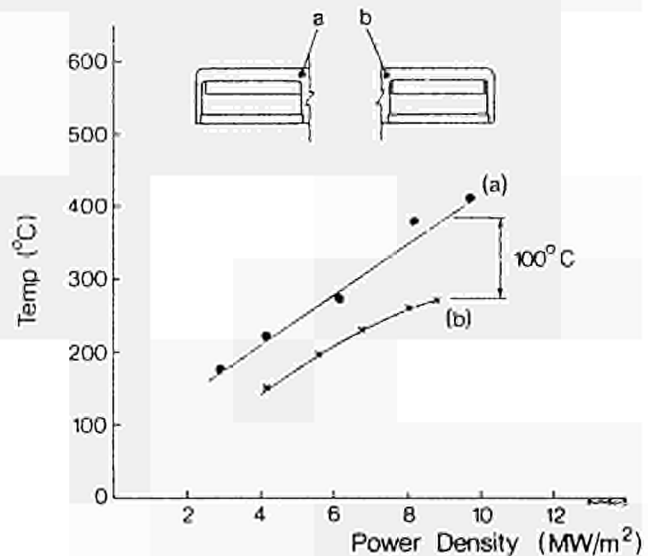
Fig. 5 A comparison of the temperature profile along the central web for (a) the single slotted hypervapotron and (b) the double slotted hypervapotron for identical total powers of 0.6 MW.

The resulting temperature profile is much flatter with the peak temperature appearing in the front plate above the finned structure. The performance of the hypervapotron was limited always by imposing a limit of 450°C on the maximum temperature of the CuCrZr alloy in order to avoid hardening of the material due to over precipitation. Hence the flatter temperature profile, and in particular the reduced temperature above the central web, allows the element to be rated for higher power densities.

The available driving head in the JET coolant system results in a flow rate of 13m³/hr in the full energy ion dumps and scrapers. At this flow rate, the peak power density and total intercepted power limits are 9.5 MW/m² and 0.710 MW respectively [2]. These limits contain a 20% safety factor to allow for any variation in flow rates through manifolded elements.

As previously reported [1] and contrary to a Thomson CSF design study prediction [3], the heat transfer coefficient improves with increasing coolant flow rate for a given power density. Figure 6 shows the peak power density capability of the modified element for a range of coolant flow rates. Taking the limiting thermocouple temperature which corresponds to 450°C at the surface, the power density can be increased by 33% for an increase in flow rate of 100%, this corresponds to an increase in total intercepted power capability of 30% to 0.940 MW.
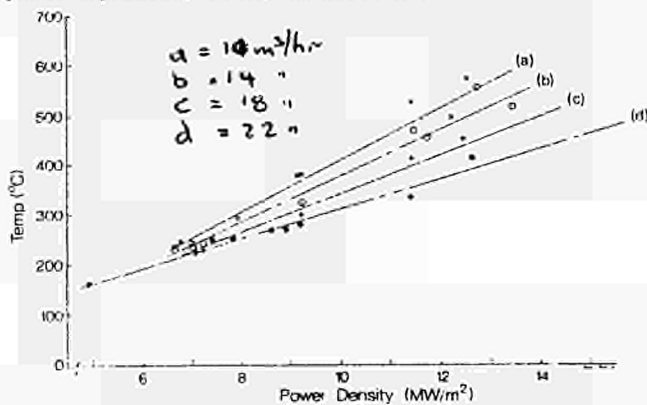
Fig. 6 The plot shows the reduction in the finned cooling structure temperature at a given power density for an increasing coolant flow rate.

The performance of the original hypervapotron element showed a dependence on total power [1], which started at around 0.3 MW and became very pronounced at 0.5 MW. A higher temperature variation was recorded along the element by the thermocouples in the central web than could be accounted for by the increase in bulk water temperature. The modified element displays the same characteristic at higher power levels (0.85 MW) Fig.7. The total power effect is not a characteristic of the central web only since thermocouples above the finned cooling structure also show the same trend.
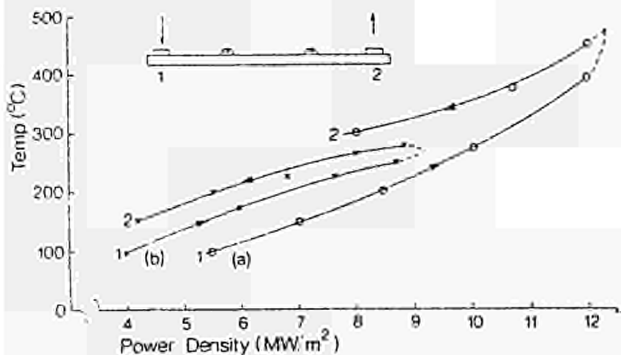
Fig. 7 Plotted are the temperatures recorded by the front face thermocouples in the hypervapotron for two pulses (a) 0.85 MW and (b) 0.6 MW total intercepted power. The lower power pulse shows a ΔT comparable to the 34°C measured by water thermocouples. The high power pulse exhibits the 'total power effect, the water ΔT is only 48°C.

Hypervapotron performance was thought to be sensitive to the hydrostatic pressure of the coolant [4]. In a controlled experiment specifically designed to investigate the pressure dependence, the coolant static pressure in an element was varied at a constant flow for a series of constant power beam pulses. No variation in performance was observed.

A 3-dimensional finite element analysis predicting the stresses in the twin slotted hypervapotron element has been performed using the thermal profile derived experimentally by measuring the temperature at various depths within the element, (a predicted thermal profile was not available as the hypervapotron effect cannot be explained by conventional boiling heat transfer). Von Mises stresses of 350 N/mm² are computed (Fig.9). The maximum surface temperature of 400°C, is equivalent to that expected for the highest operational value in the JET neutral injection beamline (~8 MW/m², 0.5 MW, 11m³/hr coolant flow). Approximately 5% of the total stress is primary stress produced by the internal pressure; the remainder being secondary stress brought about by the pulsed thermal load. These cycles of ± 160 N/mm² cause yielding and preliminary fatigue data indicates a safe fatigue limit of 2x10⁴ cycles of 400°C.
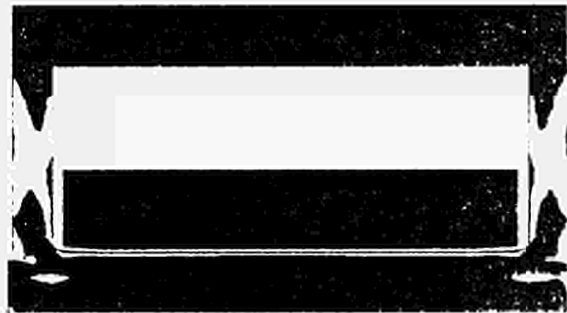

Fig. 8 Von Mises stresses for the twin slotted hypervapotron.

Results & Developments of Multitube Elements

A new 'multitube' element designed as a possible substitute for the hypervapotron element has previously been described [1]. The element, designed on the 'thermal skin' principle, allowed cooling over the whole of the front face and avoided the hot spot caused by the uncooled central web of the hypervapotron.

One of the main drawbacks of the prototype multitube element was its high coolant pressure drop. Testing showed that this was ~1.1 bar at 11m³/hr, approximately three times that of the vapotron [1]. Examination of the design identified two main areas where improvement could be made. These were the main inlet and outlet pipes and the drilled cooling channel entry and exit. The inlet and outlet pipes were changed to a race track geometry which increased the areas by ≈90%. The entry and exit of the drilled cooling channels were profiled to give a cleaner coolant flow path and the manifold area was also increased by 40%. Further improvements could only be achieved by radical changes to the overall geometry and size of the element.

Figure 9, compares ΔP versus flow for the modified and original multitube design with the hypervapotron. An improvement of ~40% in pressure drop over the multitube is apparent.
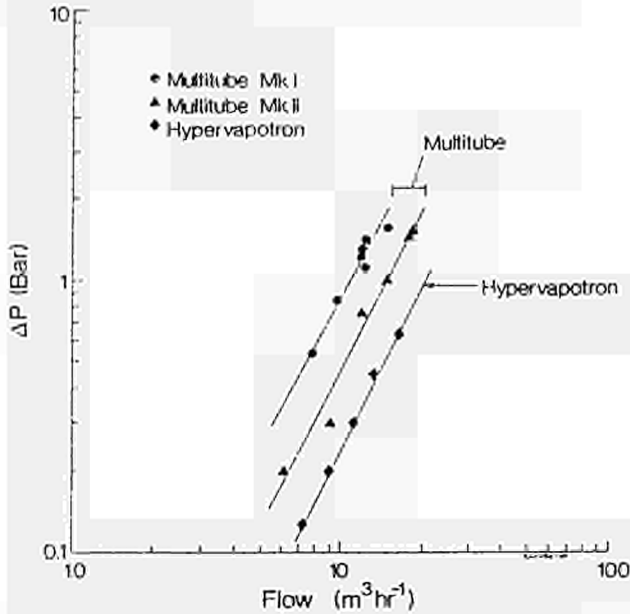

Fig. 9 A comparison pf multitube and hypervapotron pressure drop characteristics showing an average reduction in multitube ΔP of 42%.

The multitube element has handled up to 14 MW/m² in steady-state and unlike the vapotron does not exhibit any dependence on total power. The front face of the element is 3mm thick compared to 6mm for the vapotron. This results in equilibrium being reached quickly but the lower thermal capacity gives a smaller safety margin against short excursions in peak power density.

Testing has shown that for a coolant flow rate of 11m³/hr the total power limit of this multitube element is 0.8 MW [1]. Figure 10 shows a plot of temperature versus total power for 11 and 18 m³/hr coolant flow rate. Inset is a time versus temperature trace for 0.9 MW total intercepted power showing the increased rate of rise of temperature at the onset of burn-out.
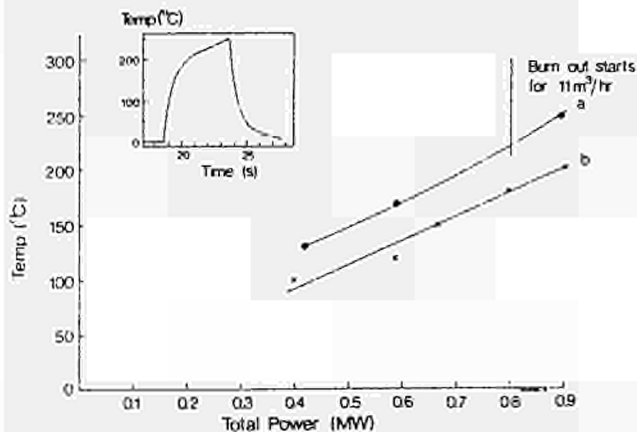
Fig.10 Multitube tube outlet temperature for a series of pulses with (a) 11m³/hr and (b) 18m³/hr. The burn-out region is shown for the lower flow. The inset figure shows the change in temperature gradient at the start of burn-out.

This temperature deviation of 16°C s⁻¹ is more than a factor two lower than measurements previously reported on a multitube element with a 6mm spacing between cooling channel centres (as opposed to the 5mm spacing reported here). Figure 11 compares the two types of multitube elements showing the improved performance of the 5mm pitch element.
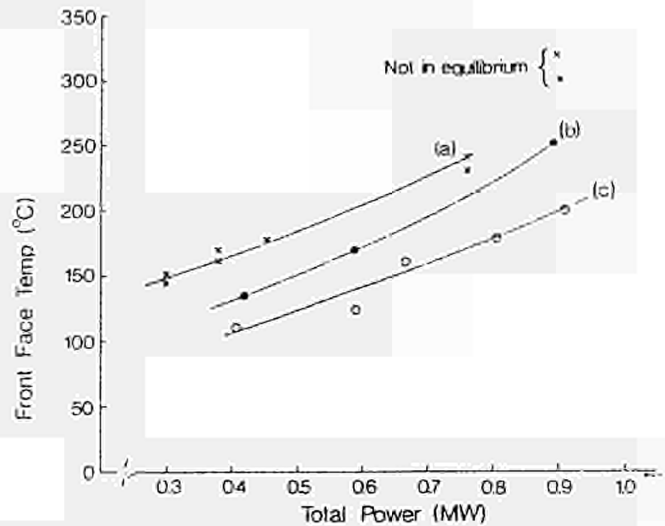
Fig.11 A comparison between multitubes for various flow rates and hole pitches (a) 14.4m³/hr and 6mm pitch (b) 11m³/hr and 5mm pitch and (c) 18m³/hr and 5mm pitch.

The thermal stress in the multitube has been computed using a calculated temperature distribution in the material. A 3-dimensional finite element programme was used. Temperature distributions in the copper were first obtained assuming convective heat transfer. Based upon these temperatures, a boiling component according to Chen [5] was added to the local convective term. The program was re-run and new temperatures were obtained. This iterative procedure was repeated until the total heat transfer to the water per cooling channel (based on the iterated local wall and water temperatures) was equal to the heat input per channel of 16 MW/m². The convective heat transfer coefficient varies from 0.02 MW/m² °C to 0.0385 MW/m² °C along the channel, while the total values (including the nuclent boiling term) vary from 0.0675 to 0.109 MW/m².

The predicted maximum Von Mises stress for a multitube without a slot between the manifolds is ~350 N/mm² and the maximum element temperature would be 475°C.

The sections in Fig.12 show the predicted temperature and stress distribution for a multitube element with a 2mm central slot, which allows free deformation of the manifolds, for a uniform surface power density of 16 MW/m². Maximum temperatures of ~500°C and stresses of 200 N/mm² are predicted.

1 = 69.8°C   5 = 262°C
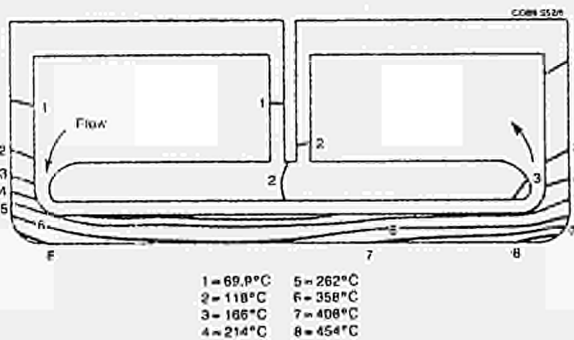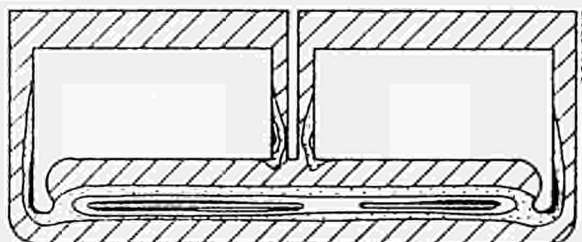2 = 118°C   6 = 358°C
3 = 166°C   7 = 406°C
4 = 214°C   8 = 454°C

Fig.12 (a) Temperature distribution in a 3-D model of
the centrally slotted multitube, for a
power density 16 MW/m³, internal pressure
3.5 bar.

▨ 11 N mm⁻² □ 109 N mm⁻²
▦ 60 N mm⁻² ▤ 157 N mm⁻²
■ 206 N mm⁻²

(b) Stress contours in a 3-D model of the
centrally slotted multitube.

The program used cannot predict the burn-out
region, the onset of which is found experimentally to
be at 14 MW m⁻² for a total coolant flow of
14.4 m³ hr⁻¹.

Using this reduced power density the maximum
stress is found to be 180 Nm⁻² and the maximum element
temperature 436°C.

The results from the finite element analysis show
that the temperatures and stresses at this power
density will be well within the limits for the CuCrZr
alloy used.

Comparison between the performance of
Hypervapotron & Multitube Elements

The main characteristics are compared in Table 1.

We have chosen to define the limit of performance
of a hypervapotron in terms of the maximum operating
temperature of the copper alloy used. Since we use
CuCrZr for its mechanical properties at elevated
temperatures [4] a maximum operating temperature of
450°C is chosen in order to prevent precipitation of
the Cr.

Exceeding the temperature limit of 450°C will
obviously not result in a short term failure but is
detrimental to long term fatigue life. Hopefully the
effect will be quantified and may lead to a cumulative
damage based performance limit.

The safe operating region for a hypervapotron
element in the plane defined by total power and the
peak power density is shown in Fig.13. Also indicated
is the (reduced) area available for operation in the
JET injection systems which is determined by the
restricted coolant flow available. Fig.13 also shows
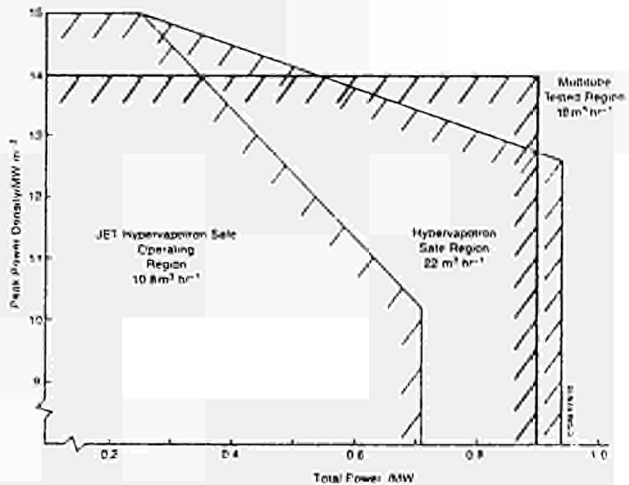the range over which the multitube element has been
operated.

Fig.13 Hypervapotron safe operating regions and
multitube tested region in terms of total
intercepted power and power density.

The violent boiling detected in vapotrons is not
observed in the multitube element. Pressure
transducers at the inlet and outlet of both elements
have recorded fluctuations ± 0.3 bar across the
multitube and ± 1.2 bar across the hypervapotron for
similar beam pulses.

The geometry of the multitube has been modified to
reduce the pressure drop by ~40%, but still remains
twice that of the vapotron. Any further changes will
only reduce this by a few percent unless radical
changes in overall geometry take place.

The particular alloy chosen for manufacturing the
elements is not widely used and as such no data base of
fatigue life exists. The material is at present
undergoing a limited study on fatigue life which will
give a better understanding of its long term fatigue
properties.

The maximum predicted Von Mises stress for the
hypervapotron and the unslotted multitube is
approximately 80% higher than that of the multitube
with the central slot.

	Hypervapotron	Multitube
Safe operating limit	Material temp <450°C	NOT DEFINED
Peak power density	15 MW/m² for ~0.25 MW total power	14 MW/m²
Total power	0.71 MW with peak power density of 10.2 MW/m² and 11m³/hr coolant flow rate	0.9 MW for coolant flow of 14.4m³/hr
	0.94 MW with peak power density of 13 MW/m² and coolant flow rate of 22m³/hr	>0.9 MW for coolant flow of 18m³/hr
Bend radius	58 m/MW/m²	100 m/MW/m²
Coolant pressure drop	0.3 bar 11m³/hr 0.5 bar 14.4m³/hr 1.1 bar 22m³/hr	.56 bar 11m³/hr 1.1bar 14.4m³/hr
Advantages	Wide operating range with no risk of burn-out Low pressure drop 5 years operation with no failures	Well defined thermo-dynamics No total power dependence
Disadvantages	Requires bend compensation bellows Violent boiling gives rise to vibration Operating mechanism not well understood	No burn-out statistics Flow distribution not known Risk of blockage of small tubes

References

[1] R Tivey, et al., Test investigating the performance limits of vapotron and multitube beam stopping elements, JET-DN-C(89).

[2] D Martin, et al., Test investigating the performance limits of modified vapotron and multitube, JET-DN-C(89)73.

[3] Thomson CSF, Technical report to JET contract JC110VHXX. Application of hypervapotron techniques to source of the JET cooling problems (1980).

[4] R Tivey, et al., Testing of beam stopping elements using hypervapotron cooling. Proc. SOFE, Monteray (1987).

[5] A B Tramschek, A A Nicol, Temperature and stress distribution in a Multitube element. Report from the University of Strathclyde, Glasgow, October 1988.

THE CONTROL OF PLASMA PARAMETERS TO AVOID
HIGH CURRENT DISRUPTIONS IN JET

A. Tanga, C. Lowry, P. Lomas, M. Garribba, M.F. Johnson, P. Noll, B. Tubbing and the JET Team
JET Joint Undertaking, Abingdon, Oxon., U.K.

Introduction

Disruptions at high plasma current in JET are a serious operational problem because of thermal overloading of in-vessel components and mechanical stresses due to induced currents. Empirically determined operating space have been mapped, which determine the operating condition free of disruptions both for x-point and limiter configurations.

In JET there are three causes of disruption : (1) MHD induced disruptions, (2) Density limit, (3) Vertical instabilities.

In order to avoid disruptions three operational diagrams have been empirically created which define operationally stable regions: (1) Gross MHD stability is described by a plasma internal inductance versus safety factor (ℓi vs q_ψ) diagram; (2) Density limit disruptions can be described by Hugill diagram; (3) Stability diagram for vertical instability, in terms of plasma elongation versus plasma current.

This paper describes the JET operation space of parameters and the means to control the plasma parameters to stay within the boundaries.

1) ℓi q_ψ diagram

MHD induced disruptions occur due to plasma current profile instability due to kink and internal modes [1]. The space of parameter can be then represented in a ℓi-q diagram [1,2] as shown in fig. 1. This diagram was compiled from the trajectories of about 1000 JET discharges in the limiter configuration [3].
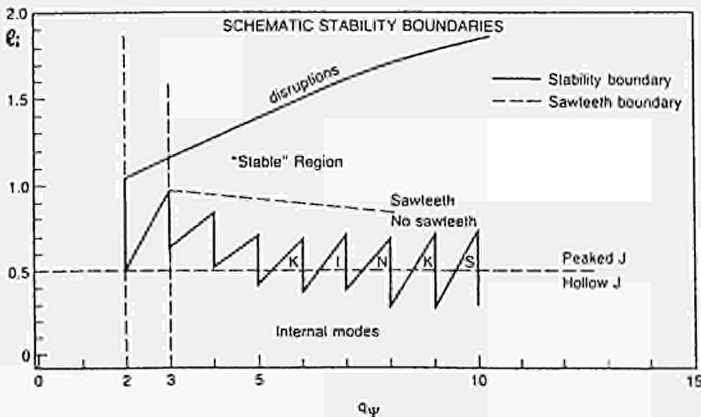

Fig. 1 Empirical stability diagram for JET. Lower boundary indicates the stability boundary for rotating MHD during the current rise.

There are three boundaries: (a) a high ℓi, (b) $q_\psi = 2$, (c) low ℓi.

The high ℓi boundary represents a disruptive boundary. The trigger of the instability is due to

steep gradient in the plasma current profile. Operationally one reaches this boundary by operating at the density limit or by rapid plasma expansion or by excessive peaking of temperature profile with central deposited radio frequency heating. In the case of x-point configuration a similar boundary has been found as shown in fig. 2. In fig. 2 the values of internal inductance are plot versus the safety factor, measured at 95% of the poloidal flux, for x-point disruptions. Most of these disruptions occurred in the formation phase of the x-point configuration when the plasma undergoes a rapid expension [4]. At present there is not a direct control of internal plasma inductance, therefore the control of ℓi is based mainly on control of temperature profiles.
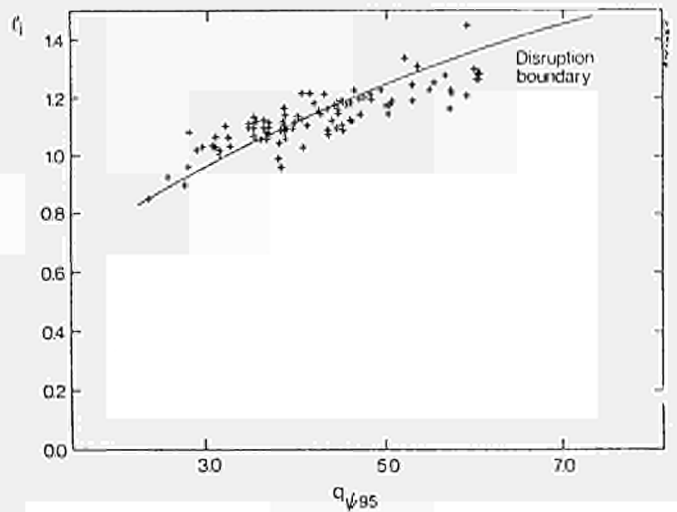

Fig. 2 Disruptive line at high ℓi for x-point configuration. On the abscissa the value of the safety factor at 95% of poloidal flux is shown.

A typical trajectory for a limiter discharge is shown in fig. 3. During the current rise the discharge trajectory is just above the lower stability boundary. The lower stability boundary limits the ramp rate of plasma current. Ramping up plasma current with constant toroidal field the maximum ramp rate is 0.3 MA/s. However, with simultaneous toroidal field and plasma current ramp with plasma expansion, required to keep q_ψ constant, higher plasma current ramp rate can be achieved, up to 1 MA/s.

The indentations at integer values of q_ψ are caused by strong external kink modes and/or by double tearing which may develop in a major disruption only at $q_\psi = 3$ and $q_\psi = 4$. At higher values of q_ψ the internal reconnection produces a rapid increase of ℓi without disruption.
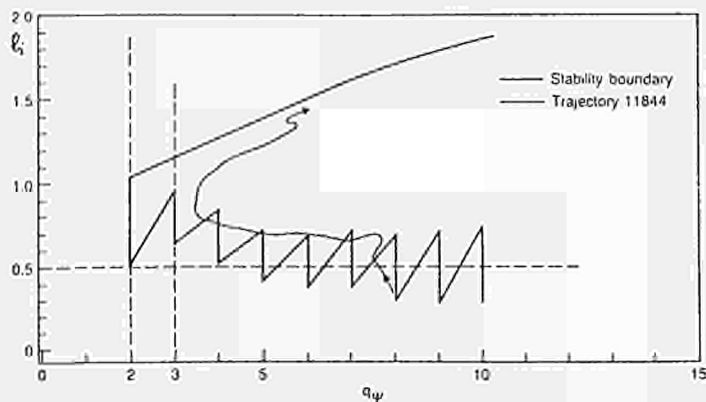
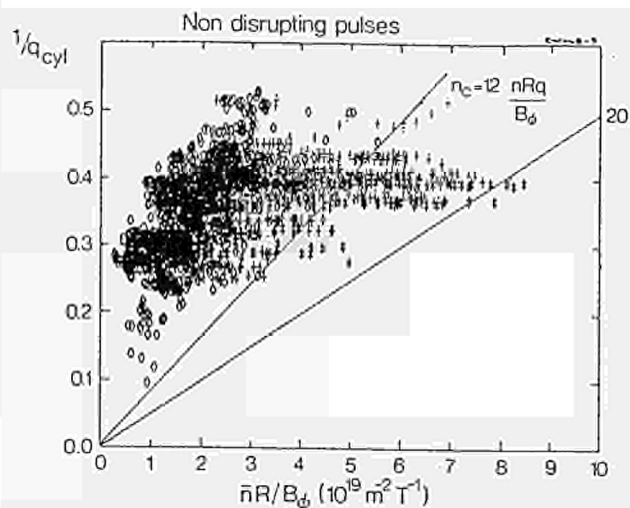Fig. 3 Typical trajectory for JET limiter discharge.

Fig. 4 Hugill plot for ohmic and additionally heated x-point discharges. Symbols: diamonds represent ohmically heated plasmas, crosses represent Neutral Beam heated plasmas, asterisks represent combined radiofrequency and Neutral Beam heated plasmas.

During plasma current decay generally the trajectory follows the upper ℓ_i boundary without disruption. Plasma current tail disruptions can be avoided by slowing down the plasma current decay rate. The q_ψ boundary has been tested experimentally in several limiter discharges [5].

2) Density limit

With carbon limiter the density limit disruptions start when 100% of the input power is radiated [5]. High edge radiation contracts the plasma channel until an MHD unstable profile is reached in the proximity of the upper boundary of the MHD stability diagram.

With Beryllium gettering, however, a high edge radiation situation (Marfe) does not necessarily lead to unstable profile and disruption. The Hugill diagram, a relation between the inverse of the safety factor and a normalised value of the plasma density [6] is similar in JET for limiter [7] and x-point configurations for gas fuelled discharges, which is shown in fig. 4.

In a well conditioned vessel the experimental point fell in the Hugill diagram within the boundary limited by the line $\bar{n}Rq_{cyl}/B_T = 12$ $(10^{19}\mathrm{m}^{-3}\mathrm{T}^{-1})$ for ohmic discharges and $\bar{n}Rq_{cyl}/B_T = 20$ for additionally heated discharges, both for limiter and x-point discharges (fig. 4). In the case of x-point high density is reached only in H-mode discharges [8]. In the H mode the density limit is normally not disruptive: first the plasma undergoes an H to L transition, then plasma density decays, especially at the edges of the plasma, then radiation also decays avoiding a disruptive effect. The H to L transition is triggered when the radiated power reaches 60% of the input power [9].

The control of plasma density is performed by plasma density feedback on a preprogrammed density waveform. Wall pumping techniques are used to reduce the plasma density during the decay of plasma current.

Both the Inner Wall and the x-point configuration (in L mode), with graphite tiles there is sufficient pumpiung of the plasma density to allow a disruption free termination of the discharges. Therefore in the operation with graphite limiter the plasma column is normally moved in contact with the inner wall during the plasma current decay phase.

3) Vertical instability

Loss of control of vertical position results in a vertical instability with consequent plasma disruption. The design of the feedback circuit allows in principle stabilisation up to growth rate of 280 s^{-1}[10]. A basic destabilising force acts on plasma with elongated cross section in JET. This is due to the quadrupolar component of the equilibrium field and to the iron image currents. These two effects can be described by a coefficient A''_{pp}. The vertical force acting on the plasma itself is:

$$F_{pself} = A''_{pp}I_p{}^2Z_p \qquad (1)$$

where

$$A''_{pp} = -\frac{2\pi R_Q}{I_p}\left[\frac{\partial B_R}{\partial z}\right]_{equilibrium\ field} + \left[\frac{\partial B_R}{\partial z_p}\right]_{iron}$$

$$\left[\frac{\partial B_R}{\partial z}\right]_{equilibrium\ field}$$

is the gradient of the quadrupolar component of the equilibrium field:

$$B_Q = \left[\frac{\partial B}{\partial z}\right]_Q Z$$

$$\left[\frac{\partial B_R}{\partial z_p}\right]_{iron}$$

is the radial field change caused by the iron circuit when the plasma is vertically displaced by an amount δz_p.

From eq.(1) a quantity related to the controlled current in the shaping coils can be derived which is called F_{number}, which is proportional to F_{pself}:

$$F_{number} = 0.098\ (I_p + K\ I_{SH})\ I_p$$

where K is a constant and the term in brackets represents the effect of the quadrupolar component of

the equilibrium field and of the image currents in the iron (proportional to plasma current). To achieve a given plasma elongation, the shaping current is normally proportional to plasma current, therefore $F \propto I_p^2$. Experimentally it is found that there is linear relation between F and I_p when the vertical instability occur. The resulting stability diagram is shown in fig. 5. The shaping currents are either preprogrammed or determined by shape control feedback [10].

Conclusions

It has been shown that for each of the three main causes of disruption, an operational diagram can be empirically determined which enables the design of discharges which are free from disruptions. However, with the exception of vertical instability, there is only an indirect control of plasma parameters. Therefore in order to avoid disruptions one relies on proven scenarios especially for the plasma ramp-up and decay. In 1990-91 JET programme there are planned experiments devoted to the control of the MHD disruptive phase via feedback control of the m=2 mode and by controlling the plasma current profile by LHCD.

References

[1] J. Wesson, Tokamaks, Clarendon Press, Oxford U.K., 1987, pp. 139-151.

[2] C.Z. Chen, H.J.P. Furth, A.G. Boozer, PPPL-2372.

[3] P. Lomas et al., in Proc. 15th European Conference on Controlled Fusion and Plasma Heating, Dubrovnik, May 16-20, 1988, Vol. I, p. 123.

[4] A. Tanga et al., in Proc. 12th European Conference on Controlled Fusion and Plasma Physics, Budapest, 2-6 September, 1985, Vol. I, p. 70.

[5] J. Wesson et al., "Disruptions in JET", JET-P(88)44, 1988.

[6] J. Hugill, Proc. 2nd Joint Grenoble-Varenna Int. Symp. Como (Italy) 1980, p. 775.

[7] A. Gibson and the JET Team, Plasma Physics and Contr. Fusion 30, 1375 (1988).

[8] A. Tanga et al., Nucl. Fus. 27, 1877 (1987).

[9] H.J. Jaeckel, P.J. Harbour, N. Gottardi et al. in Proc. 14th European Conference on Controlled Fusion and Plasma Physics, Madrid, 22-26 June 1987, Vol. II, p. 718.

[10] P. Noll, R. Aigle, M.L. Browne, D. Corbyn et al., in Proceedings of the 11th Symposium on Fusion Engineering, Austin, 1985, Vol. I, pp.33-40.
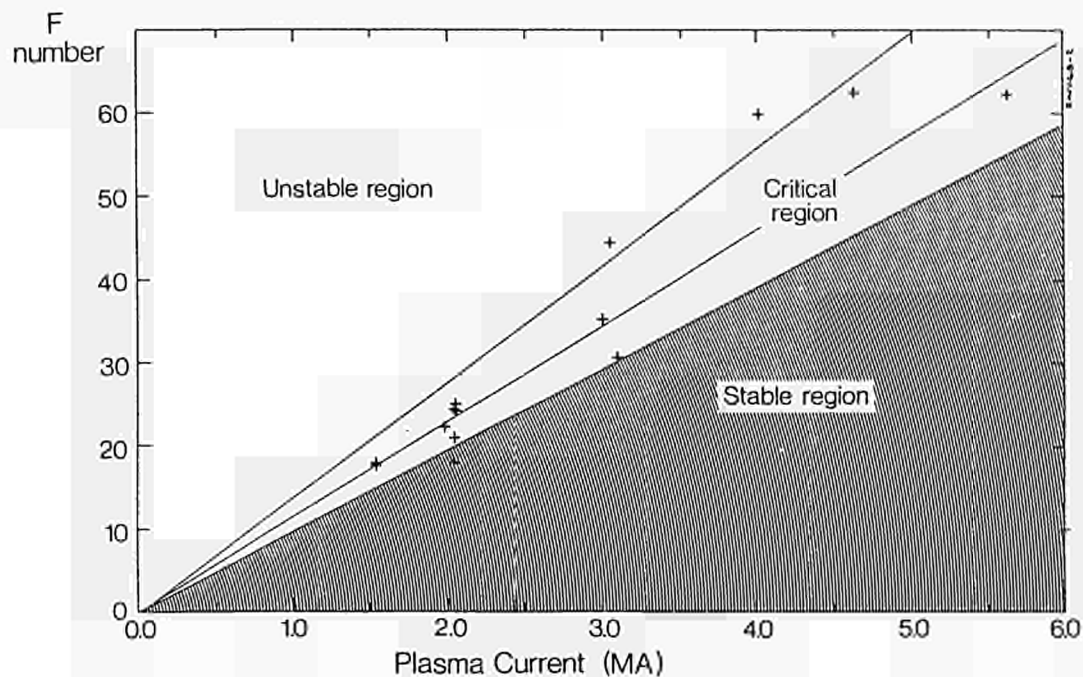
Fig. 5 Empirical plot for vertical instabilities. F number versus plasma current. For definition of F number see text.

Overview of JET Results using a Beryllium First Wall

The JET Team
(presented by M Keilhacker)

Invited Paper at the 31st Meeting of the Division of
Plasma Physics, American Physical Society,
Anaheim, California, USA. November 1989.

Overview of JET Results using a Beryllium First Wall

The JET Team
(presented by M Keilhacker)

Abstract. This paper summarizes results from the initial operation of the JET Tokamak [Plasma Physics and Controlled Nuclear Fusion Research (IAEA, Vienna, 1985) vol.1, p11.] with beryllium. JET was first operated with an evaporated Be coating on the walls and graphite limiters in June 1989. In August the graphite limiter tiles were replaced with Be tiles, and a three week experimental campaign was conducted in September/October. In the first phase oxygen was reduced to a negligible level and the carbon flux halved. In the second phase, for limiter mode operation, carbon was reduced by another factor of five, and Be became the dominant impurity. High power, long pulse additionally heated limiter mode discharges with $Z_{eff} < 1.5$ were achieved, and density limits were increased by a factor of up to two. ICRF produced H-modes were obtained in X-point operation (double null). The combination of Be gettering with new operational procedures to delay the strong influx of carbon from the X-point tiles enabled the achievement of record fusion parameters in H-mode discharges including a transient $n_d T_i \tau_E$ value of $9 \times 10^{20} m^{-3}$ keVs, corresponding to a Q_{DT} equivalent of about 0.8.

I. Introduction

This paper describes initial results obtained in JET [1] using beryllium as a first wall material [2]. The use of Be was motivated by the recognition, several years ago, that impurity/particle control is one of the most serious problems facing the development of fusion reactors. These problems have already become severe, as Tokamaks have moved out of the short-pulse mode of operation of the earlier generation devices, into the long pulse, high power operation typified by JET.

There are several requirements that the plasma-facing materials in a long-pulse Tokamak must satisfy. It should have a very low charge, Z, a low sputtering yield, and a high melting point, in order to minimize hydrogen dilution and plasma radiation. Furthermore, oxygen must be gettered effectively, and it is convenient if the high heat flux components also serve as the gettering material. In order to ensure that control of plasma density can be maintained, the plasma facing material should have favourable pumping qualities. Finally, it must also have good thermal-mechanical properties, including a high thermal conductivity and the ability to withstand repeated thermal shock.

Carbon has been widely used as a first wall material, as it possesses many of the desired qualities. In JET, however, it was felt that beryllium could provide superior performance [3]. With support from JET, an experiment was subsequently initiated on ISX-B to test a beryllium limiter. The general findings of this test were favourable [4]. The main advantages of beryllium, relative to carbon, are as follows. First, Z is 4, rather than 6, resulting in smaller dilution and lower radiation for a given impurity concentration level. Secondly, beryllium getters oxygen effectively. In addition, its long term hydrogen retention is much lower, and it pumps strongly during a discharge. The main disadvantage of Be relative to C is that it has a relatively low melting temperature of 1280°C. However, the increased self sputtering of C above 1200°C reduces the potential advantage of its higher melting point. A technological disadvantage of Be arises from its toxicity.

Beryllium is being introduced into JET in phases. Prior to June of 1989, the plasma facing components, consisting of the belt limiters, the inner wall tiles, and the X-point tiles (see figure 1), were graphite. Beginning in June, a thin coating of Be was evaporated onto the inner surface of the vacuum vessel. We refer to this phase as the Be/C phase, since most of the coating on the limiters and/or the X-point tiles was eroded after a few pulses, leaving a configuration in which the plasma-contacting components were primarily carbon, while the rest of the vessel wall remained beryllium. In July and August the carbon belt limiter tiles were replaced with (radiation cooled) Be tiles, and a short experimental campaign was carried out in late September and early October; we refer to this phase as the Be Lim phase. In spring 1990, the Be limiter tiles will be water-cooled, and the nickel RF antenna screens and its carbon protection tiles will be replaced with Be screens and Be protections. By the end of 1990, water-cooled Be X-point tiles will be added.

The principal results obtained in these first two beryllium phases can be summarised as follows. In the preceding carbon phases, carbon was the dominant impurity, with significant amounts of oxygen also present. This resulted in high values of Z_{eff} and severe plasma dilution for high power discharges. During the Be/C phase, it was found that the oxygen was reduced to an insignificant level, and that the carbon concentration, for a given power level and line density, was reduced by approximately a factor of two. In addition, greatly improved density control was obtained. These improvements resulted in reduced Z_{eff} and fuel dilution, better access to the "hot ion mode", the achievement of RF-only H modes, and improved values of fusion parameters. In the Be Lim phase, for limiter mode operation, carbon was further reduced to an insignificant level, and beryllium became the dominant impurity. This made it possible to produce high power, long heating pulses with Z_{eff} below 1.5, and corresponding values of the dilution parameter, $n_d/n_e > 0.8$-0.9. It was also found possible to double the density

limit, and a Murakami parameter of 17×10^{19} m^{-2}T^{-1} was reached. The use of strong gas puffing at the beginning of a heating pulse yielded improved performance in both limiter mode and X-Point operation. For X-point plasmas the use of beryllium, coupled with some innovative experimental techniques, resulted in transient values of $n_d T_i \tau_E = 9 \times 10^{20}$ m^{-3}keV s, corresponding to a Q_{DT} equivalent of about 0.8.

In the succeeding sections of this paper the effects of beryllium on impurity behaviour per se are first discussed (Section II), followed by an exposition of the consequences of the achieved higher plasma purity for plasma performance in limiter and X-point configurations (Section III). The paper concludes with a summary and short discussion of the implications of the experiments.

II. Impurity Results per se

A. Impurity Influx and Concentrations

The Be coatings are applied using an evaporation technique similar to that employed for titanium coatings. Properties of the coatings were measured using extractable surface probes. The deposited layer of Be is not uniform, being as thick as 2000Å at a probe located at the outer mid-plane, and averaging about 300Å over the vessel surface, corresponding to the deposition of about 10 g of Be per evaporation. It is found that the Be coating on the limiter erodes within a few discharges, establishing an equilibrium between erosion and redeposition. During these few discharges the ratio of C to Be atoms collected in the scrape-off layer increases from about 0.5 on the first pulse to 6-10 once the equilibrium phase has been established. Analysis of the surface of the limiter indicates that BeC is formed which contains only about 10% deuterium, as compared with 30-40 % for graphite limiters.

The most conspicuous change in going from the C to the Be/C phase is the reduction of oxygen in the plasma, as evidenced in figures 2a and 2b. The OII signal is reduced by a factor >20, while the CII signal decreases by ~2. Although the beryllium signals increase, carbon remains the dominant impurity for the Be/C phase.

Figure 3 illustrates the variation of the ratio of limiter carbon flux to deuterium flux for Ohmic discharges (crosses and open symbols) for the C and Be/C phases under discussion. The C phase data labelled 1988 was obtained with very well conditioned limiters, while for the 1989 C phase data the machine was less well conditioned. From this figure it can be seen that in the Be/C phase, the C/D flux ratio was consistently below that of the graphite phase for $\bar{n}_e \leq 2 \times 10^{19} m^{-3}$, although the best (1988) graphite data approaches that of the Be gettering phase for $\bar{n}_e \geq 2.5 \times 10^{19} m^{-3}$. The reduction of C in the discharge, for given conditions such as line-density and heating power, is believed to arise primarily from the elimination of the sputtering of carbon by oxygen, as can be seen from examination of the relationship

$$\frac{\Gamma_C}{\Gamma_D} = \frac{Y_{DC}}{1 - Y_{CC} - (\Gamma_O/\Gamma_C) Y_{OC}}, \quad (1)$$

where Y_{DC}, Y_{CC}, and Y_{OC} are yields for the sputtering of carbon by deuterium, carbon (self-sputtering), and oxygen respectively. For the conditions of JET, Y_{CC} is typically of order 0.3-0.5, $Y_{OC} \approx 1$, and Γ_O/Γ_C is about 0.3 for the C phase discharges, but is ≈ 0 for the Be/C phase. Carbon influx in the Be/C phase is further reduced by the fact that the (relatively small) fraction of carbon coming from the wall, rather than from the limiter or X-point tiles, is virtually eliminated by the Be coating.

The solid lines on figure 3 are from a sputtering model for the Ohmic discharges based on eqn. (1) which includes the dependence of sputtering yields on edge plasma temperature. The increase of sputtering yield with angle of incidence [5], is simulated in the model by increasing Y_{cc} by 30%. The curve corresponding to no oxygen in the discharge matches the Be/C phase data well at low and medium densities, but less accurately at higher densities, which may arise from chemical sputtering.

Figure 3 also shows (solid circles) the dependence of the C/D flux ratio for the Be/C phase for additionally-heated discharges. In this case, the decrease of the flux ratio with increasing line density (and hence decreasing edge temperature) also occurs, but is shifted to higher densities, as expected from dependence of edge plasma properties on total heating power.

In the third operating phase, that in which Be tile limiters were used, the concentration of carbon in limiter discharges was reduced by approximately another factor of 10, relative to the Be/C phase just discussed, as suggested by the spectroscopic data of figures 2b and 2c. The Be signal increased by about 10, and Be became the dominant impurity, although significant amounts of chlorine were also discovered, as is typical after any opening of the machine. The chlorine fraction decreased as the experimental campaign progressed.

B. Effective charge and Plasma Dilution.

Because of the virtual elimination of oxygen, and the replacement of carbon by Be, the effective plasma charge, Z_{eff}, was reduced significantly, first in the Be/C phase, and then more so in the Be Lim phase for both Ohmic and additionally heated discharges (figures 5 and 6). Because of the reduced impurity level in Be Lim discharges, and the resulting lower fraction of edge radiated power, it was found possible to further reduce the impurity concentration in additionally heated discharges by using a strong gas puff at the beginning of the heating pulse. Such strong gas puffing was not possible in the C phase, as it led to strong edge radiation and usually to disruption.

Figure 4 shows data from two pulses which were very similar (I_p=3.1 MA, P_{Tot}=25 MW), except that one of them had additional gas puffed in, as shown in the uppermost set of traces. The plasma line density attained was about the same in each pulse, although the limiter density was substantially higher in the case of the strong gas puff. This suggests that it is possible, in the Be Lim operating phase, to decouple the edge density from the plasma core without adversely affecting the performance of the latter, which has important implications for control of plasma surface interactions. The flux of Be from the limiter, as indicated on the "Be, Lim" traces, was the same for both discharges, indicating a lower sputtering yield (Γ_{Be}/Γ_D) for the strong puff case, consistent with a lower edge temperature. The value of Z_{eff}, was much lower for the strong puff case, indicating that a much smaller fraction of the Be produced at the limiter reached the core of the plasma. Such a reduction in impurity concentration, produced by strong gas puffing, has been seen repeatedly in Be phase operation. Some of this reduction certainly comes from increased screening of impurities resulting from the higher edge densities, although preliminary calculations indicate that this is too small to fully explain the observations.

In the Be Lim phase it has been possible to deliver large amounts of energy to the plasma while maintaining low Z_{eff}. In pulse #20687, for example, nearly 180 MJ of heating energy was supplied. Z_{eff} rose initially to about 2.5 upon initiation of the 25 MW combined heating, but then fell to less than 1.5 by the end of the heating pulse, by which time the line-averaged electron density had reached 7×10^{19} m^{-3}. The highest load to which a graphite limiter has been subjected in JET is 120 MJ. Inspection of the belt limiters after completion of the Be Lim phase showed clear signs of local melting over about 5% of the limiter surface, with a toroidal structure resembling the magnetic field ripple, but the damage was as a whole less severe than expected.

A comparison of Z_{eff} vs line density for Ohmic discharges for the three phases under discussion is presented in figure 5. The 1988 and 1989 data refer to the two carbon limiter phases referred to in connection with figure 3. It can be seen that the introduction of the Be gettering reduced Z_{eff} over the whole range of densities attainable in JET Ohmic discharges, due to the elimination of oxygen and the reduction of carbon. When the Be Lim was introduced, Z_{eff} was reduced further, primarily because of the substitution of Be for C. At high densities, where Z_{eff} can be kept small in well conditioned C limiter discharges, the differences are not so pronounced. Examination of the data for additionally heated discharges as well shows that it is possible, with the Be tile limiter, to operate at very high power per particle while maintaining a low Z_{eff}. An alternate representation of this phenomenon is given in figure 6, which shows the dilution factor, n_d/n_e, vs the total input power normalized by the volume averaged density, $P_{tot}/<n_e>$, for belt limiter discharges. Whereas it had not been possible in the graphite configuration of JET to maintain n_d/n_e much above 0.6 for moderate power pulses unless extensive conditioning was done, or to operate at all with $P_{tot}/<n_e> \geq 10$ MW/10^{19}m^{-3}, values greater than 0.8 can now be routinely achieved in limiter discharges for specific power up to 10 MW/10^{19}m^{-3}, and n_D/n_e remains above 0.6 for $P_T/<n_e>$ up to 20 MW/10^{19}m^{-3}. This, of course, enters importantly into the fusion power density, and contributes to the improved fusion performance discussed in Section III.

The results of sections IIA. and IIB. are summarized in Table I, which shows the dilution factor, and concentrations, in %, of O, C, and Be for the three phases of 1989 operation. The values listed represent averages over the data base for each phase. It is worth pointing out that in the Be Lim phase, the greatest gains were made in limiter mode operation, since, for the X-point pulses, the tiles which absorbed most of the energy were still graphite.

C. Pumping and Density Control.

The introduction of beryllium has produced a marked improvement in our ability to control the plasma electron density in JET. This comes in part from the reduction in the amount and charge of the dominant impurity, but also depends strongly upon the fact that Be pumps deuterium very effectively during the discharge. It is also found to retain very

little deuterium, relative to graphite, on longer time scales (minutes to hours); over 90% of the neutral gas admitted to JET is recovered, compared to ~50% in the carbon phase.

Figure 7 shows the decay time, τ_p^*, for the plasma deuteron content following switch-off of the gas supply for the various configurations. In the Be/C phase, a freshly evaporated coating has about the same pumping speed as the best helium-conditioned graphite cases. As the Be coating ages, its pumping speed decreases, but remains significantly better than for poorly conditioned graphite cases. For limiter mode operation with Be Lim tiles, the pumping speed is still faster, and remains so even after extended high power operation. In this sense, JET with Be tile limiters behaves very much like a "metal" machine with good pumping characteristics, but with the added benefits of low Z_{eff} and P_{rad}/P_{tot}. A final advantage which has been noted is that the vacuum vessel is no longer deconditioned by disruptions, i.e. the impurity level is largely unchanged by such occurrences. This increases the fraction of "good" pulses in a given operating period.

III. Consequences for Plasma Performance

A. Limiter Mode Plasmas.

The general results discussed in Section II led to improvement in nearly every operating scenario of JET. In this section we discuss three specific examples connected with limiter mode operation. The first two involve the Be Lim phase, and the third the Be/C phase.

The first of these concerns the density limit. The improved purity of the plasma has led to large increases of the attainable density for Ohmic (up to 60%), RF heated (up to 100%), NB and combined NB/RF heated (up to 75%) plasmas. This is illustrated in a Hugill diagram in figure 8. The dashed straight lines labelled OH/RF (C) and NBI(C) indicate the maximum values of $n_e Rq_{cyl}/B_t$ which were reached in the graphite operating phases of JET; the values were about 12 and 20, respectively. With RF heating in the C phase, values were not better than for Ohmic pulses. The introduction of Be into JET increased the Ohmic density limits to values slightly in excess of those reached for NI operation in the earlier C phase. In addition, values of the Murakami parameter, $n_e R/B_t$, with additional heating now extend up to 17×10^{19}(m^{-2} T^{-1}). Moreover, densities obtained in additionally heated discharges are now essentially independent of the mode of heating [6], a direct reflection of the improvement of the purity of RF heated plasmas. Finally, we note that the value of $n_e Rq_{cyl}/B_t$ ~36 typically reached in the Be Lim phase exceeds the scaling proposed by Greenwald et al. [7] by a factor of about 50%.

The nature of the physical processes governing the density limit is under investigation. It is clear from the Hugill diagram that the density limit depends on total power and the type and/or quantity of impurity ions in the plasma, as well as on q_{cyl}. At a fixed value of q_{cyl}, and for a fixed operating phase (corresponding to relatively fixed impurity conditions), the density limit scales roughly as $P_{tot}^{1/2}$, while a regression analysis shows $n_{max} \sim P_{tot}^{1/2} q_c^{-1/3} f(Z_{eff})$ for the entire database. Although such behaviour is clearly suggestive of a radiation caused density limit, there is also some evidence in our database for fuelling-limited maximum densities.

The general characteristics of the plasma near the density limit have also changed markedly between the C and Be phases. In the C phase, the density limit occurred when the radiated power fraction reached 100% and a large MARFE appeared. Contraction of the current channel ensued which led to MHD instability and to a disruption [8]. In the Be phases the density limit was always associated with MARFEs, but in this case they usually produced a soft, non-disruptive limit to the density with little or no evidence of MHD activity.

As a second example of improved performance of limiter mode plasmas with Be, we report on the attainment of the "hot ion mode". The strong deuterium pumping has resulted in very good control of the plasma density and permitted access to this regime in belt limiter operation for the first time in JET, and central ion temperatures $T_i(0) > 18$ keV have been recorded. With the improved density control it is now possible to peak the density profiles, using either beams or pellets. This has resulted in a trebling of the d-d neutron yield, compared with the C phase, to a value of 2×10^{16} ns^{-1}, using 17 MW of neutral beam injection. (Similar results had previously only been achieved in Inner Wall discharges).

D (^{3}He) fusion yield experiments also benefitted from reduced dilution in discharges with Be gettering. In a minority heating experiment using ^{3}He, over 100 KW of D-^{3}He fusion power was produced with 13 MW of ICRF power. In the earlier carbon-phase experiments low-Z impurities had limited the fusion power to 60 KW [9].

B. X-Point Plasmas.

As indicated above, the largest improvement in the case of the X-point plasmas came from Be gettering, and the consequent elimination of oxygen and improved ability to control the density. Installation of the Be limiter tiles had little further effect. Nevertheless, Be gettering, along with some changes in experimental procedures, resulted in major improvements in X-point plasma performance in 1989. (Most of these results were obtained in double null configuration).

One example of this is the attainment, for the first time in JET, of H-modes using ICRH heating alone [10]. This resulted from both Be gettering, which covered the nickel antenna screens, and from the use of dipole antenna phasing , which tends to produce less impurities. (At the same time, an automatic tuning system was brought into operation which allowed higher powers to be coupled to the plasma). Figure 9 shows an example of an H-mode produced by about 8 MW of ICRF (H minority scheme) coupled into the plasma. In this case a pellet was injected just prior to the heating pulse to create the proper target plasma (i.e. to maintain the density in the presence of strong pumping). As can be seen, there were two H-mode phases in this discharge, with the first lasting about 1.5 seconds, and the second about 0.8 seconds, terminated in both cases by $P_{rad} > P_{rf}$. The plasma purity, n_d/n_e, remained at around 0.8 during the heating phase, and the energy confinement time reached 0.85 s at the end of the first H-mode phase. In general, these ICRF H-modes have the same characteristics as NB heated H-modes [11], i.e. they exhibit a similar power threshold, similar particle and energy confinement times, and so forth. The ability to achieve long lived ICRF H-modes is an important step for NEXT STEP devices, such as CIT and NET/ITER.

As a second example of improvements to X-point plasma performance, the attainment of record fusion parameters in H-mode discharges is discussed. At high heating power levels ($P \geq 10 - 12$ MW) in the C phase, the discharges were always troubled, not only by a severe dilution of the plasma ($n_d/n_e \sim 0.5$), but also by a strong influx of carbon (the "carbon bloom") after 0.5 - 1.0 s, quenching the neutron production and terminating the H-mode. The use of Be gettering improved the plasma purity due to the elimination of oxygen and reduction of carbon flux (n_d/n_e rose to ~ 0.9), but did not affect the carbon bloom in a major way. It was found possible, however, to extend the H-mode period by up to 30% by either sweeping the X-point, both in the radial and vertical (double null operation) directions to reduce the X-point tile temperatures, or by using strong gas puffing in the divertor region. In addition, 6 of the 16 NI sources were converted from 80 kV to 140 kV. Tests showed that for a given power, the more energetic beams produced approximately twice the neutron yield, so that the use of 6 140 kV sources and 10 80 kV sources increased the neutron yield by about 37% over the earlier (all 80 kV) system.

By combining Be evaporation with these operational techniques it was possible to treble the neutron yield, relative to the C phase, to 3.4×10^{16} ns^{-1}, resulting in $Q_{DD} = 2.3 \times 10^{-3}$ and a D-D fusion power of about 40 kW. (Here and in the following, Q is defined as fusion power, P_{fus}, divided by absorbed neutral beam power, $P_{NB,abs}$). Figure 10 summarizes the Q_{DD} values, which were obtained during the three recent operating phases, in a scatter plot of Q_{DD} vs neutral beam power. The improved H-mode plasma performance with Be walls results from a combination of reduced plasma dilution ($n_d/n_e \sim 0.9$) and increased ion temperatures ($T_i(0)$) in the range 20 ~ 30 keV) while the energy confinement times are practically unchanged compared to those in the previous all-carbon experiments [11].

Traces from one of the record pulses (20981) are shown in figure 11. Table II lists further parameters associated with this discharge. The central ion temperature reached 22 keV, and was quenched by a strong influx of carbon ("bloom"), which reduced the beam penetration and the central power deposition. Just before this quench, at t = 11.4s, the energy confinement time, τ_E, was 1.1s, with a record fusion product $n_d^*(o) T_i(o) \tau_E$ of 9×10^{20} m^{-3}keVs (in this case, $n_d^*(o)$ includes 25% fast ions). Similar high values of $n_d T_i \tau_E$ have been obtained in H-modes with central pellet injection. In this case $T_i(o) = 9$ keV, $T_e(o) = 7$ keV and $n_d(o) = 5.10^{19}$ m^{-3} were achieved.

Figure 12 summarizes the values of the "fusion parameter" $n_d T_i \tau_E$, which were obtained during the C and Be phases. The curves parameterized by Q_{DT} refer to D-T equivalent values of the thermal Q computed for these D-D data points using realistic plasma profiles and a Z_{eff} value of 2. These Q_{DT} curves are calculated for stationary conditions whereas the plotted τ_E values are defined as $\tau_E = W/(P_{tot} - \dot{W})$, with $0 \leq \dot{W}/P_{tot} \leq 0.5$. In addition, the measured n_d values contain up to 25%, and the τ_E values up to 10% of fast ions.

More accurate Q_{DT} values are obtained from TRANSP[12] simulations using measured T_e, T_i, n_e and Z_{eff} profiles and replacing the deuterium by a D-T mixture. For pulse 20981 such simulations predict an equivalent total $Q_{DT} \sim 0.8$ (1/5 thermal-thermal, 4/5 beam-thermal) and a D-T fusion power of 13 MW for injection of 140 KV D beams into a T target plasma (see Table II) and $Q_{DT} \sim 0.6$ (1/3 and 2/3) for injection into a 50:50 mixture of D and T. They also show that in the former case the average value of Q_{DT} over an energy confinement time ($\tau_E = 1.1$ s) exceeds 0.5.

IV. Summary and Implications

The introduction of Be into JET as a plasma facing material, in the two phases described above, has led to general and substantial improvements in JET plasmas. In limiter discharges it was possible to maintain $Z_{eff} \leq 1.5$ ($n_d/n_e \geq 0.8$) at heating powers of the order of 30 MW when gas puffing was used to reduce the effective sputtering yield.

The low radiative cooling rate of Be, combined with elimination of other impurities, increased the density limit substantially, resulting in a maximum value of the Murakami parameter of 17×10^{19} m^{-2}T^{-1}.

Be pumps deuterium strongly, resulting in a degree of density control not achieved in JET with carbon as the plasma facing component. In addition, the long term retention of deuterium in the Be components is found to be very small.

The strong gettering and pumping action also led to improved H mode performance, resulting in the achievement of ICRF only H-modes, and, when sweeping and strong gas puffing were employed, enabled record values of fusion parameters to be attained.

Early in 1990, water cooling of the Be limiter tiles will be installed, and the nickel antenna screens will be replaced by Be screens. This is expected to further improve limiter mode performance. In late 1990, the graphite X-point tiles will be replaced by Be tiles, and it is anticipated that further improvements to H mode operation will result.

To demonstrate effective impurity control under very long pulse quasi-stationary conditions, a pumped divertor for JET, with plasma current capability of 6 MA, has been proposed [13]. This would become operational by the end of 1992, and is expected to provide important results for progressing towards NET/ITER.

References

1.   P.H. Rebut and the JET Team, in Plasma Physics and Controlled Nuclear Fusion Research 1984, Proceedings of the 10th International Conference, London, 1984 (IAEA, Vienna, 1985) Vol. 1, p.11.

2.   Further details of the material presented here can be found in the Bulletin of the American Physical Society 34, 9 (Oct 1989), pages 2054-2058

3.   P.H. Rebut and K.J. Dietz, in Fusion Technology 1982 (Proc. of the 12th Symposium, Julich, 1982), (Pergamon Press, New York, 1983). Vol. 1., p.85;

4.   P.K. Mioduszewski, P.H. Edmonds, C.E. Bush, A. Carnevali, R.E. Clausing, T.B. Cook, L.C. Emerson, A.C. England, W.A. Gabbard, L. Heatherly, D.P. Hutchinson, R.C. Isler, R.R. Kindsfather, P.W. King, R.A. Langley, E.A. Lazarus, C.H. Ma, M. Murakami, G.H. Neilson, J.B. Roberto, J.E. Simpkins, C.E. Thomas, A.J. Wootton, K. Yokoyama, R.A. Zuhr, K.H. Behringer, J. Dietz, E. Källne, P.J. Lomas, P.D. Morgan, P.E. Stott, A. Tanga, K.H. Sonnenberg, M.F. Smith, J. Watkins, R.D. Watson, J.B. Whitley, D.H.J. Goodall, N.J. Peacock, R. Clayton, J. von Seggern, K.G. Tschersich, Nucl. Fus. 26 1171 (1986).

5.   J. Bohdansky, Nuclear Fusion Special Issue: Data compendium for plasma surface interactions, edited by R.A. Langley et al. (IAEA, Vienna, 1984) p.61.

6.   J. Jacquinot, V. Bhatnager, M. Bures, D. Campbell, R. Giannella, K. Lawson, M. Stamp and B. Tubbing, Fusion Engineering and Design (in press)

7.   M. Greenwald, J.L. Terry, S.J. Wolfe, S. Ejima, M.G. Bell, S.M. Kaye, and G.H. Nielson, Nuclear Fusion 28 (1988) 2199.

8.   J.A. Wesson, R.D. Gill, M. Hugon, F.C. Schüller, J.A. Snipes, D.J. Ward, D.V. Bartlett, D.J. Campbell, P.A. Duperrex, A.W. Edwards, R.S. Granetz, N.A.O. Gottardi, T.C. Hender, E. Lazzaro, P.J. Lomas, N. Lopes Cardozo, K.F. Mast, M.F.F. Nave, N.A. Salmon, P. Smeulders, P.R. Thomas, B.J.D. Tubbing, M.F. Turner, A. Weller, Nucl. Fus. 29 641 (1989).

9. D.F.H. Start, V.P. Bhatnagar, D.A. Boyd, M. Bures, D.J. Campbell, J.P. Christiansen, P.L. Colestock, J.G. Cordey, W. Core, G.A. Cottrell, L.G. Eriksson, M.P. Evrard, T. Hellsten, J. Jacquinot, O.N. Jarvis, S. Kissel, S. Knowlton, H.W. Lean, P.J. Lomas, C. Lowry, A.L. McCarthy, P. Nielsen, J. O'Rourke, G. Sadler, A. Tanga, P.R. Thomas, K. Thomsen, B. Tubbing, B. van Belle, J.A. Wesson, in Plasma Physics and Controlled Nuclear Fusion Research 1984, Nice, France, 1988. (IAEA, Vienna 1989) vol. 1, p.593.

10. B.J.D. Tubbing, J. Jacquinot, D. Stork and A. Tanga. Nucl. Fusion, (in press).

11. M. Keilhacker and the JET Team, in Plasma Physics and Controlled Nuclear Fusion Research 1988, Proceedings of the 12th International Conference, Nice, France, 1988 (IAEA, Vienna, 1989). vol. 1, p.139.

12. R.J. Hawryluk, in Physics of Plasmas Close to Thermonuclear Conditions, Proceedings of the Course held in Vienna, Italy, September 1979, (European Commission, 1980, EUR FU BRU/XII/476/80), vol. 1, p.11; see also R.J. Goldston, D.C. McCune, H.H. Towner, S.L. Davis, R.J. Hawryluk, and G.L. Schmidt, J. Comp Physics 43 61 (1981)

13. P.H. Rebut and the Pumped Divertor Task Force, Bull. Am. Phys. Soc. 34 2057 (1989).

APPENDIX 1

THE JET TEAM

JET Joint Undertaking, Abingdon, Oxon, OX14 3EA, U.K.

J. M. Adams[1], H. Altmann, A. Anderson[?], S. Arrenberger[?], W. Bailey, P. Ballantyne, B. Balet, R. Barnsley[?], D. V. Bartlett, L. R. Baylor[?], A. C. Bell, P. Bertoldi, E. Bertolini, V. Bhatnagar, A. J. Bickley, H. Bindslev[?], J. Bizarro[?], S. Dhman[?], T. Bonicelli, S. J. Booth, G. Bosia, M. Botman, D. Boucher, H. Brelen, H. Brinkschulte, M. Brusati, T. Budd, M. Bures, T. Businaro, P. Butcher, H. Buttgereit, G. Caldwell-Nichols, D. J. Campbell, P. Card, G. Celentano, C. D. Challis, A. Cheetham, P. Chiron, J. Christiansen, C. Christodoulopoulos, P. Chuilon, R. Claesen, S. Clement[?], F. Clipsham, J.P. Coad, S. Conroy[?], M. Cooke, S. Cooper, J. G. Cordey, W. Core, G. Corrigan, S. Corti, A. E. Conley, G. Cottrell, J. Coulon[?], M. Cox, P. Cripwell[?], H. de Blank[?], G. Docker[?], H. de Esch, L. de Kock, E. Deksnis, G. B. Denne, G. Deschamps, G. Devillers, K. J. Dietz, J. Dobbing, N. Dolgetta, S. E. Dorling, P. G. Doyle, D. F. Duchs, H. Duquenoy, A. Edwards, J. Ehrenberg, T. Elevant[?], S.K. Erents, L. G. Eriksson[?], H. Fajemirokun[?], H. Falter, D. Flory, M. Forrest[?], J. Freiling[?], C. Froger, P. Froissard, K. Fullard, M. Gadeberg, A. Galetsas, M. Galley, M. Garribba, P. Garr, X. Gd[?], R. Giannella, A. Gibson, R.D. Gill, A. Gondhalekar, C. Gormezano, N. A. Gottardi, G. Gowers, B. J. Green, W. K. Guo[?], R. Haange, G. Hammett, C. J. Hancock, P. J. Harbour, N. C. Hawkes, P. Haynes, J. L. Hemmerich, A. Hemsworth, F. B. Herzog, R. F. Herzog, J. Hoekzema, R. Hope, J. How, M. Huart, T. P. Hughes[?], M. Hugon, M. Hugon[?], A. Hwang[?], C. Idelon, B. Ingram, M. Irving, J. Jacquinot, H. Jaeckel, G. Janeschitz[?], O.N. Jarvis, F. Jensen, E. M. Jones, L. P. D. F. Jones, T. T. C. Jones, A. Kaye, B. E. Keen, M. Keilhacker, G. J. Kelly, W. Kerner, R. Konig, A. Konstantellos, M. Kovanen[?], P. Kupschus, P. Lallia, R. Lasser, J. R. Last, B. Laundy, L. Lauro-Taroni, K. Lawson[?], E. Lazzaro, M. Lennholm, P. Lomas, M. Lorenz-Gottardi[?], M. Loughlin, C. Lowry, B. Macklin, G. Maddison[?], G. Magyar, W. Mandl[?], V. Marchese, F. Marcus, J. Mart, E. Martin, R. Martin-Solis[?], P. Massmann, K. F. Mast[?], G. McCracken[?], C. Merquet, S. F. Mills, P. Millward, S. L. Milora[?], E. Minardi[?], A. Moissonnier, F. Mompean, P. L. Mondino, P. Montvai[?], P. Morgan, H. Morsi, G. Murphy, M. Mynarends, C. Nardone, F. Nave[?], G. Newbert, M. Newman, P. Nielsen, P. Noll, W. Obert, D. O'Brien, J. O'Rourke, R. Ostrom, M. G. Pacco-Duchs, M. Pain, F. Paoletti, S. Papastergiou, D. Pasini, A. Peacock, N. Peacock[?], D. Pearson[?], V. Phillips[?], M. Pick, J. Plancoulaine, J-P. Poffe, F. Porcelli, L. Porte[?], R. Prentice, G. Radford[?], T. Raimondi, C. Raymond, P. H. Rebut, R. Reichle[?], J. Removille, G. Rey[?], F. Romini, D. Robinson[?], A. Rolfe, R. Romain, R. T. Ross, L. Rossi, P. Rutter, H. C. Sack, G. Sadler, G. Saibene, N. Salmon[?], G. Sanazzaro, A. Santaguistina, R. Sartori, C. Sborchia, P. H. Schild, M. Schmid, G. Schmidt[?], S. M. Scott, A. Sibley, R. Simonini, A. Sips[?], P. Smeulders, S. Sommers, K. Sonnenberg, R. Stankiewicz[?], M. Stamp, P. Stangeby[?], D. F. Start, C. A. Steed, D. Stork, P. E. Stott, T. E. Stringer, D. Stubberfield, D. Summers, H. Summers[?], H. Tamnen, A. Tanga, A. Taroni, A. Tesini, P. R. Thomas, E. Thompson, K. Thomsen, J. M. Todd, P. Trevalion, B. Tubbing, F. Tibone, E. Usselmann, A. Vannucci, H. van der Beken, G. Vlases, M. von Hellermann, T. Wade, C. Walker, Z. Wang[?], D. Ward, M. L. Watkins, M. J. Watson, H. Weisen[?], J. Wesson, J. Wilks, U. Willen[?], D. Wilson, T. Winkel, S. Wolfe, B. Wolle[?], D. Wong, C. Woodward, M. Wykes, I. D. Young, L. Zannelli, Z. Zheng[?], Y. Zhu[?], M. Zouhar.

PERMANENT ADDRESS

1 UKAEA, Harwell, Didcot, Oxon, UK.
2 ULB-EB Association, LPP-ERM-KMS, B-1040 Brussels, Belgium
3 Central Research Institute for Physics, Academy of Sciences, Budapest, Hungary
4 ENEA CENTRO In Frascati, I-00044 Frascati, Roma, Italy
5 Chalmers University of Technology, Goteborg, Sweden
6 Princeton Plasma Physics Laboratory, New Jersey, USA
7 UKAEA Culham Laboratory, Abingdon, Oxfordshire, UK.
8 Plasma Physics Laboratory, Space Research institute, Sao Jose dos Campos, Brazil
9 Institute of Mathematics, University of Oxford, UK.
10 CRPP/EPFL, 21 Avenue des Bains, CH-1007 Lausanne, Switzerland
11 Swedish Energy Research Commission, S-100 72 Stockholm, Sweden.
12 Imperial College of Science and Technology, University of London, UK.
13 Max Planck Institut fur Plasmaphysik, D-8046 Garching bei München, FRG.
14 Risø National Laboratory, Denmark
15 FOM Instituut voor Plasmafysica, 3430 Be Nieuwegein, The Netherlands

16 Commissariat à l'Energie Atomique, Cadarache, F-13108 St Paul Lez Durance, France
17 JAERI, Tokai Research Establishment, Tokai Mura, Naka Gun, Japan
18 Institute for Aerospace Studies, University of Toronto, Downsview, Ontario, Canada
19 University of Strathclyde, 107 Rottenrow, Glasgow, G4 ONG, UK
20 Nuclear Engineering Laboratory, Equipment University, Panama.
21 INSCT, Lisboa, Portugal
22 ENP, Milan, Italy
23 Oak Ridge National Laboratory, Oak Ridge, Tenn., USA
24 University of Heidelberg, Heidelberg, FRG
25 IPP, Academia Sinica, Beijing, P.R. China
26 Southwestern Institute of Physics, Leshan, Sichuan, P.R. China
27 RCC Cyfronet, Otwock-Swierk, Poland
28 Kernforschungsanlage Julich, FRG
29 University of Leicester, Leicester, UK.
30 University of Essex, Colchester, UK.
31 Universidad Complutense de Madrid, Spain
32 University of Dusseldorf, FRG

<div>

	C-Phase	Be/C-Phase	Be-Phase	
			Limiter	X-Point
Oxygen concentration	1	0.05	0.05	0.05
Carbon concentration	5	3	0.5	1.5
Beryllium concentration	-	1	3	1
$\frac{n_d(0)}{n_e(0)}$	0.6	0.8	0.85	0.9

Table 1. Average Impurity Concentrations (%) and Dilution Factor for the Various Operating Phases.

</div>

System Configuration

X-Point (Double Null) Discharge, H-Mode

$I_p = 4$ MA, $B_t = 2.8$ T, $P_{NB,abs} = 16$ MW

Plasma Parameters ($\pm 10\%$; at t = 11.4 sec)

$n_e(o) = 4.0 \times 10^{19} m^{-3}$ $T_e(o) = 8.6$ keV
$n_d^*(o) = 3.7 \times 10^{19} m^{-3}$ $T_i(o) = 22$ keV
$Z_{eff}(o) = 1.4$ $\tau_E = 1.1$ s
D – D Neutron Rate $= 3.4 \times 10^{16} s^{-1}$
$P_{FUSION,D-D} = 40$ kW

Fusion Product

$n_d^*(o) T_i(o) \tau_E = 9 \times 10^{20} m^{-3}$keVs
with $P_{tot} = 17$ MW and $dW/dt = +8$ MW
($n_d^*(o)$ includes 25% fast ions)

Equivalent D-T Fusion Power

$P_{FUSION,D-T} = 13$ MW for 0.1s
$\bar{P}_{FUSION,D-D} > 8$ MW averaged over an energy confinement time ($\tau_E = 1.1$s)
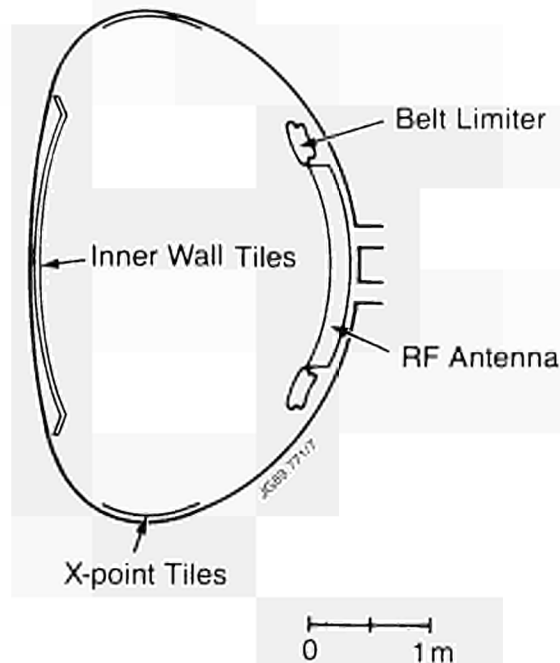
Table II. Parameters for Pulse # 20981

Fig. 1 Schematic cross section of JET showing location of key plasma-facing components
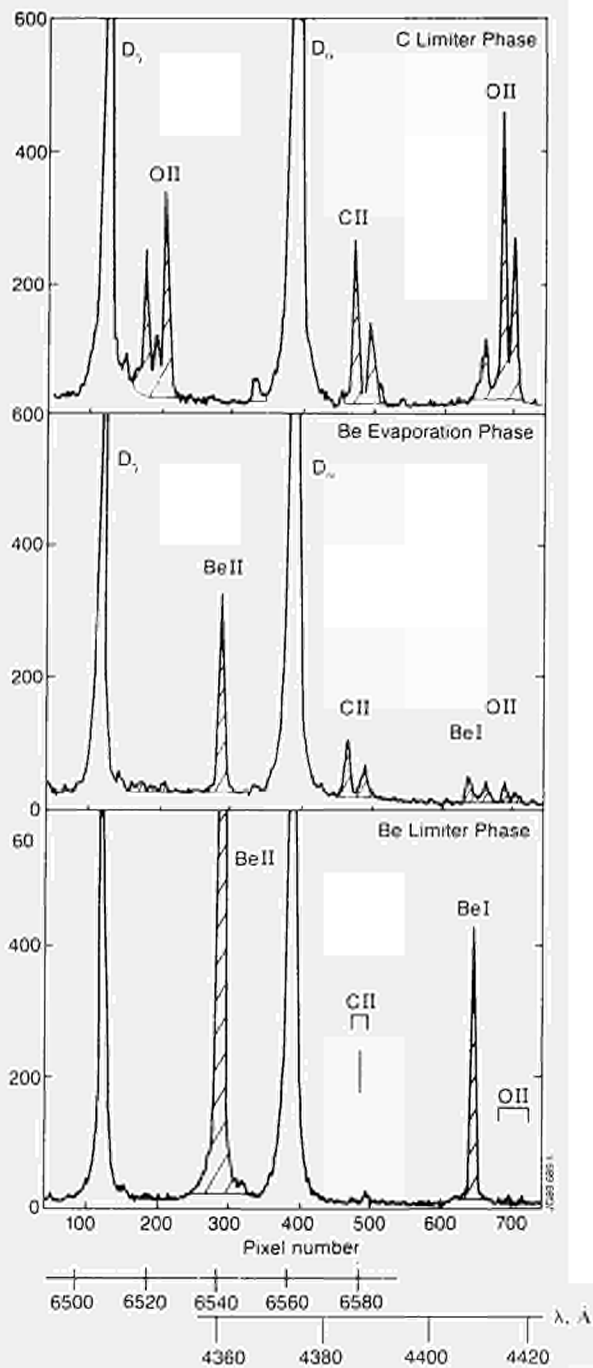
Fig. 2 Spectral lines in the visible region for the three operating phases; (a) the all Carbon phase, (b) the Be/C phase with Be evaporation and Carbon limiters, and (c) the Be Lim Phase with Be evaporation and Be tile belt limiters.
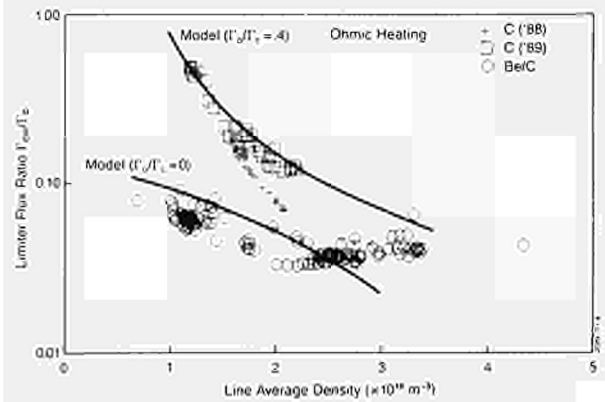

Fig. 3 Ratio of limiter Carbon flux to Deuterium flux vs line average density, $\bar{n}_e$, for ohmic discharges for the C and Be/C phases. The solid lines are from a sputtering model (see text).
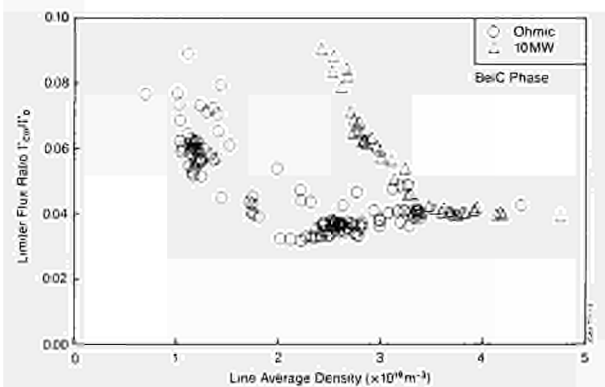

Fig. 4 Ratio of limiter Carbon flux to Deuterium flux vs, $\bar{n}_e$ for ohmic and additionally heated discharges. Be/C Phase.
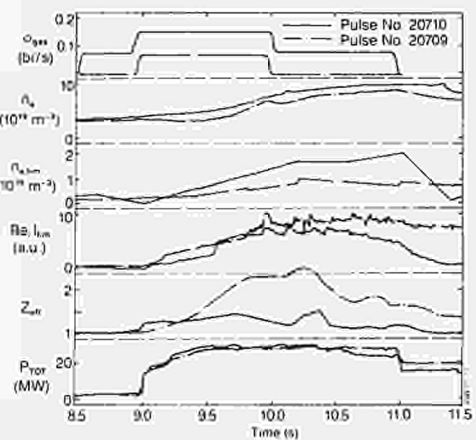
Fig. 5 Experimental data from two Be Lim phase pulses which are similar except for their gas puff histories. Note the large reduction in Z_{eff} resulting from the strong puffing at the beginning of the heating pulse.
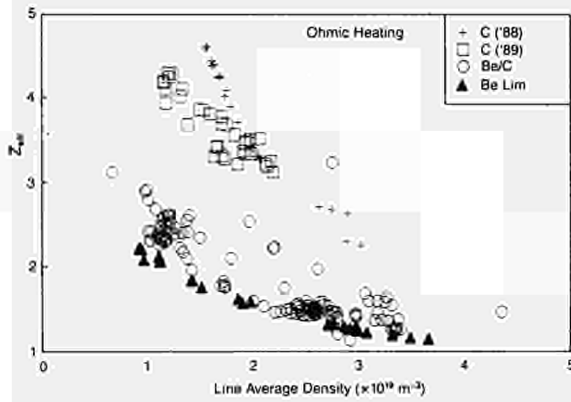
Fig. 6 Z_{eff} vs $\bar{n}_e$ for ohmic shots for two C-phase campaigns and the Be/C and Be Lim phases, showing the improvement resulting from the use of Beryllium.
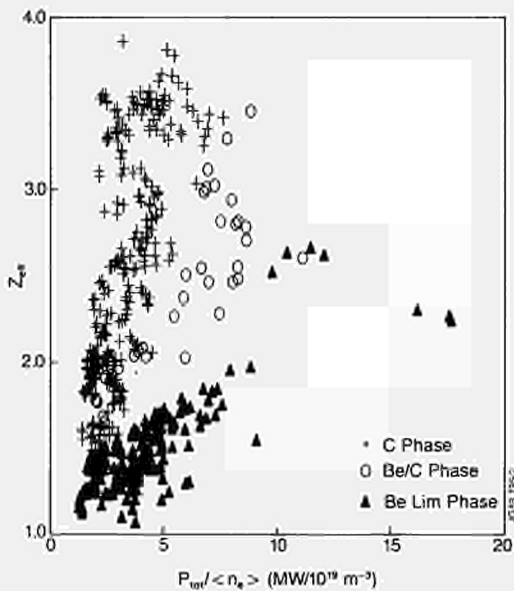
Fig. 7(a) Z_{eff} vs the ratio of total input power to volume averaged density for additionally heated discharges. $I_p = 3\,MA$, $P_{tot} \geq 4\,MW$.
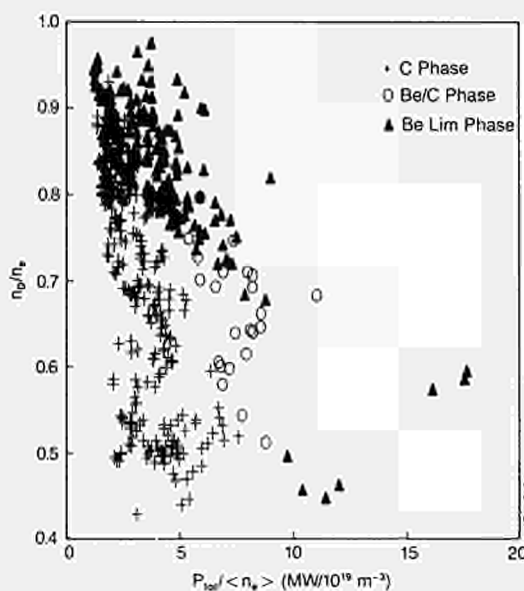
Fig. 7(b) The dilution parameter, n_d/n_e, vs ratio of total input power to volume average density, for the same data base as that of Fig. 7(a).
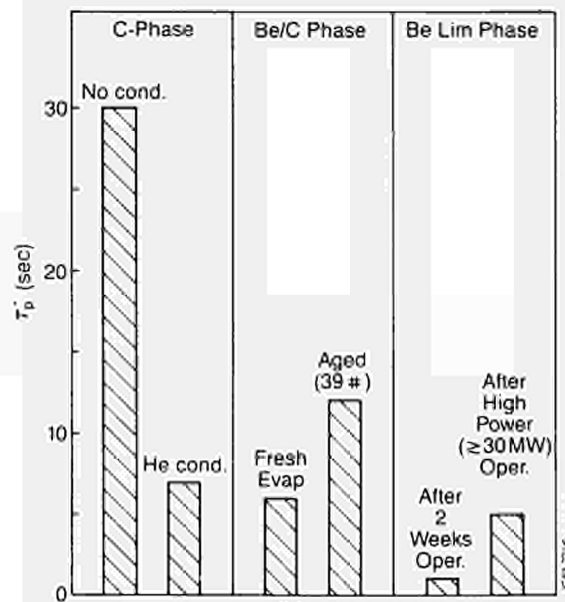
Fig. 8 Decay time of plasma Deuteron content, τ_p^*, following switch-off of gas supply for the C, Be/C and Be Lim phases. The figure illustrates the strong pumping characteristics of Beryllium relative to Carbon.
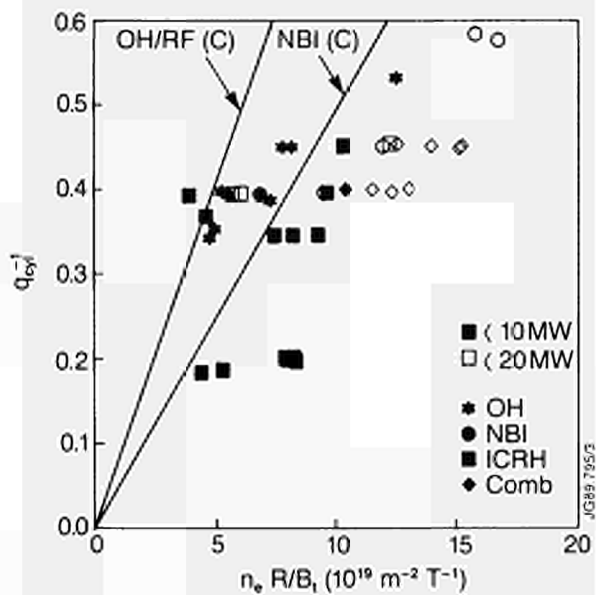
Fig. 9 Inverse cylindrical safety factor, q_{cyl}^{-1}, vs $n_e R/B_t$ ($10^{19}\,m^{-2}\,T^{-1}$) showing maximum densities obtained in JET. The experimental points are from the Be Lim phase. The two drawn curves represent operational boundaries for the C phase of 1988.
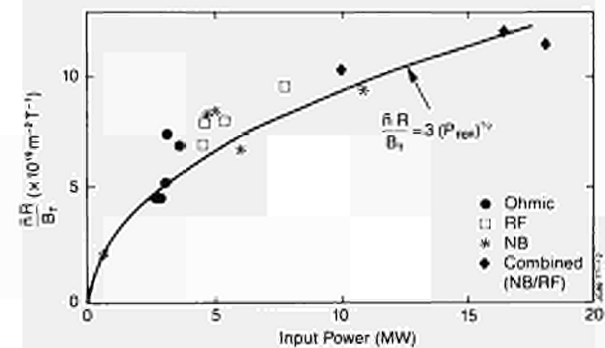
Fig. 10 The maximum Murakami parameter ($n_e R/B_t$) vs total input power, P_{tot}, for Be Lim shots with $q_{cyl} = 2.5$, showing scaling as $\sim P_{tot}^{1/2}$, independent of the mode of heating.
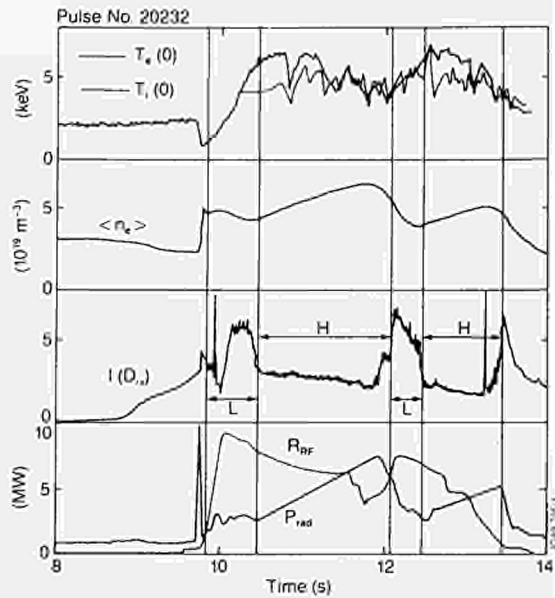
Fig. 11 Experimental traces from pulse # 20232 ($I_p = 3\,\text{MA}$, $B_t = 2.8\,\text{T}$), in which two H-mode periods were produced using RF heating alone. For this shot $\tau_E = 0.85\,\text{s}$, and $n_d/n_e = 0.8$ at the end of the first H-mode period (11.9s). A 4mm pellet was injected at 9.8s, but this has no relevance with respect to the H-mode.
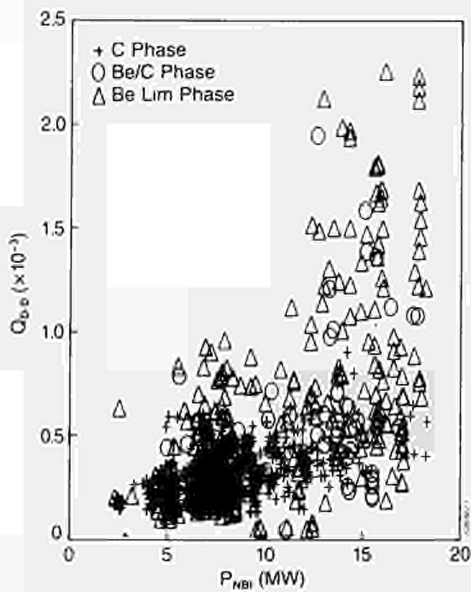

Fig. 13 Experimental traces from a high fusion yield H-mode pulse (# 20981), showing a peak D-D neutron rate (Y_n) of $3.4 \times 10^{16}\,\text{s}^{-1}$ at 11.4s, just prior to quenching by the 'Carbon Bloom'. Be Lim phase. Injected neutral beam power $P_{NB,inj} = 18\,\text{MW}$ (12.3MW 80kV/D and 5.7MW 140kV/D).

Fig. 12 Q_{DD} vs neutral beam power for the three operating phases.
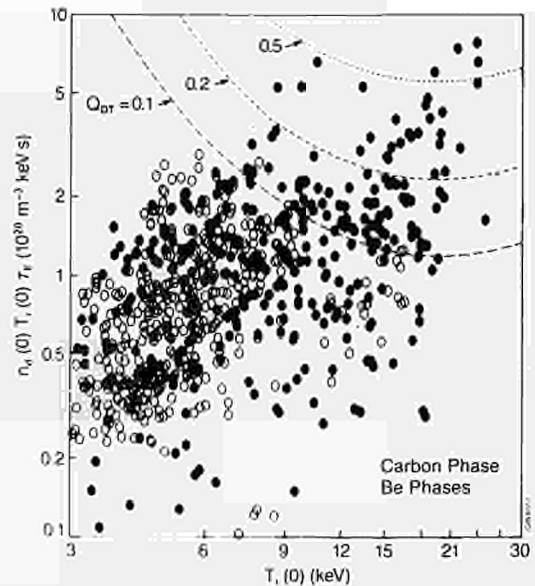
Fig. 14 The fusion parameter $n_d(0)\, T_i(0)\, \tau_E$ vs $T_i(0)$ for the C and Be phases. The curves parameterized by Q_{DT} refer to computed D-T equivalent values of the thermal Q.

Effect of Beryllium Evaporation on the Performance of ICRH on JET

J Jacquinot at al

Paper at the IAEA Technical Committee on
ICRH Edge Plasmas, 2nd – 5th October 1989.

Effect of Beryllium Evaporation on the Performance of ICRH on JET

J. Jacquinot, V. Bhatnagar, M. Bures, D. Campbell, R. Giannella,
K. Lawson, H. Stamp and B. Tubbing

Abstract

Beryllium films (150 to 300Å) have been evaporated on all JET
in-vessel components (carbon limiters, nickel screen, Inconel
walls). Immediate and lasting improvements of the plasma have been
observed in all plasma regimes. We concentrate on the results
obtained with ICRH and NBI on the density limit and on H-mode
plasmas which are particularly sensitive to impurity release.
Specific effects produced by RF waves are reduced to a negligible
level when the following 3 aspects are combined - beryllium
evaporation - dipole phasing - correct screen angle. The density
limit obtained with ICRF is now identical to NBI heated cases and
substantially higher than the values obtained in the pre-beryllium
phase. Long H-modes (1.3 s) have been obtained with RF alone. The
H mode confinement is similar to that of NBI cases. In limiter
plasmas Z_{eff} decreased to 1.2 - 1.4 at high density and for 10 MW
input power. The results are related to oxygen gettering,
suppression of nickel sputtering from the antenna screens and to
the use of dipole phasing.

1. Introduction

The performance of Tokamaks depends on the preparation of the
first wall and of the limiters. The maximum plasma density which
can be sustained and the duration of H-modes are two aspects of
plasma operation which are particularly sensitive to impurities.
ICRF has been generally inferior to NBI in these two domains. The
use of the dipole phasing[1,2,3] and of a screen aligned with the
magnetic lines of force[4] has improved the performance but has not
completely suppressed specific deleterious effects of ICRH.
Carbonization and boronization of the entire vacuum vessel made a
remarkable impact on plasma performance. Most notably,
boronization first performed in Textor[5] gave excellent results,
in particular with the reduction of oxygen release.

In this article we concentrate on the overall performance of
JET plasmas before and after evaporation of thin beryllium films.
Two companion JET papers concentrate on the impurity release[6] and
on the modifications of the edge plasma measured by Langmuir
probes[7]. In a first part we examine the density limit in Ohmic,
NBI or ICRF heated plasmas. In the second part the production and
duration of H-modes produced by NBI and ICRF are compared. Unless
stated in the text, the analysed experiments have been performed
with a hot vessel (300°C), dipole phasing and with the direction of
the field corresponding to the correct alignment of the screen bars
with the magnetic lines of force. The influence of oxygen release
from the walls and of self-sputtering of the screen material is
considered.

2. Density limits, beryllium evaporation, effect on pumping

2.1 Pre-beryllium experiments

Experiments on density limits in limiter plasmas have
been performed in 1986 and in June 1989 (Table 1). In both
cases the density was increased by opening a deuterium gas
valve during RF heating. In the 1986 experiments, monopole
(in phase) was used and the power did not exceed 5 MW. The
density could only be increased by 15% above the limit
observed with Ohmic heating alone. In both the ohmic and RF
cases, oxygen, and to a lesser extent, carbon, were the main
contributors to the radiation. Radiation from oxygen increased
steeply as the density approached the limit. The plasma
disrupted when the total radiated power was comparable to, or
larger than the input power. The radiation from Nickel did
not play a significant role in the energy balance. Experi-
ments performed with NBI during the same period could extend
further the density limit. The parameter $N = \bar{n}_e R \, q_{cyl}/B_T$ had
the following maximum values (in units $10^{19}m^{-2}T^{-1}$): 10 in
Ohmic, 11.5 with RF and 18 with NBI.

In the second period of operation (1988), no attempts
were made to reach the density limits. However it is clear
from the operating diagram (figure 1) that the 1986 limit was
actually exceeded in the course of experimentation. N reached
16 at high values of q_{cyl}. It is quite possible that this
improvement is directly related to a lower oxygen
contamination of the vessel due to systematic Helium glow
discharge cleaning overnight. Other causes cannot, however,
be ruled out; we have particularly in mind the more frequent
use of dipole phasing and the conditioning resulting from high
combined power operation (P_{tot} < 35 MW) which provoked fre-
quent carbon catastrophies covering the walls and the screens
with a layer of carbon.

2.2 Experiments after beryllium evaporation

In the third period of interest (June-July 1989, see
table 1), the vessel was first conditioned with frequent
Helium glow cleaning and high power operation for 2 weeks;
then a beryllium layer was evaporated on all in-vessel sur-
faces from four evaporators (90° aperture in the toroidal
directions). In this process, a beryllium film (150 to 300Å
thick) was deposited on the Nickel screens. The evaporation
was repeated almost every night during the operation period.
This preparation had a major impact on hydrogen pumping.
The pumping of hydrogen and deuterium was considerably
increased and the plasma density would normally decrease
during high power ICRH if the density feedback system was not
used. This pumping effect decreased progressively shot by
shot. The other major improvements concern density limits,
impurity release, fuel dilution and total radiation. This
improvement did not to degrade substantially during operation.
No attempts were made to optimise the thickness of the
beryllium.

Figure 2 shows the time evolution of the line averaged
density $\langle n_e \rangle$ for 3 MA discharges with ohmic heating alone and
with 9 MW of either ICRF (dipole phasing, H minority) or NBI

(80 keV beams). In all three cases a "marfe" (localised
region of high radiated power) starts near the top of the
vessel and prevents a further density increase despite
continuous high gas injection rate. The plasma does not
necessarily disrupt but the marfe can degrade the energy
confinement. The ohmic density limit is almost identical to
the pre-beryllium phase (N = 11). The limits with NBI and RF
are now identical, $N_{ad} = 24$, a substantial increase over the
best values achieved previously.

Figure 3 gives the evolution of the total radiated power
from bolometric measurements. The radiated power remains a
moderate fraction (40 to 50%) of the input power until just
before the appearance of the marfe. Large spikes on the
radiated power reveal the presence of the marfe which
continues until the gas flow has been reduced. Contrary to
the pre-beryllium experiments, the radiation is dominated by
the carbon contribution and oxygen plays only a minor role.

Z_{eff} values are similar in the three cases (figure 4); it
decreases slightly during the density rise. $Z_{eff} \sim 1.5$ in the
RF case; it is slightly lower in the NBI case (1.4).

The evolution of the diamagnetic stored energy is repre-
sented on figure 5. It is remarkably constant in the RF case.
Note that the heating efficiency is higher in the RF case by
20% due to better penetration of the RF power in high density
plasmas. It should be noted that the Marfe occupying a small
region in the plasma edge does not necessarily degrade the
energy confinement (see the NBI and RF cases of Figure 5).

The D-D reaction rate has also been significantly
improved. In typical 3 MA discharges with monster sawteeth
the reaction rate is about twice the pre-beryllium values
(figure 6). The overall confinement is also increased but
only slightly; quantification of the effect is awaiting
further analysis.

3. ICRF performance in the H-mode regime

The duration of the H-phase in X-point plasmas is quite sensi-
tive to the impurity influx. The electron density and the impurity
content increase during the H-phase and a transition back to the
L-mode occurs when the total radiated power exceeds the total input
power.

In 1988, before beryllium evaporation, the power radiated by
oxygen was the main contribution to the total radiation in NBI only
H-modes (Table 2). H-modes could be triggered by combined NBI and
RF power but the radiation from oxygen and nickel was considerably
increased while the contribution of carbon remained unchanged at a
low level (Table 2). From the linear combination of the measure-
ments summarised in Table 2, we find that the RF produces, for a
given power, six times more oxygen radiation and nine times more
nickel radiation than NBI. The duration of the H-mode was severely
reduced even with modest RF powers (4 MW).

Beryllium evaporation changed completely this situation.
Both the H-mode duration and the rate of increase of the
total radiated power are now comparable between the two heating
methods. A detailed spectroscopic analysis of the contributions
from the various impurities is not yet available but preliminary
data indicate that the effect of oxygen and nickel have been
considerably reduced.

H-modes have been obtained with ICRF alone in the dipole
phasing above a power threshold which is identical to the NBI case.
The energy confinement time is also similar[8]. In many cases
monster sawteeth, typical of RF heating, develop. The D-D
reaction rate is about twice the value obtained in L-mode monster
sawteeth (figure 6). The density increases, as in the NBI case,
and a large density pedestal develops at the plasma edge - the
density profile is flat. The electron temperature pedestal is
about 1 keV.

It has not been possible so far to produce long H-modes with
ICRF alone in the monopole phasing, although combined heating in
this mode has been quite successful. The power threshold for
H-modes could be higher in monopole but this point was not investi-
gated.

Figure 7 gives an example of an H mode obtained with ICRF
alone. The evolution of the H_α and of the total radiated power
trace shows that in this case the H-transition occurs in two steps
which are not correlated to sawteeth. (The discharge is sawtooth
free between 50 and 51.2 seconds). Also shown is the evolution of
the loading resistance (R_c) of one of the seven antennae. Each step
of the H-transition is responsible for a drop of about 1 ohm of
R_c. The later decrease of R_c can be attributed to an increase of
the separation between the antennae and separatrix. Also note the
disappearance of the noise on the R_c trace during the H phase.

The duration of the H mode with NBI only in the same discharge
was very similar (Table 2). Longer durations have also been
obtained with NBI only with a larger distance separating the
antenna and the plasma and with further beryllium conditioning.
Similar conditions have not yet been tested with ICRH.

4. Discussion and Conclusion

After the use of beryllium evaporation, the impurity produc-
tion specific to ICRH appears to have decreased to a negligible
level. The density limit and the characteristics of the H-mode are
now independent of the heating method.

This new situation can be attributed, to a large extent, to
the powerful gettering action of oxygen by the evaporated beryllium
layer. Since the beryllium film is quickly removed from the
limiters by the plasma and since beryllium appears also to
disappear from the screen[6] (by erosion or by coverage with the
limiter material) we must conclude that this oxygen was coming from
the vessel walls or from the weakly loaded zones of the limiter.
This proposal is also compatible with the observed prolonged action
of the beryllium film over several days. The increased sensitivity

of ICRH to oxygen could result from the very small amount of power that the RF waves dissipate near the wall.

The beneficial effect on nickel can be trivially attributed to coverage of the nickel screens by beryllium. The major step forward is that screens covered with beryllium do not release beryllium in a sufficient quantity neither to contribute to the dilution of the D fuel nor to give appreciable radiation.

Note that for 200 eV ions (the RF voltage between screen bars) the self sputtering of nickel reaches 0.5 at normal incidence, a factor of 2.5 larger than the self sputtering of beryllium; a clear clue for the physical mechanisms[9] at work near the ICRH screen. Solid beryllium appears indeed as a long term solution for ICRH as proposed by JET[10]. Beryllium screens will be installed before the next experimental campaign.

Acknowledgements

The authors are grateful to the JET team for the excellent performance of the machine systems which allowed the progress reported here.

References

[1] K. Odajima et al., Confinement studies of additionally heated plasmas in the the JFT-2M Tokamak, Proc. 11th. Conf. Kyoto (1986), Vol. 1, IAEA, Vienna, I, 151.

[2] M. Bures et al., Modification of the plasma edge and impurity production by antenna phasing during ICRF heating in JET, Plasma Phys. and Controlled Fusion, Vol. 30, II, 1988, 149.

[3] J.R. Wilson et al., ICRF heating on the TFTR Tokamak for P_{RF} up to 2.5 MW.

[4] M. Bures et al., Role of antenna screen angle during ICRF heating experiments in JET, submitted to Nuclear Fusion, also Proc. 15th EPS Conf. Dubrovnik 1988, Vol. 2B, Part II, 713.

[5] F. Waelbroek, J. Winter et al., (1989) Plasma Physics and Controlled Fusion, 31 pp. 185-192.

[6] M. Bures et al., proceedings of this conference.

[7] S. Clements et al., Effect of ICRH on the JET edge plasma with carbon and beryllium coated limiters, proceedings of this conference.

[8] B. Tubbing, J Jacquinot, D. Stork, A.Tanga, H-mode in JET with ICRH alone, accepted for publication in Nuclear Fusion.

[9] D.A. D'Ippolito, J.R. Myra et al, Impurity release by ICRF antennas, proceedings of this conference.

[10] JET Joint Undertaking Progress Report Vol. 1, 33 (1988).

PERIODS	ANTENNA	LIMITERS	CONDITIONING	RESULTS RELATED TO IMPURITIES
1986 Mid 1987	- 3 antennae with Ni screens (1 with 1 μm Cr) - 7 MW (monopole)	- Carbon tiles - 8 poloidal limiters	- Some carbonisations - D glow overnight	- Metallic impurity found in plasma originates from powered screens - Density limit (5 MW monopole) same as ohmic limit - Carbonisation lasts ∿ 20 shots
Mid 1987 End 1988	- 8 antennae (Ni screens) - 16 MW (dipole)	- Carbon tiles - 2 belt limiters	- Initial carbonisation - He glow overnight - Helium discharges - High power	- Angle of screen is important - Improved density limit - Dipole better than monopole - H mode terminated by Ni and O influx
Jun-Jul 1989	- 7 antennae - ∿ 200 Å Be on screen and walls - 18 MW (dipole, monopole)	- As above	- Initial Helium glow - Several Be evaporations ∿ 200 Å	- Oxygen disappears - Density limit as NBI ($\langle n \rangle$ Rq_{cyl}/BT = 24) - Long H modes with RF alone (7 to 12 MW)
Sep-Oct 1989 (in progress)	- 8 antennae	- Be tiles on belt limiters - Carbon X-point tiles and inner wall		
1990 (planned)	- 8 antennae - Be screens	- As above		

TABLE 1
Summary of the JET Modes of Operation with ICRF

Pulse Number (Period)	Conditions	$\frac{1}{P_{ad}} \frac{dP_{rad}}{dt}$ s^{-1}	$\frac{1}{P_{ad}} \frac{dP_o}{dt}$ s^{-1}	$\frac{1}{P_{ad}} \frac{dP_c}{dt}$ s^{-1}	$\frac{1}{P_{ad}} \frac{dP_{ni}}{dt}$ s^{-1}	Duration of the "H-phase" s
17386 mid 1988	NBI only H-mode (9.5 MW)	0.4	0.14 ± 0.04	0.05	0.1	2.5
17391 mid 1988	Combined Heating H-mode P_{NBI} = 6.5 MW P_{AF} = 4 MW (monopole)	0.9	0.4 ± 0.1	0.06	0.4	0.7
19799 June 1989 Be evaporation	NBI only H-mode (10 MW)	0.5				1.3
20230 June 1989 Be evaporation	ICRH only H-mode (8 MW, Dipole)	0.5				1.3

Table 2
Duration of the H-phase and rate of increase of the radiated power during the H-phase
(P_{ad} = additional heating power, P_{rad} = total radiated power, O, C, N_i refer to Oxygen, Carbon, Nickel)
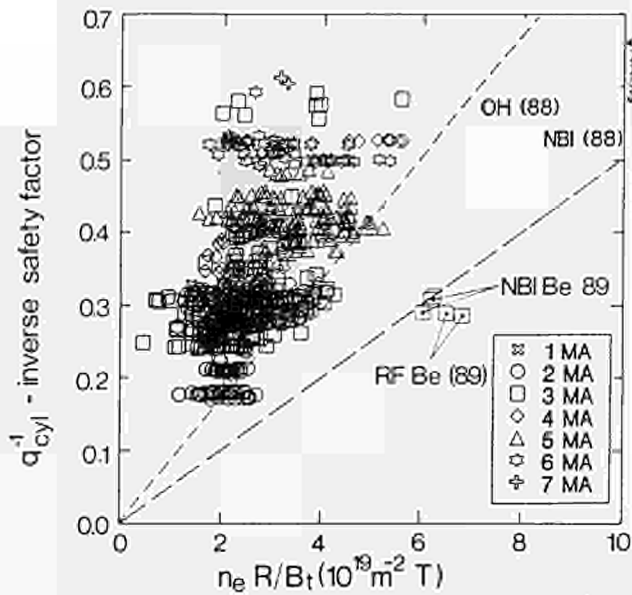
Fig. 1 Inverse cylindrical q versus the normalized average density. The figure contains the 1986-89 data base of the maximum density obtained (e.g. not necessarily a limit) in deuterium plasmas heated with ICRF as well as the recent density limits obtained with NBI and ICRF after the evaporation.
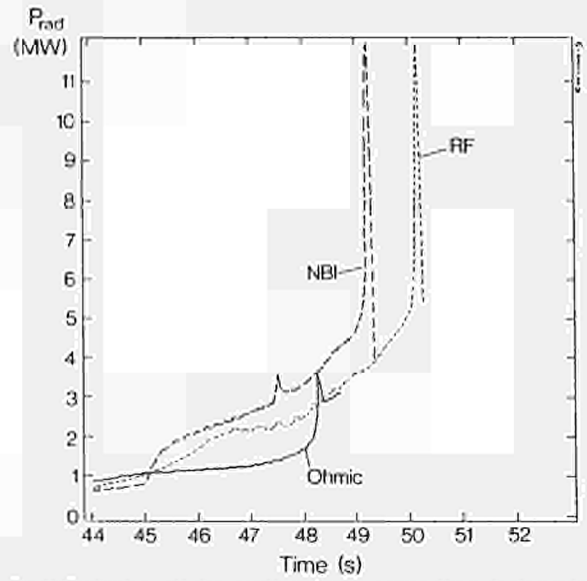

Fig. 3 Evolution of the total radiated power from bolometric measurements (plasma conditions as for Fig. 2). For clarity the traces are interrupted after the onset of the Marfe.
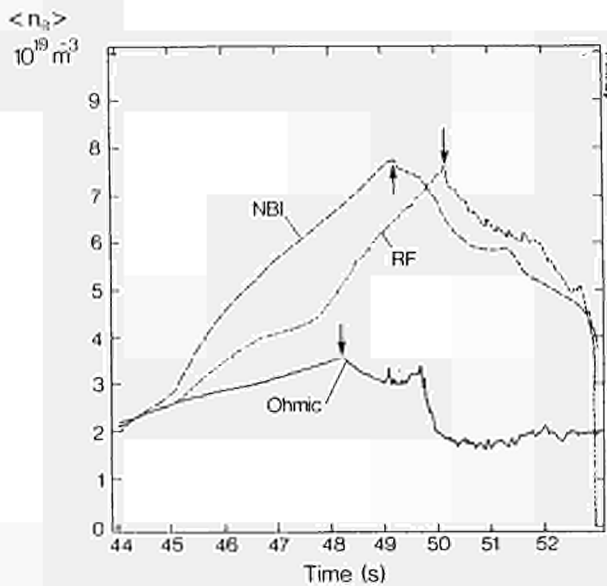

Fig. 2 Evolution of the line average density in ohmic (2.5 MW), ICRF (9 MW) and NBI (9 to 10 MW) discharges (3 MA, 3.1 T limiter plasmas). The onset of the Marfe is indicated by the arrow.
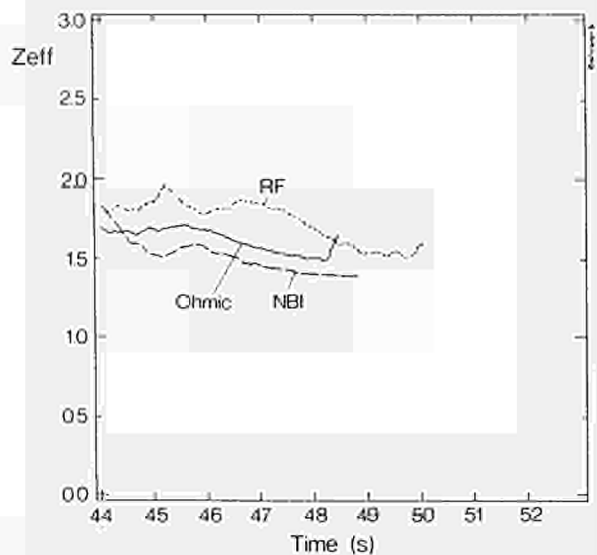
Fig. 4 Evolution of Z_{eff} from bremsstrahlung measurements along a vertical line of sight. Measurements with a horizontal line of sight give somewhat lower values (e.g. 1.3 instead of 1.5). The traces are interrupted where the Marfe starts (conditions of Fig. 2).
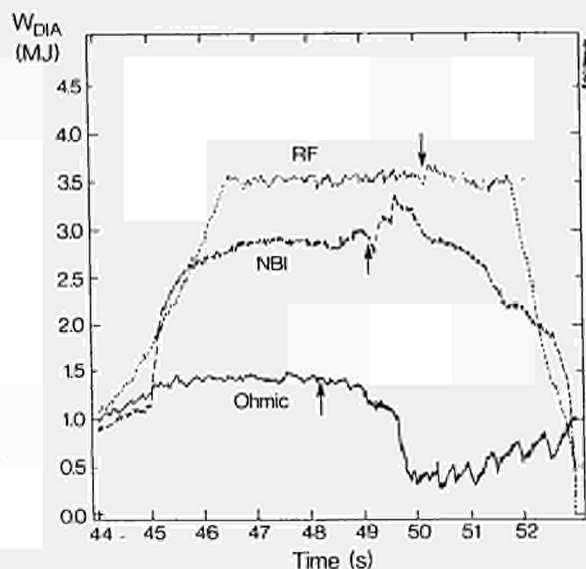
Fig. 5 Stored energy (diagmagnetic loop) versus time (conditions of Fig. 2). ICRF heating is more efficient at high density than the 80 keV beams which do not penetrate to the plasma centre.
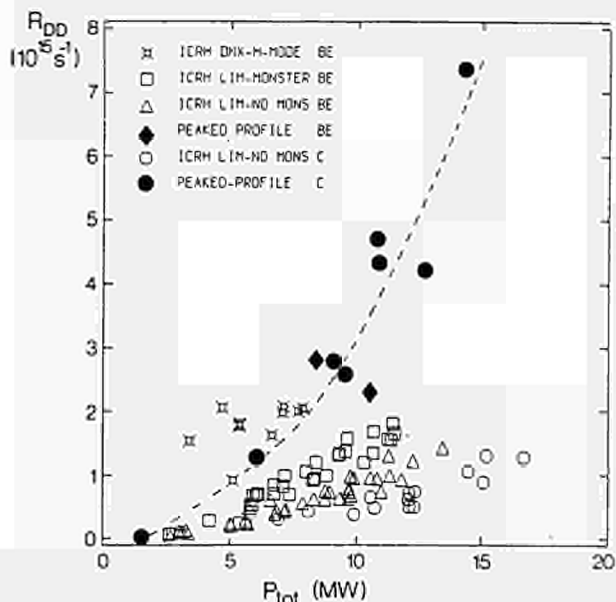

Fig. 6 D-D reaction rate of 3 MA, 3.1 T plasmas heated with ICRF (H-minority resonance near the plasma center). The various symbols correspond to different confinement regimes : double null H-modes, limiter L-modes with or without monsters and peaked density profiles created by pellet injection. Comparison of two similar regimes (non-monster limiter plasmas) show that the D-D reaction rate increases by about a factor of 2 after evaporation of beryllium. Enhanced confinement regimes give an even larger gain. Note that high power heating of peaked density profile created by pellets have not yet performed with Beryllium coated walls.
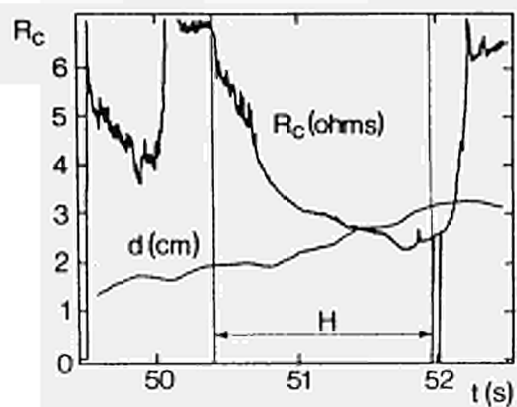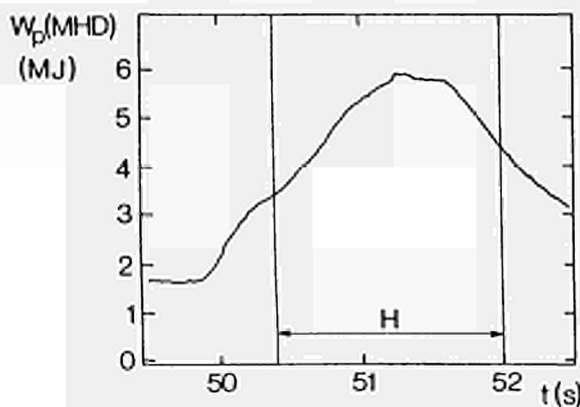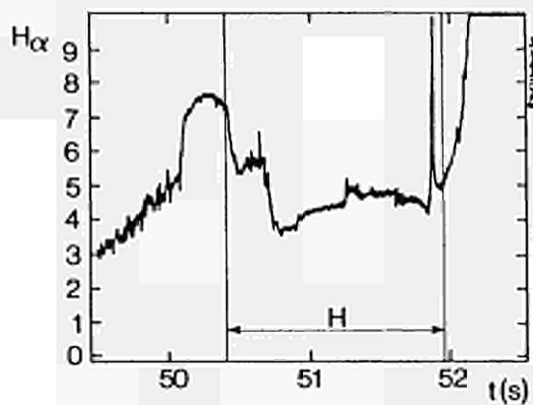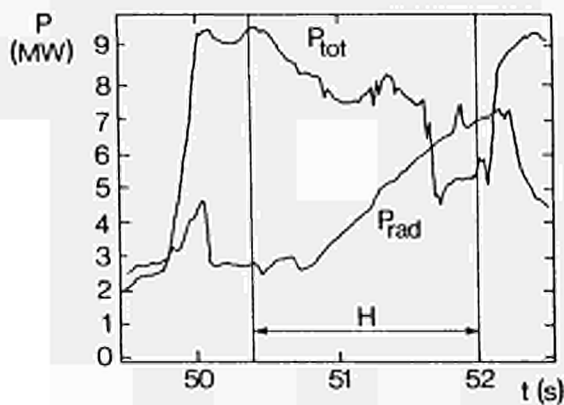

Fig. 7 Evolution several quantities during an H-mode obtained with ICRH only : Total input power (P_{tot}); radiated power (P_{rad}); stored energy from the MHD equilibrium (W_{MHD}); vertical line of sight (H_α); coupling resistance of one antenna (R_C); distance between the antenna and the separatrix (d). Note the 2-step transition to the H-mode on H_α, P_{rad} and R_C.